AD-A256 104

Active
MATERIALS
and
Adaptive
STRUCTURES

Edited by
Gareth J Knowles

DTIC
ELECTE
OCT 6 1992
S
C
D

Proceedings of the

ADPA / AIAA / ASME / SPIE

Conference on

Active Materials and Adaptive Structures

4 - 8 November 1991, Alexandria, Virginia

Best
Available
Copy

SMART MATERIALS AND STRUCTURES SERIES

Series Editor: G J Knowles

Previously published in this series

First European Conference on Smart Structures and Materials
Edited by B Culshaw, P T Gardiner and A McDonach

SMART MATERIALS AND STRUCTURES SERIES

ACTIVE MATERIALS AND ADAPTIVE STRUCTURES

Proceedings of the ADPA/AIAA/ASME/SPIE Conference on
Active Materials and Adaptive Structures,
4–8 November 1991, Alexandria, Virginia

Edited by   **Gareth J Knowles**

Price $196.00 from
IOP Publishing LTD
335 E. 45th St.
New York, NY *10017*
JK 10-5-92

92-26222

92 9 30 037

DTIC QUALITY INSPECTED **l**

FOREWORD

The 1991 Active Materials and Adaptive Structures Conference in Alexandria, Virginia, was held to address the explosion in both theory and application of recent and ongoing developments in smart, intelligent, or adaptive structures. The hope was to provide an outlet for significant developments of these maturing technologies and for their applications to be made accessible to a broad interdisciplinary community. The many areas of intelligent systems and smart structures incorporating active materials are now emerging rapidly as an exciting broad-based discipline that has already grown to include major areas of research and development. These include extensive ongoing R&D programs in filament sensors including: many fiber-optic based devices; ferroelectric, shape memory, and electro-rheological-based sensors and actuators; hybrid composites incorporating inherent sensing and actuation; biomimetics; micromachines; adaptive optics; and many others.

This volume contains a broad spectrum of theoretical, developmental, and applicational studies in intelligent materials and smart structures. For example, a wide variety of approaches to sensing and actuation are discussed that exploit the many recent developments in active materials. Such research and development activities are currently taking place in universities, industry, and government laboratories—all of which were substantially represented at the AMAS meeting. Many possible applications of these technologies are described that include already emerging applications in underwater vehicle technology, aircraft systems, smart munitions, civil engineering, biomedical, robotics, and space platforms. These technologies offer the potential of substantial advances in areas such as precision structures, damage assessment/health monitoring, adaptive optics, advanced avionics, and adaptive space structures ensuring both enhanced and more reliable systems.

The success of the AMAS Conference was due to the kind support received from the American Defense Preparedness Association, the Institute of Physics, and the various government agencies and agency representatives who lent their prestige and financial support. I would particularly like to thank Richard Claus, Andrew Crowson, Peter Dean, Bruce Holt, James Kelly, Jerry Newsome, Pamela Reis and Ben Wada for their support and encouragement.

Gareth J Knowles
Grumman Corporation

CONTENTS

\

SESSION (12)   Modeling Methods for Smart Structures

SPECIAL SESSION   Smart Materials Research and Applications in Japan

SESSION (13)   Piezoceramic Damping Techniques I: Aerospace Applications

SESSION (14)   Neural Networks for Smart Structures

A multiaxis isolation system for the French Earth observation satellite's magnetic bearing reaction wheel

By
D. Cunningham, P. Davis, and F. Schmitt

Honeywell Inc., Satellite Systems Operation; Glendale, Arizona

ABSTRACT: The design and testing of a six degree of freedom isolation system using viscous damping is presented. To avoid interactions with the reaction wheel's magnetic bearing and output torque control loops, an isolation system is required to provide very specific and tightly controlled values for the natural frequency and damping (Q) in all degrees of freedom. Low natural frequency requirements and launch loads, together with 1-G testability, require the isolators to be capable of unusually large deflections. Analysis shows that the combination of requirements can be met with a symmetric arrangement of three isolator pairs— a *hexapod*. A prototype system has been fabricated. A design description and test results are included.

1.1 SYSTEM DESCRIPTION

The function of the isolator is to reduce vibration transmission from the reaction wheel to the spacecraft during orbital operation. It is important that the system not increase loads transmitted from the spacecraft to the reaction wheel during launch, and is particularly true for certain frequencies. MATRA, the company responsible for the spacecraft, is pursuing two alternatives to reduce vibration. The primary approach is to modify the reaction wheel to improve its capability. The *hexapod* isolator, a backup system, will be pursued through the system testing of a prototype installed in a spacecraft.

The isolator system design is shown in Fig. 1 and its schematic arrangement in Fig. 2. Isolator pairs are attached to the Y structure, which holds the reaction wheel at a radius R and in a plane containing its center of mass. Each isolator is skewed by an angle α from the Z direction, with the angle measured about the line connecting the attachment point and the center of mass. Each isolator has pivots at both ends; therefore, the loads are essentially axial loads.
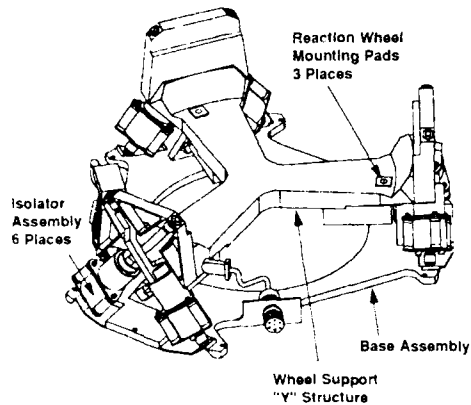
Fig. 1 Hexapod Isolator System
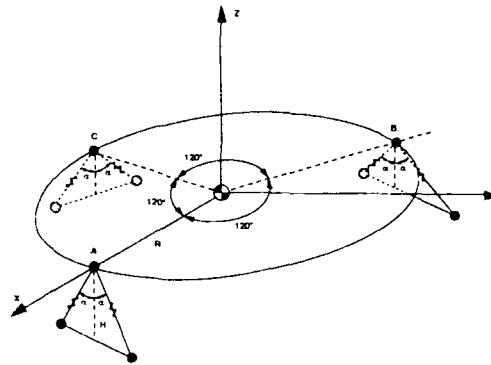
Fig. 2 Symmetrical Hexapod Geometry

The translational range of the isolated reaction wheel determines the axial stroke required at the isolators. In this application, stops are provided between the base assembly and the Y structure to limit the motion of each isolator. This *hexapod* arrangement is a kinematic mount, in that position is neither over- nor under-constrained by the isolators. All loads are deterministic; they may be calculated from the nominal geometry and the isolator axial stiffness. Alignment is greatly simplified as a consequence, and stress due to thermal strain is also eliminated. Fig.3 shows some of the relationships between system parameters in an X,Y,Z coordinate system and single isolator parameters. Subscript A denotes the axial direction of an isolator.

Motion allowed by the stops at the isolators was chosen to limit X and Y motions and prevent contact with adjacent spacecraft components. Stop stiffness was determined to provide a compromise between the peak deflections under launch conditions and peak impact loads. Isolator requirements derived from the system level requirements are shown in Fig.4.

System stiffness and damping matrices are diagonal. Therefore, cross coupling will be a second-order effect, due to asymmetries. For example, the system frequency and peaking (Q) requirements given in Fig.4 were used to derive the individual isolator requirements shown in Fig. 5. The isolator stiffness (KA), damping constant (CA), and skew angle (α) were selected to match the X and Y translational frequency (f_x), the X and Y rotational frequency ($f_{\theta x}$), and the X and Y translational peaking (Q_t).

Variable	Element to System $\alpha = 38.3$ deg
X - Y Deflection	$\delta X = \dfrac{2}{\sqrt{3}}\ \dfrac{\delta A}{\sin(\alpha)} = 1.863\ \delta A$
Z Deflection	$\delta Z = \dfrac{\delta A}{\cos(\alpha)} = 1.274\ \delta A$
X - Y Force	$F_X = 2\sqrt{3}\ \sin(\alpha)\ F_A = 2.147\ F_A$
Z Force	$F_Z = 6\cos(\alpha)\ F_A = 4.709\ F_A$
X - Y Stiffness	$K_X = 3\sin^2(\alpha)\ K_A = 1.152\ K_A$
Z Stiffness	$K_Z = 6\cos^2(\alpha)\ K_A = 3.695\ K_{ZA}$

Fig. 3 Hexapod Translational
Transformations

Axis	Frequency ($\pm 5\%$)	Q ($\pm 10\%$)
x	4 Hz	10
y	4 Hz	10
z	---Hz	---
θx	10 Hz	< 6
θy	10 Hz	< 6
θz	7 - 12 Hz	Low

Fig. 4 System
Isolator Requirements

Mounting radius	8.25 in.
Mounting height	6.22 in.
Skew angle (alpha)	38.3 deg
Stiffness	56.5 lb/in.
Damping	0.225 lb-s/in.
Stop location	0.175 in.
Stop stiffness	5000 lb/in.
Stop damping	2.25 lb-s/in.
Launch stroke	0.263 in.
Launch force	440 lb
Launch damping force	63 lb
Max end-pivot rotational stiffness	42 in.-lb/rad
Min end-pivot translational stiffness	5650 lb/in.
Min end-pivot rotational angle (launch)	4.5 deg

Fig. 5 MVIA Isolator
Requirements

1.2 OVERALL DESIGN LAYOUT

The primary requirements on the overall design layout were: the isolator system must fit within the spacecraft compartments, and use the existing spacecraft and reaction wheel mounting provisions. No changes to either the spacecraft or the reaction wheel were allowed. For functional reasons, the isolators' layout geometry must be as close as possible to that determined by the system design. Fig. 1 shows the final layout.

To maximize stiffness of the reaction wheel support structure and minimize its weight, a Y shape was chosen with the three isolator pairs attached at the ends near the three reaction wheel mounting pads.

To avoid cross-coupling, the plane of the isolator end pivots must contain the reaction wheel center of mass, so the Y-structure ends were extended in the Z direction to the level of the attachment points. To fit in the space between the reaction wheel and the spacecraft compartment, two isolators pairs were shifted 15° from the nominal 120° spacing and the isolator stems were crossed with one stem offset. The stops, one for each isolator, are located near the isolator pairs. This arrangement places the stops in parallel with the isolators, preventing the stop contact forces from passing through the isolators and the flexures. A base assembly provides the interface between isolator ends and the spacecraft. The electrical cable across the isolator system has sufficiently low stiffness to not affect operational performance.

1.3 ISOLATOR DESIGN

The schematic diagram of an isolator is shown in Fig. 6, with a cross section in Fig. 7. As one end of the isolator moves with respect to the other, damping takes place through the forcing of fluid through the annulus between the two chambers. The fluid is sealed in these chambers by metal bellows, which are also used in the temperature compensator and for a redundant seal over the lower bellows. No redundant bellows seal is required over the upper bellows, since seals are provided between the housing components that enclose it. Fluid volume variation with temperature is compensated for by a spring-loaded piston acting on the damping fluid. A small passage joins the compensator volume to the main fluid volume at the midpoint of the annular passage where the fluid pressure remains nearly constant. The damping effect is a linear function of the flow length. Three coil springs are placed in parallel with the main bellows to obtain the required stiffness. Their location allows them to be changed easily for fine adjustment of stiffness. The flexure pivots at each end of the isolator have two angular degrees of freedom. Since they consist of two bending elements machined into a solid cylinder at a right-angle, the pivots introduce no friction into the system. Having relatively low stiffness, the pivots preclude significant bending loads on the isolator.
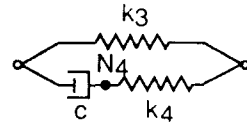
Fig. 6 Equivalent Circuit
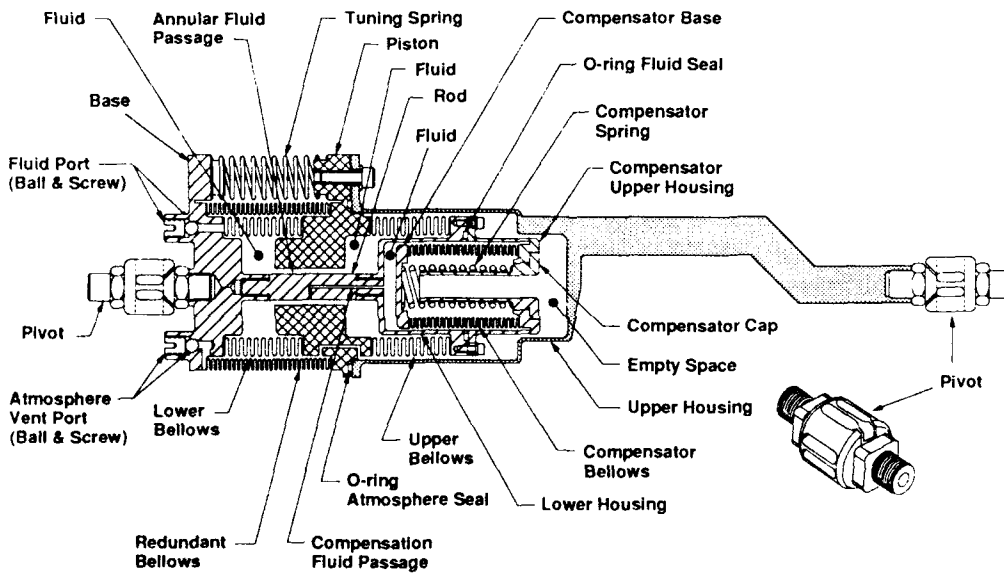
Fig. 7 Isolator Cross Section

1.4 PERFORMANCE TEST RESULTS

Testing was conducted both at the isolator level and at the system *hexapod* level. Isolator testing was carried out by mounting one end to a rigid mass while the other end was vibrated axially. Force, deflection, and acceleration were measured; from this data, the damping coefficient and the spring constants shown in Fig. 6 were determined. Fig. 8 shows the resulting values. Note that the value for K_3 can be varied by substitution of the three coil springs and the damping coefficient C can be changed significantly by using a different viscosity damping fluid. Overall, the isolator parameters are acceptable.

$C_{Low} = 0.24$ lb/in./s

$K_3 = 58$ lb/in.

$K_4 = >8,000$ lb/in.
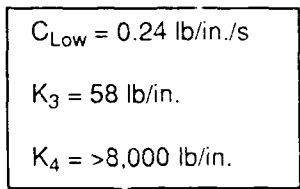
Fig. 8. Isolator Test Results

The *hexapod* isolator system was tested with a dummy mass to represent the reaction wheel. Transmissibility was measured by mounting the isolator system on a force-measurement table and introducing a force disturbance at the dummy mass. This was done in the X, Y and Z directions. The transmissibilities determined from these tests are shown in Fig. 9. Although there are differences in both resonant frequency and transmissibility, they are correctable through spring and damping fluid viscosity changes. Note that correction would not be required if the application didn't require such precision.

X Translation Transmissibility

Z Translation Transmissibility
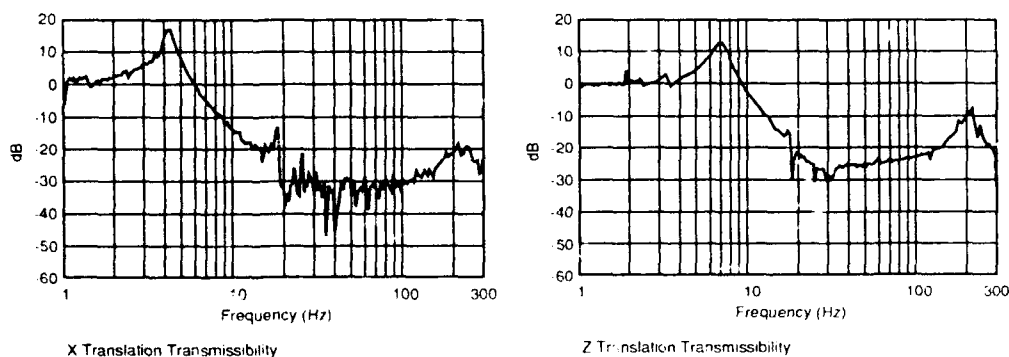
Fig. 9. Measured Transmissibility

1.5 CONCLUSIONS

At this stage of the development we can conclude that the performance requirements have been met.

- All frequency and Q requirements in Figure 4 were satisfied.
- The ability to fine tune both C and K was demonstrated.
- The use of two degree of freedom machined flexures was shown to be applicable to the **hexapod** isolator concept.

Testing for thermal/vacuum survival remains to be done and, more importantly, testing of the performance of the reaction wheel's magnetic bearing and torquing control loops while on the isolator system.

REFERENCES

1. *Line of Sight Performance Improvement with Reaction Wheel Isolation*; J. J. Rodden, et al – Lockheed Missiles and Space Co., Inc., and L. P. Davis – Sperry Corp.; Annual AAS Guidance and Control Conference, February 1986

2. *Development of the PACOSS D-Strut™*; D. C. Cunningham, Honeywell Inc., Satellite System Operation; Damping '91 Conference, February 1991

3. *An Advanced D-Strut™*; L. P. Davis and S. D. Ginter, PhD – Honeywell Inc., Satellite Systems Operation; Damping '91 Conference, February 1991

PATENT PENDING

A Hexapod Reaction Wheel Isolator – D. Cunningham, P. Davis and F. Schmitt

Passive damping design for control system stability on the SPICE testbed

Y.C. Yiu

Lockheed Missiles & Space Co., 1111 Lockheed Way, O/77-50, B551, Sunnyvale, CA 94089

Eric M. Austin

CSA Engineering, 560 San Antonio Road, Suite 101, Palo Alto, CA 94306

Steven D. Ginter

Honeywell Inc., Satellite Systems Operation, P.O. Box 52199, Phoenix, AZ 85022

ABSTRACT: The SPICE Testbed is being used to demonstrate a 100-times reduction in structural line-of-sight jitter. The reduction will be achieved through an integrated application of active control and passive damping techniques. The primary role of the passive system is to augment active control stability in the cross-over and spill-over frequency region by achieving a specified level of damping in certain critical modes. This paper describes the synthesis approach to the passive damping system and summarizes a combination of damped struts, constrained-layer treatments, and tuned-mass dampers to meet the damping objectives. Complex eigensolutions and cross-orthogonality between the undamped real modes and the damped complex modes were used to verify the damping design.

1. INTRODUCTION

The *SPace Integrated Controls Experiment (SPICE)* Testbed brings passive and active techniques together in an integrated application to a large flexible precision structure. One of the objectives of the SPICE Program is to demonstrate a factor of 100 reduction in root-mean-square line-of-sight (LOS) jitter in the presence of specified disturbances. Because of the challenging requirements, active structural control will be used to achieve primary improvement, with passive damping ensuring a robustly stable system.

This paper presents the system-level passive damping design synthesis process and the preliminary passive damping design of the SPICE Testbed for control system stability. Three types of passive damping treatments, damped struts, constrained-layer damping and tuned-mass dampers, were considered to provide sufficient passive damping to the relevant vibration modes in order to stabilize the control system.

2. THE SPICE TESTBED

The SPICE Testbed is a large precision optical structure with a large segmented primary mirror. The primary mirror is supported by a bulkhead truss structure which is comprised of approximately 250 struts. The secondary mirror is supported by a tripod system. The structure is has high modal density. The finite element model (FEM) is shown in Figure 1 and a summary of the model is provided in Table 1.

Two sets of disturbances to the structure are considered: one at the secondary mirror and the other at the three corners of the truss structure. The power spectral density functions of these disturbances have a constant amplitude at 5 to 10 Hz with fourth-order breaks at 5 and 10 Hz. The amplitudes of the power spectra are scaled to have an open-loop line-of-sight jitter of 100 μrad (RMS).

Figure 1. FEM of the SPICE Testbed

Table 1. Summary of SPICE FEM

No. of Nodes	357
No. of Elements	486
1st Tripod Bending Mode	8.88 Hz
Modes Below 100 Hz	62
Modes Below 200 Hz	105

3. PASSIVE DAMPING REQUIREMENTS

The passive damping requirements were derived from the active control system design. They were driven by the control system stability in the loop cross-over and spill-over frequency regions. The stability issues of control/structure interaction are long standing and well know, Aubrun et al (1982). The objective of the passive damping system was to reduce the resonant response characteristic in certain target modes by achieving a specified viscous damping ratio.

The active control system used a high-gain, high-authority approach similar to Aubrun et al (1982), having a 70 Hz bandwidth. The control feedback was based on a combination of the structural LOS variables and acceleration measurements from numerous points on the structure. The LOS variables were constructed from relative displacements and rotations between elements of the simu-

Table 2. Damping Requirements

Mode Number	Frequency (Hz)	Equivalent Viscous Damping
65, 66	103	0.05
71, 72	117	0.05
75, 76	123	0.10
78, 79	126	0.05

lated optical system. Proof-mass actuators (4 at each tripod leg and 6 at the bulkhead) were used. The damping requirements for control system stability are summarized in Table 2.

The damping improvement was to be achieved under several constraints. First, the structure could not admit any geometry or dimensional changes. Second, the damping design could not significantly alter the structural response characteristics in the control system bandwidth. Third, any structural alterations must not compromise structural integrity in meeting static and dynamic load requirements, and the structure's small deformation, linear response characteristics. Finally, the passive system must not increase the weight by more than 10%.

4. DESIGN APPROACH

The dynamics of the baseline structure as approximated by a finite element model can be characterized by the mass matrix (**M**) and the stiffness matrix (**K**), and the disturbances are characterized by the spatial vectors (**P**) and the forcing functions g(t)

$$\mathbf{M\ddot{u} + C\dot{u} + Ku = P} \ g(t) \tag{1}$$

Inherit damping of a structure is normally modelled as modal damping coefficients. For a *structure augmented with viscous and viscoelastic materials to enhance its damping charac-teristics*, the structural system is best described mathematically in the frequency domain by

$$[(-\omega^2\mathbf{\tilde{M}} + \mathbf{\tilde{K}}^R(\omega)) + i\,(\omega\mathbf{\tilde{C}} + \mathbf{\tilde{K}}^I(\omega))]\,\mathbf{U}(\omega) = \mathbf{P}\ G(\omega) \tag{2}$$

The goal of the passive damping design process is to identify the best and most weight efficient ways to introduce passive damping into the system for control system stability. A rigorously optimized solution based on Equation (2) is too complex and not practical, even if it is possible. The practical approach to this design problem is to understand the fundamental behavior of the structure and use simplified engineering design procedures to design various damped devices. The methods for designing damped struts, constrained-layer treatments, and tuned-mass dampers for simple structures are well established. These methods can be applied to complex systems by using simplifying assumptions. The integration and interaction of these damping devices must then be verified by a rigorous analysis to ensure that the system requirements are met.

5. DAMPING DESIGN

For the control system stability, relatively large amounts of passive damping were required in a relatively small set of modes in the high frequency range, as shown in Table 2. In order to best formulate passive damping design concepts, the modal characteristics of these modes must be well understood. For the three types of damping treatments considered, the most important modal parameters are the locations of maximum strain energy and maximum displacement. A summary of the modal strain energy (MSE) distribution is shown in Table 3. The high percentage of strain energy in the bulkhead in modes 65, 66, 75, 76, 78, and 79 suggests damped struts can be used effectively to impart system-level damping to these modes. However, they are quite ineffective for modes 71 and 72, where the highest concentration of strain energy is in the tripod legs. In this case, either constrained-layer treatments or tuned-mass dampers would be effective on the tripod legs. Special attention should also be given to modes 75 and 76 which have a high damping requirement of 10%.

Table 3. Summary of Modal Strain Energy Distribution

Modes	65,66	71,72	75,76	78,79
Freq (Hz)	103	117	123	126
Req'd ζ	5%	5%	10%	5%
Bulkhead MSE	62%	16%	65%	74%
Tripod MSE	23%	63%	0%	4%

5.1 Damped Strut Design

The modal strain energy distribution in Table 3 suggests that struts with high loss factor could be used to obtain the required damping. However, a more detailed breakdown shows that the

strain energy in these higher order modes is well distributed in many bulkhead struts. The number of struts to be replaced by damped struts is dictated by 1) the highest loss achievable at the strut level and 2) the character of the modes for which the struts are effective. The first is determined through strut design, the second through system-level analysis.

A three-parameter model was used to model a typical damped strut as suggested by Yiu and Ginter (1991). This provided a simple representation of the strut stiffness and damping characteristics and allowed sizing of the strut parameters to match the stiffness, damping, and frequency characteristics to match the system-level damping requirements. The system-level damping design followed the method suggested by Yiu (1991) which provided the basis to approximate the contribution of each damped strut to the system-level damping.

Figure 2 shows the number of struts would have to be replaced for each target mode, assuming a strut loss factor of 0.4 and that the struts with highest MSE were replaced first. Many struts were effective for providing damping to many modes at the same time. Hence, the total number of struts to be replaced is much less than the direct sum of the number of struts read from Figure 2. The approximate system-level damping predictions for the sets of damped struts can be computed rather easily and are shown in Figures 3 and 4.
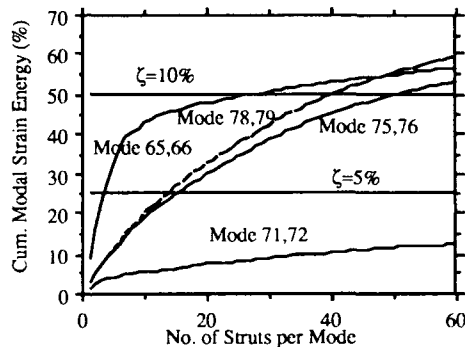
Figure 2. Modal Damping Design Curve
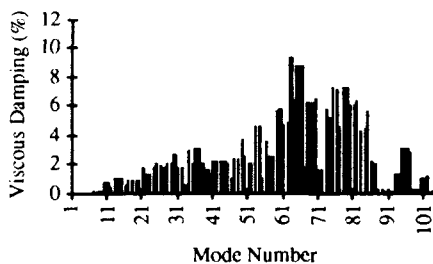
Figure 3. 60 Damped Struts System Damping
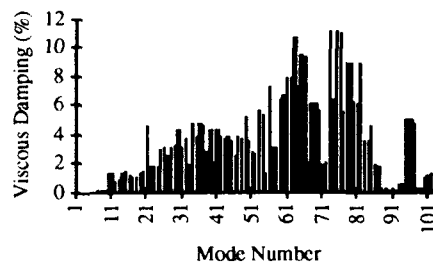
Figure 4. 94 Damped Struts System Damping

5.2 Constrained-Layer Damping Treatment

It is clear from Figure 2 that a large number of struts would have to be replaced to meet the goal of 5% damping, if possible, for modes 71 and 72. The MSE in Table 2 identifies these as modes involving primarily the tripod legs, so it is logical to augment these tripod legs with constrained-layer treatments to provide system-level damping. Trade studies were performed to determine the best combination of viscoelastic material (VEM) and constraining layer on an isolated model of a single leg treated as a pinned-end beam. Following rough guidelines outlined neatly by Kerwin (1984), the resulting design called for a relatively flexible VEM and graphite/epoxy constraining layers applied in eight circumferential and one longitudinal segments. Using a finite element model and modal strain energy method, the predicted

system-level damping of the constrained-layer design is approximately 4%. The system-level damping prediction of the constrained-layer treatments is shown in Figure 5. When this modal damping was superimposed on those provided by the the damped-strut design, the total modal damping exceeded the passive damping requirements for the modes of interest.

5.3 Tuned-Mass Dampers

The large number of struts required is driven mainly by the 10% viscous damping needed in the mode pair at 123 Hz. As an option to eliminate some struts, two tuned-mass dampers (TMDs) were design for these modes. The two attachment locations were chosen as points of highest displacements, which turned out to be points on the outer edge of the bulkhead. Design guidelines derived from discussions in Harris (1988) were used to predict the proper mass of 6.3 lbs (2.9 kg) each and loss factor of 0.66. Each TMD introduced an additional vibration mode to the system. The system-level effect of the TMDs o: ʼe control system has not yet been assessed. The TMDs were then modelled as complex springs and an complex eigensolution was solved for system level damping prediction.

Figure 5. Constrained-Layer Treatments System Damping
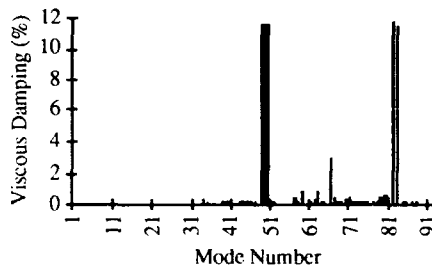
Figure 6. Tuned-Mass Dampers System Damping

6. SYSTEM-LEVEL ANALYSES

System-level analyses are required to 1) verify the applicability of the simplified design approach for each damping treatment applied to a complex structure, 2) check for possible interaction between different damping devices, and 3) predict system-level characteristics and check the perturbation of the plant modal characteristics due to damping augmentation.

Discrete damping devices such as the damped struts and tuned-mass dampers can be modelled by dashpots. An explicit system-level damping matrix was assembled for the complex eigenvalue problem which provided the system frequencies, damping, and mode shapes. For analysis of the large structural system, efficient methods by Yiu and Weston (1992) were used. Cross-orthogonality checks were used to correlate the real modes of the undamped model and the complex modes of the damped model.

For the damped strut design, the damping and frequency predictions correlated very well with the complex eigensolution. The cross-orthogonality check revealed that the introduction of the damped struts did not significantly change the mode shape of the structure. However, for the tuned-mass damper design, due to the interaction between the dampers and the structural modes to be suppressed, significant change in mode shapes in a few modes was expected and observed by the orthogonality check.

When 60 struts were replaced by the damped struts, modes 65 and 66 had 12% damping modes 78 and 79 had 8% damping; both exceeded the damping requirements. However, modes 75 and 76 had only 6.2% damping, which was less then the 10% required. A separate damping design with two TMDs targeting modes 75 and 76 resulted in four modes with 11.5% damping. The 60-damped-strut design and two-TMD design were integrated in a finite element model, and a complex eigensolution was computed. An excerpt of the cross-orthogonality check is shown in Table 4. The

Table 4. Cross-Orthogonality Check

Complex Modes 60 D-Struts + 2 TMDs			Real Modes Undamped Model - Mode/Freq			
Mode No.	Freq (Hz)	ς (%)	65 103.4	66 103.4	75 123.4	76 123.5
67	104.9	1.2	0.72	0.56	-0.05	0.05
68	105.1	3.0	-0.59	0.67	0.05	0.03
77	128.9	**14.8**	-0.01	-0.01	**-0.69**	**0.42**
78	129.3	**3.8**	0.0	0.0	**-0.52**	**0.62**
79	129.9	5.4	0.0	0.03	**0.79**	**0.40**
80	132.7	14.6	0.03	-0.04	-0.18	-0.20

complex modes that resemble the real modes 75 and 76 have cross-orthogonality coefficients of 0.69 and 0.62. Therefore, the mode shapes have been changed substantially. The damping in these modes were increased to 14.8% and decreased to 3.8% due to the addition of the two TMDs. The interaction of these two damping treatments has significant change the plant used in the control design synthesis. A control design iteration is required to verify the system performance and stability if these two passive treatments are implemented. The 94-damped-strut design increases the damping in modes 75 and 76 to 11%, and it is reasonably sure that no significant changes in the control design is required. The modal damping from damped-strut-design and constrained-layer design is superimposed as the practical modelling and techniques for such an integrated passive system have not been available so far.

7. CONCLUSION

The system-level passive damping design presented herein demonstrated that passive damping can be used effectively with a control system to achieve a high level of vibration suppression. The design synthesis process used is practical and effective; it is based on understanding structural behavior and also fundamental engineering principles. Furthermore, the integrated passive design was analyzed rigorously for performance verification. Design iterations and optimization of passive damping, active control, integrated passive and active system, and component design will further refine the preliminary design toward hardware implementation.

8. REFERENCES

Aubrun J.N. et al, *1982 RADC-TR-82-21, Final Technical Report*, 'ACOSS Five (Active Control of Space Structure)'

Kerwin E.M. and Smith P.W. 1984, *Proceedings of Vibration Damping Workshop* (Wright Lab, Flight Dynamics Directorate), 'Segmenting and Mechanical Attachment of Constrained Viscoelastic Layer Damping Treatments for Flexural and Extensional Waves'

Harris C.M. (editor) 1988, *McGraw Hill*, Shock & Vibration Handbook, 3rd Edition.

Yiu Y.C. and Ginter S.D. 1991, *Proceedings of Damping '91 Conference* (Wright Lab, Flight Dynamics Directorate), 'Dynamics of a Class of Viscously Damped Struts'

Yiu Y.C. 1991, *Proceedings of Damping '91 Conference* (Wright Lab, Flight Dynamics Directorate), 'System Level Design and Analysis of Truss Structures Damped by Viscous Struts'

Yiu Y.C. and E.L. Weston 1992, *33rd Structures, SDM Conference*, (AIAA/ASME/ASCE/AHS/ASC), 'Computation of Complex Modes in Reduced Subspaces'

Passive damping in the MIT SERC controlled structures testbed

E. H. Anderson, G. H. Blackwood, and J. P. How

MIT Space Engineering Research Center (SERC), Cambridge, MA 02139

ABSTRACT: The role of passive damping in a controlled structures technology testbed with a multipoint alignment performance metric is described. Two distinct types of damping are implemented. Low loss factor viscoelastic damper struts are distributed throughout the truss structure to uniformly add damping to all modes of interest. In addition, high loss factor viscous dampers are used to target modes required by a control strategy that employs a movable mirror to directly influence pathlength. Experimental results of the component-level characterization of the viscous dampers and system level performance of both sets of dampers are presented.

1   INTRODUCTION

Stringent requirements for future large space structures have lead to the development of numerous approaches to actively control both shape and alignment. The low inherent damping in these structures is an impediment to most active control approaches. By increasing phase margin in the controller rolloff region, passive damping augmentation improves the performance and robustness of active systems operating on the structure.

The controlled structures technology (CST) testbed (Blackwood *et al*, 1991) at the MIT Space Engineering Research Center (SERC) incorporates passive damping in the form of lossy struts that replace existing members. Two types of dampers - low-loss viscoelastic and high-loss viscous - have been employed. The viscoelastic struts are modified versions of the basic aluminum tube struts that make up the testbed. The viscous struts make use of the Honeywell D-Strut damper (Anderson *et al*, 1991). The remainder of the paper contains a description of the testbed, the damping philosophy, and an experimental demonstration of the effect of the dampers.

2   TESTBED DESCRIPTION AND APPROACH TO DAMPING

The SERC CST testbed was designed to capture the relevant physics and performance metric of an orbiting optical-wavelength interferometer spacecraft. Research addresses both the internal and external differential pathlength stability for multiple siderostat collecting telescopes in a frequency range where structural flexibility is important.

Figure 1 shows the testbed structure. Six triangular truss beams form a tetrahedron measuring 3.5 meters on a side, representing a 1/10th scale model of the reference science mission. A laser mounted to the structure at the "fourth vertex" (backright in the photo) provides a measure of optical pathlength changes between this point (representing combining optics) and three mock siderostats located on the science plane of the structure. At each siderostat location is a 3 dof articulated mirror whose position is measured by the laser metrology system. High sensitivity accelerometers, used to determine the external differential pathlength, are placed nearly collocated with the mock siderostats. A disturbance source (three orthogonal piezoceramic proof mass actuators) is located at the top vertex. Currently, four active piezoelectric struts can replace the basic aluminum struts, for a total of 13 possible actuators. The testbed structural skeleton consists of 229 aluminum nodes and 701 struts. Total mass is approximately 63 kg. There are about 30 modes below 100 Hz, with a fundamental at 25 Hz.
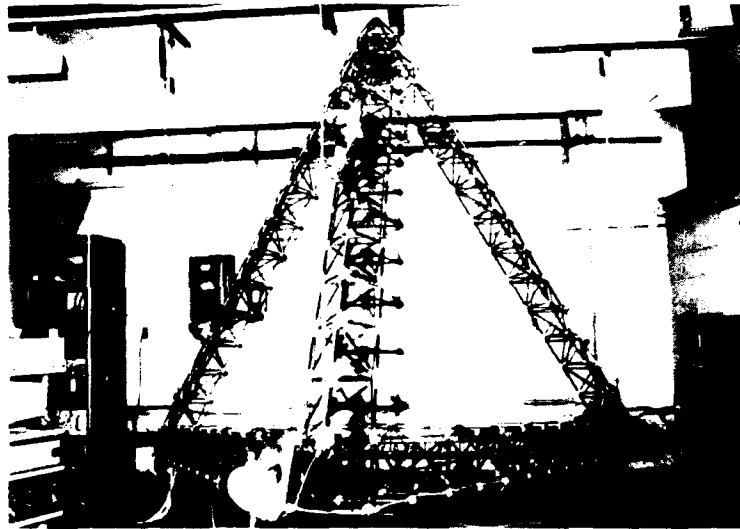
Figure 1: The SERC CST Testbed

Strut	Unit Mass (g)	Mass Added to Testbed
Nominal	39.5	–
J-Strut	57.3	1.41% (50)
D-Strut	232.9	1.53% (5)
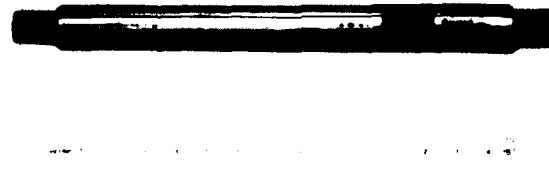
Figure 2: The J-Strut Viscoelastic Damper

The passive damping was added in the form of struts rather than at the joints of the structure. This decision was based on the desire to simplify both the modeling of damping and the physical alteration of the damping distribution, and to allow numerous damper designs (viscoelastic, viscous, shunted piezoelectric, etc.) to be employed. Future work will compare the relative effectiveness of passive vs. active dampers.

As mentioned, two types of passive damper struts have been used. The purpose of the viscoelastic struts (J-Struts) is to increase the overall level of damping in the structure, ensuring that no modes are too lightly damped. The high-loss viscous struts (D-Struts) were added to damp a smaller number of modes deemed critical by a specific control approach. The J-Struts can be considered a semi-permanent part of the testbed, but the locations of the D-Struts depend on the control approach.

In a lightly damped truss structure, the damping provided by n damped struts for a single mode can be estimated by $\eta_j = \eta_{strut} \sum_{i=1}^{n} e_{ij}$, where η_{strut} is the loss factor of an individual strut and e_{ij} is the ratio of strain energy in strut i to the strain energy of the entire structure for mode j. The linearity of the expression makes it possible to represent a placement strategy as an integer linear programming problem using $(0,1)$ variables for each location. Struts were placed based on maximizing the minimum loss factor over the first 36 flexible modes, using the program LINDO.

3 BROADBRUSH DAMPING (J-Struts)

The main design criterion for the J-Strut dampers (Figure 2) was to maximize the loss factor per mass with a minimal change in stiffness from the nominal strut. The struts were manufactured by wrapping two 0.015 inch layers of 3M ISD110 viscoelastic material
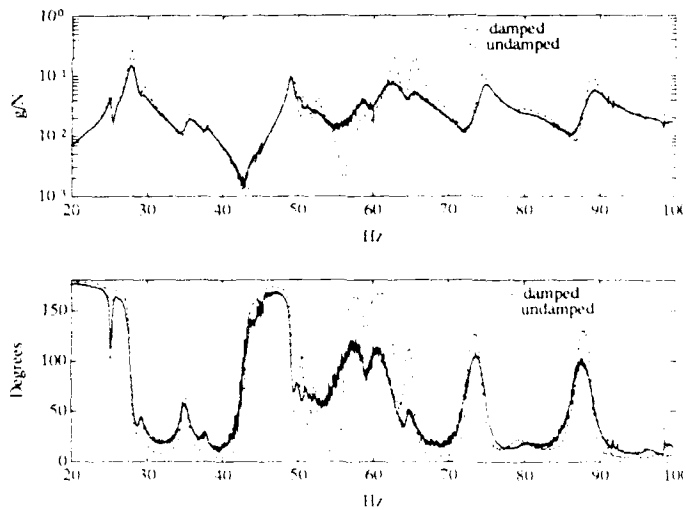
Figure 3: Collocated Transfer Function Showing Effect of the Addition of 50 J-Strut Dampers to the Testbed

(VEM) around nominal aluminum struts. A 0.5 inch outer diameter aluminum tube with 0.035 inch wall thickness was cut in half along its length and cured to the outside of the VEM layer. Total treated length was 5 inches. The fifty J-Struts were tested in an axial component tester at displacement levels of approximately 200 nm rms, and found to have a high frequency stiffness approximately 10% above that of the nominal strut and a loss factor of 0.06-0.07 over the frequency range of 20-60 Hz.

Fifty struts were placed in the structure using the algorithm described earlier. An average damping addition of 0.44%-0.52% was expected for the first 24 modes. The experimental increase in damping was determined by acquiring transfer functions from two separate shaker locations to three separate accelerometers before and after the addition of the J-Struts. Data were acquired with random input in blocks from 20-60 Hz and 60-100 Hz. A typical transfer function is shown in Figure 3. The data were fit for all modes below 90 Hz. For the 20 modes for which reliable data were obtained both with and without the dampers present, the average damping ratio rose from 0.94% in the "undamped" case to 1.34%, an increase of 0.40%.

4 TARGET DAMPING (D-Struts)

The Honeywell D-Strut damper is a device that can have loss characteristics tailored for a specific application. Earlier versions of the D-Strut were used in the PACOSS program (Morganthaler, 1991). The present D-Strut is a smaller device, similar to that used in the JPL Phase-B Testbed (O'Neal and Eldred, 1991), but with a higher loss factor. The D-Strut specifications were based on the approach of Anderson *et al* (1991). The frequency-dependent loss factor should have a maximum (η^*) in the range of control rolloff (50-100 Hz), and the frequency-dependent stiffness of the strut is matched to that of a nominal strut at the maximum loss frequency (f^*). Due to the gradual decrease in loss factor at frequencies above the peak, the peak (64 Hz) was placed near the low end of the rolloff region.

The complex D-Strut impedance represented by the lead-lag system of Figure 5 was measured using a precision axial component tester that employs a large piezoelectric driver and laser interferometer displacement measurement. Data for approximately 100 nm rms motion across the D-Struts was acquired from 1-100 Hz, and the model
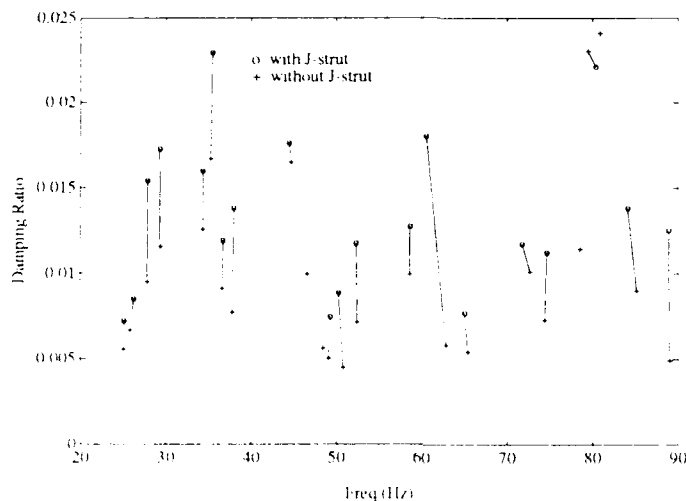
Figure 4: Average Damping for First 24 Modes Based on Curve Fits of Transfer Function Magnitude and Phase Data With and Without J-Struts

D-Strut	Component Tests				In Testbed		
	k_A (N/μm)	$f^*(Hz)$	η^*	ϕ^*	$f^*(Hz)$	η^*	ϕ^*
1	4.03	80.4	1.48	56.0°	64.7	1.13	48.4°
2	3.77	66.7	1.25	51.2°	56.9	1.01	45.2°
3	4.15	85.0	1.49	55.6°	68.4	1.11	47.9°
4	3.87	73.0	1.39	53.4°	60.8	1.06	46.7°
5	3.89	85.0	1.49	56.2°	68.7	1.14	48.7°
avg.	3.94	78.0	1.41	54.5°	63.9	1.09	47.4°
spec.	3.08	63.9	1.66	58.9°	–	–	–

Table 1: Properties of the D-Struts

parameters (DC gain, pole frequency, and zero frequency) extracted for each of five struts. Results of the fit are shown in Table 1. The average value of the DC stiffness k_A is above the specified value. It represents 35% of a nominal strut stiffness. The higher than expected stiffness resulted in an increase in the frequency (f^*) of the maximum loss factor (η^*). The values of η^* are slightly below the specified value. The quantity ϕ^* corresponds to the maximum phase lead. Note that the same quantities are given for the struts after they are placed in series with a spacer (k_{sp}=68 N/μm) and integrated into the testbed. The spacer is currently undergoing redesign (stiffening) to bring these numbers closer to the component values.

5   OPTICAL PATHLENGTH CONTROL

A subset of the testbed performance metric is the stabilization of an optical pathlength between the collecting optics and one of the siderostats. Pathlength error measured by laser metrology can be fed back by a controller to an articulating mirror to cancel motion along the optical LOS and reject pathlength disturbances. The transfer function (Figure 6) between mirror actuation and pathlength exhibits some coupling with the lightly damped structural modes, leading to a reduction in phase margin of modes in the region of the controller rolloff. The goal is to place the D-struts to increase phase margin of some particularly troublesome modes. The mode at 90 Hz is chosen a the target mode to be damped due to its contribution of 70° phase loss (beyond that caused
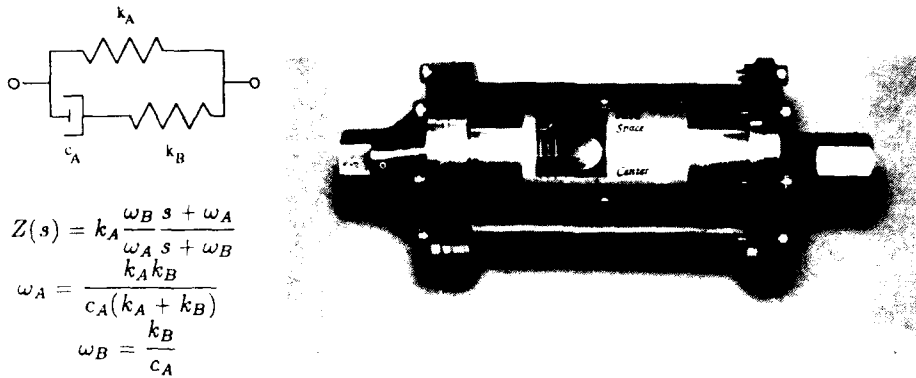
$$Z(s) = k_A \frac{\omega_B \, s + \omega_A}{\omega_A \, s + \omega_B}$$

$$\omega_A = \frac{k_A k_B}{c_A(k_A + k_B)}$$

$$\omega_B = \frac{k_B}{c_A}$$

Figure 5: Model and Photograph of the D-Strut
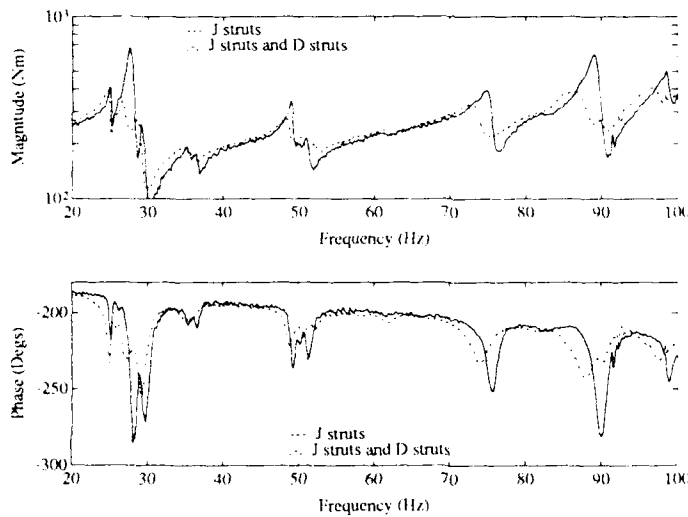
Figure 6: Mirror Mount to Laser Transfer Function Showing Reduction in Phase Excursions Due to D-Strut

by the laser sampling delay). The locations of the five D-struts were based on a strain energy ranking for this mode. To avoid placement in neighboring struts, five of the top seven locations were used.

From Garcia *et al* (1990) the expected phase loss of a particular mode (and the phase recovery due to added damping) can be determined without computing or measuring the transfer function directly. For the articulation of a light, rigid mirror using PZT displacement actuators against a flexible base structure, the structural flexibility weakly couples to the collocated transfer function between commanded and measured displacement. The pole-zero spacing in the transfer function for the rth mode is bounded to first order by

$$z_r - p_r \leq \left\{ \frac{1}{2} m (\phi_r^i)^2 \right\} p_r \tag{1}$$

where m is the mirror mass at location i and ϕ_r^i is the eigenvector of the rth mode (normalized to unity modal mass) of the flexible structure at the mirror interface along the LOS. The bound becomes tighter as the structural modal spacing becomes large.

For the collocated case, a closely spaced zero follows each pole, and the minimum phase of the pole-zero pair is

$$\Phi = -2 \arctan \left\{ \frac{m(\phi_r^i)^2}{4\zeta_r} \right\} \tag{2}$$

where ζ_r is the modal damping and the function argument remains nondimensional.

The effect of the *relative* measurement can be included by considering the eigenvector at the fourth vertex (at location k) along the LOS, ϕ_r^k. Since the mirror is articulated about an axis that does not pass through its center of gravity, rotational effects are included by the mirror inertia J, a geometric factor α relating rotation to commanded displacement, and structural rotation eigenvector ϕ_r^θ at the mirror interface location along the rotation axis. The phase loss due to the rth mode becomes

$$\Phi = -2 \arctan \left\{ \frac{1}{4\zeta_r} [m((\phi_r^i)^2 - \phi_r^i \phi_r^k) + \alpha J(\phi_r^i \phi_r^\theta - \phi_r^k \phi_r^\theta)] \right\} \tag{3}$$

The additional terms due to noncollocated and rotational flexibility tend to be small compared to the collocated term, in part because the fourth vertex is massive. Thus the transfer function of Figure 6 exhibits nearly collocated behavior.

The minimum phase of the pole-zero pair at 90 Hz calculated using eigenvectors from the finite element model, measured 0.0086 damping ratio, and a mirror mass of 1.3 kg, is 93 degrees, compared to the measured 70 degrees beyond the phase loss due to time delay. The error is attributed to finite element modelling errors, and the discrepancy between the eigenvectors of the model with and without mass loading of the mirror. From Figure 6, the addition of the D-Struts clearly reduces the phase loss in the target mode. This analytical approach permits us to calculate the phase loss due to flexible modes in the open loop mirror transfer function, identify those modes for targeted D-strut damping, and to specify the modal damping required to recover the desired amount of phase. Sufficient damping of these modes will facilitate the stable rolloff of compensators for pathlength regulation.

6   CONCLUSIONS AND FUTURE WORK

The approach to passive damping augmentation in one CST testbed has been presented. A large number of low-loss factor viscoelastic struts was used to increase damping slightly in all modes. A smaller number of very high loss factor viscous dampers was used to target critical modes which limit performance in a specific control loop. Future work will include possible construction of 50 more J-Strut dampers, stiffer D-Strut spacers, assessment of whether the high-loss D-Struts can cause complex modes, and the use of the target viscous damping in direct optical pathlength control and other global control.

7   ACKNOWLEDGEMENTS

8   REFERENCES

Anderson, E., Trubert, M., Fanson, J., and Davis, L., 1991, "Testing and Application of a Viscous Passive Damper for Use in Precision Truss Structures," *32nd AIAA SDM Conf.*, pp. 2796-2808, AIAA Paper 91-0996.

Blackwood, G., Miller D., and Jacques, R., 1991, "The MIT Multipoint Alignment Testbed: Technology Development for Optical Interferometry," SPIE Paper 1542-34.

LINDO, The Scientific Press, 507 Seaport Court, Redwood City, CA 94063.

Morganthaler, D., 1991, "Design, Analysis, and Testing of the PACOSS D-Strut Truss," *Proc. Damping '91 Conf.*, Vol. III, pp. IAB-1-23.

O'Neal, M. and Eldred, D., "The JPL Phase-B Testbed," *Symp. on AMAS*, 1991.

Von Flotow, A. and Vos, D.W., 1991, "The Need for Passive Damping in Feedback Controlled Flexible Structures," *VPI/SU Conf on Recent Adv in Active Control of Sound and Vib.*

Smart tuned-mass dampers

Kevin E. Smith*, Joseph R. Maly, and Conor D. Johnson
CSA Engineering, Inc., 560 San Antonio Road, Suite 101, Palo Alto, CA 94306

ABSTRACT: Passive damping using tuned-mass dampers (TMDs) is a well-known, weight-efficient approach to suppress vibrations of a single mode (or a group of modes). A TMD produces a high level of damping with a small amount of added weight if kept tuned to the frequency of the offending mode. A prototype TMD that will tune itself to an offending mode has been designed, built, and tested. It can keep itself tuned to the offending mode, even if that mode changes frequency. The prototype confirmed that a "smart" TMD could be built.

1. INTRODUCTION

A tuned-mass damper (TMD) is a vibration damping device consisting of a mass and a damped "spring" attached to a structure at or near an antinode of a troublesome mode of vibration. The damped spring is often composed of a viscoelastic material (VEM). This device is capable of damping either one mode or several very closely spaced modes and is usually more weight-effective than other types of damping (passive or active) It must be tuned precisely, however, in order to function properly, i.e., specific values of spring constant, damping loss factor, and mass are critical to the successful design of the TMD.

TMDs are conceptually simple, can be optimized (with special design tools), are very efficient in weight and space requirements, and produce significant damping levels, but they are seldom used. Their only real drawback is that the TMD must remain tuned within fairly narrow frequency bounds. If the TMD becomes untuned due to a change in TMD properties or if the structure to which it is attached changes, the TMD might no longer provide any damping.

The goal of this effort was to take the TMD concept and overcome its one real drawback: the need for constant tuning. The approach was to take advantage of the temperature-sensitive properties of viscoelastics to create a damped spring with a spring rate that could be continuously varied (by heating or cooling) to dynamically tune the TMD as needed. Specifically, this consisted of the following.

1. Derive an algorithm that can determine the temperature of the viscoelastic for optimum tuning. This control algorithm was developed subject to two assumptions.

   - The natural frequency and damping of the mode of the base structure is initially unknown and can change with time in a continuous or noncontinuous manner.

   - The excitation to the structure is unknown in type and level, and both may change with time. The excitation (and thus response) may also drop below the sensitivity of any sensor used by the TMD. This loss of excitation and response may not result in a wrong action by the controller.

*Currently with U.S. Windpower, Inc., Livermore, CA

2. Demonstrate the algorithm's performance on a laboratory-scale structure with a real, thermally controlled TMD.

This approach is based on assumptions that provide a broad. realistic (and stringent) view of how a TMD might be required to interact with most engineering structures. The requirements on the control algorithm are really quite severe. Restricting the algorithm to making only response measurements under unknown excitation conditions effectively rules out tuning algorithms based on estimating the current natural frequency of the structure.

Eventually, one practical assumption had to be made. Because viscoelastics have a limited range over which their stiffness can change by applying heat, the TMD obviously cannot be tuned over an arbitrarily large range. Therefore, we levied the requirement that the mode to be damped had to always remain in the operating range of the TMD.

2. SYSTEM MODEL

The physical system used to derive the controller is shown in Figure 1. An accelerometer is attached to the base structure at the point where the TMD is attached to the base structure A second accelerometer is attached to the moving mass of the TMD. A thermocouple measures the temperature of the VEM in the TMD. A resistive, ribbon heater is embedded in the VEM. The box around the VEM, thermocouple, and heater is intended to convey the idea that the elastic and lossy components of the TMD are affected by the heater. This model contains all of the physical parameters that we are allowed (by the constraints enumerated above) to measure or control.

3 TUNING ALGORITHM

The tuning scheme arises from the curves shown in Figure 2 . The curves labeled "Base" and "TMD" represent the RMS response to broad-band excitation of the base structure at the first accelerometer and the moving mass of the TMD when the VEM complex stiffness varies over the limits shown. (The loss factor of the VEM is assumed to be constant over this range.) This figure come: from solving the equations of motion for the system of Figure 1. The curve labeled "ratio" is simply the numerical ratio of the TMD RMS response to the Base RMS response. What is significant about this figure is that it shows that the maximum value of the RMS ratio occurs at the same TMD stiffness that produces the minimum base response. The minimum TMD response occurs at a significantly different stiffness.

This is believed to be a new result and represents the major step in constructing self-tuning TMDs. We now have a fundamental estimator for determining if a TMD is tuned.
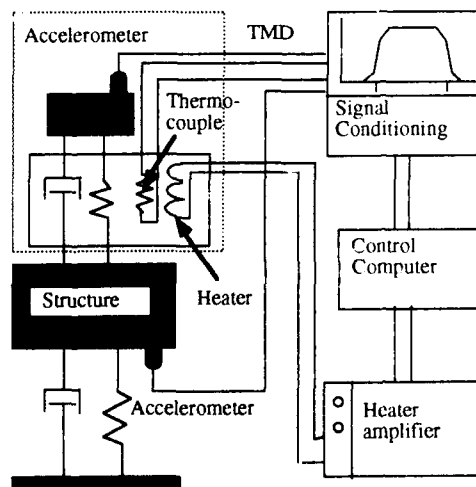
Figure 1. Schematic of the base structure, TMD, sensors, and controller.

4. CONTROLLER

By exploiting this function we were able to derive a controller that automatically and robustly tracks the underlying structure's dynamics and produces minimum response.

It needs to be kept in mind that the RMS ratio curve in Figure 2 can change with time. The change can be both in terms of where the maximum occurs (in terms of TMD stiffness and base structure) and the value of the ratio.

This approach does not require a calibrated TMD, i.e., the exact relation between TMD natural frequency and VEM temperature or stiffness and VEM temperature need not be known. What is

Figure 2. RMS of base structure, TMD, and their ratio.

known is that the natural frequency of the TMD at ambient temperature is higher than the upper limit of the allowed frequency range and that at maximum usable temperature the TMD's natural frequency is lower than the lower limit of the allowed frequency range. In other words, it is known that the TMD can change its natural frequency over the range of interest. Furthermore, the TMD stiffness versus temperature and loss factor versus temperature relations are not required to be linear, but they are assumed to be continuous.

5. CONCEPT VALIDATION

A laboratory test setup was used to prove out the tuning concept. The experiment consisted of a test structure, a thermally controlled TMD, two accelerometers, and a control computer, with excitation to the base structure provided by an electrodynamic shaker.

The test article was a square-section steel beam suspended between machinists bookends above a thick, steel baseplate. The TMD was configured as a cantilever beam attached at the point of maximum deflection of the test article's first bending mode. The TMD was a sandwich of graphite-epoxy facesheets with two inner sheets of Soundcoat DYAD 606 VEM. This material was usable over a range of 22° C to 43° C. The shear modulus changes by a factor of seven over this temperature range. The two VEM sheets surrounded a MINCO Thermofoil resistive ribbon heater. The control computer was a Macintosh IIx running the LabVIEW acquisition/control program. The shaker was driven with white noise of various levels.

Several test configurations were run; all successfully. These included tune from start-up and retune after an abrupt change in the base structure. The controller was able to find, track, and optimally damp the base structure in all cases.

5.1 Tuning from Start-up

In this test the system was initiated with a "cold" TMD, i.e., the TMD was initially too stiff. The controller develops an estimate of the RMS response of each accelerometer (base structure and

TMD) over an observation interval.[1] The ratio of the RMS estimates is stored and the first temperature update is made. It was known that the TMD had to be initially heated in order to tune. This stems from designing the TMD to be overly stiff at room temperature.

Figure 3 shows the development of the RMS ratio with time. The current gain on the TMD heater was purposely set low to allow better observation of the process. The TMD is initially so stiff (cold) that considerable heating is required to effect any appreciable change in stiffness. Eventually the VEM stiffness changes enough to affect the RMS ratio. The TMD's natural frequency approaches the optimal (not shown) and the controller stabilizes at the correct level. Some limit cycling is evident and is due to the lack of insulation on the TMD.

5.2 Abrupt Change in the Base

A more interesting case is the response of an already tuned TMD to an abrupt change in the base structure's dynamics. The test described above was repeated until the controller achieved the optimal tuning. A significant weight was then magnetically snapped onto the base structure. Figure 4 shows the development of the RMS ratio. with the abrupt change in RMS ratio and the retuning noted. The controller retuned and achieved optimal damping.

Figure 3. Tuning from start-up.

6. CONCLUSIONS

The study was successful in demonstrating all of the essential aspects of the self-tuning TMD. The controller could find and track a single structural mode and produce the maximum system damping for that particular TMD. The use of the RMS ratio as the basis for the tuning control has been shown to be essentially correct and accurate for optimum performance. The controller is capable of tuning when the base structure or TMD fall slightly outside the assumed tuning range or when the RMS detection is degraded.

Thin-film heaters were shown to be adequate for regulating the temperature of the VEM as dictated by the control system. This type of heater was ideal for the tuned beam used in this experiment since the

Figure 4. Abrupt change in base dynamics.

heater could be embedded in the VEM, providing uniform temperature regulation. In addition, the heaters can be custom-made to match any shape VEM surface.

---

[1] This interval was picked to minimize variance in the RMS. The RMS estimate was constructed from the integral of the magnitude of the Fourier transform of each signal. (Each signal was Hanning weighted.)

Smart polymeric materials for active camouflage

Dr. L. J. Buckley and Mr. D. Mohl
Naval Air Development Center
Warminster, PA 18974

Abstract

Segmented polyurethanes that contain the diacetylene
group in the molecular backbone were synthesized and studied
as potential active visual camouflage materials. The
diacetylene groups can be reacted in the solid state to
produce a chromic material that will change its absorption
behavior with strain or temperature. The morphology of
these materials dictates the ultimate length of the
conjugated polydiacetylene structure and was investigated
with small-angle x-ray scattering. This enabled the
selection of systems that were well phase separated with a
strong chromic effect. The structure is typically lamellar
and highly dependent upon processing. In addition to the
adaptive material, the active camouflage system consists of
sensors and controls. The sensors identify the ambient
wavelengths and intensity of the surroundings. The
controller processes the information from the sensors and
sends signals to modify color and intensity. Various sensor
configurations were investigated.

1. INTRODUCTION

Polyurethane block copolymers containing the diacetylene

group in the hard segment were synthesized and studied as

potential smart materials for an active camouflage system.

The diacetylene group is a highly reactive functionality

that, in correct solid-state geometry, can be topochemically

polymerized using heat or radiation into a fully conjugated

polymer with extensive electron delocalization along its

main chain backbone as shown previously by Wegner (1970).

It is possible to dynamically modify the optical properties

of these materials by changes in temperature, pressure, or

stress (see, for example, Rubner (1986)). Polyurethane-

diacetylene block copolymers were synthesized via a two step
solution polymerization technique.   The polyurethanes have a
segmented block copolymer structure consisting of
crystalline hard domains containing the diacetylenes within
soft segment amorphous regions.   The materials varied by
type of hard segment and soft segment molecular weight.   The
morphology of these systems depends upon many factors such
as: molecular weight of the soft segments; extent of
segmental mixing at the interface; hard domain size; and
extent of phase separation.   The chromaticity and absorption
shift are highly dependent upon the morphological state of
the polymer.   The overall objective of this effort was to
develop materials for an active camouflage system that is
capable of changing both, color and intensity.

2. MATERIAL CHARACTERIZATION

UV-Visible studies were performed to evaluate the
mechanochromic and thermochromic nature of these materials.
The change in absorption behavior was quantified for each of
the various polyurethane systems investigated.   An example
is shown in figure 1.   The soluble nature of these materials
before forming the polydiacetylene structure enables
efficient deposition as a coating.
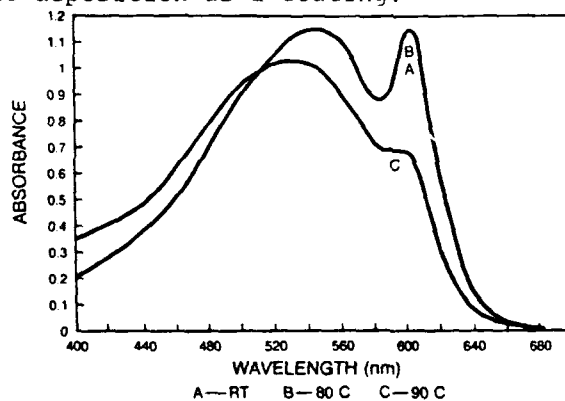
Fig. 1.   Thermochromic Behavior for HDI-5,7-2000 Material

The small-angle x-ray scattering studies indicated that the
solid-state cross polymerization reaction does not
significantly affect the morphology of the
polyurethane/diacetylene materials. From the Porod
analysis, relatively sharp interfaces were found with the
HDI systems somewhat sharper than their MDI counterparts.
The systems were ranked according to degree of phase
separation and the trends indicated a higher soft segment
molecular weight improved the degree of phase separation.
Table I shows the relative degree of phase separation as
determined by the ratio of Porod's Invariant to the
calculated electron density variance. This analysis is
thoroughly described by Tyagi, McGrath, and Wilkes (1986).

Table I. Relative Degree of Phase Separation

Sample	$\Delta\rho^2/\Delta\rho^{2\prime}$
MDI-5,7-1000	0.111
MDI-2,4-1000	0.140
MDI-5,7-2000	0.154
HDI-5,7-1000	0.184
HDI-5,7-2000	0.210

3. SENSOR AND CONTROL SYSTEM

In addition to the adaptive material, the active ca.ouflage
system consists of sensors and controls. The sensors
identify the ambient wavelengths and intensity of the
surroundings. The controller processes the information from
the sensors and sends signals to modify color and intensity.
Various sensor configurations were investigated such as: a
diffraction grating with photodetectors; a color (CCD)
camera; primary color filters with photocells; and a series
of narrow bandpass filters with silicon photodetectors. The
sensor outputs are fed through an anolog to digital
converter into the microprocessor. The digital
representation for the output voltage at each wavelength
will be stored so the microprocessor can determine the

spectral response for an unknown background and modify the
material accordingly. The narrow bandpass filters with
silicon photodetectors were chosen as the sensor system and
data is compared below in Figure 2 to a spectroradiameter
for colored transparencies.
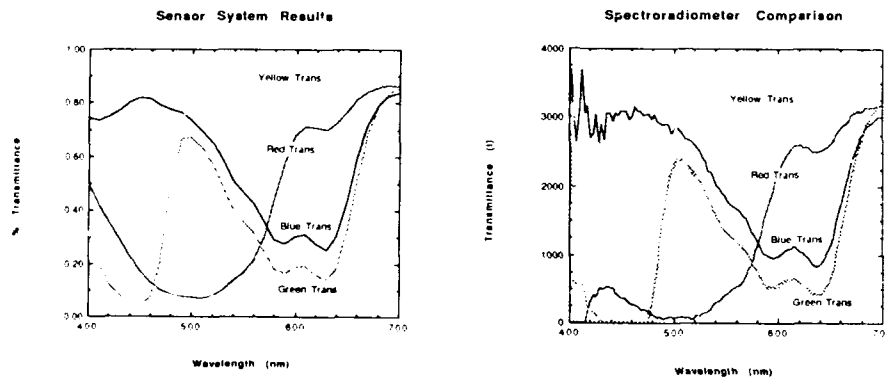
4. REFERENCES

Rubner, M, 1986, Macromolecules, 19, 2129
Tyagi, D, McGrath, J, Wilkes, G, Polym. Eng. & Sci. 26,1371
Wegner, G, 1970, Makromolekulare Che...ie, 134, 219

The new BLM system: self-assembling bilayer lipid membranes

H T Tien, Z Salamon, D-L Guo and A Ottova-Leitmannova

Membrane Biophysics Lab (Giltner Hall), Department of Physiology
Michigan State University, East Lansing, MI 48824

ABSTRACT: Supported bilayer lipid membranes (s-BLMs) were formed by the
self-assembly method on freshly fractured metallic wires. The influence
of a host of compounds in membrane forming solutions on s-BLMs were
examined and the effect of pH on the function of the s-BLM studied.
Additionally, the redox reactions of a s-BLM containing vinyl-ferrocene
as an electron mediator have been investigated by cyclic voltammetry.
The results have shown that ferrocene can be very easily immobilized in
s-BLMs. This suggests that s-BLM systems offer a novel approach to the
electrode modification by simple way of immobilization of compounds
within BLM.

1. INTRODUCTION

Planar bilayer lipid membranes (BLMs) and spherical liposomes are widely
used as realistic models of biomembranes; they have been used to study the
molecular basis of ion selectivity, membrane transport, energy
transduction, electrical excitability and redox reactions (Blank and
Findi, 1987; Yoshikawa et al., 1987; Ivanov, 1988; Davison, 1989; Gliozzi
and Robello, 1989; Mittal, 1990; Tsong, 1991). Owing to the differences in
their configuration and physical dimensions, the electrical properties of
lipid bilayers can be readily studied in BLMs (Tien, 1974). Advances in
microelectronics in recent years coupled with growing interest in
biotechnology have prompted many researchers to exploit the BLM system as a
basis for biosensors as well as for the development of molecular devices
(Kruus, 1987; Tien, 1988; Bruckner et al., 1990; Maeda et al., 1990;
Valleton, 1990; Ishii, 1991; Kato and Kunitake, 1991; Nakanishi, 1991;
Nakashima, 1991; Schuhmann et al., 1991). Unfortunately there is one
problem associated with conventional BLMs, namely, their mechnical
instability. They rarely last longer than a few hours. The new BLM system,
discovered recently and described here, possesses in contrast to
conventional BLMs, the requisite mechanical stability as well as the
desired dynamic properties. For example, the s-BLM system offers an
approach to the lipid bilayer modification by incorporating a variety of
novel compounds. In this paper, after briefly describing the new BLM
system, we report the incorporation of a ferrocene compound into s-BLMs
whose sensitivity to certain redox couples has been investigated by
membrane cyclic voltammetry (Tien, 1984; 1986).

2. EXPERIMENTAL

1.1 **Material and reagents**. A number of s-BLM forming solutions were used

including lecithin, glycerol mono- and di-oleate dissolved in squalene. In certain lipid solutions 1% of cholesterol was added to enhance the stability of s-BLMs. In most experiments either Teflon-coated stainless steel (SS) wire of 0.3 mm diameter or platinum (Pt) wire of 0.5 mm was used. For redox reaction experiments, a BLM-forming solution made of glycerol-dioleate (GDO) dissolved in squalene and saturated with vinyl-ferrocene (Fc) has been used. For ion selectivity and specificity experiments, valinomycin (Sigma) was dissolved in a GDO-squalene solution (Tien, 1974). Similar solutions were prepared with monensin, gramicidin, iodine, and TCNQ (Tien, 1986). All chemical compounds were obtained commercially and were used without further purification. Double-distilled water was used in the preparation of all solutions.

'.2 s-BLM formation. The procedure described previously were followed (Tien and Salamon, 1989).   Essentially, one end of the coated wire was immersed into a lipid membrane-forming solution, as then cut **in situ.**   In order to achieve reproducible results, a small guillotine was constructed for the cutting procedure (Martynski and Tien, 1991). The lipid-coated wire was then transferred into an aqueous solution. After approximately 1 minute the potential was adjusted to a desired value.   After another 3-4 minutes the electrical parameters (R_m = resistance, C_m = capacitance) were monitored.

'.3 Electrical measurements. Measurements were made using an IBM instrument (Model EC-225 Voltammetric Analyzer) in either the two or three electrode configuration. In the former case the lipid-coated SS (or Pt) wire was attached as a working electrode and the saturated calomel electrode (SCE) as a reference electrode.   Alternatively a three electrode configuration was used, with a Pt wire serving as an auxiliary electrode.

Cyclic voltammetry (CV) of membranes. CV is a familiar technique to electrochemists as a means of studying redox states of electrode-active species. The basics of CV consist of cycling the potential of a working electrode (WE) immersed in an unstirred solution and measuring the resulting current, i. e., a current-voltage curve or a voltammogram. The potential of the WE is maintained relative to a reference electrode (RE, eg., SCE-- saturated calomel electrode). Frequently, a third electrode, known as the auxiliary electrode (AE), is used if the current is large (uA or more) in order to prevent RE polarization, which could cause the measured potential to change (Heineman and Kissinger, 1989). This powerful and elegant CV technique was applied for the first time to membrane studies (Tien, 1984;1986) and affords a highly useful method for the study of electron-transfer and redox reactions, with the bilayer lipid membrane (BLM) serving as the working electrode. We have been using CV to investigate the effects of redox compounds, including proteins of various types, and of drugs on BLMs. Recent results indicate that CV coupled with spectroscopy studies of BLMs can give important information concerning electron transfer, with particular relevance to the membrane processes in neurons, mitochondria, and chloroplasts (Glenhurst and Niki, 1988). We have used this technique in studies of electron transfer from cytochrome c to cytochrome c peroxidase across the BLM. Further, it has been demonstrated that CV coupled with spectroscopy is potentially a very powerful tool in the study of membrane-bound cellular processes, not only for the determination of the standard $E^{o}{}'$ but also for obtaining new insight into the energetics and mechanism of the process (Tien,1986; Davison,1989).

3. RESULTS AND DISCUSSION

Since the first reports of bimolecular (black, or bilayer) lipid membrane
(BLM) in 1962 (see Tien, 1974 for a historical account) its potential use
as a biosensor has been proposed (Ivanov, 1988). The main argument is that
the lipid bilayer would provide a natural environment for ion and electron
carriers, photoactive compounds, receptors, membrane-bound enzymes, etc.
Hence it would be of potential use in biosensor technology (Tien, 1988).
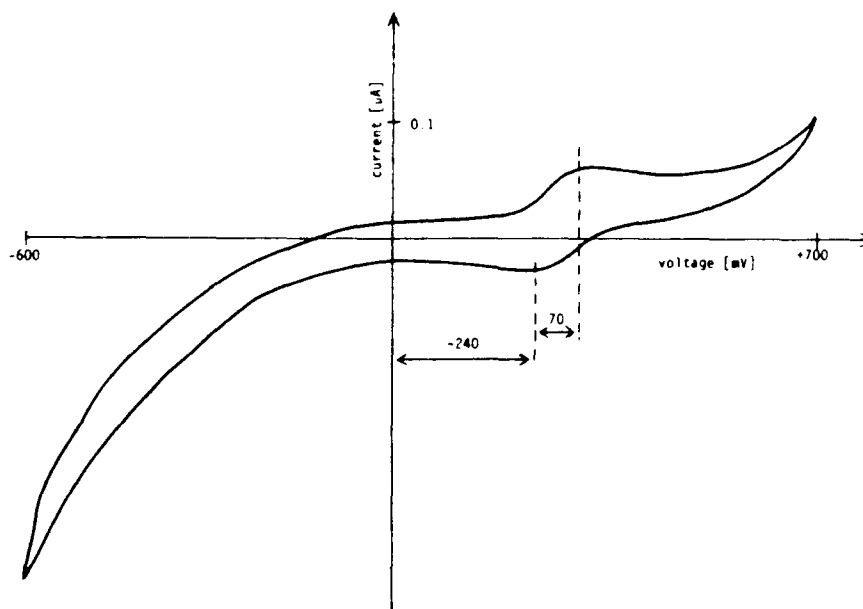
FIG. 1 The cyclic voltammogram of a GDO + Fc s-BLM on Pt wire at 100 mV/s.

Thus far, a truly functioning lipid bilayer-based biosensor, however, has
yet to be developed. This is most likely owing to the inherent instability
of the conventional BLM system which is sensitive to a number of factors
such as hydrostatic pressure, boundary effects at the Plateau-Gibbs border,
dielectric breakdown, surface contamination. Recently, the feasibility of
lipid bilayer using materials other than phospholipids has been
demonstrated (Kato and Kunitake, 1991) and single and multilayer-based
sensors have been successfully attempted (Zviman and Tien, 1991). Further,
a boost in the stability of BLMs has been recently achieved by
self-assembling the BLM on a solid support, as reported elsewhere (Tien,
1990; Martynski and Tien, 1991). This new method of a bilayer formation
solves two basic obstacles in the way of the practical utilization of BLM
structures, namely: (i) its stability and, (ii) its compatibility with a
standard microelectronic technology. Here a self-assembly of amphipathic
molecules into a bilayer, on a freshly cut metal surface takes place. This
improves the stability of the system by orders of magnitude. This

ultrathin structure (~ 5 nm), being biomembrane-like, should greatly
facilitate in the development of BLM-based biosensors and molecular
devices. Previously, we have discussed the main properties of the s-BLMs
(Tien, 1990) and also the role of a film thickness on the efficiency of an
electron transfer process occurring in such a system (Ivanov, 1989). Among
them the use of the s-BLMs in the field of ion- and enzyme-selective
sensors seems to be most promising (Tien, 1990). This is so because various
electrode-active compounds can be simply immobilized within a s-BLM. We
have already started to verify experimentally the advantages of the s-BLM
system using different chemical mediators [Wardak and Tien, 1990; Zviman
and Tien, 1991). This communication describes that such a useful electron
modifier as ferrocene can easily be immobilized in a s-BLM system using a
platinum wire substrate. The results show enhanced sensitivity of the
system to $Fe(CN)_6^{-3,-4}$ ions. It should be mentioned in passing that bare
and freshly cut SS wires used for s-BLMs are sensitive to hydrogen ions. In
the pH range 3-8, nearly theoretical Nernst slopes have been obtained,

(GDO + FERROCENE)/PT WIRE

0.1 uA (for (A))

(A)

Current

1.0 uA (B)

(B)

Voltage   700 [mV]

(A) in bathing solution (0.1 M KCl)

(B) 0.1 M KCl + 0.5 mM $K_3[Fe(CN)_6]$

ΔV ≈ 105 mV
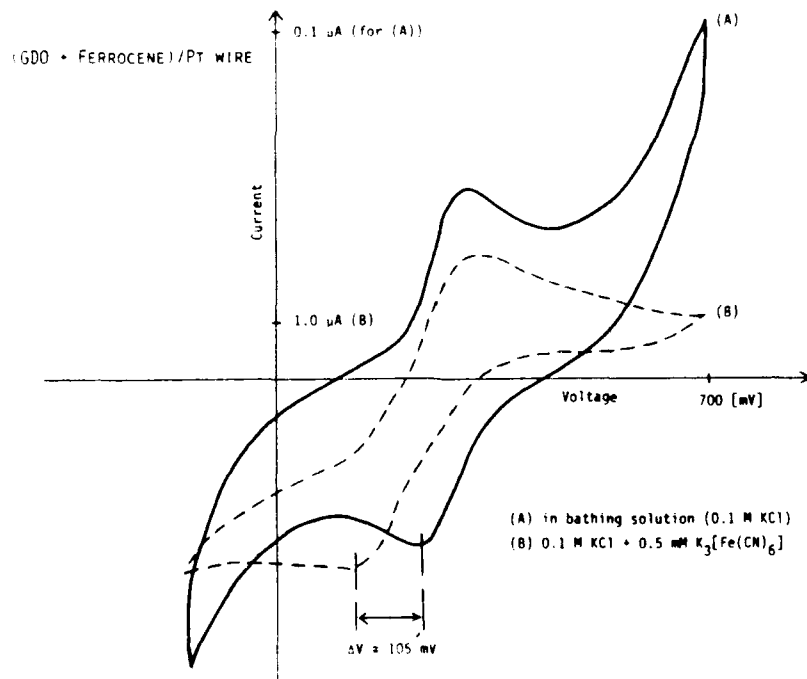
Fig. 2 The cyclic voltammograms of the system presented in Fig. 1.

whereas in alkaline pH (8 to 12.4) only 30 mV per pH unit was seen. It has
also been found that valinomycin-doped s-BLMs were sensitive to K^+ ion
exhibiting linear response in the concerntration range 10^{-3} to 10^{-1} M.
The process of a BLM formation which usually takes a few minutes to be
completed was monitored by measuring a membrane resistance and capacitance.
As has been shown previously the time-change of both parameters of a lipid
layer deposited on a surface of the platinum wire is very similar to that
observed with a conventional single BLM (Tien, 1974; Martynski and Tien,
1991). These findings indicate that the resistance decreases over the time
of thinning process reaching a constant value of the order 10^5-10^7 ohm cm^2

for different BLM forming solutions, whereas the capacitance increases up to 0.5-1.0 uF cm^{-2}. Additionally, the cyclic voltammograms of s-BLMs modified with a vinyl- ferrocene were obtained. Fig. 1 shows a typical cyclic voltammogram of a Pt-supported (GDO + Fc) bilayer in 0.1 M KCl bathing solution at a scan rate of 100 mV/s. Form this graph it can be clearly seen the redox peaks corresponding to essentially reversible redox process of the ferrocene-ferricinium couple. Figure 2 illustrates the changes in both a shape and a position of the redox peaks of the (GDO + Fc) bilayer (curve 1) after the addition into the bathing solution 500 uM (curve 2) of $K_3[Fe(CN)_6]$. The presence of the $Fe(CN)_6^{-3/-4}$ ions shifts both peaks towards less positive values of potential, however a magnitude of the shift is different. The reduction peak shift is much more pronounced and it can be related to the $Fe(CN)_6^{-3/-4}$ concentration in a bathing solution. This concentration dependent shift of the reduction peak is presented in Table 1. It can be seen a good linear relationship in the $Fe(CN)_6^{-3/-4}$

Table 1. Voltage peak separation in a s-BLM doped with vinyl ferrocene.

Electrode	Bathing solution	Peak positions [mV]	
		Reduction	Oxidation
Pt with GDO + Fc BLM	Without Fe(CN)	240	310
	With 0.5 mM $K_3[Fe(CN)_6]$	125	305
Pt	With 0.5 mM $K_3[Fe(CN)_6]$	195	255

concentration range up to about 5 mM. From this figure one can also see that Pt electrode with a (GDO + Fc) bilayer deposited on its surface senses $Fe(CN)_6^{-3/-4}$ ions present in the bathing solution at the concentration as low as in the range of 10^{-7} M. Although the same size of a bare Pt wire coated with Teflon but without a BLM deposited on its surface shows much more reversible CV signal (voltage separation between peaks is only 60 mV - see Table 1) the lowest detectable amount of Fe(CN) is however almost two orders lower (- 5 x 10^{-6} M).Such results clearly indicate that the presence of a GDO + Fc bilayer on the surface of a Pt wire modifies platinum electrode behavior on $Fe(CN)_6^{-3/-4}$ ions increasing significantly its sensitivity and changing both the peak potentials and their shapes. This specific modification of the surface of a platinum wire can also be seen in the position of the redox peaks. Table 1 shows a comparison of peak positions between a bare platinum electrode and the same platinum electrode coated with a GDO + Fc bilayer in a bathing solution with 5 x 10^{-4} M $K_3[Fe(CN)_6]$. Although in order to understand the mechanism of interaction between Pt supported (GDO + Fc) electrode and ferro-/ferricyanide ions, additional experimental results are necessary. The present findings indicate a possible way of using such type of the BLM system for a simple detection of the $Fe(CN)_6$ ions in the aqueous solutions. Although the experiments reported here are preliminary, the results suggest the possibility of advantageously using s-BLM as a biosensor by reason of its inexpensive and simple construction. The lipid bilayer of s-BLMs, as ideal environment for electroactive compounds, would therefore permit the construction of an amperometric sensor.

Finally, it is worth noting that s-BLMs with millimeter to micrometer dimensions have other attributes; they are essentially microelectrodes. As such, s-BLMs can be readily developed for a variety of practical applications. It seems highly likely that the new method for self-assembling BLM on solid support, like its predecessor, will have an impact on lipid bilayer-based research in the years to come.

REFERENCES

Blank M ed 1987 Mechanistic Approaches to Interactions of Electric and Magnetic Fields with Living Systems (New York: Plenum) pp 301-324
Bruckner C, Petelenz D and Janata J 1990 Mikroch Act 1 169
Davison S G ed 1989 Progress Surface Science 30 1-200
Fare T L 1990 Langmuir 6 1172
Fox M A 1991 Top. Cur. Chem. 159 67
Gliozzi A and Robello M 1989 Coll Surf. 35 121
Heineman W R and Kissinger P T 1989 Current Separations 9 15
Ishii T Kumazawa N Yoshikawa K and Mukasa K 1991 Fall ACS Meeting Abst 123
Ivanov I ed 1988 Thin Liquid Films (New York: Marcel Dekker, Inc.) p 181
Janata J 1987 Proc. Symp. Chemical Sensors, Turner, A.P.F. (The Electrochemical Society, Inc.) 258
Kato S and Kunitake T 1991 Chem Lett 2 261
Krull V J 1987 Anal. Chim. Acta 197 203
Martynski T, Tien H T 1991 Bioelectrochem. Bioenerg. 25 317
Milazzo G ed 1983 Bioelectrochemistry and Bioenergetics (New York: Wiley) 5 pp 157-224
Mittal K L ed 1989 Surfactants in Solution 8 (New York: Plenum Press) 133
Mountz J M and Tien H T 1978 Photochem. Photobiol 28 395
Nakanishi H and Yamaguchi H 1991 Fall ACS Meeting Abst 124
Nakashima N 1991 Fall ACS Meeting Abst 104
Reichert W M, Bruckner J and Joseph J 1987 Thin Solid Films 152 345
Tien H T 1974 Bilayer lipid membranes (BLM): theory and practice (New York: Marcel Dekker, Inc.)
Tien H T 1986 J Electroanal Chem 211 19
Tien H T 1988 J Clinical Lab. Analysis 2 256; J Surface Sci. Technol. 4 1
Tien H T 1990 Advanced Materials 2 316
Tsong T Y 1991 Biophys. J 60 297
Vassilev P M and Tien H T 1989 in Subcellular Biochemistry: Artificial and Reconstituted Membrane Systems eds J R Harris and A -H Etemadi (New York: Plenum Press) pp 97-143
Valleton J M 1990 React Polym 12 109
Wardak A, Tien H T 1990 Bioelectrochem. Bioenerg. 24 1
Yoshikawa K H, Hayashi H, Shimooka H, Terada H and Ishii T 1987 Biochem Biophys Res Commun 145 1092
Zhao K H, Xu S and Fendler J H 1991 Langmuir 7 520
Zviman M, Tien H T 1991 Biosensors & Bioelec. 6, 37

Controlled formation and properties of responsive polymers

Stephen G. Weber*, Elizabeth T. Wise, Andrew D. Hamilton*,
Erkang Fan, Cristina Vicent, Fernando Garcia Tellado, Stephen J. Geib

Department of Chemistry, University of Pittsburgh,
Pittsburgh, PA 15260

The design of 'smart materials' that show both a controlled structure and a specific response to exogenous chemicals is an important goal. We are presently taking two approaches to this problem, both centered on the use of non-covalent interactions to form the structural foundation of the material and to provide the origin of its specific response.

1 A Three-Dimensional Gel

The first system studied is commonly known as 'slime' and consists of aqueous sodium tetraborate and polyvinyl alcohol (PVA) in a weakly basic solution. The tetrahedral borate ion complexes with PVA in such a way as to create a three-dimensional network. The solvent is mainly immobilized in the network when the concentration of crosslinked chains is high, and a semisolid gel is produced. The physical properties of the borate gels - solubility in water, deformation with shear stress, thermal reversibility of crosslinks - indicate that the bonds must form, break, and reform readily. Thus, hydrogen bonding rather than covalent bonding is likely[1-4]:
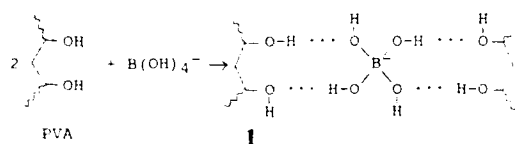
We have carried out an investigation of the phase diagram of this system at low borate concentration. Figure 1 shows changes in viscosity with borate concentration at different concentrations of PVA (recorded as diol concentration). Viscosity of the gel is dependent on the extent of borate crosslinking of the PVA. Because not all of the borate may bind with the polymer, we are presently performing experiments to determine the relationship between viscosity and the number of crosslinks. The plot also shows that diol concentration is a factor in gel viscosity. It is possible that chain tangling accounts for the viscosity at low polymer concentrations. i.e. borate causes predominantly intramolecular crosslinks. At higher PVA concentrations, intermolecular crosslinking effectively increases the polymer molecular weight and a more viscous gel results.
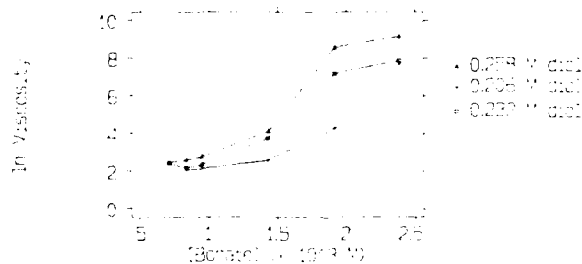
Fig. 1. Viscosity as a function
of borate concentration.

The material properties of the system depend on the activity of the borate which can be controlled with low molecular weight alcohols having a *cis* -1,2 or *cis* - 1,3 configuration[1,4-7]. The added alcohol indirectly influences the material properties by preferentially forming covalent borate complexes. The result is a reduction in the extent of crosslinking and a corresponding decrease in viscosity.

The effect of certain polyols on the PVA-borate system leads to interesting applications. We have tested its potential as a chemical valve by plugging a pipette tip with a concentrated gel and immersing it in various alcohol solutions. Table 1 lists the observations which are consistent with existing hypotheses. Complexation appears to be more favorable with acyclic molecules such as mannitol[8,9]. And in aqueous solutions fructose is present mainly in the more flexible acyclic form.

Table 1 Dilution Time for Gel Material Immersed in 0.1 M Polyol Solutions (buffered, pH 10)

Polyol	Time	Observations
Mannitol	10 minutes	Swelling, almost complete dissolution
Fructose	10 minutes	Swelling, almost complete dissolution
Sucrose	Did not dissolve	Some swelling
Glucose	Did not dissolve	Some swelling
Control		
Bicarbonate buffer	Did not dissove	Some swelling

2 Directed Hydrogen Bonding Interactions

In the past several years we have published extensively in the area of molecular recognition.[10] Our primary approach has been to use directed hydrogen bonding interactions to control both the strength and selectivity of substrate binding. This has led to artificial receptors for many important molecules including amino acids[11], barbiturates[12], diacids[13] and the different nucleotide bases.[14] More recently we have demonstrated that high energy intermediates or transition state species can be recognized and stabilized by synthetic receptors leading to accelerations in reaction rates.[15] The information and experience we have gained in these general studies form the basis of our approach to self-assembling organic structures. We have made good progress to show that the choice of complementary hydrogen bonding interactions to direct the assembly of defined molecular aggregates is a valid one.

2.1 Functional Organization of Multichromophore Structures

We have used the barbiturate/receptor interaction[12] to achieve the linear organization of two chromophores. This approach allows the formation of *functional* aggregates in which properties exist that are not present in the isolated components (Figure 2). Porphyrin barbiturate **3** and dansyl receptor
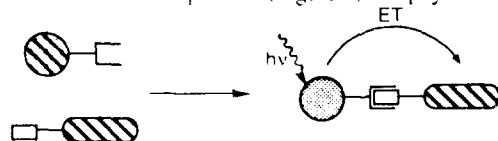
Figure 2

4 contain complementary binding regions and come together to form hexahydrogen bonding complex **5**, which positions the two chromophores ~23Å apart. A series of ^{1}H NMR, and static and dynamic fluorescence quenching experiments[16] confirm the self-assembly and energy transfer communication between the two chromophores even at concentrations as low as 10^{-6} M. The idea of preprogrammed molecules (due to their hydrogen bonding complementarity) self-assembling into defined linear aggregates with unidirectional flow of energy or electrons is a powerful one that has a

clear analogy in the photosynthetic reaction center[17] as well as potential applications in photoactive materials and molecular electronics[18]. Recent results have shown that the dansyl in **4** can be substituted by a quinone and that photoinduced electron transfer between the self-assembled subunits can occur.[19] We have also demonstrated, with a ferrocene-linked double receptor, that an extended tris-chromophore aggregate of type **6** can also be formed in solution. A critical feature of these designs (developed further below) is the relative positioning of the redox partners as well as the strong binding ($K_a > 10^6$ M^{-1}) which allows significant association of equimolar solutions even at low concentration.

3   4   5

6
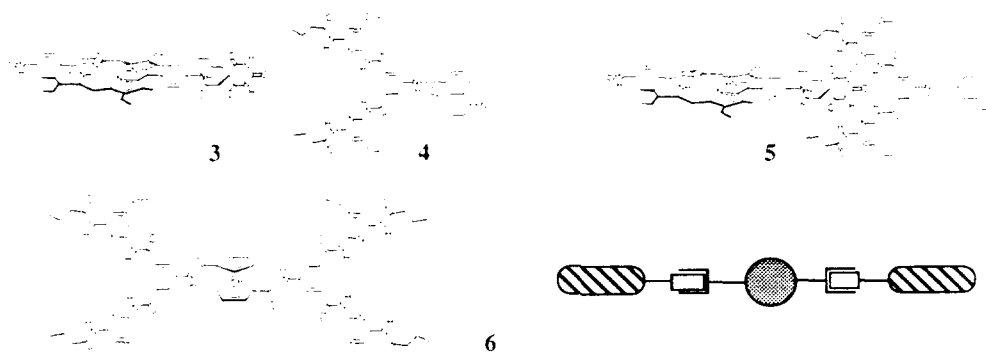
2.2 Polymeric Aggregation

In the rational design of solid state structures, directed hydrogen bonding interactions can be used to control the orientation, shape and constitution of the polymeric aggregates. In the past year we, and others[20-25] have developed specific motifs that lead, with some reliability, to predictable structures.

2.2.1 Based on Hydrogen Bonded Ribbons

Protonation of diacylaminopyridine **7** with diarylphosphoric acid causes a 180° rotation around the C-N bond and formation of two intramolecular hydrogen bonds between the pyridinium-NH and CO groups. This directs the amide-NH groups outward to form two intermolecular H-bonds with bridging diarylphosphates. The resultant cocrystal takes up a ribbon structure with the pyridinium-phosphate hydrogen bond network at its core (Figure 3).[26] This ordered arrangement leads to a segregation of anions and cations to opposite sides of the ribbon and recurs with other phosphate components including chiral binaphthyl phosphates.[26]

7
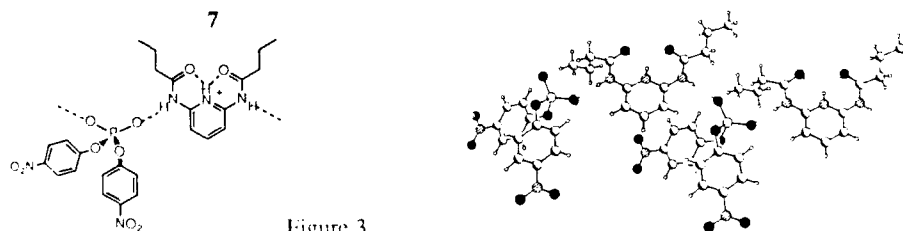
Figure 3

2.2.2 Based on Hydrogen Bonded Sheets

The common translational H-bonded packing of diamides[23] can be induced to interpose a second component by incorporating strong bidentate interactions between the crystal partners. We have shown that the 2-acylaminopyridine/carboxylic acid pair provides a stronger interaction than the single hydrogen bond between simple diamides and can lead to polymeric aggregates as in figure 4.
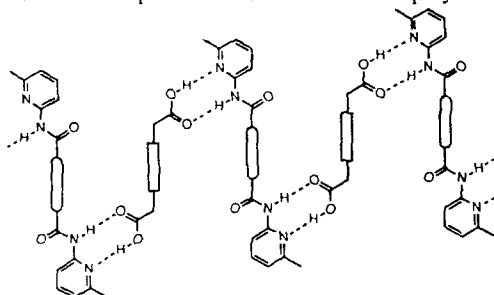
Figure 4

This represents an elongated molecular sheet whose dimensions are imposed by the hydrogen bonding network and the relative size match of the alternating components. Figure 5 shows the complex formed between biphenyldiamide 8 and 1,12-dodecanedicarboxylic acid. An almost flat sheet structure is taken up with a 73° slip or tilt angle between the polymethylene chains and the horizontal (defined by a line drawn through the pyridine-N atoms). This H-bonding motif is dominant

8
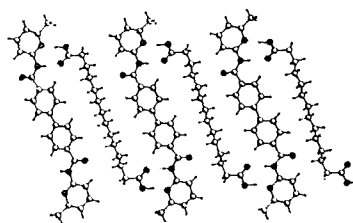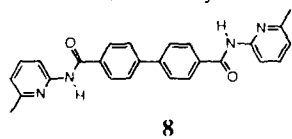
Figure 5

and is retained despite changes in size of the molecular components. Indeed, the extent of the slip angle can be varied in a systematic and predictable way by changing the size matching of the diamide and diacid. Shortening the diamide spacer from biphenyl to naphthyl (~2.2Å shorter) leads to a decrease in the slip angle to 60° (Figure 6). A subsequent shortening of the diacid to 1,8-octane di-carboxylic acid increases the slip angle to the point where the two subunits are well-matched and the angle is ~90° (Figure 7). In this work we have identified a recurring hydrogen bond packing pattern that survives changes in the component structure. Such persistent motifs can form the basis of a wide range of functional and redox active polymeric aggregates.
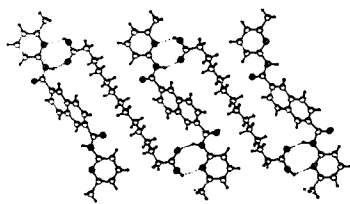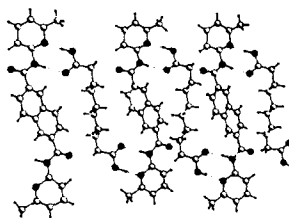
Figure 6   Figure 7

2.2.3 Based on Hydrogen Bonded Helices

The bis-amide 9 formed from 2-aminopicoline and isophthalic acid is also expected to form polymeric aggregates with dicarboxylic acids of the types similar to that seen in Figures 5-7. However, when 9 takes a convergent conformation of the two aminopyridines (as shown) two carboxylic acids can only bind in a non-planar or helical manner (as shown in 10).Propagation of this arrangement would lead to an extended, self-assembled helix. The complex between 9 and pimelic acid shows precisely this remarkable structure. A helix is formed composed of alternating

9   **10**
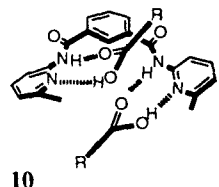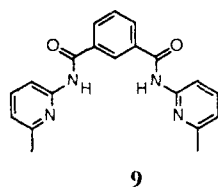
receptor-diacid components (Figure 8). Each molecules of 9 stacks parallel to the one above and the one below with an interplane distance almost 8Å. A critical stabilizing feature in the crystal is the intercalation of the isophthaloyl rings of one helix into the space between the receptors in a second helix. This intercalation can only occur if there is sufficient distance between the isophthaloyl planes. The interplane distance will be controlled by the length of the diacid and shortening the diacid should eliminate the possibility of intercalation stabilization of the crystal. Figure 9 shows the crystal structure of the complex between 9 and glutaric acid. A 'squashed' helix structure is taken up with rotation of one C-CO bond by 180° to form a more planar arrangement capable of stacking between the sheets.[27]
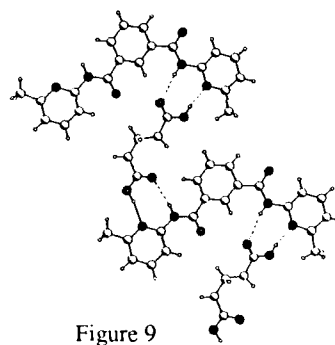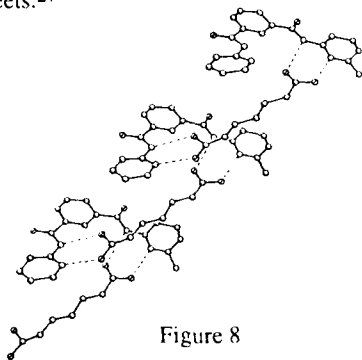
Figure 8   Figure 9

References

1.   Casassa, E. Z.; Sarquis, A. M.; Van Dyke, C. H. *J. Chem. Ed.* 63, 1986, 57.
2.   Cheng, A. T. Y.; Rodriguez, F. *J. Appl. Polym. Sci.* 26, 1981, 3895.
3.   Shibayama, M.; Sato, M.; Kimura, Y.; Fujiwara, H.; Nomura, S. *Polymer* 29, 1988, 336.
4.   Righetti, P. G.; Snyder, R. S. *Appl. Theor. Electrophor.* 1, 1988, 53.
5.   Nickerson, R. F. *J. Appl. Polym. Sci.* 15, 1971, 111.
6.   Deuel, H.; Neukom, H. *Makromol. Chem.* 3, 1949, 13.
7.   Deuel H.; Neukom, H.; Weber, F. *Nature* 161, 1948, 96.

8.   Connor, J. M. *J. Inorg. Nucl. Chem.* 32, **1970**, 3545.
9.   Hoffstetter-Kuhn, S.; Paulus, A.; Gassmann, E.; Widmer, H. M. *Anal Chem.* 63, **1991**, 1541.
10.   For a review see Hamilton, A. D. Advances in Supramolecular Chemistry, Gokel, G. Ed. Jai Press, 1991, p. 1.
11.   Pant, N.; Hamilton, A. D. *J. Am. Chem. Soc.* **1988**, *110*, 2002.
12.   Chang, S. K.; Hamilton, A. D. *J. Am. Chem. Soc. 1988, 110,* 1318. Chang, S. K.; Fan, E.; Van Engen, D.; Hamilton, A. D. *J. Am. Chem. Soc.* **1991**, *110*, 1318.
13.   Garcia-Tellado, F.; Goswami, S.; Chang, S. K.; Geib, S.; Hamilton, A. D. *J. Am. Chem. Soc.* **1990**, *112,* 7393.
14.   S. Goswami, D. Van Engen, and A. D. Hamilton, *J. Am. Chem. Soc.* **1989**, *111*, 3425. Muehldorf, A. V.; Van Engen, D.; Warner, J. C.; Hamilton, A. D. *J. Am. Chem. Soc.* **1988**, *110,* 6561.
15.   Tecilla, P.; Chang, S. K.; Hamilton, A. D. *J. Am. Chem. Soc.* **1990**, *112,* 9586.
16.   Tecilla, P.; Dixon, R.P.; Slobodkin, G.; Alavi, D. S.; Waldeck, D. H.; Hamilton, A. D. *J. Am. Chem. Soc.* **1990**, *112,* 9408.
17.   Diesenhofer, J.; Epp, O.; Miki, K.; Huber, R.; Michel, H. *J. Mol. Biol.* **1984**, *80,* 385.
18.   Hopfield, J. J.; Onuchic, J. N.; Beratan, D. N. *J. Phys. Chem.* **1989**, *93,* 6350.
19.   For alternative approaches to photoinduced electron transfer between non-covalently associated subunits see Harriman, A.; Kubo, Y.; Sessler, J. L.*J. Am. Chem. Soc.* **1992**, *114,* 388., Aoyama, Y.; Asakawa, M.; Matsui, Y.; Ogoshi, H. *J. Am. Chem. Soc.* **1991**, *113,* 6233.
20.   Seto, C. T.; Whitesides, G. M. *J. Am. Chem. Soc.* **1991**, *113,* 712.
21.   Ducharme, Y.; Wuest, J. D. *J. Org. Chem.* **1988**, *53,* 5789.
22.   Etter, M. C. *Acc. Chem. Res.* **1990**, *23,* 120. Leiserowitz, L.; Hagler, A. T. *Proc. R. Soc. Lond. A.* **1983**, *388,* 133.
23.   Leiserowitz, L.;Tuval, M. *Acta Cryst.* **1978**, *B34,* 1230.
24.   Zerkowski, J. A.; Seto, C.; Wierda, D. A.; Whitesides, G. M. *J. Am. Chem. Soc.* **1990**; *111,* 9025.
25.   Lehn, J. M.; Mascal, M.; DeCian, A.; Fisher, J. *J. Chem. Soc. Chem. Commun.* **1990**, 479.
26.   Geib, S. J.; Hirst, S. C.; Vicent, C.; Hamilton, A. D. *J. Chem. Soc. Chem. Comm.* **1991**, 1283.
27.   Geib, S. J.; Vicent, C.; Hamilton, A. D. Unpublished work.

Three-dimensional phase-strain model for embedded optical fiber sensors: experimental verification and applications to different sensor types

J. S. Sirkis

University of Maryland, Department of Mechanical Engineering, College Park, Maryland 20742, 301-405-5265

ABSTRACT: This paper describes a generalized approach to modeling the phase change in interferometric optical fiber sensors as a function of applied strain and temperature fields. The model is combined with theory of elasticity solutions transversely isotropic host materials to show how the new model is different from the classic Butter and Hocker approach. Experiments verify the new model approach.

INTRODUCTION

This paper describes a generalized approach to modeling the phase change in interferometric optical fiber sensors as function of applied strain and temperature fields. The general approach is then applied to Mach-Zehnder, Michelson, intrinsic and extrinsic Fabry-Perot, polarimetric, dual-mode and Bragg grating optical fiber sensors. The models for these sensors are then combined with theory of elasticity solutions for thermomechanical loading of both isotropic and transversely isotropic host materials. The predictions of the unified model are compared to those of the Butter and Hocker approach to illustrate the basic differences between the two when they are applied to embedded sensors. It is shown that all sensor types, with the exception of extrinsic Fabry-Perot sensors, have significant dependence on transverse strains, and that in many load cases the transverse strain dominates the sensor's output. In the process of applying the unified theory, new physical models for polarimetric and Bragg grating sensors are developed, the concept of optical fiber senor sensitivity is redefined, and the question of what exactly embedded optical fiber sensors are measuring is addressed.

UNIFIED MODEL

While it is not feasible to present a detailed development of the model under the page constraints of this manuscript, it is possible to explain the basic features of the unified model, and how it differs from the Butter and Hocker approach. The unified development provides a method for deriving the phase-strain-temperature relations for any interferometric optical fiber sensor. In all cases the phase change is a function of a linear combination of the three principle strains and the temperature all integrated along the sensing section of the optical fiber. This means that the sensor responds to both axial and transverse strains transferred from the host to the fiber. The Butter and Hocker model assumes that the transverse strains are simply Poisson contractions. This is true for surface mounted sensors but not for embedded sensors. When the fiber is embedded, it interacts with the host material to determine the strain state in the fiber (and in the host). The strain in the fiber is a complicated function of the fiber <u>and</u> host material properties. The Butter and Hocker approach assumes that the strain state in the fiber is only a function of the fiber material properties. To illustrate the differences between these two modeling approaches consider a Mach-Zehnder fiber sensor embedded in the following host composite materials: 1) Plane strain subjected to a uniform temperature distribution (Fig. 1).   2) Plane strain subjected to radial compressive stress in the far field (Fig. 2), 3) Generalized plane strain uniaxial tension with a known axial   strain (Fig. 3), 4) Case 2 under the generalized plane strain assumption, 5) Generalized plane strain subjected to transverse tension (Fig. 4).   In all cases the fiber sensor path is straight and parallel to the reinforcing fibers, the fiber is uncoated, and the reference fiber is unstrained. The first two load cases are chosen to illustrate the worst case scenario (plane strain) for both thermal and mechanical loading. The third case is chosen to show that sometimes the unified and Butter and Hocker phase-change models can give similar results, and also because it is a common specimen used to test structurally embedded optical fiber sensors. The final two cases were chosen since the generalized plane strain scenario is more realistic for optical fiber sensors. The last case, in particular, is illustrative because the loading is not axisymmetric. Data is shown only for the Mach-Zehnder sensor but the response of intrinsic Fabry-Perot, Michelson, and Bragg grating sensors can be inferred from the Mach-Zehnder sensor data since its reference fiber is unstrained. Table 1 shows the relative error between the two phase change approaches for the

Mach-Zehnder (MZ), Polarimetric (P), dual-mode (DM), and extrinsic Fabry-Perot (EFP). Relative error is defined as 100x(unified model - Butter and Hocker model)/unified model.

The most striking result in Table 1 is that the extrinsic Fabry-Perot sensor yields the same result whether it is surface mounted or embedded as attested to by the zero error between the unified approach and Butter and Hocker models. Recall that Butter and Hocker's approach is analogous to assuming the sensor is surface mounted. The phase sensitivities for Case 3 are unique in that both phase-change models yield very similar or identical results for all of the sensors.

CONCLUSION

A unified approach to phase-strain-temperature relationships for optical fiber sensors has be presented. This approach is valid for all interferometric optical fiber sensors experiencing arbitrary strain fields and configured in arbitrary geometric paths. The unified approach has been applied to all popular sensor types and has been compared the classic Butter and Hocker approach. The combination the phase-change models shows that in all cases, except for the extrinsic Fabry-Perot sensor, the Butter and Hocker model leads to false interpretation of the embedded sensor data. Experimental evidence not shown in this manuscript verifies the theoretical findings.
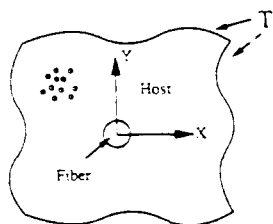
Figure 1.
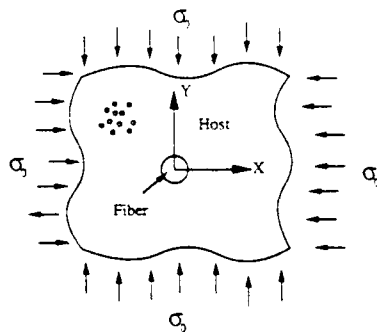
Figure 2.
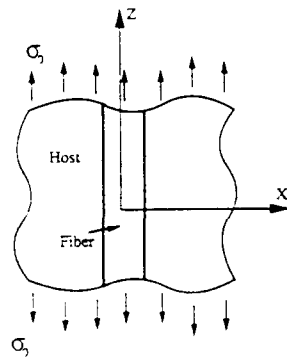
Figure 3.
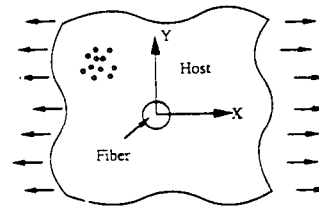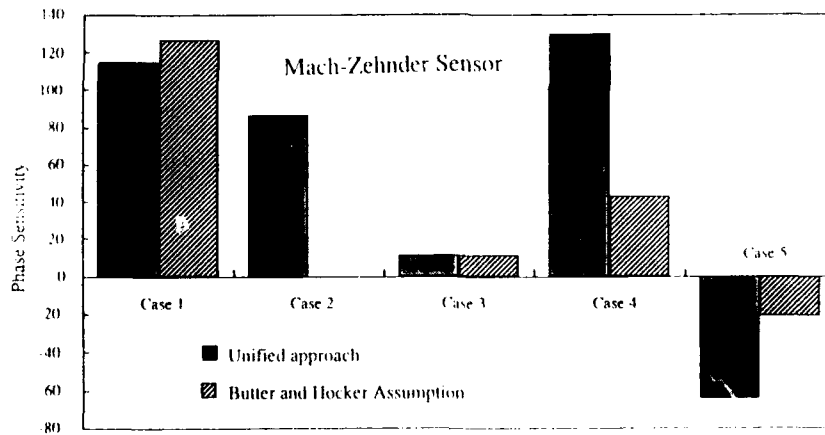
Figure 4.

Figure 5.

Table 1.

	MZ	P	DM	EFP
Case 1	-10.5	0	78.2	0
Case 2	100	0	10	0
Case 3	0.3	0	0.3	0
Case 4	66.6	0	66.6	0
Case 5	66.6	99.9	66.6	0

Spatially weighted fiber optic sensors for smart materials and structures

K. A. Murphy, B. R. Fogg and R. O. Claus, Fiber & Electro-Optics
Research Center, Bradley Department of Electrical Enginering,
Virginia Tech, Blacksburg, VA   24061 and A. M. Vengsarkar, AT&T Bell
Laboratories, Murray Hill, NJ

ABSTRACT: Two-mode, elliptical-core optical fibers are
demonstrated in weighted, distributed and selective mode
filtering applications on laboratory structural test articles.   We
demonstrate the use of tapered-sensitivity two-mode fiber
sensors and the performance of chirped two-mode fiber gratings
as spatial modal sensors for structural analysis.

1. INTRODUCTION

Two-mode, elliptical-core (e-core) optical fibers with stable output
intensity patterns were first used as strain gages and modal filters
in 1987 by Shaw and co-workers.[1,2] Murphy *et al.* subsequently
demonstrated that such proposed e-core sensors can be ruggedized,
made insensitive to external environmental perturbations along the
lengths of the lead-in and lead-out fibers, and used for the detection
of vibration in flexible metal and composite beams.[3] Vensarkar *et al.*
extended this work to investigate the use of such optical fiber
methods specifically for the weighted spatial analysis of
structures.[4] This paper reviews recent results in light of those
previous two contributions.

2. TWO-MODE E-CORE FIBER SENSORS

Two-mode, e-core "modal domain" fiber sensors have been
implemented during the past four years for applications requiring
well defined gage length sensors where the gage length is several
centimeters to many meters long. The fiber sensor operates on the
principle of differential phase modulation between the LP_{01} and
LP_{11}^{even} modes and consists of three segments of different fibers
spliced together.[3] An e-core, single-mode fiber is used as the lead-
in fiber, a two-mode e-core fiber forms the sensing section and a
circular-core multimode fiber acts as the lead-out fiber. The lead-in
fiber preserves the polarization of the input laser signal and allows
the accurate coupling of the proper input signal to the center active

sensing section. The sensing section allows the propagation of only two modes with different propagation coefficients, and the interference between these two modal fields creates a beat interference at the end of the sensing section. A circular-core multimode fiber is spliced to the sensing section and transmits a signal proportional to the strain integrated along the length of the sensing section to output detection electronics.

3. WEIGHTED FIBER SENSING

The introduction of weighted fiber sensitivity may be introduced along the length of the sensing section of the fiber using several methods, just as weighted piezoelectric film sensors may be shaped to analyze different vibrational modal characteristics.[5] The potential use of weightings in fiber sensors for such applications has been considered in particular by Lindner and coworkers.[6]

Effective weighting may be accomplished by one of three methods. First, the optical fiber sensors may be attached to the test structure in particular geometrical patterns. Analysis indicates that the output of such sensors is proportional to the difference in the slopes of the structure at the endpoints of the sensor.[5] Thus, sensors may be weighted in their sensitivity to particular structural modes by properly placing them on the structure to be interrogated. For example, the data shown in Figure 1 demonstrates that the appropriate positioning of an optical fiber sensor on a vibrating beam may lead to appropriate modal filtering. Here, the fiber has been placed on a clamped-clamped beam in such a way that the second order vibrational mode is clearly suppressed.[4]

Second, the sensitivity of the fiber may be modified along its length in such a way that output signals proportional to certain vibrational modes may be surpressed with respect to those due to other vibrational modes, specifically modes with particle motion profiles which are similar to the weighting profile of the fiber. Such gradual fiber sensitivity weightings may be achieved by longitudinally grading the V-number of the fiber, and thus modifying the modal propagation constant difference along the fiber sensor length. Figure 2 shows the output of piezoelectric and tapered optical fiber sensors for vibration in a clamped-clamped beam; note the suppression of the second and third modes.

Third, gratings may be written along the length of fibers, and the spatial periodicity of the gratings may be chirped to produce a weighted sensing function profile. Figure 3 shows the output of a
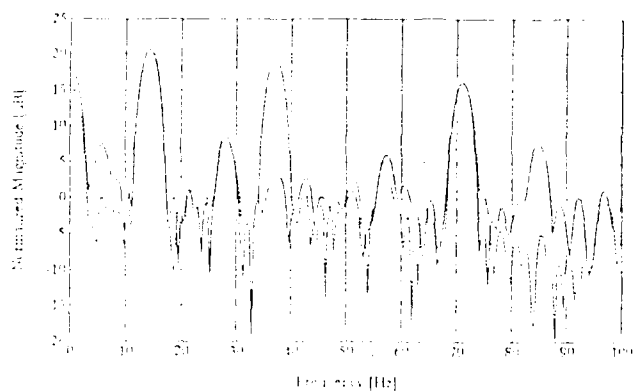
Fig. 1. Fourier transform of signals from fiber sensor (solid) placed along discrete section of a clamped-clamped beam and piezoelectric patch (dashed). Second mode information is suppressed.[4]
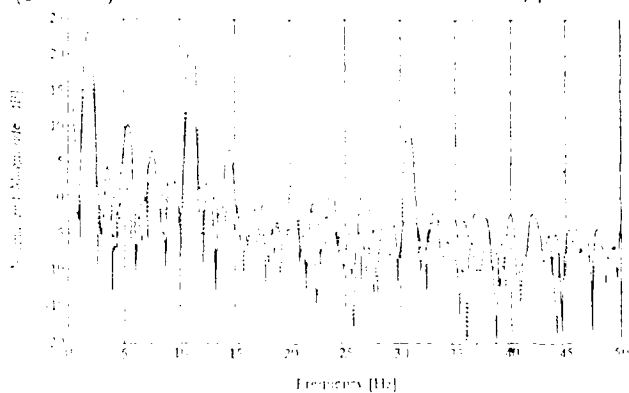
Fig. 2. Fourier transform of output signals from tapered fiber sensor (solid) and piezoelectric patch (dashed) on clamped-free beam.[4]
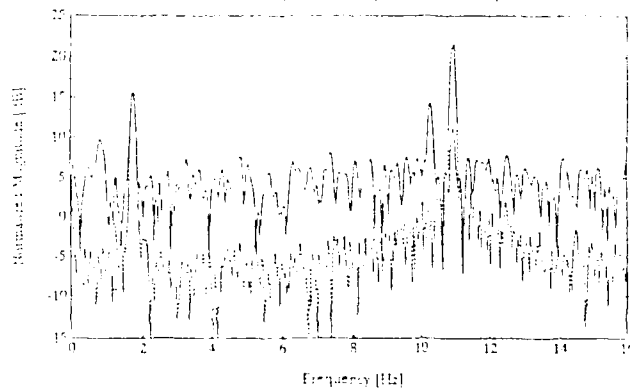
Fig. 3. Fourier transform of signals from grating-induced, first-mode enhanced e-core, two-mode fiber sensor (solid) and piezoelectric sensor (dashed) attached to beam. Second mode fiber sensor signal here is suppressed by 10 dB compared to signal of conventional e-core sensor.[4]

weighted grating-based sensor versus the performance of a conventional piezoelectric sensor. Note the suppression of the second order mode information.

4. REMARKS

Several methods are available for the effective weighting of optical fiber sensor sensitivity along the length of moderately long gage length sensors. This summary has briefly discussed three such methods. The reader is referred to the references for detailed information.

5. ACKNOWLEDGEMENTS

6. REFERENCES

[1] B. Y. Kim, J. N. Blake, S. Y. Huang and H. J. Shaw, "Use of highly elliptical core fibers for two-mode fiber devices," *Opt. Lett.*, vol. 12, pp. 739-734, 1987.

[2] B. Y. Kim, J. N. Blake, S. Y. Huang and H. J. Shaw, "Strain effects on highly elliptical core fibers," *Opt. Lett.*, vol 12, 732-734, 1987.

[3] K. A. Murphy, M. S. Miller, A. M. Vengsarkar and R. O. Claus, "Elliptical-core, two-mode optical fiber sensor implementation methods," *J. Lightwave Technol.*, vol. 8, pp. 1688-1696, 1990.

[4] A. M. Vengsarkar, K. A. Murphy, B. R. Fogg, W. V. Miller, J. A. Greene and R. O. Claus, "Two-mode elliptical-core weighted fiber sensors for vibration analysis," Proc. SPIE O/E Fibers (Boston, MA), September 1991.

[5] C. K. Lee and F. C. Moon, "Modal sensors/actuators," *J. Appl Mech.*, vol. 57, pp. 434-441, 1990.

[6] D. K. Lindner and K. Reichard, "Weighted distributed effect sensors for smart structure applications," this volume.

Single-fiber, dual modal-domain sensors

Christian V. O'Keefe

Martin Marietta Laboratories, 1450 S. Rolling Rd, Baltimore, MD 21227

ABSTRACT: Single-fiber sensors, such as modal-domain and polarimetric sensors, while useful as strain sensors, are also very susceptible to temperature effects. This simultaneous response to temperature and strain has been exploited to create a single-fiber sensor using a single light source that can measure both temperature and strain independently. Two modal-domain sensors were created along the two orthogonal axes of a two-mode polarization-preserving fiber. Since each sensor responds differently to temperature and strain, each generates an independent output, from which both temperature and strain can be extracted.

1. INTRODUCTION

Many different types of fiber optic sensors that measure strain, vibration, or pressure have been proposed and tested by various researchers such as Claus et al (1988), Valis et al (1989), and Lee et al (1989). Some of these have used single-fiber approaches based on mode-mode interference (modal domain sensors) or polarization modulation (polarimetric sensors) such as those from Grossman et al (1989) and Layton et al (1979). To determine the suitability of different fibers for sensing applications, various fibers were tested for their ability to function as modal domain and polarimetric sensors under dynamic strain conditions by O'Keefe et al (1991) and under dynamic temperature variations in this paper.
These tests were useful for determining sensor sensitivity to strain and temperature for particular optical fibers and for sensor type--modal domain or polarimetric. These characterization tests also were useful for the development of dual sensors -- those that use both the modal domain and polarimetric effects in a single fiber or those that have two modal domain sensors in the same fiber. The development of a dual sensor that has two modal domain sensors within the same fiber resulted in two sensors each of which has a different response to strain and temperature changes. This provides the ability to develop sensors which can limit ambiguities in determining the strain direction, provide higher strain resolution and a large dynamic range, and, most importantly, allow one to possibly separate strain from temperature. Such a sensor was created and used to perform these functions.

2. BACKGROUND

Modal domain and polarimetric fiber-optic sensors rely on differential phase velocities of two or more modes propagating within a single fiber. This single-fiber approach does not require separating a beam into a sensing fiber and a reference fiber with subsequent recombination of the two beams. Instead, the beam travels in a single fiber which is exposed to the parameters that are being measured simultaneously be they temperature, strain, or other phenomena, and a separate isolated "reference" fiber is not needed. The beam travels down the fiber and is separated into several modes, each of which travels with a different phase velocity. When the modes are recombined, they produce an interference pattern, which exhibits intensity changes as a function of the phase difference between the different

modes. The phase velocities of the different modes are affected by a variety of perturbations such as strain and temperature changes in the optical fiber.

If the differential propagation constants inherent in a birefringence fiber can be combined with a modal domain sensor, two independent outputs can be generated. This arrangement offers the possibility of solving for two parametric influences on the fiber such as strain and temperature. One approach was developed by Vengsarkar et al (1990) whereby an E-core fiber sensor was operated at two different wavelengths, resulting in the construction of a modal domain and a polarimetric sensor within the same fiber. Initial results with accuracies of +- 10 µm/m and +- 5°C for strain and temperature measurements, respectively were very promising. Some drawbacks include the need for two lasers, wavelength separation filters, and the optical configuration for injecting the light from the two lasers into one fiber. The dual sensor method, where two modal domain sensors are created within one birefringent optical fiber to perform simultaneous measurements of strain and temperature, can be implemented with only one laser which can be pigtailed to the end of the fiber.

3. STRAIN AND TEMPERATURE CHARACTERIZATION OF FIBERS

When two modes $\vec{E}_{l', m'}$, η' and $\vec{E}_{l'', m''}$, η'' travel within a birefringent fiber, they do so with different propagation constants such that upon recombination onto a photodetector the light intensity and hence the detector output level is a function of the phase difference between the two modes. When the optical fiber sensor is perturbed through events such as strain or temperature changes, the phase difference and hence the output of the sensor will change according to

$$\Delta\Theta = \int_{l.1}^{l.2} \beta \, dL + \int_{l.1}^{l.2} \frac{\partial\beta}{\partial\varepsilon} \, dL + \int_{l.1}^{l.2} \frac{\partial\beta}{\partial T} \Delta T \, dL + \int_{l.1}^{l.2} \beta \frac{\partial\varepsilon}{\partial T} \Delta T \, dL \qquad (1)$$

where β is the difference between the propagation constants of the two modes and L is the length of the sensing portion of the fiber. The final change in phase is therefore an integration of the perturbations over the length of the fiber sensor. It is also a function of the change in the characteristic parameter with strain $\partial\beta/\partial\varepsilon$ and with temperature $\partial\beta/\partial T$, and the change in length with temperature $\partial\varepsilon/\partial T$, which is also known as the coefficient of thermal expansion (CTE). This equation can be simplified if it can be assumed that the optical fiber sensor is uniformly loaded both mechanically and thermally. The phase change can then be written as:

$$\Delta\Theta = \beta \, \Delta L + \frac{\partial\beta}{\partial\varepsilon} \Delta L + \frac{\partial\beta}{\partial T} L \, \Delta T + \beta \frac{\partial\varepsilon}{\partial T} L \, \Delta T \qquad (2)$$

or with the common variables grouped together:

$$\Delta\Theta = \left[\beta + \frac{\partial\beta}{\partial\varepsilon}\right] \Delta L + \left[\frac{\partial\beta}{\partial T} + \beta \frac{\partial\varepsilon}{\partial T}\right] L \, \Delta T \qquad (3)$$

Substituting the coefficients $\Lambda'_{\Delta Li}$ and $\Lambda'_{L\Delta Ti}$ defined by

$$\frac{2\pi}{\Lambda_{\Delta Li}} = \beta_i + \frac{\partial\beta_i}{\partial\varepsilon} \quad (4a) \qquad\qquad \frac{2\pi}{\Lambda_{L\Delta Ti}} = \frac{\partial\beta_i}{\partial T} + \beta_i \frac{\partial\varepsilon}{\partial T} \quad (4b)$$

equation (3) can be rewritten as

$$\Delta\Theta_i = \frac{2\pi}{\Lambda_{\Delta Li}} \Delta L + \frac{2\pi}{\Lambda_{L\Delta Ti}} L \, \Delta T \qquad (5)$$

As seen in Eq. 5, the output of polarimetric and modal domain sensors is more a function of the total stretching or displacement ΔL than the actual strain. The strain does manifest itself in the output since the displacement is equal to an integration of the strain over the sensing portion of the optical fiber. The polarimetric displacement sensitivity of the fibers were tested first; the results are given in O'Keefe et al (1991). The temperature sensitivity of the same fibers is shown in Table I. As shown in Eq. 5, the outputs of the polarimetric and modal domain sensors are a function of the temperature changes and the length of the sensor exposed to these temperature changes $(L \Delta T)$. Therefore, characteristic temperature parameters for the optical fiber sensors are expressed in terms of the product of the temperature and the length of exposed fiber (°C-m).

TABLE I. POLARIMETRIC TEMPERATURE SENSITIVITY OF TESTED
POLARIZATION-PRESERVING FIBERS

Fiber Type	Length (m)	Temperature Change (°C)	°C-m/Fringe
3M FSHB3611	0.645	27.7	1.467
York HB800	4.354	28.6	1.196
York HB1250	5.43	26.4	5.655

The modal domain sensitivities of the birefringent fibers were measured by performing each test with the input light injected along each fiber polarization axis. In each case, the output was observed through a polarizer for modal domain response and for coupling effects from one polarization to the other. The coupling effects were found to be very minimal. The results of the modal domain responses under displacement are given in O'Keefe et al (1991) and under temperature changes are shown in Table II.. Again, the characteristic fiber sensor parameters are expressed in terms of the displacement (ΔL) and temperature*length $(L \Delta T)$ or (°C-m).

TABLE II. MODAL DOMAIN TEMPERATURE SENSITIVITY OF TESTED FIBERS.

Fiber Type	Polarization State	Length (m)	Temperature Change (°C)	°C-m/Fringe
York HB 800	First	4.354	25.1	20.017
	Second	4.354	30.2	12.990
York HB1250	First	5.43	28.6	8.540
	Second	5.43	28.3	13.234

4. DESIGN OF DUAL SENSOR

The results of the modal domain sensor testing clearly showed the effects of polarization on strain sensitivity in the polarization- preserving fibers. With this knowledge, a birefringent modal domain sensor in which two modal domain sensors were effectively created by using a single fiber and a single light source was constructed. Because of the diffe~ential phase velocity between the two birefringent axes in a polarization-preserving fiber, the two modal domain sensor outputs can be used for strain direction determination or separation of temperature from strain effects. This concept is shown in Figure 1 Although a gas laser was

used in the experiments, a laser diode can also be used with its advantages in terms of size, weight and power consumption. This design also can be modified to create an all optical-fiber sensor.
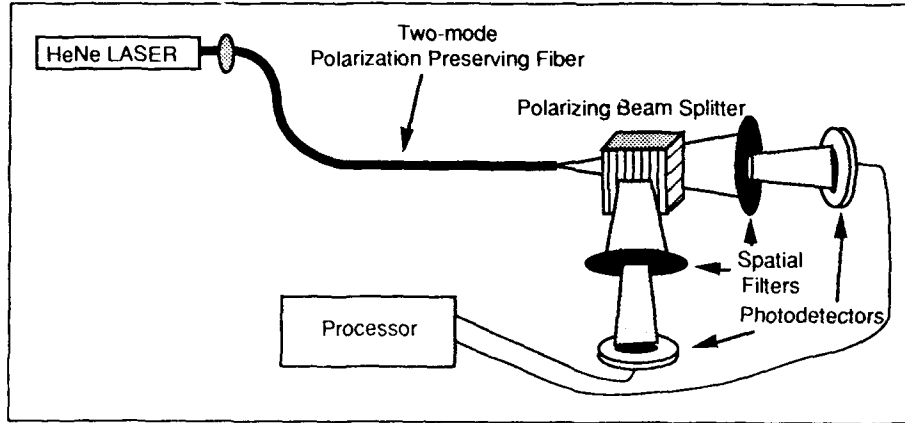
Figure 1. Dual sensor

If Eq. 5 is expanded to encompass both sensor outputs, the following two equations result:

$$\Delta\Theta_1 = \frac{2\pi}{\Lambda'_{\Delta L1}} \Delta L + \frac{2\pi}{\Lambda'_{L\Delta T1}} L\,\Delta T \quad (6a) \qquad \Delta\Theta_2 = \frac{2\pi}{\Lambda'_{\Delta L2}} \Delta L + \frac{2\pi}{\Lambda'_{L\Delta T2}} L\,\Delta T \quad (6b)$$

As was done with the polarimetric/modal domain sensor mentioned earlier (Vengsarkar et al 1990), the modified characteristic parameters $\Lambda'_{\Delta Li}$ and $\Lambda'_{L\Delta Ti}$ defined by the relations in Eqs. 4 and 6 can be expressed in matrix form as:

$$\begin{bmatrix} \Delta\Theta_1 \\ \Delta\Theta_2 \end{bmatrix} = \begin{bmatrix} \dfrac{2\pi}{\Lambda'_{\Delta L1}} & \dfrac{2\pi}{\Lambda'_{L\Delta T1}} \\ \dfrac{2\pi}{\Lambda'_{\Delta L2}} & \dfrac{2\pi}{\Lambda'_{L\Delta T2}} \end{bmatrix} \begin{bmatrix} \Delta L \\ L\Delta T \end{bmatrix} \qquad (7)$$

or

$$\overline{\Delta\Theta} = \Lambda'\,\overline{P} \quad (8) \qquad \text{where} \qquad \overline{P} = \begin{bmatrix} \Delta L \\ L\Delta T \end{bmatrix} \qquad (9)$$

$$\Lambda' = \begin{bmatrix} \dfrac{2\pi}{\Lambda'_{\Delta L1}} & \dfrac{2\pi}{\Lambda'_{L\Delta T1}} \\ \dfrac{2\pi}{\Lambda'_{\Delta L2}} & \dfrac{2\pi}{\Lambda'_{L\Delta T2}} \end{bmatrix} \quad (10)\text{ and} \qquad \overline{\Delta\Theta} = \begin{bmatrix} \Delta\Theta_1 \\ \Delta\Theta_2 \end{bmatrix} \quad (11)$$

As a result, the matrix Λ' can be inverted to yield a set of linear equations which will provide the temperature and displacement (or strain) as a function of the change in phase of the two outputs of the dual sensor:

$$\overline{P} = \Lambda'^{-1}\,\overline{\Delta\Theta}. \qquad (12)$$

Accurate results are theoretically possible if the following assumptions hold true: 1) there is no cross-sensitivity between the two parameters or polarizations, 2) the matrix Λ' components can be determined with a very high degree of accuracy, 3) the fiber response remains linear, and 4) the phases of the output signals can be measured with a very high degree of accuracy. Some degree of tolerance for variabilities in the matrix coefficients and the output phase measurements is achieved if one has a well-conditioned matrix. The condition of the matrix is a function of the strain and temperature sensitivities of the optical fiber and are inherent to that fiber type and batch. In the case of a badly conditioned matrix, small errors in determining the phase outputs of the sensor will result in large errors in determing the strain and temperature. One method for comparing the stability of the matrices of various fibers and sensor types is to calculate the reciprocal of the condition number (rcond) of each matrix as was done by Vengsarkar et al (1990). If the matrix is well conditioned, rcond is near 1.0 whereas if the matrix is badly conditioned, rcond is closer to zero. Upon applying the rcond using 1-norm for dual modal domain sensors, it was discovered that the matrix coefficients of the fibers tested here all resulted in il--conditioned matrices. Nonetheless, a dual modal-domain sensor was still successfully created using one of these fibers, specifically the York HB800, an 850nm polarization preserving fiber.

5. TEST OF DUAL MODAL-DOMAIN SENSOR AND RESULTS

The dual modal domain sensor that was created with the configuration shown in Figure 1 allowed the application of strain and/or heat. First, the sensor was strained by various amounts at a constant temperature, the phase of the two outputs was determined and Eq. 15 was used to calculate the ΔL and temperature. Similarly the sensor was heated while the strain was kept constant and the ΔL and temperature were calculated. Finally, both strain and temperature were varied and were calculated from the sensor outputs. The results are summarized in table III. The directly measured values for ΔL and ΔT are given in the columns labelled "Exp." and the values calculated from the outputs of the sensor are given in the column labelled "Calc." Accuracies for measuring the parameters and phases were $\Delta L = \pm 5 \, \mu m, \Delta T = \pm 0.1°C$, and $\Delta \Theta = \pm 0.8$ rads.

TABLE III. RESULTS OF STRAIN AND TEMPERATURE SEPARATION.

Test No.	Exp. ΔL	Exp. ΔT	$\Delta \Theta$ (rads) Pol 1	$\Delta \Theta$ (rads) Pol 2	Calc. ΔL	Calc. ΔT
1	890 μm	0.0°C	14.14	21.99	723 μm	0.6°C
2	930 μm	0.0°C	15.71	27.23	958 μm	-0.9°C
3	1655 μm	0.0°C	29.85	49.48	1696 μm	-0.5°C
4	0 μm	9.6°C	18.85	11.78	-2.5 μm	10.4°C
5	0 μm	3.8°C	6.28	3.93	-0.8 μm	3.5°C
6	0 μm	5.3°C	9.42	6.28	20 μm	5.0°C
7	500 μm	1.0°C	7.85	11.78	378 μm	0.6°C
8	1000 μm	5.9°C	24.35	29.85	803 μm	5.4°C
9	1000 μm	10.2°C	40.84	42.41	926 μm	13.2°C
10	250 μm	3.9°C	11.78	11.78	241 μm	4.1°C

6. CONCLUSIONS

It can be seen that the dual modal-domain sensor does have the ability to measure both strain and temperature. As shown in Table III, it performs best when it is sensing strain or temperature individually, but can adequately measure and separate both perturbations simultaneously. The concept behind this type of sensor is demonstrated here, and the accuracy can be improved by using of a different optical fiber, one whose characteristics will result in a better conditioned Λ' matrix. Even with the non-ideal optical fiber used in these tests, accuracy within several degrees Celsius and several hundred microns was achieved.

The temperature and strain perturbation results that were generated also were very useful for the determination of the temperature sensitivity of various fibers and sensor types combinations. These sensitivity results allow one to choose a fiber with a desired strain and temperature response for a specific application.

7. REFERENCES

Claus, R.O., S. Sudeora, K.A. Murphy, and K.D. Bennett, 1988. "Low Profile Optical Time Domain Fiber Sensors for Materials Evaluation," Proc. Rev. of Progress in QNDE, 8B, pp. 1437-1442.

Grossman, B., T. Alavie, F. Ham, J. Franke, and M. Thursby, 1989. "Fiber Optic Sensor and Smart Structures Research at Florida Institute of Technology," SPIE Fiber Optic Smart Structures and Skins II, 1170, pp. 123-135.

Layton, M.R. and J.A. Bucaro, 1979. "Optical Fiber Acoustic Sensor Utilizing Mode-Mode Interference," Applied Optics, 18(5):pp. 666-670.

Lee, C.E., Taylor, H.F., Markus, A.M., and Udd, E, 1989. "Optical Fiber Fabry-Perot Embedded Sensor," Optics Letters, 14(21):1225.

O'Keefe, C.V. and Djordjevic, B.B., 1991. "Characterization of series of modal domain and polarimetric fiber optic sensors," Proc. Fiber Optic Sensor based Smart Materials & Structures Workshop, 1991.

Valis, T., E. Tapanes, and R.M. Measures, 1989. "Localized Fiber Optic Strain Sensors Embedded in Composite Materials," SPIE Fiber Optic Smart Structures and Skins II, 1170, pp. 495-504.

Vengsarkar, Ashish M., W. Graig Michie, Ljilja Jankovic, Brian Culshaw, and Richard O. Claus, September 1990. "Fiber Optic Sensor for Simultaneous Measurement of Strain and Temperature," SPIE Fiber Optic and Laser Sensors VIII, 1367, pp. 249-260.

Weighted distributed-effect sensors for smart structure applications

Douglas K. Lindner

Dept of Elec. Eng., Virginia Tech, Blacksburg, VA 24061, and

Karl M. Reichard

Applied Research Lab, Penn State, P.O. Box 30, State College, PA 16804

ABSTRACT

Recently there has emerged a new class of sensors for structures such as piezoelectric laminate PVDF film, modal domain optical fiber sensors, and holographic sensors. These sensors have a unique capability in that they can be fabricated to locally alter their sensitivity to the measurand. Thus, these sensors act as a spatial filters. Spatial filters can be configured to measure a wide variety of structural parameters which can not be measured directly with point sensors, including modal amplitudes and travelling waves. In this paper we discuss the model of these sensors for control system design. In particular, we model the fabrication error and show that this model identifies the limitations imposed by the sensor on the control system.

1. INTRODUCTION

The suppression of vibration in flexible structures using active feedback control has received a great deal of attention in the last decade. Current research has focused on the instrumentation required to implement these control laws, particularly, through the use of embedded sensors and/or actuators - so-called Smart Structures. Recently there has emerged a new class of sensors for structures which respond over a significant gauge length; we call these sensors distributed-effect sensors. The most well known sensor of this type is piezoelectric laminate PVDF film. Two other sensors in this class are modal domain optical fiber sensors (Murphy, et. al., 1990) and holographic sensors (Welch and Cox, 1991). In some cases, these sensors have a unique capability in that they can be fabricated to locally alter their sensitivity to the measurand. These sensors act as a spatial filter. This spatial filter is defined by the spatial variation of the sensitivity of the sensor; this function of space is called the weighting function. By various choices of the weighting function, these sensors can be configured to measure a wide variety of structural parameters which can not be measured directly with point sensors such as modal amplitudes and traveling waves. In this paper we discuss the incorporation of spatial filters into control systems for vibration suppression in flexible structures.

Spatial filtering has been demonstrated by Burke and Hubbard (1987), Lee and Moon (1990), and Collins, et. al. (1991) using PVDF film. In their simplest configuration, the use of modal domain optical fiber sensors in a control loop for vibration suppression of a cantilevered beam has recently been demonstrated (Cox and Lindner, 1991). Reichard and Lindner (1991) and Lindner and Reichard (1991) suggest several ways in which these sensors may be configured as spatial filters. Vengsarkar, et al. (1991) have demonstrated a modal domain sensor with varying core radius on a flexible beam.

One application is the use of spatial filters for the active suppression of acoustic radiation (Miller, et. al., 1990; Clark and Fuller, 1991; Lindner, et al.. 1991). Collins, et. al. (1991) used this same filter in a rate feedback system for disturbance rejection. Burke and Hubbard (1987) have demonstrated vibration suppression in a cantilevered beam using a spatially shaped actuator. Chaing and Lee (1989) used weighted PVDF film to excite and control only the first mode of a cantilevered beam. Lindner, et al. (1990, 1991) used a spatial filter to implement a low order compensator on a flexible beam.

In this paper we discuss the modeling of spatial filters for control applications. In particular, we develop a model which incorporates the effects of fabrication errors in the weighting function (Reichard and Lindner, 1992; Reichard, 1991). This model predicts the limitations of the control system imposed by the spatial filter.

In Section 2 spatial filters are discussed. Section 3 develops the model of a spatial filter. Section 4 introduces the effects of fabrication errors on the performance of the spatial filter. Section 5 has the conclusions.

2. DISTRIBUTED SENSOR MODELS

Definitions: A signal, $m(z,t)$, is called a <u>distributed signal</u> if it depends on time, t, and on a spatial variable, z, which belongs to a domain, Ω, of at least dimension 1. A sensor is a <u>distributed sensor</u> if the output of the sensor, $s(z,t)$, is a distributed signal proportional to the distributed signal, $m(z,t)$, of the structure. A sensor is a <u>distributed-effect sensor</u> if the output of the sensor, $y(t)$, is a scalar function of time derived from a distributed signal $m(z,t)$.

Typically, distributed-effect sensors are modeled as

$$y(t) = K\int_{\Omega} g(z)\, m(z,t)\, dz \qquad (2.1)$$

where K is a proportionality constant and $g(z)$ is a function which depends on the sensor placement and fabrication. In some cases the sensor can be physically altered in a controlled way such that the function $g(z)$ can be selected independently of the sensor.

Definitions: If the function $g(z)$ in (2.1) can be chosen independently of the sensor, then $g(z)$ is called a <u>weighting function</u>. Any device with an input of the distributed signal $m(z,t)$ and an output of the scalar signal $y(t)$ which can be modeled as in (2.1) where $g(z)$ is a weighting function is called a <u>spatial filter</u>.

Figure 2.1 shows a control loop containing a flexible structure and a spatial filter. Sometimes it is convenient to think of a distributed-effect sensor as two separate operations: a distributed sensor followed by a processing unit which performs the integral in (2.1). From this point of view, the weighting function performs a filtering function (Lee and Moon, 1989; Lindner, et al:., 1991). From another point of view, the weighting function is a distributed control gain (Burke and Hubbard, 1987; Lindner, et. al., 1990, 1991).

3. MODELING SPATIAL FILTERS

We assume that the distributed signals of a flexible structure can be described in terms of the mode shapes, $\psi_n(z)$, and the modal amplitudes, $\eta_n(t)$, as

$$m(z,t) = \sum_{n=1}^{N} \psi_n(z)\, \eta_n(t). \tag{3.1}$$

The modal amplitudes satisfy the reduced order model

$$\ddot{\eta}(t) + K\eta(t) = Q_1 u(t) \tag{3.2}$$

where $u(t)$ is the control input force. Substituting this expression in the model of a spatial filter (2.1) yields

$$y(t) = \sum_{j=1}^{N} \left[\int_{\Omega} g(z)\, \psi_j(z)\, dz \right] \eta_j(t) = \sum_{j=1}^{N} c_j \eta_j(t) = C\eta(t) \tag{3.3}$$

Secondly, assume that there exists another set of basis functions $\{\gamma_k(z)\}$ defined over the spatial domain Ω such that

$$g(z) = \sum_{k=1}^{N} g_k \gamma_k(z). \tag{3.4}$$

Define the N x N matrix Q by

$$Q = [q_{kj}], \quad q_{kj} = \int_{\Omega} \gamma_k(z)\, \psi_j(z)\, dz. \tag{3.5}$$

Then (3.6) can be written as

$$C = [c_j] = \left[\sum_{k=1}^{N} g_k \int_{\Omega} \gamma_k(z)\, \psi_j(z)\, dz \right] = [g_1\, g_2 \cdots g_N] Q = GQ. \tag{3.6}$$

Assume that Q is invertible. Then given C, G is computed from (3.6) and conversely. This result says that selecting the weighting function is the same as choosing the output matrix (3.3) of the reduced order model of the structure.

4. WEIGHTING FUNCTION ERRORS

When a spatial filter is fabricated, the weighting function which is achieved, $g_a(z)$, will differ from the desired weighting function, $g_d(z)$. As a result the performance of the spatial filter will be degraded over the nominal system performance. Let $g_d(z)$ is the desired weighting function and $g_a(z)$ is the achieved weighting function, then

$$n(z) = g_a(z) - g_d(z)$$

is the spatial filter error. The actual sensor output is given by

$$y_a(t) = \int_{\Omega} g_a(z) m(z,t)\, dt. \tag{4.1}$$

An error in the weighting function induces an error at the filter output. The signal

$$e(t) = y_a(t) - y_d(t)$$

is called the <u>sensor output error</u>. The sensor output error written in terms of the spatial filter is

$$e(t) = \int_\Omega \left[g_a(z) - g_d(z) \right] m(z,t) \, dz = \int_\Omega n(z) \, m(z,t) \, dz . \tag{4.2}$$

If the weighting error function, $n(z)$, is expressed in term of the basis functions of the structure

$$n(z) = \sum_{i=1}^{N} n_i \psi_i(z) \tag{4.3}$$

then the output of the spatial filter using the achieved weighting function is

$$y_a(t) = \left[C + \delta C \right] \eta(t) \quad \text{where} \quad \delta C = \left[n_1 \cdots n_N \right] Q . \tag{4.4}$$

The weighting error function has been investigated in both deterministic and stochastic settings (Reichard, 1991; Reichard and Lindner, 1991). The following example is representative of the results by Reichard (1991).

Example 4.3: (modal filter) Consider a cantilevered beam and suppose that the weighting function is selected so that the spatial filter will measure exactly the first modal amplitude. The desired weighting function, $g_d(z)$, is shown in Figure 4.1. Also shown in that Figure 4.1 is the achieved weighting function $g_a(z)$ where $n(z)$ is a zero-mean, Gaussian random process with variance σ_n. The transfer function of this system is a zero-mean random variable with variance as shown in Figure 4.2. Also shown in Figure 4.2 is the desired frequency response. Figure 4.3 compares an ideal first mode filter with a strain guage. This example shows that the performance of the spatial filter with a non-ideal weighting function is degraded over the desired frequency response.

5. CONCLUSIONS

In this paper we have discussed the modeling of spatial filters for active vibration suppression for flexible structures. It was shown that the choice of the weighting function is equivalent to the choosing the output matrix of the finite dimensional model. Secondly, a model of the fabrication error of the sensor was introduced. This model shows the limitations imposed by the spatial filter on the control system.

6. ACKNOWLEDGMENT

7. REFERENCES

Burke, S. E. and J. E. Hubbard, 1988. "Distributed Actuator Control Design for Flexible Beams," *Automatica*, Vol. 24, No. 5, pp 619-627.

Chang, Wie-Wen, and Chih-Kung Lee, 1989. "Critical Damping Control of a Flexible Slender Plate Using a Distributed Modal Actuator and Sensor," *Proceedings of the 1989 American Control Conference*, Pittsburgh, PA.

Clark, R. L. and Fuller, C. R., 1991. "Active Structural Acoustic Control With Adaptive Structures Including Wave Number Considerations," *Proceedings of the*

Workshop on Recent Advances in Active Control of Sound and Vibration, Blacksburg, VA, April, pp. 507-524.

Collins, S.A., D. W. Miller, and A. H. von Flotow, 1991. "Piezopolymer Spatial Filters for Active Structural Control," *Proceedings of the Workshop on Recent Advances in Active Control of sound and Vibration,* Blacksburg, VA, pp. 219-236.

Cox, D. E. and D. K. Lindner,"Active Control for Vibration Suppression in a Flexible Beam Using a Modal Domain Optical Fiber Sensor," *ASME Journal of Vibration and Acoustics,* Vol 113, 1991, pp. 369-382.

Lee, C.-K. and F. C. Moon, "Modal Sensors/Actuators, 1990, *"Journal of Applied Mechanics,* Vol. 57, pp. 434-441.

Lindner, D. K., K. M. Reichard, W. T. Baumann, and M. F. Barsky, 1990, "Measurement and Control of Flexible Structures Using Distributed Sensors," *Proceedings of the 29th IEEE Conf on Decision and Control,* Honolulu, HI, pp. 2588-92.

Lindner, D. K., W. T. Baumann, F. Ho, and E. Bielecki, 1991, "Modal Domain Optical Fiber Sensors for Control of Acoustic Radiation," *Proceedings of the Workshop on Recent Advances in Active Control of Sound and Vibration,* Blacksburg, VA, April, pp. 839-850; submitted to the ASME Journal of Vibration and Acoustics, 1991.

Lindner, D. K. and Reichard, K. M., "Control Systems Using Modal Domain Optical Fiber Sensors for Smart Structures," to appear in the Proceedings of the ASME Winter Annual Meeting, Smart Structures and Materials Symposium, Atlanta, GA, December, 1991.

Miller, D. W., Hall, S. R., and von Flotow, A. H.,1990, "Optimal Control of Power Flow at Structural Junctions," *Journal of Sound and Vibration,* Vol. 140, pp. 475-497.

Murphy, K. A., M. S. Miller, A. M. Vengasarkar, and R. O. Claus, 1990, "Elliptical-Core Two Mode, Optical Fiber Sensor Implementation Methods," *Journal of Lightwave Technology,* Vol. 8, pp. 1688-1696.

Reichard, K. M., 1991, "Distributed-Effect Modal Domain Optical Fiber Sensors for Flexible Structure Control," Ph.D. Thesis, Bradley Department of Electrical Engineering, Virginia Tech, Blacksburg, VA.

Reichard, K. M. and Lindner, D. K., 1991, "Modeling the Effects of Arbitrary Stress on the Response of Modal Domain Optical Fiber Sensors," Internal Report, Bradley Department of Electrical Engineering, Virginia Tech, Blacksburg, VA.

Reichard, K. M. and D. K. Lindner, "The Effects of Weighting Function Errors on Spatial Filters for Structural Control," submitted to the AIAA/ASME/ASCE/AHS/ASC 33rd Structures, Structural Dynamics, and Materials Conference, Dallas, TX, April, 1992.

Vengsarkar, A., Murphy, K., Fogg, B., Miller, W., Greene, J., and R. O. Claus, "Two-Mode, Elliptical-Core, Weighted Fiber Sensors for Vibration Analysis," to appear in the *Proceedings of the Fiber Optic Sensor-Based Smart Materials & Structures Workshop*, Blacksburg, VA, April, 1991.

Welsh, S. S. and D. E. Cox, "Characteristics of a Dynamic Holographic Sensor for Shape Control of a Large Reflector," *Proceedings of the SPIE Conference on OE Aerospace Sensing,* paper no. 1480-01, Orlando, FL, April, 1991.
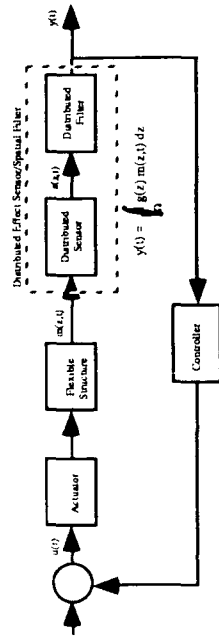
Figure 3.1.1 Control System for a Flexible Structure Containing a Spatial Filter

$$y(t) = \int_0^L g(z)\, m(z,t)\, dz$$

Figure 4.1. Ideal and Actual Spatial Filters

Figure 4.2. Variance of an Ideal and Actual Spatial Filter
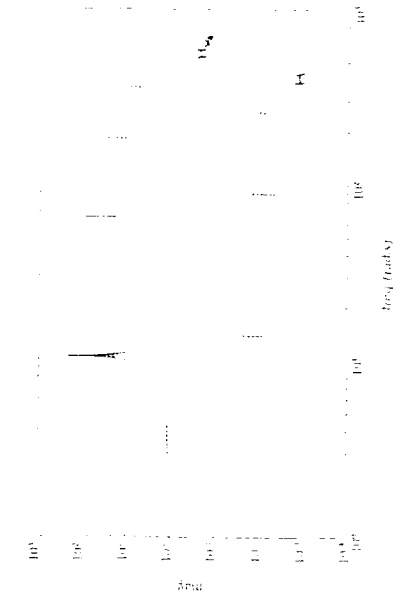
Figure 4.3. Ideal Spatial Filter and Strain Gauge Transfer Functions

Active structural control demonstrator for spacecraft applications

G.W.Game
British Aerospace Space Systems Ltd.
Earth Observation & Science Division.
Bristol, England.

ABSTRACT: This paper describes the development of a demonstrator
for the active alignment control of space structures. Initial
experiments have been based on the alignment control of a simple
aluminium cantilever beam by the use of a heater pad and angle
measurements from a laser interferometer. This work is now being
extended to a 3-dimensional truss structure controlled using
piezo-electric actuators.

1. INTRODUCTION

The increasing instrument sensitivity needs of the scientific community
are leading towards larger spacecraft structures combined with more
demanding payload pointing requirements. Typically, pointing requirements
for European spacecraft of ten years ago were in the tens of arcsec range.
The SPOT Earth observation satellite, for example, launched in 1986 had a
pointing requirement of 72arcsec. Observatory payloads in future space
missions (such as the Far Infra-Red Space Telescope FIRST) will be
required to achieve attitude stability in the sub-arcsec range which must
be maintained over many minutes. The payload pointing error budget
includes terms due to rigid body motions resulting from, for example,
measurement noise in the AOCS instruments and structural distortions
resulting from temperature gradients and structural flexibility. These
levels of attitude stability require all sources of error and disturbance
to be minimised.

Alignment stability in spacecraft is conventionally achieved using low
coefficient of expansion materials (such as CFRP) in a controlled thermal
environment. Any unacceptable residual distortions must either be measured
and used to correct the data where possible or controlled actively by
re-aligning part of the spacecraft structure. Several operational
spacecraft payloads use active thermal control (eg. the Improved
Stratospheric and Mesospheric Sounder ISAMS) and active structural control
is being applied to reduce alignment errors for large mirrors (eg. the
Hubble space telescope). The alignment requirements of future scientific
missions are now reaching the point where off-line design techniques are
no longer adequate.

Section 2 of this paper describes recent research activities within BAe,
Earth Observation & Science Division, investigating structural alignment
control. These experiments were based on an aluminium cantilever beam
controlled using a heater pad to remove distortions. Section 3 describes
our current research activities in the area leading to a technology base
and demonstrator facility allowing the alignment (and vibration) control
of large 3-dimensional structures.

2.   CONTROL OF AN ALUMINIUM CANTILEVER BEAM.

For this experiment a 0.76m long, hollow rectangular section, aluminium beam representing a spacecraft boom was clamped to a surface table at one end with the other end free. Distortions of the beam were obtained by the use of weights arranged to produce sideways forces at the free end resulting in an angular misalignment between the ends of 4 arcsec/N. Angular measurements were obtained using a laser interferometer system configured as shown in figure 1. Control of the beam was achieved by the use of a Kapton heater strip bonded to the vertical face of the beam   opposite to   the interferometer system. The output from the interferometer was fed into a standard IBM PC which included a (PID) control law. The output from the controller was used to control the power supply to the heater pad. Results showing the response of the system to a 30 arcsec initial angular   mis-alignment are shown in figure 2. The error was reduced to within 0.1   arcsecs   (which   was   the limiting   accuracy   of   the interferometer)   after approximately 50 seconds. The transient response (figure 2) was oscillatory as the result of the non-linear response of the heater pad.
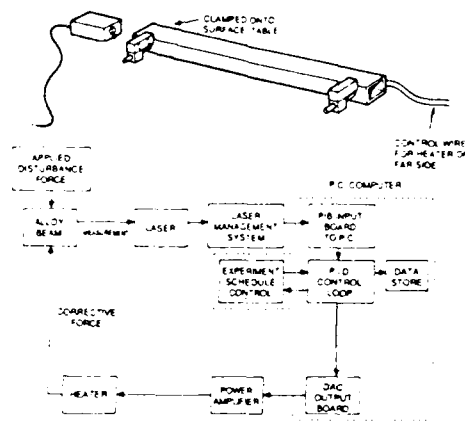
Figure 1. Configuration of cantilever beam alignment experiment

The above experiment demonstrated that active alignment control of structures is a realistic concept that can effectively produce the required accuracies for spacecraft payload requirements. In practice, spacecraft structures are often more complex than the simple beam described above while the use of heater pads for control is undesirable because of their effects on the surrounding thermal environment and their non-linear behaviour.

Figure 2. Closed loop response of cantilever beam to an initial distortion

3.   DEVELOPMENT OF A STRUCTURAL ALIGNMENT CONTROL DEMONSTRATOR.

The demonstrator was designed to represent a three dimensional spacecraft structure and is modular to permit re-configuration without incurring manufacturing costs. The ability to extend its use, eventually, to active vibration control is considered to be an important requirement.

The above requirements are met by an 'off-the-shelf' product produced by Meroform Gmbh of Germany. The system is intended for use in displays etc. and consists of a set of standard interchangeable parts. Node elements, which are spheres approximately 4cm diameter, have 18 threaded holes into

which struts of standard length may be screwed. The lengths available allow the construction of cube elements with diagonal bracing. Various materials are available, but the demonstrator is made from anodised aluminium. The structure being studied, shown in fig. 3, consists of 16 nodes and 42 struts with a total height of approximately 1m.

Distortion is introduced into the structure by the use of heater elements wrapped around four of the vertical struts. These represent disturbances generated by thermal gradients within the spacecraft.

The measurement system must be capable of measuring distortions with sub-arcsecod resolution. Absolute distortion with respect to an external reference or relative distortion between two points within the structure are required. A summary of potential systems is shown in table 1 and the use of a laser interferometer has been selected since it offers flexibility for a demonstrator. With a single laser, additional measurements can be obtained by adding mirrors, beam-splitters and interferometer blocks. A disadvantage of many of the alternatives, assuming the required resolution can be achieved, is the need to build an additional structure to support part of the measuring device (eg. capacitive micrometer).

Table 1 shows some actuation systems that were considered. Piezo-electric systems are ideal because they can be built into ' active struts' and have

Figure 3. Structural alignment rig.

been selected for the demonstrator. These have also been successfully applied to vibration reduction in truss structures[1]. Piezo-electric actuators require approximately 100V to produce distortions of 100µm but suffer from 15% hysteresis. A possible alternative is a Magnetostrictive material (Terfenol-D) which can provide larger strain levels with no hysteresis. However, the presence of a magnetic field may influence the spacecraft E-M environment while the use of current rather than voltage will make demands on the spacecraft power sub-system.

The number and placement of actuators depends upon the characteristics of the disturbances to be controlled. It is shown in (2) that it is difficult to locate actuators at positions within the structure which are effective against all conceivable disturbances. A suitable set of realistic disturbances is (as suggested in 2) composed of a linear combination of the first few vibration mode shapes or other appropriate deterministic functions. The optimal actuator locations are those which minimise the 'distortion squared' integrated over the structure. A numerical optimisation procedure, including a FE model, is used to solve the above problem[2].

Ideally, displacement sensors should be positioned at the point(s) where the distortion reduction is required. In practice this may not be possible

Actuators	Measurement systems
Piezo-electric.	Laser interferometer.
Electric motors.	Fibre optic interferometer.
Pressure transducers.	Magnetic/capacitive sensors.
Heater elements.	Quadrant detectors.
Magnetostrictive materials.	Piezo-electric.
Electrostrictive materials.	Linear/rotary transducers.
Electrorheological fluids.	LVDT.
Memory metals, composites.	Strain gauge/load cells.

Table 1 Summary of actuation and measurement devices.

because of the location of payload hardware and an estimator has to be used. An estimator for the shape of a structure is described in (3). Measurements, z_i, of displacement are obtained at a number of locations and a performance index, J, is defined;

$$J = \frac{1}{2}\int (z-y)^2 Q^{-1} dx + \frac{1}{2}\int (F)^2 R^{-1} dx \qquad 3.1$$

subject to the constraint equation;

$$y = GF \qquad 3.2$$

where   z = Measurement of true displacement y.
         F = Disturbance force vector.
         G = FE model of structure.
         Q,R are weighting matrices.

Minimisation of 3.1, which involves the solution of a set of linear equations, produces estimates of the disturbance F and measurement y which are then used to predict the shape at the points of interest.

The required control forces at the actuator locations are determined by defining another cost function, J_1, measuring the squared error between the estimated shape, y^*, and the desired shape, y_d, again subject to the FE model defined by 3.2

$$J_1 = \frac{1}{2}\int Q(y^* - y_d)^2 dx \qquad 3.3$$

Substituting 3.2 into 3.3 and performing the minimisation yields an optimal force vector. As for the estimation problem, the solution requires a set of linear equations to be solved. The above estimator/controller technique has been applied to a beam and a large antenna problem (3,4).

4.   CONCLUSIONS.

This paper has shown that accuracies of at least 0.1 arcsecs are readily achievable with simple active alignment control for boom like structures. No fundamental problems are foreseen in extending this level of control accuracy to 3 dimensional structures to meet the perceived requirements of future scientific spacecraft.

5.   REFERENCES.

1   Fremont. A.   Active damping of a truss structure using piezo-
     Dufour. J-P.   electric actuators. Proc. of 1st Int. Conf. on
     Sparavier. M.   dynamics of flexible structures in space. May 1990.

2   Haftka. R.T.   Optimum placement of controls for static deformations
                        of space structures.AIAA Journal Vol 22 No9 Sept 1984.

3   Weeks. C.   Shape determination & control for large space
                        structures.JPL, Cal. Inst. of Tech. Oct 1981.

4   Eldred. D.   Experimental demonstration of static shape control.
     Schaechter.D.   J. Guidance Vol 4 No3 1981.

Flows between structural and control designs by example of the extendable and retractable mast

J. Bals, G. Grübel

DLR Laboratory for Flight Systems Dynamics, German Aerospace Research Establishment, D-8031 Oberpfaffenhofen, Germany

W. Charon

DORNIER GmbH, P.O. Box 1420, D-7990 Friedrichshafen 1, Germany

Abstract An approach towards an integrated structure/control design is proposed. The logic to achieve the design integration is based on multiobjective parameter optimization, which allows to take care of structural and control design requirements explicitely and simultaneously. One of the key tasks within the integrated active structure design is to avoid instability caused by spillover of uncertain or truncated modes. This can be achieved by a hyperstable controller which guarantees stability robustness provided colocated sensors and actuators can be used. By example of an active Extendable Retractable Mast (ERM) the control design part of this approach is demonstrated.

1. Introduction

The active structures design is commonly sequential. In a first step a structural design is performed using finite element methods. This step is guided by structural design criteria, e.g. mass, stiffness and frequencies. Then, sensor/actuator positioning and model order reduction (e.g. truncation) is performed in order to obtain a control design model. Finally, the control system is designed based on a control specific criterion (e.g. pole location, quadratic performance index). Such a sequential design process leads more to a 'controlled structure', rather than an 'active structure', where structural and control designs should both be tuned for a best possible compromise among structural and control design criteria.

DLR, the German Aerospace Research Establishment, and the DORNIER company cooperate in exploring the benefits of Concurrent Engineering for an integrated design of active structures. The challenge is to achieve goal concurrence by a suitable goal attainment method for interactive and iterative computer-aided design experimenting. This shall allow to tackle the multi-disciplinary design problem more in parallel than in sequence.

2. Computational Flows: Integrated Structures/Control Design

The structures control design flow is sketched in Figure 1. We propose a *Structures Control Design Integration Module* (DIM) which links together a struc

tures design environment and a control design environment. The logic to achieve the design integration is multiobjective parameter optimization. which allows to take care of both structural and control design requirements individually and simultaneously in the sense that a best possible compromise can be found by an iterative engineering adjustment of procedural parameters which determine the design direction [1]. The DIM requires an open software architecture with a modular configerability of structural dynamics- and control engineering software and databased computational experimenting support to keep track of the variability of a complex design process [2, 6, 3].
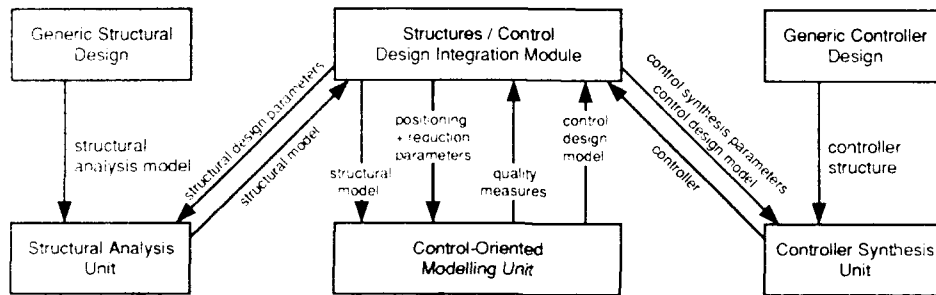
Figure 1.   Integrated structures/control design approach

The structural design analysis is assumed to be based on finite element methods Before the *structural analysis unit* can be used within the optimization. a generic structural design has to be performed. Already within the generic structural design some controller properties have to be considered in order to guarantee to the proper extend the performance of the active structure: In [3, 4] an extended modal cost technique is developed for selection of number, type and locations of sensors and actuators. Then. LQG theory is used for a rough design of a related generic controller within the generic structural design. The outcome of the generic structural design is a structural analysis model which includes the definition of the free structural design parameters and the related procedures to perform sensitivity analysis. Also. a good initial guess of the structural design parameters should be provided to the DIM. The purpose of the structural analysis unit is to compute a new structural model. if the DIM changes some of the free structural design parameters Depending on the structural analysis model the computation of the structural model requires a sensitivity analysis or a complete finite element analysis.

The *control-oriented modelling unit* has to take care of two closely related problems The specific arrangement of sensors and actuators on the structure determines good or bad "transfer functions for control". Furthermore structural dynamics models are usually not suitable for control design purposes because the dynamic order is too high. Hence. order reduction has to be performed. The parameters. which determine the quality of the sensor/actuator positioning and order reduction. are the positioning parameters (number, type, and positions) and the order reduction parameters (order of the reduced model. modes to be kept in the control design model). The purpose of the control-oriented modelling unit is to build a new control design model. whenever the structural model or the positioning and reduction parameters have been changed. Furthermore. quality measures for positioning and order reduction have to be provided to the DIM.

which give an indication whether the current positioning and reduction parameters are adequate for the current structural model or not. The positioning quality measures can be based on the extended modal cost analysis [4]. Alternatively, the positioning measures [5], using modal observability/controllability measures, are applicable. The reduction quality measure depends on the chosen order reduction method (e.g. singular values using the internal balancing method).

In a generic controller design, the controller structure has to be determined (e.g. output feedback, observer based feedback). Also the related controller synthesis procedure has to be defined, which computes a controller as a function of the controller design model and the current controller synthesis parameters. In the *controller synthesis unit* a controller synthesis is performed, whenever the controller synthesis parameters, or the control design model, have been changed.

In any design stage it is possible to fix subsets of the design parameters to their current value. This allows for example to switch between purely structural and purely control design, whenever necessary. In particular, a single design sequence, as well as an iteration loop can be emulated.

3. Structural Design of a Controlled ERM

The present paper aims to illustrate the control design part of the integrated approach looking at a realistic mast-like structure as an example. The passive version of the ERM has been developed by the DORNIER company as prime contractor to the European Space Agency. Its imagined active version is an elastic 20 m long mast fittet with piezoelectric local actuators and sensors and an offset rigid antenna whose pointing accuracy shall be improved (see Figure 2). Its generic structural design has already been described in the literature [3, 4], including the addressed methodology.
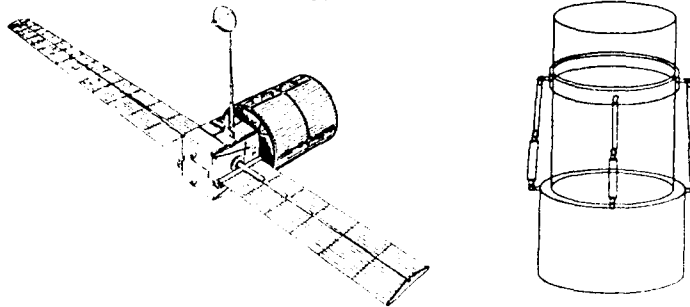
Figure 2. Solar array- and antenna-ERM on columbus resource module and deployment configuration of ERM elements. Colocated sensors and actuators are realized as piezoelectric active strut members.

The block diagram of the controlled structure is shown in Figure 3. The main source of disturbance for the ERM is a forced motion at the base of the mast due to positioning maneuvers and activities within the spacecraft the ERM is attached to. These disturbances are modelled by the vector **w**. In the generic structural design [4] two colocated sensor/actuator pairs called U1 + O1 have been selected. This configuration is represented by the control input vector **u** and the mesurement vector **ym**. The measurements and the control inputs are spoiled by additional measurement noise **v** and control input noise **n**. The output variables that are to be controlled are specified by the pointing directions of the antenna (see [4]). Accordingly, the rotations of the tip node about the x and y axes were chosen as the two output variables in the evaluation output vector **ya**. The spec-
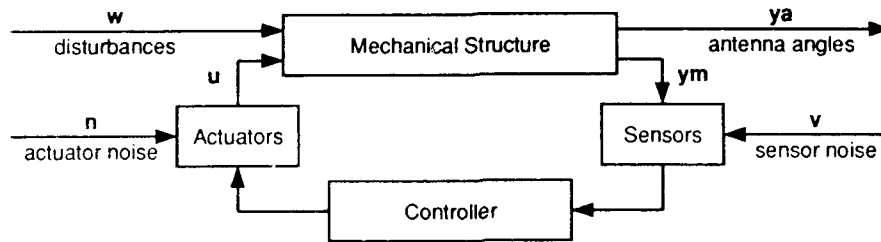
Figure 3. Block diagram of the controlled ERM

ifications for the controlled structure have been definied during the generic structural design in terms of its stochastic properties. For the disturbance input **w**, the sensor noise **v**, and the actuator noise **n**, zero mean white noise excitations with given variances **W**, **V**, and **N** have been assumed. Because of their availability on the market colocated sensor/actuator devices with 120 N maximum force, i.e. 40 N standard deviation, were chosen as a baseline. The disturbed antenna angles were defined by the output variances:

	x-angle	y-angle
open loop	3.1674E-6	6.6637E-6
closed loop (specified)	0.2500E-6	0.2500E-6

The computation of the output variances requires a covariance analysis of the closed loop system

$$\dot{x} = Ax + Er \quad , \quad y = Cx + Dr \quad .$$

where the white noise input is $r = [w, v, n]^T$ and the output y is defined as $y = [ya, u]^T$. The matrices **A**, **E**, **C**, **D** are the corresponding closed loop system matrices. The state covariance **X** is obtained from the Lyapunov equation

$$XA^T + AX = ERE^T \quad .$$

where $R = diag\{W, V, N\}$. The output covariance matrix **Y** is computed as

$$Y = CXC^T + DRD^T \quad .$$

The first two diagonal elements Y_{11}, Y_{22} of the covariance matrix contain the variances of the antenna angles, the third and fourth diagonal elemnts Y_{33}, Y_{44} are the variances of the two actuator signals, which are equal because of the symmetric actuator positioning. In this analysis, also the influence of sensor and actuator noise on the actuator covariances is considered.

4. Hyperstability/Multiobjective Control Optimization

In [8] an integrated structures/control design via multiobjective optimization was described by example of the Draper/RPL spacecraft model. The stability problem due to "spillover" was found to be one of the most important problems. This is not surprising, since, for example, changing structural parameters can decrease the quality of sensor/actuator positioning and order reduction and therefore may increase the danger of spillover. Thus, integrated structures/control design optimization requires a stability robust controller structure which can tolerate model uncertainties remaining after structural design. In [8] a modal suppression tech-

nique was applied to eliminate observation spillover from the converged solution. Here, a controller design method is used, which satisfies the stablity robustness requirement already during the design procedure by a combined hyperstability/multiobjective optimization approach [1].

The class of hyperstable controllers is of special importance since a control loop with hyperstable controller is guaranteed to be stable as long as the plant remains hyperstable despite of model uncertainties. For flexible structures hyperstability of the plant is guaranteed independent of unmodelled modes and uncertain modal parameters (frequencies, damping ratios, mode shapes), provided colocated sensors and actuators are used. In the design method [1] hyperstability theory serves to specify a computationally tractable controller structure. The multiobjective optimization approach is used to determine suitable values for the free synthesis parameters $\mathbf{p} = [p_1, \dots, p_n]^T$ of a hyperstable controller structure. In order to meet the above covariance specifications the vector performance index is defined as $\mathbf{g(p)} = [Y_1, Y_{22}, Y_{33}]^T$. Other design criteria like eigenvalue criteria or time response criteria could be added to the vector performance index, if necessary. The vector performance index is optimized by minimizing the scalar cost function

$$\gamma(\mathbf{p}) = \max_{1 \le i \le L} \ [g_i(\mathbf{p})/c_i] \ .$$

This kind of optimization procedure together with the fact that the designer can intervene via the design weighting vector $\mathbf{c} = [c_1, \dots, c_L]^T$, makes it possible to systematically explore a given controller structure in terms of the design requirements, and hence to achieve a "best possible" compromise.

Within the optimization, a 16th order control design model is used. A second order hyperstable controller structure is applied containing 7 free controller synthesis parameters. The results of a controller design case study are given in Table 1. The standard deviations for the x-angle, y-angle, and for the first actuator are shown with and without the impact of sensor/actuator noise. The controller design C1 satisfies the specifications for the antenna angle. However, the actuator limitation of 40 N is exceeded. If the limitation for the baseline actuator is kept (design C3), the specifications for the antenna angles cannot be reached. The design C2 is a compromise at the level of 200 N for the actuator standard deviation. These results indicate that either improved actuators have to be developed or the requirements for the antenna pointing accuracy have to be reduced.

signal / controller	x/noise 1.E-3	x/no noise 1.E-3	y/noise 1.E-3	y/no noise 1.E-3	u/noise 1.E+2	u/no noise 1.E+2
C1	0.4937	0.4480	0.5000	0.4476	6.4135	5.4435
C2	1.0876	1.0808	1.2047	1.1987	1.9999	1.9942
C3	1.6170	1.6158	2.1560	2.1547	0.40C0	0.3998
open loop	-	1.7790	-	2.5762	-	-

Table 1. Antenna and actuator standard deviations

The different designs have also been analyzed in the time domain. For this purpose deterministic input signals **r** have been derived which approximately represent the white noise inputs in the relevant frequency range of the mechanical structure (see also [7]). In Figure 4 the open and closed loop response are compared for controller design C1 by plotting the y-angle of the antenna versus the x-angle. The curve is parametrized by the time from zero to 32 seconds.
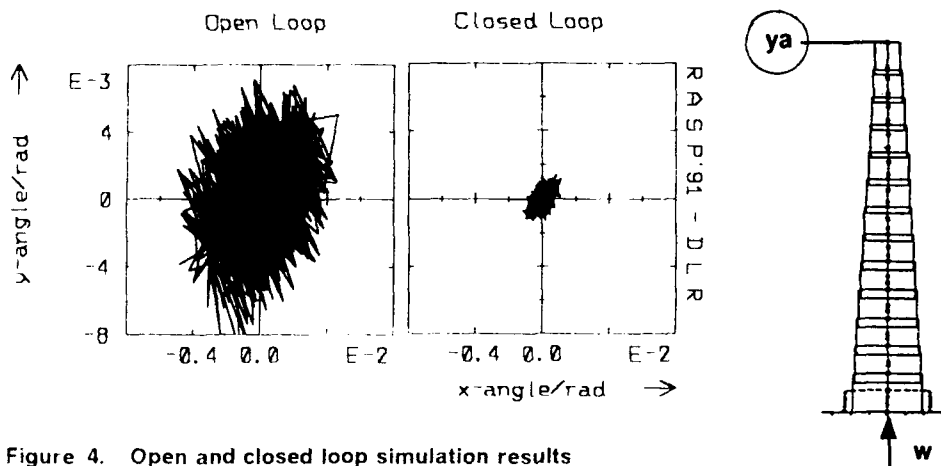
Figure 4. Open and closed loop simulation results

5. Concluding Remarks

The multiobjective/hyperstability control design approach. which guarantees robust controlled stability, was successfully applied to a given mechanical ERM design. As a next step. a software engineering implementation in a common environment is planned. which allows the simultaneous optimization of controller synthesis parameters as well as sizing parameters of the mast. like thickness of the tubes.

6. Bibliography

[1] Bals. J.. *A Hyperstability/Multiobjective Optimization Approach for Active Flexible Structures*. IFAC Symposium on Design Methods for Control Systems, Zurich. 1991.

[2] Bals. J.. *A FLEXTOOL: A Concurrent Control Engineering Tool for Control Analysis and Design of 'Active Structures'*. CADCS. Swansea. UK. July. 1991.

[3] Charon. W.. Buck. U.. Newerla. A.. *On Structural Design of Active Structures*. Dynamics of Flexible Structure in Space. Cranfield. UK. May 1990.

[4] Charon. W.. *Actuator Positioning Within the Mechanical Design of Active Structures*. DGLR 91-143. International Forum on Aeroelasticity and Structural Dynamics - Workshop on Smart Material and Structures. Aachen. FRG. June 1991.

[5] DLR and DORNIER SYSTEM. *Investigation of Attitude and Orbit Control System Modelling for Flexible Space Platforms*. ESTEC Contract No. 6839/86/NL/MA(SC) performed by DLR. Final Report. 1988.

[6] Joos. H.-D. *Automatic Evolution of a Decision-Supporting Design-Project Database in Concurrent Control Engineering Environment*. CADCS. Swansea. UK. July. 1991.

[7] Maurer. D. Charon. W.. *Active Structures: Verification of Dynamic Performance After Mechanical Design*. DGLR 91-140. International Forum on Aeroelasticity and Structural Dynamics - Workshop on Smart Material and Structures. Aachen. FRG. 1991.

[8] Schneider. G L. Calico. R.A.. Jr. *Integrated Structural/Contro' Design Via Multiobjective Optimization*. Dynamics of Flexible Structure in Space. Cranfield. UK. 1990.

Control of multiflex systems

A Silva†, R Franco‡, J Ramakrishnan§ and K W Byun§

† Agusta SpA Milan, Italy
‡ ESA/ESTEC, Noordwijk, The Netherlands
§ Dynacs Engineering Co. Inc., Palm Harbor, FL, USA

Abstract. Control-structure interaction effects are dominant in highly flexible space structures with high gain controllers. The applicability of the control structure design sensitivity (CSDS) and the dynamics and control analysis program (DCAP) for the design and evaluation of these controllers is presented in this work. Additionally, control-structure issues in a multibody setting are demonstrated using an European Data Relay Satellite (DRS) model.

1. INTRODUCTION

The integration of structural modeling and control design for a class of space structures is addressed in this work. Control-structure interaction issues become predominant for high performance control. The integrated design approaches are demonstrated using local controllers and combined optimization methods 'Ramakrishnan J R, Stornelli S, Rajiyah H, and Silva A (1991)'. Finally the dual objective of high performance and vibration suppression for a DRS model is presented.

The local controller 'Lust R V, and Schmit L A (1988)' concept lends itself to the area of smart structures since the structural member has a variable position and velocity gain associated with it. In this setting, control effort proportional to the nodal displacements and velocities is applied to the active members. The control forces modify the effective stiffness and damping parameters of the structure reducing response quantities of interest. The optimization problem is posed as minimizing the total controller forces subjected to constraints on dynamic displacements and individual controller forces.

The combined optimization problem 'Salama M, Garba J, and Demsetz L (1988)' uses a composite objective function (with a structural and control objective) to

simultaneously optimize the structure and controller. The approach is based on the concept that the minima of a sum is less than or equal to the sum of the minima.

The final example illustrates the interaction problems in the high bandwidth control of Eurostar DRS. Controller design to minimize the solar panel vibration after an attitude maneuver is presented. ESTEC funded programs CSDS and DCAP are used extensively in this work.

2. LOCAL CONTROLLER PROBLEM

The discretized equations of motion for a linear structural system subject to multiple loading conditions are given by:

$$[M]\{\ddot{u}\}_k + [C]\{\dot{u}\}_k + [K]\{u\}_k = \{P(t)\}_k \qquad k = 1,\dots,n \qquad (1)$$

where the matrices and vectors have the usual meaning. The local controller forces can be written in terms of the system level position and velocity feedback matrices $[G_p]_k$ and $[G_v]_k$ as

$$\{f_c\}_k = -[G_v]_k\{\dot{u}\}_k - [G_p]_k\{u\}_k. \qquad k = 1,\dots,n \qquad (2)$$

With this force term, the closed-loop equations of motion can be written as

$$[M]\{\ddot{u}\}_k + [C_A]_k\{\dot{u}_k\} + [K_A]_k\{u_k\} = \{P(t)\}_k \qquad (3)$$
$$[C_A]_k = [C] + [G_v]_k$$
$$[K_A]_k = [K] + [G_p]_k \qquad (4)$$

The local controller optimization problem is now cast as:

$$\text{Minimize} \sum_{i=1}^{n} |f_c(t)|_i \qquad (5)$$

subject to

$$|\delta_{max}|_i \leq \delta_{o_i}, \qquad i = 1,\dots,n_g$$
$$|f_c(t)|_i \leq f_{max}, \qquad i = 1,\dots,n_f$$

and appropriate side constraints on the gains. The local control example is skipped for the sake of brevity.

3. COMBINED CONTROL/STRUCTURE OPTIMIZATION

The simultaneous control structure optimization problem is stated as follows.

$$\min J(a,u) = \left[J_s(a) + \frac{1}{2}\rho^2 \int_o^\infty (x^T Q x + u^T R u)\, dt \right] \qquad (6)$$
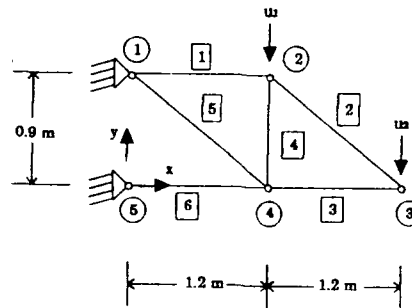
Figure 1: Combined Control/Structure Optimization
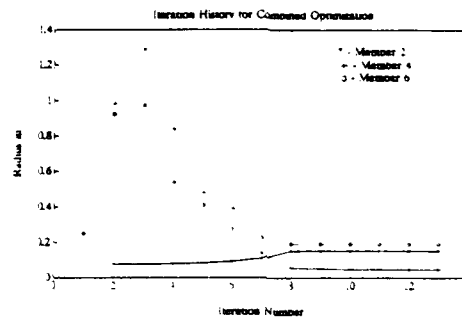
Figure 2: Iteration History for Combined Optimization

subject to the system dynamics and behavioral constraints. The structural objective J_s is only a function of the structural design variables $\underline{a}$ while the control objective in equation (6) is a function of both $\underline{a}$ and the control $\underline{u}$. Expressing the control objective as an implicit function of $\underline{a}$, the problem is recast as selecting a set of structural design variables $\underline{a}^*$ such that

$$F(a) = \left[J_s(a) + \frac{1}{2}\rho^2 x_o^T P(a) x_o \right] \tag{7}$$

is minimized. The planar structure used to demonstrate this approach is shown in figure 1. The iteration history for the radius of members 2, 4 and 6 and the open-loop frequency ω is shown in figure 2.

4. CSI ISSUES IN MULTIFLEX SYSTEMS

The EUROSTAR DRS (figure 3) is modeled as a multiflex system with a rigid core body and two flexible solar panels. The solar panel is modeled in NASTRAN using bar and membrane finite elements.

The satellite is initially modeled as three rigid bodies. A PD controller is designed to slew the satellite through 0.3 radians. The solar panels are then made flexible and
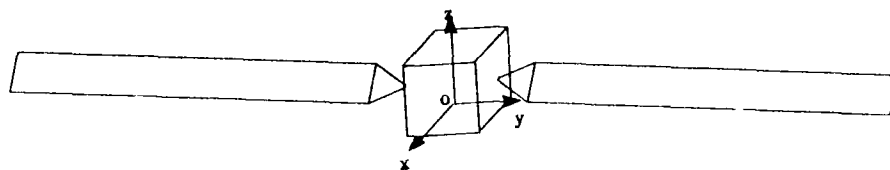
Figure 3: EUROSTAR DRS
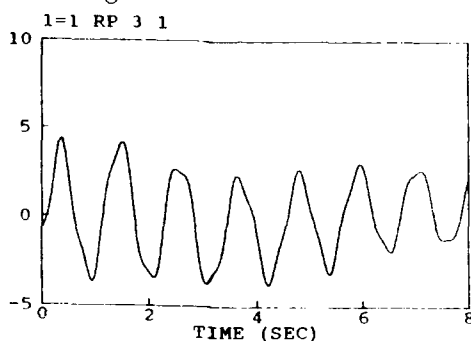
Figure 4: Flex due to Low bandwidth Control

are modeled with their first six cantilever modes. These modes range in frequency from 0.14 to 2.6 Hz. Two simple PD controllers of bandwidth π r/s and 4 π r/s and critical damping are evaluated in the multibody simulation sense. The effect of the rigid body control on flex is evident in figures 4 and 5.

To suppress the effects of panel flexibility, an LQG and pole placement controller are designed using accelerometer outputs and moment actuator input. The responses are shown in figures 6, 7, 8 and 9. The pole placement controller achieves fast slew and vibration suppression at the expense of high control gain and sensitivity. The LQG control, on the other hand, is slower but is also less sensitive to loop uncertainty. The availability of tools such as CSDS and DCAP are useful for similar design and analysis.
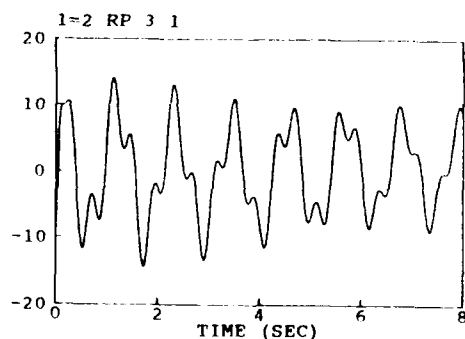
Figure 5: Flex due to high Bandwidth Control

Output y1
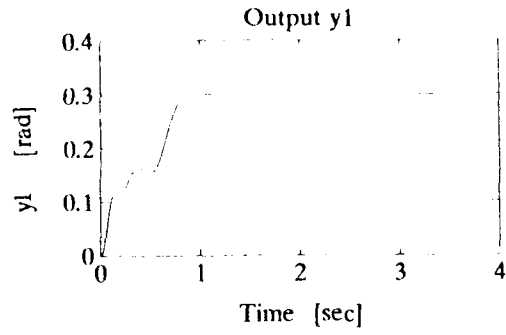
Figure 6: Pole Placement: 0 Response

Output y3
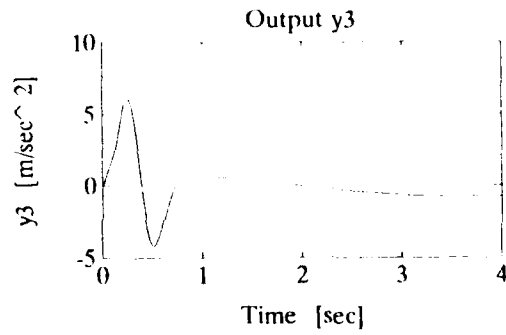
Figure 7: Pole Placement: Accelerometer Response

Output y1
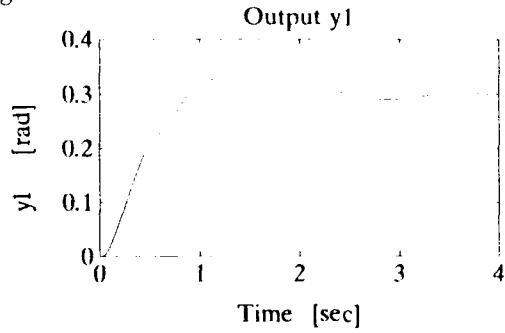
Figure 8: LQG: 0 Response

Output y3
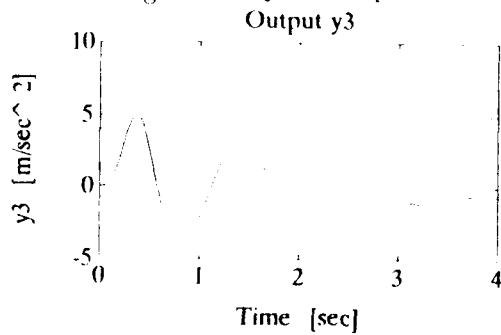
Figure 9. LQG: Accelerometer Response

5. SUMMARY

This work addresses some key CSI issues. Local and combined controller optimization formulation are presented with examples. Finally, the problem of slewing a DRS satellite without having excessive vibration is presented. The CSDS and DCAP software lend themselves to the modeling, design and analysis of such problems.

References

1   Lust R V, and Schmit L A, *Control Augmented Structural Synthesis*, NASA Contractor Report 4132, NASA Scientific and Technical Information Division, 1988

2   Ramakrishnan J R, Stornelli S, Rajiyah H, and Silva A, *Control Strategies for Space Systems* submitted for publication to the Journal of Modeling and Scientific Computation, August 1991

3   Salama M, Garba J, and Demsetz L, *Simultaneous Optimization of Controlled Structures*, Computational Mechanics, 1988 (3), pp. 275-282

Spatially distributed shell convolving sensors

H. S. Tzou [1] and **J. P. Zhong** [2]

[1] Department of Mechanical Engineering
University of Kentucky, Lexington, KY 40506–0046 USA

[1] Institute of Space and Astronautical Science, Kanagawa 229, Japan [§]

[2] Conmec Inc., Allentown, PA 18103 USA

ABSTRACT

Observation spillover of undamped distributed structural systems could be
prevented via modal filtering using distributed piezoelectric convolving sensors.
In this paper, sensor mechanics of spatially distributed piezoelectric shell
convolving sensors are analyzed and results presented. The theory suggests that
the sensor sensitivity can be divided into two components: 1) the transverse
modal sensitivity and 2) the membrane modal sensitivity in which the former is
primarily contributed by bending strains and the later is by membrane strains.
Design of spatially distributed cosine–shaped convolving sensors for circular ring
structures is proposed and evaluated.

1. INTRODUCTION

In a distributed structural control system, observation spillover can introduce
unstable dynamic responses of undamped structures (Meirovitch & Baruh, 1983).
There are several techniques to reduce the observation spillovers. One method is to
use spatially <u>distributed modal sensors</u> which only respond to a structural mode or a
group of modes. Busch–Vishniac (1990) also proposed spatially distributed
transducers with sensor and actuator applications. Lee and Moon (1987) proposed a
distributed piezoelectric modal sensor design for a flexible beam and a
one–dimensional plate. Collins et al. (1991) proposed spatially distributed shaped
piezoelectric sensors using sinc functions for monitoring beam oscillations. Tzou et
al. also derived a generic distributed piezoelectric sensor/actuator theory (1991) and a
thin piezoelectric finite element formulation (1990) for distributed sensation and
control of shells. In this paper, generic distributed piezoelectric shell convolving
sensors are proposed and detailed electromechanical behaviors (**sensor mechanics**) are
analyzed and investigated.

2. DISTRIBUTED SENSOR MECHANICS

In this section, an output signal equation of a generic distributed shell convolving
sensor is derived based on a generic piezoelectric shell theory (Tzou & Zhong, 1990).
This concept is then extended to distributed convolving ring sensors. (Due to page

limitations, only results are presented.)

2.1. Distributed Shell Convolving Sensors

It is assumed that a generic piezoelectric shell continuum made of symmetrical hexagonal materials is used as a distributed shell sensor. Output signal is measured across the top and bottom electroded surfaces, i.e., the transverse direction. A theory of distributed shell convolving sensors is derived. For a <u>distributed</u> piezoelectric shell continuum. it is assumed that the electric–field E_3 is uniformly distributed over the entire electroded surface. The signal output V_3^t from a distributed piezoelectric shell with an effective surface electrode A is

$$V_3^t = - \frac{1}{(C_a h + \epsilon_{33}) A} \left[\int_A \int_{\alpha_3} (e_{31} S_{11} + e_{31} S_{22}) A_1 A_2 (1 + \frac{\alpha_3}{R_1})(1 + \frac{\alpha_3}{R_2}) d\alpha_1 d\alpha_2 d\alpha_3 \right] . \quad (1)$$

where C_a is the capacitance; h is the thickness; ϵ_{33} is the dielectric constant; e_{31} is the piezoelectric constant; S_{11} is the principal strain in the ith direction. A_i is Lame's constant; and R_i is the radius of the ith coordinate axis. For a thin piezoelectric shell layer *bounded on or embedded in an elastic shell continuum (Figure 1), principal* mechanical strains can be further divided into membrane strains S_{ii}^o and bending strains k_{ii}. Thus, the output signal of a shell sensor becomes

$$V_3^t = - \frac{1}{(C_a h + \epsilon_{33}) A} \left\{ \left[\int_A \int_{\alpha_3} \left(e_{31} \left[(S_1^o + S_{22}^o) + \alpha_3 (k_{11} + k_{22}) \right] \right) \right] \right. $$
$$\left. A_1 A_2 (1 + \frac{\alpha_3}{R_1})(1 + \frac{\alpha_3}{R_2}) d\alpha_1 d\alpha_2 d\alpha_3 \right\} . \quad (2)$$
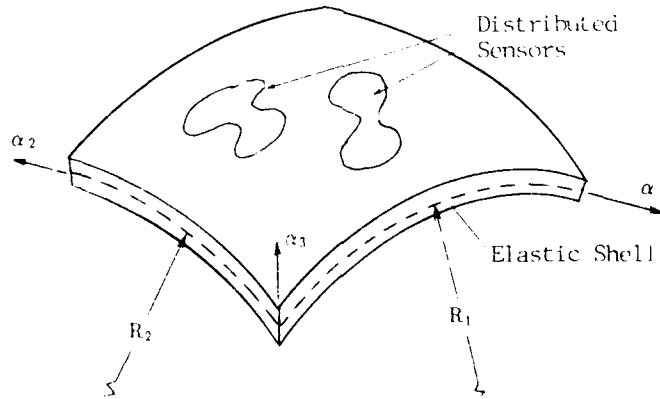
Fig.1 **Spatially distributed piezoelectric shell sensors.**

The membrane strains and bending strains are defined as

$$S_{11}^o = \frac{1}{A_1} \frac{\partial u_1}{\partial \alpha_1} + \frac{u_2}{A_1 A_2} \frac{\partial A_1}{\partial \alpha_2} + \frac{u_3}{R_1} , \tag{3}$$

$$S_{22}^o = \frac{1}{A_2} \frac{\partial u_2}{\partial \alpha_2} + \frac{u_1}{A_1 A_2} \frac{\partial A_2}{\partial \alpha_1} + \frac{u_3}{R_2} , \tag{4}$$

$$k_{11} = \frac{1}{A_1} \frac{\partial}{\partial \alpha_1} \left[\frac{u_1}{R_1} - \frac{1}{A_1} \frac{\partial u_3}{\partial \alpha_1} \right] + \frac{1}{A_1 A_2} \left[\frac{u_2}{R_2} - \frac{1}{A_2} \frac{\partial u_3}{\partial \alpha_2} \right] \frac{\partial A_1}{\partial \alpha_2} , \tag{5}$$

$$k_{22} = \frac{1}{A_2} \frac{\partial}{\partial \alpha_2} \left[\frac{u_2}{R_2} - \frac{1}{A_2} \frac{\partial u_3}{\partial \alpha_2} \right] + \frac{1}{A_1 A_2} \left[\frac{u_1}{R_1} - \frac{1}{A_1} \frac{\partial u_3}{\partial \alpha_1} \right] \frac{\partial A_2}{\partial \alpha_1} , \tag{6}$$

where u_i is the displacement in the ith direction; A_1 and A_2 are Lame's parameters; and R_1 and R_2 are radii of in–plane coordinate axes. Lame's parameters A_i and radii of curvatures R_i are geometry dependent, e.g., $A_1 = A_2 = 1$ and $R_1 = R_2 = \infty$ for a rectangular plate. Thus, the sensor equation can be further simplified according to the geometries.

It can be observed that the total output is contributed by both membrane and bending strains experienced in the piezoelectric layer. Thus, two output sensitivities: 1) *transverse modal sensitivity* and 2) *membrane modal sensitivity* can be defined accordingly and these two sensitivities are applied to distributed piezoelectric sensors. In general, transverse modal sensitivity is defined for transverse natural modes and membrane modal sensitivity for in–plane natural modes. Distributed piezoelectric shell layers placed on the neutral surface can only be used as membrane sensors. Note that the generic piezoelectric shell is fully covered with conducting electrodes on the top and bottom surfaces. Besides, the external electric charge induced effect $C_a h$ is still included, which should be neglected for sensor applications. Since $\alpha_3/R_1 \ll 1$ and $\alpha_3/R_2 \ll 1$, they can be further neglected, too. In the later derivations, the surface electrodes are spatially shaped and the electric polarization is also altered in order to design generic shell modal sensors.

It is assumed that the piezoelectric shell thickness is constant. For a spatially distributed piezoelectric shell convolving sensor, a weighting function $W(\alpha_1, \alpha_2)$ and a polarity function $\text{sgn}[U_3(\alpha_1, \alpha_2)]$ can be added to the generic shell signal equation. Note that $\text{sgn}(\cdot)$ denotes a singum function used to change the piezoelectric polarity, which $\text{sgn}(\cdot) = 1$ when $(\cdot) > 0$, 0 when $(\cdot) = 0$, and -1 when $(\cdot) < 0$; and $U_3(\alpha_1, \alpha_2)$ denotes a modal function. Electrode shape (or sensor shape) can be designed by using a weighting function, $W(\alpha, \alpha_2)$. Consider a one–dimensional structural, e.g., beam, ring, arch, etc., the mechanical strains are functions only one coordinate, say α_1. Thus, membrane strains S_{11}^o, S_{22}^o and bending strains k_{11}, k_{22} can be described as functions of coordinate α_1, i.e., $W(\alpha_1, \alpha_2) = W(\alpha_1)$. The sensor equation can be written as

$$V_3^t = -\frac{e_{31}}{\epsilon_{33}} \frac{1}{A} \int_{\alpha_1} W(\alpha_1) \, \text{sgn}[U_3(\alpha_1)] \left[h(S_{11}^o + S_{22}^o) \right.$$
$$\left. + \frac{1}{2}(h_2^2 - h_1^2)(k_{11} + k_{22}) \right] A_1 A_2 (1 + \frac{\alpha_3}{R_1})(1 + \frac{\alpha_3}{R_2}) \, d\alpha_1 , \tag{7}$$

where h_1 and h_2 are the distances measured from the neutral surface of the shell to the top and bottom surfaces of the distributed piezoelectric sensor layer, respectively. This theory is applied to distributed convolving piezoelectric ring sensors in the next section.

2.2. Distributed Convolving Ring Sensors

Distributed cosine shaped piezoelectric convolving modal sensors are designed and analyzed for flexible ring structures. *Transverse modal sensitivity* for transverse natural modes and *circumferential modal sensitivity* (equivalent to *membrane modal sensitivity* in shells) for circumferential natural modes are defined and discussed. For a ring structure, the Lame's parameters are $A_1 = 1$ and $A_2 = R$.   The radii of curvatures are $R_1 = \infty$ and $R_2 = R$. The modal equations, circumferential modes: $u_\theta(\theta,t)$ and transverse modes: $u_3(\theta,t)$, for a free–floating ring are

$$u_\theta(\theta,t) = \sum_{n=0}^{\infty} \eta_n(t) \, A_n \sin(n\theta - \varphi) , \tag{8}$$

$$u_3(\theta,t) = \sum_{n=0}^{\infty} \eta_n(t) \, B_n \cos(n\theta - \varphi) , \tag{9}$$

where $\eta(t)$ denotes the modal participation factor, or modal coordinate; φ is an arbitrary phase angle; and A_n and B_n are constants. In the following derivation, it is assumed that a reference point is defined so that the phase angle $\varphi = 0$. Based on modal orthogonality, the sensor shape function $W(\alpha)$ can be designed as a cosine function:

$$W_k(\theta) = b\cos(k\theta) , \tag{10}$$

where b is a weighting factor. Substituting $W_k(\theta)$ into the sensor equation gives

$$V_3^t = -\frac{e_{31}\pi b}{\epsilon_{33}\, A_k} \, \text{sgn}(\cos n\theta)\left[h(kA_{k_2}+B_{k_2})+\frac{1}{2R}(h_2^2 - h_1^2)(kA_{k_1}+k^2 B_{k_1})\right] \eta_k(t), \tag{11}$$

where A_{k_1} and B_{k_1} are respectively the circumferential and transverse modal oscillation amplitudes of the kth transverse natural mode with natural frequency ω_{k_1}. A_{k_2} and B_{k_2} are the circumferential and transverse modal amplitudes of the kth circumferential natural mode with natural frequency ω_{k_2}. Thus, the first part, membrane strains, is primarily contributed by circumferential modes with amplitudes A_{k_2} and B_{k_2}; and the second part, bending strains, is contributed by transverse modes with amplitudes A_{k_1} and B_{k_1}. The modal amplitudes, either A_{k_1}/B_{k_1} or A_{k_2}/B_{k_2}, are coupled by a constant (Tzou & Zhong, 1991). (Note that A_k denotes the effective electroded area and A_k is a constant for the kth mode.) k_1 denotes the transverse mode and k_2 the circumferential mode for $n = k$. Thus, two modal sensitivities: 1) *transverse modal sensitivity* and 2) *circumferential modal sensitivity* can be defined. Each of the sensitivities can be further divided into two component sensitivities defined in terms of either transverse or circumferential oscillation amplitudes.   The *transverse modal sensitivities* S_t^t and S_c^t respectively defined by the transverse oscillation amplitude B_{k_1} and by the circumferential oscillation amplitude A_{k_1} of the

distributed sensor are

$$S_t^t = \frac{V_3^t}{B_{k_1}\eta(t)} = \frac{-e_{31}\pi b}{\epsilon_{33}\,A_k}\left[\ \frac{1}{2R}(h_2^2 - h_1^2)(k^2-1)\ \right] , \tag{12}$$

$$S_c^t = \frac{V_3^t}{A_{k_1}\eta(t)} = \frac{e_{31}\pi b}{\epsilon_{33}\,A_k}\left[\ \frac{1}{2R}(h_2^2 - h_1^2)(k^3-k)\ \right] . \tag{13}$$

The *circumferential modal sensitivities* S_C^t and S_C^c respectively defined by the transverse oscillation amplitude B_{k_2} and by the circumferential oscillation amplitude A_{k_2} are

$$S_t^c = \frac{V_3^t}{B_{k_2}\eta(t)} = \frac{-e_{31}\pi b}{\epsilon_{33}\,A_k}\left[\ h(k^2 + 1)\ \right] , \tag{14}$$

$$S_c^c = \frac{V_3^t}{A_{k_2}\eta(t)} = \frac{-e_{31}\pi b}{\epsilon_{33}\,A_k}\left[\ h(k + \frac{1}{k})\ \right] . \tag{15}$$

Thus, for bending oscillation where transverse modes dominate, S^t should be used to estimate oscillation amplitude. On the other hand, for circumferential oscillations, S^c is used. Figure 2 illustrates a spatially distributed ring sensor for the mode $k = 2$.
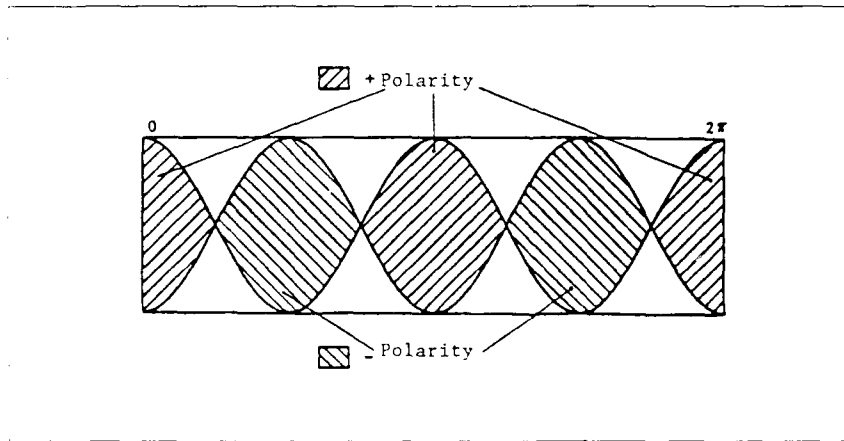
Fig.2 A spatially distributed piezoelectric ring sensor.

3. SUMMARY AND CONCLUSIONS

In this study, generic distributed piezoelectric shell convolving sensors were proposed and detailed *sensor mechanics* were analyzed. It was observed that the sensor output is contributed by membrane strains and bending strains experienced in the sensor layer. Two sensor sensitivities: 1) *transverse modal sensitivity* and 2) *membrane modal sensitivity* can be defined accordingly. In general, the transverse modal sensitivity is defined for out—of—plane transverse natural modes and the membrane modal sensitivity for in—plane natural modes.

Spatially distributed cosine shaped piezoelectric convolving sensors were designed and analyzed for ring structures. **Transverse modal sensitivity** for transverse natural modes and **circumferential modal sensitivity** (equivalent to *membrane modal sensitivity* in shells) for circumferential natural modes were defined and discussed. Proper selections of piezoelectric sensor shape and convolution can provide spatial modal filtering and prevent observation spillover in distributed control systems.

ACKNOWLEDGEMENT

REFERENCES

Busch–Vishniac, I.J., 1990, "Spatially Distributed Transducers: Part–2," *ASME Journal of Dynamic Systems, Measurements, and Control*, Vol.(112), pp.381–390.

Colins, S.A., Miller, D.W., von Flotow, A.H., 1990, "Sensors for Structural Control Applications Using Piezoelectric Polymer Film," MIT SERC Report #12–90.

Lee. C.K. and Moon, F., 1988, "Modal Sensors/Actuators," IBM Report, RJ 6306 (61975), Research Division, IBM.

Meirovitch, L. and Baruh, H., 1983, "On the Problem of Observation Spillover in Self–Adjoint Distributed–Parameter Systems," J. of Optimization Theory and Applications, Vol.(39), No.(2), pp.269–291.

Soedel, W., 1981, Vibrations of Plates and Shells, Dekker.

Tzou, H.S., 1991, "Distributed Modal Identification and Vibration Control of Continua," *ASME Journal of Dynamic Systems, Measurements, and Control*, Vol.(113), No.(3).

Tzou, H.S. and Tseng, C.I., 1990, "Distributed Piezoelectric Sensor/Actuator Design for Dynamic Measurement/Control of Distributed Parameter Systems: A Finite Element Approach," *Journal of Sound and Vibration*, Vol.(138), No.(1), pp.17–34.

Tzou, H.S. and Zhong, J.P., 1990, "Electromechanical Dynamics of Piezoelectric Shell Distributed Systems, Parts 1 and 2," <u>Robotics Research–1990</u>, ASME–DSC–Vol.26, pp.199–211, 1990 ASME Winter Annual Meetings, Dallas, Texas, Nov. 25–30, 1990.

Tzou, H.S. and Zhong, J.P., 1991 "Sensor Mechanics of Distributed Shell Convolving Sensors Applied to Flexible Rings," (w/ Zhong), <u>Structural Vibration and Acoustics</u>, Edrs. Huang, Tzou, et al., ASME–DE–Vol.34, pp.67–74, Symposium on Intelligent Structures and Systems, 1991 ASME Design Technical Conference, September 22–25, 1991.   *(C/CnvlScr–ADPA.PiezShl3)*

81

Cyclic fatigue in piezoelectric ceramics

S. W. Freiman and G. S. White

Ceramics Division, NIST
Gaithersburg, MD

ABSTRACT

This paper summarizes a study into the cyclic fatigue behavior of a lead-zirconate-titanate ceramic. The results can be divided into two categories, those for which a specimen reached a temperature > 200°C, and those which were restrained to lower temperatures. High temperature cycling was shown to cause macroscopic crack extension and extensive microcracking. Lower temperature cycling caused minimal crack extension and microcracking only near indentations; no decrease in bend strength was measured after cycling. There was no effect of temperature on K_{Ic}.

INTRODUCTION

Actuators and transducers made from piezoelectric or electrostrictive ceramics will be key elements in the development of smart materials and systems. Such materials must operate for long periods under cyclic voltage, and, consequently, cyclic strain conditions. Because of the susceptibility of all brittle materials to catastrophic failure, an understanding of failure mechanisms is an essential prerequisite to mechanical reliability of these materials. Although fracture of piezoelectric materials has been studied under static conditions[1-3], little is known of their response to cyclic loading.

Lead zirconate titanate (PZT) is a ferroelectric and piezoelectric ceramic material with applications as ultrasonic transducers or actuators. The static mechanical properties of PZT have been studied; effects of environment[1-3] and electric field[4] on crack growth in PZT and lead magnesium niobate[5] (PMN) have been explored. Some effects of cyclic loading on the strength of PZT[4,6,7] have been determined.

Recently, we have investigated the behavior of cyclically loaded PZT by direct observation of crack extension caused by the application of a cyclic electrical field. The results of this research are reported in detail in References 8 and 9. This paper summarizes the findings of this study.

EXPERIMENTAL PROCEDURES

The material used in this work[8,9] was a commercial* PZT-8 in the shape of bars $\approx$ 70 x 12.6 x 6 mm, poled perpendicular to the 70 x 12.6 mm faces. Typical grain sizes were 1-6 μm. Figure 1 shows schematics of the test apparatus and test specimens. Cyclic loading measurements were made on the bars after one of the 70 x 6 mm surfaces had been polished to a 6 μm diamond paste and a 10 N Vickers indentation had been placed into the center of the polished surface, oriented so that the radial cracks generated by the indentation were aligned parallel and perpendicular to the specimen sides. In this way we could directly observe the effect of cyclic voltages on crack extension.

(a)   (b)
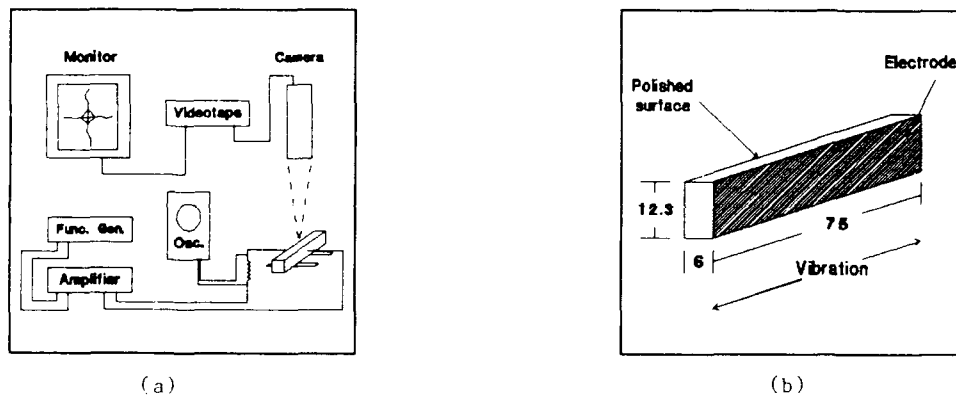
Figure 1. (a) Schematic of cyclic loading apparatus. The specimen is driven at resonance frequency by a tunable signal generator. Current through the specimen is determined by the voltage across precision resistor. (b) Specimen for cyclic loading.

A function generator supplied a sinusoidal driving voltage (50-200 $V_{peak-to-peak}$) to the specimen at a frequency chosen to excite the longitudinal resonance of the bar (f $\approx$ 23 KHz). The resultant electrical fields were 10 to 50 times smaller than typical fields used to drive PZT. The specimen was mounted in series with a precision 1 Ω resistor to provide a measure of the current at resonance. A copper-constantan thermocouple was attached to the surface of the specimen. A video camera attached to an optical microscope was used to record crack extension and changes in the appearance of the specimen surface near the cracks. Heating of the cyclically driven specimens was by internal friction during excitation. Consequently, specimen temperatures varied between room temperature (RT) and some maximum value during each period of excitation.

RESULTS AND DISCUSSION

Figure 2 is a typical plot of crack extension as a function of excitation
time for specimens in which the temperature was allowed to reach ≈200°C.
The symbols indicate measurements made while the specimen was at rest
after excitation. Crack extension is not uniform with time but occurs in
distinct increments, and appears to be equivalent in all directions. From
the symmetry of the loading geometry, we would have expected the maximum
tensile load across the crack tips to be exerted on cracks which are
oriented in the ±y directions i.e., perpendicular to the longitudinal
axis (see Fig. 1b). In fact, the bars that failed, broke precisely in this
manner: through the center of the bar perpendicular to the long axis.
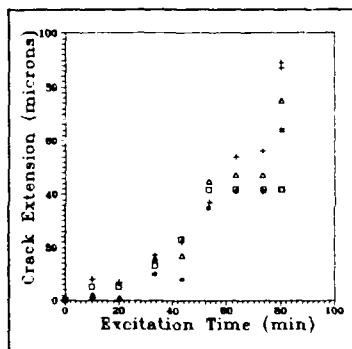
Figure 2. Crack extension plotted as
a function of excitation time for
all four radial cracks for specimen
allowed to reach ≈200°C. Crack
extension is independent of crack
direction, although only cracks in the
±y direction were expected to be
loaded. Symbols indicate crack
extension in the ($\square$) +y, (+) -x,
(*) -y, and ($\triangle$) +x directions.

Specimens for which temperatures were maintained at ≈ 80°C behaved
differently from those reaching 200°C (Figure 3). For a cumulative
excitation time < 20 minutes, the specimen temperature was kept ≤80°C,
during which time no crack extension occurred. As the temperature
increased, cracks grew slightly. After 25 minutes at T≤86°C, the specimen
was again excited and the temperature was allowed to rise without
restriction. Upon reaching 104°C (1.1 minutes of continuous excitation),
the specimen failed. This behavior was reproduced in three specimens;
after cumulative excitation periods of ≈20 minutes with maximum
temperatures ≈80°C, specimens failed within ≈1 minute of continuous
excitation (100°C<T<110°C). Specimens in which temperatures were allowed
to rise to ≈200°C, without undergoing 20 minutes of low temperature
excitation, survived well over an hour of cumulative excitation time
before failure. Therefore, excitation at the lower temperatures generates
some type of damage leading to failure as the specimen is allowed to warm
above 100°C. It should be noted that determination of critical fracture
toughness by an indentation-strength technique[10] at both RT and 150°C
showed this parameter to be 1.3 MPam$^{1/2}$, independent of temperature[8].

Figure 3. Crack extension as
function of time for specimen
maintained at T≤86°C. After 25
minutes cumulative excitation time
at these temperatures, the specimen
was excited without regard to the
temperature. At T≈°C, the specimen
failed.
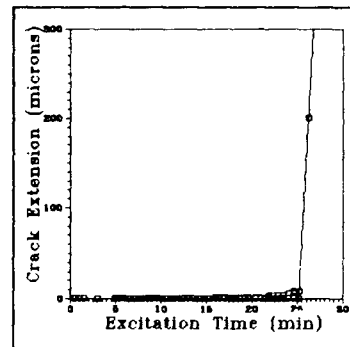
Optical microscopy of the crack structure for a specimen in which the
temperature exceeded 200°C shows a wandering crack path, mottled regions,
and crack bridging. Mottled regions are seen, particularly in the
vicinity of the crack bridges and grains which are partially surrounded by
the cracks. In addition, the mottling invariably appears in a very
pronounced fashion in the vicinity of the indentation impressions and
often in the vicinity of large pores. Frequently, though not always,
mottled regions exist adjacent to the cracks, extending as the cracks
extend. The existence of the mottling around indentation impressions
leads us to believe that the mottling may be related to surface damage in
which the grains are twisted out of the plane of the specimen's polished
surface. For those cases in which the mottling parallels crack extension,
it is not possible to state whether the surface damage or the crack
extension is the precursor; because no measurements can be made during
excitation of the specimen, only the final condition, in which both the
mottled regions and the cracks have extended, can be observed. In
addition, while many of the cracks do not appear to be adjacent to surface
damaged regions, there have been observed instances in which a mottled
region appeared and, later, a crack appeared running from one edge of the
mottled region to the other. Consequently, there appears to be a relation
between the mottled regions and crack extension, but both the details of
the relationship and the identification of the mottled regions are
presently unknown.

SEM micrographs showed no evidence of cracks on the 2-10 μm size range,
which might be expected if microcracks around the grains were to coalesce
into macroscopic cracks. Similarly, no indication of the mottled regions
was found in the SEM: i.e., no microcracked regions, no changes in
apparent surface roughness, and no compositional variations. In addition,
SEM images of the etched surfaces were unable to detect domain structure
in the specimens. X-ray diffraction measurements of the polished and
fractured surfaces indicated that the domain structure of all fracture
surfaces (for cyclic and 4-point bend loading) was randomized but that the
remaining portions of the specimen retained substantial poling. Lack of
focus made it impossible to restrict interrogation of the specimen to the
vicinity of the critical flaw to determine if slow crack extension also

affected domain orientation.

TEM observations that cracks are present in both the low and high
temperature specimens and the absence of any detected cracks in the as-
received material indicate that microcrack generation during cyclic
loading is one form of the distributed damage generated during cyclic
loading. The difference in microcrack density and distribution between
the low and high temperature specimens may provide an important clue as to
the macroscopic crack growth behavior of the two types of specimens. At
high temperature, cracks are generated in pockets distributed fairly
uniformly throughout the high stress region of the specimens. However,
the pockets are isolated from each other and do not appear to interact.
The presence of these pockets may account for the sporadic crack extension
described previously[2] in the high temperature specimens as well as for the
crack growth in all directions from the indentation. Cracks in the high
temperature specimen would not be expected to grow for values of K_I less
than K_{Ic}[8]. Therefore, if pockets of microcracks form near the tips of the
radial cracks from the indentation, the radials still would not extend
until the combined stress intensities at the radial crack tip from the
radial crack and one of the microcracks reached K_{Ic}. At that point, the
radial crack would extend discontinuously the distance of the connected
microcracks in the particular pocket. After this extension, no further
crack extension would be expected until another set of microcracks was
created near the radial tip. Since the pockets of microcracks seem to be
generated fairly uniformly over the high stress region of the specimen,
this type of crack extension could occur at any of the radials, resulting
in a discontinuous extension of each of the four cracks. The rate of
crack extension would be limited by the rate at which microcracked regions
intercepted the crack front; as the microcrack density became greater, the
crack growth rate, on average, would appear to increase.

TEM observations of the low temperature specimen suggest that microcracks
in these specimens do not link up to form a larger flaw but form a dense
cloud around the indentation during cyclic loading. When the temperature
increases, after the cloud of microcracks has been generated, the
microcracks evidently link up with the radial cracks from the indentation,
forming a critical flaw which results in catastrophic failure.

SUMMARY

The fracture behavior of PZT-8 was investigated under cyclic loading at
temperatures below 86°C and above 150°C. Crack extension was seen for
specimens loaded at ≈200°C while, for specimens loaded at T ≤ 80°C,
minimal crack extension was observed. However, specimens excited at the
lower temperatures experienced an unidentified accumulation of damage
which resulted in immediate failure when the specimens were driven at
temperatures above 100°C. Crack extension in specimens excited at the
higher temperature could not be attributed to environmentally enhanced
fracture. In addition, increased crack extension rate with increased
cumulative excitation time in the higher temperature specimens implied
possible damage accumulation at those temperatures as well as at the lower
temperatures.

REFERENCES

1. S. W. Freiman, K. R. McKinney and H. L. Smith, "Slow Crack Growth in Polycrystalline Ceramics," in Fracture Mechanics of Ceramics, Vol. 2, (D. P. H. Hasselman and F. F. Lange, eds.) Plenum Publishing Co., New York, NY pp.659-676 (1974).

2. R. F. Caldwell and R. C. Bradt, "Stressing Rate Effects on the Bond Compressive Strengths of a Piezoelectric Ceramic," J. Am. Ceram. Soc. 60 168-170 (1977).

3. J. G. Bruce, W. W. Gerberich, and B. G. Koepke, "Subcritical Crack Growth in PZT," in Fracture Mechanics of Ceramics, Vol 4, (D. P. H. Hasselman and F. F. Lange, eds.) Plenum Publishing Co., New York, NY pp. 687-709 (1978).

4. K. D. McHenry and B. G. Koepke, Electric Field Effects on Subcritical Crack Growth in PZT," in Fracture Mechanics of Ceramics, Vol. 5, (R. C. Bradt and A. G. Evans, eds.) Plenum Publishing Co., New York, NY pp. 337-352 (1983).

5. A. S. Raynes, G. S. White, S. W. Freiman and B. S. Rawal, "Electric Field Effects on Crack Growth in a Lead Magnesium Niobate Ceramic", Proceedings of the Anaheim Meeting of Am. Ceram. Soc.

6. R. C. Pohanka, P. L. Smith and J. Pasternak, "The Static and Dynamic Strength of Piezoelectric Materials," Ferroelect. 50 286-291 (1983).

7. Sumio Takahashi and Eiji Mori, "Fatigue Test of Electrostrictive Material," J. Acoust. Soc. Jap. 28 241-251 (1962).

8. G. S. White, S. W. Freiman and A. S. Raynes, "Cyclic Loading of PZT, I", submitted to Am. Ceram. Soc.

9. G.W. White and M. D. Vaudin, "Cyclic Loading of PZT, II", submitted to J. Am. Ceram. Soc.

10. P. Chantikul, G. R. Anstis, B. R. Lawn, and D. B. Marshall, "A Critical Evaluation of Indentation Techniques for Measuring Fracture Toughness: II. Strength Method," J. Am. Ceram. Soc. 64 #9 539-43 (1981).

Transmission electron microscopy study of domain wall structures in antiferroelectric materials

Marc De Graef, James S. Speck and David R. Clarke

Materials Department, University of California, Santa Barbara, CA 93106

Abstract. The antiferroelectric domain structure of a tetragonal Sn-doped PLZT ceramic was studied by means of transmission electron microscopy (TEM). The various domain walls were identified on the basis of a tetragonal unit cell with c/a = 0.993. Additionally, a long period modulation was observed along the $<110>$ directions (cubic indexing). The temperature dependence of the long period modulation and high resolution observations are presented.

1. Introduction

Ferroelectric antiferroelectric (FE AFE) transitions in ceramic materials lead to desirable electromechanical properties for the construction of energy convertors and actuators. One such system is the solid solution $Pb(Zr,Sn,Ti)O_3$ (Ishchuk 1987). The addition of La or Sn both widen the AFE phase region of the pseudo-binary PZT system and cause a "diffuse phase transition" to take place between the FE and AFE states; this transition can be induced by temperature variations, electric fields or applied mechanical stresses.

Sn-doped PZT ceramics can be tailored to exhibit a phase transition which is nearly independent of temperature. According to Jaffe et al (1971), increasing the Sn-content while maintaining a constant Ti/Zr ratio causes the low temperature rhombohedral phase to be replaced by a tetragonal antiferroelectric phase. The domain structures in these materials are complex and require further characterization. In a study on a related Sn-doped material, $Pb_{0.99}\{[(Zr_{1-y}Sn_y)_{1-x}Ti_x]_{0.98}Nb_{0.02}\}O_3$ (with x=0.03 and y=0.20) a periodic one-dimensional modulation of the AFE phase was reported (Chang 1985); these investigators interpreted the modulations to be anti-phase boundaries in the AFE order of cation displacements.

The present paper reports on room temperature and low temperature TEM observations of domain structures in a compound with nominal composition $(Pb_{0.97}La_{0.02})(Zr_{0.55}Sn_{0.35}Ti_{0.10})O_3$ (PLSnZT). The room temperature equilibrium structure of this material is believed to be tetragonal antiferroelectric.
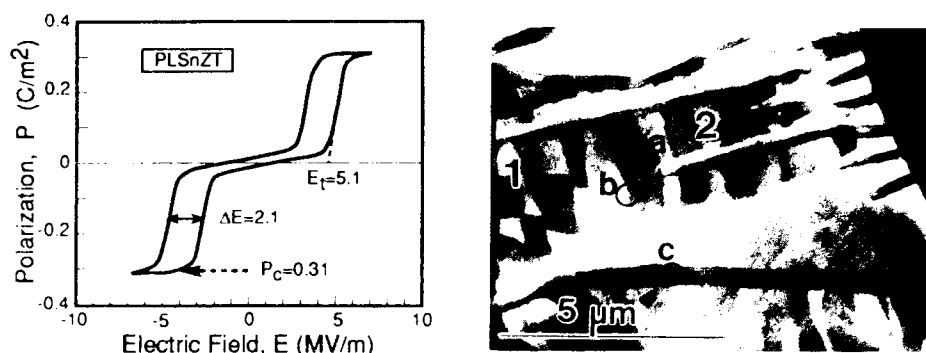
Figure 1: a) Experimental P-E curve for PLSnZT; note the extremely high coercive field of 5.1 MV/m. b) Electron micrograph (dark field (110)-reflection) showing a typical domain pattern in a grain close to the [001] zone axis orientation; a checkerboard pattern (1) and a zebra-like region (2) are indicated. The faint contrast in the intermediate bands is due to ion milling damage. The various domain walls a,b and c are discussed in the text.

2. Experimental observations

The lattice parameters of the tetragonal phase were determined by means of X ray powder diffraction and TEM : $a = 0.8220$ nm and $c = 0.8164$ nm, resulting in a tetragonality of $c/a = 0.993$ and a doubling of the cubic unit cell along the 4-fold directions. The experimental P-E curve is shown in Fig. 1a; the coercive field is very high, 5.1 MV/m. Thin sections for TEM observations were prepared using the standard specimen preparation techniques (dimpling and ion milling).

2.1. Conventional electron microscopy

At room temperature, most grains show a domain pattern (Fig. 1b) with regions which exhibit either a checkerboard or zebra-like contrast alternating with featureless regions. As will be shown further on, the zebra-like domains show a complex diffraction pattern with satellites corresponding to a one-dimensional long period modulation. Three different types of domain walls can be observed : within a dark region of the zebra-like pattern, two orientation variants of the tetragonal structure alternate periodically with a (110)-type contact plane. These domain walls are indicated by the symbol **a** in Fig. 1b. Regions with modulations perpendicular to different (110)-type planes have a different background intensity and are separated by wavy interfaces roughly parallel to (100)-type planes (indicated by **b**). Finally, regions where the periodic modulation occurs along (110) planes which are not close to the Bragg orientation do not show any modulated contrast. The tetragonality gives rise to a small orientation deviation across the boundary indicated by **c** which therefore exhibits δ-fringe contrast (asymmetric bright field symmetric dark field fringe images).

Upon cooling to liquid nitrogen temperature, the lattice parameter decreases and, in addition, the superlattice period shortens by about 5%. Figure 2a shows
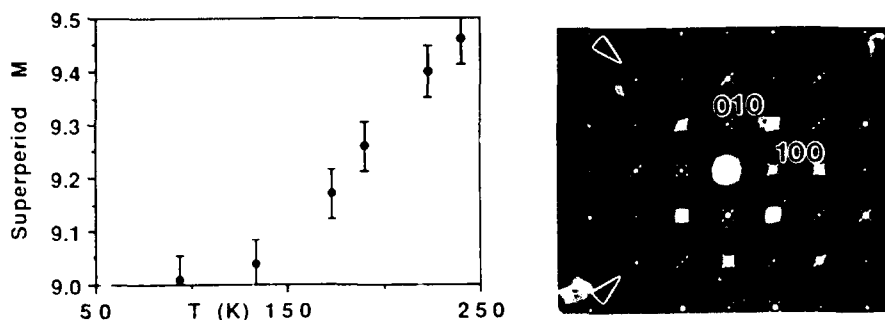
Figure 2: a) Temperature dependence of the superlattice period along [110]; b) [001] section of PbSnZr at 90K with two modulation directions along [110] and [1̄10]

the temperature dependence of the superlattice period M, in multiples of $a/\sqrt{2}$. A typical electron diffraction pattern taken along a cube axis is shown in Fig. 2b; two orthogonal orientation variants can be observed.

At low temperature, in a carbon coated sample, the domain mobility under influence of the electron beam is greatly enhanced; small displacements of the electron beam cause a complete rearrangement of the domains, including the long period superlattice modulations. In a Au/Pd coated sample such beam (or surface charge) induced domain wall motion could not be observed. It is important to note that the complete modulated structure could easily flip from one orientation variant to another. No evidence of a rhombohedral ferroelectric phase was found. This is not surprising, considering the very high coercive field. Controlled in-situ electric field experiments on this material have proven to be difficult.

In several grains, a *domain wall source* was observed at 90K in a carbon coated sample; domain walls, exhibiting the typical δ-fringe diffraction contrast, were emitted from a lattice defect (possibly a dislocation) in a periodic manner, very similar to the well-known Frank-Read source of dislocations. The domain walls were emitted from the defect, migrated through the grain and were annihilated at another stationary domain wall. The frequency of the domain wall source was strongly dependent on the intensity and position of the electron beam with respect to the lattice defect.

2.2. High resolution electron microscopy

High resolution observations along a cube zone axis show two different regions: the undistorted perovskite lattice can be observed in the thinnest specimen regions (no superlattice modulations). This suggests that the stability of the modulated phase is partially determined by a strain component. In thicker regions (Fig. 3) two perpendicular modulation patterns along the [110] and [1̄10] directions can be observed, with a (010) interface plane separating both regions. The contact plane between the bright and dark bands within one variant of the modulated structure is diffuse, in agreement with the weak intensity of the higher order satellite reflections, and is not confined to a single (110) type plane, i.e. the intensity maxima
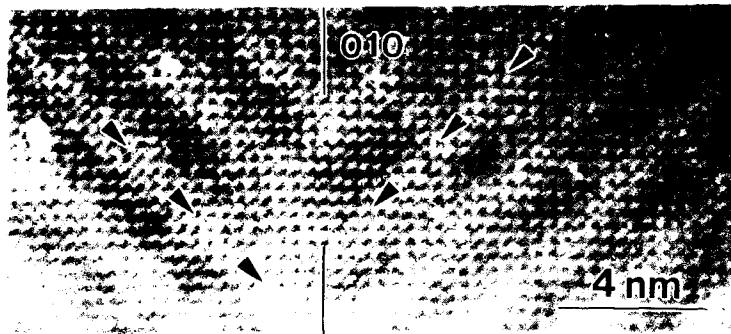
Figure 3: High resolution electron micrographs of a [001] oriented PLSnZT thin film; the change from [110] to [1̄10] modulation directions can be observed. The interface plane is almost parallel to (010).

of the modulation "wander" along the (110) plane. The low temperature mobility of the lattice modulation under influence of the electron beam precludes the possibility of compositional fluctuations. The alternating dark and bright bands in the high resolution micrograph are most likely caused by the different AFE cation displacements in both ba...s; since anti-ph... e boundaries usually do not give rise to different background int. sities on either side of the interface plane, we tentatively interpret the modulations as being du. to twin-related arrangements of the cation displacements. For a full interpretation of these high resolution micrographs the complete atom coordinates are required, including the AFE displacement pattern. To our knowledge the cation displacements of the AFE cell are unknown and hence a full image simulation was not possible.

3. Discussion and Conclusion

The domain structure of an AFE PLSnZT ceramic is complex. A full understanding of the electric properties (e.g. the high coercive field) of these materials requires a detailed study of the AFE cation displacement patterns and the stable domain wall geometries. Further crystallographic work is in progress.

References

Ishchuk V M and Zavadskii E A 1987 *Sov. Phys. Solid State* **29** 932
Jaffe B, Cook W R and Jaffe H 1971 *Piezoelectric Ceramics* (London: Academic Press) pp 174-181
Chang Y J, Lian J Y and Wang Y I 1985 *Appl. Phys.* **A36** 221

Conceptual design, kinematics and dynamics of swimming robotic structures using active polymer gels

M. Shahinpoor

Department of Mechanical Engineering
University of New Mexico, Albuquerque, New Mexico 87131

ABSTRACT: Discussed are the structural design, kinematics and dynamics of swimming of autonomous swimming robotic structures which utilize an arrangement of electrically controlled polymeric ionic gel muscles. The general structural design of such swimming robotic structures is considered to be in the form of a submarine structure which is partially encapsulated in an elastic or flexible membrane filled with a counterionic electrolyte such as water+acetone. In such an encapsulated portion of the robotic swimming structure are specifically arranged polyacrylamide or PVA−PAA polymeric cylindrical fibres or bundles. The arrangement of, say, polyacrylamide fibres is such that it is capable of generating microprocessor−based electrically controlled propagating transverse waves to propel the partially encapsulated membrane structure in any direction and in any desired manner.

1. INTRODUCTION

Kuhn(1949) and Katchalsky (1949) originally reported on the possibility that certain co−polymers may be chemically contracted and expanded like a synthetic muscle. As originally reported by Kuhn, Horgitay, Katchalsky and Eisenberg (1950) a three dimensional network, consisting of polyacrylic acid, can be obtained by heating a foil of polyacrylic acid containing a polyvalent alcohol such as glycerol or polyvinyl alcohol. The resulting three−dimensional networks are insoluble in water but swell enormously in water on addition of alkali and contract enormously on addition of acids. Linear reversible dilations and contractions of the order of more than 500 per cent have been observed in our laboratory. Furthermore, as reported recently by Li and Tanaka (1990), the structural deformation (swelling or collapsing) of these gels is homogeneous in the sense that, for example, for a long cylindrical gel, the relative changes of the length and the diameter are the same.

Polymethacrylic acid cross−linked by divinyl benzene copolymerized in methanol exhibit similar properties, as shown by Kuhn, Horgitay, Katchalsky and Eisenberg (1950). Chemically stimulated pseudo−muscular actuation has also been discussed recently by De Rossi, Chiarelli, Buzzigoli, Domenici and Lazzeri (1986), Caldwell and Taylor (1990), and Segalman, Witkowski, Adolf and Shahinpoor (1991).

The possibility of using these polymeric gel muscles or actuators for mechanochemical engines and turbines was originally discussed by Steinberg, Oplatka, and Katchalsky (1966), and Sussman and Katchalsky (1970).

Hamlen, Kent and Shafer (1965) were the first to report that the same effect can be obtained electrically. In this case a voltage is applied which causes the solution to become either acidic or alkaline depending on the direction of the current or the sign of

the voltage. If the solution becomes alkaline it forces the gel to expand. Otherwise, the solution becomes acidic and the gel contracts. Thus, a reversible expansion and contraction of the fibre is obtained with the application of an electric field. Depending on the orientation of the fibres these polymer gels may also undergo reversible bending in an electric field as shown by Kurauchi, Shiga, Hirose and Okada (1990). In the following sections, first a conceptual design for such autonomous swimming robotic structures is presented followed by a discussion on the kinematics and subsequently dynamics of such structures.

2.CONCEPTUAL DESIGN OF AN AUTONOMOUS SWIMMING ROBOTIC FISH

Consider a prismatic structure of, say, rectangular cross section. Assume that the on—board batteries, the electronics, the EPROM chips and microprocessors are housed in the volume of the robotic structure's head as shown in Fig. 1. Attached to this head is an elastic or otherwise flexible membrane structure filled with an aqueous counterionic electrolytic solution such as water+acetone. The membrane is considered to be wire—framed by means of elastic strings as shown in Fig. 1. A large number of printed wires are run from the head to various locations on the inside wall of the elastic dielectric membrane where they are connected to a number of electrodes also printed inside the membrane wall as shown in Fig. 2.
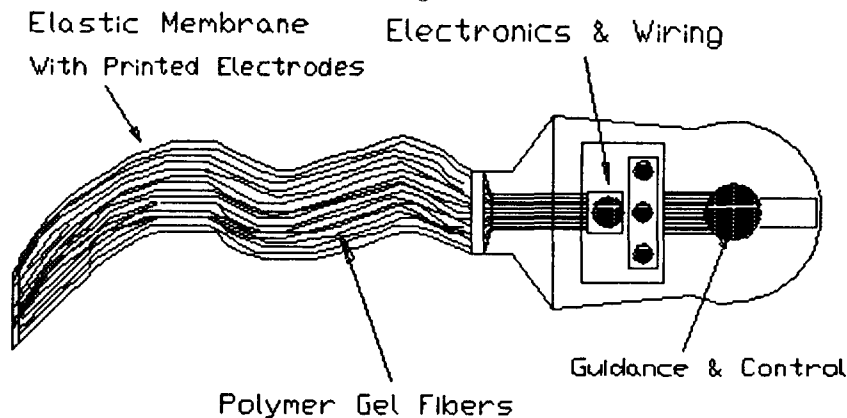
Figure 1— A proposed design for an autonomous swimming robotic fish
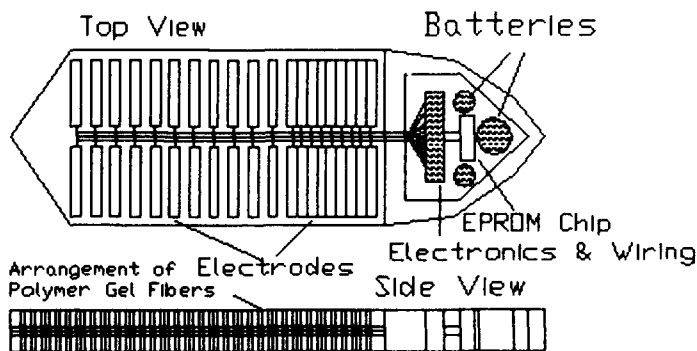
Figure 2— Mechatronic design of a swimming robotic structure

Note that with some specific arrangement of polymeric fibres, micro–processor–based, electrically controlled expansion and contraction of the tail portion of the robotic structure may be achieved, thus enabling the robotic structure to swim freely like a fish. In this regard, a variety of induced motions may be achieved ranging from eel–like to normal fish–like propulsions as shown in Fig. 3 .
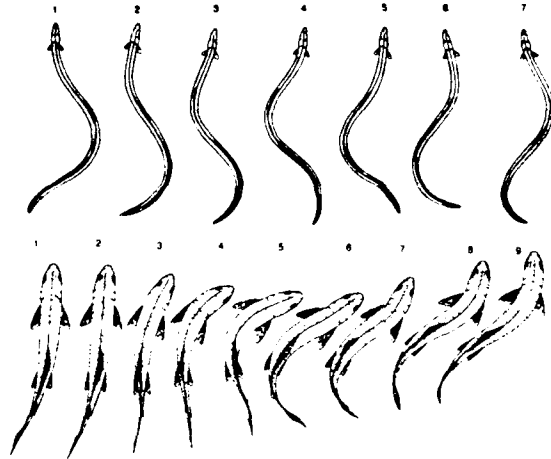
Figure 3– Comparison between the wavy motions of an eel and a fish
(from P.W. Webb(1984) with permission)

3. KINEMATICS & DYNAMICS

Referring to Figure 4, below, note that travelling body waves may be generated to move the partially–encapsulated membrane structure from the membrane head where it is attached to the robotic fish head by internally activating or flexing segments of the polymeric muscles which are floating in the electrolytic solutions inside the elastic membrane.

Thus, a travelling wave in the x direction is electrically created such that

$$Y(s,t) = y(s) \sin(2\pi/l) (s - v_x t) \qquad (1)$$

where $y(s)$ is the magnitude of the travelling wave generated by electrically flexing the polymeric muscle at various locations along the arc length s, l is the overall length of the muscle, s is the arc length, v_x is the speed of the propagating transverse travelling wave in the x direction and t is the time. Note that $v_x(s,t)$ is controlled by the speed of triggering the polymeric muscles to flex sequentially along the arc length s. Further, it is to be noted that

$$v_y = (d/dt) Y(s,t) = v_y(s,t) \qquad (2)$$

is the component of the velocity in the y direction and the slope of the muscle, i.e., (dY/dx) is controlled electrically such that

$$(dY/dx) = f(E,s,t) \qquad (3)$$

where E is the electric field strength.

The propulsive forces in a fluid medium can be either by resistance forces or by reaction forces. Here only the resistance forces are considered because of the fact that the motion of polymeric fins and muscles is very slow. Consider an encapsulated polymer muscle of unit length 1 and width b moving in water by producing travelling waves that effectively propel the robotic fish at a velocity of U as shown in Fig. 4.
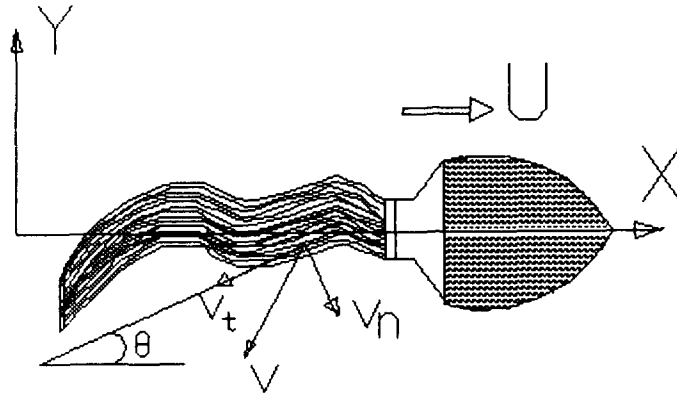
Figure 4– A simple model for a robotic fish with ionic gel muscles

The velocity vector **v** as a function of the arc length s at any point on the surface of the membrane is given by

$$v(s) = (v_x, v_y) \tag{4}$$

where the velocity components v_x and v_y are related to the normal and the tangential velocity components v_n and v_t by the following equations :

$$\begin{bmatrix} v_n \\ v_t \end{bmatrix} = \begin{bmatrix} -\sin \theta & \cos \theta \\ \cos \theta & \sin \theta \end{bmatrix} \begin{bmatrix} v_x \\ v_y \end{bmatrix} \tag{5}$$

where θ is local slope of the muscle body curvature and is given by

$$\tan \theta = (dY/dx) \tag{6}$$

The normal and the tangential components of the velocity vector in turn contribute to pressure drag and skin friction drag, respectively. The differential version of these drag forces can be written as dF_n, and dF_t such that

$$dF_n = -(1/2) \, C_n \, \rho \, b \, |v_n| \, v_n \, ds \tag{7}$$

$$dF_t = -(1/2) \, C_t \, \rho \, b \, |v_t| \, v_t \, ds \tag{8}$$

where C_n and C_t are the pressure drag and the skin friction drag coefficients, respectively, and ρ is the density of the fluid medium. The differential propulsion thrust developed can be calculated as

$$dF_x = dF_n \sin \theta + dF_t \cos \theta \tag{9}$$

which is expanded to

$$dF_x = -(1/2)\,\rho\,b\,[\,C_n|v_n|v_n\sin\theta + C_t|v_t|v_t\cos\theta\,]\,ds \qquad (10)$$

Integrating equation (10) over the entire arc length s yields the total propulsion thrust in the direction of **U** as

$$F_x = -(1/2)\rho b \int_0^1 [\,C_n|v_n|v_n\sin\theta + C_t|v_t|v_t\cos\theta\,]\,ds \qquad (11)$$

As far as the dynamics of the gel itself is concerened the reader is referred to Segalman, Witkowski, Adolf and Shahinpoor (1991) for a description of a detailed continuum theory of ionic gels. In order to control the motion of this robotic structure by an EPROM or a microprocessor chip, one has to find a relationship between the force imposed on the gel by the electric field E and the electric field strength E itself.

The solution to the combined kinematics–dynamics–continuum mechanics equations for the above simple structure is presently underway and will be reported in soon.

4. ACKNOWLEDGEMENT

5. REFERENCES

1. Caldwell, D. G., and P. M. Taylor, 1990, Chemically Stimulated Pseudo–Muscular Actuation, Int. J. Engng Sci., 8, 797–808
2. De Rossi, D. E.,Ciarelli, P., Buzzigoli, G., Domenici, C., and L. Lazzeri, 1986, Contractile Behavior of Electrically Activated Mechanochemical Polymer Actuators, Trans. Am. Soc. Artif. Intern. Organs, XXXII, 157–162
3. Hamlen, R. P., Kent, C. E., and S.N. Shafer, 1965, Electrolytically Activated Contratile Polymer, Nature, 206, 4989, 1148–1149
4. Katchalsky, A., 1949, Rapid Swelling and De Swelling of Reversibel Gels of Polymeric Acids By Ionization, Experientia, 5, 319–320
5. Kuhn,W., 1949, Reversible Dehung and Kontraction bei Anderung der Ionisation lines Netwerks Polyvalenter Fadenmolekulionen, Experientia, 5, 318–319
6. Kuhn, W., Horgitay, B., Katchalsky, A., and H. Eisenberg,1950, Reversible Dilation and Contraction By Changing The State of Ionization of High–Polymer Acid Networks, Nature, 165, 4196, 514–516
7. Kurauchi, T., Shiga, T., Hirose, Y., and A. Okada, 1990, Deformation Characterization of Polymer Gels In Electric Fields, Toyota Central Research & Development Lab. Publication, 41–1, Nagakute, Aichi, 480–11
8. Li, Y., and Tanaka, T., 1990, Kinetics of Swelling and Shrinking of Gels, J. Chem. Phys., 92, 2, 1365–1371
9. Segalman, D., Witkowski, W., Adolf, D., and Shahinpoor, M., 1991, Electrically Controlled Polymeric Muscles As Active Materials Used In Adaptive Structures, Proc. ADPA/AIAA/ASME/SPIE Conference on Active Materials and Adaptive Structures, Nov. 4–8
10 Steinberg, I.Z., Oplatka, A., and A. Katchalsky, 1966, Mehcano Chemical Engines, Nature, 210, 5036, 568–571
11 Sussman, M.V., and Katchalsky, A., 1970, Mechano Chemical Turbine: A New Power Cycle, Science, 167, 45–47
12 Webb, P.W., 1984, Form and Function In Fish Swimming, Sci. Am., 251, 1, 72–83

A study on control of a light weight robotic system using piezoelectric motor, sensor and actuator

Zhen Wu, Xiao-Qi Bao, Vijay K. Varadan and Vasundara V. Varadan

Department of Engineering Science and Mechanics, Center for the Engineering of Electronic and Acoustic Materials, The Pennsylvania State University, University Park, PA 16802

ABSTRACT: A single link flexible robotic manipulator having a actively controlled arm with attached piezoelectric vibration sensors and actuators and a servo controlled travelling wave type piezoelectric motor as driver is constructed. By using a simple control algorithm, the manipulator can be computer controlled to move to a programed destination very quickly and smoothly, with the settling time shortened by a factor of approximately 1/60. This "piezo-robot" conceptually achieves the goals of light weight, flexibility and dexterity.

1. INTRODUCTION

One of the trends in the evolution of robots is to reach the goals of light weight, compliance (or flexibility) and fast response in robotic manipulators and end-effectors in which the drivers are self-contained. However, one of the limitations of reducing volume and weight is due to the mass and bulk of conventional drivers (i.e. AC/DC electric motors, hydraulic or pneumatic actuators). Another factor is that heavy and stiff manipulating structures must be used to prevent vibration interferences during manipulating operations, because the structural deformation of flexible links severely impairs the end-point accuracy. So, many robots are "over designed" to be heavy and rigid, even though the actual tasks they perform are paint spraying or welding. This paper proposes new approaches of applying small, light weight piezoelectric sensing and actuating devices and active vibration control techniques to achieve a light weight and dextrous robotic arm.

The piezoelectric/ultrasonic motor operates on a new principle of obtaining rotation or linear motion from specially configured ultrasonic vibrations inside the stator generated by piezoelectric elements. It has the advantage of being a light weight, simple structure, fast in response for starting and stopping, direct in adaptability to low speed rotation and free from magnetic noise. Several Japanese researchers, for example Inaba *et al* (1987), Iijima *et al* (1986), Kuribayashi *et al* (1985) developed various types of piezoelectric motors in the mid-80's, among which the travelling wave type motor by Inaba *et al* is most applicable.

Piezoelectric motors are being used in automation, robotics, audio and visual appliances. Schoenwald *et al* (1988) designed a mini gripper using a linear piezoelectric motor. In this paper, a servo controlled travelling wave type piezo-motor is designed as a lightweight and dextrous driver for the robot.

Research on the control of flexible robotic manipulators has become a hot topic in recent years. Many theoretical models have been developed and some primary experimental results have been published (Biswas and Klafter 1988). Most of the work is based on control of the driver (motor) of the robotic arm to achieve smooth and precise motion of the arm tip including starting and stopping. In this paper, an independent lightweight piezoelectric vibration sensor/actuator pair is attached to the manipulating structure and the control is based on active damping concept (Sung *et al* 1989), which deals with any kind of vibration interference without restriction on the motor speed. The lightweight piezoceramic sensors and actuators have high electromechanical coupling and are ideal for active vibration control.

2. PIEZOELECTRIC MOTOR AND ITS SERVO-CONTROL

The structure of the travelling wave type piezoelectric motor is shown in Figure 1. The "stator" consists of two piezoelectric elements (piezoceramic disks) which convert electrical energy into mechanical energy, an elastic element (made of steel), and a support base. The piezoceramic disks are bonded to the elastic element, thus the electrically induced strain inside the piezoceramic disks causes deformation in the elastic element. Specially
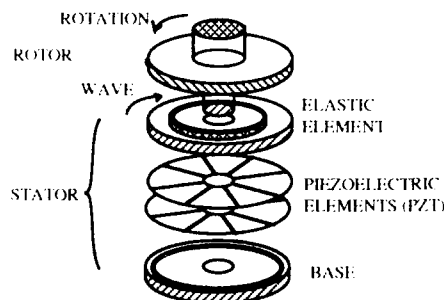
Fig. 1 Structure of the Piezoelectric Motor

configured piezoelectric elements shown in Figure 2 leads to a flexural (bending) vibration mode when an alternating electric voltage is applied at the frequency of modal resonance. Two phases of flexural vibration generated individually by two piezoceramic disks, are superimposed into a travelling wave propagating in the circumferential direction. As the wave advances, the surface particles of the elastic element move in an elliptical trajectory, and thus have a velocity component along the surface opposite to the wave direction. The rotor, which is pressed on the stator, picks up this velocity via frictional force and rotates a direction opposite to wave propagation in the stator (See Figure 3). By changing the direction of the travelling wave, the motor can be reversed.

The piezo-motor has a simple and lightweight structure which is free of magnets or coils. Its speed is several hundreds rpm, which is directly adaptable to most robotic applications. It also

has a very fast response (typically within 10^{-2} sec. or smaller) in starting, stopping and reversing, since friction force works as a brake and provides a holding torque when the motor is off. For electromagnetic motors, the braking and holding torque must be generated externally by a complicated electronic circuit.
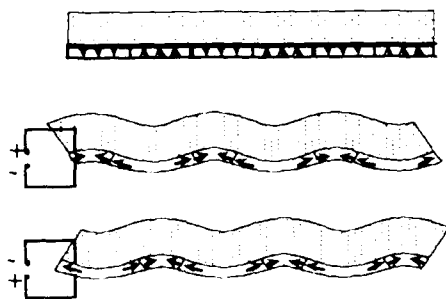
Fig. 2. Flexural Mode Vibration in Stator
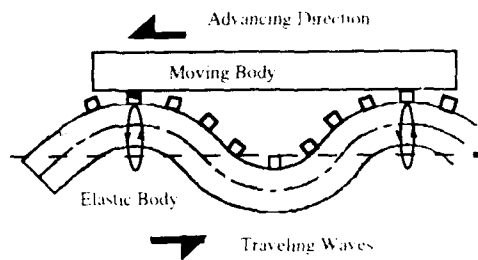
Fig. 3. Moving Mechanism of Rotor

For a piezo-motor, the rotor must overcome a starting torque due to static friction, so the motor speed cannot be linearly controlled by varying the input voltage, like for a DC motor. A new method of modulating the input power by a square wave gating signal is tried. By suitably choosing the period (or frequency) of the modulating signal, an approximate linear response of the motor speed with respect to the duty cycle (percentage of time when the motor is switched on out of one period) of the modulating signal can be obtained. From our experiences, a low modulating frequency is suitable for the control of low speed, while, a high modulating frequency is suitable for high speed control. A closed-loop servo position control system which consists of a piezo-motor, a positional sensor (encoder) and a PC controller is shown in Figure 4. Although the piezo-motor has a fast on/off response within tens of milliseconds, there is still a small amount of overshoot when the motor approaches its destination. To avoid this overshoot, the position control strategy is as follows: (1) let the motor start at its full speed (set duty cycle to 100 %); (2) when the motor gets within a certain distance to the destination, reduce the motor speed by setting a lower duty cycle; (3) turn off the motor when the destination is reached. The distance threshold value and the duty cycle should be selected depending on the load and the speed of the motor.
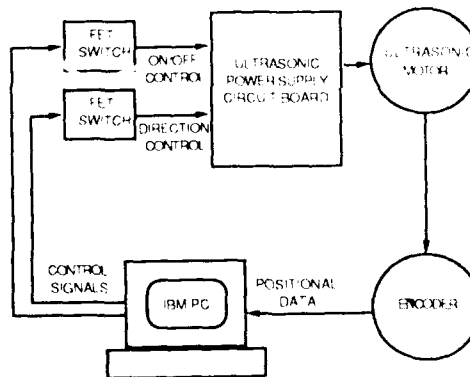
Fig.4. Schematic Diagram of Servo Control System for the Piezoelectric Motor

3. ACTIVE VIBRATION CONTROL OF ROBOTIC ARM

Most manipulating structures for robots can be roughly considered as cantilever beams. One end of the beam is clamped on the motor shaft, and the other end is usually free. The vibration interference often occurs at the lowest free bending mode of a light, flexible arm. Active vibration control is accomplished by a sensor-actuator feedback loop. The displacement, velocity, or other characteristic signals of vibrations of the structure are picked up by sensors, then the actuator produces an external force to actively suppress the vibration, in response to the signal from the sensor.

Figure 5 shows the feedback loop for the active vibration damping for a cantilever beam, piezoceramic sensors (13x9 mm) and actuators (25x9 mm) are placed on both sides of a cantilever beam (254x9 mm) and connected in parallel (bimorph arrangement). The sensors and actuators are located at the clamped end, where the curvature of the deformed beam and the electromechanical coupling are at a maximum. The constant velocity feedback control algorithm is implemented by an analog control loop. The output of the sensor (conditioned via a current pre-amplifier) is $180°$ out of phase with respect to the vibrating velocity at resonance. This signal is fed to the actuators by a power amplifier and thus suppresses the vibration. The band-pass filter picks up the signal of the mode to be controlled and the phase shifter compensates for other instrumental delay in the loop. So far, only the first bending (deflection in z-axis) mode is controlled. The experimental comparison on the residual vibration of the beam with and without the active damping are shown in Figure 6. When the arm is subject to a step impulse, the vibration amplitude decays exponentially as $V=V_0 \exp(-\alpha t)$. The damping factor α is about 0.17 for natural damping (trace a) and about 9.8 for actively controlled damping (trace b). By active damping, the residual vibration is neutralized within 0.4 second, therefore, the settling time is significantly reduced, which can even be observed by the naked eye.
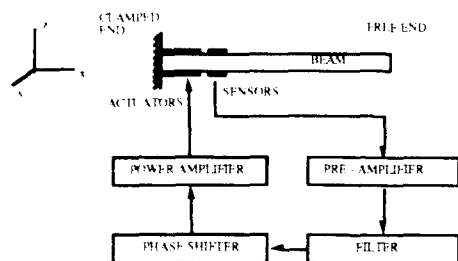
Fig. 5. Block Diagram of Active Vibration
       Control Feedback Loop
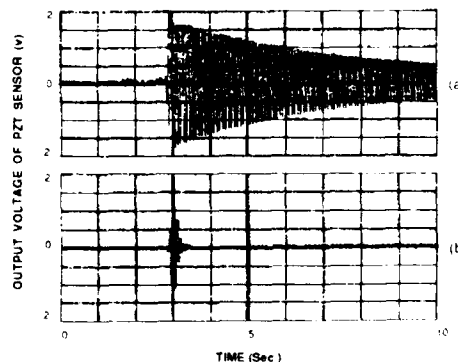
Fig. 6. Experimental Results on
       Active Vibration Control

4. "PIEZO-ROBOT" --- SUMMARY AND CONCLUSIONS

A single link, single axis flexible robotic manipulator, basically consists of a flexible arm with the piezoelectric sensors and actuators attached and a servo controlled piezoelectric motor as the driver is constructed. The unique features of light weight, quick response, and minimized residual vibrations and settling time have been achieved in this prototype "piezo-robot" as shown in Figure 7. The piezo-motor is 40 mm in diameter, and 12 mm high. It weighs only 70 grams. The maximum speed is 600 rpm, and the maximum torque is 0.07 N-m. The length of the arm is about 25 cm, and the weight of the steel arm is about 21.2 grams, including 2.2 grams of piezoceramic pieces. The total weight of the manipulator is only about 100 grams (excluding the base box). This "piezo-robot" is controlled by a PC computer and can move to a programed destination along a programed path with quick start/stop response and very short settling time.

In conclusion, the two approaches proposed for a light weight, flexible and dexterous robot, the piezoelectric motor and active vibration control using piezoelectric sensors and actuators, are shown to be feasible in practise.
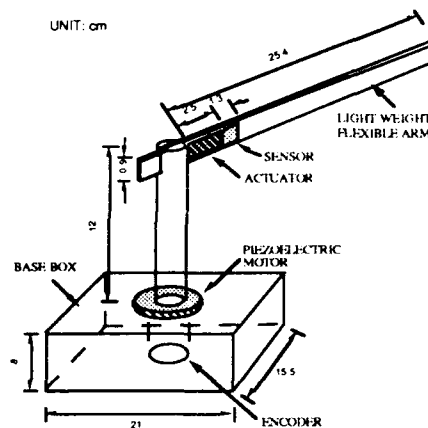
Fig. 7. Schematic Diagram of Single Link, Single Axis "Piezo-robot"

REFERENCE

Biswas S K and Klafter R D 1988 *Proc. IEEE Int. Conf. on Robotics and Automation*, pp. 15
Iijima T, Wada M, Nakagawa Y and Itoh H 1986 *Proc. 7th Symposium on Ultrasonic Electronics*, (Kyoto Japan), pp. 191
Inaba R, Tokushima A, Kawasaki O, Ise Y and Yoneno H 1987 *IEEE Ultrasonics Symposium*, pp. 747
Kuribayashi M, Ueha S and Mori E 1985 *J. Acous. Soc. Am.* **77**, pp. 1431
Schoenwald J S, Beckham P M, Rattner R A, Vanderlip B and Shi B E 1988 *IEEE Ultrasonics Symposium*, pp. 513
Sung C C, Bao X Q, Jeng J H, Varadan V V and Varadan V K 1989 *J. Wave-Material Interaction* **4**, pp. 65

Experimental verification of a nonlinear based controller for slewing of flexible multi-body systems

Farshad Khorrami   Sandeep Jain

Control/Robotics Research Laboratory
School of Electrical Engineering & Computer Science
Polytechnic University, 333 Jay Street
Brooklyn, NY 11201

ABSTRACT

In this paper, experimental results for slewing of a class of flexible multi-body systems (i.e., flexible multi-link manip^{o}tors) are given. A two-link flexible arm has been developed at the Control/Robotics Research Laboratory (CRRL) at Polytechnic university. The manipulator has been designed to study different configurations (i.e., rigidity) of the arms. This setup mimics the behavior of deployable or erectable spacecrafts. The structural frequencies of the setup is clustered in the low frequency range and is well within the control bandwidth. Furthermore, this system is nonminimum phase due to noncollocated sensing and actuation. The nonminimum phase property limits the achievable control bandwidths. These characteristics are present in many large flexible structures and rapid retargetting and pointing systems. A two-stage controller is utilized for vibration damping and end-effector trajectory tracking of a two-link flexible manipulator. The measurements utilized for vibration suppression are obtained through accelerometers mounted on the tip of flexible members. The real-time computing power is provided by a digital signal processing board (TMS320C30 based) capable of 33 Mflops.

I. INTRODUCTION

Due to earth-based and space-based applications, much attention has been given to modeling and control of flexible multi-body systems. Furthermore, studies on articulated elastic multi-body systems also enhance the knowledge in Control/Structure Interaction of large space structures. It is crucial that ground-based experimental studies be carried out on active control of flexible multi-body systems and flexible structures. We have developed a set of experimental test beds to study the Control/Structure Interaction in flexible structures. One of the test beds is a two-link flexible manipulator described in more detail later in the paper.

The complication in controller synthesis for multi-link flexible manipulators is due to the fact that the input/state map of flexible-link manipulators is not externally feedback lineariz-.able [1, 2]. In addition, the dynamics of flexible-link manipulators are much more complicated than the corresponding rigid-link manipulators. Not only the distributed parameter nature of the dynamics is a complication, but also the moving boundary conditions at the tip of the flexible links connected to the next link are major difficulties. Several modeling techniques

and different control algorithms have been proposed for flexible-link manipulators ([3, 4, 5, 6], to name a few). Several approaches for nonlinear and linear control designs are being pursued at this time. The advocated controllers are being implemented on a two-link flexible arm developed at CRRL at Polytechnic University.

II.   EXPERIMENTAL SETUP

A two-link robot arm with replaceable links has been developed (Figure 1). Different configurations (i.e., rigidity) can be studied by varying the lengths and the thickness of the arms. The actuator for the first link is a direct drive DC motor and the second link is actuated by a geared DC motor through anti-backlash gears. Each arm is instrumented with piezoelectric type accelerometer at the tip and several strain gages along the link. Furthermore, the angular positions and velocities of the arms are measured by optical encoders and DC tachometers respectively. The optical encoders for the first and sceond joint have resolutions of 0.05 and 0.075 degrees respectively. The second joint has been designed to be lightweight; however, air cushion support is available for the joint and the tip on a granite table. At this time, the tip of the manipulator is only supported by an air cushion. This will provide torsional stiffness at the joint. All the sensors are signal conditioned and filtered for anti-aliasing (the cutoff of the low-pass filters is 50Hz). A CCD camera is also being mounted above the setup to provide information on the end-effector tracking performance of the robot manipulator. The real-time computing power for the experiments is a digital signal processing board (TMS320C30 based) capable of 33 Mflops. The DSP board communicates directly with three other boards through a DSP link. The other three boards are 1) 32-channel analog input board with 12 bit A/D convereters. 2) 16-channel analog output board. 3) a custom designed 16-bit digital input/output board for accessing the optical incremental encoders on the joints.
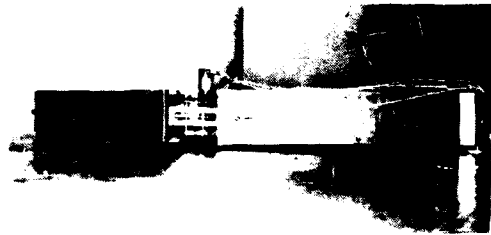
Figure 1: Experimental setup of a two-link flexible arm.

III.   MODELLING AND MODEL VALIDATION

A detailed derivation of the dynamics for open chain kinematic flexible manipulators was presented in [7, 3, 8]. The approach advocated in [3] was the extended Hamilton's principle to obtain the integro-partial differential equations representing the dynamics. Various effects such as axial displacement, shear, torsion, centrifugal stiffening, Coriolis, and gravity were considered. A finite dimesional approximation of the model through finite elements or assumed mode technique may be obtained. The generic model for the class of flexible multi-body systems are as follows:

$$\begin{bmatrix} M_{rr} & M_{rf} \\ M_{fr} & M_{ff} \end{bmatrix} \begin{bmatrix} \ddot{q}_r \\ \ddot{q}_f \end{bmatrix} + \begin{bmatrix} D_r & 0 \\ 0 & D_f \end{bmatrix} \begin{bmatrix} \dot{q}_r \\ \dot{q}_f \end{bmatrix} + \begin{bmatrix} 0 & 0 \\ 0 & K \end{bmatrix} \begin{bmatrix} q_r \\ q_f \end{bmatrix} = \begin{bmatrix} F_1(q_r, \dot{q}_r, q_f, \dot{q}_f) \\ F_2(q_r, \dot{q}_r, q_f, \dot{q}_f) \end{bmatrix} + \begin{bmatrix} I \\ 0 \end{bmatrix} u \quad (1)$$

where q_r is the vector of the rigid body variables. q_f is the vector of the flexure variables. M is the inertia matrix, f_is are the vectors containing Coriolis, centrifugal, gravitational terms.

and coupling of the flexible and the rigid (joint) variables, K is the diagonal stiffness matrix, D_r and D_f are viscous and structural damping coefficients, and u is the generalized inputs (torques) to the system.

At this point, we have tested the individual subsystems in the setup and have identified the models of the actuators. A careful model validation of the actuators have been performed taking into account the effects of stiction. Furthermore, analog velocity loops are included on the motors to reduce the effect of stiction. The actuator models have been developed through time-domain (step responses) and frequency-domain (frequency response) techniques. All the subsystems in the system have been carefully evaluated. We have developed a simulation model for the one-link flexible arm which matches the experimental results closely. At this point, we are developing an actual simulation of the two-link (flex-flex) experimental setup by including the effects of the anti-aliasing filters in addition to all the actuator and sensor dynamics. We have also implemented several simple feedback control algorithms.

IV. CONTROL DESIGN

A. Input-Output-State Properties

The class of systems under study can be put in the standard form

$$\dot{x} = f(x) + g(x)u \tag{2}$$
$$y = h(x). \tag{3}$$

For notational simplicity and due to lack of space, we consider the dynamics of one-link flexible arm here. However, the results are true for the multi-link case. These systems are not input/state linearizable under a nonlinear change of coordinate and control. However, the input-output map may be linearized, i.e.,

$$\dot{z}_1 = z_2$$
$$\dot{z}_2 = b(z_1, z_2, \eta) + a(z_1, z_2, \eta)u = L_f^2 h + L_g L_f h \ u$$
$$\dot{\eta} = \psi(z_1, z_2, \eta) \tag{4}$$
$$y = z_1 \tag{5}$$

where $z = \Phi(x)$ is given by $z_1 = h(x)$, $z_2 = L_f h(x)$, $z_i = \phi_i(x)$ for $i = 3, \cdots, 2p + 2$ where p is the number of modes retained in the approximation. ϕ_is satisfy $L_g \phi_i(x) = 0$ and $L_f(.)$ is the Lie derivative of $(.)$ in the direction of the vector field f.

It is well known that the zero dynamics play an important role in stabilization and output tracking for nonlinear systems. The zero dynamics for this system are given by the restriction of the evolution of the system on the subset

$$\Omega = \left\{ x \in \mathcal{R}^n \mid h(x) = L_f h(x) = 0 \right\}.$$

Therefore, the zero dynamics are

$$\dot{\eta} = \psi(0, 0, \eta). \tag{6}$$

The zero dynamics turns out to be asymptotically stable if viscous or structural damping is assumed to exist in the model and the output function is taken as the joint position. However, if the end-effector position (or acceleration) is chosen to be the output function, then the zero dynamics of the system is unstable. Therefore, this nonlinear system is non-minimum phase

and due to this fact there is a limitation on the achievable bandwidth. This will be seen later in the linear analysis of the arm in a later section.

The above analysis also suggests a method for control of the arm. If a given joint trajectory, i.e., y_{ref} is to be tracked, then the following control will be feasible

$$u = [L_g L_f h(x)]^{-1}[\ddot{y}_{ref} - L_f^2 h(x)] \qquad (7)$$

where η is found as the solution of

$$\dot{\eta} = \psi(y_{ref}, \dot{y}_{ref}, \eta).$$

B. *Asymptotic Perturbation*

An asymptotic expansion analysis of the dynamics of the multi-link flexible manipulators has been given [3]. Utilizing this approach, a nonlinear based controller is established. The expansion was performed by embedding a small parameter in the distributed-parameter model of the arm and performing an asymptotic expansion. The small parameters are $\epsilon_i = \frac{m_i L_i^3}{E_i I_i}$ where m_i is the mass of link i, $E_i I_i$ is the bending stiffness of link i, and L_i is the length of link i. The choice of these parameters signifies that as the link becomes shorter or as the bending stiffness of the link becomes larger, the perturbation parameter becomes smaller. In turn, this corresponds to the fact that as this parameter vanishes the manipulator behaves as if it were rigid. A nonlinear feedback based on this scheme may be derived.

C. *Linear Outer-Loop Controllers*

Robustness to parameter variations and unmodelled dynamics are central issues in design of feedback control systems. Many approaches have been proposed to satisfy and enhance the robustness of the closed-loop systems. The aforementioned nonlinear based controllers utilize the joint information for large angle slewing of the structure; however, to achieve a better performance, we are augmenting the nonlinear based controllers with an outer-loop linear control design. The linear control methodologies utilized are linear quadratic output feedback regulator, frequency shaping [9], Wiener-Hopf design, robustness through structured representation of the uncertainties [10] (to name a few).

V.   EXPERIMENTAL RESULTS

The transfer function from the system input to the end-effecter position for a typical flexible structure is non-minimum phase. The non-minimum phase behaviour is expected due to the non-collocated nature of the system output. Figures 2 and 3 depict the magnitude plot and the pole-zero locations for the transfer function of our experimental single-link flexible arm with no payload from the joint motor input voltage to the end-effector acceleration. The peaks correspond to the vibrational modes of the beam. Note that the system poles are lightly damped and due to the non-minimum phase nature of the system, this imposes limitations on the system bandwidth. Experiments were also carried out on parameter identification for a two-link flexible set-up with the following parameters: Length of link 1 = $0.45m$, Link 1 thickness $= \frac{3}{32}$", Length of link 2 = $0.61m$, Link 2 thickness $= \frac{1}{16}$", Elbow mass (comprising of joint 2 actuator assembly) = $96.4gms$, Payload mass = $100gms$.
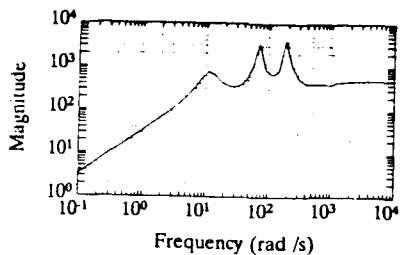
Figure 2: Magnitude plot.
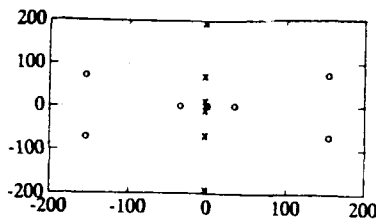
Figure 3: Pole-zero locations.

The system modes were estimated by analyzing the response of the accelerometers at the elbow and the end-effector using white noise as input to both the joint actuators. Identification of the vibrational modes using fast fourier transform techniques showed a number of "closely packed" vibrational modes at frequencies less than 2 Hz. A typical FFT plot for the end-effector acceleration is shown in Figure 4. From the plot, at least 3 modes can be distinctly identified below 2 Hz. two of which have a separation of 0.4 Hz. This is in contrast to the case of a one-link flexible arm where the system modes are relatively far apart. The denseness of the modes is attributed to the coupling of the individual modes of the two highly flexible links.
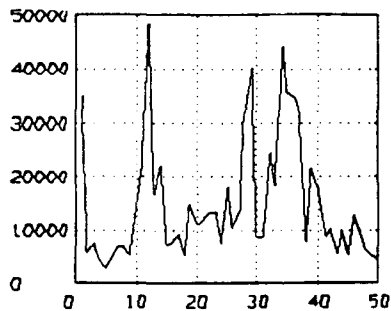
Figure 4: FFT of tip acceleration.

For the inner loop control, two different control schemes were applied. The first was an independent joint PD control and the second was a rigid body based non-linear control. Since both these controls are joint based schemes, significant vibrations at the tip are observed in both cases as shown in Figure 5. However, in the non-linear control case, the inner loop PD control operates on the linearized $\mathcal{O}(1)$ dynamics and hence results in lesser vibrations at the end-effector.

Next, an outer loop controller was designed for the closed-loop system (including the inner loop controller) for supression of the end-effector vibrations. The controller was a linear output feedback designed according to a quadratic cost criterion. This nonconvex optimization problem was solved by a software developed in house. The feedback signals were the outputs of the accelerometer signals at the elbow and the end-effector. The feedback gains obtained were fine-tuned experimentally to achieve the best response at the end-effector. The tip response for a typical slew with the accelerometer feedback in conmjunction with the rigid-body based non-linear controller in the inner loop is shown in Figure 6. From the plots, it is evident that the vibrations at the end-effector are significantly reduced as compared with the case when

only the inner loop controller is applied.
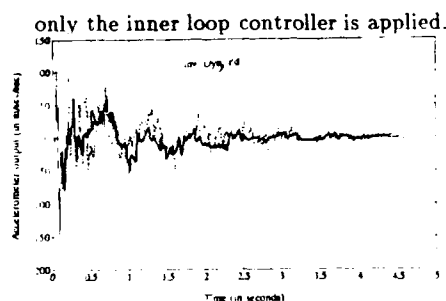
Figure 5: Inner-loop control only.
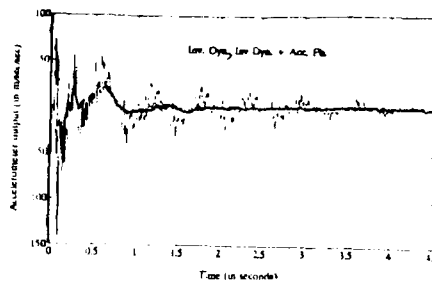
Figure 6: Inner/Outer-loop control.

VI.   CONCLUSION

In this paper, experimental results for slewing of a class of flexible multi-body systems (i.e., flexible multi-link manipulators) were given. Several approaches for control design for this class of systems were mentioned. Furthermore, these methodlogies were applied to an experimental setup developed at CRRL to mimic the behavior of a typical flexible multi-body system. Another setup developed to study the control/structure interaction is a slewing flexible structure with active members. The real-time computing power is provided by a digital signal processing board (TMS320C30 based) capable of 33 Mflops.

REFERENCES

[1] X. Ding, T. J. Tarn, and A. K. Bejczy, "A novel approach to the dynamics and control of flexible robot arms," in *Proceedings of the 27th Conference on Decision and Control,* (Austin, Texas), pp. 52–57, Dec. 1988.

[2] F. Khorrami, "Dynamical properties of manipulators exhibiting flexibilities," in *Proceedings of the IEEE International Conference on Systems Engineering,* (Pittsburg, PA), pp. 1–4, Aug. 1990.

[3] F. Khorrami, "Analysis of multi-link flexible manipulators via asymptotic expansions," in *Proceedings of the 28th Conference on Decision and Control,* (Tampa, FL), pp. 2089–2094, Dec. 1989.

[4] C. Oakley and R. Cannon, "Initial experiments on the control of a two-link manipulator with a very flexible forearm," in *Proceedings of the 7th American Control Conference,* (Atlanta, GA), pp. 996–1002, 1988.

[5] E. Schmitz, "Modeling and control of a planar manipulator with an elastic forearm," in *Proceedings of the 6th IEEE International Conference on Robotics and Automation,* (Scottsdale, Arizona), pp. 894–899, Apr. 1989.

[6] R. H. Cannon and E. Schmitz, "Initial experiments on the end-point control of a flexible one-link robot," *The International Journal of Robotics Research,* vol. 3, no. 3, pp. 62–75, 1984.

[7] W. J. Book, "Recursive Lagrangian dynamics of flexible manipulator arms," *Int. Journal of Robotics Research,* vol. 3, no. 3, pp. 87–101, 1984.

[8] K. H. Low, "A systematic formulation of dynamic equations for robot manipulators with elastic links," *Journal of Robotic Systems,* vol. 4, no. 3, pp. 435–456, 1987.

[9] F. Khorrami and Ü. Özgüner, "Frequency-shaped cost functional for decentralized systems," in *Proceedings of the 27th Conference on Decision and Control,* (Austin, Texas), pp. 417–422, Dec. 1988.

[10] A. İftar, F. Khorrami, and S. Jain, "A robust controller design approach and experiments for a slewing flexible structure," in *Proceedings of the IEEE Systems, Man, and Cybernatics Conference,* (Charlottesville, VA), Oct. 1991.

Do embedded sensor systems degrade mechanical performance of host composites?

R. Davidson and S.S.J. Roberts

AEA Industrial Technology, Harwell Laboratory, UK.

ABSTRACT: Finite element analysis techniques have been used to predict the stress concentrations around and within optical fibres embedded parallel to the reinforcement of a unidirectional CFRP composite. The effect of transverse compression and thermal stresses resulting from fabrication have been analysed. The residual thermal stresses are affected by the thickness, stiffness and the relative thermal expansion coefficient of the coating. Mechanical strength measurements on a variety of fibre sensor composite combinations support the analytical results. The results of the FE analysis can be used in the detailed design of intrinsic fibre optic sensors for embedment in composites.

1. INTRODUCTION

The development of smart composite materials relies upon building into the composite structure during fabrication a suitable nervous system which can sense the localised environment. In order to produce an adaptive structure, actuators are also necessary which respond to the sensor signals to effect shape change or vibration control. These actuators would be either embedded, as in the case of shape memory alloy wires or surface bonded as in piezoelectric ceramics.

For embedded sensor or actuator systems concern has been expressed as to the possible structural strength degradation which may result. This paper considers the modelling of stress and strain fields around and within optical fibres embedded in host carbon reinforced composites. The saturation is complex since fibre optics generally consist of a silica based core/cladding combination designed to give the waveguiding and sensing characteristics of the fibre plus a polymeric protective coating to reduce handling damage and increase environmental resistance. The optical fibre package of this type will always be significantly larger in diameter than the reinforcing fibres which are typically 5-10 μm in diameter. When such optical fibres, typically 100-300 μm in diameter, are embedded in composite laminates there will be an inevitable disruption of the reinforcing fibres in the vicinity of the fibre optic. The nature of this disruption will not only be dependent upon the diameter of the embedded fibre but also on the relative orientation of the optical fibre and the neighbouring reinforcing fibres.

In order to be acceptable the fibre sensor must:
- Produce a minimum perturbation in the distribution of reinforcing fibres;
- Not significantly reduce the strength or stiffness characteristics of the composite;
- Not suffer from excessive attenuation such that sensing techniques can not be applied;
- Provide for input and output of laser light. (This is usually done, though not ideally, through pigtails).

Several laminate/optical fibre geometries have been studied using finite element analysis to determine the magnitude and extent of stress concentrations caused by the embedded fibre when the laminate is under uniform thermal, tensile or shear loads applied in the plane of the fibre cross-section. **This paper concentrates on the results for a 125 μm diameter silica fibre embedded parallel to the reinforcement in a unidirectional CFRP composite.** Mechanical and thermal stresses are considered, using a 2D finite element technique in plane strain conditions. Results from the analysis of more general laminates, will form the basis of further publications.

2. THE MODEL

A sketch of the model is shown in **Figure 1.** The optical fibre is coated with a low modulus polymer, the thickness and modulus of which are varied in the analysis, and embedded in a typical carbon epoxide fibre composite. The material properties used in the analysis are given in **Table 1.** The analysis used an "in-house" PC based finite element program (BISEPS-LOCO). The mesh was composed of 6 noded plane strain triangular elements. Only one quarter of the model was meshed as at least two planes of symmetry exist for both the compressive and thermal load cases. All surfaces of the model were restrained to remain planar.

3. RESULTS

3.1 Compression Load Case
A uniform compressive stress of 100MPa was applied to the model. The resultant stress distribution is expected to lie between the two extremes depicted in **Figure 2.** For very low stiffness coating the model behaves as a plate with a central hole and stress flows around the outside concentrating at "B" as shown. For a very stiff coating strain is limited in the centre of the model by the coating and the stress flows preferentially through the fibre concentrating at "A" and "C". The optimum geometry to reduce stress concentrating effects would be such that the stresses were equal at all three positions. The values of stress at "A", "B" and "C" have been studied as the coating modulus and thickness are varied. These results show two effects:

(i) As the thickness of coating increases, causing the effective stiffness of the combined coating and fibre to decrease, the "yy" stress concentration decreases at "A" but increases at "B".(Note that a high "yy" stress at "B" is accompanied by a high transverse "xx" stress at "A").

(ii) For a given thickness of coating, values of "yy" stress increase as the coating modulus decreases, again because the effective stiffness of the centre of the model decreases.

In **Figure 3**, the values of "yy" stress at "A" and "B" are summarised. The optimum coating thickness, i.e. when stress at "A" and "B" are equal, is seen to increase as the coating modulus increases so as to provide the same overall stiffness of the fibre and coating. For comparison,the dotted lines show the variation in stress concentration for a polyimide ($E = 2$GPa) coated smaller diameter 80 μm fibre. The results indicate that to obtain an optimum geometry, a coating of 10 μm is required on the 80 μm fibre but must be increased to around 17 μm on the 125 μm fibre.

3.2 Thermal Load Case

The residual stress generated on cooling by 100°C, from the curing temperature to ambient, was calculated for a range of coating thickness, moduli and thermal expansion coefficients. The resultant stress distributions are axisymmetric and the hoop and radial stresses for each case are presented in **Figures 4-6. Figure 4** shows the variation in radial and hoop stress through the model with coating thickness and **Figure 5** shows the variation with coating modulus. In both cases increasing the effective rigidity of the coated fibre by decreasing thickness or increasing modulus increases stress throughout the model. **Figure 6** shows the change in stress distribution when the coating thermal expansion coefficient is changed from 20x 10 μm/ μmk to 70x 10 μm/ μk. In the first case, the coefficient is less than that of the composite (35x 10 μm/ μk) and the coating is in compression. In the second case the coating is in tension as it attempts to shrink away from the composite. Increasing the expansion coefficient is also seen to reduce stress levels in the composite and fibre. It is important for the successful implementation of some strain sensing techniques, such as quasi-distributed polarimeters, that large strains in the optical fibre core do not exist as a result of thermal effects on curing. Conversely for cure monitoring high thermal strains in the core are desirable in order to achieve the required sensitivity. By considering FE parametric analyses, sensors for particular applications with tailorable sensitivities can be designed.

4. COMPARISON WITH EXPERIMENTAL RESULTS

To determine whether the trends predicted are seen in practice, experimental results from transverse tensile testing of unidirectional samples of epoxy/CFRP with an embedded optical fibre were examined. The press moulded unidirectional specimen

samples were 1mm thick and 20mm wide and had a variety of fibre/coating combinations embedded in them parallel to the reinforcement. A summary of the results is given in **Table 2.** Full details can be found in **reference 1.**

The results are in agreement with theory in that, for a constant coating to composite modulus ratio, the stress peak at "B" increased as the coating thickness/fibre diameter ratio increased as shown by the decrease in sample strength. The results for the bare fibres may be thought to contradict theory in that it is predicted that the size of the fibre does not effect values of stress, therefore the strengths should not be greatly different. The fact that strengths are reduced according to size in these samples could be because the sample thickness was small compared to the disturbed region around the fibre. Also an important aspect in real situations which has not been considered in the analysis is the quality of the bonding between the optical fibre to coating and coating to composite. For good strength and transfer of composite strain to the fibre optic good bonds at these interfaces are necessary. Scanning electron microscopy of fracture surfaces clearly illustrate the importance of coating characteristics (1).

5. CONCLUSIONS

° The finite element analyses show that the combined stiffness of the coating and optical fibre affects the stress distribution around an embedded fibre. Thin, stiff coatings reduce stress concentrations (at B) under mechanical loads. However, residual thermal stresses are affected by the relative thermal expansion coefficient of the coating as well as its stiffness. Stresses are found to reduce with increasing coating thickness as the coating thermal constraint is reduced, but also their value may be changed by altering the coating expansion coefficient. This implies that there could be scope for using similar fibres but with differing coating properties to aid in the distinction between thermal and mechanical strain.

° Understanding the stress distributions caused by thermal and mechanical loads enables sensors to be designed to match specific sensor techniques and the required sensed properties.

° In order to accurately sense strain in the composite a good bond between the coating and the optical fibre and the coating and the composite is necessary. Though this interfacial effect cannot be analysed easily.

° Experimental results support the results of the FE analysis. It has been found that a 6.5 μm polyimide coating on an 80 μm fibre does not effect the strength of the composite, whilst at the same time bonds very well to the composite.

6. REFERENCES

1) S.S.J. Roberts and R. Davidson, "Mechanical properties of composite materials containing embedded fibre optic sensors", Fibre Optic Smart Structures and Skins IV, SPIE, Vol. 1588, September 1991, to be published.

TABLE 1 MATERIAL PROPERTIES

Material	Ex (GPa)	vxy	Ey (GPa)	Gxv (GPa)	α_x ($\times 10^{-6}$)	α_y $\times 10^{-6}$
Silica Fibre Optic	72.9	0.17	--	31.1	0.45	--
Coating	0.05 to 2.0	0.35	--	0.0185 to 0.74	20 to 70	--
CFRP Epoxy 914C HS	185.0	0.30	6.9	4.4	-0.8	35

TABLE 2 TRANSVERSE STRENGTHS OF UNIDIRECTIONAL CFRP/EPOXIDE
COMPOSITE WITH EMBEDDED OPTICAL FIBRE.

Coating	Coating Modulus (MPa)	$\frac{E\ Coat}{E\ Composite}$	Fibre Diameter (ϕ) (μm)	Coating Thickness (t) (μm)	$\frac{t}{\phi}$	Failure Stress (MPa)
De Soto 131	50	0.0063	80	10	0.125	64.3 ± 3.9
			80	20	0.25	62.3 ± 3.2
Medium Acrylate			125	57.5	0.46	57.0 ± 4.5
De Soto 131			125	62.5	0.50	54.2 ± 3.3
Lankro 2280B			125	62.5	0.50	55.0 ± 1.4
			75	132.5	1.77	51.1 ± 4.3
Medium Acrylate			140	180	1.28	51.3 ± 2.9
Polyimide	3000	0.375	60	6.5	0.052	64.0 ± 4.0
			125	17.5	0.14	47.5 ± 3.6
Bare Fibre	8000	1.0	125	0	0	62.8 ± 4.8
			300	0	0	36.6 ± 2.2
Aluminium	70000	8.75	125	67.5	0.54	52.9 ± 4.9

E composite = 8 GPa   Specimen width = 20 mm.
Specimen Strength = No fibre 65.5 ± 3.7 MPa.   Specimen Thickness = 1 mm.

CFRP Epoxy Host Composite
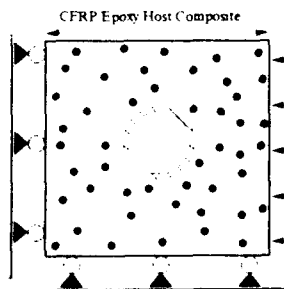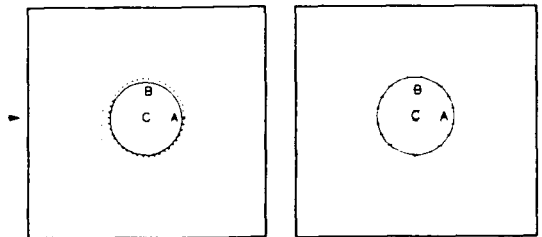
Basic Model   Compliant Coating   Stiff Coating

Compressive Stress of 100 MPa

FIGURE 1   FIGURE 2 STRESS FLOW AROUND EMBEDDED FIBRE
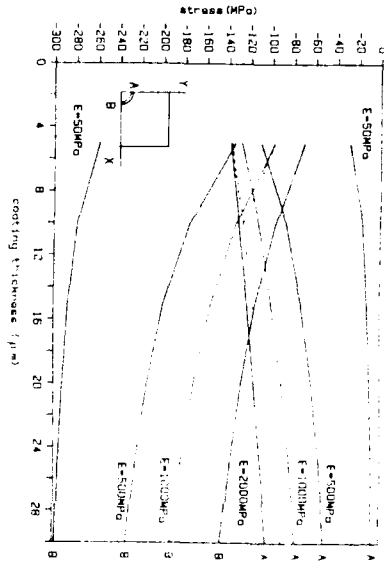
FIGURE 3 Plot of 'yy' stress at 'A' and 'B' as a function of Coating Modulus and Thickness for a 125 um Diameter Fibre.
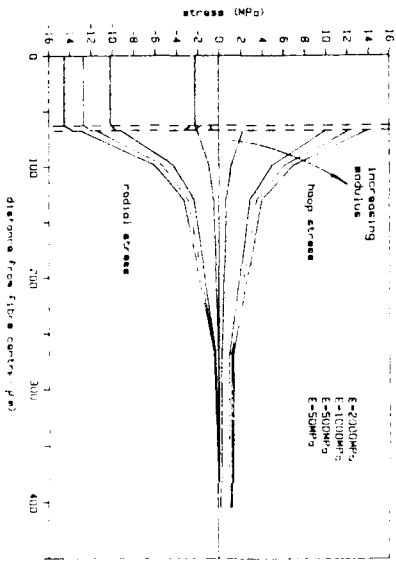
FIGURE 5 Variation in Residual Stress with Coating Modulus for a Temperature Change of -100 C: Coating Thickness = 5µm.
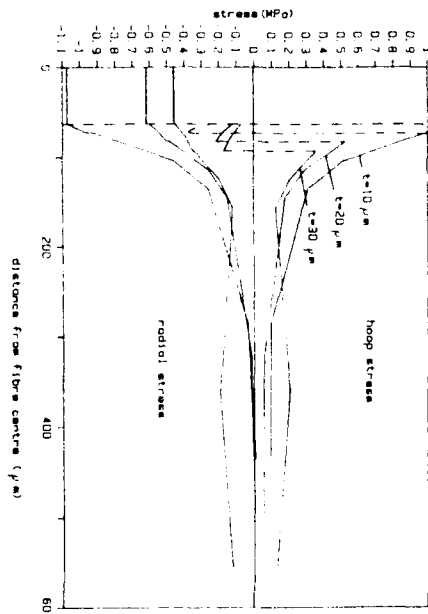
FIGURE 4 Variation in Residual Stress with Coating Thickness for a Temperature change of -100 C: Coating Modulus = 50 MPa.
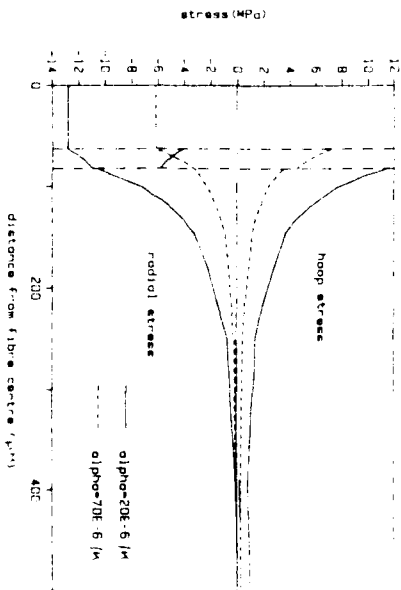
FIGURE 6 Variation in Stress Distribution with Thermal Expansion Coefficient for a Thermal Load of -100 C.

Tensile strength and stiffness reduction in graphite/bismaleimide laminates with embedded fiber-optic sensors

D W Jensen, J Pascual, and J A August

The Pennsylvania State University, 233 Hammond Bldg, University Park, PA 16802

ABSTRACT: This study quantifies the effects of the orientation and location of embedded optical fibers on the uniaxial tensile behavior of Graphite/Bismaleimide laminates. Experimental strength and stiffness data were obtained for eight different test configurations. Optical fibers embedded in various orientations modestly reduce the tensile strength and stiffness properties of composite laminates (less than 10%). The largest reductions occur in composite laminates with optical fibers embedded perpendicular to both the loading direction and the adjacent graphite fibers.

1. INTRODUCTION

The inherent benefits of optical fiber sensors (such as small size and weight) make them particularly well-suited for integration with fiber-reinforced composite structures (Jensen and Griffiths 1988). However, typical optical fiber diameters are 12 to 100 times larger than most reinforcing fiber diameters, and two to three times the thickness of a single layer of an advanced composite material. The large size and reduced mechanical properties of optical fibers in comparison to the reinforcing fibers indicate that embedded optical fibers may act as physical intrusions, which cause a degree of structural degradation.

The objective of this study was to quantify the effect of the orientation and quantity of embedded optical fibers on the tensile behavior of Graphite/Bismaleimide (Gr/BMI) laminates. Experimental strength and stiffness data were obtained from eight different test configurations.

A prior study by Measures et al (1989) included a series of experiments to ascertain the influence of embedded optical fibers on the tensile strength of Kevlar/Epoxy laminates. Results indicate that embedding optical fibers may increase the average tensile strength of the laminates. However, the variations in manufacturing the specimens reportedly gave a 10% spread in the data. In general, variations in cure cycle parameters, such as cure cycle duration or applied temperature, may induce extraneous changes in the tensile failure strength.

In a related study Jensen and Pascual (1990) compared experimental tensile strength and stiffness data from seven configurations, fabricated with varying quantities of optical fibers embedded parallel to the loading direction. Significant strength and stiffness reductions (10% to 20%) were found to occur only at relatively high optical fiber

volume fractions (4% to 5%). The present study complements this work by quantifying the effects of optical fiber orientation on the tensile behavior of Gr/BMI laminates.

2. TEST DESIGN

The test configurations were designed by selecting optical fiber locations and orientations with respect to the laminate that were assumed to represent extreme cases. Consider a laminate under tensile loading (Figure 1) with an optical fiber embedded in the center of the laminate perpendicular to both loading direction and adjacent reinforcing fibers. Due to their rigidity, the reinforcing fibers bridge over the circular optical fiber cross-section. Dasgupta *et al* (1990) showed that the span of this lenticular resin-rich region decreases with the angle between the optical fiber and the adjacent plies (Figure 2). Intuition dictates that optical fibers embedded at small angles should have less effect on the tensile strength, due to the higher fiber compaction. This study assumed that optical fibers running parallel or perpendicular to the *neighboring reinforcing fibers* have minimum or maximum impact, respectively, on the laminate mechanical performance and, therefore, represent extreme cases. Furthermore, the

Fig. 1.   Laminate with Optical Fiber Embedded Transversely

small circular cross-section of an optical fiber embedded parallel to the loading direction should reduce the load-bearing ability of the laminate to a lesser extent than the relatively larger rectangular cross-section of an optical fiber embedded perpendicular to the loading. This study assumed that optical fibers running parallel or perpendicular to the *loading direction* cause minimum and maximum degradation, respectively, of the mechanical behavior of laminates and, therefore, also represent extreme cases. Additionally, the placement of optical fibers symmetrically or asymmetrically with respect to the laminate midplane might adversely affect the laminate performance. The possible optical fiber orientations and symmetries were combined to produce the arrangements detailed in the test matrix, Table 1, and shown in Figure 3. These configurations were primarily designed to explore the significance of optical fibers embedded parallel or perpendicular to the applied uniaxial loading and/or adjacent reinforcing fiber directions on the mechanical

Fig. 2.   Laminate with Optical Fiber Embedded at an Angle

performance of advanced composites. The control configuration had no embedded optical fibers, to provide a standard against which all other strength and stiffness reductions were measured.

Table 1. Test Matrix

| Configu-ration | Number of Optical Fibers | Optical Fiber Direction Relative to: | | Number of Tension Tests |
		Loading Direction	Adjacent Graphite Fibers	
1	N/A	N/A	N/A	9
2	3	parallel	parallel	9
3	6	parallel	parallel	5
4	6	parallel	perpendicular	9
5	1	perpendicular	parallel	9
6	2	perpendicular	parallel	9
7	1	perpendicular	perpendicular	9
8	2	perpendicular	perpendicular	11

The $[0_3/90_2/0]$ stacking sequence was selected to enable embedding of optical fibers in several orientations, allow comparison of results with other studies (Jensen and Pascual 1990), and avoid the introduction of material couplings. G40-600/5245C Gr/BMI was selected as a representative material for evaluation. The material properties are listed by Jensen and Pascual (1990). The performance of this material is comparable to that of other advanced composites used throughout the aerospace industry.
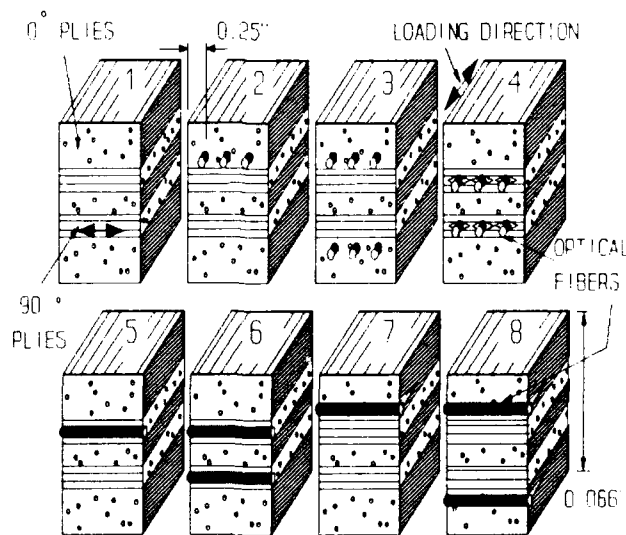
Fig. 3. Optical Fiber Configurations Studied

3. EXPERIMENT

Since composites require special test methods to quantify material properties with an acceptable degree of repeatability, due to their inhomogeneity and brittle nature, specimen manufacture and uniaxial tension testing were performed in accordance with the American Society for Testing and Materials (ASTM) Standard D3039-76. Eight 12-inch square plates were fabricated from unidirectional Gr/BMI prepreg tape with

embedded optical fibers and cured in a hot press. Acrylate-coated optical fibers with a 250-μm outer diameter were precisely positioned using a fiber-positioning jig. The laminated plates were covered with cure materials in a standard cure sequence and cured in a Tetrahedron MTP 14 programmable hot press employing the following cure cycle to ensure uniform mechanical properties: the temperature
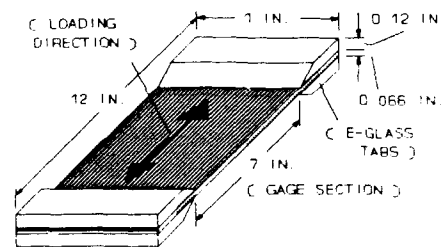
Fig. 4. Test Specimen Geometry

was raised at a rate of 5°F per minute and held at 190°F for 1 hour, 220°F for 2 hours, and 350°F for 2 hours, under a constant pressure of 50 psi. Strain-compatible loading tabs were cut from E-glass panels, beveled to a 25° angle on one side, and bonded onto the Gr/BMI plates with NARMCO NB-101 film adhesive. Subsequently, the specimens were cut from the tab-bonded plates using a diamond-coated saw (Figure 4). Variation of specimen thickness and width were within ±2%. Axial strain gages were mounted in the center of the gage sections of all specimens to measure elastic stiffness. The specimens were mounted in a screw-driven 60-kip Tinius-Olsen testing machine. Data acquisition for all the configurations was accomplished using a Micro-Measurements 2100 System 8-channel strain gage conditioner. All specimens were loaded to ultimate failure, usually exploding violently with a loud bang, and projecting graphite fibers against a plastic shield. Graphs of stress versus strain were plotted to select linear ranges for stiffness calculations (2000-8000 $\mu\epsilon$) based on Hooke's law. For each configuration, the average value and standard deviation of strength and stiffness were determined. To offset the detrimental effects of test measurements induced by unforeseen experimental error, Chauvenet's criterion was applied to each configuration to eliminate at most one data point (Holman 1989). In this manner, specimens 2-8, 3-4, 6-9, and 7-5 were not included in the calculation of the average stiffness, and specimen 5-1 was not included in the average strength calculation.

4. RESULTS AND DISCUSSION

Table 2 summarizes average tensile strength and stiffness data for each configuration. All tensile strength and stiffness reductions were less than 5%, except for Configuration 8. Note that, in general, the decrease in tensile strength and stiffness caused by optical fibers embedded in any orientation was similar in magnitude to the respective standard deviations. The effect of embedded optical fiber orientation on the laminate tensile mechanical properties was small enough to be comparable to the scatter due to the inhomogeneity and brittle nature of composites.

Strength and stiffness reductions were the largest for Configuration 8 (9% and 11%, respectively). Observe that in this configuration two optical fibers are embedded perpendicular to both the loading direction and the adjacent graphite fibers, causing geometric discontinuities in the neighboring longitudinal (0°) plies. These geometric discontinuities occur at two optical fiber locations, as opposed to a single location for Configuration 5. Awerbuch and Hahn (1977) experimentally verified that the static tensile strength of a laminate is controlled by its longitudinal plies when these are present in a sufficient number. Thus, the geometrical alteration induced by two optical fibers embedded perpendicular to the loading direction in the longitudinal plies of the

laminate caused the largest reduction in tensile strength.

There was no significant difference in strength and stiffness reduction between configurations with optical fibers embedded parallel or perpendicular to the loading direction, with the exception of Configuration 8. Specifically, Configurations 2, 3, and 4 exhibited strength and stiffness decrements of up to 3% and 2%, respectively, while Configurations 5 through 8 had decrements ranging up to 4%. Thus, neither the tensile strength nor stiffness were significantly degraded by the presence of embedded optical fibers, except when these were placed perpendicular to both loading direction and neighboring graphite fibers symmetrically about the laminate midplane.

Table 2. Average Tensile Strength and Stiffness

Configu- ration	Strength [ksi]	Stiffness [ksi]	Percent Reduction	
			Strength	Stiffness
1	229 (8)*	17.1 (0.5)	-	-
2	225 (4)	16.9 (0.3)	2	1
3	222 (9)	16.9 (0.3)	3	1
4	228 (8)	16.8 (0.6)	1	2
5	219 (9)	16.7 (0.5)	4	2
6	225 (9)	16.5 (0.2)	2	4
7	224 (6)	16.9 (0.5)	2	1
8	210 (11)	15.3 (0.6)	9	11

* Standard Deviation in parenthesis

There is no conclusive relationship between symmetry in the embedment of optical fibers and reductions. Configurations with optical fibers embedded asymmetrically about the laminate midplane did not readily induce larger strength or stiffness reductions. In this respect, the largest reduction in mechanical properties (approx. 10%, Configuration 8) occurred when the optical fibers were embedded symmetrically about the midplane, while the related asymmetrical configuration had small strength and stiffness reductions (1% and 2%, respectively, for Configuration 7). It is hypothesized that the number of geometrical discontinuities, two in the former configuration and one in the latter, had a greater effect on the laminate performance than symmetry.

The results of this study show that optical fibers embedded in various orientations at low volume fractions slightly reduce the tensile mechanical properties of composite laminates. As an exception, optical fibers embedded perpendicular to the surrounding longitudinal plies can cause modest strength and stiffness reductions. These results are limited t the effect of embedded optical fiber orientation on the tensile behavior of thin, cross-ply symmetric laminates. For example, the reductions in tensile mechanical properties induced by optical fibers embedded parallel to the adjacent plies but at an angle with respect to the loading direction might be lower in angle-ply laminates than in cross-ply laminates. These limitations are being addressed in continuing studies.

5. CONCLUSIONS

This study shows that optical fibers embedded in various orientations only slightly reduce the tensile mechanical properties of composite laminates. The effect of embedded optical fiber orientation on the laminate tensile mechanical properties was small enough to be comparable to the scatter due to the inhomogeneity and brittle nature of composites. As an exception, optical fibers embedded perpendicular to both loading direction and adjacent graphite fibers can cause modest tensile strength and stiffness reductions. Overall, the effects on tensile strength and stiffness were on the order of 10% or less. The severity of the geometrical disturbance caused by optical fibers embedded perpendicular to the reinforcing fibers was greater than the influence of symmetry in the embedment of optical fibers. These results indicate that optical fibers embedded perpendicular to the loading direction in composite laminates induce the largest degradation in their mechanical performance. By extension, optical fibers should be embedded parallel to both the loading direction and adjacent reinforcing fibers for minimal intrusion, when possible.

6. ACKNOWLEDGEMENTS

7. REFERENCES

Awerbuch J and Hahn H T 1977 *Fatigue of Filamentary Composite Materials - ASTM STP 636* ed Reifsnider and Lauraitis (New York: ASTM Intl.) pp. 248-266.

Dasgupta A, Wan Y, Sirkis J S, and Singh H 1990 *Proc. SPIE Fiber Optic Smart Structures and Skins III* **1370** pp 119-128

Holman J P 1989 *Experimental Methods for Engineers* (New York: McGraw-Hill) p 63

Jensen D W and Griffiths R W 1988 *Proc. SPIE Fiber Optic Smart Structures and Skins* **986** pp 70-76

Jensen D W and Pascual J 1990 *Proc. SPIE Fiber Optic Smart Structures and Skins III* **1370** pp 228-237

Measures R M, Glossop N D W, Lymer J, Leblanc M, West J, Dubois S, Tsaw W, and Tennyson R C 1989 *Applied Optics* **28** 2631

"Standard Test Method for Tensile Properties of Fiber-resin Composites: ASTM D3039-76" 1988 *ASTM Standards* (New York: ASTM Intl.) **15.03** pp 117-120

Micromechanics of fiber optic sensors

Y. E. Pak, V. DyReyes, and E. S. Schmuter
Grumman Corporation, Bethpage, N.Y. 11714

ABSTRACT: Coated optical fiber embedded in a host composite matrix is ana-
lyzed to study the elastic interaction between the fiber and the matrix. The optical
fiber and its coating are modeled as concentric, circular inclusions embedded in
an isotropic homogeneous matrix. Linear elasticity solutions are obtained for the
cases of a far-field longitudinal shear load and a uniaxial tensile load. The effects
of the modulus of the coating as well as its thickness is studied for the strain
transfer and the stress and strain concentrations. A boundary element analysis is
performed, and its results are in excellent agreement with the elasticity solution.

1. INTRODUCTION

Optical fibers have recently gained popularity as embedded strain sensors that can
monitor the state of strain in composite materials (Udd and Claus 1990). Embedded
optical fiber sensors can be especially useful in aircraft technology for health moni-
toring and damage assessment of aircraft structures. In order to accurately predict
the performance of the fiber optic sensors, it is important that we have an accurate
assessment of the elastic interactions that take place between the optical fiber and the
host matrix. This is particularly true in light of fact that the optical fibers can cause
stress and strain concentrations in the host structure in which they are embedded.
The coating on the optical fiber also can cause additional complications such as a loss
in strain transfer. Therefore, it is important that we employ micromechanics analysis
to study and characterize these effects. To this end mathematical and computational
analyses were performed in the framework of linear elasticity. In this paper, we sum-
marize salient features revealed by the micromechanics analysis of a coated, embedded
optical fiber embedded in a host matrix.

2. ANALYSIS

We model the coated optical fiber as infinitely long, isotropic, concentric inclusions
with radii a and b embedded in an isotropic matrix (Sirkis and Dasgupta 1990), as
shown in Figure 1. We also model the host matrix as a homogenous, isotropic medium
with the equivalent elastic constants. The matrix, assumed to be infinite in extent,
is subjected to a far-field antiplane shear, $\sigma_{zy} = \tau_\infty$, and a far-field uniaxial tension,
$\sigma_{yy} = \sigma_\infty$, parallel and transverse to the fiber, respectively. In the longitudinal shear
case, only the out-of-plane displacement, $u_z(x,y)$, is non-zero, and the equilibrium
equations simplify to a two-dimensional Laplace equation. A closed form solution was

obtained by expanding the displacement in series and invoking the far-field and the displacement and traction continuity conditions across the interfaces (Pak 1991). For the uniaxial tension case, a two-dimensional plane stress (plane strain) solution was obtained by a complex potential method (Pak 1991). A boundary element analysis was also performed, using an in-house code MRBE2D, to verify the accuacy of the boundary element model as well as to check the correctness of the elasticity solution.

3. STRAIN CONCENTRATIONS

Throughout the analysis we will let the shear modulus and the Young's modulus of the optical fiber be $\mu_F = 15\mu_M$ and $E_F = 10E_M$ for the longitudinal shear case and the uniaxial tension case, respectively. The Poisson's ratios of 0.3, 0.45, and 0.15 are respectively used for the matrix, the coating, and the fiber. The shear modulus and the Young's modulus of the coating are varied in such a way as to simulate soft epoxy coatings as well as stiff metallic coatings. This will enable us to study the effects of the coating modulus on the strain transfer and the stress and strain concentrations. We will fix the a/b ratio to be 0.8, which corresponds to the actual dimensions of the optical fiber used in our tests.

Figure 3 shows the contours of constant strain obtained from the elasticity solution for the longitudinal shear case, and the uniaxial tension case. Figure 4 shows shear strain normalized to the far-field strain along the x-axis. It can be seen that the maximum strain occurs at the coating-matrix interface when the coating is soft. Also plotted are the boundary element results for the uniaxial case ($E_C/E_M = 0.5$), which show excellent agreement with the analytical solution. It is interesting to note that for the longitudinal shear case the strain inside the fiber is constant for all values of the coating stiffness. However, in the case of uniaxial tension, the strain inside the fiber is constant only when there is no coating.

4. STRESS CONCENTRATIONS

Normalized shear stress along the x-axis is plotted in Figure 5. A high stress is induced in the optical fiber when the coating is relatively stiff, and as the coating becomes softer the maximum stress shifts to the matrix. This is because a stiffer coating will transmit more load to the optical fiber whereas a softer coating, behaving more like a cavity than an inclusion, induces higher stress in the matrix. Contrary to the strain distributions, the stresses are discontinuous along the x-axis. Unless the coating is very soft the highest stress occurs in the optical fiber. This is due to the fact that the optical fiber is the stiffest member in this model.

5. STRAIN TRANSFER

Shear strain transfer to the optical fiber as a function of the coating thickness is plotted in Figure 6 for several coating moduli. Figure 6(a) for the longitudinal shear case shows

that when the shear modulus of the coating is less than that of the matrix, greater shear strain is induced in the optical fiber by a thinner coating. At the same time, when the shear modulus of the coating is greater than that of the matrix, the thicker coating induces greater strain in the optical fiber. The figure also shows that the maximum strain transfer occurs when the coating shear modulus is greater than the matrix shear modulus. It can be shown that the maximum shear transfer occurs when the shear modulus of the coating is the geometric mean of the shear moduli for the fiber and the matrix. This is true for all coating thicknesses. The shear transfer increases uniformly with the increase in the coating thickness when the coating is stiffer than the matrix. This implies that the stiffer and thicker coating will induce more shear transfer. However, for the uniaxial tension case the maximum shear transfer occurs for the most part when there is no coating.

6. CONCLUSIONS

We have studied the strain tranfer to, and the strain and stress concentrations caused by, an optical fiber embedded in a homogenous matrix that is subjected to far-field longitudinal shear and uniaxial tension. It was shown that the longitudinal shear load and the uniaxial tensile load induce similar stress and strain concentration effects. However, they differ in the strain transfer behavior. The boundary element analysis confirmed the accuracy of the model as well as the correctness of the elasticity solution. The micromechanics analysis undertaken in this work is highly idealized; however, it reveals information essential to understanding the elastic behavior of embedded fiber optic sensors.

Acknowledgments

REFERENCES

Pak, Y. E., 1991, "Longitudinal Shear Transfer in Fiber Optic Sensors," submitted to *Smart Materials and Structures* for publication.

Pak, Y. E., 1991, "Micromechanics of Embedded Optical Fiber Under Uniaxial Tension," manuscript in preparation.

Sirkis, J. S., and Dasgupta, A., 1990, "Optimal Coating for Intelligent Structure Fiber Optical Sensors," *SPIE Proceedings on Fiber Optic Smart Structures and Skins III*, Vol. 1370, p. 129.

Udd, E. and Claus, R. O., eds., 1990, *SPIE Proceedings on Fiber Optic Smart Structures and Skins III*, Vol. 1370.
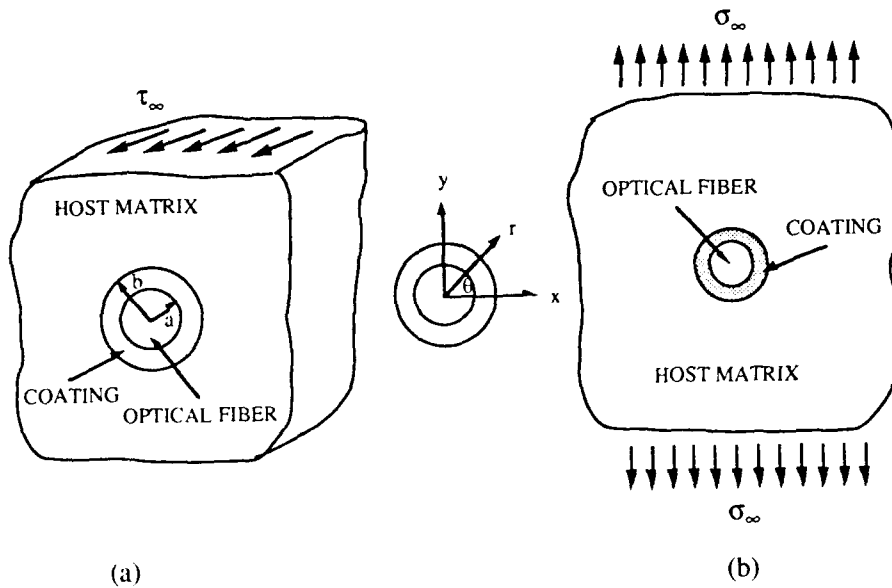
Figure 1. Embedded optical fiber subjected to (a) longitudinal shear load and (b) uniaxial tensile load.

w = 10
h = 10
a = 0.8
b = 1
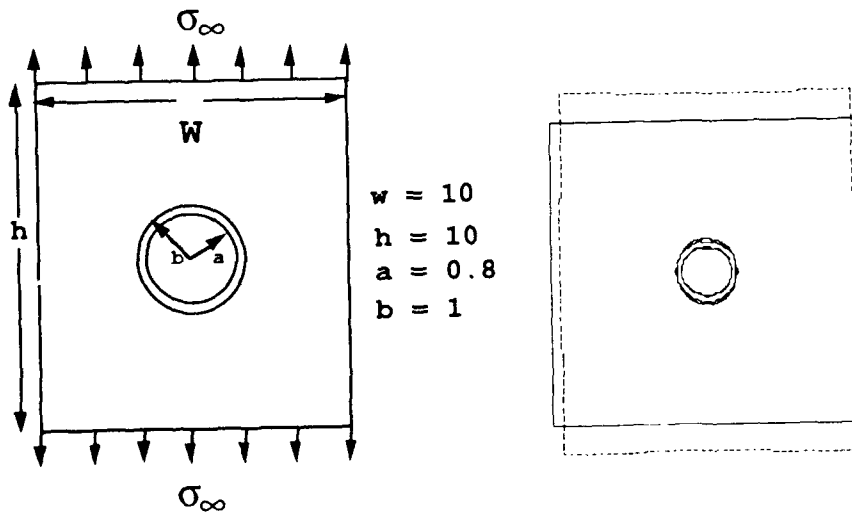
Figure 2. Boundary element analysis model and deformation plot under uniaxial tension.
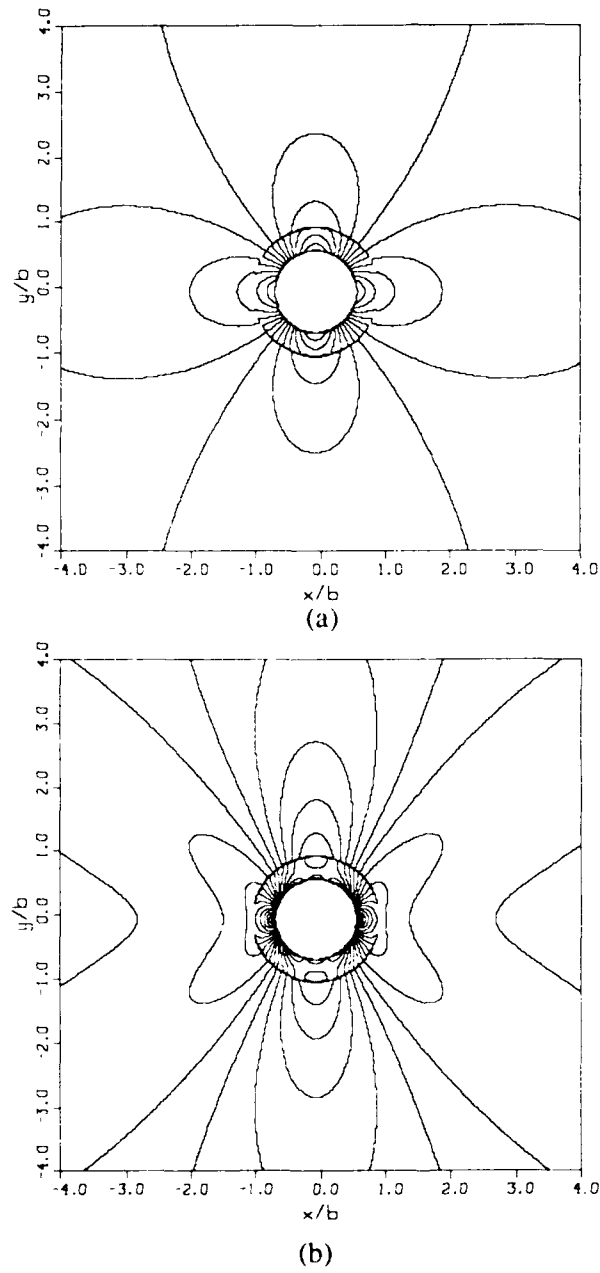
Figure 3. Contours of constant (a) shear strain under longitudinal shear load
and (b) maximum normal strain under uniaxial tensile load.
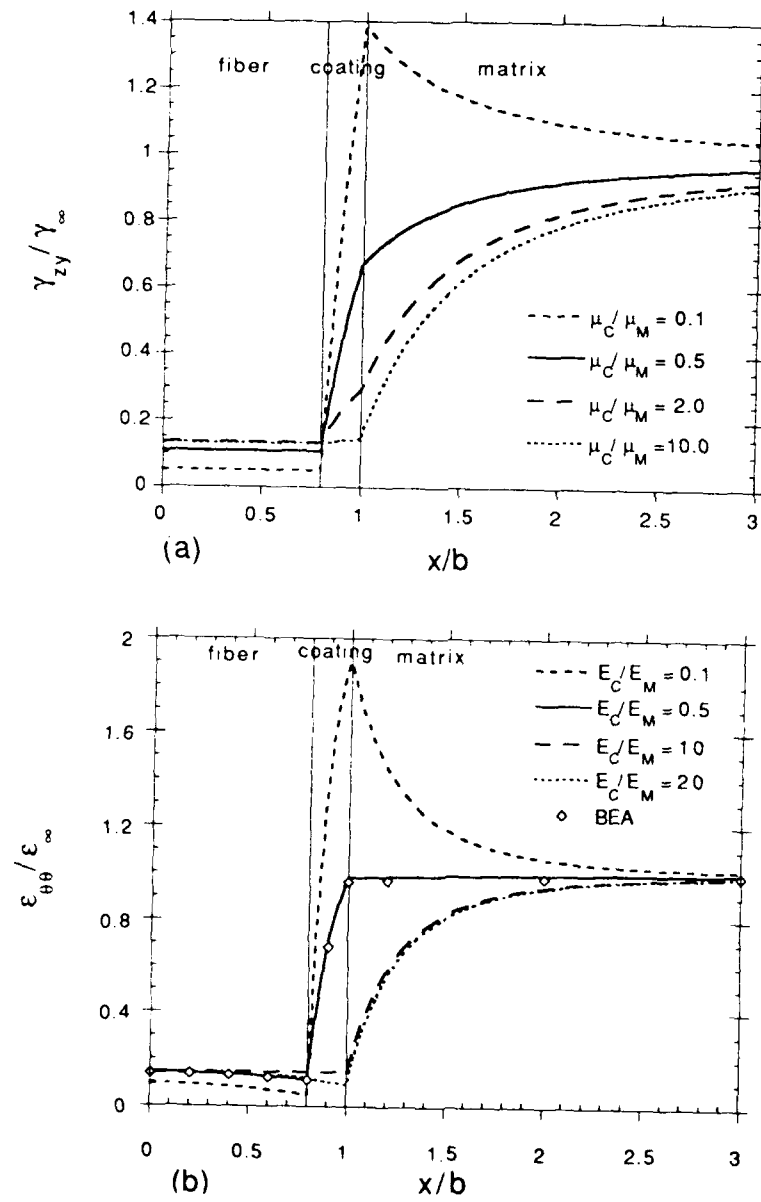
Figure 4. Normalized strain distribution along x-axis for (a) longitudinal shear load and (b) uniaxial tensile load.
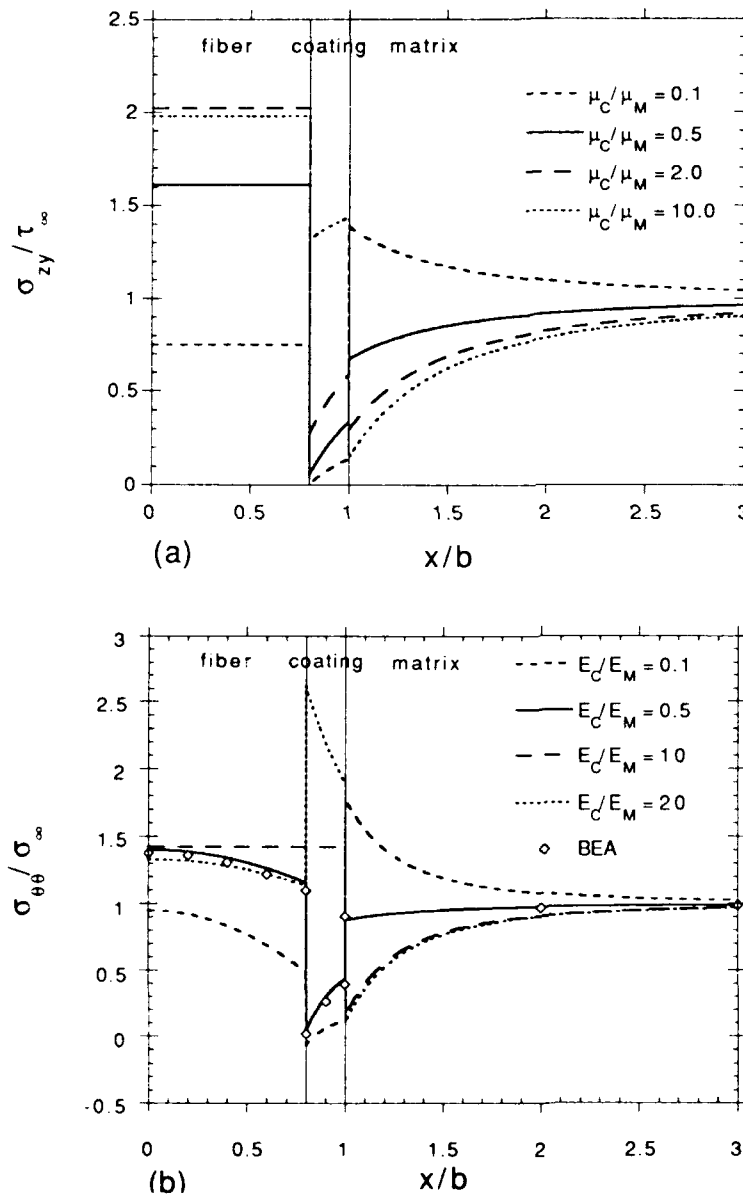
Figure 5. Normalized stress distribution along x-axis for (a) longitudinal shear load and (b) uniaxial tensile load
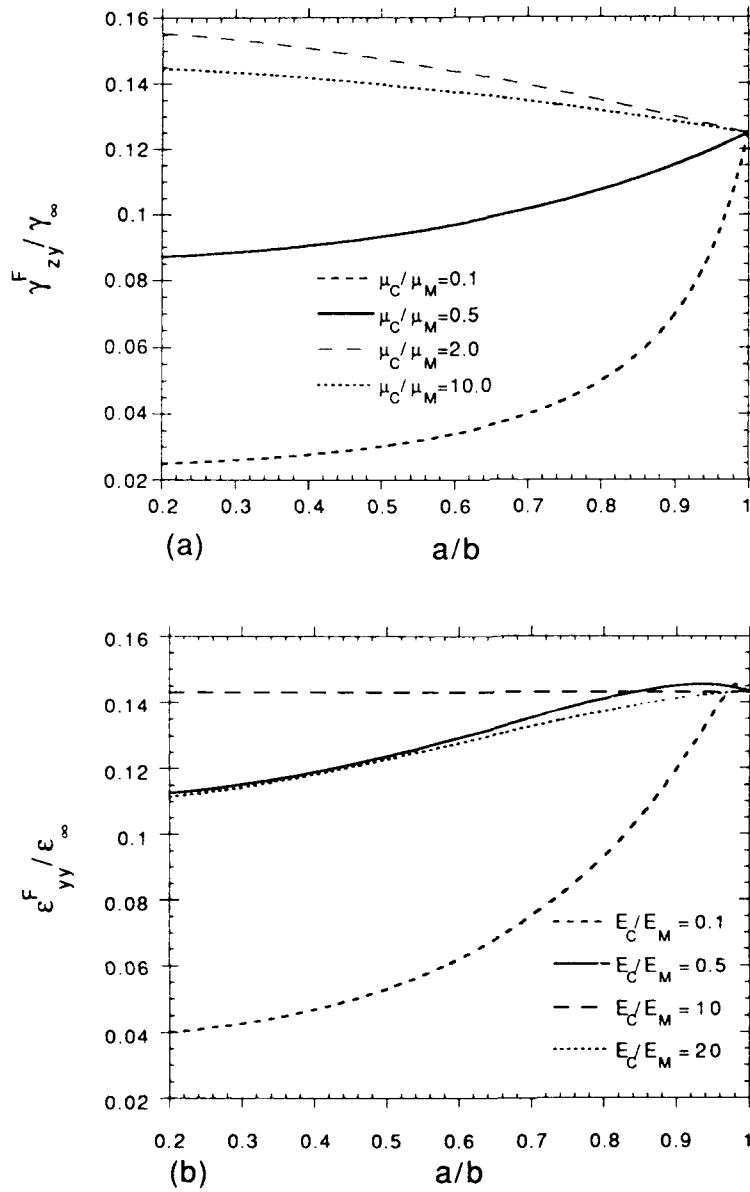
Figure 6. Strain transfer to the optical fiber as a function of coating thickness for (a) longitudinal shear load and (b) uniaxial tensile load.

Compressive strength and stiffness reduction in graphite/bismaleimide laminates with embedded fiber-optic sensors

D W Jensen, J A August, and J Pascual

The Pennsylvania State University, 233 Hammond Bldg, University Park, PA 16802

ABSTRACT: This paper summarizes an investigation into the influence of embedded optical fibers on the uniaxial compressive performance of Graphite/Bismaleimide laminates. Experimental strength and stiffness data were obtained for eight different test configurations. Results indicate that some orientations of embedded optical fibers can severely degrade the compressive performance of composite laminates. Compressive strength and stiffness reductions ranged up to 70% and 20%, respectively. Similar to previous results for tensile properties, optical fibers embedded perpendicular to the loading direction and the adjacent graphite fibers induced the largest reductions.

1. INTRODUCTION

Due to the filamentary nature of composite materials, optical fibers may be integrated in arrays within smart composite structures to recognize and measure the intensity of mechanical parameters (such as strain, pressure, or temperature) and, thus, monitor structural behavior and integrity. Predictably, the geometrical discontinuities induced by embedded optical fibers, which may range in size up to twice the thickness of a single composite ply, raise concerns about structural performance. Previous work by Jensen *et al* (1991) has shown that optical fibers embedded in various orientations only slightly reduce the tensile mechanical properties of composite laminates (5% to 10%). However, compression loads are more sensitive to geometrical imperfections in the load path and are also more likely to dominate the response of advanced composites under cyclic loading and environmental exposure (Clark and Lisagor 1981). Thus, this investigation quantifies the influence of embedded optical fibers on the performance of Graphite/Bismaleimide (Gr/BMI) laminates in uniaxial compression, including experimental strength and stiffness data for eight different test configurations.

Results from a study by Measures *et al* (1989) indicate that embedding optical fibers has a negligible effect on the average compressive strength of Kevlar/Epoxy laminates. However, these results are predictable, since the poor interlaminar shear strength of Kevlar/Epoxy composites causes substantial delamination and poor compressive properties (Strong 1989). Since glass fibers adhere better than organic fibers (such as Kevlar) to most epoxies, the optical fibers may have acted as crack arresters, slightly improving the compressive properties.

Ricci (1989) performed a preliminary investigation of the effect of embedded optical

fibers on the compressive strength of Gr/BMI laminates. Three different configurations were fabricated by embedding acrylate-coated optical fibers parallel or perpendicular to the loading and graphite fiber directions in a $[0_3/90_2/0]_s$ laminate. Compared to a control configuration without embedded fibers, the compressive strength decrement ranged from 2% to 37%, with the largest reduction occurring when the optical fibers were embedded perpendicular to both the loading and adjacent graphite fibers. The contradictory findings regarding the compressive performance of composite laminates with embedded fiber-optic sensors underscores the need for this investigation.

2. EXPERIMENT

Following the criteria detailed by Jensen *et al* (1991), optical fibers were arranged in orientations and symmetries with respect to the laminate midplane that were assumed to represent extreme cases. These cases comprise the configurations detailed in the test matrix, defined in Table 1 and depicted in Figure 1. The Control Configuration had no embedded optical fibers, providing a standard against which strength and stiffness reductions were compared. To study the effect of fiber orientation, Configurations 2 through 8 had optical fibers embedded parallel or perpendicular to the applied uniaxial loading and/or adjacent graphite fiber directions. To study the effect of fiber symmetry, Configurations 2, 5, and 7 had optical fibers embedded asymmetrically with respect to the laminate midplane; in the remaining configurations, the optical fibers were embedded symmetrically.

Table 1. Test Matrix

Configu-ration	Number of Optical Fibers	Optical Fiber Direction		Number of Compression Tests
		Relative to Loading Direction	Relative to Adjacent Graphite Fibers	
1	N/A	N/A	N/A	8
2	3	parallel	parallel	7
3	6	parallel	parallel	7
4	6	parallel	perpendicular	10
5	1	perpendicular	parallel	9
6	2	perpendicular	parallel	8
7	1	perpendicular	perpendicular	8
8	2	perpendicular	perpendicular	8

The material system chosen for evaluation in this study, G40-600/5245C Graphite/Bismaleimide, offers a similar performance to that of other advanced composites favored by the aerospace industry. As detailed by Jensen *et al* (1991), the $[0_3/90_2/0]_s$ stacking sequence enabled placement of acrylate-coated 250-μm diameter optical fibers at several convenient laminate locations. This also permits comparison of results with related studies (Ricci 1989, Jensen and Pascual 1990) and placed this study within the scope of American Society for Testing and Materials (ASTM) standard test methods for composites.
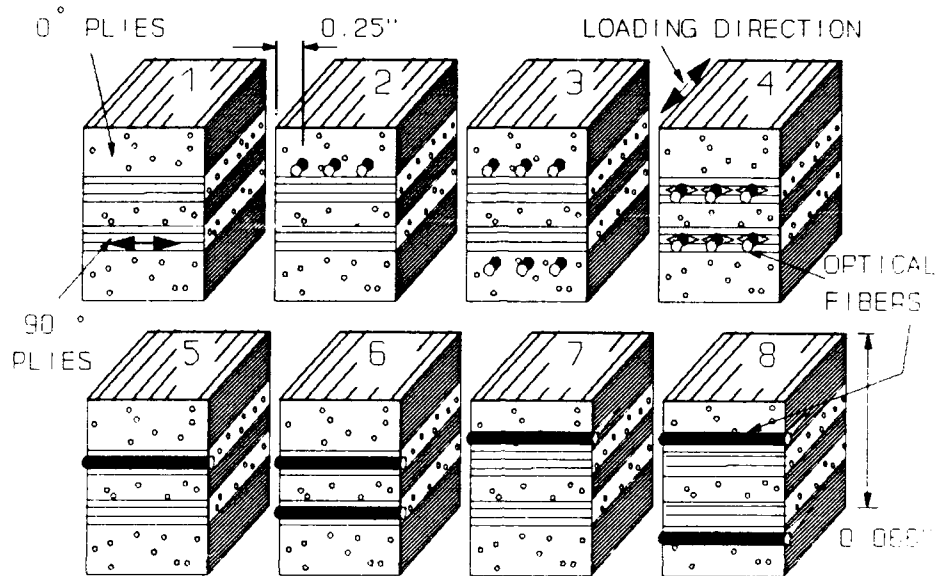
Fig. 1. Optical Fiber Configurations Studied

To quantify the material properties with an acceptable degree of reliability, specific procedures detailed in the ASTM Standard D3410-87 were followed for specimen manufacture and uniaxial compression testing. The Illinois Institute of Technology Research Institute (IITRI) fixture for compression tests was selected based on availability and ease of handling. The specimen width and gage length were chosen such that the ultimate compressive load was approximately 77% of the Euler critical buckling load, while ensuring that the 60 kip testing machine capability was not exceeded, based on the theoretical laminate strength of 14.5 ksi and modulus of 17.8 Msi. A nominal laminate thickness of 0.066 inches and a conservative assumption of pinned-pinned boundary conditions led to a 6.3 inches wide by 0.66 inches long maximum test section. To maintain a reasonable factor of safety and satisfy ASTM specifications, a gage length of 0.5 inch was selected (Figure 2).

Eight 12-inch composite square plates were laid up and cured following the procedures detailed by Jensen *et al* (1991). The composite plates were cut to specimen size using the diamond saw. Hot-rolled steel plates were 2.5 inches long by 1.0 inch wide were bonded on both sides of each specimen end using NB-101 film adhesive. Axial
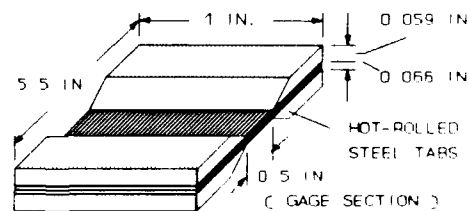
Fig. 2. Test Specimen Geometry

strain gages were mounted back-to-back in the center of the gage sections of each specimen to measure elastic stiffness and provide indications of out-of-plane bending and/or buckling. Width and thickness measurements of each specimen were taken at several points and averaged for use in data reduction.

As mentioned above, the specimens were tested in an IITRI fixture. The fixture was mounted inside a Tinius-Olsen universal testing machine which has been modified to interface with an OMEGA 900 PC data acquisition system. Strain plots were checked during data reduction to detect bending caused by fixture misalignment. The experimental data was reduced as described by Jensen *et al* (1991). Since the test configurations failed at different levels, three different ranges were used for determining the compressive moduli based on a least-squares method of linear regression. The 2000-8000 $\mu\epsilon$ range was used for Configurations 1, 2, 3, and 4; the 1000-5000 $\mu\epsilon$ range was used for Configurations 5 and 6; and the 500-2500 $\mu\epsilon$ range was used for Configurations 7 and 8. Chauvenet's criterion was applied to each configuration to set limits for data point rejection and to remove at most one data point outside each prescribed configuration range (Shenck 1979). Specifically, compression specimens 5-9 and 6-8 were excluded when calculating the average stiffness of Configurations 5 and 6, respectively.

3. RESULTS AND DISCUSSION

All of the compression specimens failed by fiber fracture, with cracks splitting the gage section across the width. Tables 2 and 3 list average compressive strength and stiffness and the respective standard deviation and percentage reduction values for each test configuration. The compressive strength and stiffness reductions ranged up to 70% and 20%, respectively; significantly more than for tension, which was less than 10%.

Table 2. Average Compressive Strength

Configuration	Strength [ksi]	Standard Deviation [ksi]	Strength Reduction [%]
1	136	11	-
2	116	17	15
3	134	13	1
4	119	6	13
5	90	19	34
6	85	24	38
7	40	8	70
8	42	7	69

Several trends are evident in the degradation of compressive strength. Compressive strength reductions ranged from 1% to 15% and from 34% to 70% for configurations with optical fibers embedded parallel or perpendicular to the loading direction, respectively. For the latter case, optical fibers embedded in the longitudinal plies caused larger compressive strength reductions, 69% to 70%, than optical fibers embedded in the transverse (90°) plies, 34% to 38%. These results indicate that the compressive strength was sensitive to the optical fiber orientation with respect to the loading direction. Specifically, optical fibers embedded perpendicular to the loading direction caused larger compressive strength reductions than optical fibers embedded

parallel to the loading direction. In addition, the degradation induced in the former case was larger for configurations where the optical fibers were embedded perpendicular to the neighboring graphite fibers, forming resin-rich lenticular discontinuities, than for configurations where the optical fibers were embedded parallel to the neighboring graphite fibers, forming smaller circular discontinuities. Therefore, the largest compressive strength reductions (up to 70%) occurred in composite laminates with optical fibers embedded perpendicular to the loading direction and the adjacent graphite fibers.

Table 3. Average Compressive Stiffness

Configuration	Stiffness [Msi]	Standard Deviation [Msi]	Stiffness Reduction [%]
1	14.5	1.0	-
2	11.6	0.5	20
3	12.7	0.6	13
4	12.2	0.9	17
5	13.1	1.2	12
6	13.2	1.0	7
7	12.3	0.8	15
8	11.6	0.9	20

Overall, the presence of embedded optical fibers had a large effect on the compressive strength of the specimens, while stiffness was affected to a far lesser extent (up to 20%). Compressive stiffness reductions ranged from 13% to 20% and from 12% to 20% for configurations with optical fibers embedded parallel and perpendicular to the loading direction, respectively. For the latter case, optical fibers embedded in the longitudinal plies caused larger compressive stiffness reductions (15% to 20%) than optical fibers embedded in the transverse plies (7% to 12%). It might be inferred that the compressive stiffness is not sensitive to optical fiber orientation with respect to the loading direction, since the ranges caused by optical fibers embedded parallel or perpendicular to the loading direction were similar. However, the degradation induced in the latter case was largest when the optical fibers were embedded perpendicular to the neighboring graphite fibers, forming crack-like lenticular discontinuities, than when optical fibers were embedded parallel to the neighboring graphite fibers, forming smaller circular discontinuities. This is the same trend observed for compressive strength reductions.

4. CONCLUSIONS

In summary, optical fibers embedded in various orientations have been shown to severely degrade the compression performance of composite laminates, even though tensile properties are only modestly reduced. Overall, the presence of embedded optical fibers has a larger effect on the compressive strength than on the compressive stiffness of composite laminates. In this respect, optical fibers embedded perpendicular

to the loading direction cause similar stiffness reductions to, and larger strength reductions than, optical fibers embedded parallel to the loading direction. Both compressive strength and stiffness are reduced further if optical fibers oriented perpendicular to the loading direction are embedded in the longitudinal plies as opposed to the transverse plies. As it might be expected, the largest compressive strength reductions occur in composite laminates with optical fibers embedded perpendicular to both the loading direction and the adjacent graphite fibers.

These results are restricted to the effect of embedding relatively large acrylate-coated optical fibers in various orientations inside thin, symmetric cross-ply laminates subjected to uniaxial compression. These limitations are being addressed in related studies to develop thorough guidelines for optical fiber embedding with minimal structural degradation.

5. ACKNOWLEDGEMENTS

6. REFERENCES

Clark R K and Lisagor W D 1981 *Test Methods and Design Allowables for Fibrous Composites-ASTM STP 734* ed Chamis (New York: ASTM Intl.) pp 34-53

Jensen D W and Pascual J 1990 *Proc. SPIE Fiber Optic Smart Structures and Skins III* **1370** pp 228-237

Jensen D W, Pascual J, and August J A 1991 *Proc. ADPA/AIAA/ASME/SPIE Conf. on Active Materials and Adaptive Structures*

Measures R M, Glossop N D W, Lymer J, Leblanc M, West J, Dubois S, Tsaw W, and Tennyson R C 1989 *Applied Optics* **28** 2631

Ricci J A 1989 *B.S. Thesis* The Pennsylvania State University

Schenck H 1979 *Theories of Engineering Experimentation* (New York: McGraw-Hill) pp. 228-230

"Standard Test Method for Compressive Properties of Unidirectional or Crossply Fiber-resin Composites: ASTM D3410-87" 1988 *ASTM Standards* (New York: ASTM Intl.) **15.03** pp 132-139

Strong B A 1989 *Fundamentals of Composites Manufacturing: Materials, Methods, and Applications* (New York: SME) p 62

Flexible piezoelectric materials: application to pressure and vibration sensing

AUTHORS: F. Geil and L. Matteson; Westinghouse, Oceanic, Annapolis, MD

ABSTRACT

Piezoelectric materials can be attached to structures for the purpose of sensing sound pressures or structure vibration. The signals of interest to be sensed by piezoelectric materials must be "AC" by nature, as in sound pressure and vibration. The signals to be ignored are the "DC" components; these are barometric/hydrostatic pressure or static strain. The two flexible piezoelectric materials of greatest availability are piezorubber (PZR) and polyvinylidene fluoride (PVdF) film. This paper will compare piezoelectric constants for both materials and discuss some of the tradeoffs necessary when choosing a piezoelectric material for pressure and vibration sensing applications. This paper also covers the preferred application of each sensing materials and presents experimental data showing the performance attained. In an active control application where vibration is to be minimized, electrical self-noise must also be minimized.

INTRODUCTION

Flexible piezoelectric materials can be attached to structures for the purpose of sensing sound pressures or structure vibration. Of particular interest is the sensing of vibration of an underwater vehicle in order to minimize the energy that is radiated as sound to the far field. This vibration signal can be thought of as the "error" signal for a processor which in turn drives a noise canceling actuator. This paper will cover the use of flexible piezoelectric materials to sense the shell structural vibration and illustrate the differences between sensors used as traditional hydrophones and used as vibration pickups. Also, the pertinent piezoelectric material characteristics and electrical self-noise will be examined. Some experimental work will be presented but the work is in progress and therefore incomplete, however future experimental plans will be presented.

If the structure is underwater, the vibration is detected by either sensing displacement or sensing circumferential strain or strain rate. These two sensing modes are shown in Figure 1. One advantage of using a sensor that senses displacement is that the sensor may also be able to sense sound resulting from structure vibration. This signal could be included as part of the "error" signal to the processor. An advantage of area sensing in general over point sensing (accelerometers) is that "area averaging" may be employed to reduce turbulent flow noise.

$$V = \frac{F \cdot g_{33} \cdot th}{A}$$

F: FORCE
A: AREA
s: STRAIN
E: MODULUS OF ELASTICITY
th: THICKNESS
g: PIEZOELECTRIC CONSTANT

$$V = s \cdot E \cdot g_{33} \cdot th$$
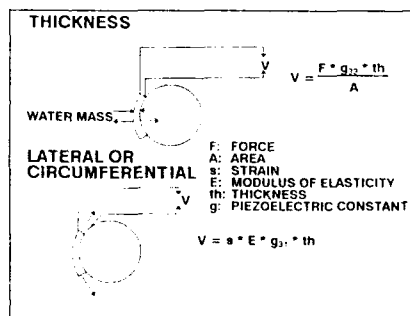
Figure 1. Two Vibration Sensing Modes

CANDIDATE SENSOR MATERIAL

Two types of piezoelectric materials which are readily available and currently being tested are piezorubber (PZR) and piezofilm. PZR is a piezoelectric composite in tile form composed of lead titanate powder in a neoprene matrix. The piezofilm is a flexible lightweight polymeric piezoelectric film with polyvinylidene fluoride(PVdF) as the base resin. Neither material has natural piezoelectric behavior but are polarized during the manufacturing process by subjecting them to a high electric field imposed across the thickness dimension, while cooling from a high temperature.

THE PIEZOELECTRIC CONSTANTS

The piezoelectric stress constant, g, defines the voltage generated by the material when subjected to mechanical stress. The piezoelectric materials are anisotropic. The voltage produced by a given stress depends upon the axis in which the stress is applied. Figure 2 shows the active axes in a piezoelectric material while Figure 3 shows a comparison of piezoelectric stress constants for various materials. Modes of vibration can be detected in several ways depending on the mode of interest. The relative values of stress constants give a good indication of which sensor material is most appropriate for each sensing mode.
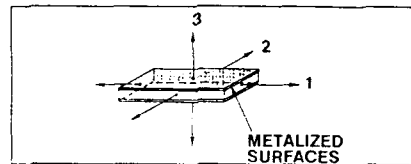
Figure 2. Active Axes in Piezoelectric Materials

Piezoelectric Stress Constant [x 10^{-3} Vm/N]	Piezorubber Type 307	PVdF Film	Copolymer Film	PZT
g_{33}	+132	-339	-220	+25.2
g_{32}	-10	~+20	+140	-11
g_{31}	-10	+216	+140	-11
g_h	+112	-109	+40	+3.2

Figure 3. Some Piezoelectric Material Coefficients

For example, the PZR is an appropriate choice for displacement or thickness sensing (the material is squeezed between the shell and the water), while PVdF film and the copolymer film are good choices for sensing circumferential strain. One important advantage of copolymer film is the equality of g_{31} and g_{32}. With PVdF, its unequal lateral sensitivities require two layers with crossed "1" axes, if true area sensing is required.

THE NATURE OF THE SIGNALS

As described earlier, the piezoelectric sensor on an underwater vehicle may sense displacement or strain. One important point to remember is that the signal is AC in nature, not DC. This is fortunate for underwater vehicles since depth-induced signals, which are DC, should be ignored. Piezoelectric materials naturally ignore the DC component because of the charge path to ground through the amplifier input circuit. This input resistance also bleeds off slowly changing signals such as temperature-induced (pyroelectric) charge.

HYDROPHONE VS. VIBRATION SENSOR

A piezorubber sensor can be used as a hydrophone or as a vibration sensor. For a hydrophone, the incoming sound is converted to voltage, and one concern is that vehicle vibration produces a voltage that may mask the signal of interest. When using PZR as a vibration sensor, the signal becomes weaker as the vehicle vibration is reduced by the processor, and self-noise (electrical and/or flow) may mask the lower levels of vibration. In addition, self-noise may be an unwanted processor input. These self-noises will be discussed further later.

ATTACHMENT CONSIDERATIONS

In our application, it is necessary to attach the sensor directly to the shell structure. This necessity causes a problem. If the sensor is attached to the structure with the ground or signal return on the outside as shown in Figure 4a, then the signal electrode will be electrically shorted or at least severely loaded by the capacitance to the shell. There is,

Figure 4. The Sensor Configuration Dilemma

however, the advantage that the sensor is shielded against EMI. If the signal electrode is on the outside as shown in Figure 4b, the signal is susceptible to EMI but there is no loading or shorting of the signal, assuming a thick enough waterproofing layer. These problems and advantages pose a dilemma for attaching the sensor to the structure, but there are

two solutions. The first one is shown in Figure 5a. The signal electrode can be inside, which shields from EMI, with a thick dielectric standoff, thick enough to have a capacitance to the shell that is small compared with the sensor capacitance. One concern with this solution for piezofilm is that the lateral stress

FIGURE 5A PROBLEM (FOR FILM): LATERAL STRESS MUST BE CARRIED THROUGH THE STAND OFF INSULATOR

FIGURE 5B PROBLEM: SENSOR COST IS DOUBLED

Figure 5. Two Solutions to the Sensor Dilemma

must be carried through the standoff material. The second solution is to make a "sandwich" of two back-to-back sensors which, if the signal electrode is inside, can shield form EMI and also attach directly to the vibrating surface with no signal loss. This configuration, shown in Figure 5b, has been used successfully with both PZR and PVdF film

FABRICATION OF SENSOR

To fabricate this "sandwich" using PZR, two pieces of PZR and a printed circuit board (PCB) substrate are needed (Figure 6). The PCB is thin glass epoxy which keeps the "sandwich" flexible and provides the electrical connection between the two PZR tiles. No direct connection between the PZR tile and the PCB is needed as long as the epoxy joint is thin, less than 0.001 inch. This is necessary in order to insure that the bond capacitance is large

Figure 6. Three Elements Form a Multi-Element PZR Sandwich

compared to the sensor capacitance. A major advantage of the PCB substrate is the ease with which an electrode pattern may be formed for the purposes of sensing spatial wavelengths smaller than the sensor area. For this configuration corresponding grooves are cut through the PZR inner electrodes.

When using the PVdF film for the "sandwich," the PCB might also be used but its stiffness needs to be low compared with the stiffness of the structure so that the sensor does not diminish the structure's vibration. A possible variation of the sandwich could be to etch the electrical connection pattern into the electrode coating on the inner sides of the film. We have not used or investigated this possible solution.

TESTING

The objective of the testing is to find the best material and configuration for the sensor portion of an active noise control system. A test box was built in order to comparatively test several piezoelectric materials. The experimental setup is shown in Figure 7 and a picture of the test box is shown in Figure 8. As the picture shows, the test box was made of one inch thick aluminum. This heavy construction is to insure that no radiated sound is produced from the sides or the back. A thin aluminum plate is placed in a window and driven at various locations by a shaker. Several plates with different piezoelectric sensors will be placed into the window and tested. We already have fabricated a plate with a sandwich of 100μ PVdF film (parallel 31 directions) and one with
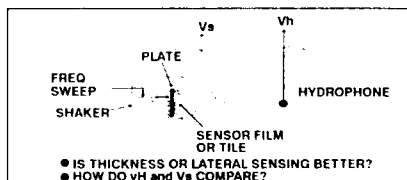
Figure 7. Experiment for Selection of Sensor Type

Figure 8. Photo of Underwater Test Box With Shaker

copolymer film. Figure 9 shows a sample of
data taken in air using an aluminum plate
with PVdF film sensor attached. This test
data illustrates how a mode might be
ignored (response nulls) and how the
response varies for a different shaker drive
point position. In the near future, we will use
the test box to drive a frequency sweep from
the shaker onto the sensor plate and into the
water. The sensor signal and the
hydrophone signal picked up in the far field
will be compared over the frequency range

Figure 9.   Two Examples of Sensor Signals
With Nulls; Driving Point is Varied From
On-Center to Off-Center

of interest. The sensor of choice will be the type that has the best correlation between
the sensor signal and the far field hydrophone response.

IMPORTANCE OF SELF NOISE

When the vibration is low or has been driven to a low level, the self-noise of the sensor
may predominate in the net signal to the processor. The flow noise level produced by the
turbulent boundary layer is reduced by a sufficiently thick outer stand off layer and by the
"area averaging" provided by the area of the sensor.

Electrical self noise minimizing requires
control of several factors. These include
maximizing of the sensor capacitance, voltage
sensitivity (g constant times thickness), and
amplifier input resistance, while minimizing
the capacitance loading, sensor electrical loss
(tan delta), and amplifier internal noise
components (input voltage noise and current
noise). The sensor and its interface to a
state-of-the-art low noise amplifier has been
modeled, to show the effects of parameter
variation. The amplifier is an Analog Devices
AD743 FET op amp chip. Figure 10 shows

Figure 10.   Electrical Self-Noise Compared
to Vibration Signal — Three Examples

the total noise voltage over the 10 Hz to 10 kHz frequency range. Curve 1 shows the total
electrical self noise voltage spectrum level for the case of a sensor whose area is 4 square
inches with an amplifier input resistance of 100 megohms. A hypothetical minimum
expected vibration spectrum level is also shown, assumed to be not masked by this
electrical noise level. Curve 2 shows the effect of a smaller area sensor, in this case one
square inch. Curve 3 illustrates the still higher noise if the input resistance is reduced to 1
megohm. The point that the curves illustrate is that in all but the first case (Curve 1) the
electrical self noise signal is stronger than the signal level.

CONCLUSION

Area-sensing of vibration levels on underwater vehicles is achieved using either
displacement or circumferential strain sensors, incorporating piezorubber tiles or
piezo-film. The sensor installation is optimized using the sandwich construction
technique which achieves self-shielding without capacitance loading. Early experiments
show that area sensing can cancel vibration modes that have a spatial wavelength that is
small compared to the area of the sensor, useful for ignoring non-propagating modes.
Lastly, the importance of low electrical self noise in the sensor-preamplifier design
is demonstrated.

Large area piezoelectric-polymer composites

SD Darrah[1], HD Batha[1], D Damjanovic[2], LE Cross[3]

[1]Fiber Materials, Inc., 5 Morin Street,, Biddeford, Industrial Park,
Biddeford, Maine 04005-4497, [2]EPFL, Departement des materiaux, Laboratoire
de ceramique, MX-D Ecublens, Ch-1015 Lausanne, Switzerland, [3]Pennsylvania
State University, Materials Research Laboratory, University Park,
Pennsylvania 16802

ABSTRACT: Large area 1-3 fiber reinforced PZT composites
are being fabricated and the relationships between
composition and performance are being investigated.

1. INTRODUCTION

Large area 1-3 fiber reinforced piezoelectric polymer composites have
potential use as sensors, acoustic generators and active sound and
vibration damping materials on large structures. Previously, small area
composites have been successfully demonstrated, but fabrication
limitations prevented consideration for large systems. Advanced composite
manufacturing techniques now allow fabrication of these large area
composites with precise location of PZT rods and continuous glass fibers
in the transverse plane.

A program is being conducted at FMI to develop fabrication techniques and
to establish the relationships between composite design and performance.

2. PIEZOELECTRIC COMPOSITE DESIGN

The 1-3 composite specimens are fabricated with PZT rods extending through
the thickness of the material as shown in Figure 1. Continuous glass
fiber is woven in the transverse plane and the entire specimen is
impregnated with resin. The large area surfaces are coated with

conductive electrode material and the specimen is poled with the field between the electrodes, i.e. parallel to the PZT rods.

The composite performance is a function of PZT type, size, shape and concentration; fiber reinforcement type and concentration; and resin type. All specimens have been prepared with PZT-5H type material. The rods are square in cross-section with cross-sectional widths of 0.50, 0.75 or 1.00mm and concentrations range from 2 to 36%. Continuous glass fibers in 5 to 12% concentration and 11% random fiber reinforcements have been used. Specimens have been fabricated with several different formulations of epoxy type resins. Resin choice is determined by fabrication issues such as pot life, viscosity, shrinkage and cure cycle as well as by electrical and mechanical properties. Young's modulus and Poisson's ratio give important information on transfer of stress and acoustic velocity. A low dielectric loss tangent is desirable for the resin. The overall dimensions of the composite specimen are also important because they determine the frequencies of significant resonances.
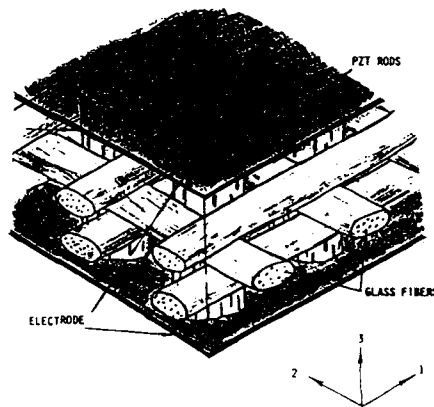
Figure 1.   Structure of PZT Composites

3.   MEASUREMENTS OF PIEZOELECTRIC PERFORMANCE

The relationships between PZT rod spacing and polymer resin type to composite performance have been studied. Complex impedance spectra were recorded with an HP 4194A impedance/gain phase analyzer in order to characterize resonance behavior in the specimens. In addition to the thickness resonance and its overtones, transverse resonances due to periodic discontinuities or overall plate dimensions may also be observed. The frequencies at which resonances occur are governed by the separation

between reflecting surfaces and by the velocity of the waves through the media. Figures 2,3 and 4 illustrate these points. In Figure 2, a specimen with 1mm PZT rods at 4.5mm periodicity in a low modulus resin exhibits only a thickness resonance and its overtones. Figure 3 shows a spectrum for the same type rods and resin but with 2.25mm periodicity. At this spacing, a transverse resonance is observed at a frequency near the frequency of the thickness resonance. A specimen with the wider (4.5mm) spacing but higher modulus resin exhibits not only the thickness and transverse resonances but also the low frequency planar resonance across the entire specimen.
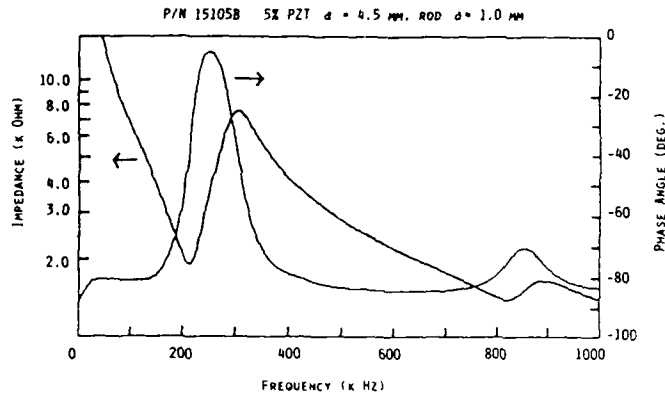
Figure 2. Spectrum of PZT composite with soft resin
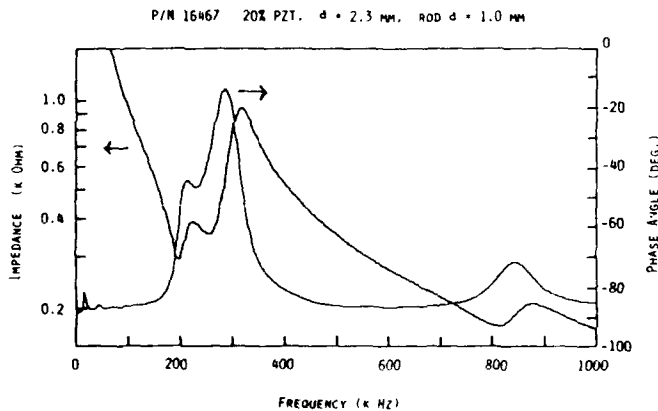
Figure 3. Spectrum of PZT composite with soft resin

P/N 16725   5% PZT   d = 4.5 MM,   ROD d = 1.0 MM
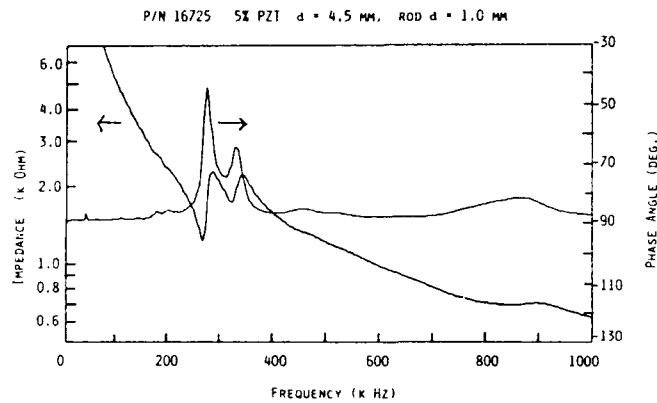
Figure 4.   Spectrum of PZT composite with hard resin

4.   CONCLUSIONS

In designing PZT composite specimens, consideration must be given to the ultimate application. Important factors are frequency range, bandwidth, sensing or actuating mode and temperature. In the sensing mode, where a flat response is desirable over a specified frequency range, resonances should be avoided in that range. In the actuating mode, however, it could be advantageous to design the specimen so that the thickness resonance could be used. The specimen must be fabricated with PZT resins, reinforcements and dimensions which meet the requirements. Preliminary results have been achieved which allow correlations to be drawn between properties and performance and work is continuing toward a better understanding of these relationships.

Metal-ceramic composite actuators

Yutaka Sugawara, Katsuhiko Onitsuka, Shoko Yoshikawa, Q. C. Xu, R. E. Newnham and K. Uchino

Materials Research Laboratory
The Pennsylvania State University
University Park, PA 16802

ABSTRACT

A new type of actuator composed of metal end caps and piezoelectric ceramics has been developed as a displacement transducer. Shallow cavities positioned between the metal caps and the central ceramic disk convert and amplify the radial displacement of the piezoelectric ceramic into a large axial motion of the metal end plates. Large d_{33} coefficients exceeding 2500 pC/N were obtained with the composite actuators. The behavior of the electrically-induced strain with geometric variables such as the thickness of the brass end caps, as well as with pressing force and driving frequency, have been evaluated. Sizeable strains were obtained with both PZT (piezoelectric lead zirconate titanate) and PMN (electrostrictive lead magnesium niobate) ceramics.

Introduction

In recent years, piezoelectric and electrostrictive ceramics have been used as displacement transducers, precision micropositioners, and in many other actuator applications (1). An important drawback to these devices, however, is the fact that the magnitude of strain in piezoelectric ceramics is limited to about 0.1%. Magnification mechanisms have, therefore, been developed to produce sizeable displacements at low voltages. The two most common types are the multilayer ceramic actuator with internal electrodes, and the cantilevered bimorph actuator. The multilayer actuator produces a large force at low voltages, but large displacements are not obtained. Bimorphs, on the other hand, produce large displacements up to hundreds of microns but the forces are very small. Therefore, there is a need for another type of magnification giving sizeable displacement with sufficient force to carry out actuator applications.

A cross-section of the newly patented ceramic-metal composite (2) is shown in Figure 1. It is called the "Moonie" because of the moon-shaped spaces between the metal end caps and the piezoelectric ceramic. Originally, this composite was designed as a hydrophone, and the hydrostatic piezoelectric properties have been reported elsewhere (3).

Referring to Figure 1, the radial motion of the piezoelectric ceramic is converted into a flextensional motion in the metal end caps. As a result, a large displacement is obtained in the direction perpendicular to the ceramic disk. This is the basic principle of the composite actuator described in this paper.

Effective Piezoelectric Coefficient

It is well known that poled PZT [Pb(Zr,Ti)O$_3$] ceramics are strongly piezoelectric (4). Under an applied electric field, the ceramic expands longitudinally through d_{33}, and contracts transversely through d_{31}. Therefore, in the Moonie structure, the axial displacement comes from two different sources. One is the longitudinal displacement of the ceramic itself through d_{33}, the other is the flextensional motion of the metal arising from the radial motion of the ceramic and d_{31}. The two contributions add together to give unusually large displacements which can be described by an effective d_{33} coefficient.

The d_{33} coefficient relates strain and electric field in the poling direction and is often used to compare different piezoelectric materials. In a weak piezoelectric such as quartz, d_{33} is approximately 1 pC/N, and is about an order of magnitude smaller than an average piezoelectric
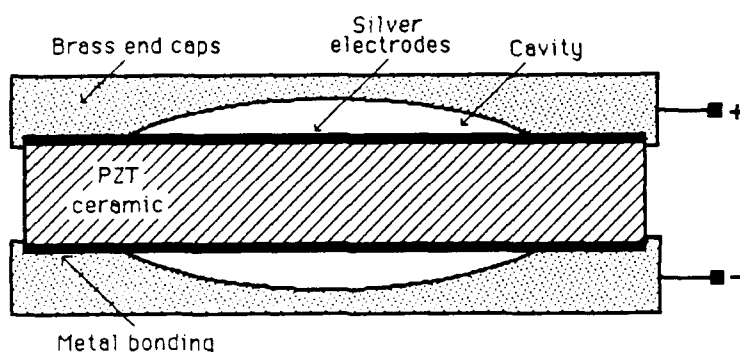
Fig. 1.   Composite Moonie Actuator

like polyvinylidene fluoride. Strong piezoelectrics such as $BaTiO_3$ or Pb (Zr,Ti) O_3 (PZT) have piezoelectric coefficient larger than 100 pC/N. Effective d_{33} values in excess of 1000 pC/N are obtained for the composite structures reported in this paper.

Sample Preparation and Measurement Technique

The initial objective of the research is to make an actuator capable of very large displacements, and to evaluate its performance under DC and AC drive.

The composite actuators were made from electroded PZT 5A disks (11 mm in diameter and 1 mm thick) and brass end caps (13 mm in diameter and thicknesses ranging from 0.4 to 3 mm). Shallow cavities 6 mm in diameter and 150 µm center depth were machined into the inner surface of each brass cap. The PZT disk and the end caps were bonded around the circumference taking special care not to fill the cavity or short circuit the ceramic electrodes. Silver foil (25 µm thickness) and silver paste were used as bonding materials. The composite was heated to 600°C under stress to solidify the bond. After cooling, the actuator was encapsulated around the circumference in Spurrs epoxy resin followed by curing at 70°C for 12 hours. Electrodes were attached to the brass end caps and the ceramic was poled at 2.5 MV/m for 15 minutes in an oil bath held at 120°C.

The direct piezoelectric coefficient was measured at a frequency of 100Hz using a Berlincourt d_{33} meter. The converse piezoelectric coefficient of the ceramic was determined with a laser interferometer. Displacements of the composite actuator were measured linear voltage differential transducer (LVDT) having a resolution of approximately 0.05 µm. The effective d_{33} coefficient of the composite is obtained by dividing the strain by the applied electric field. In comparing the resulting d_{33} with that of a ceramic, it is important to use the total thickness of the composite in calculating the field-induced strain. Resonant frequencies were obtained with a Hewlett Packard L. F. Impedance Analyzer No. 4192A.

Experimental Results

Fig. 2 shows the d_{33} coefficient and resonant frequency plotted as a function of the brass thickness. As expected, thinner end caps flex easier resulting in larger piezoelectric coefficients.
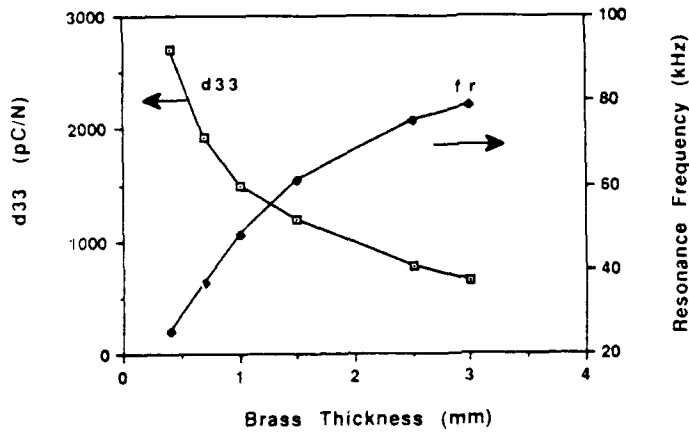
Fig. 2.   Resonance frequency f_r and d_{33} coefficient plotted as a function of the thickness of the brass endcaps

The d_{33} values were measured at the center of the brass end caps using a Berlincourt d_{33} meter. Values as high as 2500 pC/N, approximately five times that of PZT 5A, were obtained with the Moonie actuator. A spectrum analyzer was used to measure the fundamental flextensional resonant frequency. The resonant frequency decreased rapidly with decreasing brass thickness, dropping to less than 20 kHz for a thickness of 0.4 mm.

Piezoelectric effects are largest near the center of the transducer where the flexural motion is largest. The d_{33} values measured as a function of position with a Berlincourt meter are shown in Fig. 3. Plots are shown for two brass thicknesses of 0.4 and 3.0 mm. Ample working areas of
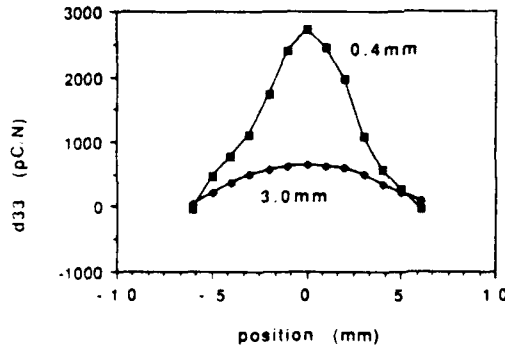
Fig. 3. Positional dependence of the d_{33} coefficient for two actuators with brass thickness of 0.4 mm and 3.0 mm

several mm² are obtained with the actuators.

Maximum displacements obtained with the Moonie actuators are shown in Fig. 4. The values were recorded with the LVDT system and a field of 1 MV/m which is well below the
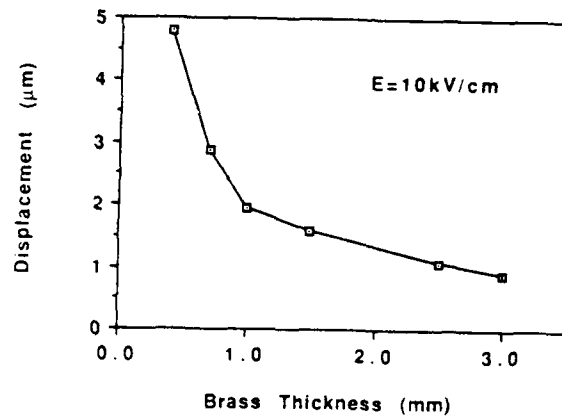
Fig. 4. Maximum displacement plotted as a function of brass thickness

breakdown field of PZT. The largest displacements were obtained with actuators having thin end caps. By loading the actuators with weights it was demonstrated that even thin end caps are capable of exerting forces in excess of 2kg*f*.

A few experiments were also carried out with actuators incorporating PMN (lead magnesium niobate) ceramics. PMN does not need to be poled because it utilizes the electrostrictive effect rather than piezoelectricity. As shown in Fig. 5, displacements as large as 10
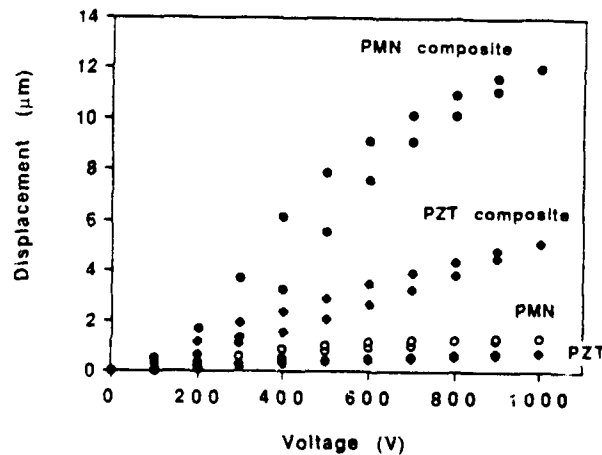
Fig. 5. Displacements measured for composite actuators driven by PZT and PMN ceramics. Displacement for the uncapped ceramics are shown for comparison.

μm were obtained with PMN and brass end caps 0.4 mm thick. Corresponding curves for the composite containing PZT, and for the uncapped PZT and PMN ceramics are shown in Fig. 5 as well. The composites produce a strain amplification of about five times.

Conclusions

A new type of actuator has been constructed from piezoelectric PZT ceramics bonded to metal end caps. Shallow spaces under the end caps produce substantial increases in strain by combining the d_{33} and d_{31} contributions of the ceramic. Even larger displacements were obtained using PMN electrostrictive ceramics. Further improvements in actuator performance are expected using improved materials and design. Driving voltages can be reduced using multilayer ceramics, and larger displacements can be obtained using multimoonie stacks (Fig. 6).
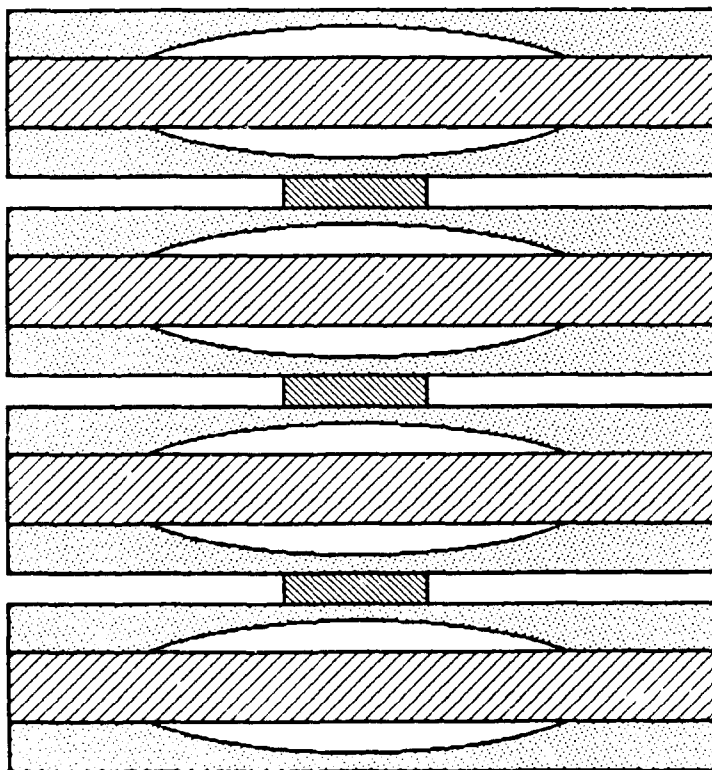
Fig. 6. Illustration of Stacked Composite

References

(1)   Uchino, Kenji, "Piezoelectric/Electrostrictive Actuators", Morikita Publishers, Tokyo, Japan, 1986.

(2)   Newnham, R. E., Qichang C. Xu, (patent) Transformed Stress Direction Acoustic Transducer (to The Pennsylvania Research Corporation) U.S. 4,999,819 (March 12, 1991).

(3)   Xu, Q. C., J. Belsick, S. Yoshikawa, T. T. Srinivasan and R. E. Newnham. "Piezoelectric Composites with High Sensitivity and High Capacitance for Use at High Pressures," IEEE Transactions on UFFC (submitted).

(4)   Jaffe, H., W. Cook and B. Jaffe, Piezoelectric Ceramics, Academic Press, NY, 1971.

Benefits of controls-structures interaction technology for future NASA mission needs

William L. Grantham

NASA Langley Research Center, Hampton, VA 23665-5225

ABSTRACT: Example "case studies" are presented in this paper to show how Controls-Structures Interaction (CSI) technology, when used in the design and control of large space structures, can increase mission performance and enable certain future NASA missions. Many future NASA missions have common CSI technology needs due to their inherent flexibility which requires the lower structural frequencies and spacecraft control system to occupy the same spectral bandwidth. These studies have been used to help formulate and direct the CSI technology development program being jointly pursued at the Langley Research Center (LaRC), Jet Propulsion Laboratory (JPL), and Marshall Space Flight Center (MSFC).

Several CSI benefit studies have been completed by LaRC to date as part of an ongoing assessment process: 1) missions requiring large antennas, and 2) missions requiring the use of closed-loop controlled flexible remote manipulator arms for in-space assembly. Also reported are the recent results concerning Space Station Freedom user accommodations and the influence of routine in-orbit disturbances and other effects, such as astronaut movement, which critically affect precision pointing and microgravity experiments.

1. INTRODUCTION

This paper addresses the questions of which future missions need Controls-Structures Interaction (CSI) technology for implementing large spacecraft in-orbit, and what specific benefits are to be derived if the technology is available? The answers have been used to help formulate and direct the CSI technology development program being jointly pursued at NASA Langley Research Center (LaRC), Jet Propulsion Laboratory (JPL), and NASA Marshall Space Flight Center (MSFC) (Newsom, 1990). Since many future NASA missions have common CSI technology needs, a technology development program focused to the needs of one or two missions can, in fact, provide many benefits to a large number of missions. Focusing the technology development in the direction of selected future missions also involves greater interaction between the technology developer and the technology user so that each is more sensitive to the needs of the other.

Three specific CSI benefit studies presented herein are part of an ongoing assessment process at LaRC: 1) missions requiring large antennas, 2) missions requiring the use of flexible remote manipulator arms for in-space assembly, and 3) in-space experiments on Space Station Freedom requiring precision pointing and low micro-g levels.

2.   LARGE SPACE ANTENNA MISSIONS

Many future missions need antennas larger than the 9-meter antenna flown on ATS-6 in 1973 (Grantham, 1990). For these larger antennas, CSI technology will be required to maintain their precise shape and beam pointing stability. This is because larger antennas will be more flexible and more subject to distortion and because they must work at shorter wavelengths requiring much higher quality control on antenna dimensions than ever before.

The first large antenna-related focus mission selected for study was the Mission-To-Planet-Earth Geostationary Platform (Geoplat). In order to provide the needed precipitation maps of the Earth every 30 minutes for Mission-To-Planet-Earth, precision pointing and beam scanning are necessary for the large microwave radiometer antennas on each end of the geostationary platform. Since the beam scanning will most likely be accomplished mechanically by moving some parts of the antenna, this and other spacecraft disturbances will cause feed-mast flexure and antenna distortion resulting in beam pointing jitter. Jitter up to 10 percent of the resolution cell size is allowed without seriously degrading the quality of the precipitation map developed by the beam raster scan.

The CSI benefits study results for the Mission-To-Planet-Earth show that significantly larger antennas (80 meters) can be used if CSI technology is available as compared to much smaller (20 meters) antennas if it is not (Grantham, 1990 & NASA CR-187471, 1990). Likewise, the science benefits study for the precipitation mapper shows it is possible to meet science requirements of maximum measurable rain rate and resolution cell size using CSI technology to suppress antenna beam jitter whereas, without that control ability, the science requirements simply can not be met (Grantham, 1990).

Once developed, the CSI technology will enable a number of important missions, such as the Mission-To-Planet-Earth, and assure improved performance capability for similar large space antenna missions such as the Very Long Baseline Interferometer (VLBI) for radio astronomy, advanced communication systems, and aircraft surveillance systems.

3.   BENEFITS OF CSI TECHNOLOGY TO SPACE STATION FREEDOM
      ASSEMBLY BY ROBOTIC MANIPULATOR SYSTEMS (RMS)

Based on experiences from many previous Shuttle flights, the oscillations of the RMS/payload system have been found to add significant time to payload deployment, retrieval, and maneuvering. For example, the crew must wait for the oscillations to damp sufficiently to determine the results of the last input; this insures that the next input is not phased so as to enhance the oscillation. A robotic system with a CSI controller might significantly reduce settling time during Freedom assembly and later for Moon and Mars vehicles assembly.

To quantify the settling-time reduction, a benefits study was conducted for a CSI controller applied to the flexible Space Shuttle RMS during assembly of Space Station Freedom (Lamb, 1989). The CSI case was compared with assembly times using the present Space Shuttle RMS. The comparison was for baseline assembly sequence #20/13. The number designation indicates 20 flights are required to accomplish complete assembly (for the first 13 flights Freedom is unmanned). This was the most detailed assembly sequence defined at the time the study began. There were 101 items in the 20 flights and RMS settling time was estimated as a function of the payloads for 8 different weight classes. In the study it was found that 65 percent of the RMS settling times--without CSI technology--are predominantly related to payloads in two weight classes (3000 lbs ± 2000 lbs and 7500 lbs ± 2500 lbs).

A typical RMS maneuver during normal operations induces arm tip oscillations up to 2 inches (peak-to-peak). The RMS settling time without the CSI controller was computed for each of the 20 missions relative to the total RMS activity time. Following that, the potential settling time reductions for a CSI controller with different assumed damping factor improvements were calculated.

Results from the RMS benefit study, assuming use of CSI technology, show a decrease in the amount of RMS settling time by a factor of five which would significantly speed up the Space Station Freedom assembly. Total time cut out of the assembly process-- waiting for the arm to settle--could be as much as 10 hours (Lamb, 1989).

4. IN-SPACE EXPERIMENT PAYLOADS ON EVOLUTIONARY SPACE STATION FREEDOM

The next benefit study initiated was to determine if CSI technology could improve user accommodations on the Evolutionary Space Station Freedom. Early studies have already shown that some baseline activities on Freedom, such as crew treadmill and RMS activities, are most likely to require schedule work-arounds to avoid conflicts with user requirements for microgravity and precision pointing.

In the LaRC-sponsored benefits study at McDonnell Douglas, user requirements and related disturbances were defined for input to a finite element model of Freedom (Extended Operating Capability - XOC Configuration) developed at LaRC (NASA CR-184037, 1990). The study determined the extent of environment improvement possible using CSI technology.

Routine Freedom disturbance sources such as treadmill jogging, tethered soaring, attitude jet firings, and other events were used in the finite element model to compute spacecraft vibrations and micro-g effects at seven payload locations; the disturbing forces were located at their most likely Freedom positions with the excitation imposed in each axis. Acceleration levels above 2 milli-g's were computed at the US lab module due to treadmill jogging--more than three decades higher than is allowable for crystal growth. Pointing jitter calculations exceeded 70 arc sec/second at a number of attached payload positions, which is more than an order of magnitude higher than allowed for candidate precision pointing payloads.

Given that the Freedom environment needed to be improved, several ameliorative steps were considered: disturbance isolation, active control of Freedom, passive damping, and payload gimbaling and isolation. Disturbance isolation from the rest of

the spacecraft was the most effective way of reducing micro-g jitter due to jogging. Predicted improvement of 49 dB was forecast for a 0.01 Hz isolator. The primary improvement for precision pointing was through the use of two-axis gimbals for payload mounts, and the pointing jitter improvement was forecast at 71dB for a 0.5 Hz bandwidth control system. Although the Freedom geometry has changed recently, the results of this study are indicative of the measures that must be taken in order to assure that the Freedom environment is useful for scientific experiments and attached payloads.

It is also clear that the CSI technologist must have a good understanding of what specific types of environmental improvements the researcher needs in order to provide design countermeasures. Just as in the Geoplat case where the physics of the precipitation measurement played an important part in choice of electromagnetic frequency (and thus antenna diameter, Grantham, 1990), it is important that the physics of preferred microgravity environment be understood in order to design countermeasures to improve it (Naumann, 1979 & Feuerbacher, 1988).

REFERENCES

Control-Structures-Interaction (CSI) Technologies and Trends for Future NASA Missions NASA CR-187471 December 1990

Feuerbacher B, Hamache H, and Jilg R 1988 *Compatibility of Microgravity Experiments with Spacecraft Disturbances* A Flugwiss Weltraumforsch 12 pp 145-151

Grantham W L, and Laskin R A 1990 *NASA CSI Technology Focus Mission and Benefit Studies* 4th NASA DOD CSI Technology Conference November 5-7

Lamb B A, and Nowlan D R 1989 *Benefits of Control-Structure Interaction (CSI) Technology to Space Station Assembly by Flexible Robotic Systems (RS)* NASA CR-187523 November

Lockheed Missiles & Space Company, Inc 1990 *Geostationary Platform Study* NASA CR-184037 August

Naumann Robert J 1979 *Susceptibility of Materials Processing Experiments to Low-Level Accelerations* Spacecraft Dynamics as Related to Laboratory Experiments in Space Edited by G H Fichtl, B N Antar and F G Collins NASA Conference Publication 2199 May 1-2 pp 63-68

Newsom Jerry R, Layman W E, and Hayduk, R J 1990 *The NASA Controls-Structures Interaction Technology Program* Presented at the 41st Congress of the International Astronautical Federation Dresden GDR October 6-12

The controls-structures interaction guest investigator program

Rudeen Smith-Taylor and Sharon E. Tanner

NASA Langley Research Center

ABSTRACT: The Guest Investigator (GI) Program is one of the five elements of the NASA Controls-Structures Interaction (CSI) Program. Through the GI Program, researchers from industry and academia use government testbeds to validate advanced control techniques and integrated controls-structures designs. The objective of the GI program is to support CSI technology advancement by 1) involving CSI research experts from academia and industry, 2) providing the researchers with the most advanced CSI test facilities for conducting experimental validation, and 3) disseminating the experimental results to the research community.

1. INTRODUCTION

The behavior of large flexible space structures of the future will necessitate that control system designers be cognizant of the structural dynamics of the spacecraft. The integration of high performance control systems and flexible structures must be designed so as to improve system performance and prevent any detriment to system stability. Because of the uncertainties involved in controlling flexible structures, the design of these advanced control systems cannot rely solely on analytical development but will require experimental validation on dynamically realistic and structurally complex test facilities. This integrated approach, referred to as controls-structures interaction technology, is the focus of the NASA Controls-Structures Interaction (CSI) Program. The Program is a multidisciplinary research activity whose objective is to develop and validate the technology needed for future spacecraft to meet increasingly demanding mission requirements. The five CSI program elements addressing these issues are: 1) configurations and concepts, 2) integrated analysis and design methods, 3) ground testing methods, 4) in-space flight experiments, and 5) a Guest Investigator (GI) program. Three NASA Centers, the Langley Research Center (LaRC), the Marshall Space Flight Center (MSFC), and the Jet Propulsion Laboratory (JPL), are cooperatively developing this technology.

Because the advancement of CSI technology greatly benefits from the participation of researchers from academia and industry, a general solicitation for participation in the GI program is made to obtain the most promising research approaches. The selections for award are based on technical merit, utilization of test facilities, and cost. Technical monitors are provided by each test facility. In the recently completed Phase I, researchers participated in a 2-year research activity in which government testbeds were

used to test system identification methods and controller design techniques. Following is a description of the Phase I test facilities.

2. CSI GROUND TEST FACILITIES

The Mini-MAST facility is a 20-meter long deployable/retractable truss, located at the NASA Langley Research Center, Hampton, Virginia. Mini-MAST is a flight-quality laboratory model of a 60-meter MAST flight truss. The graphite/epoxy cantilevered truss is supported vertically from a rigid foundation. Longerons run parallel to the beam axis, battens form triangular cross-sections, and diagonals lie in the beam face planes. The longeron and diagonal members are hinged with pinned connections to titanium corner-body joints. The battens are rigidly connected to the corner bodies. The beam has 18 bays which are deployable and retractable, 2 bays at a time. A stiff platform at the tip and one near the mid-point hold servo accelerometers for linear acceleration measurements and rate gyros for angular rate measurements. Noncontacting displacement sensors are mounted alongside the truss for observing lateral displacement. Three torque wheel actuators (TWA's), mounted on the tip platform and weighing approximately 85 pounds each, are available for control. Disturbance input to the structure is provided by the TWA's or by 3 Unholtz-Dickie 50 lb shakers. (Tanner 1991)

The Advanced Control Evaluation for Structures (ACES) ground test facility is located at the NASA Marshall Space Flight Center, Huntsville, Alabama. The test article is a vertically suspended deployable beam approximately 14 meters in length, supporting a 3 meter offset antenna. The beam was built as a flight backup for the Voyager magnetometer boom, is extremely lightweight, lightly damped, and very flexible. It is symmetric and triangular in cross section with three continuous longerons forming the corners. The cross members divide the beam into 91 bays, each having equal length and mass and similar elastic properties. The inverted beam is attached to a payload mounting plate at the gimbaled base, with an antenna and two counter-balance legs appended to the beam tip forming a configuration having modal characteristics of large space structures. An optical system consisting of a fixed position laser, 2 mirrors, and a 2-axis detection plane provides a measure of control system performance. One of the mirrors of the optical system is mounted to a 2-axis advanced pointing gimbal system located on an extension arm appended to the base of the beam. This gimbaled mirror is used in a closed-loop image motion compensation system for the primary measure of controller effectiveness. (Jones 1991)

3. PHASE I RESEARCH TRUSTS

Each GI was required to perform validation testing at both government testbeds described above, concentrating on a single testbed for a year. The techniques employed by each researcher is discussed below.

3.1 Arizona State University

Dr. Bong Wie demonstrated the simplicity and effectiveness of applying classical control designs to realistic CSI testbeds. Various single-input/single-output (SISO) controllers were simultaneously applied to bending and torsional motion. Nonminimum phase compensation was employed for periodic disturbance rejection. With Mini-MAST, sensor output decoupling was required since the individual displacement sensors are inherently coupled. Both collocated and noncollocated SISO

controllers were demonstrated. At ACES, Dr. Wie used four separate SISO loops which were identified by the Harris Corporation researchers. None of the ACES feedback signals were collocated.

3.2 California Institute of Technology

Dr. John Doyle and Dr. Gary Balas used μ-analysis and synthesis for their research effort. Control design using μ-synthesis is an iterative process which alternates between solving an H_∞ optimal control problem and a structure singular value (μ) analysis problem. μ-synthesis can directly account for known and unknown errors such as structural modes eliminated from the reduced order design models, unmodeled sensor and actuator dynamics, or inaccurate damping, frequencies, or mode shapes. Modeling difficulties created the need for excessively large uncertainty values, which in turn severely penalized controller performance emphasizing the importance of accurate models.

3.3 University of Cincinnati

Dr. Randall Allemang led the effort to develop reliable state space models which Dr. Gary Slater used for control law development. In applying system identification techniques to actuator/structure/sensor systems, the complexity that time delays add to the model was evident. While the positivity approach guarantees stability if sensors and actuators are ideal, application of this technique to real hardware showed its limitations. Application of the controllers to real hardware resulted in instabilities which in turn led to the development of multivariable scaling and phase compensation. To maintain the positive definiteness of controller matrices when coupled with the compensators, comparable scale factors had to be applied to both the inputs and outputs of the system. Such scaling holds promise for future 'arge space structures. This procedure can tolerate a zero scale factor, thus compensating for a sensor or actuator failure without requiring a redesign of the controller.

3.4 Harris Corporation

Dr. David Hyland used the Optimal Projection Approach for Uncertain Systems (OPUS), with the Maximum Entropy/Optimal Projection (MEOP) controller process, in the design of robust, high performance controllers. The MEOP process begins with low- to moderate-authority controllers to which robustness is added through application of the homotopy algorithm, creating a maximum entropy design. Maximum entropy designs increase gain stability, allow order reduction in the controller bandwidth, and improve the controller's tolerance of uncertainties in damping, frequency, and location of system zeros. At each testbed, a decentralized controller architecture was developed, integrating several reduced-order controllers, each operating on an individual loop within the system. At ACES, four SISO loops dominating the system dynamics were identified which were subsequently used by other GI.

3.5 Massachusetts Institute of Technology

Dr. Wallace Vander Velde demonstrated failure detection and isolation (FDI) techniques. Generalized parity relations and failure detection filters were the two methods selected for investigation since both are applicable to sensors and actuators alike. The FDI using the generalized parity relations method, produces a scalar residual

r(t). This residual will be zero only when the input measurements are noise-free in an accurately modeled system with all sensors functioning perfectly. With non-ideal systems, the goal is to ensure that when a sensor fails the residual produces an identifiable signature distinctive from the background noise created by unmodeled dynamics and measurement noise. Single Sensor Parity Relations (SSPR) and Double Sensor Parity Relations (DSPR) were compared. SSPR are simpler to create and implement.; however, the magnitude of the failure signature with SSPR's can be inadequate if the sensor fails in the off mode. DSPR's involve decision logic to isolate the failed sensor but are preferred for increased reliability.

3.6 Purdue University

Dr. Robert Skelton used Modal Cost Analysis (MCA) with self-tuning Output Variance Constraint (OVC) controller design to develop multiple-input/multiple-output (MIMO) controllers. An iterative procedure was applied, integrating both system identification and control law development. Model order reduction was required to make the complex dynamics associated with realistic large space structures more manageable. Controller performance was used as the criteria in the model reduction process, ensuring the appropriateness of the analytical model for a particular controller design. MCA includes a closed-form solution for the weighted quadratic cost functions associated with each chosen system output. Specifications influence the weights assigned to modes and noise, thereby influencing weights assigned to estimator gains and input signals. The iterative process acts as a self-tuning mechanism, producing a series of controllers from low to high gain.

4. CONCLUDING REMARKS

During the 2-year activity of Phase I, principal investigators using ground test facilities at LaRC and MSFC, conducted experiments to validate CSI techniques in system identification and controls development. The primary goal of all the researchers was to better understand the practical limitations of simplifying theoretical assumptions. Phase I results have shown that without knowledge of the structural dynamics to be controlled, many of the most accepted control techniques demonstrated only marginally improved performance results. When these same techniques were integrated with knowledge of the structural dynamics, the results showed considerably better performance. The GI program has been instrumental in advancing CSI technology, producing valuable experience to be shared with the research community. With these results at hand and improved government test facilities, the research effort from subsequent phases promises to result in even more impressive demonstrations of integrated design.

REFERENCES

Jones V L, Bukley A P, Waites H B and Patterson 1991 A *NASA/MSFC Large Space Structures Ground Test Facility* IFAC Workshop, Huntsville, AL

Tanner S E and et al 1991 *Mini-MAST CSI Testbed Preliminary User's Guide* NASA TM 102630

Actuation and control with Ni-Ti shape memory alloys

D Stoeckel, J Simpson

Raychem Corporation, 300 Constitution Drive, Menlo Park CA 94025

ABSTRACT: Ni-Ti shape memory actuators respond to temperature changes with a shape change. The change in temperature can be caused by a change in the environment or by electrically heating the Ni-Ti element. In the first case, the shape memory alloy acts as a sensor and an actuator (thermal actuator). In the second case, it is an electrical actuator that performs a specific task on demand. Thermal as well as electrical Ni-Ti actuators combine large motion, rather high forces and small size, thus they provide high work output.

1. INTRODUCTION

"Shape Memory" describes the effect of restoring the original shape of a plastically deformed sample by heating it. This phenomenon results from a crystalline phase change known as "thermoelastic martensitic transformation". The shape memory effect in Ni-Ti alloys can be used to generate motion and/or force in actuators, fasteners and couplings. At temperatures below the transformation temperature, Ni-Ti alloys are martensitic. In this condition they are very soft and can be deformed easily (like soft copper). Heating above the transformation temperature recovers the original shape and converts the material to its high strength, austenitic, condition (like steel).

2. MECHANICAL PROPERTIES

The mechanical properties of the austenite and the martensite are quite different. As shown in Figure 1, the austenitic curve looks like that of a "normal" material. However, the martensitic one is quite unusual. On exceeding a first yield point, often called "plateau stress, several percent strain can be accumulated with only little stress increase. After that,
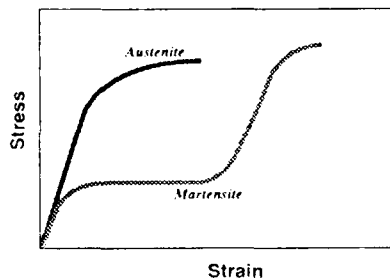
Fig. 1. Tensile Behavior of Ni-Ti alloys
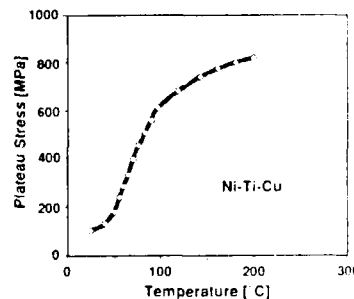
Fig. 2. Influence of temperature on the plateau stress of a Ni-Ti-Cu alloy

stress increases rapidly with further deformation. The deformation in the "plateau region" is non-conventional in nature. It is fundamentally different from the conventional deformation by gliding, and can be recovered thermally. I.e. heating above the transformation temperature will restore the original shape. Deformation exceeding the second yield point cannot be recovered. At this point, the material is plastically deformed in a conventional way. Plotting the plateau stress or the first yield point versus temperature produces a curve as shown in Figure 2. A similar curve is obtained, when the modulus is plotted versus temperature.

3. HYSTERESIS

The transformation from austenite to martensite and the reverse transformation from martensite to austenite do not take place at the same temperature. A plot of the volume fraction of martensite, or more practically, the length of a wire loaded with a constant weight, as a function of temperature provides a curve of the type shown schematically in Figure 1. The complete transformation cycle is characterized by the following temperatures: austenite start temperature (As), austenite finish temperature (Af), martensite start temperature (Ms) and martensite finish temperature (Mf).
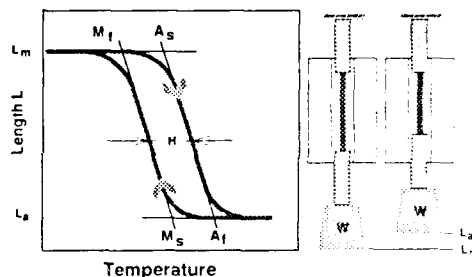
Fig. 3. Schematic length/temperature hysteresis of a shape memory wire loaded with a constant load

The hysteresis is an important characteristic of the heating and cooling behavior of shape memory alloys and actuators made from these alloys. Depending on the alloy used and/or its processing, the transformation temperature as well as the shape of the hysteresis loop can be altered in a wide range. Binary Ni-Ti alloys typically have transformation temperatures (As) between 0°C and 100°C with a width of the hysteresis loop of 25°C to 40°C. Copper containing Ni-Ti alloys show a narrow hysteresis of 7°C to 15°C with transformation temperatures (As) ranging from -10°C to approx. 80°C. An extremely narrow hysteresis of 0 to 5°C can be found in some binary and ternary Ni-Ti alloys exhibiting a premartensitic transformation (commonly called R-phase). On the other hand, a very wide hysteresis of over 150°C can be realized in Niobium containing Ni-Ti alloys after a particular thermomechanical treatment.
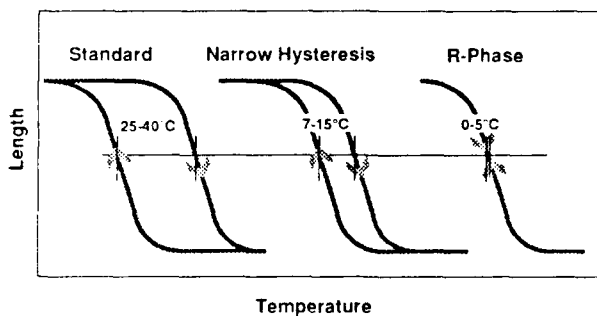
Fig. 4. Schematic length/temperature hysteresis of different Ni-Ti alloys

The standard thermomechanical processing of Ni-Ti alloys generates a steep hysteresis loop (a greater shape change with a lesser change in temperature), which generally is desirable in applications where a certain function has to be performed upon reaching or exceeding a certain temperature. Special processing can yield a hysteresis loop with a more gradual slope, i.e. a small shape change with temperature. This behavior is preferred in applications where proportional control is required.
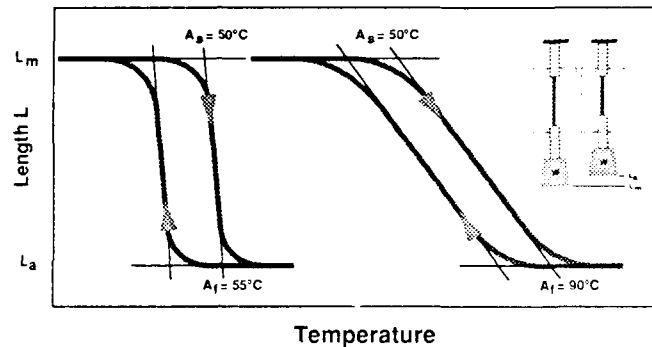
Fig. 5. Influence of processing on the shape of the hysteresis loop

The shape of the hysteresis loop is not only alloy and processing dependent, but is also influenced by the application itself. If a wire (standard processing) works against a constant load, e.g. by lifting a certain weight, the transition from martensite to austenite or vice versa occurs in a very narrow temperature range (typically 5°C). However, if the wire works against a biasing spring, the transition is more gradual and depends on the rate of the spring. The reason for this behavior is the stress dependency of the transformation temperatures. As can be seen from Figure 6, the transformation temperatures increase with increasing operating stress.
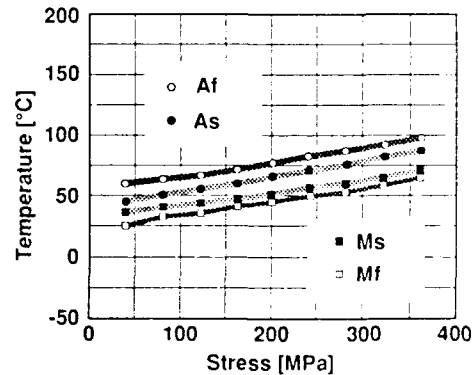
Fig. 6. Influence of the applied stress on the transformation temperatures

4. ACTUATOR DESIGN

The shape memory effect in Ni-Ti alloys is not limited to the linear contraction of wires. Even larger shape changes can be achieved in the bending or torsional deformation mode. Accordingly, there are many possibilities regarding the shape of the actuator. Preferred configurations are :

- straight tensile wires (high force, small motion)
- helical compression springs (large motion, less force)
- helical extension springs (large motion, less force)
- cantilever springs (bending)
- "Belleville"-type disc springs (high force, small motion)

The design of shape memory elements for thermal actuators is based on the different stress/strain curves of the austenite and the martensite. As an example, Figure 7 shows the force/deflection curves of a helical compression spring at high and low temperatures. The high temperature shape of the spring with no load is Lo (A). If the spring is loaded with a constant load W in the austenitic condition (at temperatures above Af) the spring is compressed along A - B with the displacement Δl (B). Upon cooling below Mf the spring transforms into martensite. Now the load W compresses the spring to point C on the

martensite curve with the displacement ΔL.
Repeated heating/cooling cycles between
points B and C. If, instead of a constant load,
a steel biasing spring is used, the
force/deflection curve for this spring has to
be superimposed to the austenitic and
martensitic spring characteristics of the
Ni-Ti spring.

Under optimum conditions and no load the
shape memory strain can be as high as 8%.
However, for cyclic applications the usable
strain is much less. The same applies for the
stress; for a one-time actuation the austenitic
yield strength may be used as maximum
stress. Much lower values have to be
expected for cyclic applications. The
following numbers may be used as
guidelines:

Fig. 7. Design concept for actuators working
against constant load

Number of Cycles	Max. Strain	Max Stress
100	4%	275 MPa/43 ksi
10000	2%	140 MPa/20 ksi
100000+	1%	70 MPa/10 ksi

5. APPLICATIONS OF SHAPE MEMORY ACTUATORS

Ni-Ti shape memory actuators respond to a temperature change with a shape change. The
change in temperature can be caused by a change of ambient temperature or by electrically
heating the Ni-Ti element. In the first case, the shape memory alloy acts as a sensor and an
actuator (thermal actuator). In the second case, it is an electrical actuator that performs a
specific task on demand. Thermal as well as electrical Ni-Ti shape memory actuators
combine large motion, rather high forces and small size, thus they provide high work output.
They usually consist of only a single piece of metal, e.g. a straight wire or a helical spring,
and do not require sophisticated mechanical systems.

Shape memory thermal actuators have been
successfully used in the areas of thermal
compensation, thermal actuation and thermal
protection. They often fit into tight spaces in existing
designs, where other thermal actuators, like
thermostatic bimetals or wax actuators, would require
a major redesign of the product. In flow-control or oil
pressure control valves, for example, helical springs
can be placed in the fluid path, without restricting the
flow. Thus, they provide fast response to changes in
temperature.

Fig. 8. Shape memory flow control
valve

Electrical actuators have been used to replace
solenoids, electric motors etc. in applications, where
quiet operation, small dimensions, small or large
forces and simplicity of the design is required. By
controlling the power during electrical actuation,
specific levels of force and/or specific positions can be maintained. A variety of triggering
devices, animated objects, toys etc. are presently being marketed. The integration of Ni-Ti
wires in composite structures has been suggested, to allow the structure to change shape on
demand.

Shape memory and related effects

C. M. Wayman

Department of Materials Science and Engineering, University of Illinois at Urbana-Champaign,
1304 West Green Street, Urbana, Illinois 61801

ABSTRACT. Many materials are now known to exhibit a shape memory effect by means of which an article deformed at some lower temperature will regain its original undeformed shape when heated to a higher temperature. This behavior is basically a consequence of a martensitic phase transformation. The various shape memory materials are found to have common characteristics such as atomic ordering, a thermoelastic martensitic transformation which is crystallographically reversible, and a martensite phase which forms in a self accommodating manner. Explanation of the shape memory phenomenon is now well in hand, at least for metallic materials. In addition to the "one-way" memory, shape memory alloys also exhibit a "two-way" memory and a "mechanical" shape memory resulting from the formation and reversal of stress-induced martensite.

1. OVERVIEW

Martensitic transformations, the means by which steels are quench hardened, have long been a cornerstone of technology. Apart from this strengthening, attention has recently focussed on other mechanical aspects of martensitic materials, such as TRIP (Transformation Induced Plasticity) steels and transformation (martensitic) toughened ceramics. Most recently, a new class of behavior known as *shape memory* has been found to be associated with martensitic transformations in certain materials, mostly metallic alloys. Accordingly, a material when deformed after martensitic transformation regains its undeformed shape when heated to a sufficient temperature so that the martensite transforms back to the parent "austenite" phase. This shape memory response after deformation and thermal stimulation constitutes "smart" behavior.

Principal applications of shape memory effect (SME) alloys in high performance products include aircraft hydraulic couplings and electrical connectors. Because of their dramatic strength in response to temperature, SME alloys have continuously been proposed as alternatives to solenoids, motors, and bimetallic or wax type actuators. Alternatively, a SME approach to electrochemical actuation offers advantages which conventional approaches would find difficult or impossible to achieve.

- Large amounts of recoverable strain offer work densities up to ten times higher than conventional approaches. Applications concerned with maximizing the work volume or work/weight of a device find the SME approach attractive.
- High electrical resistivity permits direct electrical actuation without extra parts and with efficient use of available energy.
- Large available material strains permit extremely long strokes, constant force during the stroke, and high starting force.
- SME actuators can be linear, rotary or a combination of each.

Most frequently shape memory is viewed as a one time operation, for example, shrinking a ring around hydraulic tubing. However, it should be noted that if the material is returned to its martensitic state, it can be redeformed, reheated, re-recovered, etc. repeatedly. The memory function must be "informed" each time before shape recovery.

The SME is the consequence of a crystallographically reversible martensitic phase transformation occurring in the solid state. Although there are many ways (orientations) to produce the martensite phase from its parent phase during cooling, once the lower symmetry martensite is formed it has a unique reversion path during the reverse transformation because of crystallographic restrictions. The transformation of the parent phase into martensite is basically a deformation process, but because the individual units of martensite self-accommodate, the overall macroscopic deformation (strain) upon transformation is zero. When the shape memory martensite is deformed, a particular orientation of the various self-accommodating units that most favorably oriented with respect to the applied stress—grows at the expense of others, eventually leading to a single orientation of martensite. This orientation has only one reversion path, which is the essence of the shape memory—a deformed and reoriented martensitic phase which is thermally responsive. Strains on the order of seven per cent are typically recoverable in this manner.

Shape memory alloys (SMA) also display superelasticity, a mechanical type of shape memory as opposed to the thermally induced (by heating) shape memory described above. In this case, when the parent phase is deformed above the martensite start temperature, the martensitic transformation occurs "prematurely" because the applied stress substitutes for the thermodynamic driving force usually obtained by cooling. When the applied stress is basically uniaxial, only one orientation (out of many) of martensite is selectively formed, which imparts an overall deformation to the specimen. This deformation disappears when the stress is removed and the original specimen shape is restored leading to a mechanical shape memory with fully recoverable strains on the order of 12%.

In addition, a "two-way shape memory" can be realized whereby a specimen is programmed by means of thermomechanical treatment. Typically, a specimen deformed in the martensitic condition is intentionally constrained during heating in order to suppress the normal (one-way) shape memory. This process generates "built in" microstresses in the parent phase which in turn program the specimen to behave as in a stress-induced martensitic transformation. That is, the microstresses promote only a single orientation of martensite upon subsequent cooling, which produces a spontaneous deformation. When the specimen is heated, the normal shape memory process occurs and its original shape is reproduced. The two-way process can be repeated indefinitely (as with a thermoset) as opposed to the one-way memory, which is a one time only operation (as in making a mechanical connection).

2. Some Behavioral Details

2.1 The Formation of Martensite in Shape Memory Alloys

A typical plot of property changes vs. temperature for an SMA is shown in Fig. 1, where symbolically the parent phase (usually called austenite) is represented as a two-dimensional square lattice, and the martensite is a rhombus, derived on cooling by a spontaneous distortion of the parent. Note that the formation of martensite is really a deformation process. Various temperatures, M_s, M_f, A_s and A_f are indicated in the graph and are explained in the legend to the figure. It is to be noted that, comparing the formation of martensite between M_s and M_f, and the reversal of martensite (formation of parent) between A_s and A_f, there is a certain hysteresis, which is usually on the order of 20 C. As indicated at the y axis, plots such as Fig. 1 are obtained when a variety of physical properties are measured during the course of a martensitic transformation upon cooling and its subsequent reversal during heating.

2.2 The Nature of the Shape Memory Effect

The SME can be described with reference to the cooling and heating curves such as shown in Fig. 1 and this is done in Fig. 2. There is no change in shape of a specimen cooled from above A_s to below M_f. When the specimen is deformed below M_f it remains so deformed until it is
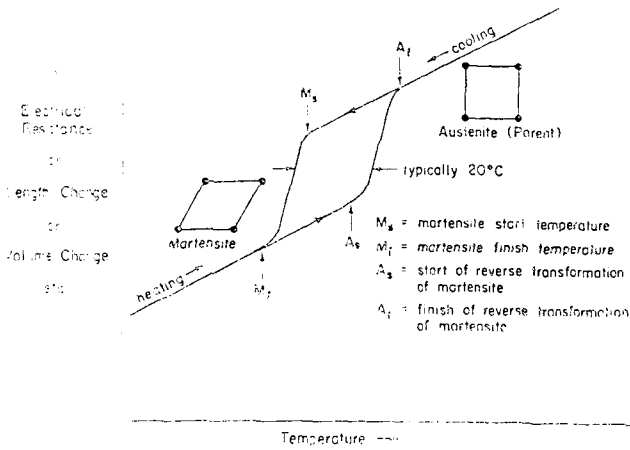
Fig. 1. Hypothetical plot of property change vs. temperature for a martensitic transformation occurring in a shape memory alloy. The parent phase (austenite) is represented by the square lattice, which upon transformation is distorted into the rhombic product phase (martensite). Characteristic temperatures are defined in the inset.
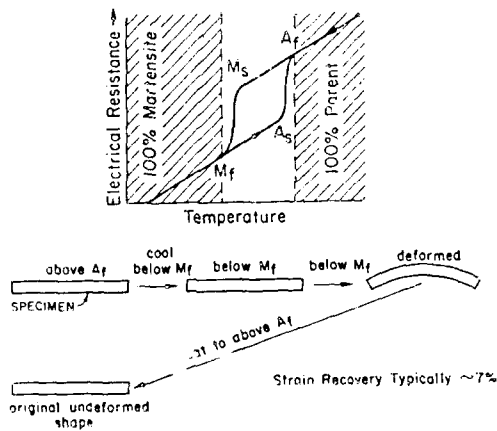
Fig. 2. The shape memory effect is described with reference to Fig. 1

heated. The shape recovery begins at A_s and is completed at A_f. At the inflection point between A_s and A_f, about 50% of the original shape is recovered. Once the shape has recovered at A_f there is no change in shape when the specimen is cooled to below M_f, and the

shape memory can only be reactivated by deforming the martensitic specimen once again. In other words, the SME is a one time only occurrence and because of this is frequently referred to as the one-way shape memory, in contrast to the two-way shape memory described later. As Fig. 2 indicates, recoverable strains on the order of 7% are typical of SMA's, but some show recoveries as high as 10%.

Figure 3 is a stress strain curve for a Cu39.8%Zn SMA deformed in the martensitic condition below 25°C below the M_f temperature. Two features are worthy of note. First, the martensite was strained to over 5%, yet all of this strain was recovered when the specimen was heated to above the A_f temperature. Secondly, the yield stress of the martensite is fairly low, about 35 MPa (5 Ksi). Above A_f the yield stress of the parent was found to be about 350 MPa (50 Ksi). In fact, a good rule of thumb for SMA's is that the martensite yield stress is about 10% of that of the parent phase. Usually the design stress (i.e., recovery stress) of SMA's is taken to be the yield strength of the parent phase. This would be the stress generated for making a coupling, powering an engine, etc.
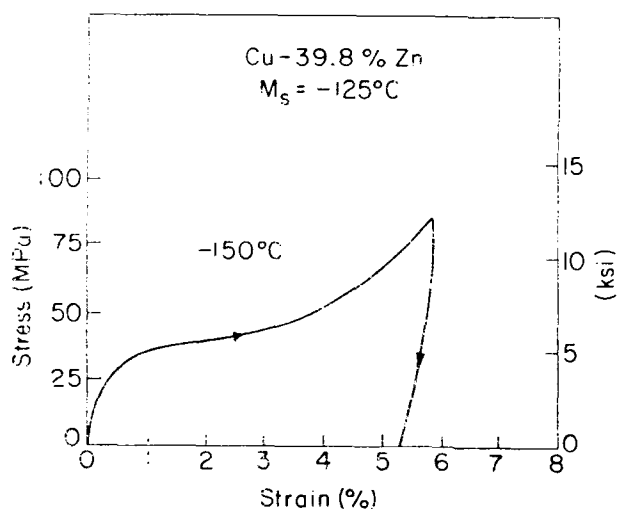
Stress strain curve for a martensitic Cu-Zn shape memory alloy. The strain of over five percent is completely recovered when the unloaded specimen is heated above the A_f temperature.

Superelasticity and Stress-Induced Martensite

The discussion up to now shows that the SME is both a thermal and mechanical one. The martensite initially formed by cooling is then deformed below the M_f temperature. The deformed martensite is then heated to above the A_f temperature to cause the shape recovery, i.e., the shape memory is caused by heating deformed martensite.

We now consider another type of shape memory which is temperature independent — superelasticity. Normally, on cooling, the martensite forms at M_s under no stress. But in the same material, martensite can form above M_s if a stress is applied, and the martensite so formed is termed stress induced martensite (SIM). The driving force for the transformation is now mechanical, as opposed to thermal, as in the case of "cooling martensite." The SIM reverts when the applied stress is released, giving rise to a mechanical shape memory

Figure 4 shows a "superelastic" stress-strain curve (actually a superelastic loop) for a Cu-39.8%Zn SMA. The upper plateau corresponds to the formation of SIM under stress while the lower plateau represents the reversion of the SIM when the stress is released. Note that 9% strain is fully recovered, and this corresponds to the mechanical shape memory.
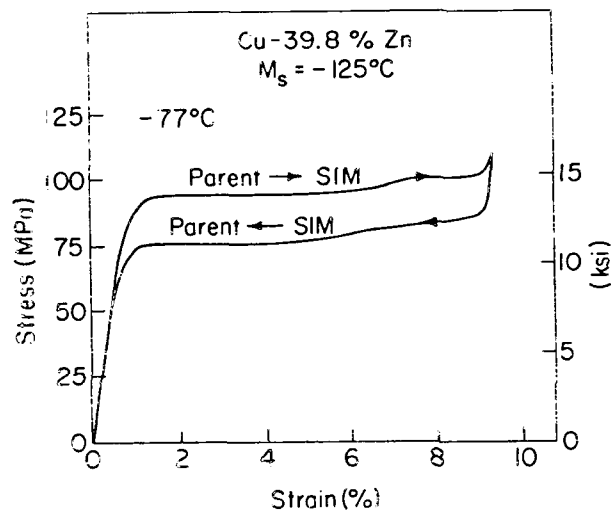
Fig. 4. Stress-strain curves for a Cu-Zn single crystal loaded in tension above the M_s temperature. As the M_s temperature is approached, the stress required to induce martensite is lowered.

2.4 The Two-Way Shape Memory

Lastly, we consider the two-way shape memory effect (TWSM). This is illustrated for spring-type specimens in Fig. 5. In the upper part of the figure a collapsed SMA spring is deformed by extension below M_f. The contracted spring shape is recovered following heating to above A_f. The contracted shape remains when the specimen is again cooled to below M_f. This is the
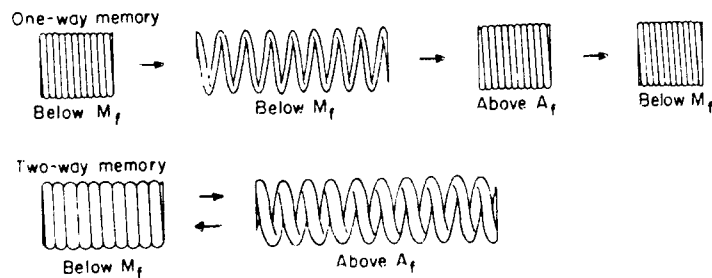
Fig. 5 Comparison of one-way and two-way memories

one-way shape memory behavior, where, as noted before, is a one time only deployment. In contrast, the TWSM is depicted in the lower half of the figures, in which case a contracted spring below M_f extends when heated to above A_f. But now, the extended spring spontaneously contracts again when cooled below M_f. This behavior repeats indefinitely. To produce the two-way behavior, thermomechanical treatment is required, usually involving several transformation cycles.

3. Summary

The shape memory effect is a consequence of a crystallographically reversible martensitic phase transformation occurring in the solid state. Although there are many ways (orientations) to produce the martensite phase from its parent during cooling, once the lower symmetry martensite is formed it has only one unique reversion path during the reverse transformation because of crystallographic restrictions.

Shape memory alloys also display superelasticity, a mechanical type of shape memory as opposed to the thermally induced (by heating) shape memory described above. In this case, when the parent phase is deformed above the martensite start temperature, the martensitic transformation occurs "prematurely" because the applied stress substitutes for the thermodynamic driving force usually obtained by cooling.

Finally, a two-way shape memory can be realized in shape memory materials, whereby a specimen is programmed by means of thermomechanical treatment. Typically, a specimen deformed in the martensitic condition is intentionally constrained during heating in order to suppress the normal one-way shape memory. This process generates in-built microstresses in the parent phase which in turn program the specimen to behave as in a stress-induced martensitic transformation. That is, the microstresses favor only a single orientation of martensite during cooling.

REFERENCES

Duerig T W, Melton K N, Stockel D and Wayman C M eds 1990 *Engineering Aspects of Shape Memory Alloys* (Boston: Butterworths-Heinemann)
Perkins J ed. 1975 *Shape Memory Alloys* (New York: Plenum Press)
Schetky L McD 1979 *Scientific American* **241** 74
Wayman C M 1980 Some Applications of Shape Memory Alloys *Journal of Metals* **32** 129

Active buckling control of nitinol-reinforced composite beams

A.Baz, J.Ro, M.Mutua and J.Gilheany

Mechanical Engineering Department, The Catholic University of America, Washington, DC 20064

ABSTRACT

The buckling characteristics of flexible fiberglass composite beams are actively controlled by activating optimal sets of a shape memory alloy (NITINOL) wires which are embedded along the neutral axes of the beams. With such active control capabilities, the beams can be manufactured from light weight sections without compromising their elastic stability. This feature will be invaluable in building light weight structures that have high resistance to failure due to buckling.

A finite element model is developed to analyze the individual contributions of the fiberglass-resin laminate, the NITINOL wires, and the shape memory effect to the overall performance of the composite beams. A closed-loop computer-controlled system is built to validate the finite element model. The system is used to control the buckling of a fiberglass polyester resin beam which is 63.75 cm long, 0.45 cm thick and 2.54 cm wide reinforced with 8 NITINOL - 55 wires that are 0.55 mm in diameter. The results obtained confirm the developed theoretical model and indicate that the critical buckling load can be increased three times when compared to the uncontrolled beam.

1. INTRODUCTION

Considerable attention has been devoted recently to the utilization of the Shape Memory NIckel-TItanium alloy (NITINOL) in developing SMART composites that are capable of adapting intelligently to external disturbances (Ikegami et al. 1990, Rogers et al.1991, and Baz et al 1990 and 1991). Such wide acceptance stems from the fact that NITINOL acts as an actuator converting thermal energy into mechanical energy (Perkins 1975 and Duerig et al 1990) as it undergoes its unique phase transformation from low temperature martensite to high temperature austenite. During this phase transformation process large phase recovery forces are generated and thereby alter the strain energy of the composite inside which the NITINOL fibers are embedded. With such capabilities, the static and dynamic performance of the SMART composites can be optimized and tailored to match changes in the operating conditions.

Emphasis is placed, in the present work, on using the shape memory effect of the NITINOL fibers in controlling the buckling of fiberglass composite beams. The NITINOL fibers are embedded inside vulcanized rubber sleeves placed along the neutral axes of these composite beams as shown in

Figure (1).   In this arrangement, the fibers are free to move during the
phase transformation process in order to avoid degradation and/or
destruction of the shape memory effect which may result when the fibers are
completely bonded inside the composite matrix.   The **NITINOL** fibers are
trained to **memorize** the shape of the unbuckled beam and when the beam is
deflected under the action of external compressive loads, the controller
activates the **NITINOL** fibers by heating them above their transformation
temperature.   The generated phase recovery forces bring the beam back to
its **memorized** undeflected position.   The present study is motivated by the
work of Baz and Tampe (1989) where external helical shape memory actuators
are used to enhance the buckling characteristics of long slender beams.
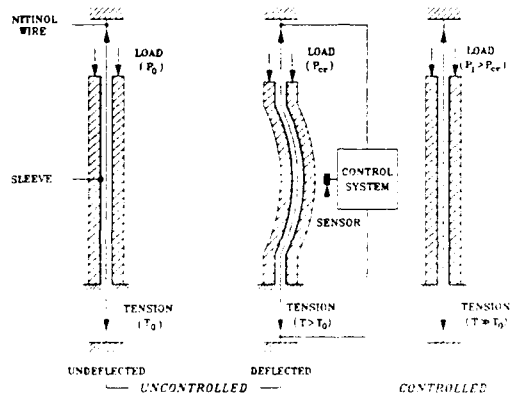
Figure (1) - Principle of buckling control of NITINOL-reinforced composites

2. STATIC CHARACTERISTICS OF NITINOL-REINFORCED BEAMS

The static characteristics of NITINOL-reinforced composite beams are
primarily governed by their stiffness.   The overall beam stiffness is made
up of the following components: the flexural rigidity of the beam, the
geometric stiffness that accounts for the axial and thermal loading as well
as the stiffness imparted by the elasticity of the NITINOL fibers.   These
individual components of the beam stiffness can be determined by
considering the NITINOL-reinforced beam element shown in Figure (2) with
the forces acting on it and the associated displacements.   The combined
stiffness of the element can be obtained using the principle of
conservation of energy and equating the work done by external loads to the
strain energies stored in the element. In the present analysis, the theory
of Bernoulli-Euler beams is used with the assumption of small deflections.
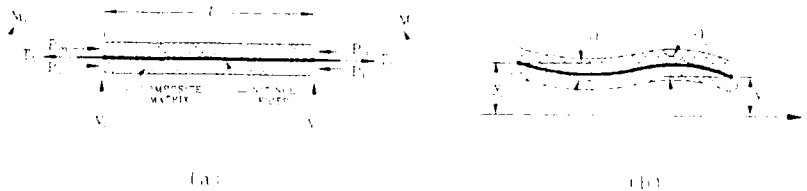
Figure (2) - NITINOL-reinforced beam element with forces and displacements

2.1 External Work

The work done by the external loads includes:

a. work done by transverse loads and moments (W_1): This work is given by

$$W_1 = 1/2 \ [\delta]^T \ [F],\tag{1}$$

where $[\delta]$ is deflection vector and $[F]$ is transverse load vector.

b. work done by the axial mechanical loads (W_{2m}): W_{2m} is given by

$$W_{2m} = P_m \ / \ 2 \int_0^L (dw/dx)^2 \ dx,\tag{2}$$

where P_m is the external axial compressive load acting on the beam.

c. work done by the axial thermal loads (W_{2t}): W_{2t} represents the work done by the thermal loads P_t on the beam element due to changes in the temperature $\Delta\Theta$ of the element caused by changes in the ambient temperature or during the activation and de-activation of the NITINOL fibers. It is given by

$$W_{2t} = P_t \ / \ 2 \int_0^L (dw/dx)^2 \ dx,\tag{3}$$

where P_t is

$$P_t = \alpha \ \Delta\Theta \ E_m \ A_m,\tag{4}$$

where α is the thermal expansion coefficient of the composite, E_m is its modulus of elasticity and A_m is the beam cross sectional area.

2.2 Stored strain energy

The stored strain energy consists of two components:

a. strain energy of beam (W_3): The energy stored in the beam element due to its bending is given by

$$W_3 = E_m \ I_m \ / \ 2 \int_0^L (d^2w/dx^2)^2 \ dx,\tag{5}$$

where $E_m \ I_m$ is the flexural rigidity of the beam.

b. strain energy of NITINOL fibers (W_4): Considering the NITINOL fiber as a string with a tension T which is displaced laterally a distance w from the neutral axis of the beam. Then its stored strain energy W_4 is given by

$$W_4 = T \ / \ 2 \int_0^L (dw/dx)^2 \ dx.\tag{6}$$

Equating the sum of the work done by the external forces F, P_m and P_t to the sum of the strain energies stored in the beam and the NITINOL fibers gives

$$W_1 + W_{2m} + W_{2t} = W_3 + W_4.\tag{7}$$

Substituting equations (1), (2), (3), (5) and (6) into equation (7) yields

$$[\delta]^T[F] = E_m \, I_m \int_0^L (d^2w/dx^2)^2 \, dx - P_n \int_0^L (dw/dx)^2 \, dx, \qquad (8)$$

where P_n is the net axial force give by

$$P_n = (P_m + P_t - T). \qquad (9)$$

Defining a proper displacement function for the composite beam element, one can write the beam deflection **w** as

$$w = [A] \, [\delta], \qquad (10)$$

where the elements of matrix [A] are function of **x** (Fenner 1975).

Accordingly, dw/dx and d^2w/dx^2 can be obtained by differentiating equation (10) with respect to x to yield

$$dw/dx = [C] \, [\delta] \quad \text{and} \quad d^2w/dx^2 = [D] \, [\delta]. \qquad (11)$$

If the stiffness matrix $[K_e]$ of the element is defined by the following relationship

$$[F] = [K_e] \, [\delta], \qquad (12)$$

then, $[K_e]$ can be determined by combining equations (8), (11) and (12) as follows

$$[K_e] = E_m \, I_m \int_0^L [D]^T[D] \, dx - P_n \int_0^L [C]^T[C] \, dx. \qquad (13)$$

The element stiffness matrix $[K_e]$ of equation (13) consists of two components: the conventional transverse stiffness and the geometric stiffness that combines the effect of the axial mechanical loads, axial thermal loads and the tension of the NITINOL reinforcing fibers. Equation (13) also represents the basic equation for understanding the role that the NITINOL fibers can play in controlling the static characteristics of the composite beam. For example, if the beam is not reinforced by NITINOL fibers (i.e. **T** = 0) and the mechanical and thermal loads induce compressive stresses in the beam, then the geometric stiffness will increase and the total element stiffness will decrease. When the combined effect of the mechanical and thermal loads reaches a critical magnitude such that the geometric stiffness becomes equal to the flexural stiffness of the beam, the beam stiffness vanishes and the beam becomes elastically unstable. Subjecting the beam to any additiona! external disturbance will cause the beam to buckle.

It should be pointed out that the thermal loading, as it increases the geometric stiffness, also decreases the flexural stiffness of the beam because it reduces its effective modulus of elasticity E_m. Such a dual effect makes the beam buckle under smaller thermal loads than under pure mechanical loading.

However, the critical load of the un-reinforced beam can be increased by embedding pre-strained NITINOL fibers into the beam. If the tension **T**, resulting from the pre-strain alone, is high enough to counter-balance the mechanical and thermal effects then the beam stiffness can be maintained unchanged. For higher pre-strain levels, the beam stiffness can be enhanced. Further enhancement can be achieved when the shape memory effect of the NITINOL fibers is activated by heating the fibers above their phase transformation temperature. The additional tension, induced into the fibers by the phase recovery forces, makes the net axial load P_n negative and accordingly increases the overall stiffness of the beam element. However, it is essential that the total tension in the NITINOL fibers, i.e., the sum of the tension due to the pre-strain and the phase recovery force, must exceed the mechanical and thermal loads and compensate for the softening effect in the matrix resulting from heating the NITINOL fibers inside the composite matrix.

Therefore, effective control of the stiffness of NITINOL-reinforced composites can be achieved by proper selection of the initial pre-strain level of the NITINOL fibers. This selection is particularly crucial as the pre-strain level determines the generated levels of recovery forces.

3. THE EXPERIMENTAL SET-UP AND RESULTS

3.1. Experimental set-up

Figure (3) shows a schematic drawing of the experimental set-up used in actively controlling the buckling of a NITINOL-reinforced beam. The beam dimensions are 63.75 cm by 2.5 cm by 0.44 cm. The beam is reinforced by eight 0.55 mm NITINOL fibers which are embedded symmetrically along the neutral axis of the beam.
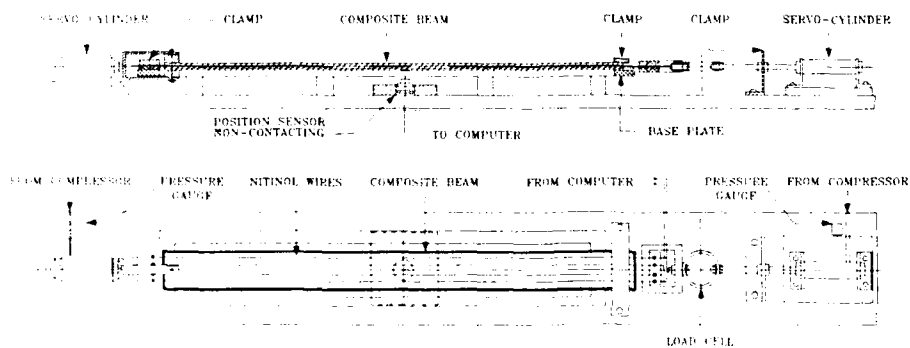
Figure (3) Schematic drawing of the active buckling control experiment.

The right end of the beam is clamped to a fixed base and the left end is connected to the piston of a loading cylinder. The cylinder is pressurized by compressed air from the storage tank of an air compressor. The increasing compressive load applied by the load cylinder to the beam will eventually cause the beam to buckle. The resulting deflection of the beam is monitored continuously by a non-contacting sensor which is placed at the mid-span of the beam. The sensor also serves as physical stop to prevent excessive deflection once buckling has occured. The output signals of the sensor is sent to a micro-computer via a set of analog-to-digital

converters.   The processing of the sensor's signal is shown in the
controller block diagram shown in Figure (4).   When the beam deflection
exceeds a pre-set value of a dead-band, the controller is turned on using a
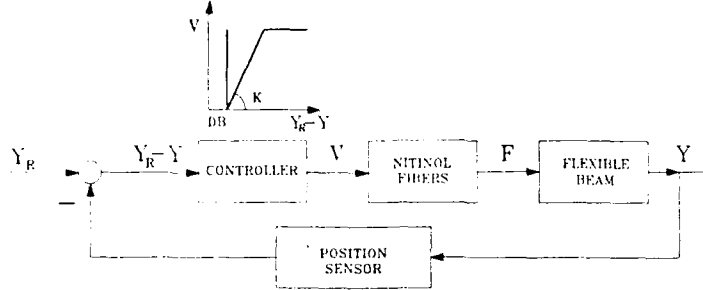
Figure (4) - Block diagram of the active buckling control system

proportional controller with a saturation limit.   The control action is
sent via a digital-to-analog converter to a power amplifier to activate the
NITINOL fibers embedded inside the compressively loaded composite beam.
The activation of the NITINOL fibers will compensate for the monitored
deflection and the phase recovery forces developed in the fibers will
attempt to bring the beam back to its undeflected position.

In the active buckling control system described, the NITINOL
reinforcing fibers are clamped at one end to the fixed base and at the
other end to pre-tensioning cylinder via a load cell.   The load cell
monitors the initial value of the pre-tension applied to the NITINOL fibers
by the pre-tensioning cylinder.   The load cell also continuously measures
the phase recovery forces developed in the NITINOL fibers as they undergo
their phase transformation.

3.2. Experimental Results

Figure (5) shows a comparison of the performance with and without the
active buckling control.   The results displayed are for a
NITINOL-reinforced beam with each of the eight fibers has an initial
tension of 33.7 N which corresponds to an initial pre-strain of 0.35%. For
the controlled cases, the controller dead band corresponds to deflection
error of 0.0176 mm and the controller gain is 2727 volt/mm. The saturation
limit is 6 volts/fiber and the maximum current is 1.6A.
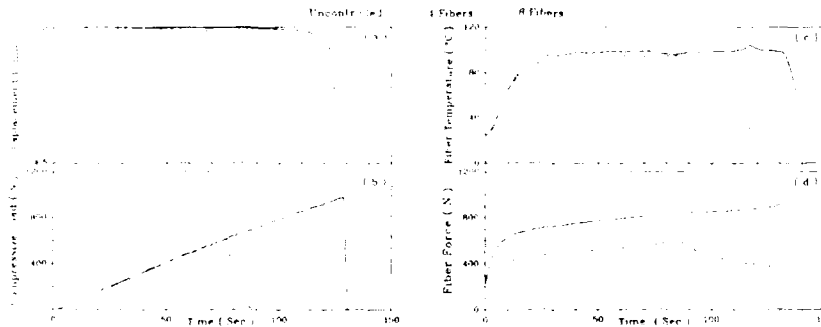
Figure (5) - Performance of buckling controller with 0, 4 and 8 NITINOL
fibers activated (dead band = 0.0176 mm, gain = 2727 volts/mm).
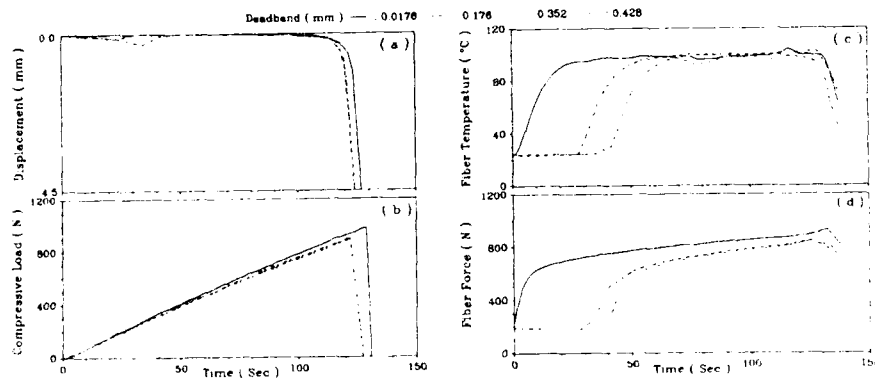
Figure (6) — Effect of dead band (gain = 2727 volts/mm, initial pre-tension/fiber = 33.7N and 8 fibers are activated).
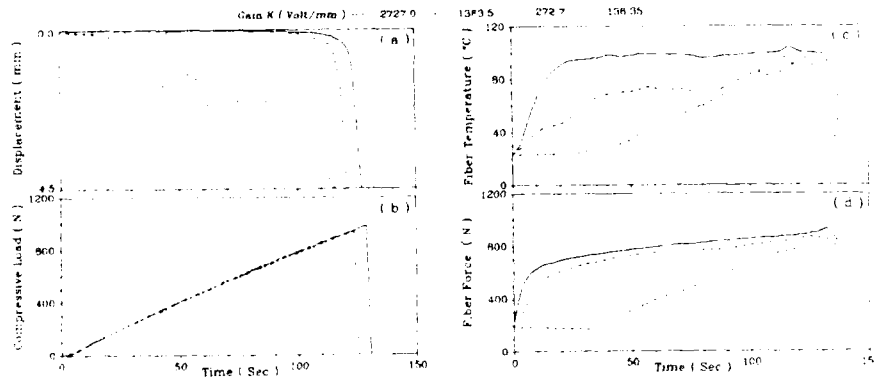
Figure (7) — Effect of controller gain (dead band = 0.0176 mm, initial pre-tension/fiber = 33.7N and 8 fibers are activated).
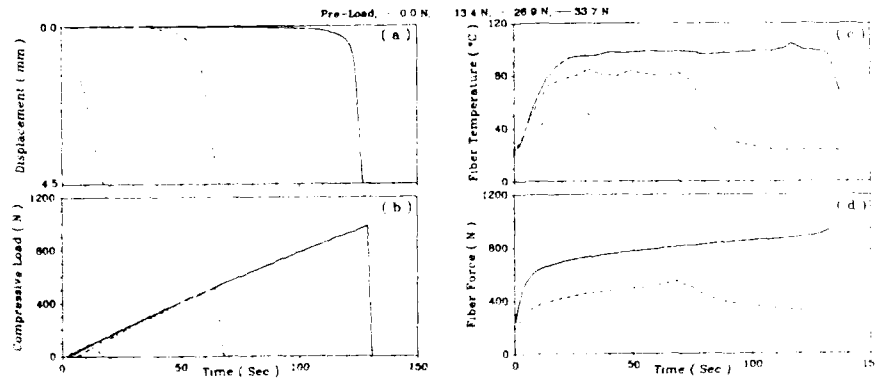
Figure (8) — Effect of initial pre-tension (dead band = 0.0176 mm, gain = 2727 volts/mm and 8 fibers are activated).

In Figure (5-a), the deflection of the beam resulting from the application of a gradually increasing compressive load is shown. The rate of load increase is 500 N/min as shown in Figure (5-b). It can be observed that the uncontrolled beam buckles when the increasing compressive axial load exceeds 330 N. However, when all eight NITINOL fibers are activated, the beam can withstand axial loads up to 950 N before it begins to buckle. Therefore, with the NITINOL reinforcement it is possible to almost triple the critical buckling load of the beam. With four activated fibers, the critical buckling load is about 700 N which corresponds to about double the critical load of the uncontrolled beam. Figure (5-c) shows the corresponding time history of the temperature of the NITINOL fibers due to the activation and de-activation of the controller. In Figure (5-d), the time history of the phase recovery forces developed in the NITINOL fibers is shown. The tension in the fibers remains equal to the initial pre-tension, i.e. $33.7N \times 8 = 269.6N$, for the uncontrolled case. However, the tension increases to approximately 1000 N when eight NITINOL fibers are activated.

It is also possible to energize different sets of the NITINOL fibers to counterbalance the external loading condition in order to prevent buckling of the composite beam. For small external loads it is only necessary to energize a few fibers, but if the load increases the controller can energize a larger number of fibers to maintain the beam in its undefelected form.

The effect of varying the controller parameters on the performance of the active control system is shown in Figures (6), (7) and (8). In Figure (6), the effect of varying the control dead-band on the system performance is shown. In this case, the control action is only generated when the beam deflection exceeds the dead band. This is accomplished by the heating of the NITINOL fibers and the development of the phase recovery forces as shown in Figures (6-c) and (6-d), respectively. For the range of dead bands considered, between 0.0176 mm and 0.528 mm, the effect on the critical buckling loads is insignificant.

The effect of decreasing the controller gain from 2727 volt/mm to 136.35 volt/mm on the system performance is shown in Figure (7). This effect decreases the slope of temperature rise of the NITINOL fibers and, in turn, the rate at which the corresponding phase transformation forces are recovered. Changing the controller gain is found to influence to some extent the critical buckling load. For example, when the controller gain is 2727 volt/mm the critical buckling load is 950 N and when the gain is reduced to 136.35 volt/mm the critical buckling load become about 850N. Therefore, reducing the controller gain by a factor of 1/20 only results in a 10.5% reduction in the critical buckling load.

The effect that the pre-tension has on the system performance is shown in Figure (8) for a dead band of 0.0176 mm and controller gain of 2727 volts/mm. It is clear from the results obtained that , the pre-tension plays the most crucial role in controlling the buckling of the beam. Increasing the tension from 0.0 N/fiber to 33.7 N/fiber increases the critical buckling load from about 100 N to 950 N, respectively.

4. COMPARISON BETWEEN THEORY AND EXPERIMENTS

The mechanism of actively controlling the buckling of the NITINOL-reinforced beam can best be understood by considering Figure

(9-a). The figure represents the theoretical prediction of the buckling characteristics of actively controlled NITINOL-reinforced beams. In the figure, the applied axial load is increased gradually at a linear rate of 500 N/min. For the uncontrolled beam, the critical buckling load is fixed at 320 N and remains unchanged with time. This load corresponds to a pre-tension of 33.5 N/fiber. When the applied load becomes equal to the critical buckling load, the beam is on the verge of elastic instability. The beam will buckle once the applied load exceeds the fixed critical buckling load. At time $t = 0$, the controlled beam has the same buckling load as the uncontrolled beam. But, when the controller senses any deflection greater than the dead band due to the application of the external load, the buckling characteristics of the beam is enhanced as represented by the dashed characteristics. The activation of the NITINOL fibers makes the beam less susceptible to buckling as the critical buckling load is increased to become 850 N instead of the original uncontrolled load of 320 N. Accordingly, the controlled beam will not buckle until the applied load exceeds the theoretically predicted limit of 850 N. The effect of varying the pre-tension levels on the theoretical prediction of the critical buckling load is shown in Figure (9-b) along with the corresponding experimental results. It is evident that there is a close agreement between theory and experiment.
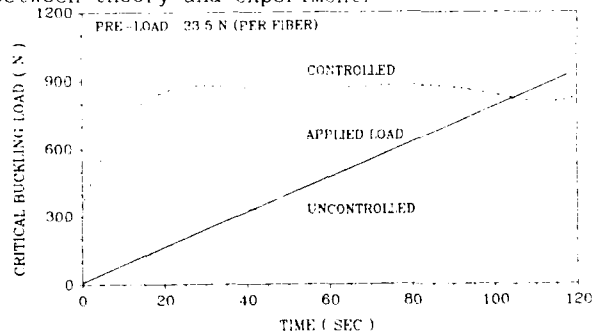
Figure (9-a) – Theoretical prediction of critical buckling load of controlled and uncontrolled beams.
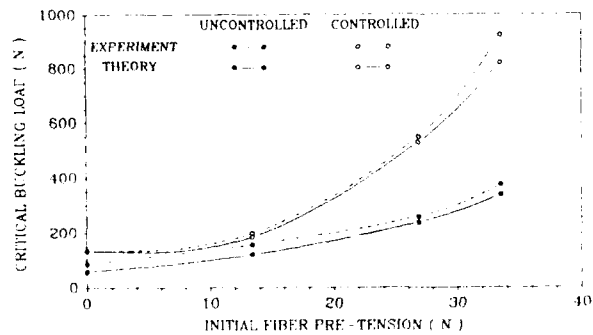
Figure (9-b) – Comparison between theoretical and experimental critical buckling loads as function of the initial fiber pre-tension.

5. CONCLUSIONS

The buckling characteristics of NITINOL-reinforced composite beams have been presented. The fundamental issues governing the behavior of this new class of **SMART** composites have been introduced. Applications of NITINOL reinforcing fibers in the control of buckling have been successfully demonstrated.

Emphasis has been placed in the presentation on the actuation capabilities of the NITINOL fibers. Extensive efforts are, however, in progress to use the NITINOL fibers to extract modal and physical displacements of structures with multi-modes of vibration (Baz, Poh and Gilheany 1991).

With such built-in sensing and controlling capabilities, NITINOL-reinforced composites can provide a means for continuously tuning their structural characteristics to adapt to changes in the operating conditions. These features will be particularly useful in many critical structures that are intended to operate autonomously for long durations in isolated environment such as defense vehicles, space structures and satellites.

REFERENCES

Baz, A., and Tampe, L., "Active Control of Buckling of Flexible Beams", Proc.of ASME Design Technical Conference, Montreal, Canada, Vol. DE-16, pp.211-218, Sept. 1989.

Baz, A., Iman, K. and McCoy, J., "Active Control of Flexible Beams using Shape Memory Actuators", *J. of Sound & Vibration*, Vol.140, No.3, pp.437-456, 1990.

Baz, A., Poh, S. and Gilheany, J., "A Multi-mode Distributed Sensor for Vibrating Beams", ASME Winter Annual Meeting, Atlanta, GA., Dec. 1991.

Duerig, T.W., Melton, K.N., Stockel, D. and Wayman, C., *Engineering Aspects of Shape Memory Alloys*, Butterworth and Heinemann Ltd., London, 1990.

Fenner, R.T., *Finite Element Methods for Engineers.*, Macmillan Press Ltd., London, 1975.

Ikegami, R., Wilson, D. and Laakso, J., "Advanced Composites with Embedded Sensors and Actuators (ACESA)", Edwards AFB Technical Report # AL-TR-90-022 (F04611-88-C-0053), 1990.

Perkins, J. *Shape Memory Effect in Alloys*, Plenum Press, New York, 1975.

Polymer Laboratories, Ltd., "PL-DMTA, MKII Dynamic Mechanical Thermal Analyser", Loughborough, United Kingdom, 1990.

Rogers, C., Liang, C. and Jia, J., "Structural Modification of Simply-Supported Laminated Plates using Embedded Shape Memory Alloy Fibers", *Computers & Structures*, Vol.38, No.5/6, pp.569-580, 1991.

ACKNOWLEDGEMENTS

Recent advances in nitinol technology

Frederick E. Wang

Innovative Technology International, Inc.
Beltsville, MD   20705

ABSTRACT

Despite the discovery of the shape-memory effect in
NITINOL (Nickel - Titanium - Naval Ordnance Laboratory)
in early 1960, its practical uses have been far smaller
than expected. The reasons for the slow progress are
discussed and recent advances made in Nitinol applica-
tions are given through specific examples.

More than 30 years has elapsed since the discovery of 'memory
effect' in TiNi (generic name - NITINOL).   During this time
interval, no less than 139 papers have appeared in various Journals
on the subject of Nitinol.   The break-down of the publications
according to the field of investigation is given in Table I.
Meanwhile, more than 4,000 patents have been filed on the use of
the shape-memory effect.   But, the fact remains that we have not
gained much understanding about Nitinol, and the actual application
of Nitinol, thus, remains elusive - only a handful of applications
are in practical use (out of 4,000 patented ideas).

The reason for the poor advancement of Nitinol application is
traceable to the inability of the Nitinol manufacturers to provide
material that meets the engineering specifications and requirements
of the potential user.

I shall now describe three specific cases of Nitinol application in
the medical field in which ITI was able to overcome the specific
requirements imposed on the products by the user.

SINOSAUR® MICRO-GUIDE CATHETER

The first one is known as Sinosaur® Micro-guide catheter (Fig. 1).
This device is to make a catheter steerable by placing thin strips
of Nitinol at the tip of the catheter.   The Nitinol strips are
activated (heated) by passing electric current.   Thus, the wider
the A_s - A_f interval, the greater the amount of current is required
to activate the catheter, and vice-versa.   Ideally, to obtain
F.D.A. (Federal Drug Administration) approval, the smaller the
current, the better.   This meant the Nitinol activation interval A_s
- A_f should be small.

ITI made the Nitinol strip with the A_s - A_f interval of only 6°C (Fig. 2-a) compared to the conventional interval of 15°C (Fig. 2-b). Should this temperature interval have remained at about 15°C - 20°C, the F.D.A. approval probably could not have been obtained and another wonderful patented idea would have gone for nought.

Another problem associated with this device was how to overcome the thermal hysteresis that is inherent in the martensitic transformation, i.e., the existence of M_s, M_f temperatures that are always 15°C - 30°C below the A_s, A_f temperatures. To illustrate the problem, let us assume a thermal hysteresis of 15°C. This means a Nitinol strip activated (in heating) between A_s (43°C - just above body temperature) and A_f (49°C) can only be restored to its original condition by cooling to 25°C (45°C - 15°C). But, the body temperature being 37°C, there is no means of providing 25°C temperature to restore the Nitinol strips for another round of activation.

ITI provided a solution to the problem by thermo-mechanically training Nitinol strips that have a 0°C - 1°C of thermo-hysteresis (see Fig. 2-a,b); thus, making it possible to restore the original condition by body temperature. In this manner, both problems were overcome.

'SIMON NITINOL FILTER'

The second application of Nitinol is know as the 'Simon Nitinol filter'. This is a vascular filter that is placed in the aorta of a patient to filter blood clots and prevent them from passing to the heart, lungs or brain, thus preventing heart-attack, stroke, etc. The advantage of this application is that a filter made of Nitinol can be collapsed into a small tubing below its TTR (transition temperature range) and can be delivered to the desired position via catheter. By setting the A_f to be at $\approx$ 30°C, the filter can be deployed (automatically) in the 37°C blood temperature. This procedure of deploying the filter via catheter, eliminates the conventional, invasive (and risky) surgery.

The problem in this case was, unlike the catheter guide, not in the 'thermo-hysteresis' or in the narrow temperature interval between A_s, A_f, but, rather, in the requirement of F.D.A. that the pre-loaded filter (in the tubing), prior to delivery to the hospitals, must be sterilized in-situ the tubing - not chemically, but thermally. This meant the Nitinol filter in-situ the tubing which has been 'programmed' to open (Fig. 3) at 37°C, must stay strained in the tube and be heated to 80°C - 90°C, far above its 'programmed' transition temperature. Yet, upon cooling to R.T., the filter is expected to open (without ill effect) once deployed into a 30°C - 35°C bath (Fig. 3).

ITI was able to 'thermo-mechanically' train the Nitinol filter to perform in this manner. This aspect of retaining memory after extreme sterilization temperature in a restricted configuration, virtually gained the F.D.A. approval.

ELASTORQ®

The third case has to do with catheter guide wire. Heretofore, 'guide wire' utilizes the 'superelastic' property of Nitinol. The advantage being the flexibility of Nitinol wire that allows doctors to maneuver guide wire through tortuous passages in the vascular system, biliary system, etc., without the worry of permanent bending. Nevertheless, this easy elastic bending of superelastic Nitinol wire, while extremely helpful, it also made it difficult for the doctor to transmit 'torque' motion faithfully from proximal to distal end which results in an ill-effect known as 'whipping'. In general, torsion transmission and bending motion are related to shear-modulus and Young's modulus. In turn, 'Young's' and 'shear' moduli are related through a constant known as 'Poisson's ratio'. In a given material, the Poisson's ratio is a fixed constant and cannot be changed. Thus, if a material has a low Young's modulus (thus, easy to bend), it also has a low shear modulus (that shows up as 'whipping').

The question is, can shear modulus be enhanced without enhancing Young's modulus at the same time in Nitinol? If this was possible, we would have the desired Nitinol guide wire which is easily bendable, and yet, eliminate the problem of 'whipping'. This was accomplished at ITI and is being produced and marketed under the trade name ELASTORQ®.

These three cases of Nitinol application illustrate clearly the distinct problems associated with each application. In other words, a data-base of material property which may be available and useful in other materials is not possible in Nitinol. This is to say, Nitinol is not an 'off shelf' material and that for each application, the material must be engineered. Only in a 'low-tech' application of Nitinol is the specific engineering not necessary.

TABLE I

NITINOL

"NEVER BEFORE, A SUBJECT MATTER INVESTIGATED BY SO MANY FOR SO LONG
AND YET YIELD SO LITTLE UNDERSTANDING"

Between 1960 and 1990

Physical Characterization	Number of Investigation
Structure (Lattice)	46
Mechanical Property	39
Transport Property	23
Applications	18
Phase Diagram	10
Review Article	3
Total	139.

Featured in more than 50 magazine articles, while six major
international conferences have been held, and more than 4,000
patents filed between the US and Japan.

FIG._1

The CRI Cynosar Steerable Catheter:

- directs laser probes into peripheral vessels
- directs angioscopes and guides micro-instruments
- guides lasers for other surgical procedures
- utilizes a steerable tip
- deflects up to 90 degrees and straightens back to center
- holds any degree position
- utilizes a remote table-side control unit
- has a one-to-one torque ratio
- has an open center lumen, adaptable for micro-instrumentation or drug delivery
- has traditional catheter handling characteristics

FIG. 2

(A)   Modified S Element 5

(B)   MOD S ELEMENT 1 RETEST 10/23/91

TIP FORCE GRAMS

TEMPERATURE C

HEATING CYCLE   COOLING CYCLE

FIG. 3

Development of a low atomic number, sensitive strain gage

R. L. Donovan

A. W. Raskob, Jr.

APTEK, Inc.

1257 Lake Plaza Drive

Colorado Springs, CO 80906

Abstract: Conventional strain gages are of limited use in certain radiation environments. A study was conducted to evaluate the feasibility of using polyvinylidene fluoride as a very sensitive and radiation resistant strain gage. Gages were formed from thin films of the polyvinylidene fluoride, and compared in operation with standard resistive gages. Heating due to radiation deposition was predicted using a computer model. Laboratory and analytical results indicate that polyvinylidene fluoride performs well as a very sensitive dynamic strain gage with reduced thermal response to radiation as compared to standard resistive gages.

Introduction. Radiation environments containing high levels of x-radiation present harsh physical and electrical conditions to transducers and instrumentation alike [1]. There are two chief problems which combine to limit the usefulness of standard resistive strain gages: 1) radiation deposition in the gage and its leads induces heating, and 2) severe electrical noise in the instrumentation creates a high level background signal.

Conventional strain gages cannot be used in regions where significant x-ray shine through exists. Typical strain gages are made of high atomic number (high-Z) metals such as copper, constantan, nichrome, etc. When these gages are used to measure strain on irradiated low-Z materials (such as carbon-carbons, carbon-pitch-dies, aluminum, etc.) they are susceptible to radiation-induced heating. This heating will compromise the gage's ability to yield an accurate, calibrated strain signal. Precautions may be taken, such as shielding the gage, but these measures may compromise the effectiveness of the gage or the conditions of the experiment [1,2].

Radiation induced ionization can give rise to significant electrical noise currents in the signal carrying cases. Very small strains ($\sim$ 10's of μstrain) produce only μvolts from a standard resistive gage bridge. This small signal requires a large degree of amplification and often the use of special buffers, circuitry and cabling in an attempt to attain an acceptable signal to noise ratio.

A study was conducted to evaluate the feasibility of using polyvinylidene fluoride (PVDF or PVF$_2$), a piezoelectric polymer, as a highly sensitive and low atomic number (Z) dynamic strain sensing element. Such a gage is attractive for two reasons: 1) it possesses a high level electrical response to strain, and 2) it is relatively transparent to x-rays. These gages were tested for correlation to resistive strain gages. Modelling of the gage and electrical circuit was performed to design parametric experimental studies to determine effects of various gage parameters on performance.

Description of Work and Results. A lumped parameter electrical response model was derived for the gage and associated circuitry. Solutions for dynamic amplitude and phase behaviour were obtained for a number of combinations of gage area, aspect ratio, and PVDF thickness. This was used to design a parametric study test matrix. A number of runs were made using PSPICE [3] (a circuit analysis code) to validate the simpler lumped parameter model. Heating effects due to x-ray radiation were computed using an energy deposition code (GRAD [5]).

Standard resistive gages were compared to PVDF gages for a variety of dynamic strain inputs. The gages were attached to prismatic, cantilevered beams of various
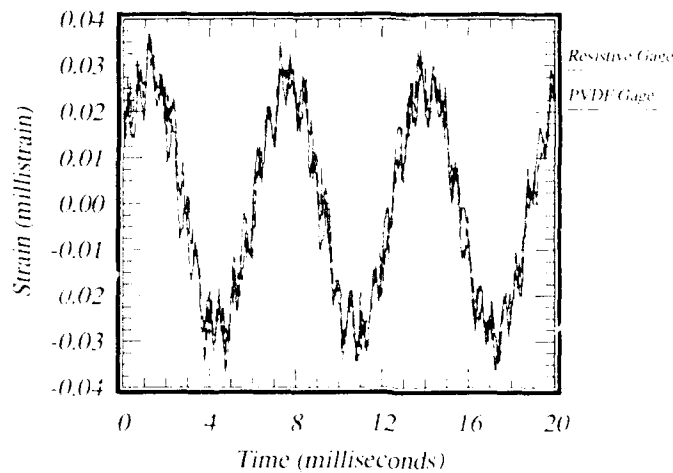
Figure 1: Comparision of PVDF and resistive strain gage outputs.

dimensions. Their positions on each beam were chosen so they would experience similar strains (for at least the lowest beam mode). A fixture was used to provide repeatable and analytically verifiable excitations to a wide variety of beams. In this way, many different strain frequencies and magnitudes, representative of typical experimental data as collected with resistive gages, could be modelled.

Calculations using GRAD showed that the heating expected in a typical gage installation as a result of energy deposition will not raise the gage temperatures enough to significantly degrade performance. Analytical modelling of the PVDF gage and recording instrumentation circuit gave good correlation with actual gage performance. PSPICE circuit analysis results were consistent with the lumped parameter model (thus validating it).

A range of different strain frequencies and magnitudes were input to the beams using the test fixture. Recorded strain data showed excellent frequency and amplitude correlation between the standard resistive and PVDF gages as shown in Figure 1. The greater sensitivity of the PVDF gage enabled it to reliably measure lower amplitude strain signals which were obscured in the resistive gage records by signal noise. This is shown in Figures 2 and 3. The resistive gage in Figure 2 exhibits an noise level
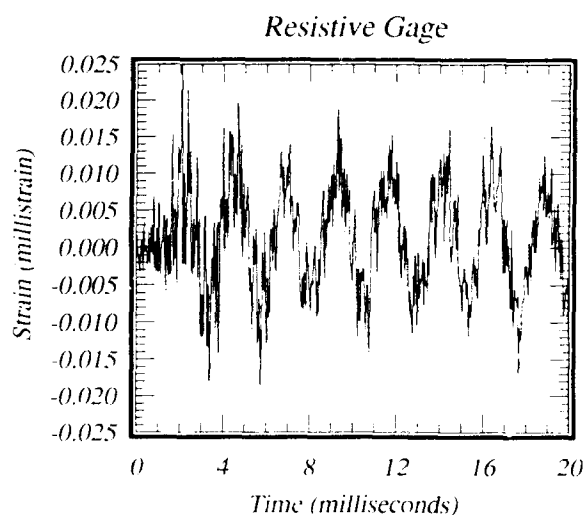
Resistive Gage

Figure 2: Resistive strain gage output.

which is roughly the equivalent of a 5 μstrain peak-to-peak signal, whereas the PVDF gage noise level in Figure 3 is substantially lower.   The PVDF and resistive gages agreed over all strain magnitude ranges tested which included peak-to-peak strains between 10 μstrain to 1.5 millistrain.

The analytical model provided a basis for extrapolating laboratory performance to actual test/instrumentation environments. Table 1 presents a comparison of predicted output levels for a resistive strain gage and a PVDF gage with and without cable loading.

Conclusions. The feasibility of using PVDF as a low-Z, sensitive strain gage was demonstrated. The lower-Z composition leads to reduced thermal response to x rays, and allows for forward placement in radiation environments. The gage works well with standard strain gage instrumentation.

PVDF is excellent for measuring dynamic response and extremely low strains. Its output is at least two orders of magnitude greater than that of resistive gages, resulting in a much higher signal-to-noise ratio.   PVDF response is linear over a wide range of strain amplitudes and over a wide dynamic range of frequencies. Its
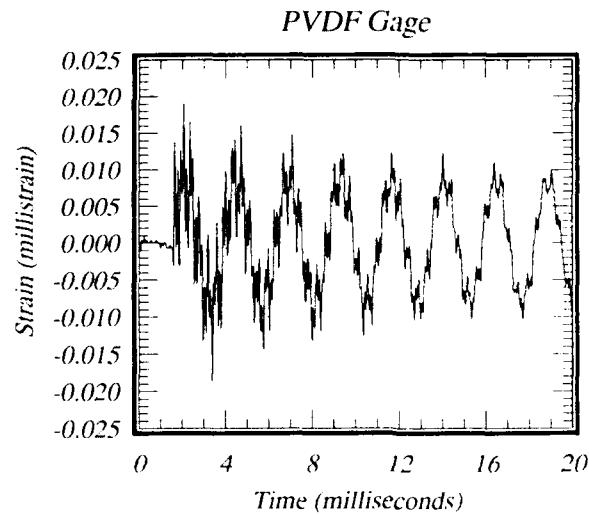
PVDF Gage

Figure 3: PVDF strain gage output.

Table 1: Comparison of Predicted Resistive and PVDF Gage Outputs

Input Strain	Resistive Gage Bridge	Low-Z Gage (mV)	
(μstrain)	Output[1] (mV)	No-Load Gage[2]	100' Cable[3]
2000	3.84	11.9×10^3	2.59×10^3
1000	1.92	22.5×10^3	1.29×10^3
500	0.96	11.2×10^3	$.646 \times 10^3$
100	.192	2.25×10^3	$.129 \times 10^3$
50	.096	1.12×10^3	$.065 \times 10^3$
10	.019	$.221 \times 10^3$	$.013 \times 10^3$

All outputs are prior to amplification

[1] Resistive gage bridge excitation voltage 4.0V, gage factor 2.05

[2] PVDF film without any external capacitance

[3] RF-21 cable (@ 10pF/foot), 0.175×0.25 inch gage area

sensitivity makes it ideal for use in the study of precision structures, such as space structures.

Acknowledgements. This work was sponsored by the Defense Nuclear Agency (DNA) under a Phase I Small Business Innovative Research (SBIR) project.

References

[1] DeMuth, N., Meiers, D., "Impulsive Response Investigation of S-200-E Beryllium Rings," Kaman Sciences Corp., AFWL-TR-72-223, May 1973

[2] Oscarson, J., Seitz, D., "Impulsive Load Response of Soft-bonded Rings and Arcs," Kaman Sciences Corp., DNA3862F, 12 Dec. 1975

[3] PSPICE, MicroSim Corp., Jul. 1989

[4] "Experimental-Theoretical Correlations of Impulsively Loaded Rings," Kaman Nuclear Report KN-71-89(R), 25 Feb. 1971

[5] Williams, G.C., **Program GRAD User's Guide**, APTEK, Inc., 1989

Smart materials for sensing and/or remedial action to reduce damage to materials

Carolyn Dry, Associate Professor

Architecture Materials Research Lab, Architecture Research Center, School of Architecture, University of Illinois, Urbana-Champaign, Illinois, U.S.A.

ABSTRACT

Cracking, due to loading, is a major problem in materials durability because the cracks increase permeability. The sensing of cracking or corrosion of a settable material by a chemical or physical sensor which, in the process of sensing, starts the activation of a remedial process is the topic of this research. Specifically, materials containing various types of hollow porous fibers filled with a chemical which release into the matrix at appropriate times, or over time, are designed to address some issues of material brittleness and durability; i.e. cracking and corrosion.

1. SMART MATERIALS FOR SENSING AND REMEDIAL ACTION

In these smart materials sensing and repair actuation occur by the activation of a timed release of a repair chemical into the matrix due to a stimulus which is itself the environmental agent of attack. These are passive smart materials requiring no outside feedback loop nor continuous monitoring. Rather, they are activated by each environmental loading or impetus. The sensors and actuators are disturbed throughout the structure, thus providing remedial action where and when needed.

2. CRACKING

Loading over time has a cumulative effect which can lead finally to complete deterioration of the component or structure. The design to alleviate this problem consists of hollow porous fibers containing crosslinking crack-closing chemicals, adhesives, polymers, or crystallizing rehydrater which close the cracks. The chemicals are released from fibers when they deform due to loading. This is the ideal situation in which the agent of environmental degradation, namely loading, is the stimulus to release the repair chemical by fiber deformation, breakage, unlinking, or coating debonding. (See Figure 1.)

Internal Release

Repair of Condition

Condition Leading to Deterioration
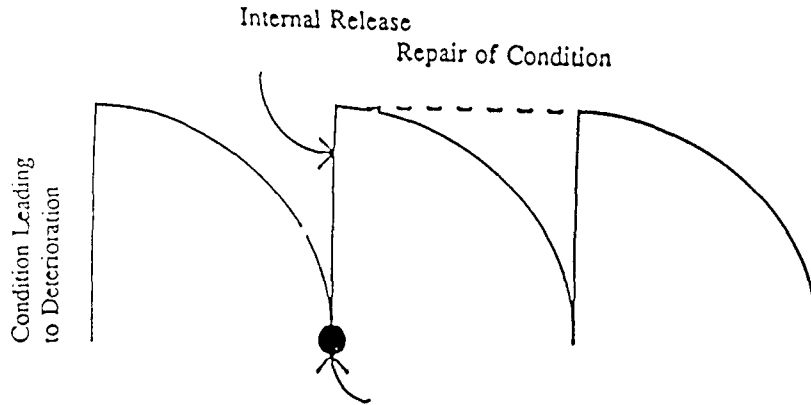
Trigger Release of Repair Chemical Occurs Due to Loading Which Causes Cracking and/or Fiber Deformation Alkalinity Charge Which Activates Corrosion

Figure 1.   Sensing and Repair of Material by Timed Release of Chemicals from Fibers

A specific application of the cracking repairing idea is a material in which the release of crack filler from stretched, cracked, or debonded fibers heals matrix cracks and rebonds debonded fibers to the matrix. Several designs for this are:

1.) Tensile loading stretches the fiber, causing contraction (Figure 2) due to Poisson's effect, thus releasing the chemicals from the porous fiber wall.

2.) Tensile loading causes debonding of a hollow porous fiber from matrix and stripping away of coating, thus releasing its chemical through the pores of the fiber. (Figure 3)

PULLING CHANGES FIBER'S POISSON'S RATIO, FORCING CHEMICAL THROUGH MEMBRANE'S PORES

Figure 2.

COATING YIELDS FROM MATRIX LEAVING COATING BEHIND; CHEMICAL IS RELEASED FROM UNCOATED FIBER PORES
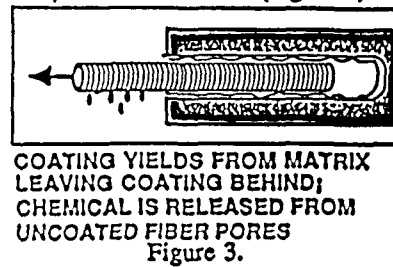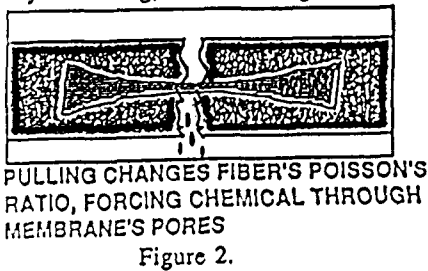
Figure 3.

3.) Tensile loading breaks the hollow fiber, thus releasing its chemical. (See Figure 4.)

FIBER BREAKS DUE TO LOADING; CHEMICAL IS RELEASED AT BREAK
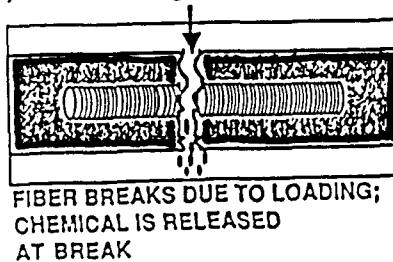
Figure 4.

4.) Compressive loading causes the unlinking of a twisted fiber bundle, from which the chemical is released into the crack. (See Figure 5.)
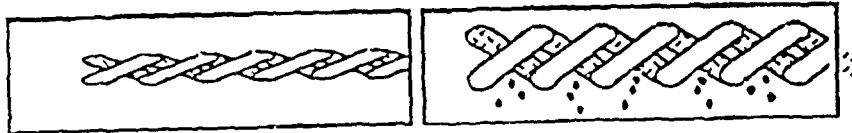
Figure 5.

5.) Heat of 120° F. melts the fibers' wax coating, releasing a monomer, drying out the matrix. Then a higher temperature polymerizes the monomer in the matrix (Figure 6).

HEAT MELTS FIBER'S WAX COATING; ALSO CEMENT MATRIX IS DRIED

MONOMER IS RELEASED THROUGH POROUS WALLS: GOES INTO THE DRIED MATRIX

MORE HEAT POLYMERIZES THE MONOMER IN THE MATRIX
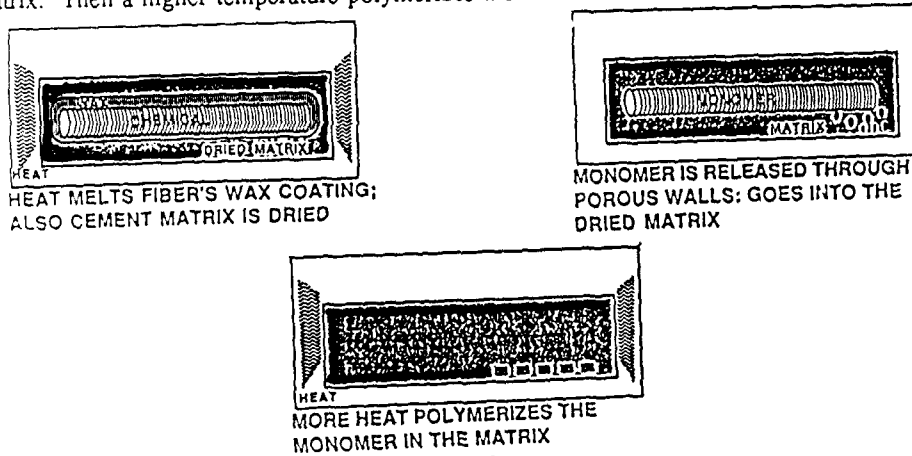
Figure 6.

CORROSION

Corrosion is an electrochemical process that requires an electrical current in a moist and oxygenated condition. The entry of chloride ions or carbonation can cause the pH to be reduced to 11.5 pH, at which point corrosion begins. The addition of calcium nitrite, an anticorrosion chemical, protects the steel. In this design calcium nitrite is put into hollow porous fibers coated with polyol. Polyol dissolves in an alkalinity of appropriate pH (11.5), thus, releasing the anticorrosion chemical (see Figures 7 and 8). The cause of deterioration, reduction of alkalinity due to chloride or carbonation which causes the corrosion is the sensor (coating dissolution) also which actuates the remedial action (release of calcium nitrite).

ANTICORROSION CHEMICAL IS RELEASED THROUGH FIBER PORES NEAR THE REBAR AT THE TIME WHEN THE Ph IS APPROPRIATE FOR START OF CORROSION

FIBER COATING DISSOLVES AS Ph CHANGES OVER TIME
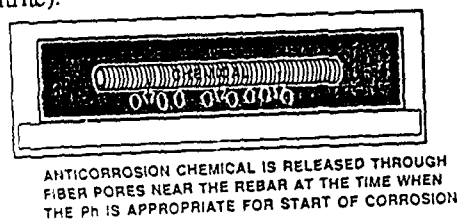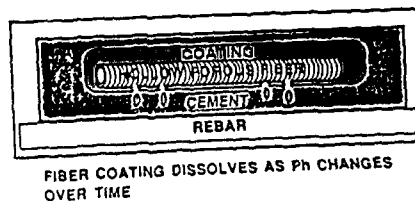
Figure 7.

Figure 8.

Preliminary results show that the design to prevent corrosion damage will work (see Figure 9).
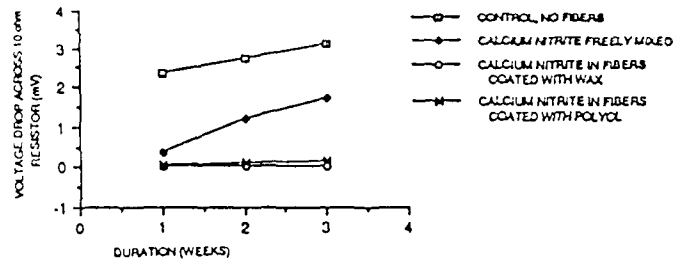
COMPARISON OF VOLTAGE DROP (mV) ACROSS A 10 ohm RESISTOR
OF VARIOUS SAMPLES UNDERGOING CORROSION TESTING
Figure 9.

The successful release of chemicals from fibers was documented using a scanning electron microscope.   Photo 1.

SUMMARY

Known smart materials such as piezoelectric materials, martensitic transformation materials, etc. sense a change in a particular physical parameter and actuate in response. They are well characterized materials which, because of their unique properties, have many applications. The smart materials using time release are different from those; a design is made for each application from individual components. These tailor-made smart materials consist of several parts, including: 1.) an agent of internal deterioration, for instance dynamic loading which causes cracking, 2.) a stimulus to release the repairing chemical, 3.) a fiber, 4.) a coating or fiber wall which can be removed or changed in response to the stimulus, 5.) a chemical carried inside the fiber, also 6.) sometimes a way of hardening or linking the chemical in the matrix. Fibers and mechanisms to release the chemicals such as fiber breakage, coating dissolution are the sensors, while the stimulus such as crack energy, change in pH, and actual release of the chemical work together as actuators. These smart materials containing sensors and actuators acting together are thus designed to be passive, automatically activated, and are distributed throughout the material to provide remedial action anywhere it is needed.

Measurement of strain and stress in a piezoelectric actuator for collocated control

Jeffrey J. Dosch* , Daniel J. Inman[+], and Ephrahim Garcia[+*]

* Graduate Research Assistant, Mechanical Systems Laboratory, Department of Mechanical and Aerospace
Engineering, State University of New York at Buffalo.
[+] Professor and Chair, Mechanical Systems Laboratory, Department of Mechanical and Aerospace Engineering,
State University of New York at Buffalo.
[+*] Assistant Professor, Department of Mechanical Engineering, Vanderbilt University.

ABSTRACT: A technique has been developed which allows a single piece of piezoelectric
material to concurrently sense and actuate in a closed loop system. The motivation behind
the technique is that such a self-sensing actuator will be truly collocated and has applications
in active and intelligent structures, such as vibration suppression. The usefulness of the
proposed device was experimentally verified by actively damping the vibration in a
cantilever beam. A single piezoceramic element bonded to the base of the beam functioned
both as a distributed moment actuator and strain sensor. Using a positive position feedback
law the first two modes of vibration were suppressed; the first mode five percent settling
time was reduced from 35 to 0.3 seconds and the second mode settling time was reduced
from 7 seconds to 0.9 seconds.

INTRODUCTION

This paper describes a technique in which a piezoelectric actuator and sensor are combined
into a single piezoelectric element called a self-sensing actuator. One benefit of a self-sensing
actuator is that the sensor and actuator are truly collocated. Collocated control has been shown
to have a number of advantages relating to the closed loop stability of the structure. For
instance, Goh and Caughey (1985) have shown that in the absence of actuator and sensor
dynamics, structures controlled with collocated velocity feedback are unconditionally stable at
all frequencies.

The self-sensing actuator has a number of desirable properties, related to collocated control,
not easily achieved with a separate piezoelectric sensor and actuator. As mentioned, one
property is that the self-sensing actuator is truly collocated. The best that can be achieved with
a separate sensor and actuator is to have the two elements in close proximity. Another
desirable property is the elimination of possible closed loop control problems arising from the
capacitive coupling between the sensor and the actuator elements. This is not an issue with the
self-sensing actuator because only a single element is used.

DESCRIPTION AND VERIFICATION OF THE SELF-SENSING ACTUATOR

Figure 1 shows a model of the piezoelectric material used here to illustrate the operation of the self-sensing actuator. A voltage is produced in a piezoelectric material which is proportional the applied strain. In Figure 1 this voltage is indicated by v_p. In an actuator there will also be a voltage applied from the controller and this is indicated by v_c in the figure. The capacitor C accounts for the dielectric properties of the material. The capacitance is measured either at constant stress C^T or at constant strain C^S. In a traditional piezoelectric sensor there is no applied voltage v_c and thus v_p can be directly measured to determine the strain. In an actuator there is an applied voltage v_c across the actuator which makes it impossible to directly measure voltage modelled by v_p.

The bridge circuit shown in Figure 2 is used indirectly measure v_p, and thus indirectly measure the strain in in a piezoelectric actuator. The bridge circuit accomplishes this task by eliminating the signal due to the controller v_c. The capacitor C_3 is chosen to be equivalent to the constant strain capacitance of the piezoelectric material. The two capacitors indicated by C_2 form AC voltage dividers with the two capacitors C_p^S and C_3. The output from the voltage dividers are at outputs at v_1 and v_2. The sensor signal v_s is determined by subtracting v_2 from v_1. The sensor signal v_s will be proportional to piezoelectric strain voltage v_p and it can be shown that:

$$v_s = v_1 - v_2 \quad = \frac{C_p^S}{C_p^S + C_2} \, v_p. \tag{1}$$

Thus the voltage due to the controller v_c has been eliminated.

The use of the self-sensing actuator bridge circuit was experimentally verified by actively damping the first two modes of vibration in an aluminum cantilever beam of dimensions $38.7x$ $2.3x\,0.08$ centimeters. Bonded to the base of the beam was a single piezoelectric element which acted both as the sensor and actuator. The bridge circuit shown in Figure 2 was used to determine the strain in the actuator. The strain signal from the bridge circuit was fed back to the piezoelectric element through a Positive Position Feedback (PPF) controller (Fanson 1987), which was designed to suppress vibration in the beam's first two modes. The beam was excited in one of its modes by a second piezoelectric element and then allowed to free decay. The free decay time responses for the first two modes of vibration of the experimental beam, both with and without the self-sensing control are compared in Figure 3.

The bridge circuit used here determined the strain in a piezoelectric actuator. Using similar methods the stress could also be determined. This could be accomplished by making the

capacitance C_3 in Figure 2 equal to the constant stress capacitance of the piezoelectric material instead of the constant strain capacitance.

REFERENCES

Fanson, J. L. and T.K. Caughey. 1987. "Positive Position Feedback Control For Large Space Structures," *Proceedings 28th AIAA/ASME/ASC/AHS Structures Structural Dynamics and Materials Conference, Monterey, California.* AIAA Paper No. 87-0902, pp. 588-598.

Goh, C. J. and T. K. Caughey. 1985. "On the Stability Problem Caused By Finite Actuator Dynamics In the Control of Large Space Structures," *International Journal of Control.* 1985, vol. 41, No. 3, pp 787-802.

FIGURES
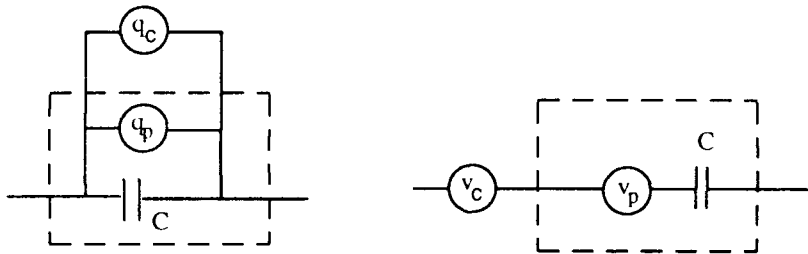
Figure 1. *Two equivalent electrical models for the piezoelectric actuator. v_c and q_c are respectively applied voltage and charge generators; v_p and q_p are respectively the equivalent voltage and charge generators due to polarization of the material, attributed to the piezoelectric effect. For a strain sensor v_p is proportional to strain and the capacitance is the value at constant strain $C = C^S$. For a stress sensor v_p is proportional to stress and the capacitance is measured at constant stress $C = C^T$.*

$$v_s = v_1 - v_2$$
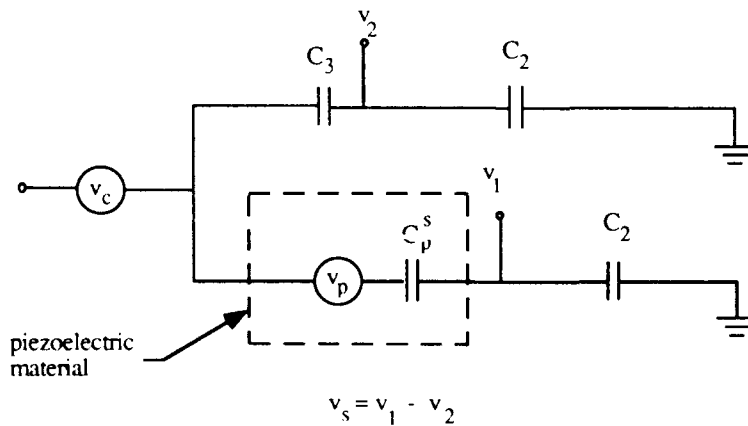
Figure 2. *Self-sensing actuator circuit for position sensing (strain sensing). C_p^S is the capacitance of the piezoelectric material measured at constant strain and C_3 is chosen such that $C_3 = C_p^S$. The sensor signal is v_s.*
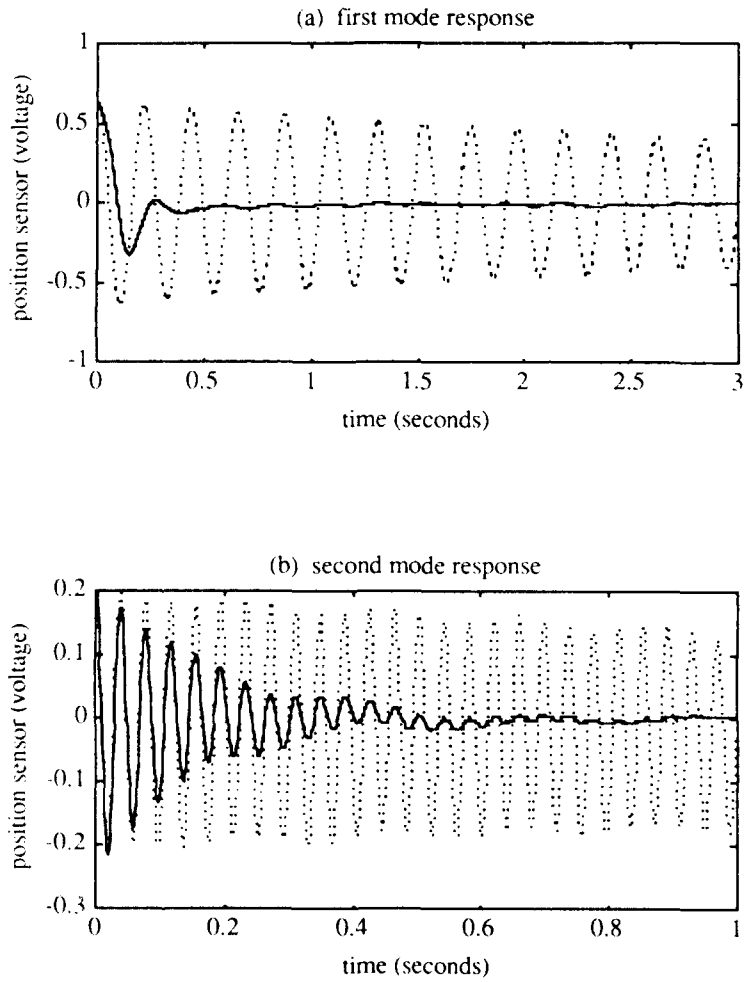
Figure 3. Comparison of the free decay time response of an active cantilever beam. A single piezoelectric element bonded to the base of the beam was used for both sensing and actuation in a position feedback loop (PPF). The closed loop response is the solid line and the open loop response is the dotted line for the first mode (a) and the second mode (b).

199

A novel sensor for adaptive and smart structures

Nisar Shaikh
Department of Engineering Mechanics and
Center for Materials Research and Analysis
University of Nebraska-Lincoln
Lincoln, NE 68588-0347
U.S.A.

ABSTRACT

One of the most important characteristics of an adaptive or "smart" structure is its ability to sense its own state as well as environmental stimuli. The sensing function is performed by sensors which are integral parts of structural members. The optical fiber is a typical example of a state-of-the-art sensor. A novel sensor is developed by sputtering a piezoelectric film on a metal fiber. This sensor, similar in configuration to an optical fiber, is active and shows great potential for application of sensing dynamic strain in structures.

INTRODUCTION

Adaptive and smart structures have the capability of actuation, such as the ability to maintain a prescribed or programmed state (Wada, Fanson, Chen, and Kuo 1990). Integral to the above operation is a continuous sensing ability. Optical fiber and piezoelectric transducers and skins have been incorporated into the structure for vibration and shape control (Swigert and Forward 1981), (Claus, McKeeman, May, and Bennet 1989). The need for a durable, efficient, and multi-functional sensor has motivated continuing research into new sensors (Shaikh and Dillon 1990). A novel sensor is developed by coating piezoelectric material on a metallic fiber. Similar in application to optical fiber, the new sensor is active and does not require an external signal, and subsequent conversion to an electrical output. The sensor is most suited for fibrous composites, where it can be easily incorporated into filament and strands. Several of these sensors can be conveniently dispersed or distributed along the entire structure.

PIEZOELECTRIC FILM SENSOR

Piezoelectric layers have been used as sensors, and are often referred to as "smart-skins." The feasibility of a strain-sensing property by a piezoelectric film was demonstrated by conducting vibration measurements on beams made of stainless steel strips deposited with Zinc Oxide (Shaikh and Dillon 1990). In the past, piezoelectric films have been used for ultrasonic transducers in the frequency range of Mega Hz to Giga Hz. In contrast, the Zinc Oxide coated strips were successfully tested at frequencies of the order of 100 Hz, to simulate the vibrations of a structure. Thus the piezo-films are effective at frequencies much lower than their resonance.

PIEZO-FIBER SENSOR

A fiber sensor is developed by coating piezoelectric Zinc Oxide on an Ni-Cr wire of 14.5 microns in diameter. In an elegant arrangement, the metal fiber functions as one electrode, while the structural member in which the sensor is embedded acts as another electrode.

STRUCTURAL CONFIGURATION

To test piezo-fiber sensors, cantilever beams were constructed with two brass strips. The piezo-fiber sensor was sandwiched between the strips and held with epoxy. Graphite-epoxy composite beam samples were also made with sensor wires placed between the carbon layers. The cross sections of these beams are shown in Figures 1a and 1b.

PERFORMANCE TESTS

Each beam was tested for its inherent ability to sense vibration. The two electrodes described earlier were directly attached to a digital scope. Adequate signal was generated without the need of an amplifier. The tests consisted of forced vibration through a shaker table as well as natural vibration by impulse.

The plot of natural vibration of the cantilever beam made of brass strips is shown in Figure 2a. A damped natural vibration containing both low and high frequency modes is seen.
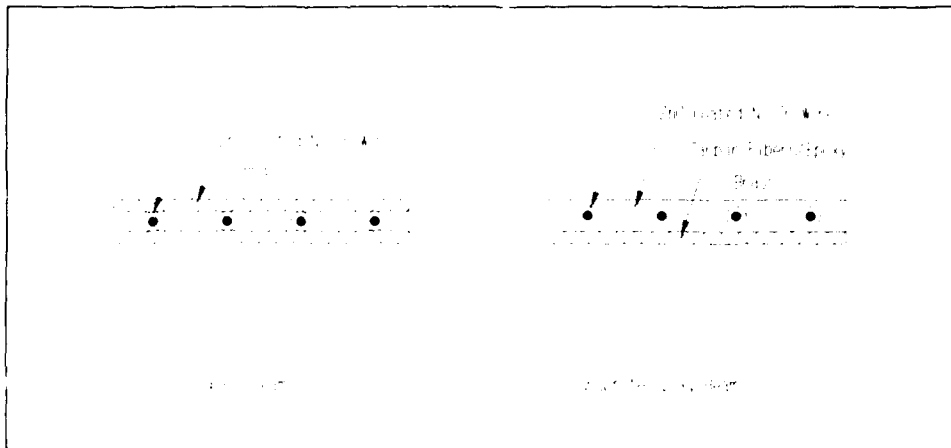
Figure 1a   Figure 1b

Cross-sections of beams with embedded piezo-fiber sensors

The forced vibration tests consisted of exciting the base of each beam on a shaker, which goes up to 5 kHz in frequency. The forced vibration response of the carbon-epoxy sample is shown in Figure 2b. The top signal is from the embedded sensor, while the bottom signal is from an accelerometer mounted on the cantilever base.
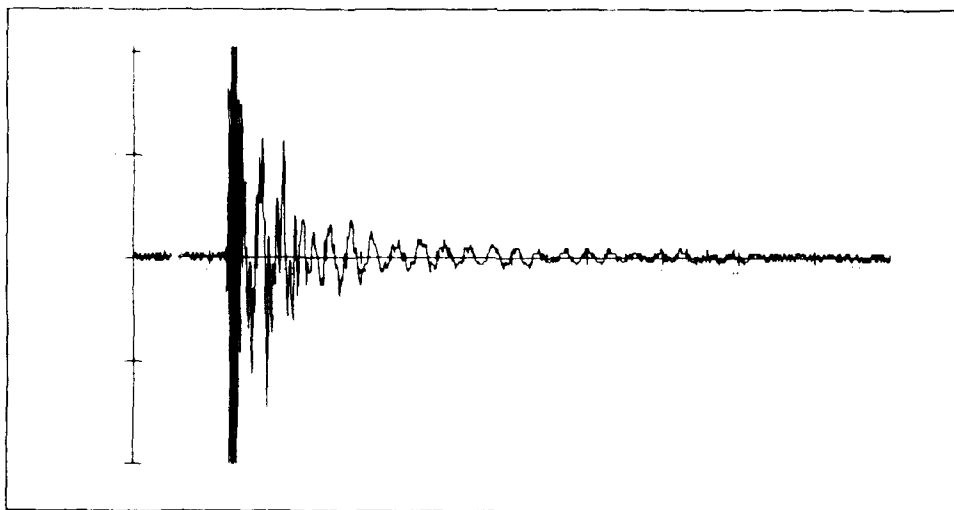
Figure 2a
Natural Impulse Response
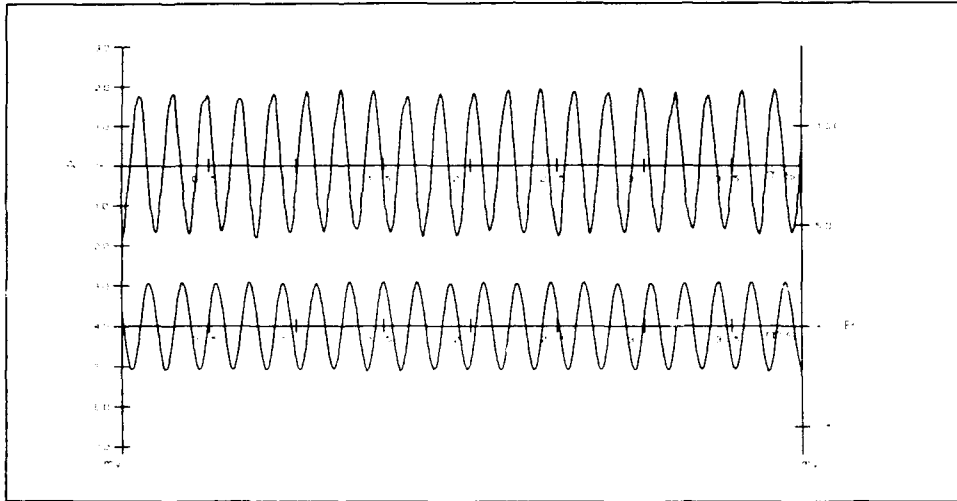
Figure 2b
Forced Vibration Response

ACKNOWLEDGEMENTS

REFERENCES

Claus, R.O., McKeeman, J.C., May, R. G., Bennet, K.D., "Optical Fiber Sensors and Signal Processing for Smart Material and structures," Smart Materials, Structures and Mathematical Issues, Technomic Publishing Co., 1989, pp 29-38.

Shaikh, Nisar and Dillon, Rod, "Smart Structural Composites," Proceedings of U.S./Japan Work Shop on Smart/Intelligent Materials and Systems, 1990, pp 287-293.

Swigert, C.J. and Forward, R.L., "Electronic Damping of Orthogonal Bending Modes in a Cylindrical Mast-Theory," AIAA Journal of Spacecraft and Rockets, Vol. 18, No.1, 1981, pp 5-11.

Wada, B.K., Fanson, J.L., Chen, G., Kuo, C., "Adaptive Structures: Space Systems," Proceedings of the International Workshop on Intelligent Structures, Taiwan, 1990.

203

Time-scale effects in shape-memory alloys

Eugene M. Cliff

Aerospace and Ocean Engineering Department
and
Interdisciplinary Center for Applied Mathematics
Virginia Polytechnic Institute and State University
Blacksburg. VA 24061-0531

ABSTRACT

We study a mathematical model of a thermo–mechancial process includ-
ing phase–transition. Two time scales appear in the model; one arises from the
thermal process, while the second relates to the phase transition. A numerical
simulation is used in a preliminary study of these phenomena.

INTRODUCTION

The dynamics of mechanical systems with components that exhibit a *shape–memory effect* is
an interesting and important topic. The design of such mechanical systems is certainly made
more tractable by the availability of accurate mathematical models. The purpose of this paper
is to describe some efforts with a numerical simulation for one such model, and to examine
some of the effects of system parameters on the dynamic response. The model we use has been
studied by Hoffmann *et al* (1989), and is based on work by Colli, Frémond and their co-workers
[Frémond (1987), Colli *et al* (1988), Colli (1989)].

MATHEMATICAL MODEL

We have in mind an alloy with three crystalline phases which we canonically name Martensite-
plus (M^+), Martensite-minus (M^-) and Austenite (A). We consider a model in one spatial
dimension and adopt a macroscopic view so that at a given time–space point $[(t, x)]$ each
crystalline phase exists in some phase–fraction $[0 \le \beta_i(t, x) \le 1, \quad i = 1, 2, 3]$ and these phase-
fractions sum to unity.

The 'state' of the alloy can be described by four variables: the temperature, the phase–
fractions of the two Martensitic phases; and the longitudunal displacement. The evolution of
each variable is be described as a function of time and space. The underlying physics for this
evolution is given by: conservation of energy, conservation of linear momentum and, a mixture
evolution rule.

$$\rho c_0 \dot{\vartheta} - \rho \ell (\dot{\beta}_1 + \dot{\beta}_2) - \rho \vartheta \alpha'(\vartheta)(\beta_1 - \beta_2)\dot{\varepsilon}(u) - \rho (\vartheta \alpha'(\vartheta) - \alpha(\vartheta))\varepsilon(u)(\dot{\beta}_1 - \dot{\beta}_2) = k \vartheta_{xx} \qquad (1)$$

$$\left(-\nu u_{xxx} + (\lambda + 2\mu)\varepsilon(u) - \alpha(\vartheta)(\beta_1 - \beta_2) \right)_x = 0 \qquad (2)$$

$$\kappa \begin{pmatrix} \dot{\beta}_1 \\ \dot{\beta}_2 \end{pmatrix} - \zeta \begin{pmatrix} \beta_{1xx} \\ \beta_{2xx} \end{pmatrix} + \rho \begin{pmatrix} -\alpha(\vartheta)\varepsilon(u) + \frac{\ell}{\vartheta_0}(\vartheta - \vartheta_0) \\ +\alpha(\vartheta)\varepsilon(u) + \frac{\ell}{\vartheta_0}(\vartheta - \vartheta_0) \end{pmatrix} + \rho \vartheta \partial I(\beta_1, \beta_2) \ni 0 \qquad (3)$$

where for $t \in [0, T]$ and $x \in [0, L]$ for some $T > 0$, $L > 0$,

$\vartheta(t,x)$	—	absolute temperature
$\beta_1(t,x), \beta_2(t,x)$	—	the fractions of the two martensitic phases
$u(t,x)$	—	longitudinal displacement
ε	—	strain given by $\varepsilon = u_x$
ℓ	—	latent heat for Austenite
ρ	—	material denisty $\rho > 0$
c_0	—	heat capacity $c_0 > 0$
ϑ_0	—	critical temperature
k	—	thermal conductivity > 0
λ, μ	—	Lamé constants
$\alpha(\vartheta)$	—	thermal expansion function
	—	(see Figure 1) $\Longrightarrow$
κ	—	relaxation time–constant
ζ	—	diffusion coefficient
I	—	is the indicator function of the closed convex subset

$$\mathcal{K} \subset \{(\beta_1, \beta_2) \in \mathbf{R}^2 : \beta_1 \geq 0, \ \beta_2 \geq 0, \ \beta_1 + \beta_2 \leq 1\}$$
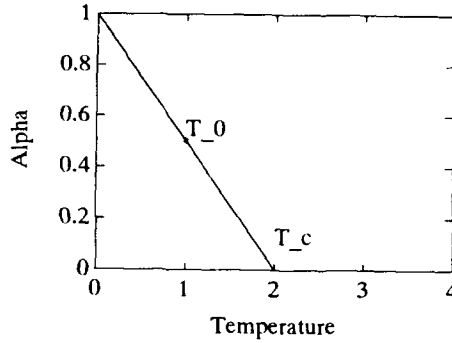
$$I(\beta_1, \beta_2) = \begin{cases} 0 & \text{for } (\beta_1, \beta_2) \in \mathcal{K} \\ +\infty & otherwise \end{cases}$$

Equation (1) results from a energy balance equation. Equation (2) results is the quasi-static form of the linear momentum equation and Equation (3) describes linear viscous behavior and diffusion of the phase ratios β_i. The phase ratio of austenite β_3 is given by

$$\beta_3 := 1 - \beta_1 - \beta_2$$

The special form of the Indicator function I forces the β_i to take admissible physical values between 0 and 1 with the sum equal to 1. The variational inequality (3) is needed because of the sub-gradient ∂I. This arises because the set $\mathcal{K}$ has sharp corners.

The initial and boundary conditions are:

$$\vartheta(0,x) = \vartheta^0(x), \tag{I1}$$

$$\left. \begin{aligned} \beta_1(0,x) &= \beta_1^0(x) \\ \beta_2(0,x) &= \beta_2^0(x) \end{aligned} \right\} \tag{I2}$$

$$\left. \begin{aligned} k\vartheta_x(t,0) + a(\vartheta(t,0) - \vartheta_0) &= 0 \\ k\vartheta_x(t,L) + a(\vartheta(t,L) - \vartheta_L) &= 0 \end{aligned} \right\} \tag{B1}$$

$$\beta_{1x}(t,0) = \beta_{2x}(t,0) = \beta_{1x}(t,L) = \beta_{2x}(t,L) = 0 \tag{B2}$$

$$\left. \begin{aligned} u(t,0) &= 0 \\ u(t,L) &= u_L(t) \\ u_{xx}(t,0) = u_{xx}(t,L) &= 0 \end{aligned} \right\} \tag{B3}$$

where

$\vartheta^0(x)$ — initial temperature of the alloy
$\beta_1^0(x), \beta_2^0(x)$ — initial phase fractions for the two martensitic fractions
ϑ_0, ϑ_L — prescribed constant boundary temperatures
a — Newton cooling coefficient
$u_L(t)$ — prescribed displacement function

TIME-SCALING

While many of the parameters in the model are well-understood, several of them are more difficult to measure. In particular, the relaxation-time-parameter κ and the diffusion-parameter ζ in the phase-transition dynamics must be estimated. We have in mind a parameter-identification problem wherein, the physical system is subjected to some external excitation (e.g. $u_L(t)$ in (B3)) and some measurements of the time-varying response are recorded. These 'data' are then used in conjunction with mathematical optimization to produce 'best fit' parameter estimates. As a preliminary step we examine some of the effects of parameter values on the mathematical predicitons. We focus on the time-scale issue.

The parameters in the dynamical equations (1–3) can be grouped to more clearly illustrate the time-scale issue. Since time-derivatives appear in only first and third equations we can write:

$$\dot{\vartheta} - p_1 \cdot (\dot{\beta}_1 + \dot{\beta}_2) - \vartheta\alpha'(\vartheta))(\beta_1 - \beta_2)\dot{\varepsilon}(u) - (\vartheta\alpha'(\vartheta) - \alpha(\vartheta))\varepsilon(u)(\dot{\beta}_1 - \dot{\beta}_2) = \vartheta_{xx} \qquad (1')$$

$$\mathcal{T} \cdot \begin{pmatrix} \dot{\beta}_1 \\ \dot{\beta}_2 \end{pmatrix} - \zeta \cdot \begin{pmatrix} \beta_{1xx} \\ \beta_{2xx} \end{pmatrix} + \begin{pmatrix} -\alpha(\vartheta)\varepsilon(u) + p_2(\vartheta - \vartheta_0) \\ +\alpha(\vartheta)\varepsilon(u) + p_2(\vartheta - \vartheta_0) \end{pmatrix} + \vartheta\partial I(\beta_1, \beta_2) \ni 0 \qquad (3')$$

The length of the 'wire' has been normalized to unity and the temperature scale has been defined so that $(\vartheta_c - \vartheta_0)$ is the unit. The time unit is $\tau \equiv \rho \cdot c_0 \cdot L^2/k$, which is the length-squared divided by the thermal diffusivity. The parameters are given by

$$p_1 \equiv \frac{\ell}{c_0(\vartheta_c - \vartheta_0)}, \qquad p_2 \equiv \frac{\ell}{c_0\vartheta_0}, \qquad \mathcal{T} \equiv \frac{\kappa c_0}{k}$$

NUMERICAL RESULTS

The existence proof in Hoffmann *et al* (1989) is based on a fixed-point argument applied to an iteration map. The numerical results presented here were generated by a fully discrete, finite difference scheme that is patterned on the iteration map. We used this code to predict the response to a smooth loading $u_L(t)$ in (B3). We have taken $p_1 = p_2 = 1$ and $\zeta = 0$ and we will vary the time-scale parameter $\mathcal{T}$. For a 1 ft metallic wire the thermal time constant (our unit time) is about 600 seconds. It is expected that the phase-transition dynamics are much faster, so we use 'small' values for $\mathcal{T}$. The total time-interval is about 180 sec.

Shown in Fig. 2 is the response for the case $\mathcal{T} = 10^{-4}$. From the upper-left the four component figures are: $u(t, x)$ – displacement, ; $\vartheta(t, x)$ – temperature, ; $\beta_1(t, x)$ – phase fraction of M^+, and $\beta_3(t, x)$ – phase-fraction of A. Note that the M^+/A boundary propagates about 15% from each boundary.

In contrast, Fig. 3 is the response for the case $\mathcal{T} = 10^{-1}$. To save space here we only show the ϑ and β_3 responses. The u response is about the same as in Fig. 2, while β_1 and β_3 are complementary. It's clear that the 'slower' phase-dynamics produces smoother responses. The vertical scales in Figures 2 and 3 are **not** the same. In Fig. 2 the A fraction varies from 100% to 0%, while in Fig. 3 the lower bound is about 99%. As expected, the slower dynamics produces less $A \Rightarrow M^+$ phase change.

Figure 2.

Figure 3.

REFERENCES

Colli, P, Frémond, M and Visitin, A (1988), "Thermo-mechanical evolution of shape memory alloys", Publ No. 607, IAN, CNR, Pavia, Italy.

Colli, P (1989) "An evolution probelm related to shape memory alloys", Publ No. 656, IAN, CNR, Pavia, Italy.

Frémond, M (1987), "Mécanique des milieux continus: matériaux à mémoire forme", Proceedings of the Paris Academy of Sciences, Vol 304, Series II, No. 7, pp239 244.

Hoffmann, K-H, Niezgódka, M and Songmu, Z (1989) "Existence and Uniqueness of Global Soltutions to an Extended Model of the Dynamical Developments in Shape Memory Alloys", pre print University of Augsburg, Germany

Finite element approximation of a shape memory alloy

John A. Burns and Ruben D. Spies

Interdisciplinary Center for Applied Mathematics

Department of Mathematics

Virginia Polytechnic Institute and State University

Blacksburg, Virginia 24061, USA

Abstract. In this paper we use a finite element scheme to approximate the solutions of a dynamical model of phase transitions in Shape Memory Alloys with Landau-Devonshire potential. Numerical results are shown and open problems are discussed.

1. INTRODUCTION

Consider the system of partial differential equations

$$\rho u_{tt} - \nu \rho u_{xxt} - (\Psi_\epsilon)_x - (\Psi_{\epsilon_x})_{xx} = f \tag{1.1}$$

$$-\theta (\Psi_\theta)_t - k\theta_{xx} - \alpha k\theta_{xxt} - \nu \rho u_{xt}^2 = g \tag{1.2}$$

for $x \in \Omega \subset \mathbb{R}$ and $0 \leq t \leq T$. System (1.1-2) formally describes the dynamics of phase transition in a one-dimensional pseudoelastic material and arises from the conservation laws for linear momentum and energy. The parameters, functions and variables involved in (1.1-2) are defined by: $u = u(x,t)$ - displacement; $\theta = \theta(x,t)$ - temperature; ρ - constant mass density; ν - viscosity constant; k - thermal conductivity coefficient; $f = f(x,t)$ - distributed loads; $g = g(x,t)$ - density of heat sources; α - short thermal memory coefficient; $\Psi = \Psi(\epsilon, \epsilon_x, \theta)$ is the Helmholtz free energy density, and $\epsilon(x,t) = u_x(x,t)$ is the linearized (macroscopic) strain. We refer to [5] and [9] for the details about the derivation of equations (1.1-2). Our system is complemented by the following initial and boundary conditions:

$$u(x,0) = u_0(x), \qquad u_t(x,0) = u_1(x), \qquad \theta(x,0) = \theta_0(x), \qquad \text{for } x \in \Omega \tag{1.3}$$

$$\frac{\partial}{\partial \epsilon}\Psi(u_x, u_{xx}, \theta) = \sigma_\Gamma(t), \qquad k\frac{\partial}{\partial \nu}\theta(x,t) = k_1(\theta_\Gamma - \theta), \qquad \text{for } x \in \partial\Omega, \quad 0 \leq t \leq T \tag{1.4}$$

where ν is the outward normal unit vector to $\partial\Omega$. k_1 is a positive constant and θ_Γ is the temperature of the surrounding medium.

There are several results on the existence and uniqueness of solutions to system (1.1-2) for different types of initial and boundary conditions and for different forms of the free energy Ψ ([3], [4], [5], [7], [8], [10]). See [1] for a brief summary.

2. NUMERICAL APPROXIMATIONS

In this paper we are concerned with numerical approximations of the solutions of the initial boundary value problem (1.1)-(1.4) when the free energy density is given by the Landau-Devonshire potential

$$\Psi(\epsilon, \theta) = \Psi_0(\theta) + \alpha_2(\theta - \theta_1)\epsilon^2 - \alpha_4\epsilon^4 + \alpha_6\epsilon^6 \tag{2.1}$$

with $\Psi_0(\theta) = -C_v \theta ln\left(\frac{\theta}{\theta_2}\right) + C_v\theta + C$, where α_2, α_4, α_6 are positive constants, θ_1 and θ_2 are critical temperatures, C_v is the specific heat and C is a constant.

Consider the particular case in which $\Omega = (0,1)$, $\alpha = 0$, $v = 0$ and the free energy density Ψ is given as in (2.1). Then system (1.1-2) can be writen in the form

$$\rho u_{tt} - \left(2\alpha_2(\theta - \theta_1)u_x - 4\alpha_4 u_x^3 + 6\alpha_6 u_x^5\right)_x = f \tag{2.2}$$

$$C_v\theta_t - 2\alpha_2\theta u_x u_{xt} - k\theta_{xx} = g \tag{2.3}$$

to be satisfied in $\Omega = (0,1)$ for $0 \leq t \leq T$ where u and θ satisfy the initial and boundary conditions (1.3-4). We propose the following finite dimensional approximations for u and θ:

$$u^N(x,t) = \sum_{i=-1}^{N+1} a_i^N(t)o_i^N(x), \qquad \theta^N(x,t) = \sum_{i=-1}^{N+1} b_i^N(t)o_i^N(x) \tag{2.4}$$

where the o_i^N's are the usual cubic splines in $(0,1)$, $a_i^N(t)$ and $b_i^N(t)$, $-1 \leq i \leq N+1$, are coefficients to be computed and $N+3$ is the order of the approximation. The projection into $V^N = \text{Span}\{o_i\}$ of the weak formulation in $L^2(0,1)$ of equations (2.2-3) yield the following finite dimensional system

$$\begin{cases} \rho M A''(t) = F_1(t) + F_2(t) + P(A,B) \\ C_v M B'(t) = (-kS + \dot{S})B(t) + G_1(t) + G_2(t) + Q(A,B) \end{cases} \tag{2.5}$$

where $A(t) = col[a_{-1}(t) \; a_0(t) \; \ldots \; a_{N+1}(t)]$, $B(t) = col[b_{-1}(t) \; b_0(t) \; \ldots \; b_{N+1}(t)]$.

$M = [< o_j, o_i >]$, $S = [< o_j', o_i' >]$, $F_1(t) = col[< f(\cdot,t), o_j >]$.

$F_2(t) = col[\sigma_1(t)o_j(x) |_{x=0}^{x=1}]$, $G_1(t) = col[< g(\cdot,t), o_j >]$, $G_2(t) = col[k_1\theta_\Gamma(0,t)o_j(0)+$

$k_1\theta_\Gamma(1,t)o_j(1)]$, $P(A,B) = col[- < \Psi_1(u_x^N, \theta^N), o_j' >]$, $Q(A,B) = col[2\alpha_2 < \theta^N u_x^N u_{xt}^N, o_j >]$.

and $\dot{S} = k_1 \begin{bmatrix} T & 0 & 0 \\ 0 & 0 & 0 \\ 0 & 0 & T \end{bmatrix}_{(N+3)\times(N+3)}$, where $T = \begin{bmatrix} -1 & -4 & -1 \\ -4 & -16 & -4 \\ -1 & -4 & -1 \end{bmatrix}$.

We have dropped the index "N" where it was clearly understood by the context. Here A, B, F_1, F_2, G_1, G_2, $P(A,B)$ and $Q(A,B)$ are all $(N+3)$-dimensional vectors, M, S and $\dot{S}$ are $(N+3)\times(N+3)$ matrices and $< \cdot, \cdot >$ denotes the inner product in $L^2(0,1)$. By defining $C(t) = A'(t)$ system (2.4) can be written as the following system of first order ODE's:

$$\begin{cases} A'(t) = C(t) \\ C'(t) = \rho^{-1}M^{-1}(F_1(t) + F_2(t)) + \rho^{-1}M^{-1}P(A(t), B(t)) \\ B'(t) = C_v^{-1}M^{-1}(-kS + \dot{S})B(t) + C_v^{-1}M^{-1}(G_1(t) + G_2(t)) + C_v^{-1}M^{-1}Q(A,B) \end{cases} \tag{2.6}$$

or, equivalently

$$X'(t) = \tilde{A}X(t) + F(t) + NL(X(t)) \tag{2.7}$$

where

$$X(t) = [A(t)^T \; C(t)^T \; B(t)^T]^T, \qquad \tilde{A}(t) = \begin{bmatrix} 0 & I_{N+3} & 0 \\ 0 & 0 & 0 \\ 0 & 0 & C_v^{-1}M^{-1}(-kS + \dot{S}) \end{bmatrix}$$

$$F(t) \doteq \begin{bmatrix} 0 \\ \rho^{-1}M^{-1}(F_1(t) + F_2(t)) \\ C_r^{-1}M^{-1}(G_1(t) + G_2(t)) \end{bmatrix} \quad \text{and} \quad NL(X(t)) \doteq \begin{bmatrix} 0 \\ \rho^{-1}M^{-1}P(A(t), B(t)) \\ C_v^{-1}M^{-1}Q(A(t), B(t)) \end{bmatrix}$$

where I_{N+3} denotes the identity matrix of order $N + 3$. The initial condition for (2.7) is obtained as usual by postulating the error at time $t = 0$ to be orthogonal to $V^N = \text{Span}\{\phi_i\}$. Thus, we obtain

$$X(0) = X_0 \doteq [A(0)^T \quad C(0)^T \quad B(0)^T]^T$$

with $A(0) = M^{-1}U_0$, $C(0) = M^{-1}U_1$ and $B(0) = M^{-1}\Theta_0$, where $U_0 \doteq col[< u_0, \phi_i >]$, $U_1 \doteq col[< u_1, \phi_i >]$, and $\Theta_0 \doteq col[< \theta_0, \phi_i >]$.

Summing up. we want to approximate the solutions of the IVP

$$(\Sigma^N) : \begin{cases} X'(t) = \hat{A}X(t) + F(t) + NL(X(t)) \\ X(0) = X_0 \end{cases} \tag{2.8}$$

for $0 \leq t \leq T$.

3. NUMERICAL RESULTS

For the alloy $Au_{23}Cu_{30}Zn_{47}$. the following data was reported in [2]: $\alpha_2 = 24$ J cm^{-3}K^{-1}, $\alpha_4 = 1.5 \times 10^5$ J cm^{-3}. $\alpha_6 = 7.5 \times 10^6$ J cm^{-3}. $\theta_1 = 208$ K, $C_v = 2.9$ J cm^{-3} K^{-1}, $k = 1.9$ W cm^{-1} K^{-1}. $\rho = 11.1$ g cm^{-3}. We took $\theta_0(x) \equiv 200$ K, $u_0(x) \equiv 0$, $u_1(x) \equiv 0$, $\theta_\Gamma(t) \equiv 200$ K and $\sigma_\Gamma(t)$ as in Fig.1. Notice that the maximun stress, $\sigma_\Gamma(10^{-3}) = 250$, is slightly above the plastic yield corresponding to the temperature $\theta = 200$ K. We used a sixth order Runge-Kutta-Verner method to solve (Σ^N) for this alloy. The program was run in an IBM 3090 with vectorization facilities.
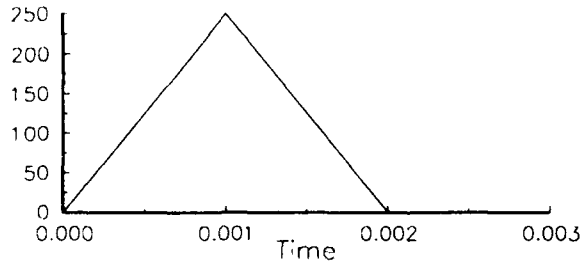
Fig.1: Boundary Stress input

Fig.2 shows the evolution in time of displacement, temperature and deformation obtained with $N = 10$ and $k_1 = 100$. Notice how the stress-induced phase transition produces large deformations and increases the temperature near the boundary. Fig.3 corresponds to $N = 10$ and $k_1 = 500$. No significant change in deformation is observed with this increase in k_1. However, the boundary starts to cool off faster due to the greater influence of the external temperature.

We are currently investigating the influence of the parameters α_2, α_4, α_6 and C_v. The goal of this effort is to develop computational schemes for the identification of system parameters which will allow us to validate the model. Validation of the model will enable us to proceed to develop computational algorithms for control of this system. Finally, by introducing new parameters in the stress-strain relations. local and global memories can be captured ([1]). The resulting system is now a partial functional differential equation. Similar schemes for this modified model are also been studied.

Displacement   Temperature   Deformation
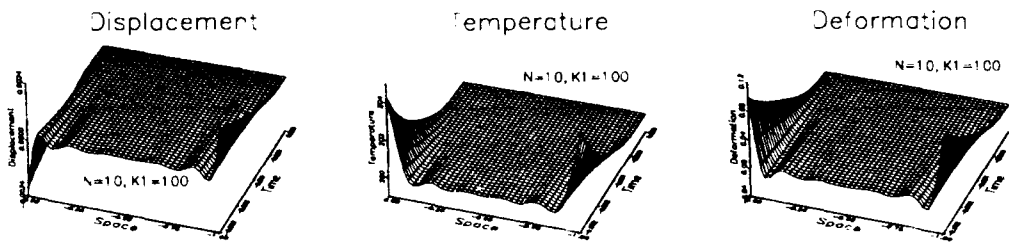
Fig.2: Evolution of displacement, temperature
and deformation. $N = 10$, $k_1 = 100$.

Displacement   Temperature   Deformation
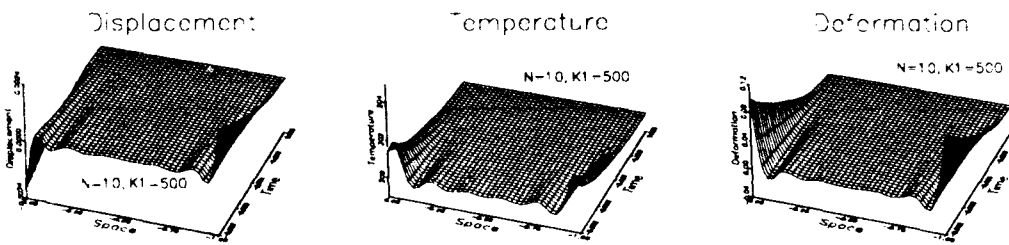
Fig.3: Evolution of displacement, temperature
and deformation. $N = 10$, $k_1 = 500$.

REFERENCES

[1] Burns, John A. and Spies, Ruben D., *Modelling for Control of Shape Memory Alloys*, Proceedings of the 30th IEEE Conference on Decision and Control, Dec. 1991, Brighton, United Kingdom..

[2]. Falk, F., *Ginzburg-Landau Theory of Static Domain Walls in Shape Memory Alloys*, Z. Physik B-Condensed Matter **51** (1983), 177-185.

[3]. Hoffmann K.H. and Songmu Z., *Uniqueness for Nonlinear Coupled Equations Arising from Alloy Mechanism*, Preprint #118. Institut für Mathematik. Ausburg.

[4]. Hoffmann K.H. and Songmu Z., *Uniqueness for Structural Phase Transitions in Shape Memory Alloys*, Mathematical Methods in the Applied Sciences **10** (1988). 145 151.

[5]. Niezgodka M. and Sprekels J., *Existence of Solutions for a Mathematical Model of Structural Phase Transitions in Shape Memory Alloys*, Mathematical Methods in the Applied Sciences **10**, 1988, 197-223; II, Preprint # 89. Institut für Mathematik, Universität Ausburg, 1985.

[6] Perkins, Jeff (Ed.), "Shape Memory Effects in Alloys," Proceedings of the International Simposium on Shape Memory Effects and Applications, Toronto, May 19 22, Plenum Press, New York and London, 1975.

[7]. Songmu Z., *Global Solutions to Thermomechanical Equations with Nonconvex Landau-Ginzburg free energy*, Journal of Applied Mathematics and Physics (ZAMP) **40** (January 1989), 111-127.

[8]. Sprekels J., *Global Existence for Thermomechanical Processes with Nonconvex Free Energies of Ginzburg-Landau Form*, Journal of Mathematical Analysis and Applications **141** (1989), 333-348.

[9]. Sprekels, Jürgen, *Shape Memory Alloys: Mathematical Models for a Class of First Order Solid-Solid Phase transition in Metals*, "Schwerpunktprogramm der Deutschen Forschungsgemeinschaft," Anwendungsbezogene Optimierung und Steuerung, Report # 241, 1990.

[10]. Sprekels J. and Songmu Z., *Global Solutions to the Equations of a Ginzburg-Landau Theory for Structural Phase Transitions in Shape Memory Alloys*, Physica D. **39** (1989), 59 76.

Constitutive modeling of phase transition in smart materials

Mehrdad Negahban, Department of Engineering Mechanics and the Center for
Materials Research and Analysis, University of Nebraska-Lincoln, Lincoln, NE
68588-0347

1   Introduction

Smart, intelligent, and adaptive materials and structures have recently received particular attention due to their active, as opposed to passive, interaction with their working environment. This interaction can range from sensing the material's structural integrity to actively sensing and appropriately responding to different stimuli. Real and pseudo phase transitions are one mechanism which can be used to make a material smart. Shape memory alloys and rheological fluids are two examples of materials which can be made smart by taking advantage of their phase transitions.

Many polymers in a way similar to shape memory alloys remember their previous shape and can be stimulated to return to this shape. Polycarbonate and polystyrene[1] are two materials which after plastic forming below the glass transition temperature will recover their original shape upon heating above their glass transition temperature.

Figure 1 shows a sample of cold rolled polymethyl methacrylate (PMMA) before and after cooling it to above 200 C. The sample has reduced in length and width and increased in thickness. The sample shows little warping or any other kind of loss in geometric integrity. The glass transition temperature of PMMA is about 100 C and its melting temperature is about 200 C.

Figure 2 shows samples put in a preheated oven and quenched in water at different times. The oven was heated to 195 C. The samples had warped before the quenching step. The quenching in water did not contribute to the final shape shown other than freezing it. The entire process took about four minutes for the sample to first bend and then unbend. In another set of experiments in which the oven was preheated to 220 C the stress in the sample was so large that it induced small tension cracks on the side with the larger strains. These cracks opened and closed as the sample

See Martin, H and ... Watson 1972

(a)

(b)
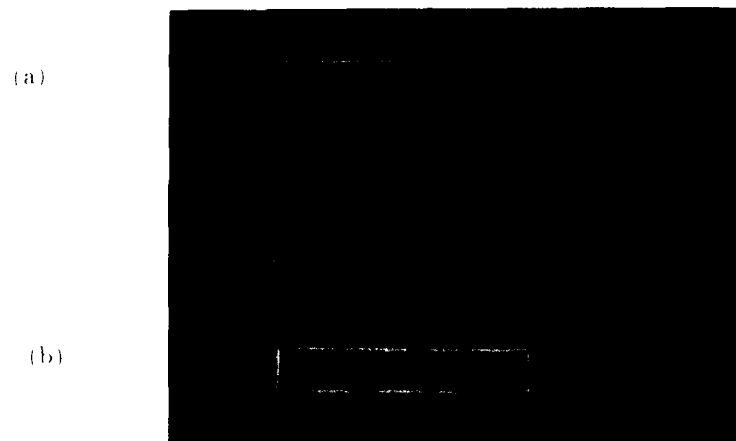
Figure 1: Sample of poly(methyl methacrylate) (a) as cold rolled, and (b) after gradually heating to 200 °C.

deformed. After four minutes the sample underwent no further deformations. This large deformation is most likely attributed to the thermal gradient in the oven since the sample always bends towards the back of the oven which is hotter. Residual stresses should not significantly contribution to the deformation. Samples were also put into an oven which was preheated to 150 °C, and 180 °C. The results were similar, but the samples did not show the cracks. In all cases the axial direction had an approximate -45% strain, the width of the sample also had an approximate -45% strain, and the thickness increased to give an approximate strain of 250%. The volume change was small and of the order of several percent strain. The time needed for the sample to reach a final shape was increased to about ten minutes for the lower temperature.

This change in shape can be used for developing large strain actuators, self healing members, and members which can perform complex motions. In addition, since these materials are transparent and their response is very predictable, localized heating can be used to manufacture parts of complex shapes in an automated system which allows the production of precision parts in small quantities.

2   Mathematical Modeling

Complex deformations can be studied once a mathematical model to characterize the behavior of the material has been developed.

The most simple model developed must at least be able to (a) handle large deformations of several hundred percent strain, and (b) capture the characteristic of shape recovery. The following model can handle both these requirements and is based on
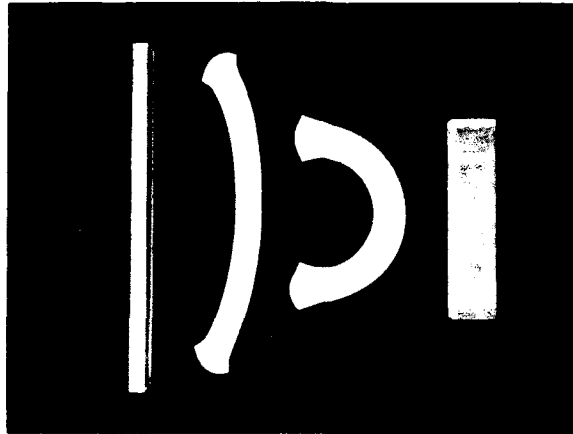
Figure 2: Samples of poly(methyl methacrylate) put in an oven which was preheated to 195°C. Left: sample before putting into the oven; Center: samples quenched in water at different points of the heating process; Right: sample after fully deforming due to the heating. Total process took four minutes.

the extension of ideas originally developed for nonlinear plasticity. This model can not capture all of the viscoelastic behavior seen in actual polymers. It is simple to extend this model to capture the viscoelastic behavior.

The basic structure of a simple mathematical model which can account for shape memory is as follows. The material will be considered an elastic-plastic material bellow the transition temperature. In a manner similar to nonlinear thermo-plasticity, it will be assumed that the second Piola-Kirchhoff stress, $\mathbf{S}(t)$, is given by a function of the current value of the right Cauchy strain, $\mathbf{C}(t)$, the corresponding plastic strain, $\mathbf{C}^p(t)$, and the temperature, $T(t)$. This relational dependence will be written as

$$\mathbf{S}(t) = \mathcal{S}\{\mathbf{C}(t), \mathbf{C}^p(t), T(t)\}.$$

where $\mathbf{C}^p(t)$ is given by a flow rule of the form

$$\dot{\mathbf{C}}^p(t) = \frac{\partial \mathbf{C}^p}{\partial T} \dot{T} + \frac{\partial \mathbf{C}^p}{\partial \mathbf{C}} : \dot{\mathbf{C}} + \frac{\partial \mathbf{C}^p}{\partial t}.$$

Omitting the last term, this would correspond to a fully strain spaced formulation of the model originally developed by Green and Naghdi (1965). The last term in the equation implies that the plastic strain can change without the introduction of any changes in the total strain or temperature (normally considered as material aging). This term is the key feature needed to model shape memory materials.

To better understand the characteristics of the model consider a material which is plastically deformed below the transition temperature and is subsequently heated

to above the transition temperature and held at a constant strain and temperature. If the term $\dot{C}^p$ is negative above the transition temperature, then the plastic strain will gradually reduced. Since the total strain is kept constant, the elastic strain will increase to compensate for the reduction in plastic strain and the stress in the material will increase. This added stress will be available to do work.

It will be assumed that the first two terms in the equation for the rate of plastic strain will go to zero above the transition temperature. The last term in this equation, $\dot{C}^p$, will be taken as negative above the transition temperature and normally zero below this temperature. Since the rate of change of plastic strain must go to zero as the plastic strain goes to unity, an equation of the form $\frac{d C^p}{dt} = \alpha(T)(C^p - 1)$ is a possible selection, where $\alpha(T)$ is zero below the transition temperature and negative above it.

3   Bending of a Bar Due to Nonsymmetric Heating

As a simple example consider the following one-dimensional problem. A sample is cold rolled in a way which results in a uniform plastic strain λ_p in the axial direction. The sample is heated to above its glass transition temperature in a chamber which initially has a small temperature gradient which gradually vanishes. As shown in the experiments, the sample should bend, contract and straighten.

Let the behavior of the material be given by a simple equation for the stress, σ, in the form

$$\sigma = E \frac{T_m - T}{T_m} (\lambda - \lambda_p)$$

where T is the temperature, T_m is the melting temperature, E is the modulus at zero temperature, λ is the stretch ratio from the initially undeformed configuration, λ_p is the plastic stretch ratio. Even though this model is one-dimensional and over simplifies the softening or hardening resulting from temperature changes, it will suffice for this problem.

Let the material be plastically strained to an initial plastic stretch ration of λ_p, and let it initially be at temperature T. Let T be less than the glass transition temperature of the material T_g. Assume that the material does not undergo further plastic deformation due to straining or temperature change and that it only changes plastic strain due to temperature induced time dependent relaxation of the plastic strain above the glass transition temperature. Assume the rate of change of λ_p is zero below the glass transition temperature and is given by an evolution equation

$$\dot{\lambda}_p = \alpha(T - T_g)(\lambda_p - 1)$$

above the glass transition temperature.

Assume the sample has a thickness of w and that the temperature field is given by an expression of the form

$$T = T_o + T_1 + T_2 t + \cdots$$

Change of curvature for different gradients of temperature
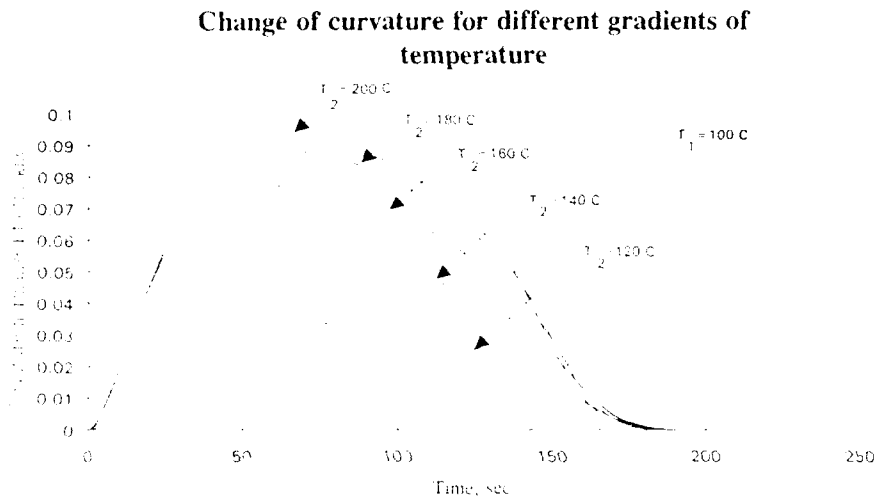
Figure 3. Theoretical evaluation of change in the radius of curvature as a function of time for uniform heating. All samples are assumed to start with one side at 100 C. The different curves are for different temperatures on the second side.

where ... is the normalized coordinate along the thickness, T_e is the final equilibrium temperature, T_1 is the initial temperature at $\xi = 0$, T_2 is the initial temperature at $\xi = 1$, t is time, and τ_1, τ_2, δ_1 and δ_2 are constants representing the rate of heat transfer. Even though this temperature distribution does not satisfy the classical Fourier law of heat conduction, it represents a reasonable temperature distribution.

Making the standard assumptions of pure bending with axial contraction, the stretch ratio will be given by ... where y is the distance from the surface of zero stress and ρ is the radius of curvature to that surface. The expression for the stress will, therefore, be given by

$$ \sigma = E \frac{T}{T} \cdots $$

Integrating the equation for ... and making the standard arguments of zero axial load and balance moment, one can evaluate the location of the surface of zero strain and the corresponding radius of curvature ρ. From ρ one can obtain the value of the curvature of the beam. Typical plots of the curvature are given in Figure 3.

... continuum theories ... flow applies in this problem.

4   Acknowledgement

The author would like to thank Dr. N. Shaikh for providing the cold rolled PMMA and for sharing his initial observations.

5   References

Green A E and Naghdi P M 1965 *A General Theory of an Elastic-Plastic Continua*
    Arch. Rational Mech. Anal. 18 pp 251-281
Murphy B M, Howard R N and White E F T 1971 J. Pol. Sci. V 39 87

Nonlinear constitutive relations for piezoceramic materials

Shiv P. Joshi

Center for Composite Materials, Aerospace Engineering Departments, University of Texas at Arlington, Arlington, TX 76019

ABSTRACT: Piezoelectric material produces electric charges when mechanically deformed and an electric potential causes a mechanical deformation. This property makes it suitable for sensor and transducer applications. The understanding of the electroelastic constitutive behavior is critical to predicting the response of a structure with embedded piezoelectric material. A concise formulation of relevant nonlinear constitutive relations is presented in this paper.

1. INTRODUCTION

Although the behavior of piezoelectric materials in non-structural applications has been investigated extensively, the treatment is often simplistic. The recent interest in "Smart Structures" has put especial emphasis on the rigorous understanding of elctroelastic behavior of piezoceramics as an integral part of a structure.

The nonlinear theory of dielectrics has been studied by Toupin (1983), Nelson (1978) and Tiersten (1981). The relation between the equations of linear piezoelectricity and the more general electroelastic equations is discussed by Tiersten (1981). Nelson(1978) presented a completely deductive derivation of the dynamical equations and constitutive relations for elastic, electric, and electroelastic phenomena based on the fully electrodynamic Lagrangian theory of elastic dielectrics. Penfield and Hans (1967) developed a linear piezoelectric theory which does not account for gradient of polarization and electrostatic interference. Mindlin (1974) derived a system of two dimensional equations for high frequency motions of crystal plates accounting for coupling of mechanical, electrical and thermal fields. Readers interested in this area may refer to books by Nye (1964), Berlincourt et.al. (1964), and Landau and Lifshitz (1960). A phenomenological description of the dynamic response of piezoceramics to an external electric field, including domain reorientation processes and the dynamics of dipole moment in each domain, has been developed by Chen et.al. (1979, 1980, 1981, 1983).

A concise formulation of linear constitutive equations for piezoelectric materials is presented by Joshi (1991). This paper extends the formulation to include some important nonlinear effects encountered by piezoceramics in "smart structures" applications.

2• LINEAR CONSTITUTIVE EQUATIONS

The physics involved in the piezoelectric theory may be regarded as a coupling between Maxwell's equations of electromagnetism and elastic stress equations of motion. The coupling takes place through the piezoelectric constitutive equations.

We will adopt index notations in this paper for convenience. We will employ the thermodynamic Gibbs potential to derive constitutive equations and will consider the σ_{ij} (stress components), E_k (electric field components), and T (absolute temperature) as independent variables.

$$G = U - \sigma_{ij}\varepsilon_{ij} - E_k\hat{D}_k - TS \qquad \text{(EQ 1)}$$

where G is the Gibbs potential, S is the entropy, and U is the internal energy. For adiabatically insulated reversible system, the total differential of internal energy is

$$dU = \sigma_{ij}d\varepsilon_{ij} + E_k d\hat{D}_k + TdS \qquad \text{(EQ 2)}$$

and therefore the total differential of Gibbs potential is

$$dG = -\varepsilon_{ij}d\sigma_{ij} - \hat{D}_k dE_k - SdT \qquad \text{(EQ 3)}$$

Expressing the Gibbs potential in Taylor series and neglecting higher order terms, we obtain,

$$dG = \left(\frac{\partial G}{\partial \sigma_{ij}}\right)_{E,T} d\sigma_{ij} + \left(\frac{\partial G}{\partial E_k}\right)_{\sigma,T} dE_k + \left(\frac{\partial G}{\partial T}\right)_{\sigma,E} dT \qquad \text{(EQ 4)}$$

From eqs.3 and 4

$$\varepsilon_{ij} = -\left(\frac{\partial G}{\partial \sigma_{ij}}\right)_{E,T} \qquad \hat{D}_k = -\left(\frac{\partial G}{\partial E_k}\right)_{\sigma,T} \qquad S = -\left(\frac{\partial G}{\partial T}\right)_{\sigma,E} \qquad \text{(EQ 5)}$$

The total differentials of dependent variables ε_{ij}, $\hat{D}_k$, and S is given as a function of independent variables as

$$d\varepsilon_{ij} = \left(\frac{\partial \varepsilon_{ij}}{\partial \sigma_{lm}}\right)_{E,T} d\sigma_{lm} + \left(\frac{\partial \varepsilon_{ij}}{\partial E_n}\right)_{\sigma,T} dE_n + \left(\frac{\partial \varepsilon_{ij}}{\partial T}\right)_{\sigma,E} dT$$

$$d\hat{D}_k = \left(\frac{\partial \hat{D}_k}{\partial \sigma_{lm}}\right)_{E,T} d\sigma_{lm} + \left(\frac{\partial \hat{D}_k}{\partial E_n}\right)_{\sigma,T} dE_n + \left(\frac{\partial \hat{D}_k}{\partial T}\right)_{\sigma,E} dT \qquad \text{(EQ 6)}$$

$$dS = \left(\frac{\partial S}{\partial \sigma_{lm}}\right)_{E,T} d\sigma_{lm} + \left(\frac{\partial S}{\partial E_n}\right)_{\sigma,T} dE_n + \left(\frac{\partial S}{\partial T}\right)_{\sigma,E} dT$$

where

$$s_{ijlm}^{E,T} = \left(\frac{\partial \varepsilon_{ij}}{\partial \sigma_{lm}}\right)_{E,T}, \qquad d_{ijn}^{T} = \left(\frac{\partial \varepsilon_{ij}}{\partial E_n}\right)_{\sigma,T} = \left(\frac{\partial \hat{D}_n}{\partial \sigma_{ij}}\right)_{E,T}, \qquad \alpha_{ij}^{E} = \left(\frac{\partial \varepsilon_{ij}}{\partial T}\right)_{\sigma,E} = \left(\frac{\partial S}{\partial \sigma_{ij}}\right)_{E,T},$$

$$\varepsilon_{kn}^{\sigma,T} = \left(\frac{\partial \hat{D}_k}{\partial E_n}\right)_{\sigma,T}, \qquad p_k^{\sigma} = \left(\frac{\partial \hat{D}_k}{\partial T}\right)_{\sigma,E} = \left(\frac{\partial S}{\partial E_k}\right)_{\sigma,T}, \qquad \frac{\rho c^{\sigma,E}}{T_0} = \left(\frac{\partial S}{\partial T}\right)_{\sigma,E}$$

are elastic compliance coefficients, piezoelectric strain constants, coefficients of thermal expansion, dielectric permittivities, pyroelectric coefficients, respectively; and $c^{\sigma, E}$ is the specific heat and ρ is the mass density. Integrating eq. 6, we obtain,

$$\varepsilon_{ij} = s_{ijlm}^{E,T}\sigma_{lm} + d_{ijn}^{T}E_n + \alpha_{ij}^{E}\Delta T$$

$$\hat{D}_k = d_{klm}^{T}\sigma_{lm} + \varepsilon_{kn}^{\sigma,T}E_n + p_k^{\sigma}\Delta T$$

$$\Delta S = \alpha_{lm}^{E}\sigma_{lm} + p_n^{\sigma}E_n + \frac{c^{\sigma,E}}{T_0}\Delta T$$

(EQ 7)

Piezoceramics are widely used, therefore we will specialize eq. 7 for them. The constitutive equations of the polarized piezoceramics are equivalent to the equations for a piezocrystal of the hexagonal 6mm symmetry class. In abbreviated subscript notation these equations may be written as

$$\varepsilon_{11} = s_{11}^{E,T}\sigma_{11} + s_{12}^{E,T}\sigma_{22} + s_{13}^{E,T}\sigma_{33} + d_{31}^{T}E_3 + \alpha_1^{E}\Delta T$$

$$\varepsilon_{22} = s_{12}^{E,T}\sigma_{11} + s_{11}^{E,T}\sigma_{22} + s_{13}^{E,T}\sigma_{33} + d_{31}^{T}E_3 + \alpha_1^{E}\Delta T$$

$$\varepsilon_{33} = s_{13}^{E,T}\sigma_{11} + s_{13}^{E,T}\sigma_{22} + s_{33}^{E,T}\sigma_{33} + d_{33}^{T}E_3 + \alpha_3^{E}\Delta T$$

$$\varepsilon_{23} = s_{44}^{E,T}\sigma_{23} + d_{15}^{T}E_2, \qquad \varepsilon_{13} = s_{44}^{E,T}\sigma_{13} + d_{15}^{T}E_1, \qquad \varepsilon_{12} = \left(\frac{s_{11}^{E,T} - s_{12}^{E,T}}{2}\right)\sigma_{12}$$

(EQ 8)

$$\hat{D}_1 = d_{15}^{T}\sigma_{13} + \varepsilon_{11}^{\sigma,T}E_1 + p_1^{\sigma}\Delta T, \qquad \hat{D}_2 = d_{15}^{T}\sigma_{23} + \varepsilon_{11}^{\sigma,T}E_2 + p_1^{\sigma}\Delta T$$

$$\hat{D}_3 = d_{31}^{T}(\sigma_{11} + \sigma_{22}) + d_{33}^{T}\sigma_{33} + \varepsilon_{33}^{\sigma,T}E_3 + p_3^{\sigma}\Delta T$$

$$\Delta S = \alpha_1^{E}(\sigma_{11} + \sigma_{22}) + \alpha_3^{E}\sigma_{33} + p_1^{\sigma}(E_1 + E_2) + p_3^{\sigma}E_3 + \frac{c^{\sigma,T}}{T_0}\Delta T$$

In cases where temperature variation is negligible, neglecting temperature terms and writing eq. 8 in compact matrix notation, we obtain

$$\{\varepsilon\} = [S^E]\{\sigma\} + [d]\{E\}$$

$$\{\hat{D}\} = [d]^T\{\sigma\} + [\varepsilon^\sigma]\{E\}$$

(EQ 9)

Where,

$$[S^E] = \begin{bmatrix} S_{11} & S_{12} & S_{13} & 0 & 0 & 0 \\ S_{12} & S_{11} & S_{13} & 0 & 0 & 0 \\ S_{13} & S_{13} & S_{33} & 0 & 0 & 0 \\ 0 & 0 & 0 & S_{44} & 0 & 0 \\ 0 & 0 & 0 & 0 & S_{44} & 0 \\ 0 & 0 & 0 & 0 & 0 & \frac{S_{11}-S_{12}}{2} \end{bmatrix} \quad [d] = \begin{bmatrix} 0 & 0 & d_{31} \\ 0 & 0 & d_{31} \\ 0 & 0 & d_{33} \\ 0 & d_{15} & 0 \\ d_{15} & 0 & 0 \\ 0 & 0 & 0 \end{bmatrix} \quad [\varepsilon^\sigma] = \begin{bmatrix} \varepsilon_{11} & 0 & 0 \\ 0 & \varepsilon_{11} & 0 \\ 0 & 0 & \varepsilon_{33} \end{bmatrix}$$

(EQ 10)

The alternative constitutive formulations may be obtained by considering other potentials. The final linear constitutive relations in compact matrix notation are presented below. The temperature change is assumed negligible and therefore not included in the relations.

$$\{\sigma\} = [C^E]\{\varepsilon\} - [g]\{E\}$$
$$\{\hat{D}\} = [g]^T\{\varepsilon\} + [\varepsilon^\varepsilon]\{E\}$$

or   (EQ 11)

$$\{\sigma\} = [C^D]\{\varepsilon\} - [h]\{\hat{D}\}$$
$$\{E\} = -[h]^T\{\varepsilon\} + [\beta^\varepsilon]\{\hat{D}\}$$

Where,

$$[C^E] = [S^E]^{-1} \qquad [g] = [C^E][d] \qquad [\varepsilon^\varepsilon] = [\varepsilon^\sigma] - [g]^T[d]$$
$$[C^D] = [C^E] + [g][\beta^\varepsilon][g]^T \qquad [h] = [g][\beta^\varepsilon] \qquad [\beta^\varepsilon] = [\varepsilon^\varepsilon]^{-1}$$

(EQ 12)

Eqs. 11 gives alternative forms of linear constitutive relations. The coefficients are related to each other as given by eq. 12.

3• NONLINEAR CONSTITUTIVE EQUATIONS

The strain, electric displacement and entropy are assumed to depend linearly on the stress, electric field and temperature (eq. 6) in deriving eq. 7. Some higher order effects can be brought about by including second order terms in eq. 6, as follows:

$$d\varepsilon_{ij} = \left(\frac{\partial\varepsilon_{ij}}{\partial\sigma_{lm}}\right)_E d\sigma_{lm} + \left(\frac{\partial\varepsilon_{ij}}{\partial E_n}\right)_\sigma dE_n + \frac{1}{2}\left[\left(\frac{\partial^2\varepsilon_{ij}}{\partial\sigma_{lm}\partial\sigma_{pq}}\right)_E d\sigma_{lm}d\sigma_{pq} + \left(\frac{\partial^2\varepsilon_{ij}}{\partial E_n\partial E_r}\right)_\sigma dE_ndE_r + 2\left(\frac{\partial^2\varepsilon_{ij}}{\partial\sigma_{lm}\partial E_n}\right)d\sigma_{lm}dE_n\right]$$

$$dD_k = \left(\frac{\partial D_k}{\partial\sigma_{lm}}\right)_E d\sigma_{lm} + \left(\frac{\partial D_k}{\partial E_n}\right)_\sigma dE_n + \frac{1}{2}\left[\left(\frac{\partial^2 D_k}{\partial\sigma_{lm}\partial\sigma_{pq}}\right)_E d\sigma_{lm}d\sigma_{pq} + \left(\frac{\partial^2 D_k}{\partial E_n\partial E_r}\right)_\sigma dE_ndE_r + 2\left(\frac{\partial^2 D_k}{\partial\sigma_{lm}\partial E_n}\right)d\sigma_{lm}dE_n\right]$$

(EQ 13)

where,

$$S^E_{ijlmpq} = \left(\frac{\partial^2\varepsilon_{ij}}{\partial\sigma_{lm}\partial\sigma_{pq}}\right)_E \qquad d_{ijnr} = \left(\frac{\partial^2\varepsilon_{ij}}{\partial E_n\partial E_r}\right)_\sigma = \left(\frac{\partial^2 D_k}{\partial\sigma_{lm}\partial E_n}\right)$$

$$\kappa_{ijlmn} = \left(\frac{\partial^2\varepsilon_{ij}}{\partial\sigma_{lm}\partial E_n}\right) = \left(\frac{\partial^2 D_k}{\partial\sigma_{lm}\partial\sigma_{pq}}\right)_E \qquad \varepsilon_{knr} = \left(\frac{\partial^2 D_k}{\partial E_n\partial E_r}\right)_\sigma$$

(EQ 14)

are nonlinear elastic compliance coefficients, electrostriction coefficients, elastostriction coefficients and nonlinear dielectric permittivity coefficients, respectively. Integrating equation 13, we obtain,

$$\varepsilon_{ij} = S^E_{ijlm}\sigma_{lm} + d_{ijn}E_n + \frac{1}{2}S^E_{ijlmpq}\sigma_{lm}\sigma_{pq} + \frac{1}{2}d_{ijnr}E_nE_r + \kappa_{ijlmn}\sigma_{lm}E_n$$

$$D_k = d_{klm}\sigma_{lm} + \varepsilon^\sigma_{kn}E_n + \frac{1}{2}\kappa_{klmpq}\sigma_{lm}\sigma_{pq} + \frac{1}{2}\varepsilon_{knr}E_nE_r + d_{klmn}\sigma_{lm}E_n$$

(EQ 15)

Piezoceramics are brittle materials and elastically behave linearly up to the failure. Electrostriction coefficients are important at high electric field strengths. In cases, where mechanical stresses are applied in addition to electric field (piezoceramic is constrained from freely deforming), the elastostriction coefficients should be included in constitutive relations.

We will neglect nonlinear elastic compliance coefficients and nonlinear dielectric permittivity coefficients, and write eqs. (15) in an abbreviated subscript notation.

$$\varepsilon_\alpha = S^E_{\alpha\beta}\sigma_\beta + d_{\beta n}E_n + \frac{1}{2}d_{\alpha nr}E_nE_r + \kappa_{\alpha\beta n}\sigma_\beta E_n$$

$$\hat{D}_k = d_{k\beta}\sigma_\beta + \varepsilon^\sigma_{kn}E_n + \frac{1}{2}\kappa_{k\beta\gamma}\sigma_\beta\sigma_\gamma + d_{k\beta n}\sigma_\beta E_n$$

(EQ 16)

Where greek subscripts take values one to six and others one to three. The electrostriction coefficients and elastostriction coefficients are reduced for a piezoceramic poled in the 3-direction which is also an axis of symmetry. These coefficients are written in abbreviated matrix form in the following equations.

$$[d_{\alpha nr}] = \begin{bmatrix} d_{111} & d_{122} & d_{133} & 0 & 0 & 0 \\ d_{122} & d_{111} & d_{133} & 0 & 0 & 0 \\ d_{133} & d_{133} & d_{333} & 0 & 0 & 0 \\ 0 & 0 & 0 & d_{423} & 0 & 0 \\ 0 & 0 & 0 & 0 & d_{423} & 0 \\ 0 & 0 & 0 & 0 & 0 & \frac{1}{2}(d_{111}-d_{122}) \end{bmatrix}$$

(EQ 17)

$$[\kappa_{\alpha\beta n}] = \begin{bmatrix} \kappa_{111} & \kappa_{121} & \kappa_{131} & 0 & 0 & 0 & \kappa_{121} & \kappa_{121} & \kappa_{132} & 0 & 0 & 0 & \kappa_{131} & \kappa_{132} & \kappa_{133} & 0 & 0 & 0 \\ \kappa_{121} & \kappa_{121} & \kappa_{132} & 0 & 0 & 0 & \kappa_{122} & \kappa_{111} & \kappa_{131} & 0 & 0 & 0 & \kappa_{132} & \kappa_{131} & \kappa_{133} & 0 & 0 & 0 \\ \kappa_{131} & \kappa_{132} & \kappa_{133} & 0 & 0 & 0 & \kappa_{132} & \kappa_{131} & \kappa_{133} & 0 & 0 & 0 & \kappa_{133} & \kappa_{133} & \kappa_{333} & 0 & 0 & 0 \\ 0 & 0 & 0 & \kappa_{441} & 0 & 0 & 0 & 0 & 0 & 0 & 0 & 0 & 0 & 0 & \kappa_{443} & 0 & 0 \\ 0 & 0 & 0 & 0 & 0 & 0 & 0 & 0 & 0 & 0 & \kappa_{441} & 0 & 0 & 0 & 0 & 0 & \kappa_{443} & 0 \\ 0 & 0 & 0 & 0 & 0 & 0 & 0 & 0 & 0 & 0 & 0 & 0 & 0 & 0 & 0 & 0 & 0 & \kappa_{663} \end{bmatrix}$$

(EQ 18)

Similar expressions can be obtained by considering strain and electric field or strain and electric displacement as independent variables. These alternative forms of nonlinear constitutive relations are presented as eqs. 19 and 20.

$$\sigma_{ij} = C^E_{ijlm}\varepsilon_{lm} - g_{ijn}E_n + \frac{1}{2}C^E_{ijlmpq}\varepsilon_{lm}\varepsilon_{pq} - \frac{1}{2}g_{ijnr}E_nE_r - \gamma_{ijlmn}\varepsilon_{lm}E_n$$

$$\hat{D}_k = g_{klm}\varepsilon_{lm} + \varepsilon^\varepsilon_{kn}E_n + \frac{1}{2}\gamma_{klmpq}\varepsilon_{lm}\varepsilon_{pq} + \frac{1}{2}\varepsilon^\varepsilon_{ijnr}E_nE_r + g_{klmn}\varepsilon_{lm}E_n$$

(EQ 19)

$$\sigma_{ij} = C^D_{ijlm}\varepsilon_{lm} - h_{ijn}\hat{D}_n + \frac{1}{2}C^D_{ijlmpq}\varepsilon_{lm}\varepsilon_{pq} - \frac{1}{2}h_{ijnr}\hat{D}_n\hat{D}_r - \tau_{ijlmn}\varepsilon_{lm}\hat{D}_n$$

$$E_k = -h_{klm}\varepsilon_{lm} + \beta^\varepsilon_{kn}\hat{D}_n - \frac{1}{2}\tau_{klmpq}\varepsilon_{lm}\varepsilon_{pq} + \frac{1}{2}\beta^\varepsilon_{knr}\hat{D}_n\hat{D}_r - h_{klmn}\varepsilon_{lm}\hat{D}_n$$

(EQ 20)

Relationships between coefficients given by eq. 12 are not applicable to nonlinear constitutive equations.

4• ACKNOWLEDGEMENT

5• REFERENCES

1. Berlincourt, D.A., Curren, D.R., Jaffe, H., 1964, *Physical Acoustics*, Ed. W.P. Mason, Vol. 1-Part A, (New York: Academic Press).

2. Chen, P.J., Peercy, P.S., 1979, *Acta Mech.*, Vol. 31, No. 3, pp. 231-241.

3. Chen, P.J., 1980, *Int. J. Solids Struct.*, Vol. 16, No. 12, pp 1059-1067.

4. Chen, P.J., Tucker, T.J., 1981, *Acta Mech.*, Vol. 38, No. 3-4, pp. 209-218.

5. Chen, P.J., 1983, *Acts Mech.*, Vol. 47, pp. 95-106.

6. Joshi, S.P., 1991, *Constitutive Laws for Engineering Materials: Recent Advances and Industrial and Infrastructure Applications* (Ed: C.S. Desai, E. Krempl, G. Frantziskonis, H. Saadatmanesh), ASME Press, pp.605-608.

7. Landau, L.D., Lifshitz, E.M., 1960, *Electrodynamics of Continuous Media*, Oxford-London-New York-Paris: Pergamon Press.

8. Mindlin, R.D., 1974, *Int. J. Solids Struct.*, Vol. 10, No. 6, pp. 625-637.

9. Nelson, D.F., 1978, *J. Acoust. Soc. Am.*, Vol. 63, pp. 1738-1748.

10. Nye, J.F., 1964, *Physical Properties of Crystals*, Oxford, Clarendon Press.

11. Penfield, P. Jr. and Hans, H.A., 1967, *Research Monograph, No. 40*, Massachusetts Institute of Technology Press, Cambridge, Massachusetts.

12. Tiersten, H.F., 1981, *J. Acoust. Soc. Am.*, Vol. 70, pp. 1567-1576.

13. Toupin, R.A., 1983, *Int. J. Eng. Sci.*, Vol. 1, pp 101-126.

Intelligent materials for future electronics

K. TAKAHASHI

Department of Electrical and Electronic Engineering
Tokyo Institute of Technology
Ookayama, Meguro-ku, Tokyo, Japan

ABSTRACT

Up to now, electronic devices have been made using materials with given characteristics. In the future, however, materials should be designed to give the desired characteristics to electronic devices. As may be inferred from the widespread use of semiconductors in electronic devices, semiconductors are at present indispensable to the electronics industry. However, if we rely exclusively upon semiconductors, we run the risk of material shortage. Consequently, there is a need for new, alternative materials. Such new materials are already being referred to by a recently coined term, "Intelligent Materials".

There is little hope for finding such intelligent materials in nature. It may, however, be possible to develop them through a kind of "Genetic Engineering in Material Science".

This paper discusses "Intelligent Materials" from the viewpoint of an individual whose experience is in the field of electronics.

1. INTRODUCTION

Descartes remarked that man was a machine-- but one so precise that it moved automatically. With the technological developments of the present century, we are moving beyond the level of precision that Descartes had in mind. But when we speak of the advance of machine-like precision, we are speaking of an advance limited to a few areas of science, and we are thinking in terms of the mechanical ideas of precision, speed, and capacity.

It would seem in this very area of "precision" that man and machine find their greatest difference. Human thinking and behavior are characterized by a certain

"FUZZY".

If one were to ask where this fuzzy originates, the answer could be given in a single word

"INTELLIGENCE".

Intelligence, and not precision, separates men from machines.

Still, this distinction, too, is becoming endangered by scientific progress. We have recently heard talk of "artificial intelligence," "intelligent sensors," "intelligent offices," "intelligent factories," and "intelligent cities." "Intelligence" has taken on a technological meaning and finds its way into an ever-growing number of technical expressions. Below, then, we will consider the concept of "intelligent materials."

What is an intelligent material? A definitive answer is not available. Intelligent materials may be reasonably defined, however, as

MATERIALS WHICH POSSESS CHARACTERISTICS CLOSE TO-- AND, IF POSSIBLE, EXCEEDING--THOSE FOUND IN BIO-MATERIALS.

2. THE TREND IN MATERIALS DEVELOPMENT

Materials development is progressing, and has progressed, along the lines suggested as follows:

STRUCTURAL MATERIALS

FUNCTIONAL MATERIALS

INTELLIGENT MATERIALS

FUZZY MATERIALS.

Until recently, the main demand on materials has been for mechanical strength. The main question regarding building materials, are example, has been whether or not they were strong; similarly, the concern about nylon was whether it was more durable than silk. Materials developed from this perspective may be referred to as "structural materials."

At present, however, demand on materials has come to focus more on their functional characteristics than on their durability. The explosive advancement in computer technology, for example, has been supported by integrated circuits made of silicon. These integrated circuits do not benefit from silicon's mechanical strength, but rather than its electrical characteristics. In other words, silicon is important as a "functional material."

The movement from "structural" to "functional" materials will be extended to "intelligent materials" as we move into the 21st century. Intelligent materials will support the technological progress of the coming century.

3. WHAT ARE INTELLIGENT MATERIALS?

Intelligent materials expand on the qualities hitherto offered by functional materials, incorporating additional functions as follows:

ENVIRONMENT-JUDGE/ADJUST FUNCTIONS

SELF-RESTORATIVE FUNCTION

SELF-DIAGNOSTIC FUNCTION

TIME-DEPENDENT FUNCTION

For example, the ability to judge and adjust to the environment is not absent from conventional functional materials, and many devices have been developed based on this function. The temperature sensors referred to as thermistors are an excellent example. These are based on a material whose resistance increases as the temperature changes--in other words, on a material which can be said to incorporate the ability to judge and adjust to the environment.

The pattern, however, will move to one where materials, such as biological materials, will possess the ability not only to "sense" the environment and change in response to a change in the environment but also to restore themselves. Such materials should be able to repair themselves when broken, or even to diagnose potential problems and generate a warning before difficulty occurs. This function could be referred to as "self-diagnostic".

In addition, there will be efforts to use materials whose particular characteristics are programmed to change over time. Such materials may grow or even multiply. We can refer here to a "time-axial function," analogous to the "metabolic" functioning of biological materials.

Indeed, the organic materials which constitute living organisms ("bio-materials") possess the full range of these functions. "Bio-materials, in fact, would seem to be synonymous with what we think of an intelligent materials.

Biological materials are the most complex of all materials. It is out of such complexity that intelligent functions can become realized.

Silicon, the material supporting so much of today's modern technology, is actually one of the simplest materials. The element itself is not complicated, crystallizes almost perfectly, and creates a product with extremely few impurities. Slightly more complicated is GaAs, the most common of the III-V compounds used for semiconductors. Semiconductors based on III-V compounds, however, cannot yet be perfectly crystallized. With the considerably more complicated II-VI compounds, p-n junctions cannot even be formed at present.

Even more complicated than these materials are amorphous materials and ceramics. Although ceramics have recently received a great deal of attention, application still remains

MORE "ARTISTIC THAN TECHNOLOGICAL".

In other words, the materials that we are presently able to make full use of are only of the simplest types.

As we move into the future, however, it will become possible to plan and control the physical, functional, chemical, and other basic values of the materials we develop. This will allow us to create "intelligent materials" far surpassing the materials in conventional use today.

4. DO INTELLIGENT MATERIALS REALLY EXIST?

The greatest power of bio-materials lies in their time-axial functioning. Indeed, bio-materials regenerate themselves. This is their most important capacity.

Among the more notable of recent materials are shape memory alloys which have the capacity to "remember" shape. It may be through such materials that we will reach intelligent materials with time-axial functioning.

The rusting of metals may be seen, from another viewpoint, as a self-diagnostic function. In addition, when common semiconductors are exposed to radiation, their qualities diminish; the qualities of InP, however, return to their former state following such exposure. This is an example of the "self-restorative" function.

Thus, even present-day materials give us an indication of functioning intelligently. Intelligent materials, therefore, do not appear to be an unrealizable dream.

5. FROM NATURAL-RAW MATERIAL PROCESSING TO MATERIAL DESIGNING

Despite the aforementioned glimpse of intelligent materials, it remains true that natural materials which are not of a biological nature do not offer much promise in themselves. It will therefore be necessary to create new materials.

Materials that have been used up to now have been processed from materials found in nature. IC's and optical fibers, for example, are based on natural silicon or on derived alloys.

Polymers, however, are artificially created, and are thus, as materials, far more useful than the silicon used in electronics. Nylon, for example, which is an artificial substitute for silk, is stronger than silk. Polymers such as nylon may be seen as structural materials (or molecules) designed to meet problems of strength.

The next step will be to design materials which are not structural but rather functional, after which there will be a further move forward to the design of truly intelligent materials. This will require the bringing together of mutually desirable qualities of the component substances, the creation of compound substances out of simple ones, and the performance of material design at the molecular or even atomic level. This process may be referred to as

"GENETIC CONTROL WITHIN MATERIALS SCIENCE," or as

"GENETIC ENGINEERING".

6. GENETIC CONTROL WITHIN MATERIALS SCIENCE

In formulating compound molecules, one method available is through molecular designing. Recently, however, new materials are being created based on atomic designing. This type of designing can be referred to as "genetic control within materials science."

The idea behind genetic control of solids, and in particular of semiconductors, may be divided into the following two tendencies:

1) Even numbered atoms form materials which are insulators, while odd-numbered atoms form conductors.

2) The energy band structure within a solid body is determined by the electric potential cycle structure.

Both of these ideas are based on the band theory, which may be considered this century's most important theory in solid physics.

From the idea of (1) above (and as shown with GaAs), substances not found in nature are being synthesized, and, although they are discontinuous, it is possible to control the forbidden band widths, which are extremely important features of semiconductors. With ternary alloys, it is possible to control forbidden band widths continuously. With quaternary alloys, forbidden bands and lattice constants can be controlled independently.

The first of the ideas above corresponds to the macroscopic combination of host and guest substances in the creation of compound substances.

The second idea suggests that it is possible to form new energy ordering by creating "super-lattices," or artificial lattices. This would be based on the creation of new materials by perfectly controlling both host and guest at the atomic level.

In what is called a super-lattice, a cyclical piling of monatomic layer orderings is used to create a multi-layered structure formed of two (or more) substances.

It is possible to form new electron cycle potentials from such structures. As a result, quantum effects, such as the creation of "minibands" for energy levels, are produced. By making use of such "minibands," the forbidden bands, which are so important to electronic devices, can be freely controlled.

The new electronic potentials achieved through super-lattices show Brillouin zone folding effects. As a result, indirect transition semiconductors can be made to become direct transition semiconductors; optical absorption coefficients can be increased; and the degree of freedom in designing photoelectronic materials can thereby be expanded.

Further, the energy band structure, which is based on the momentum space, is changed as a result of the Brillouin zone reducing effect. Electron effective mass, and, in turn, the mobility, become controllable. If the degree of movement can be increased, the response time of semiconductor devices can be improved.

One of the possibilities brought about by such super-lattices would seem to be high-temperature superconductors. The mechanism of ceramics-based superconductors, which have received so much attention, is not yet clear, but could have something in common with high-temperature, super-lattice based conductors. That is to say, the two-dimensional conduction in the super-lattice based interface may also occur at the interface of ceramics particles. If high temperature superconductors become possible, SQUID-type devices operating at room temperatures may begin to appear.

In this context, one might consider that migratory birds, after flying half-way around the world, faultlessly find their way back to where they started. This ability is said to be related to magnetic perception. It has also been said that such birds possess SQUID-type magnetic sensors. This would mean that these birds already possess superconductors which function at normal environmental temperatures.

With super-lattices, physical constants no longer need to be inherent to particular materials, but could be controlled at will. Thus, super-lattices may be the key to the "genetic control" of materials.

7. THE FUTURE OF GENETIC CONTROL

The type of thinking outlined above may create the illusion that, with super-lattices, virtually anything can be created. Such an idea would be based on a very large premise--namely, that electronic potentials can, in fact, be controlled at will. Only if such control can be realized, would free creation become possible.

Today, it is only possible to achieve multi-layered structures between two semiconductors. Full control of electronic potentials will be possible only when various multilayers can be created from mono-atomic layer ordering.

There are actually an infinite number of combinations. Besides semiconductors, these include combinations of conductors and insulators, inorganic materials and organic materials, crystalline structures and non-crystalline structures, as well as three-kinds combination, four-kinds combination, etc.

Furthermore, while today's super-lattices are oriented along only one dimension, ultimately it will be necessary to create three-dimensionally oriented structures. At the present stage, efforts are slowly moving ahead in the formation of two-dimensional types. There is not yet a clue, however, as to how to create three-dimensional super-lattices.

9. FROM MAN-MADE LATTICES TO MAN-MADE ATOMS

With a three-dimensional super-lattice, the one-dimensional square well potentials would be formed in three dimensions, so that the sub-bands would also be formed in three dimensions. Such a three-dimensional sub-band corresponds precisely with the orbital energy for hydrogen. This means that it would be possible to design atomic orbital energies at will. This would correspond to the free creation of atoms.

"ARTIFICIAL ATOMS,"

in other words, could be created.

From a different perspective, we might categories superfine powders as "artificial atoms." In this regard we may to the three conventionally accepted states of matter--"solid," "liquid," and "gas"--add a fourth: "powder." Ceramics, which at present are of considerable interest, are based on sintered powder. At the moment, therefore, ceramics might be seen as a natural arrangement of artificial atoms. So long as this arrangement remains "natural," ceramics will remain in the realm of "art." When it becomes possible to achieve artificial arrangements, ceramics will move into the realm of science

When artificial atoms of all sorts can be freely arranged in three dimensions, the creation of intelligent materials will become a true possibility.

10. THE MERGING OF MATERIALS, DEVICES, AND SYSTEMS

When it becomes possible to freely design and create materials at the atomic level, the categorizing of materials into various groups--metals, insulators, organic or inorganic matter, complex atoms, bio-materials, etc.--will lose its meaning.

In exactly the same way, when it becomes possible to make free three-dimensional atomic arrangements, it will also be possible to fabricate intelligent materials. It will then no longer be possible, nor desirable, to distinguish between "materials" and "devices."

One result will be that systems themselves will move toward true integration. At present, for example, integrated circuits are in fact only a wired arrangement of discrete devices. Today's electronic devices are discrete and are capable of processing only electronic signals. They are, in other words, electric-based systems.

If we think in terms of systems, we may think of the following division:

1) Electric systems
2) Mechanical systems
3) Energy systems

Present-day devices are all too clearly delineated along these lines. Integrated circuits are electrical systems, for example, while motors are mechanical systems. The true union of such systems is something to be hoped for in the future.

Cells--the basic units of life--seem monolithically to unite all three of the above systems. In the future, we should move first to create integrated systems that incorporate mechanical systems, and then to those which incorporate energy systems.

At present, it is not possible to incorporate energy itself directly into systems. Batteries or other electrical sources must be attached. The light-induced electric power effect and the Seebeck effect are being considered as possible ways of introducing energy into systems. Ultimately, it may be possible to fully utilize the principle of relativity that "mass is energy."

One hopes that, with the appearance of intelligent materials, monolithic integrated systems will begin to become a reality.

With the appearance of intelligent materials, it will become impossible to distinguish among materials, devices, and systems, and the borders separating these will become vague. We may consider this as a move away from the digital to the analog. This "FUZZY" will be the basis for "intelligence."

II. CONCLUSION

It is not yet possible to design intelligent materials. Such materials are, therefore, being borrowed directly from living materials and are being used to make bio-sensors and in efforts to make bio-chips that can serve as computer elements. Because it is necessary to keep these bio-materials alive, there are considerable limits to this approach. In the future, it may be possible to create devices which need not be kept alive but which will meet or surpass those found in life. In order to achieve this, however, it will be necessary to develop intelligent materials.

Perhaps we need not stop at materials which incorporate merely "intelligence." Perhaps one day we may develop materials which incorporate true "wisdom." Or perhaps, again, this would be blasphemous.

Applications of piezoelectric ceramics in smart actuators and systems

KENJI UCHINO
Materials Research Laboratory
The Pennsylvania State University
University Park, PA 16802-4801

Permanent Address:
Department of Physics
Sophia University, Kioi-cho 7-1
Chiyoda-ku, Tokyo 102
JAPAN

In these several years piezoelectric and electrostrictive actuators have become very popular for micro-positioning in optical and precision machinery fields.[1] Aiming at wide commercialization of these actuators, many investigations have been made in the improvement of ceramic materials for actuators, designs of the devices and control and systematization of the actuators.   This paper reviews recent applications of piezoelectric/electrostrictive ceramics from a viewpoint of "smart" actuators and systems.

A passively smart material is exemplified by the lead magnesium niobate (PMN) based ceramic, which can exhibit a large electrostriction ($\Delta l/l \sim 10^{-3}$) without any hysteresis and aging effect during an electric field cycle.[2] A composite actuator structure called "moonie" has been developed to amplify the small displacement induced in a multilayer piezoelectric device. Passive damper application is another smart usage of piezoelectrics, where mechanical noise vibration is radically suppressed by the converted electric energy dissipation through Joule heat when a suitable resistance is connected to the piezoelectric plate.[3] Piezoceramic: carbon black: polymer composites are promising useful designs for practical use.

An actively smart material is exemplified by the video tape head positioner made from a lead zirconate titanate (PZT) bimorph with sensor and actuator-divided electrodes.[4]

Monomorphs and shape memory ceramics belong to very smart materials. A monomorph device made of a semiconductive piezoelectric plate generates the Schottky barrier when metal electrodes are coated on the faces, providing non-uniform distribution of the electric field even in a compositionally uniform ceramic. A superimposed effect of piezoelectricity and semiconductivity leads to a bending deformation in a total ceramic plate.[5] The strains associated with phase transitions such as an antiferroelectric-to-ferroelectric transition in lead zirconate stanate-based ceramics reach up to 0.4%, which is much larger than that expected in electrostrictors. Moreover, this field-induced transition exhibits a shape memory effect in appropriate compositions, and such ceramics are useful for the applications to latching relay and a mechanical damper.[6]

A photostrictive actuator is the best example of intelligent materials including sensing, actuating and drive/control functions in a unique material.[7] In certain ferroelectrics a phenomenon in by which a constant electromotive force is generated with exposure of light has been observed A photostrictive effect is expected as a result of the coupling of the photovoltaic and inverse piezoelectric effects A remote control miniature walking robot, which is activated with illumination, is currently being fabricated. Two photostrictive PLZT bimorphs were combined together and each plate exhibits a minute photo-induced displacement on the order of 150 µm. Alternative illumination causes a slow moving of the ceramic device.

A flight actuator consisting of a pulse-driven piezoelectric element and a steel ball is a very suggestive mechanism, even if it would not be denoted as a smart system. A 2mm steel ball can be hit up to 20 mm by a 5 µm displacement induced in a multilayer actuator with quick response.[8]

A smart system is typically exemplified by a precision lathe machine. A micro displacement actuator has been manufactured using an electrostrictive multilayer actuator, a magneto-resistive strain sensor and an adaptive control circuitry. The feedback control has suppressed the position deviation of the cutting edge when pushing stress is produced during cutting process. The cutting accuracy in less than ±0.01 µm is now available.

A very smart system contains a reliability test system, which can stop an actuator system safely without causing any serious damages on to the work, e.g. in a lather machine. Acoustic emission measurement of a piezo-actuator under a cyclic electric field is a good candidate for estimating the life time of the actuators.[9]

The bright future of piezoelectric/electrostrictive actuators has been initiated and even greater commercial participation in their continued growth and application is anticipated.

REFERENCES

1.   K. Uchino, Piezoelectric/Electrostrictive Actuators, Morikita Pub. Co., Japan (1986).

2.   L. E. Cross, S. J. Jang, R. E. Newnham, S. Nomura and K. Uchino, Ferroelectrics 23, 187 (1980).

3.   K. Uchino and T. Ishii, J. Ceram. Soc. Jpn. 96, 863 (1988).

4.   A. Ohgoshi and S. Nishigaki, Ceramic Data Book '81, Industrial Products Tech. Assoc., Japan, p. 35 (1981).

5.   K. Uchino, M. Yoshizaki, K. Kasai, H. Yamamura, N. Sakai and H. Asakura, Jpn. J. Appl. Phys. 26, 1046 (1987).

6.   K. Uchino, Proc. MRS Int'l. Mtg. on Adv. Mats. 9, 489 (1989).

7.   M. Tanimura and K. Uchino, Sensors and Mater. 1, 47 (1988).

8.   S. Sugiyama and K. Uchino, Proc. 6th IEEE Int'l Symp. Appl. Ferroelectrics, p. 637 (1986).

9.   T. Hirose and K. Uchino, Ferroelectrics 87, 295 (1988).

The mace active member

Warren Hoskins and Lee Klynn, LMSC, Inc
David Miller, Space Engineering Research Center, MIT
Javier de Luis, Payload Systems, Inc

ABSTRACT

This paper covers the derivation of requirements, characterization of the active member as a component and its effect on the system level performance. The disturbance levels are established by the top level requirement to attenuate the vibration by 40 db while being 20 db above the sensor noise floor level. By integrating the active member into the broad band pointing test simulation the moment requirement is established. The active member provides a small amount of pointing error attenuation and introduces about 2% modal damping. The actuator sizing equations and trade study is presented.

1.0 INTRODUCTION

The MACE program (Mid-deck Active Control Experiment) is a flight experiment conducted in the shirt sleeve environment of the mid-deck of the Shuttle sponsored by NASA LaRC and designed by the Space Engineering Research Center at MIT with PSI as subcontractor and LMSC as a corporate sponsor. MACE is scheduled to fly in 1994. The objectives of MACE are to validate the modeling tools associated with flexible body dynamics and active structural control and to examine issues associated with non-zero gravity ground testing. The approach is to design a small flexible testbed (2 Hz) and perform a set of experiments which captures the essential physics of large precision spacecraft structures. The testbed consists of a multi-segmented beam, a torque wheel for attitude control, and an active member for vibration suppression/damping. Attached to both ends are two axes gimbals which point rigid payloads (see Figure 1). A series of experiments are planned: the first experiment is an on-orbit system identification test. Space and ground test results will be compared and system gains will be updated. The second experiment is a pointing test using the torque wheels for broad band disturbance. The active member inconjunction with the gimbal maintains payload pointing. The third experiment is a pointing test of one payload while slewing the other payload.

2.0 DESIGN REQUIREMENTS

The top level requirement is to attenuate the vibrations by two orders of magnitude (40 db) as measured by the pointing error of Payload 2 (PL2). The performance threshold has not been established but will be set at the resolution capability of the sensor. For the purposes of this study the performance level was determined from the Sample Problem as described in Reference 1. With both payloads locked in place and a white random moment disturbance of 0.0015 newton-meters squared per Hertz intensity applied at Payload 1 (PL1), the pointing error of PL2 was computed. The finite element model with its dynamical characteristics is

shown in Figure 1 . The pointing error response of PL2 is shown in Figure 2. As can be seen from the running RMS error (24 milli-rad), nearly all the error is attributable to the first three modes. This establishes the top level error which is to be attenuated by a factor of 100. For this experiment the active member is responsible for attenuating only a small portion of the error and the remaining error is divided between the torque wheel assembly and PL2 gimbal as shown in Figure 3. Normally an error tree shows the flow down of residual error of all the elements that contribute to the performance; however, this figure shows which actuators are responsible for pointing error cancellation and the amount of error cancellation.

(a) MACE Testbed

NO	FREQ (HZ)	DAMP (%)
1	1.37	0.4
2	4.48	0.4
3	6.61	0.4
4	11.65	0.4
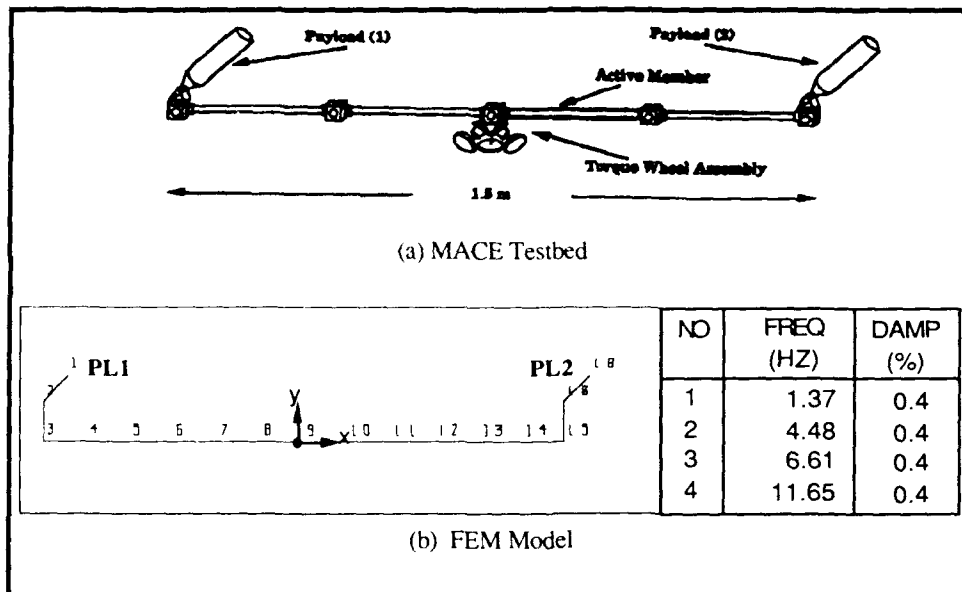
(b) FEM Model

Figure 1 MACE Testbed and FEM Model
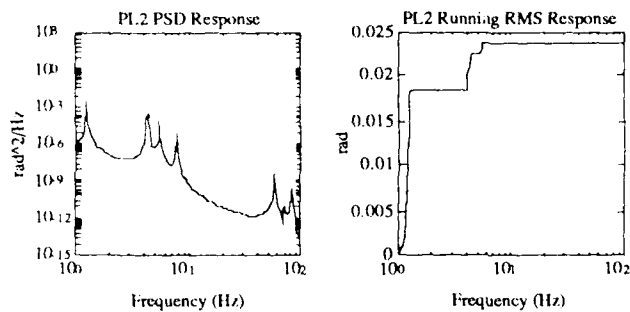
Figure 2 PL2 Random Response Due To PL1 Disturbance
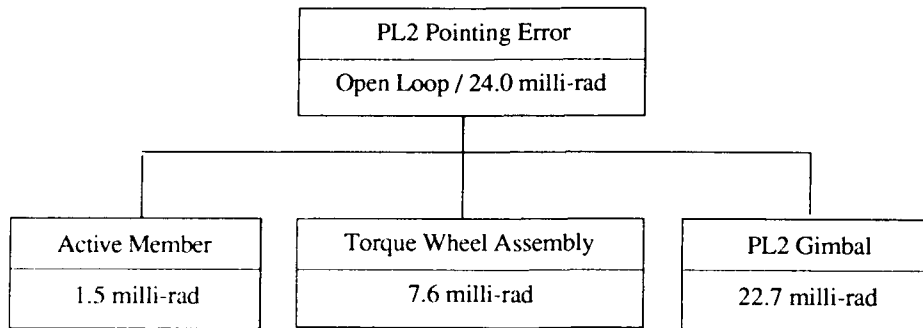
Figure 3 Pointing Error Flow Down

To determine the effectiveness of the active member on the pointing error, an uniform random couple of intensity 10×10^{-6} NM^2/rad per sec was applied to two nodes: to the center node and in the opposite direction to the node toward PL1. The resulting pointing error of PL2 is shown in Figure 4 (1.5 milli rad) where the active member has only a small influence on the pointing error. Thus the active member should be able to handle its allocated error if an actuator can be built that produces the required moment. Using a three sigma estimate for the peak moment, the PZT (lead zirconate titanate) actuator is required to produce a moment of 0.240 newton-meters.
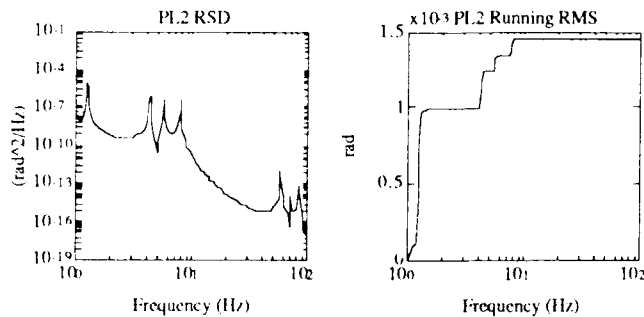
Figure 4 PL2 Random Response Due To Active Strut

3.0 ACTIVE MEMBER DESIGN

In recent years the piezoelectric actuator technology (Ref 2-8) has evolved to a maturity capable of supporting a design activity. Several research efforts have validated that using simple strength of materials approach provide reasonable estimates of the actuator performance. By applying standard design factors to the equations adequate margins can be

guaranteed. Review of this database indicates that the actuator can be designed to meet the requirements.

The active member consists of a lexan tube which is one inch in diameter and about one foot in length and represents one of the four segments. This tube is thicker than the other tubes and is machined flat on all four sides producing an equivalent stiffness to the other four members (see Fig. 5). A piezo ceramic (PZT-G-1195) thin sheet is epoxied to all four machined sides along the full length. On one side the PZT is energized positively causing a tensile strain while on the opposite side the PZT is energized negatively causing a compressive strain. In this way a pure moment is induced along its length which can be represented with two end moments in opposite directions. With the PZT actuator attached to all four sides control is provided in both axes. This active member is used to provide modal control and active damping over the bandwidth of the disturbance.
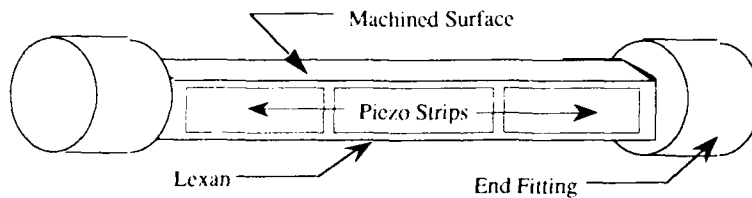
Figure 5 MACE Active Member

The design equation is:

$$M_a = \frac{(EA)_a \, b_s \, d_{31} \, V_{31}}{1 + Y_b} \quad \text{where:} \quad Y_b = \frac{b_s^2 \, (EA)_a}{2 \, (EI)_s}$$

The geometry associated with the actuator segment only is depicted in Figure 6. The "s" subscript refers to the lexan strut and the "a" subscript refers to the piezo actuator. The piezoelectric constant d_{31} relates the strain to applied field and V_3 is the applied field. The outer fiber distance for the lexan strut is b_s. The $(EA)_a$ and $(EI)_s$ are the stiffness associated with the actuator and strut. The derivation of this equation is obtained by allowing the actuator strips and lexan tube expand/contract freely and then apply the plane sections remain plane constraint. A sensitivity study was performed to determine an optimum choice of parameters. The principle quantity is the moment (M_a) that the actuator can generate and the principle parameter is the thickness of the actuator coupled with the applied voltage. The moment is maximum by having a very stiff strut so that the stiffness ratio, Y_b, goes to zero. The $(EI)_s$ is of the same order of magnitude as $b_s^2 \, (EA)_a$ and limits the induced moment the actuator can generate.

E_a	Modulus	6.3×10^{10} pascals
t_a	Thickness	Variable (meters)
L_a	Length	0.203 meters
W_a	Width	2.54 cm
EI_s	Stiffness	32.2 pasals-meters^4
b_s	Width	2.54 cm
d_{31}	Constant	166×10^{-12} strain/volt*
V_3	Field	$400/t_a$ volts/m

* See Reference 9
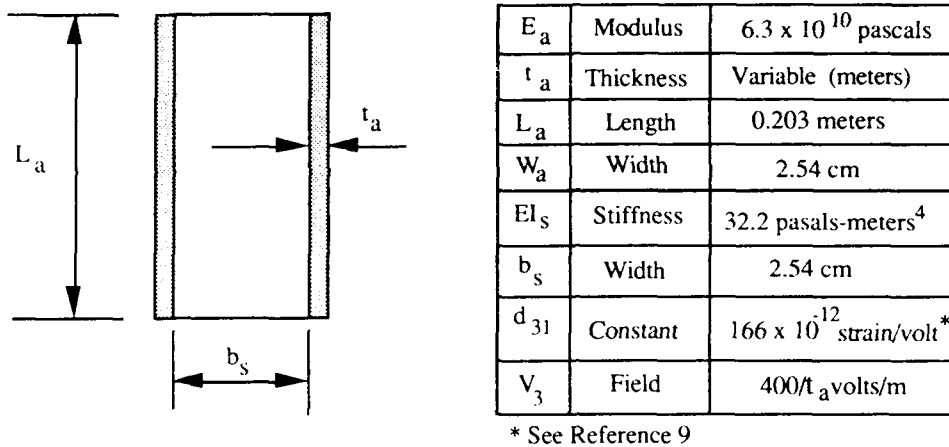
Figure 6 Actuator Geometry and Parameters

Figure 7 demonstrates how the actuator moment is affected by the actuator thickness while using the values for the other parameters as shown in Figure 6. A conservative moment is achieved using an upper voltage value of 400 volts to insure that the actuator is not saturated or depoled. In addition, the design equation assumes a 100% moment transfer while there are some losses due to the epoxy adhesive. By selecting an actuator thickness of 0.254 mm an induced moment of 0.5 newton-meter can be achieved while allowing for transfer loss and possible 4 sigma peaks. Thus this design meets the requirement of 0.24 newton-meter peak induced moment.
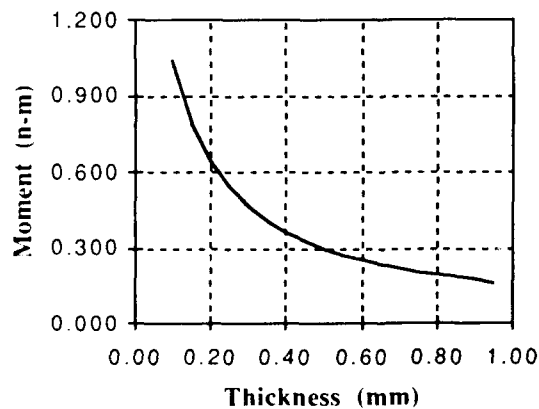
Figure 7 Actuator Induced Moment

The next step is to fabricate the active member and then to characterize its performance. Four tests are contemplated: (1) energize cantilever strut and measure the tip displacements and rotations over the spectrum of interest; (2) constrain both strut ends and measure the loads generated; (3) place the active strut in the MACE testbed, apply an uniform random signal to the actuator and then measure the PL2 pointing error; and (4) excite PL1 gimbal, close an active damping loop and measure the effective damping.

4.0 CONCLUSIONS

The active member for the MACE testbed is designed to provide the high precision control while introducing active damping. The next step is to assemble and characterize the active strut over the frequency spectrum.

5.0 ACKNOWLEDGMENTS

6.0 REFERENCES

1. Mercadal, Mathieu, "Sample Problem I: Sensor And Actuator Selection, Sensor And Actuator Pairing", SERC #6-91-R, Space Engineering Research Center, MIT, June 1991.

2. Swigert, Charles and Forward, Robert, "Electronic Damping of Orthogonal Bending Modes in a Cylindrical Mast - Theory", J. Spacecraft Vol 18, No.1, Jan.- Feb 1981.

3. Forward, Robert, "Electronic Damping of Orthogonal Bending Modes in a Cylinder Mast - Experiment", J. Spacecraft Vol 18, No. 1, Jan.-Feb. 1981.

4. Crawley, Edward and de Luis Javier, "Use of Piezoelectric Actuators as Elements of Intelligent Structures", AIAA Journal, Vol 25, No. 10, October 1987.

5. Crawley, Edward and Anderson, Eric, "Detailed Models of Piezoceramic Actuation of Beams", AIAA Paper B9-1388-CP, 1989.

6. Freymann, Raymond and Stumper, Edmond, "Active Damping of a Large Lightweight Structure using Piezoelectric Sensors and Actuators", Proceedings of SDM, April 1991, pp 2852-2864.

7. Bronowicki, A.J., Mendenhall, T.L., Betros, R.S., Wyse, R.E., Innis, J.W., "ACESA Structural Control System Design", First Joint US/Japan Conference on Adaptive Structures, November 1990.

8. Fanson, J.L., Chu, C-C., Lurie, B.J., Smith, R.S., "Damping And Structural Control Of THe JPL Phase 0 Testbed Structure", First Joint US/Japan Conference on Adaptive Structures, November 1990.

9. Piezo Systems, Inc., Company Literature, Cambridge, Mass. 1991.

Neural control of smart electromagnetic structures

Michael Thursby, Kisuck Yoo and Barry Grossman
Department of Electrical and Computer Engineering
Florida Institute of Technology,Melbourne, Fl 32901
Tele (407) 768-8000 X6160 EMail mthursby@zach.fit.edu

Abstract

We are studying a new class of smart structures-smart electromagnetic structures(SEMS). These structures are "smart" in that they integrate sensing elements (e.g.,antennas), processing elements (neural networks) and control elements(diodes) in a manner not previously considered. Smart Electromagnetic Structures(SEMS) have the potential to provide an adaptive electromagnetic(EM) environment to the structure on which they can be mounted. Based on their sensing capabilities they may be able to detect and modify the EM fields around them as well as their far field image. The ability to adapt derives from the closed loop nature of the SEMS, hence the speed of adaptation is determined by the speed of the loop. Factors including bandwidth of the control structure do influence the speed of the system. The speed of the response is primarily determined by the technology of the computational elements. The implementation we are studying includes an Artificial Neural Network(ANN) as the processor. The neural net can respond in no more than three gate delays for each iteration of the loop. We have found that the network takes from three to five iterations of the loop to complete its control task. This results in a total time for system response of less than fifteen gate delays.

Artificial neural networks(ANNs) and their ability to model and control dynamical systems for smart structures, including sensors, actuators, and plants, are directly applicable to the SEMS concept. By incorporating a neural network into the control structure of a single microstrip patch element its electrical characteristics can be changed in response to a received signal. This change can be used to alter the antenna's performance in real time.

The Neural Net Antenna

The micropatch antenna has many advantages including simplicity and size, and a few drawbacks, e.g., narrow bandwidth. The electrical characteristics of the antenna can be adjusted using control elements embedded in the patch itself. We will describe research being carried out in the Autonomous Systems Laboratory(ASL) of Florida Institute of Technology(FIT) into the control of such patch antenna elements using a neural network (NN) in the feed back loop to enhance the operating characteristics of the The neural net can make the required determinations in near real time. The ability of the net to adapt to unknown inputs (generalization) and its fault tolerance makes the neural antenna an ideal candidate for flexible tactical antennas for the future. The combination of a simple neural network with a microstrip patch antenna is shown in Figure 1.
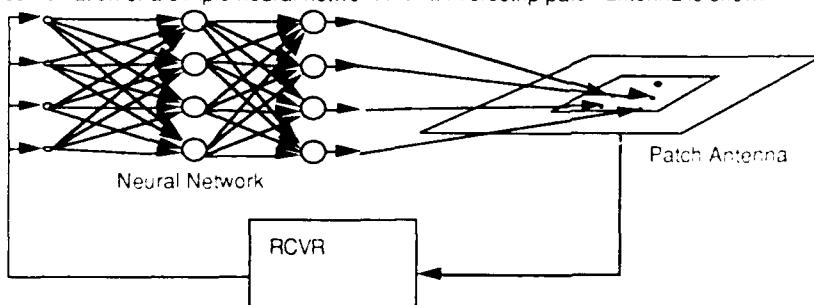
Figure 1. The microwave patch antenna with tuning points and a neural network to drive the points can be considered a smart antenna structure.

The patch neural network antenna system has been developed and this analytical model as well as experimental models of the antenna are being tested and compared. The model and prototypes are being taught to adapt to the magnitude and phase response of incoming signals.

In order to test the ability of such a system to tune to the frequency of incoming signals a series of experiments were conducted on the trained simulation of the neural antenna system. The ability of the neural antenna to follow the center frequency of incoming signals with time

varying frequency characteristics will be presented. Experiments requiring the network to tune the antenna in a stepped frequency environment. The ability of the antenna to follow a continuously varying frequency signal will also be presented. We demonstrate that the patch can be given autonomous adaptive capabilities using neural networks.

Several applications for such an antenna can be postulated. First such an device would improve receiver characteristics in a frequency agile environment. The adaptability of the neural antenna would reduce the manufacturing and siting tolerance requirements normally placed on such conformal antennas. An array of such smart patches could be assembled to create an even more adaptable antenna system.

Acknowledgements

Multicomputer networks for smart structures

Scott F. Midkiff and John T. McHenry

Bradley Department of Electrical Engineering
Virginia Polytechnic Institute & State University, Blacksburg, Virginia 24061

ABSTRACT: This paper discusses the use of multicomputers to meet the high data throughput and real-time computational requirements of smart structures. The mapping of neural network computational models onto multicomputer networks is presented as an example.

1. INTRODUCTION

Smart structures require the integration of a number of technologies including structures, materials, sensors, control, and actuators. Given the advances in technologies for composite materials and fiber optic sensing, there is now motivation to better understand system-level issues for smart structures. This paper examines the processing capabilities that must be a key component of smart structures and, specifically, the use of multicomputer networks. The paper first describes multicomputers and discusses processing requirements for smart structures. The paper then explains how multicomputers can be used to fulfill those needs. As an application example, the implementation of neural network computations using a multicomputer is discussed. The paper concludes with a discussion of a three-node test network designed and implemented at Virginia Tech to examine computing and communication issues for smart structures.

2. MULTICOMPUTER NETWORKS

Multicomputers, or distributed memory computers, are a type of parallel processing system consisting of multiple processing nodes interconnected by a communications network. Each processing node in a multicomputer has memory, computing resources, and interprocessor communication facilities. The computing resources are used to perform the processing assigned to the node. The memory stores both program and data. The communications facilities access the interconnection network and support other input and output operations. A multicomputer contains no shared memory.

Data and other information is shared between tasks executing on different processing nodes via the interconnection network. Communication is particularly important to the overall performance of a multicomputer. Communication performance in a multicomputer de-

pends on four general factors: (1) link and protocol speed, (2) node speed, (3) traffic characteristics, and (4) interconnection network topology.

In general, topologies may consist of either point-to-point links or shared busses and may be either general-purpose or application-specific. General-purpose topologies provide small average and worst-case distances between nodes, and thus minimize the number of links that must be traversed for a variety of different traffic patterns. Application- specific topologies match the communication patterns of a particular application.

3. PROCESSING REQUIREMENTS FOR SMART STRUCTURES

Processing and data communication are required in a smart structure to acquire and condition signals from one or more sensors, process sensor data, and, based on system state, control actuators and or indicate failures. These tasks can be partitioned functionally and physically. With functional partitioning, different types of tasks are computed separately. Physical partitioning uses separate tasks for different regions of the structure. Data communication is needed to acquire sensor data, transfer the data to one or more processing elements, and send outputs to actuators or indicators. In addition, if tasks are partitioned, interprocessor communication is needed to coordinate and share information among tasks executing on different processors. The computation and communication must be performed in real-time. Real-time performance is more than just fast computing, rather it implies that operations are correct only if the results are valid and the time at which the results are produced meets all timing constraints (Stankovic 1988).

The physical characteristics of smart structures place unique constraints on the design of the processing system. The shape of the structure influences physical partitioning and limits the topology of the communications network. Additional physical design issues include the need to embed components in materials, size and weight limits, and power distribution and consumption.

For some smart structures, it is essential that the processing system be modular and scalable. A modular and scalable processing system allows the structure to be constructed incrementally, expanded after initial deployment, and easily repaired. In addition, pieces of the system can be tested independently before and during operation.

4. MULTICOMPUTER NETWORKS FOR SMART STRUCTURES

Multicomputers have a number of attractive features for smart structures. Multicomputers allow concurrent processing and high-speed data transfer needed for real-time operation. The network topology can be adapted to the physical topology of the structure and to the traffic patterns of specific algorithms. Finally, multicomputers are modular and scalable; the nodes provide modularity and a system can be grown by adding nodes and links. However, if a multicomputer is to meet the requirements of smart structures, it is necessary to address the design of processing nodes and the interconnection network within an application-specific context including the contributions the sensors, actuators, and control algorithms.

In a smart structure, sensor data acquisition and signal processing, local control functions, and actuator control operations map naturally onto individual multicomputer nodes, as shown in Figure 1. The integration of *sensor and actuator interfaces with single-chip* processing nodes must be addressed for smart structure applications. It is also conceivable that processing nodes can be embedded in the material of a smart structure, and thus be located near sensors and actuators. Alternatively, nodes can be interfaced to sensors and actuators along structure boundaries.

The design of an interconnection network for a smart structure involves three primary issues: (1) the network topology should support the application's communication pattern, (2) links must be fast, reliable, and testable, and (3) protocols must provide predictable delays and high throughput.

Optical communication links offer a number of benefits for smart structures, including high bandwidth, immunity to electromagnetic interference, and the potential for hybrid sensing and communication. In addition, optical links provide the opportunity to exploit hybrid sensing and communication, i.e. performing both sensing and communication on single fibers, as described by McHenry et al. (1991).

An application-specific topology may exploit task partitioning. For example, a hierarchy of interconnected nodes can be envisioned. At the lowest level, local control or health monitoring functions are performed at each node, while at the highest level, global functions provide control of failure detection for the entire structure.

5 EXAMPLE NEURAL NETWORK IMPLEMENTATION

The neural network or connectionist paradigm is a candidate model for computations in smart structures. Grossman et al. (1990) propose a neural network that receives sensor data as input and drives actuators with outputs. Ghosh and Hwang (1988) show that the inherent parallelism and distributed state in a neural network allow it to be effectively realized by a multicomputer network. The use of a multicomputer for neural network
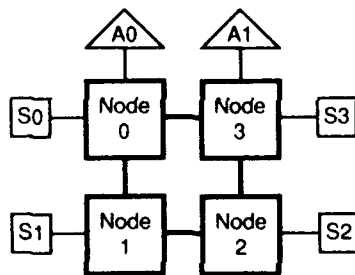
Fig. 1 Multicomputer network
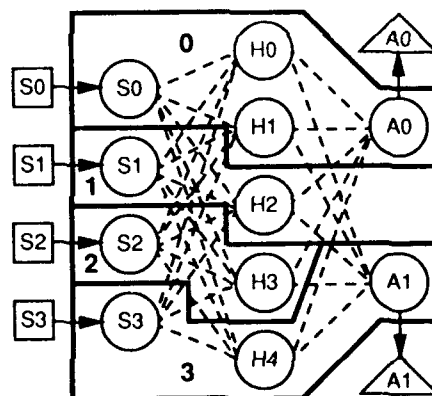
Fig. 2. Neural network example

paradigms is particularly attractive for applications where different levels of processing are needed in addition to neural network operations and timing constraints do not dictate the use of dedicated neural network hardware. For example, signal processing functions that condition sensor outputs, neural network operations to determine local actuator outputs, and system-wide coordination tasks can all be implemented by a multicomputer.

To illustrate a multicomputer implementation of a neural network computation, consider the simple neural network of Figure 2 with four input layer cells (denoted by S) receiving sensor inputs, two output layer cells (A) driving actuators, and five hidden layer cells (H). Figure 2 indicates a mapping of the eleven neural network cells onto the four multicomputer nodes of Figure 1. For this mapping, multicomputer node 0 computes S0, H0, H1, and A0; node 1 computes S1 and H2; node 2 computes S2 and H3; and node 3 computes S3, H4, and A1. This mapping is one of several that are optimal assuming time division multiplexing of nodes and links, bidirectional links, and synchronous operation. The time for one iteration must include four computation cycles, with node 0 being the bottleneck since it implements two hidden layer cells, and four communication cycles, two to move input layer outputs to hidden layer cells and two to move hidden layer outputs to output layer cells.

6. CURRENT WORK

Experimental investigation of multicomputer networks for real-time computation and communication in smart structures is currently underway at Virginia Tech (McHenry et al 1991). A three-node test bed has been created to study the integration of computing, communication, control, and optical sensing. Nodes are personal computers connected by a fiber optic MIL-STD-1773 bus. Wavelength division multiplexing is used to incorporate intensity-based sensing on the same fiber used to carry data. A multicomputer for actual use in a smart structure could be implemented using much simpler and more compact nodes and a different network structure might be advantageous.

7. ACKNOWLEDGEMENTS

8. REFERENCES

Ghosh J and Hwang K 1988 *Proc. Int. Symp. Computer Arch.* (Washington: IEEE Computer Society) pp 3-11

Grossman B, Hou H, Nassar R, Ren A and Thursby M 1990 *Fiber Optic Smart Structures and Skins III* ed E Udd and R O Claus (Bellingham, WA: SPIE) pp 205-211

McHenry J F, Midkiff S F, Wiencko J A and Reed T W 1991 *Proc. Fiber Optic Sensor-Based Smart Materials and Structures Work.* (Lancaster, PA: Technomic Publishing)

Stankovic J A 1988 *Computer* **21** 10

Neural network/knowledge based systems for smart structures

J M Mazzu, S M Allen, and A K Caglayan

Charles River Analytics, 55 Wheeler Street, Cambridge, MA 02138

ABSTRACT: Presented is a design approach for intelligent structural monitoring systems, which consists of integrating artificial neural networks (ANNs) and knowledge based expert systems (KBs) to achieve maximum benefits from both. This approach is based on an object oriented class hierarchy where the ANN classes are determined from structural CAD models. Using finite element strain distributions, classes of ANNs are trained to estimate undamaged structural strain measurements based on each sensor's spatial neighborhood. The KBs evaluate the estimates to detect sensor failures, isolate structural damage, and perform damage assessments.

1. INTRODUCTION

A smart aerospace structure is defined as a structure instrumented with arrays of sensors, computers and actuators that monitor its load environment and structural integrity throughout its life and take corrective action where required (Jaeger and Rogers 1988, Wada and Fanson 1990). In analogy with living organisms, the sensor arrays will play the role of the nervous system, a computer architecture will play the role of the brain, and actuators will play the role of muscles (Gerardi 1990). Here, a hybrid ANN/KB system serves as the "brain" which relies on fiber-optic and/or conventional strain gauge sensors to detect and isolate structural damage while providing assessments for reconfiguration (Mazzu, Caglayan and Allen 1991).

The primary development objective is to use the complementary capabilities of neural networks and expert systems within appropriate tasks and to determine integration strategies for creating structural monitoring systems. The smart structures system development takes place within the in-house developed *NueX* ™ Hybrid Environment (Mazzu, Caglayan and Jonas 1991). Within this system, shown in Figure 1, ANN input and output nodes are represented as objects within the knowledge base, thereby supporting the inheritance of structural information. The executive controller for the smart structures system is handled by a specialized KB; *NueX* ™ allows the executive KB to directly pass information to and from the ANNs. Structural information regarding geometry and sensor locations is stored within an object oriented structural KB, which also performs structural reasoning on the relationships between sensor locations and critical aircraft components. *NueX* ™ automatically maps the

CAD structural representations into KB objects. Failure Detection and Isolation (FDI) is accomplished by both ANNs and KBs. The results from the FDI are evaluated within the Damage Assessor (DA), which also includes ANNs and KBs. The DA is responsible for determining the structural residual strength and the effects of damage on critical components such as hydraulic lines.
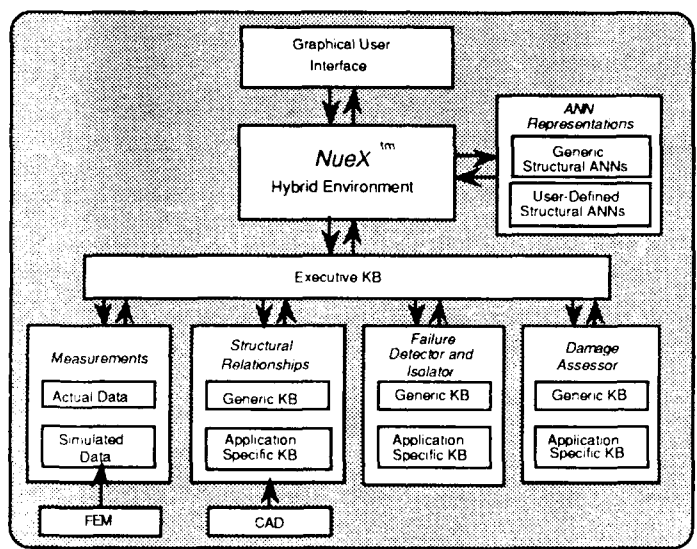
Fig. 1. Hybrid Smart Structures System

2. FDI NEURAL NETWORKS

In our hybrid smart structures methodology, ANN development is accomplished using a structural class based approach. Typically for large aircraft structures, finite element models are only available for specific critical locations, hence it is desirable to minimize the need for further analyses. Therefore, a variety of general structure classes are defined such that the majority of the structure is represented; finite element models need only be available for a representative of each of these general locations. For each of these general classes, specialized ANNs are developed to process the sensor measurements which relate to that particular structural class. ANN training data are obtained by subjecting each section's finite element model to the largest range of loading conditions that its particular class may encounter over the structure and over the load spectrum of the aircraft. In doing so, the resulting ANN can be used over any location on the structure that matches its class. The specific ANN task for FDI involves estimating each sensor's undamaged strain measurement based upon its neighboring strain distribution. For example, in Figure 2, sensor 5's undamaged strain measurement is based upon its neighboring sensors (1, 2, 3, and 4).
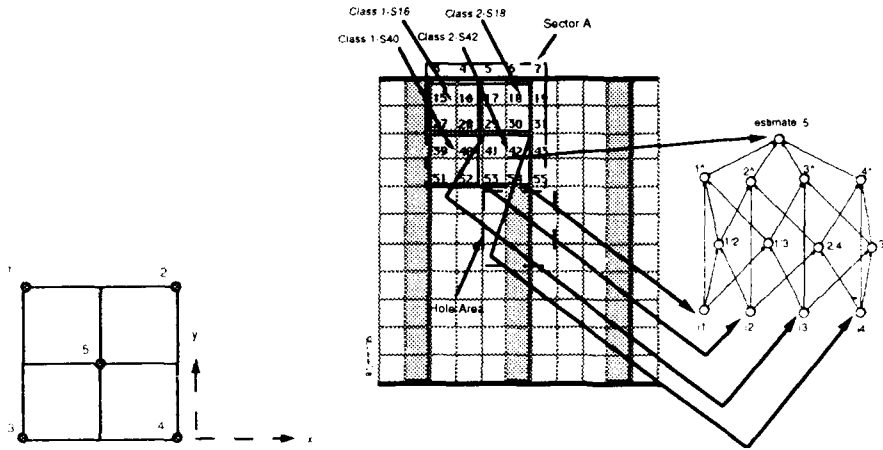
Fig. 2. Spatial Neighborhood   Fig. 3. Mapping from FEM Description to ANN Classes

Consider a representative airframe section, illustrated in Figure 3, consisting of a skin cover with three attached spars. Here, a 144 node finite element model illustrates sensors grouped into two classes, Skin and Skin/Spar. Class 1 (Skin ANN) consists of four adjoining skin plates, while Class 2 (Skin/Spar ANN) represents any area where two skin plates border two spar sections (shaded in grey). There are numerous instances of these classes throughout the structure, however, only four have been selected for illustration. Together, these four classes form what is labeled as Sector A. The labeling of classes, as in "Class 1-S16", symbolizes the relationship between that particular class instance and its associated neural network processor (Class 1-S16 uses sensors 3, 5, 27 and 29 to estimate the undamaged strain measurement of sensor 16).

3. FDI EXPERT SYSTEMS

The FDI rules set the status of each sensor to one of seven states: *OK, candidate, suspect, true_alarm, false_alarm, failed,* or *damaged* (Figure 4). The absolute value of the difference between ANN undamaged strain estimates and the actual strain measurement is defined to as an *error signal*. If a sensor's error signal is less than an alarm threshold, its status is set to *OK*, if its error signal is over the threshold, its status is set to *candidate*. If the average error signal for the neighborhood associated with a *candidate* sensor is less than the alarm threshold, then its status is set to *false_alarm*, otherwise its status is set to *true_alarm*. When a sensor is not functioning, its status is set to *suspect*. The FDI KB similarly uses a damage threshold to determine if the sensor has *failed* or the structure is *damaged* at that location.

Figure 4 illustrates the smart structures system results, which include the FDI expert system and neural network strategies, for the airframe section with centrally located damage. Shaded

squares represent alarm signals indicating damage nearby. Therefore, dark squares indicate highly abnormal strain distributions due to structural damage. As indicated, false alarms have been distinguished from true alarm signals. The system has correctly distinguished between four sensors which are not functioning due to structural damage and one which has been purposely failed by the designer.
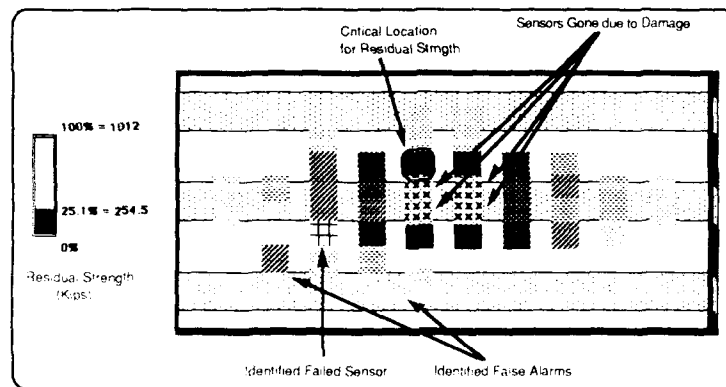
Fig. 4. System Results for Damaged Airframe Section

These damage isolation results are then used by the Damage Assessor KB to determine what critical structural components have been affected and to estimate the structure's residual strength; determined here to have been lowered to 25.1% of its maximum strength.

4. CONCLUSIONS

Since the system performance is dependent upon sensor positioning, structural class definitions, neural network training, and threshold determinations, the *NueX* ™ Smart Structures Design Tool has been developed based upon the hybrid strategies presented here. These steps will be performed iteratively by the structural designer using this tool, along with CAD and finite element programs. In this manner, engineers will be able to create intelligent structural monitoring systems designed specifically for their applications.

5. REFERENCES

Gerardi T G 1990 "Health Monitoring Aircraft" *J. of Intelligent Material Systems and Structures* Vol. 1 No. 3: 375-385

Jaeger C A and Rogers C A 1988 "An Overview of Smart Materials & Structures" *SmartMaterials, Structures and Mathematical Issues* Blacksburg VA

Mazzu J M, Allen S M and Caglayan A K 1991 *A Hybrid Neural Network Knowledge Base System for Intelligent Structural Monitoring* F33615-89-C-3219

Mazzu J M, Caglayan A K and Jonas M R 1991 *A Hybrid Neural Network Expert System Environment* NAS9-18479

Wada B K and Fanson J I 1990 "Adaptive Structures" *Mechanical Engineering* November

Application of a neural network to the active control of structural vibration

M. R. Napolitano, C. I. Chen

Department of Mechanical and Aerospace Engineering, West Virginia University, Morgantown, WV 26505-6101.

R. Nutter

Department of Electrical Engineering, West Virginia University, Morgantown, WV 26505-6101.

ABSTRACT: The application of a Neural Network (N.N.) for state estimation purposes in the overall problem of Active Control of Structural Vibrations is here suggested. The results related to the training session and to the numerical implementation of the state estimation for a vibrating cantilevered beam are presented. The influence of parameters such as number of hidden layers, number of neurons for each hidden layer, size of the input data pattern on the training section is shown.

1. INTRODUCTION

Active control of structural vibrations has been the focus of extensive research in recent years. It has been shown that active control methods that use "intelligent" structures have several advantages over time-proven passive control techniques. Different types of actuators have been used for damping structural vibrations, such as piezoelectric actuators, shape memory alloys and magnetostrictive alloys. Along with these advances in material sciences, in the past few years several control strategies implementing these actuators have been suggested (Baz and Poz 1987a,1987b,1990,Baz 1991a,1991b). All the introduced control strategies require at each computational step the physical (nodal) or modal position and/or velocity for each node of the finite element model of the structure. Therefore these control algorithms are not particularly attractive for practical implementation unless a state estimation structure is introduced.

2. A NEURAL NETWORK

Consider a system whose dynamics is described by the discrete equations:

$$X(k) = A\ X(k\text{-}1)\ +\ B\ U(k\text{-}1)\ +\ W(k) \qquad (1)$$
$$Y(k) = C\ X(k)\ +\ V(k) \qquad (2)$$

When the dynamics of a vibrating structure has to be described the A and B matrices will be related to the stiffness and inertial matrices of the vibrating structure. The state

vector X will contain nodal displacements and velocities. The size of the vectors U and Y will be given by the number of actuators and sensors to be used by the Active Control System. The vectors W and V represent random disturbances acting on the system and measurement errors respectively. For the system described by the Eqs. (1-2), using a classic estimation such as any type of Observer or a Kalman Filter (Ogata 1987), the state estimation will be obtained in such a way that the estimation structure "has to learn" about the dynamics of the system at each time step starting from ground zero. It can be easily understood that this task is computational very demanding for high order systems. Besides there will be actuators saturation problem during the transient, that is before the estimation error is driven to zero. An alternative approach can be given by the application of a NEURAL NETWORK or NEURAL OBSERVER (N.N. or N.O.) system used for the estimation task (Baz 1991a,1991b, Nielsennn 1990, Rumelhart and McClelland 1986, Simpson 1990, Widrow 1986). A very basic architecture of a N.N. is shown in Figure 1 which represents a state estimation structure for a dynamic system with 4 states of which only 2 can actually be measured.
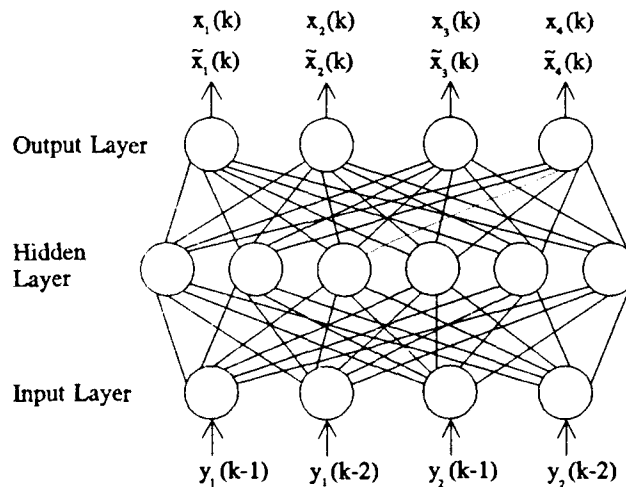
Figure 1 General Architecture of a Neutral Network

X$_i$(k) represents the state measurement vector at the time step k and y$_j$(k-p) represents the measurement from sensor j at time step (k-p). In other words, the state variables

of the system can be determined by a combination of past measurements. A key feature of this structure is that it will "learn" the dynamics of the vibrating system during a training section made of several training cycles, with training data coming from either previous computer numerical simulation or from experimental data, if available. The training section can be considered successful when a selected parameter related to the estimation error converges to a small acceptable margin. A typical choice for such parameter is:

$$ERRTOT = \frac{1}{2} \sum_{j=1}^{m} \sum_{i=1}^{n} \left(X_i(k) - \tilde{X}_i(k) \right)^2 \qquad (3)$$

where n is the number of state variables and m is the number of input time steps. A remarkable feature of a N.N. is the ability of learning the dynamics of both linear and non-linear systems; the only difference is that nonlinear systems require a longer training. Once the N.N. has been designed and implemented in a microprocessor, the input data at each time step of such N.N. structure would be the data coming from the reduced number of sensors that we can actually place on the structure; the output data are the correct estimates ($\tilde{X}$) at each time step of all the states of the system. A N.N. must contain at least 3 layers: 1 input layer, 1 hidden layer and 1 output layer. Note that it may contain more than 1 hidden layer. For the purpose this study let us consider only 1 hidden layer, as shown in Figure 1. Each cell shown in Figure 1 is called Processing Element (P.E.), also known as Neuron. The number of P.E.s for input and output layers depends respectively on the number and the pattern (the previous time instants) of available measurements and on the number of states to be estimated, the number of P.E.s in the hidden layers can be arbitrary. Each P.E. of the hidden layer sends its output to the output layer and receives its input from the input layer. The output of each P.E. is calculated as a manipulation of the weighted sum of the output of all the P.E.s of the lower layer (with the option of adding a threshold parameter) through an activation function "f" which must be non-decreasing and differentiable. A typically used activation function is the sigmoid function:

$$f(x) = (1 + e^{-x})^{-1} \qquad (4)$$

The set of weights associated with each layer are calculated during the training session with the goal of minimizing the previously introduced parameter ERRTOT. The

process of minimizing such parameter is practically the learning process. For our purposes will consider a N.N. of feedforward type with inter-layer connections with supervised learning. The design of the N.N. structure, that is the determination of the sets of weighting coefficients and relative thresholds, will be performed using the Back-Propagation algorithm (Rumelhart an McClelland 1986, Simpson 1990) which is essentially a gradient-based optimization method. This Back-propagation method is the most widely used method for the design of the structure of feedforward type of N.N. with supervised learning. The method performs the input to output mapping by minimizing a cost function. Such task is accomplished by making weight connections adjustments according to the error between the computed and desired output values of the P.E.s of the output layer. The details of the algorithm are shown in Rumelhart and McClelland 1986, Simpson 1990.

3. STATE ESTIMATION IN A VIBRATING BEAM

A numerical study simulating the application of a N.N. for state estimation of a vibrating cantilevered beam has been performed. Particularly the N.N. has been designed to furnish the state estimation of the nodal displacements of an aluminum cantilevered beam subjected to a random excitation at the tip with a force of ± 2 Newton. The beam has been modeled with 10 elements and has therefore 20 linear and angular degrees of freedom. It is assumed that the input to the N.N. are given by the data of the vertical displacements of the node #2 and #3 from time instant (k-1) down to (k-p). Intuitively it can be understood that the use of previous instants data helps the accuracy of the estimates of the N.N. The output of the N.N. will be accurate estimates of the displacements at time instant k. The results are relative to two phases: the TRAINING PART and the SIMULATION PART. The structure of the N.N. has been designed with a training section made of 50000 training cycles. At each training cycle the algorithm is implemented through a 5 seconds time history of the dynamics numerical simulation of the vibrating beam. The learning rate for the training is kept small and is a linear decreasing function in order to avoid oscillations of the parameter ERRTOT. Figure 2 shows that the parameter ERRTOT decreases more for a N.N. with an higher number of hidden layers. In each case each hidden layer contains 10 P.E.s. This implies that better estimates are obtained from more complex N.N. Figure 3 shows that, using 1 hidden layer, the influence of the number of P.E.s on the accuracy of the

estimates is minimal, as we can see for 10, 20 and 30 P.E.s. Finally Figure 4 shows that the convergence of ERRTOT and, therefore, the accuracy of the estimates is helped if a certain number of data from previous instants are available. Figures (5-7), relative to the SIMULATION PART, shows the comparison of the vertical displacement of nodes #1, #3 and #5 between the numerical simulation and the N.N. simulation with 1 hidden layer, 10 P.E.s and 10 input pattern; they are practically coincident.
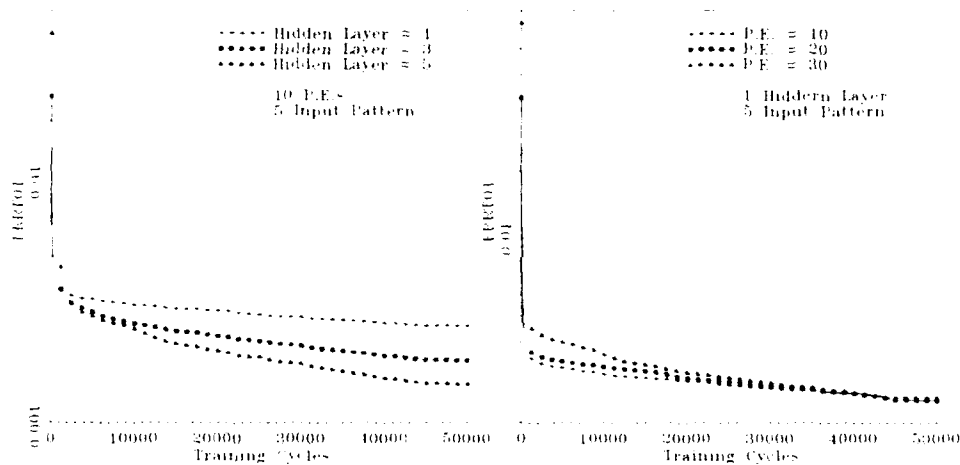
Figure 2 ERRTOT vs. Training Cycles for Different Number of Hidden Layers

Figure 3 ERRTOT vs. Training Cycles for Different Number of P.E.s
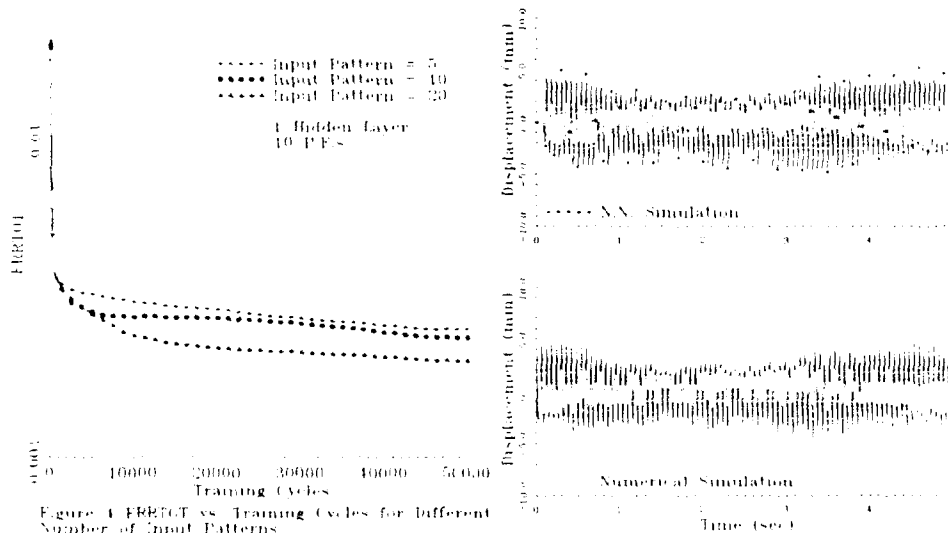
Figure 4 ERRTOT vs. Training Cycles for Different Number of Input Patterns

Figure 5 Comparison of Displacement at Node 1
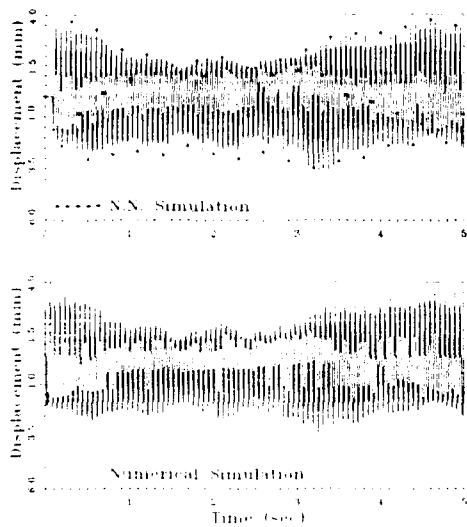
Figure 6 Comparison of Displacement at Node 3   Figure 7 Comparison of Displacement at Node 5
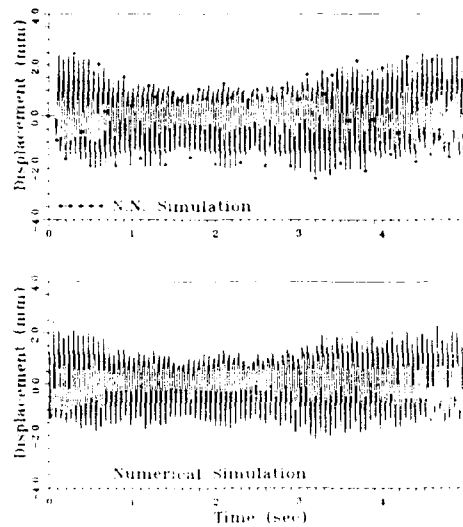
4. CONCLUSIONS AND RECOMMENDATIONS

A N.N. has shown to be a potentially very useful alternative approach for the difficult task of state estimation of a vibrating structure within the overall problem of Active Control of Structural Vibrations. Further studies are of course necessary. Particularly the authors are investigating the numerical implementation of a N.N. with a control algorithm driving piezoelectric actuators placed on the beam such that closed loop performance can be finally assessed.

REFERENCES

Baz A. Poh S, 1987a, NASA Technical Report Number N87-23980, *Modified Independent Model Space Control Method for Active Control of Flexible Systems*.

Baz A, Poh S, 1987b, NASA Technical Report N87-25605, *Comparison Between M.I.M.S.C., I.M.S.C. and P.I. Methods in Controlling Flexible Systems*.

Baz A, Poh S, 1990, *J. of Intelligent Materials, Systems and Structures*, (1), pp. 273-287.

Baz A, 1991a, *J. of Sound and Vibration* (1), pp. 151-157.

Baz A, 1991b, *Proc. 8th VPI & Su Symposium on Dynamics & Control of Large Structures*, Blacksburg, VA.

Nielsen R B, *Neurocomputing*, Addison-Wesley Pub. Co., Reading, Ma, 1990.

Ogata K, *Discrete-Time Control System*, Prentice-Hall Inc., Englewood Cliff NJ, 1987.

Rumelhart D, McClelland J, *Parallel Distributed Processing*, MIT Press Cambridge, Ma, 1986.

Simpson P K, *Artificial Neural Systems*, Pergamon Press Inc., Fairview Park, NY, 1990.

Widrow B, Stearns S, *Adaptive Signal Processing*, MIT Press, Cambridge, Ma 1986.

Modeling and identification of the JPL phase B testbed

John T. Spanos and Andrew Kissil

Jet Propulsion Laboratory, California Institute of Technology, Pasadena, CA 91101

Abstract. This paper represents a case study in modeling and identification of an experimental flexible structure designed and built at the Jet Propulsion Laboratory to study the problem of control-structure interaction. Finite element models and experimentally identified transfer function models are developed and compared. The identification approach is described and analytical and experimental results are presented.

1. Introduction

The work described in this paper addresses the modeling and identification of an experimental flexible structure designed and built at the Jet Propulsion Laboratory. Referred to as the "JPL Phase B Testbed," the structure was designed to duplicate the control-structure interaction problems that are expected to limit optical performance of future space telescopes and interferometers. The Testbed is a lightly damped truss structure cantilevered to the ground and standing approximately eight feet tall. A detailed description of the hardware is given by Eldred and O'Neal (1991).

In this paper we develop finite element and input-output transfer function models for future use with actuator-sensor placement and control system design. Comparisons between the analytically and experimentally derived models reveal that finite element models may not be sufficiently accurate for high performance control design.

2. Finite Element Model

The finite element model of the JPL Phase B Testbed is illustrated in Figure 1. An optical motion compensation system, also referred to as "Trolley", is mounted on the end of the $-X$ boom and a four-cable gravity offload mechanism supports its weight from the ceiling. These two elements add complexity to an otherwise "clean" truss structure.

The model was assembled using the NASTRAN finite element code and consists of 129 grid points for a total of 774 elastic degrees of freedom. From these only 252 degrees of freedom carry mass. There are 255 CBAR, 83 CONM2, 52 MPC, 33 CELAS2, 4 CTRIA2, 4 CQUAD4, 2 CRBE2, 2 CRIGD1, and 1 CROD elements. The four-cable offload mechanism was modelled using CBAR elements and the geometric stiffness effect of the preloaded cables was embedded into the CBAR element stiffness properties. However, only one midspan grid point was used in modeling each cable and as a result only the first cable mode was captured. In addition, a small mirror mounted on the $-Y$ boom was modeled as a concentrated mass rigidly attached to the midspan of one of the $-Y$ boom truss members.
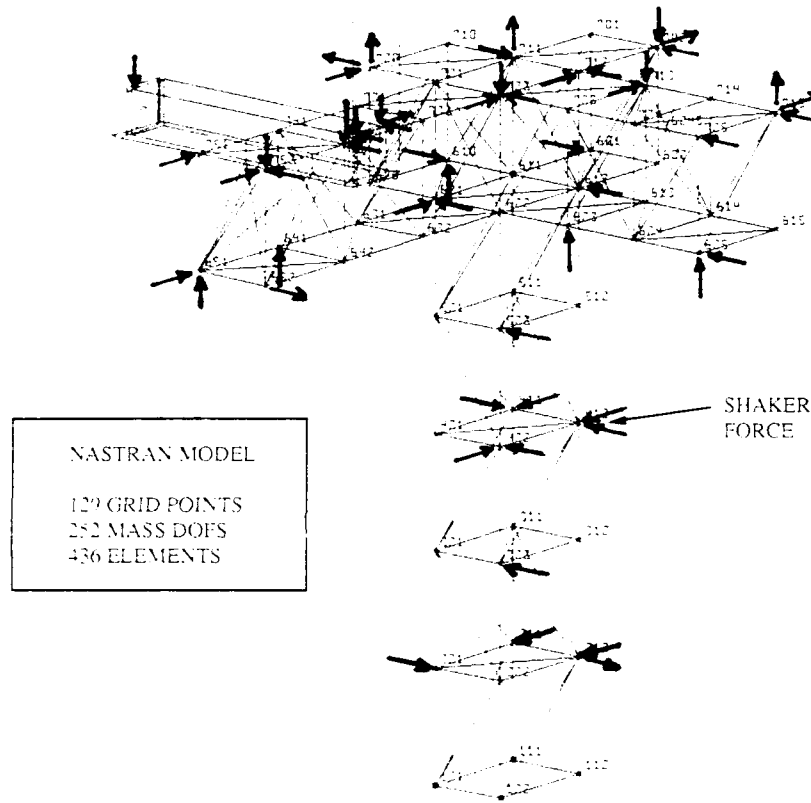
Figure 1. NASTRAN finite element model of the JPL Phase B Testbed showing accelerometer locations and directions

The total mass of the model is 45.3 kg. The Trolley box has a mass of 11.6 kg and its mounting frame along with miscellaneous components has a mass of 7.96 kg. The small mirror attached to the +Y arm has a mass of 0.7 kg. The nodes of the truss have a concentrated mass of 0.1 kg each, however, their masses were slightly increased by lumping the contribution of truss member mass density at the nodes. Although the truss grid points have rotational stiffness, they were assigned zero mass moments of inertia. The only grid points which were given nonzero mass moments of inertia were the Trolley box, and +Y arm mirror.

Normal modes analysis was performed using RPK's version of COSMIC NASTRAN on an AST 386/33 computer. The full order model, 252 mass degrees of freedom, was used for modal analysis. The first 22 structural modes in the frequency range 4-108 Hz were extracted and their natural frequencies are listed in the second column of Table 1. We note that the eight modes occurring at 38 Hz are due to the four-cable gravity offload mechanism which suspends the Trolley from the ceiling. The frequency of the first global structural mode occurs at 5.5 Hz and its shape represents torsional motion of the vertical truss column. Similarly, the second structural mode occurs at 7.6

Hz and is primarily bending of the Testbed about the Y-axis. Higher modes, up to 100 Hz, represent other global modes of the structure while several of the modes occuring above 100 Hz are local strut bending modes.

3. System Identification

The system identification process was carried out as follows. First, the frequency response of the structure was measured using a single shaker and several accelerometers. Second, a transfer function was parameterized to match the corresponding *modal* transfer function obtained from diagonalizing the finite element model. Third, each frequency response measurement was fitted with a scalar transfer function parameterized by the ratio of two polynomials and good estimates of modal frequency and damping were obtained. The natural frequency and damping estimates were subsequently used to fit the modal transfer function to each frequency response measurement thereby yielding estimates of the mode shapes at each measurement location.

3.1 Measuring the Frequency Response

The measurement stage of system identification consisted of exciting the Testbed with a single shaker and measuring the acceleration at 56 different locations on the structure as shown in Figure 1. The experiment was conducted using a 2630 Tektronix data acquisition system which allows 4 channels to be monitored at a time. One of these channels was used to measure the shaker excitation force (i.e., output voltage of a load cell connected to the shaker via a stinger) while the remaining three channels were connected to three roving Kistler accelerometers. The shaker excitation force was band-limited white noise and the time domain data were windowed to reduce leakage, transformed in the frequency domain using the Fast Fourier Transform (FFT), and averaged to reduce noise. Four thousand ninety six frequency points were taken for each of four frequency ranges: 2.812–12.812 Hz, 10.31–30.31 Hz, 25–125 Hz, and 100–500 Hz. As a result, each transfer function was measured at a total of $4 \times 4096 = 16384$ frequency points. The number of averages for the four frequency ranges were 10, 20, 30, and 50, respectively.

3.2 Transfer Function Parameterization and Curve Fitting

The objective of frequency-domain system identification is to find a transfer function whose frequency response matches the measured response. We are particularly interested in a transfer function that is defined directly in terms of the modal frequencies, dampings, and mode shapes of the structure. The classical modal model obtained from finite element analysis has the form:

$$G(s, r) = \sum_{k=1}^{m} \frac{\begin{bmatrix} a_{1k} \\ a_{2k} \\ \vdots \\ a_{ik} \end{bmatrix}}{s^2 - 2\zeta_k \omega_k s + \omega_k^2} - \begin{bmatrix} d_1 \\ d_2 \\ \vdots \\ d_a \end{bmatrix} ; \qquad r = \{\omega_k, \zeta_k, a_{rk}, d_r\}$$

where $k = 1, 2, \ldots, m$ and $r = 1, 2, \ldots, a$. In the parameter vector r, $a_{rk} = \phi_{rk}\phi_{1k}$ where ϕ_{1k} is the kth modal displacement at the shaker location and ϕ_{rk} is the kth modal displacement at the rth accelerometer location. The parameters $\{\omega_k, \zeta_k\}$

denote modal frequency and damping while the constants d_r represent the static contribution of the high frequency modes.

Equation (1) represents the desired parameterization of the unknown transfer function. The parameter vector x which defines $G(s, x)$ can be determined from the solution of the frequency weighted least squares curve-fitting problem:

$$\min_{x} \sum_{i=1}^{p} \sum_{r=1}^{u} \left| W_r(\omega_i) [H_r(j\omega_i) - G_r(j\omega_i, x)] \right|^2 \tag{2}$$

where $H_r(j\omega_i)$ is the rth frequency response measurement. $W_r(\omega_i)$ is a positive weighting scalar corresponding to the ith frequency and r^{th} measurement, and p is the number of frequency points at which the transfer function was measured.

It is evident from (1) that the least squares curve-fitting problem (2) is *nonlinear* in the modal frequency and damping parameters while it is *linear* in the mode shape parameters α_{rk} and constants d_r. This observation motivates an approximate two-step solution to the optimal curve fitting problem. First, identify the modal frequencies and dampings $\{\omega_k, \zeta_k\}$ using a suitable nonlinear least squares algorithm and, subsequently, solve a linear least squares problem to obtain the modal residues α_{rk}.

3.3 Identifying Modal Frequencies and Dampings

Although the problem of identifying modal frequencies and dampings is nonlinear, a highly effective linear least squares algorithm has been proposed by Sanathanan and Koerner (1963). The algorithm fits transfer functions to frequency response measurements by iteratively solving a sequence of weighted linear least squares problems. However, it requires that the unknown transfer function $G_r(s)$ be parameterized as a ratio of two polynomials in contrast to the partial fraction parameterization of (1). The details of the algorithm are beyond the scope of this paper but additional information can be found in (Spanos, 1991).

FORTRAN software implementing the Sanathanan-Koerner algorithm were developed by Dailey and Lukich (1987) who parameterized the numerator and denominator of the unknown transfer function as sums of Chebychev polynomials (Chebychev polynomials are numerically better conditioned than power polynomials). Upon convergence of the algorithm, the Chebychev polynomials are transformed to power polynomials and the state space quadruple is formed by realizing the power polynomials into controllable canonical form. The output from the curve fitting program is a state-space "A" matrix from which the modal frequencies and dampings are easily extracted. 216z Although the algorithm implementation of Dailey and Lukich (1987) can fit a *vector* transfer function to a *vector* frequency response measurement, we have used it only as a scalar curve-fitter to avoid numerical problems due to the large amount of frequency response data and accelerometer outputs. Furthermore, to avoid having to identify several modal parameters simultaneously, we divided each measurement record into four frequency bands: 4.5-15 Hz, 14.3-32 Hz, 30-49 Hz, and 32-100 Hz. In this way we were able to identify less than eight modes at a time. A total of nineteen distinct modes in the frequency range 4.5-100 Hz were identified.

Since there were 56 measurement records, 56 estimates of modal frequencies and dampings for each of the 19 identified modes were obtained. To arrive at a single estimate, a weighting was assigned to each modal parameter based on the quality of the curve fit: if a particular fit was visually bad, then the modal parameters from that fit were given a zero weighting factor and were not taken into account when
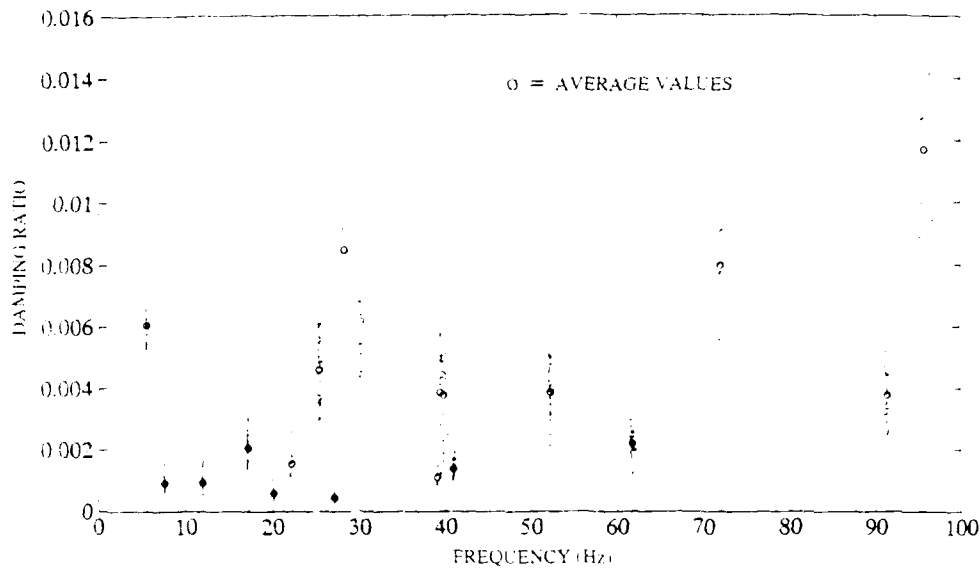
Figure 2. Modal frequency versus damping for each curve-fitted transfer function

computing the average estimate. Table 1 gives the averaged modal frequency and damping estimates along with 3-sigma variations while Figure 2 plots modal frequency versus damping for all modes and measurement records. It is shown that the variation in modal frequency is on the order of 1% while the variation in modal damping is on the order of 100%. This indicates that it is considerably more difficult to identify modal damping than it is to identify modal frequency. We also note that the average modal dampings varied from 0.04% for mode 8 to 1.2% for mode 19 which qualifies the structure as "lightly damped".

3.4 Identifying Mode Shapes

Once the modal frequencies and dampings were found, the modal residues at the measurement locations were determined from the solution of the linear least squares problem:

$$\min_{\alpha_r, d_r} \sum_{i=1}^{p} W_r(\omega_i) |H_r(j\omega_i) - G_r(j\omega_i, \alpha_r, d_r)|^2 ; \qquad r = 1, 2, \ldots, q \qquad (3)$$

where $\alpha_r = \{\alpha_{r1}, \alpha_{r2}, \ldots, \alpha_{rm}\}$ represents the vector of modal residues associated with the rth measurement location. After the modal residues α_{rk} were determined, the normalized eigenvectors were obtained from $\phi_{rk} = \alpha_{rk} \phi_{1k}$ where $\phi_{1k} = \sqrt{\alpha_{1k}}$. Figure 3 shows a typical transfer function obtained from the curve-fitting procedure.

4. Comparison of Finite Element and Identified Models

Several comparisons were made between the finite element model and the identified transfer function model. Specifically, comparisons were made between modal frequencies, mode shapes, and transfer functions.

Table 1. Modal frequencies and dampings

FINITE ELEMENT MODEL		IDENTIFIED MODEL				
MODE No.	FREQUENCY (Hz)	MODE No.	FREQUENCY (Hz)	3 σ VARIATION (%)	DAMPING (%)	3 σ VARIATION (%)
1	5.49	1	5.49	1.46	0.605	44.5
2	7.63	2	7.63	0.53	0.092	57.7
3	11.53	3	12.05	0.53	0.091	75.8
4	17.16	4	17.19	0.72	0.205	75.6
5	20.54	5	20.14	0.15	0.058	69.6
	.....	6	22.24	1.17	0.153	116.4
6	25.48	7	25.45	1.21	0.461	78.1
	.....	8	27.11	0.08	0.044	90.2
	.....	9	28.30	1.85	0.848	120.4
7	29.63	10	30.27	1.38	0.646	64.8
8	38.36	11	39.11	0.28	0.130	67.1
9	38.36	12	39.46	0.30	0.386	122.6
10	38.36	13	39.86	1.39	0.378	107.7
11	38.36		.....	....	.....	.....
12	38.36		.....	....	.....	.....
13	38.36		.....	....	.....	.....
14	38.36		.....	....	.....	.....
15	38.36		.....	....	.....	.....
16	40.04	14	40.95	0.53	0.137	64.0
17	50.62	15	52.30	0.40	0.386	58.8
18	64.11	16	64.20	0.79	0.218	75.0
19	71.71	17	72.65	0.80	0.795	44.2
20	75.72		.....	....	.....	.....
21	86.55	18	91.40	0.49	0.376	56.4
22	108.48	19	95.73	1.96	1.367	51.8

4.1 Comparison of Modal Frequencies

Table 1 presents a comparison of the modal frequencies obtained from the finite element model and those obtained from curve-fitting. The first two modal frequencies have a discrepancy of less than 0.2%, which is less than the 1.5% 3-sigma variation of the identified first modal frequency. The third mode shows a relatively large discrepancy (4.5%), however, we point out that discrepancies of 5% or less are generally considered good in the modal survey arena. Furthermore, we found a number of analytical modes that could not be paired with experimentally identified modes and vice versa. We suspect that the multiple modes associated with the gravity offload mechanism near 39 Hz were not distinctly identified by the curve-fitter. A comparison of the mode shapes provided additional insight into how the modes should be paired.

4.2 Comparison of Mode Shapes

Since the normalization of the eigenvectors is arbitrary, the identified modes were normalized so as to minimize the sum of the squares of the differences between the modes being compared; i.e.,

$$\min \sum_{i=1}^{l} \left(\phi_{ik} - c_k \tilde{\phi}_{ik} \right)^2 , \qquad k = 1, 2, \ldots, m \qquad (4)$$

where $\phi_k = \{\phi_{1k}, \phi_{2k}, \ldots, \phi_{lk}\}$ represents the kth analytical mode, and similarly $\tilde{\phi}_k$ is the kth identified mode. To obtain a measure of the correspondence between the analytical and identified modes, let $\tilde{\phi}_k^* = c_k \tilde{\phi}_k$ and define the relative error quantity:

$$\epsilon_k^2 = \sum_{i=1}^{l} \left(\phi_{ik} - \tilde{\phi}_{ik}^* \right)^2 \bigg/ \sum_{i=1}^{l} \phi_{ik}^2 , \qquad k = 1, 2, \ldots, m \qquad (5)$$
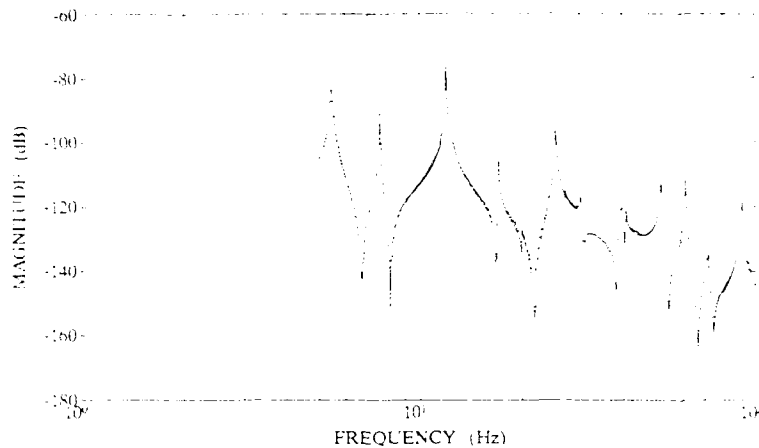
Figure 3. Comparison of a *curve-fitted* transfer function (722 y-displ. / 412 force) with the corresponding measurement data

The quantity $1 - \epsilon_{ik}$ was used as a measure of the correspondence between modes. Clearly, a correspondence value of 1.0 would indicate an exact match of the modes. In this way each of the first 22 analytical modes was compared with each of the 19 identified modes and the pairing order of Table 1 was obtained.

4.3 Comparison of Transfer Functions

The most direct method of evaluating the quality of the two models is by plotting their frequency response along with the measured data. In order to make meaningful comparisons, the modal model obtained from finite element analysis was assigned the modal dampings of the identified model. Figures 3 and 4 show how a typical frequency response measurement compares with the identified model and the finite element model respectively. The transfer function corresponding to the finite element model (Fig. 4) is a considerably worse fit to the measurement than its curve-fitted counterpart (Fig. 3). As expected, the finite element model performs best in the low frequency range (up to 17 Hz) capturing the lowest four modes while the identified model fits the data closely throughout the frequency range 4.5-100 Hz.

5. Future Work

For system identification with a single excitation, modes with vibration nodes near the excitation location may not appear in the frequency response measurement and, as a result, they may not be identified by the curve-fitter. Multiple excitation locations should alleviate this problem. Furthermore, new and existing methods for tuning finite element models with experimental measurements will be evaluated and the most promising ones will be applied on the JPL Phase B Testbed.
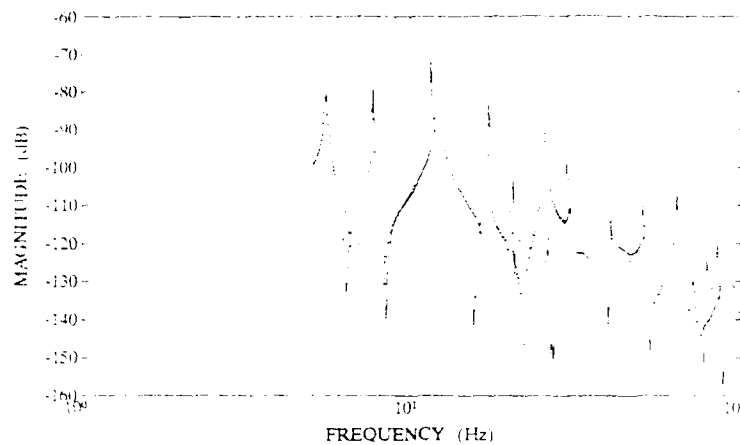
Figure 4. Comparison of a *finite element* transfer function (722 y-displ. / 412 force) with the corresponding measurement data

6. Conclusions

In this paper we have presented the results of modeling an experimental flexible structure. Finite element and experimentally identified transfer function models were developed and compared. A frequency domain system identification methodology based on transfer function curve-fitting was described and was shown to be effective. Having compared modal frequencies, mode shapes, and transfer functions, we found the finite element model to be inferior to the identified model. The discrepancy was more pronounced at frequencies beyond the first four global modes of the structure. In addition, we found that the variations in the modal damping estimates were approximately 100 times larger than the variations in the modal frequency estimates indicating that modal damping was more difficult to identify than modal frequency.

Acknowledgements

References

Dailey R L and Lukich M S 1987 "Recent Results in Identification and Control of a Flexible Truss Structure" Proceedings of the American Control Conference Atlanta GA June 15-17.

Eldred D B and O'Neal M C 1991 "The JPL Phase B Testbed Facility" ADPA Active Materials & Adaptive Structures Symposium & Exhibition Alexandria VA Nov. 5-7

Sanathanan C K and Koerner J 1963 "Transfer Function Synthesis as a Ratio of Two Complex Polynomials" IEEE Trans on Auto Control Vol. AC-8 pp 56-58

Spanos J T 1991 "Algorithms for l_2 and l_∞ Transfer Function Curve Fitting" Guidance Navigation and Control Conference New Orleans LA Aug. 12-14

Placement of a limited number of sensors for modal identification of a space station photovoltaic array

Daniel C. Kammer

Department of Engineering Mechanics, University of Wisconsin, Madison, WI 53706

Leehter Yao

Department of Electrical and Computer Engineering

ABSTRACT: An iterative method, called Effective Independence, is used to place a small number of sensors on a representative Space Station photovoltaic array for identification of a set of target mode shapes. The method ranks sensor locations based upon their contribution to the linear independence of the target modes.

1. INTRODUCTION

On-orbit system identification will be a vital component of the successful operation of proposed large space structures (LSS). The vibration data obtained from either deliberate input or external disturbances will be used to design control systems and correct analytical models for structural dynamic analysis. In many cases, a modal representation will be desired. An on-orbit modal identification of an LSS will present many difficulties for experimentalists which are not present in a ground vibration test of a smaller structure. One of these problems is the placement of sensors. In the case of an on-orbit test, the number of sensors will be extremely limited due to weight and cost considerations. A small allotted number of sensors must be placed on the structure to identify a limited number of dynamically important target modes.

While many authors have considered sensor placement for control purposes, only Kammer (1991) has considered sensor placement for modal identification from the standpoint of using the test data to perform test-analysis correlation and analytical model updating. The modal partitions obtained from the test data must be linearly independent otherwise correlation analysis will fail because the test mode shapes will be spatially dependent. This paper applies the Effective Independence method presented by Kammer (1991) to place a small number of sensors for modal identification of a Space Station photovoltaic (PV) array. The utility of the proposed sensor placement methodology is demonstrated through numerical simulation of modal identification analyses using the Eigensystem Realization Algorithm (ERA) (Juang and Pappa 1985) and a realistically sized example.

2. SENSOR PLACEMENT METHODOLOGY

Initially, a set of modes is selected for identification from the finite element representation of the structure. This set, called the target modes, is chosen based upon some measure of

X,(k) represents the state measurement vector at the time step k and y,(k-p) represents
the measurement from sensor j at time step (k-p). In other words, the state variables

dynamic importance and should in general include mode shapes which are strongly excited by
the proposed inputs. Next, a large set of candidate sensor locations is designated from which
the smaller final sensor configuration will be selected. The objective of the Effective
Independence sensor placement strategy is to select sensor locations which render the target
mode shape partitions as linearly independent as possible.

The sensor placement problem is approached from the standpoint of estimation theory. The
target mode independence requirement implies that at any time t, the sensors can be sampled
and the target modal response can be estimated. A static Fisher model is assumed for the
output equation in the form

$$u_s = \Phi_{fs} q + v \tag{2.1}$$

in which u_s is the response at the sensor locations, Φ_{fs} is the matrix of finite element model
target mode shapes partitioned to the sensor degrees of freedom, q is the target modal
response, and v is the sensor noise. Noise v is assumed to be a stationary additive random
observation disturbance with zero mean and positive definite covariance intensity matrix R.
An efficient unbiased estimator yields an estimate error covariance matrix of the form

$$P = E[(q - \hat{q})(q - \hat{q})^T] = [\Phi_{fs}^T R^{-1} \Phi_{fs}]^{-1} = Q^{-1} \tag{2.2}$$

where Q represents the Fisher Information Matrix (Middleton 1960). Maximization of Q
results in the minimization of the error covariance matrix P which results in the best estimate
$\hat{q}$. The initial candidate sensor set is selected such that Φ_{fs} is full column rank implying that
Q is positive definite.

The method begins by computing the Effective Independence distribution vector E_D using the
expression

$$E_D = (\Phi_{fs} \Psi)^{\wedge 2} [\lambda]^{-1} \{1\}_r \tag{2.3}$$

where Ψ are the orthonormal eigenvectors of positive definite Q and $[\lambda]$ are the corresponding
eigenvalues, $(\ )^{\wedge 2}$ represents a term by term square of the enclosed matrix, and $\{1\}_r$ is a
column vector of 1's with dimension r corresponding to the number of target modes. Terms
within the vector E_D represent the fractional contribution of each sensor location to the
independence of the target modes. Entries in vector E_D are sorted by magnitude and the
lowest ranked sensor is deleted from the candidate set. Remaining sensor locations are then
ranked and sorted again. In an iterative fashion, the initial candidate set of sensor locations is
rapidly reduced to the number allotted for the test.

A modal analysis was performed for a finite element representation of a Space Station PV
array. These modes were calculated with the PV array fixed at its base which is consistent

with the connection of the array to the Space Station. Dynamically important array modes are defined here as those modes which are strongly excited by the motion of the rest of the station. These are precisely the fixed interface array modes which contribute strongly to the forces and moments at the array base. Selected target modes and corresponding frequencies are listed according to fractional contribution to interface loads, M_I, in Table 1.

Table 1. PV array target modes selected based upon interface load contribution

Mode	Freq. (Hz.)	M_I
5	0.155	0.237
3	0.123	0.123
6	0.194	0.062
78	1.412	0.055
2	0.114	0.052
1	0.112	0.046
4	0.133	0.033
11	0.306	0.013
21	0.454	0.012
10	0.288	0.010

The initial candidate set of sensor locations consisted of three mutually perpendicular linear motion sensors at 107 node points evenly distributed over the array. The Effective Independence method was employed to reduce the initial 321 sensor locations to 15 locations which were to be used for identification of the target modes. One sensor was deleted during each iteration. The derived sensor configuration, designated the EfI sensor set, is illustrated in Figure 1. For comparison, three other sensor configurations were selected, each containing 15 sensors. The first set was based upon modal kinetic energy and will be referred to as the KE configuration. The candidate sensor location containing the largest kinetic energy for each target mode and the next five highest ranked locations over all the target modes were selected for this sensor configuration which is illustrated in Figure 2. The other two 15-sensor configurations were selected based upon engineering judgement which is so often used in sensor placement. These two sets will be designated as EJ1 and EJ2 and are pictured in Figures 3 and 4, respectively.

Table 2 presents the determinant and condition number of the information matrix for each of the four selected sensor configurations. While the size of the determinant gives a measure of the amount of target modal response information contained in the sensor data, the condition number in the spectral norm gives a measure of the linear independence of the target modal partitions. A value of 1.0 indicates that the partitions are orthogonal and of equal Euclidean length and are thus as independent as possible. Out of all four candidate sensor configurations, the set based upon Effective Independence yields the largest determinant and the smallest condition number.
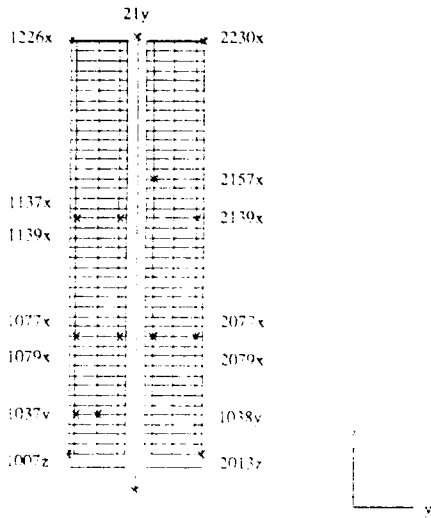
Fig. 1 Effective Independence
sensor configuration (EfI)
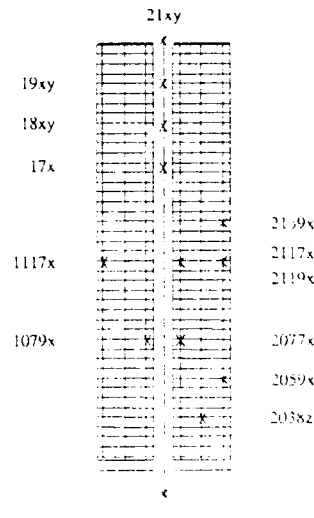
Fig. 2 Kinetic Energy
sensor configuration (KE)
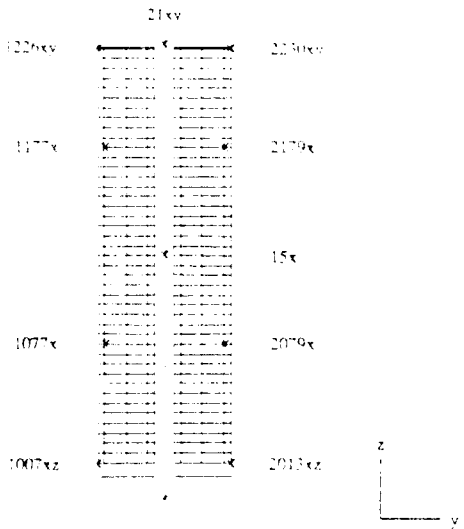
Fig. 3 Engineering Judgement
sensor configuration 1 (EJ1)
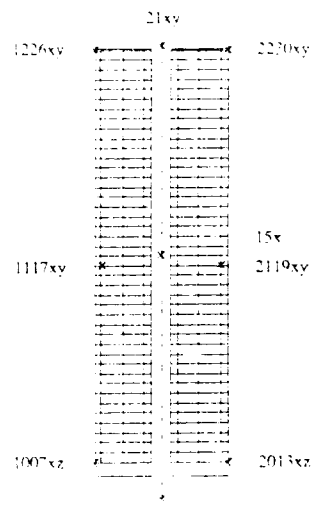
Fig. 4 Engineering Judgement
sensor configuration 2 (EJ2)

Table 2. Fisher Information matrix determinant and condition number for each sensor set

	EfI	KE	EJ1	EJ2
Determinant	3.36×10^6	7.41×10^3	5.17×10^{-1}	5.05×10^{-5}
Condition Number	1.71×10^1	4.58×10^3	5.15×10^2	3.96×10^5

3. MODAL IDENTIFICATION OF SPACE STATION PV ARRAY

The Eigensystem Realization Algorithm was used to extract mode shapes and frequencies from simulated response to initial conditions for each of the four sensor configurations described in the previous section. The displacement at the ith sensor location was simulated using the relation

$$u_{s_i} = \sum_{j=1}^{r} \phi_{ji} e^{-\varsigma_j \omega_j t} \cos(\sqrt{1 - \varsigma_j^2} \, \omega_j t + \psi_j) q_{oj} + v_i$$

(3.1)

where ϕ_{ji} is the ith coefficient in the jth target mode, ς_j is the corresponding damping ratio, ω_j is the natural frequency, ψ_j is the phase angle, and q_{oj} is the initial condition. The time series was sampled at 20.0 Hz. providing approximately fourteen data points per period for the highest frequency target mode. Noise v_i was added to the sensor data at each sample as a zero-mean Gaussian sequence with variance σ^2. Sensor data was generated for three linearly independent vectors of target mode initial conditions given by $q_1 = \{1\ 1\ -1\ 0\ 1\ 1\ 1\ 0\ 1\ 1\}^T$, $q_2 = \{-1\ 1\ 1\ 0\ -1\ 1\ 1\ 0\ 1\}^T$, and $q_3 = \{1\ 1\ -1\ 0\ 1\ 1\ 1\ 0\ 1\ 1\}^T$. Phase angles were assumed to be zero. In all the ERA identification analyses performed, the block Hankel matrix possessed 90 rows and 1,050 columns. Details of the ERA formulation can be found in Juang and Pappa (1985).

Seven cases were considered for each of the four candidate sensor configurations. Table 3 lists the percentage modal damping and noise level for each case. The simulated test data was generated using the finite element representation of the PV array, therefore the analytical model was assumed to be correct. Once the test modal parameters were computed from the corresponding sensor data, test-analysis correlation was performed to determine the accuracy with which the target modes were extracted. Frequencies were compared directly. Test and analysis mode shapes for each sensor configuration were compared using the cross-orthogonality computation (Chen and Garba 1985) given by

$$C = \Phi_{test}^T M_{TAM} \Phi_{fs}$$

(3.2)

in which Φ_{test} are the identified test modes and M_{TAM} is a test-analysis model mass matrix.

Table 3. Percentage modal damping and noise in sensor data

	Case 1	Case 2	Case 3	Case 4	Case 5	Case 6	Case 7
Damping	1.0	1.0	1.0	1.0	1.0	5.0	10.0
Noise	0.1	0.5	1.0	5.0	10.0	0.1	0.1

The ith target mode is said to be accurately identified from the sensor data if its corresponding diagonal term from the cross-orthogonality matrix C_{ii} is greater than or equal to 0.90 and its corresponding frequency error is less than or equal to 5.0%. The accuracy criterion was applied to the correlation results to determine the total number of target modes identified in

each instance. Figure 5 illustrates the results for cases 1 through 5. In each case, the EfI sensor configuration resulted in a larger number of accurately identified target modes. If the noise level is held fixed and the damping increased, as in cases 1, 6, and 7, the EfI sensor configuration, once again, yields a larger number of accurately identified target modes than the other three sensor sets as illustrated in Figure 6.
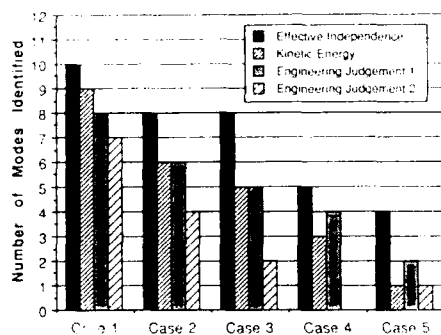
Fig. 5 Accurately identified
modes, cases 1-5
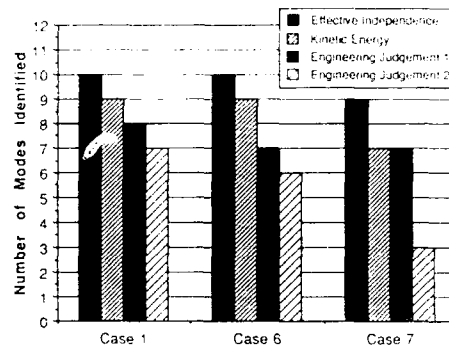
Fig. 6 Accurately identified
modes, cases 1, 6, and 7

4. CONCLUSION

This paper demonstrates the utility of using the Effective Independence procedure for sensor placement in the case of on-orbit modal identification where a limited number of sensors will be available. The method ranks sensors based upon their contribution to the linear independence of a set of target modes. In an iterative manner, sensors with low ranking are eliminated from a large candidate set resulting in the final configuration. The Eigensystem Realization Algorithm was used to extract mode parameters from simulated response data. In all cases considered, the EfI sensor configuration identified more target modes than the other sensor sets considered.

5. REFERENCES

Chen J. C. and Garba J. A. 1985 *Proceedings of the Joint ASCE/ASME Mechanics Conference* pp 109-137.
Juang, J. N. and Pappa R. S. 1985 *Journal of Guidance, Control, and Dynamics* 8 pp 620-7.
Kammer D. C. 1991 AIAA *Journal of Guidance, Control, and Dynamics* 14 9 pp 251-9
Middleton D. 1960 *An Introduction to Statistical Communication Theory* (New York: McGraw-Hill)

Aircraft structural integrity and "smart" structural health monitoring

P. S. Rutherford, E. A. Westerman
Boeing Defense & Space Group
Military Airplanes Division
Seattle, Washington

ABSTRACT: A "Smart" Structural Health Monitoring System (SHMS) would consist of a network of advanced photonic sensors integrated into an airframe. SHMS would detect and/or monitor fatigue cracks, corrosion, impact events, disbond, and temperature to ensure flight safety at a minimum cost to performance without reducing aircraft availability or increasing maintenance costs. Complementing U.S. Air Force Airframe Structural Integrity Program (ASIP) with SHMS in an aircraft offers significant benefits by enabling individual structural "status."

INTRODUCTION

A "Smart" Structural Health Monitoring System (SHMS) would consist of a network of advanced photonic sensors integrated into an airframe. SHMS would reduce current aircraft maintenance and yield performance and cost benefits. However, system integration issues have not been resolved. This paper discusses the benefits and integration issues of a "Smart" SHMS with the current Airframe Structural Integrity Program (ASIP) to ensure aircraft structural integrity throughout the economic life of the aircraft.

TODAY'S ASIP

Structural integrity of today's aircraft is achieved in part through disciplined durability and damage tolerance designs and full-scale test validation procedures. It is maintained by an on going force management program. The U.S. Air Force ASIP is an umbrella effort that promotes these activities to ensure aircraft structural design provide the required strength, stiffness, and margin of safety for the least cost throughout the aircraft economic life.

Minimum detectable flaw size, flaw growth rates, load path plurality, component accessibility, and replacement costs must be considered when selecting a safe and least-cost design approach. Based on the expected aircraft operational usage and flaw growth rates, a maintenance plan can be implemented that continuously checks for the detectable flaws during scheduled inspections.

The Loads/Environment Spectra Survey (LESS) collects data to determine the aircraft usage and flight load spectra using appropriate instrumentation on selected aircraft in the fleet. These data are input into the Individual Aircraft Tracking Program (IATP), which is used to modify inspection schedules.

SHMS OVERVIEW

The figure below illustrates the "Smart" SHMS concept as a network of advanced photonic sensors integrated into an airframe on a future fighter aircraft. SHMS would detect and/or monitor fatigue cracks, corrosion, impact events, disbond, and temperature to ensure flight safety at a minimum cost to performance without reducing aircraft availability or increasing maintenance costs.
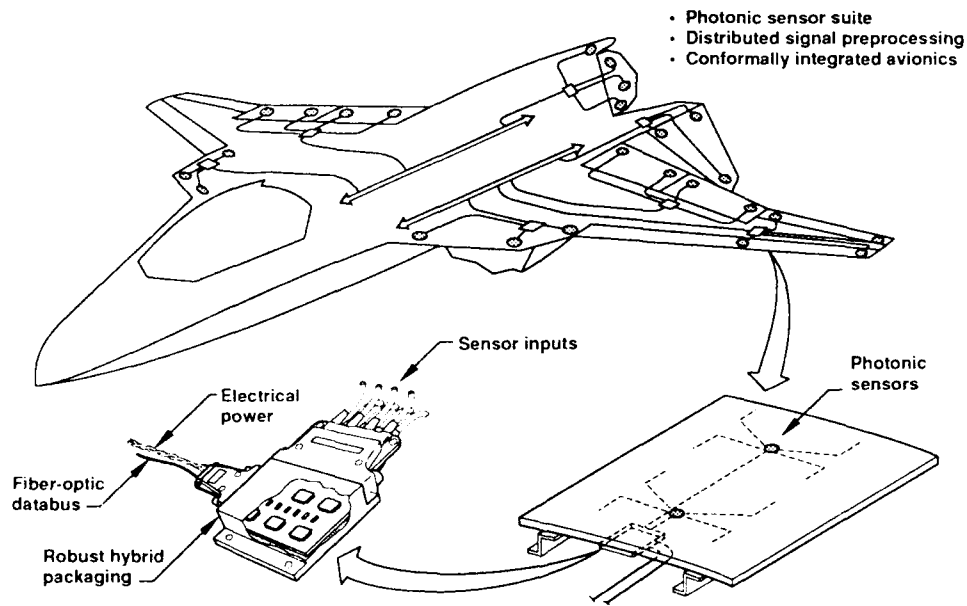
Figure 1. "Smart" Structural Health Monitoring System Concept

Complete sensor coverage would be implemented in critical areas and parts. These parts would be identified during the aircraft damage tolerance and durability analysis, full-scale testing, and/or during vehicle service in response to incurred damage. Additional monitoring capability would be built into the SHMS to allow for a significant growth of sensor coverage during the life of the aircraft, enabling service-critical part or repair part coverage. Structure that is simply difficult and costly to access and inspect with photonic sensors would receive lesser coverage. Monitoring areas and parts with minimum sensor coverage would rely on individual aircraft usage and flight load spectra in a classic ASIP sense.

Sensors would be conformal, unobtrusive, and easy to install in the field without sacrificing aircraft performance. To acquire data, sensors would be locally interfaced into a distributed

network of conformally integrated avionics modules using a robust hybrid package. After preprocessing, redundant or unusable sensor data would be discarded. Pertinent preprocessed sensor data would be transmitted to the aircraft central computer for further evaluation, storage, and action. Ground support personnel would download sensor information from the central computer and interpret it to determine maintenance and/or damage repair action required before the next sortie.

ADVANTAGES OF SHMS

SHMS in an aircraft offers significant benefits by enabling individual structural "status," which increases availability and reduces maintenance costs. Improved aircraft availability would result from a significant reduction in today's precautionary manual and tear down inspections, which frequently indicate no damage. Improved aircraft structural "status" would result from real-time structural health monitoring, enabling immediate condition awareness for inflight assessment of structural integrity. Reduced life cycle costs would result from applying sensor networks to monitor both structure and other highly integrated systems. Operational and maintenance-induced damage can also be detected and monitored using SHMS. Continual flaw monitoring will permit some maintenance to be deferred, allowing greater aircraft availability and flexibility. This flexibility could allow additional sorties from battle-damaged aircraft. Repaired damage could also be instrumented and incorporated into the SHMS for a continuous assessment of repair performance.

Future aircraft will require new structural materials and design technologies to meet signature requirements. Accessibility to the internal structure to perform inspections will be limited because of the congestion created by burying engines, avionics, antennas, and cooling systems within the structure. Inspection of internal structural components will require removal of all interfering systems. Specialized maintenance personnel will be required to perform all system remove-and-replace actions. In addition, those panels and components removed for inspection access will have to be replaced and checked before the aircraft is available for sorties. SHMS has the advantage of isolating damage locations without part removal. Therefore, access to the internal structure for inspection is not required.

FUTURE ASIP

Complementing ASIP with a "Smart" SHMS would affect both the structural design and maintenance philosophy. Damage tolerant designs would be influenced by a new set of flaw size assumptions based on the minimum detectable flaw size using SHMS sensors, thereby reducing the nondestructive inspections (NDI) experienced in today's ASIP. The design engineer will position SHMS sensors in the area of structural concern, similar to the NDI location, and define guidelines for data interpretation and evaluation.

The duration for which structure is required to withstand damage would be reduced because damage would be detected earlier. Also, periodic manual inspection on future structures may not always be afforded. Since human error significantly reduces the effectiveness in manual NDI, further conservatism is built into the inspection intervals. Therefore, less design conservatism

could be employed if a sufficient understanding of real-time flaw growth and location is available.

During individual part strength and fatigue testing, photonic sensors would be incorporated to validate the ability of the sensors to detect critical flaw sizes. SHMS would also be used during full-scale development to validate the environmental changes and interaction of other components. Such validation would give the design engineer confidence that critical flaws will be detected accurately in actual operation. Today's ASIP requires that a structure be durable enough to tolerate a detectable flaw size the entire inspection interval or longer. This requirement reduces the allowable inspection interval. The immediate detection of structural anomalies would allow design options that normally require inspection frequencies that are too short to be practical with today's NDI techniques.

The proposed SHMS would complement force management plans. With immediate interpretation of structural "health," locations requiring immediate damage verification could be inspected with portable base-level NDI techniques, giving the base-level maintenance personnel the ability to assess temporary repair potential.

CONCLUSION

A "Smart" SHMS would reduce maintenance, extend economic life, and decrease life cycle costs while improving individual aircraft structural integrity and increasing performance. Issues to be considered are component economic life design (replacement costs) compared to the added costs of sensor installation, network integration, weight, and power requirements. When determining if a "Smart" SHMS should complement ASIP the engineer must take a global system view and weigh the added costs of sensor coverage against the advantages of a SHMS on a life-cycle cost basis. This system may increase costs in the design, development, and production of an aircraft, but add significant savings over the life of the aircraft.

Development of an intelligent rotor

Inderjit Chopra
Center for Rotorcraft Education & Research
University of Maryland, College Park, MD 20742

The principles of smart structures technology are applied to the rotary-wing field in order to build an intelligent rotor with reduced vibration. A higher harmonic control (HHC) system based on piezoelectric technology is being developed to suppress vibration. This system will use piezoelectric crystals for both sensing and actuation and will require the development of an active feedback control system. An analytical model of the piezoelectric HHC system is being formulated and incorporated into a comprehensive rotorcraft code (UMARC). This model will then be validated against numerous experimental data. To then prove the feasibility of this concept, a six foot diameter Froude-scaled bearingless intelligent rotor model is being built in house using modern composite technology. The model rotor will be systematically tested at the University of Maryland in a vibration laboratory, a 10 foot diameter vacuum chamber, a hover stand, and finally in the Glenn L. Martin Wind Tunnel. The fabrication, testing, and analysis procedures proposed for this research effort are outlined below. This work will be an important step towards demonstrating the feasibility of the intelligent rotor concept, a concept which may revolutionize future rotor designs.

Recently, there has been an increased emphasis on research activities in the area of smart structures. Much of this work has focused on the application of piezoelectric technology to space related activities, such as the control of large space structures (Refs. 1-2). Some of the initial work in applying this emerging technology to the rotor has been pioneered at Maryland by Barrett (Ref. 3). Using a simple feedback system, it was demonstrated that the forced flap vibration of a rotating blade in a vacuum could be significantly reduced. The objective of the proposed research will be to expand on this initial work by developing a higher harmonic control system for vibration reduction based on piezoelectric technology and incorporating an active feedback control system. The use of HHC systems to suppress helicopter vibration is not new and in fact has been widely investigated (Refs. 4-5). The most common system involves blade pitch control through excitation of the swash plate with servo-actuators. This action results in the generation of new unsteady aerodynamic forces which in

turn suppress vibration. Although this method has been proven to be quite effective, a number of significant drawbacks do exist. The power requirements needed to drive the servo-actuators can be substantial, particularly at extreme flight conditions where vibration becomes most pronounced (Refs. 6-7). In addition, current systems are limited to blade root control for both the multi-blade and individual blade control systems. However, with the application of piezoelectric technology, these seemingly inherent limitations may be overcome.

For the fabrication of the model blades, rigid foam is cut to the desired airfoil shape, joined with a glass-epoxy spar, and covered with a fiber-glass skin. The complete blade assembly is then installed in a numerically machined aluminum mold having a NACA 0012 airfoil section and cured in an autoclave. Tantalum masses are placed in the foam at various locations in order to achieve the desired cg locations. Specially cut piezoelectric crystals are embedded in certain directions along the blade spar. These crystals are used as both sensors and actuators. To achieve appreciable signals or actuation forces, a large number of crystal banks are embedded in the blade at several locations. Also, the structural couplings associated with various composite layups, such as bending-twisting and extension-twisting, will be exploited in order to magnify the actuation strains. Such couplings are achievable with symmetric and antisymmetric ply layups, respectively (Ref. 8).

After the fabrication is completed, static and dynamic tests will be performed on the individual flexbeams, torque tubes, and blades in order to determine their stiffness and inertial properties. Considerable effort will be expended to ensure that the properties of each blade assembly are as nearly identical as possible. Where ever possible, comparison with known properties will be made in order to assess the accuracy of the experimental procedures. These experimentally determined properties will also be used as input data for theoretical analyses.

A 10 foot diameter vacuum chamber facility, located at the University of Maryland, will be used to determine the dynamic characteristics of the model blades in a rotating environment. Signals acquired in the rotating frame will be transmitted to the fixed frame via a 100 channel slip ring. This type of facility is useful since aerodynamic forces are not present. Blade natural modes will be identified by exciting piezoelectric crystals with a function-generator and measuring the response with piezoelectric sensors. A FFT analyzer and various other instrumentation will be used for data acquisition and analysis (Ref. 9). In addition to obtaining vibration characteristics, the vacuum chamber will be used to aid in developing an efficient piezoelectric HHC system which is capable of suppressing vibration. Initially, a very simple feedback system, which uses piezoelectrics for both excitation and actuation, will be employed to suppress flap vibration. Then, a more advanced distributed control system will be developed which will use

crystals, placed at predetermined locations along the blade, to identify and suppress vibration. The system proposed for this research will use a selected number of crystals to excite the blades at higher harmonics of the rotational speed. Additional crystals will then be used as sensors in order to measure the level of vibration present at various blade stations. Finally, the remaining crystals will be used as actuators to absorb the vibration. Thus, the vibration will be suppressed at its source through the use of an active feedback control system. A hover stand, which is located immediately adjacent to the vacuum chamber, will be used to evaluate the feedback system in an aerodynamic environment and may be used to investigate the stability of the rotor in hover.

The vacuum chamber/hover stand can be used for preliminary design of the piezoelectric system and to verify its operation. However, the final design or fine tuning of the HHC system must be performed in a wind tunnel under forward flight conditions. It is under such conditions that vibratory excitation of the blades occurs due to the unsteady aerodynamic forces associated with forward flight. The rotor model will be tested in the Glenn L. Martin Wind Tunnel using our bearingless rotor rig (Ref. 10). This tunnel is capable of a maximum speed of 230 mph in the 8 by 11 foot test section. The goal of this stage of the proposed research will be to examine the functioning of a higher harmonic control system based on piezoelectric technology in a realistic aerodynamic environment. Some crystals will be used to sense vibration while others will be used to excite the blade at various stations. This will result in a time varying radial distribution of blade twist or effective camber thereby creating new unsteady aerodynamic forces which may suppress vibration. Since excitation is not limited to root control, this may yield significant improvements in performance and efficiency over existing HHC systems.

Along with the experimental work outlined above, a parallel and complimentary analytical analysis is undertaken. A comprehensive rotorcraft code (UMARC) has recently been developed at the University of Maryland (Ref. 11). Within UMARC, rotor blades are represented as elastic beams undergoing flap and lag bending, elastic twist and axial extension. The resulting equations of motion are discretized by using a finite element method in space and time. A number of blade aerodynamic options are available including simple quasisteady aerodynamics, unsteady attached flow, and unsteady separated flow. Wake analyses range from simple inflow models all the way to a complex free wake analysis. The code has the capability to perform a dynamic analysis of bearingless rotors in both hover and forward flight. NASA Ames is currently upgrading the code in order to simulate higher harmonic control of helicopter vibration. The powerful capabilities of this comprehensive code will be used throughout the course of the proposed research. In addition, an analytical model of the piezoelectric

system will be incorporated into UMARC and validated against the experimental results.

Finally, a study is being made to examine the feasibility of implementing the intelligent rotor concept on a full scale rotor. This is being performed in collaboration with Ames Research Center scientists, to investigated the implementation of a piezoelectric HHC system on a full scale rotor for testing in the Ames 40 by 80 foot tunnel. This project may be incorporated into the active rotor control program currently existing at NASA Ames which involves HHC/IBC testing of several different rotor systems. It is hoped that the research effort proposed here will provide an important step towards determining whether such systems are practical and indeed possible for routine use in the future.

References

1. Crawley, E.F., and de Luis, J., "Use of Piezoelectric Actuators as Elements of Intelligent Structures," AIAA Journal, Vol. 25, (10), October 1987.

2. Anderson, E. H., and Crawley, E. F., "Detailed Models of Piezoceramic Actuation of Beams," 30th AIAA/ASME/ASCE/AHS/ASC Structures, Structural Dynamics and Material Conference, Mobile, Alabama, April, 1989.

3. Barrett, R., *Intelligent Rotor Blade and Structures Development Using Directionaly Attached Piezoelectric Crystals*. MS. Thesis, University of Maryland.

4. Shaw, J., *Higher Harmonic Blade Pitch Control: A System for Helicopter Vibration Reduction*. Ph.D. Thesis, Massachusetts Institute of Technology, May 1980.

5. Ham, N. D., " A Simple System for Helicopter Individual-Blade-Control Using Modal Decomposition," Vertica, Vol. 4, (1), 1980.

6. Nguyen, K., *Higher Harmonic Control Analysis for Vibration Reduction of Helicopter Rotor Systems*. Ph.D. Thesis, University of Maryland.

7. Miao, W., Kottapali, S. B. R. and Frye, H. M., "Flight Demonstration of Higher Harmonic Control (HHC) on S-76," 42nd Annual Forum of the American Helicopter Society, Washington, D.C., June 1986.

8. Smith, E. C. and Chopra, I., "Formulation and Evaluation of an Analytical Model for Composite Box-Beams," Proceedings of the 31st AIAA SDM Conference, Long Beach, California, April, 1990.

9. Chandra, R. and Chopra, I., "Influence of Elastic Couplings on Vibration Characteristics of Thin-Walled Box Beams under Rotation," Accepted for Publication in the AIAA Journal of Aircraft.

10. Wang, J. M., et. al., "Theoretical and Experimental Investigation of the Aeroelastic Stability of an Advanced Bearingless Rotor in Hover and Forward Flight," AHS National Specialists Meeting on Rotorcraft Dynamics, Arlington, Texas, Nov. 1989.

11. Bir, G. S., Chopra, I. and Nguyen, K., "Development of University of Maryland Advanced Rotorcraft Code (UMARC)," Proceedings of the 46th Annual Forum of AHS, Washington, D.C., May 1990.

Design, modeling, analysis, and tests of sensors and actuators utilized in a mission adaptive wing

Charlie D. Turner

Nichols Research Corporation, 4040 So. Memorial Pky, Huntsville, Alabama 35802

ABSTRACT: This paper presents the design development of a combined set of sensors and actuators that provides for health monitoring and static/dynamic control for a mission adaptive wing. The mission adaptive wing employes both conventional aerodynamic control surfaces and internal actuators to provide for static and dynamic control/load distribution. The primary focus of the paper is the dual distributed segmented sensors that are employed for both health monitoring and static shape control along with the segmented distributed actuators that are used for both dynamic and static control.

1. INTRODUCTION

Much of the growing technology base in active materials and adaptive structures is due to the requirements that were established by the need for precision control of large space structures, but the highly distributed sensor/actuator/control concepts have also found applications within the surface ship, submersible, building, optics, aircraft, and helicopter communities. In order for the next generation of advanced structures to meet more demanding performance requirements, advances in critical technology areas are needed. These areas include dynamics and control of structures; system identification and health monitoring; computation control hardware and software; design, modeling, and analysis of advanced structures; and adaptive structures. In order to insure that the needed advances are made Nichols Research Corporation is developing a series of Controls Structures Interaction (CSI) Testbeds. The advanced wing concept and large space structures testbeds are being developed in parallel. This paper presents the advanced wing concept CSI testbed.

The early combat aircraft designers were faced by conflicting requirements for a stable, but highly maneuverable aircraft. The response time of the aircraft is related directly to the static stability, inertia and control moments. These are fixed by size, loading, center of pressure (CP),center of gravity (CG), and the control surface size/deflection for the aircraft. The CP and CG may vary greatly for a given aircraft mission or during the mission as fuel is used, but would be considered fixed during a maneuver. The use of fly-by-wire computer controled aircraft such as the F-16 and F-18 has added a totally new dimension to the design concept.

By using a computer to control the aircraft, the designer may now develop an aircraft that is statically unstable; then use the flight computer to provide the necessary flight stability. By designing combat aircraft in this manner, maximum aerodynamic performance can be achieved from the airframe while providing the pilot with a "stable" aircraft to fly. The use of the flight computer has now been expanded to include gust load alleviation, vibration suppression, and adaptive control of wing/store flutter as presented by Harvey *et al* (1979). In each case the control system has been expanded to include additional sensors, but control forces are still provided by the currently available aerodynamic control surfaces.

By taking full advantage of distributed sensor/actuator/control concepts future generations of aircraft will be able to utilize a combination of aerodynamic controls and distributed internal actuators. Each of the internal distributed actuator/sensor pairs must be controlled by the flight computer for shape control, but also must respond quickly for acoustic or dynamic control. To provide the quick response time, a neural network computer may be used to control the distributed actuators as described by Turner (1991a). Communication between the flight computer and the neural network will provide for real time wing shape/load distribution control. In addition the distributed sensors associated with each actuator will provide a means of determining in real time airframe "health" such as a result of battle damage and then allow the flight computer to adjust airframe loading to prevent further damage and/or loss of the aircraft. The NRC Testbed based on a set of aero-servo-elastic scaled wings will be used to address CSI, "health", and scaling issues.

2. CSI TESTBED

As shown in Figure 1 the NRC Advanced Wing Concept Testbed is composed of four aero-servo-elastic models. The first of the models, Figure 1 (a), is composed of one full scale model and two subscale models. Both the full scale model and the two subscale models are foam filled composite construction having two internal spars - a primary and secondary member allowing for both bending and torsion control of the wing. The models have been designed for testing in the same wind tunnel at the same test conditions obtaining the same maximum strain/stress in the spar caps. Each spar is an active beam containing eight sensors and sixteen actuators. This approach has resulted in six different active beam that will be used in studying scaling of piezo effects; structure, sensor, and actuator boundary effects; and internal damping effects. This design can take advantage of shear damping, but Kim *et al* (1990) demonstrated that the effective bending moment decreases

Figure 1. CSI Testbed Models

with increasing damping and therefore will require optimization of the beam,sensor, actuator design. The internal damping will be much more important for space structures than for aircraft structures which can take advantage of aerodynamic damping. Details of the active beam design is given in the following section. The fourth model which is in preliminary design, Figure 1(b) is also of foam filled composite but with three internal spar. One spar is being designed with an internal structural disconnect for modeling in flight damage thus allowing for real time wind tunnel "health" monitoring and active control response.

3. SENSOR/ACTUATOR BEAM DESIGN

Each beam to be used in the aero-servo-elastic models will contain eight sensors and sixteen actuators distributed across four regions of each beam. Each region will contain two two sensors located on the top and bottom of the beam and four actuators located internal to the beam as shown in Figure 2. The actuators were embedded in the beam as a means of improving the passive damping performance which will be critical for large space structures. No attempt was made at this time to optimize the active/passive performance of the actuators by either sizing or placement. Once the scaling boundary effects are determined then the beams used in the fourth model will be optimized for active control and passive damping.
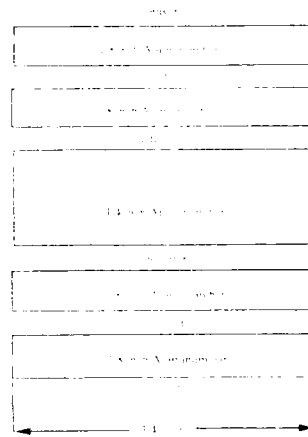
Figure 2. Spar Cross Section

4. SUMMARY

The design of the four foot aero-servo-elastic model has been completed. Problems with a new material used in bounding of the sensors/actuators have delayed assembling the two spars for this model. Extensive dynamic testing is planned for the two spars prior to assembling the first aero-servo-elastic model.

5. ACKNOWLEDGMENT

The designs of the piezoelectric polymer sensors and actuators were done by Christopher Henry a Senior Project Engineer with Atochem North America, Inc.

6. REFERENCES

Harvey C A, Johnson T L and Stein G 1979 *Adaptive Control of Wing/Store Flutter* (Honeywell Systems and Research Center)

Turner C D 1991a *Proc. 32nd Structures, Structural Dynamics, and Materials Conference* (AIAA) pp 2261-8

Kim S J and Jones J D 1991b *Proc. Recent Advances in Active Control of Sound and Vibration* (VPI & SU) pp78-91

A compliant wing section for adaptive control surfaces

B.J. Maclean, B.F. Carpenter, J.L. Draper, and M.S. Misra

Martin Marietta Defense Space and Communications Group, Denver, CO 80201

ABSTRACT: Shape memory alloy wires can be utilized as embedded actuator
elements in a compliant wing section to generate the foil curvature changes necessary
for attitude control or adaptive litting. A "flex-biased" winglet section with chord-to-
thickness ratio of twelve was developed for evaluation of tip displacement, power
requirements and dynamic response in air and water. A closed-loop control approach,
based on positional sensor feedback, was utilized to demonstrate foil shape stability
under adverse static and ambient loading conditions.

1. INTRODUCTION

Shape memory alloys (SMAs) utilize a reversible crystalline phase transformation to
recover their original heat-treated shape when heated above a critical transformation
temperature range (recoverable strain can be as high as 8%) or to generate recovery stresses
(as high as 100 ksi). More detailed descriptions of the shape memory effect can be found in
the works of Jackson et al (1972), Miyazaki et al (1989) and Perkins (1975). SMA wire
"tendons" can be used as embedded actuator elements to control the level of facesheet strain
in adaptive structural components which utilize sandwich panel construction. As facesheet
strain is varied, the degree of curvature and magnitude of tip deflection of a panel section
can be controlled. Figure 1 shows the results of a finite element model used to analyze this
approach on a winglet wedge section with chord to thickness ratio of 12. The upper
facesheet was modeled as a conventional composite laminate with varying degrees of strain
imposed on the active facesheet on the bottom side of the winglet. Tip deflection on the
order of 40% chord was predicted for 4% facesheet strain (operational strain for a high
lifecycle SMA would be necessarily limited to less than 3%). The fact that large
deformation is possible in a fully elastic manner, the winglet is said to be "compliant".

Electrical resistance heating of the SMA wires can be used to control facesheet contraction
via a displacement sensor feedback loop. However, one of the primary issues regarding
utility of SMAs as actuator elements for compliant lifting surface applications is the
intrinsic design trade between response rate and electrical power requirements, as discussed
in the next section. The purpose of this work was to demonstrate the ability to control the
shape of a winglet panel section and evaluate its heating and cooling performance under
varying ambient and loading conditions.

2. APPROACH

A 1" wide by 12" long winglet wedge section, 1" thick at the root, was fabricated utilizing a 0.125" thick fiberglass epoxy laminate on the underside bonded to an aluminum honeycomb core. The top facesheet was pre-fabricated with tunnel holes for the SMA elements using an elastomeric thermoplastic material with elastic modulus of 30 ksi and elastic limit of >30%. The sheet was subsequently bonded to the upper side of the honeycomb core using a silicone rubber-based adhesive.

4% Lower Facesheet Strain
(Chord / Thickness = 12:1)
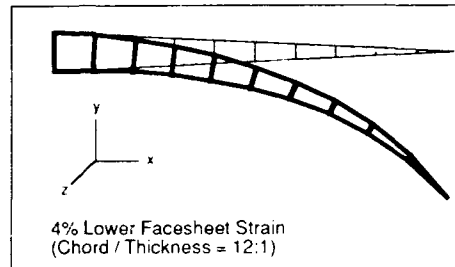
Figure 1 Wing Section Deformation as a Function of Lower Facesheet Strain

NiTi-10%Cu SMA wires (0.020" in diameter with a nominal austenitic finish temperature of 50°C) were procured from a vendor and then annealed for 20 minutes at 900°F. A wire "conditioning" procedure was then employed to develop a "two-way memory" effect by isothermally straining 12" long bundles of wires at 70°C over a range of 4% strain at 1 Hz for a total of 1000 cycles. This process produced a spontaneous elongation of 2.1% upon cooling down from the cycling temperature, with zero applied stress. This process of isothermal cycling and associated two-way memory is an important facet of SMA development as described by Johnson (1978) and Proft et al. The conditioned wires were then cut to length and inserted into the 12 facesheet tunnel holes in the 1" wide facesheet.

Electrical circuit plates were then fabricated to create three parallel circuits of four wire lengths each to produce a favorable electrical resistance of 2.2Ω. Next, the SMA wires were pre-strained to approximately 4% (relative to their length at temperatures above 50°C) and "terminated" by melting the ends, using an arc welder, to produce a ≈0.04" diameter "ball". These balls provide the mechanical stop to pull against during contraction, as well as the electrical contact with the circuit plates.

An important point to be made regarding the design of the winglet is its ability to balance externally applied loads. With 12 each 0.020" diameter wires contracting with a potential of 65 ksi operational recovery stress (= 245 lbs. total contraction force potential), against a facesheet stiffness of 150 lbs./in. 4% wire recovery corresponds to only 72 lbs. of wire tension, leaving a wire operating margin of 173 lbs. This means that with a lever arm of 12:1, the 1.0" wide winglet is capable of lifting almost 15 lbs. at its tip.

A closed-loop, displacement sensor feedback approach (Figure 2) was utilized to evaluate winglet performance using operational amplifiers for monitoring current and voltage into the active SMA elements. A proportional/integral/differential (PID) control law provided the ability to supply electrical power to the SMA wires based on sensed displacement error.

The bandwidth for shape control of an adaptive sandwich panel is dependent on the rate of heat transfer in and out of the SMA wires. This, in turn, is a function of transient effects between the facesheet material and the SMA wires, as well as the rate of cooling of the facesheet to ambient conditions. Bandwidth improves with enhanced cooling of the facesheet but enhanced cooling requires greater power levels to maintain wire temperature

for a given command position. The winglet could be cycled through most of its range of motion at about 0.1 Hz in air. This bandwidth response was improved by a factor of 5 to 10 by placing the winglet in water, albeit with the associated increase in required power to hold any particular position.
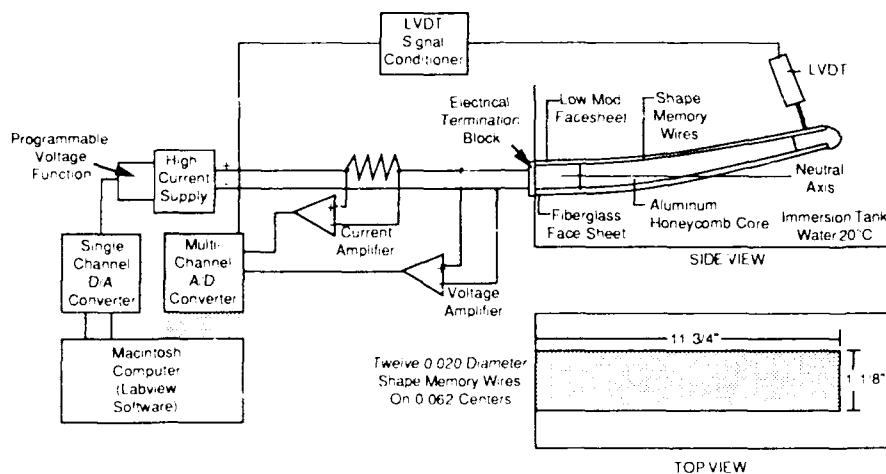
Figure 2 Schematic of closed-loop, displacement sensor feedback approach.

3. RESULTS & DISCUSSION

Two series of tests were performed; the first test series measured the power necessary to hold the wing section at a commanded deflection, and the second test series determined deflection rate versus power.

Power-to-Hold Testing -- The testing conducted to determine the power required to hold the winglet tip at a certain position was accomplished through use of LVDT signal feedback. A control algorithm was developed to accept a command input and calculate the difference between LVDT and command signals. This difference represents an error signal which is further modified and ultimately controls the power supplied to shape memory elements embedded in the winglet. Figure 3 shows power as a function of tip displacement. The high thermal conductivity of the water causes a substantial increase in the quantity of power required to hold the winglet tip at a specified position, as compared to the air environment. Tip deflections up to 1.5 inches were obtained using 80 watts. Dividing applied power by the twelve each, one foot lengths of shape memory wire embedded in the winglet gives seven watts dissipated per foot of 0.020 inch diameter NiTi-Cu wire (with 60°C transformation temperature).
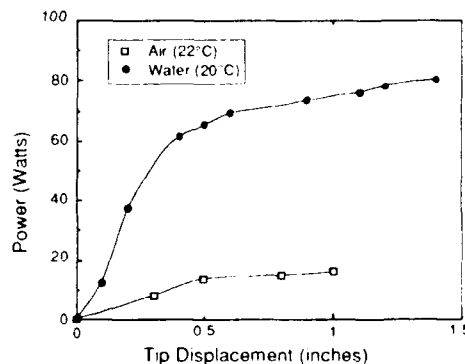
Figure 3 Power as a Function of Winglet Tip Deflection

Deflection Rate Testing -- The tip deflection rate as a function of applied power was also investigated. The LVDT output as a function of time for a stepped power input of 400 watts is given in Figure 4. Deflection rate is nearly constant at 0.5 in/sec up to a tip deflection of 1.75 in. (3.7 Volts LVDT output). Upon termination of the power input, cooling of the shape memory wires causes the tip of the winglet to return to its neutral position. Approximately 60 percent of deflection is recovered at a constant rate of 0.9 in/sec. The remaining deflection is recovered at a steadily decreasing rate. Deflection rates were determined from tests at various power levels to generate tip deflection rate versus applied power shown in Figure 5. Measurements were limited due to the source's inability to supply power in excess of 400 watts. However, as shown by the curve in Figure 5, the data does suggest a limit on the maximum achievable deflection rate. Rates of 0.5 inch/second were achieved at 400 watts (35 watts per foot of 0.020 inch diameter wire).
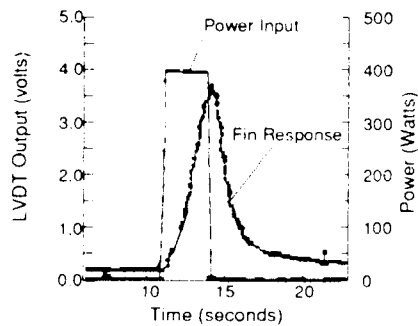
Figure 4 Flex Biased Winglet Tip Displacement as a Function of Time
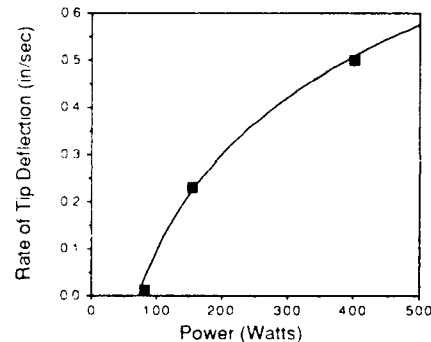
Figure 5 Tip Deflection at Increasing Power Levels

4. CONCLUSIONS

This work demonstrates the ability to control the uniform deformation of a sandwich panel winglet section using embedded shape memory actuator elements and implementing a control approach based on positional sensor feedback. Because this approach is employed to maintain a certain wing "shape", variations in applied loads and ambient conditions (changes in air or water temperature, or convective heat losses) can be compensated within the dynamic response capability of the system. Advanced adaptive foil designs can be envisioned, based on this approach, where control of discrete actuator/sensor segments across the chord provide the ability to fine tune airfoil camber to minimize drag and flow separation over a broad range of speed and angle of attack.

5. REFERENCES

Jackson C M, Wagner H J, and Wasilewski R J 1972 *55-Nitinol-- The Alloy with a Memory: Its Physical Metallurgy, Properties, and Applications* NASA--SP 5110
Johnson A D 1978 *Proc. of the NITINOL Heat Engine Conf.* NSWC MP 7° 441 pp 10-1 to 10-30
Miyazaki S and Otsuka K 1989 *ISIJ International* 29 1 pp 353-377
Perkins J ed 1975 *Shape Memory Effects in Alloys* (New York: Plenum)
Proft J L, Melton K N., and Duerig T W "Transformational Cycling of Ni-Ti and Ni-Ti-Cu Shape Memory Alloys" Raychem Corp. to be published

The JPL phase B testbed facility

Daniel B. Eldred and Michael C. O'Neal

Jet Propulsion Laboratory, California Institute of Technology, Pasadena, CA

Abstract: This paper describes an experimental facility being developed at Jet Propulsion Laboratory for demonstration and validation of control concepts arising out of NASA's Control Structure Interaction program. The facility is meant to be a ground testbed with relevance to a broad class of future precision optical space systems. The objective of the experimental program is to investigate a multi layer control approach to the maintenance of nanometer-level optical pathlength stability in the presence of external disturbances and multiple structural resonances.

1. INTRODUCTION

The development of future space and lunar-based astronomical instruments such as telescopes and optical interferometers will require major advances in the control, alignment, and pointing of distributed optical systems mounted on large flexible space structures. For example, a feasibility study performed at the Jet Propulsion Laboratory (JPL) of a space-based optical interferometer called the Focus Mission Interferometer (FMI) showed that a combination of disturbance isolation, active and passive structural vibration suppression, and active optical pathlength compensation would be required in order for the interferometer to function at full effectiveness.

No single layer of this multi-layer architecture would be sufficient, by itself, to ensure success of a system where micron-level open loop response needs to be quieted to the nanometer regime to meet the strict optical tolerances. In order to investigate the proper blending and interactions between the layers in this architecture at the nanometer level, JPL has constructed an experimental ground testbed, the "Phase B Testbed," as part of its ongoing effort in the NASA-wide Control Structures Interaction (CSI) program. The Phase B Testbed is part of an evolutionary chain of testbeds at JPL.

The configuration of the Phase B Testbed consists of a scaled subset of the FMI, and it exhibits many of the same problems as the actual instrument but is much simpler and more manageable in a laboratory environment. This is an important consideration in order for the Testbed to be successfully constructed and brought into working order within the budgetary and manpower constraints imposed on the program. Components of the Phase B Testbed include: a structure with multiple resonances within the bandwidth of interest; an optical path which is correlated with structural motion; sensors and actuators for isolating the disturbances, suppressing structural vibrations, and compensating the optical pathlength; and real-time computers for implementation of the control algorithms and recording the results.

An important aspect of the CSI program is the integrated development environment that is associated with the development of the CSI methodology. In particular, since one of the CSI objectives is to design structures and control systems simultaneously, it was deemed important that the structural analysts and the control analysts work closely together so that engineers in one discipline have an appreciation of the demands of the other, if not the analytical skills. Towards this aim, the offices of the CSI design team at JPL were collocated and cross-disciplinary training has been strongly encouraged. In further support of this, nearly all analysts' computers have been linked together on a local network. As evidence of the success of this interdisciplinary cross-training, structural analysts have designed and implemented working controllers, and control analysts have modeled the structures together with their controllers and performed structural identification on the Phase B Testbed.

2. TESTBED STRUCTURE

The structure comprising the Phase B Testbed (Fig. 1) consists of a 2.5 m vertical tower with two horizontal arms attached to its top and oriented perpendicular to one another. The structure is constructed from 1.27 cm diameter aluminum tubes. Together with stainless steel end fittings threaded into the tubing, the tubes are bolted to aluminum nodes which have multiple holes drilled in them at different angles to allow assembly in a variety of geometries. The end fittings are designed such that an individual strut can be removed and replaced without any other disassembly or disturbance to the structure, and furthermore they can be adjusted to compensate for slight length variations in the tubes. In all, the Testbed is comprised of 186 aluminum tubes and 60 nodes.

3. TESTBED OPTiCS

A two-stage compensation system is used to provide precise, high bandwidth control of the optical light pathlength. This system consists of a "trolley" containing primary and secondary reflectors, coupled via Bendix flexures and lever arms to a rigid base. The optical elements are configured as a cat's eye retroreflector, which reflects outgoing light parallel to the incident direction, though translated in position. Out of concern for thermal stability of the trolley, critical components

Fig. 1. Phase B Testbed Structure

are constructed from Invar, an alloy which exhibits extremely low thermal expansion. The system is virtually identical to one currently being used in a ground-based stellar interferometer to equalize the optical pathlengths along two separated optical trains such that white light interferometry can be performed.

The coarse stage of optical compensation consists of moving the entire trolley relative to its base via a voice coil actuator driven by a current amplifier. Maximum output of this actuator is about 62 N over a stroke of about 6 mm, with approximately 100 Hz bandwidth possible. The relative displacement between the trolley and its base is measured by an eddy current sensor. The fine stage of compensation is achieved with a reactionless piezoelectric actuator which controls the position of the secondary mirror. This actuator, which itself

includes both a coarse and a fine stage, has a resolution of better than 1 nm over a 30 micron range and potentially has a bandwidth as high as 10 kHz, though the amplifier this actuator uses limits the actual bandwidth to about 1 kHz in practice.

A heterodyne laser interferometer manufactured by Hewlett Packard is used to measure optical pathlength, both to provide input for control algorithms and to verify their performance. Resolution of the interferometer is 2.5 nm; however, since the laser light makes four passes through the optical system, the resolution in terms of relative spacing of optical components is actually better than 1 nm. The optical elements associated with the interferometer are mounted on a small optical bench atop a separate, rigidly constructed tower. The optics on the structure and on the tower can be easily modified, if desired, to change the degree of structural coupling with optical pathlength.

4. OTHER SENSORS AND ACTUATORS

Active struts, which employ piezoelectric elements to control their lengths, can be substituted for the aluminum tubes virtually anywhere on the structure, and can be used in active feedback schemes to suppress structural vibrations. These struts also employ eddy current sensors to measure elongation and load cells to monitor applied load. D-struts manufactured by Honeywell, which employ a viscous fluid to achieve a desired level of passive damping, can also be substituted. In addition, both piezoelectric and force-rebalance accelerometers can be mounted virtually anywhere on the structure.

5. DISTURBANCE INPUTS

Disturbances to the Phase B Testbed can be input via shakers attached to nodes of the structure. A shaker is essentially a proof-mass actuator suspended from a cable attached to a hanging fixture. The force output to the structure is recorded with a load cell attached in series with the load path. Attachment to the nodes is via a slender rod which transmits primarily longitudinal force due to compliance in other directions and which will break under excess loading to protect the structure against renegade shaker commands. The shakers can be excited with virtually any disturbance profile, including broad-band and narrow-band white noise, to either simulate a disturbance source in a stellar interferometer or to perform accurate modal identification with good signal to noise ratio.

Ambient disturbances result in as much as 100 microns motion in the optical pathlength, as compared to the nanometer level control desired. Considerable effort was made to identify the disturbance sources, which included seismic noise from local traffic, acoustic and turbulent noise from a large number of equipment fans in the laboratory and air conditioning, and even 60 and 120 cycle per second acoustic hum from a nearby transformer. Ambient vibration in the tower supporting the interferometer optics was particularly troublesome because the tower functions as the reference against which optical pathlength is measured, and accordingly the tower was retrofitted with damping material between all its joints to reduce its vibration level.

6. REAL-TIME COMPUTERS

The Testbed is controlled using single board computers in a VME chassis. Included are three processors boards based on the 68030 processor, an array processor based on the 860 processor, 16 bit analog to digital and digital to analog conversion, a custom laser interferometer interface card, and a 16 megabyte memory card. The VxWorks real time operating system, which features a Unix-like interactive shell, is used to run, synchronize and debug control software. Performance of the single board computers is very high, with control loops running as rapidly 2 kHz for a 40 state controller running on the array

processor, to 13 kHz for a simple piezoelectric actuator controller running on one of the 68030 boards.

Control algorithms are written in the programming language C. General routines for initializing the hardware, reading input data from disk files, accessing sensors and actuators, timing, and saving experiment experiments have been written with the result that the analyst only need concentrate on the logic of his control algorithms to implement it. Three Unix workstations are used in the laboratory for program development and experiment monitoring: a Sun Sparc, a Sun 3/60, and a Masscomp. GNU's cross compiler is used to develop object-compatible code for the single board computers.

The real-time computers are linked to the development workstations via ethernet and function as hosts on JPL's computer network. Thus the real-time computers are accessible from any workstation connected to JPL's ethernet network. This makes it possible for analysts to develop and debug their algorithms from their offices, and has proved very successful. In fact, remote access has been demonstrated from across the country. The network also makes virtually unlimited disk storage space and other resources available to the real-time computers, and greatly facilitates the transfer of experiment data to analysts both at JPL and at remote facilities.

7. CONCLUSIONS AND FUTURE WORK

Experiments to date have included structural vibration suppression using both active struts and passive dampers and optical pathlength compensation using the trolley voice coil and piezoelectric actuators. Details can be found in the references. Future experiments will combine these control layers to achieve greater disturbance rejection while the level of disturbance is increased. In addition experiments demonstrating disturbance isolation will be performed, and a special fixture for this purpose is currently being constructed.

8. ACKNOWLEDGEMENTS

9. REFERENCES

Fanson J L, Anderson E H, Moore D M, and Ealey M A, *Development of an Active Truss Element for Control of Precision Structures* , Optical Engineering, Vol 29 No 11, Nov 1990, pp 1333-1341

Fanson J L, Briggs H C, Chu C C, Lurie B J, Smith R S, Eldred D B and Liu D, *JPL CSI Phase 0 Experiment Results and Real Time Control Computer*, 4th NASA/DoD Control/Structures Interaction Technology Conference, Orlando FL, Nov 5-7 1990

O'Neal M, Eldred D, Liu D, and Redding D, *Experimental Verification of Nanometer Level Optical Pathlength Control on a Flexible Structure*, 14th Annual AAS Guidance and Control Conference, Keystone CO, Feb 2-6 1991

Laskin R A and San Martin M, *Control/Structure System Design of a Spaceborne Optical Interferometer*, AAS/AIAA Astrodynamics Specialist Conference, Stowe VT Aug 1989

Spanos J T and O'Neal M, *Nanometer Level Optical Control on the JPL Phase B Testbed*, ADPA/AIAA/ASME/SPIE Conference on Active Materials and Adaptive Structures, Alexandria VA, Nov 1991

Numerical analysis of multiple frequency interference in photorefractive media

David E. Cox and Sharon S. Welch

NASA Langley Research Center
Hampton, Virginia, 23665-5225

ABSTRACT: Photorefractive crystals are materials which exhibit light induced refractive index variations. Because the index variations change with illumination, photorefractive crystals provide the potential for dynamic recording of holographic information. This paper describes the dynamic behavior of a photorefractive crystal exposed to light waves at multiple frequencies. Results from numerical simulations demonstrate the effect of off-Bragg diffraction on both the recording and readout of dynamic holograms. These results are compared to those obtained for a static recording media, such as photographic film, where multiple frequency holography has been successfully used to generate images with superimposed depth contours.

1. INTRODUCTION

The photorefractive effect, a change in refractive index exhibited by certain crystalline materials when exposed to light, was discovered over 25 years ago[1] and has received much attention since that time[2]. The phenomenon can be described in simple terms as follows. An optical power distribution in a photorefractive crystal causes migration of charge carriers in the medium. The displaced charge carriers become trapped by acceptor sites in the crystal lattice, creating a nonequilibrium charge distribution. A static electric field is thus established in the crystal which, in turn, causes refractive index variations to occur through the electro-optic effect. A phase hologram or grating will be recorded in a photorefractive crystal when two, or more, coherent light beams interfere within the crystal. The recording is dynamic in that, if the volume containing the grating is re-illuminated with a different interference pattern, charges will

again migrate, leading to erasure of the existing grating and formation of a new grating or hologram. It is this dynamic holographic recording capability which makes photorefractive crystals attractive as a sensor material.

A noncontacting distributed sensor based on photorefractive crystals has been proposed for measuring the surface distortions of large reflectors[3]. The proposed sensor relies on holographic reconstruction from interferograms recorded at multiple frequencies. In multiple frequency or contour holography, a hologram of an object is recorded at two different optical frequencies. The hologram is subsequently illuminated with light of a single frequency, and two object waves, one slightly magnified relative to the other, are thereby reconstructed. When imaged, these object waves interfere to produce fringes across the image which correspond to lines of constant contour. For certain recording geometries, the light intensity across the image can be used to determine the position of every resolved point on the surface of the object[4].

Contour holography, as described above, has been demonstrated previously using static recording media[5]. When a hologram is recorded in static media such as photographic film, diffraction is negligible during recording since typically the media must be developed before the grating becomes apparent. The processes of recording and readout are therefore decoupled. This decoupling is of significance in contour holography. Contour holography requires image reconstruction from two different holograms superimposed in the same recording medium. One of the holograms is Bragg matched to the readout wave, while the other experiences a slight Bragg mismatch. This mismatch is responsible for the generation of the fringes which appear across the reconstructed image. It is assumed that this same Bragg mismatched diffraction has no effect on the formation of the grating. This assumption is valid only when recording and readout occur independently of one another, as in the case of static media. In the case of dynamic media, recording and readout are coupled, and, therefore, off-Bragg diffraction will affect the formation of the grating itself.

Coupled wave equations can be used to describe the spatial variation of the electric field due to volume diffraction, as well as dynamic formation of index gratings due to an intensity distribution[6,7,8]. In order to evaluate the potential of photorefractive crystals for performing holographic contouring, we have extended the standard coupled wave equations to allow for the creation of additional waves due to Bragg mismatched diffraction. This analysis is quite general

and has applications to other areas such as multiple hologram storage[9], simultaneous read-write of holograms[10], and achromatic beam coupling[11].

2. THEORY

The coupled wave equations which describe diffraction from volume variations in refractive index can be derived from Maxwell's equations. If the time dependence of the index variation is small with respect to the phase velocity of the electric field, each frequency of the electric field will obey the scalar wave equation,

$$\nabla^2 E - (\beta^2 - 2j\alpha\beta)E = 0 \tag{1}$$

where

$$\beta = \frac{2\pi}{\lambda}(n_0 + n_1(r,t))$$

The parameter α is the loss coefficient, λ is the free space wavelength, n_0 is the nominal index of refraction, and $n_1(r,t)$ is the induced refractive index variation. For the case of two-frequency interference the refractive index variation will have the form,

$$n_1(r,t) = n_{K1}\cos\left(K_1 \cdot r + \psi_1\right) + n_{K2}\cos\left(K_2 \cdot r + \psi_2\right) \tag{2}$$

where n_{K1}, n_{K2} are the grating amplitudes, K_1, K_2 are grating vectors, and ψ_1, ψ_2 describe phase shifts between the intensity pattern and the grating.

The electric field for two-frequency interference has eight components, four incident waves, and four additional waves due to off-Bragg diffraction (figure 1). Using this form for the electric field, equation (1) can be used to derive a set of eight coupled wave equations which describe the spatial dependence of the fields. The grating amplitudes grow exponentially in time towards steady state values which are determined by the intensity distributions. The values at steady-state are determined using an iterative approach. The coupled wave equations are solved at time t equals zero given some assumed initial field amplitudes. The calculated field amplitudes are then used to predict the temporal evolution of the gratings for a small time step and new solutions to the coupled wave equations are obtained using the new grating amplitudes. This process is repeated until the amplitudes of the gratings converge.

3. SIMULATION RESULTS

Two numerical simulations were conducted, each assuming a crystal 1 cm in length, with a coupling coefficient of 5 cm^{-1}, no absorption, and

a nominal refractive index of 2.25. The waves $\{R_i, S_i\}$ made angles of +5 and -5 degrees with the z axis, respectively. The wavelengths were 500 nm and 501 nm, to yield image contours every 250 μm. The time constant of the crystal was equal to unity. In one case the recording medium was assumed to have an intrinsic phase shift of zero degrees, in the other it was assumed to be 90 degrees. These values correspond to the intrinsic phase shifts of two different classes of photorefractive materials, drift-dominated materials such as bismuth silicon oxide, and diffusion-dominated materials such as barium titanate. The distinction is significant since diffusion-dominated materials have highly nonuniform gratings due to beam coupling effects.
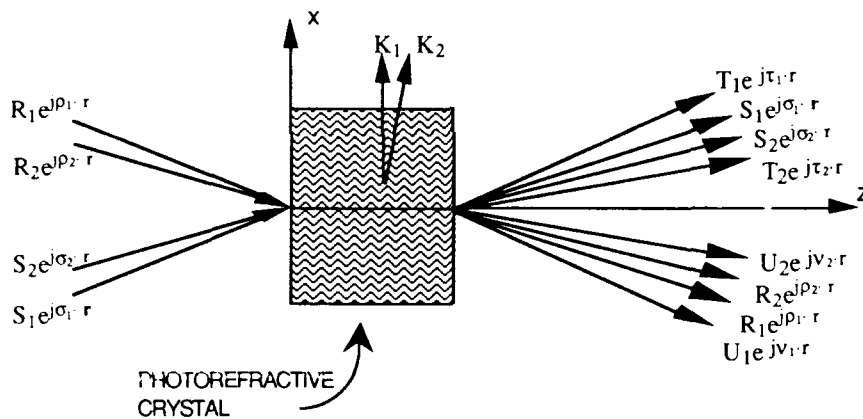
Figure 1. Electric fields resulting from interference of light of two frequencies in a dynamic recording medium with off-Bragg diffraction. Waves R_i and S_i on the left of the medium are incident reference and signal waves. Waves R_i and S_i on the right are the incident waves altered by Bragg matched diffraction. Waves T_i and U_i are waves resulting from off-Bragg diffraction of waves R_i and S_i.

To illustrate the effect of off-Bragg diffraction on the photorefractive recording process the steady-state refractive index modulation was calculated and compared to the index modulation which would form in the absence of diffraction during recording. Figure 2 shows this comparison for both drift-dominated and diffusion-dominated materials. In both cases off-Bragg waves caused changes in the grating amplitude. In the drift-dominated material off-Bragg diffraction caused the two gratings to have different amplitude distributions. This can have a considerable effect on readout of the hologram. Figure 3 shows the dynamic readout from the gratings of figure 2. In the drift-dominated material the diffraction efficiency depends upon which grating is Bragg matched to the readout wave, as
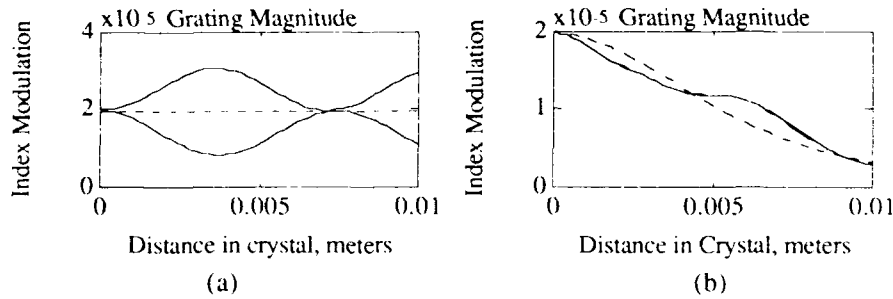
Figure 2. Graphs of refractive index modulation along the z axis of the crystal. Dotted lines assume no off-Bragg diffraction, solid lines consider off-Bragg diffraction. Boundary conditions are $R_1 = R_2 = S_1 = S_2 = 1$ (a) Drift-dominated material, i.e. no intrinsic phase shift (b) Diffusion-dominated material, i.e. 90 degree intrinsic phase shift.
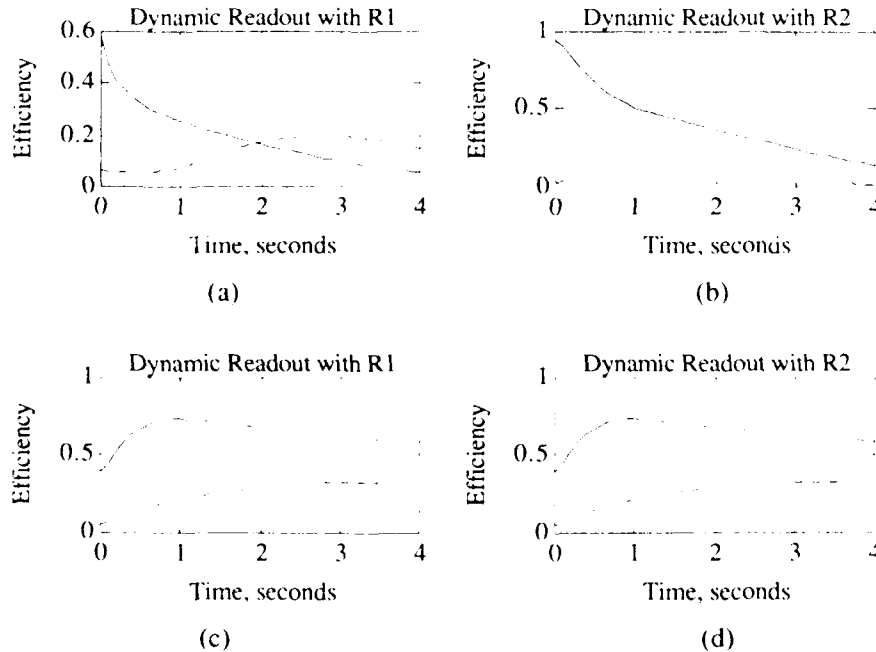
Figure 3. Graphs of diffraction efficiency as a function of time for readout with waves R_1 and R_2. Solid line is Bragg matched diffraction, dotted line is off-Bragg diffraction. (a) and (b) result from grating formed when intrinsic phase shift equals 0 degrees. (c) and (d) result from grating formed when intrinsic phase shift equals 90 degrees.

shown in figures 3a and 3b. Diffraction efficiency in the diffusion-dominated material is independent of which beam is used for readout, as shown in figures 3c and 3d.

4. CONCLUDING REMARKS

Coupled wave equations which allow for off-Bragg diffraction in the reading and writing of dynamic holograms were proposed and numerically solved. Temporal characteristics of the diffracted waves and the induced gratings were accounted for based on the dynamics of charge migration in two types of photorefractive materials.

Contour holography using photorefractive materials holds promise as a technique for making dynamic distributed position measurements. This research has shown that in photorefractive crystals the effect of diffraction during the recording process and erasure upon readout introduce complexities which are not present in photographic film. Further study is required to qualify these differences and fully evaluate the potential of dynamic contour holography.

5. REFERENCES

1)   Ashkin, A., Boyd, G., Dziedzik, J., Smith R., Ballman, A., and Nassan, K., 1966, App. Phys Lett. **9** 72.

2)   Gunter, P., and Huignard, J. P., 1988, *Photorefractive Materials and Their Aplications I* Topics in Applied Physics Volume 61 (Germany: Springer-Verlag).

3)   Welch, S. S., and Cox ,D. E., 1991, Proc. of SPIE 1480, pp 2-10.

4)   Hildebrand, B. P., and Haines, K. A., 1967, J. Opt. Soc. of Am, **57** 155.

5)   Friesem, A. A., and Levy, U. ,1976 ,Applied Optics **15** 3009.

6)   Kogelnik, H., 1969, Bell System Tech Journal **18** 2909.

7)   Kukhtarev, N. V., Markov, S. G., Odulov, S. G., and Vinetskii, V. L., 1979, Ferroelectrics **22** 941.

8)   Saxena, R. ,Claire, G. ,and Yeh, P., 1991, J. Opt. Soc. Am. B **8** 1047.

9)   Wu, S., Qiwang, S., Mayers, A., Gregory, D., Yu F., 1990 ,App. Opt. **29** 1118.

10) Saxena, R., Vachss, E., McMichael, I., and Yeh, P., 1990, J. Opt. Soc. Am. B **7** 1210.

11) Rabinovich, W. S., Feldman, B. J., and Gilbreath, G. C. ,1991, Opt. Lett. **16** 1147.

High temperature and ultrasonic wave optical fiber sensor instrumentation for aerospace applications

Kent A. Murphy, Anbo Wang, Michael F. Gunther, Brian R. Fogg
Ashish M. Vengsarkar and Richard O. Claus

Fiber & Electro-Optics Research Center, Bradley Department of Electrical Engineering
Virginia Polytechnic Institute and State University, Blacksburg, Virginia 24061-0111

ABSTRACT: We demonstrate the operation of a silica-based quadrature phase-shifted extrinsic Fabry-Perot fiber optic sensor for the detection of the amplitude and the relative polarity of dynamically varying strain. The sensor is demonstrated from -275 to 975° C. Also presented are results from a sapphire fiber interferometer used as an ultrasonic wave detection device with 1500° C capabilities.

1. INTRODUCTION

Two distinct high temperature sensors using phase-modulated techniques are described in this paper. The first sensor consists of a silica-based quadrature phase-shifted extrinsic Fabry-Perot fiber optic sensor and the second sensing method uses a sapphire optical fiber Fabry-Perot interferometer.

Phase-modulated fiber optic sensors have been shown to possess high sensitivities for the measurement of strain, temperature, vibration, pressure and other parameters.[1] Fabry-Perot (FP) sensors that are based on multiple beam interference eliminate the need for a reference arm and do not require sophisticated stabilization techniques as in the case of Mach-Zehnder and Michelson interferometers.[2] Several techniques to create intrinsic optical fiber Fabry-Perot interferometers have been described in the past.[3-5] In a recent paper, we described a silica optical fiber extrinsic FP interferometer and used it as a sensor of microdisplacements and thermally-induced strain.[6] The fiber interferometer was classified as extrinsic because the FP cavity was an air-gap between two fiber ends and the sensor output was immune to perturbations in the input/output fiber.

A similar sensor design using sapphire optical fiber has recently been demonstarted.[7,8] Sapphire optical fiber waveguides typically are manufactured as single crystal or multicrystalline material in either rod or tube form with outer diameters of 50 microns or more, a uniform index of refraction of approximately 1.76 at room temperature, lengths of several tens of centimeters, and attenuation on the order of 10dB or more per meter. Relatively large diameter sapphire fiber rods have been used in the past as transmissive

elements for blackbody and fluorescent temperature probes. Because the melting temperature of single crystal c-axis sapphire is approximately 2040°C, these types of sapphire fiber rod-based sensors have been demonstrated to operate at correspondingly high temperatures.

The silica fiber Fabry-Perot sensor will be desribed and demonstrated in Sections 2 and 3. Sections 4 and 5 will include the construction and experimental results for the sapphire fiber sensor.

2. SILICA FIBER FABRY-PEROT SENSOR DESCRIPTION

We describe the construction of the extrinsic FP interferometer with reference to Figure 1. A single mode fiber (λ_o= 1300 nm), used as the input/output fiber and a multimode fiber, used purely as a reflector, form an air gap that acts as a low-finesse FP cavity. The far end of the multimode fiber is shattered so the reflections from the far end do not add to the detector noise. The Fresnel reflection from the glass/air interface at the front of the air gap (reference reflection) and the reflection from the air/glass interface at the far end of the air gap (sensing reflection) interfere in the input/output fiber. Although multiple reflections occur within the air gap, the effect of reflections subsequent to the ones mentioned above can be shown to be negligible. The two fibers in the silica tube are allowed to move longitudinally which results in changes in the air gap length thus changing the phase difference between the reference reflection and the sensing reflection. The phase difference can be monitored as intensity modulations at the output of a fused biconical tapered coupler.

The interference of the two-wave interferometer can be evaluated in terms of a plane-wave approximation. The observed intensity at the detector is a superposition of the two reflections. For a strain sensor, it is useful to plot the detected intensity versus gap-separation s, as shown in Figure 2. We see that the fringe contrast drops as the displacement increases; this is to be expected since the relative intensity of the sensing reflection recoupled into the input/output fiber starts dropping with respect to the reference reflection.

The extrinsic FP interferometer has been tested as a displacement sensor by attaching one fiber to a stationary block and the second fiber to a micropositioner which produces a known displacement between the fiber ends. For comparison with the theoretical results, we show in Figure 3 an oscilloscope trace of the continuously monitored output intensity of the sensor for s = 0 to s = 203 μm. The experimentally counted number of fringes for the displacement was 310.5 which corresponds to a displacement of 202 micrometers.

The reduction in fringe contrast as a function of displacement has been improved by splicing a multimode optical fiber onto the end of the input/output fiber and then polishing the multimode fiber until the output light is somewhat collimated. The length of multimode fiber is on the order of a few millimeters and serves as a quarter-pitch GRIN lens. The experiment described in Figure 3 was repeated with the lensed fiber and the results are presented in Figure 4.

The principle of operation of a quadrature phase-shifted Fabry-Perot (QPS-FP) sensor has been described in detail.[6] A method of obtaining two signals 90° out of phase with respect to one another are shown in Figures 5. To test the validity of the quadrature phase-shifted sensors, a sensor (using the scheme shown in Figure 5) was attached to a cantilever titanium beam with an epoxy. The fiber sensor was attached parallel to the length of the beam and beam vibrations were monitored. A typical oscilloscope trace is shown in Figure 6. The figure clearly shows the shift in the lead/lag properties of the two signals as the relative direction of the strain in the beam changes from increasing to decreasing.

A QPS-FP sensor was tested as a thermally-induced strain gauge on a ceramic cross-flow (CXF) filter at Westinghouse Science and Technology Center, in Pittsburgh. CXF filters are used for hot gas clean-up of coal-fired power generation systems, such as pressurized fluidized-bed combustors and integrated gasifier-combined cycles. Figure 7 shows the QPS-FP sensor output as a function of time during the heat-up portion of the test compared to the filter temperature measured using a conventional thermocouple. The sensor performed equally well during the cool-down cycle.

A one centimeter gauge length QPS-FP sensor was attached to a cantilever beam and then submerged in a liquid nitrogen (-273° C) bath. The tip of the cantilever beam was displaced and then released several times. a typical oscilloscope trace can be seen in Figure 8. The fringes correspond to 276 microstrain which is within 10% of the calculated value of strain. The minimum detectable phase shift was 0.0996° which corresponds to a minimum detectable strain of 0.01 μstrain for a gauge length of 19.03 mm. Static and dynamic loading data obtained from the sensors show a high degree of accuracy and a strain resolution of 0.01 μm/m.
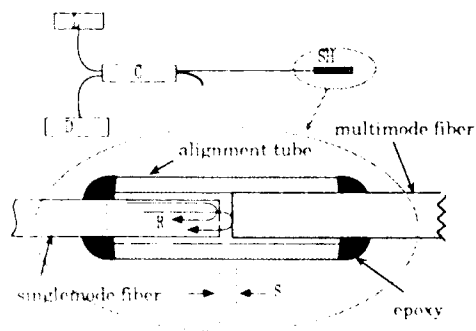
Fig. 1. Sensor system and sensor detail. L-laser, D-detector, C-coupler, SH-sensor head, R-reflections, S-gap seperation.
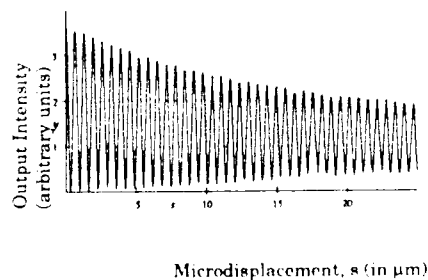
Fig. 2. Theroticial output vs. gap separation.
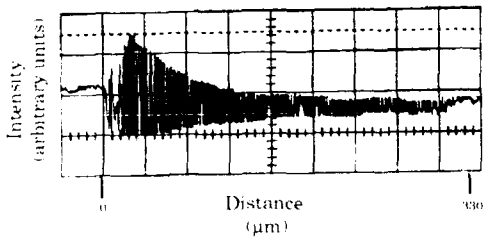
Fig. 3. Fringe contrast without lensed sensor.
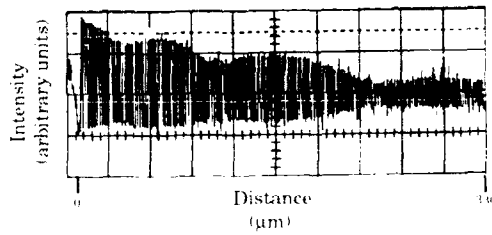
Fig. 4. Fringe contrast with lensed tip.
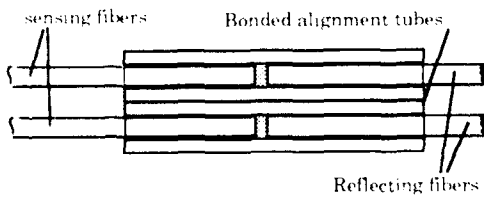
Fig 5. Detail of quadrature phase-shifted sensor.
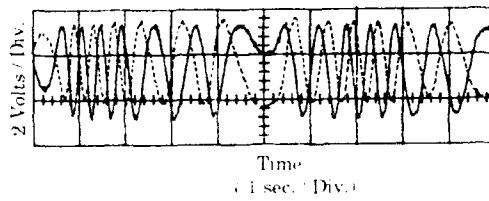
Fig. 6. Quadrature phase-shifted sensor trace showing lead-lag phenomenon.
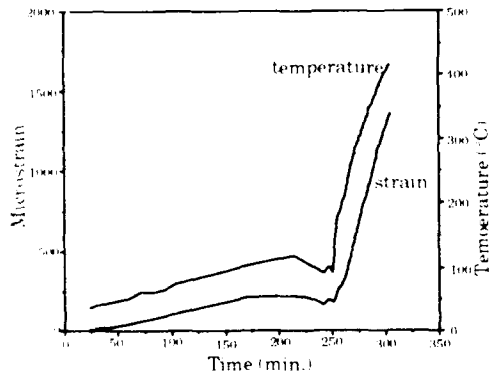
Fig. 7. Results of F-P sensor during on-site testing at Westinghouse.
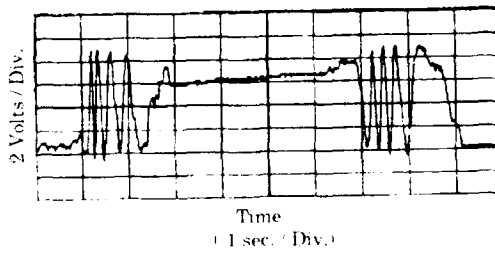
Fig. 8. Oscillograph of FP sensor attached to cantilever beam at -273° C during bending and release.

3. SAPPHIRE OPTICAL FIBER SENSOR FABRICATION

Sapphire optical fiber Fabry-Perot sensors have been fabricated as shown in Figure 9. Here, coherent light from a 1300nm laser is coupled into a single mode fiber and subsequently divided by a 2x2 fused biconical tapered coupler. Light from one of the output fibers is collimated using a GRIN lens and launched into a length of sapphire fiber rod waveguide. The collimated optical beam propagates the length of the guide and is partially reflected at two locations, thus producing two output fields which interfere. A Fabry-Perot etalon is formed by the surfaces which produce the reflections, and reflective coatings on each of the surfaces may be employed to increase the finesse of the etalon. The reflected output signal is coupled back through the lens and the input fiber, to the coupler and a photodetector.

4. MEASUREMNT OF ULTRASONIC SURFACE ELASTIC WAVES

The sapphire fiber rod sensor was supported above the surface of a material specimen as shown in Figure 10 to measure the out-of-plane particle displacements associated with ultrasonic surface elastic waves propagating on the surface. If the density and moduli of the material are known, this component information may be used to determine the entire surface wave displacement field. For this geometry, the etalon again is formed by the gap between the end of the sapphire rod and the facing surface.

Figure 11 shows the photodetector output for a 2.2 MHz wave generated on the surface using a conventional piezoelectric transducer. Here, an averaging effect is observed due to the relative size of the probing beam and the acoustic wavelength of the surface wave. The ultrasonic transducer produces a surface elastic wave having a maximum out-of-plane displacement on the order of 10 Å, so the resulting maximum optical phase change corresponds to much less than one fringe, and the output signal remains in the linear range of the system.
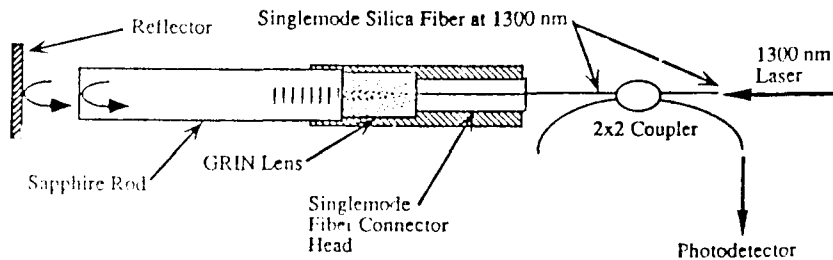
Fig. 9 Geometry of sapphire rod EFPI sensor with a reflector.

300   *Active Materials and Adaptive Structures*
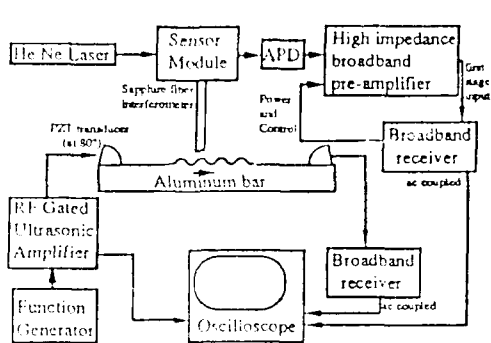
Fig.10 Experimental set-up for SAW detection.

Fig.11 Plot A PZT input. Plot B is FFT of A.
Plot C is output of sapphire interferometer.
Plot D is FFT of sapphire interferometer.

5. SUMMARY

The silica fiber Fabry-Perot sensor was successfully demonstrated as a thermally induced strain monitor in an industrial environment up to 450° C (the limitation of the fiber coating not the sensor itself). The sensor has been used successfully in a laboratory up to 975° C with no coating.

We have developed a sapphire rod waveguide-based extrinsic Fabry-Perot sensor, and have demonstrated its use in an ultrasonic surface elastic wave detection configuration. Current research includes the measurement of displacement, temperature, and pressure.

ACKNOWLEDGMENT

REFERENCES

1. J. Dakin and B. Culshaw, Optical Fiber Sensors: Principles and Components, Artech House, Boston, MA 1988.
2. T. Yoshino, K. Kurosawa, K. Itoh, and T. Ose, "Fiber-optic Fabry-Perot interferometer and its sensor applications," IEEE J. Quantum Electron., vol. QE-18, pp. 1624-1632, 1982
3. K. L. Belsley, J. B. Carroll, L. A. Hess, D. R. Huber, and D. Schmadel, "Optically multiplexed interferometric fiber optic sensor system," Proc. - SPIE Int. Soc. Opt. Eng., vol. 566, pp. 257-264, 1985.
4. A. D. Kersey, D. A. Jackson, and M. Corke, "A simple fibre Fabry-Perot sensor," Opt. Comm., vol. 45, pp. 71-74, 1983.
5. C. E. Lee and H. F. Taylor, "Interferometric optical fibre sensors using internal mirrors," Electron. Lett., vol. 24, pp. 193-194, 1988.
6. K. A. Murphy, M. F. Gunther, A. M. Vengsarkar, and R. O. Claus, "Quadrature phase shifted extrinsic Fabry-Perot fiber optic sensors," Opt. Lett., vol. 16, pp. 273-275, 1991.
7. K. A. Murphy, "Sapphire fiber interferometer for measurements at high temperature," Proc. Smart Materials and Structure Workshop (Blacksburg, VA), April 1991, Technomic Press.
8. K. A. Murphy, B. R. Fogg, A. M. Vengsarkar and R. O. Claus, "Sapphire fiber interferometer for microdisplacements at high temperature," Proc. SPIE vol. 1588 (Boston, MA), September 1991.
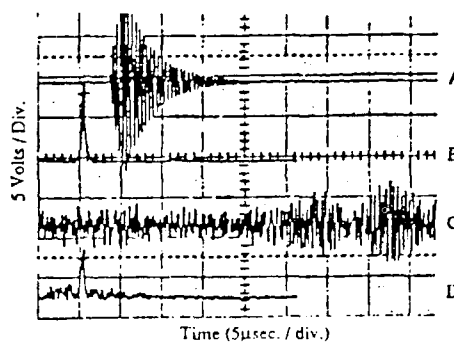
Fiber optic sensing system critical issues and developments for smart structures

R. M. Measures, K. Liu, and S. Melle.
University of Toronto Institute for Aerospace Studies, 4925 Dufferin St., Downsview, Ontario,
M3H-5T6, Canada

ABSTRACT: The development of Smart, or Active, materials will require the perfection of
structurally integrated fiber optic sensing systems. We will indicate some of the critical issues
facing this development and report on our advances in this context.

1. INTRODUCTION

In the 70's new approaches to complex engineering systems like aircraft were adopted. These assume
that each major component contains one or more critical flaws at a level not detected initially. This led
to new engineering strategies, such as:

1. *Lifetime System Monitoring;*   2.   *Retirement for Cause;*   3. *Designed-in Inspectability*

The earlier approach of retiring an entire batch of structural components once a potentially critical flaw
(crack) was discovered in one component led to an enormous cost. Retirement for Cause involves
periodic inspection of each component with expensive and elaborate NDE systems. Once a critical
flaw is detected that component is retired. Although this ASIP (*Aircraft Structural Integrity Program*)
program has been successful in preventing loss of aircraft from structural failures, it is expensive and
not always accurate, furthermore, it leads to greatly increased downtime and a commencerate increase
in life cycle costs. The introduction of components with built-in inspectability should significantly
reduce costs, improve maintenance and shorten downtime. In addition, monitoring the loads and
deformations of a component on a continuous basis will permit its true fatigue life to be estimated at
any time.

The past five years has seen the emergence of a new field of engineering termed "Smart Materials and
Structures" or some times "Active Materials and Adaptive Structures". This multidisciplinary field
will lead to a revolution in engineering principles and a radical change in our thinking about building
structures as diverse as: Aircraft and Space Platforms, Marine Vehicles and Installations and
Terrestrial Structures.

The development of *structurally integrated fiber optic sensing systems* represents a necessary first step
in the evolution of this field and will lead to advances in process control of material fabrication and to
improvements in safety and economics of many diverse industrial products. Built-in sensing systems
are equally likely to be found in future aircraft as in new bridges. In terms of advanced composite
materials the greater confidence instilled by this intrinsic inspectability will lead to their increased use
as primary structures and could avoid overdesign with its multiplier effects, particularly in the
Aerospace Field. The second part of this new field is concerned with structures that not only sense
their state but can modify it through some form of control actuation. The perfection of reliable and
accurate structurally integrated sensing systems would also constitute a necessary first step in the
evolution of Adaptive Structures. These kinds of structures have particular relevance to the Aerospace
Field leading to: aircraft with adaptable wings, active noise suppression and space structures that
constantly adjust their shape and damp out unwanted vibration.

The primary structural measurement domains are: *strain, damage, temperature and fabrication.* If we
include advanced composite materials the measurement of strain would permit: load, deformation,
vibration, stress concentration to be determined while damage assessment would follow from: crack,
delamination, corrosion and debonding monitoring. Cure state and residual stress measurements
could lead to improved fabrication control. It is obvious that the economics of implementation would
be most favoured if one type of sensor can be used for all of these measurements.

CRITICAL ISSUES AND DEVELOPMENTS

The critical areas of research and development needed to implement practical Smart Materials and Structures are indicated in **Figure 1**.
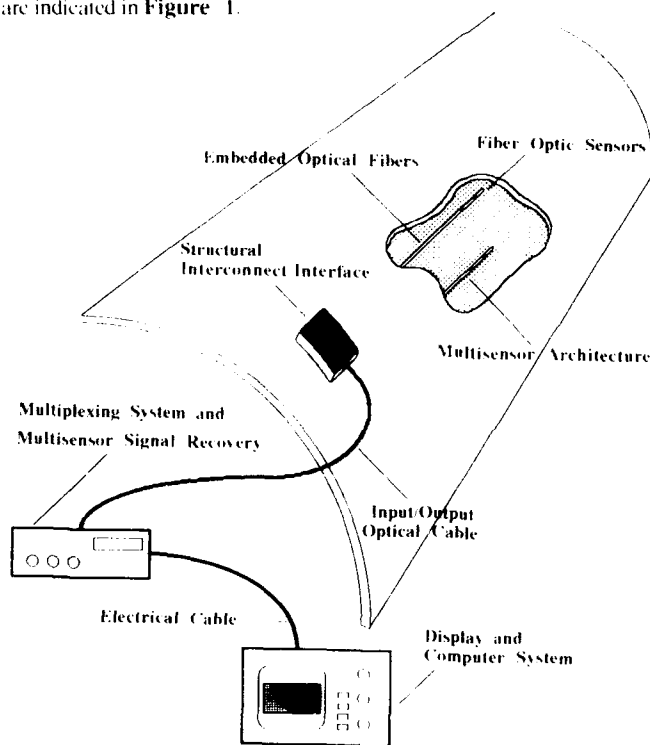
Figure 1.   Schematic of a Fiber Optic Smart Structure Indicating the Critical Areas of Development Required

1.1 Fiber Optic Sensors

The ideal sensor for Smart Materials and Structures will have to be capable of undertaking the wide range of measurements alluded to above and it would have to be:

-*Intrinsic* for minimum perturbation and stability
-*Localized*, to operate *remotely* with *insensitive leads*
-Able to *discern* the direction of measurand field change
-*Well-behaved* with *reproducible* response
-Able to determine *measurand field directly*
-*All-fiber* for operational stability
-Able to provide a *linear response*
-A *single optical fiber* for minimum perturbation
-*Single-ended* for ease of installation and connection
-Sufficiently *sensitive* with adequate *dynamic range*
-*Insensitive* to phase interruption at structural interface
-*Nonperturbative* to structure and *robust* for installation
-Interrupt immune and capable of *absolute measurement*
-Amenable to *multiplexing* to form sensing networks
-*Easily* manufactured and adaptable to *mass production*

The most important sensor performance indicators are: *dynamic range; spatial and measurand resolution and frequency response*, while some of the most critical issues to be addressed include: *interrupt immunity* and the need for absolute measurements, *signal fading* due to load induced birefringence, and thermal *apparent strain*.

The two fiber optic sensors with the most promise at this time are based on the:

Intracore Bragg Grating	Intrinsic Fabry-Perot
Merits	*Merits*
• absolute measurement	• high sensitivity
• automated fabrication	• fast response time (demodulation limited)
• minimal strength degradation (rebuffering	• localized with mm. spatial resolution
problem)	• absolute measurement with coherent
• multiplexed/demultiplexed	multiplexing
• fast response time (with wavelength ratiometric	*Demerits*
technique)	• limited strength unless localized mirror
• localized with few mm. spatial resolution	• difficulty in automated fabrication.
Demerits	• slow time response with coherent multiplexing
• sensitivity may not be adequate	• possible performance degradation with
• limited availability	mirrored end
• limited power with broadband light source	

1.2 Embedded Optical Fibers

In terms of embedded optical fibers the key issues are:
• *Influence on the Material Properties*
If optical fibers are to be embedded within practical composite material structures they must not: *compromise the tensile or compressive strength, increase the damage vulnerability or reduce the fatigue life of these materials*. Although preliminary evidence suggests that degradation of the material properties is minimal providing that the diameter of the optical fiber is less than about 125 μm, fractographic studies reveal that optical fibers embedded at an angle to the adjacent ply directions of the composite material create resin cavities (termed "resin-eyes" because of their shape). The formation of resin-eyes leads to high stress concentrations at the host/optical fiber interface which may over a period of time and under occassional high loading conditions lead to debonding of the optical fiber from the host. Clearly, more definitive research will be needed before optical fibers can be imbedded with *confidence* within composite structures intended to have a 20 (plus) year working life.
• *Sensor/Host Interface and Coatings*
It is possible that this high stress concentration around the optical fiber may be diminished with coatings of appropriate size and stiffness. Clearly, careful consideration will have to be given to the diameter of optical fibers and their type of coating if they are to be embedded within composite structures and *function correctly* with no performance degradation for the useful life of the structure. Professor J. Sirkis and his group are starting to study these issues.
• *Performance Life of the Sensing System*
When the optical fibers are embedded coilinear with the ply direction there is no appearance of a resin eye and minimal stress concentration is expected. However for this configuration a resin void is formed on the end of the optical fiber and this could lead to initiation of debonding from the host material. This suggests that it may not be prudent to locate the sensing region at the end of an embedded optical fiber intended for extensive use. More research is needed to ascertain the seriousness of this problem.
• *Sensing System Damage Vulnerability and Degradation*
A sensing system within a practical Smart Structure will have to be fairly robust and degrade gracefully when the structure suffers modest damage. Special coatings and a judicious choice of location and orientation may help to avoid premature fracture of the optical fiber but in the long term rerouting of optical information through the sensing network may be necessary.

1.3 Multisensor Architecture and Multiplexing Strategy

• *Sensing System Architecture*
The type of measurement to be undertaken will dictate whether the fiber optic sensors should be : *point, long path or distributed* while the nature of the structure will determine if they are multilayered or limited to form a single layer. Optical fiber orientation, placement in the composite layup, spatial

resolution and constraints imposed by the finite bend radius are all important factors to be considered. It will also be important to identify any special structural features or regions of high stress concentration. The power budget and signal to noise factors will certainly play a key role in defining the sensing system architecture. Sensing system damage vulnerability and ease of fabrication represent other considerations to be taken into account.

• *Multiplexing Strategies*

Multiplexing is the merging of data from several channels into one channel, while demultiplexing is the inverse. The primary parameters used in optical multiplexing schemes are: wavelength, time, frequency, phase and space. Consequently, there are five multiplexing techniques:

• *Wavelength Division Multiplexing* (WDM) - each sensor operates at a different wavelength. The relevant wavelength encoding can be performed by either: the light source, spectral filters, resonant cavities or dispersive elements. Demultiplexing is acheived by means of a spectral analyser.

• *Time Division Multiplexing* (TDM) - light pulses are simply combined and differences in the transit time for the light signals propagating along the various channels are used for demultiplexing. For practical structures this would require very narrow pulses. This would lead to low signal strength and very fast demodulation.

• *Frequency Division Multiplexing* (FDM) - each interferometric sensor operates with a signal that is modulated at a different frequency. Demultiplexing of the various signals is acheived by means of appropriate bandpass filters to ensure that each detector only receives signals from a specific sensor.

• *Phase Division Multiplexing* (PDM) - or coherence multiplexing, uses pairs of interferometres each with a cavity length greater than the coherence length of the source so no interference arises until the lengths of the two interferometers are made to match.

• *Spatial Division Multiplexing* (SDM) - this often involves some scanning mechanism to physically connect, in sequence, each of the sensors to the data link.

Currently, none of these multiplexing schemes can be developed into a microsystem that could either be embedded or form part of a small robust structural interface. This implies that the interconnect might have to involve a ingress/egress of the number of optical fibers used to constitute the sensing system. If a fast response, high resolution (few mm and about 10 µstrain) distributed strain sensing system was available this might reduce the severity of this problem, but no such system has been developed.

1.4 Multisensor Signal Recovery and Structural Interconnect/Interface

• *Multisensor Signal Recovery*

A multisensor signal recovery system should be reliable, compact, inexpensive and involve as few components as possible. Many approaches under consideration today are based on the use of a single signal recovery system to service a number of sensors by means of some multiplexing scheme. Invariably this leads to sequentially sampling the output from each sensor. The alternative approach of providing a signal recovery for each sensor is likely to be expensive and impractical unless the system can be built on an optoelectronic chip and either embedded within the structure or incorporated into the structural interface or connector.

• *Structural Interconnect/Interface*

The nature of the structural interconnect problem hinges on whether the output from the structure is optical or electrical. Current thinking is predicated on optical signals flowing into and out of the structure via the structural interface. In general this interface must have minimal structural perturbation; be easy to fabricate and introduce into the production of the structure. If multiplexing is not used each sensor would have its own output and a ribbon or bundle of optical fibers would have to egress from the structure. This may be the case even with multiplexing since most schemes do not lend themselves to sufficient miniaturization to be embedded or included in the structural interface. Although, structural interconnects can be made to a broad surface or an edge, the former tends to be favored in many cases as edges are often trimmed or used for structural support. The development of a "reliable" and "convenient" structural interconnects is likely to represent one of the most critical steps in the implementation of Smart Structures for in many of the situations where this technology could be of significant benefit interconnection will have to be performed by unskilled personnel, possibly in hostile environments, such as an aircraft on a subzero runway in a blizzard.

The structural interconnect problem would be greatly simplified if a single electrical cable could be used, the interface would then serve as both a structural and electrical/optical interface. This is clearly

only practical if a single optoelectronic chip can be developed that would generate the light signals used to interrogate the array of fiber optic sensors integrated into the structure and to convert the subsequent optical sensing signals back into electrical signals, **figure 2**.
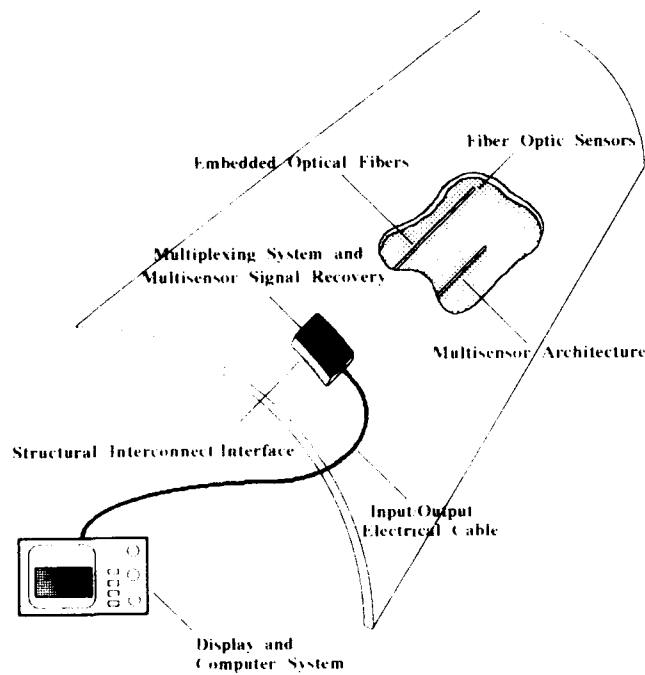
Figure 2. Schematic of Fiber Optic Smart Structure with Structurally Integrated Signal Processing

PASSIVE WAVELENGTH DEMODULATED BRAGG MULTI-LASERSENSOR SYSTEM

Our recent development of a simple, passive and fast method of wavelength demodulating optical fiber intracore Bragg grating sensors lends itself to an approach that could conform to a multisensor electrical optical structural interface as suggested above. The concept involves using each in-fiber Bragg grating sensor to control the wavelength of a laser and monitoring this wavelength with our *wavelength ratiometric technique*, **figure 3** [Melle et al 1991]. In **figure 4** we propose one possible system based on this approach that could be built on an optoelectronic chip, handle a large number of sensors, yet be small enough to be mounted inside the structural interconnect or embedded within the structure. Either way the connection to the structure would be through a conventional type electrical interconnect. In this approach each laser would be switched on (or excited) in sequence so that only one wavelength demodulation detection system would be necessary. If, however, fast time response is required then a parallel system would be used and each laser sensor would have its own wavelength ratiometric detection system, as in figure 3
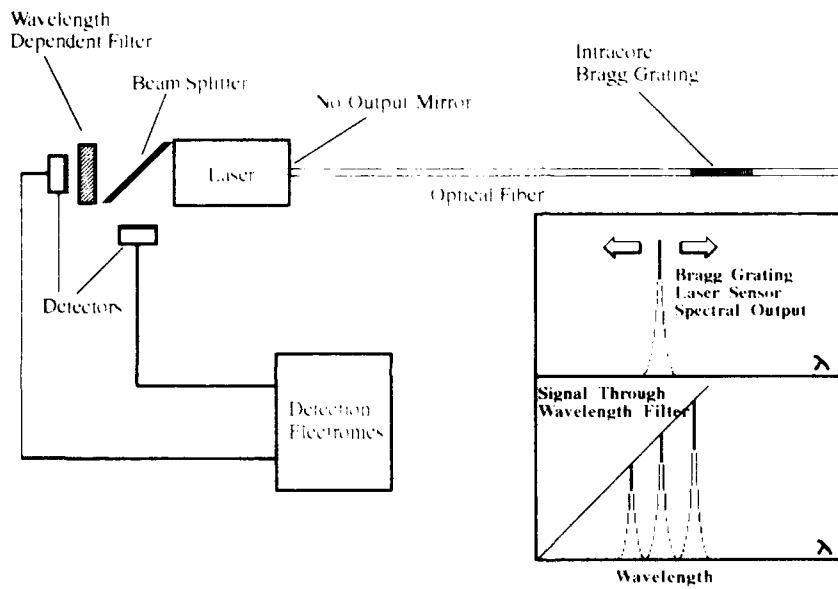
**Figure 3.   Schematic of Wavelength Dependent Ratiometric
Bragg Grating Laser Sensor**
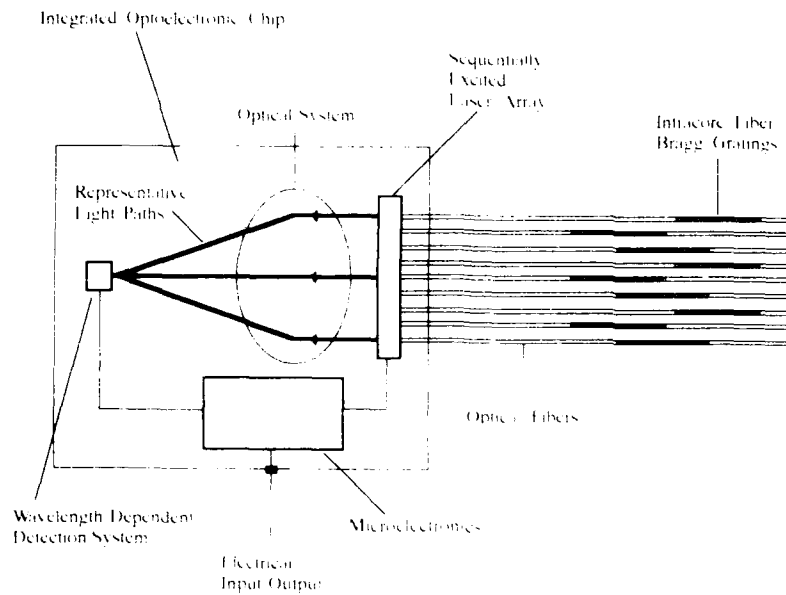
Figure 4. Schematic of Wavelength Dependent Ratiometric Multiplexed
Multiple Bragg Laser Sensor System

SUMMARY

A number of the important issues facing the development of fiber optic based smart structures is discussed. One of the most critical, from the standpoint of implementation of this technology, involves the interconnect to practical structures, like aircraft wings. These structural interfaces will have to function in operational environments, be extremely robust yet nonperturbative of the structure. We have suggested that this might be achievable with a set of structurally integrated fiber optic Bragg grating laser sensors that are interrogated with the simple wavelength demodulation scheme we have devised since this would permit the signal processing system to be build on a small optoelectronic chip which could be mounted within the structural interface. This would permit a single electrical cable to be used with a conventional type electrical interconnect to the structure.

ACKNOWLEDGEMENTS

REFERENCES

Melle S.M., Liu K. and Measures R.M.,1991, "Strain Sensing Using a Fiber Optic Bragg Grating", SPIE OE Fibers'91 Conference Fiber Optic Smart Structures and Skins IV. Boston, September 5-6.

Fiber-optic interferometric sensors for ultrasonic NDE of composite materials

Kexing Liu and Raymond M. Measures
*University of Toronto Institute for Aerospace Studies (UTIAS),
4925 Dufferin Street, Downsview, Ontario M3H 5T6, CANADA*

ABSTRACT: Interferometric fiber optic sensors using ordinary single-mode fibers
were studied to detect elastic strain waves for nondestructive evaluation of
composite materials. This fiber sensor has been embedded in both graphite/epoxy
and Kevlar/epoxy composite specimens. Applications and limitations of the sensor
are also discussed.

Composite materials are finding a widespread use in the aerospace and other industries.
Because of their special properties, it is desirable to establish new non-destructive
evaluation (NDE) techniques for in-service (in-situ) monitoring of composite structures.
These advanced NDE techniques should be capable of sensing damage arising within a
structure in real-time. The use of a dielectric sensor is preferable for embedding in
composite materials. The fact that optical fibers are dielectric material, free from
electromagnetic interference, small in size and light in weight and can survive high
temperature and high pressure has led to the investigation of embedding optical fibers into
solid materials, particularly the advanced composite materials for nondestructive testing and
structure integrity monitoring [1].

Optical fibers as intrinsic sensing elements have been studied for the detection of ultrasonic
strain waves within composite materials since more than a decade ago [2]. More recently,
an ultrasonic detection system based on fiber Michelson interferometry for composite
damage monitoring was reported [3]. The system employed an active homodyne
demodulation technique to maintain linearity and maximum sensitivity. The fibers were
embedded in both Graphite/epoxy and Kevlar/epoxy composite specimens. Acoustic
emission signals were detected for both tensile loading and out of plane loading. The
system provided single-ended sensing with real-time monitoring capabilities, and had a
broadband response of 100kHz to 2MHz.

The use of interferometers based on ordinary single-mode fibers for the detection of low
frequency strain [4] and ultrasonic waves [3] within composite materials has the obvious
advantages of simpler configuration, higher sensitivity and lower cost compared with those
based on polarization preserving fibers. However, the problems associated with the
embedded ultrasonic strain wave sensors based on ordinary single-mode fibers such as
localization and sensitivity variation due to the state of polarization (SOP) have drawn little
attention in the smart structures sensing community [5][6]. In this paper, the results of a
sensitivity analysis will be given for the detection of elastic strain waves with embedded
ordinary single-mode fibers. Problems of localization and visibility variation due to SOP

and birefringence effects will be discussed. The application and limitations of embedded ordinary single-mode fibers in the form of a Michelson interferometer for ultrasonic strain wave detection will be briefly presented.

The response of an embedded optical fiber to propagating elastic waves is determined by the propagation and polarization direction of the ultrasonic waves with respect to the orientation of the optical fiber and the state of polarization (SOP) of the optical beam in the fiber [6]. In the frequency range where the acoustic wavelengths are of the order of the fiber sensor length, the output is an integral for the ultrasonic-wave component along the direction of the optical fiber.

Visibility variation is often referred to as polarization-induced fading (PIF) [5]. Assuming that the 2x2 fiber directional coupler has splitting ratio of 1:1, and the losses are equal in both sensing and reference fibers, for a uniform strain field in the core of the fiber, such as in the hydrostatic case, the visibility is determined by the relative SOP's in the two fibers and the input polarization orientation [5]. It is known that the visibility variation can be compensated by controlling the input SOP of the light beam, thereby, maintaining maximum visibility [5]. However, for non-uniformed strain field in the core, as is the case in this paper, the visibility will be affected by an additional factor, i.e. the ultrasonic field induced birefringence [6] This component cannot be nulled out by using the suggested feedback control of the input SOP, because the feedback servo control will not follow the high speed SOP change.

Nevertheless, embedded interferometric sensors based on ordinary single-mode fibers can still be used in many non-absolute ultrasonic measurements, such as ultrasonic pulse delay measurement or relative ultrasonic spectrum distribution measurement.

Absolute localization cannot be realized with an embedded ultrasonic sensor based on a pair of ordinary single-mode fibers. This is due to the fact that the two very-well paired fibers have different birefringencies and thus different SOP's, even though they may be subject to the same ultrasonic field (if the ultrasound wavelength is much greater than the fiber diameter and both fibers are well bonded to the matrix). As a result, the ultrasonic induced phase changes in the lead section of both fibers do not cancel each other upon recombination at the directional coupler [6].

However, localization will still be achieved if the ultrasonic field is localized. This is often the case in laboratory experiments where the emission sources are fairly close to the sensing section of the fiber, or specimens are small such that the embedded lead section of fibers is relatively short.

Ultrasonic detection using embedded Michelson/Mach-Zehnder interferometric sensors based on polarization preserving fibers will provide localization if the principle axes of the two fibers are aligned. The polarization induced visibility variation will be eliminated. Therefore, for precision measurement and field applications, polarization preserving fibers and components are recommended [6]. This, nonetheless, is subject to the availability of

the high performance fiber polarization components, such as polarizing directional couplers and connectors and involves the difficult tasks of laying the two optical fibers into the composite material with their polarization axes aligned.

In our experiments, the sensor was configured as Michelson interferometer with active homodyne phase demodulation [3] as shown in Fig.1a. The sensor response to high frequency, low amplitude acoustic signals is linearized and at maximum sensitivity. The signal fading due to random orientation of the SOP in the fiber was minimized in the laboratory experiments by adjusting the input SOP and securing the lead fibers against vibration and air current flow.
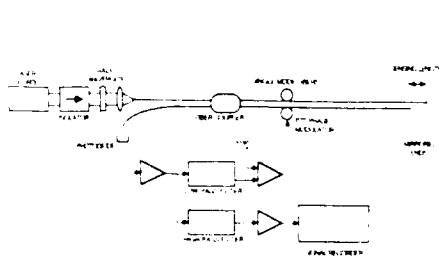
Fig.1(a) The Sensor Configuration.   Fig.1 (b) Experiment for Pulse Measurement.
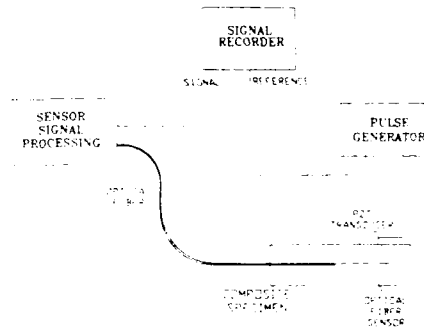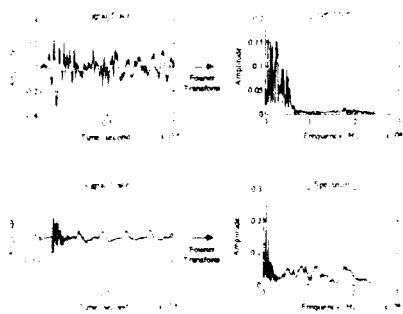
Fig.2 Acoustic Emission Spectrum.   Fig.3 Ultrasonic Pulses Detected.
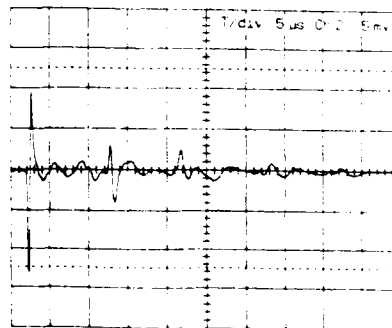
In the first instance, the fiber optic sensor (FOS) was embedded in a graphite/epoxy composite specimen (1" x 10"). The layup of the specimen was [0/0/90/90{90}90/90/0/0], where {90} denotes the position and orientation of optical fibers. The specimen was subject to a tensile loading with an MTS-880 testing system. Fig.2 shows acoustic emission signals detected by the FOS resulting from damage (crack and delamination) created during the loading. Using Fourier analysis, the relative spectral characteristics of signals detected were examined.

The second example demonstrates a measurement result of ultrasonic pulse delay with the optical fiber sensor. The sensor is embedded in an epoxy specimen (Hysol TE6175/HD3561) of approximately 1" x 1" x 1" in dimension and the experimental setup is revealed by Fig.1b. The ultrasonic pulses was generated by the broadband longitudinal transducer. Fig.3 shows the detected pulse and the echoes reflected from the surfaces of the cube.

In conclusion, detection of elastic strain waves for nondestructive evaluation with embedded ordinary single-mode fibers in an interferometric setup was discussed. Sensors based on ordinary single mode fibers can be used for relative ultrasonic spectrum analysis and pulse delay measurement for confined/localized elastic strain waves. However, in addition to the visibility variation due to random fluctuations of the birefringence of the optical fibers and the input SOP orientation, which can be compensated, the ultrasonic strain wave induced birefringent phase retardation in the fiber will also cause sensitivity variation and non-localization in the sensor, which cannot be easily compensated. In general, absolute ultrasonic amplitude measurement cannot be realized using ordinary single mode fibers, due to the anisotropic nature of the elastic strain waves. However, interferometers based on polarization preserving fibers and polarization components can, if used correctly, overcome these difficulties.

REFERENCES

1. Measures, R.M., "Smart Structures with Nerves of Glass", *Prog. Aerospace Sci.* Vol.26, pp.289-351, (1989).

2. Claus, R.O., and Cantrell Jr., J.H., "Detection of Ultrasonic Waves in Solids by an Optical Fiber Interferometer", *Proc. IEEE Ultrasonic Symposium*, pp.719-721, (1980).

3. Liu, K., Ferguson, S.M., and Measures, R.M., "Fiber-Optic Interferometric Sensor for the Detection of Acoustic Emission within Composite Materials", Optics Letters, Vol.15, No.22,pp.1255-1257, (1990).

4. Valis, T., Tapanes, E., Liu, K., and Measures, R.M., "Passive Quadrature Demodulated Localized Michelson Fiber Optic Strain Sensor Embedded in Composite Materials," *J. of Lightwave Technology*, Vol.9, pp.535-544, (1991).

5. Kersey, A.D., Marrone, M.J., Dandridge, A., and Tveten, A.B., "Optimization and Stabilization of Visibility in Interferometric Fiber-Optic Sensors Using Input-Polarization Control", *J. of Lightwave Technology*, Vol.6, pp.1599-1609, (1988).

6. Liu, K., and Measures, R.M., "Detection of High Frequency Elastic Strain Waves with Ordinary Single-Mode Optical Fibers", to be published.

Resin sensors for composite cure monitoring

B. Zimmermann*, M. de Vries**, R. Claus**

* FIMOD Corporation, P.O. Box 11192, Blacksburg, VA 24062
** Fiber & Electro-Optics Research Center, Virginia Tech, Blacksburg, VA 24061

ABSTRACT: The performance of a novel fiber optic composite cure monitor, developed for thermoset composite fabrication process control, is discussed. The monitoring system includes a sensing fiber manufactured from the composite resin itself. This avoids incorporation of foreign materials into the composite for cure monitoring purposes. Embedded all-glass fibers can negatively affect the composite structure, or cause inhomogeneities which result in composite delamination. By choosing the material of the monitoring optical waveguide to possess similar thermo-elastic properties to those of the resin of the composite, the inhomogeneities and associated negative effects within the composite are avoided. Proof of principle was shown using neat resin specimens and pre-impregnated graphite/epoxy coupons.

1. INTRODUCTION

The work described in this manuscript was prompted by process monitoring requirements which include the capability of determining the cure state of composites during fabrication. In addition to being able to perform an in-situ measurement on the state of cure, it is desirable to do so by using sensors which can be embedded deep within the composite without affecting the integrity of the finished component. This is especially critical for thick composites, where conditions in the center of the specimen may be very different from those on the outside surfaces where temperature and pressure are usually monitored. The sensor elements to be embedded must therefore be as non-intrusive as possible either by minimizing their size or by manufacturing them out of materials which are either identical or very similar to those of the composite itself. Embedded fiber optic sensors have been proposed by Druy et al (1988), and used for cure monitoring applications. Many of these sensors, however, are intrusive due to their large size and/or "incompatible" material type, often deteriorating the composite's structural integrity. Afromowitz (1988) suggested to utilize optical fiber sensors made out of the composite resin itself such that the cure can be monitored in the composite without affecting its structural integrity. Preliminary experiments were conducted with industrial grade, fast cure epoxies, and feasibility was demonstrated. It has been shown that the concept can be used not only with fast cure epoxies, but also with typical composite resins and pre-impregnated laminates.

2. THEORY

The proposed composite cure monitor correlates the resin refractive index to its state of cure. The refractive index change of the resin is monitored using optical fiber waveguide techniques. A waveguide fiber is manufactured using the resin material of the organic matrix composite itself. After insuring that the resin fibers have been allowed to cure completely, they are embedded in the resin to be monitored. An optical signal launched into the cured resin fiber will excite a number, M, of optical "modes" given approximately by:

$$M = \frac{v^2}{2} \ ,$$

(1)

where v, the waveguide normalized frequency, is given by :

$$v = \frac{2\pi a}{\lambda} (n_1^2 - n_2^2)^{\frac{1}{2}} \ .$$

(2)

In Equation (2), **a** is the resin fiber diameter, λ the operating wavelength, n_1 the refractive index of the cured resin fiber, and n_2 the refractive index of the resin to be monitored. As the resin cures, the optical power, P, transmitted through the resin fiber changes according to:

$$\frac{dP}{dt} = \frac{dP}{dn_2} \frac{dn_2}{dt} \ ,$$

(3)

where dP/dn_2 is assumed to be proportional to dM/dn_2, that is:

$$\frac{dP}{dn_2} = K \frac{dM}{dn_2} \ .$$

(4)

K depends on several factors including optical launch conditions into the lead fiber, fiber interaction length, cure temperature, and cure pressure. As will be explained in the experimental section, a reference signal, P_{ref}, will be tapped from the optical source to compensate for source output drift. The Normalized Transmitted Power (NTP), which will be related to the state of cure, is given by:

$$NTP = \frac{P}{P_{ref}} \ .$$

(5)

3. RESULTS
The resin's optimum operating wavelength, i.e., the wavelength at which optical loss was minimized, was found using a commercially available fiber spectrum analyzer. The resin used in the experiments was found to have minimum signal attenuation between 800 and 1100 nm. It was therefore chosen to perform the experiments using a CW 816 nm laser source.

Subsequent to manufacturing and curing the resin fiber sensors, they were placed in a heating assembly as shown in Figure 1. This assembly allowed cure monitoring using neat resin specimens. The assembly consisted of a laser, a fiber optic splitter, two photodetectors, an optical power meter, two lead fibers, a resin fiber sensor, a heating block, and a GPIB interface to a personal computer. The output of the laser was split into two arms; the output of one of the splitter arms was sent directly to photodetector # 1 as reference signal, while the output of the other arm was launched into the resin fiber through a lead-in fiber. The output of the resin fiber was picked up by a lead-out fiber and directed to photodetector # 2. The power levels of the two detectors were processed by the optical power meter and passed on through a GPIB bus to a computer for data acquisition. An A/D board in the computer also allowed acquisition of the temperature in the heating block.

Figure 2 shows the results of monitoring the cure of thermoset neat resin specimens using the assembly of Figure 1. A graph of Normalized Transmitted Power (NTP) and its numerical derivative (dNTP/dt) versus time of cure shows how NTP decreases steadily as the resin cures, while dNTP/dt which is indicative of the rate of cure approaches zero.
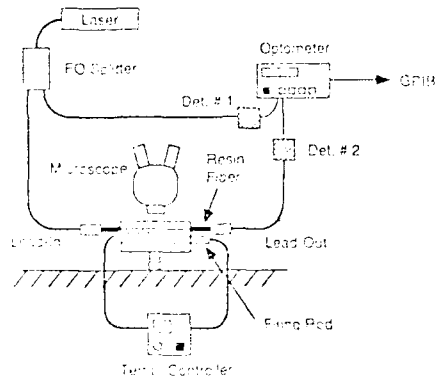
Fig. 1. Thermoset Neat Resin Cure Monitoring Set-Up.
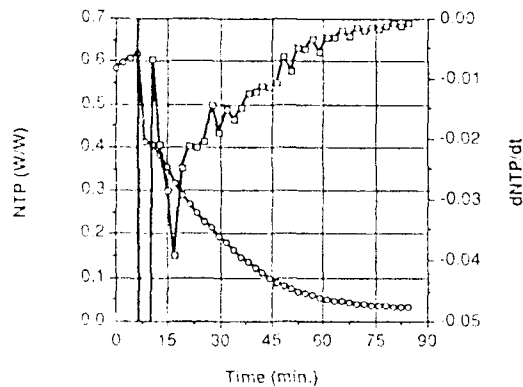
Fig. 2. Graph Showing NTP and dNTP/dt Versus Cure Time for the Neat Resin Process.

The assembly shown in Figure 1 was also used to monitor the cure of a pre-impregnated laminate composite coupons. The prepreg laminates were placed in an aluminum mold which contained access ports through which the resin fiber sensor was routed. A total of 32 prepreg plies (0°-90° orientation) was used; the resin fiber was placed between the 12th and 13th ply, parallel to the matrix fibers. Pressure and temperature in the mold were applied using a 1 ton hot press. A pre-cure temperature of approximately 125 °C was used for 45 minutes to condition the specimen before ramping up the temperature to 175 °C.

Figure 3 shows NTP and temperature versus cure time, and clearly demonstrates the sensor's behavior both during the pre-cure conditioning cycle as well as the cure cycle. During the 45 minute conditioning period NTP falls slowly, already indicating the presence of resin gelation. As the temperature is increased to 175 °C, NTP first increases due to a

decrease in the resin fiber density, then drops off sharply once curing sets in. Figure 4, on the other hand, shows the numerical derivative of NTP and temperature versus cure time. Again, dNTP/dt approaches zero as the composite reaches its fully cured state.

4. SUMMARY

The feasibility of a non-intrusive, in-situ fiber optic composite cure monitor has been demonstrated. Experiments were conducted using both neat resin and pre-impregnated graphite/epoxy specimens. Results indicate that the cure state of a composite can be determined by monitoring Normalized Transmitted Power (NTP) through the resin fiber waveguide. Furthermore, numerical differentiation of NTP seems to allow monitoring of composite cure rate. Future work will include testing of the cure monitor in autoclave environments, as well as implementing algorythms for process control purposes.
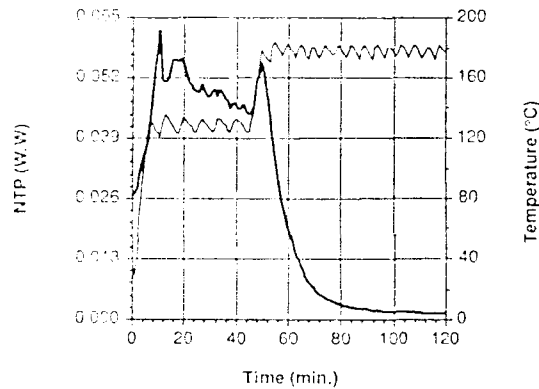
Fig. 3. Composite Cure Monitoring Results (NTP vs Time).
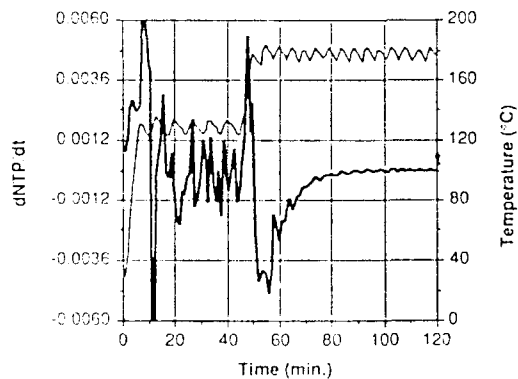
Fig. 4. Composite Cure Monitoring Results (dNTP vs Time).

6. REFERENCES

Afromowitz M A 1988 J. of Lightwave Technology, Vol. 6, No. 10
Druy M A, Elandjian L and Stevenson W A 1988 SPIE Proceedings Vol. 986, 130

Fiber optic sensors and architectures for large structures

Eric Udd
McDonnell Douglas Electronic Systems Company
Santa Ana, California 92705

Abstract

This paper provides an overview and design considerations for fiber optic sensors and architectures that are particularly well suited to large structures. Issues that are addressed include embedding fiber optic sensors into large composite structures, performance criteria and reliability and maintainability.

Introduction

Advanced aerospace platforms will require sensor technology to monitor the environment surrounding the platform as well as the structural integrity of the platform itself. Size, weight, immunity to electromagnetic interference, and environmental ruggedness, low cost and reliability are key characteristics of successful candidate technology. Recently fiber optic sensor technology has demonstrated several advantages when compared to electronic technology for advanced aerospace platforms [References 1-3], including being lightweight and nonobtrusive, all passive configurations, low power utilization, immunity to electromagnetic interference, high sensitivity and bandwidth, compatibility with optical data transmission and processing, long lifetimes and low cost.

These features can be key drivers in reducing the overall weight and size of advanced aerospace platforms while providing increased capability. With respect to weight savings the fibers may be embedded directly into composite materials without degrading the strength of the parts resulting in no net increase in space. The small size, environmental ruggedness and passive nature of the optical fiber makes this feasible. The fiber sensors may also be attached to the surface of the structure in analogy with current sensor technology and still offer significant advantages as the absence of electromagnetic interference eliminates the need for costly and heavy shielding and cabling while hardening the aerospace platform to electromagnetic jamming, damage due to electromagnetic pulses and lightning strikes. Because advanced aerospace platforms can be expected to be called upon to perform in increasingly challenging environments the number and performance requirements can be expected to increase. Fiber optic technology is uniquely suited to this task as the sensors may be multiplexed and their high sensitivity potential merges neatly with the high bandwidth capability of fiber optics.

This paper overviews the usage of fiber optic sensor technology in large aerospace platforms that could be used to support health monitoring and damage assessment functions to augment survivability, repairability, and maintainability while enhancing performance and control systems by providing flexible sensor information channels. Technical issues and tradeoffs that remain to be addressed are described in association with the system.

Fiber Optic Sensor System

A possible configuration of a fiber optic sensor system is shown in Figure 1. A series of fiber optic sensor strings that contain in line multiplexed fiber optic sensors are embedded or attached to the structure to be monitored. These sensor strings are configured to support a limited number of fiber sensors, nominally ten, in order to (1) improve yield and hence lower the cost of the sensor strings, (2) simplify processing requirements, (3) allow for rapid reconfiguration and graceful degradation of the system when damaged and (4) improve repairability and maintainability. To support this architecture an optical switch is used to sequentially interrogate the sensor strings. This switch could be a mechanical switch for multimode or single mode fiber optic sensor strings or it could be an integrated optic switch to support single mode sensor strings. While it is anticipated that some systems might allow the relatively

slow access available with mechanical switches it is expected that future high performance systems will use single mode integrated optical switches supporting single mode fiber optic sensor strings. Once each string is accessed by the switch a fiber sensor string demodulator will be used to separate the signals from the in line sensors using multiplexing techniques that are likely to include time, wavelength and frequency division methods. The output from the demodulator is then formatted into data packets and sent via a fiber optic transmitter to a system signal processor that does preprocessing necessary to support the onboard control systems such as vehicle health management and damage assessment.

Figure 2 illustrates how the embedded fiber optic sensor system might be integrated into an avionics system specifically the Air Force Pave Pillar structure. The output from the embedded sensor system could enter the avionics through a number of paths. One of the most likely scenarios would be for the output of the system signal processor to be fed directly into the vehicle health management bus. This data would then be used by the vehicle health management system processors to format the data into a form usable by the mission avionics multiplex bus. This information would then be processed for display to the pilot and or used to correct mission profiles. The information from the embedded sensor system could also be used for flight control and used to directly support instrumentation displays.

Fiber Sensor Considerations

While there are many fiber optic sensors that have been or are being developed there are a number of issues that limit the number of sensors that currently appear to be good candidates. Specifically because connectors and points of ingress and egress out of the parts are relatively difficult (1) a single point of ingress and egress is highly desirable. This is especially important for the case of large structures that are made using material winding techniques such as those employed in making a composite tank for a launch vehicle as is shown in Figure 3. Here the fiber sensors would be wound into the part with the composite filament and could be used to support the manufacturing process. The embedded sensors could then be used to augment nondestructive evaluation and support vehicle health management systems. In order to avoid issues associated with the structural integrity of the part (2) the sensors should be no larger than the fiber diameter. Due to the large number of sensors expected to be needed for large structures (3) the sensor strings should be readily manufacturable at low cost and (4) the sensors should be resistant to fluctuations in signal level caused by connector and cable loss. When these conditions are evaluated two of the most promising candidates are etalon [References 4-5] and grating [References 6-8] based sensor strings. Each of these sensor types can be multiplexed [Reference 9] using time and wavelength division techniques in single ended configurations. They can be designed to be no larger than the fiber diameter and appear to be amenable to low cost manufacturing. Because these sensors use spectral encoding of their signals they also meet the criteria for resistance to signal degradation due to connector or cable attenuation fluctuations. For large structures however there are still issues for these sensors that involve the cost of very large numbers of sensors and the signal processing needed to support them.

One way to address these issues is to use two sets of sensors. One set would be a very low cost set of sensors based on microbending or distributed sensing which would support a large low cost array that would be used to sense the general location of damage or a change in status of the structure. The finer, high performance sensor string consisting of etalon and or grating sensor strings would then be configured to accurately assess the situation.

Aerospace Applications

There are many potential applications of embedded sensor systems on board aerospace platforms and the advantages of light weight, small size and immunity to electromagnetic interference are compelling. Examples would include monitoring icing conditions on wings, excess vibration in jet engines, weight distribution prior to take off, and in flight and routine structural assessments to augment flight control and improve maintenance.

As an example of the problems that must be solved consider a wing structure that is 10m by 2m. Ideally structural information for this wing might be supported by strain sensors with 10 cm spacing. This would involve 2000 strain measurement per surface of the wing. If ten sensors were supported by each sensor string this would result in 200 strings that would have to be integrated and processed. Eventually this type of system may be realizable, the more likely near term scenario is a limited number of sensor strings supporting a less capable vehicle health management system that would still be substantially better than the best systems used today.

Other examples of aerospace applications would include the usage of fiber optic sensors to provide stabilization and damping of vibrations on large lightweight space platforms of the future and advanced launch systems.

Summary

An architecture for an embedded sensor system has been described and consideration given for the selection of embedded sensors to support it.

References

1. E. Udd, "Fiber Optic Smart Structures", in Fiber Optic Sensors: An Introduction for Engineers and Scientists, Edited by Eric Udd, Wiley, 1991.

2. R. M. Measures, "Smart Structures with Nerves of Glass", Prog. Aerospace Sci., 26, p. 289, 1989.

3. C. J. Mazur, G. P. Sendeckyj, and D. M. Stevens, "Air Force Smart Structures/Skins Program Overview", Proceedings of SPIE, 986, p. 62, 1988.

4. C. E. Lee and H. F. Taylor, "Interferometric Fiber Optic Temperature Sensor Using a Low Coherence Length Light Source", Proc. of SPIE, 1370, p. 356, 1990.

5. C. E. Lee, H. F. Taylor, A. M. Markus and E. Udd, "Optical Fiber Fabrey-Perot Embedded Sensor", Optics Letters, 14, p. 1225, 1989.

6. J. R. Dunphy, G. Meltz, F. P. Lamm and W. W. Morey, "Multi-function Distributed Optical Fiber Sensors for Composite Cure and Response Monitoring", Proc. of SPIE, 1370, p. 116, 1990.

7. W. W. Morey, "Distributed Fiber Grating Sensors", Proceedings of OFS 7, p. 285, Sydney, Australia, Dec. 2-6, 1990.

8. R. J. Campbell et. al., "Narrow-Band Optical Fibre Grating Sensors", Proceedings of OFS 7, p. 237, Sydney, Australia, Dec. 2-6, 1990.

9. A. Kersey, "Distributed and Multiplexed Fiber Optic Sensors", in Fiber Optic Sensors: An Introduction for Engineers and Scientists, Edited by Eric Udd, Wiley, 1991.
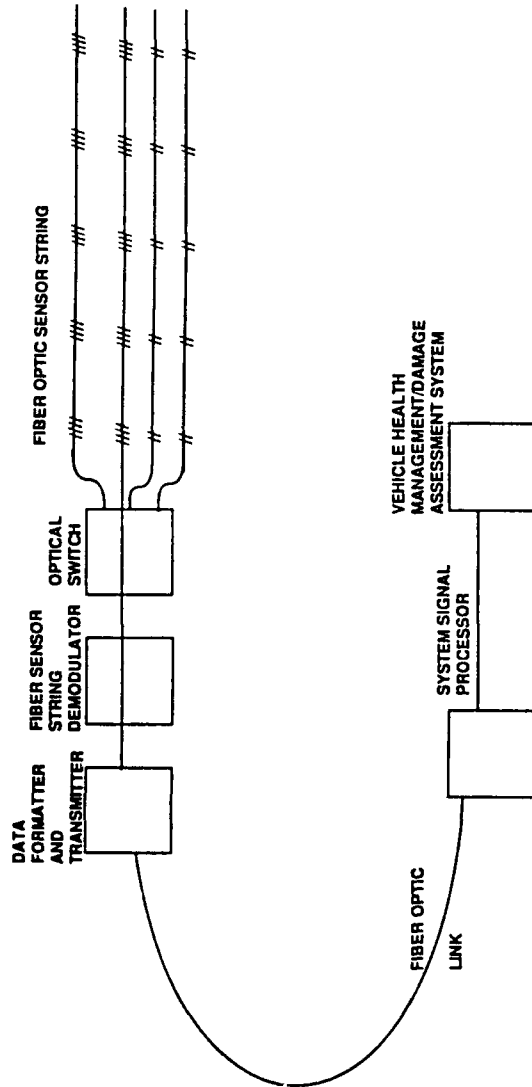
FIGURE 1. FIBER OPTIC SMART STRUCTURE ARCHITECTURE
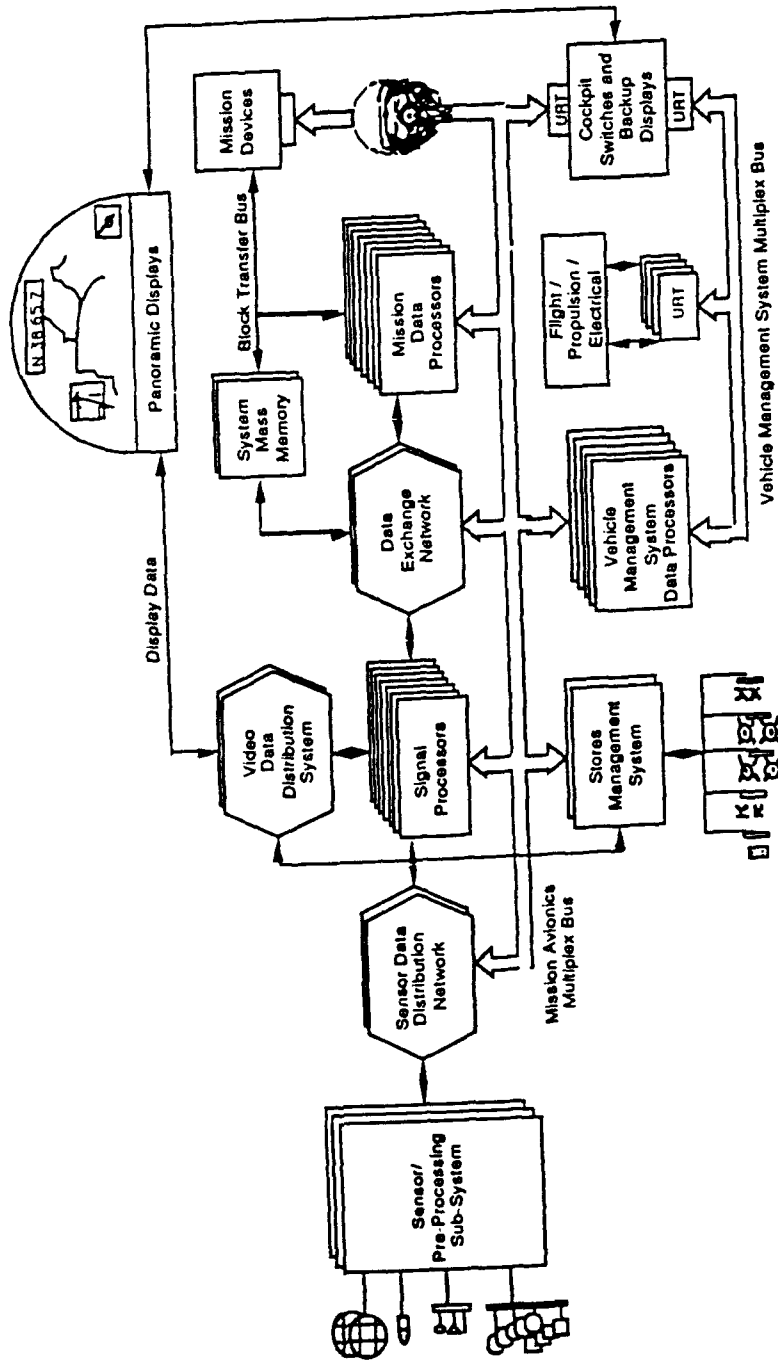
FIGURE 2. INTEGRATED AVIONICS SYSTEM USING THE AIR FORCE PAVE PILLAR ARCHITECTURE.
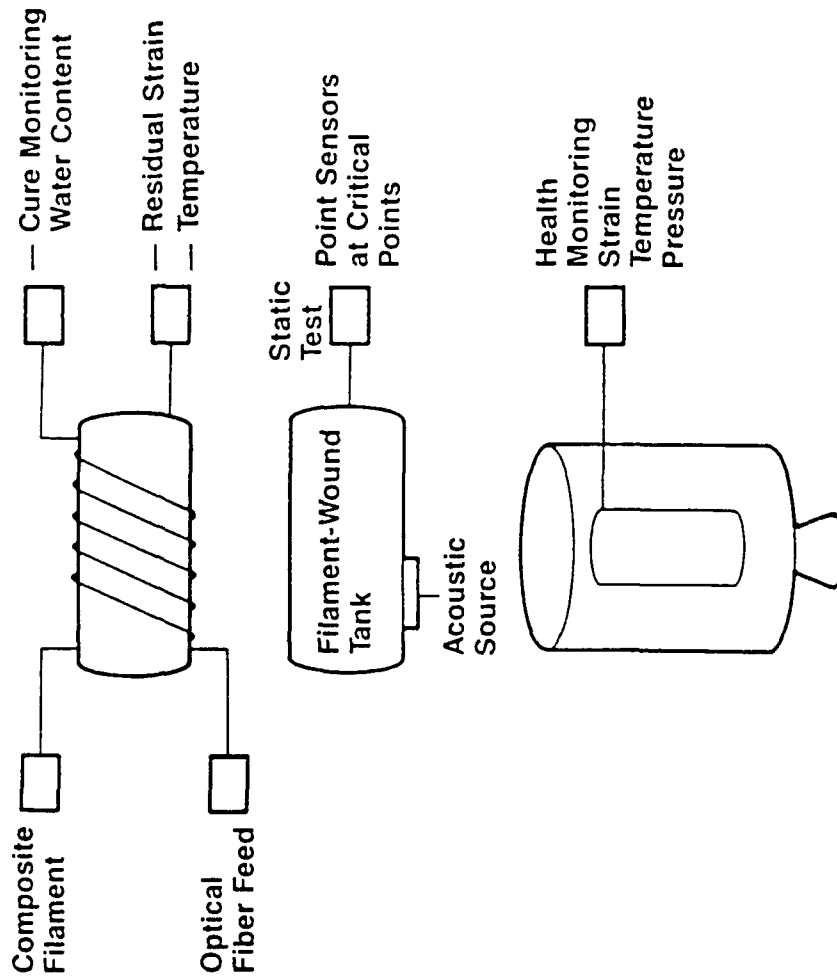
FIGURE 3.   EMBEDDING FIBER OPTIC SENSORS INTO A COMPOSITE TANK.

Distributed fiber optic sensors

JP Kurmer and AA Boiarski

Battelle, 505 King Avenue, Columbus, Ohio 43201

SA Kingsley

Fiberdyne Optoelectronics, 545 Northview Drive, Columbus, Ohio 43209

ABSTRACT: A summary of Battelle's recent efforts in distributed fiber optic sensor technology is discussed. The first is a temperature sensor based on optical time domain reflectometry; while, the second utilizes an interferometric technique to sense acoustic waves for the detection of leaks within gas or fluid filled pipes.

1. INTRODUCTION

A significant advantage of the distributed sensing approach is its ability to provide continuous high-spatial resolution monitoring of the measurand at many locations within a structure using a single length of optical fiber. This is in contrast to the point sensor approach in which an optical fiber is required to be routed from the data collection point to the sensing point for each and every measurement to be made.

We present two distributed fiber optic sensor systems currently being developed by Battelle for the electric power industry. The first is a temperature sensing system based on Rayleigh backscattering from the fiber cladding and utilizes optical time domain reflectometry (OTDR) techniques. The second system is an acoustic sensor for detecting and locating leaks within high pressure fluid-filled (HPFF) pipes.

2. DISTRIBUTED TEMPERATURE SENSING

Distributed fiber optic temperature sensing is currently an active area and several review articles have been written (Rogers 1986, Twerdochlib 1989). In Battelle's approach, the temperature sensitive fiber is formed by coating a modified, ultraviolet-light-curable polymer material onto a core glass during fiber production. By monitoring the changes in Rayleigh backscattered light from the fiber, local temperature changes can be measured along the fiber length. An OTDR in conjunction with a personal computer are used to collect and analyze the Rayleigh backscattered data. A 15 meter long sensing fiber was used in the demonstration experiments, shown in Figure 1. The fiber is looped twice through a 0.5 meter long tube heater to provide two hot spots of identical temperature located approximately 2.5 meters apart.

Typical relative backscattered light intensity data are shown in Figure 2. The reference signal shows the backscattered intensity as a function of distance while the heater is at room temperature. Also shown is the backscattered intensity when the heater is at 105 C. Notice that as the temperature is increased in localized regions of the fiber the relative backscattering decreases. A theoretical model, used to predict the change in scattering intensity due to the elevated temperature, (dB_s), is based on the work of Gloge (1971) and is in good agreement with the experimental data. The value of dB_s changes slightly with distance along the length of the fiber and can be easily corrected for in the data reduction. It is presently postulated that the length effect is associated with mode mixing effects within the optical fiber. Figure 3 shows both the dB_s length-corrected and original temperature data along the length of the fiber.

The spatial temperature resolution along the fiber is shown in Figure 4. Here, several hot zones were established with variable lengths. The fiber can accurately track the hot regions of 50 cm, 25 cm, and 10 cm lengths. Current spatial resolution of the system is on the order of 8 cm.
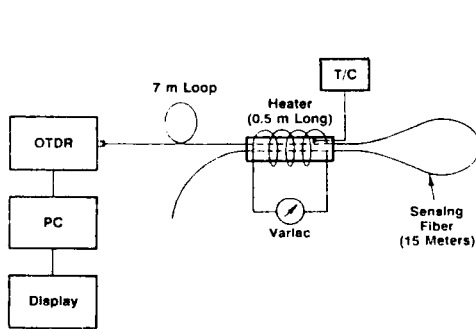
Fig. 1. Schematic of sensor system test setup
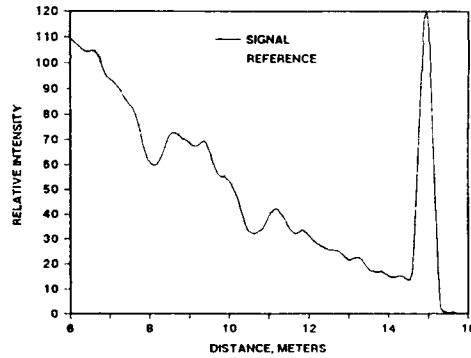
Fig. 2. Relative OTDR signal and reference intensities for two 105 C hot spots
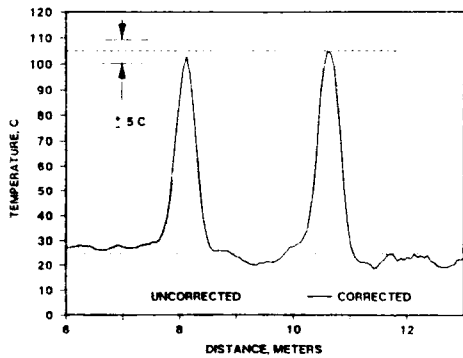
Fig. 3. Temperature data along fiber for two 105 C hot spots
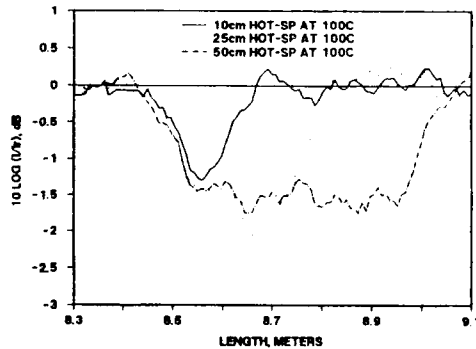
Fig. 4. Relative OTDR signal for variable hot spot width

A summary of the overall performance goals for the system developed were:

- Temperature accuracy: $\pm$ 2 C
- Temperature range: 20-150 C
- Sensor length: $\geq$ 20 meters
- Length resolution: 0.1 meters

The current application of this system is in temperature and performance monitoring of generator windings and switch gear circuit breakers for the power industry. Future applications include the monitoring of transmission lines, and transformers.

3. DISTRIBUTED ACOUSTIC SENSING

Another fiber optic sensor system being developed by Battelle is based on the Sagnac interferometer and will be used to sense the acoustic emission at HPFF pipe leak sites. In the Sagnac interferometer, Figure 5, commonly employed as a rotation sensor, the output of a laser or light emitting diode is split into two beams and directed into two counter-propagating directions around a coil of optical fiber. By rotating the fiber, the optical path lengths become imbalanced, the two beams arrive out of phase, and destructive interference can occur. This is known as the Sagnac effect and is one of the few non-reciprocal effects in such an interferometer (Culshaw 1984, Dakin 1988, Dakin 1989, Ezekial 1982). This system can also be employed to detect localized, pressure disturbances impinging on an optical fiber (Dakin 1987, Dakin 1990).

The theoretical pressure sensitivity for the fiber optic phase modulator currently being designed is approximately 3.1×10^{-5} radians/meter/pascal at an operating wavelength of 1.3 μm. The theoretical carrier to noise ratio (CNR) for the Sagnac interferometer is 147.6 dB re 1 mW re 1 Hz. The 1 mW reference is the input into the interferometer. From the CNR, we can calculate that the minimum detectable phase deviation is 3×10^{-8} radians/$\sqrt{Hz}$ re 1 mW. From the phase modulation sensitivity and the
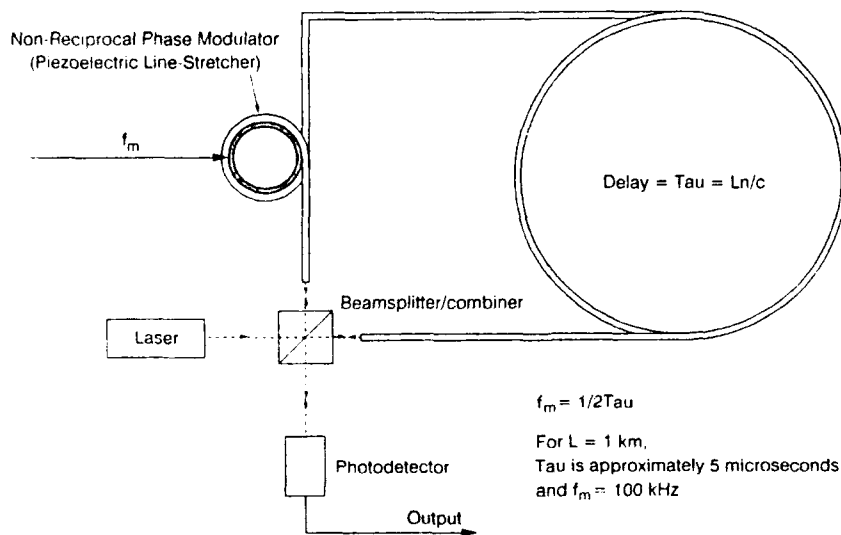
Fig. 5. The Sagnac interferometer

minimum detectable phase deviation, we find that the minimum detectable pressure is 1000 μPa/m $\cdot \sqrt{\text{Hz}}$ re 1 mW, which is equivalent to 60 dB re 1 μPa/$\sqrt{\text{Hz}}$ re 1 mW.

4. SUMMARY

The temperature sensor system developed met or exceeded the measurement goals for monitoring generator windings. The temperature measurement range for the sensor was 0-150 C and the estimated measurement accuracy was ± 5 C. Approximately 20 meters of sensor fiber could be interrogated with a length resolution of 10 cm. Modification of the fiber core and cladding materials should provide a sensing fiber length greater than 200 meters. Additionally, changes in the numerical algorithms should increase the temperature accuracy of the system.

The acoustic sensor being developed has a theoretical sensitivity of 1000 μPa/m $\cdot \sqrt{\text{Hz}}$ re 1 mW. An HPFF test chamber has been designed and built to evaluate its applicability for leak sensing and leak location determination. The system currently being developed should be applicable to both liquid and gas systems. The fiber optic system has been built, and preliminary tests indicate very good agreement with theory. Further work is under way to improve the sensitivity of the interferometer system to allow detection of very weak acoustic emissions.

The fiber sensing technology being developed for the electric power industry is believed to be directly applicable to the manufacturing, dynamic performance health monitoring and failure mode analysis of smart structures.

5. ACKNOWLEDGEMENTS

6. REFERENCES

Culshaw B 1984 *Optical Fibre Sensing and Signal Processing* (Peter Peregrinus Ltd.)
Dakin J P, Pearce D A J, Strong A P, and Wade C A 1987 *Journal of Optical Sensors* **2** 6 pp 403-406
Dakin J P, and Culshaw B 1988 *Optical Fiber Sensors: Principles and Components Vol 1* (Boston & London: Artec House)
Dakin J P, and Culshaw B 1989 *Optical Fiber Sensors: Systems and Applications Vol 2* (Boston & London: Artec House)
Dakin J P 1990 *The Distributed Fibre Optic Sensing Handbook* (U.K.: IFS Publications Ltd.)
Ezekial S, and Arditty H J 1982 *Springer Series in Optical Sciences Vol 32* (Springer-Verlag)
Gloge D 1971 *Applied Optics* **10** 10 pp 2252-2258
Rogers A J 1986 *J Phys D: Appl Phys* **19** pp 2237-2255
Twerdochlib M, Emery F T, and Brandt G B 1989 *EPRI Report 2487-1 (GS-6338)*

Optical fiber sensor-based smart materials and structures

R. O. Claus, K. A. Murphy, A. M. Vengsarkar and R. G. May
Fiber & Electro-Optics Research Center, Virginia Tech,
Blacksburg, VA   24061

ABSTRACT: Optical fiber sensors may be used to analyze the
properties of materials and structures during their fabrication, in-
service and degradation phases. Fiber sensor methods allow the
measurement of a wide range of physical observables and the fibers
themselves may be attached to or embedded within polymer, ceramic
and metal-based materials. This paper outlines fiber sensor
technology for "smart" materials and structures.

1. INTRODUCTION

Optical fibers have been developed for applications in measurement
science during the past fifteen years. Fiber sensors may be configured
to measure a wide variety of physical observables including strain,
temperature, vibration, chemical concentrations, acoustic and
ultrasonic waves, and displacement [1]. More than ten years ago, fiber
sensors were embedded in advanced polymer-based composites by the
first author to measure strain and temperature [2]. Since that time,
fiber sensor methods have progressed to allow more quantitative
measurements of these primary effects as well as information
concerning secondary materials effects such as crack propagation, ply-
ply delaminations in composite laminates, and material damage caused
by impacts. At the same time, parallel developments in specialized
fiber and coating materials and signal processing have allowed the
application of fiber sensor methods to a broader class of materials
analysis problems with improved signal analysis capabilities. This
paper outlines uses of fiber sensors for the analysis of material and
structural properties and suggests future directions.

2. EMBEDDED OPTICAL FIBER SENSORS IN MATERIALS

The usual concept of "smart" materials assumes that sensor, signal
processing and actuation functions are somehow built into the material,
either by the incorporation of individual elements or by the development
of materials with inherent sensory and actuation capabilities. Optical
fibers embedded as sensors are of potential concern because they may

perturb the integrity of the material and because their connectorization and networking pose technological challenges. Recent work has shown that major concerns here are 1) the orientation of the sensor fiber with respect to the host, 2) the size of the sensor fiber with respect to the host composite fibers, 3) the properties of the fiber coating, and 4) how the fiber-to-matrix interface fails under load. Additionally, application-related systems problems demand solutions to sensor repair and connectivity.

Recent research has addressed some of these problems and perhaps identified solutions to others. Initial studies of fiber embedding were performed by Czarnak and coworkers at Virginia Tech in 1987 [3]; similar work has been considered by others [4, 5]. Czarnak found that strain concentrations of as much as twenty occurred at the interface between embedded optical fiber sensor elements and the surrounding matrix in composite laminates. More recent work has considered the movement of fiber sensors during the embedding and curing process [6], methods for the manufacturing of so-called "low profile" fibers having outer glass waveguide diameters of as little as 35 microns [7], thus improving embedding properties, and the effect of the quality of the fiber-to-matrix bond on material failure characteristics [8].

Also, methods have been suggested to allow the repair and retrofitting of damaged fiber sensor elements [9]. Practical connector technology has not emerged to allow the interconnection of materials containing optical fiber sensor elements or networks [10].

3. OPTICAL FIBER SENSORS FOR MATERIALS ANALYSIS

Optical fiber sensors may be used to measure numerous material properties. This section reviews current applications and limitations.

During the lifetime of material and structural systems, optical fiber sensors may first be applied to the measurement of their fabrication. For some composite materials, this means cure monitoring and the general concern often is what set of parameters is required to determine properties to insure quality of resulting parts. Methods which use specialized optical fibers to determine changes in 1) the local resin chemistry [11], 2) the index of refraction of the resin near the tip of a fiber probe [12], and 3) local modulus via the monitoring of ultrasonic wave propagation [13], have been developed and demonstrated. Generally more complicated optical fiber sensor methods have been employed to additionally monitor the fabrication conditions for such materials, including material removal operations.

During the normal lifetime of "smart" materials, fiber sensors have

temperature may be measured using a variety of optical fiber methods. Recent developments have been extrinsic Fabry-Perot interferometric (EFPI) devices [14] and in-line fiber gratings [15]; both yield short gage length information and may offer multi-element multiplexing.

Vibration has been measured most effectively using two-mode elliptical-core fiber sensors, having limited gage lengths from centimeters to tens of meters in length and with insensitive lead-in and lead-out fiber sections [16]. The analysis and control of specific mode shapes in vibrating structures has been approached both by controlling the location of the sensors on the vibrating structures, and by varying the sensitivity of the sensor fibers along their lengths. Such weighted sensors may have applications in sensor array functions for environmental fields other than vibrational [17].

Optical fiber sensors have also been used for the analysis of damage in composites in several ways. One has been to use embedded arrays of selectively etched fibers which break locally when the host material is impacted [18]. Although this method is destructive in that the fiber sensor is not operational after one impact, it does give qualitative information concerning impact-induced events. Quantitative analyses of impact, delamination and crack initiation and propagation have been obtained using in-line EFPI sensors to detect ultrasonic waves [19], crack opening displacements [20], and strain field variations [21].

4. SUMMARY

Optical fiber sensors have been developed during the past decade for applications in the analysis of materials and structures. This brief discussion has outlined some of the major application areas. The following references should provide more detail.

5. ACKNOWLEDGEMENTS

6. REFERENCES

[1] E. Udd, ed.. *Fiber Optic Sensors*, Wiley Interscience, New York, 1991.

[2] R. O. Claus and J. H. Cantrell, Proc. IEEE Region 3 Conf, 1989.

[3] R. Czarnek. Proc. SPIE O/E Fibers (Boston, MA), 1989.

[5] A. Tay et al., Proc. SPIE O/E Fibers (San Jose, CA), 1990.

[6] K. A. Murphy, M. S. Miller et al., *JCTRER* **13**, 1 (1991), pp. 29-35.

[7] K. A. Murphy et al., Proc. SPIE vol. 1588, September 1991.

[8] C. DiFrancia et al., Proc. SPIE vol. 1588, September 1991.

[9] R. Claus et al., Proc. SEM Conf. (Milwaukee, WI), July 1991.

[10] G. Orcel, R. G. May and R. O. Claus, this volume.

[11] M. Druy et al., Proc. SPIE O/E Fibers (San Jose, CA), 1990.

[12] M. Afromowitz, Proc. Review of Progress in QNDE (San Diego, CA), July 1989.

[13] W. V. Miller et al., Proc. Review of Progress in QNDE (San Diego, CA), July 1989.

[14] K. Murphy et al., *Optics Letters* **16**, 4 (1991), pp. 273-276.

[15] D. Lyons, this volume.

[16] K. A. Murphy, B. R. Fogg, A. M. Vengsarkar and R. O. Claus, this volume.

[17] D. K. Lindner and K. Reichard, this volume.

[18] R. M. Measures, Proc. SPIE O/E Fibers (San Jose, CA), 1990.

[19] K. A. Murphy et al., Proc. SPIE Vol. 1588, September 1991.

[20] K. A. Murphy and R. O. Claus, in preparation.

[21] K. A. Murphy, R. O. Claus and S. B. Desu, Proc. Pittsburgh Energy Technology Conference (Pittsburgh, PA), September 1990.

The use of adaptive structures in reducing drag of underwater vehicles

K.J. Moore, M. Noori, J. Wilson and J.V. Dugan, Jr.

Cortana Corporation, 520 North Washington Street, Suite 200, Falls Church, VA 22046

ABSTRACT: Experimental and theoretical studies by researchers in several countries over the last 30 years have shown that the generation of a traveling wave on the surface of a moving body may reduce drag. A laboratory-scale investigation using wave parameters identified in recent CFD studies will further understanding of the physics of traveling wave behavior. Requirements for an active wall test device are discussed in the light of previous experience and new developments in active materials and adaptive structures.

1. TRAVELING WAVE CONCEPT

The possibility of using vortical flow to reduce drag has been known for a number of years. Suitably positioned transverse slots can result in entrained vortices and a significant reduction in end drag over the closure of a bluff body. In addition, experiments at NASA Langley have shown that ordered periodic vorticity injected into a turbulent boundary layer near a wall results in about 25% drag reduction over nominal flat plate values.

A related concept in fluid flow dynamics has been investigated with a view to improving the hydrodynamic performance of underwater vehicles. A traveling wave with specified and controllable phase velocity, amplitude, wavelength and shape is used to generate and trap vortices in the troughs of a flexible wall (Figure 1). The resulting secondary flow condition cannot be classified as conventional laminar, transitional or turbulent flow, but rather constitutes a new regime described as "controlled vortical flow". Analytical studies (Wu et al., 1990) have shown that an appropriate tailoring of traveling wave to flow parameters results in ordered vortical flow and an associated reduction in drag to a level substantially below flat plate values. Further computational verification of the traveling wave concept will likely be costly, and may not engender the same level of confidence as an experimental demonstration. Thus the need for a practical investigation has been identified.
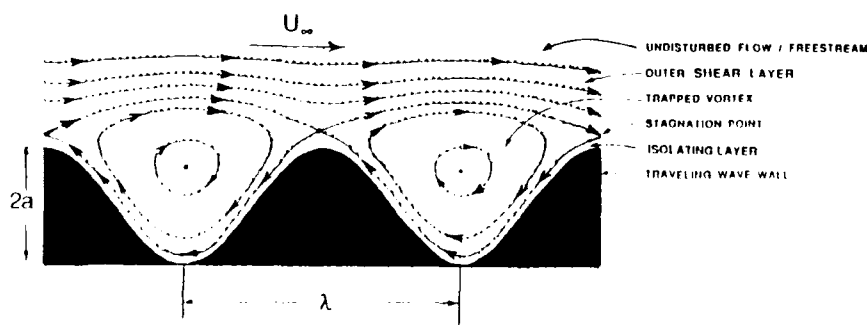
Figure 1. Elements of Traveling Wave Flow

2.   PROOF-OF-CONCEPT INVESTIGATION

The principal objectives of the proposed experimental investigation of traveling wave behavior are to demonstrate vortex entrapment in the troughs of a traveling wave using flow visualization techniques, to determine the combinations of wall and flow parameters giving drag reduction, and to assess the trade-off between the energy required for wall activation and the energy gained through drag reduction.

Experimental demonstration of the traveling wave concept is a multidisciplinary problem involving aspects of hydrodynamics, materials, and control systems technologies. In particular, practical demonstration of a controlled vortical flow regime will involve the design and fabrication of some kind of flexible wall device. A traveling wave with specified parameters (see below) will be used to generate and trap vortices in the troughs of a flexible wall. An active wall is defined as one which uses energy from an external source for deformation, in contrast to a passive wall which uses energy from the flow to deform. For the purposes of the proposed proof-of-concept investigation an active wall has been identified as the more attractive option, since it offers the experimenter a high degree of control, thereby eliminating the need for extensive instrumentation to measure traveling wave parameters.

3.   ACTIVE WALL TEST DEVICE

Computational fluid dynamics (CFD) studies of traveling wave behavior have shown that the amplitude-to-wavelength ratio, a/λ, and ratio of wave velocity to freestream velocity, c/U_∞, are critical parameters influencing vortex entrapment and establishment of a controlled vortical flow. Parameter ranges of interest are:

$$0.10 \leq \frac{a}{\lambda} \leq 0.25 \tag{1}$$

$$\frac{c}{U_\infty} \approx 0.5 \tag{2}$$

Target ranges for active wall parameters have been defined on the basis of the above values, together with information on wavelength, freestream velocity, and Reynolds number (based on wavelength) for practical applications. The need to reduce complexity and minimize costs has also been taken into account. Wavelengths (λ) should be in the range 5 to 20 cm, and the active device length (L) should incorporate at least 10 wavelengths, i.e. $L \geq 10 \lambda$. Amplitudes of oscillation should be in the range 0.5 to 5 cm such that (1) is satisfied. Frequencies of 10 to 100 Hz and wave velocities of 2 to 5 m.s^{-1} are required.

One of the major design goals for an active wall test device is that the wave amplitude, together with two of the three related parameters - wavelength, wave velocity and frequency - should be independently controllable. The potential to investigate various waveforms would be an added advantage. No definitive conclusions have been reached regarding the relative merits of 2-D (plate) and 3-D (axisymmetric body of revolution) devices. It has been postulated that drag measurements may be easier using a towed 3-D device, whereas investigation of ranges of wall and flow parameters and flow visualization experiments may be more readily performed using 2-D test plates.

4.   PREVIOUS EXPERIENCE

A number of active wall devices have been reported in the literature over the last 20 years. The relevant articles have been reviewed in some detail in order to avoid unnecessary duplication of existing results and to benefit from the experience of previous researchers. The choice of actuator type is seen to be critical in determining traveling wave parameters, notably amplitude and frequency. The majority of devices discussed in the literature are mechanically-

driven systems of the type shown schematically in Figure 2. These devices utilize a series of cams positioned on a camshaft with a successive phase difference between adjacent cams. These systems are generally fixed amplitude and wavelength devices, although frequency and wavespeed can be varied by altering the speed of rotation of the camshaft. The number of actuator elements per wavelength is important in determining the wave profile. Since the cost of any traveling wave device increases with the total number of actuators used, it is desirable to select the minimum number of driving elements to achieve the required waveform. Eight actuators per wavelength are generally believed to be necessary to achieve a satisfactory sine wave profile.
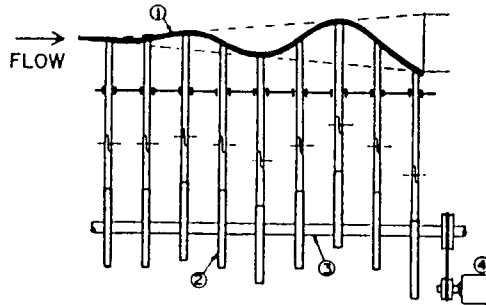
Figure 2: Schematic of Mechanically - Driven Active Wall Device
1=rubber, 2=cam, 3=camshaft, 4=motor

Most of the active wall devices described in the literature were designed for amplitude-to-wavelength ratios, a/λ, significantly lower than the desired range identified in the present CFD studies. Unfortunately, most investigators who claim to have measured a reduction in drag (or even a thrust force) using an active wall device have not documented their experiments in sufficient detail for parameter ranges to be identified unambiguously.

5.   CANDIDATE ACTUATOR SYSTEMS

The active wall test device required for a traveling wave proof-of-concept experiment constitutes an adaptive structure. In order to achieve the shape control associated with traveling wave generation, actuators must be incorporated in the active wall system. The following candidate actuators have been reviewed in the light of present requirements and recent developments in active materials technology:

* mechanical
* pneumatic
* hydraulic
* piezoelectric and electrostrictor
* shape memory alloy
* electromagnetic
* magnetostrictor
* electrically conductive polymer

The requirement for wave amplitudes ≥ 0.5 cm combined with frequencies in the range 10 to 100Hz imposes severe restrictions on actuator systems, many of which are either frequency- or amplitude-limited. In general, the requirement for wavelengths on the order of 10 cm can be readily accommodated.

The frequencies of mechanically-driven active wall devices described in the technical literature are generally ≤ 30 Hz. Some difficulties may be anticipated in combining amplitudes on the order of 1 cm with frequencies greater than ~ 30 Hz and a mechanical device designed to operate under these conditions would need to be reasonably robust. Ideally, a test device would be designed such that wavespeed, amplitude and frequency could be varied independently. However, the feasibility of achieving this degree of flexibility with a mechanically-driven device has not been demonstrated to date.

Recent progress in developing shape memory alloys (SMA's), such as Nitinol, has resulted in helical actuators which can produce deformations on the order of 1 cm. However, difficulties

in rapid cooling of SMA wires limit the frequency-response of state-of-the-art actuators to a few Hertz, even using active cooling. Both pneumatic and hydraulic systems are also limited to frequencies below 10 Hz.

Piezoelectric, electrostrictor and magnetostrictor actuators are all amplitude-limited (< 0.01 cm), despite recent significant enhancements in maximum strain values. An active wall device using piezoelectric ceramic actuators (PZT) has been developed (Park, Silvus and Cerwin, 1985). Amplitude, frequency and velocity of the traveling wave are all independently controllable, making this device extremely flexible in terms of parameter refinement. The use of an electronic drive system permits the generation of a traveling surface wave of arbitrary shape. However, wave amplitudes are small (≤ 13 microns), and even the use of state-of-the-art piezoelectric actuators could not produce deformations on the order of 1 cm.

The possibility of using the attractive and repulsive forces between electromagnets, or between an electromagnet and a permanent magnet, has been proposed as a means of generating a traveling wave. A device described in a Soviet Inventor's Certificate (Kim, Afonin and Bondarenko, 1972) uses damping fluid between the hull and outer skin, and a hull mounted inductor provides a variable electromagnetic field. The purpose of the device is "to reduce the frictional drag of underwater vessels". Unfortunately, no performance data are available by which to assess the suitability of electromagnetic systems for a traveling wave proof-of-concept experiment, or for practical applications.

Electrically conductive polymers are generally made by doping of insulating polymers. Certain dopant/polymer combinations exhibit dimensional changes of up to 10% in length associated with the insulating/conducting transition. Hence, these materials may be used as actuators converting electrical to mechanical energy. However, conductive polymer actuators have not yet been sufficiently investigated to be considered serious candidates for an active wall test device.

6.   CONCLUSIONS

A laboratory-scale experimental investigation has been identified as a logical next step in furthering current understanding of the physics of the traveling wave. The most cost-effective near-term option for an active wall device appears to be a mechanically-driven system with variable wavespeed and frequency, together with variable amplitude or wavelength. Such a device is expected to be noisy and cumbersome, and unsuited to underwater vehicle applications. Practical implementation of the traveling wave concept to reduce drag will likely involve significant developments in state-of-the-art active materials and adaptive structures, or the implementation of a tailored auto-oscillatory system.

7.   BIBLIOGRAPHY

Kim K I, Afonin A A and Bondarenko V I 1975 *Opisanie Izobretaniiak Avtorskomy Svidetel'stvy*
Park J T, Silvus H S and Cerwin S A 1985 *Review of Scientific Instruments* **56** 732
Wu J M, Wu J Z, Wu C J and Vakili A D 1990 *International Symposium on Nonsteady Fluid Dynamics* ed JA Miller and DP Telionis (ASME) pp 359-68

Electrically-controlled polymeric gels as active materials in adaptive structures

D. Segalman, W. Witkowski, D. Adolf

Sandia National Laboratories
Albuquerque, New Mexico
87185

M. Shahinpoor

Department of Mechanical Engineering
University of New Mexico
Albuquerque, New Mexico
87131

Abstract. This paper presents several applications of ionizable polymeric gels that are capable of undergoing substantial expansions and contractions when subjected to changing pH environments, temperature, or solvent. Conceptual designs for smart, electrically activated devices exploiting this phenomenon are discussed. These devices have the possibility of being manipulated via active computer control as large displacement actuators for use in adaptive structures.

The enabling technology of these novel devices is the use of compliant containers for the gels and their solvents, removing the difficulties associated with maintaining a batn for the gels. Though most of these devices are designed using properties well discussed in the literature, some presented near the end of this paper make use of conclusions that the authors have drawn from the literature and their own experimental work.

Those conclusions about the basic mechanisms of electromechanical gels are discussed in the third part of this paper and a complete set of governing equations describing these mechanisms are presented in the fourth section.

This paper concludes with a discussion of some of the ramifications of the above system of equations and a discussion on gel-driven devices and on the control of such devices.

1. Introduction

The contractile and expansile properties of polyelectrolyte gels has been a subject of diverse study since the original observations of Kuhn (1949) and Katchalsky (1949). The phenomenon involves the modulation of the affinity of the polymer for

solvent by changing the pH of the solvent, by changing temperature or solvent, or
 as originally discussed by Hamlen, Kent and Shafer (1965) — subjecting the bath
to an electrostatic field. The effect of the change in pH can produce a homogeneous
deformation of as much as four hundred percent (Li and Tanaka 1990). An electro-
static field can produce even a nonhomogeneous deformation such as bending.

Various discussions of applications have occurred over the years. The possibility
of using these polymeric gel muscles or actuators for chemomechanical engines and
turbines was originally discussed by Steinberg, Oplatka, and Katchalsky (1966),
and Sussman and Katchalsky (1970). Such applications have been discussed by
Eric Cross (1989), Crawly, de Luis, Hagood and Anderson (1988) Tzou and Tseng
(1990) in the context of piezoelectric sensors and actuators, by Gandhi, Thompson,
Choi and Shakir (1989), Choi, Gandhi and Thompson (1989) and Choi, Sprecher
and Conrad (1990) in the context of electro-rheological fluid sensors and actuators,
and by Hanagud, Wan and Obal (1988) and Tadjbakhsh and Su (1989) in the
context of optimal placement of generic sensors and actuators in adaptive and
intelligent structures.

2. Electromechanical Devices

The major conceptual advantages of gel actuated devices are

- compactness

- simplicity

- modest weight

- small power requirements

- low material costs

In principle, there need be only one moving part, and that is the actuating gel itself.
There is not the attendant weight and complexity of electric motors or hydraulic
pumps and actuators. All that is required is an electric field of the order of a few
volts per centimeter.

The major disadvantages of such devices are

- in general, the response times of these gels are much longer than conventional
  actuator components;

- there is the inconvenience that the gel must be contained within a solvent
  bath.

In what follows, applications and designs which exploit the advantages of these gels
and for which the disadvantages are without consequence are identified.

To make the electromechanical gels more useful, it is necessary to remove the
bath. This is done by containing the gel and its bath in a container. The designs
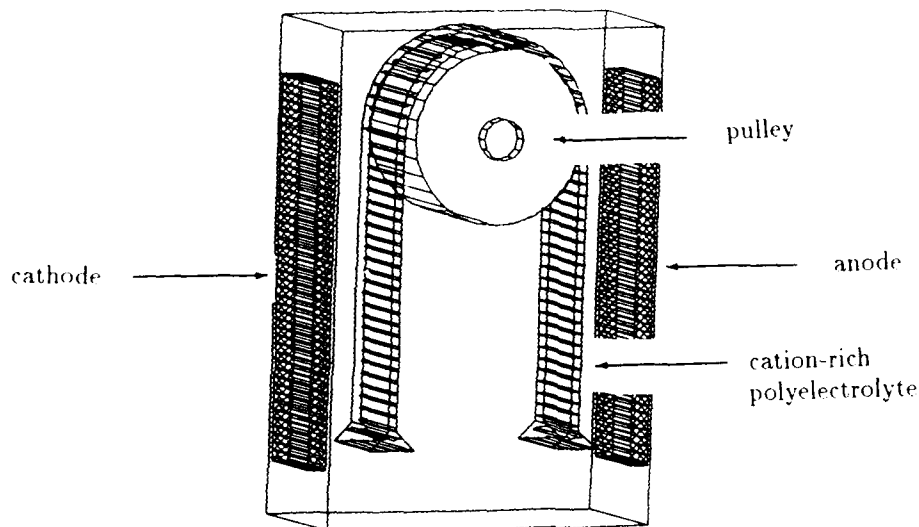
Figure 1: A very simple motor using the electromechanical properties of a polyelectrolyte

presented here use rigid containers where appropriate and use flexible and foldable membranes where needed.

Figure 1 shows a very simple device based on a more sophistocated design first presented by Steinberg, Oplatka, and Katchalsky (1966). This device takes advantage of the observation that for electrolytic polymer impregnated with cations (+), the polymer closer to the anode tends to swell while that closer to the cathode shrinks. The combined deformations cause the pulley about which the polymer is wrapped to undergo rota.ion. An AC voltage supply and will cause oscillatory motion of the pully. In this case a reasonable inflexible container is used.

Figure 2 shows a very simple extensional device. This cylindrical device has a bellows-like container that permits both longitudinal extension and the associated lateral contraction that leaves the overall volume of the container essentially unchanged. In this device, the polymer is attached on one side to the anode and is attached on the other side to a spacer which is itself attached to the cathode. When the electric field is applied, the polymer absorbs solvent and swells, pushing against the spacer and extending the cylinder. Reversing the field causes the device to contract. Polymer is placed only on one side of the cylinder since polymer placed by the cathode deforms in a manner so as to exactly cancel out the deformations of the polymer near the anode.

A sphincter-type valve is shown in Figure 3. Here the doughnut-shaped polymer is ordinarily in a closed configuration in its unactivated state: the inner radius is zero. The doughnut, being situated near the annulus, swells after the field is turned on and the inner radius opens to permit flow through the annulus.

We see that one of the deficiencies of the electromechanical gels presented in the above two examples is that only one part of the electric field can be exploited at
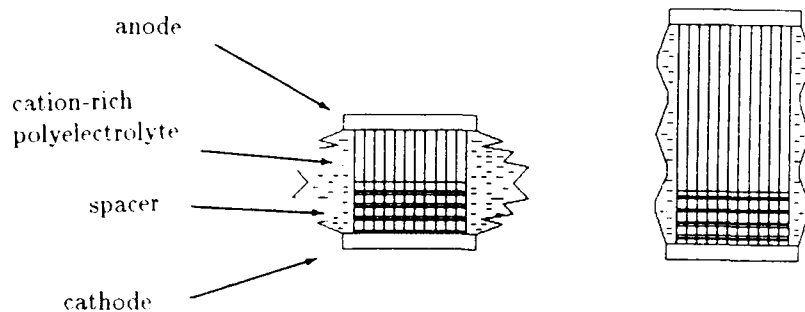
Figure 2: A simple extension/contraction actuator using the electromechanical properties of a polyelectrolyte
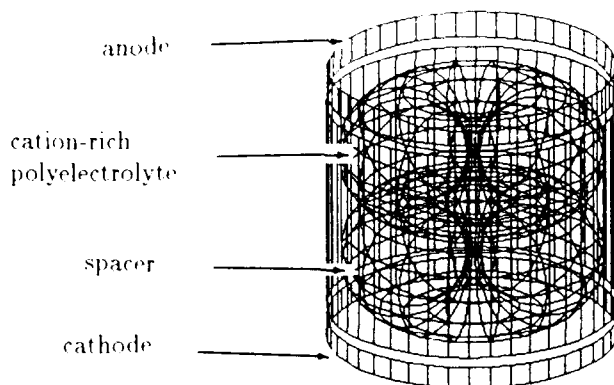
Figure 3: A sphinctering actuator using the electromechanical properties of a polyelectrolyte

a time. A collection of more efficient configurations, using the full electric field, is presented below.

To make more effective use of the electric field, we must employ a more mechanistic understanding of the electromechanical phenomenon than has been exploited in the above examples.

3. Laboratory Observations

To develop more intelligent designs of electromechanical devices, the fundamental physical chemistry of the problem must be understood. A characteristic of polymer electrolyte gels is volume collapse. In the above discussion, that collapse is sparked by changing the electric field applied to the bath or changing the pH of the bath.

Identical collapse can be caused by changing solvent or lowering the temperature (Tanaka et al. 1982).

What distinguishes the behavior of polyelectrolyte gels from other polymers is that the volume change associated with modulating the affinity of the solvent for the polymer results in a *catastrophic* volume change. This effect, which is crucial to the performance of electro-mechanical gel devices, can be rationalized as follows: the counter ions associated with the polyelectrolyte form an "ion gas" which cannot escape the gel due to charge neutrality constraints. Therefore, there is an increased osmotic pressure tending to swell the gel and oppose volume collapse. When collapse finally does occur in a polyelectrolyte gel, it is catastrophic, resulting in a first-order phase transition. The general features of this phase transition are captured by standard mean-field theories such as that of Flory (1953), as used by Tanaka and Fillmore (1979) and Li and Tanaka (1990).

As stated above, though, there are several unresolved issues. First, all polyelectrolyte gels are white when they are collapsed by solvent substitution (diluting a good solvent with miscible, but less good solvent). This is extremely interesting since it implies that there are spatial concentration fluctuations frozen in the gel on length scales of visible light. Our laboratory observations indicate that the origin of these frozen inhomogeneities is due to the vitrification of the polymer during phase separation. That is, unswollen polyelectrolyte gels have extremely high glass transition temperatures (T_g) due to their ionic nature. Of course, when they are swollen, their T_g is dramatically decreased (well below room temperature). However, as phase separation progresses, the polymer phase becomes more concentrated, with a concomitant increase in T_g. At some point during this process, the polymer phase T_g reaches room temperature, the polymer relaxation times become effectively infinite, and phase separation stops, resulting in the observed frozen inhomogeneities. The relative impermeability of these regions severely retards any further kinetics.

The vitrification discussed here does not seem to happen when contraction is caused by change in ph, however. This would appear to be because of the chemical change that the pH has on the polymer works against vitrification, replacing bound counterions with $[H^+]$ or $[OH^-]$ ions.

The second major unresolved issue is the effect of the electric field. While several theories exist, we believe the most promising approach rests on the observation that, at the voltages normally used (an overpotential of 2 volts), hydrolysis abounds, resulting in a pH gradient at both electrodes (DeRossi et al. 1986). Since the dissociation of the polyelectrolytes is pH dependent and the volume collapse depends crucially on that dissociation, one can envision how the electric field will cause collapse at one electrode and swelling at the other. However, there are several studies in the literature which cast doubt on this simple explanation (Irie 1986), (Osada et al. 1988).

The issue of vitrification in the above discussion will serve as a constraint on the control strategies and might play a role in calculating the response rate of the structure, but it is not anticipated that vitrification will play much of a role in actuator design.

The first enhancement to our design strategy is to add anion-rich polyelectrolytes
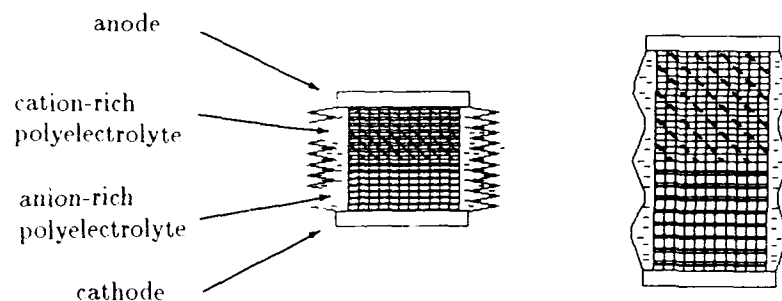
Figure 4: An extensional actuator employing both anion-rich and cation-rich poly-electrolytes.

to our collection of gels. The above discussion on the role of the electric field suggests that such gels will swell in low pH environments and shrink in high pH environments, and such an observation was made by Kishi et al. (1990). A design enhancement exploiting such polyelectrolytes is indicated in Figure 4, in which a anion-rich polyelectrolyte is placed near the cathode of the cell to complement the cation-rich polyelectrolyte originally placed by the anode. One sees that invoking the electric field causes both gels to swell, causing both to contribute to the extension of the actuator. Reversal of the electric field reverses pH environment near the electrodes and cases both gels to collapse. A similar enhancement for the sphincter valve in Figure 5, in which the inner portion of the doughnut is anion-rich and the outer is cation-rich and the electrodes have been moved to the inner and outer portions of the doughnut. Series of these devices could be used to constitute a peristaltic pump.

A further modification to the design strategy suggested by our understanding of the electromechanical mechanism is to decouple the acid/base generation from the actuator. This strategy is indicated in Figure 6. In this figure, a separate cell is used to make acidic and basic solutions which are then pumped into the actuators. (Since there is no back pressure, the solvent pump can be extremely small.) This configuration permits greater efficiency since the electrolysis cell can be dimensioned smaller than the actuator. Further, the reaction time of the actuator can be reduced since stored activating solvent can be pumped into the actuator as needed.

4. Governing Equations

Since it is believed that the electrical stimulus leads to a chemical effect, the describing equations for a chemically-activated gel structure deformation are presented. The mathematical representation involves properly describing the expanding or contracting polymer matrix, fluid transfer of solvent into and out of the
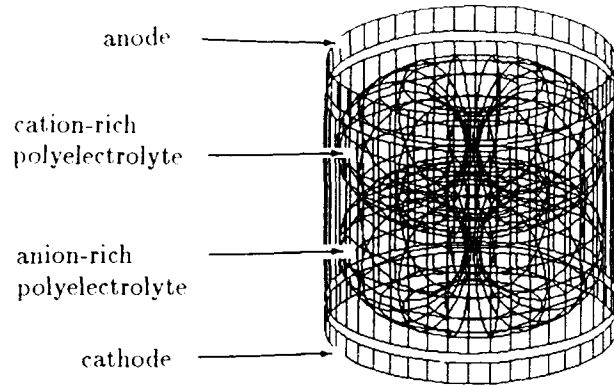
Figure 5: A sphincter type actuator employing both anion-rich and cation-rich polyelectrolytes.
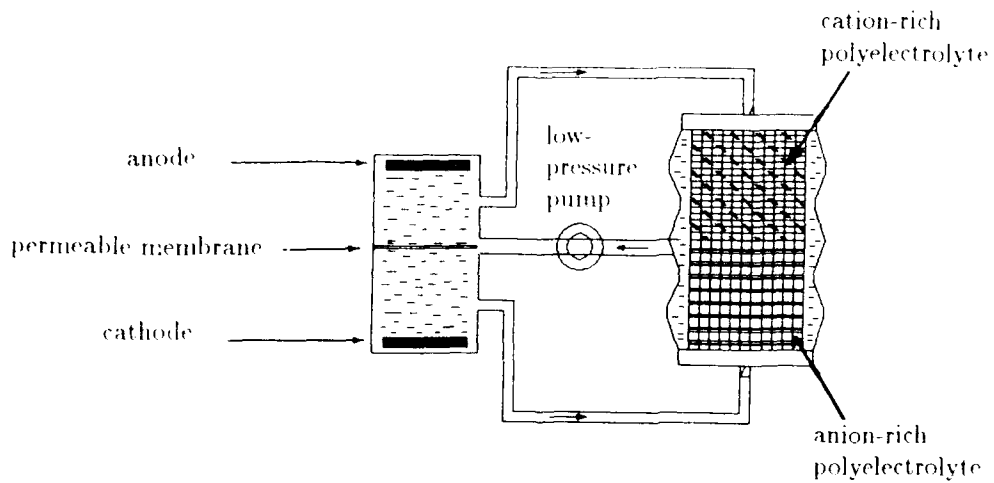
Figure 6: An actuator motivated by acidic/basic solvent drawn from an electrolysis cell.

substructure and the coupled effects between the two phenomena. In what follows, governing equations are derived in the current, deformed configuration.

The velocity of solvent within the polymer is that of the polymer plus the differential velocity due to diffusion. The diffusion is driven by osmotic-pressures which are themselves functions of two internal coordinates or states, concentration, c, and pH, H. The variable c is the mass of solvent per unit volume of swollen polymer, and H is mass of H^+ ions per unit volume of swollen polymer.

The diffusion equation describing the evolution of the solvent concentration is (Bird 1960)

$$\frac{\partial c}{\partial t} = \nabla \cdot [D_{1,1}(c,H)\nabla c + D_{1,2}(c,H)\nabla H] - \nabla \cdot (c\dot{\boldsymbol{x}}_g) \tag{1}$$

where the terms $D_{i,j}$ are diffusivities and $\dot{\boldsymbol{x}}_g$ is the local gel velocity.

[Some insight can be gained by observing that for the situation where the gel is in a constant pH environment and the polymer is fixed in space, the above equation reduces to

$$\frac{\partial c}{\partial t} = \nabla \cdot [D\nabla c]. \tag{2}$$

This is identical in form to the equation for heat conduction, and much of our intuition about heat conduction applies to some regimes of this chemo-mechanical phenomenon.]

The transport of H is similar to that of c but it also involves sources:

$$\frac{\partial H}{\partial t} = \nabla \cdot [D_{2,1}(c,H)\nabla c + D_{2,2}(c,H)\nabla H] - \nabla \cdot (H\dot{\boldsymbol{x}}_g) + \dot{H}_s \tag{3}$$

where H_s accounts for creation or neutralization of H. Note that $\partial H/\partial t$ is a tunable parameter that may be varied through electrical or chemical means.

The stress relationships for large deformation elasticity require the use of large deformation strain quantities. The deformation gradient $\mathcal{F}(t)$ is defined as

$$\mathcal{F}(t) = \frac{\partial \boldsymbol{x}_g}{\partial \boldsymbol{X}_g} \tag{4}$$

where $\boldsymbol{X}_g$ is the location of the particle in the unstrained state. In this problem, it is useful to factor the deformation gradient into its unimodular part and a part representing isotropic swell:

$$\mathcal{F}(t) = \mathcal{F}_{\text{uni}}(t) \cdot \mathcal{F}_{\text{iso}}(t) \tag{5}$$

where

$$\mathcal{F}_{\text{uni}}(t) = \mathcal{F}(t)/\alpha(t) \tag{6}$$

$$\mathcal{F}_{\text{iso}}(t) = \alpha(t)I \tag{7}$$

and

$$\alpha(t) = (\det[\mathcal{F}(t)])^{1/3} \tag{8}$$

For a solvent-concentration dependent neo-Hookean type solid, the stress result-ing from a given deformation is:

$$\mathcal{S}(t) = G(c)[\mathcal{E}(t) \cdot \mathcal{E}(t)^T - \mathcal{I}] + p\mathcal{I} \tag{9}$$

where $\mathcal{S}$ is the stress.

$$\mathcal{E}(t) = \mathcal{F}_{\text{uni}}(t)^{-1}. \tag{10}$$

G is the Young's modulus, and p is a Lagrange multiplier dual to the incompress-ibility constraint on the swollen polymer. Because of the assumed incompressibility of the gel/solvent system, the above equation presents stress only up to an unknown pressure.

A viscoelastic rather that the above elastic constitutive equation could be used for the gel if the diffusion process is so fast that the viscoelasticity of the polymer becomes important. The simplest such model is that of Lodge (68):

$$\mathcal{S}(t) = \int_{-\infty}^{t} \mu(c, t - \tau)[\mathcal{E}(\tau) \cdot \mathcal{E}(\tau)^T - \mathcal{I}] d\tau + p\mathcal{I} \tag{11}$$

The incompressibility condition on the swollen polymer is simply a statement that the volume of that material is not a function of the imposed pressure. Assuming no volume change of mixing, this condition becomes:

$$\frac{\partial \alpha^3}{\partial t} = \alpha^3 \dot{c}/\rho_r \tag{12}$$

where ρ_r is the density of pure solvent.

The conservation of momentum for the gel is:

$$\rho_g \ddot{x}_g = \nabla \cdot \mathcal{S} + \rho_g f_b \tag{13}$$

where ρ_g is the mass density of the swollen gel, and f_b contains all local body forces, such as gravitational or electromagnetic loads.

Together the above are a complete set of equations - providing as many scalar equations as scalar unknowns. That pairing of equations with variables in Table 1 relates each vector or scalar variable with a corresponding equation of the same rank. All of the variables in Table 1 are functions of time and location in the gel.

The initial conditions are initial values of x_g, c, and H. The boundary conditions are: all stress components of the fluid boundary on the gel, displacent conditions on the gel imposed by other parts of the actuator, and stress conditions imposed by other parts of the actuator. Note, that the hydrodynamics of the bath may add additional damping to that due to the diffusive process and that due to the viscoelasticity of the gel.

This development shows that it is the diffusion process, Equation 1, which gov-erns the reaction time of the actuator. As with other diffusion processes (such as heat transfer) the speed of the process can be accelerated tremendously by changing the dimensions of the medium. Another observation is that in the case of swell, the

variable	corresponding equation
$c(t, \boldsymbol{X}_g)$	Eq 1
$H(t, \boldsymbol{X}_g)$	Eq 3
$\boldsymbol{x}_g(t, \boldsymbol{X}_g)$	$\begin{cases} \text{Eqs 9 \& 10 \& 13} \\ \text{or} \\ \text{Eqs 11 \& 10 \& 13} \end{cases}$
$p(t, \boldsymbol{X}_g)$	Eq 12

Table 1: Tabulation of equations and unknowns

diffusion and the convection terms in Equation 3 are additive, while those terms are of opposite effect in the case of shrinkage. We can expect that the reaction rates of these two processes to be very different.

The system of equations summarized in Table 1 can be solved with standard numerical methods such as finite element analysis. The authors are now developing such a simulation program.

It should be mentioned that the formulation presented here is unique in that it presents a diffusional driving force to the mechanics. This novel formulation avoids some of the deficiencies in other developments (Li and Tanaka 1990). which preclude such phenomena as stress-free rigid-body motion. Further, it accommodates large deformation through the use of appropriate strain measures and explicitly includes body forces.

5. Conclusion

Actuators exploiting the chemical/mechanical properties of polyelectrolytes have strong application in environments where weight is at a premium and there exists a handy source of electricity. Conditions in space structures are paradigmatic of those for which gel-based actuators have a competative advantage. The utility of such actuators depends significantly on the design of appropriate containers and the exploitation of the best understanding of the physical chemistry of the process.

There currently exists enough fundamental understanding to theoretically analyze the process, though some of the relevant parameters must be deduced from experiment. A novel and complete formulation of the diffusion and the rubber elasticity phenomena has been presented.

Acknowledgments

References

Bird R B, Stewart, W E, Lightfoot, E N, 1960, *Transport Phenomena*, John Wiley and Sons, 567

Choi B S, Gandhi M V, and Thompson B S, 1989, *Proc. 1989 Am Cont. Conf.*, Vol. *1*, 694-699

Choi Y, Sprecher A F, and Conrad H, 1990, *J. Intelligent Mater. Syst. and Struct.*, Vol. *1*, 91-104

Crawley E F, de Luis J, Hagood N W, and Anderson E H, 1988, *Proc. 1988 Am. Cont. Conf.*, *vol. 3*, 1890-1896

Cross L E, 1989, California Institute of Technology, 9-17

De Rossi D E, Chiarelli P, Buzzigoli G, Domenici C, and Lazzeri L, 1986, *Trans. Am. Soc. Artif. Intern. Organs*, Vol *32*, pp 157-162.

Flory P J 1953 *Principles of Polymer Chemistry*, Cornell University Press, Ithica, NY

Gandhi M V, Choi B S and Shakir S, 1989 *Trans ASME. J. of Mechanisms. Transmissions, and Automation in Design*, Vol. *111* 328-336

Hamlen R P, Kent C E, and Shafer S N, *Nature*, Vol. *266*, No. 4989, 1148-1149, (1965).

Hanagud S, Won C C, and Obal M W 1988 *Proc. 1988 Am. Control. Conf.*, Vol. *3*, 1884-1889

Irie M 1986, *Macromolecules*, 2890-2892

Katchalsky A, 1949 *Experientia*, Vol. *5*, 319-320

Kishi R, Masebe M, Hara M, and Osada Y 1990 *Polymers for Advanced Technologies*, Vol. *1* 19-25

Kuhn W 1949 *Experientia*, Vol., *5*, 318-319

Li Y, and Tanaka T 1990 *J. Chem. Phys.*, *92*, 1365-1371

Lodge A S 1964 *Elastic Liquids*, Academic Press, New York, 62

Lodge A S 1956 *Trans. Faraday Soc.* *52* 120

Osada Y, Umezawa K, and Yamauchi A 1988 *Macromo. Chem.* Vol. *189* 597-605

Steinberg I Z, Oplatka A, and Katchalsky A 1966 *Nature*, Vol. *210*, no. 5036 568-571

Sussman M V and Katchalsky A 1970 *Science*, Vol. *167* 45-47

Tadjbakhsh I G, and Su Y, 1989 *Trans. ASME. J. Appl. Mech.*, Vol. *56*, pp. 941-946

Tanaka T, and Fillmore D 1979 *J. Chem. Phys.* Vol *70*, N. 3, 1214-1219

Tanaka, T, Nishio, I, Sun, S, and Ueno-Nishio, S 1982 *Science*, Vol. *218* 467-470

Tzou H S and Tseng C I 1990 *Computers in Engineering*, Vol. *1*, ASME 473-480

On-line adaptive stiffness control to tailor modal energy content in structures

R A Osegueda, D C Nemir and Y J Lin

College of Engineering, The University of Texas at El Paso, El Paso, TX 79968

ABSTRACT: This paper describes a structural motion control theory that is based upon adaptive stiffness changes. An enhanced dissipation of the vibrational energy is accomplished by changing stiffness in the system in such a way that the energy in low modes of vibration is transferred into higher modes which have accelerated rates of damping. Simulation studies are presented on a simple unforced system and on a truss model subjected to sinusoidal forced excitations. Applications range from the control of wind or seismically induced motion in civil structures to the motion control of a large space structure.

1. INTRODUCTION

When a structure exhibits a high degree of flexibility, the control of motion within that structure becomes important. Structures can have a significant flexibility due to size (eg: a suspension bridge), geometry (eg: a skyscraper where the height to base area ratio is large), or material (eg: a space station where structural members are necessarily lightweight and hence compliant). In a civil structure, motion can occur due to the influence of earthquakes or wind. In an aerospace structure, motion can occur due to attitude adjustments, crew movements or wind. For lightly damped structures in particular, disturbances are dissipated slowly and even small amplitude periodic disturbances can eventually lead to large oscillations, leading to occupant discomfort, performance degradation and structural damage. For this reason, active and semi-active structural motion control remain research areas of great interest.

In multistory buildings, active control has been successfully demonstrated on both scale models and actual buildings using techniques such as active mass dampers and active tendons (Soong 1990). An active mass damper works to damp out vibrations in a structure by transferring momentum between the structure and an auxiliary mass. This type of system has been successfully demonstrated in the laboratory and in the field. An example is Kajima Corporations's computer-activated mass damper system in the 13 foot wide, 11 story Kyobashi Seiwa building in Tokyo (Kobori 1990b). An active control using tendons can be implemented in a building by controlling tensions in structural tendons via hydraulic actuators, thus implementing corrective forces to counteract motion (Soong 1990). This technique has been successfully implemented on a 1:4 scaled model at the State University of New York at Buffalo (Chung, Lin, Soong and Reinhorn 1989). One advantage to the tendon approach is that many buildings, most bridges, and all oil platforms already make

use of passive tendons for structural support.   Incorporating active tendons in future construction is a reasonable extension.

The problem with active control techniques, particularly as applied to civil structures, is that they require a great deal of energy to implement.   Furthermore, if not correctly implemented, this class of controls can result in the introduction of unwanted excitations into the system, a phenomenon known as modal spillover (Meirovitch, Baruh and Oz 1983). An alternative class of controls, known as semi-active control, involves making structural changes in the system. With semi-active control, a small amount of energy can be used to leverage a large influence on the system.   One example of semi-active control is the semi-active damper proposed for automotive suspensions (Karnopp 1990). In these systems an auxiliary damper is either engaged or disengaged depending upon the relative velocity between the wheel and chassis. The damper is activated by a low energy means such as an electromagnetically controlled valve. A second example of semi-active control is the impact mass damper discussed by Dehghanyar, et al (1987) wherein structural damping is enhanced by collisions between an auxiliary and a primary mass. A third example of a semi-active control is that proposed by Kobori and coinventors (1990a and 1991), wherein active bracing is used in a building to alter dynamical characteristics. The main objective in those patents is to remotely sense seismic tremors and then adjust structural stiffness so that resonant modes in the building are made different from the dominant frequencies associated with the seismic power spectra at each instant.

This paper describes a theory for motion control based upon the semi-active redistribution of modal energies in structural systems. The approach falls within the domain of "smart structures" since the structure itself is automatically tailoring local system properties to achieve a specified global system objective. Like the frequency steering approach of Kobori (1990a and 1991), our approach entails the dynamic alteration of structural stiffness. Our primary objective, however, is not based upon the avoidance of resonance, but rather the transference of system energies from low modes to higher modes. Since structural passive damping is more effective at higher frequencies, the proposed technique accelerates the passive removal of vibrational energy. The technique can also be used to limit structural motion in a specified direction.

2. THE MODAL ENERGY TRANSFERENCE TECHNIQUE

The proposed modal energy transference approach for structural motion control can be explained by using the idealized lumped spring-mass-dashpot of Figure 1. This structure has baseline idealized springs, dashpots and lumped masses of magnitudes k_i, c_i and m_i. Additional springs Δk_i can be actively connected or disconnected in parallel with the baseline (additional damping is also possible).

In the simulation studies described in this paper, the connection and release of a given auxiliary spring is constrained to occur only when the strain energy in the spring is zero. Since changing the spring constant of a relaxed spring does not introduce energy into the system, the technique qualifies as a semi-active control.
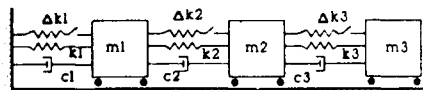
Fig. 1. Example lumped system

The dynamic motion of the nominal structure (no added parallel springs) is described by:

$$M \ddot{y}(t) + C \dot{y}(t) + K y(t) - f(t) \qquad (1)$$

where **M**, **C** and **K** are the global mass, damping and stiffness matrices of the nominal structure, f(t) is the external force vector, and y(t) is the vector of structural displacements. The characteristic equation associated with (1), assuming proportional damping, is:

$$[K - \lambda M] \Phi - 0, \qquad (2)$$

where λ is the undamped eigenvalue and Φ is the nxn modal matrix. The eigensolution of (2) yields n eigenvalues λ_i with eigenvectors ϕ_i. Because of the orthogonality conditions and the assumed proportional damping matrix, (1) can be decoupled by applying the modal transformations $y(t) = \Phi q(t)$ and $\dot{y}(t) = \Phi \dot{q}(t)$, where, q(t) and $\dot{q}(t)$ are modal displacements and velocities. The transformation gives

$$m_j^* \ddot{q}_j(t) + c_j^* \dot{q}_j(t) + k_j^* q_j(t) - f_j^*(t) \qquad j-1,2,\ldots,n \qquad (3)$$

where f_j^* is the modal force, and m_j^*, c_j^* and k_j^* are the modal mass, damping and stiffness of the jth mode and are given by

$$m_j^* - \phi_j^T M \phi_j, \qquad c_j^* - \phi_j^T C \phi_j, \qquad k_j^* - \phi_j^T K \phi_j. \qquad (4)$$

If the system is elastic and linear during a period of time, then the total energy (TE) of the system is the sum of the strain energy (PE) and kinetic energy (KE). The total energy can be decoupled into modal energies:

$$TE(t) - \frac{1}{2} \sum_{j-1}^{n} k_j^* q_j^2(t) + \frac{1}{2} \sum_{j-1}^{n} m_j^* \dot{q}_j^2(t) - \sum_{j-1}^{n} PE_j(t) + \sum_{j-1}^{n} KE_j(t) \qquad (5)$$

where $PE_j(t)$ and $KE_j(t)$ are respectively the jth mode potential and kinetic energies at time t. If at some time $t=t_o$ one or more of the springs are relaxed, the corresponding active connections can be triggered or released, modifying the structure without an input of additional energy. Let the new structure's dynamic motion be given by:

$$M \ddot{\hat{y}}(\tau) + \hat{C} \dot{\hat{y}}(\tau) + \hat{K} \hat{y}(\tau) - \hat{f}(\tau) \qquad (6)$$

subject to the initial conditions $\hat{y}(\tau=0) = y(t=t_o)$ and $\dot{\hat{y}}(\tau=0) = \dot{y}(t=t_o)$. Under the proportional damping assumption, the eigensolution of the new structure is given by:

$$[\hat{K} - \hat{\lambda} M] \hat{\Phi} - 0 \qquad (7)$$

to give new eigenvalues $\hat{\lambda}_j$ with new eigenvectors $\hat{\phi}_j$. Since the eigenvectors have changed, the modal parameters of the modified structure are:

$$\hat{m}_j^* - \hat{\phi}_j^T M \hat{\phi}_j, \qquad \hat{c}_j^* - \hat{\phi}_j^T \hat{C} \hat{\phi}_j, \qquad \hat{k}_j^* - \hat{\phi}_j^T \hat{K} \hat{\phi}_j, \qquad (8)$$

and the total energy of the system is given by:

$$TE(t) - \frac{1}{2}\sum_{j=1}^{n} \hat{K}_j \cdot \hat{q}_j^2(t) + \frac{1}{2}\sum_{j=1}^{n} \hat{m}_j \cdot \dot{q}_j^2(t) - \sum_{j=1}^{n} PE_j(t) + \sum_{j=1}^{n} KE_j(t) \quad \textbf{(9)}$$

Since the engagement/release of a relaxed control spring does not add to the total energy of the initial system, the total energy at time $t=t_0$ is equal to the total energy in the modified system at time $\tau=0$. However, modifying structural stiffness in this way will result in a redistribution of modal energies. If the spring can be engaged/released in such a manner as to shift the energy distribution from lower modes to higher modes, the result will be an accelerated passive dissipation of the total energy of the system.

3. CONTROL RULE

Our control objective is to change the distribution of the modal energy at any time $t=t_0$ (every time an active brace (spring) is in a relaxed state) so that the modal energy content of the new system is steered to a desired state. Generally, it will be desirable to minimize energy in the lower modes since in real materials and structures, the viscous damping of vibrational energy is more pronounced for energy in the higher modes because of the faster energy absorption during cyclic straining. Suppose that at a given time, t_0, there are a possible m control actions that can be taken, where we again note that a valid control action consists of either connecting or releasing a relaxed spring in the system. We define the cost functions

$$J_k(t_0) - \sum_{i=1}^{n} \alpha_i \left[PE_i{}^k(t_0) + KE_i{}^k(t_0) \right] \quad k - 1, 2, \dots m \quad \textbf{(10)}$$

where α_i, $i=1,2,\dots n$ is a set of weighing factors and $PE_i{}^k(t_0)$ and $KE_i{}^k(t)$ are respectively the potential and kinetic energies in the ith mode if the kth control action is taken. For example, if at time t_0 there are d relaxed springs in the system, then there are a possible $m=2^d$ control actions that can be taken (with each relaxed spring allowed to have either a connected or released state). Then there are m costs that can be computed from equation (10), each corresponding to one possible set of control actions. The particular control action that is chosen will correspond to the set of connection conditions that results in a minimum cost.

The algorithm is summarized in Figure 3. First, sensors in the structure detect when there is a disturbance to the structure and initiate the control algorithm (Block A). Next, the strains are monitored in each active brace/spring (Block B). If the strains in any springs are close to zero, those springs are identified as being relaxed and become control candidates (Block C). Sensor readings from the structure are then used to determine global displacements and velocities y and $\dot{y}$ (Block D). Equation (5) is used to compute the total energy in the system. If the total energy falls below some threshold level the algorithm terminates (Block E). If the system still contains an unacceptable level of vibrational energy, global coordinates are converted into modal coordinates for each of the candidate eigenstructures. We note that if there are d relaxed springs, there will be 2^d control candidates and consequently, 2^d different modal matrices and 2^d sets of different modal coordinates. Fortunately, the modal matrices will be characteristic of the system structure and can be computed ahead of time. Equation (9) allows the determination of modal

potential and kinetic energies in each of the control candidates. Equation (10) generates a cost for each of these candidates (Block F). The control action that yields the minimum cost is chosen (Block G) and the algorithm repeats.
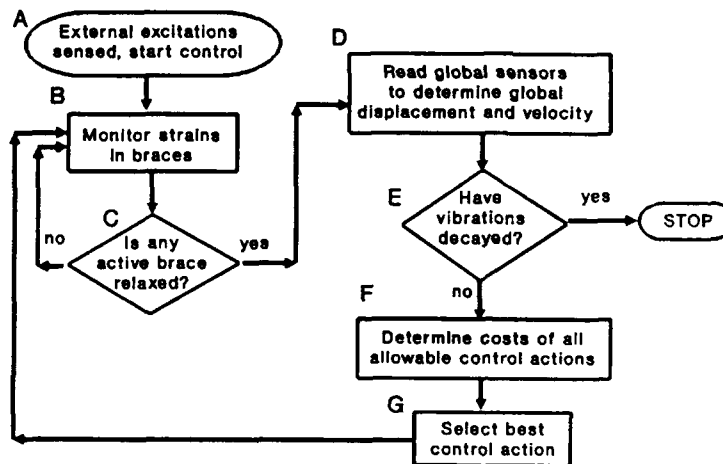
Fig. 2. Flowchart of control algorithm

4. FREE VIBRATION EXAMPLE

The undamped system of Figure 1 is used to illustrate the algorithm using nominal springs of $k_1 = k_2 = k_3$, masses of $m_1 = m_2 = 2 m_3$ and controllable springs $\Delta k_1 = \Delta k_2 = \Delta k_3 = k_1$. The excitation comes as a result of an initial first mode displacement condition; afterwards, the system is unforced. The control objective is to minimize the energy contents of the first and second modes according to the control rule of section 3. Figure 3 shows the displacement history at the tip

Fig. 3. Displacement history for unforced-undamped system

normalized to the initial displacement. The time scale is normalized with respect to the period of the first mode of the nominal structure (T_1). As Figure 3 illustrates, after about 8 cycles, the vibrations are predominantly of a higher frequency (third mode).

Figure 4 illustrates the corresponding time history of the three modal energies. At time $t = 0$, the energy content is $E_1 = 1$, $E_2 = 0$ and $E_3 = 0$. As time increases the energy in mode 1 decreases and the energy of mode 3 increases. The total energy remains constant because the example is undamped and because the engagement/release of the additional springs is performed when the springs are in equilibrium. After 10 cycles, Figure 4 shows that the vibrations are of a pure third mode content.
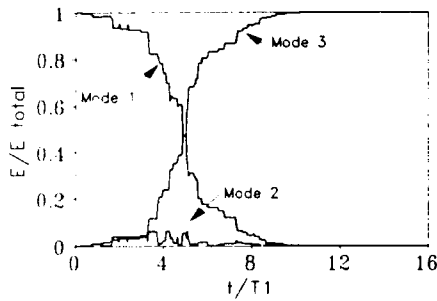
Fig. 4. Modal Energies versus time
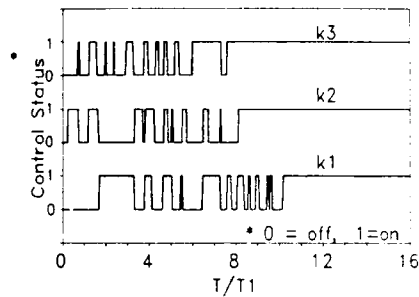
Fig. 5. Time history of control actions

Figure 5 depicts the status of the controllable springs as a function of time. The three plots in this figure indicate the control status via values of 0 or 1. A value of 0 indicates that the control element is not clamped; a value of 1 indicates that it is clamped. This figure also illustrates the assumption that the added stiffness occurs instantaneously.

5. FORCED VIBRATION RESPONSE

A second simulation study considers the truss depicted in Figure 6. All elements of the planar truss have the same geometric and materials properties. The control elements k_1, k_2 and k_3 (k_1 is at the left) have twice the stiffness of the nominal diagonal brace elements. The structure is initially at rest and is acted upon by a sinusoidal load of $p(t) =$ $\sin \Omega t$ as shown. The loading frequency Ω, was varied from 1 to 10 rad/sec. The control rule of section 3 was implemented to minimize the energy content in the first mode by connecting or releasing the control elements dynamically. The damping of the structure was assumed to be proportional solely to the mass with a first mode damping ratio of 0.01. Table 1 lists the frequencies of the first three modes of all eight candidate structures.
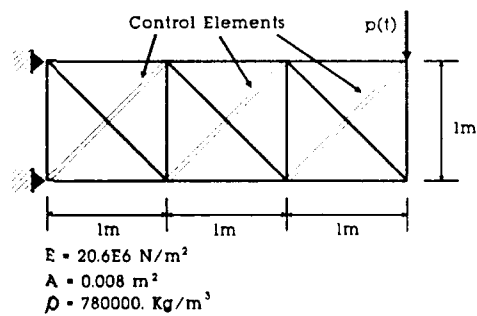
Fig. 6. Planar truss with three control elements

Figure 7 portrays the maximum observed normalized vertical displacement as a function of the loading frequency. The efficacy of the control scheme is contrasted with the two limiting cases. These cases are a no control when all control elements are disengaged (0-0-0) and a no control case when all elements are engaged (1-1-1). The 0-0-0 case nas a maximum normalized deflection of 58 occurring when the loading frequency is the resonant one. For the 1-1-1 case the maximum is 46. For the control case, the maximum is about 28 and occurs at a loading frequency that is intermediate to the two limiting structures.

Table 1. Truss resonant frequencies of three lowest modes
for all control configurations

Candidate Structure	Status k_1 k_2 k_3			Angular Frequency (rad/s) Transverse 1	Transverse 2	Axial 1
1	0	0	0	3.90	13.3	16.7
2	0	0	1	3.98	13.8	17.4
3	0	1	0	4.30	13.3	17.0
4	0	1	1	4.35	13.8	17.7
5	1	0	0	4.38	19.2	16.6
6	1	0	1	4.50	20.8	16.9
7	1	1	0	4.79	19.8	17.0
8	1	1	1	4.89	21.5	17.4

Figure 8 portrays the tip vertical deflections, normalized to the static deflections, for the uncontrolled system (0-0-0) in resonance. It should be noted that the maximum amplitude of Figure 8 corresponds to the point of Figure 7 at $\Omega = 3.90$ rad/s. Figure 8 clearly shows that the avoidance of resonance was a byproduct of the control objective of minimizing first mode energy. It is important to emphasize that the proposed control rule did not always result in a reduced deflection amplitude over the uncontrolled nominal structures. This is seen in Figure 7 at a resonant-like peak at a loading

Fig. 7. Maximum normalized displacement versus loading frequency

frequency of 4.30 rad/sec. The time history corresponding to this point is shown in Figure 9.
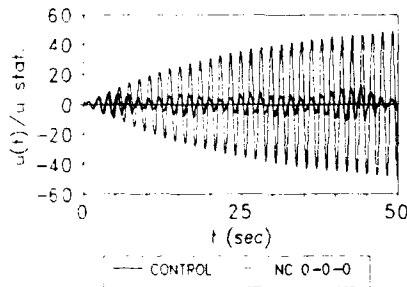
Fig. 8. Deflection of control and no control (0-0-0) cases at $\Omega = 3.90$ rad/s
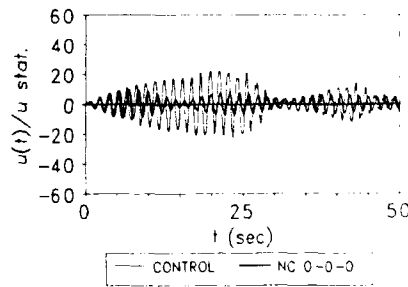
Fig. 9. Deflections of control and no control (0-0-0) cases at $\Omega = 4.30$ rad/s

6. DISCUSSION

The algorithm presented in this paper assumed that control actions consisting of adding and removing stiffness dynamically can only take place when the candidate control element is in a relaxed position. It may well be that these elements can be controlled to release their stored energy in such a way as to oppose external forces, thus functioning in a similar manner to the impact mass damper discussed by Dehghanyar et al (1987). Such an approach would also serve the objective of transferring low mode energy into higher modes. Although simulations assumed that control actions can be made instantaneously, real world actuators have delays and time constants that must be incorporated into any realistic model. Ongoing work addresses these issues and we are proceeding with experiments on a laboratory model.

It is important to note that although the results of Figure 7 demonstrate that there are some excitation frequencies at which having no control is better than having control, a strategy based upon this requires an a priori knowledge of the excitation. Kobori and coauthors (1990a,1990b,1991) have proposed the sensing of earthquake excitations remotely, analyzing the spectral content, and then adjusting system stiffness in such a way as to avoid resonance. The difference between the Kobori approach and the approach proposed in this paper is that our approach is based solely upon the measurement of structural response and does not require forecasting.

7. CONCLUSION

This paper described a structural motion control theory based upon adaptive stiffness changes. By changing system springs dynamically, modal energies were transferred from initial modes to different modes. The approach can be used to achieve an enhanced dissipation of the vibrational energy by transferring low mode energies into higher modes which have accelerated rates of damping. This objective also leads to reduced structural deflections. Simulation studies were presented on a simple unforced system and on a truss model subjected to sinusoidal forced excitations.

8. REFERENCES

Chung L L, Lin R C, Soong T T and Reinhorn A M 1989 *J. Eng. Mech.* 115 8 pp 1609-27

Dehghanyar T J, Masri S F, Miller R K and Caughey T K 1987 *Proc. 2nd Int. Symp. on Structural Control* (Boston: Martinus-Nijhoff) pp 141-59

Karnopp D 1990 *J. Dynamic Systems, Measurement and Control* 112 pp 448-455.

Kobori T, et al 1991 *U.S. Patent 5,036,633*

Kobori T, Yamada S and Kamagata S 1990a *U.S. Patent 4,922,667*

Kobori T 1990b *Proc. U.S. National Workshop on Structural Control Research* ed G W H and S F M pp p1-p21

Meirovitch L, Baruh H and Oz H 1983 *J. Guidance* 6 4 pp 302-10

Soong T T 1988 *Engineering Structures* 10 pp 74-84

Soong T T 1990 *Active Structural Control: Theory and Practice* (Essex: Longman Scientific)

Frequency-shaped passive damping using resistively-shunted piezoceramics

George A. Lesieutre, Assistant Professor of Aerospace Engineering
Christopher L. Davis, Graduate Student

The Pennsylvania State University, University Park, PA 16802

ABSTRACT: The provision of adequate passive damping is an essential aspect of design for practical broadband LTI control of uncertain structural dynamic systems. Resistively–shunted piezoceramics offer potential for significant damping with advantages over more conventional approaches. Tailorable frequency-dependence is especially notable, as damping plays different roles within and beyond the control bandwidth. Guidelines for effective material selection, placement, and shunting are presented in the form of a modified modal strain energy method. Applications to the development of damped structural composite materials are also noted.

1. INTRODUCTION

Vibration damping is essential to the attainment of performance goals for many engineering systems. The ability to tailor frequency-dependence of damping is especially important in practical active structural control applications employing linear, time–invariant compensation. At frequencies above some crossover, robust gain–stabilized performance is attained by assuring, loosely, that modal damping "rolls off" no faster than control authority (Greene and Stein 1979). At frequencies within the control bandwidth, robust broadband phase stabilization of uncertain structural dynamics requires a minimum level of passive damping commensurate with the level of uncertainty (von Flotow and Vos 1991).

The use of piezoelectric materials in combination with resistive and resonant shunting circuits to achieve passive vibration energy dissipation and resonant response reduction has been demonstrated by several researchers, including Hagood and von Flotow (1991). This paper extends earlier work by addressing the use of multiple resistively-shunted piezoceramic elements to achieve specified frequency-dependent damping. Resistive shunting is emphasized because of its relative broadband effectiveness and insensitivity to tuning errors.

Resistively-shunted piezoceramics appear to offer several advantages over more conventional approaches to passive damping. These include: 1) insensitivity of properties to temperature; 2) tailorable frequency–dependent properties; 3) high stiffness; and 4) ability to serve as actuators. Disadvantages include high density and gradual changes in properties with time.

2. DAMPING DUE TO ELECTROELASTIC RELAXATION

Piezoelectric materials are potentially effective for damping because of strong coupling between mechanical and electrical behavior: vibratory strains produce potential gradients, and the resulting currents dissipate energy through joule heating in some resistance. Interpretation of the operative physical mechanism as an anelastic relaxation permits the use of classical relations (Nowick and Berry 1972) and the extension of established tools for design purposes.

The electroelastic relaxation strength may be found from consideration of the appropriate material constitutive equations, often specialized to the case of a single non-zero stress. The relaxation strength corresponding to a scalar material modulus, c^E, is given by:

$$\Delta = \frac{e^2}{c^E \varepsilon^S}$$

(Where c^E is a modulus, e a piezoelectric coupling, and ε^S a permittivity; superscript "E" indicates constant field, "S" strain)

This relaxation strength is a measure of the coupling between the displacement and electrical fields. It is related to the square of the electromechanical coupling coefficient, k, another measure often used to describe the properties of such materials. From classical internal friction relations, the corresponding peak material damping loss factor associated with this relaxation, η_{max}, is given by:

$$\eta_{max} = \frac{\Delta}{2(1+\Delta)^{1/2}}$$

Using the complex modulus representation of material properties ($M = M_1 + i\,M_2$), and assuming multiple discrete relaxations, the frequency-dependence of the storage modulus, M_1, the loss modulus, M_2, and the loss factor, η, are given by:

$$M_1(\omega) = M_R\left[1 + \sum_{i\ relaxations} \Delta_i \frac{(\omega\tau_{\varepsilon i})^2}{1+(\omega\tau_{\varepsilon i})^2}\right]$$

$\tau_{\varepsilon i}$ is the ith characteristic relaxation time at constant strain and M_R the relaxed (low-freq.) modulus

$$M_2(\omega) = M_R \sum_{i\ relaxations} \Delta_i \frac{(\omega\tau_{\varepsilon i})}{1+(\omega\tau_{\varepsilon i})^2}$$

$\tau_{\varepsilon i} = R_i C_{tot}^S$ where R_i is the shunting resistance and C_{tot}^S the total capacitance at constant strain

$$\eta(\omega) = \frac{M_2(\omega)}{M_1(\omega)} = \eta_{max}\frac{2(\omega\bar{\tau})}{1+(\omega\bar{\tau})^2}$$ for a single relaxation   and $\bar{\tau} = \tau_\varepsilon(1+\Delta)^{1/2}$

The through-the-thickness capacitance of a single piezoelectric plate is given by:

$$C^S = \frac{A\varepsilon^S}{L}$$

(A is the electrode area, L the thickness)
(C_{tot}^S is twice C^S for two identical capacitors in parallel.)

3.   DESIGN GUIDELINES

3.1   Material Properties, Structural Participation, and Frequency-Dependence

The total modal damping of a built-up structure (or composite material) can be estimated as the sum of constituent damping weighted by the relative contribution of each to the total strain energy of the mode. This notion can be extended to the case of resistively-shunted piezoceramics by defining a "coupled strain energy fraction" as follows:

$$V_P^* = \frac{V_P}{U_0 + U_P}$$

U_0 is the strain energy in the base structure;
U_P is the strain energy in the piezoceramic; and
V_P is the effective coupled portion of U_P

For a piezoceramic element bonded to the surface of a bending beam, V_P is given by an expression of the form:

$$V_P = \tfrac{1}{2}(EI)_P \left| \int_{length} \left(\frac{\partial^2 w}{\partial x^2} \right) \left| \frac{\partial^2 w}{\partial x^2} \right| dx \right| \qquad \text{(Volume integral of non-positive semidefinite quantity)}$$

Note that it is possible for V_P to be nearly zero even when U_P is not; for example, when a small piezoceramic element is nearly centered on a "strain node," or when the characteristic length of vibration is smaller than the piezo length. This characteristic is closely related to the spatial filtering property of continuously distributed sensors as described in Collins *et al* (1991). The effects of piezoceramic placement on mode shapes and strain energy distribution must also be considered in design, as should the frequency-dependence of material modulus.

The piezoelectric damping added to a structural vibration mode "j" may be considered approximately (for small damping) as the sum of frequency-dependent contributions from each of "i" elements, each with its own relaxation time.

$$\zeta_j(\omega) = \sum_{i\,piezos} \underbrace{\tfrac{1}{2}\eta_{max\,i}}_{material} \underbrace{V^*_{Pj\,i}}_{structural} \underbrace{\frac{2(\omega\bar{\tau}_i)}{1+(\omega\bar{\tau}_i)^2}}_{frequency\,(R)} \qquad \begin{array}{l}\zeta_j \text{ is a \textbf{modal damping ratio}, but} \\ \eta_i \text{ is a \textbf{material damping loss factor}.}\end{array}$$

3.2 Experimental Validation

The validity of these guidelines were explored using a series of cantilevered beam tests following those described by Hagood and von Flotow (1991). Surface-mounted piezos with transverse coupling (k_{31}) were used (longitudinal strains and transverse voltage gradients).

Figure 1 summarizes the results, which agreed fairly well with theory. Peak damping was slightly less than that predicted using manufacturer-furnished property data, but in good agreement with published results. The discrepancy may be due to material aging, imperfect bond load transfer, or use of baseline mode shape to estimate strain energy distribution. For the material used, the value of k_{31} was approximately 0.35.
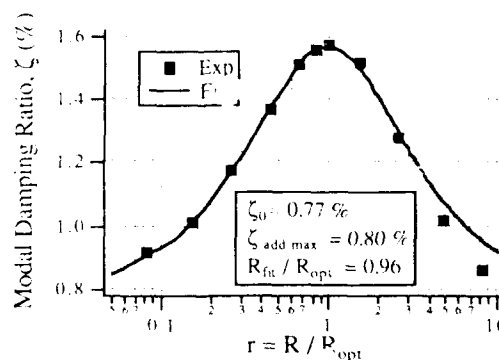
Figure 1: Experimental Results for Single R

3.3 Frequency Shaping

The ability to specify the electroelastic relaxation time through the selection of a shunt resistor is one of the most important features of passive piezoelectric damping. A designer can, by carefully defining a combination of material and structural parameters, tailor the frequency-dependence of damping to suit the requirements of a specific application. Such design variables include the piezoelectric material used (and its constitutive properties); the primary mode of deformation; electrode locations; the amount, shape, placement, and orientation of the piezoelectric material on the structure; and the shunting resistances.

As shown in Figure 2, different kinds of typical material damping behavior can be approximated—however, a designer need not be constrained to duplicate such "classical" behavior. In general, for a fixed amount of piezoelectric material, there is a trade between peak damping and effective frequency range. The design problem is similar to that faced in obtaining a discrete relaxation spectrum from an experimentally-determined material dynamic response function.
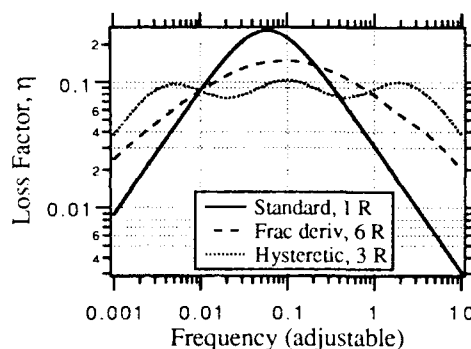
Figure 2: Examples of Tailored Damping

4.   POTENTIAL APPLICATIONS TO COMPOSITE MATERIALS

As noted in the preceding, piezo placement has a significant impact on achievable structural modal damping. However, if the elements could be scaled down and proliferated throughout a structure, possibly as reinforcement in a structural composite material, significant material damping could be achieved without sensitivity to placement. Using higher longitudinal 3-3 coupling could result in peak loss factors in excess of 25%, even at low volume fractions.

Basic research in progress at Penn State is addressing the possibility of developing such a composite (Yoshikawa *et al* 1991). Key challenges include the fabrication of piezoceramic whiskers, poling and electroding, and providing an integral, tailorable resistive path. Needs in the area of modeling / optimization may be met through the development of multi-field finite elements (Lesieutre 1992) or network impedance models (Hagood and von Flotow 1991).

5.   SUMMARY

Resistively-shunted piezoceramics offer potential for significant damping with advantages over more conventional approaches. A modified modal strain energy method has been developed and tested to guide material selection, placement, and shunting in the pursuit of tailored frequency-dependent damping for structural control applications.

6.   REFERENCES

Collins S A, Miller D W and von Flotow A H 1991 *Proc.Conf. on Recent Advances in Active Control of Sound and Vibration* eds Rogers C A and Fuller C R (Lancaster: Technomic) pp 219-234 ("Piezopolymer Spatial Filters for Active Structural Control")
Greene C S and Stein G 1979 IEEE Paper CH1486-0/79/0000-0230 ("Inherent Damping, Solvability Conditions, and Solutions for Structural Vibration Control")
Hagood N W and von Flotow A H 1991 J. *Sound and Vibration* **146** 1 ("Damping of Structural Vibrations with Piezoelectric Materials and Passive Electrical Networks")
Lesieutre G A 1992 in press *Int'l J. of Solids and Structures* ("Finite Elements for Dynamic Modeling of Uniaxial Rods with Frequency-Dependent Material Properties")
Nowick A S and Berry B S 1972 *Anelastic Relaxation of Crystalline Solids* (New York: Academic Press) pp 55-56: 63-73
von Flotow A H and Vos D W 1991 *Proc.Conf. on Recent Advances in Active Control of Sound and Vibration* eds Rogers C A and Fuller C R (Lancaster: Technomic) pp 593-603 ("The Need for Passive Damping in Feedback Controlled Flexible Structures")
Yoshikawa S, Kurtz S K, Xu Q C, Ramachandran A R and Hayek S 1991 *Proc. 14th ONR Review of Piezoelectric and Electrostrictive Materials for Transducer Applications*, Penn State University, April 22-23, 1991 ("Passive Damping using Piezoelectric Ceramics")

A case study in passive piezoceramic, viscous, and viscoelastic damping

A. H. von Flotow, N. W. Hagood, Massachusetts Institute of Technology
K. L. Napolitano, E. M. Austin, CSA Engineering, Inc.
L. P. Davis, Honeywell, Inc.

Abstract: This paper presents a comparison of three approaches for the passive damping of the ASTREX structure. Open loop performance from specified disturbances (thrusters) to specified responses (line-of-sight) is considered. A computational model is used to select important eigenmodes on the basis of their contribution to the line-of-sight error. Important structural components are selected on the basis of their line-of-sight weighted modal strain energy fraction. Damped replacements for these components are designed using piezoceramic, viscous, and viscoelastic damping mechanisms. The components incorporated into the model and the relative improvement in structural damping response are compared.

No subtleties are attempted. The paper does not consider either structural configuration redesign for damping or possible synergism between passive damping and active control.

1. INTRODUCTION AND BACKGROUND

The purpose of this paper is to demonstrate three passive damping technologies on a common testbed: the ASTREX structure. Obviously, there are situations where each of the technologies shine. However, this is not an attempt to showcase one technology. Rather, it is an attempt to show the advantages of each technology on a realistic structure. In the end, we should all hope that the aerospace community will recognize that an integrated approach, perhaps one using a combination of the three technologies, is the best way to approach complicated problems.

The overall approach is to choose a dynamics-based figure of merit, define a set of target modes and structural members that affect it greatly, do component-level designs for each technology, and assess each concept's effect on the figure of merit. A logical measure for effectiveness of a damping treatment on this type of structure is line of sight disturbance due to slew thruster input.

2. PASSIVE DAMPING TECHNOLOGIES ADDRESSED

2.1 Passive Piezoelectric Damping

Piezoelectrics materials are elastic ceramics and polymers which have the ability to efficiently convert mechanical energy to electrical energy and vice-versa. This property has made them popular as actuators and sensors in active vibration control systems. This dual transformation ability also makes them useful as passive structural dampers. In passive energy dissipation applications, the electrodes of the piezoelectric are shunted with a passive electric circuit. The electrical circuit is designed to dissipate the electrical energy that has been converted from mechanical energy by the piezoelectric.

The effectiveness of the piezoelectric damper is dictated by its coupling properties and the configuration in which it is used. The fundamental material property is the electromechanical coupling coefficient, k, whose square represents the percentage of applied mechanical strain energy which is converted into electrical energy and vice-versa. The value of the coupling coefficient (and hence the piezoelectric effectiveness) is dependent on the configurations of operation can be described as: Longitudinal (stress and field applied parallel to the poling direction), Transverse (stress perpendicular and field parallel to poling), and Shear(stress applied about an axis perpendicular to poling while the field is perpendicular to both). The coupling coefficient in the longitudinal and shear configurations is approximately 2.5 times that in the transverse direction.

The simplest electrical shunt circuit for passive damping is a resistor. Other circuits can be visualized and have been reported elsewhere [1]. A resistor provides a means of energy dissipation on the electrical side and thus increases the total piezoelectric loss factor above that of the unshunted piezoelectric. With a shunted resistor, the ceramic behaves like a standard first-order viscoelastic material. The material properties of the resistive shunted piezoelectric can be represented as a complex modulus as is typically done for viscoelastic materials, $E^{eff}(\omega) = \bar{E}(\omega)(1 + i\eta(\omega))$, where $\bar{E}$ is the ratio of shunted stiffness to open circuit stiffness of the piezoelectric and η is the material loss factor. The nondimensional expressions for η and E are

$$\eta(\omega) = \frac{\rho k^2}{(1-k^2)+\rho^2}, \quad \bar{E} = 1 - \frac{k^2}{1+\rho^2}, \quad \rho = RC^s\omega = \frac{\omega}{\omega_d}, \tag{1}$$

where ρ is the nondimensional frequency ratio, k is the electromechanical coupling coefficient, R is the shunting resistance, and C^s is the clamped piezoelectric capacitance. These relations have been plotted versus ρ, the nondimensional frequency (or the nondimensional resistance) in Figure 1 for a typical value of the longitudinal coupling coefficient. As illustrated in the graphs, for a given resistance the modulus of the piezoelectric changes from its short circuit value at low frequencies (about that of aluminum) to its open-circuit value at high frequencies. The transition is first order, with the transition frequency being RC^s, where C^s is the capacitance of the piezoceramics electrodes. R is the resistance. The material loss factor peaks at this transition frequency at a value of 44% for longitudinal or shear use and 8% for transverse use. The point of maximum loss factor can be assigned to the desired frequency by appropriate choice of resistor.

While the loss factor levels are not as high as those for viscoelastic materials, the high stiffness (63 GPa, 9 135 × 10⁶ psi) of the shunted piezoelectric materials (typically a ce-
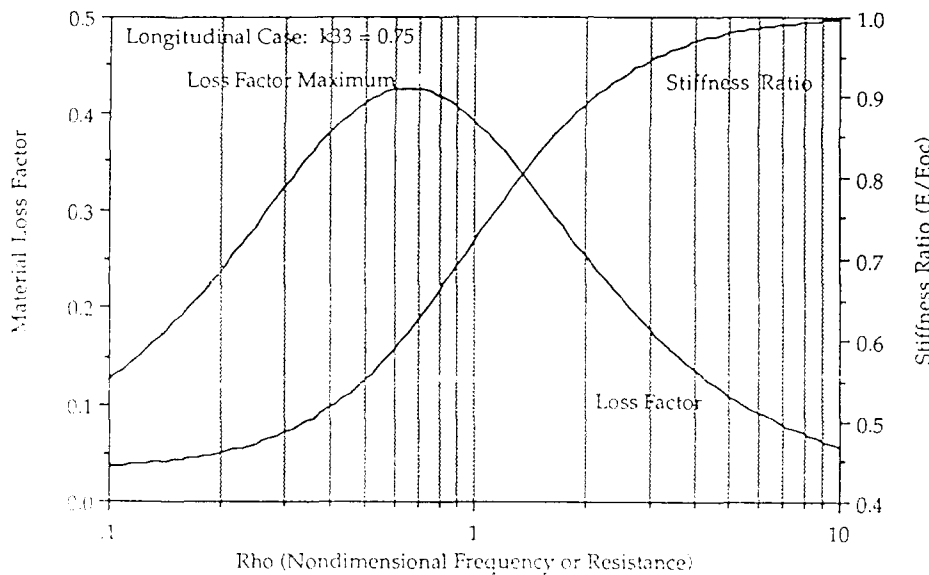
Figure 1. Effective material properties of a resistively shunted piezoelectric in the longitudinal case

r·unic) allows them to store many times the strain energy of the viscoelastic for a given strain. The piezoelectric material properties are also relatively temperature independent below their Curie temperature (temperature at which they lose their piezoelectric properties, typically in the range of several hundred °C). The piezoelectric material density (~ 7.5 gm/cm^3, 0.27 lbs/in^3) is much higher than that of viscoelastic materials, however.

Passive piezoceramic damping is a recent development [1, 2] and has yet found no application outside the research laboratory. In principle, one should compare this material directly with polymer viscoelastic materials described in Section 2.2. In this comparison, piezoceramics shunted with a resistor are stiffer, more dense and more brittle and have a lower peak loss factor. A further potential consideration is that they may be used simultaneously as actuators and as damping elements [2]. One purpose of this paper is to make this comparison more quantitative.

2.2 Viscoelastic

Passive damping using viscoelastic materials(VEM's) is used widely in both commercial and aerospace applications. Viscoelastics are elastomeric materials whose long-chain molecules cause them to convert mechanical energy into heat when they are deformed. Perhaps the most important advantage of VEM's is their high ratio of loss modulus to storage modulus. The properties of viscoelastic materials when deformed in shear are characterized by the loss modulus G'', the storage modulus G', and the loss factor $\eta = G''/G'$. The loss factor is a measure of the energy dissipation capacity of the

material, and the storage modulus is a measure of the stiffness of the material. The storage modulus (often called simply the shear modulus) is important in determining how much energy gets into the viscoelastic, and the loss factor determines what fraction of that energy is dissipated.

Typical applications for VEM's are constrained-layer treatments, damped struts, and tuned-mass dampers. VEM's are particularly well suited for damping local and global bending modes via constrained-layer treatments. When integrated into a structure during the initial design, constrained-layer treatments can results in net weight savings. VEM's are good for damped struts because it provides a loss mechanism for bending, axial, and torsion deformations. VEM's are most useful in moderate-band temperature environments and can be quite sensitive to operating temperatures

2.3 Viscous

A viscous-damping technique offering high damping for spacecraft truss structures has been under development now for several years [4, 5, 6]. The technique, known as the D-Strut^{TM}, employs a small, mechanical viscous damper configured in an inner-outer, tube-strut configuration. The D-Strut serves as a basic element in a truss structure, replacing the nominal-type strut. The viscous-damping concept, employed in more compliant isolation systems, has been qualified for at least three space applications and is currently flying in the Hubble Space Telescope, where its function is to isolate disturbances emanating from the attitude control Reaction Wheel Assemblies [7, 8].

The United States Air Force, the Jet Propulsion Laboratory (JPL), and NASA's Lewis Research Center (LeRC) are independently investigating the use of D-Struts in high specific-stiffness truss structures. The D-Strut is simple in design and construction, easy to model, and readily incorporated into the overall structure design and analysis process. Key features include high damping, low temperature sensitivity, large dynamic range, damping independent of stiffness, and linear purely viscous performance.

3. ANALYSIS AND LOS RESPONSE TO SLEW TORQUES

A line-of-sight equation was entered into the baseline ASTREX finite element model that accounted for motion in the tertiary mirror, and individual action of each of the six segmented mirrors. Undamped modes were calculated up to 100 Hz using MSC/NASTRAN. Since actual input forces were unknown, equal and opposite forces were applied at the location of the thrusters to simulate a slew maneuver. Rather than having NASTRAN calculate a response function for the LOS, a technique using the modal residues, R, was employed. This is a little more precise than the response function. Since the mean square, σ_{LOS}^2, for low modal overlap is proportional to $R^2/\zeta\omega_n^3$, a merit factor of R^2/ω_n^3 was calculated for each mode and normalized so that its sum was 1. This allowed the modes to be ranked according to their contribution to LOS.

The next step was to assess which elements have the most modal strain energy in the modes that have the greatest effect on LOS. A simple way to do this is to multiply the vector of residuals R^2/ω_n^3 by the modal strain energy for each element. This amounts to the matrix product of the MSE vector ($n_{elem} \times n_{modes}$) and the vector of x and y LOS residuals ($n_{modes} \times 2$). The $n_{elem} \times 2$ resultant is the LOS-weighted MSE for LOS$_x$ and LOS$_y$. The highest values in each column represent elements having the most influence

Mode No.	Freq. (Hz)	Contribution to RMS (%) (0-100 Hz)	Percent Modal Strain Energy			
			Tracker Struts		Tripod Legs	
			extension	bending	extension	bending
29	48.6	25.6	11.44	1.38	1.78	43.76
16	26.2	21.8	9.79	1.15	0.57	6.44
18	28.9	15.6	17.07	14.78	2.51	2.67
20	30.0	6.1	0.34	0.17	2.74	1.79
9	15.9	4.8	4.49	0.49	1.10	18.77
38	64.3	3.5	5.11	1.66	4.28	1.37
7	11.9	2.8	0.49	0.11	4.77	64.35

$$\Sigma \approx 80\%$$

Table 1: Breakdown of MSE in modes important to LOS_x

Mode No.	Freq. (Hz)	Contribution to RMS (%) (0-100 Hz)	Percent Modal Strain Energy			
			Tracker Struts		Tripod Legs	
			extension	bending	extension	bending
9	15.9	34.8	4.49	0.49	1.10	18.77
16	26.2	21.3	19.78	16.27	1.09	1.60
18	28.9	6.0	17.07	14.78	2.51	2.67
29	48.6	4.2	11.44	1.38	1.78	43.76
25	40.3	4.0	8.94	0.88	7.53	5.33
22	33.2	3.3	0.93	0.55	7.99	4.78
38	64.3	2.8	5.11	1.66	4.28	1.37

$$\Sigma \approx 76\%$$

Table 2: Breakdown of MSE in modes important to LOS_y

on the LOS over the set of n_{modes} modes. This was used to choose the set of elements as targets for passive damping.

Elements were sorted according to their weighted MSE value to determine which contributed the most to overall jitter. Tables 1 and 2 list the top few jitter-critical modes for each direction along with the modal strain energy in some key groups of members. The tripod legs and the truss members connecting the trackers to the baseline truss contributed the most to jitter, and were therefore chosen to be damped. As Tables 1 and 2 show, the majority of the energy in the tracker struts is extensional, and the majority in the tripod legs is bending.

4. COMPONENT DESIGNS

A few basic requirements were set for the damping designs so that comparisons of effectiveness would be easier. The specifications on stiffness and weight were as follows: EI of tracker struts evaluated at 0.1 Hz be at least 75% that of the undamped version, EI and AE evaluated at 0.1 Hz of the tripod legs be at least 75% that of the undamped version, extensional stiffness AE evaluated at 0.1 Hz of both the tracker struts and tripod leg struts be at least 75% that of the undamped version. For simplicity, the end fittings parts were perfectly rigid and massless.
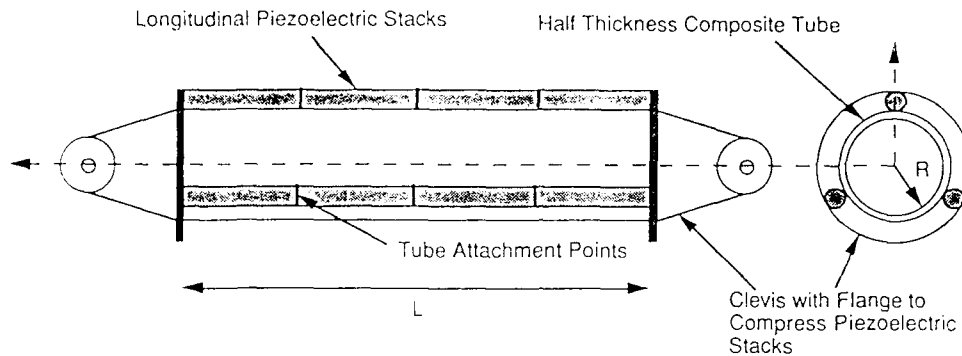
Figure 2: Schematic of piezoelectric damped member design showing internal composite tube and external piezoelectric stacks

4.1 Piezoelectric

The challenge is to select a geometry for incorporating the quite stiff piezoceramic material into the aluminum/graphite-epoxy strut. The goal is to bring as large a fraction as possible of the strain energy into the piezoceramic material, both in extension and in bending within the stiffness constraints outlined above. The methodology of designing the struts will be presented in the following paragraphs. The methodology, but not the actual dimensions was identical for the tracker and tripod designs.

It is necessary to reduce the stiffness of the undamped material in the strut, the graphite/epoxy, and replace this stiffness with that due to the piezoceramic. We considered reducing the graphite/epoxy wall thickness from 120 milli-inches (12 ply) to 30 milli-inches (3 ply at 45°, 0°, and 45°), but rejected that idea as too radical and chose instead to reduce the graphite/epoxy tube wall thickness by half to 60 milli-inches. In order to recover the strut's stiffness, the removed graphite/epoxy is replaced with three long stacks of longitudinally oriented piezoceramic wafers of 100-milli-inch thickness interlaced with copper-beryllium electrodes of 1-milli-inch thickness. These long, slender piezoceramic stacks must be constrained from buckling by restraining them to the remaining graphite/epoxy tube. They must also be compressed to avoid tensile stresses during operation. This is accomplished by end plates compressing the stacks and putting the composite tube in tension. Figure 2 is a sketch of the concept.

The half-wall thickness halves the EA and EI of the members. This must be recovered by the addition of the piezoceramic elements. The total area of the piezoelectric stack is chosen such that the total EA of the damped member (tube plus piezo-stacks) would equal the EA of the original member. Since the piezoelectric stiffness is a function of frequency, Eq. (1), this stiffness matching was done at the nondimensional frequency corresponding to the maximum piezoelectric loss factor. From (1), the value of this maximum loss factor and ρ value at which it occurs is given by:

$$\eta_{max} = \frac{k^2}{2\sqrt{1-k^2}} = 0.44, \quad \rho_{max} = R C^{''} = \sqrt{1-k^2} = 0.6614 \qquad (2)$$

Component	Units	Tracker	Tripod
Composite Tube Area	$m^2(\times 10^{-4})$	3.64	6.17
Piezo-Stack Area	$m^2(\times 10^{-4})$	3.02	7.14
Total Area	$m^2(\times 10^{-4})$	6.66	13.33
Composite Tube Inertia	$m^4(\times 10^{-6})$	0.58	2.01
Piezo-Stack Inertia	$m^4(\times 10^{-6})$	0.49	2.33
Total Inertia	$m^4(\times 10^{-6})$	1.07	4.34
Effective Stiffness, E^D_{Eff}	GPa	81.20	96.05
Mass/Unit Length	kg/m	2.72	6.98

Table 3: Section Properties of Damped Trucker and Tripod Tubes

The frequency at which this maximum material loss factor occurs is selected through appropriate choice of the shunting resistor. In the damped member designs the peak loss factor was arbitrarily set to 30 Hz by selecting a resistor such that RC was equal to 35×10^{-3} rad/sec. The particular value of the resistance depends on the capacitance and lengths of the specific member under consideration. Better performance could have been obtained through more careful loss factor tuning of the individual members independently.

Having determined the total area of the individual members independently, it is possible to determine the effective frequency dependent stiffness of the member. The total EA of the piezoelectric stacks (subscript p). It takes the form

$$E_{Eff}(\omega) = \frac{A_c E_c + A_p E_p(\omega)}{A_c + A_p} = E^D_{Eff} \frac{(a^2 + \omega^2)}{(b^2 + \omega^2)} (1 + i\frac{c\omega}{a^2 + \omega^2}) \qquad (3)$$

where

$$a = 36.58 \text{ Hz}, b = 45.36 \text{ Hz}, c = 15.86 \text{ Hz}$$

ω is frequency in Hz, and the values of E^D_{Eff} for the tracker and tripod members are given in Table 3.

The next step is to determine the bending stiffness of the damped members. The stiffness constraint on the bending moments is that EI/ml^2 of damped members must be no less than 75% of the original. Since the piezoelectric is very dense this requirement drove the moment of inertia of the designs. The total EI of the damped member must obey the relation

$$EI_{damped} = \frac{3}{4} EI_{old} \frac{m_{damped}}{m_{old}} \qquad (4)$$

Once the EI of the damped member is fixed, the inertias can be obtained. The composite tube was arbitrarily chosen to contribute half of the bending stiffness, EI. This required increasing the radius of the composite tube 40%. The inertia of the piezoelectric stacks
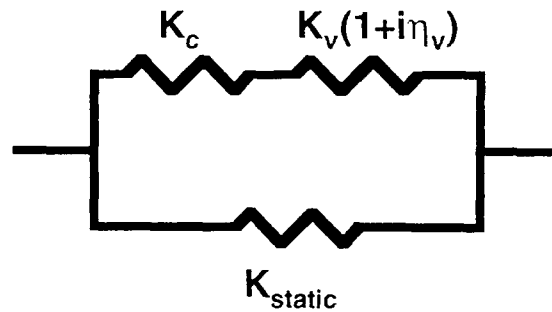
Figure 3: Spring model of a damped strut

was then calculated using the piezoelectric stiffness at maximum loss factor as was done for the area design. As a result of this design method the effective modulus for bending is the same as that for extension and thus the same loss is achieved in bending or extension of the damped member.

The above discussion has omitted detailed redesign of the aluminum end fittings, of the restraint between the piezoceramic stacks and the graphite/epoxy tubes, of the mechanism by which the piezoceramic stacks would be pre-loaded in compression, and of other details. We cannot claim to have much design experience with these details. Piezoceramic damping has never been attempted at this scale and as such this design should be considered high risk (though feasible). Half-meter-long piezoelectrically damped struts have been previously manufactured and shown [3] to perform as predicted. The damping achieved in [3] is much larger than that achieved from those designed since resonant passive circuits were used rather than simple resistors.

4.2 Viscoelastic

4.2.1 Tracker Struts
To gain insight into how this damped strut operates, one can represent the strut as a combination of complex springs, as shown in Figure 3. To concentrate the strain energy in the VEM and therefore obtain a higher strut loss factor, K_c should be maximized. This is analogous to two springs in series. In order to maximize the strain energy in one spring, the other must be relatively stiff. Therefore, constraining layer should be as stiff as possible. Only the weight requirement limits its maximum stiffness. Likewise, K_{static} must be minimized. This corresponds to two springs in parallel. In order to maximize the strain energy in one spring, the other must be relatively compliant. Therefore, one wants to minimize the static stiffness of the strut and minimize the stiffness of the static load path. A physical interpretation is as follows. The constraining layers restrain the VEM when a load extends the static tube. The relative displacement between the static tube and constraining layer puts the VEM in shear, causing energy to be dissipated. A schematic of the design is shown in Figure 4.

VEM struts have several inherent advantages. First, VEM's are robust and can take high shock loads without fear of catastrophe. They can easily handle over 100% strain due to static loads, and the VEM damping element is very light-weight. In this design, the viscoelastic material weighs less than 0.07 lbs per strut. VEM struts can damp a combination of bending, extension, and torsional deformations. Proper selection of viscoelastic materials and viscoelastic material dimensions ensures a high loss factor at

Constaining Layer(4 staves)   **VEM**

Load-Carrying Tube
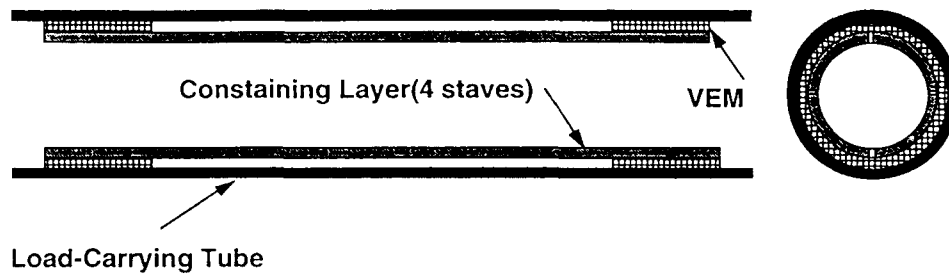
Figure 4: Schematic of viscoelastic damped strut

a desired frequency. VEM damped struts can also sustain a respectable loss over a wide frequency range by selecting a VEM with a moderate loss over a wide frequency range.

This strut design has several advantages. The static load carrying tube will counter any and all static loads placed on the strut. VEM creep is not an issue because the static tube provides a robust, elastic load path. Because the VEM is placed inside the static tube, it is protected from the environment. The constraining layer is a unidirectional composite, an ideal application because the dynamic loads seen are axial to the material. This reduces strut weight significantly. As composite materials become lighter and stiffer, the strut weight will be determined by the weight of the damping element, which for VEM damped struts is very small. It is easy to fabricate. The VEM selected is commercially sold as a structural adhesive, and will be used to bond the constraining layers to the static load-carrying tube. Any local resonance of the constraining layers should be well-damped.

It was decided that the total cross-section area of the strut should be no more than twice that of the baseline strut. If more material is used, strut performance is enhanced. The constraining layer chosen is a unidirectional composite with the properties E = 33Msi and $\rho = 0.055 \frac{lb}{in^3}$. The load-carrying member is the same composite material used in the baseline strut. The VEM chosen is 3M Y966, with the properties evaluated at 73°F. The final dimensions were static tube thickness = 0.08", constraining layer thickness = 0.15", and VEM thickness = 0.014". A finite element model of the strut was built. By reducing the static tube's area by one-third and applying the rest of the area to the constraining layer, a stiffness of 0.77 that of the baseline tube at 0.1 Hz, was achieved. The extensional stiffness and loss were measured via a DFR. Because the frequencies considered are well-below strut resonance, the mass terms in the equation of motion can be ignored, so

$$\eta_s = -\frac{u_i}{u_r}, \text{ and } K_s = \frac{u_r}{u_r^2 + u_i^2} \tag{5}$$

Calculating bending loss is not as straight forward. Two end static loads were applied
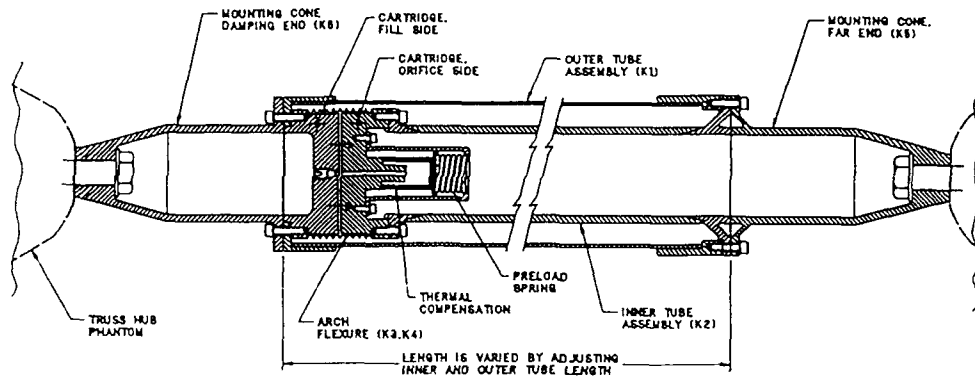
Figure 5: Cross-sectional view of a D-Strut

to the strut FEM: a bending moment and then a lateral force. For both loading case, all end DOF's except that of the load were constrained. The rotation (displacement) of the moment (lateral force) was measured along with the applied force and the constrained force fixed DOF's. The corresponding stiffnesses were calculated and used to back out a corresponding EI for each type of loading. The average EI was used in the FEM. The bending loss was calculated by multiplying the average percent strain energy of the two deformed shapes by the VEM loss factor at the desired frequency.

4.2.2 Tripod Legs

An excellent feature of VEM's is that they can be used to design add-on damping treatments to existing structures. The tripod leg damping treatment was designed as such. Since the MSE of tripod leg modes 9 and 29 was in the top 3/4 of the tripod legs, a constrained layer damping treatment on the top 3/4 was designed. Eight unidirectional composite staves (E = 33Msi, $\rho = 0.055\frac{lb}{in^3}$, t = 0.09 in), were placed on the tripod leg as constraining layers to a 40-mil-thick VEM. A finite element model of the tube was built with simply supported end conditions. In first bending mode of the tripod leg, 18 percent of the strain energy entered the VEM, which roughly corresponds to a loss of 0.21. More loss could be achieved with a stiffer constraining layer. With CL thickness of 0.13 in., 22 percent MSE enters the VEM. Approximately 15.3 pounds was added to each tripod leg, bringing the total weight of one tripod leg to 50.3 lbs.

4.3 Viscous

A cross-sectional view of a D-Strut is shown in Figure 5. Primary elements are the damping cartridge and the inner and outer tubes. The damper cartridge is placed in series with the inner tube. The damper and inner tube are then placed in parallel with the outer tube. An axial displacement across the strut produces a displacement across the damper. Under an axial displacement, the damper forces fluid through a small-diameter orifice, thereby causing a shear in the fluid. This fluid is proportional to the displacement rate across the damper and produces a force directly proportional to deflection velocity.

k$_1$ - Outer Tube Stiffness

k$_2$ - Inner Tube Stiffness

k$_3$ - Damper Static Stiffness

k$_4$ - Damper Volumetric Stiffness

c - Viscous Damping Coefficient
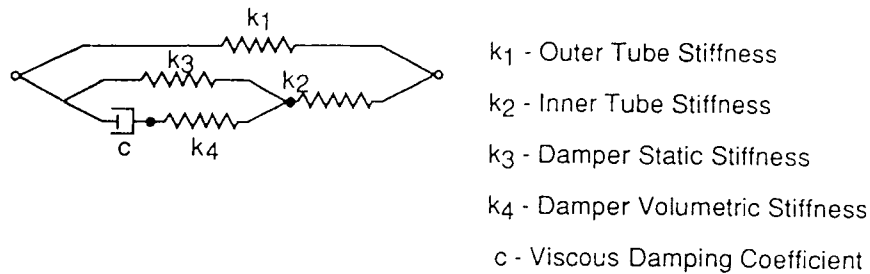
Figure 6: D-Strut equivalent model

Compliance of the damper and the inner and outer tubes is key to the damping element performance of the D-Strut. The damper is the most compliant element; the inner tube is the least compliant element. The outer tube provides the basic static stiffness of the strut, making it pertinent to applications where the strut is a critical load-bearing element in the structure.

4.3.1 D-Strut Model

A D-Strut is accurately modeled by five physically lumped parameters. as indicated by Figure 6. If there is an element such as a quick disconnect device in series with the D-Strut, or if there is hub compliance, a fifth spring (k$_5$) is placed in series with the above model.

The primary parts of the D-Strut contributing to the stiffnesses k$_1$ through k$_5$ are identified in Figure 1 by the k values located next to the part names. Best performance is obtained when the inner tube (k_2) is several times as large as the outer tube (k_1); when the volumetric stiffness of the arched flexure (k_4) is very large compared to the axial stiffness (k_3) (100:1 or more); when the series or hub stiffness (k_5) is at least as large as (k_2); and when (k_4) is two or more times as large as (k_2). These stiffness values dictate the magnitude of the damping. When the above conditions are satisfied, loss factors of 50% to 100% occur. The damping coefficient (c) can be established by selecting fluid viscosity, diameter, and length of the shear annulus. Ranges from 1 to 10,000 lb-sec/in. have been obtained. A much larger range is obtainable. The selection of c sets the frequency range in which the damping occurs. A high value of c provides low-frequency damping while a low value provides high-frequency damping. the selection of (k_2) carries with it the primary weight penalty; thus, a trade between weight and damping factors is essential. The weight of the damping element is relatively small; however, it is a function of diameter and a secondary trade is sometimes indicated. (k_1) is approximately the static stiffness of the strut and is generally dictated by the system or modal requirements.

4.3.2 D-Strut Design and Results

To be consistent with the viscoelastic strut, the D-Strut design was restricted so that cross sectional area of the undamped strut would not be increased more than 2 to 1. The static stiffness of the new design was to be no less than 75% of the undamped tube that

it replaced. The inner tube modulus was to be 33,000,000 $\frac{lb}{in^2}$ and its density 0.055 $\frac{lb}{in^3}$. Its outside diameter, ranging from 2.6 to 2.75 in., was selected to fit inside the original or outer tube whose inside diameter was 2.83 to 2.845 in. A load limit of 5000 lb was also selected. Review of the modal data suggested that best results would be obtained by selecting the damping coefficient to provide peak damping in the vicinity of 30 Hz. For realism, an existing D-Strut design from the SPICE program was selected as the baseline (see Figure 5), and the inner tube and outer tubes were modified. The flexure provided a $k_3 = 950$ lb/in. and a $k_4 = 1,950,000$ lb./in was not altered. The end fittings for this design, also remained the same, provided a $k_5 = 1,000,000$ lb/in. With this, the new design was roughly optimized by trading off wall thickness for the inner tube to balance performance and weight. Very high damping was achieved without further increases in tube thickness. (See Element Damping Factor %) The damping coefficient was selected to center the maximum damping at or near 30 Hz.

4.3.3 Viscous Bending Mode Damping

Bending mode damping by viscous techniques has not been included in this analysis. As a result, significant performance loss will result, particularly due to the lower bending modes of the tripod legs. Two schemes that provide viscous damping do exist. One uses two bellows arranged with the annulus between them, similar to the viscous isolator used on the Hubble Space Telescope. The other is a multiport arrangement that can be implemented within the D-Strut damping cartridge. Time limitation, along with space limitation within this paper, precluded consideration or evaluation of these approaches.

5. EFFECT ON LOS

5.1 Analysis Methods for the Damping Treatments

The LOS will be assessed via a direct frequency response (DFR) of the line-of-sight equation from 1 to 100 Hz (minus the contribution of rigid body modes). The RMS of this curve will be the figure of merit. The jitter reduction will be the ratio of this integral to a baseline integral having a baseline 0.5% structural damping (Q = 200).

5.1.1 Piezoelectrics

Functions of Young's modulus, $E^*(\omega) = E(\omega)(1 + i\eta(\omega))$, the areas, and moments of inertia, were supplied for both tracker struts and tripod leg damping treatments. Both the bending and extensional stiffnesses exhibited a peak loss factor of 0.22 at 35 Hz. E and η were evaluated at 6, 16, 30, 49, and 75 Hz. To account for the frequency dependent properties of the damping treatment, DFR's from 1-10 Hz, 10-20 Hz, 20-40 Hz, 40-60 Hz, and 60-100 Hz were applied using the corresponding values of E and η. Frequencies at 16, 30, and 49 Hz apply to the already determined significant modes to be damped. Performance at the modes of interest should be fairly accurate.

5.1.2 Viscoelastics

The same analysis as above was applied to the viscoelastic struts. However, each strut was separated into bending and extension elements to account for the different bending and extensional loss. Since no accurate method of representing the VEM-damped tripod legs as a series of beams could be devised, the detailed finite element model used to design the tripod legs was directly inserted into the system-level model. Again, VEM storage modulus and loss factor were varied according to the desired frequency range.
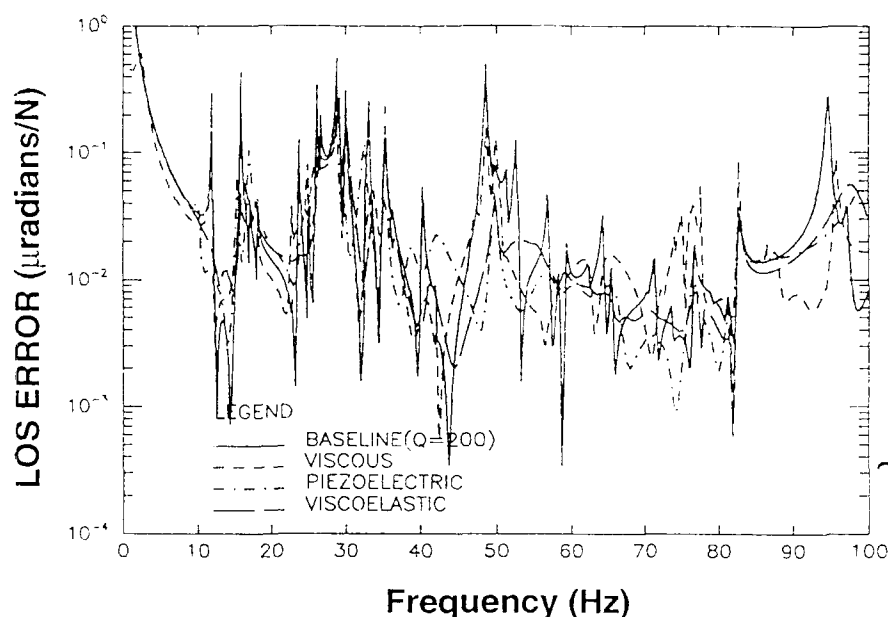
Figure 7: Comparison of LOS$_x$ PSD's resulting from each damping technology

5.1.3 Viscous Struts

A three parameter model of the viscous strut was supplied. The static tube was represented as a bar element with both bending and extensional stiffness. The tube carrying the dynamic loads was represented as an axial element only. A dashpot was inserted directly into the model to simulate the damping element. A DFR from 1 to 100 Hz was then performed.

Figures 7 and 8 show PSD's of the X and Y LOS between 1 and 100 Hz. Assessing the effect of each of the damping treatments on the line of sight is a difficult task; one that requires more than just comparing the RMS values of the LOS over a broad frequency range. None of the designers of the damping treatments was given complete freedom to exploit their damping technology, due to the specifications described earlier. Since modes were attacked selectively, the results must be interpreted selectively. In general, there is a fair amount of coupling between the tracker struts and tripod legs in the modes most important to LOS. Consequently, each damping technique addresses each mode, with varying degrees of success. Rather than identifying modes in which particular damping treatments were effective, we will look at how each addresses two important "classes" of modes: extensional energy in the tracker struts and bending of the tripod legs.

While bending of tripod legs are typically the greatest single source of LOS error for structures such as ASTREX, this is not entirely the case here. There is no local mode of the tripod legs that contributes significantly to LOS. Tables 1 and 2 show that the largest single portion of the MSE in the two modes contributing the most to LOS (modes 29 and 9, respectively), there is enough extensional energy in the tracker struts for the viscous technology to provide respectable system-level loss. Figure 9 shows this for modes 9 at 15.9 Hz and 29 at 48.6 Hz
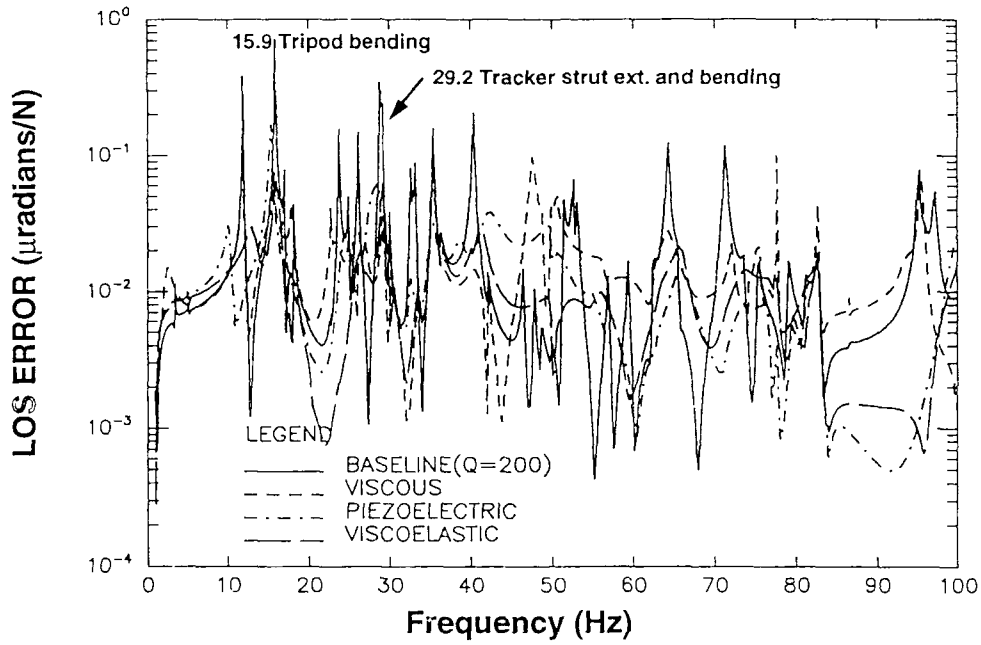
Figure 8: Comparison of LOS$_y$ PSD's resulting from each damping technology
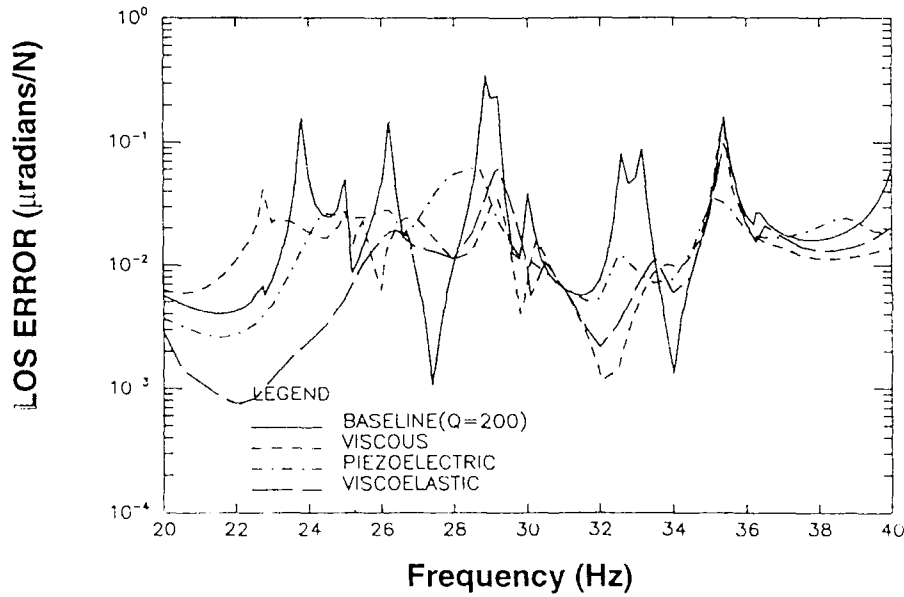
Figure 9: LOS$_y$ for each damping technology plotted against baseline between 20 and 40 Hz

Strut Length (inches)	Baseline (pounds)	VEM Strut (pounds)	Viscous (pounds)	Piezoelectrics (pounds)
42.48	2.03	3.84	3.52	6.50
30.79	1.55	2.78	3.02	4.71
50.58	2.39	4.52	4.83	7.74
39.50	1.65	3.55	3.81	6.04
TOTAL	22.4	42.6	43.4	72.4

Table 4: Weight of damped tracker struts

Freq. (Hz)	VEM Strut (exten/bending)	D-Strut (exten/bending)	Piezo. Strut (exten/bending)
6	.17/.061	.27/0.0	.069/.069
16	.27/.10	.59/0.0	.16/.16
30	.31/.11	.69/0.0	.22/.22
50	.34/.12	.61/0.0	.21/.21
75	.34/.13	.47/0.0	.17/.17

Table 5: Average extension and bending loss of damped tracker struts at selected frequencies

Modes 16, 18, and 19 are characterized by concentrations of modal strain energy in both extension and bending of the tracker struts. Each of the three damping treatments addresses these modes well. Even addressing only extension, the D-Strut has such a high loss factor near 30 Hz that it is the most effective. Both the piezoelectric and viscoelastic concepts are effective also, mainly because the same damping mechanism addresses both bending and extension.

Table 4 presents the weights of the damped tracker struts. The weight of the viscous and viscoelastic elements are essentially the same. The piezoceramic element is heavier because its damping element is inherently dense. Table 5 presents the average extension and bending loss of each damped strut concept at different frequencies. Of the three the viscous strut performs best in extension, but has no bending loss is implemented currently. The VEM performs well in extension and fair in bending. The piezoceramic performs equally well in both. Depending on the strut deformation, a different strut can be chosen.

The add-on damping treatment for the VEM damped tripod leg adds 15.31 lb/leg, bringing the total weight of each tripod leg to 50.31 lb. Each piezoceramic damped tripod leg is 79.19 lb. The loss factor of the tripod leg is the same as the piezoelectric struts. The loss factor of the VEM damped tripod cannot be assigned because the end conditions cannot be defined. However, the first bending mode of a simply supported tripod leg has a predicted loss factor of 0.21.

6. CONCLUSIONS

Each of the damping treatments performed well, given the requirements on weight and minimum static stiffness, and each is capable of playing an important roll in providing passive damping for a variety of structures. Table 6 gives RMS values over some selected

Case	LOS$_x$			LOS$_y$		
	10-100 Hz	20-40	24-31 Hz	1-100 Hz	20-40 Hz	26-31
Undamped	1.0	1.0	1.0	1.0	1.0	1.0
Viscous*	0.83	0.86	0.84	0.89	0.72	0.56
Piezoelectric	0.78	0.83	0.80	0.80	0.76	0.75
Viscoelastic	0.80	0.86	0.87	0.71	0.65	0.62

*no tripod leg damping treatment

Table 6: Scaled RMS values over selected frequency bands

frequency ranges. As can be observed, selected the frequency range can "influence" which damping treatment performs best. The total ASTREX FEM weight, excluding pedestal weight is 8,394 pounds. The heaviest damped struts make up less than 0.63% of the weight (see Table 7). Even including the piezoceramic tripod legs, the added mass due to passive damping is only 2.2%.

There are many factors that must be considered is choosing an approach to damping: effectiveness, cost, schedule, maintenance, etc. Again, the goal of this paper was not to choose a "winner." Rather, it was to look at the strengths and weaknesses of each objectively. With that in mind, here are a few observations:

Piezoelectric:

- Has the advantage that the loss mechanism is also a structural material, albeit an undesirable one (brittle with the stiffness of aluminum and density of steel).

- Is temperature insensitive (up to about 250 C) and can also be used as an actuator.

- Limited experience base.

Viscoelastic:

- Effective for bending, axial, and torsional strains.

- Temperature sensitivity depends on peak loss factor; it can be very high

- Temperature control needed for uncontrolled environments, but small amounts of VEM require small amounts of heat.

- Designs are generally fairly simple, and the materials are robust in the presence of shock and high-strain loads.

- Large experience base, including many operating flight applications.

- Generally very inexpensive to fabricate.

Viscous:

- Though possible to adapt for bending deformations, this mechanism is by far best suited for axial deformations.

	Tracker Struts		Tripod Legs		Total	
Treatment	mass added	% of ASTREX	mass added	% of ASTREX	mass added	% of ASTREX
Viscous	21.0	0.25	n/a	0	21.0	0.25
Piezoelectric	52.9	0.63	132.6	1.58	185.5	2.21
Viscoelastic	20.2	0.24	45.9	0.55	66.1	0.79

Table 7: Weight added to ASTREX Structure

- The fluids are somewhat sensitive to temperature variations, but much less than high-loss VEM's.

- Large experience base; many flight miles logged.

- Loss mechanism inherently requires precision fabrication; this could lead to high per-unit costs unless volumes are high.

References

[1] Hagood, N. W., von Flotow, A., "Damping of Structural Vibrations with Piezoelectric Materials and Passive Electrical Networks," *Journal of Sound and Vibration*, Vol. 146, No. 1, April 1991.

[2] Hagood, N. W., Chung, Walter H., von Flotow, A., "Modelling of Piezoelectric Actuator Dynamics for Active Structural Control," *Journal of Intelligent Material Systems and Structures*, Vol. 1, No. 3, July 1990, pp. 327-354.

[3] Hagood, N. W., Crawley, E. F., "Experimental Investigation into Passive Damping Enhancement for Space Structures," To appear in the *Journal of Guidance, Control, and Dynamics,* Vol. 14, No. 6, Nov.-Dec. 1991, pp. 1100-1109.

[4] Davis, L. P., Wilson, J. F., "Very High Damping in Large Space Structures," *ASME Vibrations Conference,* Boston, MA, 1987.

[5] Davis, L. P., Wilson, J. F., "New Structure Design Criteria Offer Improved Pointing and Lower Weight," *59th Shock and Vibration Symposium,* Albuquerque, NM, Oct. 1988.

[6] Cunningham, D. C., "Final Technical Report, ACOSS D-Strut Development," Prepared for *Martin Marietta, Honeywell, Inc., Satellite Systems Operation,* Glendale, AZ, Aug. 1990.

[7] Roddeb, J. J., Dougherty, H. J., Reschke, L. F., Hasha, M. D., Davis, L. P., "Line of Sight Performance Improvement with Reaction Wheel Isolation," *AAS Guidance and Control Conference,* Keystone, CO, Feb. 1986.

[8] Davis, L. P., Wilson, J. F., Jewell, R. E., "Workshop on Structural Dynamics and Control Interactions of Flexible Structures," *NASA Marshall Space Flight Center,* Huntsville, AL, Apr. 1986.

Design and development of passive and active damping concepts for adaptive space structures

D. L. Edberg
A. S. Bicos

McDonnell Douglas Space Systems Company. Huntington Beach, CA 92647

ABSTRACT: Many types of spacecraft are expected to need shape control and structural vibration suppression systems to meet their performance requirements. Because the operational lifetimes of these spacecraft will be long, changes may occur which necessitate that the vibration control subsystems adapt to maintain performance. This investigation is concerned with the development of two different vibration suppression techniques that use piezoelectric energy conversion to enhance vibration dissipation. The ultimate goal is to develop structural struts which incorporate these techniques that may be installed in a generic truss structure.

1. ENHANCEMENT OF DAMPING USING A TUNED ELECTRONIC SHUNT

When a structure is vibrating, its components are mechanically strained. Piezoelectric materials can convert this mechanical strain to electric potential, allowing an electrical network to be added to extract energy. Hagood et al [1988,1990] have shown the results of adding a passive shunt to a truss with piezoelectric members. The work reported here is a further development of that work.

For passive and active control investigations, MDSSC designed and fabricated a number of piezoelectric struts, each consisting of lead zirconate titanate (PZT) hollow cylinder segments wrapped with a fiberglass/epoxy outer coating. The design was modified from one used by Hagood et al [1988,1990] by the addition of an electrically-isolated PZT element that could be used as a sensor independently of the other elements in the strut. Figure 1 shows the design of the MDSSC-fabricated piezoelectric struts. An electric field applied between the outer radius and the inner radius created axial deformation. Mechanically, the segments were connected in series, and electrically all but one of the cylindrical rings were connected in parallel. The strut has a static force constant of approximately 0.45 N/V, and it exhibits the hysteresis commonly found in piezoelectric materials.

The MDSSC CSI truss is shown in Figure 2, and is used as a testbed for the shunting experiments. It uses Meroform components as did the MIT truss,

however it is longer (9.5 vs 5 meters) and has half as many piezoelectric struts (two vs four).
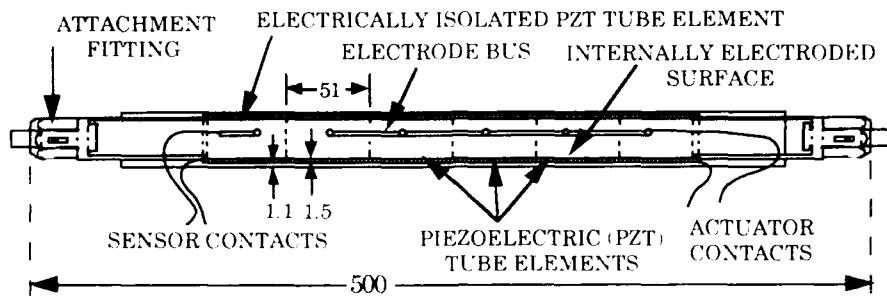
Figure 1. The MDSSC Piezoelectric strut (dimensions in mm).
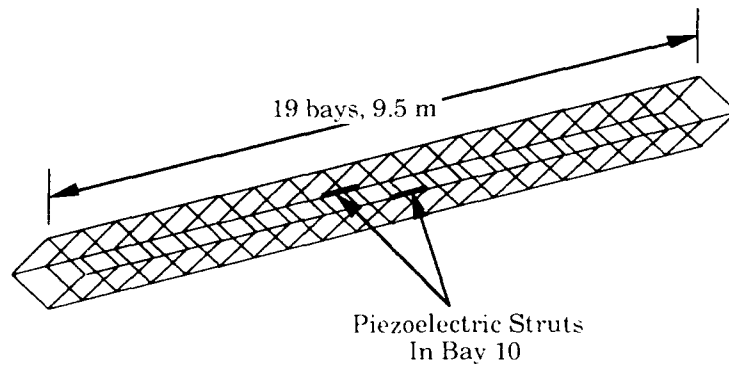
Figure 2. The location of the piezoelectric struts within the MDSSC CSI truss (diagonals, node spheres, and suspension cables omitted for clarity).

Piezoelectric materials under mechanical excitation behave similar to a capacitance electrically in parallel with a voltage source (see Figure 3). A pure resistance is the only means to dissipate energy, because both capacitive and inductive elements can store energy, but not dissipate it. There are optimal values for either both types of shunts, and the optima are determined by energy dissipation relationships [Hagood et al 1988,1990].
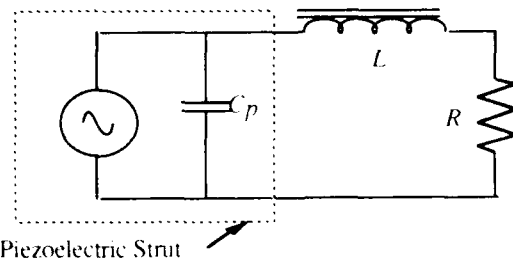
Figure 3. Electric Circuit Equivalent of Piezoelectric Material and external RL-Shunt

Large values of inductance are usually required because of the low natural frequencies involved. The natural frequencies f_n of the shunted piezoelectric strut are related as follows, where L is the added inductance, and C_p is the capacitance of the piezoelectric:

$$f_n \sim \frac{1}{2\pi\sqrt{LC_p}}$$

With f_n around 10 Hz and C_p about 1 μF, the value of L is in the hundreds of henries. Inductors in this size range are very heavy and possess significant internal resistance, usually higher than that for optimum dissipation. Reducing the resistance or increasing the "Q" of the inductors may be accomplished at the expense of additional mass, by increasing the gauge of the wire and the mass of the inductive material. This is contrary to mass/payload constraints for large space structures.

To eliminate the large mass associated with the necessary values of inductance, we developed a "simulated inductor" (patent pending) composed of operational amplifiers and passive circuitry connected as a gyrator, which can produce any desired inductance with just a few simple electronic components. The value of the simulated inductance may be easily changed by a variable resistor, meaning that it may be possible to have passive damping circuits monitor the frequencies to which they are subjected and alter their own characteristics in order to optimize their behavior. The electronic circuit used to simulate a large inductance is shown in Figure 4.
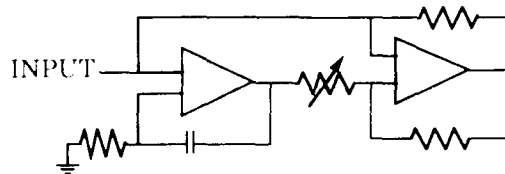
Figure 4. Inductor simulated by operational amplifier circuit.

The measured results of applying a single-mode tuned shunt containing an active inductor to the first bending mode of the MDSSC CSI Truss are shown in Figure 5. The figure shows the first mode resonance peak with the piezoelectric strut in an open-circuit condition together with the first mode resonance with the active inductor shunt connected. Comparison shows that both the amplitude and frequency drop upon application of the tuned shunt. The amplitude dropped 11 dB, corresponding to a damping ratio increase from 0.068% to 0.25% of critical.

To be practical, a vibration dissipation system must work on a range of frequencies, not just a single mode of vibration. We set out to attempt to enhance the damping of two modes simultaneously with the addition of a second shunt circuit tuned to the added mode, as shown in Figure 6. We quickly learned that adding a second shunt circuit tuned to the third mode "detuned" both itself and the first mode shunt, meaning that mutual loading effects had to be considered. Our analysis assumed that the values of the resistances R_1 and R_2 were proportional to the numerical values of the corresponding inductances, because resistance is proportional to the length of copper wire which in turn is proportional to the value of inductance. Values for L_1, L_2, and C_2 were chosen in order to set the two frequencies of the

denominator as near to the first and third mode frequencies as possible. With C_p = 472 nF, the values used for L_1, L_2, and C_2 were 144 H, 37.45 H, and 196 nF respectively.
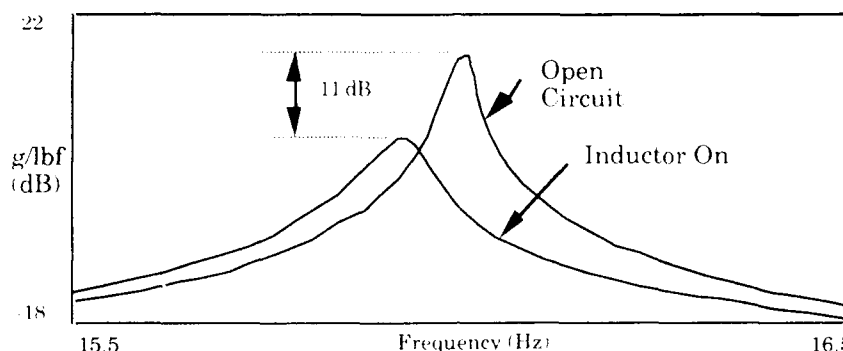
Figure 5. An 11 dB damping increase in the first bending mode of the MDSSC CSI Truss was obtained through the use of a shunt containing a simulated inductor.
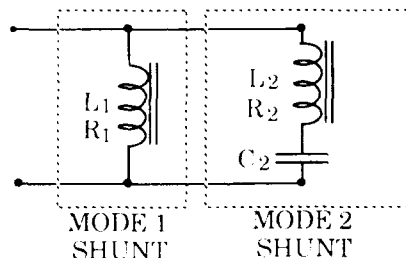
Figure 6. Electric Circuit Depiction of Two-Mode Shunt

This configuration was breadboarded from passive components and successfully used to simultaneously damp the first and third mode of the MDSSC CSI truss, as shown in Table I. The second mode was not targeted because the piezoelectric struts have little participation and thus effectiveness on this mode. Over 10 dB of reduction was achieved for each of the two targeted modes.

TABLE I. RESULTS OF TWO-MODE SHUNT DAMPING EXPERIMENT

Mode No.	Damping Ratio ζ (% Critical)		ζ Increase (%)	Reduction (dB)
	Unshunted	Shunted		
1	0.0397	0.146	368	11.3
3	0.0381	0.200	525	14.4

2. A SELF-MODULATED SHEAR LAYER TO ENHANCE DISSIPATION

The concept of a constrained layer damping treatment may be augmented by using piezoelectric ceramics to increase the amount of shear strain energy in the viscoelastic material (VEM) layer. This will increase the damping provided by the constrained VEM layer. The classical constrained layer treatment uses a rigid constraining layer on top of a flexible VEM to increase

the amount of shear in the VEM over that of a free VEM layer alone. Our concept replaces part of the structure with PZT_E, and the constraining rigid layer with PZT_C, as shown in Figure 7. The piezoelectric effect causes the embedded structural PZT to produce a voltage when the structure deforms. By electrically connecting the embedded PZT to the constraining layer PZT in opposite polarity, we can increase the amount of shear strain energy in the VEM layer and hence increase the damping of the system without adding energy.
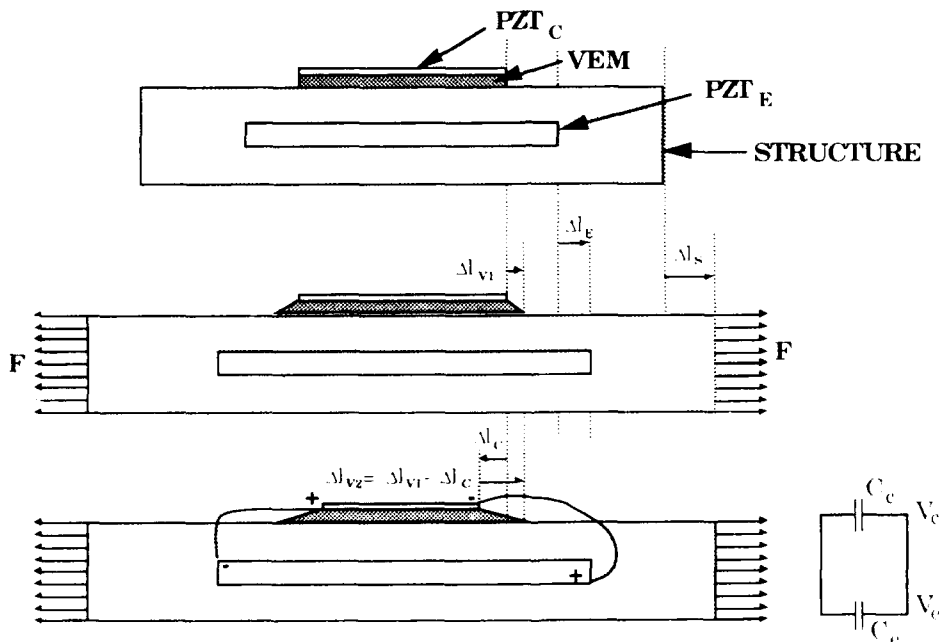
Figure 7. The top view shows the geometry of the modulated shear layer. The middle view shows a conventional constrained layer, and the bottom figure shows how the length of the constraining layer is modulated to increase the shear in the viscoelastic material (dark shading), which in turn is attached to the structural member (light shading).

The two PZTs are electrically modelled as two capacitors, C_E and C_C. When the embedded PZT_E is strained due to structural vibration, a voltage is generated and appears at the constraining layer PZT_C. Once the voltage across the PZTs is determined, PZT_C and the VEM then act approximately as a surface-bonded actuator with finite bonding layer and the analysis proceeds similarly to that of de Luis and Crawley [1985] and Anderson and Crawley [1989]. PZT parameters are chosen to maximize the strain in the VEM.

Figure 8 shows the normalized system damping versus the VEM thickness divided by the PZT thickness for the layup shown subjected to a sinusoidally varying axial load. The two curves plotted represent analytical results for two different models. These results indicate that from a few percent up to five

times more damping can be obtained when the PZTs are connected compared to when they are unconnected (shown as shaded region). The unconnected case is similar to a classical constrained layer damping treatment with a rigid constraining layer. Experiments are planned to determine the best model.
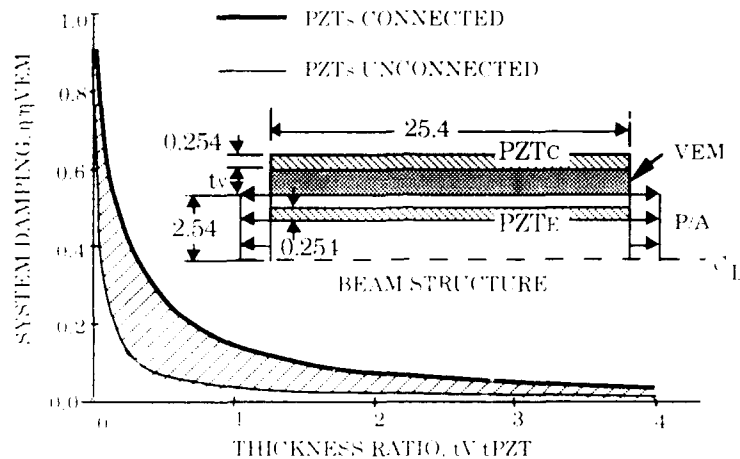
Figure 8. System damping can be significantly increased when PZTs are connected over that of a classical constrained-layer damping treatment (unconnected PZTs).

4 CONCLUSIONS

A shunt employing an inductor simulated by lightweight electronic circuits was shown to be an effective means of increasing the damping of the system without the added mass of passive inductors. A tuned electronic shunt was made to simultaneously dissipate two modes of vibration. The design of multiple-mode shunts must consider the system as a whole rather then each shunt independently because of loading effects.

The PZTVEM concept analysis showed that with typical materials a potential damping increase of as much as five times over a conventional constrained layer was possible.

REFERENCES

Hagood N, Crawley E 1988 "Development and Experimental Verification of Damping Enhancement Methodologies for Space Structures," MIT Space Systems Laboratory Report #18-88

Hagood N, Chung W, and von Flotow A 1990 "Modelling of Piezoelectric Actuator Dynamics for Active Structural Control," *Proc. 31st Structures, Structural Dynamics, and Aeroelasticity Conf.*

de Luis J and Crawley E 1985 "The Use of Piezo-Ceramics as Distributed Actuators in Flexible Space Structures," MIT Space Systems Laboratory Report #20-85

Anderson E and Crawley E 1989 "Piezoceramic Actuation of One- and Two-Dimensional Structures," MIT Space Systems Laboratory Report #5-89

An acousto-electromagnetic piezoelectric waveguide-coupler

Tomas Valis, Andreas H. von Flotow, and Nesbitt W. Hagood

Department of Aeronautics and Astronautics
Massachusetts Institute of Technology
Cambridge, MA 02139, U.S.A.

Abstract

Theory and experiment are presented for a device which couples
travelling waves in an electrical transmission line with flexural waves
in an elastic beam. Coupling of the two wave types is achieved using
a segmented piezoelectric layer adhered to the beam and connected to
the transmission line. The key design parameter is the nondimensional
coupling length. A simple expression for calculating its magnitude is
derived. For the design used, this length was predicted to be four
wavelengths. Experiments yielded a similar value.

1 Introduction

Efficient coupling of electrical and structural-acoustic power opens up the
possibility of electrically modifying the structural-acoustic properties of 'ac-
tive materials and adaptive structures'. A commercial application of such
coupling is the development of ring-type piezoelectric travelling-wave motors
which are used as autofocus drives on 35 mm cameras[1]. The motor con-
verts an electrical drive-signal to a circulating flexural wave in a steel-ring
'stator' which generates a torque on a mated 'rotor'. Linear travelling-wave
motors[2] are difficult to design, owing to the need for efficient coupling of
flexural waves into and *out of* a linear stator-track. One can envisage large-
scale applications of this technology to generate and absorb travelling-waves
in structures.

  The standard device for coupling travelling electromagnetic waves is the
'2×2' coupler used in both microwave and optical waveguide circuits. Its
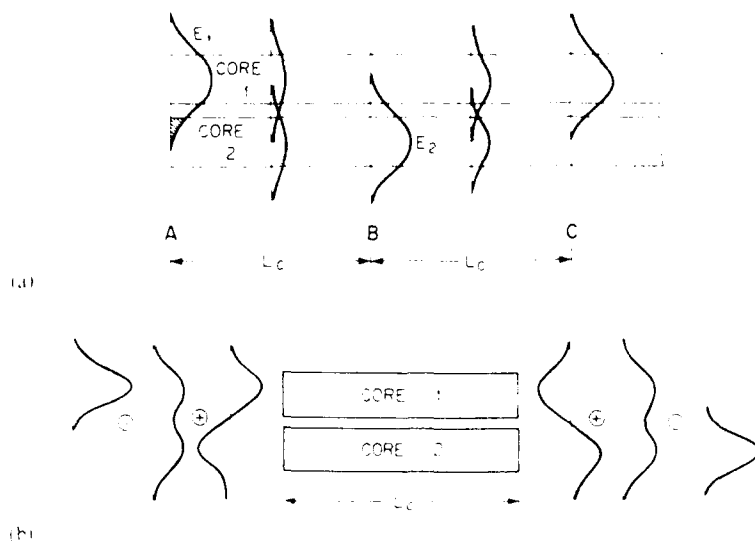
Figure 1: Evolution of the energy distribution along two parallel, coupled optical-fiber cores, according to (a) the coupled-mode concept, and (b) the normal-mode concept. In the case of an acousto-electromagnetic waveguide coupler, one guide is electromagnetic, the other one is acoustic. After Dakin and Culshaw[3].

theory of operation (illustrated in Fig. 1), analogous to the transfer of energy between two coupled pendula, is described in most waveguide texts[4]. The present work takes the idea of a waveguide-coupler and extends it to the case of coupling between an electrical transmission line and an elastic beam. Similar work was done by Baer and Kino[5], who considered coupling a transmission line to longitudinal acoustic waves, and by Hagood and von Flotow[6] who considered tuned L-C-R coupling to vibrating structures.

2   Coupled Wave Equation

The following section presents a description of coupled modes between waveguides with second- and fourth-order spatial derivatives. The analysis is for continuous-impedance media; spatial discretization is smeared.

The (temporally) Fourier-transformed coupled wave equation for two codirectional waves propagating in reciprocally coupled, lossless, single-mode waveguides takes the form

$$\begin{bmatrix} K_{11} & K_{12} \\ K_{12} & K_{22} \end{bmatrix} \begin{Bmatrix} x_1'' \\ -x_2'''' \end{Bmatrix} = -\omega^2 \begin{bmatrix} M_{11} & 0 \\ 0 & M_{22} \end{bmatrix} \begin{Bmatrix} x_1 \\ x_2 \end{Bmatrix} . \qquad (1)$$

Phase speed matching occurs at a frequency

$$\omega = \frac{K_{11}}{M_{11}} \sqrt{\frac{M_{22}}{K_{22}}} \; . \tag{2}$$

Efficient (i.e., phase speed matched) coupling is narrowband.

The eigenvalue problem for phase speed matched guides yields the characteristic equation:

$$(1 - \kappa^2)\beta^6 - \beta^4 - \beta^2 + 1 = 0 \; , \tag{3}$$

where the propagation constants are normalized to their uncoupled values. The roots of the above equation consist of two pairs (forward and backward) of complex conjugate roots representing propagation in the two waveguides, and two real roots corresponding to two evanescent modes.

The two pairs of propagating roots consist of β_O and β_E (where subscripts O and E denote 'odd' and 'even'), and subject to initial conditions. $\underline{x}(0, \omega) = \left\{ \begin{array}{c} 1 \\ 0 \end{array} \right\}$, the guide amplitudes will evolve spatially as,

$$\underline{x}(z) = \left\{ \begin{array}{c} \cos \beta_\Delta z \cos \overline{\beta} z \\ -\sin \beta_\Delta z \sin \overline{\beta} z \end{array} \right\} \; . \tag{4}$$

where $\beta_\Delta \equiv \frac{\beta_O - \beta_E}{2}$ and $\overline{\beta} \equiv \frac{\beta_O + \beta_E}{2}$. Complete power transfer occurs after a coupling length, l_c, such that $\underline{x} = \left\{ \begin{array}{c} 0 \\ 1 \end{array} \right\}$.

The nondimensional coupling length is given by

$$\frac{l_c}{\lambda} = \frac{1}{4} \frac{1}{\beta_\Delta} \; . \tag{5}$$

If the guides are lossy, the coupled-mode propagation constants become complex. For the case of phase speed matched, low-loss guides coupled by a lossless medium,

$$\gamma_{O,E} = \overline{\alpha} + \imath\beta_{O,E} \; . \tag{6}$$

where $\overline{\alpha} = \frac{\alpha_1 + \alpha_2}{2}$ (i.e., the mean loss-factor of the two guides) and the propagation constants are well approximated by their undamped values. That the coupled modal loss factor is the mean is a result of the normal modes being symmetric with respect to power flow. For low-loss guides, the amplitudes will evolve spatially as

$$\underline{x}(z) = \left\{ \begin{array}{c} \cos \beta_\Delta z \cos \overline{\beta} z \\ -\sin \beta_\Delta z \sin \overline{\beta} z \end{array} \right\} e^{\overline{\alpha} z} \; . \tag{7}$$
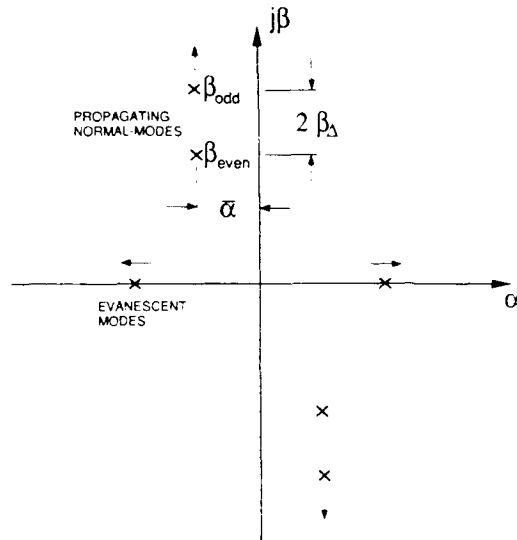
Figure 2: Coupled-mode propagation constants plotted in the complex plane. Arrows indicate increased coupling coefficient, κ, in Eqn. 3. If the waveguides are uncoupled and lossless, the propagating roots coalesce to the same radius as the nonpropagating (evanescent) ones.

subject to the same initial conditions as those in Eqn. 4. The system propagation constants that result are plotted in Fig. 2 .

By performing numerical experiments, it was found that for values of the coupling coefficient: $\kappa < 0.3$, the nondimensional coupling length is well approximated by:

$$\frac{l_c}{\lambda} \cong \frac{1}{\sqrt{2\kappa}} \, . \tag{8}$$

A corresponding equation for coupling to longitudinal acoustic-waves was derived in Baer and Kino[5] (their Eqn. 4).

3   Flexural Acoustic Waves

The system considered consists of identical (but oppositely polarized) piezoelectric layers adhered on either side of a passive (host) layer. Since flexure imposes strain on both piezoelectric layers, their charge outputs are summed. Subscripts p and h denote the piezoelectric and host layers, respectively.

The state variables chosen are:

q charge on the electrode segments.

w out-of-plane beam displacement.

The two governing equilibrium equations are

$$V_3' = L \ddot{q} \, , \tag{9}$$

and

$$M_2'' = \overline{\rho} A \ddot{w} \, . \tag{10}$$

where primes denote spatial differentiation in the '1' direction (as per coordinates in Fig. 4), V_3 and M_2 are voltage and moment. L is the transmission line inductance per unit length, $\overline{\rho}$ is the volume-weighted mean density of the beam, and A is the cross-sectional area of the beam. Assuming Bernoulli-Euler behaviour of a perfectly laminated beam, the appropriate constitutive equation is

$$\left\{ \begin{array}{c} q' \\ w'' \end{array} \right\} = \left[\begin{array}{cc} C_{p3}^T & \frac{a}{s_{11}^E (EI)} \left(\frac{t_h}{2} + \frac{t_p}{4} \right) d_{31} \\ \frac{b}{t_p} d_{31} & (EI)^{-1} \end{array} \right] \left\{ \begin{array}{c} V_3 \\ M_2 \end{array} \right\} \, . \tag{11}$$

where superscripts E, D, and T denote values taken at constant field (short circuit), electrical displacement (open circuit), and stress (free), and C_{p3} is the piezoelectric capacitance, a is the width of the beam, d_{31} is piezoelectric charge coefficient, s_{11} is the piezoelectric compliance and

$$(EI) = \frac{w}{12} \left[E_h t_h^3 + E_p^E (t^3 - t_h^3) \right] \, . \tag{12}$$

and

$$b \equiv \frac{\frac{6}{t_h} \left(1 + \frac{1}{2t^*} \right)}{3 + \frac{E_h}{E_p^E} t^* + \frac{3}{t^*} + \frac{1}{t^{*2}}} \, . \tag{13}$$

where t^* is the thickness ratio of the host and piezoelectric layers, $\frac{t_h}{t_p}$, and t is the total thickness of the beam.. The latter quantity, b, which relates the beam curvature to mean piezoelectric strain-actuation, is derived by Crawley and Anderson[7]. Inversion of Eqn. 11 and substitution into the equilibrium equations (Eqns. 9,10) yields a coupled wave equation of the form of Eqn. 1. The coefficient, κ, of the associated characteristic equation (Eqn. 3) is

$$\kappa = k_{31}^{\text{eff}} = \sqrt{\eta_b} k_{31} \, . \tag{14}$$

where k_{31} is the electromechanical-coupling-coefficient of the piezoelectric material (for G1195 PZT, $k_{31} = 0.35$), and η_b is the composite piezoelectric efficiency-factor for bending, such that

$$\eta_b \equiv \frac{1}{1 + \frac{E_h}{E_p^D} \tau} \, . \tag{15}$$
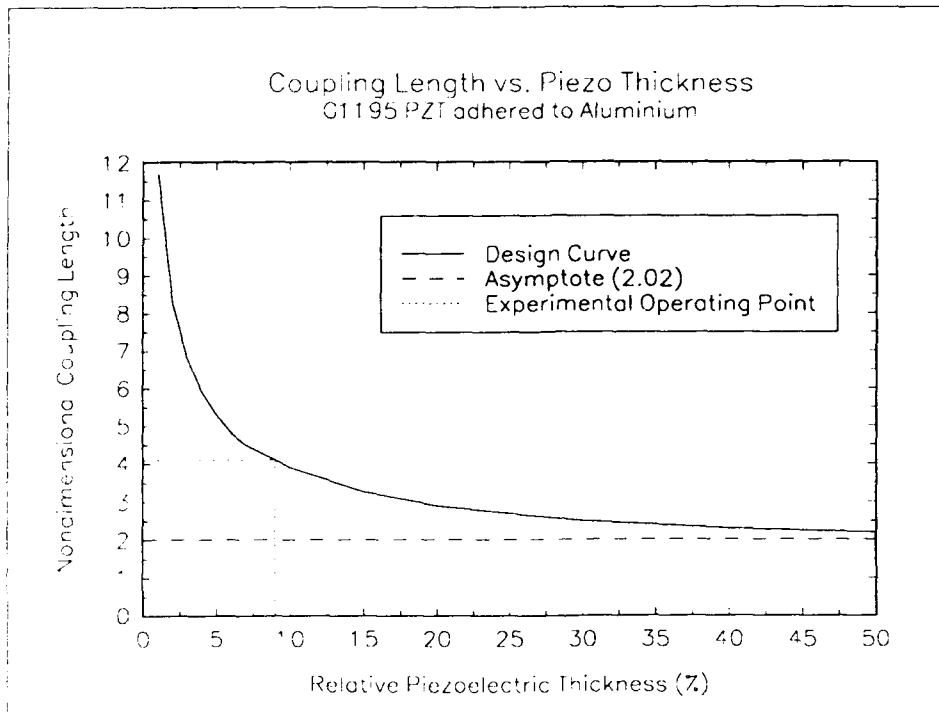
Figure 3: Nondimensional coupling-length as a function of the relative thickness of the piezoelectric, $\frac{t_p}{t}$, and host material layers. The slope is calculated from Eqn. 16. The asymptote correspond to $\eta_b = 1$

where $r \equiv [(\frac{t}{t_h})^3 - 1]^{-1}$ and $\frac{E_h}{E_p^D}$ is the open-circuit modulus ratio of the host to the piezoelectric layer. Substitution into Eqn. 8 yields the coupler design equation:

$$\frac{l_c}{\lambda} = \frac{1}{\sqrt{2\eta_b^D k_{31}}} \; . \tag{16}$$

As depicted in Fig. 3, the relative thickness of the piezoelectric layer determines the coupling length. The above analysis is not applicable to the case of a 'thick' piezoelectric layer, as the modelling assumptions start to break down.
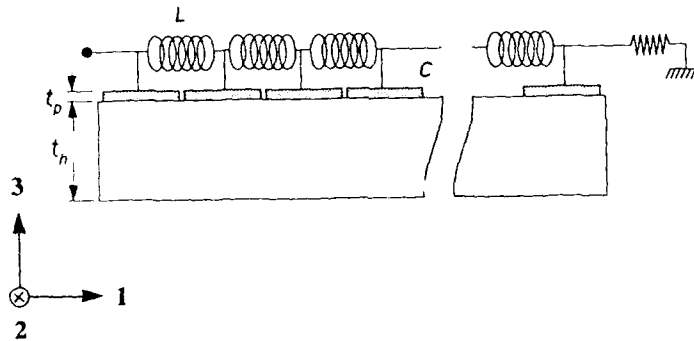
Figure 4: A cross-sectional schematic of the coupler arrangement.

4 Experimental Design

The experimental design consisted of a single-sided lamination of piezoelectric segments to an aluminum beam. Although it is a one-sided lamination, the symmetric lamination equations developed in the previous section should provide a good approximation, as the flexural phase speed is much slower than the longitudinal one, and $\frac{t_h}{t_p} > 10$. A phase-speed matched set of inductors bridged the piezoelectric segments as illustrated in Fig. 4. Small diameter ($\approx 100\ \mu$m) copper wire was used to connect the inductors to the piezoelectric segments. The inductors connected to the piezoelectric capacitance formed an L-C ladder network. The electrical input consisted of a sinusoidal function-generator driving an audio amplifier. The electrical output consisted of an impedance-matched termination resistor. Based on the predicted coupling length, the length of the coupling region was chosen to correspond to two coupling-lengths. This choice serves to demonstrate both coupling into and out of the beam. By choosing this length, there should (in principle) be no acoustic power propagated to the end of the beam; the termination impedance of the beam should be irrelevant. Expecting some acoustic power to be uncoupled, a crude attempt was made to apply a matched termination to the beam using wet mud. The design coupler parameter values are listed in Table 1.

The loss-factor of the electrical waveguide is given by,

$$\alpha_{\text{line}} \cong \frac{1}{2} R \sqrt{\frac{C}{L}} \tag{17}$$

which is the well-known expression[8] for low-loss transmission lines. The loss-factor for the beam is difficult to model owing to the presence of a adhesive layer between the host and piezoelectric layers. It was roughly

Parameter	Value
beam length	670 mm
beam width	12.7 mm
piezo segment length	6.35 mm
interaction length	370 mm
Al thickness	2 mm
PZT thickness	191 μm
Line Capacitance	970 nF/m
Line Inductance	7.9 H/m
Line Resistance	11 kΩ/m

Table 1:   Design parameter values used in the experimental acousto-electromagnetic waveguide coupler.

Parameter	Value
frequency	7.8 kHz
wavelength	46 mm
phase-speed	360 m/s

Table 2: Operating parameters for the experimental coupler at maximum coupling.

estimated to be 1-2% per half-wavelength. Using the design parameters: $\alpha_{line} \approx 1.8$ Np/m, and $\alpha_{beam} \approx 0.8$ Np/m.

5   Experimental Results

By measuring RMS voltages at each segment, the voltage profile in the transmission line could be compared to theory. The frequency of the input was adjusted until maximum coupling was observed; the corresponding profile is plotted in Fig. 5. The operating parameters are listed in Table 2.

End effects were evident in the form of reflections from both ends of the beam. These reflected waves couple to the transmission line and create standing waves. Their effects need to be removed to realize purely codirectional coupling.
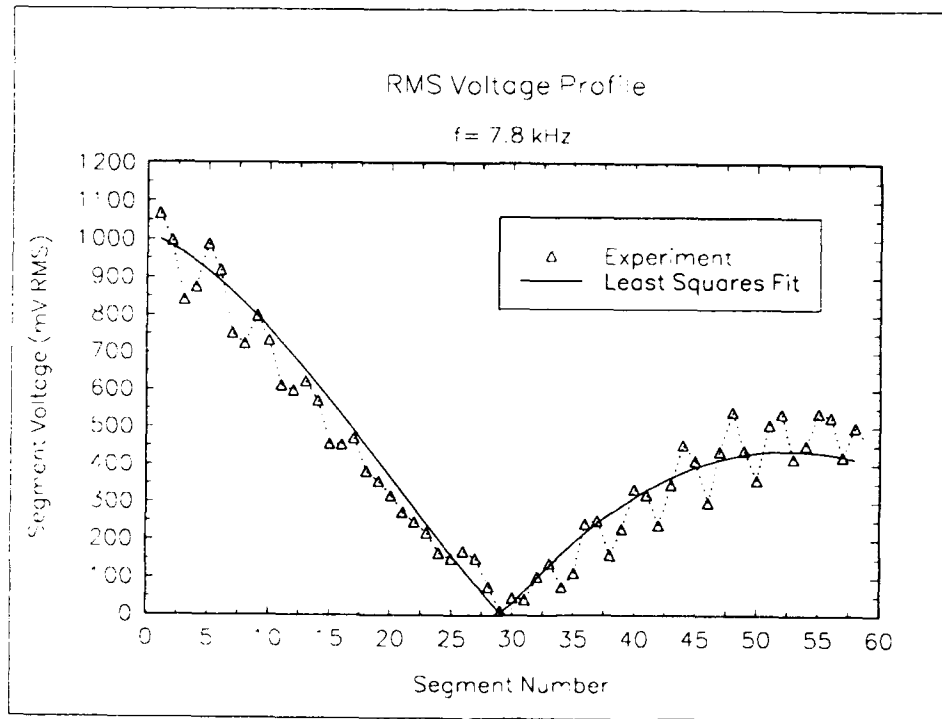
Figure 5: Recorded voltage profile on the beam-coupled transmission line at phase speed matched conditions. The continuous line is least-squares curve fit to $|\cos(\beta z)e^{-\alpha z}|$, serving to suppress standing-wave effects. Power flow into and out of the beam is evident.

Quantity	Theory	Experiment
l_c/λ	4.1	3.9
α [Np/m]	1.3	2.4

Table 3: Comparison of theoretical and experimental values of the design coupler.

A least-squares curve fit using $|\cos(\beta z)e^{-\alpha z}|$ on the voltage profile was performed to yield estimates for l_c and α. The comparison between theory and experiment is shown in Table 3. Correlation between theory and experiment for the coupling length is remarkably good, considering that a 'zeroth order' model was used, and the experimental design was a first attempt. The predicted loss factor was considerably lower than the observed one, this may be attributable to parameter uncertainty or modelling errors.

6   Conclusions

The voltage profile illustrates substantial coupling between guides. The predicted and observed coupling-lengths were in agreement. The discrepancy in the decay constant may be attributed to uncertainty in the values of the loss-factors for the transmission line and the elastic beam, and coupling of power into other wave-modes. Standing-wave effects degraded coupler performance; they result from incomplete coupling generating reflections from the impedance mismatched beam-terminations. Ideally, they should not arise at all if the coupling-length and operating frequency are chosen correctly. A disappointing result was that they could not be eliminated in spite of tuning both of the above. Design improvements to achieve 'complete' coupling are, no doubt, possible.

Among the most promising applications of the acousto-electromagnetic waveguide coupler is to build 'lapjoints' between electrical and mechanical waveguides, as illustrated in Fig. 6. Two lapjoints, closing a recirculating-loop around a linear stator-track would make an efficient linear servo. Such a design would make linear travelling wave motors functionally equivalent to rotary ones, except that the stator would be a hybrid electromechanical device. The other interesting application is the efficient absorbtion of narrowband structurally-borne noise (e.g., gear meshing noise) that affects
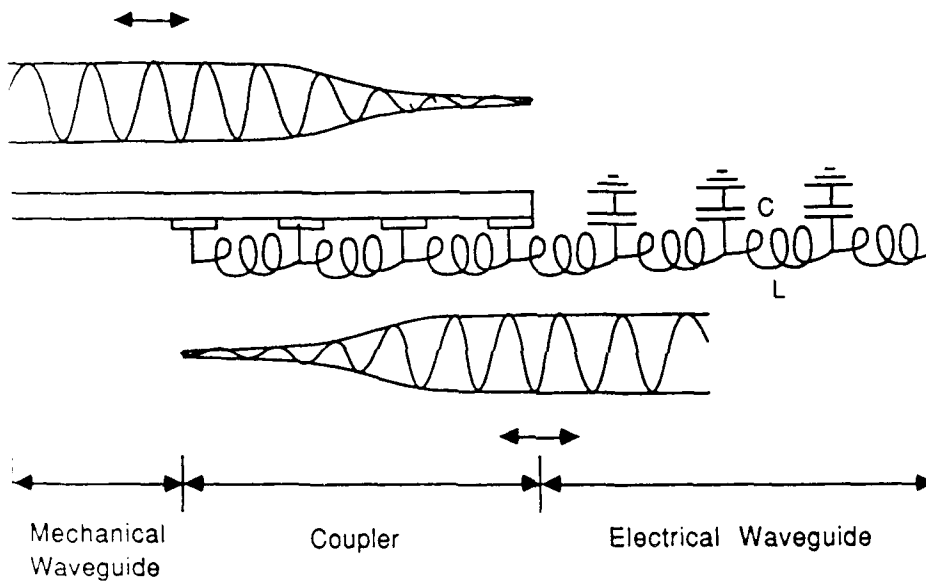
Figure 6: A 'lapjoint' between an elastic beam and an electrical transmission line. Coupling can occur in either direction.

the performance of undersea vehicles. Finally, there is also the possibility of structural-acoustic impedance tailoring of flexible structures.

References

[1] Canon EF35 - 135 mm lens for the EOS series camera.

[2] Kawamura, A., and N. Takeda, 'Linear Ultrasonic Piezoelectric Actuator,' *IEEE Trans. Industry Applications*, vol. 27, no. 1, pp. 23–26, 1991.

[3] Dakin, J. and B. Culshaw, *Optical fibre sensors: principles and components.*, Artech House: Norwood, MA, 327 p., 1988.

[4] Tamir, T., Ed., *Guided-Wave Optoelectronics*, Springer-Verlag: Berlin, 401 p., 1989.

[5] Baer, R.L., and G.S. Kino, 'A Travelling Wave Ultrasonic Transducer,' in Proc. *1982 Ultrasonics Symposium*, pp. 498–501, San Diego, Oct. 27–29, 1982.

[6] Hagood, N.W., and A.H. von Flotow, 'Damping of Structural Vibrations with Piezoelectric Materials and Passive Electrical Networks,' *J. Sound and Vibration*, vol. 146, no. 2, pp. 243–268, 1991.

[7] Crawley, E., and E. Anderson, 'Detailed Models of Piezoelectric Actuation in Beams,' *J. Intelligent Material Structures and Systems*, vol. 1, no. 1, pp. 1–25, 1990. (Eqns. 8–22).

[8] Cheng, D.K., *Field and Wave Electromagnetics*, Addison-Wesley: Reading, MA, 703 p., 1989.

Embedded optical fiber sensors for damage detection and cure monitoring

Kexing Liu, Andrew Davis, Myo M. Ohn, Byung Park, and Raymond M. Measures

University of Toronto Institute for Aerospace Studies, 4925 Dufferin Street
Downsview, Ontario, Canada M3H 5T6

ABSTRACT: This paper will report on the use of interferometric fiber optic sensors for
damage detection and cure monitoring. These sensors have been used to detect acoustic
emission (AE) associated with the growth of delaminations in composites. Preliminary
efforts directed towards the generation and detection of ultrasonic waves using optical fibers
for cure monitoring are also discussed.

1. INTRODUCTION

As the use of advanced fiber reinforced composite materials in aerospace engineering has
increased, it has become highly desirable to establish new nondestructive evaluation (NDE)
techniques for in-service (in-situ) monitoring of structures fabricated from these materials.
In particular, in-situ strain and acoustic emission measurements would be very useful for
assessing the structural integrity of composite structures. Furthermore, the monitoring and
control of the curing process is essential for the reliable production of robust composite
structural elements with given thermal and mechanical properties.

The sensor employed in the experiments reported in this paper consists of a fiber optic
Michelson interferometer with active homodyne demodulation and is described elsewhere
(Liu et al. 1990). The active homodyne demodulation system serves to eliminate the
response to slowly varying measurands and perturbations (e.g. DC strain, temperature, air
currents, etc.) and maintains the interferometer at its quadrature point (Jackson et al. 1980).

2. DYNAMIC DAMAGE MONITORING EXPERIMENTS

Acoustic emission is generally defined as the release of internally stored energy in a material
under load and appears as transient stress waves. More specifically, in composites these
stress waves are caused by several microfailure mechanisms: matrix cracking, fiber breakage,
and fiber/matrix debonding. They appear as broadband acoustic waves, mainly in the
100kHz-1MHz region (Zimcik et al. 1988). Acoustic emission detection has been widely
used for testing composites in various modes of loading because of its relatively simple
detection setup and in-situ and real-time mode of operation (Fowler 1989). Statistical

analysis of the acoustic events detected with piezoelectric sensors has been shown to yield information about the type, geometry, and possibly the location of defects (Ferguson 1990).

The NDE method that is used herein simultaneously employs three different techniques: a) acoustic emission detection using an embedded fiber optic Michelson interferometric sensor, b) optical fiber fracture and c) image enhanced backlighting. Using FFT analysis, the spectral characteristics of AE signals obtained from the following laminates have been examined: a) square (10 cm x 10 cm) 8-ply Kevlar/epoxy cross-ply coupons with a stacking sequence of [0/0/90/90/{90}/90/90/0/0] under quasi-static, transverse loading (Ferguson 1990) and b) 4 ply laminates (10 cm x 19 cm) with a stacking sequence of [+45/{-45}/-45/-45/+45] under compressive loading (Park 1991). In case b) a circular piece of heat-resistant nonbonding tape (0.026 mm thick and 18 mm diameter) and 4 treated fibers were embedded in the -45° direction between the first and second plies. This was done to yield the optimum configuration for fiber fracture. Numerous tests have shown that all fibers running through the delaminated area were fractured and thus this method represents a reliable triggering method for the growth of delaminations. The experimental arrangement is illustrated in Figure 1. The fracturing of the treated fibers, which was caused by crack propagation and/or delamination, triggered the Michelson interferometer. Figure 2 shows an oscilloscope trace of an AE signal and the trigger signal (horizontal line) during the growth of a delamination.
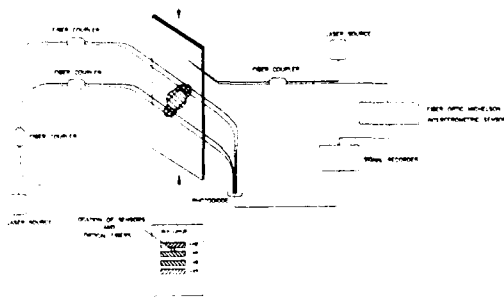
Figure 1. Schematic of fiber optic AE detection system.
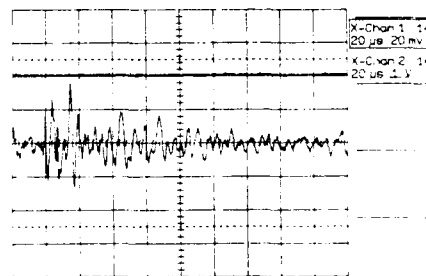
Figure 2. Oscilloscope trace of AE signal during delamination growth.

3. ALUMINUM PLATE EXPERIMENTS

Laser generated ultrasound has been the subject of many papers (Hutchins 1986). For solids, a narrow, high power laser pulse is absorbed at the surface of the material providing transient localized heating. The resulting thermoelastic expansion leads to the generation of ultrasonic waves. Bulk longitudinal waves, bulk shear waves, Rayleigh waves, and Lamb waves have been generated by pulsed lasers (Scruby and Drain 1990).

Aussel and Monchalin (1989) have used laser generated ultrasound and laser interferometry to determine ultrasonic velocity in a number of materials. Their technique involved the

cross-correlation of successive echoes In order to determine whether the fiber optic Michelson interferometer could be used to measure the velocity of ultrasound generated by either a laser of by a piezoelectric transducer, a proof of concept experiment involving an aluminum test plate was conducted. Light pulses from a Q-switched Nd:YAG laser are directed onto the top surface of the plate. Ultrasonic pulses so generated then propagate back and forth across the thickness of the plate and are detected by an optical fiber sensor adhered to the underside of the plate. A similar experiment was conducted using a piezoelectric transducer as the source of ultrasound. In both cases the plate thickness and the time difference between the peaks of the first and second arrivals was measured. The laser generated ultrasound experiment yielded a value of (6360 ± 50)m/s while the experiment involving the piezoelectric transducer yielded a value of (6360 ± 40)m/s. These values are comparable to those of Krautkramer and Krautkramer (1990) who state a value of 6320m/s.

4. CURE MONITORING EXPERIMENTS

The knowledge of the degree of cure of epoxy resins is extremely important in the fabrication of strong and reliable composite materials, especially for thick structures. Hence, a method for the determination of the degree of cure is desirable. The autoclave curing process presents a number of difficulties and so present engineering practice commonly employs overcure to ensure a uniformly cured sample. This is both time consuming and expensive.

Winfree (1983) has characterized the curing of epoxy resins by measurement of the attenuation and velocity of ultrasonic longitudinal and shear waves. As crosslinking bonds between polymer chains form, the epoxy resin changes its state from a viscoelastic liquid to a viscoelastic solid. The viscoelastic moduli (bulk and shear moduli) of the material change accordingly, which in turn produces a change in the acoustic properties of the material, yielding a good indicator of the state of cure. The opto-ultrasonic approach to cure monitoring introduced in this paper is a hybrid employing fiber optic sensors for the detection of ultrasound generated by either a laser or a piezoelectric transducer.

(a) Ultrasound generated by laser.   (b) Ultrasound generated by PZT.
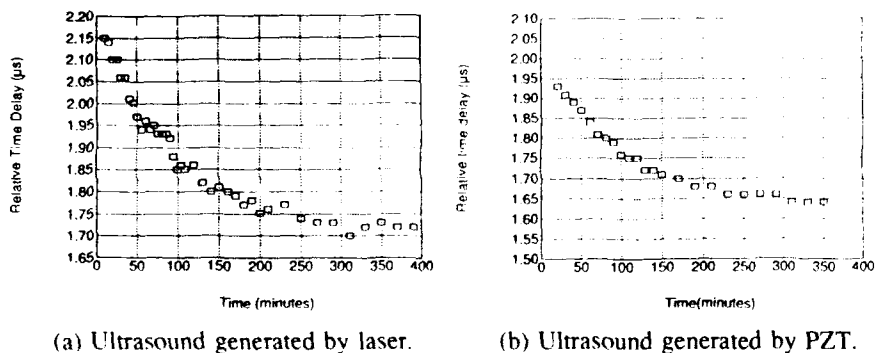
Figure 3. Relative ultrasonic propagation delay vs. curing time.

In light of this, two preliminary experiments were conducted in an attempt to see if an embedded fiber optic ultrasound detection system could be used to infer changes in ultrasonic velocity as an epoxy cures. One experiment involved the use of a Q-switched Nd:YAG laser as the source of ultrasound while the other experiment utilized a piezoelectric transducer (VP-1093). For simplicity a room temperature cured epoxy (Hysol EPK 907) was used. The experiments essentially consisted of measuring the "relative time delay" in the arrival of ultrasonic signals as a function of cure time. The arrival time of the first peak measured with respect to the trigger point is referred to as the "relative time delay." Since ultrasonic velocity increases as an epoxy cures it is expected that the "relative time delay" should decrease with time. This trend is evident in Figure 3.

5. CONCLUSIONS

Fiber optic ultrasonic sensors have been used for the detection of AE during the growth of delaminations in composite plates. The velocity of ultrasound in an aluminum plate was measured using fiber optic sensors. Finally, a preliminary epoxy cure monitoring experiment using embedded fiber optic sensors yielded results that followed an expected trend.

6. ACKNOWLEDGEMENTS

7. REFERENCES

Aussel J-D and Monchalin J-P 1989 *Ultrasonics* **27** 165-177

Ferguson S M 1990 *"The Detection of Damage-Induced Acoustic Emission in Advanced Composite Materials Using Embedded Optical Fiber Sensors"* Master's Dissertation, University of Toronto

Fowler T J, Blessing J A and Conlisk P J 1989 *Third International Symposium on Acoustic Emission from Composite Materials* 16-27

Hutchins D A 1986 *Can. J. Phys.* **64** 1247-1264

Jackson D A, Priest R, Dandridge A and Tveten A B 1980 *Appl. Opt.* **19** 2926-2929

Krautkramer J and Krautkramer H 1990 *Ultrasonic Testing of Materials, 4th edition* (New York: Springer-Verlag)

Liu K, Ferguson S M and Measures R M 1990 *Opt. Lett.* **15** 1255-1257

Park B 1991 Master's Dissertation, University of Toronto

Scruby C B and Drain L E 1990 *Laser Ultrasonics: Techniques and Applications* (Bristol: Adam Hilger-IOP)

Winfree W P 1983 *Proc. 1983 IEEE Ultrasonics Symposium* 866-869

Zimcik D G, Proulx D, Roy C and Mashouli A 1988 *SAMPE Quarterly* **19** 5-11

Thermal-plastic metal coatings on optical fiber sensors for damage detection

J. S. Sirkis and A. Dasgupta

Department of Mechanical Engineering, University of Maryland, College Park, Maryland 20742

ABSTRACT: Optical fiber sensors coated with linear work hardening elastic-plastic materials are analytically explored to determine the effects which the coating material properties and thickness have on the sensor performance. The optical fiber system is subjected to both an axial load and an arbitrary thermal gradient. This non-linear analysis reveals a mechanism for designing coatings which provide a "memory" to the fiber optical sensor by forcing the sensor system to undergo permanent deformations in response to predefined excursions in the strain field.

1. INTRODUCTION

A passive memory of sorts can be added to optical fiber sensors by coating them with elastic plastic-metals. This memory is provided as a result of permanent deformations in the coating, and therefore in the fiber sensor, as a result of load history which exceeds the yield surface of the given coating material. A sensor with an elastic-plastic metal coating has obvious potential as a damage sensor working on the same principal as the fiber breakage sensor, except that in this case the fiber sensor is available for post damage measurements. This damage sensor concept can be used with most every intrinsic optical fiber sensor type, and finds great advantage in its simplicity of operation.

2. MODELING

The analytical description of the stress and strain fields developed in a

metal coated optical fiber subject to axial loading and arbitrary radial thermal gradients is used to investigate the amount of permanent strain which is coupled from the ductile coating to the optical fiber. The optical fiber is modeled as linear elastic, while the metal coating is modeled as linear work hardening obeying a von Mises yield criterion. The optical fiber is assumed to be operating as an interferometric strain sensor, so that the elastic-plastic analysis can be coupled with a three-dimensional phase-strain theory to predict the sensor output. Detectable damage is arbitrarily defined to occur when the optical phase shift of the light propagating in the sensor corresponds to that of an uncoated optical fiber experiencing a 500μ axial strain. This axial strain level represents one quarter of the .02% offset condition typically used to define the yield point on a uniaxial stress-strain curve.

3. RESULTS

Figures 1 and 2 respectivelyshow the response of an aluminum coated optical fiber sensor to a damped sinusoid-like axial force and uniform thermal gradient history. The dashed lines in these graphs show the purely elastic response and the solid lines show the elastic-plastic response. Notice the residual phase shift between the two responses in both curves. The other important feature exhibited by these two graphs is that the residual phase shift is greater for the axial loading than for thermal loading. This behavior is a result of the thermal stresses being highly localized at the fiber/coating interface, while the stresses caused by the axial loading effect the entire coating in nominally the same manner.

The sensitivity of the sensor response to the coating Young's modulus, Poissons's ratio, yield strength, thermal coefficient of expansion, and thickness are explored for a fixed temperature and a varying axial load, and then a fixed axial load and a varying temperature. As one might expect, the yield strength and coating thickness dominate all other parameters in the sensor performance under both thermal and mechanical loading. As the yield strength increases, larger stresses are required to produce permanent

deformations. As the coating thickness goes to zero, the elastic recovery stresses in the fiber dominate the elastic-plastic stresses in the coating so that permanent deformation in the fiber never occurs. Under only mechanical loading, the axial force must approach infinity as the coating thickness does the same in order to produce permanent deformation in the fiber. The coating Young's modulus has an order of magnitude lower influence when compared to the yield strength, and Poison's ratio plays almost no part in determining the amount of permanent deformation occurring the fiber. The mismatch between the thermal coefficients of expansion plays a critical role in determining the performance of the metal coated fiber sensor experiencing thermal loading. Interestingly, the temperature levels required to cause damage level permanent deformations must exceed roughly 500°F for any combination of the other coating parameters. For many coating parameter combinations the threshold temperature is much higher. The implication here is that the thermal and mechanical behavior of this type of damage sensors is automatically decoupled. One should note that all material properties are consider independent of temperature in this analysis.

4. CONCLUSIONS

This paper presents the mathematical analysis of an optical fiber sensor that is coated with an elastic-plastic metal. Parameter studies have been performed to find the important geometric and material characteristics which control the level of residual strain (and phase) developed in the fiber/coating system. The sensor system discussed in this paper is a passive alternative to the fiber breakage sensors used for damage detection, can be used with any intrinsic (and some extrinsic) optical fiber sensor configurations, and can survive damage events so that post damage measurementsare possible.
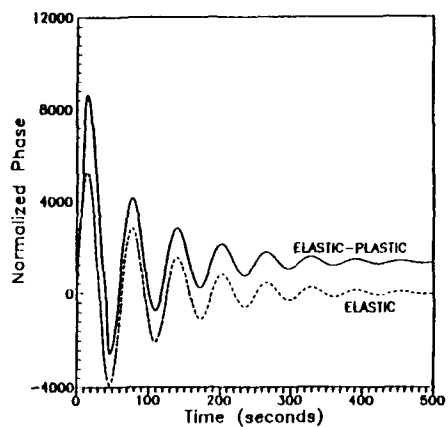
Fig.1   Response to Axial Load.   Fig.2   Response to Thermal Load.
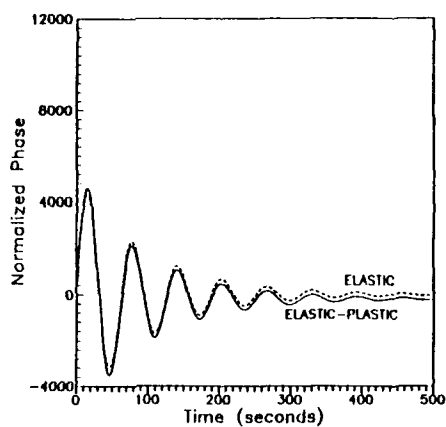
Health monitoring system for aircraft

J Gerardi and G Hickman

Innovative Dynamics, Langmuir Labs, Ithaca, New York 14850

ABSTRACT: Work is currently in progress to develop an advanced structural integrity monitoring system to increase safety of aging aircraft. This system is based on the concept of smart structures which integrates sensory systems into the structure, analogous to a central nervous system. Structural abnormalities are determined by continuously monitoring the vibration signature using a network of active sensor modules. Pattern recognition techniques are used to analyze the vibration signatures and identify structural damage in real-time. Conventional minimum distance algorithms as well as neural networks have provided high recognition rates in classification of corrosion damage and wing leading edge ice accretion.

1. INTRODUCTION

A Structural Integrity Monitoring System based on analysis of vibration signatures is being developed at Innovative Dynamics to detect structural abnormalities on aircraft. Current nondestructive evaluation techniques such as hand-held eddy-current or x-ray scans are so costly and time consuming that retiring some of the oldest jets may be more effective than maintaining them. An on-line inspection system such as SIMS holds the promise of solving these maintenance and diagnostics problems. The system described here consists of small surface-mount sensor module designs with integrated electronics that can be retrofit to existing aircraft. The objective is to integrate these modules into vulnerable or inaccessible areas of the airframe to reduce or eliminate the need for whole aircraft NDE scans or tear downs.

The principle underlying the operation of SIMS is the use of structural vibration signatures to determine mechanical properties. Damage to a structure often manifests itself as a change in the dynamic response of the structure, corresponding to changes in the physical properties. SIMS applies this concept for obtaining failure mode characterization of structural components. The system works by mechanically exciting the structure with broadband energy and monitoring changes in the structural response. Shape, amplitude and distortion of the vibration signals provide useful information concerning the location and severity of the damage.

Neural networks are attractive for vibration signature analysis. These techniques have been shown to be useful in solving complicated signal processing problems such as in NDE acoustic emission detection (Barga 1991). Neural networks require far less restrictive
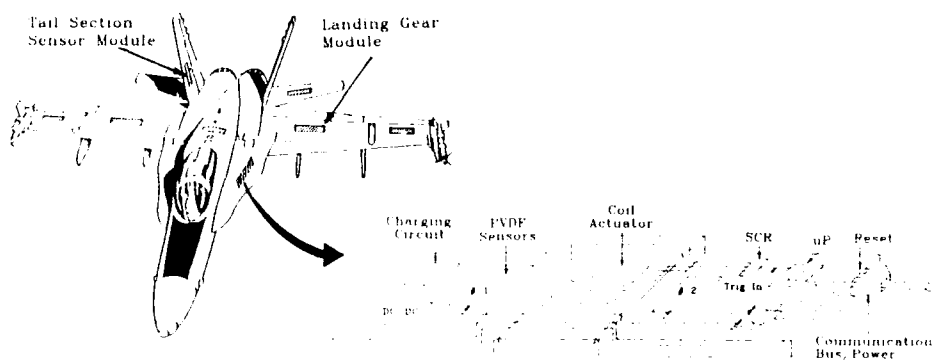
Fig. 1. Structural integrity health monitoring system concept

assumptions about the structure of the input signal compared to other pattern classification techniques. In addition, the inherent parallelism of these networks allows very rapid parallel search and best-match computations required for monitoring complex aircraft structures.

Prototype system hardware and software have been developed and tested to determine the feasibility of a neural network based health monitoring system. Networks were trained to classify signatures from representative aircraft structures with simulated rivet line corrosion and with ice accretion. The neural network performance data are compared to that of the traditional nearest neighbor classifier used in earlier studies (Hickman 1991). This classifier serves as a good performance benchmark since it can be used to obtain upper and lower bounds on the Bayes probability of correct classification as the number of sample signals increases (Cover 1967).

2. SYSTEM ARCHITECTURE

Key components of SIMS are smart sensor modules daisy chained to a host central processor via a serial data communications link as depicted in Figure 1. The host processor interrogates individual structural components which contain the attached or embedded sensor modules that then relay digitized vibration signatures back to the host computer. The modules contain several piezoelectric vibration sensors, a pair of 12 bit microcontroller chips, an eddy-current actuator, and associated power and signal conditioning electronics. A network of these modules serves as a nervous system in detecting and recording the health of the structure. The eddy-current provides the impulse excitation source to the structure. When a pulse of current is sent through the eddy coil, currents are induced in the metal skin of the structure, creating a repelling force or impulse. A dual coil version can be used for composite structures. Excitation energy is on the order of 1 to 10 Joules, depending on the size of the structure. The piezoelectric sensors detect the dynamic structural response. Once the signals are processed by the host computer, diagnostic information is stored and the address code of the next module is selected on the bus. After all the modules have been interrogated, the data is displayed and/or removed from the aircraft processor with a removable storage disk for further analysis and routine maintenance logging procedures.

3. NEURAL NETWORK ALGORITHM

The neural network used was a multilayered perceptron trained using backpropagation learning (Rumelhart 1986). The network is composed of three layers of processing elements that perform a nonlinear transformation on their summed inputs and produce continuous-valued outputs between -1 and 1. A schematic diagram of the network is shown in Figure 2. A number of signal representations could be used as input to the neural network. The simplest would be to use the digitized waveform directly. For this study, however, a feature extraction procedure was used before processing with the neural network for easy comparison with previous results obtained using the nearest neighbor classifier. This procedure consists of generating an appropriate set of features for discrimination between classes. Both time and frequency domain parameters including damping ratio, peak amplitude, and spectral energy in different frequency bands have been found useful for vibration signal analysis (Hickman 1991).
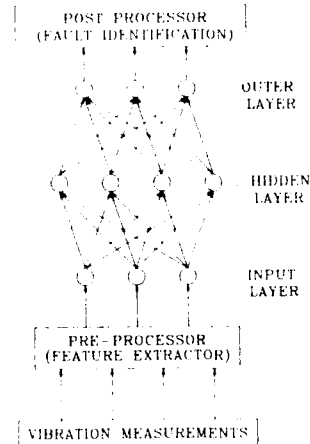
Fig. 2. Neural network architecture

4. CLASSIFICATION EXPERIMENTS AND RESULTS

Experiments were designed to determine the ability of a neural network based diagnostic system to identify corrosion damage and ice accretion. Training the network consisted of repeated presentations of input-output pairs representing the damage case to be learned. The trained network was presented with a set of test returns excluded from the training set to determine its ability to generalize.

Laboratory experiments were performed on a 24" square 0.080" thick aluminum plate. Aircraft screws were used to clamp the edges of the test panel to a jig which provided rig'd support to the test panel. A sensor module was attached to the bottom center of the test panel. The system was trained to recognize simulated corrosion by loosening a series of 4 and 8 consecutive screws at different locations around the plate. To illustrate the variation in vibration signatures, Figure 3 displays the frequency response of the plate without any damage and with 8 loosened screws. The neural network results were outstanding, 100% of the responses were correct in indicating the severity of the damage. The nearest neighbor classifier did not fair as well, 84% of the responses were correct. Of note is the sensitivity of the nearest neighbor to proper selection of the input features. If two nonrelevent features were also used, the nearest neighbor performance dropped to 62% while the
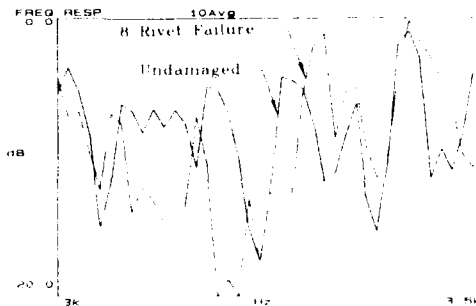
Fig. 3. Typical sensor frequency response showing baseline (undamaged) and an 8 rivet failure case

network performance was unaffected. Work is currently in progress to reliably identify the location of the damage as well as severity.

Sensor modules were also installed on the inside surface of a prototype leading edge wing section for in-flight testing (Hickman 1990). This prototype wing section is a 50" long wing cuff or glove designed to slide onto the DHC-6 Twin Otter main wing. The system was initially trained in the NASA Lewis icing research tunnel. Ice was allowed to build up continuously on the wing cuff and the system was trained in increments of 0.05 inch of ice up to a maximum thickness of 0.5 inch. Figure 4 displays one of the features that was used in the pattern classification. This figure shows the energy present in the frequency band 1150-1800 Hz as the ice thickness

Fig. 4. Sensor response on wing cuff during NASA Lewis icing tunnel tests (partial power in 1150-1800 Hz for different angle-of-attack and liquid water content)

increases. Corrosion was also simulated by loosening aircraft screws as was done in the laboratory tests. Once trained, the system was tested in-flight. Comparable performance was observed using the network and nearest neighbor classifier, 94% of the responses gave the correct ice thickness. Corrosion was also reliably identified, with results similar to those obtained in the flat plate laboratory experiments. These flight tests demonstrated the capability of the system to duplicate results in the high noise environment of turboprop aircraft.

5. CONCLUSIONS

Smart structures comprised of attached sensor/actuator modules were found to be highly effective in gathering structural vibration data with good S/N and acceptable size, weight, and power requirements for aircraft applications. Initial laboratory and flight tests showed the system to perform well in identifying structural abnormalities using pattern recognition techniques. Work is in progress to develop a damage assessment methodology based on analytical and experimental modal analysis to reduce the training procedure. A concurrent effort is devoted to develop neural network topology that will have the ability to recognize and immediately incorporate new input data that fall into classes for which the network has not been trained.

REFERENCES

Barga R S and Meador J L 1991 *SPIE* 1469 pp 602 - 611
Cover T M and Hard P E 1967 *IEEE Trans on Information Theory* IT-13 pp 21-27
Hickman G, Gerardi J and Feng Y 1991 *Journal of Intelligent Material Systems and Structures* 2(3) pp 411-430
Hickman G, Gerardi J, Feng Y and Khatkhate A 1990 *ID Report NAS3-25200*
Rumelhart D E and McClelland J L 1986 *Parallel Distributed Processing: Explorations in the Microstructure of Cognition* (MIT Press)

Materials characterization for micromechanics using deep etch lithography

J. B. Warren
Brookhaven National Laboratory, Upton, NY 11973

ABSTRACT: Deep etch lithography uses x-ray radiation at the National Synchrotron Light Source to expose polymethyl methacrylate (PMMA) resist in layers up to 0.5 mm in thickness. The processed PMMA is used as a mandrel for the fabrication of metallic microstructures by electrodeposition or chemical vapor deposition. The yield strength, ductility, and notch toughness of the microstructures are strongly dependent on the deposition method. If the surface finish and internal grain size are determined by electron microscopy, finite element analysis can be used to predict their behavior and mode of failure.

1. EXPERIMENTAL RESULTS AND DISCUSSION

Deep etch lithography is a microfabrication method (Ehrfeld et al., 1987) that makes use of synchrotron x-ray radiation to expose thick layers of an x-ray resist such as PMMA. The highly collimated beam, with a divergence of 11 milliradians, minimizes the penumbra effect caused by divergent radiation from the extended UV source used in traditional optical mask alignment tools. For x-ray lithography, resist layers need not be in contact with the mask for sub-micron resolution and the height of the developed resist layer is limited only absorption effects. After exposure, the irradiated regions of resist are dissolved in a developer. Resist protected by an opaque X-ray mask forms a rigid microstructure that can be up to several hundred microns high with wall widths of only a few microns. In deep etch lithography, this microstructure is used as a sacrificial mandrel for electroforming or it is left intact as part of a multi-layer structure. Component size, dimensional accuracy, and surface smoothness are all determined by the characteristics of the exposure source and the mask used to transfer the pattern to the resist.

Since the X-ray beam used for exposure is several millimeters wide at the mask position, component size is seriously limited only by absorption in the direction parallel to the beam. Generally, white radiation is used to minimize exposure time. The maximum resist thickness that can be exposed is governed by the absorption equation: $I = I_o e^{-(\mu/\rho)\rho x}$. The dosage at a given depth in the resist will thus vary according to the absorption coefficient

for a given wavelength in the incident beam. For PMMA at 4 Kev, (a typical value for the NSLS x-ray ring at Brookhaven National Laboratory) the absorption equation predicts that the intensity will decrease by a factor of 10 at a distance of 330 um below the resist surface. At this distance, the beam intensity is still sufficient to break the bonds in the PMMA polymer so the exposed areas can be dissolved in solutions such as methyl isobutyl ketone -

isopropanol. This maximum thickness limitation still permits the fabrication of microstructures two orders of magnitude thicker than the microactuators developed with silicon-based fabrication technology.

Minimum wall thicknesses and surface smoothness are determined by the characteristics of the absorbing regions in the X-ray mask. These regions consist of electroplated gold lines that can be less than 1 um in width. An electron beam pattern generator is used to write the initial pattern in e-beam sensitive

Fig. 1   Developed PMMA Microstructure

resist and the absorbing lines are built up to 1 um in thickness by electrodeposition on an x-ray-transparent silicon membrane. Resist exposed with such a mask is shown in Fig. 1, where the PMMA microstructure is 10 um high. While the resist walls are almost perfectly vertical, close examination shows a very fine grooved structure caused by roughness on the

mask absorber lines being transferred to the resist. The pattern is maintained from the top to the bottom of the wall by the collimation of the beam. These grooved structures always appear with current mask technology and place limits on the surface quality of microcomponents formed with deep etch lithography.

A copper grating with a 5 um pitch formed by electrodeposition is shown in Fig. 2. In this case, PMMA is spun on a silicon wafer with a conductive metal underlayer. After development of the PMMA, the wafer is made cathodic in a

Fig. 2   Electrodeposited Copper Grating

electrodeposition cell so the copper deposit grows upward from the conductive wafer surface between the non-conductive resist walls. The deposition is stopped before the copper is higher than the resist walls and the PMMA then is dissolved to expose the grating.

Although electrodeposition has been used in industry for many years, it is an experimentally complex method where variables such as bath composition, current density, and surface quality will affect the grain size, orientation, and internal stress of the deposit. Control of these variables becomes essential as the dimensions of the electroformed component shrink to the extent that its minimum dimensions may be on the same order as the dimensions of the internal grain structure. For example, in acid-bath copper sulphate plating solutions, grain size tends to be quite coarse and may be columnar in character (Dennis, 1986). Stress analysis for microcomponents made with this process would be impossible unless the orientation for each grain in the structure could be determined by selected area electron diffraction. Estimates of mechanical properties will improve if the grain size is minimized or if alternative methods that produce an inherently small grain size are used for deposition. Such methods as

Fig. 3 CVD Tungsten Grating Microstructure

vacuum evaporation or sputtering, while producing fine grained or even amorphous deposits, are line-of-sight techniques incapable of coating complex geometries. Large amounts of internal stress often result if thick coatings are attempted with these methods.

Two technologies that can deposit very fine-grain or amorphous coatings at the thicknesses required for deep etch lithography are chemical vapor deposition (CVD) or plasma enhanced chemical vapor deposition (PECVD). Fine-grained tungsten coatings can be deposited with both these methods by reducing WF_6 with H_2 at pressures of a few hundred millitorr and temperatures from 200° C to 600° C. Fig. 3 shows a tungsten grating formed by CVD on grooved silicon surface formed by anisotropic chemical etching of a <100> silicon wafer. After deposition, the silicon was dissolved in aqueous KOH

Fig. 4 PMMA Micromold for Tensile Specimen

solutions which do not attack tungsten. Selected area electron diffraction demonstrated the average grain diameter to be < 0.1 um.

Once a component's microstructure has been determined, finite element analysis (FEA) is used to determine how the microcomponent will behave under load. In Fig. 4, deep etch lithography has been used to prepare a micromold for a tensile specimen that can be fabricated with one of the methods described above. By supporting the flanges of the specimen on a piezo controlled stage the central beam can be subjected to either tensile or bending stresses. The stress states can be predicted by FEA as long as the grain size is sufficiently small that an isotropic elastic solution is possible and that the surface roughness is characterized in the model with a reasonable amount of precision.
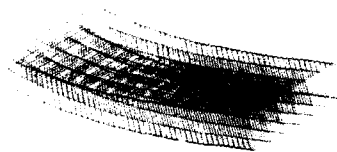
Fig. 5 FEA Model of Deformed Microbeam

In Fig. 5, the central microbeam of the test specimen is represented by an three dimensional FEA model composed of 4000 elements. If the beam is loaded as shown, (deformation has been exaggerated) the maximum principal stresses values can be determined. The grooved features inherent in the deep etch lithography process will act as stress raisers and, as shown in Fig. 6, the maximum stresses will occur at these locations. Large numbers of nodes are needed to accurately model a complete three dimensional beam with surface roughness, but it is generally sufficient to use a coarse mesh for the complete model to determine the maximum stress areas and then refine the mesh in these locations for more accurate analysis.
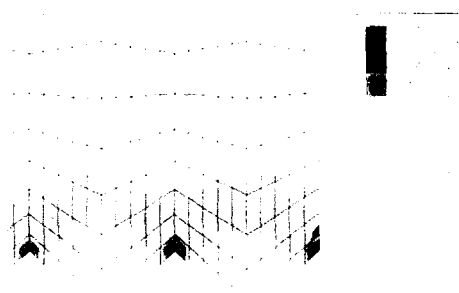
Fig. 6 Maximum Principal Stress Regions in FEA Model of Microbeam

2. REFERENCES

Ehrfeld W et. al. IEEE Solid State Sensor and Actuator Workshop Hilton Head South Carolina June 1988 pp 1-4

Dennis J K and Such T E Nickel and Chromium Plating Butterworth and Co. London 1986 pp. 28.

Investigation of shape memory properties of electrodeposited indium–thallium alloys

C.H. Sonu, T.J. O'Keefe, S.V. Rao, and L.R. Koval

Departments of Metallurgical Engineering, Electrical Engineering, Mechanical Engineering, and Graduate Center for Materials Research, University of Missouri-Rolla, Rolla, Missouri 65401 USA

ABSTRACT: A process was developed for the electrodeposition of In-Tl alloys in a composition range where this system exhibits the shape memory effect. The results show that the composition of the alloy deposits is mainly dependent on pulse peak current density and that the electrodeposited alloy undergoes phase transformation similar to standard equilibrium alloys. However, the temperature range over which the transformations occur is substantially increased. Qualitative shape memory tests were made and shape recovery was confirmed on electrolytically produced In-Tl alloys.

1. INTRODUCTION

Materials which exhibit the shape memory effect are finding increased usage as both sensors and actuators in smart or adaptive structures (Bergamasco 1990, Neukomm 1990, Hashimoto 1985). The essential requirement for metal alloys to be classified as shape memory alloys is a martensitic transformation upon cooling, with the appropriate phase change. Advantage is then taken of the dimensional change which accompanies the alteration in structure with temperature to perform some corrective action in a structure. Recently, studies in our laboratories have demonstrated that it is possible to produce alloys which exhibit the shape memory effect using electrodeposition techniques. This unique processing method offers a number of potentially attractive features, which in time might be incorporated into advanced responsive control systems. The alloys can be deposited in place, at ambient temperature, in thin films or layers, and in a variety of structures and compositions.

In this research, the objective was to produce alloys electrolytically which had compositions in a range where the shape memory effect was known to occur. The indium-thallium system was chosen to show the feasibility of the concept and research was focused on the production of these alloys in a composition range of 15 to 38 at% Tl. It was determined that homogeneous, dense alloy films could be electrodeposited using pulsed current from a sulfate electrolyte and the effect of pulse parameters on the composition and morphology was investigated. The phases existing in the electrodeposited alloys above room temperature were determined by high temperature X-ray diffraction techniques.

2. THE SHAPE MEMORY EFFECT

The mechanism responsible for the shape memory effect involves the presence of a martensitic phase transformation during temperature change. The temperature at which the martensitic transformation starts on cooling is called the Ms temperature and the temperature at which the martensitic transformation stops is called Mf. For the reverse transformation, these temperatures for conversion back to the parent phase are called As and Af, respectively. The shape memory effect can be explained by the

Fig. 1. Illustration of the shape memory effect

stress-strain-temperature relationship of the alloy, shown in Figure 1. The alloy is cooled below its Mf temperature (a to b). Then, the alloy is deformed in the martensitic state (b to c) and unloaded (c to d). There is a permanent strain present but it is not restored when the load is removed. However, when the alloy is heated, martensite is converted to the parent austenite phase and the material is restored in its original shape. In the case of the In-Tl system, the martensite phase is a FCT (face centered tetragonal) and the parent phase is FCC (face centered cubic).

3. PULSE PLATING

Fig. 2. Effect of peak current density on thallium content of the deposits obtained at 25 C without agitation

Indium-thallium alloys were electrodeposited from the electrolyte containing 40.6 g/l of indium sulfate, 2.2 g/l of thallium sulfate, and 28 ml/l of sulfuric acid with the peak current densities from 6.7 mA/cm^2 to 67 mA/cm^2. Platinum foil was used as an anode and the cathode was a glassy carbon plate. The effect of peak current density on the composition of the alloy deposit is shown in Figure 2. The alloy deposits obtained at low current densities in the range of 6.7 to 10 mA/cm^2 show high thallium content of 30-40 at% and an increase in current density decreased the thallium content in the deposit.

As the current density increases, the effect on composition seems to diminish. In the current density region used in this study, thallium is deposited at its limiting current value. Therefore, any increase in current density actually leads to an increase in the rate of indium deposition. At the high current density region from 50 to 70 mA/cm^2, the thallium content approaches the limiting value, 5.3 at%, which was the concentration of thallium in the electrolyte. The composition of the alloy doesn't seem to be dependent on the other pulse parameters such as duty cycle and off time.

4. SCREENING DESIGN TEST

A Plackett-Burman statistical design test (Lipton 1973) was performed to investigate the effect of selected controllable process variables on the composition of the deposit. This design is based on a simplified first order empirical model, but will also yield information indicating overall curvature, or deviation from the linear model and gives an indication of the presence of interaction effects among variables. An eight-run screening design was chosen, and the experimental procedure employed follows basically that described in the literature (Murphy 1977).

Pulse plating parameters used in this test were on time, off time, peak current density, and temperature. The factor levels and the calculation of factor effects are shown in Table 1. The screening test, as given in Table 2, shows that the peak current density is the only significant factor in changing the composition of the alloys, with the results indicating that an increase in peak current density causes a decrease in thallium content.

Table 1 Statistical design results for pulse plating of Indium-Thallium alloy

Table 2 Summary of factor effect intervals at 95% confidence limit

5. PHASE TRANSFORMATION AND SHAPE RECOVERY
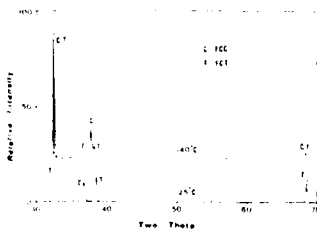
Fig 3 X-ray diffraction profiles of In-21at% Tl alloy deposit

In-Tl alloys in a certain composition range have a FCC structure as a parent phase and undergo a martensitic transformation to a FCT structure on cooling (Nittono 1982). Figure 3 shows the X-ray diffraction profiles of 21 at% Tl alloy deposit. The figure indicates that the electrodeposited alloy undergoes the phase transformation with change in temperature. According to the experimental results on thermally prepared equilibrium alloys (Guttman 1950), the transformation temperature (As) of a 21 at% Tl is around 60°C and the alloy transforms completely by 63-65°C. Since the electrodeposited alloy shows a mixture of FCC and FCT phases in 140°C, it seems the transformation was not complete, even when the temperature was well in excess of that expected for thermally prepared alloys. Figure 4 shows the grain structures of both thermally prepared alloys and electrodeposited alloys of similar composition. The electrodeposited alloy has small

Fig. 4 The grain structures of Indium-
Thallium alloys
(a) Thermal, 22at%Tl
(b) Electrodeposited, 21at%Tl

grains, a few μms in diameter and somewhat varied in grain size while the thermally prepared sample has much larger grains approximately hundreds of μms in size. Some qualitative tests were made to see if the electrodeposited alloys exhibit the shape memory effect. An electrodeposited alloy was cut into a narrow strip and bent at room temperature. When the sheet was heated, movement toward its original flat shape was observed showing at least a partial recovery and the shape memory effect. The deformation-recovery test was repeated several times and recovery was reproduced in every instance.

6. SUMMARY

Indium-thallium alloys can be successfully deposited from a sulfate electrolyte using pulsed current. An increase in peak current density causes a decrease in thallium content in the deposit. The results from the screening test show that the peak current density is the only significant factor which affects the composition of electrodeposited alloys. The electrodeposited alloy shows a martensite to parent phase transformation, FCT to FCC upon heating. The temperature interval for the transformation of the electrodeposited alloys is much wider than those of the thermally prepared alloys but the electrodeposited alloy does show the shape recovery. The ability to produce these new types of shape memory materials by electrolysis appears to offer some exciting possibilities for incorporation into adaptive structures. However, considerably more research is required to more clearly define and characterize these materials in order to optimize their potential applications in actual control systems. Future plans call for optimizing the properties of the In-Tl electrodeposited alloys and investigate their use as possible sensors in the active control of a simple cantilever beam.

7. ACKNOWLEDGEMENT

8. REFERENCES

Bergamasco, M. et.al 1990 *Sensors and Actuators* **A21-A23** 253
Guttman, L. 1950 *Trans. AIME* **188**(12) 1472
Hashimoto, M. et.al 1985 *J. Robotic System*, **2** 3
Lipton, C. and Sheth, N.J. 1973 Statistical Design and Analysis of Engineering
   Experiments McGraw-Hill Co. N.Y.
Neukomm, P.A. et.al 1990 *Sensors and Actuators* **A21-A23** 247
Nittono, O. and Koyama, Y. 1982 *Trans. Inst. Met. Japan* **23**(6) 28
Murphy, T.D. 1977 *Chem. Eng.* June 168

The energy transfer effectiveness of a piezoelectric on silicon bimorph micromotor

Jan G. Smits, Wai-shing Choi, Tom K. Cooney,
Department of Electrical, Computer and Systems Engineering
Boston University, Boston

ABSTRACT

Piezoelectric on silicon bimorph micromotors could offer an atractive alternative to electrostatic micromotors in the sense that they are much less sensitive to disturbances of their environment. A major disadvantage of the electrostatic motor is its requirement of an electric field, which precludes the operation of the motor in a dirty environment or in a conductive medium, such as water.

In deriving the effectiveness of the heterogeneous bimorph, a work cycle is assumed for the bimorph. The work cycle depends on the nature of the load. For a constant load, such as gravity, the workcycle differs from that when a spring type load is applied. The energies stored in the bimorph and the work done are derived for each combination of boundary conditions. The performed work is related to the electrical energy taken in by the bimorph. The effectiveness λ for constant load is defined as the ratio of the energy transferred by the bimorph to the energy put in by the generator.

For the spring type load the results are more complicated because the effectiveness depends on the springconstant of the loading spring. In our laboratory we have experimentally fabricated ZnO on SiN heterogeneous bimorphs with dimensions of $3000 \times 400 \times 3\mu$.

INTRODUCTION

Bimorphs have been invented by Sawyer, who in his paper of November 1931 gave a full account of their use up to that time [1]. Bimorphs have been used since for many appications of which we will mention a few: the changing of displays [2,3], to record sound [4], for precision displacement [5], for optical scanners [6,7], for pumps [8,9], and for air flow generation[10, 11]. They have also been used to bend mirrors,[12], to rotate the head of a magnetic tape drive for a video tape recorder [13], to bring diaphragms in vibration, [14] and to make motors [15,16,17]. Piezoelectric bimorphs have also been used to control structural vibrations [18, 19,20,21] . The bimorphs are used as a gripping device [22,23] or as a fine positioner [24,25].

Whatever the application, the total energy transfer in static applications can not exceed the limits which are set by the piezoelectric material, as the are calculated by Lucas [26]

CONSTITUENT EQUATIONS

The constituent equations of piezoelectric bimorphs have been formulated in terms of the canonical pairs $(M, \alpha), (F, \delta), (p, \mathcal{V})$ and (V, Q), where M is the external moment at the tip, α is the rotation, F is the force at the tip and δ is the deflection, p is the force per unit area (pressure) and $\mathcal{V}$ is the volume diplacement of the bimorph . V is the voltage across the electrodes, and Q is the charge on them. The constituent equations are given as:

$$
\begin{pmatrix} \alpha \\ \delta \\ \mathcal{V} \\ Q \end{pmatrix} = \begin{pmatrix} \dfrac{3s_{11}^E L}{2wh^3} & \dfrac{3s_{11}^E L^2}{4wh^3} & \dfrac{s_{11}^E L^3}{4h^3} & \dfrac{3d_{31} L}{4h^2} \\[2mm] \dfrac{3s_{11}^E L^2}{4wh^3} & \dfrac{s_{11}^E L^3}{2wh^3} & \dfrac{3s_{11}^E L^4}{16h^3} & \dfrac{3d_{31} L^2}{8h^2} \\[2mm] \dfrac{s_{11}^E L^3}{4h^3} & \dfrac{3s_{11}^E L^4}{16h^3} & \dfrac{3ws_{11}^E L^5}{40h^3} & \dfrac{d_{31} w L^3}{8h^2} \\[2mm] \dfrac{3d_{31} L}{4h^2} & \dfrac{3d_{31} L^2}{8h^2} & \dfrac{d_{31} w L^3}{8h^2} & \dfrac{\epsilon_{33}^T L w}{2h}\left(1 - k_{31}^2/4\right) \end{pmatrix} \begin{pmatrix} M \\ F \\ p \\ V \end{pmatrix} \qquad (1)
$$

or

$$\begin{pmatrix} \alpha \\ \cdot \\ \cdot \\ Q \end{pmatrix} = B \begin{pmatrix} M \\ \cdot \\ \cdot \\ V \end{pmatrix} \tag{2}$$

where B is the bimorphmatrix.

Consider the case that the bimorph is loaded with a constant force. How much energy is it able to tranfer into the the object that exerts the force? It has been shown [27] that it is possible to calculate the effectiveness λ_F as

$$\lambda_F = \frac{18k_{31}^2}{16 + 23k_{31}^2} \tag{3}$$

Similar equations hold for the effectivenesses against a constant moment M working at the tip and for a constant pressure p on the beam.

$$\lambda_M = \frac{3k_{31}^2}{2 + 4k_{31}^2} \quad \lambda_p = \frac{5k_{31}^2}{6 + 6k_{31}^2} \tag{4}$$

In the case that the bimorph acts against spring, as opposed to a constant force the effectiveness becomes dependent on the spring constant. We use the symbols μ_M, μ_F, μ_p to distinguish it from the case with the constant boundary condition [28]

$$\mu_M = \frac{k_M \left(\frac{b_{14}}{1+k_M b_{11}} \right)^2}{b_{44} - \frac{k_M b_{14}^2}{1+k_M b_{11}}} \quad \mu_F = \frac{k_F \left(\frac{b_{24}}{1+k_F b_{22}} \right)^2}{b_{44} - \frac{k_F b_{24}^2}{1+k_F b_{22}}} \quad \mu_P = \frac{k_p \left(\frac{b_{34}}{1+k_p b_{33}} \right)^2}{b_{44} - \frac{k_p b_{34}^2}{1+k_p b_{33}}} \tag{5}$$

As is obvious in equation 5 the effectiveness depends on the spring constants k_M, k_F, k_p. Obviously. when the spring constants go to zero, the effectiveness will vanish too, on the other hand, if the springs become infinitely stiff, then the effectiveness will also go to zero. It is clear that there is an optimum spring constant for which there will be a maximum energy transfer. To find that spring constant we take the derivative of the effectiveness with respect to the springconstant and set it equal to zero and solve for the springconstant. We find for $\mu_{M_{max}}$:

$$\mu_{M_{max}} = \frac{3k_{31}^2}{4 \left(1 - \frac{k_{31}^2}{4} \right) \left(2 - \frac{3k_{31}^2}{4 \left(1 - \frac{k_{31}^2}{4} \right)} + 2 \sqrt{1 - \frac{3k_{31}^2}{4 \left(1 - \frac{k_{31}^2}{4} \right)}} \right)} \tag{6}$$

We observe in these equations that the effectiveness λ_i and the maximum efectiveness $\mu_{i_{max}}$ where $i = M, F, p$ are largest in the case of a moment, smaller in the case of a force, and smallest in the case of a pressure. It has been stated [29] that $0 \leq k_{31}^2 \leq 1$ and we can use these limits to find :

$$\lambda_M \geq \lambda_F \geq \lambda_p \quad \mu_{M_{max}} \geq \mu_{F_{max}} \geq \mu_{p_{max}} \tag{7}$$

This seems striking and rather important: When a piezoelectric bimorph is used as a motor element, it is most effective as a "moment"-motor, less effective as a "force"- motor and least effective as a "pressure"-motor. In particular the last case is important for the design of piezoelectric pumps. because if the medium to be pumped is in direct contact with the deflecting bimorph then the pump is the least effective. It may be necessary to look at a different design for the pump.

As it may be convenient in micromachining to fabricate a piezoelectric film on top of a Silicon cantilever beam, we have a new type of element which we call an enakemesa morph, (from the Greek ena kai meso which means one and a half), which is called by others [7] "heterogeneous bimorph " or "30' " monomorph". Its constituent equations have been analyzed and can be summarized as:

$$
\begin{pmatrix} \alpha \\ \delta \\ \mathcal{V} \\ Q \end{pmatrix} = E \begin{pmatrix} M \\ F \\ p \\ V \end{pmatrix}. \tag{8}
$$

The enakemesomatrix E in its full form is given by:

$$
A \begin{pmatrix}
\frac{12L}{Kw} & \frac{6L^2}{Kw} & \frac{2L^3}{K} & \frac{-6d_{31}BL}{K} \\
\frac{6L^2}{Kw} & \frac{4L^3}{Kw} & \frac{3L^4}{2K} & \frac{-3d_{31}BL^2}{K} \\
\frac{2L^3}{K} & \frac{3L^4}{2K} & \frac{3L^5 w}{5K} & \frac{-d_{31}BL^3 w}{K} \\
\frac{-6d_{31}BL}{K} & \frac{-3d_{31}BL^2}{K} & \frac{-d_{31}BL^3 w}{K} & \frac{Lw}{Ah_p}\left(\epsilon_{33}^T - \frac{d_{31}^2 h_{\bullet\bullet}(s_{11}^{np}h_p^3 + s_{11}^p h_{np}^3)}{K}\right)
\end{pmatrix} \tag{9}
$$

with

$$
A = s_{11}^{np} s_{11}^p (s_{11}^p h_{np} + s_{11}^{np} h_p) \quad B = \frac{h_{np}(h_{np} + h_p)}{(s_{11}^p h_{np} + s_{11}^{np} h_p)} \tag{10}
$$

$$
K = (s_{11}^{np})^2 (h_p)^4 + 4 s_{11}^{np} s_{11}^p h_{np}(h_p)^3 + 6 s_{11}^{np} s_{11}^p (h_{np})^2 (h_p)^2 \\
+ 4 s_{11}^{np} s_{11}^p h_p (h_{np}^3) + (s_{11}^p)^2 (h_{np})^4 \tag{11}
$$

where h_{np} and s_{11}^{np} are the thickness and the elastic compliance of the non-piezoelectric material, while h_p and s_{11}^p are the corresponding counterparts of the piezoelectric material. d_{31} and ϵ_{33}^T are, respectively, the direct piezoelectric coefficient and the dielectric constant under constant stress of the piezoelectric material. L and w are the length and width of heterogeneous bimorph.

If we again define the effectiveness as λ_F we find

$$
\lambda_F = \frac{2e_{24}^2}{e_{22}e_{44} + 3e_{24}^2} \tag{12}
$$

and similar expressions for λ_M and λ_p.

Substitution of the matrix elements of equation (17) gives:

$$
\lambda_F = \frac{18k_{31}^2 nt^2(1 + t^2)}{4H - k_{31}^2(4n^2t - 23nt^2 - 54nt^3 - 23nt^4 + 4t^5)} \tag{13}
$$

where

$$
H = n^3 + 5n^2t + 4nt^2 + 6n^2t^2 + 6nt^3 + 4n^2t^3 + 5nt^4 + t^5 \tag{14}
$$

$$
n = \frac{s_{11}^{np}}{s_{11}^p} \quad t = \frac{h_{np}}{h_p} \quad k_{31} = \frac{d_{31}}{\sqrt{\epsilon_{33}^T s_{11}^p}} \tag{15}
$$

Similar equations for λ_p and λ_M are found.

By normalizing the expressions we can rewrite them as :
It can be verified by coefficient inspection that

$$
\lambda_M > \lambda_F > \lambda_p \quad for \quad n, t > 0 \quad ; \quad 0 \leq k_{31} \leq 1. \tag{16}
$$

λ As Function Of k_{31}

It is noted that for fixed values of n and t, λ_F, λ_M and λ_p increase almost parabolically with increasing k_{31} and reach maxima at $k_{31} = 1$. Thus piezoelectric heterogeneous bimorphs made out of piezoelectric materials with higher coupling factor will be more effective.

Optimal Film Thickness Ratio, t_o

From (13), we observe that λ_F, λ_M and λ_p are functions of k_{31}, n and t. In order to make the analysis mathematically tractable, we will let n equal to 1. Such assumption will be a reasonable approximation to some of the piezoelectric and non-piezoelectric systems. For examples, s_{11}^E of ZnO is 7.75 $(TPa)^{-1}$ and s_{11} of Si is 7.74 $(TPa)^{-1}$. However s_{11} of Si varies with the dopant concentration and can have values between 7.5 to 7.9 $(TPa)^{-1}$ [31]. Thus for the ZnO and Si system, $n = 1$ indeed can be achieved.

With $n = 1$, we can rewrite (13), (25) and (27) as :

$$\lambda_F = \frac{18k_{31}^2 t^2 (1 + t)^2}{4 + 20t + 40t^2 + 40t^3 + 20t^4 + 4t^5 - k_{31}^2 \left(4t - 23t^2 - 54t^3 - 23t^4 + 4t^5\right)} \tag{17}$$

To obtain values of optimal thickness ratio t_o for maximum values of the effectiveness, we establish the following conditions:

$$\frac{\partial \lambda_F}{\partial t} = \frac{72k_{31}^2 t(1 + t)(2 + t - k_{31}^2 t - t^2 + k_{31}^2 t^2)}{(-4 - 12t + 4k_{31}^2 t - 12t^2 - 31k_{31}^2 t^2 - 4t^3 + 4k_{31}^2 t^3)^2} = 0 \tag{18}$$

Solving the above equations separately yields the following sets of roots:

$$\left\{ t_{o1}^F, \dots, t_{o4}^F \right\} = \left\{ -1, \ \frac{1}{2}\left(1 - \sqrt{1 + \frac{8}{1 - k_{31}^2}}\right), \ 0, \ \frac{1}{2}\left(1 + \sqrt{1 + \frac{8}{1 - k_{31}^2}}\right) \right\} \tag{19}$$

There are 4 real and distinct roots in this solutions set, which are also found for λ_M and $\lambda - p$. This implies that for a given value of k_{31}, the optimal geometrical design of the bimorph, i.e. t_o, for use as a moment motor will also be optimal for use as a force motor or a pressure motor.

Of the four roots in the solutions set, t_{o1}, t_{o2} are negative definite and t_{o3} is zero, they are not of physical interest. t_{o4} is positive definite and shows a dependence on k_{31}. For a practical system like ZnO on Si, k_{31} for ZnO is 0.18 and n is 1. Hence t_{o4} is determined as 2.02.

For the PZT and Si system, k_{31} for PZT is 0.3. s_{11}^{PZT} is 12.3 $(TPa)^{-1}$ and n is 0.6. Repeating the previous computation procedures with $n = 0.6$, the optimal value of film thickness ratio, t_{o4} is determined as 1.41.

We can summarize the previous results in the following table:

TABLE 1.   RESULTS OF OPTIMATIZATION WITH RESPECT TO t

Materials	k_{31}	n	t_o	$\lambda_{M_{max}}$	$\lambda_{F_{max}}$	$\lambda_{P_{max}}$
ZnO on Si	0.18	1.0	2.02	0.0278	0.0210	0.0157
PZT on Si	0.30	0.6	1.41	0.0777	0.0600	0.0455

The above results suggest that for a system with weak piezoelectric coupling factor, the non-piezoelectric film should be approximately 1.5 to 2.0 times as thick as the piezo-electric film.

IV. Conclusion

The effectiveness of a heterogeneous bimorph in converting electrical energy into mechanical work is a function of the piezoelectric coupling factor, the thickness ratio and the elastic compliance ratio between the non-piezoelectric and piezoelectric material comprising the bimorph.

It has been found that the heterogeneous bimorph has the largest effectiveness in performing work against a constant load applied as a moment. Effectiveness of the bimorph in performing work against a constant load applied as a force at the free end is larger than that of an applied pressure.

The set of optimal values of k_{31}, n and t leading to maximum λ_M will also lead to maximum λ_F and λ_p.

For systems of practical interest, such as the ZnO on any substrate, maximum effectiveness occurs at $t = 2.02$ and $n = 0.687$, where the non-piezoelectric film is about twice as thick as the piezoelectric film. For ZnO on Si, $\lambda_M = 2.78\%$ $\lambda_F = 2.10\%$ and $\lambda_p = 1.57\%$

For PZT on any substrate, we find that maximum effectiveness occurs at $t = 1.45$ and $n = 0.405$. For PZT on Si, we find $\lambda_M = 7.77\%$ $\lambda_F = 6.00\%$ and $\lambda_p = 4.55\%$

REFERENCES

[1] C.B. Sawyer, The Use of Rochelle Salt Crystals for Electrical Reproducers and Microphones Proceedings Institute of Radio Engineers, Vol. 19, No. 11, Nov. 1931, pp.2020-2029.

[2] J.T.McNaney, Electrostrictive apparatus for changing displays. United States Patent. 3,146.307. Aug. 25, 1964.

[3] M.Toda, S.Osaka, and E.O.Johnson, A new electromotional device. RCA Engineer, Vol. 25. No. 1. June/July 1979, pp.24-27.

[4] B.B.Bauer, Sound recording method and apparatus. United States Patent. 3,490,771, Jan. 20 1970.

[5] E.A.Ivanov, V.V.Silchenkova, A.A.Sazonov, and N.S.Budkin. Device for the precision displacement of an article within a plane. 3,928,778, Dec. 23, 1975. United States Patent.

[6] J.K.Lee. Piezoelectric bimorph optical scanners: analysis and construction. Applied Optics. Vol 18, 1979, pp 454-459.

[7] M.R. Steel, F. Harrison and P.G. Harper. The Piezoelectric Bimorph: An Experimental and Theoretical Study of its Quasistatic Response. J. Phys. D Appl. Phys. Vol. 11 1978, p.979.

[8] W.J.Spencer, W.T.Corbett, L.R.Dominguez and B.D.Shafer, An Electronically Controlled Piezoelectric Insulin Pump and Valves. IEEE Transactions on Sonics and Ultrasonics, Vol. SU-25, No. 3, May 1978, pp.153-156.

[9] J.G.Smits, Piezoelectric Micropump with Three Microvalves Working Peristaltically. Sensors and Actuators, A21-A23 (1990) pp203-206

[10] Piezoelectric motor actuator kit manual, Corporate Brochure, Piezosystems Inc. Cambridge Massachusetts.

[11] M.Toda, Theory of Air Flow Generation by a Resonant Type PVF$_2$ Bimorph Cantilever Vibrator. Ferroelectrics, Vol 22, pp911-918 (1979).

[12] S.A.Kokorowski, Analysis of adaptive optical elements made from piezoelectric bimorphs. J. Optical Soc. Am., Vol. 69, 1979, pp.181-187.

[13] Y.Kubota, Rotating Magnetic head Piezoelectric assembly and drive circuitry for video tape recorder. 4,233,637, Nov. 11, 1980, United States Patent.

[14] J.G. Smits. Resonant diaphragm pressure gauge, Proceedings of the Symposium on Force. Displacement, Pressure and Flow Sensors, September 1982, Twente University, pp135-151.

[15] S.Osaka and M.Toda, Rotative motor using plural arrays of piezoelectric elements. 4,399,386. Aug. 16, 1983, United States Patent.

[16] J.G.Smits, Integrated Micromechanical Piezoelectric Motor, U.S. Patent 5,049,775

[17] Jan G. Smits, Is Micromechanics Becoming A New Subject For Academic Courses Or The Design Of A Piezoelectric On Silicon Microbot. Proceedings of the Eighth Biennial University/ Government/ Industry Symposium held in Westborough Massachusetts, 12-15 July, 1989.

[18] E.F.Crawley and J.de Luis, Use of Piezoelectric Actuators as Elements of Intelligent Structures. AIAA Journal, Oct. 1987, pp1373-1385.

[19] H.S.Tzou and M.Gadre, Theoretical Analysis of a Multi-Layered Thin Shell Coupled With Piezoelectric Shell Actuators for Distributed Vibration Controls. J. Sound and Vibration, Vol. 132, No. 3, 1989, pp433-450.

[20] A.Baz and S.Poh, Performance of an Active Control System with Piezoelectric Actuators. J. Sound and Vibration, Vol. 126, No. 2, 1988, pp327-343.

[21] T.Udagawa, T.Akatsu and Y.Hamada, Grip Device. 4,667,997, May 26, 1987, United States Patent.

[22] D.J.Peters and B.L.Blackford, Piezoelectric bimorph-based translation device for two dimensional, remote micropositioning. Rev. Sci. Instrum., Vol. 60, No. 1, Jan. 1989, pp.138-140.

[23] Y.Hatamura and K.Ono, Fine positioning device. 4,686,440, Aug. 11, 1987, United States Patent.

24. C.W.Staufenberg Jr.   and R.J.Hubbell, Piezoelectric Multiaxis Micropositioner 1,727,278, Feb. 23, 1988, United States Patent.

25. I.Lucas, Transformation of Energy in Piezoelectric Drive Systems. Siemens Forsch. u. Entwickl. Ber. Bd. 4 (1975) Nr. 6

26. J.G.Smits and T.K. Cooney, The Effectiveness of a Piezoelectric Bimorph Actuator to Perform Mechanical Work Under Various Constant Loading Conditions Ferroelectrics, 1991 pp 89-105.

27. J.G.Smits, The Effectiveness of a Piezoelectric Bimorph Actuator to Perform Mechanical Work Against Various Spring Type Loads. Accepted for Publications by Ferroelectrics.

28. J.G.Smits, Eigenstates of Coupling Factor and Loss Factor of Piezoelectric Ceramics, Ph. D. Thesis, Twente University, 1978.

29. C.P. Germano. Flexural Mode Piezoelectric Transducer, IEEE Audio, 1971, p.6.

30. Landolt-Börnstein, Neue Tabelle Vol. 17, Springer Verlag, Berlin.

Robustness issues in model adaptive controllers

S.Hanagud and G.L.NageshBabu

School of Aerospace Engineering,Georgia Institute of Technology, Atlanta, Ga-30332

ABSTRACT

Smart, adaptive or intelligent structures can be used to actively control vibrations. For smart structures, to perform selected functions autonomously, variations in the a priori model due to added pay loads, flaws or failures should be accommodated. One way of accommodating such variations is by adaptively changing the plant model. These changes can also be accommodated by designing robust controllers. In this paper such model adaptive controllers and robust controllers are designed for a specific flexible body system to optimize the design for either the robust controllers or the model adaptive controllers.

INTRODUCTION

During the past several years there has been a considerable amount of research activity to use bonded or embedded piezoceramic (or PVDF) sensors and actuators to control vibration (or jitter) in light weight structures(Olson 1956, Forward 1979,1981a,1981b,1983, Hanagud et al 1986a,b,c,1988, Crawley et al 1985, Fanson et al 1987). Bonded piezoceramic sensors and detection circuits can be designed such that the rate of deformation of a beam structure will result in a signal that is proportional to the difference of the slope rate at the two ends of the transducer (Hanagud, Obal and Calise 1986a,b,1988). Similar results can be derived for voltage time histories as a function of the deformation rates of other types of structures. The detected signal can be conditioned by operations such as filtering, phase shift and amplification. The conditioned signals are used as inputs to bonded or embedded piezoceramic actuators to transmit energy to the structure. The objective of the operations of sensing, conditioning and feedback to selected actuators is to design a vibration or jitter control of the structure.

Most of the work in the area of flexible structural controls assumes a time invariant system. However, in practice flexible structures may undergo discontinuous changes due to failures, induced defects, added pay loads or configuration changes. Controllers designed with a priori time invariant assumption will be inefficient and in many cases may lead to instability. This necessitates the usage of adaptive controllers in such cases. Some of the existing adaptive controllers include self tuning regulators(Stien and Saridis 1979, Deshpande et al 1973, Wittenmark, 1979) and model adaptive controllers(Hanagud et al 1990, Glass et al 1990).

In self tuning regulators, model parameters are identified based on a time invariant form obtained from the initial assumptions. These methods may not be able to adapt

to large changes in the a priori model. In model adaptive controllers, initially appropriate model is identified by using Artificial Intelligence (AI) first best, heuristic search techniques. After the model is identified, based on the identified model, parameters are identified similar to self tuning regulators. Cost involved in such model adaptive controls include the creation of an elaborate model space, selection of the most likely model from the model space and selection of the model parameters for the selected model.

The discontinuous changes in the model parameters from the a priori model, from here referred as nominal model, can also be accommodated by considering the changes in the model parameters as uncertainities and then designing robust controllers using techniques like μ control theories (Doyle et al 1982,1988, Packard et al 1988). But accommodating these uncertainities using robust controllers may involve excessive control forces and elaborate controllers. The purpose of this paper is to compare the relative merits of the both robust adaptive controllers and model adaptive controllers.

A specific example of a single link flexible arm with varying tip masses is considered as the time varying flexible system. As the tip mass varies, the dynamics of the system changes. The controller designed for one configuration of dynamic equations may lead to instability in another configuration of dynamic equations. The varying tip mass is considered as the uncertainity and robust adaptive controllers are designed. Heuristic search methods (Hanagud et al 1990, Glass et al 1990) are used to select a proper model and based on that model, model adaptive controllers are designed. Performance is compared for both the controllers.

DYNAMIC EQUATIONS

An adaptive structure of a single link flexible arm made of aluminum with the geometric configuration as shown in figure 1 is considered. The structure consists of piezoelectric sensors, piezoelectric actuators, detecting circuit and a controller. The piezoelectric sensor converts the mechanical energy due to disturbances into an electric field. The detection circuit attached to the sensor converts this electric field into a voltage which in turn is transmitted through a controller to the actuator. The plant equations with the bonded piezoceramic sensors and actuators can be written as follows(Hanagud et al 1986a,b)

$$r = Ar + B_d f + Br_d \quad r \in R^{2n}$$
$$y = Cr \quad y \in R^{2p} \tag{1}$$

Now a dynamic compensator is designed to suppress the vibration caused by the external disturbance by using H_∞ control procedure (Doyle et al 1982,88). In this control procedure, the compensator is designed for the worst case error due to the disturbance. The controller thus designed is based on the time invariant a priori model and is known as nominal model. This model can not accommodate any variations in the plant model. To accommodate the variations in the plant model due to the changes in the dynamics of the system, adaptive controllers need to be designed. Two such adaptive controllers are robust adaptive controllers and model adaptive controllers.

ROBUST ADAPTIVE CONTROLLER

The robust adaptive controller is designed using μ synthesis. The governing differential equation with added tip mass can be written with $(A + \Delta A)$, $(B_1 + \Delta B_1)$ and

Once the model is identified by using the artificial intelligence based heuristic search methods, parameters like mass, stiffness and damping are identified using conventional structural dynamic identification algorithms (Hanagud et al 1986c) with the model chosen through model identification procedure as the a priori model. With the chosen model and chosen parameters, a nominal μ controller is designed which will be termed as model adaptive controller. It differs from the earlier designed nominal controller in the sense that the dynamic model used for the design of controller is different.

RESULTS AND DISCUSSIONS

A five degree of freedom structural dynamic model is generated by the identification procedure (Hanagud et al 1986c) for the single link flexible arm shown in figure 1. Using the procedure given in (Doyle et al, 1982,1988), a nominal H_∞ controller is designed. Tip rotation with and without nominal controller is shown in figure 3. Control force required for the suppression is shown in figure 4. Effectiveness of the nominal controller is tested by considering the flexible manipulator with a tip mass equal to the 25 percent of the total mass of the arm. The tip rotation with and without nominal controller is shown in figure 5. It can be seen from the figure 5 that the system resulted in to instability due to the presence of tip mass. To account for this tip mass, two options are available, one being the robust adaptive controller and the other one is model adaptive controller.

With a tip mass of 25 percent of the total mass of the arm, a robust controller is designed. The tip rotation of the arm with and without robust controller with this tip mass is shown in figure 6. The control force required for this configuration is shown in figure 7. The tip rotation and control force for the manipulator with out tip mass with robust controller are shown in figures 8 and 9. From figures 4 and 9, it can be seen that the control force requirement for a robust controller is higher than the control force requirement of a nominal controller. But the controller can accommodate the tip masses up to 25 percent of the total mass of the beam. Thus using robust adaptive controllers, we can design controllers that can accommodate certain amount of variation from the a priori model at the expense of control force. Second option that can be considered is the model adaptive controller which involves using the Artificial Intelligence based heuristic search methods.

With this first best search approach, model for the cantilever beam with the tip mass of 25 percent of the total weight has been identified. Using this model as the nominal model, a μ controller is designed. The tip rotation and controller forces for such controller designed is are shown in figures 10 and 11. It can be seen that the control force levels are similar to the control force levels when a nominal controller that is designed for the arm with out tip mass.

CONCLUSIONS

Time varying flexible systems require adaptive controllers to accommodate the varying dynamic models. Two types of adaptive models are considered. Robust adaptive control models assume the variation from the a priori model as the uncertainity and a μ controller will be considered to accommodate that uncertainity. In the model adaptive controller, the artificial intelligence based heuristic search methods select a new model from the created most probable model space. Usage of robust adaptive controllers results in elaborate controllers and excessive control forces. But it does not require design of many controllers for the creation of model space. The model adaptive controller requires less control force when compared with robust adaptive controllers but it requires design

$(B_2 + \Delta B_2)$ in equation 1 where

$$\Delta A = \begin{bmatrix} 0 & 1 \\ -m^{-1}k & -m^{-1}d \end{bmatrix} - \begin{bmatrix} 0 & 1 \\ -[m+\Delta m]^{-1}k & -[m+\Delta m]^{-1}d \end{bmatrix}$$

$$\Delta B_d = \left\{ \begin{array}{c} 0 \\ m^{-1} \end{array} \right\} - \left\{ \begin{array}{c} 0 \\ (m+\Delta m)^{-1} \end{array} \right\}$$

$$\Delta B = \left\{ \begin{array}{c} 0 \\ m^{-1}k_d \end{array} \right\} - \left\{ \begin{array}{c} 0 \\ (m+\Delta m)^{-1}k_d \end{array} \right\} \tag{2}$$

Here m,k,d are mass, stiffness and damping matrices and k_d is the actuator related piezoelectric constant. This can also be arranged in as

$$\dot{r} = Ar + B_d f + Bv_d + v$$
$$v = \delta z$$
$$z = \Delta A r + \Delta B_d f + \Delta B V_d$$
$$y = cr \tag{3}$$

Here δ is the uncertainity due to the presence of the tip mass. This can be represented in a block diagram as shown in 2. Now the problem is in the frame work of μ synthesis (Doyle et al 1982,1988, Packard and Doyle, 1988). A robust controller is designed that can accommodate the addition of tip mass using μ synthesis. It should be noted that the designed robust controller is based on the same dynamic model as the nominal controller with the variations of nominal model being considered as uncertainity. That is this robust adaptive controller can accommodate both the nominal model and varied model.

MODEL ADAPTIVE CONTROLLERS

The basic idea of model identification is to improve the accuracy of parameter identification by starting it with an a priori model which more closely resembles the actual structure than an initial time invariant model. Design of model adaptive controllers involve the identification of both the model and the parameters based on the identified model. In a time varying flexible structure (TVFS), a model ν is defined by means of differential operators, boundary and initial conditions. The parameters θ_i that need to be identified in a chosen model include the mass, stiffness and damping matrices. Thus the identification in a model adaptive controller procedure indicates the selection of ν and parameters θ_i such that the error function $J(\nu, \theta)$ is minimized among all possible models in a model search space and all possible parameters. The form of the model search space is discontinuous and include infinite set of all possible TVFS models. Since it is impractical to use J in an infinite set, the model subspace is restricted to a finite set of most likely models, R. R is chosen such that individual model responses $H(\nu, \theta_i)$ for an a priori set of parameters are distinct. However, there exists a possibility that the model to be identified may not exist in the chosen most likely subset R. In addition, noise due to various reasons also result in error in the measurements used in the evaluation of error function J. This necessitates the selection of best model in terms of minimization of error J if exact match is not found in R. As the model space R is discontinuous, minimization can not be defined by $\frac{\partial J}{\partial \nu}$ and J cannot be minimized by numerical methods. Therefore symbolic methods such as heuristic methods are required to find the optimal model in R.

of many possible controllers to create model space. Both the methods can be used for the large changes in the system. Trade off should be made when selecting a suitable adaptive controller. Optimal selection could be design of robust controllers in the model space accommodating a band of variations in the model form for each element of robust controller in the model space.

ACKNOWLEDGEMENTS

REFERENCES

Crawley, E.F. and Luis, J. de. 1985, *AIAA/ASME/ASCE/AHS 26th SDM Conference*, AIAA No. 85-0626.

Deshpande, J.G. Upadhyay, T.N. and Lainiotis, D.G., 1973, *Automatica*, pp 107-115.

Doyle,J.C., Wall,J.E. and Stein,G., 1982, tainities,", *Proc. 21 CDC*, pp. 629-636.

Doyle,J.C., Glover,K., Khargonekar,P.P, and Francis B.A., 1988 *American Control Conference.*

Fanson, J.L. and Caughey, T.K.,1987, *AIAA/ASME/ASCE/AHS 28th SDM Conference*, pp. 588-598.

Forward, R.L., 1979, *Applied Optics*, pp. 690-697.

Forward, R.L. and Liu, C.P., 1981a *Proceedings AIAA/ASME/ASCE/AHS 22nd Structures, Structural Dynamics and Materials Conference*,Paper No. 81-0556.

Forward, R.L. and Swigert, C.J., 1981b, *J. Spacecraft and Rockets*.

Forward, R.L. and Swigert, C.J., 1983, *Shock and Vibration Bulletin*, pp. 51-61.

Glass, B.J. and Hanagud, S., 1990, *31 st AIAA SDM Conference*, paper no AIAA-90-1170-CP.

Hanagud, S., Obal, M.W., and Mayyappa, M., 1986a, *AIAA/ASME/ASCE/AHS 27th SDM Conference*, pp. 443-453.

Hanagud, S., Obal, M.W. and calise. A.J., 1986b, *AIAA/ASME/ASCE/AHS 27th SDM Conference*.

Hanagud, S. Meyappa,M., Cheng.Y.P. and Craig, J.L. 1986 c *AIAA Journal*.

Hanagud, S., Obal, M.W. and Calise, A., 1988, *Smart materials, structures and mathematical issues*, Ed by C A Rogers, Technomic Publishing Co. pp. 69-80.

Hanagud, S. Glass, B.J. and Calise, A J. 1990, *AIAA J. Guidance Control and Dynamics*, pp. 534-549, 1990

Olsen, H.F., 1956, *J. Acous. Soc. Am.* pp. 966-972.

Packard,A. and Doyle,J.C., 1988, *ACC Conference*

Stein, G. and Saridis, G.N., 1969, *Automatica*. pp 731-739.

Wittenmark, B., 1979, *Automatica*. pp 85-89.
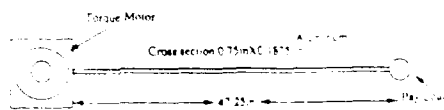
FIGURE 1 SINGLE LINK FLEXIBLE MANIPULATOR
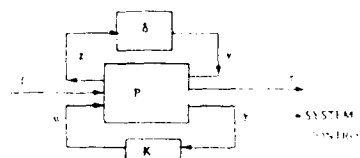
FIGURE 2 BLOCK DIAGRAM FOR THE UNCERTAIN SYSTEM

Figure 3 Tip rotation of a single flexible link manipulator with a tip mass and with nominal controller (zero tip mass)
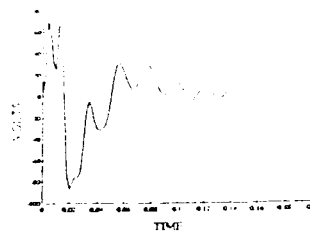
Figure 4 Control force with a nominal controller
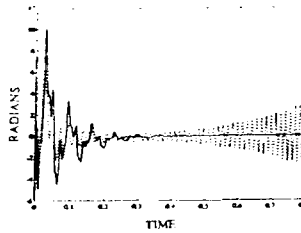
Figure 5 Tip rotation of a single flexible link manipulator with a tip mass and with nominal controller (25 % of total mass)

Figure 6 Tip rotation of a single flexible link manipulator with a robust controller (with 25 % of total mass as tip mass)

Figure 7 Control force with robust controller

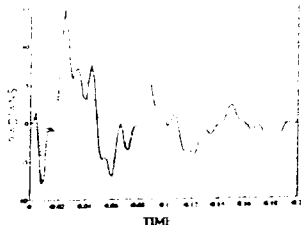Figure 8 Tip rotation of a single flexible link manipulator with a robust controller (with zero tip mass)
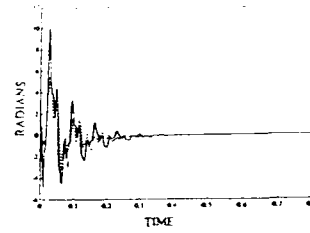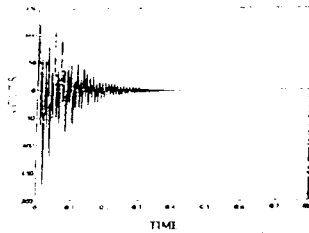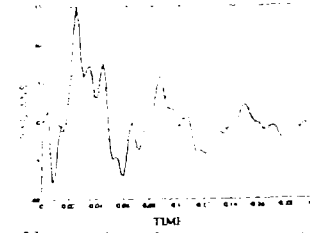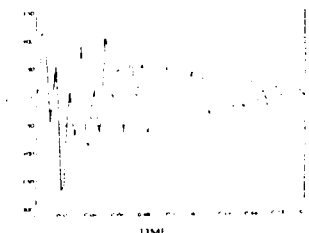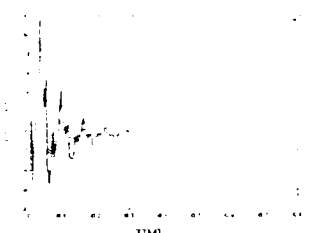

Figure 9 Tip rotation of a single flexible link manipulator with a model adaptive controller (25% of tip mass)
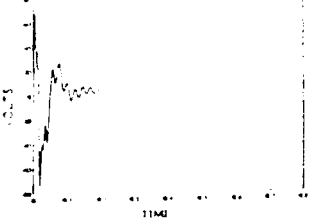

Figure 11 Control force with model adaptive controller

Preliminary design of optimal H_2 and H_∞ controlled structures

Robert N. Jacques and David W. Miller
Space Engineering Research Center
Massachusetts Institute of Technology

Abstract

Recent trends in spacecraft design which yield larger structures with more stringent performance requirements place many flexible modes of the structure within the bandwidth of active controllers. The resulting complications to the spacecraft design make it highly desirable to understand the impact of structural changes on an optimally controlled structure. This work uses low order structural models with optimal $\mathcal{H}_2$ and $\mathcal{H}_\infty$ controllers to develop some basic insight into this problem. This insight concentrates on several basic approaches to improving controlled performance and how these approaches interact in determining the optimal designs.

1   Introduction

Traditionally, control and structure subsystems in spacecraft have been designed separately. This was an efficient approach when the required bandwidth of rigid body controllers was well below the frequencies of the flexible modes of the structure. Recently however, increasing size in spacecraft structural designs have resulted in ever decreasing frequencies for flexible modes, while more stringent pointing and alignment requirements have resulted in control designs of increasing bandwidth. The net result is that several to many flexible modes of a spacecraft structure can lie within the bandwidth of onboard controllers. The strong interaction of structure and control that arises from this makes simultaneous design of these two subsystems highly desirable.

One approach to this problem can be called numerical control/structure optimization [1]. In this method, one first selects a basic structural and control design (*e.g.* a ten bay truss with full state feedback). Several structural parameters (*e.g.* truss member thicknesses) and control gains are designated as design variables and a dynamic performance metric is formulated. A numerical algorithm is then employed to search over the space of allowable designs for a particular one which optimizes the dynamic performance metric with a suitable constraint on the overall mass or size of the structure.

The Achilles Heel of this approach lies in the lack of physical insight yielded by the numerical solution. This insight is crucial in designing any controlled structure, including one which will ultimately be designed numerically. A good understanding of how changes in the structure influence controlled performance is essential in formulating the optimization problem to be solved numerically. For example, physical insight will hopefully lead to a wise, rather than arbitrary selection of the design variables. Otherwise selection of design variables can place design objectives at odds and thereby yield a needlessly compromised solution.

One can envision four basic ways that a change to the structure of a spacecraft can alter its controlled performance. First, it can alter the way that disturbances influence the dynamics of the structure (disturbability). Second, it can affect the influence of control actuators (controllability). Third, it can change the way in which the dynamics of the structure appear in the performance metric (observability). And finally, it can change the frequencies and damping ratios of the structure. It should be noted that

there is also a fifth way that one can alter the performance of a controlled structure, and that concerns changes which affect the robustness of the controllers. However, this is beyond the scope of this work. The next section describes the basic mathematical controlled structure problem and formulates a low order problem (typical section) useful in studying how these different approaches interact.

2 Problem Description and Typical Section

A general linear structure can be described by the equation of motion:

$$
\begin{aligned}
M(\alpha)\ddot{r} + D(\alpha)\dot{r} + K(\alpha)r &= F(\alpha)u + G(\alpha)v \\
y &= N(\alpha)r
\end{aligned}
\tag{1}
$$

where r is a vector of physical displacements on the structure, y is a vector of displacements (either physical or modal) to be controlled, u is a vector of control forces, and v is a vector of disturbance forces. The vector α is an array of real values which represent quantities in the structure which can be varied by the engineer in the design process. For example, the elements of α could represent the diameters of members in a truss structure. The goal of control/structure optimization is to find a suitable combination of structural parameters and control force which minimizes the performance metric.

$$
(\alpha^{*}, u^{*}(t)) = \arg \min_{u(t), \alpha \in \mathcal{D}} J(M(\alpha), D(\alpha), K(\alpha), F(\alpha), G(\alpha), N(\alpha), u(t))
\tag{2}
$$

The set of allowable designs, $\mathcal{D}$, is usually constrained to contain only designs that are below some maximum value of size or mass.

Equation 1 can be transformed into a modal state space representation where the state vector is modal displacement, q, and frequency normalized modal velocity, q':

$$
\frac{d}{dt} \begin{bmatrix} q \\ q' \end{bmatrix} = \begin{bmatrix} 0 & \omega \\ -\omega & -2\zeta\omega \end{bmatrix} \begin{bmatrix} q \\ q' \end{bmatrix} + \begin{bmatrix} 0 \\ \omega^{-1}\Phi^{T}F \end{bmatrix} u + \begin{bmatrix} 0 \\ \omega^{-1}\Phi^{T}G \end{bmatrix} v
$$

$$
y = \begin{bmatrix} N\Phi & 0 \end{bmatrix} \begin{bmatrix} q \\ q' \end{bmatrix}
\tag{3}
$$

The matrices ω and ζ are diagonal matrices containing the natural frequency and damping ratio of each mode and Φ is the modal transformation matrix:

$$
r = \Phi q \qquad q' = \omega^{-1}\dot{q} \qquad \Phi^{T}M\Phi = I \qquad \Phi^{T}K\Phi = \omega^{2} \qquad \Phi^{T}D\Phi \approx 2\zeta\omega
\tag{4}
$$

Altering certain matrices in Equation 3 corresponds exactly to the approaches for altering controlled performance mentioned above. It is useful to make the following definitions.

Frequency Matrix	ω
Damping Matrix	ζ
Controllability Matrix	$\mathcal{F} = \omega^{-1}\Phi^{T}F$
Disturbability Matrix	$\mathcal{G}_{v} = \omega^{-1}\Phi^{T}G \quad$ or $\quad \mathcal{G}_{d} = \omega^{-2}\Phi^{T}G$
Observability Matrix	$\mathcal{N} = N\Phi$

$$
\tag{5}
$$

Note the appearance of inverse frequency in the expression for controllability. It reflects the inherent resistance of higher frequency modes to impulsive control forces. Similarly, there are frequency terms in the disturbability expressions, except that there are two forms. The first corresponds to impulsive (velocity) disturbance forces, the second corresponds to static (displacement) disturbance forces. The choice of exponents in these expressions is clarified below.

Any alteration to the structure can be perceived as having two stages of effects. First, a change to the structure alters its frequencies, damping, controllability, disturbability, and observability. Second the changes in these quantities alter the controlled performance of the system. This view of the problem is useful because it is relatively easy to understand how a change to the structure will influence its frequencies, damping, controllability, disturbability and observability. If one could then understand the relative importance of these quantities in determining controlled performance, then one would have a good understanding of the entire problem. To develop this understanding, it is useful to study the system shown in Figure 1.
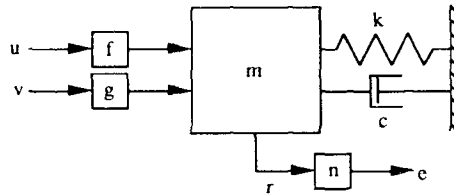
Figure 1: Typical section

This system is typical of a single mode of a flexible structure. For this reason this model and its associated controller are called a controlled structure typical section. The frequency, damping, controllability, disturbability, and observability matrices for the typical section are simply scalars:

$$\omega = \sqrt{\frac{k}{m}} \quad \zeta = \frac{c}{2m\omega} \quad \mathcal{F} = \frac{f}{\omega} \quad \mathcal{G}_v = \frac{g}{\omega} \quad \mathcal{G}_d = \frac{g}{\omega^2} \quad \mathcal{N} = n \tag{6}$$

and the equation of motion in state space form is:

$$
\begin{aligned}
\dot{x} &= Ax + Bu + Lv \\
y &= Cx \qquad C = \begin{bmatrix} \mathcal{N} & 0 \end{bmatrix} \\
x &= \begin{bmatrix} q \\ q' \end{bmatrix} \quad A = \begin{bmatrix} 0 & \omega \\ -\omega & -2\zeta\omega \end{bmatrix} \quad B = \begin{bmatrix} 0 \\ \mathcal{F} \end{bmatrix} \quad L = \begin{bmatrix} 0 \\ \mathcal{G} \end{bmatrix}
\end{aligned}
\tag{7}
$$

The next sections show how the above parameters influence the controlled performance for the optimally controlled system when two different performance metrics are used.

3 $\mathcal{H}_2$ Problem

One of the most common dynamic performance metrics is the infinite horizon, $\mathcal{H}_2$ performance metric:

$$J = E\left[\int_0^\infty \left(y^T(t)y(t) + u^T(t)Ru(t)\right) dt\right] \tag{8}$$

where $E[\cdot]$ is the expectation operator and R is a symmetric, positive-definite control weighting matrix. The disturbance is specified as an expected value of the outer product of the initial state. In this case, it is assumed that the initial state comes about due to either static or impulsive forces applied to the disturbance inputs of the system:

$$
S = E\left[x(0)x^T(0)\right] = \begin{bmatrix} E[q(0)q^T(0)] & 0 \\ 0 & 0 \end{bmatrix} \qquad \text{displacement disturbance}
$$

$$
= \begin{bmatrix} 0 & 0 \\ 0 & E[q'(0)q'^T(0)] \end{bmatrix} \qquad \text{velocity disturbance}
$$

$$
E\left[q(0)q^T(0)\right] = \mathcal{G}_d V \mathcal{G}_d^T \qquad E\left[q'(0)q'^T(0)\right] = \mathcal{G}_v V \mathcal{G}_v^T \tag{9}
$$

where V is the expected value of the outer product of the disturbance force v. It should be noted that there is also a stochastic formulation of this performance metric. However,

Table 1: $\mathcal{H}_2$ Performance Costs

Control Type	Disturbance Type	
	Velocity	*Displacement*
Open Loop or Heavy Damping	$J_{\text{opt}} = \frac{\mathcal{G}^2 \mathcal{N}^2}{4\zeta\omega}$	$J_{\text{opt}} = \frac{\mathcal{G}^2 \mathcal{N}^2}{4\zeta\omega}\left(1 + 4\zeta^2\right)$
Expensive Control, Light Damping	$J_{\text{opt}} = \frac{\mathcal{G}^2 \rho |\mathcal{N}|}{|\mathcal{F}|}$	$J_{\text{opt}} = \frac{\mathcal{G}^2 \rho |\mathcal{N}|}{|\mathcal{F}|}$
Cheap Control, Light Damping	$J_{\text{opt}} = \frac{\mathcal{G}^2 \sqrt{|\mathcal{N}|\rho^3\omega}}{\sqrt{|\mathcal{F}|^3}}$	$J_{\text{opt}} = \frac{\mathcal{G}^2 \sqrt{|\mathcal{N}|^3\rho}}{\sqrt{|\mathcal{F}|\omega}}$

if V is taken to be the intensity of a Gaussian White Noise disturbance, then the resulting analysis would be completely analogous to that for the velocity disturbance.

Notice that frequency does not appear in the above disturbance expressions. This was the chief reason for including frequency in the original definitions for the disturbance matrices, as it reflects the differing resistance of higher frequency modes to static and impulsive forces.

A well known result of optimal control theory, is that for an optimally controlled system described by Equations 7 and 9 the $\mathcal{H}_2$ cost is [2]:

$$J_{\text{opt}} = \text{tr}\left\{PS\right\} \tag{10}$$

where P is the symmetric, positive-definite solution of:

$$PA + A^T P + C^T C - PBR^{-1}B^T P = 0 \tag{11}$$

For the typical section problem, these equations can be solved in closed form with the control penalty defined as $R = \rho^2$ [3]:

$$J_{\text{opt}} = \frac{\rho^2 \mathcal{G}_d^2 V \omega}{\mathcal{F}^2}\left(\sqrt{\beta^2 + 1}\sqrt{4\zeta^2 + 2\sqrt{\beta^2 + 1} - 2} - 2\zeta\right) \quad \text{displacement disturbance}$$

$$J_{\text{opt}} = \frac{\rho^2 \mathcal{G}_v^2 V \omega}{\mathcal{F}^2}\left(\sqrt{4\zeta^2 + 2\sqrt{\beta^2 + 1} - 2} - 2\zeta\right) \quad \text{velocity disturbance}$$

$$\text{where} \quad \beta = \frac{\mathcal{N}\mathcal{F}}{\omega\rho} \tag{12}$$

Equation 12 is too complicated to make any easy inferences about the relationship between frequency, damping, controllability, disturbability, observability and performance. However, the two values, ζ and β completely determine the character of the equations, and it is illustrative to consider the asymptotic behavior of the performance with respect to these values.

Table 1 shows how Equations 12 behave for limiting values of control effort, β and damping ζ. The top row of this table shows the behavior of the cost as the control forces become ineffective compared to the internal forces of the damping. In that case, the control terms ($\mathcal{F}$ and ρ) drop out, leaving an expression that represents the performance of the open loop system. The expressions for both disturbance cases are very similar with the exception of how damping influences performance. For damping levels less than 50%, increased damping improves performance, however, for larger levels, increased damping actually inhibits performance for the displacement disturbance. This reflects the tendency of heavily damped systems to recover slowly from initial displacements.

The second and third rows of the table show the behavior of the system when the control forces exceed the influence of the damping. In that case, the system shows two
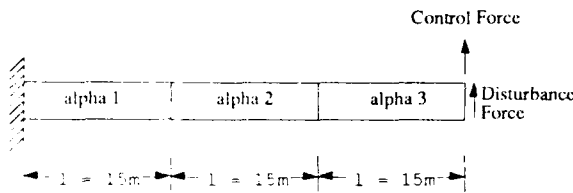
Table 2: Results

λ	Optimal Design		
	α_1	α_2	α_3
0.0000	.10	.10	.10
0.0001	.10	.10	1.59
0.0010	.10	.31	5.00
0.0100	0.38	1.18	15.72
0.1000	2.50	5.48	53.04
0.2000	4.57	8.93	81.48
0.3000	6.58	12.02	108.66
0.4000	8.65	15.10	137.97
0.5000	10.95	18.56	171.79
0.6000	13.77	22.66	213.96
0.7000	17.59	28.22	271.95
0.8000	24.06	37.32	364.60
0.9000	40.21	60.07	565.21
0.9200	47.49	70.68	644.24
0.9400	58.71	87.88	756.79
0.9600	79.40	122.91	937.62
0.9800	136.80	233.95	1307.86
0.9900	230.35	402.91	1779.25

Figure 2: Beam example of Milman *et.al.*

different types of behavior depending on the level of control effort. For low control effort (expensive control), the costs for both disturbance cases are identical. This is because the low control is providing a small amount of active damping and the response of the system takes several cycles to attenuate. The phase difference in the responses imposed by the disturbance type has little effect. For higher control levels (expensive control), the response of the system attenuates in only one or two cycles and the phase difference becomes more important. Hence the displacement and velocity disturbances render different performance in the third row of the table.

It is interesting to note that the addition of control reduces the sensitivity of the system to observability and controllability (although the amount of reduction depends on the control level and disturbance type), however the sensitivity to disturbability remains unchanged. This is because changing the observability or controllability changes the bandwidth of the controller and altering the disturbability does not.

Using the information contained in this Table 1, and information about the sensitivity of frequency, damping, controllability, observability, and disturbability to the design parameters, α, one can infer which of these quantities should be adjusted and which should be ignored in designing a good controlled structure.

As an example, consider a case worked out by Milman *et.al.* [1] (Figure 2) This system consists of a three element, cantilevered, Bernoulli-Euler beam with a tip actuator and an impulsive disturbance also at the tip. The control in this case is optimal full state feedback and the design variables are the thicknesses of the three elements. The metric optimized was a combination of a dynamic performance metric penalizing strain and kinetic energy and a metric penalizing total mass.

$$J \quad \lambda W(\alpha) + (1 - \lambda) \int_0^\infty \left(r^T K r + \dot{r}^T M \dot{r} + \rho u^2 \right) dt \tag{13}$$

The parameter, λ, is adjusted to obtain different levels of tradeoff between weight and performance. An important feature of this problem is that the actuator and the disturbance are collocated. Examining the first column of Table 1 reveals that reducing the magnitude of the disturbability and increasing the controllability will both have favorable effects on the performance. However, the table also shows that when the sensitivity of the disturbability, $\mathcal{G}$, and controllability, $\mathcal{F}$, to the design variables are equal (as in this case), then greater gains can be attained by reducing disturbability at the expense of controllability for all levels of control. Table 2 confirms this suspicion. For almost all values of λ, the design obtained through optimization placed the bulk of the mass at the tip of the beam, where its inertia could help resist any forces applied to the tip.

4 $\mathcal{H}_\infty$ Problem

Another performance metric in common use is the $\mathcal{H}_\infty$ metric:

$$J = \sup_{\omega} \left(y(\imath\omega)^T y(-\imath\omega) + u(\imath\omega)^T R u(-\imath\omega) \right) \tag{14}$$

where the disturbance in Equation 7, v, is Gaussian White Noise of unit intensity. It can be shown that when there is a minimum positive value, γ, such that there exists a symmetric, positive-definite solution to the equation:

$$PA + A^T P + C^T C - P\left(BR^{-1}B^T - \frac{1}{\gamma^2}LL^T\right) = 0 \tag{15}$$

Then for optimal full state feedback control, the value of the performance metric is the square of this limiting value of γ [4].

For the typical section, it is possible to solve for this γ in closed form:

$$J_{\mathrm{opt}} = \gamma_{\mathrm{min}}^2 = \begin{cases} \mathcal{G}^2\left(\frac{\mathcal{F}^2}{\rho^2} + \frac{\omega^2}{\Lambda^2}4\zeta^2(1-\zeta^2)\right)^{-1} & \zeta \le \frac{1}{\sqrt{2}} \\ \mathcal{G}^2\left(\frac{\mathcal{F}^2}{\rho^2} + \frac{\omega^2}{\Lambda^2}\right)^{-1} & \zeta \ge \frac{1}{\sqrt{2}} \end{cases} \tag{16}$$

The same proportionality to $\mathcal{G}^2$ that was present in the $\mathcal{H}_2$ case is also present in the $\mathcal{H}_\infty$ case. However, the dependence on the remaining terms has an interesting form. For very expensive control ($\rho \to \infty$), the term containing the controllability drops out and the cost reverts to the open loop cost. This solution implies that for problems in which the disturbability is relatively insensitive to parameter changes ($\frac{\partial \mathcal{G}}{\partial \alpha} = 0$), then a structure which was optimized for open loop response will also have optimal closed loop response. In other words, sequential design of the structure and control will achieve the same result as simultaneous design. The insensitivity of a system to disturbability can occur frequently in controlled structure design. This is most likely to happen when the disturbance is not well known, or widely distributed and uncorrelated. Hence, there is a possibility that it may actually be easier to design $\mathcal{H}_\infty$ controlled structures than there $\mathcal{H}_2$ counterparts. However, it still remains to be shown that this result applies to higher order systems.

5   Conclusions and Future Work

The typical section is a useful tool for understanding the implications of structural changes under different types of control. The ability to formulate closed form solutions makes it very easy to understand the functionality of the performance on disturbability, controllability, observability, frequency, and damping. As long as the coupling between modes in a structure remains light, the typical section results, which exactly capture the behavior of a single controlled mode, should be reliable in higher order systems. However at high control levels, the modal coupling becomes more severe and the typical section insights become less reliable. More work needs to be done in understanding how complex systems behave at high control levels.

References

1 M. Milman, M.Salama, R. Scheid, R. Bruno, and J.S.Gibson, JPL Technical Report D-6767, October, 1989.

2 R. Kwakernaak and R.Sivan, *Linear Optimal Control Systems*. John Wiley and Sons, Inc., 1972.

3 R. N. Jacques and D.W. Miller. MIT SERC Report 1-91, February 1991.

4 J.C. Doyle, K. Glover, P.P. Khargonekar, and B.A.Francis. *IEEE Transactions on Automatic Control*, 34(8), August 1989.

Control of Grumman large space structure using H_∞ optimization

Chien Y. Huang and Gareth J. Knowles

Corporate Research Center, Grumman Corp., MS A08-35, Bethpage, NY 11714, USA

ABSTRACT: The control design for a large space structure using H_∞ methods is described. The plant is modeled using mass-spring units, from which the first 69 modes are kept. Artificial damping is first added to the system using rate feedback and a reduced-order model is obtained. The H_∞ optimization technique is then applied to achieve a bandwidth of 150 Hz and an overall disturbance rejection of over 2400:1. Caveats regarding sensor and actuator dynamics are put forth along with other issues relevant to the control design of a large space structure.

1. INTRODUCTION

Studies on the dynamics and control of the large space structure (LSS) have been actively conducted since the Apollo program [1]. With the upcoming launch of Space Station Freedom (SSF), there is a renewed interest in this area. This is partially due to anticipated experiments that require SSF modules to perform maneuvers that, because of the flexibility of their frames, can cause significant control-structure interaction. Furthermore, requirement to align and point the structure with high precision can only be met using active control.

Two major problems (A third problem is placement of actuators and sensors, see [2]) are associated with the control of an LSS. One of them is the modeling. High-fidelity mathematical description of an LSS inevitably leads to a high-order system from which, due to numerical considerations, a reduced-order model must be extracted for control design. The question becomes that of modeling just enough dynamics to account for all motions of interest without incurring control and observation spillovers [3] (the former is excitation of uncontrolled modes and the latter is excitation of unobservable modes). A typical approach is to use modal decomposition to incorporate explicitly the desired modes, carry out the control design, and then perform tests to validate the result.

The other problem is control design itself. Several control techniques have been applied to LSS. They include pole-placement [4], modal control [5], LQG [6], LQG/LTR [7], etc. The main difficulty in this phase is generation of a stabilizing feedback control to a large-order plant. Although most of these approaches have shown to be successful in computer simulations, none of them are conclusive as it is impossible to test an LSS in 1-g conditions (the strength of the frame is not sufficient to support the mass without deformations). Therefore, in an effort to validate the techniques, several experiments [8,9] are being carried out using small-scale space structure.

Past LSS control design methods do not directly address modeling uncertainties. H_∞ optimization [10,11] is a new control synthesis method that allows the designer to shape frequency response characteristics of the plant to achieve desired performance and, more important, robustness to account for unmodeled dynamics. The objective of this paper is to apply the H_∞ control design methodology to the control of a large space structure. The goal is to conduct a feasibility study, with intent to point out areas for further research.

The organization of the paper is as follows. The dynamic model and the design approach are described first. The inner-loop feedback design is then addressed, followed by model reduction. Next, H_∞ optimization is examined and simulation results are shown. Finally, practical concerns of adding sensor and actuator dynamics are studied and additional comments are offered as conclusions.

2. GRUMMAN LARGE SPACE STRUCTURE

The Grumman Large Space Structure (GLASS) is a generic truss structure intended for precision pointing (Fig. 1). It is modeled in NASTRAN code using 112 nodes connected as mass-spring units from which dynamic modes can be calculated. The first 69

modes, ranging from 2 Hz to 66 Hz, are included in this study. The actuators and rate sensors are assumed to be collocated and situated near the nodes. Forty-eight actuators (and sensors) are present and they are found in groups of three (for x-, y-, z-axes) evenly distributed across GLASS around nodes 2, 3, 17, 20, 34, 35, 53, 56, 58, 59, 77, 80, 94, 95, 109, and 112. Note that this is a relatively small number; a full set would consist of over 336 actuators. Two additional line-of-sight (LOS) sensors are located in the middle of GLASS for precision-pointing. Random disturbances of normal distribution are assumed to exist at six distinct nodes (9, 26, 41, 66, 89, and 102). The control of GLASS is necessary because it has very low (actually none due to our modeling) damping and a large number of resonant modes. As a result, environmental disturbances can induce unacceptable vibrations. The design goals in this study are to attenuate LOS error by a factor of at least 2000:1 from 0 to 15 Hz and nominally to push the bandwidth of the system to 150 Hz.

3. DESIGN PROCEDURE

The design procedure is to first add damping to the system using collocated rate-feedback control[*]; this is the inner-loop design. After the plant is stabilized, an outer-loop H_∞ controller is added to reduce LOS error and to expand the system bandwidth. This design phase is iterated with simulation runs until the responses are satisfactory. A simplified control system block diagram is shown in Fig. 2. The approach used in this study follows closely the methodology outlined in [12].
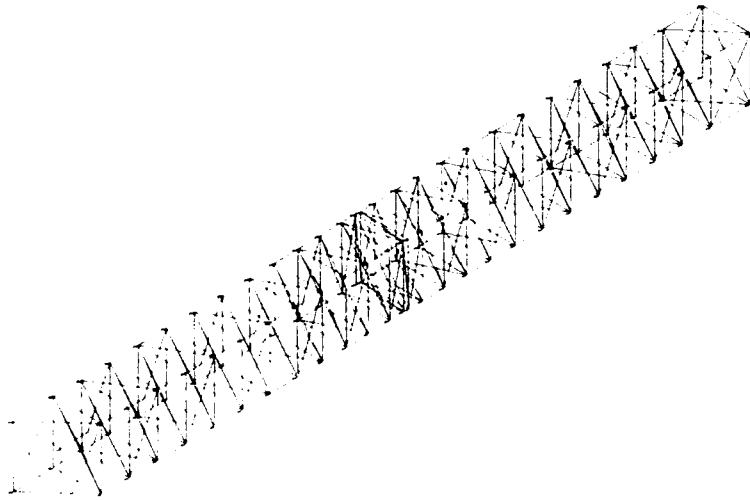

Fig. 1 Grumman Large Space Structure

---

[*]   There are strong reasons for utilizing collocated rate feedback [8]. However, physical constraints may force non-collocated measurements, which present additional problems.
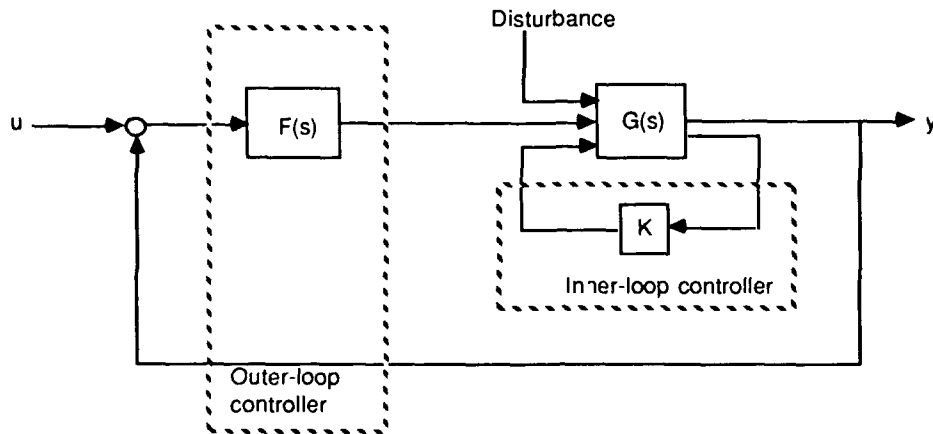
Fig. 2 Control system block diagram.

For GLASS, there are 138 states (69 modes), and 48 controls. Due to collocation, the number of outputs is also 48, while the dimension of disturbance vector is 18. That is:

$$\dot{x}_{138} = A_{138 \times 138} x_{138} + B1_{138 \times 48} u_{36} + B2_{138 \times 18} \eta_{18} \tag{1}$$

$$y_{48} = C_{48 \times 138} x_{138} \tag{2}$$

where x consists of modified generalized displacement, matrices A, B, C are formed from mass matrix, stiffness matrix, and generalized force, and η is the external disturbance.

These equations are used for inner-loop control design. For outer-loop control, only actuators at nodes 53, 56, 58, and 59 are used to further reduce the LOS deviations, and only the LOS sensors are used as measurement. That is,

$$\dot{x}_{138} = A_{\cdot 38 \times 138} x_{138} + \bar{B}_{138 \times 12} u_{12} \tag{3}$$

$$\bar{y}_2 = \bar{C}_{2 \times 138} x_{138} \tag{4}$$

where $\bar{B}$ is the appropriate submatrix of $B1$, and $\bar{C}$ is the corresponding submatrix of C.

IV. Inner-Loop Control Design

Because there is no damping in our modeling of GLASS, artificial damping must be provided before H_∞ control design can be applied (since H_∞ requires no poles to be on $j\omega$ axis). By energy considerations, it is easy to see that any system described by positive semidefinite matrix is guaranteed to be stabilized by collocated constant-gain rate-feedback control (although this is not necessarily true with the addition of actuator and sensor dynamics, see Section VII). Experimentation and extensive simulation led to the choice of feedback gain K of 1400 I_{48}. The time responses of the line-of-sight sensors due to disturbances with the rate-feedback are shown in Fig. 3. Although not shown, these responses are on the order of 30 times less than system responses without the compensation.

V. Model Reduction

After the system is stabilized, the order of the model must be reduced so that the outer control loop can be designed. To do so, the singular values of the modified plant
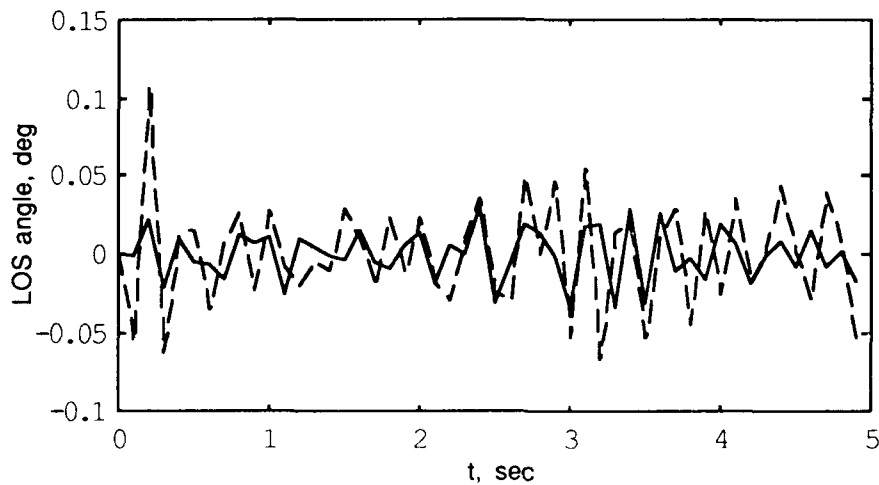
Fig. 3 LOS responses due to random disturbances after rate feedback.

dynamics $\mathbf{G'}(s) = \bar{\mathbf{C}}(s\mathbf{I}-\mathbf{A})^{-1}\bar{\mathbf{B}}$ are plotted (Fig. 5) to ascertain the important dynamics and the corresponding approximation for a particular frequency range. From Fig. 5, $\mathbf{G'}(s)$ is divided into slow, medium, and fast modes, that is

$$\mathbf{G'}(s) \;=\; \mathbf{G'}_s(s) + \mathbf{G'}_m(s) + \mathbf{G'}_f(s) \tag{5}$$

It can be seen from Fig. 4 that most of the dynamics is concentrated in the medium frequency range, with small contributions from slow and fast modes. This leads us to make the approximation

$$\mathbf{G'}(s) \;=\; \mathbf{G'}_m(s) + \Delta\mathbf{G'}(s) \;\approx\; \mathbf{G'}_m(s) \tag{6}$$

Fig. 4 Singular values of the system after rate feedback.

This quasi-equality holds as long as the modeling error Δ is below the robust frequency [12], which is defined as the lowest frequency where the minimum singular value of $G'_m(s)$ is greater than the maximum singular value of $\Delta G'(s)$. For GLASS, it is found after some test that there are 32 slow-mode states, 77 medium-mode states, and 29 fast-mode states. Seventy-seven states is still a very large system to work with; therefore, further model-reduction is necessary.

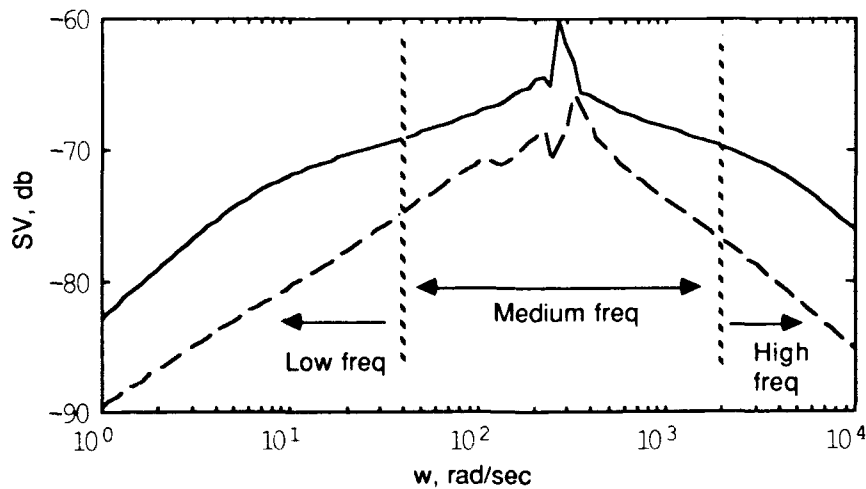There are several model-reduction techniques [13,14]. The Schur method for balanced model reduction [14] is employed in this case. The methodology computes matrices V_r and V_l containing the bases for the right and left eigenspaces of RQ, where R is the reachability (or controllability) Grammian and Q is the observability Grammian. This is done via Schur vector decomposition only for those states associated with large Hankel singular values. The reduced-order model is then found by multiplying the original model to the bases of singular value decomposition of V_r and V_l.

Because of the small number of actuators and sensors (12 for the outer loop design) involved (unlike other reported studies), GLASS is not strongly controllable or observable. Consequently, the smallest model that was found to give satisfactory match for medium modes is of the 25th-order. The singular value plot of the full (77 states) and reduced (25) models are shown in Fig. 5.
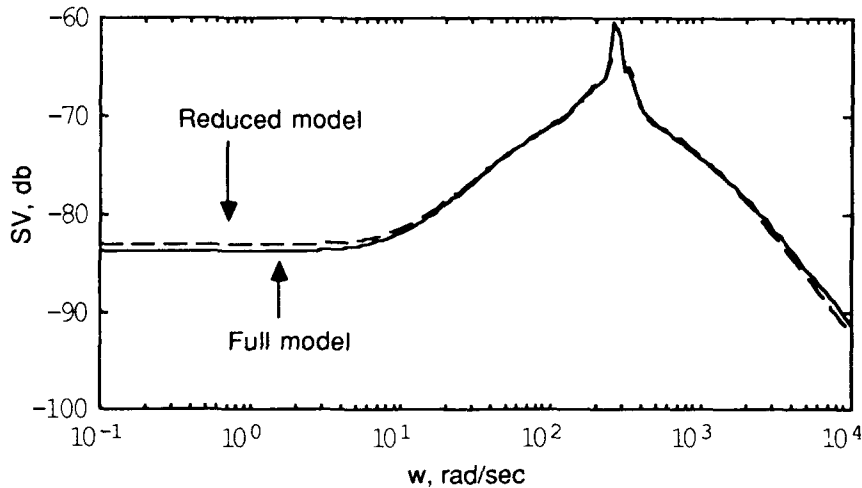
Fig. 5 Comparison of 77-state medium model and 25-state reduced model.

VI. H_∞ Control Design

H_∞ optimal control design is carried out by formulating the equations into a 2-block mixed-sensitivity H_∞ problem. In this framework, the objective is to minimize the inequality $\|T\|_\infty \leq 1$, where $\|\cdot\|_\infty = $ H-infinity norm

$$T = \text{closed-loop transfer function} = \begin{bmatrix} \gamma W_1^{-1} S \\ W_3^{-1}(I\text{-}S) \end{bmatrix}$$

$$S = \text{sensitivity matrix} = (I + G'F)^{-1}$$
$$F = H_\infty \text{ controller.}$$

The optimization technique hinges on the selection of the weighting matrix W_1 and W_3, which trades the performance and robustness specification in frequency domain. γ is a parameter that must be varied until the transfer function T assumes desired shape.

The reduced-order system must first be "squared-down" before H_∞ methods can be applied. That is, the number of inputs and outputs must be made equal. Since we have two

LOS outputs and 12 actuators, a pre-compensator **P** must be designed. An easy solution is to use the left pseudo-inverse of the first Markov parameter $(\mathbf{C_s B_s})$ of the slow mode system. The rationale is that any contribution due to low-order dynamics behaves like a first-order lag, which essentially is captured by the first Markov parameter. Therefore, we set **P** to be $(\mathbf{C_s B_s})^{\#}$.

The weighting functions for this design are chosen based on desired bandwidth and disturbance rejection. Weighting matrix $\mathbf{W_1}$, which is intended to minimize sensitivity function, is chosen to be

$$\mathbf{W_1}(s) = \gamma \cdot \text{diag}(6.25e^{12} \, (\frac{s+2500}{s+50}), \ 6.25e^{12} \, (\frac{s+2500}{s+50})) \tag{7}$$

This weighting matrix is chosen to provide adequate low and medium frequency gains that are necessary to achieve performance. Weighting matrix $\mathbf{W_3}$, which is used for robustness purpose, is chosen to be

$$\mathbf{W_3}(s) = \text{diag}(\frac{s}{1000}, \frac{s}{1000}) \tag{8}$$

This weighting matrix ensures that the system bandwidth is roughly 1000 rad/sec or 150 Hz.

With these weighting matrices, we can compute the H_∞-optimal controller $F(s)$, which is of the same order as the system (25th-order in this case). With this controller, the LOS error is further attenuated by an additional factor of over 80 as can be seen in Fig. 6, where the responses of the line-of-sight sensors due to random disturbances are shown for the H_∞ controller turned on at a 2 sec mark. Thus, with the H_∞ controller we have accomplished disturbance attenuation and increased the total system bandwidth at the same time.
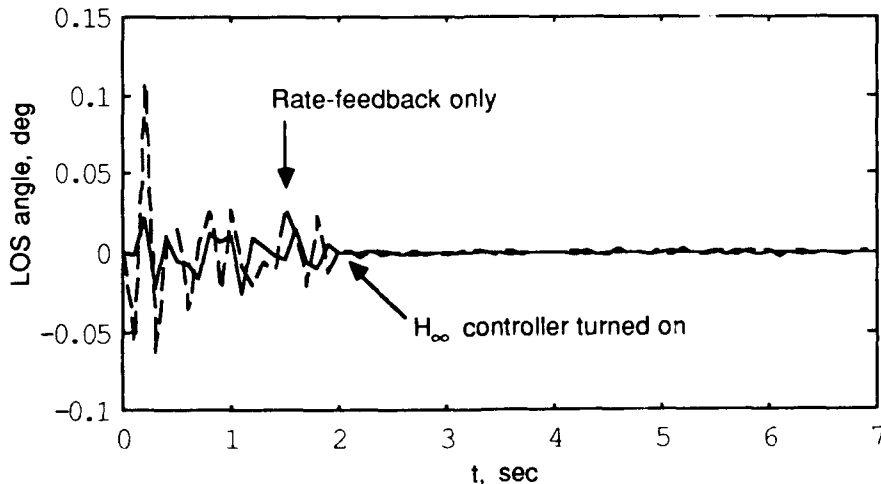

Fig. 6 System responses with rate-feedback and H_∞ controller.

VII. Impact of Actuator and Sensor Dynamics

Previous results were obtained without considering sensor and actuator dynamics. However, upon close examination, they turned out to be important and have to be included. This is especially true for the inner-loop design, where rate-feedback was used to provide

artificial damping. When both actuator and sensor dynamics are present, such scheme actually may destabilize the system. To see this, consider the following formulation:

plant: $\dot{x} = Ax + Bu$ (9)

sensor: $\dot{z} = A_s z + B_s y$ (10)

actuator: $\dot{w} = A_a w + B_a u_a$ (11)

Assuming constant feedback, that is $u_a = -Kz + L\delta$, we have as the closed-loop system

$$\dot{x}_c = \begin{bmatrix} A & 0 & B \\ B_s C & A_s & 0 \\ 0 & -B_a K & A_a \end{bmatrix} \begin{bmatrix} x \\ z \\ w \end{bmatrix} + \begin{bmatrix} 0 \\ 0 \\ L \end{bmatrix} \delta \qquad (12)$$

It can be shown that if position feedback is used, the system described by Eq. 16 is always unstable regardless of K. If rate feedback is used, then some (but small) damping can be achieved for small and medium values of K, and large K will destabilize the system. Finally, if both position and rate-feedback is used, a greater amount of damping can be obtained, but large values of K will still lead to instability.

A graphical explanation of the problem can be obtained using the root-locus techniques. Poles and zeros always interlace along (or close to) $j\omega$-axis. If position feedback is used, then there is no zero at origin. If rate feedback is used, there is a zero at the origin. And if both rate and position feedbacks are used, the zero is along the real-axis. For simplicity, we assume that both actuator and sensor dynamics are of first-order with different time constants. Higher-order dynamics will make the situation worse.

As the feedback gain K increases, most of the poles go to the zeros. The net count of poles minus zeros will determine the angles of the asymptotes of "free" poles. If the zero at the origin is not present (i.e., position feedback), the net count is four and the angles are ± 45 degrees to the perpendicular. In this case, two poles on the $j\omega$-axis depart immediately to the right-half plane. If rate feedback is employed, the net count is three and the angles are $60°$, $180°$, and $300°$. In this case, the "free" poles are pulled toward left-half plane before heading back to right-half plane. When both rate and position feedbacks are present, the situation is similar, except the poles are pulled further into left-half plane due to movement of the zero which was at the origin. The amount of damping on all poles is determined by how far they move into left-half plane. This is dependent on the original position of the poles and zeros. An additional problem arises when the same gain is used for all feedback paths. In that case, zeros also move when the gain is changed (because the problem is no longer single-input single-output).

This analysis tells us that constant gain feedback alone may not be sufficient to provide artificial damping needed to stabilize GLASS when actuator and sensor dynamics are present; thus other means must be conceived. One solution is to use dynamic feedback to further redistribute the pole-zero locations. This procedure may not be straightforward due to the dimensions of the plant model. Another approach is to assume damping. It turns out that our original model is not realistic since some form of mechanical damping is always available, although its modeling may not be well-known. Incorporation of this damping effect may alleviate the need to provide artificial damping. A third solution is to add passive damping. Currently, there is effort to further augment damping of the LSS using visco-elastic materials and piezoceramic attachments [15]. This may be necessary in order for any of the active control strategies to be successful.

VIII. Conclusions

The control design for a large space structure using H_∞ methods is described. The design is carried out by first stabilizing the system using rate-feedback as inner-loop control and then applying the H_∞ controller as the outer-loop control to extend the system bandwidth

and exert higher signal attenuation at specific frequency ranges. The methodology has shown to be able to tradeoff performance versus robustness, something that most of the modern control techniques lack.

As mentioned in the main body, the system is weakly controllable and observable. As a result, the final H_∞ design resembles a high-gain controller. This is unavoidable given the requirement to extend the bandwidth and at the same time achieve desired attenuation. The situation will improve as more actuators and sensors are added. In addition, rate-limiting and control saturation have been ignored. In a more detailed design, their effects on the system stability and response must be addressed. The structure used does not possess any damping. This poses a great demand on inner-loop stabilization. It is expected that some passive damping be built into the structure to alleviate the requirement. This will also address concerns of actuator and sensor dynamics, which have been shown to be important. Finally, limited experimentation was conducted with the weighting matrices. In a more thorough design, they should be extensively studied to arrive at a more optimum setting.

References

1.   Nurre, G. S., Ryan, R. S., Scofield, H. N., and Sims, J. L., "Dynamics and Control of Large Space Structures," *J. of Guidance, Control, and Dynamics*, Vol. 7, No. 5, Sept.-Oct., 1984, pp. 514-526.

2.   Wu, Y. W., Rice, R. B., and Juang, J. N., "Sensor and Actuator Placement for Large Flexible Space Structures," *Proc. of JACC*, 1979, pp. 230-238.

3.   Balas, Mark J, "Trends in Large Space Structure Control Theory: Fondest Hopes, Wildest Dreams," *IEEE Trans. Automatic Control*, Vol. AC-27, No. 3, June 1982, pp. 522-535.

4.   Wu, Y. W., Rice, R. B., and Juang, J. N., "Control of Large Flexible Space Structures using Pole Placement Design Techniques," *J. of Guidance, Control, and Dynamics*, Vol. 4, No. 3, May-June, 1981, pp. 298-303.

5.   Meirovitch, L., Baruh, H., and Oz, H., "A Comparison of Control Techniques for Large Space Structure," *J. of Guidance, Control, and Dynamics*," Vol. 6, No. 4, Aug. 1983, pp. 302-310.

6.   Gran, Richard, Rossi, Michael, and Moyes, H. Gardner, "Optimal Digital Control of Large Space Structures," *J. of Astronautical Sciences*, Vol. 27, No. 2, April-June 1979, pp. 115-130.

7.   Sundararajan, N., Joshi, S.M., and Armstrong, E. S., "Robust Controller Synthesis for a Large Flexible Space Antenna," *J. of Guidance, Control, and Dynamics*, Vol. 10, No. 2, March-April, 1987, pp. 201- 207.

8.   Knowles, G., and Rossi, M., "Broadband Control of a Cantilevered Triangular Plate." *IEEE Control and Decision Conference*, Tampa, FL, 1989.

9.   Chu, Cheng-Chih, Smith, Roy S., and Fanson, "Robust Control of an Active Precision Truss Structure," *Proc. of American Control Conference*, San Diego, CA, May, 1990, pp. 2490-2495.

10. Francis, B. A., *A Course in H_∞ Control Theory*," Springer Verlag, Heidelberg, Germany, 1987.

11. Doyle, J. C. *et al.*, "State-Space Solutions to Standard H_2 and H_∞ Control Problems," *IEEE Trans. Automat. Contr.*, Vol. AC-34, No. 8, pp. 831-847, Aug, 1989.

12. Safonov, M. G., Chiang, R. Y., and Flashner, H., "H_∞ Robust Control Synthesis for a Large Space Structure," *Proc. of Automatic Control Conf.*, Atlanta, Georgia, pp. 2038-2045, 1988.

13. Moore, B.C., "Principal Component Analysis in Linear Systems: Controllability, Observability, and Model Reduction," *IEEE Trans. Automat. Contr.*, Vol. AC-26, No. 1, pp. 17-31, Jan, 1981.

14. Safonov, M. G., and Chiang, R. Y., "Schur Balanced Model Reduction," *Proc. of Automatic Control Conf.*, Atlanta, Georgia, pp. 1036 - 1040, 1988.

15. Su, J., Rossi, M., Knowles, G., and Huang, C., "Piezoceramic/DSP-Based Integrated Workstation for Modal Identification and Vibration Control," Proc. of AMAS Conference, Alexandria, VA, Nov. 5-8, 1991.

Influence of controller gains on system parameters of feedback controlled flexible structures

James A. Fabunmi

AEDAR Corporation, Landover, MD 20785

ABSTRACT: The system consisting of the baseline flexible structure modified by the active controllers is considered. Computer algebra is used to derive expressions for the system transfer functions, using the known transfer functions of the baseline flexible structure and the feedback gains of the active controllers. The roots of the characteristic polynomial of this transfer function give the system resonant frequencies and damping parameters. These results permit the parametric study of the placement of the resonant frequencies and damping parameters of the combined system, as functions of the feedback gains.

1. INTRODUCTION

The technology of active control of structures has been the subject of considerable research interest over the past decade in part because of the need to suppress excessive vibrations associated with the deployment of large flexible structures in space (Various Authors, 1986; Atluri and Amos (Ed.), 1988). The most popular approach to the design of the active control schemes follows the paths of modern control theory which involves optimal state-space feedback control (Various Authors, 1984, 1986; Atluri and Amos (Ed.), 1988; O'Donoghue and Atluri, 1985; Horner and Walz, 1985), or output feedback control (Meirovitch, 1988; Garcia and Inman, 1990). The objective of this paper is to present the results of recent research aimed at the development of simple algorithms for calculating actuator feedback gains, based on specified modal characteristics of the closed-loop system.

Techniques based on computer algebra were reported by Fabunmi (1989), which permit the derivation of the transfer functions (Laplace transform of the Green's Functions) of the system resulting from the attachment of discrete dynamic substructures to a distributed parameter base-line structure. It is assumed that the algebraic forms of the transfer function of the base-line structure as well as those of the discrete attachments are known. The mathematical form chosen for system transfer functions permits the direct determination of the system parameters as the complex values of the Laplace variable at which singularities of the transfer function occur.

2.   MODELLING OF ACTIVE CONTROLLER ATTACHMENTS

The class of controllers used to illustrate the proposed technique comprises of those in which the output displacements and velocities at a discrete number of locations on the structure, are linearly combined to produce the applied control forces. The implementation of the active controller design involves the application of excitation forces at some spatial coordinate $x = b_i$, which are proportional to displacements and velocities measured at $x = a_i$. Figure 1 is a schematic representation of the interconnection of contollers to the baseline structure.
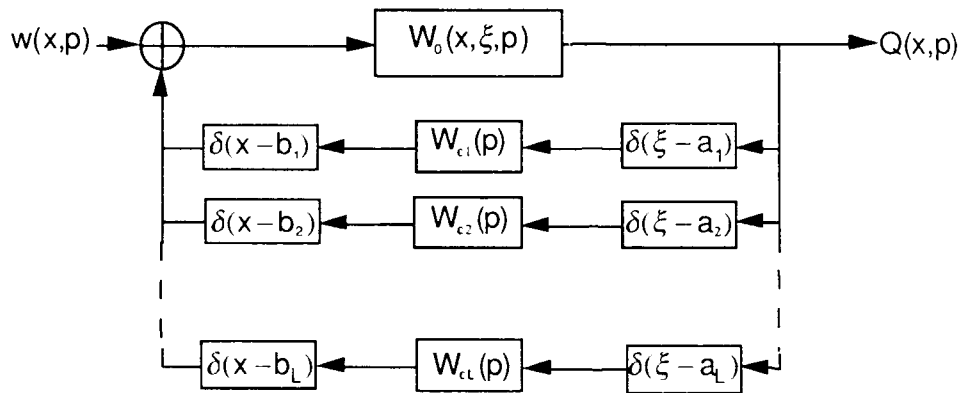

Figure 1.   Schematic of Interconnection of Linear Feedback Controllers to Distributed
Parameter Baseline Structure

For example, the ith controller excitation force could be written as:

$$w_c(b_i,t) = g_i Q(a_i,t) + h_i \dot{Q}(a_i,t) \tag{1}$$

where g_i and h_i are the displacement and velocity feedback gains of the ith controller respectively, $i = 1,2,...L$, L being the total number of controllers; $w_c(x.t)$ is the controller force, $Q(x,t)$ is the measured displacement. The Laplace transform of Equation (1) results in a relationship which is used to define the transfer function of the ith controller as:

$$W_{ci}(p) = \frac{w_c(b_i,p)}{Q(a_i,p)}$$

$$= g_i + h_i p \tag{2}$$

The general algebraic form of the transfer function of the baseline distributed system is taken to be (Chen, 1966; Stakgold, 1979; Butkovskyi, 1982, 1983; Keener, 1988; Fabunmi, 1989):

$$W_0(x,\xi,p) = \sum_{k=1}^{\infty}\left(\frac{1}{\beta_k^2} \frac{\varphi_{0k}(x)\varphi_{0k}(\xi)}{p^2 - p_{0k}^2} \right) \tag{3}$$

where $\varphi_{0k}(x)$ is the kth orthonormal modal function for the baseline structure, p_{0k} is the corresponding modal parameter, and β^2_k is a weighting factor or generalized mass.

The transfer function of the combined system is given by the following integral equation (Butkovskyi, 1983):

$$W(x,\xi,p) = \int W_T(x,\eta,p)W(\eta,\xi,p)d\eta + W_0(x,\xi,p) \tag{4}$$

where,

$$W_T(x,\xi,p) = \int W_0(x,\eta,p)\sum_{i=1}^{L}\delta(\eta - b_i)W_{ci}(p)\delta(\xi - a_i)d\eta$$

$$= \sum_{i=1}^{L} W_0(x,b_i,p)W_{ci}(p)\delta(\xi - a_i) \tag{5}$$

3.   CALCULATION OF CONTROLLER FEEDBACK GAINS

Consider a baseline structure with negligible damping, i.e. $p_{0n1} = i\omega_{0n1}$, the frequencies and exponential growth rates of the closed-loop modes are;

$$\omega_{tn_i} = \sqrt{\omega_{0n_i}^2 - \left\{\frac{1}{2\beta^2}\sum_{i=1}^{L}\{h_i\,\varphi_{0n_i}(a_i)\,\varphi_{0n_i}(b_i)\}\right\}^2 - \frac{1}{\beta^2}\sum_{i=1}^{L}\{g_i\,\varphi_{0n_i}(a_i)\,\varphi_{0n_i}(b_i)\}} \tag{6}$$

$$\sigma_{tn_i} = \frac{1}{2\beta^2}\sum_{i=1}^{L}\{h_i\,\varphi_{0n_i}(a_i)\,\varphi_{0n_i}(b_i)\} \tag{7}$$

The damping of the closed-loop system is controlled by the velocity feed-back gains, whereas the frequency is affected by both the velocity and displacement feedback gains. If L velocity feedback gains are to be calculated directly based on specified values of the growth rates of L system modes, Equation (7) provides a set of L equations for the L desired values of h_i. It may also be desired that there be no shift in the frequencies of these or some other L modes. In that case, a set of L equations for the L values of the displacement feedback gains, g_i, can be set up as follows:

$$-\left\{\frac{1}{2\beta^2}\sum_{i=1}^{L}\{h_i\,\varphi_{0n_i}(a_i)\,\varphi_{0n_i}(b_i)\}\right\}^2 - \frac{1}{\beta^2}\sum_{i=1}^{L}\{g_i\,\varphi_{0n_i}(a_i)\,\varphi_{0n_i}(b_i)\} = 0 \tag{8}$$

Having obtained the values of the velocity and displacement feedback gains in this manner, it is necessary to check the exponential growth rates of the modes that were not included in the analysis, using Equation (7). The purpose of this check is to verify that there are no modes for which the exponential growth rate is positive - an indication that instability of that mode can be induced by the controller.

4.   CONCLUSION

This paper has presented results of computer-algebraic derivations of the characteristic parameters of systems consisting of a distributed baseline structure and output feedback linear active controllers. Expressions which show the explicit dependence of the system parameters on the displacement and velocity feed-back gains as well as the measurement and actuator coordinates were obtained. These results can be applied to the calculation of displacement and velocity feed-back gains based on requirements that certain closed loop modes have specified damping ratios. Because of the simplicity of the calculations involved in this process, it becomes practical to conceive embedded systems which permit the "smart" structure to readjust its feedback gains in order to increase the damping of those of its modes which are most strongly excited by the external dynamical forces.

5.   ACKNOWLEDGEMENTS

REFERENCES

Atluri, S.N., Amos, A.K., (Ed.), 1988, "Large Space Structures: Dynamics and Control". Springer-Verlag.

Butkovskyi, A.G., 1982, "Green's Functions and Transfer Functions Handbook". Ellis Horwood Ltd., Halsted Press.

Butkovskyi, A.G., , 1983, "Structural Theory of Distributed Systems". Ellis Horwood Ltd.

Chen, Y., 1966, "Vibrations: Theoretical Methods", Addison-Wesley.

Fabunmi, J.A., 1989, "Analysis of Modes and Frequencies of Modified Structures Using Computer Algebra", Proceedings International Conference on Noise and Vibration '89, Aug. 16-18,Singapore.

Garcia, E., Inman, D.J., 1990, "Control Formulations for Vibration Suppression of an Active Structure in Slewing Motions", ASME Publication DSC-Vol. 20 - Advances in Dynamics and Control of Flexible Spacecraft and Space-Based Manipulations - (S.M. Joshi, T.E. Alberts, Y.P. Kakad, Editors),   pp. 1-5.

Horner, G.C., Walz, J.E., 1985, "A Design Technique for Determining Actuator Gains in Spacecraft Vibration Control", AIAA/ASME/ASCE/AHS 26th Structures. Structural Dynamics and Materials Conference, Part 2, Orlando Florida, pp. 143-151.

Keener, J.P., 1988, "Principles of Applied Mathematics: Transformation and Approximation". Addison-Wesley.

Meirovitch, L., 1988, "Control of Distributed Structures", pp. 195-212 of (Atluri and Amos, 1988).

O'Donoghue, P.E., Atluri, S.N., 1985, "Control of Dynamic Response of A Continuum Model of A Large Space Structure", AIAA/ASME/ASCE/AHS 26th Structures. Structural Dynamics and Materials Conference, Part 2, Orlando Florida, pp. 31-42.

Stakgold, I., 1979, "Green's Functions and Boundary Value Problems", Wiley Interscience.

Acoustic waveguide embedded sensors for submarine structures

R. T. Harrold and Z. N. Sanjana

Westinghouse Science & Technology Center, 1310 Beulah Rd., Pittsburgh, PA
15235

ABSTRACT: Acoustic waveguides embedded within composite materials offer
the monitoring of internal conditions both during manufacture and
throughout the material lifetime. Consequently these sensors are now
being evaluated as part of a DARPA program called "Embedded Sensors for
Submarine Structures (ES^3)".* Objectives of this program include
monitoring and control of manufacturing processes and assessment of the
relative integrity and load response of the structure.

In this paper, the influence of waveguides on composite strength is
evaluated; their cure, impact and strain monitoring performance
assessed; and a submarine structural monitoring scheme proposed.

1. BACKGROUND AND INTRODUCTION

Acoustic waveguides (AWG) are robust and easy to use, and are ideally
suited for monitoring maufacturing processes and the structural health of
composites (Harrold and Sanjana (1986-1991). These AWG are typically small
(<0.5 mm) diameter rods of polyester-fiberglass or Nichrome with a low
(<0.3) Poisson's ratio. They have the capability to transmit soundwaves
into and out of a material for interrogation, and also to extract
soundwaves (vibrations or acoustic emissions (AE)) from inside a material.
A key feature is that any small changes in the value of the acoustic
impedance (ρc), where ρ is density and c is the acoustic wave velocity of
the medium surrounding an AWG, will greatly change the attenuation of
soundwaves travelling inside the AWG. For example, orders of magnitude
attenuation changes occur during cure monitoring of materials because of
large changes in the viscosity of the curing material.

2. WAVEGUIDE EMBEDMENT

Composite panels were made (within a heated press or autoclave and then
post cured) with four embedded 0.5 mm diameter AWG of Inconel 600
(Nichrome), Fig. 1. A scanning electron microscope (SEM) picture of a
cross section through the laminate, Fig. 2, shows good bonding to the AWG
sensor, but the large (0.5 mm diameter) sensor has caused severe distension
of the fiber pattern in which the ply thickness is ~0.125 mm (~5 mil). In

---

*This DARPA submarine technology program which is managed by James Kelley
is being integrated by McDonnell Douglas (MCAIR), St. Louis, Dan King,
Program Manager. Besides Westinghouse, other subcontractors are McDonnell
Douglas Electronic Systems, Martin Marietta A&N, Martin Marietta Labs,
Stanford University and Virginia Polytechnic.

In order to accommodate the large sensor, some plies were cut in panels made later, but to avoid this problem it is also planned to use smaller sensors of 0.125 to 0.25 mm (5 to 10 mil) diameter. A picture, Fig. 3, shows a 0.5 mm diameter AWG exiting from a composite panel with its termination bonded to an acoustic transmitter/receiver.
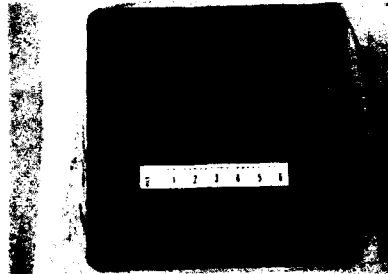

Fig.1-Composite panel of 41, 0-90 cross-plied prepreg sheets. of AS4/3501-6 graphite-epoxy with 4 embedded AWG.

3. CURE MONITORING

Usually with large composite parts, careful control of temperature, pressure and time are the criteria used to ensure uniform cure and quality. Actual monitoring of cure is often carried out only in discrete areas using dielectrometry. Embedded AWG, by virtue of acoustic signal attenuation, Harrold and Sanjana (1986a), allow an integrated measure of the curing over large areas of a part. The AWG cure monitoring results reported here were obtained when the composite was cured within a heated press at a pressure of 50 lb/in^2 (3.45 x 10^5 Pa) and temperatures reaching 180°C during a 5 hour cycle. A typical AWG signal during cure is shown in Fig. 4.
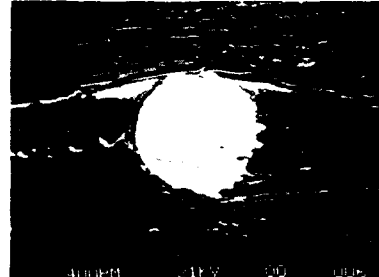

Fig. 2-SEM picture of laminate cross-section.

Throughout the cure cycle, the peak value of the acoustic signal received at the far end of the AWG (10 mil and 20 mil diam. AWG in separate panels) varies over several orders of magnitude, Fig. 5. This occurs because of large changes in resin acoustic impedance and gelation (resin transition from a liquid to a rubbery-gel) can be pinpointed by a minimum value in the WGD transmitted signal, and also by a change in acoustic wave velocity as the acoustic waves travel along the WGD/resin interface. Later in this program it is planned to examine the cure at different depths within thick (50 mm) graphite-epoxy panels.

Fig. 3-Acoustic AWG of 0.5 mm diameter Nichrome exiting from composite panel and bonded to acoustic sensor.

4. WAVEGUIDE TERMINATIONS

In order to improve the AWG connections, experiments are being conducted by using 60° aluminum cones at the AWG terminations to help match the small AWG to the large transducer. This gives
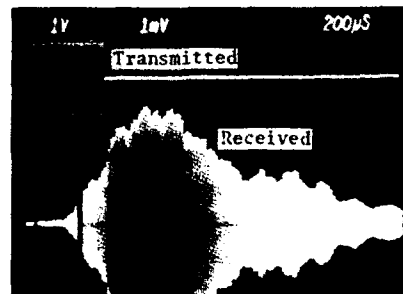

Fig. 4-Typical AWG signal recorded during cure monitoring.

repeatable results upon reconnection and also similar signal transmission levels in both directions along the AWG. With further development an order of magnitude increase in AWG signal sensitivity is anticipated which will be valuable when 5 mil (125 μm) diameter AWG with less signal transmission are evaluated.

5. MECHANICAL PROPERTIES OF LAMINATES WITH EMBEDDED AWG SENSORS

The rationale for the mechanical tests was to subject the site of the embedded AWG to the worst case stress situation for any given test. Key tests performed were apparent interlaminar shear (ILS) strength (ASTM D2344) and flexural strength (FS) (ASTM D790). The environments selected were room temperature (RT) and at 80°C after exposure to 90% relative humidity (RH) for 96 hours at 65°C. Tests were carried out with the AWG sensor in positions which were both parallel and transverse to the principal stress direction, Fig. 6 (four point loading mode for the FS to avoid placement of loading head directly over transverse placed AWG). The sensor was placed in the middle (maximum shear stress zone) of the laminate for the transverse direction test in flexure and also for both ILS tests. For the FS, in which the sensor was parallel to the stress direction, the sensor was embedded in the fifth ply from the top which is in the region of maximum compressive stress. For each test series on specimens with embedded AWG, tests were also made on specimens without AWG and cut from the same laminate. The results of the ILS (each value an average from three replicates) are outlined in Table I and the FS tests in Table II.

Fig. 5-AWG cure curves for thin (5 mm) epoxy-graphite composite panels. Dielectrometry results added for comparison.
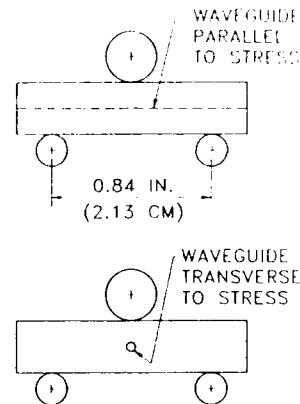
Fig. 6-Arrangement for ILS tests of graphite-epoxy specimens (~3 cm × ~0.5 cm × ~0.5 cm) both with and without embedded Nichrome AWG.

The results show no significant change in ILS with specimens having embedded AWG sensors. A 43% reduction in FS occurs with the sensor transverse to the stress direction and the carbon fibers bent around the AWG, Fig. 2. With the fibers not bent around the AWG the FS only reduces ~14%. This small reduction should be avoided with the use of smaller diameter AWG. With all the tests, and considering specimens with and without embedded sensors, the results demonstrate the same (8 to 9%) reduction in strength at 80°C compared with room temperature. This infers that the thermal expansion coefficients of both the Nichrome AWG and graphite-epoxy composite match well.

In future use in seawater it is possible that galvanic effects between the composite and embedded Nichrome AWG could influence the composite strength. This is not anticipated to be a problem, because in tests of graphite-epoxy specimens with embedded Nichrome AWG in boiling simulated seawater for 10
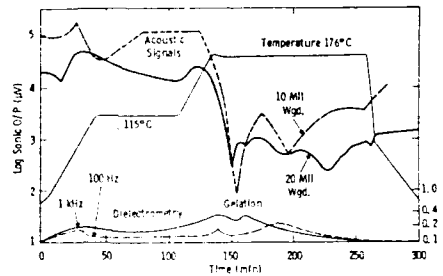
Table I-Apparent Interlaminar Shear Strength Testing of Laminate (ASTM 2344)

Table II-Flexural Strength and Modulus Testing of Laminates (ASTM D790): Specimen 25.4 cm × 0.5 cm × 1.27 cm

Specimen	Shear Strength (RT) GPa (ksi)	Shear Strength (80°C) GPa (ksi)	Flexural Strength (RT) GPa (ksi)	Flexural Modulus (RT) GPa (Msi)	Flexural Strength (80°C) GPa (ksi)	Flexural Modulus (80°C) GPa (Msi)
Control (Without Sensor)	0.06 (8.65)	0.056 (8.09)	0.83 (120.9)	58.7 (8.5)	0.71 (102.4)	62 (9.0)
Sensor Parallel	0.054 (7.89)	0.054 (7.89)	0..4 (107)	58.7 (8.5)	0.71 (102.8)	60.6 (8.8)
Sensor Transverse	0.06 (8.72)	0.051 (7.42)	0.47 (68.8)	69 (10.0)	0.37 (53)	69 (10)
Sensor Transverse (Carbon Fibers Not Bent Around Sensor)	———————→		0.73 (104.3)	66.2 (9.6)	0.66 (95.8)	65.6 (9.5)

minutes, erratically varying potential differences of only 20 to 60 mV were measured between the AWG and composite. At 80°C this voltage was less than 2 mV, and at room temperature no voltage was measured. However, it was observed that the edges of the composite above the water level became encrusted with salt, whether or not a waveguide was embedded.

6. RESPONSE OF EMBEDDED ACOUSTIC AWG TO LAMINATE STRAIN

A four point strain test was carried out on a carbon-epoxy specimen (~2.5 cm x ~32 cm x ~0.5 cm) with a 0.5 mm (20 mil) diameter Nichrome AWG embedded between the 5th and 6th plies below the surface (in a region of maximum compressive stress during the test). As the specimen was strained with a load up to 79.4 kgm (175 lbs) measurements of acoustic signals transmitted through the AWG were recorded for comparison with simultaneous measurements from conventional strain gauges bonded to the specimen surface. At the maximum load, the specimen deflection was ~4.5 mm (180 mils), the strain approximately 2100 microstrain (μin/in), and the bending stress 21.4 MPa (3100 lb/in^2). This test was repeated with the specimen turned over so that the AWG was located near the bottom surface (in a region of maximum tensile stress), and another test was carried out using a new specimen with the AWG located in the center (a site of zero stress during the strain test). The results, in the form of AWG transmitted signals in mV at 67 kHz, are plotted versus microstrain (μ in/in) in Fig. 7. These curves clearly show that the AWG transmitted signals reduce as strain increases for the AWG embedded near the specimen upper surface (compression), and lower surface (tension), and does not change significantly for the AWG embedded in the specimen center (zero strain). The different acoustic signal levels are due to losses at the AWG terminations and are not related to the AWG locations.

7. RESPONSE OF EMBEDDED 0.125 mm (5 MIL) DIAMETER INCONEL 600 (NICHROME) ACOUSTIC WAVEGUIDE TO IMPACT ON SURFACE OF GRAPHITE-EPOXY COMPOSITE PANEL

The first composite panel has been made with 0.125 mm (5 mil) AWG and important issues with the smaller AWG are the sensitivity to impact and sonic ranging capability, and some preliminary investigations have been carried out in these areas. It was found that the impact of a salt grain (~0.000075 gm) dropped from a height of 25 cm onto the panel surface could be sensed via the small diameter waveguide. Compared with previous data, Harrold and Sanjana (1986a), obtained using larger diameter AWG, the trend with increasing impact is similar, and the impact signal is approximately proportional to the square of the AWG diameter.
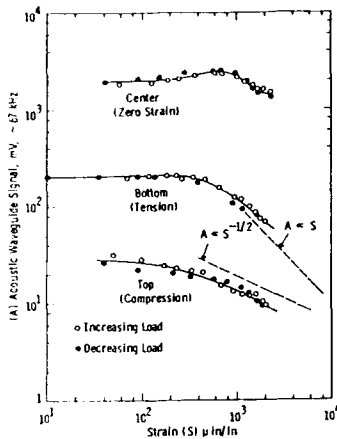
Fig. 7-AWG signals versus strain for four point strain test on epoxy-graphite specimens.

8. TRANSIENT TIME METHOD (SONIC RANGING) FOR LOCATING IMPACT SITE ON SURFACE OF GRAPHITE-EPOXY COMPOSITE

Sonic ranging techniques will be useful for locating both impact sites and highly stressed regions within submarine hulls which generate acoustic emissions (AE). Longitudinal acoustic waves from these events could reach the acoustic sensors at the AWG terminations by different paths and at different velocities. For example, at a velocity of ~7500 m/sec within graphite to the nearest implanted AWG or nearest waveguide exit and then through this waveguide at ~4500 m/sec to reach the termination. In addition, a possible longitudinal wave velocity is ~5000 m/sec, which would be the average of 7500 m/sec for graphite, and ~2500 m/sec for epoxy. Also, shear waves and surface waves with different velocities will be present.

Typical transient signals recorded at AWG terminations and triggered by the first arriving signal are illustrated in Fig. 8. The impact site was near one corner of the panel and the signal, Fig. 8, indicating 50 μsec transit time was recorded at the AWG termination in the opposite corner. This agrees with the value which can be calculated based on the wave velocity in graphite and distance traveled. It should also be noted that the signal frequency is ~60 kHz and it is modulated at ~8 kHz, which is the panel resonant frequency based on an average velocity of ~5000 m/sec for graphite-epoxy.
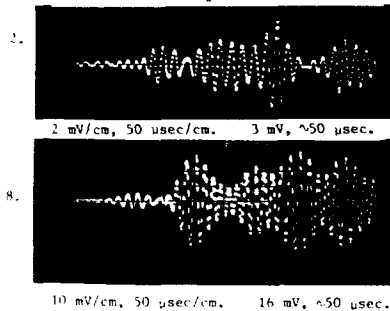

Fig. 8-Typical transient signal recorded at 5 mil Nichrome AWG termination due to surface impact. 135 mgm steel ball dropped from 25 cms.

9. ACOUSTIC WAVEGUIDE OPERATING MODES

Embedded AWG are versatile and can be used in three useful operating modes. Firstly, in the transmit/receive mode either along individual AWG or between distant AWG, for cure monitoring (Fig. 5), strain monitoring (Fig. 7) or composite quality measurement. The next important operating mode is receive only, for impact measurement (Fig. 8) and eventual damage location by sonic ranging. The third useful operating mode is transmit/receive and simultaneous impact. Stress waves from the impact modulate the original transmitted wave. This mode provides another method for sensing impact on a panel surface and locating the impact site.

10. EMBEDDED ACOUSTIC WAVEGUIDE SENSING CONCEPT FOR SUBMARINE STRUCTURE

In the sensing concept, Fig. 9, AWG would be embedded within the hull in a hoop-like fashion every 15 meters (~50 feet). During submarine operation, the hull stresses, strain and sounds from possible microcracks would be
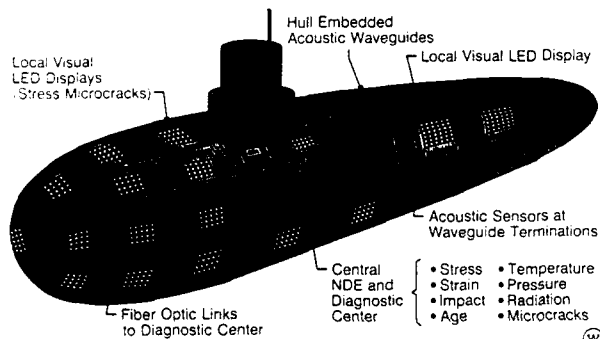
Fig. 9-Smart structure with embedded acoustic
waveguide array for submarine NDE and diagnostics.

monitored via the AWG terminations. This information would be available both locally, via a visual display (LED-type of oscilloscope, Mims (1979)), and remotely at a central NDE and diagnostic center after transmission via a fiber optic data transmission link. The basic AWG sensors can be modified by adding special coatings to also monitor other phenomena such as temperature and radiation. Consequently, before implantation, an important consideration will be future monitoring requirements throughout the submarine lifetime.

11. SUMMARY

Mechanical tests on graphite-epoxy composite specimens with large (0.5 mm) diameter Nichrome AWG embedded show only a ~14% strength reduction under the worst case stress conditions which should be eliminated with the use of smaller, 0.125 to 0.250 mm diameter AWG. The mechanical tests at 80°C reveal no problems with the large diameter embedded AWG, which infers that the thermal expansion characteristics of Nichrome and graphite-epoxy match well. Galvanic effects between graphite and Nichrome have been shown to be minimal and problems are not anticipated. It has been shown that AWG embedded sensors are valuable for cure monitoring of graphite-epoxy composites during manufacture and on completed specimens, proof of principle tests have demonstrated strain monitoring, impact sensing and location. Three operational modes have been identified for the AWG sensors. In addition, for large area cure and condition monitoring, acoustic waves can be transmitted between distant AWG. Anticipated related benefits of embedded metallic AWG are lightning protection and EMI shielding via improved conductivity within the composite, and resistive heating to improve the curing process or for deicing in service. As this developmental program proceeds it is planned to determine the performance of smaller (0.125 to 0.250 mm) diameter embedded AWG sensors, monitor the cure of thick (50 mm) panels, optimize the AWG terminations, and investigate impact damage sensing and location.

12. ACKNOWLEDGMENT

Ed Diaz of (W) STC for mechanical test expertise and facilities

13. REFERENCES

Harrold and Sanjana 1986a J. Polym. Sci. 26 5
Harrold 1986b U.S. Pat. 4,590,803
Harrold and Sanjana 1991 Rev. Prog. Quan. NDE 10B, ed. D. O. Thompson,
   D. E. Chimenti (New York:Plenum) pp. 1267-1272.
Mims 1979 Popular Electronics

Surface impedance modification of plates in a water-filled waveguide

P S Dubbelday

Naval Research Laboratory, Underwater Sound Reference Detachment,
P.O.Box 568337, Orlando Fl 32856-8337

ABSTRACT: The interaction of parallel waves, propagating in a water-filled cylindrical waveguide, with a plate perpendicular to its axis is determined by the plate's specific acoustic impedance, the product of density and wave speed. By means of an attached piezoelectric disk-shaped double transducer, (sensor and actuator), the apparent surface impedance of the plate is modified to equal the impedance of the medium, thus establishing a no-reflection situation. The actuator voltage is regulated by a feedback loop, based on an algorithm for complex-root finding.

1. INTRODUCTION

In this investigation, plane waves propagate in a cylindrical waveguide, and interact with a disk-shaped plate with specific acoustic impedance $\rho_s c_s$, where ρ_s is the density and c_s the dilatational wave speed in the plate material. In a previous study (Dubbelday and Homer 1991), it was shown that by attaching a layer of piezoelectric material (actuator) to the plate, one can establish a condition of no-transmission through the plate, by regulating the voltage of the actuator through a feedback loop that reduces the voltage output of a sensor, placed behind the plate, to zero. The feedback loop was closed by a computer that performs its task by means of an algorithm from complex-root-finding concepts.

To establish a no-reflection condition, one needs two items of information to drive the actuator, in order to distinguish the incoming wave from the reflected wave. These could be derived from two pressure transducers, or one pressure transducer and one velocity transducer. In the analysis presented here it is shown that one may establish a no-reflection condition by means of two active layers attached to the plate. The voltage of one of these, the actuator, is governed by a feedback loop, based on the same algorithm as referred to above, that uses the voltage signal from the other layer, the sensor.

WAVEGUIDE AND TRANSDUCERS

A sketch of the waveguide used in this
experiment is shown in Figure 1. This
is an NRL-USRD (Naval Research
Laboratory, Underwater Sound Reference
Detachment) type G19 calibrator (Naval
Research Laboratory 1982). A plane
wave is created in the water-filled
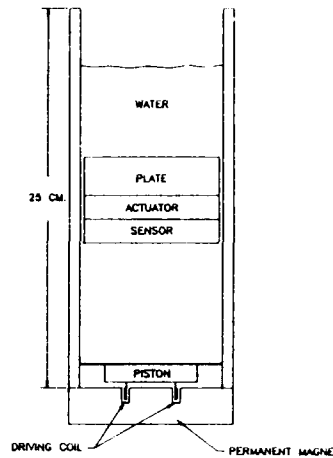tube by a coil-driven piston in the
bottom.

The double transducer is constructed
from two layers of active material,
each 3.3 mm thick. The active material
is NTK Piezorubber, PR-306.
(Piezorubber is a trademark of NTK
Technical Division, NGK Spark Plug Co.,
Nagoya, Japan.) It consists of PbTiO$_3$

Fig. 1. Experimental arrange-
ment in G19 calibrator.

particles embedded in a neoprene elastomer matrix. The center
electrode is common to both transducer disks, and is kept at ground
potential. The shields of the transducers and the shields of the
coaxial cables are electrically connected together and to ground. The
polarization of the two transducers is antiparallel.

ANALYSIS OF DOUBLE TRANSDUCER

It is assumed that the operation of
the two transducers, attached to the
plate, may be adequately described
by a model sketched in Figure 2.
The second subscript indicates the
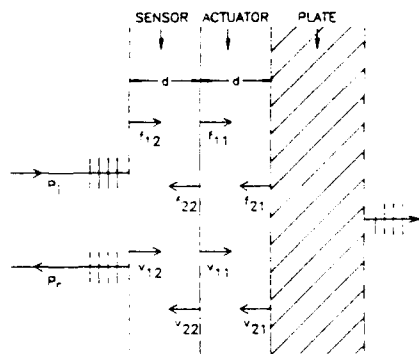transducer, 1 for the actuator, and
2 for the sensor.

The basic equations are derived in
Auld (1973) in the thin-disk
approximation, for which the lateral
dimension is much larger than the
thickness. They form a set of six
linear relations between the four

Fig. 2. Interaction of incoming
wave with plate and double
transducer.

surface forces per unit of area f_{ij} and the four surface velocities v_{ij}
(where $i,j = 1,2$), the two voltages V_1 and V_2 for the actuator and
sensor, respectively, and the current density J_1 in the actuator. It
is assumed that the sensor does not draw current. For the sake of
better insight into the analysis it is assumed that the actuator and
sensor consist of the same material, and have identical dimensions. Of

course this assumption is not essential to the principle of the method. Lafleur *et al* (1991) give relations for the case where the two layers are not identical.

At the interface between the transducers one has the conditions $f_{22} - f_{11} = 0$ and $v_{11} + v_{22} = 0$, thus there is a total of eight equations for the eight unknowns. In the experiment, the quantity V_1 is set, and the quantities V_2 and J_1 can be measured. Thus, in principle, one can express the eight unknowns in terms of these observable quantities. When the algebra is carried out one finds the physically plausible result that the current density J_1 is mainly determined by the specific capacity of the transducer, and only a small fraction of J_1 plays a part in the computation, thus posing impossible demands on the accuracy of the current measurement.

Therefore a different approach is followed. Without any voltage impressed on the actuator and its terminals not connected, one observes two voltages V_{10} and V_{20}. Since the current density J_1 is now "known", being equal to zero, it is possible to express the eight forces and velocities in terms of the voltages V_{10} and V_{20}.

From these expressions one may infer the impedance to the wave at the interface between actuator and plate, $z_p = - f_{21} / v_{21}$. With this experimentally determined value of z_p, one may solve the original equations for f_{12} and v_{12}, in terms of the set actuator voltage V_1, and the observed sensor voltage V_2.

It is assumed that z_p stays constant for a sufficiently long time, to establish the zero condition for the function $w = f_{12} - z_i \, v_{12}$, where z_i is the desired impedance of the sensor surface to the incoming wave. For the no-reflection condition $z_i = \rho_o \, c_o$, the specific acoustic impedance of the medium.

FEEDBACK ARRANGEMENT

The establishment of the desired input impedance of the plate-transducer combination amounts mathematically to finding the zero of the function w. The right-hand side may be considered as a composite function of the voltage impressed on the actuator V_1 (considered as the independent complex variable z). Both f_{12} and v_{12} are determined in terms of V_1 and V_2 by solution of the basic equations, as sketched above. The observed sensor voltage V_2 is a function of V_1 through the physical setup. Thus a complex function $w = f(z)$ is identified, partly defined by mathematical expressions and partly by the experimental arrangement. This function does not have to be linear, but it should be analytic. Mathematically the problem reduces to finding the root(s) of the analytic complex function f. From the various methods for root-finding available, the secant method proved quite successful, because

the function is almost linear, and may be supposed to have only one root.

In the present study of no-reflection, whereby the impedance z_i is set equal to the impedance $\rho_o c_o$ of the watercolumn, the root-finding algorithm worked as well as before. The desired status of a traveling wave between piston and plate was not established, however. A comparison was made between the values computed for the stress and velocity at the sensor separately and values measured by a miniature hydrophone near the sensor and an accelerometer mounted on the sensor, respectively. The agreement for pressure was reasonably good, Figure 3, but not so for the velocity, Figure 4. Various causes were investigated, but thus far no solution has been found.
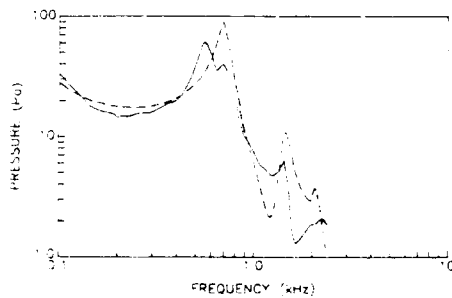

Fig. 3. Comparison of pressure from double transducer (solid) with measurement by hydrophone (dashed).
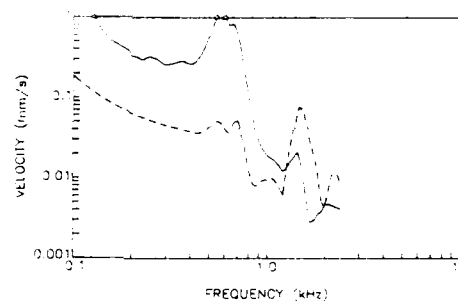
Fig. 4. Comparison of velocity from double transducer (solid) with measurement by accelerometer (dashed).

ACKNOWLEDGEMENTS

REFERENCES

Auld B A 1973 *Acoustic Fields and Waves in Solids* (New York: Wiley) I p 330

Dubbelday P S and Homer R 1991 *J. Intell. Mater. Syst. Struct.* **2** 129

Lafleur L D Shields F D and Hendrix J E 1991 *J. Acoust. Soc. Am.* **90** 1230

Naval Research Laboratory USRD Orlando FL 1982, *Underwater Electro-acoustic Standard Transducers Catalog*, pp 73-77

Shape memory alloy articulated (SMAART) control surfaces

Charles H. Beauchamp, Richard H. Nadolink, and Laurence M. Dean

Naval Underwater Systems Center (NUSC), Newport, Rhode Island

ABSTRACT: The SMAART concept is a variable camber (articulated) foil which is actuated by shape memory alloy wires to control flight of hydrodynamic or aerodynamic vehicles. An operational model of a SMAART control surface was fabricated and demonstrated in a water tunnel. Lift measurements in the water tunnel indicated that the articulated foil produces 40% higher lift (turning) force than rigid foils at angle of attack. Flow visualization showed that the wake behind an articulated foil was a factor of 3 smaller than the rigid foil at equivalent lift.

1. BACKGROUND

Numerous naval vehicles employ conventional NACA rigid foils which are rotated at an angle of attack (AOA) to control flight path. It is known that uncambered foils separate at relatively small angles of attack. This limits the lift coefficient that can be obtained and disturbs the flow entering a downstream propulsor. SMAART control surfaces are a viable method of developing flexible control surfaces with variable camber and AOA. The SMAART foil produces a larger lift coefficient at a given AOA than the equivalent rigid foil. This results in less separation and smaller resultant wakes at equivalent lifts.

The origin of the SMAART concept came from biological structures which have articulated bone or flexible cartilage structures which are actuated by contracting muscle fibers contained within a pliable skin. The original SMAART concept used a hinged aluminum structure which was actuated by contracting shape memory alloy (SMA) wires. The structure and wires were covered by a pliable elastomer skin to produce a flexible foil shape. Later variations of the concept replaced the hinged structure with a spring steel back bone and move the actuating SMA wire outside the foil. All of these variations have potential applications to aircraft or marine vehicles. This technology is covered by patents by Crosswell (1976), Cincotta and Nadolink (1990), Beauchamp, et. al. (1991).

The objective of the work describe in this paper was to develop an operational model of the SMAART control surfaces concept and to demonstrate its hydrodynamic performance improvements relative to an equivalent rigid control surface.

2. APPROACH

A typical rigid underwater vehicle control fin was selected as the baseline for this study. The fin shape was a low aspect ratio swept wing with a tip winglet. A NACA 0012 foil section

was used over its entire span. Prior to the experimental work the performance of a rigid NACA 0012 foil was compared to an articulated NACA 0012 foil using a two dimensional potential flow and boundary layer codes from Gentry and Warzan (1976). The codes were used to predict lift, drag and separation on each foil as a function of AOA.

An operational SMAART model with shape equivalent to the baseline fin was fabricated. Both the rigid baseline and the articulated fin models were tested in the NUSC Research Water Tunnel. This tunnel is capable of flow up to 30 ft/sec through a 12-inch square test section. Flow visualization techniques were used to investigate the separation on the models as a function of AOA. Both models were also mounted on a force balance in the water tunnel to measure lift, drag, and torque as a function of AOA and speed.

3. RESULTS

3.1 Actuator Mechanism

Three actuator concepts were developed. The first two used hinged structures which were actuated by SMA wires. Operational actuators were fabricated and tested for these earlier concepts. With some further development these actuators have potential for some control surface applications. However, it was determined that complete operational control surfaces could not be fabricated within time and cost constraints of this demonstration project using these earlier actuators.

The third actuator concept (shown in figure 1) was used for demonstrating a SMAART control fin. In this concept the SMA wires were located outside the foil shape and the hinged structure was replaced with a flexible spring steel backbone. The foil shape was formed by molding elastomer over stiff leading edge and trailing edge plates which were joined by the spring backbone. The model was articulated by fixing the leading edge and applying a force to the trailing edge (via SMA wires) to bend the spring-back. This simultaneously applied both camber and AOA to the fin.

The actuator employed two sets of SMA wires which were attached to opposite sides of a post extending below the trailing edge of the foil. The wires were wrapped around a series of pulleys to a terminal post. An electrical voltage was applied to one set of SMA wires to heat them above a critical temperature at which a crystal phase change caused them to contract and pull the trailing edge of the foil. SMA technology is described by Duerig and Melton (1989). Upon removal of the voltage the wires were cooled by ambient fluid and the spring backbone returned the foil to the uncambered position. Actuation in the opposite direction was accomplished by applying voltage to the opposing set of wires.

Locating the wires outside the foil had two major advantages over the internal actuator concepts. First, a higher mechanical advantage was obtainable resulting in fewer SMA wires and lower power to actuate the foil against the equivalent hydrodynamic forces. Secondly, there was no constraint on the wire length resulting in less severe constraints on the AOA that
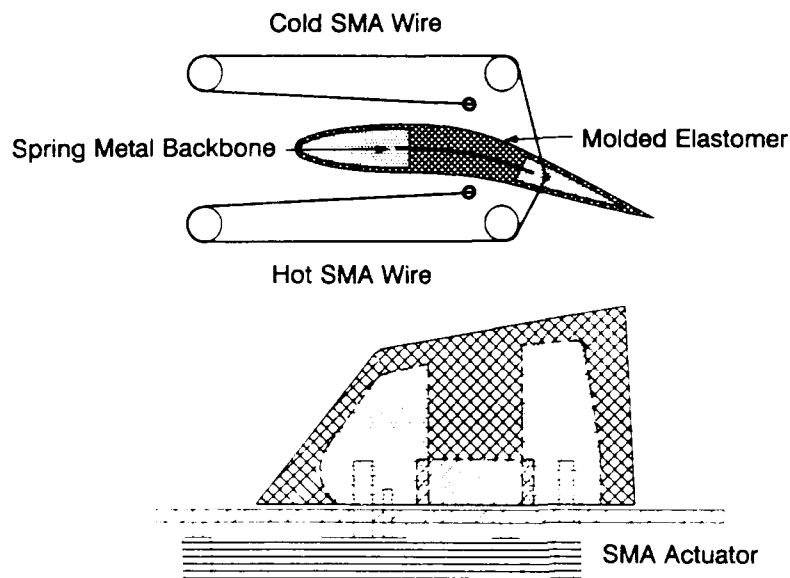
Fig. 1 Shape Memory Alloy Actuator

could be obtained. The spring backbone had the advantage over the hinged structure of providing continuous curvature in the foils camber resulting in smoother more efficient hydrodynamic shapes.

This SMAART model was tested in the water tunnel and the following performance was obtained. Actuation up to a 7° AOA with the associated camber was obtained. Slew rates exceeding 7 °/sec were obtained in both heating and cooling modes on the SMA wires. The SMA wires were successfully electrically insulated so that they were cooled direct by contact with ambient water. Power requirements for full (7°) actuations at maximum slew rate was 1.3 kw with up to 3 ft/sec of water flow. Note that 1.3 kw was the limit of the power supply. Above flow speeds of 3 ft/sec the angle of the maximum actuation diminishes until at 7 ft/sec the maximum actuation was less than 4 degree. It is believed that this decrease in maximum angle was due to increased cooling from increased flow over the wires resulting in insufficient power to completely heat the SMA wires above the critical temperature. Force measurements indicate that the actuator which was built should have been able to produce seven degrees of actuation at flow speeds in excess of 15 ft/sec.

Actuator force limitations could have been increased by adding additional SMA wires. AOA limitations could be extended by increasing the length of the wires. Slew rates in heating mode could be increased by increasing the instantaneous power. Slew rates in cooling mode could be increased by increasing the fluid flow rate over the wires by either active or passive means. By controlling ambient flow over the wires it would be possible to control cooling rate and minimized power requirements during the heating mode.

3.2 Hydrodynamic Analysis

Figure 2a shows the predicted lift vs. AOA for both the uncambered and articulated foils. The lift coefficient, C_L, is defined as $C_L = F_L / 1/2 \, \rho V^2 A$ were F_L is the lift, ρ is the density of the water, V is the velocity of the flow, and A is the area of the wing. The rigid foil reaches a maximum lift coefficient of approximately 1.5 at approximately 15° AOA. The articulated foils obtained a lift coefficient of 2.0 at an AOA of 10°. This two dimensional analysis showed that the cambered fin produce twice the lift of the rigid fin at the same AOA.

The analysis indicates that at 15° the rigid foil has 35% separation and at 20° it has 95% separation. Data from Abbott and von DoenHoff (1959) indicates lift coefficient on the rigid foil drops off at AOA larger than 16°. This is apparently due to the large degree of separation on the foil. Analysis shows that at AOA of 10° the articulated foil has only reached 25% separation. AOA was used to relate % separation to lift coefficient as show in figure 2b. The analysis predicts that at a lift coefficient of 1.5 the articulated foils produce less than 1/2 the separation of the rigid foil.
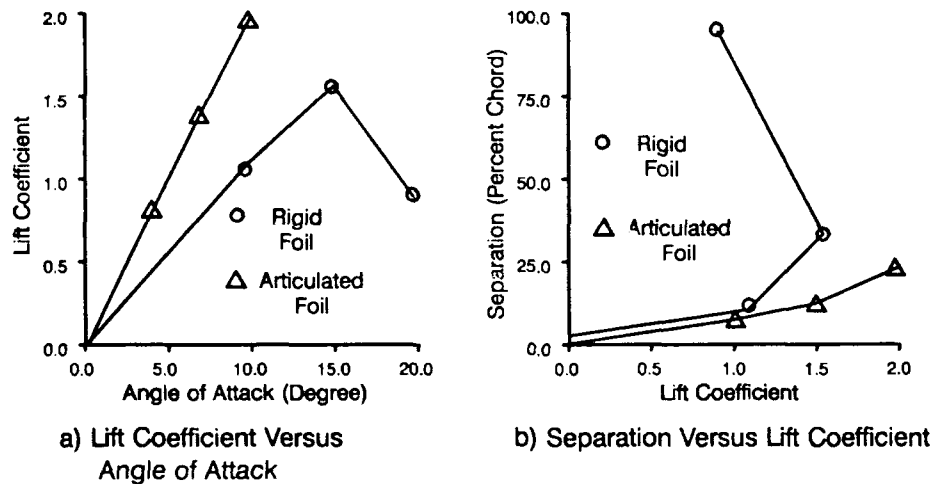

a) Lift Coefficient Versus Angle of Attack

b) Separation Versus Lift Coefficient

Fig. 2 Two Dimensional Analysis

3.3 Lift Measurements

The force measurements were made under steady states conditions. The articulate foil was held in camber by a tensioned strip located between the actuator post and the balance strut. Both articulate and rigid fin were clamped to the balance strut at the appropriate AOA. Figure 3 shows a comparison between lift measurements for the articulated and rigid fins. The statistical error bars on this figure are the 95% confidence level. The results indicate that on the average the articulated foil produce 40% more lift than the rigid foil at a given angle of attack. That is at 18° AOA the articulated foil had the same lift coefficient as the rigid foil at

24° AOA. This is less than 100% increase in lift coefficient predicted by the two dimensional analysis but the low aspect ratio fin which was tested exhibited highly 3-dimensional flow. Furthermore, it was observed during the measurements that the articulated foil showed significant flattening of the camber and deflection of the tip when flow was applied. This effect was not fully accounted for when the AOA was measured thus the reported AOA should be lower for the articulated foil. Based on this observation it is believed that the lift performance of the articulated foil could be significantly improved by designing a structure and actuator which better maintained the foil shape. It should be noted that no attempt was made in this project to optimize the foils shape. Development of improved SMAART designs are currently in progress.
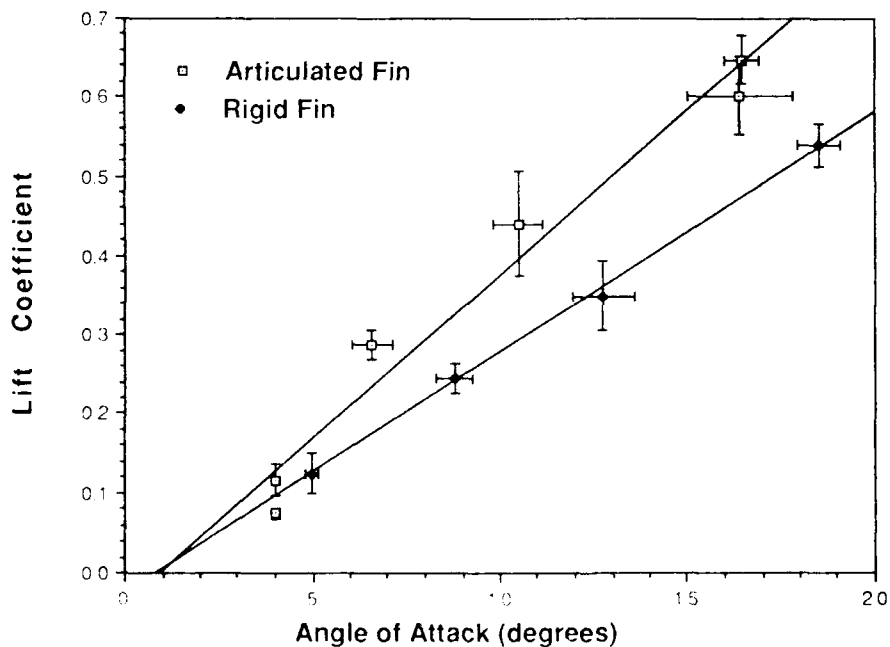

Fig. 3 Comparison of Articulated and Rigid Fins, Lift vs. Angle of Attack

3.4 Flow Visualization

Flow visualization with dye streaks was conducted in a water tunnel to compare the wake behind the articulated and rigid foils. Figure 4 shows traces of the dye patterns in the wakes of the rigid and articulated foil at equivalent lift value (i.e.18 AOA for the articulated is equivalent to 24° for the rigid). The rigid foil showed a tip vortex developing at AOA above 15°. It produces a wake width of 30 % of chord length immediately downstream of the foil. The articulated foil did not show any tip vortex up to the 18° AOA. The maximum width of

the wake behind the articulate foils was 10% of chord. This represents a factor of 3 smaller wake at equivalent lift.
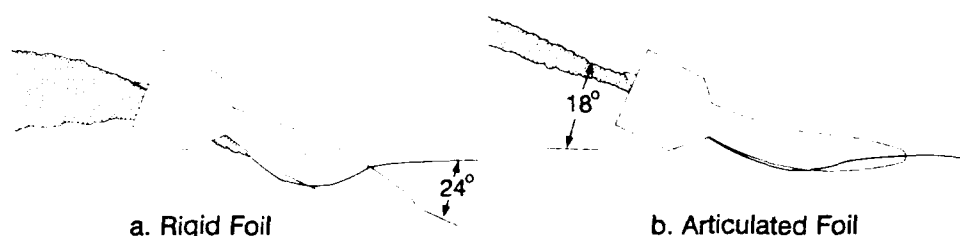

a. Rigid Foil   b. Articulated Foil

Fig. 4 Dye Streak Flow Visualization Comparison of Rigid and Articulate Foil Wakes

4. SUMMARY AND CONCLUSIONS

The SMAART concept for development of articulated foils with SMA wire actuators for application to flight control of hydrodynamic or aerodynamic vehicles has been demonstrated. Analysis has indicated that the articulated foil produces higher lift (turning) force and less flow separation than the conventional rigid foils. An operational demonstration model of the articulated control fin concept has been fabricated and tested. The results of lift measurements indicate the articulated foil fabricated here produced a 40% increase in lift relative to the rigid foil at the same AOA. The results of flow visualization indicate that the articulated foils had a factor of three smaller wake at equivalent lift. Current efforts are being directed towards optimizing the foil shape and improving the actuator and structural designs.

5. ACKNOWLEDGEMENTS

6. REFERENCES

Abbott, I. H. and von Doenhoff, A. E., (1959), Theory of Wing Sections, Dover Publications.
Beauchamp, C., Cincotta, M., Gauthier, B., and Raffa, A. (1991), Patent Disclosure, Navy Case Number 73152.
Cincotta, M. and Nadolink, R. N. (1990), Patent Application Number 07/591,532
Crosswell, T. L., Jr. (1976), Patent #3,930,626.
Duerig, T. W., and Melton, K. N. (1989), "Designing with the Shape Memory Effect" Material Research Society, International Meeting on Advanced Materials, Vol 9.
ry, A.E., and Wazzan, A. R., (1976), "The Transition Analysis Program System, Vol. I - Theory", Report MDC J7255-01, McDonnell Douglas, Hunting Beach CA

Distributed control concepts using neural networks

J. J. Helferty
Temple University
Philadelphia, PA 19122

D. Boussalis and S. J. Wang
Jet Propulsion Laboratory
Pasadena, CA 91109

ABSTRACT: A method for employing artificial neural networks for the decentralized control of flexible space structures is investigated. The basic approach is to couple the concept of the overlapping expansion/contraction method, developed by Ikeda and Siljak (1984), to the design of a decentralized artificial neural network controller. In this paper we develop a decentralized neuromorphic controller (NMC) and demonstrate its application to the vibration control of local sections of large space structures. An illustrative simulation example is given for the local control for a finite-dimensional model of the JPL/AFAL Flexible Control Experimental facility.

1. INTRODUCTION

The performance required of future precision large space structures such as orbiting interferometers and segmented reflector telescopes places very stringent requirements on the alignment and stability of optical components which are attached to large lightweight structural frameworks. The control system for the supporting structure, along with the rest of the system, must exhibit properties such as quietness (i.e., no vibration), high precision figure and position alignment, and system stability in the nanometer regeme. These performance requirements have motivated a new approach to spacecraft design, where decentralized feedback control principles coupled with advances in embedded sensing and actuation are applied to the design of high performance structural systems.

Presently, control system designers rely heavily on an "accurate" model of the structure where the space structure is generally modelled as a linear time-invariant system. Although such a model may describe the physical system adequately, any model is only an approximation to the physical system. There is always some uncertainty present in the structure due to physical parameters not being known exactly, neglecting high frequency dynamics, or invalid assumptions made in the model formulation. In this paper we suggest a distributed control system architecture for large space structures based on multi-processor systems known as artificial neural networks (ANN) which do not require accurate knowledge of the structure to be controlled but rather learn to formulate control strategies from their operational experience. We shall exploit both the distributed nature and the learning capabilities of ANN for the design of a robust, distributed control system for precision space structures. A distributed architecture is developed in which an ANN controller is employed at each actuator for local control of a section of the structure. The objective is to determine the feasability of using ANN control strategies to provide accurate vibration suppression along with figure and position alignment over a wide range of frequencies for the entire structure.

This paper is organized as follows. Section 2 briefly reviews the method of overlapping expansion/contraction method and how it is applied to finite-element models of flexible space structures. Section 3 discusses the Neuromorphic Control (NMC) algorithm and presents a simulation example of the NMC algorithm for the local control of a section of JPL/AFAL structure.

2. REVIEW OF THE INCLUSION PRINCIPLE FOR FLEXIBLE STRUCTURES.

The inclusion principle, built around the concept of overlapping expansions and contractions and was found to be ideally suited for the decentralized control of flexible space structures and has been investigated by Youseff (1988) and Ozguner et. al. (1990). The basic idea for the application of the inclusion principle to flexible structures was to view the structure as consisting of many "loosely" coupled subsystems. In brief, the procedure based on the inclusion principle developes an expanded model of the original finite-dimensional model of the structure such that the expanded model "includes" the original model - that is, the dynamics of the original model can be extracted fom the expanded model.

Consider a pair of linear-time invariant systems S and $\underline{S}$ described by

$$S: \quad \dot{x} = A\,x + B\,u; \quad y = C\,x \tag{2.1}$$

$$\underline{S}: \quad \underline{\dot{x}} = \underline{A}\,\underline{x} + \underline{B}\,\underline{u}; \quad \underline{y} = \underline{C}\,\underline{x} \tag{2.2}$$

where $x \in P^n$ and $\underline{x} \in R^{\underline{n}}$ and $\underline{n} \geq n$.

Definition 2.1(Definition 2.3 of Ikeda and Siljak (1984): We say that a system $\underline{S}$ includes a system S if there exist an ordered pair of matrices (U,V) such that $UV = I_n$, and for any initial state x(0) of S and any input u(t) we have

$$x(t; x(0),u) = U\underline{x}(t; Vx(0), u); \tag{2.3}$$

$$y[x(t)] = \underline{y}[\underline{x}(t)] \text{ for all } t \geq 0 \tag{2.4}$$

This definition implies that the system $\underline{S}$ contains all the necessary information about the behavior of the system S. We can extract any property of S from $\underline{S}$, and evaluate the properties of $\underline{S}$ using S as a reduced order model. This is the underlying idea of the inclusion principle. Consider a model of a flexible structure in its state space form:

$$\dot{x} = A\,x + B\,u; \quad y = C\,x \tag{2.5}$$

where A id a block diagonal matrix, i.e., A=block diag($A_1, A_2, ..., A_n$) and

$$A_i = \begin{bmatrix} 0 & 1 \\ -\omega_i^2 & 0 \end{bmatrix} \tag{2.6}$$

where ω_i is the natural frequency of the ith mode. Ozguner (1990) developed an overlapping expansion method such that each subsystem model for the flexible structure is controllable and observable. Modes were chosen for a particular subsystem by considering the influence coefficients in the B and C matrices. Based on this expansion we shall next develop a NMC algorithm for each subsystem of a flexible structure.

3 THE NEUROMORPHIC CONTROL ALGORITHM

Figure 1 shows a block diagram of the control system which is employed for the local control of a subsystem. Before discussing the specific function of each block in Fig. 1, a brief description of the overall control system is given. The NMC can be viewed as a self-tuning regulator from modern control theory with adjustable parameters and is comprised of two feedback loops. The goal of the NMC is to develop a local control signal u, as a function of both the current state of the subsystem structure $\underline{x}$, and a set of tunable weighting parameters $\underline{\theta}$. so that the system state is regulated about a desired control setpoint or trajectory $\underline{x}_d$. The primary feedback loop (shown with the bold line) simple maps the current state of the structure into the next control signal through the regulator. The regulator in the form of a three-layer

feedforward neural network (FNN). The input state vector $\underline{x}$ is propogated through the FNN, layer by layer, to produce a control signal $\underline{u}$ at its output which is then fed into the structure as the control input. The secondary loop employs a parameter adaptation technique which *teaches* the FNN, through adaptation of the parameter vector $\underline{\theta}$, how to construct a proper control signal. In the secondary loop, the new state is then compared to the desired state and an on-line nonlinear reccursive least square (NRLS) estimation technique is used to adjust the weighting parameters of the FNN by sequentially minimizing a weighted quadratic performance index of the error between the desired state $\underline{x}_d$ and current plant states $\underline{x}$. It should be noted that once the FNN *learns* how to map the current state into the appropriate control action, the secondary loop is no longer necessary and can be removed.
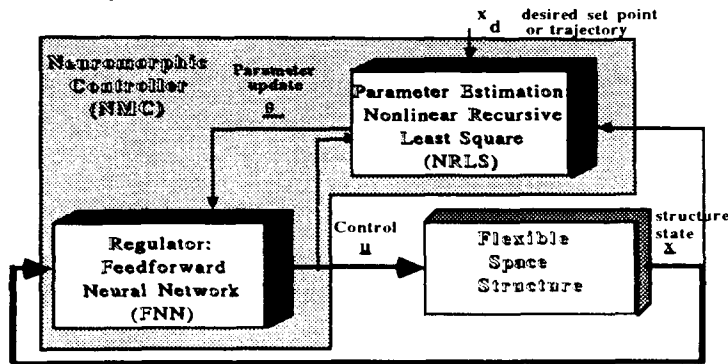

Fig. 1: Block diagram of the Neuromorphic Controller

3.1 Feedforward Neural Network. Figure 2 shows the specific network topology that will be used as the regulator. The network is arranged into three layers; an input, hidden, and output layer and we employ two types of "neurons", namely; linear (L) and sigmoidal (S). The input layer consist of n linear neurons and receives signals in the form of plant states $\underline{x}$, where $\underline{x}$ is an n-dimensional vector. Note that we assume that all of the plant states are measureable and accessible. The output layer consist of m linear neurons and emits m control signals to the structure ($\underline{u}$ is an m-dimensional vector). The hidden layer is used to encode environmental information and develop sophisticated input/output mappings and consists of h sigmoidal neurons whose outputs are denoted by the h-dimensional vector $\underline{\sigma}$. Note that we only show typical feedforward paths for a single neuron in each layer.
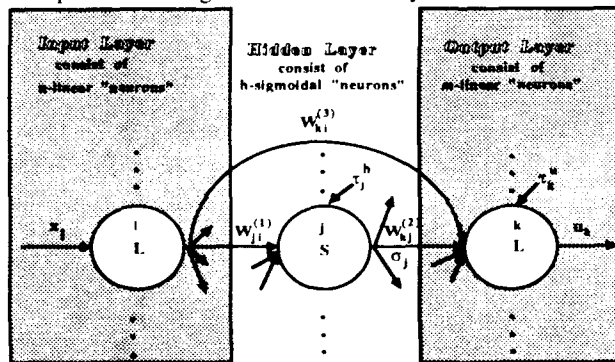

Fig. 2: Topology of the regulator implemented as a three-layer feedforward neural network. Note that not all of the connections and neurons are shown.

The output layer constructs a control signal of the form

$$\underline{u} = [W^{(2)}] \underline{\sigma}([W^{(1)}], \underline{x}, \underline{\tau}^h) + [W^{(3)}] \underline{x} + \underline{\tau}^u \tag{3.1}$$

where $[W^{(2)}]$ is an m x h matrix connecting the hidden layer to the output layer, $\underline{\sigma}([W^{(1)}], \underline{x}, \underline{\tau}^h)$ is an h-dimensional vector of hidden layer outputs, $[W^{(1)}]$ is an h x n matrix connectsing the input layer to the hidden layer, $\underline{x}$ is an n-dimensional vector of plant states, $\underline{\tau}^h$ is an h-vector of hidden layer thresholds, $[W^{(3)}]$ is an m x n matrix of direct connections from the input layer to the output layer, $\underline{\tau}^u$ is an m-vector of output layer thresholds, and $\underline{u}$ is an m-vector of control signals. Finally, a vector of tunable parameters comprised of all the synaptic weights and thresholds is defined as

$$\underline{\theta} = [W_{11}^{(1)}, ..., W_{ji}^{(1)}, ..., W_{hn}^{(1)}, W_{11}^{(2)}, ..., W_{1h}^{(2)}, W_{kj}^{(2)}, ..., W_{mh}^{(2)},$$

$$\tau_1^h, ..., \tau_h^h, W_{11}^{(3)}, ..., W_{ki}^{(3)}, ..., W_{mn}^{(3)}, \tau_1^u, ..., \tau_m^u]^T \tag{3.2}$$

which has dimension $p = n \cdot h + h \cdot m + h + n \cdot m + m$.

3.2 Local Flexible Structure Model and the Control Objective.

We first assume that the original finite-dimensional model for the structure has been expanded according to the inclusion principle as given by Ozguner et. al (1990), then we consider each local subsystem model for the flexible structure to be of the form:

$$\underline{x}^{(i)}(k+1) = \underline{A}^{(i)} \underline{x}^{(i)}(k) + \underline{B}^{(i)} \underline{u}^{(i)}(\underline{x}^{(i)}(k), \underline{\theta}(k)) \tag{3.3}$$

where k is discrete time $(k=0,1,2,...)$, $\underline{A}^{(i)}$ is a matrix of locally controllable modes and $\underline{B}^{(i)}$ is the control influence matrix. Here we shall make the following assumptions:

(i) $\underline{A}^{(i)}$ is **unknown**;
(ii) $\underline{B}^{(i)}$ is **known**;
(iii) the order of the subsystem (i.e., the number of states) is known;
(iv) all of the local modes are measurable and controllable;

The state $\underline{x}^{(i)}(k+1)$ becomes a function of the FNN weighting parameters $\underline{\theta}(k)$ through the dependence on the local contol $\underline{u}^{(i)}(\underline{x}^{(i)}(k), \underline{\theta}(k))$.

The control objective is to find a set of parameters $\underline{\theta}(k)$ such that the computed control commands, or ce applied to the structure will cause the output $\underline{x}^{(i)}(k+1)$ to approach the desired set point $\underline{x}_d$. Adaptation of the FNN control parameters $\underline{\theta}$ is achieved by minimizing the following performance index:

$$J(N,\underline{\theta}) = \sum_{k=0}^{N-1} (\underline{x}_d(k+1) - \underline{x}^{(i)}(k+1))^T [Q(k+1)] (\underline{x}_d(k+1) - \underline{x}^{(i)}(k+1)) \tag{3.4}$$

where N is the total number of samples and $[Q(k+1)]$ is a sequence of positive definite n by n weighting matrices. The sequential minimization of Eq. (3.4), in real-time, is performed using the Nonlinear Recursive Algorithm described in Helferty (1991).

3.3 Example for a 3-mode subsystem.

A finite-dimensional model of the JPL/AFAL Flexible Spacecraft simulator will be considered as a test for our decentralized NMC. Ozguner (1990) has perviouly studied this model and has shown it can be decoupled into 14 subsystems using the inclusion principle. We shall consider one of the finite-dimensional subsystem models for the JPL/AFAL facility which incorporates 3 modes of the structure.

The model is given in modal coordinates so that the state variables represent modal amplitudes and velocities. We shall also assume that the control influence matrix B and the output matrix C are known while we have **no** knowledge of the plant matrix A. Let us consider the problem of vibration suppression given an initial deflection of the structure. This basically means that we desire to drive all the states (i.e., modal displacements) to zero.

The 3-mode subsystem model is given by:

$$\dot{x} = \underline{A}\,x + \underline{B}\,u; \quad y = \underline{C}\,x$$

$$\text{where } \underline{A} = \begin{bmatrix} 000.00 & 000.00 & 000.00 & 001.00 & 000.00 & 000.00 \\ 000.00 & 000.00 & 000.00 & 000.00 & 001.00 & 000.00 \\ 000.00 & 000.00 & 000.00 & 000.00 & 000.00 & 001.00 \\ -14.93 & 000.00 & 000.00 & -00.07 & 000.00 & 000.00 \\ 000.00 & -111.98 & 000.00 & 000.00 & -00.21 & 000.00 \\ 000.00 & 000.00 & -931.54 & 000.00 & 000.00 & -00.61 \end{bmatrix}$$

$$\underline{B} = [0, 0, 0, .009, .0279, -.0702]^T; \qquad \underline{C} = [1, 1, 1, 0, 0, 0]^T$$

with an initial deflection $\underline{x}(0) = [.5,.5,.5,0,0,0]^T$. Figure 3 illustrates the open loop time response and Fig. 4 llustrates the closed loop time response using NMC to generate the control signals. The NMC learns to construct the proper control signal to dampen out the initial deflection in 5 sec.

Fig. 3

Fig. 4
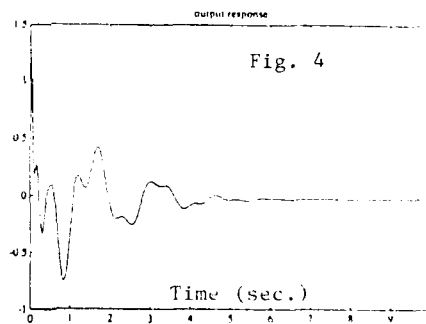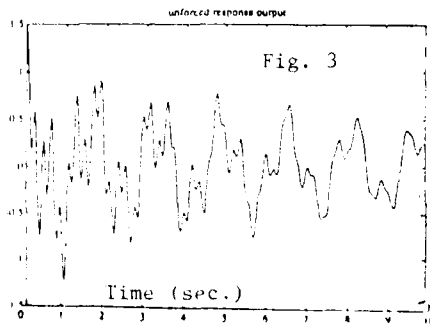
4. CONCLUSIONS

A Neuromorphic Control algorithm has been developed decentralized control of flexible space structures, where a model of the structure is incomplete. A single feedforward neural network is employed to compute the appropriate control sequences to suppress vibration. The neural network is trained by a Nonlinear Recursive Least Square algorithm, which has better convergence properties than most of the currently used weight adaptation algorithms. In this approach we avoid the heuristic "backpropogation" neural network algorithms that are currently used extensively in the literature to train neural network models.

5. REFERENCES

M. Ikeda and D. Siljak (1984), "An inclusion principle for Dynamic Systems", *IEEE Trans. on Auto. Control.*, Vol.AC-29, No. 3, pp.244-249

A. Youseff (1988),"Application of the Inclusion Principle to Mechanical Systems", *Proc. of the 1988 American Control Conference*, Atlanta, GA.

O. Ozguner, K. Ossman, J. Donne, M. Boesch, and A. Ahmed (1990)," Decentralized Control Experiments on the JPL Flexible Spacecraft", *Proc. of the 1990 American Control Conference*, San Diego, CA, pp. 368-373

J. Helferty (1991),"Adaptive Control and System Identification for Flexible Space Structures using Artificial Neural Networks" Final Report from an ASEE Summer Faculty Fellowship

Vibration control of cylinders using piezoelectric sensors and actuators

Hartono Sumali, Harley Cudney and Jeffrey Vipperman

Mechanical Engineering Department, Virginia Polytechnic Institute and State University,
Blacksburg, VA 24061, USA

ABSTRACT: Experiments were done to demonstrate that the vibrations and the noise
field surrounding an elastic cylinder can be actively controlled using structure-borne
sensors and actuators. Piezoelectric polymer film was used to sense the vibration, and
piezoceramic actuators were used to impart vibration-canceling forces. Two controllers
were used: an analog-based controller for wave cancellation and a digital controller
programmed with an adaptive control algorithm. Results showed a 68 dB reduction
in error signal and a 29 dB reduction in overall sound pressure level measured in a
reverberant environment.

1. INTRODUCTION

In elastic cylindrical structures for underwater applications, vibration and the resulting
sound have to be controlled to enhance the structure's ability to evade detection. Passive
vibration and acoustic damping methods are often incapable of achieving the goal, or
simply not feasible. Active control can be performed by introducing forces on the structure
that cancel the effect of vibration.

In certain applications such as torpedoes, microphones -- which are the most common
error sensors -- are not feasible feedback sensors. In this case, structure-borne sensors have
to be utilized. Film made of piezoelectric polyvinylidene fluoride (PVDF) is a good
structure-borne sensor for this application because it occupies almost no space, it does not
load the structure, and it can be bonded to the structure very easily. Moreover, PVDF film
has a unique advantage of being able to be shaped so that it is selectively sensitive to
certain vibration modes. The actuators that can be used are also ones that need no external
support. Again, structure-borne actuators are needed. Compared to proof mass actuators,
piezoceramic lead zirconate titanate (PZT) crystals have many advantages such as compact
size, low mass, simplicity of a single-component device, large force-to-weight ratio, low
cost and minimal maintenance requirement.

To demonstrate the ability of structure-borne PVDF film sensors and PZT actuators to
control the vibration of the cylinder, harmonic steady-state disturbance rejection
experiments were done.

2. THE CYLINDER

The structure controlled was an aluminum cylindrical shell 16 inches long, 10 inches in
outside diameter, 0.25 inch thick. Control experiments were done both on the cylinder
shell alone (referred to as the open cylinder) and on the cylinder with solid circular plates
bolted tightly on both ends (closed cylinder). A shaker inside generates a steady state
harmonic point force disturbance. A PVDF film sensor and PZT actuators were bonded
on the outer surface of the cylinder (see Figure 1).

The natural frequencies and approximate mode shapes were analytically predicted t, a method given by Blevins (1979). This method approximates the mode shape function with a product of the axial part and the circumferential part of the function. The circumferential part is a cosine function. The axial part is a mode shape function of a beam with boundary conditions corresponding to the end conditions of the cylinder. For the open cylinder, the boundary conditions are like those of a free-free beam. The closed cylinder boundary conditions were modeled as pins with torsional springs whose stiffness constant was determined experimentally. The eigenvalues and mode shape function for this type of boundary conditions were computed with formulas given by Gorman (1975). Subsequent experiments using accelerometers on the cylinder verified the predicted natural frequencies and mode shapes of the open cylinder within 8 percent (see table 1). For the closed cylinder, however, the analytical prediction was only accurate for those modes where the axial mode index is 1. The frequencies are shown in Table 2. In this paper, mode shape (i,j) means a mode shape where the circumferential part is i sinusoids and the axial part is like the jth mode shape of a beam with corresponding boundary conditions.

Because only on-resonance single-tone disturbance rejection was studied, vibration modes were selected for case studies. Acoustic experiments revealed that for the open cylinder the most powerful acoustic radiator is the fourth Rayleigh mode. (The ith Rayleigh mode shape is a mode shape where the circumferential part is i periods of sinusoids around the cylinder and where lines parallel to the cylinder's axis remain parallel to that axis, that is, there is no axial variation at any fixed radial position.) The natural frequency associated with this mode is 1425 Hz. For the closed cylinder, a very powerful acoustic radiator is mode (4,1), whose natural frequency is 1545 Hz.

Table 1 Open Cylinder Natural Frequencies   Table 2 Closed Cylinder Natural Frequencies

| Mode	Ana-lytical (Hz)	Experi-mental (Hz)	% er-ror	Mode	Ana-lytical (Hz)	Experi-mental (Hz)	% er-ror
Rayleigh 2	261	263	0.77	3,1	1019	1010	-0.88
Rayleigh 3	737	747	1.36	2,1	1121	1050	-6.33
Rayleigh 4	1413	1425	0.85	4,1	1526	1545	1.24
Rayleigh 5	2285	2250	-1.53	5,1	2358	2400	1.78
Rayleigh 6	3353	3350	-0.09				
3, 1	1586	1570	-1.01				
4, 1	1860	1850	-0.54				
5, 1	2637	2630	-0.27				
6, 1	3684	3680	-0.11				
2, 2	4118	3825	-7.12				
3, 2	3005	2880	-4.16				
4, 3	3877	3735	-3.66				
5, 3	4139	4030	-2.64				
6, 3	4927	4825	-2.07				
5, 4	5182	4895	5.54				
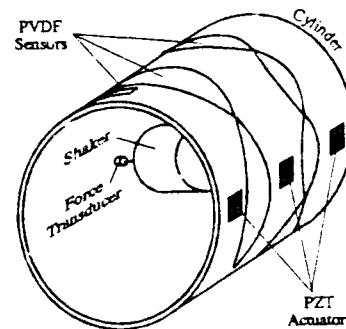
Figure 1 Cylinder with a Shaker, PVDF Sensors and PZT Actuators

3. PVDF FILM SENSOR

When the open cylinder is excited with a 1425 Hz disturbance, Rayleigh mode 4 is excited most, but all other modes are also excited, sending signals through the error sensor to the controller. These signals, although much weaker than the intended 1425 Hz feedback signal, may be amplified by the analog controller and fed back to the structure, resulting in an ever-increasing excitation if the feedback signal is in-phase with the excitation. What can help eliminate this problem of instability is an error sensor which is sensitive only to a selected mode. Modal sensor theory developed by Lee (1987) basically explains how to create such a sensor. Lee has verified his theory experimentally on a beam. Furthermore, Zhou et. al. (1991) applied modal sensor on a plate, demonstrating experimentally that a one-dimensional modal sensor on a two-dimensional structure filters out other modes other than a family of intended modes and thereby reducing control spillover.

Modal sensors and other types of distributed sensors can be made of piezoelectric polymer PVDF commercially available as thin film sandwiched between two metal electrode layers. With an electronic interface providing a sufficiently high input impedance, the charge developed in the PVDF layer can be converted to voltage proportional to strain. (Alternatively, a sufficiently low input impedance could also be used to convert the sensor's output current to a voltage signal proportional strain rate.) The film can be cut to shapes to create modal sensors and then bonded on the structure. One-dimensional modal sensor theory can be applied directly to the Rayleigh modes of the open cylinder, since the mode shapes are one dimensional. A mode (4,j) sensor is shaped such that its width varies around the cylinder according to a function $b(x) = \mu_{40} \cos(4x/R_o)$ where μ_{40} is the width amplitude and $x = R_o \theta$. R_o is the outside radius and θ is circumferential position. The modal filtering effect of this sensor is demonstrated in Figure 2, which shows the magnitude ratio of the modal sensor output voltage to excitation force (solid line), compared to the magnitude ratio of a commonly-used rectangular PVDF film sensor to excitation force (dotted line). It is clear that the modal sensor filtered out other modes than Rayleigh mode 4 (1434 Hz), mode (4,1) (1833 Hz), and mode (4,3) (3730 Hz). (Mode (4,2) was not strongly excited because the

Figure 2 Modal Filtering Effect of PVDF Modal Sensor

shaker point of action was very close to the nodal line of this mode.) This result also shows that the modal filtering effect of the mode (4,j) sensor does not only apply to Rayleigh (one dimensional) modes, but also to other vibration modes of the cylinder. This effect was taken advantage of in implementing the analog vibration control scheme on the cylinder. This sensor will be refered to as the mode 4 sensor in the rest of this paper.
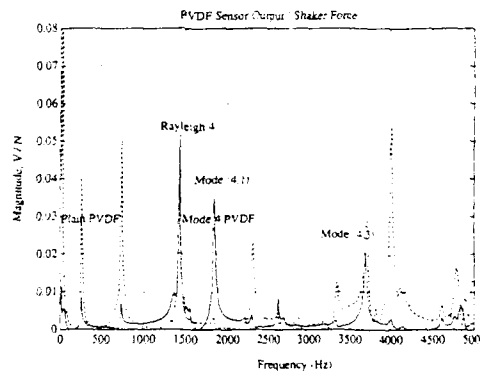
4. PZT ACTUATORS

As showed by Fuller and Jones (1987), Piezoceramic PZT bonded on a structure can be used to produce vibration to control acoustic emission from the structure. The converse piezoelectric effect causes the PZT patches to impart strain on the cylinder when electric voltage is applied to them. Piezoceramic PZT available commercially in the form of thin chips coated with metal electrodes were cut into 1.5" x 1.25" rectangles and then

bonded to milled-flat surfaces on the cylinder. Experiment on the open cylinder at 1425 Hz showed that applying 36.6 V (0-peak) to two actuators located in the middle of the cylinder's length created a 36.5 g radial acceleration on an antinode, equivalent to applying a 14 N point force at the same location. The maximum recommended operating voltage for the type of PZT chip used is 212 V. A zoomed swept sine frequency response analysis shows that the PZT actuators excite the same structural response (Figure 3). Results from an acoustic test on the closed cylinder in an anechoic chamber showed that at 1545 Hz (the frequency of mode (4,1)) the directivity pattern of the sound generated by the cylinder under the PZT excitation is very similar to the directivity pattern of the sound generated by the cylinder under shaker excitation (Figure 4). These results demonstrate that the PZT chips are indeed capable of inducing vibration and sound at levels sufficient to cancel the shaker disturbance.
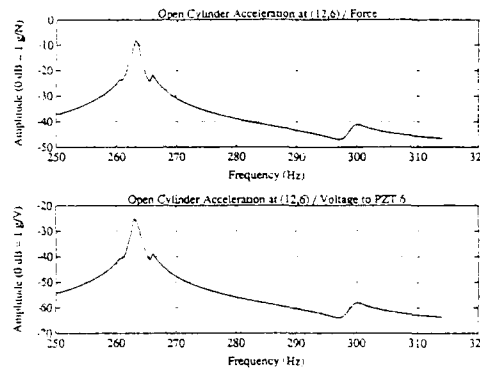

Figure 3 Magnitude Ratio of Acceleration to Force (Upper Graph); Magnitude Ratio of Acceleration to PZT Voltage (Lower Graph)
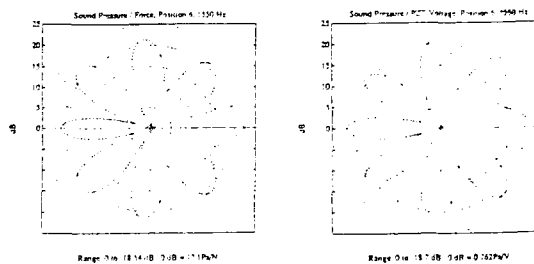

Figure 4 Acoustic Directivity Patterns of the Closed Cylinder: Under Shaker Excitation (Left Graph); Under PZT Excitation (Right Graph)

5. CONTROL EXPERIMENTS

Experiments were done with two separate control schemes. The first one used analog filter in a feedback path, and the second one implemented a Least Mean-Square adaptive control algorithm on a digital signal processing board. Both experiments were done in a reverberation chamber and the sound pressure level (SPL) generated by the vibrating cylinder was monitored with a microphone to investigate how the controllers reduced the acoustic emission from the cylinder. The disturbance excitation was applied by the shaker. The PVDF film modal sensor and the PZT Actuators were used. The analog control experiments were done on the open cylinder only. The adaptive control experiments were done on both the open and the closed cylinders. The disturbance frequency was 1420 Hz for the open cylinder and 1515 Hz for the closed cylinder.

In the analog control experiment, vibration feedback signal from the PVDF modal sensor was sent to an eight-pole Bessel filter with a cut off frequency of 1440 Hz. The output of the filter was amplified with a power amplifier and elevated to a high voltage with a transformer when necessary. The output from the transformer drove three PZT actuators to counteract the vibration disturbance from the shaker. Figure 5 shows that the feedback control reduced the feedback error signal by 15 dB, acceleration at an antinode by 16 dB, and overall sound pressure level by 23 dB. The control voltage needed to drive the actuators to reduce the SPL from 88 dB to 73 dB was only 3.6 V.

The adaptive control scheme implemented the filtered-x least-mean-square (LMS) algorithm on a TMS320C30 digital signal processing board. The control schematic is

shown in Figure 6. At time step k, the output u_k of the two-weight feedforward controller is a linear combination of x_k and x_{k-1}, where the reference signal x_k is tapped directly from the signal generator which generates the shaker disturbance signal. The two weights w_{0k} and w_{1k} are adjusted by the LMS algorithm based on the information from the PVDF sensor error signal e_k and a reference signal $\hat{x}_k$, which is obtained by filtering the original reference signal x_k through a filter that simulates the transfer function T_c of the plant. This transfer function T_c is measured off-line before the execution of the control program. This technique is based on the version of filtered-x LMS algorithm given by Widrow and Stearns (1985).

When applied to the open cylinder, the adaptive control resulted in a 32 dB reduction in PVDF error signal and a 26 dB reduction in overall sound pressure level. Figure 7 and Table 3 show that the performance of the adaptive control is superior to that of the analog control. The adaptive control appeared to induce a vibration at about 4600 Hz, probably because of aliasing problem. However, the SPL peak caused by this vibration is about 25 dB lower than the uncontrolled SPL. Moreover, this vibration can easily be eliminated by filtering the output of the digital controller.

6. PERFORMANCE OF DIFFERENT SENSOR TYPES

To compare the performance of the PVDF film modal sensor to the performance of an error microphone and a plain PVDF film sensor, experiments were done on the closed cylinder in the reverberation chamber. The reduction in sound pressure level resulting from LMS control using the three sensors is shown in Table 4. The plain PVDF sensor was a rectangular PVDF film whose position with respect to the shaker point of action was
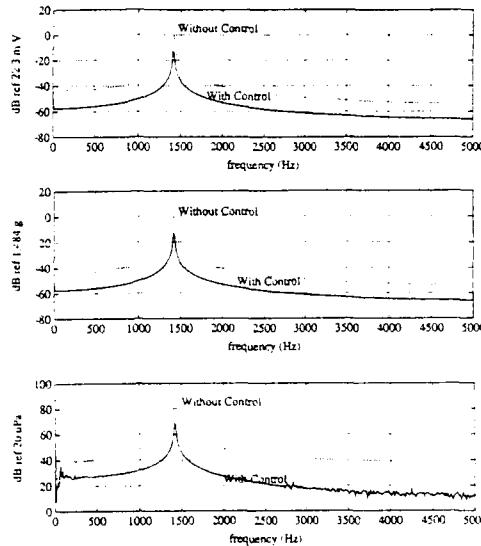

Figure 5 Results of Analog Control on Open Cylinder: Error Signal (Top Graph), Acceleration (Middle Graph) and Sound Pressure Level(Bottom Graph).
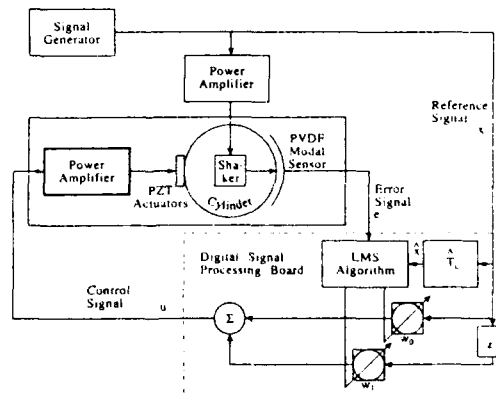

Figure 6 LMS Control System

Table 3 LMS versus Analog Control

Con-troller	Error Signal Reduc-tion (dB)	SPL Reduction (dB)	
		1420 Hz	Over-all
analog	15	23	23
LMS	32	34	26

symmetric with the position of the mode 4 sensor. This sensor was used for comparison with the modal sensor. It is clear that the SPL reduction achieved by using the PVDF modal sensor is comparable to the SPL reduction achieved by using an error microphone. These results show that PVDF modal sensors have a good potential to replace error microphone in various applications.

Figure 7 Sound Pressure Level of Open Cylinder: LMS versus Analog Control
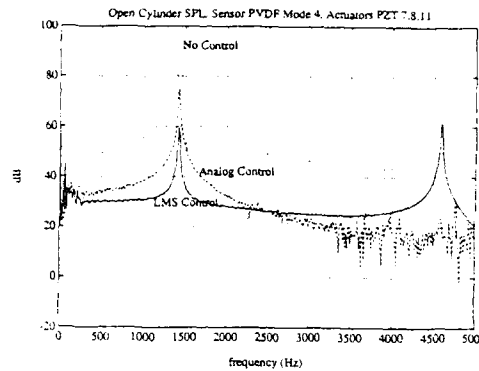
7. CONCLUSIONS

From the series of experiments done on the cylinder, the following conclusions can be drawn. First, one-dimensional modal sensors made of PVDF film can be applied to the cylinder to reduce spillover and stability problem. Second, PZT actuators have sufficient authority to generate the same vibration modes and acoustic directivity as the shaker. Third, the LMS adaptive control creates greater reductions in error signal, acceleration and overall sound pressure level than analog feedback control. And fourth, the control performance achieved with the PVDF modal sensor is comparable to the control performance achieved with a microphone as an error sensor.

Table 4 SPL Reduction Achieved with Three Different Sensors. LMS Control on Closed Cylinder

Sensor	Error Signal Reduction (dB)	SPL Reduction (dB)	
		1513 Hz	Overall
Plain PVDF	42	14	14
PVDF Mode 4	68	33	24
Microphone	26	36	26

8. ACKNOWLEDGEMENT

The authors gratefully acknowledge the support from Westinghouse Electric Corporation for this research.

9. REFERENCES

Blevins, R. D., 1979. *Formulas for Natural Frequency and Mode Shape* (Florida: Krieger), pp. 291-318

Fuller, C. R., and Jones, J. D., 1987. "Experiments on Reduction of Propeller Induced Interior Noise by Active Control of Cylinder Vibration", *J. Sound and Vibration* 112 389-395

Gorman, D. J., 1975. *Free Vibration Analysis of Beams and Shafts* (New York: Wiley) p. 31

Widrow, B. W., and Stearns, S. D., 1985. *Adaptive Signal Processing* (Englewood Cliffs, NJ: Prentice Hall) pp. 99-116 and 288-292

Zhou, N., Sumali, H., and Cudney, H., 1991. "Experimental Development of Piezofilm Modal Sensors and Characterization of Piezofilm Strain Rate Gages", *Proc. 32nd AIAA/ASME/ASCE/AHS/ASC Structural Dynamics and Materials Conf.* pp 735-743

Structural vibration suppression via adaptable damping and stiffness

Y. S. Kim, K. W. Wang and H. S. Lee

Mechanical Engineering Department, The Pennsylvania State University, University Park, PA 16802, USA

ABSTRACT: This paper presents a control strategy to suppress structural vibrations by on-line varying the system damping and stiffness. The feasibility of using ER-fluid-based structures for such purposes is illustrated.

1. INTRODUCTION

It has been recognized that some features of semi-active systems could be attractive to vibration suppression of flexible structures. The main idea is to combine feedback controls with devices whose damping and stiffness characteristics can be varied according to the controller commands. This approach will have the advantages of both the passive and active systems. Since energy is always being dissipated, it is insensitive to the spillover problem encountered in fully-active controls (Balas 1982), while at the same time reserves the benefit of feedback control of an active system. With the recent development of smart materials such as electro-rheological (ER) fluids (Gandhi et al 1987; Coulter et al 1987; Stanway et al 1987), on-line damping and stiffness variations can be physically achievable.

The major consideration in applying semi-active action on structures, other than the distributed nature of the problem, is the nonlinear characteristic of the control system due to the state dependent damping and stiffness parameters, the system uncertainties from unmodelled modes and external disturbances, and the constraints imposed upon the actuators (positive damping and stiffness constants). This paper first presents some experimental results showing the dynamic characteristics of a ER-fluid-based beam structure, and its feasibility for vibration control. We then introduce a novel strategy, based on the theory of sliding mode, for semi-active vibration suppression of flexible structures by on-line varying the damping and stiffness characteristics of the actuators. The main advantage of employing the sliding mode control technique is that it can be adequately applied to nonlinear systems, and the system can be designed to be robust with respect to unmodelled dynamics, system variations and external disturbances.

Although the feasibility of using an ad-hoc sliding mode control for semi-active structures with adjustable damping has been shown by Wang and Kim (1990), it is recognized that the important issue of actuator constraints needs to be addressed to fully utilize the theory. In a recent paper (Kim and Wang 1991), the ad-hoc control law is augmented and modified to compensate for the constraint problem. This present research extended the results of Kim and Wang (1991) to incorporate variable stiffness and Coulomb friction forces of the actuators (which has been experimentally identified in ER-fluid-based systems (Gandhi et al 1987; Stanway et al 1987)) into the control law design.

2. EXPERIMENTAL STUDY

To study the feasibility of using ER-fluid-based structures for vibration suppression, an

experimental fixture has been set up (Fig.1). A composite cantilever beam specimen (30mm x 5mm x 250mm), consists of a 2 mm ER-fluid layer sandwiched between two layers of aluminum glued to plastic plates, has been fabricated. The thin layers of aluminum were used as electrodes. A high voltage (0 to 8K volts) supply is used to activate the system. An accelerometer attached to the end of the beam is used to measure the transverse vibration signals. An impact hammer and a spectrum analyzer are used to perform frequency response analysis of the beam.

Figure 2 illustrates the time response of the beam under free vibration. Given the same initial displacement, the response of the beam damped out much faster when the ER fluid is activated. The system frequency response function is shown in Figure 3. As the actuator voltage increases, both the modal frequency and damping vary. A 8 dB drop of the first two modal transfer function amplitude is observed when the voltage source increases from 0 to 4 kV/mm.

These experimental results show that it is feasible to actively change the structure damping and stiffness by using a distributed adaptive material. It has also been shown that lumped ER-fluid dampers can be very effective in on-line changing their viscous and Coulomb friction dampings (Stanway et al 1987). With these smart actuators, a feedback control algorithm is presented in the following sections to integrate the system and on-line suppress structural vibrations.
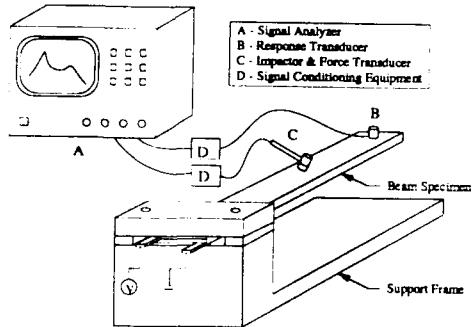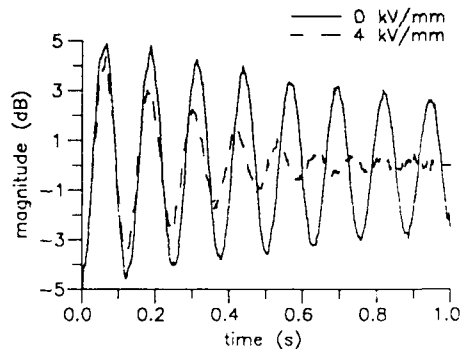
Figure 1. Experimental fixture

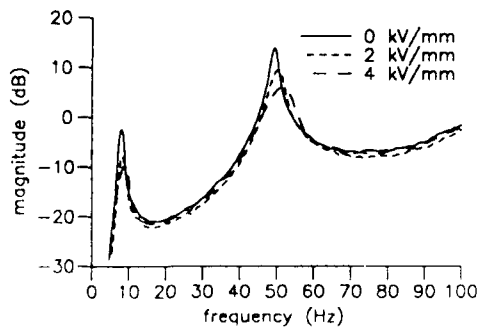Figure 2. Time response of the beam
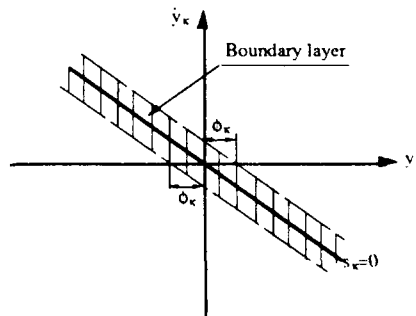
Figure 3. Frequency response of the beam

Figure 4. Sliding surface with boundary layer

3. CONTROL ALGORITHM SYNTHESIS

For the purpose of controller design, a distributed parameter system is normally discretized into a set of ordinary differential equations through the finite element method or other classical techniques, such as Rayleigh-Ritz or Galerkin's method. The model can further be transformed into the modal equations:

$$\ddot{y}(t) + [C] \, \dot{y}(t) + [\Omega] \, y(t) + F_f(y(t), \dot{y}(t)) = f(t) \tag{1}$$

Here $y(t)$ is an $N \times 1$ generalized displacement vector, $[C]$ and $[\Omega]$ are the $N \times N$ variable damping and stiffness control matrices with state-dependent elements, F_f is the Coulomb friction control force vector, and $f(t)$ is the vector consists of external disturbances.

The N modes described in (1) are usually separated into N_m controlled modes and N_R residual modes. Equation (1) can thus be rewritten as

$$\begin{bmatrix} \ddot{y}_c(t) \\ \ddot{y}_R(t) \end{bmatrix} + \begin{bmatrix} C_{cc} & C_{cR} \\ C_{Rc} & C_{RR} \end{bmatrix} \begin{bmatrix} \dot{y}_c(t) \\ \dot{y}_R(t) \end{bmatrix} + \begin{bmatrix} \Omega_{cc} & \Omega_{cR} \\ \Omega_{Rc} & \Omega_{RR} \end{bmatrix} \begin{bmatrix} y_c(t) \\ y_R(t) \end{bmatrix} + \begin{bmatrix} F_{fc}(\dot{y}(t)) \\ F_{fR}(\dot{y}(t)) \end{bmatrix} = \begin{bmatrix} f_c(t) \\ f_R(t) \end{bmatrix} \tag{2}$$

It has been assumed that the relationship between the damping and stiffness variations in ER-fluid-based structures is linear (Gandhi et al 1987). It can also be assumed that the viscous damping constant and the friction force constant are linearly related in ER dampers. These relationships can be determined experimentally. For the control algorithm design, only the controlled modes are considered and therefore the following equation is used:

$$\ddot{y}_c(t) + [\bar{\Omega}_{cc}] \, y_c(t) + [D(\dot{y}_c(t), y_c(t))] \, u(t) = f_c(t) \tag{3}$$

where $u(t)$ is an $M \times 1$ vector consists of the control actions (variable damping constants) from the M actuators, $[D]$ is an $N \times M$ state-dependent matrix and $[\bar{\Omega}_{cc}]$ is an $N \times N$ diagonal constant stiffness matrix. The control actions are computed on the basis of the sliding mode control theory (Kim and Wang 1991; Slotine 1984; Utkin 1977).

Selecting the sliding surfaces (Figure 4) as

$$s(t) = \dot{y}_c(t) + [\lambda] \, y_c(t), \tag{4}$$

and with the sliding condition

$$s_\kappa \dot{s}_\kappa < -\eta_\kappa \, |s_\kappa|, \qquad \kappa = 1, \dots, N_m. \tag{5}$$

the control values become

$$u(t) = [D(\dot{y}_c(t), y_c(t))]^{-1} \, \{ -[\bar{\Omega}_{cc}] \, y_c(t) + [\lambda] \, \dot{y}_c(t) + [\eta + \alpha_c] \, l(s) \} \tag{6}$$

where $s = |s_1, \dots, s_{N_m}|^T$, $u = |u_1, \dots, u_{N_m}|^T$, $[\lambda] = \begin{bmatrix} \lambda_1 & & 0 \\ & \ddots & \\ 0 & & \lambda_{N_m} \end{bmatrix}$,

$[\eta + \alpha_c] = \begin{bmatrix} (\eta_1 + \alpha_1) & & 0 \\ & \ddots & \\ 0 & & (\eta_{N_m} + \alpha_{N_m}) \end{bmatrix}$, and $l(s) = \begin{bmatrix} \text{sat}\left(\dfrac{s_1}{\lambda_1 \phi_1}\right) \\ \vdots \\ \text{sat}\left(\dfrac{s_{N_m}}{\lambda_{N_m} \phi_{N_m}}\right) \end{bmatrix}$.

where $\lambda_\kappa > 0$, η_κ is a small positive number, and α_κ is the upper bound of the κth

generalized disturbance ($\kappa = 1,...,N_m$). The saturation function (Slotine 1984) is introduced to form a boundary layer in state space and eliminate control chatter (Figure 4), i.e.,

$$
\text{sat}\left(\frac{s_\kappa}{\lambda_\kappa \phi_\kappa}\right) = \begin{cases} 1 & \text{with} & 1 \leq \dfrac{s_\kappa}{\lambda_\kappa \phi_\kappa} \\[2mm] -1 & \text{with} & \dfrac{s_\kappa}{\lambda_\kappa \phi_\kappa} \leq -1 \\[2mm] \dfrac{s_\kappa}{\lambda_\kappa \phi_\kappa} & \text{with} & -1 < \dfrac{s_\kappa}{\lambda_\kappa \phi_\kappa} < 1 \end{cases}
$$

The control action for every time step is implemented as follows:

a) Compute the control inputs u_κ ($\kappa=1,..., N_m$) according to equation (6)

b) If all $u_{min} \leq u_\kappa \leq u_{max}$, continue to the next time step. Here u_{min} and u_{max} are the lower and upper constraints of the actuator action, respectively.

c) If N_o number of u_κ have $u_\kappa < u_{min}$ or $u_\kappa > u_{max}$, let these $u_\kappa = u_{min}$ or $u_\kappa = u_{max}$ and re-compute the remaining N_m-N_o u_κs based on the N_m-N_o sliding surfaces. That is, the system is under the effect of N_o number of passive dampers and (N_m-N_o) number of active dampers. In this case, (N_m-N_o) number of modes will be under sliding mode control and satisfy the sliding condition and the other N_o modes will still be under damping.

If singularity occurs during the matrix inversion when computing the control actions, the controls are set to their previous computed values.

4. EXAMPLE AND SIMULATION RESULTS

The presented algorithm is generic and can be applied to various mechanical systems. However, for the purpose of illustration and without loss of generality, a simple-supported beam is used as an example to demonstrate the concept. The structure is modelled as an Euler Bernoulli beam with a uniformiy distributed variable viscous damping layer and lumped adaptable dampers applying on it.

The equation of motion describing the transverse vibration of the beam is:

$$
EI\frac{\partial^4 w(x,t)}{\partial x^4} + u\left[\frac{\partial w(x,t)}{\partial t} + \beta\frac{\partial^4 w(x,t)}{\partial x^4}\right] + m\frac{\partial^2 w(x,t)}{\partial t^2}
$$

$$
+ \sum_{i=1}^{N} \delta(x-x_i)\, u_i \left(\frac{\partial w(x,t)}{\partial t} + f_r \text{sgn}(\frac{\partial w(x,t)}{\partial t})\right) = F(x,t) \tag{7}
$$

The boundary conditions are:

$$
w(0,t) = \frac{\partial^2 w(0,t)}{\partial x^2} = w(L,t) = \frac{\partial^2 w(L,t)}{\partial x^2} = 0
$$

Here, $w(x,t)$ is the transverse displacement of the beam in Figure 5. F is the external disturbance. E is the elastic modulus, I is the beam moment of inertia, and m is the beam mass per unit length. $\delta(x-x_i)$ is a spatial Dirac delta function. The $u\left[\frac{\partial w(x,t)}{\partial t} + \beta\frac{\partial^4 w(x,t)}{\partial x^4}\right]$ term represents the uniformly distributed, variable viscous damping and stiffness. The variable damping and stiffness constants are u and uβ, respectively. The summation terms in equations (7) describe the characteristics of the lumped variable dampers, where $u_i^{(*)}$ is the variable damping constant of the ith actuator located at position x_i, and $u_i f_r$ is the Coulomb friction force of the ith damper, and sgn($\bullet$) is the sign function.

In order to analyze and evaluate the performance of the control system, computer simulations are performed for two cases and the results are discussed in the following paragraphs. For the purpose of analysis, two controlled modes and three residual modes are considered. The parameter values used in these simulations are shown in Tables 1 unless stated otherwise.

Table 1. System parameters

$\dfrac{EI}{mL^4}$	$187.5 \ (1/s^2)$
Experimentally-determined coefficient β	$141.7 \ (m^4/s)$
Experimentally-determined coefficient f_r (*)	$0.04 \ m/s$
u_{min} in the ER-fluid-based structure	$19 \ Ns/m^2$
u_{max} in the ER-fluid-based structure	$33.7 \ Ns/m^2$
u_{min} in the ER damper	$10 \ Ns/m$
u_{max} in the ER damper	$135 \ Ns/m$

(*): f_r and u_i are determined from Stanway et al (1987).

CASE ONE :

To examine the residual mode effects on the structure dynamics, the total energy function of a semi-active system is compared to that of a fully-active system. Here, the fully-active system is also designed based on the sliding mode theory using lumped forces as control inputs. Two lumped actuators are located at $x=L/3$ and $2L/3$ in both the active and semi-active cases. No constraints are imposed on the fully-active actuators. No distributed control is appl.ed. Assuming no observation spillover, the influence of the control spillover phenomenon is studied. Control gains are tuned such that the response of the controlled modes are similar for the active and semi-active cases. In fully-active systems, energy is pumped into the residual modes through the actuators. Therefore, the residual modes are excited when the control actions are on. Once the control actions are turned off after the controlled mode vibrations are eliminated, the system still maintain a constant energy level contributed by the residual modes (Figures 6). In the semi-active case, the energy in all modes are reduced due to the dissipative nature of the system.

CASE TWO :

The flexible beam is controlled by the uniformly distributed element with damping constant u and a lumped damper (u_1) located at $x=2L/5$. The unit impulse response of the beam (impact at $x=3L/5$) is used to compare the semi-active system with two passive cases. Figure 7 illustrates that the performance of the semi-active system compared favorably to that of the $u = u_{max}$ and $u = u_{cr}$ (first critical modal damping without Coulomb friction). This illustrates the advantage of using adaptable damping actions.
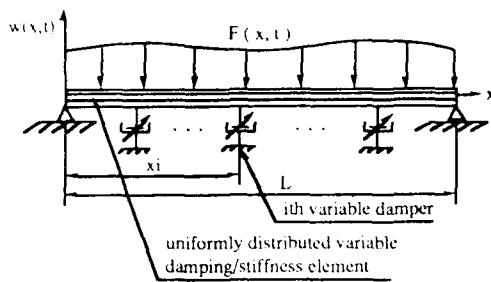
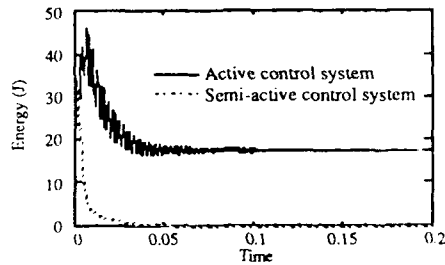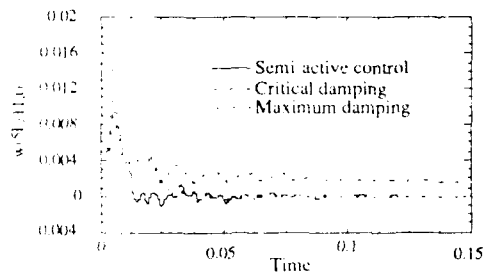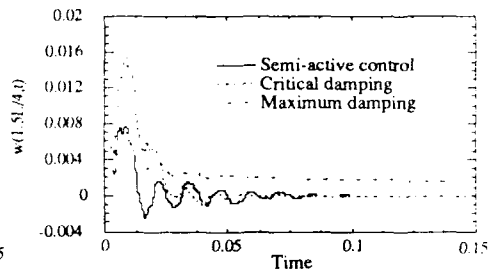Figure 5. Schematic of a beam structure

Figure 6. Total energy of the beam with unit impulse at x=L/3.

a)

b)

Figure 7. Impulse response of the beam at a)=5L/11 and b)x=1.5L/4. Unit impulse is applied at x=3L/5.

5. CONCLUSIONS

Experimental results show that it is feasible to actively vary the structural stiffness and damping by using a distributed ER-fluid material in the structure.

A semi-active control algorithm based on the sliding mode control theory is developed for vibration suppression of flexible structures. The semi-active system compared favorably to two passive systems, the critical and maximum damping cases. The semi-active system is insensitive to the spillover problem when compared to a fully-active system.

REFERENCES

Balas M J 1982 IEEE Trans of Automatic Control AC-27, 3 pp 522-535.

Coulter P. Duclos T G and Acker D N 1989 Damping'89, Palm Beach , FL, pp CAA 1-19.

Kim Y S and Wang K W 1991 to appear in Mechanical Systems and Signal Processing," On the Sliding Mode Control of Structural Vibrations via Variable Damping".

Slotine J E 1984 Int. J. Control 40, 2 pp 421-432.

Stanway B. Sproston J L and Stevens N G 1987 J. of Electrostatics pp 1-19.

Gandhi M V. Thompson B S and Choi S B 1987, "Smart Ultra-Advanced Composite Materials Incorporating Electro-Rheological Fluids for Military, Aerospace, and Automated Manufacturing Applications", pp 23-30.

Utkin V I 1977 IEEE Trans Automat Control AC-22, 2 pp 212-222.

Wang K W and Kim Y S 1990 Proc of ASME Computers In Engrn Conf v.1 pp 449-454.

Beam vibration control through strain-actuation and bending-twist coupling

Lt. Gregory S. Agnes* and Dr. Sung W. Lee**

*USAF Wright Laboratory, WL/FIBGC, Wright Patterson AFB OH 45433
**Department of Aerospace Engineering, Univ. of Maryland, College Park MD 20742

ABSTRACT: Combining strain actuation and structural coupling allows bending
and torsional vibration control of beams. Transverse shear and out-of-plane
warping are identified as important for the modelling of composite beams. A finite
element model for composite beams which includes these effects along with
piezoceramic actuation is developed and applied to a sample problem. The results
show a significant increase in damping in addition to meeting sensitivity and
bandwidth performance specifications. The results show that the use of stiffness
couplings can allow multi-directional active vibration control of beams.

1. INTRODUCTION

Adaptive control of structures through strain actuation shows promise in expanding the
performance envelope of aerospace systems. Within the range of materials currently
available for strain actuation, piezoelectric materials have been studied extensively for
application to actively controlled structures since their response to applied voltage is suitable
within control bandwidths typical of aerospace structures. The piezoelectric effect is isotro-
pic in nature making concurrent bending-twist actuation difficult.

On the other hand, composite materials offer an opportunity to realize beneficial structural
tailoring in aircraft and spacecraft design by introducing stiffness couplings produced when
orthotopic materials are laminated with varying ply angles. For example, in rotary wing
aircraft applications, bending-torsional stiffness coupling can improve pitch-flap stability of
rotor blades while extension-torsional stiffness may be used to change the twist distribution
in two speed tilt rotors. The stiffness couplings of laminated composites, used in
conjunction with strain actuation, can also be exploited to actively control the vibration
response of aerospace structures.

Accordingly, the objective of this paper is to study vibration control of composite beams through the combination of piezoelectric strain actuation and stiffness coupling. This allows the benefits of structural tailoring to be incorporated with strain actuation providing both bending and torsional vibration control of beams.

2. FINITE ELEMENT MODELING

To model composite beams, both the transverse shear and out-of-plane warping effects are important—especially for beams with stiffness couplings. Consequently, a finite element model that allows piezoelectric actuation, transverse shear deformation and cross-sectional warping was developed.

The piezoelectric effect, assuming linearity, may be written:

$$\varepsilon_{Piezo} = K_{piezo} V \tag{1}$$

with ε_{Piezo} the induced strain being proportional to the applied voltage, V. The matrix K represents the relation between applied voltage and induced strain and is both material and geometry dependant. The piezoelectric layers, along with the adhesive layer which bonds the piezoceramics to the beam, may, therefore, be treated as laminae in the beam cross section. Accordingly, the constitutive relation must include the induced strain in the total strain and may be written:

$$\sigma = C(\varepsilon_{Total} - \varepsilon_{Piezo}) \tag{2}$$

where ε represents the strain and C the elasticity matrix. Therefore, piezoelectically induced strain is included in the model in a manner analogous to thermally induced strain.

The second effect, transverse shear, can be included in the model by using shear-flexible beam theory which relaxes the constraint in Bernoulli-Euler theory that cross sections remain perpendicular to the beam axis. Under these assumed kinematics, the beam has constant shear through the cross section. However, under torsional deformation, plane sections do not remain planar and the shear strain is not constant, a phenomenon referred to as out-of-plane cross sectional warping, making shear-flexible theory inaccurate. Out-of-plane warping must therefore also be included in the model.

Cross-sectional warping may be modelled by using a displacement field normal to the cross-section that relaxes the assumption that plane sections remain planar. If the displacement field is continuous in the cross section and weighted by parameters which are functions of the axial coordinate integration through the cross-section may be performed *a priori* and the beam vibration problem is still posed in terms of cross sectional properties. Accordingly, a truncated polynomial series in the cross sectional direction whose weighing terms are functions of the axial coordinate only was chosen. Denoting the axial coordinate as "x" and the cross sectional coordinates as "y" and "z", the displacement field, **u**, is:

$$
\begin{aligned}
u &= \sum_{i=0}^{p} \sum_{j=0}^{q} f_{ij}(x) y^i z^j \\
v &= v_0(x) - z\theta_1(x) \\
w &= w_0(x) + y\theta_1(x)
\end{aligned}
\tag{3}
$$

Only terms linear in the y or z direction are traditionally included in shear-flexible beam theory.($f_{00}=u_0$, $f_{10}=\theta_1$, $f_{01}=\theta_2$) Including terms non-linear in y and z in the assumed kinematics allows modeling of beams which experience out-of plane warping.

Therefore, by including the assumed kinematics of Eqn. 3 and the constitutive relation given by Eqns. 1 and 2, formation of dynamic finite element models of composite beams with piezoelectric actuation is possible. The composite beam models were verified for both static and dynamic cases.(see Agnes 1991) From the mass and stiffness matrices determined from the finite element model, state space models may be formed and controllers designed to suppress beam vibration.

3. EXAMPLE PROBLEM

As an illustrative example, a cantilevered angle ply fiberglass(S glass) beam with piezoelectric crystals bonded as shown in Figure 1 is used. The example beam was modeled using eight three-node beam elements. Using the mass, stiffness, and actuation matrices obtained from the finite element model and assuming modal damp-
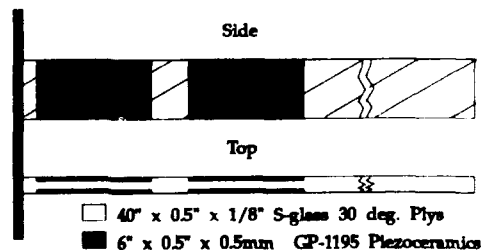

□ 40" x 0.5" x 1/8" S-glass 30 deg. Plys
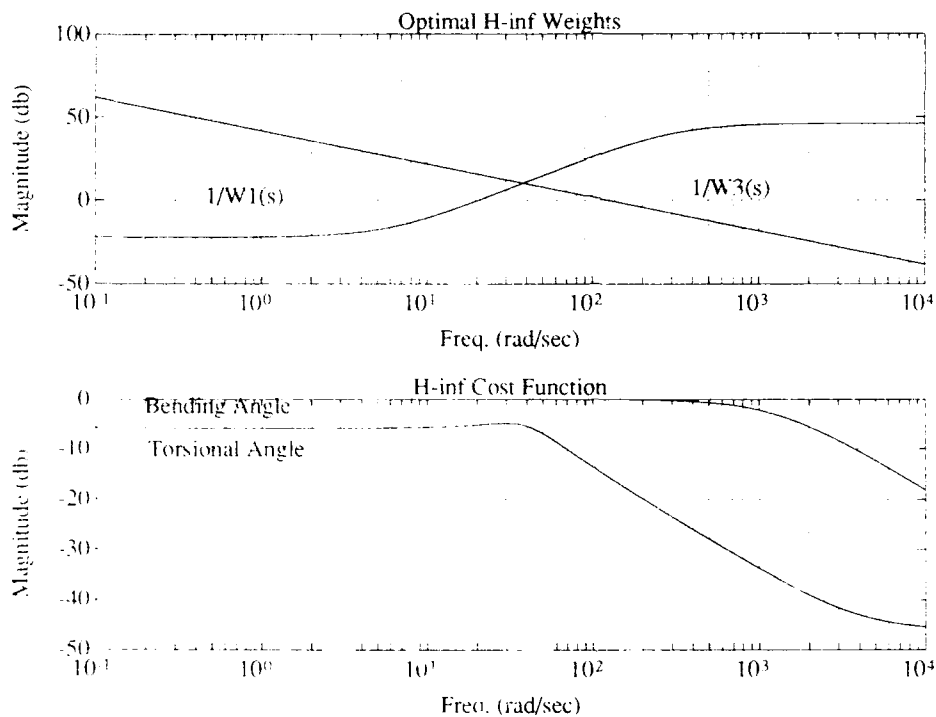■ 6" x 0.5" x 0.5mm GP-1195 Piezoceramics

Figure 1 Beam geometry.

Figure 2 H∞ Weights/Cost Function

ing of 0.5%, a 10*mode approximation was formed. Using model reduction techniques resulted in a six state state-space design model with resonate frequencies of the beam occurring at approximately 4, 18, and 49 hertz.

Next, a controller was designed. Following the H∞ control algorithm presented by Safonov(1988), collocated velocity feedback was first used to increase the damping to 25% and 36% for modes 1 and 2. Mode three split into two first order modes. Velocity sensing was performed using piezoelectric strain rate sensors which produce a current proportional to the integral of the strain rate over the area of attachment.(Obal86) The H∞ weighing matrices were then established to provide at least 10% disturbance attenuation at frequencies less that 1hz and a control bandwidth of approximately 20 hz.

An H∞ optimal controller was found via gamma iteration. A plot of the optimal weights and the cost function may be seen in figure 2. The controller performance was then verified by performing time simulations to a random excitation(0-20 hz) on the model(see figure 3a).
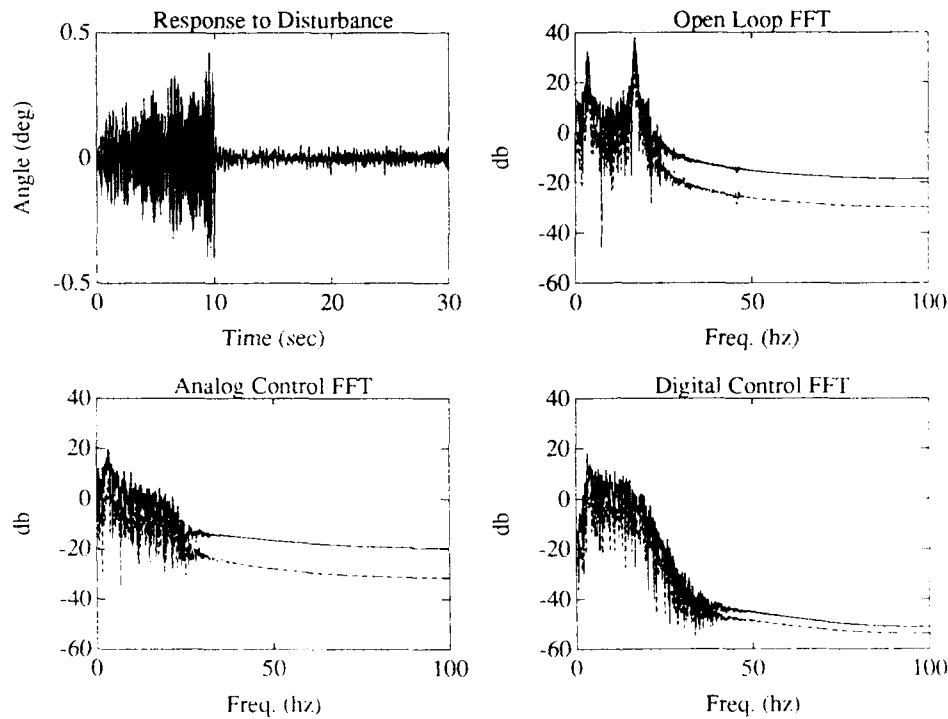
Figure 3 Digital Simulation Results

The excitation consisted of a random bending force and torsional moment acting at x=8 in. Analog velocity feedback was begun at t=10 sec.; both analog and digital H_∞ control at t=20 sec. From the time simulation, the increase in damping is evident. Figures 3b-3d show fast fourier transforms of the digital simulation. Comparing the open loop(Figure 3b) with closed loop(Figure 3d) shows a decrease in response amplitude by almost 20 db. Addition of the digital H_∞ controller results in both the low frequency disturbance attenuation(tracking) and high frequency rolloff specified in the performance goals.

4. CONCLUSIONS

The results show that simultaneous bending and torsional vibration control was made possible through the combination of strain actuation with stiffness couplings. An increase in damping from 0.5% to over 25% was possible for the first three modes. Future work will focus on experimental validation of the model and application of combined strain actuation/stiffness coupling to wing flutter suppression.

5. REFERENCES

Agnes G S 1991, *Vibration Control of Composite Beams Through Strain Actuation and H-infinity Control Theory* Masters Thesis, University of Maryland

Crawley E F and de Luis J 1987 *AIAA Journal* **25** 10 AIAA Paper 86-0878

Obal M W 1986 *Vibration Control of Flexible Structures using Piezoelectric Devices as Sensors and Actuators* Phd Thesis, Georgia Tech

Safonov M G, Chiang R W and Flashner H 1988 *Proc. ACC* pp 2038-2043

Analytical studies on adaptive control of a flexible structure

Anthony P. Tzes

Mechanical Engineering Department

Polytechnic University

333 Jay Street

Brooklyn, NY 11201

Farshad Khorrami

Electrical Engineering Department

Polytechnic University

333 Jay Street

Brooklyn, NY 11201

Abstract

The application and effectiveness of an indirect decentralized adaptive control scheme to the vibration damping control problem of a slewing flexible structure is addressed in this paper. The advocated algorithm comprises of the following parts: 1) the decentralized frequency shaped dynamic compensator penalizing the high frequency contents of the input signal, 2) the input preshaping resulting in a feedforward term that convolves the reference input with a sequence of impulses, and 3) the frequency domain identification algorithm for estimating the system transfer function and adjusting the parameters of the input preshaping scheme. The proposed control algorithm is applied in simulation studies on the slewing truss structure, which has been developed at the Control/Robotics Research Laboratory (CRRL), in order to experiment with control/structure interaction problems.

I. Introduction

The control/structure interaction problem is primarily centered on the design of controllers to compensate for, or to be robust in the presence of structural flexibility imbedded in a flexible structure system.

Application of indirect adaptive schemes in the control problem of large flexible structures is motivated by several factors, such as providing a closed loop system with reduced sensitivity due to modeling uncertainties caused by potential aging structure deformation, parameter variations due to varying payloads, and others. Indirect adaptive control schemes attempt to decrease the effects of plant uncertainty by identifying the system on-line, and subsequently updating the controller parameters. Such adaptive schemes therefore consist of two components the controller and the identification scheme.

Transfer function identification algorithms can been classified into either frequency or time domain schemes. The main characteristic of frequency domain identification methods is that the input signal is transformed to frequency domain before adaptive filtering is applied. The proposed controller structure shown in Figure 1, is comprised into 1) a decentralized frequency weighted low-order output feedback controller, and 2) an input precompensator which shapes the reference input in such a way that the vibrational modes are not excited. The advocated algorithm is demonstrated in simulation studies on the CRRL flexible structure testbed facility.

In the next sections the experimental setup and the advocated control algorithms are described analytically, while several issues related to their real-time implementation are addressed.
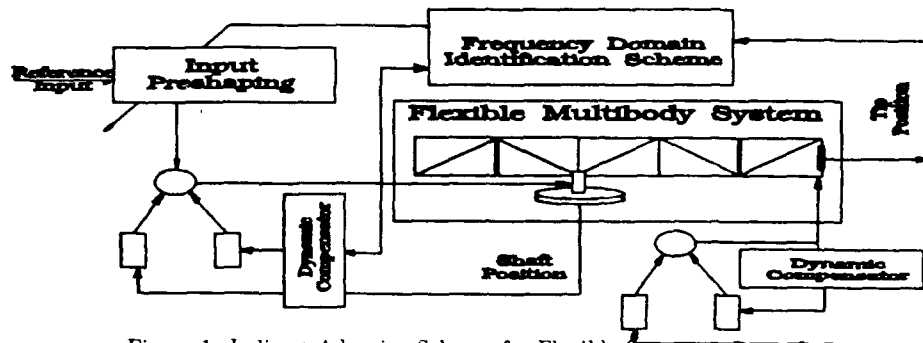
Figure 1: Indirect Adaptive Scheme for Flexible Structure Control

II.   Slewing Flexible Structure Experimental Setup

In this section a brief description of the apparatus considered in this work is provided. The CRRL control/structure interaction testbed facility consists of a two dimensional truss structure with one active member situated on the horizontal plane as shown in Figure 1. The struts and the nodes of the truss are the same as the ones used in NASA's testbed facilities. One of the struts has been replaced with a threadless mechanical screw-type linear actuator with backlash less than 0.001 inches manufactured by Rohlix. One of the nodes is attached, through a hub assembly, to a direct drive dc-motor manufactured by Dynaserve (DM1015B) capable of producing 15 N-m torque. The Dynaserve motor has ±2 arc-sec repeatability, and can be utilized for large angle maneuvers as well as micropositioning due its high encoder resolution ($655,360 \frac{pulse}{rev}$). The servo driver incorporates an analog speed input signal and includes temperature, low voltage, encoder and CPU abnormal alarms. Additional sensing devices include Kistler accelerometers, and an F/T 15/50 Force Sensor manufactured by ATI, Inc. capable of sensing forces and torques in all three directions. The primary computing facility includes two IBM 386-machines equipped with digital signal processor boards (TMS320C30-based) for the number crunching requirements of the proposed real-time control algorithm.

The reduced finite element model of the structure provides the following modal frequencies, with their associated mode shapes shown in Figure 2. From a control viewpoint, the system has two inputs, the voltage applied to the motor u_1 and the force exerted by the active member u_2, while the outputs include the shaft angular position and the truss structure tip displacement measured in the plane of revolution (Figure 1).

III.   Controller Design

A.   Decentralized Compensator

A frequency weighted linear quadratic regulator in a decentralized structure framework is employed in order to suppress the vibrations. The reasons for utilizing a frequency dependent weighting is due to the fact that the available model may neither reflect accurately the effects of high frequencies nor include the high frequency effects all together. Furthermore, actuator and sensor dynamics may inhibit inputs in the neighborhoods of these frequencies. Moreover, the decentralized framework will allow a simpler and more feasible implementation of the feedback controllers.
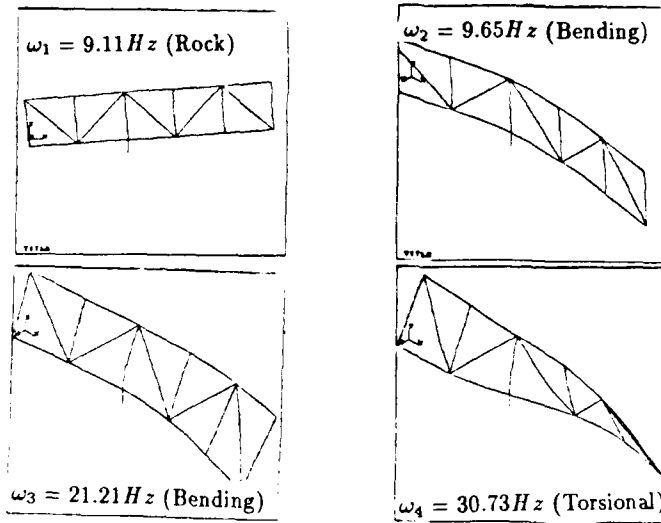
Figure 2: Truss Structure Mode Shapes.

Consider the following truncated model of the truss structure

$$M\ddot{x} + Kx + (\alpha M + \beta K)\dot{x} = \sum_{i=1}^{2} B_i u_i, \qquad y_i = C_i x, \ i = 1, 2, \tag{1}$$

where x is the state vector, M and K the mass and stiffness matrices respectively, α and β parameters resulting in a 5% structural damping over the frequencies of interest, y_1 and y_2 correspond to the shaft angular position and tip position respectively. The decentralized dynamic stabilizing compensator

$$\dot{z}_i = F_i z_i + G_i y_i, \qquad u_i = H_i z_i + M_i y_i; \qquad i = 1, 2. \tag{2}$$

that minimizes the following cost function

$$J = \frac{1}{2} \int_{-\infty}^{\infty} [x^T Q x + \sum_{i=1}^{2} U_i^*(j\omega) R_i(\omega) U_i(\omega)] \, d\omega , \tag{3}$$

where $Q > 0$ is a positive semidefinite Hermitian matrix, $R_i(\omega) = \frac{\omega^2 + \omega_2^2}{\omega^2 + \omega_4^2}$ $i = 1, 2$ are the frequency dependent matrices, and ω_1 and ω_4 correspond to the first and last modal frequencies (Figure 2) from the structure truncated model reduces to the solution of a non-convex nonlinear optimization problem [1, 2].

Effectively, this choice of $R_i(\omega)$ penalizes more the high frequencies than the low frequency controls in channel i, which causes a reduction in the ith loop gain of the closed-loop system at the high frequencies which in turn also compensates for the high frequency uncertainties in the plant model related to channel i.

B. Adaptive Precompensation

Despite the rapid growth of feedback algorithms for control/structure interaction, there has been relatively little focus upon the idea of shaping the input in such a way that the vibrational modes are not excited.

Input shaping schemes adjust the input command to the structure so that vibrations are eliminated [3, 4]. The input compensators can be designed in either the frequency domain
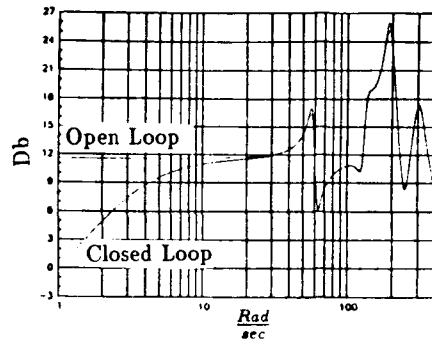
Figure 3: Transfer function magnitude response.

resulting in bandstop or notch filter structure centered around the modal frequencies [5], or in the time domain [5, 6, 7, 8] corresponding to a feedforward term that convolves in real-time the desired reference input with a sequence of impulses having appropriate magnitudes and spacing within the time domain.

In the sequel, the basic relationships for the amplitudes $A_{f,j}$ and the spacing $t_{f,j}$ between the impulses are presented. Assume that the modal frequencies ω_f and modal damping ζ_f of the system governed by the equations (1) are known *a priori*; then the solution for the advocated impulse amplitudes and their relative spacing is :

$$A_{f,j} = \frac{\binom{N_1-1}{j-1}K_f^{j-1}}{\sum_{i=0}^{N_1-1}\binom{N_1-1}{i}K_f^i}, \quad t_{f,j} = (j-1)\frac{\pi}{\omega_f\sqrt{1-\zeta_f^2}}, \quad K_f = e^{-\frac{\zeta_f\pi}{\sqrt{1-\zeta_f^2}}}, \quad (4)$$

where the impulses with amplitudes $A_{f,j}$ are responsible for producing a vibration free output from the effects ω_f^{th} modal frequency. Internal system balancing [9] indicates that the second modal frequency state component is the dominating one between the motor voltage and tip displacement transfer function. This can be further verified from the aforementioned transfer function magnitude frequency response shown in Figure 3 (prior and after the application of the decentralized feedback control).

The robustness of time domain precompensators to modal frequency variations is improved by convolving the input with a longer sequence of impulses, the tradeoff being a decrease in the transient response speed.

An adaptive precompensator [8] can be implemented by estimating on-line the modal frequencies and subsequently updating the spacing between the impulses. The combined adaptive input preshaping scheme provides the most rapid slew that results in a vibration free output, since it can provide the same robustness with less number of impulses.

C. Transfer Function Identification Scheme

The frequency domain identification scheme, called Time-varying Transfer Function Estimation (TTFE) [10, 11] is employed for the on-line identification problem of the flexible truss structure transfer function, denoted accordingly by $H(k)$.

Let the input signal $u(n)$ and output $y(n)$ are accumulated into buffer memories to form N-point data blocks These blocks are then transformed by N-point Fast Fourier Transforms

(FFTs) to their equivalent frequency transformed blocks U, Y at the kth time instant; that is,

$$
U(k)=\begin{bmatrix} U_0(k) \\ U_1(k) \\ \vdots \\ U_{N-1}(k) \end{bmatrix} = \mathcal{F} \begin{bmatrix} u(k) \\ u(k-1) \\ \vdots \\ u(k-N+1) \end{bmatrix} = \mathcal{F}\vec{u}(k), Y(k)=\begin{bmatrix} Y_0(k) \\ Y_1(k) \\ \vdots \\ Y_{N-1}(k) \end{bmatrix} = \mathcal{F} \begin{bmatrix} y(k) \\ y(k-1) \\ \vdots \\ y(k-N+1) \end{bmatrix} = \mathcal{F}\vec{y}(k)
$$

(5)

where $\mathcal{F}$ corresponds to the Fourier operator applied to an $(N \times 1)$ vector, $(\mathcal{F}_{i,j} = e^{-\frac{2\pi ij}{N}i}, i = 1, \ldots, N, j = 1, \ldots, N)$, and the notation $\vec{u}(k), \vec{y}(k)$ has been adopted for the indicated vectors. Within this frequency domain framework, the simplest form of frequency domain identification, called Empirical Transfer Function Estimate (ETFE), is to form an estimate of the transfer function at time k, $\Theta_i(k)$, as the ratio of the output transform to input transform in the manner $\Theta_i(k) = \frac{Y_i(k)}{U_i(k)}$ for $i \in \{0 \le i \le N - 1, U_i(k) \ne 0\}$, where i corresponds to i^{th} bin in the frequency domain, and $\Theta_i^*(k)$ is the complex conjugate of $\Theta_i(k)$.

TTFE updates the frequency components in the time domain through a recursive adaptation algorithm such as recursive least squares, or least mean squares. The adjacent frequency components need not necessarily be independent, so that a smoothing of the transfer function is realized. The weighted complex RLS algorithm based on the input-output model $Y_i(k) = H_i(k - 1)U_i(k - 1)$ is utilized in the manner

$$
\Theta_i(k) = \Theta_i(k-1) + \frac{P_i(k-1)U_i^*(k-1)}{\alpha_i + U_i(k-1)P_i(k-1)U_i^*(k-1)}[Y_i(k) - \Theta_i(k-1)U_i(k-1)]
$$

$$
P_i(k) = \frac{1}{\alpha_i}\left[P_i(k-1) - \frac{P_i(k-1)U_i^*(k-1)U_i(k-1)P_i(k-1)}{\alpha_i + U_i(k-1)P_i(k-1)U_i^*(k-1)}\right],
$$

(6)

where $i = 1, \ldots, N$, the forgetting factor α_i satisfies $0 < \alpha_i \le 1$, and P_i corresponds to the covariance matrices of RLS. In case of a sudden change of system dynamics, this recursion results in a smooth transient from the old transfer function to the new one. This represents a substantial difference with the nonrecursive ETFE technique which suffers a less smooth transition due to the assumption of orthogonalized input–output data blocks.

The large computational burden of TTFE related to the frequent calculation of input and output Fast Fourier transforms, can be alleviated by recursively updating the FFTs rather than explicitly computing them at each time instant. The recursive implementation of the FFT can be exploited by utilizing the circular symmetrical property arising from the definition of the FFT operator [12, 13].

The final step of the TTFE algorithm is to determine the locations of poles and zeros from the frequency domain representation of the transfer function. By determining the locations of the poles and the zeros of the system, as the peaks and the valleys of the magnitude frequency response, TTFE can detect changes to the system and tune the controller parameters accordingly.

IV. Conclusion

A decentralized adaptive controller was applied through simulation studies on the CRRL flexible truss structure dynamic model for reducing the residual vibrations. The resulting controller penalizes the high frequency contents of the input signal, and reshapes the reference input in such a way that the vibrational modes are not excited. Research is currently undergoing on applying the aforementioned scheme on the experimental setup.

Acknowledgments

References

[1] F. Khorrami, S. Tien, and Ü. Özgüner, "DOLORES: a software package for analysis and design of optimal decentralized control," in *Proceedings of the 40th National Aerospace & Electronics Conference*, pp. 434–441, Dayton, Ohio, May 1988.

[2] F. Khorrami and U. Özgüner, "Frequency-Shaped Cost Functionals for Decentralized Systems," in *Proceedings of the IEEE Conference on Decision and Control*, pp. 417–422, Austin, TX, December 1988.

[3] N. C. Singer and W. P. Seering, "Controlling vibration in remote manipulators," in *ASME Design Automation Conference*, Boston, MA, September 1987.

[4] N. C. Singer and W. P. Seering, "Using acausal shaping techniques to reduce robot vibrations," in *Proceedings of the IEEE International Conference on Robotics and Automation*, pp. 1434–1439, Philadelphia PA, April 1988.

[5] A. Tzes and S. Yurkovich, "Adaptive Precompensators for Flexible Link Manipulator Control," in *Proceedings of the IEEE Conference on Decision and Control*, pp. 2083–2088, Tampa, FL, December 1989.

[6] F. Khorrami, S. Jain, A. Tzes, W. Grossman, and W. Blesser, "Nonlinear Control with Input Preshaping for Flexible Link Manipulators," in *Proceedings of the Fifth International Conference on Advanced Robotics*, pp. 832–852, Pisa, Italy, June 1991.

[7] N. C. Singer and W. P. Seering, "Preshaping command inputs to reduce system vibration," Technical Report A.I. Memo No. 1027, MIT Artificial Intelligence Laboratory, 1988.

[8] A. Tzes, M. Englehart, and S. Yurkovich, "Input Preshaping with Frequency Domain Information for Flexible Link Manipulators," in *Proceedings of the AIAA Guidance, Navigation and Control Conference*, pp. 1167–1175, Boston, MA, August 1989.

[9] B. C. Moore, "Principal component analysis in linear systems: Controllability, observability, and model reduction," *IEEE Transactions on Automatic Control*, vol. AC–26, no. 1, pp. 17–31, February 1981.

[10] A. Tzes and S. Yurkovich, "A Frequency Domain Identification Scheme for Flexible Structure Control," *Trans. ASME, J. Dyn., Meas., and Control*, vol. 112, pp. 427–434, September 1990.

[11] S. Yurkovich, F. Pacheco, and A. Tzes, "On-Line Frequency Domain Information for Control of a Flexible-Link Robot with Varying Payload," *IEEE Transactions on Automatic Control*, pp. 1300–1304, December 1989.

[12] S. Yurkovich and A. Tzes, "Experiments in Identification and Control of Flexible Link Manipulators," *Control Systems Magazine*, vol. 10, no. 2, pp. 41–47, February 1990.

[13] A. Tzes, "Self-Tuning Controllers for Flexible Link Manipulators," Ph.D. Thesis, The Ohio State University, June 1990.

491

Nonobstructive particle damping nonlinear characteristics

H.V. Panossian

Rockwell International/Rocketdyne Division, 6633 Canoga Avenue, Canoga Park, CA 91303

ABSTRACT: This paper presents the nonlinear characteristics of Nonobstructive Particle Damping (NOPD). NOPD is a new passive vibration damping technique that consists of making small diameter holes (or cavities) at appropriate locations inside the main load paths of a vibrating structure and filling these holes to appropriate levels with metallic or nonmetallic particles in powder, spherical, or liquid form (or mixtures). The test results, which indicate clear nonlinear behavior, are presented and discussed briefly.

1. INTRODUCTION

Viscoelastic materials obey differential and integral stress–strain relationships relating to stresses, strains, and their time derivatives (Hilton 1991). The energy dissipation mechanism is mainly a complex, highly frequency–dependent, material–sensitive viscous process with one or more viscosity coefficients unrelated to structural damping (Hilton 1964). In general, viscous damping entails Newtonian flow, with stresses and strain velocities proportional to each other. Moreover, structural damping is fairly well characterized, and damping coefficients for regular materials are abundant. Its interpretation in terms of viscous damping, however, is not so clear (Dahl 1976). Linear and nonlinear formulations have appeared in the literature on solid friction–damping mechanisms in mechanical oscillations. Oscillation amplitude decay has been linked to coulomb friction, viscous damping, and structural damping at various frequency and amplitude conditions.

The nonobstructive particle damping (NOPD) technique entails making small holes (or cavities) at analytically determined (and, when possible, experimentally verified) locations inside the main load paths of a vibrating structure in appropriate areas and filling these holes to proper levels with such particles as to yield maximum damping effectiveness. A specific vibration mode, or several modes, can be addressed in a given structure. Powders, spherical, or irregular particles in metallic, nonmetallic, or liquid form (or even mixtures) with different densities, viscosities, and adhesive or cohesive characteristics can be used. (Panossian 1990, 1991a, and 1991b).

2. NOPD NONLINEAR CHARACTERISTICS

Experimental modal survey tests were carried out in the Rocketdyne Engineering Development Laboratory (EDL) on two 24-inch by 3-inch by 3/4-inch aluminum beams under free-free conditions, and various modal and vibration data were generated. Acceleration and strain measurements were taken on five equidistant points on each beam. One of the beams had seven 2-mm diameter holes along the length, and the other had thirteen 2-mm diameter holes along the width. The holes were filled with various particles and tested for damping effectiveness under different excitation levels.

The tests were performed by suspending each beam from two rubber bands and exciting it using an electomechanical exciter with a load cell at the stinger tip near one of its ends (Figure 1). Five acceleration and four strain measurements were taken at equidistant points on the beam with the two accelerometers placed at the opposite corners of both ends. Frequency response functions (FRFs), power spectral densities (PSDs), time histories, and other appropriate data were evaluated to study the damping ratios, mode shapes, and frequencies.

The seven equidistant 2-mm diameter holes drilled along the length (in the neutral plane) of the first aluminum beam were partially filled (about 90%) with tungsten powder, zirconium oxide powder, and steel shots (0.011 in. diameter). The beam was excited with a shaker with slow swept sinusoidal inputs between 10 to 1,600 Hz applied at one corner of the beam from the opposite side of the accelerometer. The FRFs were generated under empty and filled conditions and overlaid (Figure 2). The plot is that of the first bending mode at about 273 Hz when empty. The overall FRF up to 1,600 Hz is shown in Figure 3.

Figure 4 shows the dramatic response reduction by two of the many kinds of particles used. As can be seen, the accelerance amplitude when the holes are empty is 55g/lb at 275 Hz frequency while with steel shots, it reduces down to 0.88 g/lb at 267 Hz. The corresponding damping ratios at an input excitation level of 3 lbf are 0.01% of critical when empty, 1.3% with steel shots, and 3% with tungsten powder. The damping effectiveness is increased with amplitude of excitation in a rather nonlinear behavior. Figures 5 and 6 show the overlays of FRFs for steel and tungsten powder under input forces of 1 lbf, 2 lbf, 3 lbf, 4 lbf, and 5 lbf. The accompanying Nyquist plots show a clear indication of nonlinear behavior. Normally, the presence of coulomb friction and other nonlinear damping characteristics exhibit such behavior (Ewins 1986). There have been other test results that also provide sufficient proof to conclude that the NOPD mechanisms involve friction type of nonlinearities, among others.

Recent tests on particle impact force profiles have exhibited what can perhaps be characterized as exponential nonlinearities of impact force relations with beam velocity and displacement. This effect is being further analyzed.

3. CONCLUSIONS

The NOPD technique is a very effective vibration damping technique that has potential applications in all areas of structural vibration and acoustics. The test results show
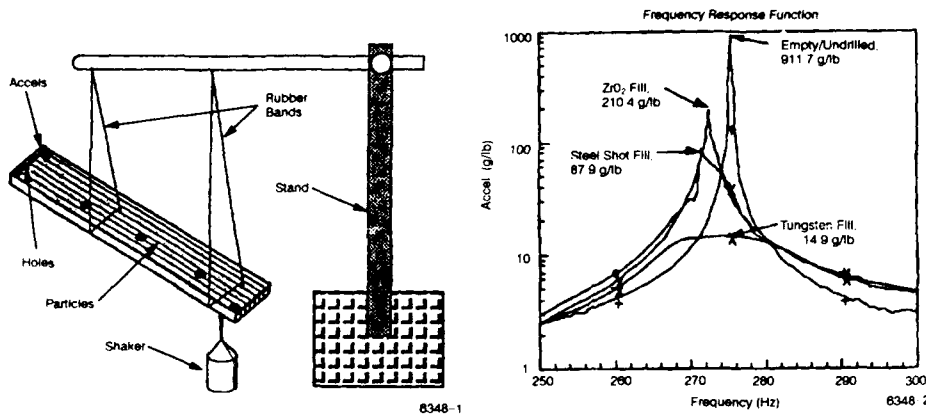
Figure 1.   Free–Free Beam Tests in Air   Figure 2.   First Free–Free Bending Mode

effectiveness in both high and low frequency ranges. Moreover, the NOPD concept is simple, easy to implement (holes and particles can be imbedded as part of the manufacturing process of the structure), and is relatively inexpensive. It has advantages over viscoelastic damping because its effectiveness is independent of environments and frequency. It has more mechanisms for energy dissipation, does not add mass (it can often reduce mass), and does not degrade in time (among others). Furthermore, damping can be optimized through experiment and analyses by choosing the right locations and size of holes in a structure, and by determining the optimal size–shape–kind–mixture of particles used.

Further research is necessary to characterize the nonlinearities analytically as well as understand and model the mechanisms involved in vibration energy dissipation. A whole new technology similar to and complementing viscoelastic damping can result from this approach given sufficient research and development with analytical modeling capabilities.

REFERENCES

Dahl, P R, 1976, *AIAA Journal*, 14, pp. 1675–1682.

Hilton, H H, 1991, *Proc. Damping '91*, Wright Laboratory Flight Dynamics Directorate, OH, pp. ICB-1, ICB-15.

Hilton, H H, 1964, *Engineering Design for Plastics*, (New York:Reinhold) pp. 199–276.

Panossian, H V, 1991, *Shock & Vibration Technology Review*, pp. 4–10.

Panossian, H V, 1991, *Journal of Vibration and Acoustics*, to appear.

Panossian, H V, and Bice, D L, 1990, *Proc. Shock & Vibration*, pp 241–151.

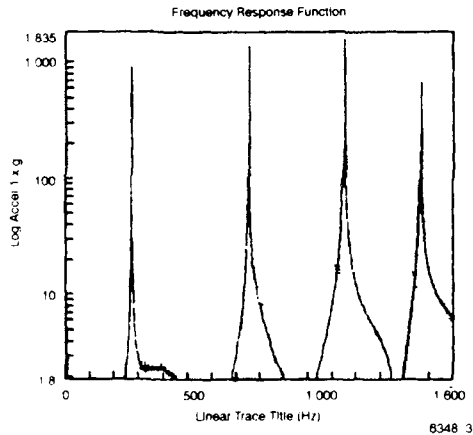Ewins, D J, 1986, *Modal Testing: Theory and Practice*, John Wiley & Sons Inc., NY.

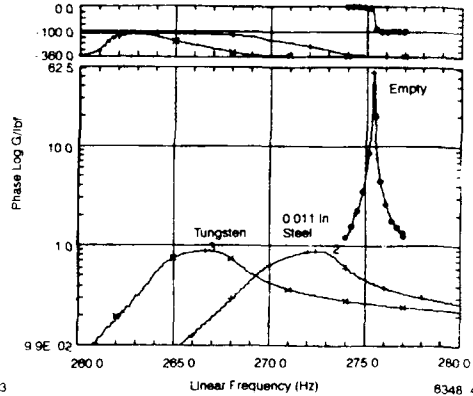**Figure 3.   FRF of Empty Cross-Holed Beam Free-Free in Air**

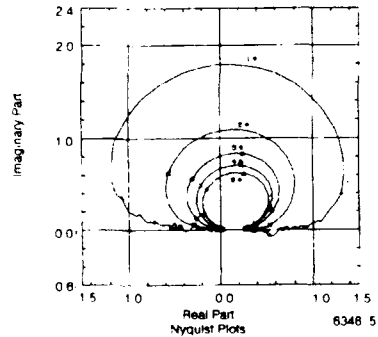**Figure 4.   Damping Effectiveness of NOPD with 3 lbf Excitation**
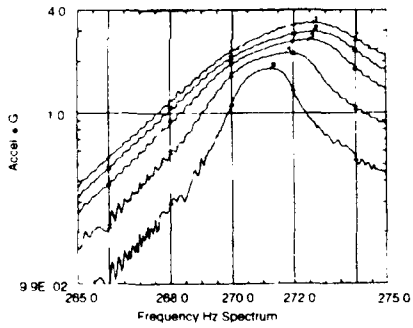

Figure 5.   Free-Free Beam Excitation Level Comparison Under NOPD Treatment With 0.011 in. Steel Shots.
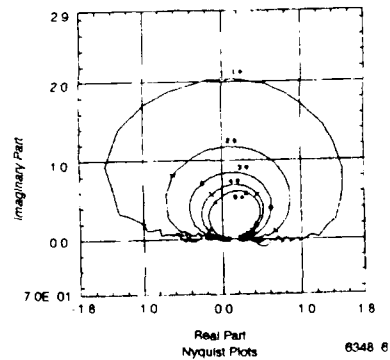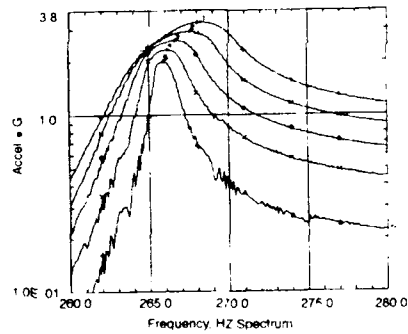

Figure 6.   Free-Free Beam Excitation Level Comparisons Under NOPD Treatment With Tungsten Powder.

Structural motion control by analytic determination of optimum viscoelastic properties

Harry H Hilton and Sung Yi

Aeronautical and Astronautical Engineering, University of Illinois at Urbana-Champaign, Urbana, IL 61801-2997

ABSTRACT: Master relaxation curves are analytically generated and their parametric influences on complex moduli, stored and dissipated energies for and responses to several loading conditions are evaluated. These pilot studies provide the basic knowledge on how to control viscoelastic structural motion through proper slection of material properties and what "designer materials" are to be manufactured for given service environments and requirements.

1. INTRODUCTION

Material selection must be based on service performance in prescribed environments. Viscoelastic damping materials may be used to reduce vibration amplitudes and/or to decay motion in prescribed times by converting mechanical energy into heat. Gottenberg and Christensen (1964) experimentally obtained complex shear moduli for isotropic viscoelastic materials in the frequency domain and relaxation functions by taking Fourier transforms of complex moduli. Bert (1973) reviewed the various mathematical models necessary to represent material damping behaviors and the experimental techniques needed to determine damping characteristics. Jones (1981) studied complex moduli of damping materials at reduced temperatures and in reduced frequency domains. Rogers (1981) proposed that the damping characteristics of viscoelastic materials can be analyzed using fractional derivative representations and Sim and Kim (1990) proposed a method to estimate material properties of isotropic viscoelastic materials. An extensive literature review may be found in Hilton and Yi (1991b).

2. DISCUSSION OF RESULTS

Hilton and Yi (1991b) have shown that the important characterization parameters for viscoelastic material master relaxation curves are the maximum $G(0)$ and minimum G^∞ modulus values, the slope of the transition region and the time span of the relaxation. The relaxation modulus curves are analytically generated for each parameteric set defining the 5 regions shown in Fig 1. These master relaxation curves are then curve fitted by least squares onto Prony series (Hilton 1964) using the multidata method of Cost and Becker (1970) and the relaxation time approximations of Schapery (1962). Figs 1 to 3 illustrate the seven distinct relaxation shear moduli curves for viscoelastic materials generated for each parameteric set. The curve M1 is the "standard" with which comparisons are made. Three master curves for the relaxation modulus with
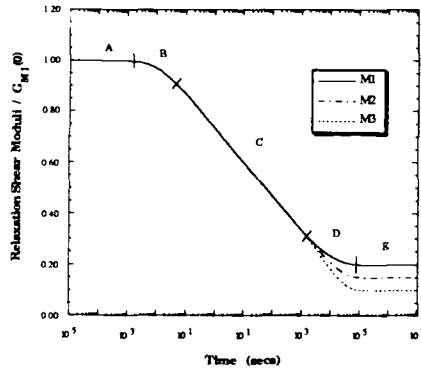
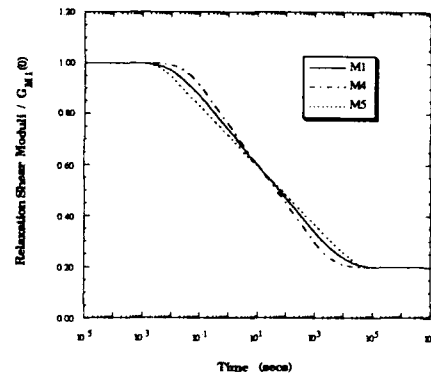Fig 1 Time dependent shear moduli
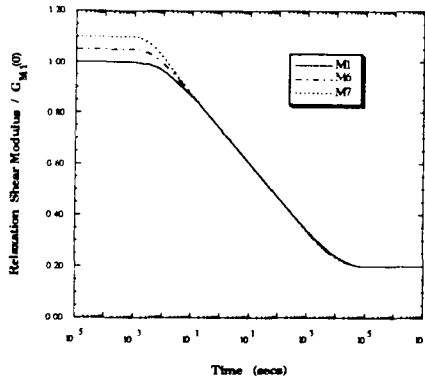

Fig 2 Time dependent shear moduli
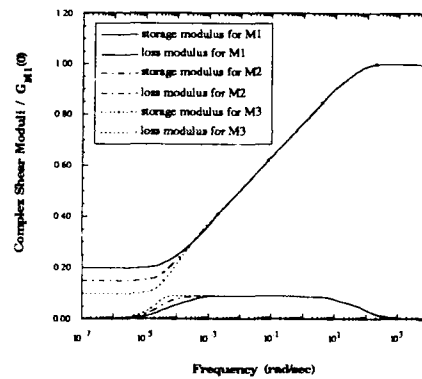

Fig 3 Time dependent shear moduli

Fig 4 Storage & loss moduli vs frequency

different G^∞ values are plotted with the $G^\infty/G_{M1}(0)$ values taken as 0.2, 0.15, and 0.1 respectively while all other parameters do not change for the three curves M1, M2 and M3. Similarly, curves M1, M4, M5 with different slopes of the relaxation modulus of 1.0, 1.05 and 1.1 are depicted. The three curves M1, M6, M7 with the different normalized $G(0)$ values with respect to the M1 $G(0)$ value are also shown.

The complex moduli can be obtained by taking Fourier transforms of the constitutive equations in the time domain and curves M1, M2, M3, M4, M5, M6 and M7 are plotted in Figs 4 to 6. Rapid relaxation of the storage modulus (the real part of complex shear modulus) from the unrelaxed to the relaxed values are observed while the peaks in the loss modulus (the imaginary part of complex modulus) occur during the same frequency range. At the two storage modulus values $G(0)$ and G^∞, the loss moduli converge to zero. The results show that the storage modulus curves in the ω plane are mirror images of the relaxation modulus curves in the time plane. The maximum and minimum storage modulus values correspond to the maximum and minimum values of the relaxation modulus respectively. The frequency span from the minimum storage modulus value to the maximum one covers approximately the same number of decades as the time duration from the initial modulus to the relaxed value with $\omega \approx 1/t$. Decreases in G^∞ result in decreases of storage modulus values and increases in loss

modulus values in the low frequency region. Fig. 5 shows that increases of transition region slopes result in increases of loss modulus maximum peak values in the frequency domain. Fig 6 shows that an increase in the initial modulus $G(0)$ values yields increases in both storage modulus and loss modulus values in the high frequencies region.
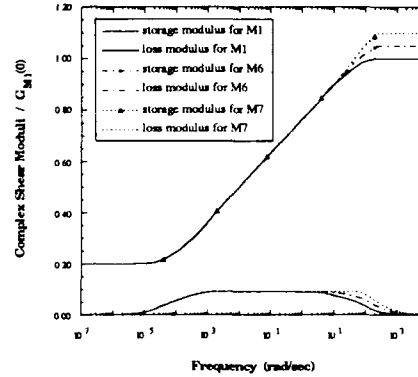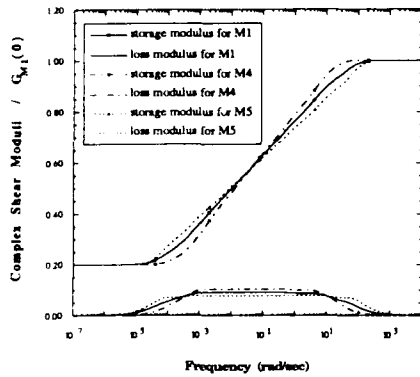

Fig 5 Storage & loss moduli vs frequency   Fig 6 Storage & loss moduli vs frequency

In Figs 7 to 9, the energies dissipated by a one dimensional unit step shear strain loading are compared. The same energies for curves M1, M2 and M3 are dissipated up to $t=10^3$ secs since the material properties change only after $t=10^3$ secs. However, the loss energies after $t=10^3$ secs are directly proportional to the decreasing values of G^∞. For these examples changes in relaxation modulus slopes do not influence the total dissipated energy up to 10^6 sec. Fig 9 shows that an increase in initial modulus values results in an increase of energy loss throughout the loading history. After the moduli are fully degraded, the amounts of dissipated energy for M2 and M3 are the same as those for M6 and M7 respectively. The amounts of energy lost for the unit step loading are proportional to the rate of relaxation i.e., $(G(0) - G^\infty)/(t_0 - t_\infty)$. However, in the transition region cases, M6 and M7 dissipate more energies than M2 and M3, since the viscoelastic material properties for M6 and M7 change at early times and then influence the energy loss through the remaining loading history.
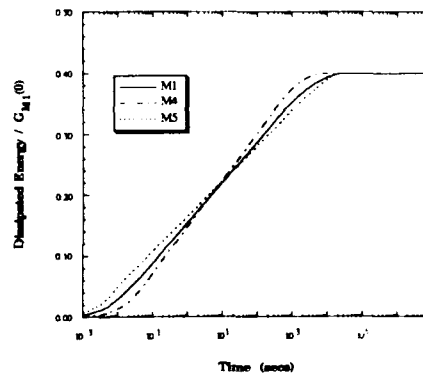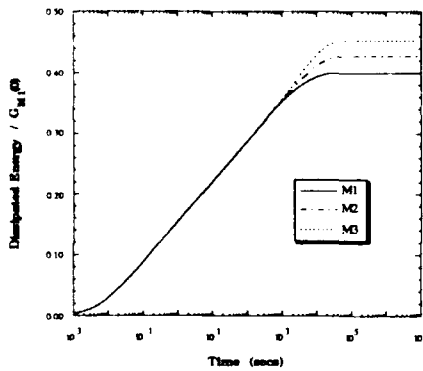

Fig 7 Dissipated energies for a unit step   Fig 8 Dissipated energies for a unit step
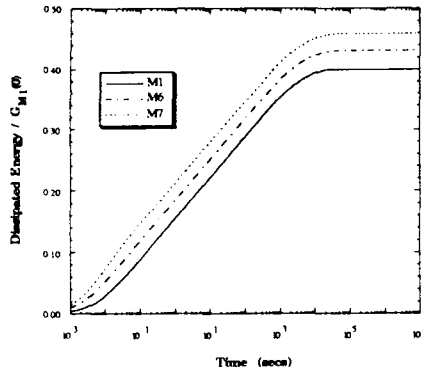   strain loading   strain loading.

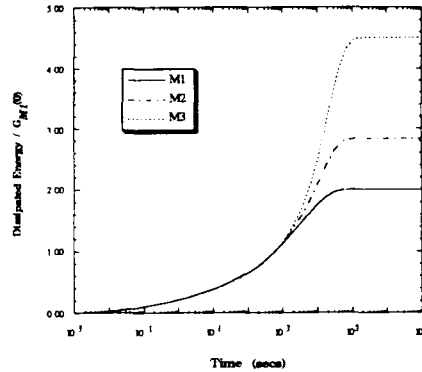Fig 9 Dissipated energies for a unit step strain loading

Fig 10 Dissipated energies for a unit step stress loading

A unit step stress is applied to a viscoelastic bar and the results show that the amount of energy dissipated by unit stress excitations is larger than that obtained by a unit strain loading. For the strain loading cases, the energies dissipated in M1, M2, and M3 are linearly proportional to the changes in initial modulus. However, as shown in Fig 11, the loss energies for the stress loading are highly non-linear. After the viscoelastic materials are fully relaxed, large differences in energy losses for cases M1, M2, and M3 are observed in Fig 10. In Fig 12, it is seen that changes in relaxation region slopes do not affect the total dissipation energy after the full degradation of viscoelastic material properties takes place, but they affect energy losses in transition regions. Fig 12 illustrates that changes of $G(0)$ values also do not greatly influence the energies dissipated by a unit step force excitation.
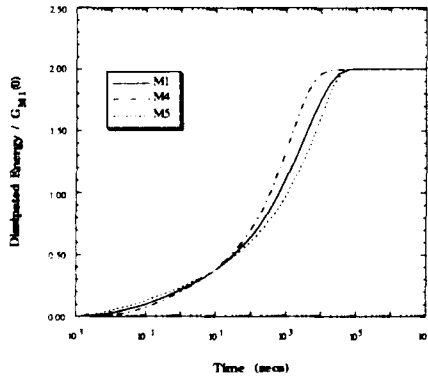
Fig 11 Dissipated energies for a unit step stress loading

Fig 12 Dissipated energies for a unit step stress loading

Next shear excitation strains $\gamma(t) = \gamma_0 \cdot \sin(\Omega t)$ are investigated. When steady-state harmonic conditions are considered, the viscoelastic stresses will also respond sinusoidally, however, stresses will lag behind strains by a phase angle since viscoelastic responses are dependent on time, frequency, temperature and moisture. The energy

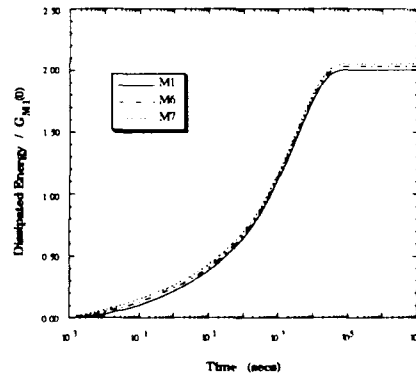dissipated per cycle and the maximum energy stored per cycle are calculated and plotted in Figs 13 to 15 against the driving frequency. The energies stored by the spring components over a complete loading cycle are zero and the shapes of curves for peak energies stored per cycle and for energy losses per cycle are similar to the complex moduli real and imaginary parts respectively. The results show that no energies are dissipated at low and high driving frequencies where viscoelastic materials behave like elastic materials. The peaks in the energy loss curves and the spans of those peaks in the frequency domain cover the same number of decades as the relaxation time periods. Figs 13 and 15 show that decreasing the fully relaxed modulus values and increasing the instantaneous modulus result in expanding the peaks of the dissipated energy curves
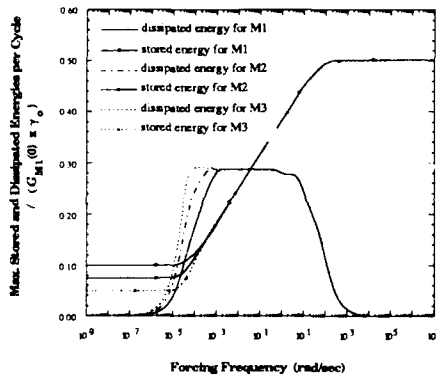

Fig 13 Max stored & dissipated energies
per cycle vs driving frequency
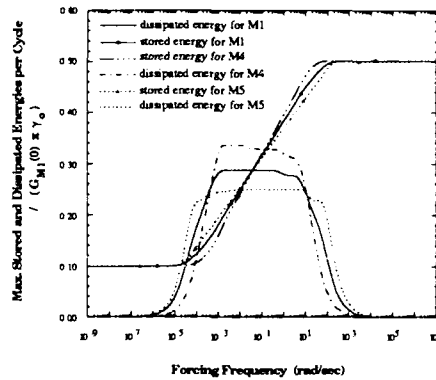
Fig 14 Max stored & dissipated energies
per cycle vs driving frequency
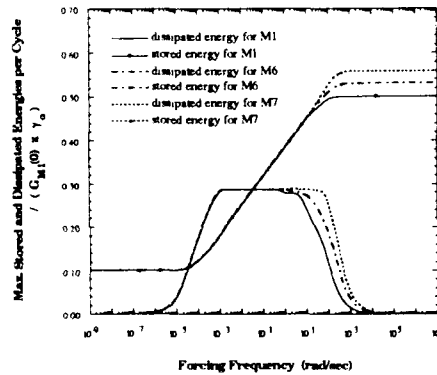
Fig 15 Max stored & dissipated energies
per cycle vs driving frequency

to the lower and higher driving frequency regions respectively. Fig 14 illustrates that increasing the slope of the transition region in the master relaxation curves yields increases in the peaks of the dissipated energy.

Additional examples were calculated using finite element techniques for anisotropic viscoelasticity (Hilton and Yi 1990,1991a) are given by the authors in (1991b).

3. CONCLUSIONS

The foregoing pilot studies indicate that by properly shaping master relaxation modulus curves in the real time plane, it is possible to control rates of dissipation energy as

well as the time occurrence of such dissipation phenomena. These in turn dictate the motion of viscoelastic bodies. It must, of course, be noted that each set of loadings and geometries produce unique conclusions and further detailed investigations are necessary for other types of loading and boundary conditions and for more complicated material characterizations, such as nonhomogeneous anisotropic viscoelasticity which directly relates to composites. The latter will then answer questions of how to best manufacture the polymeric matrix itself as well as how to best orient fibers and stack composite layers for specific service conditions. Additional independent constraints, such as cost and minimum structural weight, can also be imposed on this analytical formulation of such "designer materials".

REFERENCES

Bert C W 1973 Material Damping: An Introductory Review of Mathematical Models, Measures and Experimental Techniques *J of Sound and Vibr* **29** 129-153

Cost T L and Becker E B 1970 A Multidata Method of Approximate Laplace Transform Inversion *Int J Num Meth Eng* **2** 207-219

Gottenberg W G and Christensen R M 1964 An Experiment for Determination of the Mechanical Porperty in Shear for A Linear, Isotropic Viscoelastic Solid *Int J Eng Sci* **2** 45-57

Hilton H H 1964 Viscoelastic Analysis *Engineering Design for Plastics* Reinhold Pub Corp New York 199-276

Hilton H H and Yi S 1990 Bending and Stretching Finite Element Analysis of Anisotropic Viscoelastic Composite Materials *Proc of Third Air Force/NASA Symposium on Recent Advances in Multidisciplinary Analysis and Optimization* 488-494

Hilton H H and Yi S 1991a Dynamic Finite Element Analysis of Viscoelastically Damped Composite Structures *Proceedings of 2nd International Conference on Applications of Supercomputers in Engineering* C A Brebbia et al eds 495-511

Hilton H H and Yi S 1991b Analytical Formulation of Optimum Viscoelastic Properties for Structural Motion Control *University of Illinois TR UILU ENG 91-5009*

Jones D I G 1981 A Reduced-Temperature Nomogram for Characterization of Damping Material Behavior *The Shock and Vibration Bulletin* **51** Part 1 13-22

Rogers L 1981 Temperature Shift Consideration for Damping Materials *The Shock and Vibration Bulletin* **48** Part 2 55-69

Sim S and Kim K J 1990 A Method to Determine the Complex Modulus and Poisson's Ratio of Viscoelastic Materials for FEM Applications *J Sound and Vibr* **141** 71-82

Schapery R A 1962 Approximate Methods of Transform Inversion for Viscoelastic Stress Analysis *Proc 4th US Natl Congr Appl Mech* ASME 1075-1085

Building vibration damping into tubular composite structures using embedded constraining layers

S. S. Sattinger and Z. N. Sanjana

Westinghouse Science & Technology Center, Pittsburgh, PA 15235

ABSTRACT: The effectiveness of active control systems for suppressing structural vibration is augmented by introducing passive damping. Embedding damping materials inside the walls of tubular, organic-matrix composite structures can overcome certain limitations of add-on damping treatments. Described is a novel construction featuring a segmented, embedded constraining layer that provides high damping of all vibration modes, including the hard-to-damp, extensionally stressed modes. Discussed are the fabrication approach, attained damping performance, and advantages of the construction.

1. INTRODUCTION

The effectiveness of active control systems for suppressing structural vibration is heightened when they are used in conjunction with passive damping (Book et al 1986; von Flotow and Vos 1991). Providing passive damping can augment active vibration and noise control performance by reducing algorithm convergence time, reducing the controlled responses at system resonances, lessening control spillover, and providing attenuations at high frequencies. This paper deals with a novel approach to the task of adding passive damping to tubular structural components whose vibrations may be of concern.

Add-on constrained-layer treatments using viscoelastic materials (VEM's) have been successfully used to introduce passive damping in many types of structures, but there are a number of factors that have tended to limit their use. It may be difficult to gain access to interior regions of a structure that would otherwise be plausible locations for the installation of damping treatment. The treatment, once installed, may also create obstructions or mechanical hazards to personnel. The treatment may also cause toxicity, flammability, or other environmental problems due to outgassing and combustibility of the damping material. Conversely, exposed areas of this material may be susceptible to the effects of moisture, lubricants, oxygen, or vacuum conditions. The limited static and creep strength properties of many of these materials may also pose obstacles to the use of these treatments, as in the case of rotating components having high centrifugal acceleration levels.

Embedding damping materials inside the walls of organic-matrix composite beam or shell structures during fabrication as shown in Figure 1 can overcome these limitations. Described is a particular form of this construction (patent pending) that provides high damping of all vibration modes, including the extensionally stressed modes that tend to be
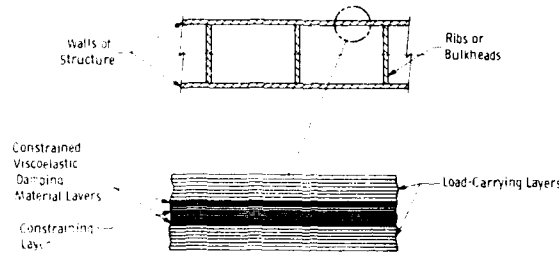
Fig. 1. Concept for embedding constrained-layer damping inside the walls of tubular composite structures

difficult to damp. This paper discusses the fabrication approach, attained damping performance, and advantages of the construction.

2. THE EMBEDDED CONSTRAINING LAYER CONCEPT

The specific vibration modes to be damped may be the global (long-wavelength) bending modes, which normally are the lowest-frequency modes of a beam or extended shell structure, or the higher-frequency local bending modes, whose shapes are contrasted in Figure 2. The local bending modes may include either the plate-bending modes of the individual panels of a flat-sided tube, or the shell-bending (lobar) modes of a cylindrical tube. Other types of modes that may need to be damped are the column modes and in-plane shear modes, which include lower-frequency torsional modes but generally are associated with the higher frequencies. A state of in-plane extensional or shear strain which is nearly uniform through the thickness of the tube wall is associated with all of these vibration mode types except the local bending modes, in which the strain is linearly varying and undergoes a reversal in sign from the inside surface to the outside surface.
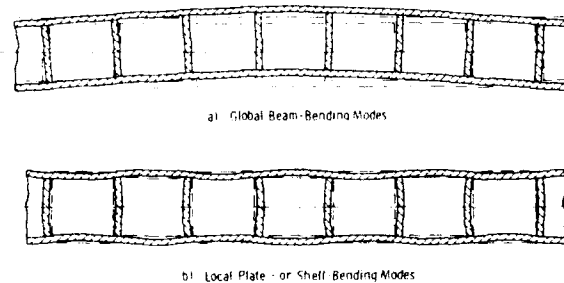

Fig. 2. Global vs. local vibration mode shapes of tubular structures

Although it is feasible to use add-on passive damping treatments to control the uniformly-stressed modes of tubes and other thin-walled structures (Torvik 1980; Sattinger 1990), most applications have been for purposes of controlling the local modes. Add-on constrained-layer damping of the uniformly-stressed modes requires deliberate axial segmentation of the constraining layer to induce energy-absorbing cyclic shear deformation of the damping polymer film, whereas the local bending modes can be damped either with or without this segmentation. If, instead, a properly sized layer of VEM damping polymer is embedded midway through the thickness of a tube wall, it can very effectively damp the local bending

modes without the use of a constraining layer, because the two equal-thickness wall portions will fulfill the mutual role of constraining layers for each other. Damping of the uniformly-stressed modes, however, still requires the use of a segmented constraining layer, and it necessary to place this internal constraining layer between two separate layers of VEM.

3. DESIGN AND FABRICATION OF SPECIMENS

We have designed and fabricated a set of filament-wound tubular fiberglass/ epoxy specimens, each 36 inches in length by 5 inches in diameter, for proof-of-principle bench testing of this construction. A graphite/ epoxy embedded constraining layer and adjoining Soundcoat Dyad 601 viscoelastic damping polymer layers are embedded in two of the specimens; this constraining layer is segmented in one case and continuous in the other. The total wall thickness for each of the damped specimens is 0.54 in. The segmentation of the first specimen is both axial (cuts running perpendicular to the tube axis) and circumferential (cuts running parallel to the tube axis). *A third specimen is a control specimen featuring conventional fiberglass/ epoxy construction. The cross-sections of the two internally damped specimens are illustrated in Figure 3. The merging together and bonding of the load-carrying inner and outer portions of the tube walls at the ends totally encapsulates the VEM and provides structural rigidity at the locations where the tube would interconnect with other structural components. These features give decided advantages over other damped composite tube constructions which rely on relative motions of the inner and outer wall portions to produce shear deformation in interleaved VEM layers (Barrett 1989; Belknap and Kosmatka 1991). The tube walls were wound from S-2 glass filaments using a symmetric 90°, ± 20° winding pattern. The continuous constraining layer was wound from IM6 graphite filaments using a similar symmetric pattern, whereas the segmented constraining layer pieces were machined from a precured tube, filament-wound separately using the same pattern. A low-temperature-curing (75°C) epoxy resin matrix was used throughout.
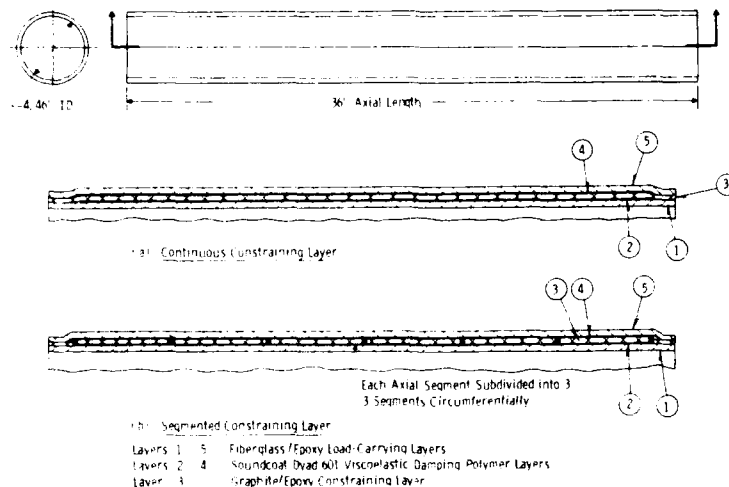

Fig. 3. Cross-section views of the internally damped specimens. Views are enlarged and proportions exaggerated for clarity.

---

*The need for circumferential segmentation of axially continuous, add-on constrained-layer treatments on tubes was shown by Vinogradov and Chernoberevskii (1980).

Although the segments were precured and epoxy-cemented to the VEM layers in this proof-of-principle fabrication, a less costly alternative would be to place prepreg patches which would be co-cured during the final cure. The ratio of the constraining layer modulus-thickness product to that of the tube wall was C 7⁷ for the specimens with both the segmented and the continuous constraining layers. This represents a fairly stiff damping design. In both specimens the damping layers comprised approximately a 44% addition to the weight of the base layers.

4. STRUCTURAL FREQUENCY-RESPONSE COMPARISONS

Figures 4 and 5 compare magnitudes of axially directed transfer accelerance (acceleration/force) frequency-response functions for the damped specimens versus that of the undamped fiberglass specimen. These are overlaid plots of measurements in a free-free configuration using filter-shaped, banded-random shaker excitation applied in 16
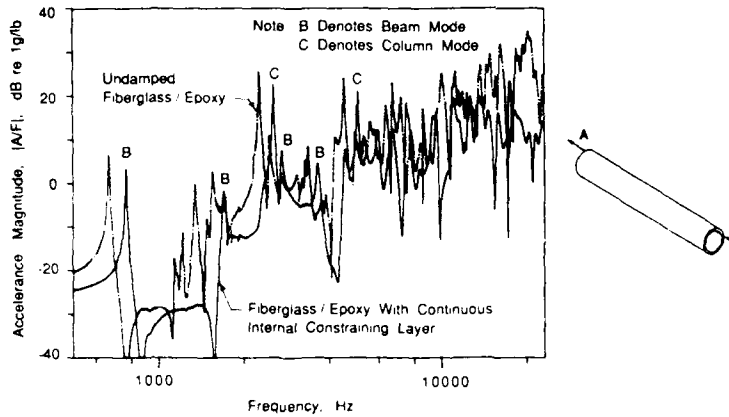

Fig. 4. Axially directed transfer accelerance for specimen with continuous embedded constraining layer versus that of undamped fiberglass/epoxy
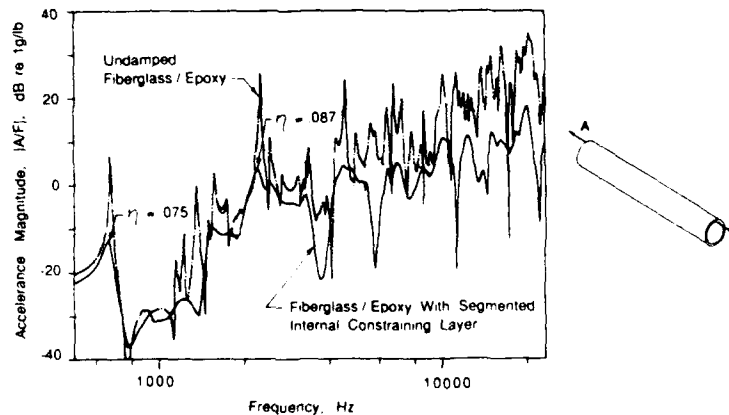

Fig. 5. Axially directed transfer accelerance for specimen with segmented embedded constraining layer versus that of undamped fiberglass/epoxy

separate frequency bands per test. Figure 4 shows that at low frequencies the shell-bending or lobar modes are strongly damped in the specimen having the continuous embedded constraining layer. However, neither the global beam-bending modes nor the lower-order, in-plane extensional modes are damped; the response peaks corresponding to these modes appear as sharply resonant as those of the undamped fiberglass specimen. Figure 5 shows that the segmented embedded constraining layer, on the other hand, strongly damps all of the modes that are excited by the axial vibration excitation. The segmented-layer specimen attains about a 15 dB average attenuation over the 36-inch specimen length across the entire frequency range.

5. DAMPING VALUES

The frequency-response tests covered a range of frequencies which was quite high in relation to some possible applications. To supplement ¹ .gh-frequency damping data from these tests with lower-frequency damping measur· .· .₃ on the segmented-layer specimen, we mounted it between solid-steel discs .;,·ⁱ .neasured decays from beam-bending, extensional, and torsional mode reso;.ances.

Figure 6 compares predicte ⁝ and measured room-temperature damping values for the uniformly-stressed vibra'ion modes of the segmented-layer specimen. All predictions were generated using a pre· .ously described method for calculating the extensional damping performance of constrained-layer treatments (Torvik 1980; Sattinger 1990). The good overall agreement between predictions and measurements seen in Figure 6 confirms that the damping of extensionally-stressed modes in segmented-layer constructions is reasonably predictable. Not included among the measured damping data plotted in Figure 6 is a torsional-mode loss factor of 0.052.

The local shell-bending or lobar modes are strongly damped in both the segmented-layer and the cc tinuous-layer specimens, with loss factors in the range from 0.1 to 0.4.
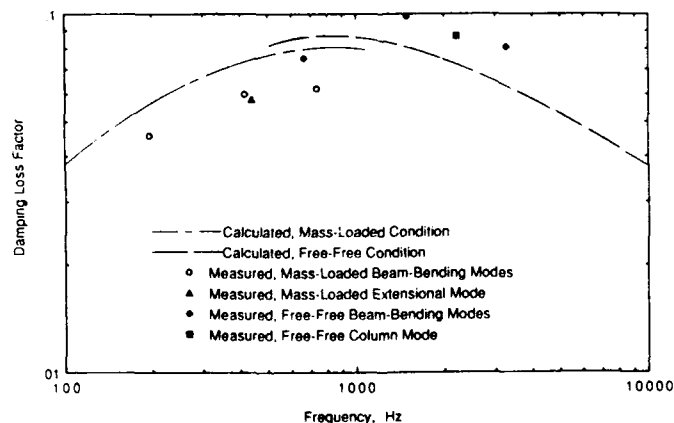

Fig. 6. Predicted vs. measured damping performance for extensionally stressed vibration modes of the segmented- constraining-layer specimen

6. CONCLUSIONS

In addition to surmounting application obstacles associated with access, strength, and environmental factors, the damping of tubular composite structures by embedded constraining layers offers much higher local-mode damping performance than is attainable with add-on treatments of comparable thickness. Segmentation of the constraining layer enables the low-frequency global beam-bending and torsional modes to be damped. Peak measurements of damping loss factors in the vicinity of 0.08 for these extensionally stressed vibration modes of the specimen with segmented constraining layer are reasonably well predicted and represent high damping of these hard-to-damp modes. The advantages of this construction over certain other internally damped composite tube constructions include total encapsulation of the VEM and better load transfer at locations where the tube would interconnect with other structural components. Likely applications of this passively damped construction, used alone or in conjunction with active vibration control, include marine and aerospace tubular composite structures and shafting for both military and commercial uses.

7. REFERENCES

Barrett D J 1989 *Proc. of Damping '89* U S Air Force Flight Aeronautical Laboratories, Flight Dynamics Laboratory, WRDC-TR- 89-3116, Paper HCB

Belknap F M and Kosmatka J B 1991 *Proc. of Damping '91* U S Air Force Wright Laboratory, Flight Dynamics Directorate, WL-TR-91- 3078, Paper HAC

Book W J, Alberts T E and Hastings G G 1986 *Computers in Mechanical Engineering* 5.2 pp 26-33

Sattinger S S 1990 *Vibration Control of Mechanical, Structural, and Fluid-Structural Systems* Amer Soc Mech Engrs PVP Vol. 202 pp 45- 53

Sattinger S S 1991 *Proc. of Damping '91* U S Air Force Wright Laboratory, Flight Dynamics Directorate, WL-TR-91-3078, Paper HBA

Torvik P J 1980 *Damping Applications for Vibration Control* Amer Soc Mech Engrs AMD Vol. 38 pp 85-112

Vinogradov B D and Chernoberevskii V V 1980 *Soviet Phys Acoust* 26 4 pp 328-30

von Flotow, A H and Vos, D W 1991 *Proc. of Damping '91* U S Air Force Wright Laboratory, Flight Dynamics Directorate, WL-TR-91- 3078, Paper GBB

507

Business opportunities in smart materials systems

Subramaniam Ramamurthy, Ph.D.   Ravi Soni
Senior Scientist   Research Engineer

                    Quantum Consultants, Inc.
              Hannah Technology and Research Center
                    East Lansing, MI 48823

INTRODUCTION

A cursory review of the history of materials science will
certainly reveal the profound influence of this scientific discipline
upon the evolution of civilization during the millennia. Thus, it is
inevitable that the new generation of smart materials and structures
technologies featuring at the most sophisticated level a network of
sensors and actuators, real-time control capabilities, computational
capabilities and a host structural material will not only have a
tremendous impact upon the design, development, and manufacture of
the next generation of products in diverse industries but also the
economic climate in the international marketplace. Those countries
and businesses with the ability to harness and coordinate the diverse
technologies associated with smart structural systems, will reap a
bountiful harvest while those countries which adopt a less aggressive
posture will surely be afflicted by a draught.

The applications for these new generations of smart materials
and structures will be diverse, but a common denominator for the
deployment of the most sophisticated class of systems featuring
sensors, actuators and microprocessors will probably be the
unstructured environment in which a system must operate. Thus the
uncertainty associated with the behavior of the relevant external
stimuli which govern the system response relative to prescribed
design criteria will largely dictate the deployment of smart
materials and structures. The necessity for synthesizing materials
and structures with autonomous self-adapting, self-correcting
characteristics is governed by the desire to achieve optimal
performance at all times under variable service conditions and while
operating in unstructured environments. There are several
characteristics of these smart materials and structures which have
been the foci of research activities, and these include changing the
mass-distribution, the stiffness, and the energy-dissipation
characteristics for vibration-control purposes, for example. This
work has permitted engineers to synthesize systems with controllable
vibration amplitudes, natural frequencies, resonances and transient
response settling-times. Other work has focused on actively changing
the geometries of structures.

The field of smart materials and structures is very broad and
will ultimately include a variety of diverse disciplines including
biotechnology, neural networks, photonics, nanotechnology and
artificial intelligence. However, at this time, significant
developments have occurred in a somewhat limited area of this diverse
field because teams of engineers and scientists have focused on
employing a network of embedded sensors, microprocessors, and an
array of dynamically-tunable actuator materials interfaced at a
global level with traditional structural materials. In this novel
class of structural systems, the structural materials provide the
skeleton of the system; the network of actuators provide the muscles
to make things happen; the network of sensors and data transmission

systems provides the nervous system, to monitor and communicate the characteristics of the external stimuli to the microprocessor-based computational facilities; and the microprocessors provide the brains which ensure the optimal performance of the overall system in the presence of variable and unstructured stimuli.

COMMERCIAL AND INDUSTRIAL APPLICATIONS

The insatiable demand for new generations of industrial, military, commercial, medical, automotive and aerospace products has fueled research and development activities focused on advanced materials. This situation has been further stimulated by the intellectual curiosity of *homo sapiens* in synthesizing new classes of biomimetic materials, and of course global competition by the principal industrial nations is also a parameter in the equation governing the rate of technological progress.

By integrating the knowledge-bases associated with advanced materials, information technology and biotechnology, these three megatechnologies are facilitating the creation of a new generation of biomimetic materials and structures with inherent brains, nervous systems and actuation systems which are currently a mere skeleton compared with the anatomy perceived in the not-too-distant future. A vigorous research thrust has been prosecuted on adaptive materials with the ability to change in real time the mass-distribution, the stiffness, and the energy-dissipation characteristics for vibration-control purposes. Thus, the research has focused upon developing adaptive materials with controllable properties.This work has permitted engineers to synthesize systems with controllable amplitudes of vibration, natural frequencies, resonances, and transient response characteristics. Other work has focused on actively changing the geometries of structures, so that initially straight members can develop a curved shape in a controlled manner upon command, for example.

Experimental results of the frequency response of beams containing embedded electro-rheological fluid domain have shown that by controlling the voltage imposed upon the fluid, the global dynamic response of a smart beam can be actively tuned to provide a desired response. Thus, natural frequencies can be changed, the damping characteristics can be changed, mode shapes can be changed, and resonances can be changed. These capabilities can be exploited in many engineering applications. Thus automobile suspension leaf-springs embodying this technology will permit the suspension characteristics of the vehicle to be actively controlled in order to ensure passenger comfort on diverse road surfaces. Robot arms employed for repetitive tasks would be able to increase the damping properties of the arm in order to minimize the settling-time upon completion of a manoeuvre. Robotic devices subjected to dynamic excitations at the end effectors that cause resonance conditions in structural members would be able to change the natural frequencies in order to avoid this state of resonance. Other robotic applications have involved shape memory alloys in the design of robot grippers while other work has involved piezoelectric materials to undertake sensing tasks which replicate the characteristics of the human dermis and epidermis.

Smart materials possessing the innate ability to change their inherent mass, stiffness and damping properties have considerable utility in medicine. This utility is evident from the number of devices featuring shape memory materials that have been employed in blood clot filters, prostheses, devices for the treatment of scoliosis, and in various pins, nails and plates employed by orthopedic surgeons. Other devices that would benefit from the ability to change the properties of the materials from which they are

fabricated include colonoscopes and catheters which must typically function in an unstructured environment within the tubular members of the human body.

The diverse range of products marketed by the sporting goods industry will also benefit from smart materials technologies. Anglers will be able to change the stiffness and energy dissipation characteristics of their fishing rods in order to enhance the pleasure associated with the task of attempting to catch a particular species or size of cold-blooded vertebrate animal, or to enhance the angler's casting technique. Rackets employed for tennis, or squash, for example could feature adaptive materials in order to enhance player performance under a variety of different playing conditions.

Structures which must operate autonomously in space are also ideal candidates for the incorporation of several types of smart structural systems because of the variable service conditions and the nature of the unstructured environment in which they must operate. The deployment of large space structures such as platforms, telescopes or solar arrays from the confinement of the payload envelope of the launch vehicle and the payload constraints imposed by launch vehicles mandates that these large space structures be lightweight, and a consequence of this is that they are somewhat flexible. Thus once the spacecraft is on station in orbit, engineers are then confronted with the tasks of accurately controlling the shape of the structure and also vibration control.

Vibration control situations would typically occur as a result of meteor impact, and in the case of an orbiting laboratory as a consequence of imperfect docking between a space shuttle and the laboratory, or an astronaut exercising on a tread mill. These classes of transient and dynamic responses could be controlled by hybrid schemes of actuators operating in concert with a network of sensors throughout the structure. Other classes of space structures involve geometrical control scenarios. Consider the proposed NASA large deployable reflector program in which the surface contour of a 20 meter diameter paraboloidal reflector must be accurately maintained to within a few microns when in the observation mode. This is a challenging task when considered in the context of manufacturing errors, structural creep, and thermal gradients. Furthermore the telescope must typically be in the observation mode for 20-minute time intervals. Structural members incorporating embedded piezoelectric materials have been proposed to control the critical geometry of the reflector.

Aircraft continually operate in unstructured environments because of uncertainties in the weather conditions, turbulence, temperatures, payloads, and the duration of the flights. Several smart structures programs have been initiated for both commercial aircraft and also military airplanes. The focus of these "smart skins" programs, so named because of the monocoque design of these structural systems, are dependent upon the specific application. The commercial aircraft programs focus primarily upon monitoring the health and flight worthiness of aircraft. Arrays of sensors throughout the wings, control surfaces and the fuselage will monitor the structural properties in the context of fatigue cracks and incipient failures. Other types of sensors will monitor the ice build up on wings and control surfaces which can adversely affect aerodynamic performance at take-off and also the controllability of the machine.

Smart materials and structures technologies will have a tremendous impact in reshaping the technological and economic bases of the international business environment during the next two decades. It is crucial to recognize that significant order-of-magnitude payoffs will arise in various applications as a consequence of the implementation of smart materials technologies. Some of these

payoffs are highlighted below.

Technological Impact
- Technological developments that are considered impossible today will become routine realities as a result of smart materials technologies, e.g., National Aerospace Plane.
- Completely unforeseen markets will be created and the dominant players will carve out distinct segments of these markets.
- The design of smart parts and subassemblies for smart mechanical and structural systems will be simplified, and significant order-of-magnitude advantages will accrue due to design-cascading effects.
- Smart materials technologies will result in simplified and efficient design and manufacturing processes.
- Performance characteristics of smart mechanical and structural systems will not only be significantly superior to today's systems, but they will also be optimal while operating in variable service conditions and unstructured environments.
- Significant reductions in costs will accrue due to the integration of sensing, actuation, and quality monitoring functions in smart structures.
- Maximum utilization of microprocessor technologies due to the unique ability of smart materials to interface with modern solid state electronics will permit the quantum leaps in the electronics area to be immediately transformed into technological advances in the smart materials and structures arena.
- Smart structural and mechanical systems will exhibit significantly superior response characteristics and capabilities due to reduced inertia, as compared with conventional technologies.
- Smart materials and structures will provide designers with a unique capability in the history of humankind to optimize system performance under various service conditions and unstructured environments.

Economic Impact
It is clearly evident from the market topology that the impending revolution in smart materials technologies will impact every segment of the world marketplace. Therefore, the economic impact of these technologies on the international marketplace is very significant. There is no such thing as the "best smart materials technology," and no one is in a position to definitively assess which technology is the best for various specific applications. One can anticipate that as the field of smart materials technologies matures, individual technologies will be integrated to yield hybrid smart materials technologies that will permit the stringent performance specifications of various smart part and subsystems to be adequately satisfied. Therefore, it is somewhat premature to project the market share and the market growth associated with each of the key smart technologies.

Smart materials and structures technologies will significantly impact every conceivable sector of the marketplace. The most significant impact of these technologies will be in the following sectors of the economy:
- automotive and transportation industries
- aerospace industry
- defense industry
- biomedical devices
- advanced manufacturing, robotics, and industrial machinery
- consumer products and sporting goods
- high precision instruments and electronic packaging

- highways, buildings, and bridges

Specific applications in each of these market sectors will be motivated by substantial order-of-magnitude improvements in performance characteristics due to the implementation of smart materials and structures technologies for variable service conditions and unstructured environments. Economics will be the other driving force in the implementation of smart materials technologies since the cost of these smart products will be substantially lower due to a smaller number of moving parts, the ability of smart materials to interface with opto-electronic devices, and several other design cascading advantages at the system level.

Typical applications of smart materials technologies in each of these sectors of the economy are highlighted below.

Automotive and Transportation Industries
- engine mounts (minimize vibration and noise)
- active suspensions (improve ride and handling)
- steering systems (improve driver comfort)
- shock absorbers
- smart windshields
- smart bumpers (improve crashworthiness)
- pumps, valves and actuators (improve system performance)
- clutches and transmission systems
- anti-lock braking systems
- new generation of engines
- automotive springs

Aerospace Industry
- smart skins containing phased-arrays (to permit aircraft to sense and communicate in various frequency bands and in any direction)
- smart wings (improve aerodynamics and system performance in service, detect damage and impending failure)
- smart control surfaces
- smart rotor-craft systems
- vibration suppression systems
- instrument panels (improved ergonomical design)
- undercarriage, shock absorbers, landing gear
- hydraulic pumps, actuators and valves
- missile actuation systems
- large space structures
- commercial aircraft
- space robots
- self-deploying space structures

Defense Industry
- submarines (reduce drag and noise)
- surface vessels (reduce drag, quieter)
- hydraulic valves, actuators and pumps
- switches
- variable radar and acoustical signature
- smart skins (life-through-death health monitoring capabilities, manufacturing, service, battlefield damage)
- ammunition-supply systems
- smart armor
- materials handling equipment
- SDI (structures supporting weapons and antenna for retargetting maneuvers without detrimental jitter and thermal-flutter)
- stealth technologies (to evade enemy emitter and platform identifications to make more specific threat determinations)
- Field-repairable airframe structures
- acoustically-damped torpedo propellers

Biomedical Devices
- prostheses: artificial limbs, hands and joints
- orthodontic braces
- sclerosis
- wheelchairs
- treatment of sporting injuries (fractures)
- implants

Advanced Manufacturing, Robotics, and Industrial Machinery
- active balancing
- dynamically-tunable robot arms
- noise reduction
- vibration control of machine-tool structures
- hydraulic actuators, valve and pumps
- joint actuators for articulating robotic systems
- robotic end-effectors
- smart flexible fixtures and grippers
- material handling
- farm equipment
- oil drilling and mining equipment
- textile machinery

Consumer Products and Sporting Goods
- skis
- tennis rackets
- golf clubs
- fishing poles
- baseball bats
- snowmobiles
- bicycle industry
- switches
- washing machines
- snow blowers

Highways, Buildings, Bridges
- smart foundations
- smart skins
- dynamically-tunable optical and thermal characteristics for doors and windows (energy efficiency and comfort)
- smart structures, bridges, buildings
- building elevators

ACKNOWLEDGEMENTS

REFERENCES

1.   Gandhi, M.V. and Thompson, B.S., *Smart Materials and Structures: The Impending Revolution*, Technomic Publishing Co., Lancaster, PA, 1990.
2.   Gandhi, M.V. and Thompson, B.S. *Smart Materials and Structures*, Chapman and Hall, London, 1992 (in press).

513

Implementing smart composites: organizational/environmental issues

Michael J. Martin - Michigan State University

"Smart" Composites Technology will not automatically be
implemented simply because they provide mechanical and
economic advantages. There are significant organizational
and environmental issues which need to be understood and
dealt with. This paper will focus on implementing
composites in a mature organization and cost
modeling/economics.

Composites are unique from traditional materials of
construction because they require an integrated approach to
"design for manufacturing." Utilization of these new
materials can be the basis for the initiation of a cultural
change in a firm. The Michigan State University Composite
Cost Comparison Model attempts to provide an evaluation tool
for these "new" cost justification techniques.

I. Manufacturing Strategies for the Ninities

Peter Drucker points out in an article entitled, "The
Changed World Economy," that there are two distinct types of
manufacturing industry: material-based and
information/knowledge based. He demonstrates that the major
driving force for the world economy is no longer the
availability of raw materials, but the availability of
technology-based innovation.

Successful corporations that are competing on a global basis
have an organization that is able to identify profitable
niches /segments in a market--whether that niche be
culturally-based (geographical) or psychographic-based
(trendsetters vs. traditionalists). These companies
organize and locate the necessary
design/manufacturing/marketing teams in the center of that
market in order to satisfy the customer's needs--not to
satisfy an immediate financial measurement. These
corporations are not competing globally. They are
developing, manufacturing, and marketing globally.

"Global" firms recognize that the markets are now highly
segmented. The manufacturing strategies that these firms
evolve employ the necessary level of technology in order to
provide flexibility. Both their manufacturing and marketing

arms are organized to react to the smaller volume runs required by these niches. A smaller market niche can be highly attractive if one can provide an economic basis for shorter production runs.

The increased segmentation of various global markets also brings another demand: "fast to market." A number of studies of Japanese manufacturing firms show that their ability to gain over 30% of the U. S. automotive market was not based completely on lower cost performance. It was also their ability to translate customer needs into products at approximately 70% of the development time of U. S. automotive firms. Most of the difference is due to their ability to trust their suppliers and make them a part of their developmental team. Customers are no longer asking for traditional supplier relationships. They are demanding that suppliers become part of their team to meet their customer's needs.

These teams are based on a true win-win relationship, not a zero-sum game. Zero-sum games are based on the customer driving costs down while the supplier attempts to raise prices. A win-win relationship focuses upon the customer establishing the value of the product in the marketplace, while the supplier identifies opportunities for improvement and passes through the benefits of these process improvements.

Thompson and Gandhi of Michigan State University have described such a "design for manufacture" model for composites. The "design for manufacture" composite model starts with the customers' specifications, which typically include static and dynamic load, geometrical (space) constraints, fatigue life projection, environmental conditions and abrasion resistance. The market can also provide the design with constraints on weight, costs and the relative value of a particular function of the part.

Traditionally, the designer then selects the materials to meet the specification within a given cost range. Here, composites represent both an advantage and a quandary. The advantage is the potential cost savings due to consolidation resulting from the ability to localize stress/strain reduction by selective placement of reinforcement. The quandary is that selection of the material eliminates certain fabrication techniques, and the lack of a coherent design data base for prediction of properties in a variety of geometric forms limits the materials selection to "cut and try."

The objective is to select materials that will meet the design specifications within cost limitation with an understanding of the function of fiber and resin plus the advantages of a mixed anisotropic and isotopic load transfer.

The use of slightly different fabrication technique or any
deviations or problems could result in a composite of
different quality with a totally different number and
distribution of defects. The aesthetic requirements of the
product impacts upon the material selection for certain
processes. How the product will be assembled can impact at
the fabrication level because of requirements for metal
inserts, surface finish for adhesive joining, or various
alternative joining techniques between metals and
composites.

Once the various types of constituents and the fabrication
systems have been identified, the design problem is now
reduced to establishing viable geometric form and design
parameters such as stacking sequence, fiber orientation and
volume fractions of various constituents in order to satisfy
the product design specifications. This phase of the
program is computer intensive and involves significant use
of finite element techniques.

"Global" firms recognize that all companies have
approximately equal access to capital and technology. The
only major difference is their people and how they organize
them. The cause of most of the failures of advanced
manufacturing technologies is implementation. Poor
implementation is often the result of "over the transcom"
organization.

Members of an "over the transom" manufacturing company look
upon themselves as black boxes that produce units to meet
customer specifications. There is no need to communicate
with in the firm as long as everyone does their "job". When
you visit these firms you often wonder who is the
competition - most often it looks like they spend most of
their time competing with each other. In these firms the
task of accounting is to identify sources of blame for not
meeting cost projections or customer specifications. The
task of marketing is to raise prices so that uncontrollable
costs can be passed through to the customer.

"New" manufacturing organizations counter this commodity
based mentality by developing integrated teams with total
access to information. Not surprisingly, those firms that
can organize into "design for manufacturing teams" have a
distinct competative advantage over traditional "over the
transom" engineering. The real advantage to the new
organization is not meeting some recent fad in order to
retain quality workers but in the synergy that occurs when
persons of different backgrounds and training focus on the
solving of a customer's problem/need.

Traditional metal based "over the transom engineering"
companies cannot justify the advanced manufacturing
technologies required for "smart" materials with the
existing cost accounting techniqes.

"Global" companies require "new" accounting tools that
recognize the value of the new "design for manufacturing"
teams, automated manufacturing technologies, composite
materials, and the impact of "fast to market" strategies.
The "new" cost analysis systems would recognize that:

* Cost identifies opportunities for improvement--not
  potential for blame.

* Cost opportunities are not to be found solely in
  labor reduction or lower cost materials but more
  importantly in the various components of
  overhead/burden.

The "fast to market" strategies have forced new
supplier/customer relationships and has embraced the "total
quality" audit. No longer do customers audit just the SPC
charts. Now the audits cover leadership/management,
quality, delivery, technology and costs. "Global" customers
need to understand that their "new" partners can identify
all of their opportunities for improvement, and pass them
along.

Most quality audits now require standard costs..for labor,
material, and overhead. Overhead can be broken down into
the burden for:

* Labor--direct supervision, indirect supervision,
  payroll, pension, benefits, taxes, etc.

* Material--purchasing, handling, inventory carrying
  charges, plant space,etc.

* Direct--utilities, machine depreciation, insurance,
  etc.

* Indirect--marketing, engineering, plant space,
  customer service, production planning, etc.

The value of this overhead information has been pointed out
by various surveys. The average cost of U.S. manufacturing
is: material 55%, labor 10%, and overhead 35%. Peat
Marwick has demonstrated that even with the most advanced
manufacturing technology, the average reduction of labor
content has been only to 4 or 5%.

II. MSU Cost Comparison Model

Composites appear to offer the design flexibility necessary
for "fast-to-market" marketing, and an apparent economic
advantage in the shorter production runs that niche
marketing requires. The economic advantages of composites
include: reduced labor costs due to the reduction of
assembly operations; opportunities for automation; and
potentially lower cost, interchangeable tools that could be

used over a broad range of models. The economies are not
only in direct charges, but also in indirect charges such as
inventories, plant space savings and flexibility of design.
Presently, there is no way to quantify the value of these
reducing indirect overhead waste.

MSU Cost Analysis Model for Composite Manufacturing is a
Lotus(TM) spread sheet based on industry experience. The
MSU model will provide a total cost estimate (the sum of
material, labor, overhead/burden, equipment, tooling, and
energy) for five composite fabrication processes: Injection
Molding (IM), Thermoforming (ThF), Resin Transfer Molding
(RTM), Sheet Molded Compression Forming (SMC), and Reaction
Injection Molding (RIM).

A brief description of the process requirements and
potential applications for each system is provided in the
user's manual. After the designer has selected the
processes to be compared, he/she can then modify the cost of
tooling for a flat plate with an estimate on the number of
inside radii, molded in holes, draft angles, ribs, etc.
required to meet the customer specifications. The model
does not consider any part performance requirements.
However, if the designer chooses a design feature that is
not feasible with a specific process based on industry
experience, then an error message will be shown. The user
now estimates the basic parameters for all of the processes:
part desired/yr., maximum surface area (sq.in.), volume
(cu.in.), time for production, cost/KW, part dimensions, and
whether the equipment would be dedicated to this one part.

The user now provides inputs or uses default values for the
specific processes have chosen--specifically material, scrap
rate, cycle time, mechanical and process efficiency, and
burden/overhead rates. The model provides a material data
base that can be searched for specific properties or cost.

The amount of material utilized reflects not only the
required production and estimated volume of the part, but
also the scrap rates in material handling fabrication, and
whether the material can be recycled. Some materials are
purchased as a raw material and others can be
self-manufactured such as SMC. Labor, capital, equipment
and tooling are influenced by production volume requirements
and cycle time of the different composite processes. Cycle
time of the various processes depends upon the thickness of
the part, the surface area of the part, the number of
cavities that could be designed in a mold, cure rate of the
resin, and the ability of the process to be automated.

The correlation equations for capital investment in tooling
and process equipment were established by industry survey
and are based upon surface area and press/clamp tonnage,

depending upon the fabrication technique. For example, the equation for Sheet Molded Compression is (e ^((press tonnage)^(-.001))*(-2180776)   + 2007828).

After the user has reviewed the inputted, defaulted, and/or calculated values, he/she can view the costs per part for that volume...or request a graph (figure 1) for that process over a volume range...or request a graph to compare selected processes over a volume range (figure 2).

The advantages of "smart" materials/composites--part consolidation, strength-to-weight ratio, and design flexibility--can be fully realized by recognizing that composites are a unique process, as well as a material of construction. The MSU Cost Analysis Model is a computational tool that will broaden the design evaluation to include all aspect of the product development process, and will integrate the design process further into a manufacturing team. Composites represent a "leap frog" opportunity for U.S. manufacturers to provide unique products to their global customers.

Acknowledgments
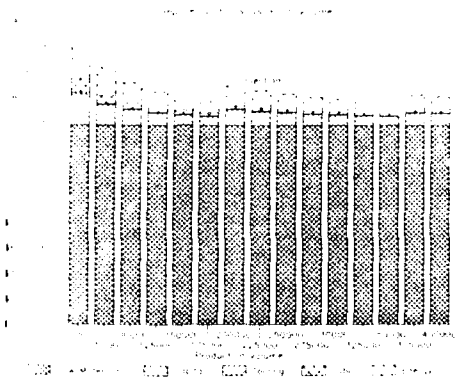
FIGURE 1   sensitivity analysis comparison of various products
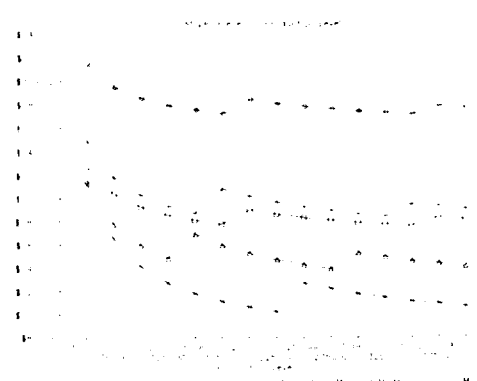
FIGURE 2   sensitivity analysis cost per piece vs. production level

Activities of the Smart Structures Research Institute

P.T.Gardiner, B.Culshaw, A.McDonach, W.C.Michie, R.Pethrick
University of Strathclyde, Glasgow G1 1XW, Scotland, U.K.

ABSTRACT: To meet the demanding multi-disciplinary challenge of smart structures and materials technology, on the 14th February 1991, the Smart Structures Research Institute was officially inaugurated on the campus of the University of Strathclyde, Glasgow. The Institute is decentralised in structure in that it acts as a project office to plan, co-ordinate and manage research projects, which are jointly undertaken between a number of scientific, engineering and administrative departments. This paper will describe the rationale for the establishment of the Institute and will review the research activities and plans for the future.

1. INTRODUCTION

The proliferation in interest and published literature in smart structures and materials technology in the late 1980s, stimulated the University of Strathclyde to undertake a comprehensive feasibility study on its status and prospects.

The results of this study are summarised below:

- the technology is truly multi-disciplinary.
- considerable *user pull* exists and the level of interest will continue to grow.
- a wide range of applications are being addressed and lie in the short, medium and long term.
- activities in the US and Japan have led to extensive networking of knowledge/ excellence; although not technologically behind, effort in Europe is fragmented.
- the availability of multifunction smart materials will have a dramatic affect upon the approaches to structural design.
- technology is immature and the science base needs to be developed.
- the University of Strathclyde has a near ideal mix of enabling skills/experience to take on board scientific developments in this field.
- The time is right for a European based multi-disciplinary world centre of excellence in this key 21st century technology.

As a result the Smart Structures Research Institute was formed and has been active since February 1991.

2. ORGANISATION OF THE SMART STRUCTURES RESEARCH INSTITUTE

The mission of the Institute is simple: to ensure the University of Strathclyde becomes a world centre of excellence and leader in Smart Structures and Materials research.

The main stream activity of the Institute is scientific research, operating in a project based manner, with research teams established from the relevant disciplines to meet the target objectives of the project. By this approach, the most efficient use of available resources is made, with minimum duplication of effort. The organisation is shown in Figure 1, showing the various contributory departments and affiliates.
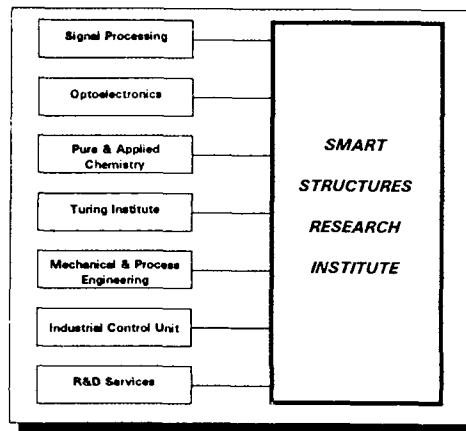
Figure 1

The key to this initiative is effective project management, and associated with this, the Institute Director and his staff perform a number of important functions in close collaboration with academic staff:

- identification and planning of research with academic staff.
- organisation and coordination of project teams from the relevant departments/ affiliates.
- proposal preparation to secure funding.
- management of research projects.
- encourage and stimulate communications between various University departments and affiliates.
- to interface with the outside world in Smart Structures and Materials Technology.

3. PROGRAMME OF WORK

As already discussed, applications fall into short, medium and long term timescales, all of which need to be supported by a strong fundamental science base. In response to this, a flexible, multi-tier programme of work has been defined:

- Level 1 - Fundamental Science
- Level 2 - Collaborative Research
- Level 3 - Independent Research
- Level 4 - Institute Membership

3.1 Fundamental Science Programme

The Fundamental Science programme is viewed as the 'backbone' of the Institute, and a number of projects have already been initiated:

- Embedded Sensor Systems
- Adaptive Structures
- Molecularly Smart Materials

3.2 Collaborative & Independent Research Programme

The Collaborative and Independent Research programmes are designed to accommodate a wide range of research objectives and commitments from cooperating industrial partners and government laboratories.

Collaborative programmes already identified include:

- Composite cure monitoring
- Damage detection/structural integrity monitoring
- Distributed sensing
- Novel actuator systems
- Monitoring civil engineering structures
- Strain indicative climbing rope.

3.3 Institute Membership Programme

The objective of the Institute Membership Programme is to provide companies, organisations and individuals with a cost-effective means of tracking the development of Smart Structures technology. The task of monitoring technical developments world-wide is not easy, even for major corporations. In the case of Smart Structures and Materials systems, the task is particularly difficult since the inter-relationship between several technical disciplines needs to be monitored and interpreted.

By tracking developments in these various disciplines, the Institute Membership Programme will provide invaluable input to Managers and Directors of Research in answering some important questions:-

- Is the proof-of-concept sufficiently established for a specific application?
- What are the major technical challenges which need to be addressed?

- Where are the critical cost parameters?
- How strong is the science base for specific research developments?
- Is the timing right for applied research?
- What level of commitment should be made now, and within the 5-year time frame?

Input for these and similar questions will cover developments both in the enabling technologies and in the growing applications base.

The Institute Membership Programme is an *information club*, its product facilitated through four main services:

- Quarterly information newsletter
- Data Base
- Annual Conference
- Seminars & Workshops

4. CONCLUSIONS

Smart structures and materials technology will undoubtedly yield a wide range of new materials plus new material sensing and actuation technologies and this will have a radical effect on current approaches to structural design. To date, a considerable amount of resources have been applied, but the technology is still largely immature and there is a necessity to develop the underpinning interdisciplinary science base. To meet this need, the Smart Structures Research Institute is the first initiative to be established in Europe and is dedicated to the development of this new and exciting technology.

Technology integration requirements for adaptive structures in space

J.P.Henderson

Materials and Vibration Engineering, 383 Ridgewood Dr, Fairborn, OH 45324

P.E.Stover

Nichols Research Corporation, 4141 Col Glenn Hwy, Dayton, OH 45431

ABSTRACT: Successful application of adaptive structures technology for vibration suppression of future space systems will require the integration of several technologies. The integration of control electronics systems with space adaptive structures systems is discussed. Some of the recent developments in the areas of passive vibration damping, active control of vibratory response, embedded sensors and actuators, and electronic systems including sensors and actuators are discussed. To take advantage of the fast moving developments in these several technologies it is necessary to define parameters for optimization of integrated vibration control systems.

1. INTRODUCTION

Future space systems will require stable precision structures to accommodate sensors with stringent limitations on line-of-sight (LOS) errors and jitter caused by vibratory response of the structure. Vibration can be excited by rapid retargeting maneuvers; onboard equipment such as cryo-coolers , momentum wheels, or control moment gyros; and propulsion or attitude control systems. Numerous studies have been conducted of vibration suppression systems to achieve this high level of performance including systems with passive damping, active control, embedded sensors and actuators, and combinations of each of these. Several investigators have reported that one of the major limitations of active control systems is the electronic compensator; stating concerns with weight, power consumption, speed and computing capacity and robustness. Others have reported that augmented passive damping is required to maintain stability in an actively controlled structure with several modes in the control bandwidth. This paper reviews some of the recent investigations into the synergistic effects of passive damping and active control of structures to be used in space, as well as emerging electronics technology that could significantly improve active vibration control systems. The obvious conclusion to this review is that the most effective approach to developing adaptive structures for vibration control of space structures is to couple rapidly improving electronics technology with modern control

theory, new sensor and actuator technology, and latest developments in the design of passively damped structures.

II. VIBRATION SUPPRESSION

There have been several investigations of utilizing feedback control systems for active vibration suppression of space structures. Many of these systems , such as Gehling (1991), Voth and Stroughton (1991), have utilized proof mass actuators (PMA) to apply corrective forces to the structure for the control of structural vibration. Others such as Obal (1986), and Bronowicki (1990) have demonstrated the feasibility of utilizing piezoelectric devices as both sensors and actuators. Independent of the type of actuators, it has been shown that the problem of active control becomes increasingly difficult with increases in the amount of vibration suppression required as well as increases of the modal density of the structure to be controlled. Obal used a band pass filter and phase shifting circuit tuned to each of the fairly well separated modes of a beam. As the structure becomes more complex and modal densities increase so does the difficulty of establishing an accurate analytical model of structural response. Stability of the control system is highly dependent on the accuracy of the plant.

von Flotow and Vos (1991) pointed out that, for structures with many closely spaced modes in the control band, uncertainties in the plant will cause compensators to become unstable unless significant passive damping is present. Even in the case of carefully characterized laboratory structures, with single input single output (SISO), passive damping in the range of 1 to 4% critical viscous is required for phase stability in the control bandwidth. In uncertain structures the required passive damping levels would be much higher. Significant damping is also required for gain stability at frequencies higher than the control bandwidth where poorly modeled modes are likely.

Structures of typical space systems have high modal densities and multiple input multiple output (MIMO). Applying modern control design, with position as well as velocity feedback, to such systems can become very cumbersome when dealing with high order systems. Accuracy and speed of the control system decreases as the size of the model increases. This forces the designer to reduce the order of the model and iterate until the desired performance and stability is achieved. This reduced order controller is subject to "spillover" instabilities caused by unmodeled modes, often requiring several design iterations of the model. Experiences with both LQR/LTR (Gehling 1991a) and H∞ (Voth and Stoughton 1991) indicate that stable active control on a typical MIMO space craft structure could not be achieved without significant levels of passive damping.

Passive damping can be achieved through a number of techniques including incorporation of viscoelastic materials (VEM), viscous struts, passively shunted piezoelectric devices, and magnetic damping devices. In fact, "passive" damping can in effect be achieved through low authority active control with local direct velocity feedback. This type of low authority controller does not exhibit the stability problems, nor does it have the performance of the high authority

control systems. Of course, the system designer must trade off the benefits, risks, costs and complexity of active versus the various passive approaches. Case studies comparing passive piezoceramic, viscous, and viscoelastic damping approaches are being presented at this conference (von Flotow et al 1991b).

Increasing passive damping through the use of viscoelastic materials is a mature technology with several well developed design techniques available. Although properties of VEMs are temperature and frequency dependent, and effective optimization of VEM damped structures require careful consideration of modal strain energies and wave lengths, these materials have been successfully used in airframes, turbine engines, automotive and naval systems for several years (Nashif et al 1985). Considerable recent progress has been made in resolving technical questions pertaining to the use of VEM in space structures, including better correlation VEM mechanical property tests, greatly improved VEM data bases, and improved finite element based design procedures. Additional questions need to be answered including a better understanding of space environmental effects on VEM and quantified outgassing information on VEM in representative configurations. The time has come to identify and resolve those areas that are hampering the integration of a powerful body of VEM damping technology into adaptive structures vibration control strategies.

III. ELECTRONICS AND POWER

The application of adaptive structures concepts to vibration control of operational systems will require the marriage of structural dynamics, active control, passive damping, and electrical and electronics technologies. It is common to assume that the phenomenal growth in the electronics arena will continue and will provide for all future needs. Such may not be the case.

In an adaptive structure the value of a parameter that indicates the status of a structural element is measured and a corrective action is taken to compensate for any undesired deviation in that status. The elements of an active vibration suppression system are the sensors that measure strain, displacement or acceleration, the force generators that apply the corrective action, and the electronics that process the sensor signals and produce the instructions to power the force generators. The interactions among these elements are controlled by the electronics system and the optimization of that system presents both a challenge and an opportunity.

The heart of any adaptive structures system is the sensor suite and the associated force generators. While strain is the most common parameter measured, there will be other measurements that are important to the system. Strain sensors may include metallic strain gauges, piezoelectric gauges (both ceramic and polymeric), digital sensors and any of several fiber optic concepts under development. Piezoelectric force generators are the baseline for many advanced adaptive structures applications. Many sensors and force generators require an analog bias and produce an analog output and many of the electronics system's reliability, accuracy and operational problems will stem from the generation, conditioning and transmission of these analog signals. From an electronics and electrical stand point, total power and power profile are

the overriding issues in the generation of forces. The analog output from the sensors will have to be converted to digital form for processing. This conversion should be accomplished as close to the source as possible and the ultimate solution would be to generate a digital signal directly. Integrated sensors that produce a digital signal are under development. These sensors are produced by micromachining techniques similar to those used to make integrated circuits and may be configured to measure strain, acceleration, pressure, flow or humidity. Auxiliary circuitry may be fabricated directly on the sensor substrate. The complexity, size, weight and reliability of the electronics may drive the sensor and force generator selection in a space application.

The electronics system that controls an adaptive structure will perform a number of functions. While many of these functions are similar for a test system and a flight system, design parameters are quite different and the differences must be considered in the technology development if a robust technology is to be available for technology transition. The electronics must accept signals from a number of sources distributed throughout the structure, condition and usually digitize those signals, transmit the signals to processing sites, provide bias and housekeeping power to a variety of components, solve algorithms that may be quite computationally intensive, produce appropriate control signals for the force generators, generate and hand-off data to the host system, regenerate itself after any number of disruptive events and recalibrate the system as required. Redundancy, lifetime, noise-immunity and reliability issues complicate the electronics system design and compensation must be provided for environmental effects. The availability of processors should not be a problem unless radiation hardness becomes an issue but the architecture should be addressed early in the development cycle to give time to optimize the system. Multiplexing to minimize cabling will be important and bus systems should be evaluated to take advantage of recent and projected developments.

Random access memory is required to support the processors and, if multiple processors are used, there are a number of options for sharing or mutually accessing sections of the memory. Nonvolatile memory is needed to store critical parameters and code for system start-up and for reinitialization after an interruption. Archival memory may be required to store system history for troubleshooting or for a reference to modify control algorithms to compensate for aging or damage effects. As with the processors, commercially available memory should suffice unless there is a radiation hardness requirement.

The speed that is achieved on modern integrated circuit chips is lost between chips because of the packaging. Multichip packages and innovative ways of attaching chips to substrates are being developed and the adaptive structure system should take advantage of those developments. Connectors are historically a weak point in any electrical system and a distributed adaptive structures system may have very severe connector problems. In this as in other technology areas discussed, the adaptive structures community may be able to influence the direction of development.

The power budget on any space craft is critical and every milliwatt is jealously accounted

for. The total energy consumed over the life of the space craft is important whether its impact is measured in terms of solar cell life or consumable weight. Passive damping has been shown to save as much as 99% of the power expended for active vibration control. The schedule on which the power is demanded may also be critical because the power source or distribution system may be overtaxed resulting in burn-out or unacceptable voltage drops if an adaptive structures demand surge happens to coincide with a demand from another load. Transients and interruptions in the prime power supply must be expected and the system must be designed to recover from a variety of power system malfunctions. Power systems are notorious sources for electronic noise. Many problems can be avoided with good power system design practice but some types of loads are inherently more noisy than others and this should be considered early in the development cycle. Rapid switching of a load will produce transients that radiate electromagnetic energy that, in turn, will be coupled into other circuits in the vicinity. Common solutions to this problem tend to be heavy and can introduce thermal management problems in a spacecraft. It is usually desirable to transmit power at the highest practical voltage to minimize conductor weight and inverter circuitry that generates an alternating or pulsed current is often employed. If this pulsed power could be applied directly to the force generator the entire system could be simpler, lighter, more reliable and more responsive. This is just one example of synergism that could be realized from an integrated approach to system development.

Radiation hardness is a very important issue. The radiation levels a given electronics device will experience are a function of mission, scenario and shielding and the ability of a device to withstand radiation is a function of device material, device design, device fabrication, circuit design, operational requirements and software design. All space systems must be able to withstand the natural environment and, depending on the scenario adopted, may have to withstand a nuclear weapon event. It seems risky to develop a military technology that cannot withstand at least some nuclear weapon induced radiation. An electronic device is much more susceptible to both hard (nonrecoverable) and soft (recoverable) damage if it is in operation during the time it is subjected to high radiation levels. It is very important to determine whether or not the device must be operating during a nuclear event. A requirement that the electronics be turned off when radiation levels are high could have significant effects on the stability of the system and on the form of the algorithms. It may seem that this is an issue the adaptive structures developer can defer but the availability of radiation-hard electronics is very limited and unless requirements for hardened components are identified to the device developer, the research and development of such parts may never be accomplished.

IV. SUMMARY AND RECOMMENDATIONS

Adaptive structures faces a dilemma that is all too common when many technologies must be married. Rapid progress is being made in several related technologies, but the direction of future progress depends heavily on the integration of the output of divergent technical

communities that have not communicated well in the past.

The vibration suppression community, has made tremendous strides in developing both active control and passive damping technologies applicable to space systems. A few investigators are now looking at the synergistic benefits of both active control and passive damping on the response of test systems, such as in the PACOSS program (Gehling 1991a, Voth and Stroughton 1991), in the SPICE program (Yiu 1991), and at the Air Force Institute of Technology (Gaudreault et al 1991). More effort should be concentrated on integration applicable to flight systems.

The adaptive structure specialist tends to view electronics as a catalog of capabilities and asks for an index to the catalog. The electronics specialist asks for a detailed definition of the problem so that he can develop an ideal electronics sub-system. Neither the catalog nor the detailed definition exists and cannot without an iterative, cooperative program. Ideally, a balanced approach will lead to early, cost-effective use of all these technologies.

V. ACKNOWLEDGEMENT

REFERENCES

Bronowicki A J, Menenthall T L, Betros R S, Wyse R E, and Innis J W 1990 *First Joint U.S./Japan Conference on Adaptive Structures* ed B K Wada, J L Fanson, and K Miura (Lancaster Pa: Technomic) pp 373-401

Gaudreault M L D, Liebst B S, and Bagley R L 1991 "Simultaneous Design of Active Vibration Control and Passive Viscous Damping" AIAA Conference on Guidance Navigation & Control, New Orleans,Paper 91-2611

Gehling R N 1991 "Active Vibration Suppression via LQG/LTR; Analytical and Experimental Results for the PACOSS Dynamic Test Article" *Proceedings of Damping '91* WL-TR-91-3078 vol I pp CAA-1-22

Gehling R N 1991 "The PACOSS Dynamic Test Article" *Proceedings of Damping '91* WL-TR-91-3078 vol II pp EDA-1-19

Nashif A D, Jones D I G, and Henderson J P 1985 *Vibration Damping* John Wiley & Sons NY

Obal M W 1986 "Vibration Control of Flexible Structures Using Piezoelectric Devices as Sensors as Actuators" PhD Thesis, Georgia Inst of Tech

Yiu Y C 1991 "Passive Damping Design for Control System Stability on the SPICE Testbed" Symp on Active Materials & Adaptive Structures, Alexandria VA

von Flotow A H and Vos D W "The Need for Passive Damping in Feedback Controlled Flexible Structures" *Proceedings of Damping '91* WL-TR-91-3078 vol II pp GBB-1-12

von Flowtow A H, Hagood N, Johnson C, and Keinholz D 1991 "Case Studies in Passive Piezoceramic, Viscous and Viscoelastic Damping" Symp on Active Materials & Adaptive Structures, Alexandria VA

Voth C T and Stroughton R M 1991 "H∞ Control for the PACOSS DTA" *Proceedings of Damping '91* WL-TR-91-3078 vol I pp CAB-1-17

Exploratory study of the acoustic performance of piezoelectric actuators

O. L. Santa Maria
NASA Langley Research Center
Hampton, Virginia

and

E. M. Thurlow, M. G. Jones
Lockheed Engineering & Sciences Co.
Hampton, Virginia

ABSTRACT: The proposed ducted fan engine has prompted the need for increasingly lightweight and efficient noise control devices. Exploratory tests at the NASA Langley Research Center were conducted to evaluate three piezoelectric specimens as possible control transducers: a Polyvinylidene Flouride (PVDF) piezofilm sample and two composite samples of Lead Zirconate Titanate (PZT) rods embedded in fiberglass. The tests measured the acoustic output efficiency and evaluated the noise control characteristics when interacting with a primary sound source. The results showed that a PZT sample could diminish the reflected acoustic waves. However, the PZT acoustic output must increase by several orders of magnitude to qualify as a control transducer for the ducted fan engine.

1. INTRODUCTION

The unique noise generating properties of the proposed ducted fan engines are forcing the aeroacoustician to consider new techniques to reduce the sound levels of these engines to acceptable levels. The proposed engine will be about 10 ft in diameter, and 10 ft. long. This design is predicted to generate noise levels over 150 dB inside the engine, with very limited space for noise attenuation devices or liners. Among the techniques being considered as a solution for this unique problem is active noise control. One of the primary difficulties of providing an active noise control system for this application is the need for extended spatial control of the spinning modes inside a duct (ref 1). One possible method for achieving extended spatial control is to use a distribution of highly efficient, lightweight sound sources.

A current program at NASA Langley Research Center is investigating alternative sound sources and their application to the noise control problem. As a first step in the development process, two exploratory tests were conducted to evaluate the acoustic transduction properties of three piezoelectric samples. Piezoelectric materials vibrate and produce sound when driven by an input voltage. If sufficiently large acoustic outputs that would match the predicted levels of the proposed engine can be obtained directly from these piezoelectric samples, they may be used as direct in-duct acoustic actuators. However, if the direct acoustic outputs are insufficient, the piezoelectric material may have to be coupled with a heavier or larger structure to amplify the acoustic outputs.

2. DESCRIPTION OF PIEZOELECTRIC SAMPLES

Three piezoelectric samples, one Polyvinylidene Flouride (PVDF) piezofilm sample and two Lead Zirconate Titanate (PZT) composites were tested. The first sample evaluated was a 28-μm-thick PVDF piezo film embedded in a block of foam. Figure 1(a) illustrates the sample in its test configuration and indicates the relative motion of the film. The other two samples were composites of PZT rods embedded in fiberglass. The cross-sectional areas of the PZT rods in the two composites were 1 mm^2 and 0.25 mm^2, spaced 4.5 mm and 2.3 mm apart, respectively. Both PZT samples had a surface density of 5% PZT. Figure 1(b) shows the configuration of the PZT composites.
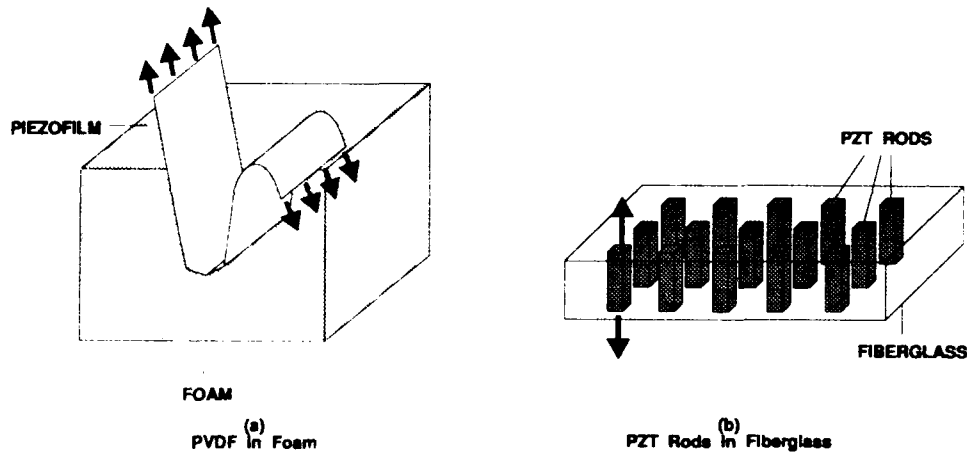
Figure 1. Piezoelectric Samples.

3. ACOUSTIC RESPONSE MEASUREMENT

The first test was to ascertain the acoustic response of the samples as functions of frequency and excitation voltage. This was done by mounting each sample normal to the axis of a 2-in. by 2-in. duct with a nonreflecting termination and measuring sound levels approximately one meter from the sample. The samples were driven at various input voltages over a frequency range of 200 to 2500 Hz in 100 Hz increments. Figure 2 shows a schematic of the setup.
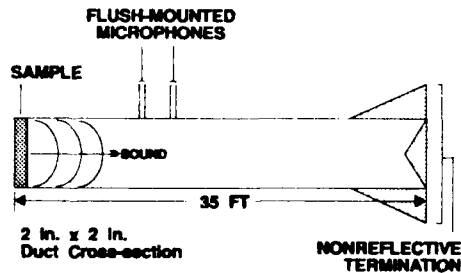
Figure 2. Progressive Wave Tube used to measure acoustic efficiency.

Figure 3 shows a frequency response plot of the acoustic output for the PVDF piezofilm. The piezofilm was driven by an input of 150 V_{rms}, the maximum voltage the PVDF-foam configuration could sustain. A peak sound pressure level (SPL) of 64.9 dB (re 20 μPa) was measured. To test for linearity of acoustic output vs. voltage input, an input of 75 V_{rms} was used. The acoustic response for both input voltages, shown in figure 3, illustrates that for most frequencies, the change in acoustic output is directly related to the change in excitation voltage or:

Figure 3. Acoustic output data for the PVDF Piezofilm.

$$\Delta dB = 20 \log \frac{V_2}{V_1}$$

for this range of excitation voltage, indicating linearity. Some points in figure 3 did not exhibit a linear increase with the change in voltage, most likely because the sound pressure levels were below the range of the acoustic measurement system.

The PZT piezoceramic samples were driven at 250 V_{rms}. Figure 4(a) shows the frequency response of the PZT sample with 1-mm^2-cross-section rods. The peak in the response curve (78.3 dB) indicates a resonant response of the sample for the frequency range tested. Figure 4(b) shows the frequency response of the PZT sample with 0.25-mm^2-cross-section rods. The response curve is similar to that of the previous PZT sample, but with a higher maximum SPL of 86.4 dB (re 20 μPa) measured. A shift in the peak and slope of the curves can be observed in Figures 4(a) and 4(b). Both samples were also driven at 100 V_{rms} to check linearity. Figures 4(a) and 4(b) illustrate that with an increase from 100 V_{rms} to 250 V_{rms}, the change in decibels satisfied the equation above ($\Delta dB = 8$ dB), thus exhibiting linear behavior.

(a)
1 mm^2 Rod X-Section

(b)
0.25 mm^2 Rod X-Section

Figure 4. Acoustic output data for PZT piezoceramic samples.

4. NOISE CONTROL EVALUATION

The second test was conducted to investigate the ability of a piezoelectric sample to alter a simple standing wave field by controlling the termination boundary condition or acoustic impedance in a standing wave tube. The standing wave tube is a closed duct in which incident and reflected acoustic waves combine to create a standing wave (ref. 2). The standing wave tube was used to determine if the active sample could act as a nonreflecting termination for various phase settings relative to a primary sound source. The PZT sample with 0.25 mm^2 cross-section rods was used as the secondary source in this test since it gave the highest acoustic output of all three samples tested.

The sample was mounted at one end of a 2-ft long standing wave tube, as shown in figure 5, with acoustic drivers on the other end to produce an incident sound field. The acoustic drivers and the sample were adjusted to produce the same acoustic output levels at each frequency tested. The standing wave produced in the tube was determined by fitting the data measured by the axially traversing probe microphone with the equation for a standing wave (ref. 2). Changes in the standing wave pattern were then measured as the PZT sample was driven at various phase settings relative to the acoustic drivers. A significant reduction in the standing wave ratio SWR would indicate that the reflected wave from the sample was being minimized.
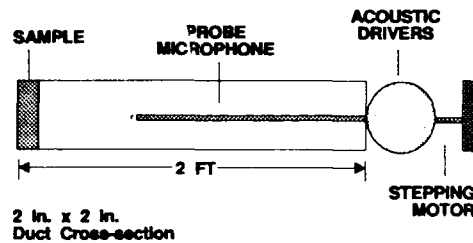
Figure 5.   Standing Wave Tube

The PZT sample was driven at 250 V$_{rms}$ input, over a frequency range of 500 to 2500 Hz, in 100 Hz increments. The relative phase was varied from 0 to 180 degrees in 30 degree increments. Changing the relative phase settings varied the SWR at all frequencies tested. For this range of frequencies, the change in SWR ranged from 4.2 dB to 44 dB. The relative phase settings at which the maximum and the minimum SWR were observed were different for each frequency tested. Figures 6(a) and 6(b) are plots of measured standing waves. Each plot shows SPL (re 20 µPa) vs. distance from the face of the sample. A typical SWR variation (in this case, an increase) is shown in figure 6(a). Figure 6(b) illustrates one of the significant reductions. The maximum standing wave ratio for this frequency was 18 dB when the sample was at a phase setting of 180 degrees. When the phase was set to 90 degrees, the SWR was reduced to 1.2 dB.

A survey of SWR versus phase setting at 1900 Hz, in increments of 1 degree, determined that the optimal phase setting was 82 degrees, which provided a SWR of less than 1 dB. This result indicates that the reflected wave from the sample is nearly eliminated.

$\Delta\Phi = 0°$ $\Delta\Phi = 90°$

(a)

900 Hz Frequency

$\Delta\Phi = 90°$ $\Delta\Phi = 180°$

(b)

1900 Hz Frequency

$\Delta\Phi$ = Relative Phase Setting
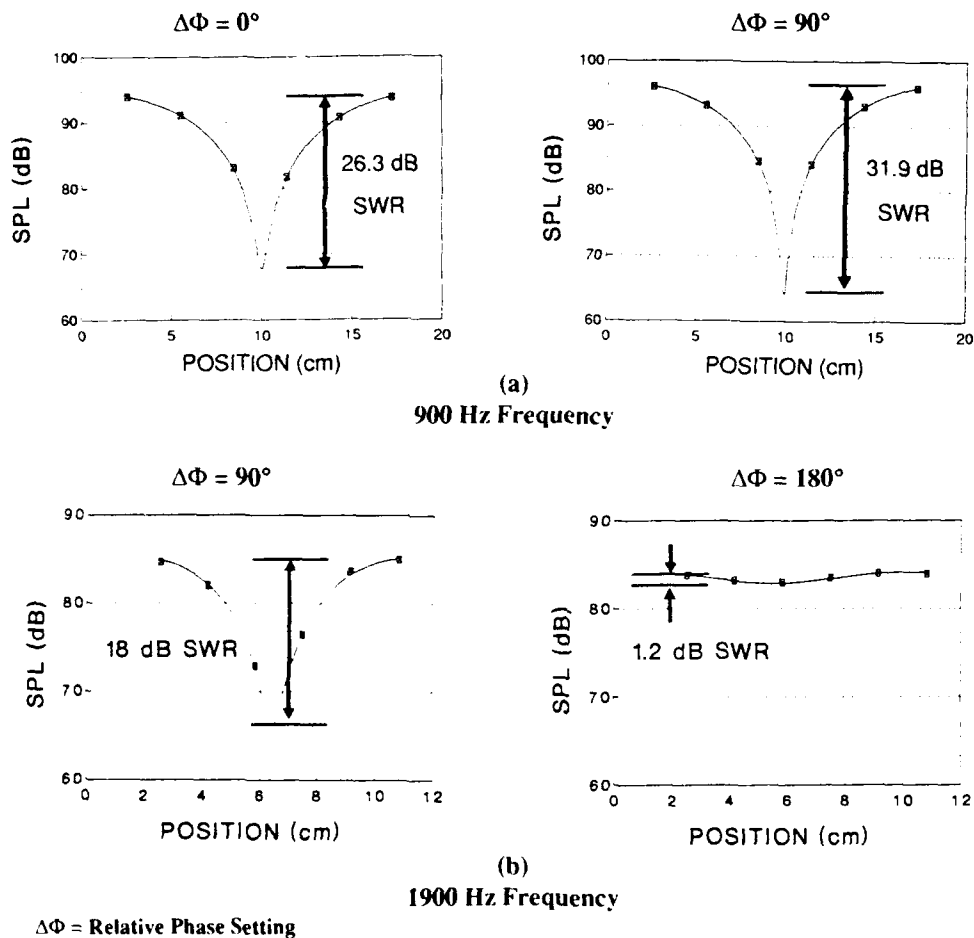
Figure 6. SWR Plots for Various Relative Phase Settings.

5. CONCLUSIONS

The acoustic ouputs of the three piezoelectric samples were found to vary linearly with input voltage. The sample with the largest acoustic output was used as an active termination in a standing wave tube. A significant reduction in standing wave ratio was achieved, demonstrating that an active piezoelectric sample can eliminate a reflected wave. The acoustic output of the samples was far below the level necessary to control the ducted fan engine. To be useful for active noise control. the response of piezoelectric materials must be increased by several orders of magnitude. Amplifying the acoustic output of piezoelectric materials remains a challenge for the active noise control and advanced materials community.

REFERENCES

1   Rice, Edward J.: "Spinning Mode Sound Propagation in Ducts with Acoustic Treatment and Sheared Flow," <u>Aeroacoustics; Fan Noise and Control; Duct Acoustics; Rotor Noise; Progress in Astronautics and Aeronautics</u>, Vol. 44, AIAA, New York, NY, 1976.

2   Jones, Michael G. and Parrott, Tony L.: "Evaluation of a Multi-Point Method for Determining Acoustic Impedance," <u>Mechanical Systems and Signal Processing</u>, Vol. 3, No. 1, 1989.

Comparison of feedforward versus feedback design in sound radiation suppression

J. Thi, E.A. Unver
AT&T Bell Laboratories, Arlington, VA

ABSTRACT

This paper presents two design approaches for the active control of acoustic radiation. The two approaches discussed employ spatial modal filters with feedforward and feedback designs, respectively. Broadband feedback control systems have the advantage over feedforward control systems in that they do not require the decoupling (neutralization) of a suitable reference signal. In the formulation of both control systems, the transfer functions associated with the actuators and sensors are modeled by different group delays. The effects of these group delays on the bandwidth performance between the feedforward and feedback designs are compared. The study described here illustrates the fundamental performance differences between the modal based feedforward and feedback active control systems that are constrained to act causally. Comparisons of the controlled and uncontrolled vibration energy and the acoustic energy are discussed. The analysis and simulation results use the dynamics of a simply supported plate in air. The results indicate that if the sensor group delay is small compared with the actuator group delay then feedback design can achieve the same cancellation performance as the perfectly neutralized feedforward design. Furthermore, the results also show that special care must be taken whenever the active control system is designed to suppress only the high efficiency radiating modes, since it is possible to increase the radiation efficiency of an uncontrolled mode without increasing its vibration level. This can be accomplished by changing the relative phasing of the modal response without changing its magnitude.

INTRODUCTION

Much of the research in active control of sound radiation employs adaptive filtering techniques or the so-called feedforward system. Adaptive filtering methods for acoustic suppression have been applied successfully in a number of practical problems, such as noise control in a fan duct, aircraft cabins and the silencing of an engine exhaust system. If the active control system is to suppress the acoustic response at locations where acoustic measurements are available, then adaptive feedforward filters can be used to cancel the measured sound from an error microphone. This type of active control system is referred to as a feedforward design with system identification. An alternative approach which does not require acoustic measurements is to control the vibrational modes that contribute the most to the radiated acoustic energy.

It has been shown that modal based active control can minimize the number of actuators, sensors, and control energy. This is especially true if the vibration problem is known to involve only a few significant radiating modes. The advantage of modal based active control strategy is that the vibration motion from individual modes can be estimated without introducing time delay into the cancellation path. A time delay will be introduced by the acoustic propagation where acoustic measurements are used. Therefore, it is possible to develop a modal based active control system using feedback design since acoustic propagation delay can present stability problems in the feedback design.

There are many factors that will influence the success of an active control system in any given application. One of the main factors is the selection of either feedforward or feedback control approach. The objective of this paper is to compare the feedforward and feedback approaches in the design of a modal-based active control system. There are major differences between feedforward and feedback approaches. Reference signals without the effects from the control signals, the so called perfect neutralization, are desired in the feedforward approach, whereas the feedback approach requires the availability of residual error signals. Furthermore, it can be shown that if the effects on the reference signals from the control signals cannot be removed perfectly, then a feedback loop exists in the cancellation path which can degrade cancellation performance and present stability problems.

In this paper, the design of the modal-based feedforward and feedback active control systems with different actuator and sensor group delays are presented. The simulation results use the dynamics of a simply supported plate in air. The effects of non-perfect neutralization in the feedforward design are also examined.

Comparison of the uncontrolled and controlled plate response indicate that feedback design can achieve the same vibration suppression as the feedforward design whenever the sensor group delay is much smaller than the actuator group delay. Furthermore, feedback design is not possible if the sum of the actuator and sensor group delay is sufficiently large, since this can present stability problems. Evaluations of the farfield acoustic pressures indicate that it is also necessary to control the low efficiency radiating modes, since it is possible to increase the radiating efficiency of an uncontrolled mode without increasing its vibration level. This can be accomplished by changing the relative phasing of the modal response.

THE FEEDFORWARD MODAL BASED CONTROLLER

The broadband adaptive filtered-X least-mean-square (FXLMS) algorithm [1,2] is used in adaptive noise cancellation application to adaptively remove undesired components of a signal that are correlated with a given reference signal. Figure 1 shows a block diagram of the algorithm for a real passband cancellation path transfer function Y_a. The reference signal r is obtained by filtering the disturbance signal d by the reference structural transfer function H_r. The application of the weight W to the reference signal r forms the cancelling signals, which drives F_p, the actuator spatial filter [3] and Y_a, the structural transfer function from actuator to vibration sensor to cancel the primary disturbance signal. The actuator and sensor transfer functions are modeled by the group delays $e^{-j\omega\tau_a}$ and $e^{-j\omega\tau_s}$, respectively. The adaptive weight is computed by the FXLMS algorithm, whereby the update is formed by filtering the reference signal r by an estimate of the equivalent cancellation path transfer function $F_m e^{-j\omega(\tau_a+\tau_s)} \hat{Y}_a F_p$, correlating with the vibration error signals, and scaling by the convergence gain factor μ. F_m is the modal filter [3] which allows the extraction of m modes to be controlled with L sensors.

If the adaptive weight W in Figure 1 is allowed to converge to W_{op} in Figure 2, then Figure 2 represents the steady state case of Figure 1, where the adaptive LMS algorithm has been removed. In this equivalent form, the algorithm resembles a conventional feedforward control system with neutralization residual transfer function $\Delta = Y_{ar} - \hat{Y}_{ar}$, where Y_{ar} and $\hat{Y}_{ar}$ are the structural transfer function from actuator to the reference sensor and its estimate equivalent transfer function, respectively. It can be seen in Figure 2 that if Y_{ar} is not exactly equal to $\hat{Y}_{ar}$, the perfect neutralization condition, then a feedback loop with loop gain $(Y_{ar} - \hat{Y}_{ar})$ Fp W_{op} exists in the cancellation path which can degrade cancellation performance and can present stability problems in some applications.

For independent spatial modal control it is desirable to form linear combinations of the sensor signals in order to extract estimates of the modal amplitudes. Ideally each linear combination will pass one specific mode and reject all the other modes. Thus, for L error sensors and M modes to be controlled, the ideal modal filter must map L inputs into M uncoupled outputs. In practice, however, modal filters $\Phi_1, \Phi_2, \ldots, \Phi_M$ based upon the discrete sampling of the continuous eigenfunctions $C_\Phi(x)$ (see Equation (A16)), do not necessarily produce the best estimates of the desired model amplitudes. A better approach, described in Reference [3] is to design modal filters that extract from sensor measurements the best least mean square estimate of the modal participation factors while rejecting as well as possible the interference from the undesired modes. In that study the modal filters were designed to minimize the average normalized cross response power. The objective function described in Equation (1a) is minimized with respect to f_n, subject to the constraint of Equation (1b), where $f_1, f_2, f_3, \ldots, f_M$ represent a set of N dimensional filter vectors and M denotes the number of actuators in the control system:

$$J = \sum_{m=1}^{M} (f_n^T \Phi_n)^2, \quad n=1,2, \ldots, N \tag{1a}$$

$$f_n^T \Phi_n = 1 \tag{1b}$$

Using vector differentiation with the method of Lagrange multipliers as described in Reference [3], the solution to Equation (1) is given by

$$F = (C_\Phi C_\Phi^T)^{-1} C_\Phi A \tag{2}$$

$$F = [F_{m1}^T \; F_{m2}^T \; \ldots \; F_{m10}^T]^T \tag{3}$$

where F_{mi} is the modal filter which allows the extraction of mode i from the L sensor measurements. A being a diagonal scaling matrix that is calculated to enforce the constraint of Equation (1b). A more detailed analysis of the modal based approach including weighted sum modal powers and performance degradation for a limited number of sensors can be found in reference [3].

THE MODAL-BASED FEEDBACK CONTROLLER

In this section, a formulation of the feedback control system is developed using the multi-input multi-output state space controller to minimize the vibration energy of selected modes.

Figure 3 shows a block diagram of the feedback control system, where the actuator and sensor transfer functions are modeled by the group delay $e^{-j\omega\tau_a}$ and $e^{-j\omega\tau_s}$, respectively. It is known that the feedback control system suffers a basic limitation of the cancellation bandwidth and out-of-band response whenever the loop transfer function exhibits non-minimum phase. In this case, the loop transfer function is given by $Ya \, e^{-j\omega(\tau_a + \tau_s)}$ which is clearly a non-minimum phase transfer function. Under these conditions, the disturbance source bandwidth can exceed the maximum stable cancellation bandwidth if the group loop delay is large. It is interesting to note that in the feedback design as shown in Figure 3, the cancellation bandwidth depends on both the actuator and sensor group delays of the loop transfer function, whereas in the feedforward design as shown in Figure 2, the cancellation bandwidth depends only on the actuator group delay.

The closed loop response as shown in Figure 3 is given by

$$H_c(\omega) = [1+L(j\omega)]^{-1} e^{-j\omega\tau_s} C_\Phi(j\omega I-A)^{-1} B_d \tag{4}$$

where, $L(\omega) = G(\omega) C_\Phi(j\omega I-A)^{-1} B_f e^{-j\omega(\tau_a + \tau_s)} \tag{5}$

and, $G(\omega) = C_c (j\omega I-A_c)^{-1} B_c$

where A, B_d, B_f, C_Φ are the state space matrices associated with the structure (see appendix) and A_c, B_c, C_c are the state space matrices associated with the MIMO model-based controller. $L(\omega)$ is defined as the loop gain. There are many methods one can apply to design the MIMO Controller. For the broadband active control system considered in this paper, the Loop Transfer Recovery (LTR) [4] design methodology was used. The controller can be designed in two steps. First a LQR regulator gain matrix K_c is computed to minimize the selected vibration modes to be controlled, thereby realizing the loop gain response,

$$L(\omega) = K_c e^{-j\omega(\tau_a + \tau_s)} (SI-A)^{-1} B_f \tag{6}$$

Note that the group delay $e^{-j\omega(\tau_a + \tau_s)}$ can be approximated by a state space equation using the Pade approximation. Therefore, the regulator gain K_c is computed based on an augmented state space equation, $[A', B'_f, C''_\Phi]$, between the space state matrices $[A, B_f, C'_\Phi]$ and the state space matrices associated with the group delay. Second, a Kalman filter gain matrix K_f is computed so that the resulting loop gain is as close to Equation (6) as possible. The resulting composite loop gain is given by

$$L(\omega) = [K_c(SI-A' + B'_f K_c + K_f C''_\Phi)^{-1} K_f] C''_\Phi (SI-A')^{-1} B'_f \tag{7}$$

Thus, by equating (5) and (7), the feedback controller can be obtained as

$$G(j\omega) = K_c(SI-A' + B'_f K_c + K_f C''_\Phi)^{-1} K_f \tag{8}$$

For small values of τ_a and τ_s, the feedback controller is determined by the regulator gain matrix K_c, Kalman filter gain matrix K_f, and the augmented state space matrix A', B'_f, C''_Φ.

APPLICATION TO A SIMPLY SUPPORTED FLAT PLATE

Once the surface velocity distributions of interest are calculated the corresponding farfield pressure can be determined. Since this paper considers active sound radiation suppression of a plate in air, the mass loading of the surrounding medium on the plate can be neglected. The farfield pressure generated by this plate can be found by using Rayleigh's formula [5]:

$$p(R) = \frac{\rho_0}{2\pi R} \int_L e^{jk|R-R_0|} \ddot{y}(R_0)\,dL(R_0), \quad R_0 << R \quad (9)$$

where $\ddot{y}(x)$ is the plate acceleration and $R-R_0$ is the distance between a field point and a point on the plate. Based on Equation (9) the radiated farfield pressure of the plate can be written as follows:

$$p(\theta) = \frac{\rho_0}{2\pi R} e^{jk(R+l\sin\theta/2)} \int_0^L e^{jkx\sin\theta} \ddot{y}(x)\,dx \quad (10)$$

where k is the acoustic wavenumber. Discretizing the integration in Equation (10) and noting that $\ddot{y}(x) = \omega^2 y(x)$, the farfield pressure $p(\theta)$ may be expressed as:

$$p(\theta) = \sum_{p=1}^{n_s} E(\theta, x_p)\, y(x_p) \quad (11)$$

where n_s is the number of surface sensors, x_p the coordinate of a surface sensor, and ω is the angular frequency and,

$$E(\theta, x) = \frac{\rho_0}{2\pi R} e^{jk(R+l\sin\theta/2)}(\omega^2) e^{jkx_p\sin\theta} \quad (12)$$

Here, $E(\theta, x)$ is the matrix operator which maps the plate response, $y(x)$ to the farfield pressure.

The locations of actuators, sensors and disturbance signals as well as the plate parameters are given in the Appendix.

The feedforward controller W_{op} in Figure 2 with τ_a equal to 5 and 25 milliseconds was computed based on minimizing the vibration energy of mode 1 and mode 3. Mode 2 was not selected for control since it is an even mode [6]. An even mode is an acoustically inefficient mode due to the radiation cancellation process that occurs when the in phase and out of phase half waves negate. For comparison, the feedback MIMO controller $G(\omega)$ in Equation (5) was also designed to minimize the vibration energy of mode 1 and mode 3 with $(\tau_a + \tau_s)$ equal to 0, 5, 15, and 25 milliseconds. Figure 4 shows the frequency response from disturbance to sensor 1 with and without feedforward control for τ_a equal to 5 and 25 milliseconds, where Y_{ar} equal to $\hat{Y}_{ar}$ and H_r equal to unity were assumed in Figure 2. Comparisons of Figure 4 and Figure 5 indicate that feedback

design can achieve the same vibration cancellation performance as the feedforward design for this case, when τ_a in the feedforward design is approximately equal to $(\tau_a + \tau_s)$ in the feedback design. It can be recognized that for sufficiently large τ_s as the use of feedback design is not possible due the gain bandwidth limitation. Although the gain bandwidth limitation can be improved by using the so-called Pseudo Cascade configuration [7,8], it is still the primary limitation for many applications with acoustic sensing using feedback design since acoustic propagation can increase τ_s significantly. Figure 6 and Figure 7 show the farfield pressures with feedforward ($\tau_a = 25$ ms) and feedback controls ($\tau_a + \tau_s = 25$ ms) at mode 1 and mode 3 frequencies, respectively. The reduction in farfield pressure of mode 1 is better while using feedforward design, whereas the reduction in farfield pressure of mode 3 is slightly better while using feedback design. In order to evaluate quantitatively the effects of non-perfect neutralization in the feedforward design, different neutralization residual $\Delta = Y_{ar} - \hat{Y}_{ar}$ is used in Figure 8 to obtain the cancellation performance in Figure 9, where the actuator and sensor group delay were neglected. Figure 10 shows the vibration cancellation level at mode 1 as function of the neutralization residual.

Finally, Figure 11 shows the farfield pressures using feedback control with the selection of mode 1 and mode 3 vs the selection of mode 1, 2 and 3 are as the modes to be controlled. Farfield enhancement in the frequency band of mode 2 (18 Hz) is observed in Figure 11. Examination of the spatial response of mode 2 in Figure 12 indicates that a relative phasing has been changed without a significant increase in its magnitude level. Therefore, it is possible to convert a low efficiency radiating mode to a high efficiency radiating mode without increasing its vibration level. This result indicates that special care must be taken whenever the active control system is designed to suppress only the high efficiency radiating modes.

ACKNOWLEDGEMENTS

APPENDIX . SIMPLY SUPPORTED PLATE MODEL

In this Appendix, the simply supported plate model used for the analysis in the main text will be defined. It is assumed that the plate is uniform and of length L and width b. The mass per unit length m is assumed constant, with modulus of elasticity E. The undamped homogeneous partial differential equation for the plate is given by

$$EI\frac{d^4 y}{dx^4} + m\frac{\partial^2 y}{\partial t^2} = 0 \quad (A1)$$

The eigenfunction mode shapes of this equation are given by [10]

$$\Phi_n(x) = A_n \sin(\frac{n\pi x}{L}) \quad (A2)$$

where A_n is a normalized constant chosen such that

$$\int_0^L \Phi_n^2(x)\,dx = 1 \qquad (A3)$$

and

$$\{A_n\} = \sqrt{\frac{2}{L}} \qquad (A4)$$

with corresponding natural frequencies

$$\omega_n = (\frac{n\pi}{L})^2 \sqrt{\frac{EI}{m}} \qquad (A5)$$

where I is the second area moment.

When damping and loading are introduced, Equation (A1) is modified to [1]

$$EI\frac{\partial^4 y}{\partial x^4} + c_s I \frac{\partial^5 y}{\partial x^4 \partial t} + m \frac{\partial^2 y}{\partial t^2} + c \frac{\partial y}{\partial t} = f(x,t) \qquad (A6)$$

where c_s is the strain velocity damping coefficient (internal), c is the absolute velocity damping coefficient (external), and f(x,t) is the loading force per unit length as a function of location x and time t. The displacement and the loading force are decomposed into modal components

$$f(x,t) = \sum_{n=1}^{N} F_n(t)\,\Phi_n(x) \qquad (A7)$$

$$y(x,t) = \sum_{n=1}^{N} y_n(t)\,\Phi_n(x) \qquad (A8)$$

where the Φ_n are defined in Equation (A2). By substituting Equation (A7) and Equation (A8) into (A6), multiplying by $\Phi_n(x)$, integrating, and using the orthogonality conditions results in the time differential equation [6]

$$\ddot{y}_n(t) + 2\zeta_n \omega_n \dot{y}_n(t) + \omega_n^2 y_n(t) = F_n(t,x)/m \qquad (A9)$$

where

$$\zeta_n = \frac{c_s \omega_n}{2E} + \frac{c}{2m\omega_n} \qquad (A10)$$

is the damping coefficient. For the special case of a line force excitation at location x_a, the force is expressed as

$$f(x,t) = f(t)\,\delta(x - x_a) \qquad (A11)$$

where each

$$F_n(t,x_a) = f(t)\Phi_n(x_a) \qquad (A12)$$

The response y(x,t) can be expressed in the state space representation using Equations (A8), (A9), and (A12) as following,

$$\dot{x} = Ax(t) + B f(t) \qquad (A13)$$

$$y(x,t) = C_\Phi(x)\,x(t) \qquad (A14)$$

where

$$A = \begin{bmatrix} A_1 & 0 & 0 & 0 \\ 0 & A_2 & 0 & 0 \\ \hdotsfor{4} \\ 0 & 0 & A_n & 0 \\ \hdotsfor{4} \\ 0 & 0 & 0 & A_N \end{bmatrix}, \; B = \frac{\sqrt{2}}{m} \begin{bmatrix} \frac{1}{2\beta_1}\sin(\pi x_a/L) \\ 0 \\ \hdotsfor{1} \\ \hdotsfor{1} \\ \frac{1}{2\beta_N}\sin(N\pi x_a/L) \\ 0 \end{bmatrix} \qquad (A15)$$

$$C_\Phi(x) = [\,\Phi_1(x)\,|\,\Phi_2(x)\,|\dots|\,\Phi_N(x)\,],$$
$$C_\Phi'(x_0) = [\,0\,|\,F_1(x)\,|\dots|\,0\,|\,\Phi_N(x)] \qquad (A16)$$

$$A_n = \begin{bmatrix} \alpha_n & \beta_n \\ -\beta_n & \alpha_n \end{bmatrix}, \qquad (A17)$$
$$n = 1,2,\dots,N$$

$$\alpha_n = \zeta_n \omega_n \qquad (A18)$$

$$\beta_n = \omega_n \sqrt{1 - \zeta_n^2} \qquad (A19)$$

A special case for N=10 is used in this paper. The following parameter values were used in the numerical calculations

Dimensions:
Length, $l = 1$ m
Width, $w = 0.01$ m
Thickness, $t = 0.002$ m
Second moment of area,
$I = w t^3/12 = 2/3 \times 10^{-11}$ m^4

Material Properties:
Modules of Elasticity, $E = 2 \times 10^{11}$ N/m^2
Mass density per unit volume,
$\rho = 8 \times 10^3$ kg/m^3

Damping Parameters:
$c_s/E = \{15500, 1550, 116, 46, 38, 31, 23, 15, 8, 8\} \times 10^{-6}$ s
$c/m = 0.202$ s^{-1}
$m = \rho w t = 0.16$ kg/m
with the above values, the natural frequencies are then calculated from Equation (A5) as

$$\{f_n\} = \{\omega_n/(2\pi)\} = \{4.5344, 18.1379, 40.8104,\dots\} \qquad (A20)$$

The above damping parameters were selected so that $\zeta_1 = \zeta_{10} = 0.01$ from Equation (A10) for the first and tenth modal frequencies since only the first ten modes are considered in here. The plate was discretized using 161 points with:
Actuator locations at points 15, 30, 45, 60, 75, 90, 105, 120, 135, and, 150
Sensor locations at points 8, 16, 24, 32, 40, 48, 56, 64, 72, 80, 88, 96, 104, 112, 120, 128, 136, 144 and, 152
Disturbance location at point 50

REFERENCES

[1]   S. J. Elliott, I. M. Stothers, and P. A. Nelson, "A Multiple Error LMS Algorithm and Its Application to the Active Control of Sound and Vibration," *IEEE Trans. Acoust., Speech, Signal Processing* ASSP-35, 1423-1434 (Oct.1987).

[2]   D. R. Morgan "An Analysis of multiple correlation loops with a filter in the auxiliary path", *IEEE Trans. Acoust*

Speech, Signal Processing, ASSP-28, 454-467, (Aug. 1980)

[3] D. R. Morgan "An Adaptive Modal-based Active Control System" *J. Acoust. Soc. Am.*, 89, 248-256, (Jan. 1991).

[4] G. Stein, M.Athans, "The LQG/LTR Procedure for Multivariable Feedback Control design", *IEEE Trans. Automatic Control*, AC-32-2, (Feb. 1987).

[5] M. C. Junger and D. Feit, *Sound Structures and Their Interaction* (MIT, Cambridge, MA, 1982) 2nd ed.

[6] J. Thi, E. Unver, M. Zuniga, "Comparison of Design Approaches in Sound Radiation Suppression", Proceedings of the Conference on Recent Advances in Active Control of Sound and Vibration, VPI, (Apr. 1991)

[7] D. R. Morgan, J. Thi "A Multi-tone Pseudo-cascade Filtered X LMS Adaptive Notch Filter," submitted for publication *IEEE Trans. Acoust. Speed and Signal Processing*.

[8] J. Thi, D. R. Morgan "A Broadband Pseudo-Cascade Active Control System", submitted for publication in *Proc. IEEE ICASSP 92*, (Mar.1992)

FIGURES
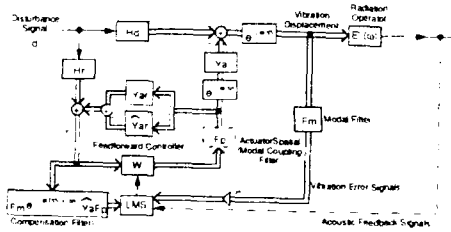
Figure 1 Broad band Feedforward Adaptive FXLMS Algorithm with Modal Filter
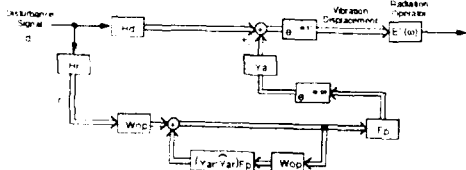
Figure 2 Steady State Equivalent of Figure 1 After Convergence to Optimum Weight
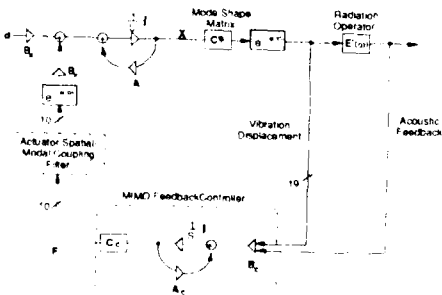
Figure 3 Broad band MIMO Feedback Active Control System
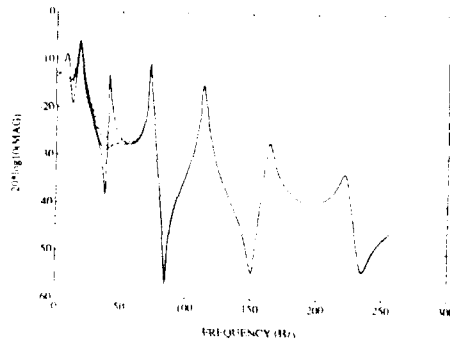
Figure 4 Frequency Response from Disturbance to Sensor 1 without Control and with Feedback Control (Delays 0, 5, 15, 25 ms)
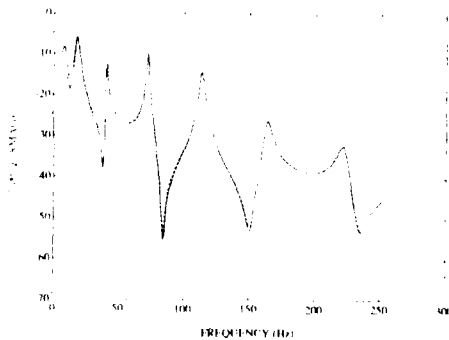
Figure 5 Frequency Response from Disturbance to Sensor 1 without Control and with Feedforward Control (Delays 5, 25 ms)
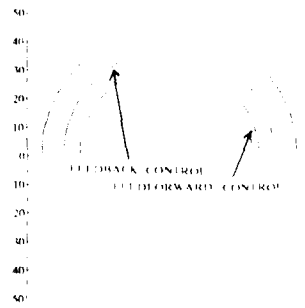
Figure 6 Farfield Pressure at Mode 1 frequency without Control, with Feedforward and Feedback Control (Delay 25 ms)
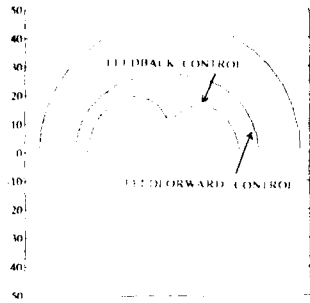
Figure 7   Farfield Pressure at Mode 3 frequency without
Control, with Feedforward and Feedback Control
(Delay 25 ms)

(a)

(b)

Figure 8 Feedforward Active Control System with Imperfect Neutralization
(a) System with Neutralization Residual Transfer Function Δ
(b) Equivalent Representation to (a)

Figure 10   Vibration Suppression at Sensor 1 as function of
Neutralization Residual
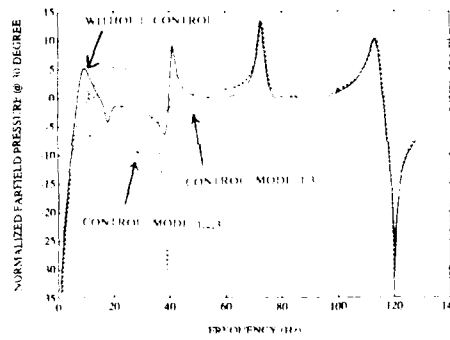
Figure 11   Farfield Pressure without Control and with Feedback
Control of Modes 1 and 3 vs Modes 1,2, and 3
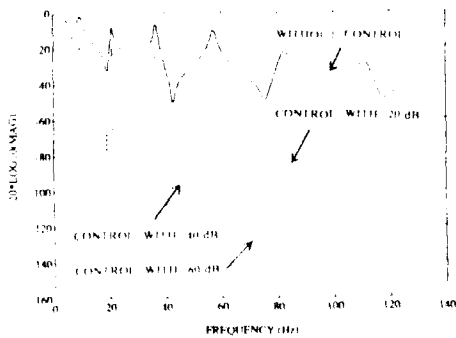
Figure 9   Frequency Response from disturbance to Sensor 1
without Control and with Control for Neutralization
Residual equal to -20, -40, -60 dB (Delay = 0 ms)
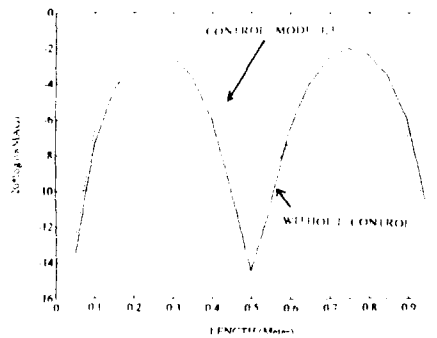
Figure 12   Spatial Response at Mode 2 frequency without
Control and with Feedback Control of only Modes 1
and 3 (Delay = 25 ms)

Active control of acoustic radiation from structures

K. Naghshineh, G. H. Koopmann, and W. Chen
The Pennsylvania State University
Center for Acoustics and Vibration, 157 Hammond Building, University Park, PA 16802

ABSTRACT: A general strategy is devised for achieving minimum radiation of sound from structures subjected to a harmonic excitation force. This strategy is based on quadratic optimization of acoustic power expression written in terms of the force vector exciting the structure. A set of actuator forces is found that results in minimum radiated sound power by altering the vibration response of the structure. This strategy is verified experimentally using a clamped-clamped beam excited with a shaker. The theoretical development along with the experimental verification of this strategy are presented.

1. INTRODUCTION

The goal of this research is to exploit the emerging actuator technologies to minimize the sound field radiated from a structure by actively altering its vibration characteristics. Good candidates for such structures include compressor casings, transformer enclosures, airplane fuselage panels, or submarine hulls.

2. THEORETICAL DEVELOPMENT

The method centers on writing a quadratic expression for the acoustic power radiated by a structure and then minimizing it subject to constraints that are dictated by the particular strategy adopted. The minimum value of this function defines the ultimate limit of suppression of the total power due to the specific arrangement of control forces. This approach is general in that it can be applied to structures of any degree of complexity. The question posed is: Given an arbitrary structure subject to known excitation forces and an arrangement of actuators already in place, what magnitude and phase of the actuators will minimize the total radiated sound power? The excitation forces are assumed to be deterministic (complex periodic).

The power radiated from any vibrating structure can be written in terms of its normal surface velocity vector, $\underline{v}$ as

$$W = \frac{1}{2} \underline{v}^T \underline{B} \, \underline{v}^* .$$

(1)

The tilde indicates that the variable is a vector or a matrix and the superscript T refers to its transpose. The matrix operator $\underline{B}$ is the surface radiation impedance which is positive definite and Hermitian. Such a quadratic expression has been derived by Cunefare and Koopmann (1990, 1991a, 1991b), and Mollo and Bernhard (1989, 1990) for three dimensional radiators. As shown in a previous paper (Naghshineh *et al* 1991a), a similar expression can be derived for the case of a beam in an infinite rigid baffle where, the matrix operator $\underline{B}$ is real and symmetric. The response of any structure due to harmonic excitation forces can be written in terms of its structural mobility matrix $\underline{Y}$ such that

$$\underline{v} = \underline{Y}\,\underline{f}\,, \tag{2}$$

where $\underline{f}$ is the external force vector exciting the structure which includes the primary as well as the control excitation forces. The mobility matrix $\underline{Y}$ is a complex, symmetric matrix. For a complex structure, the elements of this matrix could be obtained experimentally via a modal analysis, or numerically by a finite element analysis of the structure. Substituting Eq. (2) in Eq. (1) gives the expression,

$$W = \frac{1}{2}\underline{f}^{T}\underline{Q}\,\underline{f}^{*}\,, \tag{3}$$

for the radiated sound power radiated from an arbitrary structure in terms of the external force vector $\underline{f}$ and a matrix operator $\underline{Q} = \underline{Y}^{T}\underline{B}\,\underline{Y}^{*}$ which is Hermitian and positive definite. Thus given a non-trivial force excitation vector will always result in a real and positive value for the radiated sound power.

Up to this point, a quadratic expression has been derived for the acoustic power in terms of a combined excitation force vector which is a superposition of the primary and the control excitation force vectors. Since the proposed method does not require total cancellation of the structural response and instead a less demanding 'weak radiator' response, primary and control forces are assumed to be at locations that are not coincident. The challenge is to find a force vector such that the following constrained optimization problem is satisfied

$$\text{Minimize: } W = \frac{1}{2}\underline{f}^{T}\underline{Q}\,\underline{f}^{*} \tag{4}$$

$$\text{such that: } f_{pi} = a_{i}\,. \tag{5}$$

The subscript p in Eq. (5) represents the primary excitation force vector, the subscript i represents the ith component of this vector, and a_{i} is a complex number specifying the value of the primary excitation force at location i. The force vector, $\underline{f}$, satisfying the above problem has been shown (Naghshineh *et al* 1991a) to be the solution to the following system of equations.

$$\underline{Q}\,\underline{f}^{*} = c\,\underline{a}^{*}\,. \tag{6}$$

where c is a real, large (compared to the elements of the Q matrix) number, $\overline{Q}$ equals the matrix Q with the constant c added to its diagonal elements at the locations corresponding to the location of the primary forces, and q is a vector whose elements correspond to the prescribed primary excitation force values. Since the matrix Q is Hermitian and positive definite, the force vector f, solution of Eq. (6) corresponds to a global minimum value for the radiated sound power from the vibrating structure. This power value is unique for the prescribed location and values of the primary excitation forces.

3. COMPARISON OF NUMERICAL AND EXPERIMENTAL RESULTS

Equation (6) can be used to solve for the actuator (control) forces needed to drive the structure as a weak radiator. The method described in the previous section will be applied to a finite baffled aluminum beam of 914 mm (36 inches) long, 38.1 mm (1.5 inches) wide and 6.35 mm (0.25 inch) thick with clamped-clamped boundaries. Four PZT actuators (PKI type 550 made by Piezokinetics of Bellefonte, PA) are bonded to the top surface of this beam using an adhesive (EPY-150 sold by BLH electronics of Canton, MA). These actuators are 101.6 mm (4 inches) long, 12.7 mm (0.5 inches) wide, and 1 mm (0.04 inches) thick. Since it has been shown that the PZT type actuators are accurately modelled as moments applied at the edges of the actuator (Crawley *et al* 1987, Clark *et al* 1991), the power expression is formulated using finite element concepts in terms of normal point forces and moments located at each node (Naghshineh *et al* 1991a, 1991b). To further correlate this analytical model with the physical beam, adjacent moments are restricted to be equal and out of phase with respect to each other (see Fig. 1). The primary excitation to this beam is provided at a single frequency by a shaker at a point 101.6 mm (4 inches) away from its left boundary. Only the controlled and the uncontrolled vibration response of the beam are compared. Since the power radiated from the beam is directly related to its vibration response via Eq. (1), once the beam vibration response closely matches that of the predicted response, it follows that the power radiated from the beam will also match the predicted values.
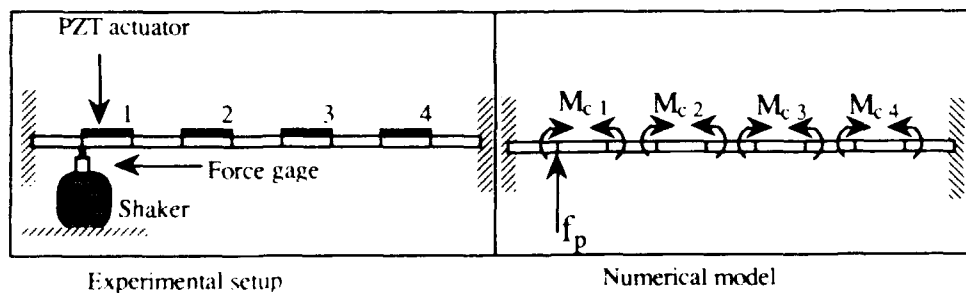
Figure 1 - The experimental setup and its representative model.

As a first step, the experimentally obtained resonances and loss factors of the beam are used to find the control moments needed to achieve the weak radiator response on-resonance at 941 Hz. This frequency coincides with the seventh beam resonance. The shaker force input to the beam is measured to be equal to 0.008 N. Using this force as the primary excitation to the beam, a set of control moments is found using the numerical procedure described in the previous section. The predicted reduction in the radiated sound power is 30.5 dB. A comparison of the experimental results against the numerical predictions for the uncontrolled and the controlled beam response is given in Fig. 2. This figure shows excellent correlation between the experimental and the predicted beam responses.
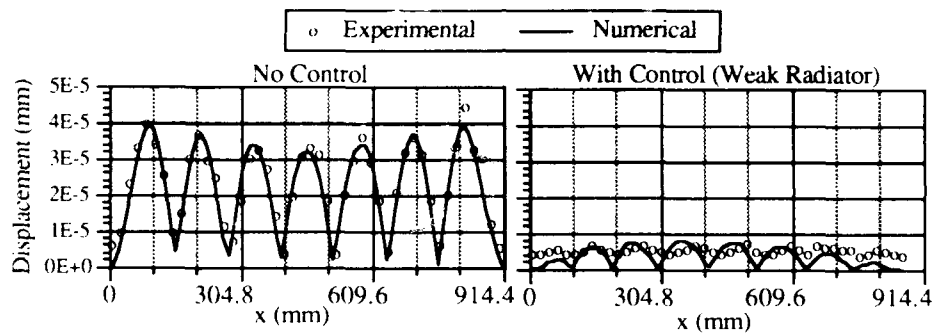
Figure 2- Comparison of the experimental versus numerical prediction of beam displacement magnitude with and without control at 941 Hz (on-resonance).

Next, an examination of this strategy is conducted at an off-resonance frequency of 850 Hz. The shaker force input to the beam is measured to be equal to 0.0283 N. The predicted reduction in the radiated sound power is 15 dB in this case. A comparison of the experime.ital results against the numerical predictions is given for the uncontrolled and the controlled beam response in Fig. 3. This figure shows excellent agreement between the experimental results and the numerical predictions.
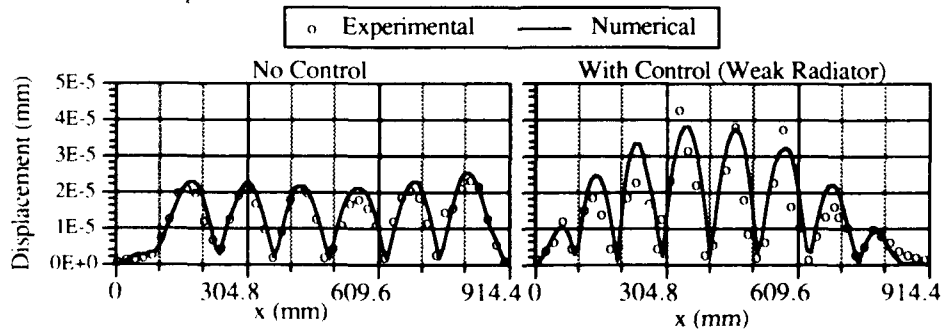
Figure 3- Comparison of the experimental versus numerical prediction of beam displacement magnitude with and without control at 850 Hz (off-resonance).

It is interesting to note that the controlled beam response magnitude is at some places nearly twice the uncontrolled response magnitude. This is significant since one may expect for the magnitude of the controlled beam response to be less than the magnitude of the uncontrolled beam response. While the controlled response magnitude is at some places nearly twice the uncontrolled response magnitude, the controlled radiated power is still predicted to be 14.5 dB lower than the uncontrolled radiated power. This is due to the fact that the supersonic wavenumber content of the weak radiator (controlled) beam response is much less than that of the uncontrolled beam response as shown in Fig. 4.
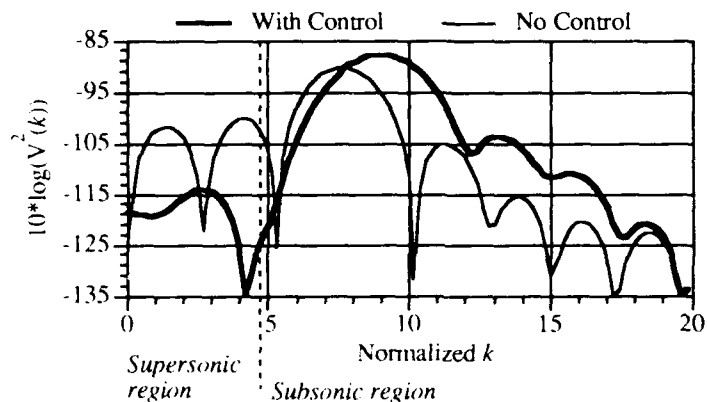
Figure 4- Comparison of the wavenumber contents of the controlled versus uncontrolled beam response at 850 Hz. The wavenumber k has been normalized by a $\pi_{,l}$ factor. The vertical dashed line corresponds to the normalized acoustic wavenumber, $\omega/\pi c$.

4. CONCLUSIONS

A method has been described for achieving weak radiator structures using active vibration control. This method is based on the minimization of a quadratic expression for the radiated sound power in terms of the primary and the control excitation forces. Given a set of primary excitation forces, a set of control forces is found that results in minimum sound power radiation at a single frequency. It should be noted that the method achieves this minimum radiation condition by selectively controlling the response rather then through complete cancellation of the structural vibration response. Although the method presented here is general, the example of a finite baffled beam is used to demonstrate the application of this method for commonly used actuators (e.g., PZT surface actuators and shakers). A close examination of the vibration response of a weak radiator baffled beam reveals three important results. First, the weak radiator beam response amplitudes are much lower than the uncontrolled beam at resonance. Second, these amplitudes decrease in areas near the beam boundaries at both off and on-resonance frequencies. Third, most of the wavenumber content of the weak radiator beam response shifts from the supersonic to the subsonic region. These

observations provide a better understanding of physical mechanisms involved in quieting structures using active vibration control.

Finally, it should be noted that the method presented here is general and is not limited to a specific problem size or boundary conditions. The quadratic expression for the acoustic power could be formulated for structures using any one of several available numerical methods.

ACKNOWLEDGEMENT

REFERENCES

Clark R L, Fuller C R and Wicks A 1991 *J. Acoust. Soc. Am.* **90**(1) 346-357
Crawley E F and Luis J D 1987 *AIAA Journal* **25**(10) 1373-1385
Cunefare K A and Koopmann G H 1990 *ASME J. Vib. Acoust.* accepted for publication
Cunefare K A and Koopmann G H 1991a *ASME J. Vib. Acoust.* **113**(3) 387-394
Cunefare K A and Koopmann G H 1991b *J. Acoust. Soc. Am.* **90**(1) 365-373
Mollo C G and Bernhard R J 1989 *AIAA*, **27**(11) 1473-1478
Mollo C G and Bernhard R J 1990 *ASME J. Vib. Acoust.* **112** 230-236
Naghshineh K and Koopmann G H 1991a *J. Acoust. Soc. AM.* accepted for publication
Naghshineh K and Koopmann G H 1991b *J. Acoust. Soc. AM.* accepted for publication

Active structural acoustic control using fiber sensors and piezoelectric actuators

Robert L. Clark and Chris R. Fuller
Vibration and Acoustics Laboratory
Mechanical Engineering Department

Brian R. Fogg, William V. Miller, Ashish M. Vengsarkar, and Richard O. Claus
Fiber & Electro-Optics Research Center,
Bradley Department of Electrical Engineering

Virginia Polytechnic Institute and State University
Blacksburg, Virginia 24061

ABSTRACT: We present a novel closed loop adaptive control system employing fiber optic strain sensors. The discussion and results in this paper will be based on preliminary experimental studies of sound radiation from a simply supported plate residing in a baffle. The filtered-x version of the adaptive LMS algorithm is implemented on a TMS320C25 DSP board resident in an AT computer. The disturbance is created with a shaker, and control is achieved with a single piezoceramic actuator. All tests conducted are based on a narrow band, stationary disturbance.

1. INTRODUCTION

Interest in adaptive structure development for active structural acoustic control (ASAC) has prompted many theoretical and experimental investigations (Clark *et al* 1990a, Dimitriadis *et al* 1989, Fuller *et al* 1989, Fuller *et al* 1990a, Wang *et al* 1990). Much has been documented concerning the modeling and application of piezoelectric actuators for control of structural vibration as well as sound radiation from structures (Clark *et al* 1990b, Crawley *et al* 1989, Fanson *et al* 1986). To implement control of structure-borne sound, error information related to far-field sound radiation must be supplied to the controller. Since the goal is to develop an adaptive structure with sensing capabilities embedded within the structure, many different types of sensors come to mind. Previous studies by Clark and Fuller (Clark *et al* 1990c,d) have been devoted to developing sensors from polyvinylidene fluoride (PVDF), which can be attached directly to the surface of the structure. An alternative sensing technique with similar response characteristics can be constructed from two-mode, elliptical-core (e-core) optical fibers (Murphy *et al* 1991, Vengsarkar *et al* 1991). Many previous studies have been devoted to vibration control of structures by implementing e-core optical fibers as error sensors (Cox *et al* 1991). The goal of this preliminary study is to demonstrate that optical fibers can also be used as error sensors for controlling structure-borne sound radiation.

2. DESCRIPTION OF CONTROLLER

To achieve control, an adaptive controller based on the multi-channel version of the Widrow-Hoff Filtered-X control algorithm was implemented. This algorithm is described in detail by Elliott, *et al* (1987). The output of an error sensor can be modeled at the nth time step as

$$e_\ell(n) = d_\ell(n) + \sum_{m=1}^{M} \sum_{j=0}^{N-1} P_{\ell mj} \sum_{i=0}^{N-1} \omega_{mi}(n-j) \, x(n-i-j) \, , \tag{1}$$

where $d_\ell(n)$ is the the ℓth error sensor, $x(n)$ is the input reference source, ω_{mi} are the coefficients of the adaptive finite impulse response (FIR) filters and $P_{\ell mj}$ is the jth coefficient of the transfer function between the output of the mth adaptive filter and the ℓth error sensor. The number of control actuators and filter coefficients are designated by M and N respectively. The outputs of the fixed filters, $\widehat{P}_{\ell mj}$, at each time step n, were used by the LMS algorithm to minimize the mean square error signal by modifying the coefficients of the adaptive filter as follows:

$$\omega_{mi}(n+1) = \omega_{mi}(n) - \mu \sum_{\ell=1}^{L} e_\ell(n) \, r_{\ell m}(n-i) \, , \tag{2}$$

where

$$r_{\ell m}(n - i) = \sum_{j=0}^{N-1} \widehat{P}_{\ell mj} \, x(n - i - j) \, . \tag{3}$$

Rather than computing the expectation of the squared error signal, the square of the error signal was simply taken as an estimate of the desired expectation in the LMS algorithm. As a result, the gradient components contain a large contribution of noise; however, the noise is attenuated with time due to the adaptive process (Widrow *et al* 1985). In Equation (2), L is the total number of error sensors utilized, and $L \geq M$. The coefficients $r_{\ell m}(n)$ are the outputs of the compensating filters $\widehat{P}_{\ell mj}$ which are estimates of the actual coefficients, $P_{\ell mj}$ measured prior to starting the control algorithm. This procedure is necessary since the LMS algorithm assumes that the error $e_\ell(n)$ is the instantaneous result of the control input for which the signal $r_{\ell m}(n)$ is a better estimate than $x(n)$ (Elliot *et al* 1987). The factor μ in Equation (2) is the gain constant that regulates the speed and stability during convergence.

3. EXPERIMENTAL SETUP

Experiments were performed in an anechoic chamber with dimensions $4.2 \times 2.2 \times 2.5$ meters and a cut-off frequency of 250 Hz. The test plate, which was mounted in a rigid steel frame, was cut from steel and measured $380 \times 300 \times 1.96$ mm. The simply supported boundary conditions were achieved by attaching thin shim spring steel to the boundaries of the plate with small set screws and a sealing compound. Previous testing has shown that this arrangement adequately models the simply supported boundary conditions (Ochs *et al* 1975). The test rig was then placed in the chamber where it was rigidly supported on a structure configured with a $4.2 \times 2.2 \times 19$ mm wooden baffle.

To achieve a steady state sinusoidal noise input, the plate was driven with a shaker attached to the structure with a stinger. Control was achieved with a single piezoceramic actuator for narrow band applications by way of the filtered-x version of the adaptive LMS algorithm implemented on a TMS320C25 digital signal processing board. The shaker used to create the disturbance was located at plate coordinates of (240 mm, 130 mm). The piezoelectric actuator was constructed from two piezoceramic elements of dimensions 38.1 × 21 × 0.19 mm bonded symmetrically (front and back). The symmetrically located patches were wired in a bimorph configuration, resulting in uniform bending about the neutral axis of the plate (Dimitriadis *et al* 1989). The optical fiber for sensing strain on the plate is oriented symmetrically about the vertical centerline of the plate. The sensor was configured such that response from odd-odd plate modes [i.e. (1,1), (3,1), etc.] would be most dominant.

The plate was instrumented with nine Bruel and Kjaer mini accelerometers and the output of these accelerometers was analyzed by solving a set of simultaneous equations to recover the amplitudes of independent modes on the panel (Fuller *et al* 1990b). The directivity pattern of the acoustic field along the plate mid-plane was quantified with a Bruel and Kjaer microphone situated on a traversing system. The radius of the traverse was approximately 1.6 m and measurements were taken in nine degree increments to map the sound radiation directivity with and without control. In addition, a few microphones were randomly located in the chamber to provide a measure of the global attenuation.

4. RESULTS

Three tests were conducted using optical fiber sensors to provide error information for controlling sound radiating from vibrating structures. More emphasis should be placed on results from the off-resonance test cases since both the structural and acoustic response of the plate depend on interaction from multiple structural modes.

4.1 On-Resonance Test Case

The first test case was conducted at an excitation frequency of 88 Hz, corresponding to the resonance condition of the (1,1) mode of the simply supported plate. The directivity pattern for the acoustic response is presented in Figure 1(a) and modal amplitudes for the structural response are illustrated in Figure 1(b). As indicated in Figure 1(a), the sound radiation was attenuated by approximately 25 dB along the mid-plane of the plate. (Similar levels of attenuation were observed throughout the acoustic field.) Control was achieved by suppressing the response of the (1,1) mode as is evident in Figure 1(b). In addition, the residual modes (i.e. modes other than the resonant mode) were attenuated as well. This method of control has been previously termed "modal reduction", since all modes observed were attenuated during the control process (Fuller *et al* 1990b).

4.2 Off-Resonance Test Cases

For the second test case the plate was driven at 320 Hz, corresponding to off-resonance excitation between the (1,2) and (2,2) modes of the plate. The radiated sound was attenuated by approximately 10 dB as illustrated in Figure 2(a). Upon achieving control, all of the modal amplitudes were observed to decrease as depicted in Figure 2(b). The dominant (3,1) mode, which is an efficient acoustic radiator, was reduced by approximately 40 dB. The remaining modes were attenuated to lesser degrees; however, all modes were reduced, thereby subscribing to the "modal reduction" method of control.

The final test case was conducted at an excitation frequency of 349 Hz, which is an off-resonance frequency lying between the (2,2) and (3,1) mode of the plate. Acoustic attenuation on the order of 10 dB was observed as depicted in Figure 3(a). The modal response for this particular case is more complex than that of the previous test cases as can be seen in Figure 3(b). Before applying control, the (3,1) mode is dominant in response; however, significant response is observed in the (1,1), (2,1), (2,2), and (2,3) modes of the structure. Upon achieving control all modes were attenuated except the (2,2) mode. The most significant attenuation was again observed in the (3,1) mode of the structure as in the previous test case. Since the modal response of the (2,2) mode increased upon achieving control, the method of control is termed "modal restructuring" (i.e. the modal response was rearranged as opposed to being reduced).

5. CONCLUSIONS

Results from this preliminary study suggest that two-mode e-core optical fibers can be used as error sensors for controlling sound radiation from the surface of vibrating structures. Sound radiation was attenuated for both on-resonance and off-resonance operating conditions for a narrow band disturbance. In the on-resonance case, approximately 25 dB of acoustic attenuation was achieved, while off-resonance control resulted in approximately 10 dB of attenuation for the cases studied. The optical fiber was oriented on the plate such that the sensor response was most sensitive to modes with a high radiation efficiency. Since the response of the optical fiber is proportional to the integral of strain over the path of the fiber, the sensor can be oriented on a structure for specific applications.

REFERENCES

Clark R L and Fuller C R 1990a *Submitted to J. of Acoustical Society of America.* (also presented at the 120th ASA meeting, Nov. 1990)
Clark R L, Fuller C R, and Wicks A L 1990b Accepted for publication in the *J. of Acoustical Society of America.* (also presented at the 119th ASA meeting, April 1990)

Clark R L and Fuller C R 1990c Presented at *First Joint U.S./Japan Conf. on Adaptive Structures* November 13-15 Maui Hawaii

Clark R L and Fuller C R 1990d Submitted to *J. of Acoustical Society of America*, (also presented at the 120th ASA meeting, Nov. 1990)

Cox D E and Lindner D K 1991 Accepted for publication in the *Journal of Sound and Vibration*

Crawley E F and de Luis J 1989 *AIAA Journal* **25** (10) pp 1373-85

Dimitriadis E K, Fuller C R and Rogers C A 1989 *Proc. of ASME 8th BiennialConf. on Failure Prevention and Reliability* Montreal Canada pp 223-33

Elliott S J, Stothers I M, and Nelson P A 1987 *IEEE Transaction on Acoustic Speech and Signal Processing*, ASSP-**35** (1) pp 1423-34

Fanson J L and Chen J C 1986 *Proc. of NASA/DOD Control-Structures Interaction Conf.* NASA CP-2447 Part II

Fuller C R, Hansen C H and Snyder S D 1989 *Inter-Noise* **89** pp 509-11

Fuller C R, Gibbs G P. and Silcox R J 1990a *J. of Intelligent Material Systems andStructures* **1**
1 (2) pp 235-47

Fuller C R, Hansen C H, and Snyder S D 1990b Accepted for publication in the *J. of Sound and Vibration*

Murphy K A, Miller M S, Vengsarkar A M, and Claus R O 1991 *J. Composites Tech & Res*.
13 (1) pp 29 - 35

Ochs J and Snowdon J 1975 *J. of the Acoustical Society of America* **58** pp 832-40

Vengsarkar A M, Fogg B R, Miller W V, Murphy K A, and Claus R O 1991 *Electronics Letters* **27** (17) pp 931 - 32

Wang B T, Dimitriadis E K, and Fuller C R 1990 *Proc. of AIAA SDM Conf.*, AIAA Paper 90-
1172-CP Long Beach California

Widrow B and Stearns S D 1985 *Adaptive Signal Processing*, (Englewood Cliffs, N. J.: Prentice Hall Inc)

(a) Acoustic Directivity Pattern of Plate/Baffle System

(b) Modal Response of Plate

Figure 1: Excitation of (1,1) at 88 Hz

(a) Acoustic Directivity Pattern of Plate/Baffle System   (b) Modal Response of Plate
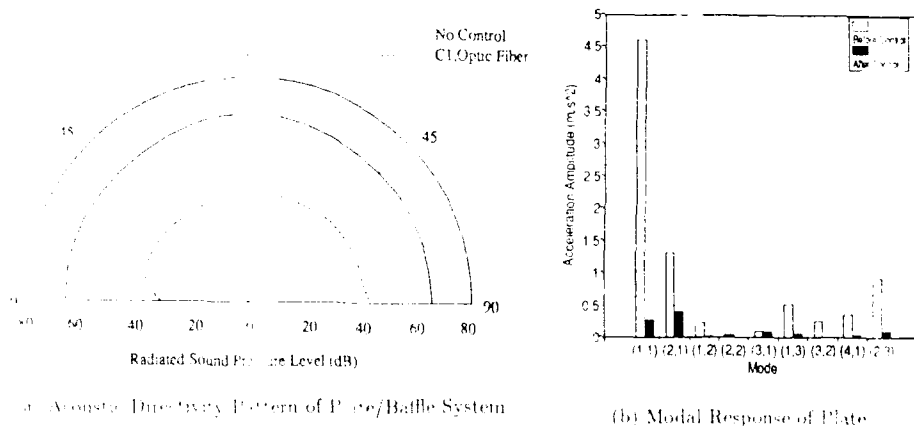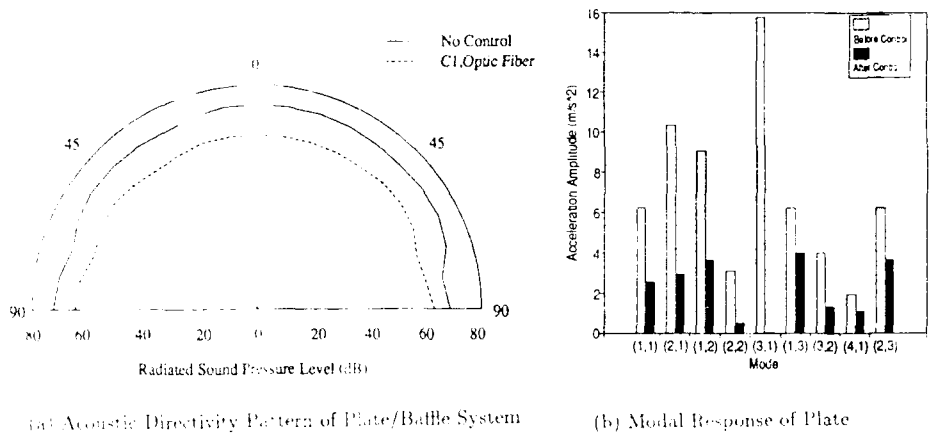
Figure 2: Off-Resonance Excitation at 320 Hz

(a) Acoustic Directivity Pattern of Plate/Baffle System   (b) Modal Response of Plate
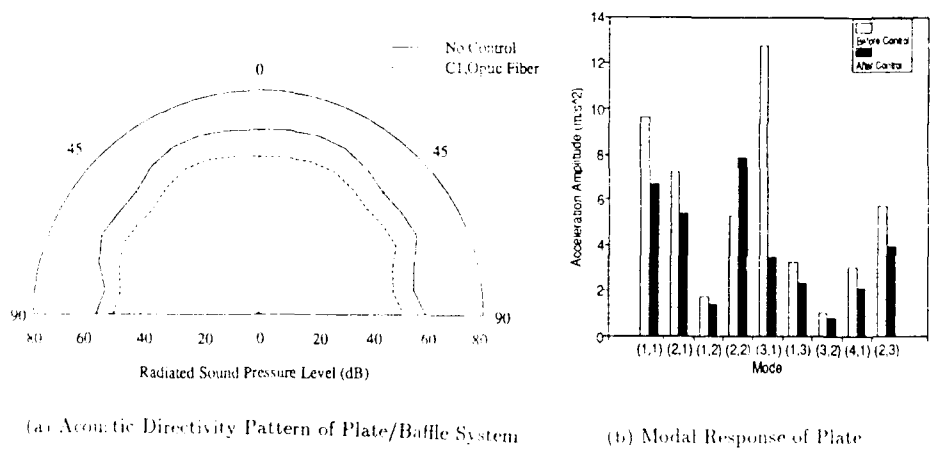
Figure 3: Off-Resonance Excitation at 349 Hz

Active acoustic echo reduction using piezoelectric coating

Xiao-Qi Bao, Thomas R. Howarth*, Vasundara V. Varadan and Vijay K. Varadan

Department of Engineering Science and Mechanics, Center for the Engineering of Electronic
and Acoustic Materials, The Pennsylvania State University, University Park, PA 16802

ABSTRACT: An active echo reduction system containing piezoelectric coating and a
digital delay line controller was developed and tested in a water filled acoustic pulse
tube. The system is able to reduce the echo of normally incident acoustic waves from
an air backed plate. An echo reduction of about 35 dB was obtained over the frequency
range of 5 to 11 KHz. In addition, the concept of active cancellation of reflection and
transmission simultaneously by bilaminar actuator was proved experimentally.

1. INTRODUCTION

The traditional solution to the problem of sound echo reduction from objects has been to use
highly damping materials with acoustic impedances well matching the impedance of the
surrounding medium. In recent years, active control techniques such as active noise control
and active vibration control have received growing attention. These techniques now offer a
new solution to problem of sound echo from objects.

In this paper, the results of our experimental research of active echo reduction are presented.
We used a multilayer piezoelectric coating, consisting of sensor sublayers to sense the incident
wave and an actuator sublayer to send out a counteractive wave to cancel the reflection. A
testing system containing the piezoelectric composite coating and the digital delay line
controller was developed and tested in a water filled acoustic pulse tube. An echo reduction of
about 35 dB was obtained over the frequency range of 5 to 11 KHz. In addition, the concept
of active cancellation of reflection and transmission simultaneously by a bilaminar actuator
was proved experimentally.

2. CONCEPT

The conceptual drawing of the active coating layer on a flat plate is shown in Fig. 1. The
active composite layer contains three piezoelectric sublayers encapsulated in an inactive

* Current address: Naval Research Laboratory, Underwater Sound Reference Detachment,
P.O. Box 568337, Orlando, FL 32856-8337

material. Two of them are identical and functioned as sensors. The other is used as an actuator. The diagram of the controller is presented in Fig. 2.
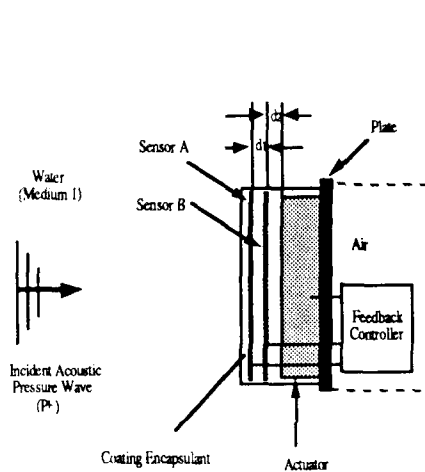
Fig. 1   Conceptual of active acoustic coating
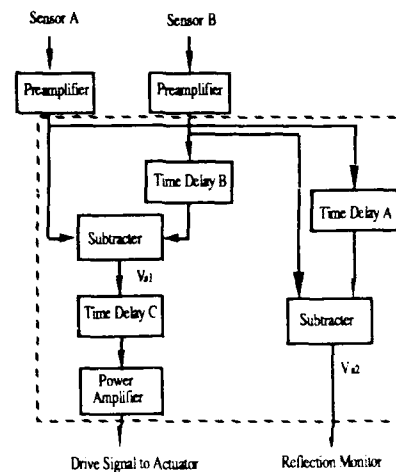
Fig. 2   Diagram of the controller

If the delay times of both delay lines A and B are set to the wave traveling time from sensor A to B, then the output voltage V_{s1} is only sensitive to incident wave while the the output voltage V_{s2} is only sensitive to the reflected wave. Output V_{s1} is compensated by the delay line C and sent through an amplifier to the actuator. The actuator is excited in such a way that the impedence of the coating matches well with the surrounding medium and the reflection is thus cancelled by the surface velocity produced by the actuator . The output V_{s2} is used as an error output. The details of the principles involved are presented in reference (Howarth). The difference between our current system and the system reported in the reference is use of delay lines rather than phase shifters in the controller. The delay lines have an advantage over the phase shifters in that the setting of the delay lines A and B is independent of frequency. This will greatly simplify the design of an adaptive controller for the system, which is the next step of this R&D program.

3. DESCRIPTION OF THE EXPERIMENT SETUP

The experiment was conducted in a water filled pulse tube of 6.35 cm in diameter and 4.27 m in length. A transducer, mounted at the bottom of the tube, generated a multicycle sinusoidal wave and received the echo from the top of the tube.   The signal source was a signal generator connected to the transducer through a gating system, a power amplifier and a transmitting/receiving switch. The received signal was displayed and recorded by a digital oscilloscope connected to a computer. The active echo reduction coating was mounted at the

top of the tube. The reflection from the free surface of water at the top was recorded as a reference.

In the coating layer, two PVDF sheets with a thickness of 0.5 mm were used as the sensors. The host material was Rho-c rubber. Both the Rho-c rubber and the piezoelectric polymer PVDF have characteristic acoustic impedances close to the impedance of water and therefore allow the acoustic wave to pass through. The actuator was a layer of 1-3 piezocomposite material backed by air. This type of material consists of piezoelectric rods spaced evenly within a polymer. The material has improved acoustic impedance matching with liquids, high electromechanical coupling factor for thickness mode, large bandwidth, and weak lateral resonances. In the 1-3 piezocomposite that was used in this experiment, PZT-4 rods with dimensions 3.17 mm by 3.17 mm by 10.4 mm (length) were encapsulated in a soft polymer with a Young's modulus of 0.85 MPa. The volume fraction of PZT was 0.30. Stiffeners of 1.57 mm glass epoxy were put on both surfaces of the composite to increase the transmission efficiency and broaden the bandwidth. The distances between the sensors (d_1) and from sensor B to the actuator (d_2) were 6 cm.

The three real time delay lines and two subtracters in the controller are digital devices. Eight bit A/D converters with a sampling rate of 5 million samples per second are used. The input bandwidth is 50 KHz. Basic operating principle of these digital delay lines involves sequentially writing the sampled data to random access memories (RAM) and reading them out at the desired time. The delay times are adjustable from 10 μs to 1.6 ms with step size of 0.2 μs. The dynamic range of the delay line is 45 dB.

4. EXPERIMENTAL RESULTS

The waves generated in the pulse tube were pulse modulated sinusoid waves. The typical echoes received by the bottom transducer with and without active control are presented in Fig. 3. The wave forms of the echoes in the time domain were converted to frequency spectrum by using FFT. The values at the center frequency were recorded and compared with that of the echo from the free water surface in order to calculate the attenuation at that frequency.

This measurement was done over the frequency range of 4 to 11 KHz with steps of 0.5 KHz. The delay time setting for delay lines A and B were fixed for all the frequencies. Since this system did not include adaptive control in this stage, the gain and delay line C were manually adjusted according to the error output, V_{c2}, for each frequency. The results are shown in Fig. 4. The curve indicated as 'Passive' is the echo reduction without active control. This echo reduction was due to the wave attenuation in the composite coating layer. These values are in the range of 5 to 9 dB. The curve marked 'Total' was obtained with active control on. Over the frequency range of 5 to 11 KHz, the total echo reduction is about 35 dB.
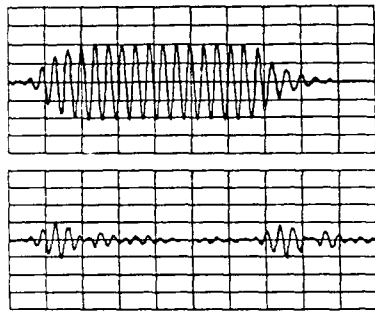
Fig. 3 Typical echo waveform at 5.6 KHz
         Top: without active control
         Bottom: with active control
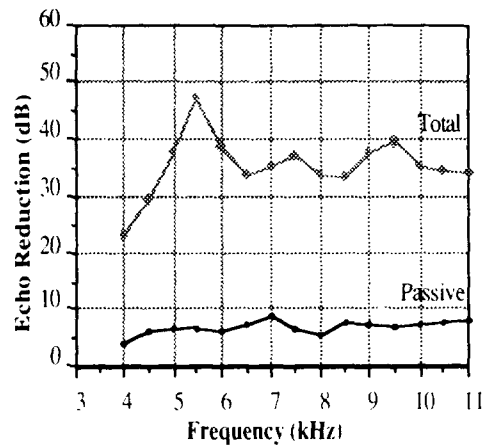
Fig. 4 Echo reduction of active coating with
         digital delay line controller

Comparing with previous results obtained by a phase shifter controller (Howarth), the value of the reduction is decreased by about 5 dB. It should be noted that the phase shifter controller was adjusted according to the signal received by the bottom transducer in the pulse tube. The signal may be not available in certain applications. In delay line controller, the error output was from the sensing sublayers in the coating.

The results show that the active acoustic coating with digital delay line control achieved great echo reduction over quite a broad frequency range.

5. REDUCING REFLECTION AND TRANSMISSION SIMULTANEOUSLY

The realization of the described echo reduction system will be more difficult if the backing medium has a complicated structure. In this case, the wave transmitted into the backing will be reflected from somewhere making the original echo structure complicated. This in turn will make the echo more difficult to be cancelled. An approach using a bilaminar actuator to prevent the transmission to the backing while actively cancelling the reflection was suggested and theoretically analyzed by Bao et al (1990). An experiment has been done to prove the concept. In this experiment, analog phase shifters were used instead of the delay lines and the actuator used was a bilaminar 1-3 composite. The second 1-3 composite layer was identical to the first, but excited by an additional channel including a phase shifter and a power amplifier. The backing medium used was water, using a hydrophone to detect the transmitted wave. The results are presented in Fig. 5. An echo reduction of 12 dB and a transmission reduction of 22 dB were achieved simultaneously by using the active control.
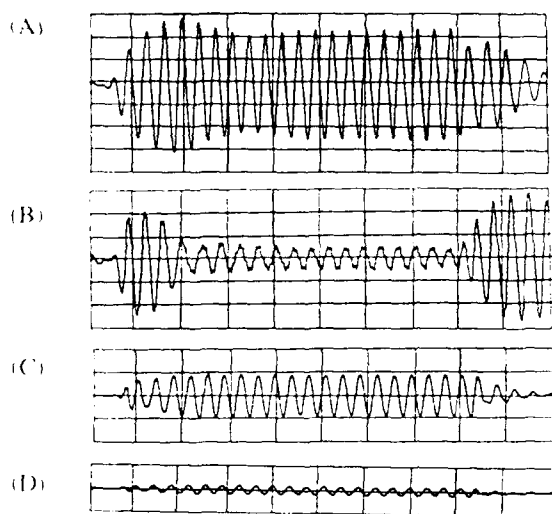
Fig. 5 Waveform at 5.6 KHz with bilaminar actuator
   (A) Reflection without active control, (B) Reduced reflection by active control.
   (C) Transmission without active control, (D) Reduced transmission by active control.

6. SUMMARY

The echo reduction of about 35 dB over the broad frequency range of 4 to 11 kHz was successfully achieved by using the active acoustic coating with the digital delay line controller. These results encourage the development of an active echo reduction system with an adaptive controller, which will be a system closer to practical application. The concept of a bilaminar actuator for reduction of both reflection and transmission was proven experimentally. This shows the feasibility of designing an active echo reduction system functioning independently of the backing structures.

7. REFERENCES

Bao X -Q. Varadan V K, Varadan V V and Howarth T R 1990 *J. Acoust. Soc. Am.* **87** 1350
Howarth T R, Bao X -Q. Varadan V K and Varadan V V 1991 accepted by publication in *J. Acoust. Soc. Am.* "Piezocomposite coating for active under water sound reduction."

Damage detection in smart structures using neural networks and finite element analysis

J. N. Kudva, N. Munir and P. Tan
Northrop Corporation, Hawthorne, CA 90250

ABSTRACT: An important aspect of the smart structures concept is automated structural health monitoring of aircraft structures. This requires detecting damage and assessing its effect on structural performance. This paper presents a new approach to detecting and defining large area damage on a structure. The approach is based on using a neural network to deduce the damage size and location from measured strain values at discrete locations. The neural network is trained using results from finite element analyses. Several examples illustrating this approach are presented.

1. INTRODUCTION

Automated health monitoring of aircraft structures has significant potential benefits including reduced life cycle costs, increased survivability and improved aircraft turnaround times. Health monitoring requires detection of various types of damage to a structure and assessing its effect on structural performance. Damage detection and definition involves processing signals from sensors while assessing the effects of the damage requires appropriate structural analysis. Since damage sustained by a structure will not necessarily be at sensor locations, the monitoring system will have to have the ability to detect damage at essentially any location. This can be achieved in two ways - 1) detect damage directly using 'remote sensing' technologies such as acoustic emission; and, 2) deduce the damage using readings from strain gages at discrete locations. This second approach is used here. The approach is based on using a neural network to deduce the damage size and location from measured strain values at discrete locations. The neural network is trained using results from finite element analyses.

2. TECHNICAL APPROACH

For a typical structural component under a given loading condition, the first step involves determining the effects of canonical damage (e.g., a circular hole) of various sizes and at several locations using finite element analyses. The results of these analyses are represented by sets of strain values at 'L' locations as follows:

$$\text{Strain-pattern}(i,j) = (S1,S2,S3,...SL)_{ij}$$

where i and j represent damage size and location respectively and S1, S2, etc., are the corresponding strain values. The 'L' locations represent arbitrary but convenient and judiciously chosen strain sensor locations on the structure. For each loading condition, these sets of strain values are determined from M*N finite element analyses (where M is the number of locations considered and N is the number of different damage sizes considered at each of the locations).

The next step involves training the neural network using the finite element results. The strain patterns are used as inputs and the damage location and size as outputs to train the neural network to a desired level of accuracy. The trained network can then be used to determine the location, size and effects of any unknown damage using measured strain values (at the same locations as before) as inputs.

3. EXAMPLES
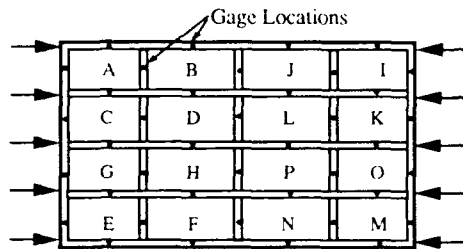
Figure 1. Stiffened Panel (48" by 32")   Figure 2. Neural Network
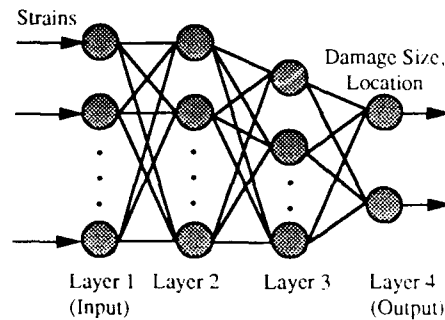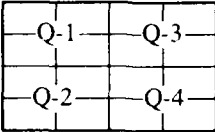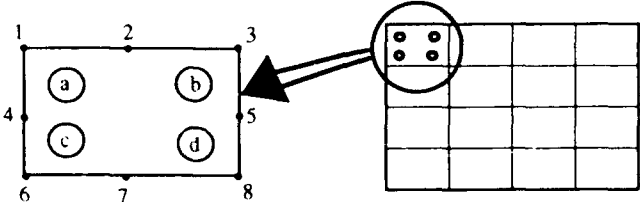
To demonstrate the approach, several example problems were run. All the examples are for the 16 bay stiffened panel under uniaxial compression shown in Figure 1. The finite element results were generated using the 'Applied Structures' P-finite element code from Rasna Corporation; the neural network used was 'N-Net' from AI-Ware running on a 386 PC. In all cases, two hidden layers with numbers of nodes per layer equal to number of inputs was used. The data was normalized by subtracting out the strain values corresponding to the undamaged structure and 'back propagation' was used to train the network. These options gave the best overall results.

The results are summarized in Table 1. The time taken to train the network varied from a few seconds to around ten minutes on the 386 PC. For examples 1 to 3, strain values at the forty locations shown in Figure 1 were used. For example 4, the gage locations are shown in Table 1. In all the examples, only damage in the form of circular holes (R=0.5 inches to 2.5 inches) was considered. The neural network was trained using results from a few values of the hole radii and the trained network was used to predict the damage size and location from input strain values corresponding to other values of the hole radii. In this manner the predicted results could be compared to actual damage.

In example 1, only damage at the center of bay A was considered. While the predicted results show the correct trend, the errors are significant. This is because of the limited number of patterns (three) used to train the network. In example 2, twelve patterns with

Table 1: Summary of Results

Example Details	Radius		Location	
	Actual	Predicted	Actual	Predicted
Example 1. Training Set: R = 0.5, 1.5 and 2.5 inches in Bay A Input = 20 and 40 Gages Output = Damage Radius	1	0.5		
	2	2.2		
	1	0.6		
	2	2.4		
Example 2. Training Set: R = 0.5, 1.5 and 2.5 inches in Bays A, B, C, & D Input = 40 Gages Output = Damage Radius and Location	1	0.73	A	A
	2	2.5	A	A
	1	1.1	B	B
	2	2.0	B	B
	1	0.6	C	C
	2	1.4	C	C
	1	0.6	D	D
	2	2.4	D	D
Example 3. Training Set: R = 1.5 and 2.5 inches Inputs: 40 Gages - (i) Damage in all 16 Bays (ii) Damage in Bays in Quad 1 only Outputs: (i) Quad Location & Radius (ii) Bay Locations	2	2.04	Q-1/A	Q-1/A
	2	1.88	Q-1/B	Q-1/B
	2	2.05	Q-1/C	Q-1/C
	2	2.08	Q-1/D	Q-1/D
Example 4. Training Set: R = 0.5 and 1.5 inches at Locations a, b, c, & d in Bay A Input = 8 Gages at Locations Shown Output = Damage Radius and Location	1	1.45	a	a
	1	1.50	b	b
	1	0.65	c	d
	1	1.46	d	d

damage at the center of bays A, B, C, and D were used for training. In all cases the damage locations were predicted correctly. The accuracy of damage size prediction was erratic, but again the trend was correct.

In example 3, damage in all sixteen bays were considered and 32 patterns (R=1.5 and 2.5 inches in each of the bays) were used for training. This resulted in 'saturation' of the network and the network failed to converge. Because of this, a hierarchical, two step approach was used. First, the trained network (using all 32 patterns) was used to predict the hole radius and just the quadrant locations. (Bays A, B, C, D are in quadrant 1; E, F, G, H are in quadrant 2; and so on.) Next, the network was trained using patterns with damage in a single quadrant and this was used to predict the damaged bay location within the quadrant. This procedure gave excellent results for both damage size and locations.

The final example involved locating damage within a bay when the damage was off-center. Eight patterns (damage of radius = 0.5 and 1.5 inches near the four corners of bay A) were used for training. The trained network was used to predict the size and location of 1.0 inch radius holes at the four corners. Because the training patterns correspond to damage close to each other within a single bay, the patterns are quite similar to each other. This, coupled with the limited number of training patterns used, lead to significant errors in the results. The locations were predicted correctly except in one case (damage at location c was predicted to be at location d; the strain patterns for damage at these two locations are very similar).

4. CONCLUDING REMARKS

The examples demonstrate that a neural network can be used to determine damage location and size in a typical structure. Several points are noted in this regard:

> 1. The training sets have to be carefully chosen - too much information and too little information both lead to inaccuracies and even lack of convergence.
> 2. It is easier to predict damage location than size. This is to be expected since location is a discrete variable and size output is a continuous variable (for instance, a location output of between 0.5 to 1.5 inches can be considered to be location 1).
> 3. It is more efficient to use an hierarchy of networks rather than one big network. This is significant because it would reduce the computational requirements and can also be used to provide redundancies for implementation on large structures.

Future work will be focused on using this approach for large structures such as aircraft wing torque boxes under complex loading cases. An interesting variation of the approach currently being examined is using the network to directly predict the reduced load carrying capacity of the damaged structure.

Experimental determination of damage and interaction strain fields near active and passive inclusions embedded in laminated composite materials

J. S. Sirkis, H. Singh, A. Dasgupta, and C.C. Chang

University of Maryland, Department of Mechanical Engineering, College Park, Maryland 20742, 301-405-5265

ABSTRACT: This paper presents some experimental observations of failure mechanisms of optical fiber sensors and piezoceramic actuators embedded in laminated composites. The observations are made using optical microscopy and moire' interferometry for many different loading conditions.

INTRODUCTION

Some micro-mechanical interaction issues associated with developing "intelligent" structures with embedded passive or active inclusions are addressed in this paper. The emphasis is on experimentally identifying possible damage and failure mechanisms caused by embedded optical fibers acting as passive inclusions within a composite structure. Damage in such structures can occur on the macroscale or microscale, each scale having different implications. Damage on the macroscale generally reduces the stiffness and/or strength of the host material thereby leading to structural degradation. Damage on the microscale will effect the sensoral/actutoral functions of the inclusions by altering strain/force transfer. Microscale damage can also coalesce into macroscale damage which can ultimately influence structural integrity.

The brevity of this manuscript precludes any discussion of the experimental details used in recording the data which will be presented. This data that is presented is intended to be "food-for-thought" in the sense that embedded sensors/actuators/processors are foreign inclusions in host structures, and these structure have mechanisms which "reject" the inclusion much like the biological rejection of transplanted organs. The mechanical rejection appears as high stress or strain concentrations, microcracking, macrocracking, etc. In a sense, this paper strives to raise the awareness of some of the "intelligent" structures community to interaction mechanics issues.

OBSERVED INTERACTIONS

Several graphite/epoxy composite lay-ups are considered with optical fibers of several different diameters and coating systems embedded within them. Also considered are the effects of both embedded piezoceramic actuators and local processors on the strain states in the host structure. All specimens are investigated using moire' interferometry or optical microscopy.

The first set of data that is presented provides a visual feeling for how host laminated structures respond to embedded optical fibers of various diameters and coating systems. Fig. 1 shows the vertical displacement field of unidirectional laminated composites, with optical fibers embedded perpendicular to the indigenous reinforcing fibers, and loaded parallel to the reinforcing fibers. One sees that the larger inclusions have more pronounced the effect. This result is intuitive, and has ramifications in embedded actuators. Fig. 2 shows the horizontal displacement fields for a specimen of similar make-up as those in Fig. 1, and also provides the strain distribution along the horizontal symmetry line. Residual strain fields have also been measured in similar specimens with similar methods.

The next set of data describes the macroscale and microscale effect of optical fibers on the impact characteristics of laminated composites. Fig. 3 shows x-radiographs of $[0_2/90_4/OF/90_4/0_2]$ clamped-clamped impact specimens with the same six embedded optical fibers used in Fig. 1. In all cases the radiographs show horizontal matrix cracks and bi-lobed delaminations typical of orthotropic laminates with no embedded optical fibers. Volume Visualization Ultrasound techniques show that the larger fiber diameters do influence which plies delaminate first. Figure 4a shows that the smallest optical fiber directly under the impact zone does not attract microcracks, while Fig. 4b shows that the largest optical fiber 1.5cm from the impact zone is responsible for significant transverse, longitudinal, and interfacial cracking.

The final set of data shows the displacement and strain fields caused by embedded piezoceramic and microelectronic circuits. Fig. 5a shows the vertical displacement field generated by a piezoceramic actuator embedded in a laminated composite which is subjected to three point bend loading. The high displacement gradients at the interface between the actuator and host material are clearly evident. Fig. 5b shows the strain distribution along a representative through-the-thickness line. Microcracking in piezoceramics due

to actuation loads and due to stress concentrations caused by the solder joint during the composite curing process are not shown, but are quite common. The Fig. 6 shows the vertical displacement field and the strain distribution along the vertical symmetry line of an embedded 741 operation amplifier. The loading in this case is due solely to the thermal dissipation of the microelectronic circuit.

CONCLUSIONS

This paper has presented representative results of a wide variety of tests in an ongoing research program aimed at elucidating the important interaction mechanics between embedded passive and active inclusions and the host structure. The goal of this research is to determine how these interaction mechanics effect the performance of "intelligent" structures. (The authors would like to thank Dr. R. Claus of Va. Tech. for manufacturing the specimen used in Fig. 6.)
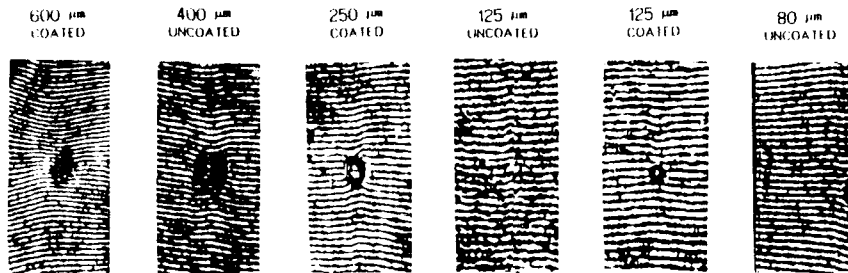
Figure 1.
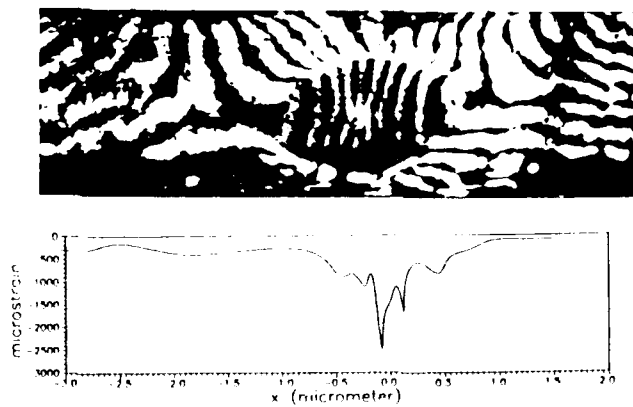
Figure 2.
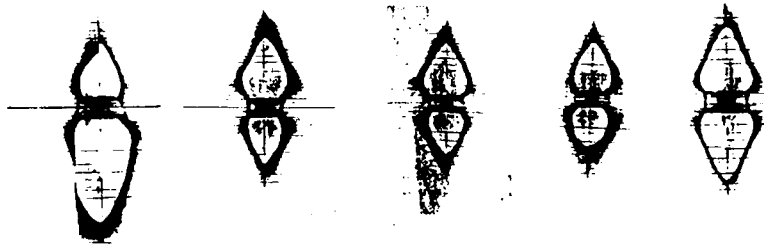
Figure 3.

Figure 4a.
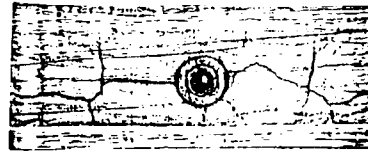
Figure 4b.
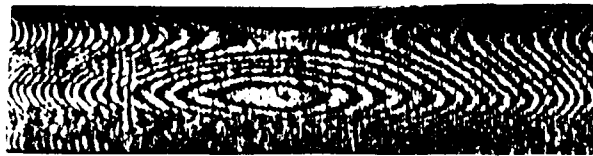
Figure 5a.
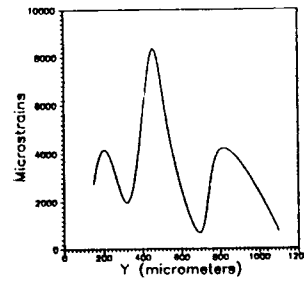
Figure 5b.
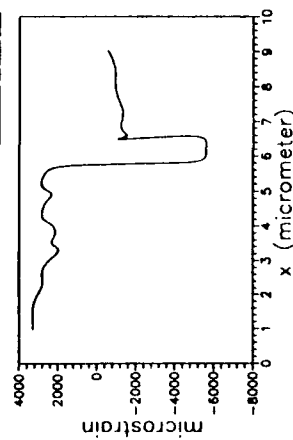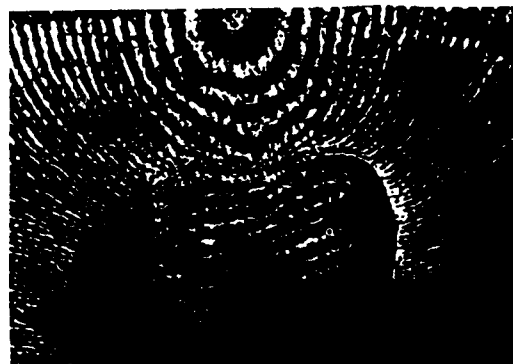
Figure 6.

Micro-damage analysis with embedded sensors in macro-composites

Gregory P. Carman, John J. Lesko, Kenneth L. Reifsnider [1], Ashish
Vengsarkar, Bill Miller, Brian Fogg, & Richard Claus [2]

(1) Engineering Science and Mechanics, (2) Electrical Engineering
Virginia Tech., Blacksburg Va., 24061

ABSTRACT: A scaled up version of a composite material is utilized to
investigate the interaction between internal damage and embedded sen-
sors. The quantitative measurements generated are utilized to validate
current micromechanical representations describing the stress redis-
tribution around a fiber fracture. Data is presented to substantiate
the ability of fiber optic strain sensors to locate damage by a tri-
angulation scheme. This is shown to be possible for sensors outside
the perturbed stress region. With the use of accurate micromechanical
models and statistical methods global level strength predictions are
shown to be possible. Thus, these analysis are key elements for the
processing of data obtained from embedded sensors in actual material
systems for strength predictions.

1. INTRODUCTION

Micro level damage events which occur in material systems are extremely
important issues when addressing the remaining strength and life of the
structure. These phenomenon include fiber fracture, matrix cracks, and
fiber end effects. The ability to understand and quantify these events
during the life of the composite require the use of internal sensors (i.e.
resistant strain gauges and Fabry Perot fiber optic strain sensors) in
conjunction with accurate micromechanical analysis. Internal sensors are
a necessity to monitor the local damage events which occur in materials
under service conditions. The data generated by the sensors can subse-
quently be analyzed to determine the location and magnitude (i.e. with
the appropriate micromechanical representations) of the damage in an at-
tempt to accurately derive a quantitative measure of the remaining

structures life. We have developed a unique system (Carman et al 1992a) which is capable of providing base line information on measurements made with embedded sensors in the vicinity of fiber fractures (presently being extended to study compression failures). This methodology is shown to provide accurate quantitative measurements of local point-wise strains in a composite, and is used to validate current micro-mechanical representations of this damage. This provides a unique capability to understand and incorporate the correct physical mechanisms in the analytical developments of micro-models. These two capabilities give the scientific community a method to understand embedded sensor technology and a technique to directly verify analytical micromechanical models. The quantitative results presented will demonstrate the relationship between internal measurements, micromechanical analysis, and laminate level strength predictions.

2. ANALYSIS & EXPERIMENTS

This techniques involves an experimental macro-model composite (i.e. scaled up 100x version shown in Figure 1) with the appropriate constituents; fiber, matrix, and interphase. With the use of Fabry-Perot fiber optic sensors and resistance strain sensors embedded in the macro-model, direct measurements of internal strains at the fiber diameter level in the composite are achieved. These measurements have been verified with an appropriate comparison to classical external measurement techniques and well accepted theoretical methodologies (Figure 2 Lesko et al 1992) By introducing into the composite a highly controlled internal damage (e.g. fiber fracture) of known magnitude and location accurate representation and measurements of the local strain redistribution is achieved. This provides base line data on the response exhibited by the embedded resistant and fiber optic sensors in the vicinity of localized damage. The tests performed demonstrate the sensor's ability, not only to measure the initiation of damage, but to also provide accurate data in the presence of the internal anomaly. The fiber-optic sensor actually detects the compressive shock wave generated during the fiber fracture process at locations outside the effected region. In fact with multiple embedded sensors, the capability to locate the damage event by triangulation methods can be achieved. In Figure 3 we present data obtained from two

fiber optic strain sensors located at relatively different positions from
the shock wave initiation site. A measured delay of 80 microseconds is
found for the relative onset of the shock wave generated by an energy
pulse (e.g. fiber fracture). The distance between the two gauges is ap-
proximately 16.0 cm. This corresponds to a measured wave velocity of 2000
m/sec. Utilizing a smeared composite approach, a wave velocity of 2300
m/sec is theoretically predicted. This demonstrates the plausibility of
employing triangulation methods to locate damage in actual composites
with experimental data obtained from embedded sensors and knowledge of
wave speed calculated theoretically. Utilizing strain energy methods,
the extent of the damage can be inferred from the amplitude of the shock
wave. That is, a fiber fracture releases more energy into the system than
a matrix crack and thus causes a larger disturbance in the material.

In addition to providing baseline data on measurements with the embedded
sensors in the presence of internal anomalies, the test generates data
on local strains in the damaged region which are utilized to verify and
improve current analytical micromechanical representations Carman et al
1992b. This latter capability is a necessity to predict real time com-
posite strength and suggest the resulting failure modes. The methodology
presented permits the ability to vary independent parameters which may
influence the stress redistribution in the neighborhood of the anomaly
(e.g.fiber spacing). The ability to systematically change these quanti-
ties enables the researcher to analyze the effect each parameter has on
stress redistribution based on direct data obtained with the embedded
sensors. This work has been extended to include a study of interphase
coatings on the fiber optic sensors to provide an optimal response in the
presence of the localized damage event (Carman & Reifsnider 1992).

With the use of accurate micromechanical models, laminate level strength
predictions can be accomplished. Recently Gao et al 1992 employed a sta-
tistical approach along with a micromechanical development to demonstrate
the functional dependence of strength on various micromechanical parame-
ters. They demonstrated that with improved representations of fiber
fracture at the local level, accurate global level predictions are pos-
sible. As can be seen in Figure 4, their theoretical development is an
improvement over Hahn's classic bundle theory. Theoretical development

such as these can be utilized in conjunction with embedded sensors to predict remaining strength and life of a composite in real time. This is accomplished with: 1) knowledge of the location of the damage, 2) understanding of the extent of damage, 3) an accurate micromechanical representation of the damage, and 4) an appropriate statistical approach to relate the damage to global level strength. We believe that the results discussed in this paper demonstrate that 1, 3, and 4 have been and can be achieved.

3. CONCLUSIONS

In conclusion, a model composite was utilized to understand the interrelationship between embedded sensors and a fiber fracture. The sensors have been shown to provide accurate internal measurements. The data obtained with these devices corroborated a micromechanical model of fiber fracture which includes a correct physical interpretation of various internal parameters. Multiple embedded sensors were shown to be able to detect the onset of a shock wave which could be used to locate the damage with the use of triangulation methods and knowledge of wave speed in the material. Through the use of micromec'anical methods and statistical approaches, laminate level strength predictions were formulated.   These three topic areas (i.e. delay measured, micromechanical representation, and statistical approach) can subsequently be utilized to make real time life predictions of composite structures through the use of data obtained from embedded sensors.

4. REFERENCES

Carman G.P., Lesko J.J., Reifsnider K.L., & Razvan A., 1992a, Composite Materials: 4TH Symposium ASTM, submitted.

Carman G.P., Lesko J.J., & Reifsnider K.L., 1992b, Composite Materials: 4TH Symposium ASTM, submitted.

Carman G.P. & Reifsnider K.L., 1992 April Recent Advances in Adaptive & Sensory Materials , submitted.

Gao Z., Reifsnider K.L., and Carman G.P., 1992 Jan Journal of Composite Materials, in press.

Lesko J.J., Carman G.P., Fogg B.R., Miller W.V., Vengsarkar A.M., Reifsnider K.L., and Clau- R.O., 1992 Jan, Optical Engineering SPIE, in press.
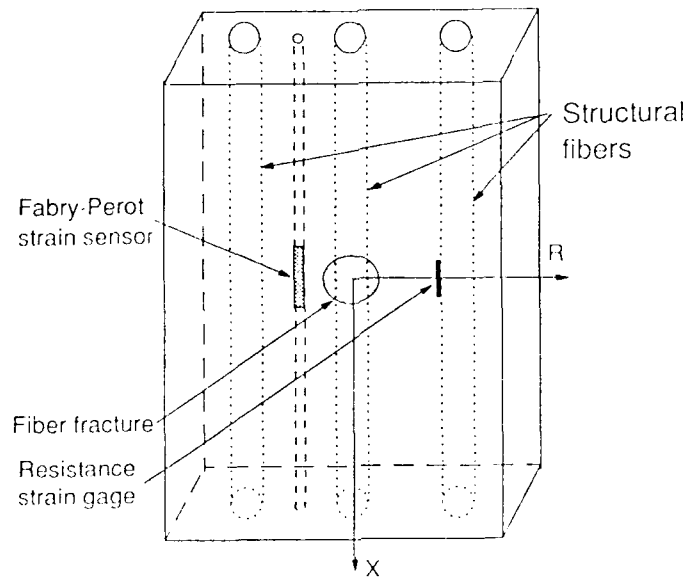
Figure 1:Illustration of the model composite with embedded strain sensors and their respective locations.
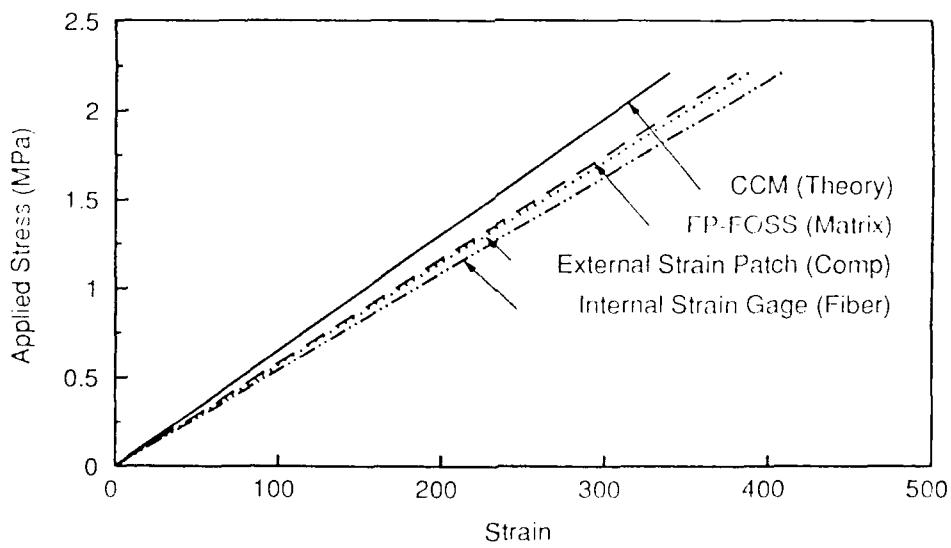
Figure 2: Comparison of strain measurements obtained from an external strain patch, an internal strain gauge, and a fiber optic strain sensor to a theoretical prediction from a CCM model.
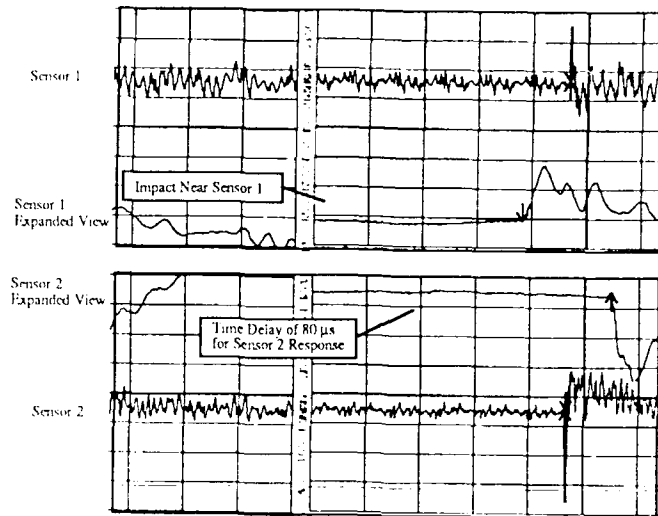
Figure 3: Depiction of the time delay measured by internal fiber optic strain sensors in a material system subjected to a energy pulse.
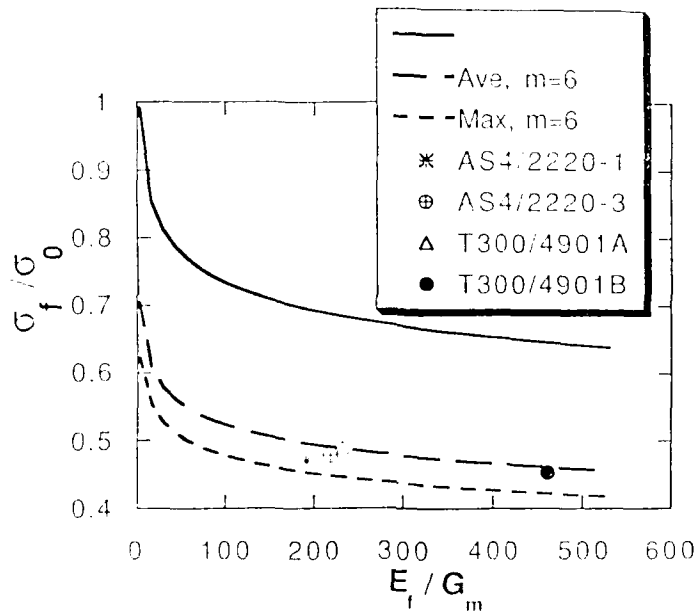
Figure 4: Global level strength predictions as a function of material stiffness ratios for Hahn's classic bundle theory (solid line) and a maximum and average micromechanical representation. Note the microme-chanical representation bracket the experimental data.

Intelligent sensor systems for smart aerospace structures

J. Schoess

Honeywell Systems and Research Center, 10701 Lyndale Avenue South, Bloomington, MN 55420

ABSTRACT: Future advanced aerospace vehicles will require smart embedded sensor systems and data links to monitor structural integrity and flight environment characteristics. This health management system, referred to as a *smart structure* will be capable of assessing vehicle structural damage in real time and reconfiguring flight controls to ensure mission performance and flight safety. This paper describes a health management approach for smart structures that integrates smart sensor and conventional sensor technology with dedicated sensor supervisory management processors to effectively interpret and manage information provided by multiple sensors. The description of this sensor architecture approach and implementation of sensor hardware including optically powered sensors and optical sensor avionic interfaces are discussed.

1. INTRODUCTION

In recent years, fiber-optic sensors have been developed to efficiently monitor the manufacturing, health, and performance of smart structures. These sensors can provide benefits of immunity to electromagnetic interference (EMI), high-temperature capability, high bandwidth, electrical isolation, light weight, and the implementation of a single fiber for signal multiplexing. However, the development of fiber-optic sensors has been limited to R&D applications with few products currently available. Although fiber-optic sensors offer great potential, they fail to meet some basic system requirements. These requirements include the provision for standardized optical sensor interfaces that allow different types of fiber-optic sensors to be installed and maintained in smart structures. In addition, smart structure sensors should provide reliable measurement of structural integrity parameters without sensitivity to secondary environmental effects and be easily integrated into today's metallic structure aircraft. The optically powered sensor (OPS) approach promotes the idea of standardized optical sensor avionic interfaces without comprising basic smart structure system requirements.

2. OPTICALLY POWERED SENSOR

The OPS approach is a novel system approach that incorporates a *standardized interface* concept and facilitates the integration of both fiber-optic and electronic sensors for smart structures applications. The key to the approach is to use a fiber cable to transfer optical power to a remotely located sensor module, acquire sensor data, and transmit the data back to the control electronics in a time-multiplexed fashion. Figure 1 illustrates the remotely powered OPS concept. The optical power transmitted to the remote sensor located on the end of the fiber link is converted to electrical power via a series of matched photodiodes. The sensor module contains a micropower analog-to-digital converter circuit to convert multiple sensor inputs such as pressure, temperature, strain, and acoustic mission to an 8-bit
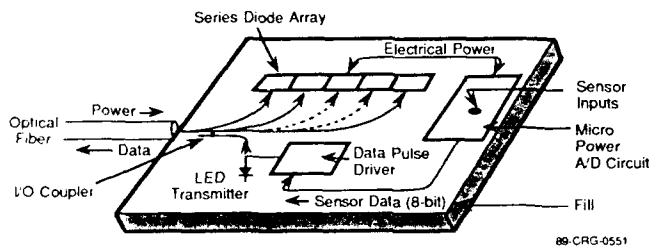
Figure 1. Honeywell Optically Powered Sensor Concept

equivalent word. The sensor data is then routed to a data pulse driver circuit that controls a light-emitting-diode transmitter. The 8-bit serial data is sent back to control electronics a bit at a time via the optical fiber link. The power-by-light concept provides the benefits of optical-fiber sensors for near-term and long-term application without having to compromise on optical fiber sensor present-performance limitations. Instead, the optically powered sensor approach promotes the idea of integrating power-by-light sensors with fiber-optic sensors by sharing a common compatible optical fiber and control electronics.

The OPS approach also provides several additional advantages for smart structure applications as follows:

- Uses proven electronic sensors that meet the necessary performance and environmental requirements,
- Uses existing sensor technologies for meeting a wide variety of applications.
- Uses a simple yet ruggedized optical packaging technique developed by fiber-optic communications technology,
- Uses a standardized single optical fiber interface at both the sensing and the receiving end of every sensor application.

2.1 Design Approach

In the OPS, sufficient optical power is transmitted to the remote sensor via the fiber link so that a significant level of optically generated electrical power is available for data acquisition and transmission. The wide variety of reliable, inexpensive electronic transducers can then be used as sensor elements. Several significant developments in optical and micropower electronics technology have made the concept feasible. Commercially available laser diodes are able to supply up to 1.0 W of optical power into the fiber at a wavelength of 850 nm. A new generation of CMOS micropower analog-to-digital converters developed at Honeywell consume only microwatts of power.

These are key components in a system in which a single 100-micron-core multimode optical fiber is used to provide optical power, address one of several multiplexed, electrically isolated EMI-shielded sensor modules, and provide a data return path. A set of matched photodetectors arranged in series is used to convert the incoming light to a dc voltage. Data communication is provided by standardized off-the-shelf light-emitting diodes and photodiodes.

3. DISTRIBUTED SENSOR ARCHITECTURES

Multisensor integration is the key to providing integrated health monitoring for high-integrity systems such as smart structures. The distributed sensor architecture approach (Schoess 1988, 1989), as shown in Figure 2, supports the idea of multisensor integration at both the sensor level and structural integrity assessment level through key building blocks such as smart sensors and smart sensor supervisors.

Network
• Standardized I/O
• Command and reports
• Reconfiguration
• *Network management*
  (extensible)

Sensor Supervisor
• Sensor data
  management
• Sensor correlation/
  analysis reduction
• Network command
• Sensor selection
  (redundancy management)

Sensor/Actuator
• BIT and self-test
• Error compensation
• Local qualification
  and decisionmaking
• Standard I/O
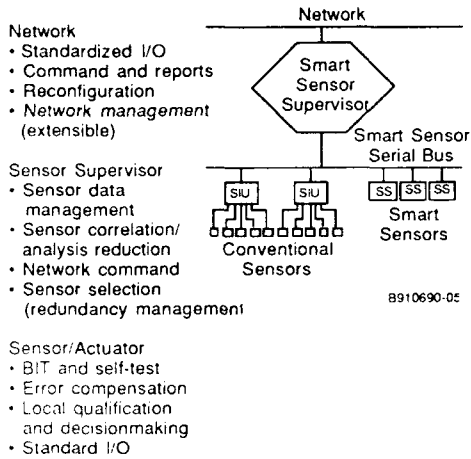
Figure 2. Distributed Sensor Architecture
Concept

Figure 3 shows a smart structure distributed network concept based on the distributed sensor architecture design philosophy. Structural integrity monitoring occurs at remote locations in the smart aerospace vehicle in the wingbox and higher temperature outer skin areas. The concept can be described in terms of two separate modules: a *remote transducer module* and the *sensor interface module*. Power to the electronics in the remote transducer module is optically transmitted from the sensor interface module. Remote transducer modules are embedded or attached to the smart aerospace vehicle's structure. Inputs provided by strain, temperature, pressure, and acoustic emission sensors are acquired by the remote transducer module and converted to an equivalent digital word. The data is then transmitted back to the sensor interface module, which contains a low-power microprocessor, laser drive electronics, and data decoding electronics handle synchronization and sensor addressing. The OPS network concept supports the networking of several remote transducer modules to a single sensor interface module.

4. OPS APPLICATION TO STRUCTURAL INTEGRITY MONITORING

Figure 4 illustrates how the network concept could be applied to monitor wingbox structural integrity. This figure shows an embedded fiber sensor system that uses low-cost power-by-light sensors and fiber-optic sensors on a shared multidrop fiber bus. The benefits of this approach include simplicity of design, commonality, producibility, and maintainability. The simplicity of this approach is achieved by implementing a common-shared redundant optical bus that transmits optical power and sensor address information to both power-by-light sensor modules and embedded optical fiber sensors. Sensor data is sent back on the same fiber for structural integrity analysis and assessment.
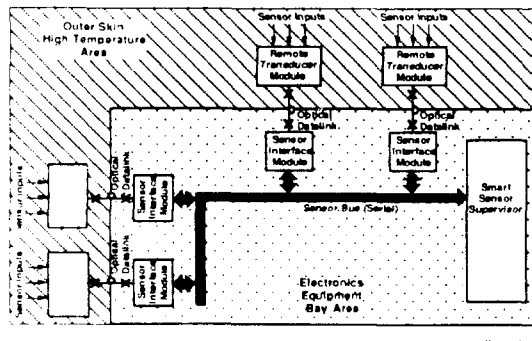
Figure 3. NASP Smart Instrumentation Design
Concept
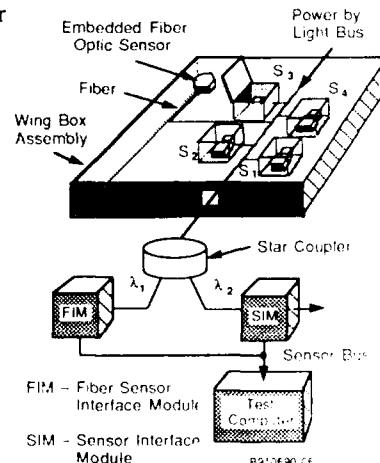
Figure 4. Wingbox Structural
Integrity Concept

The sensor interface module electronics will transmit optical power and address information to the individual remote sensors at a wavelength of 850 nm as previously described. The module will also handle optically powered sensor bus synchronization and data decoding of sensor data sent by individual sensors. It will share the multimode fiber with one or more fiber-optic sensors controlled by a fiber sensor interface module. The fiber sensor will operate at a wavelength that will be compatible with the network detection electronics. A fiber sensor interface module will have appropriate laser drive electronics, local intelligence, and decoding electronics to detect sensor data returned on the network. This approach would be compatible with fiber sensors that modulate the intensity of the light output for measurement. Reflective fiber sensors such as a fiber-optic temperature sensor incorporating bimetallic elements are good examples of compatible sensors.

Figure 5 illustrates the system-level approach illustrating remote transducer module electronics, which include an optical interface, sensor analog-to-digital conversion electronics, and an integral piezo-acoustic transducer array. Acoustic soundwaves that propagate through the aerospace structure are detected by the acoustic emission transducer array to isolate internal structural damage processes. The sensor module hardware is fabricated as a high-temperature avionic hybrid to meet aircraft environmental requirements. This approach provides the significant benefit of maintaining and repairing structural monitoring hardware without compromising the logistics issues of embedding fiber sensors.

5. REFERENCES

Schoess, J.N. (1988) "A Distributed Sensor Architecture for Advanced Aerospace Systems," SPIE Vol. 931, Sensor Fusion, Orlando, Florida, April 4, 1988.

Schoess, J.N. (1989) "Smart Sensor Technology for Advanced Launch Vehicles," AIAA-89-2755 25th Joint Propulsion Conference, July 10-12, 1989.
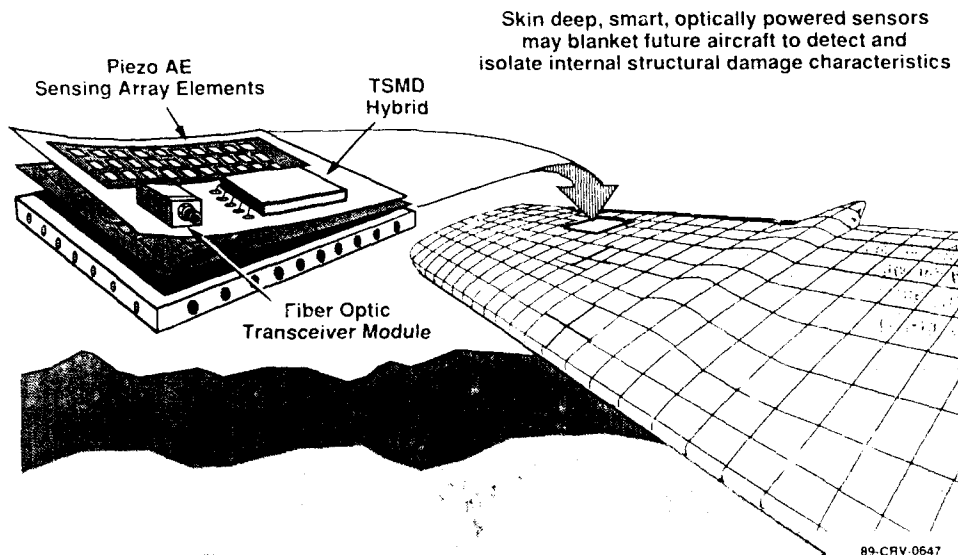
Figure 5. Optically Powered Smart Acoustic Sensor

Research activities on active control technology of aircraft in Japan

Hiroshi Matsushita*   and   Yuji Matsuzaki**
National Aerospace Laboratory   Nagoya University
Mitaka, Tokyo, Japan   Chikusa, Nagoya, Japan

ABSTRACT: The research activities in Japan, related to the active control tech-
nology of aircraft, especially in the field of aeroservoelasticity, are reviewed. The
mathematical modeling and control law synthesis method for aeroservoelastic
system established at National Aerospace Laboratory is described. As theoretical
works in the related fields, robust control system design method with multiple
model approach and multidisciplinary optimization by goal programming method
are briefly reviewed. Experimental investigations in wind tunnels are stated.

1. INTRODUCTION

The closely related topics to the adaptive structure, the aircraft active control technology
(ACT), especially in the field of aeroservoelasticity (ASE) has been pursued worldwide for
more than two decades. Among these research activities, Japan has also been conducting
the continuous research efforts on this topics. Fig. 1 summarizes these activities.
Motivated by the pioneering research conducted in the United States, some basic studies
concerning the aeroservoelastic system were initiated around the mid 70s in Japan. They
include the theoretical studies such as the unsteady aerodynamic modeling, the synthesis
method of aeroelastic control system and subcritical response identification (Matsuzaki *et al*
1981) executed at the National Aerospace Laboratory (NAL), the experimental study of
controlling beam vibration using magnetic force done by Kawasaki Heavy Industries Co.
Ltd. (KHI), and the series of experimental investigations of controlling 2-dimensional
airfoil flutter conducted at the University of Tokyo.
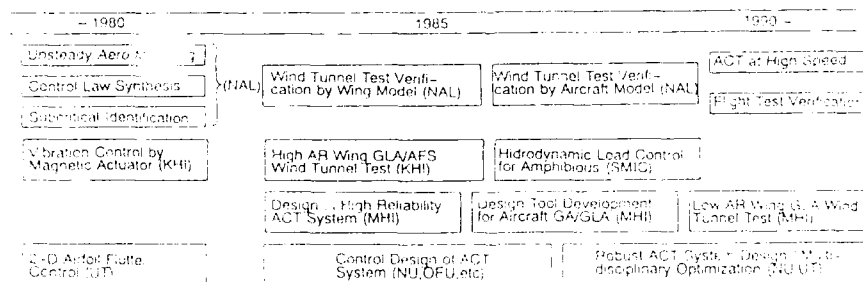
Fig.1 Research activities on aircraft ASE system in Japan

* Group Leader, Advanced Aircraft Research Group
** Professor, Department of Aeronautical Engineering

During the 80's the research increased in scope. Based on the previous basic research, validation experiments, feasibility studies and extended theoretical investigations were carried out at every research sectors in Japan; the universities, the research institutes and the aircraft manufacturers.

Wind tunnel studies to verify the previously proposed ASE synthesis method were conducted at NAL. Meanwhile, Japanese aircraft manufacturers were involved in the advanced aircraft technology studies sponsored by the Society of Japan Aerospace Industries Association. Within this program, major manufacturers conducted active control related research. At KHI, wind tunnel studies were conducted concerning the gust load alleviation and active flutter suppression for a high aspect ratio wing. At Mitsubishi Heavy Industries Co. Ltd. (MHI), a conceptual design study on the redundant ACT system with high reliability was conducted. A feasibility study to alleviate the hydroelastic forces on the stabilizer of a seaplane was carried out at Shin-Meiwa Industry Corporation. Many analytical investigations were conducted at universities concerning the application of advanced control theory to the ASE system (Ohta *et al* 1989). In the following, the typical research among these activities are presented.

2. THEORETICAL RESEARCH

The representative theoretical research in Japan presented here are research of control law synthesis method validated by the series of wind tunnel tests done in NAL, research on robust control with multiple model approach, and research on multidisciplinary optimization of ASE system.

2.1 Finite-state modeling and control law synthesis

Fig.2 shows the synthesis flow established at NAL along with the aeroservoelastic system which resulted from implementing the control laws into the on-board computer. The controlled plant of flexible aircraft is in itself the distributed system; its dynamics are inherently expressed by the partial difference equation. In order to apply the fully cultivated optimal control theory, it is necessary to express these distributed systems in the form of a lumped
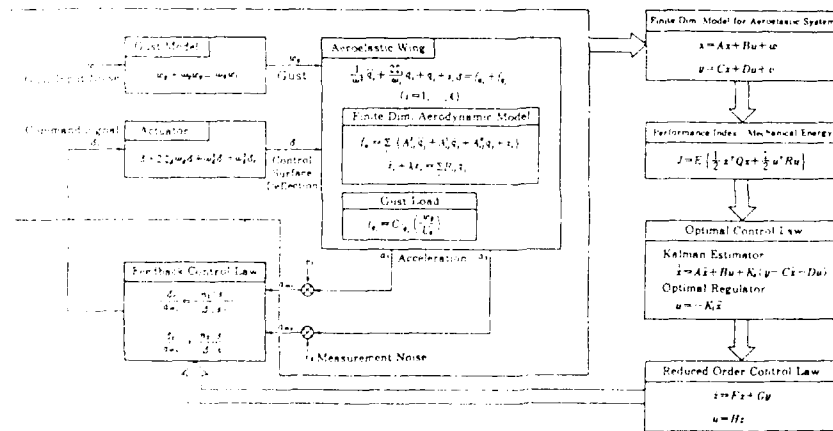
Fig.2 Control law synthesis procedure for ASE system

parameter mathematical model. With the aid of the modal approach and the truncation of the higher modes, we can obtain the lumped parameter math model for the structural dynamics. We have proposed the method to obtain the finite state math model to the unsteady aerodynamics (Miyazawa 1981 1982 1983, Matsushita 1982) using the efficient CFD program developed by Ueda (1982). The unsteady aerodynamics are approximated introducing the augmented variables which express the fundamental characteristics of delay in the unsteady aeroforces. The observable outputs of the system can be expressed as a linear combination of the state variables, so that the whole mathematical model can be reduced in the finite dimensional form.

When the ASE system can be expressed in this form, we can easily find the flutter characteristics by eigenvalue analysis, and furthermore, we can then apply the optimal control theory by defining the appropriate cost function to get the optimal control laws. As the cost function, we adopt the mechanical energy in the form of quadratic function of the state variables along with the control cost (Miyazawa 1981). With this cost function we can obtain the ordinary regulator with the state estimation by the Kalman filter. The optimal control laws thus obtained, however, have the same order as the original control plant. Because the order is too high to implement into the on-board computer for real time calculation, it is necessary to reduce it by some appropriate order reduction method. We can finally obtain the control law of a sizable order. These procedures of math modeling incorporated with optimal control theory make up the synthesis method for the ASE system established by NAL.

Besides these fundamental research work, two representative theoretical investigations were carried out in Japan; the robust control system design with multiple model approach and the multi-disciplinary optimization research using the goal programming.

2.2 Robust control system design with multiple model approach

In order to handle a multiple design point problem, Miyazawa (1988 1989) defined multiple models corresponding to each design point with the multiple equations. Control law of a constant and the same gain for each model is sought with the performance index of the summation for each model weighed by the probability. The solution is obtained with the aid of some numerical optimization method.
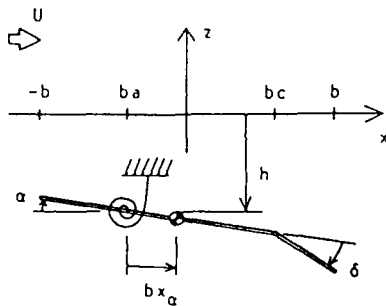
Fig.3 Airfoil model
in incompressible flow
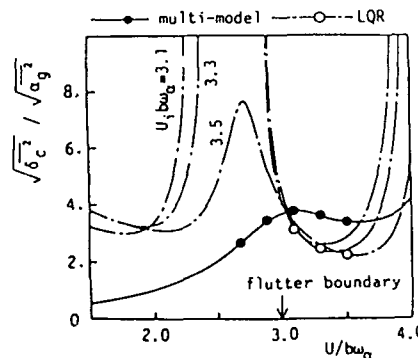
Fig.4 Control command rms
against flow velocity change

As a numerical example, he took a flutter control problem for a two dimensional airfoil in incompressible flow with pitching and plunging motion (Fig.3). In this example, he defined the performance index to be minimized as the sum of control surface movement for four different design velocities. The results are shown in Fig.4 which shows the control performance v.s. the flow velocity. For comparison, optimal control laws at each different design velocity are also shown. Though optimal solutions give the best performance at its own design velocity than any other solutions, it loses the optimally outside the design velocity. On the other hand, the controller designed by the multiple model method gives reasonable performance over a wide range of flow velocity. This controller can be said robust, and with a sophisticated computer aided design environment, the multiple mode approach will be a more powerful approach to design robust control systems.

2.3 Structure/control design synthesis by goal programming

Another theoretical work related to ASE system design is multidisciplinary optimization work conducted by Suzuki (1990). Fig. 5(a) shows the result obtained by LQR optimal control design for the active flutter control of a typical wing section. Though the system is stabilized with control, stable speed range is very narrow and wide range of instability at lower speed range is appearing. To obtain the wing which overcome this defects by optimal parameter modification is the design objective

(a) Original system   (b) Optimized system
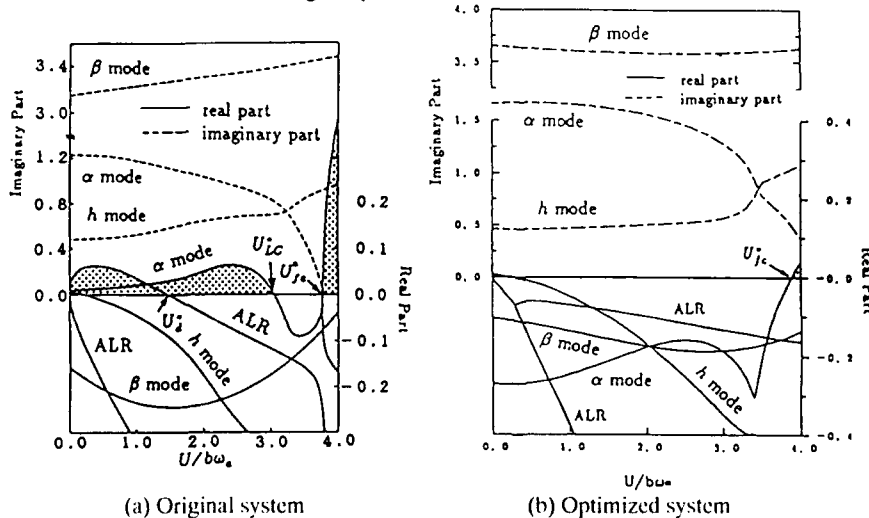
Fig.5 Eigenvalue locus of closed-loop system

Suzuki treated a problem to optimize the control system parameter and the structural parameters simultaneously. He placed the design constraints that the closed loop system should be stabilized in the hole speed range below the design speed, open loop system has to be stable below the speed not less than the original flutter speed, the control surface deflection should not be too excessive and finally, the structural design parameters change should be minimized. In the goal programming the priority to each restriction is first determined, and thereby the restrictions become the objective function weighted according to the priority. The objective function is, then expressed as the summation of the differences at each optimization step and minimized. The results of the optimization are shown in Fig.5(b). The closed loop system was stabilized whole the speed range below the design speed and the optimally modified wing was obtained.

3. EXPERIMENTAL RESEARCH IN WIND TUNNEL

3.1 High aspect ratio wing wind tunnel study

KHI carried out a wind tunnel test study of active control technology using a high aspect ratio wing (Horikawa *et al* 1986). They developed and constructed a flutter model incorporating a miniature high performance electric d-c servo motor which was installed near the control surface. They were able to attain 7.5% increase in flutter speed with the proper adjustment of the control gain as shown in Fig.6.
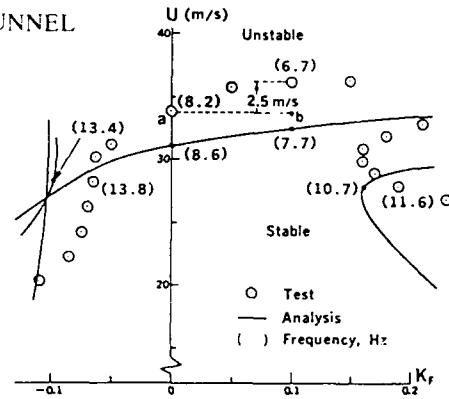
Fig.6 Flutter boundary against control gain

The first experiment which was done at NAL for validation of the control synthesis method is gust load alleviation (GLA) for a rectangular cantilevered wing (ACT Study Group 1984). The wing has the first bending mode separated from the other higher modes in its frequency. The mathematical model of the total order seven, therefore, could be represented only with this first mode. The second order control law was obtained by the order reduction. The power spectral density of Fig.7 shows that the response of the wing bending moment is greatly alleviated with GLA system engaged. The amount of the alleviation in this case is 45% in rms sense. The correspondence of the analytical expectation and the test results is excellent.The fundamental validation of our control law synthesis method was therefore confirmed by this experiment.
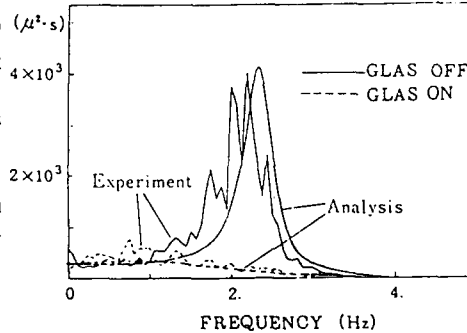
Fig.7 PSD of wing root bending moment

NAL moved to the experiment of the wing of the more realistic and complicated vibration characteristics (Matsuzaki *et al* 1989). The wing has the same plan form as the KHI model except for the leading edge surface provision. The mathematical model has 16th order with the first four vibration modes included. The wing equipped with two accelerometers and the strain gages for vibration sensing. For gust load control we used only the trailing edge control surface. With the control laws designed, NAL was able to alleviate the bending moment response due to gust especially at the peak of the first bending mode as shown in Fig.8. Again the analytical estimation predicts well the experimental results. The alleviation of gust load with control was 25% rms (Fig.9). These results confirmed again the effectiveness of our synthesis method.
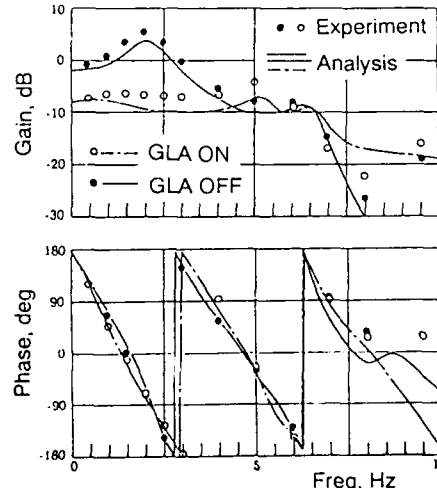
Fig.8 Bending moment frequency response due to gust
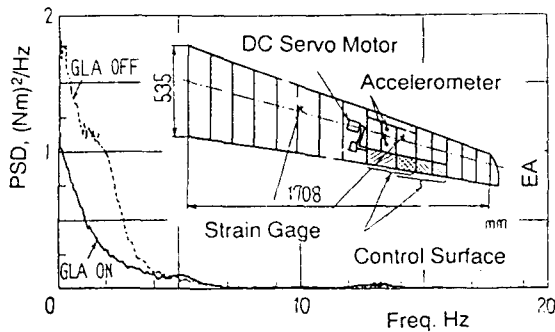
Fig.9 PSD of root bending moment
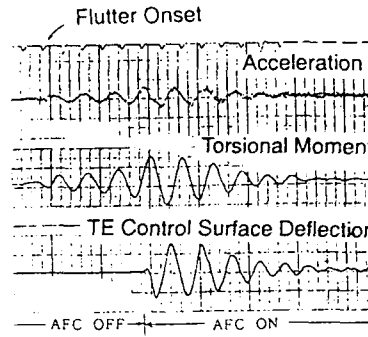
Fig.10 Time history of flutter suppressed

Next to GLA experiment NAL treated the flutter control problem using the same wing as for GLA (Ueda *et al* 1988, Matsushita *et al* 1989). The control law designed could successfully suppress the flutter as shown in Fig.10. The flutter onset indicated by the torsional moment growing up is suppressed by activating the control surface. Using both the leading edge and the trailing edge control surfaces simultaneously we were able to succeed in increasing the flutter velocity by 13%. The prediction in this case was about twice the higher than the tested results. The difference between the analytical and tested results can be attributable to the excessive estimation of the control surface effectiveness by the CFD analysis. It was concluded that the synthesis method is effective for flutter control as well.

3.2 Gust load alleviation for a low aspect ratio wing.

Another wind tunnel test was started and is still on–going by MHI (Arakawa *et al* 1988). They treated a wing with a low aspect ratio of three (Fig.11). One of the purposes of this study was to develop and verify the analytical tool for an aeroservoelastic system.

Their typical experimental result for gust response / gust load alleviation is shown in Fig.12. They were able to alleviate the response of the wing due to gust as both frequency ranges not only at rigid motion but also at the elastic vibration. They are now planning to conduct the flutter control experiment using the same model.
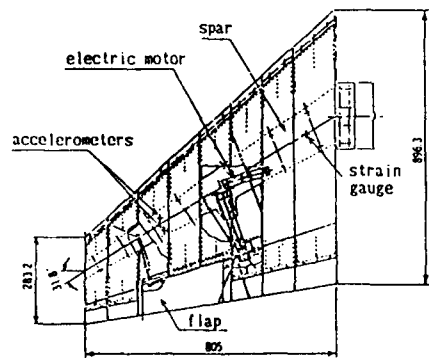
Fig.11 Low aspect ratio wing model
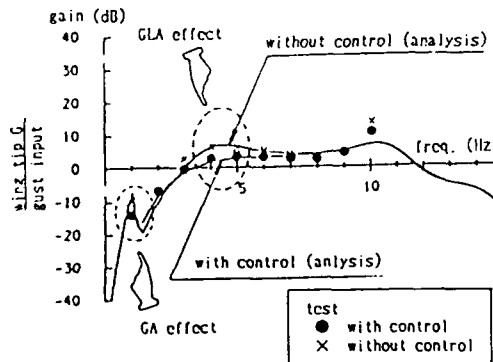
Fig.12 Frequency response of the wing

3.3 Complete aircraft model ACT experiment

The last one of the series of wind tunnel tests carried out at NAL in the low speed range was for the complete aircraft model (Matsushita *et al* 1990, Fujii *et al* 1991). The model was supported in the wind tunnel test section with the three degree of rigid motion freedom of heaving, pitching and yawing (Fig.13). The supple mental vertical force was supplied by the tension controlled torque motor winding up the model with the constant forces through the cable. The bending moment responses at the short period mode as well as at the first bending mode are reduced by the controls. Table summarizes the experimental results and compares them with analytical data. Control law A is the acceleration feedback, while, B is the acceleration plus the bending strain feedback. Control law C was designed for the purpose of fulfillment of gust load alleviation with flutter margin augmentation. The correspondence between the test and the analysis are again fairly good so that a synthesis tool for ASE system have been established.
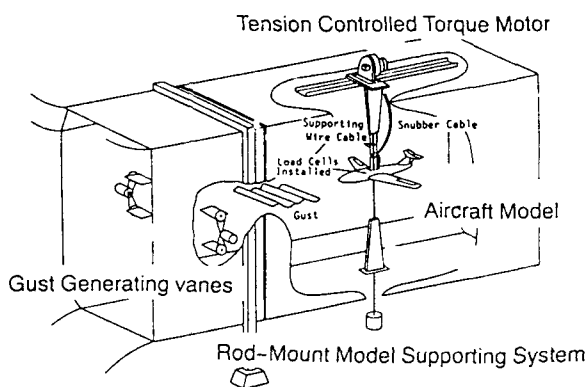
Fig.13 Aircraft model ACT experiment set-up

Table Complete aircraft model ACT experiment results

Control Law	Feedback Variable	Order	GLA			FMA	
			Analysis	Experiment		Analysis	Experiment
			Strain Energy	Bending Moment	Accele- ration	Velocity Increment	Flutter Margin Increment
A	a*	4	58%	93%	67%	3%	X 1.7
B	a/ε_B**	4	68%	80%	69%	5%	X 1.5
C	a	4	60%	---	---	18%	

* a : Acceleration
** ε_B : Bending Strain

GLA : Gust Load Alleviation
FMA : Flutter Margin Augmentation

4. CONCLUDING REMARKS

1. The control law synthesis method for an aeroservoelastic system is basically established in Japan by the efforts of the laboratory and the manufacturers, especially in the low speed range. The next step is to extend the method to the high speed range. Future subjects on the theoretical side are to establish a method to adopt the system robustness against its parameter uncertainty.

2. The active aeroelastic control technology has reached a mature situation by these research efforts, so that now flight validation is needed to provide the technology readiness.

3. Multidisciplinary optimization research should be further pursued in order to pave the way for realizing the fully control configured vehicles. In this regards active materials, adaptive structures and controlled structures will play an important role.

REFERENCES

ACT Study Group 1984 NAL TR–846 (in Japanese)

Arakawa H, Toda N, Shirai Y, Taneda H, Sakura, K 1988 *Proc. the 26th Aircraft Symposium*, Sendai, Japan, pp 160–163

Fujii K, Matsushita H, and Miyazawa Y 1991 *Proc. the International Forum on Aeroelasticity and Structural Dynamics*, Aachen, FRG,

Horikawa H and Saito K 1986 *AIAA Paper* 86–0956 pp 484–492

Matsushita H 1987 *J.The Japan Society for Aeronautical and Space Sciences*, **35** 3 (in Japanese) pp 20–28

Matsushita H, Miyazawa Y, Ueda T, and Suzuki S 1989 *Proc. the European Forum on Aeroelasticity and Structural Dynamics*, Aachen, FRG, pp 519–527

Matsushita H, Ueda T, Fujii K, Miyazawa Y, Hashidate M, and Ando Y 1990 ICAS'90, Stockholm, Sweden

Matsuzaki Y and Ando Y 1981 *J. Aircraft*, **18** 10 pp 862–868

Matsuzaki Y, Ueda T, Miyazawa Y, and Matsushita H 1989 *J. Aircraft*, **26** pp 322–327

Miyazawa Y 1981 Ph.D. Dissertation, Univ. of Tokyo, Japan (in Japanese).

Miyazawa Y 1982 NAL TR–721T

Miyazawa Y and Washizu K 1983 *AIAA J.*, **21** 2 pp 163–171

Miyazawa Y 1988 *Int. J. Control*, **47** 6 pp 1937–1946

Miyazawa Y 1989 AIAA Paper 89–3578, *AIAA Guidance, Navigation and Control Conf.*, Boston, pp 1267–1276

Ohta H, Fujimori A, Nikiforuk P N and Gupta M M 1989 *Journal of Guidance, Control and Dynamics*, **12** 2 pp 188–194

Suzuki S and Matsuda S 1990 AIAA Paper 90–3326–CP, *AIAA Guidance, Navigation and Control Conf.*, Portland, pp 96–104

Ueda T and Dowell E H 1982 *AIAA J.*, **20** 3 pp 348–355

Ueda T, Matsushita H, Suzuki S, Miyazawa Y, and Matsuzaki Y 1988 ICAS'88, Israel, also as 1991 *J. Aircraft*, **28** pp 139–145

Active stabilization of a beam under nonconservative force

Junji Tani and Yuzhou Liu
Institute of Fluid Science
Tohoku University
Katahira 2-1-2, Aoba-ku
Sendai, Japan

Abstract

In this paper, the galloping behavior of the cantilever beam in an uniform smooth wind stream is formulated by means of the transfer matrix method. Then, an optimal feedback gain matrix is designed by using the optimal regulator theory. As the actuator, a pair of piezoelectric columns is fixed between two aluminium plates in which the cantilever beam is clamped. The characteristics of the flow around cantilever beam was examined in an uniform smooth wind stream. It is found that the self-excited oscillation of the cantilever beam was suppressed sufficiently by the optimal control.

1. INTRODUCTION

Among every kind of aerodynamiclly unstables, galloping is the typical one. It can arise in any lightweight, flexible structure exposed to a flow. A wide variety of cross sections, including square, rectangular, right angle, and stalled airfoil, are potentially unstable owing to aerodynamic galloping. The galloping unstable can produce large amplitude oscillation on the structure, and some times it will destroy the structure. Therefore, it is necessary to control the galloping unstable.

In this paper, a method for stabilizing galloping unstable is reported. As an analytical model, a cantilever beam in an uniform smooth wind stream is used and it is formulated by means of the transfer matrix method. Further, the optimal regulator technique is intruduced for determining the control algorithm. As the actuator, a pair of piezoelectric columns is used.

According to the control algorithm designed above, an expriment was performed using the low-turbulence wind tunnel. The characteristics of the flow around cantilever beam with a square section was examined in an uniform smooth wind stream. It is found that the self-excited oscillation of the cantilever beam was suppressed sufficiently by the optimal control. The differences in flow characteristics behind the beam between with and without optimal control became clear.

2. THEORETICAL ANALYSIS

The analytical model is shown schematically in Fig. 1. A pair of piezoelectric devices is fixed below the clamped end of the cantielever beam and used as actuator. The moving

equation describing the vibration of the beam in the uniform smooth wind stream can be obtained in mode coordinate system by using the transfer matrix method[1].

$$\ddot{q}_k(t) + c\omega_k \dot{q}_k(t) + \omega_k^2 q_k(t) = b_k \ddot{\theta}(t) \qquad (k = 1, 2, \cdots, n) \tag{1}$$

where, $\theta(t)$ is produced by the effect of the piezoelectric actuator as shown geometrically in Fig. 1, c is a constant which depends on internal damping of the beam and velocity of the wind stream, ω_k is the natural angle frequency of the beam, $q(t)$ is an unknown function of time, and b_k can be determined by using the natural vibration modes of the beam and the distance of two piezoelectric actuators.

Table 1. Natural frequencies of beam
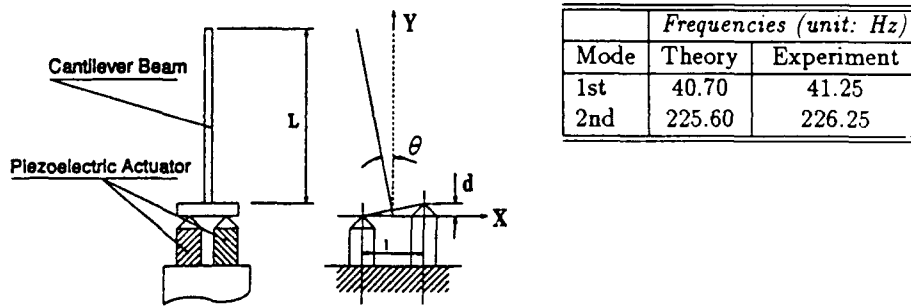
	Frequencies (unit: Hz)	
Mode	Theory	Experiment
1st	40.70	41.25
2nd	225.60	226.25

Fig.1 Analytical model and coordinate system

In order to establish the state equations of the control system, a state variable vector is introduced firstly. Then we can obtain a continuous time state equation. Further, discretizing the continuous time system with a sampling interval ΔT, the difference equations of the discrete time system are given by

$$\mathbf{X}[(i + 1)\Delta T] = A\mathbf{X}(i\Delta T) + Bu(i\Delta T) \tag{2}$$
$$Y(i\Delta T) = C\mathbf{X}(i\Delta T) \tag{3}$$

in which, Y represents the displacement of the beam at the free end, while u is called control input, the displacement of the piezoelectric actuator and determinted by means of the digital optimal regulator theory.

3. RESULTS OF EXPERIMENT AND DISCUSSION

The equipment used in the experiment is depicted schematically in Fig. 2. The experiment was carried out by using a wind tunnel which is set up at the Air Current Measure Research Institution of the Institute of Fluid Sciense, Tohoku University. The test model is cantilevered vertically in a low turbulent wind tunnel, and is made of aluminium (Young's modulus is $63.18GPa$ and density is $7.74 \times 10^3 kg/m^3$). The length,

width and thickness of the beam are $200mm$, $2.4mm$ and $2.0mm$ respectively. The experimental and theoretical values of the natural frequency of the cantilever beam used in the experiment are shown in Table 1.
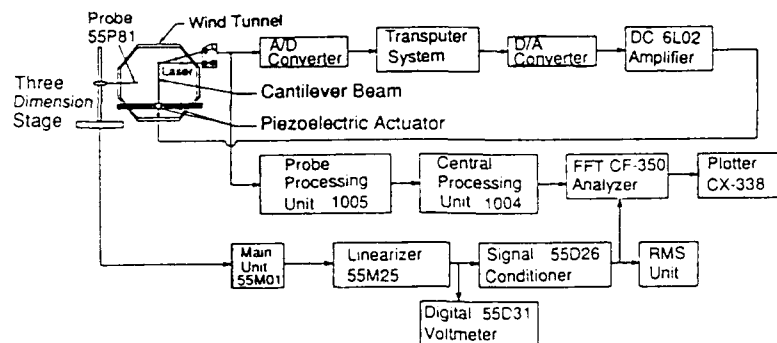
Fig.2 Schematic diagram of the experimental equipment

In this study, the velocity domain with the fundamental vibration mode was taken into account only, because this mode produced a large amplitude oscillation comparatively. When velocity of the wind was set up $U_0 = 8.0m/s$, the responses of the beam displacement measured with a laser sensor are shown in Fig. 3. In this experiment, the displacement $1mm$ was equivalent to the output voltage, $0.309V$. It is clear that the self-excited oscillation of the beam is sufficientlly suppressed when the control is applied. In this figure, symbol ↑ indicates the starting time of the control.
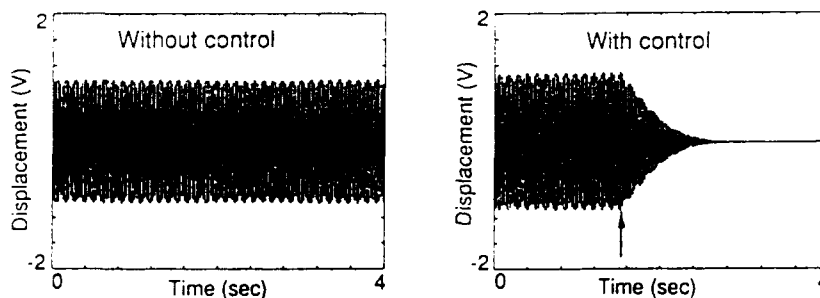
Fig.3 Effect of vibration suppressed with the optimal control

Also, in order to elucidate how the air flow is affected by the structure vibration, we examined the velocity fluctuating of the wake. The output signal of the fluctuating velocities measured with a hot-wire anemometer are shown in Fig. 4. The hot-wire probe was fixed at $x/L = 0.05$, and $z/L = 0.05$, then it was traversed in y-direction. Here, z is the distance from the free end of the beam. Without control, the values of the velocity fluctuating became largely when the probe was made approach to the beam. While, a peak value appeared in the velocity fluctuating when the probe came to $y/L = 0.02$. However, a oscillation with low vibration freqency appeared nearby

$y/L = 0.02$. The beam would be induced to produce a self-excited vibration by this oscillation with the low vibration frequency. However, though there was a peak value in the velocity fluctuating at $y/L = 0.02$ same as above, the vibration compoents with the low freqency had disappered when the control was applied.
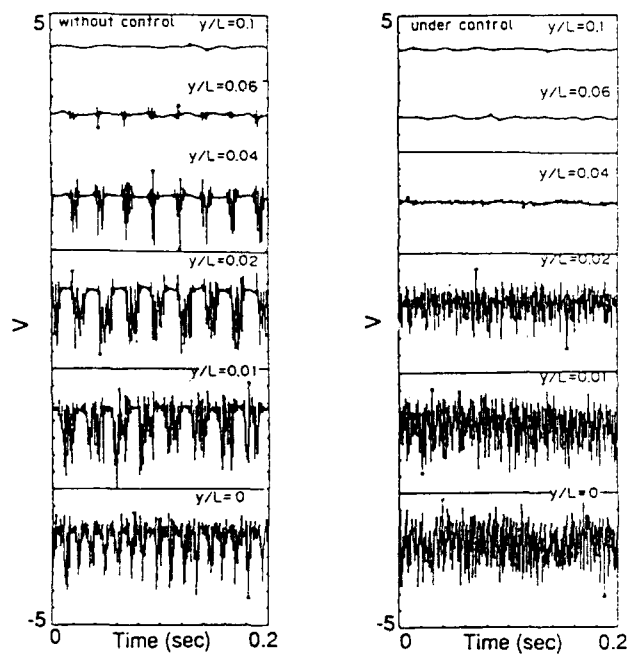
Fig.4 Velocity fluctuation of the wind stream

4. CONCLUSIONS

In this paper, the vibration control for a cantilever beam in an uniform smooth wind stream was carried out with the optimal control and the characteristics of the flow around the beam was investigated. The results obtained are summarized as follows:

1) The self-excited oscillation of the beam is sufficientily suppressed by using the optimal control.

2) The velocity fluctuating of the wake becomes very samll when the control is applied.

5. REFERENCES

1. J.Tani, S.Chonan, Y.Z.Liu, F.Takahashi, K.Ohtomo and Y.Fuda, Prepaper. Jpn. Soc. Mech. Eng., (in Japanese), No.56-525,C,(1989), p.1147.

Statistical estimates of identified modal parameters for a scale model precision truss

Lee D. Peterson

Department of Aerospace Engineering Sciences, University of Colorado
Boulder, Colorado 80309-0429

Steven J. Bullock, Scott W. Doebling

School of Aeronautics and Astronautics, Purdue University
West Lafayette, Indiana 47907

ABSTRACT: A method for determining the error in measured modal parameters is experimentally investigated on a modally rich truss structure. Modal frequency and damping error estimates are calculated from the statistical sensitivity of a form of the Eigensystem Realization Algorithm. Noise variances are estimated for the data using the frequency domain coherence for each input-output pair. It is shown that the sensitivity to a given data set can be very low, even when the sensitivity remains high to adding more data to the analysis.

1. INTRODUCTION

To achieve high reliability from an adaptive structure, it may be necessary to obtain more than simply an accurate, nominal modal of the vibration dynamics. Structural controllers often compensate for disturbances whose temporal variation is not well known. Consequently, they must rely on a model of the structural dynamics to reject the disturbances, and can be very sensitive to errors in the model. To desensitize control laws to changes or errors in the structural model, experimental modal analysis must quantify the degree of uncertainty in a given measurement.

One method for estimating the confidence in modal parameters was introduced by Longman, Bergmann, and Juang (1988) and Bergmann and Longman (1989). Their approach is based on the analytical perturbation of the Eigensystem Realization Algorithm (Juang and Pappa, 1985). Since an identified modal parameter will be a nonlinear function of the data used in the identification, it can be expanded in a Taylor series in terms of small noise perturbations in the data. Prior applications of this method have focused primarily on simulated vibration data. This paper presents an application to experimentally measured data, for which several hundred modes lie within the disturbance bandwidth.

2. THEORETICAL BACKGROUND

2.1 Eigensystem Realization Theory

The Eigensystem Realization Algorithm (ERA) (Juang and Pappa, 1985) can be best understood as a systematic curve fit of experimentally measured transfer function data. It is systematic in the sense that the order of the model (the number of parameters used in the fit) is

a natural consequence of the selected rank of the Hankel matrix formed from the data. The assumed form of the model is the general discrete state-space model:

$$x(k+1) = A\,x(k) + B\,u(k)$$
$$y(k) = C\,x(k) + D\,u(k) \tag{1}$$

The general response of this model to any input in the convolution sum:

$$y(k) = \sum_{r=0}^{k} M(k\text{-}r)\,u(r) \tag{2}$$

in which $M(i,k,j)$ is the k-th time sample of the i-th measurement to a unit pulse applied to the j-th input, and is also called the Markov parameter.

The ERA method uses measurements of M to estimate $\{A, B, C, D\}$. The details of this computation are found in Juang and Pappa (1985), and are not repeated here. We note, however, that in all our applications of ERA, we use a particularly efficient formulation, motivated by the Q-Markov COVER, which can speed up the ERA calculation by a factor of 10 or more. This was reported in Peterson and Bullock (1991) and Peterson (1992).

2.2 Error Analysis of the ERA Results

Measurements of the modal parameters can be derived from an eigenanalysis of the identified $\{A, B, C, D\}$ matrices. For instance, the n-th modal frequency is given by

$$\omega_n = \frac{1}{T}\,\text{Im}\left[\text{Ln}\!\left(\lambda_n\right)\right] \tag{3}$$

in which T is the sample period and λ_i is the i-th (complex) eigenvalue of A. In a general sense, each such parameter can be considered a function of each data point $M(i,k,j)$. By differentiating the ERA computations, the following truncated Taylor series can be derived:

$$\omega_n = \tilde{\omega}_n + \sum_{i}\sum_{j}\sum_{k} \frac{\partial \omega_n}{\partial M(i,k,j)}\,\Delta M(i,k,j) \tag{4}$$

Suppose that we know the variance of $\Delta M(i,k,j)$ to be $\varepsilon^2(i,k,j)$. Then, assuming each $\Delta M(i,k,j)$ is uncorrelated from the other data perturbations, the variance of the modal frequency is given by

$$VAR\,[\omega_n] = \sum_{i}\sum_{j}\sum_{k} \left[\frac{\partial \omega_n}{\partial M(i,k,j)}\right]^2 \varepsilon^2(i,k,j) \tag{5}$$

Similar expressions can be derived for modal damping and mode shapes (Longman, Bergmann, and Juang, 1988). In addition, bias estimates can also be derived, although we do not consider these in this paper.

2.3 Estimate of the Noise Variance from Data

As can be seen above, a key to using this error analysis procedure is to find an estimate of $\varepsilon^2(i,k,j)$. We propose finding these estimates from the statistics of the transfer function measurements themselves. This procedure, presented in Bendat and Piersol (1986), uses the

frequency domain coherence estimate to determine the statistics of the transfer function estimates.

Suppose that for the j-th input and the i-th measurement, we have measured Discrete Fourier Transforms (DFT):

$$U(f) = DFT\left[u_j(k)\right]$$
$$Y(f) = DFT\left[y_i(k)\right]$$

(6)

Assume that our knowledge of both input and measurement are corrupted by Gaussian white noise of unknown intensity.

To estimate the corresponding transfer function, form the auto and cross spectra for these signals:

$$G_{uy} = U^*Y$$
$$G_{uu} = U^*U$$
$$G_{yy} = Y^*Y$$

(7)

and average these spectra over n_d uncorrelated repetitions of the same experiment. The resulting smooth estimate of the transfer function is

$$H_{uy} = \frac{G_{uy}}{G_{uu}}$$

(8)

The coherence estimate of this transfer function is

$$\gamma_{uy}^2 = \frac{|G_{uy}|^2}{G_{uu}G_{yy}}$$

(9)

From these estimates, the statistics of the transfer function can be estimated. In particular, the variance of the magnitude of the transfer function is

$$VAR\left[|H_{uy}|\right] \approx \frac{\left(1-\gamma_{uy}^2\right)|H_{uy}|^2}{2\gamma_{uy}^2 n_d}$$

(10)

To derive the variance of the Markov parameters $\varepsilon^2(i,k,j)$, it is necessary to transform from the frequency domain variances at each frequency, f, to the time domain at each time sample, k. Since the Markov parameters are the inverse discrete Fourier sum of the frequency domain data, their variance is the sum of the variance of the magnitude of the transfer function over all frequency samples, divided by the number of samples squared. This variance is the same for all time samples for a particular transfer function.

3. EXPERIMENTAL APPARATUS AND PROCEDURE

Our research collected data from a 1:10 dynamic scale model of an interferometric imaging telescope.(Figure 1) This structure has a triangular base, for which each leg consists of 11 bays constructed from a 1-foot long pyramidal truss network. A fourth leg extends vertically to above the center of the triangular base to form an image collecting plane. The structure was lightly suspended during our tests to simulate a free-free condition. The damping levels observed in this structure were typically 0.5 % critical or less.
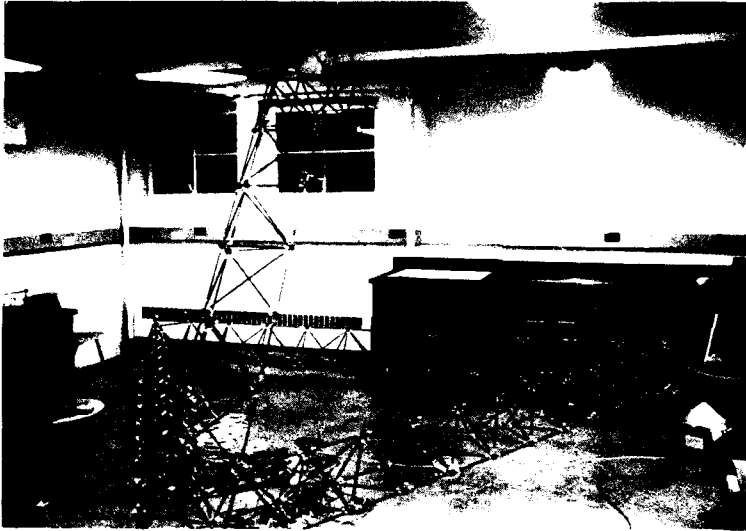
Figure 1. Experimental test structure used in this research

Pseudo-random burst force inputs were applied using a 50 pound modal shaker in three orthogonal directions from each corner of the structure. The bandwidth of the synthesized force input signal was sharply cut at 250 Hz. Vibration measurements were collected at 11 locations by piezoelectric accelerometers mounted to the nodes of the structure. The accelerometer signals were filtered and amplified by a programmable signal conditioner. The amplification gain factor was set to use the entire dynamic range of each sensor for a given measurement. The signals were simultaneously digitized with a 12 bit analog to digital converter at a sampling rate of 1000 Hz. Typical noise levels observed during the measurements were approximately 2 to 3 bits RMS.

4. RESULTS

Figures 2 and 3 present the frequencies and damping ratios identified for a typical data set analysis. For this analysis, the ERA Hankel matrix size was 100 by 54. The identification analysis required 3 seconds on a Sun SPARCStation 2, but the error analysis required 1099 seconds. (Note that we use the efficient formulation of the ERA algorithm reported in Peterson (1992).) The calculated standard deviations due to noise in the data are also shown. Calculated variances for this data set varied among all the input-output pairs, but were typically 10-4 (m/s2/N)2. These noise levels correspond to approximately 30 mvolts RMS in a 10 volt full scale measurement.

As seen in Figure 2, the uncertainty in the identitifed modal frequencies is very small. Most of the modes are identified to the same accuracy, but the higher frequency modes are generally identified better than the low frequency modes. This is due to the length of the data window used in the ERA analysis. In Figure 3, the standard deviations of the damping ratios are plotted as high and low values about a mean. Notice that the damping values identified were very high for this identification analysis.

Both the identified frequencies and damping ratios which are identified from the data set change significantly when more data is used in the analysis. For instance, when the Hankel matrix size becomes very large (of the order 1000 by 5000) the modal damping ratios approach 0.5% or less. Clearly, the error associated with noise in a given data set does not predict the error in the nominal measurement due to the truncation of the data set. The perturbation error analysis can measure the sensitivity to noise in the data set, but it cannot alone indicate whether the identification results will change if more data is added to the analysis.
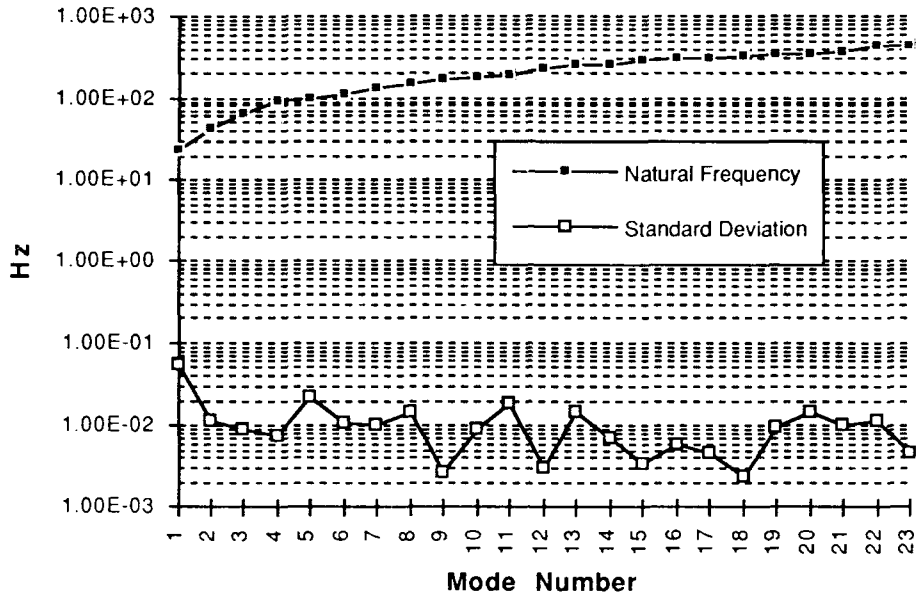
Figure 2. Identified modal frequencies and standard deviations
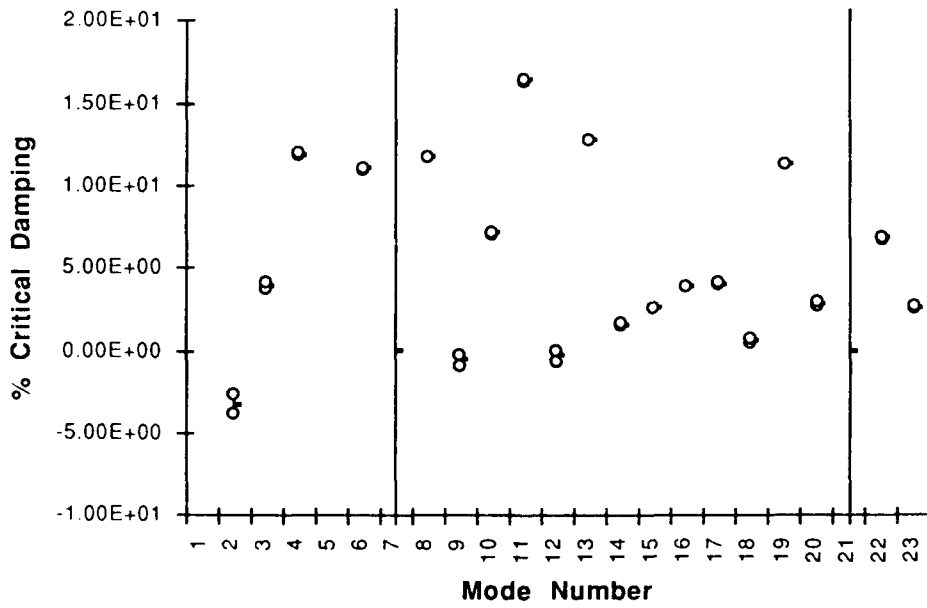
Figure 3. Identified modal damping ratios with error bars

5. CONCLUSIONS

This paper presented an experimental application of the perturbation error analysis of the Eigensystem Realization Algorithm. Noise variances in the measured Markov parameters were estimated using the coherence function for each input-output pair. It was shown that the frequency and damping errors due to noise in a given data set can be significantly smaller than the variation found when the data set size is increased. This means that the error analysis should be used only when the data set size is of sufficient size to have converged the identified parameters.

Current research is focusing on several additional issues. First, to judge the precision of the measured modal parameters, it is necessary to compare the estimated error to the minimum error bound given by Cramer-Rao theory for unbiased estimators. Also, we are investigating how to quantify the sensitivity to truncation in the data set. Longman, Bergmann and Juang (1988) considered the effect of truncating singular values, but assumed the data set was complete.

The computational requirement is one of the major impediments to applying this approach in a practical situation. For the larger data set presented here, the total identification and eigenanalysis process took only about 2 seconds of CPU time, but the variance calculation required almost 9 hours. To improve this performance, we are investigating the possibility of extrapolating the variance estimates from only a few of the sensitivities. The variance estimate from the entire data set can itself be estimated from a randomly selected subset of data points. This may make practical the application of perturbation error analysis to large data set sizes.

6. REFERENCES

Longman, R.W., Bergmann, M., and Juang, J.N. "Variance and Bias Confidence Criteria for ERA Modal Parameter Identification" AIAA Paper No. 88-4312. *AIAA Astrodynamics Conference*, 1988.

Bergmann, M., and Longman, R.W., (1989) "Variance and Bias Computation for Enhanced System Identification" 28th Conference on Decision and Control, Tampa.

Bendat, J.S. and Piersol, A.G. (1986) *Random Data: Analysis and Measurement Procedures*, 2ed., John Wiley and Sons, New York.

Juang, J.N. and Pappa, R.S. (1985) "An Eigensystem Realization Algorithm for Modal Parameter Identification and Model Reduction" *J. Guidance, Control and Dynamics*, Vol 8, No 5, pp 620-627.

Peterson, L.D. (1992) "Efficient Computation of the Eigensystem Realization Algorithm" *Proceedings of the Tenth International Modal Analysis Conference*, San Diego.

Peterson, L.D. and Bullock, S.J. (1991) "A Comparison of the Eigensystem Realization Algorithm and the Q-Markov COVER" *Proceedings of the 32nd Structures, Structural Dynamics, and Materials Conference*, Baltimore. AIAA Paper No. 91-1191.

Approximation of parameter uncertainty in nonlinear optimization schemes—case study of a truss structure

W. R. Witkowski and J. J. Allen

Sandia National Laboratories
Albuquerque. New Mexico
87185-5800

Abstract. Often theoretical models are developed using experimental data to estimate the model parameters but an evaluation is not always made of the model's reliability or robustness. Errors can exist in the theoretical model for many reasons including inadequate model formulation and poor parameter estimates. This paper investigates the approximation of second-order statistics (confidence regions) of parameters estimated using nonlinear optimization schemes to evaluate parameter reliability. An optimal set of parameters are calculated to minimize the difference between theoretical model predictions and experimental data. This metric was formulated in terms of a weighted least squares objective function. A truss structure was analyzed to evaluate nonlinear optimization and confidence region approximation techniques. It was found that since the truss model was linear and parameter interaction was small, the confidence region approximations were reliable.

1. Introduction

A mathematical model is only as good as its estimated parameters. The ability to accurately model physical processes mathematically is vital in all areas of scientific research. In the structural engineering field, the ability to predict a system's behavior leads not only to the efficient design of new structures, but also to the optimal operation and control of existing ones. Unfortunately, an exact model is usually unavailable and an approximate one must be used. Model parameters are typically determined by fitting the model to experimental data. The procedure of formulating a mathematical model, estimating its parameters, and validating its structure is referred to as *model identification*, which can involve both state and parameter estimation.

Nonlinear optimization schemes have become very popular for use as parameter estimation methods. This popularity stems from the fact that the analysis is independent of both the model form and the type of experimental data available. The

---

minimization of the summed squared error between model predictions and experimental data is commonly used as a criterion of optimality. Least squares theory states that at the optimum, linearized estimates of higher order statistics can be approximated for the estimated parameters - assuming that the measurement errors have zero mean, are independent, and have constant variances.

Unfortunately, these linearization schemes provide reliable confidence intervals only when the objective function is linear at the optimum. When this is not the case the approximation schemes can provide confidence intervals that are severely underestimated, providing a false measure of parameter reliability. Several investigators have devised techniques to evaluate the objective function curvature (Bates and Watts 1988).

This paper further analyzes the model identification results achieved by Allen and Martinez (1990) for a truss structure. In this analysis, parameter estimates were found using the MSC/NASTRAN software package for finite element analyses and optimization.

The truss parameters that were estimated, using eigenvalue data, included Young's modulus of the members and the stiffness value of the truss support structure. Confidence intervals for the parameter estimates are calculated using different approximation schemes. Reliability of these approximations with respect to objective function curvature is also discussed.

2. Nonlinear Parameter Estimation

Nonlinear parameter estimation schemes have been successfully used to approximate model parameters (Witkowski,1990). In this approach, the difference between theoretical and experimental data is minimized. This is done by finding the optimal set of parameters that "best" fit the experimental data. Therefore, an accurate mathematical model is of primary importance to provide reliable theoretical predictions. Otherwise, an ill-conditioned problem can be formulated or erroneous parameter estimates can be predicted.

An objective function, Φ, is chosen to suitably measure the error between the model and data. The choice of Φ must properly describe the experimental error and best utilize available measurements. The most commonly used formulation is the method of weighted least squares. The objective function,

$$\Phi(\hat{y}, y; \Theta) = \sum_{i=1}^{m} \sum_{j=1}^{n} w_{ij}(\hat{y}_{ij} - y_{ij})^2 \tag{1}$$

is chosen to be the weighted summed square error between model predictions, $\hat{y}_{ij}$, and experimental measurements, y_{ij}, where m is the number of experiments and n is the number of observations per experiment. The model parameters are contained within the parameter vector Θ. The weighting factors, w_{ij}, are use to scale variables of different magnitudes and to incorporate known information about measurement uncertainty. Assumptions used in this formulation include that the measurement

error is normally distributed with zero mean, independent, and has a known variances that remains constant. These assumptions are verified via residual analysis.

For an unconstrained problem, an important requirement to estimate the optimal set of parameters, Θ^*, is that the objective function have a minimum. Necessary and suffucient conditons for a local minima to exist are given in Gill, Murray and Wright (1981). However, it should be noted that for parameter estimate uniqueness, $\Phi(y, y; \Theta^*)$ must have a global, not just a local, minimum. That is, it should be shown that $\Phi(\bar{y}, y; \Theta^*) = \Phi^*$ is convex in the parameter space of interest. If this is not the case, a non-unique solution may be formed at a local minimum.

The parameter vector, Θ^*, is found when the convergence criterion,

$$\Phi(\Theta) - \Phi^* \leq \epsilon \tag{2}$$

is met. To evaluate the reliability of Θ^*, a confidence interval is evaluated. The confidence interval of a parameter estimate provides a qualitative assessment of the reliability and precision of the value. If a large confidence interval is calculated, the reliability of the model's prediction is low. However, if the parameters are identified with high precision (i.e., small confidence intervals), confidence in the model's predictions is increased.

The confidence intervals are commonly estimated by expanding Φ around its minimum using a truncated Taylor series,

$$\Phi(\Theta) \approx \Phi^* + \mathbf{q}^{*^T} \delta\Theta + \frac{1}{2}\delta\Theta^T \mathbf{H}^* \delta\Theta \tag{3}$$

where $\delta\Theta = \Theta - \Theta^*$ are the differences in the parameter estimates from the optimal values and $\mathbf{q}^*$, and $\mathbf{H}^*$ are the gradient and Hessian of Φ evaluated at Θ^*, respectively. Since Θ^* is an unconstrained optimum of Φ,

$$\Phi(\Theta) \approx \Phi^* + \frac{1}{2}\delta\Theta^T \mathbf{H}^* \delta\Theta \tag{4}$$

because $\mathbf{q}^* = 0$ at the optimum. Using the convergence criterion shown in Equation 2,

$$\left|\delta\Theta^T \mathbf{H}^* \delta\Theta\right| \leq 2\varepsilon \tag{5}$$

where ε is defined as the indifference criterion. Therefore, the "best" linearized confidence intervals are calculated by solving Equation 5. Because the solution to Equation 5 is computationally intensive and numerically unstable, several approximate schemes have been adopted with simplified calculations. Donaldson and Schnabel (1987) evaluated five different methods to approximate confidence intervals. Three variants of linearization schemes, a likelihood method, and a lack-of-fit technique were analyzed. The major distinction between the linearization schemes and the other two methods is that the former assumes that the nonlinear function can be adequately approximated by a linear function at the optimum. Bard (1974) and Donaldson and Schnabel (1987) stated that the most common approach used in practice is a linearization scheme in which the Hessian matrix is approximated using gradient information and the interaction between parameters is neglected. This

approach is convenient because it is computationally inexpensive and numerically stable. Therefore, the confidence interval for parameter α is calculated using

$$\delta\Theta_\alpha \leq \left(\frac{2\varepsilon}{A_{\alpha\alpha}}\right)^{\frac{1}{2}} \tag{6}$$

where $\mathbf{A}$ is an approximation to the Hessian matrix and $A_{\alpha\alpha}$ is the diagonal element corresponding to the parameter α. Bard (1974) showed that the Hessian can be approximated using the Gauss method by

$$\mathbf{A}^{-1} \approx \mathbf{H}^{*^{-1}} \approx \sigma^2 \left(\sum_{i=1}^{n} w_i \left(\frac{\partial f_i}{\partial \theta_i^*}\right)\left(\frac{\partial f_i}{\partial \theta_i^*}\right)^T\right)^{-1} = \mathbf{A}_a \tag{7}$$

where f_i is the ith observation and σ^2 is the residual variance. This is considered a good approximation if the second derivatives of the model equations, which are multiplied by the estimation error, ε, are small. Other approaches used to estimate the covariance matrix of Θ include: 1) using finite differences to approximate the Hessian, $\mathbf{A}_b = s^2\mathbf{H}^{-1}$ and 2) using gradient and Hessian data, $\mathbf{A}_c = s^2\mathbf{H}^{-1}(\mathbf{J}^T\mathbf{J})\mathbf{H}^{-1}$ where s is the standard deviation. The last formulation can be obtained from sensitivity analysis.

If the residual variance is unknown in Equation 7, and no replicated data is available, it is typically estimated by dividing the sum of squares of the residuals by the number of degrees of freedom,

$$\sigma^2 = \frac{1}{n-l}\sum_{i=1}^{n} e_i^{*^2} = \frac{1}{n-l}\Phi^* \approx s^2 \tag{8}$$

where l is the number of unknown parameters.

For a specified confidence level γ, linear least squares theory states that the joint confidence region is

$$\delta\Theta^T\mathbf{V}_\Theta^{-1}\delta\Theta \leq l\,s^2\,F_{l,n-l,1-\gamma} \tag{9}$$

in which $F_{l,n-l,1-\gamma}$ is the F-statistic with l and $n-l$ degrees of freedom (Bates and Watts 1988). Whereas, if the parameters are assumed independent, the marginal confidence interval is

$$\delta\Theta_\alpha \leq (\mathbf{V}_{\alpha\alpha})^{\frac{1}{2}}\,s\,t_{n-l,1-\frac{\gamma}{2}} \tag{10}$$

in which $t_{n-l,1-\frac{\gamma}{2}}$ is the t-statistic with $n-l$ degrees of freedom (Bates and Watts 1988). The population standard deviation, s, is approximated by the sample σ. The covariance matrix is defined as

$$\mathbf{V}_\Theta = E(\delta\Theta^*, \delta\Theta^{*^T}) \tag{11}$$

where $E(\cdot)$ is the operator of mathematical expectation. The covariance matrix is commonly approximated by

$$\mathbf{V}_\Theta \approx \mathbf{H}^{*^{-1}} \tag{12}$$

The matrix V_Θ contains all of the correlation information between parameters. The diagonal elements estimate the parameter variances and the off-diagonals estimate their covariances which determine the parameter interaction. If the parameter interdependicies are large, reparameterization schemes are often used to minimize this effect (Ratkowsky 1983). The Gauss approximation is typically considered a good estimate unless the curvature at the optimum is large. Bates and Watts (1988) suggested methods to measure the curvature, or the nonlinearity of the objective function, to assess the accuracy of the linearization approximations.
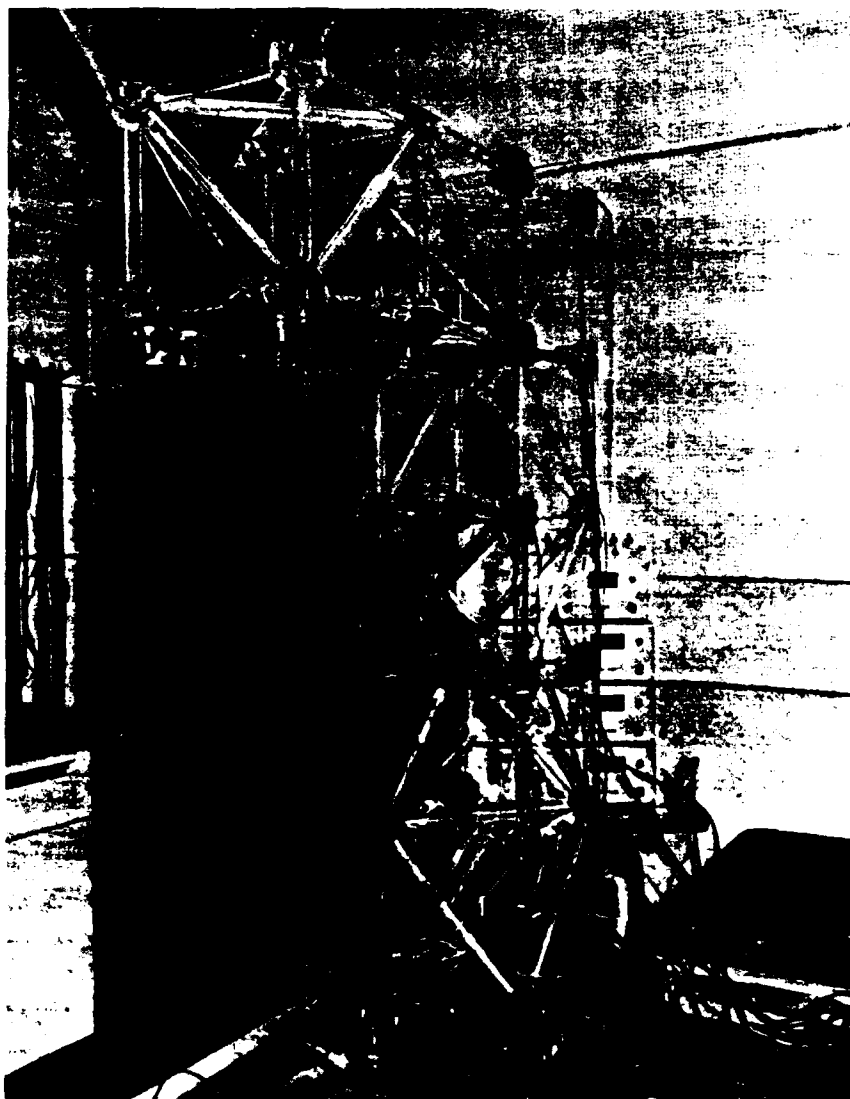
Figure 1: The Truss Structure

3. Truss Structure Description

Figure 1 shows the truss structure which was analyzed. The truss was designed and constructed to have linear characteristics. The truss structure is made of polycarbonate one inch diameter tubing. The truss has one foot cubic bays, which are assembled with the tubes bonded to polycarbonate corner blocks. The truss is mounted on a 2000 pound inertial mass, which is supported on airbags. Finite element modeling of the truss and airbags was straightforward, since the geometry and load paths were well defined.

4. Model Analysis

The **NASTRAN** model of the truss contained two unknown parameters, Young's modulus, E, and the air bag support stiffness, K. Since the restrictions of **NASTRAN** prohibited optimization on material properties directly, properties that were specified on the element definition cards were used. Therefore, E and K were indirectly changed through the use of two normalized parameters, α and β. These parameters were estimated using a nonlinear optimization approach described above (**NASTRAN** uses a modified method of feasible directions approach). A weighted least squares formulation of the objective function was used to compare the theoretical model predictions and experimental data. Normalized parameter values were used to eliminate any scaling difficulties that could cause problems in the optimization routine. Also, the objective functions were formulated such that normalized frequencies were used.

Three different sets of data combinations were used to estimate the structure's parameters and their uncertainties. The first data set included seven elastic modes (modes 2-8), the second introduced one "bounce" mode (mode 1) in place of the last elastic mode (mode 8), and the last set contained only one bounce (mode 1) and one elastic (mode 2). Table 1 shows the experimental observations and the resulting natural frequencies of the identified system for each of the data sets (cases 1-3). All of the data sets provided significant information to accurately predict the modal frequencies with maximum error less than 2.3%. Resulting parameter estimates are shown in Table 2 where $\delta\alpha$ and $\delta\beta$ are deviations from the mean value of α and β, respectively. Marginal confidence intervals (95 percentile) are given for each parameter based on Equation 10.

As expected, when using the first data set the normalized support stiffness, β, was not identified with great confidence (0.923 ± 0.265). This is because the parameter was not highly sensitive to the elastic frequencies. However, when mode 1 was added to the data set (case 2) β was accurately identified. Case 3 was analyzed to see if one bounce and one elastic mode contained sufficient information, which they did, to identify the parameters. Even the predicted frequencies for the data not used specifically in the regression, compared extremely well to experimental values.

As can be seen, the parameter estimates were nearly identical for each of the three data sets. The choice of the the covariance approximation did not make a significant difference either. This was because the problem was linear.

The marginal confid⋅ ⋅ intervals shown in Table 2 are based only on the individual parameter, not a joint probability region as in Equation 9. Therefore, using Equation 10 to estimate a joint confidence region, using a rectangular approximation, typically underestimates the theoretical confidence region (Himmelblau 1980, Bates and Watts 1990) especially if there is any parameter interaction. The joint confidence region for case 2 ($\mathbf{A}_a$) is defined by

$$0.346\delta\alpha^2 - 0.126\delta\alpha \ \delta\beta + 1.67\delta\beta^2 \leq 1.70e - 3 \tag{13}$$

where $\delta\alpha$ and $\delta\beta$ are deviations from the nominal value of α and β, respectively. Figure 2 shows both the marginal confidence intervals (represented by straight dashed lines) and the joint confidence region (represented by the ellipsodial solid line). The shadowed region is the estimated joint confidence region approximated using the marginal confidence intervals. Note how this approximation severely underestimates the confidence in α.
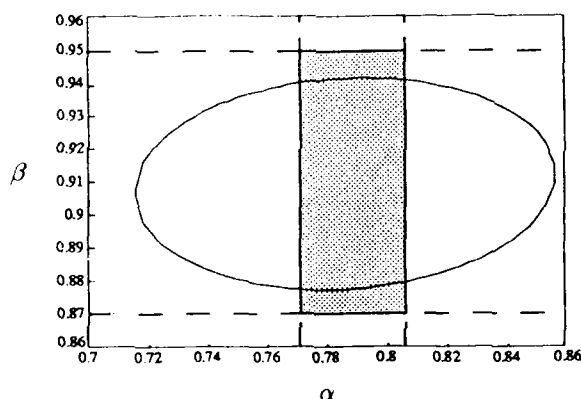
Figure 2: Marginal and Joint Confidence Regions for Case 2

A singular value decomposition (SVD) (Strang 1988) of the covariance matrix was used to further assess the influence of the parameter interaction on the confidence interval approximation. The Hessian matrix was used to approximate the covariance matrix. Since $\mathbf{H}$ is symmetric and positive definite, the matrix factorization,

$$\mathbf{H} = \mathbf{Q}_1 \mathbf{\Sigma} \mathbf{Q}_2^T$$

decomposes $\mathbf{H}$ into $\mathbf{Q}_1 = \mathbf{Q}_2$ that contain the eigenvectors of $\mathbf{H}\mathbf{H}^T$ and the diagonal matrix $\mathbf{\Sigma}$ that contains the singular values (σ_i). The singular values ar the square roots of the nonzero eigenvalues of $\mathbf{H}^T\mathbf{H}$. This information defines a hyperellipsoid, corresponding to an unscaled confidence region, whose axes positions are described by the eigenvectors of $\mathbf{Q}_1$ and relative axes lengths are determined by $1/\sqrt{\sigma_i}$. For

case 2, the eigenvectors are

$$\mathbf{Q}_1 = \begin{bmatrix} 0.999 & -0.046 \\ 0.046 & 0.999 \end{bmatrix} \tag{14}$$

and the singular values are

$$\mathbf{\Sigma}_1 = \begin{bmatrix} 2.94 & 0 \\ 0 & 0.550 \end{bmatrix} \tag{15}$$

It is seen that there was not significant interaction between the parameters since $\mathbf{Q}_1$ is essentially diagonal.

The fact that the problem was quite linear and the parameter interaction was low made the confidence interval approximation quite good. Figures 3 and 4 show the sum of squares contours for cases 2 and 3 over the parameter space. The sum of squares were also elliptical for case 1, however, they were very elongated since the sensitivity of β was smaller than that for α. It is evident that the nonlinearity is small since the contours are quite elliptical or circular. This indicates that the linear approximations using the joint probabilities will give reasonable estimates for the confidence intervals in this problem.

An analysis of the residuals, difference between predicted and fitted values, is commonly used to see qualitively how the model and data met the assumptions of the measurement errors having a zero mean, being independent, and having constant variance. Checking the residuals, values were scattered randomly around a zero mean without any bias, thereby verifying all of these assumptions.

5. CONCLUSIONS

This paper demonstrates that the nonlinear optimization approach to parameter estimation is a flexible and effective method. Although computationally intensive, for large problems, this method lends itself to a wide variety of analytical model formulations and can provide an assessment of the uncertainty of the parameter estimates. Other factors, such as measurement error distributions and instrumentation reliability can be incorporated into the estimation procedure.

An analysis of a truss structure was performed to evaluate the estimation scheme. The truss structure was easily modeled via a finite element model using **NASTRAN**. Parameter estimation was used to identify two crucial parameters yielding a model that gave excellent results. Since the model was linear and accurate, and the parameter interaction was negligible, the linearization schemes used to approximate the confidence intervals worked well.

6. ACKNOWLEDGEMENTS
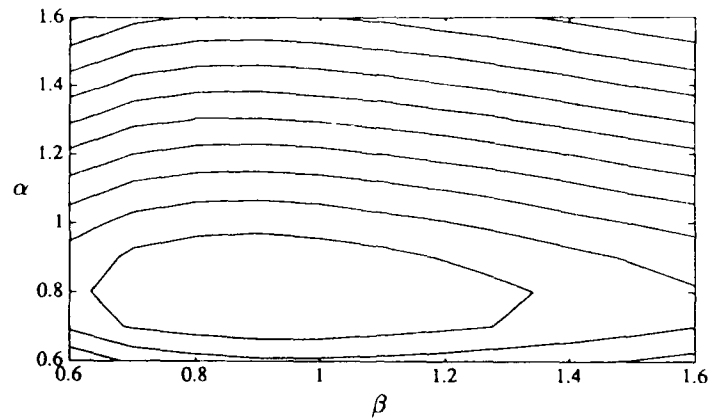
Figure 3: Sum of Squares Contours for Case 2
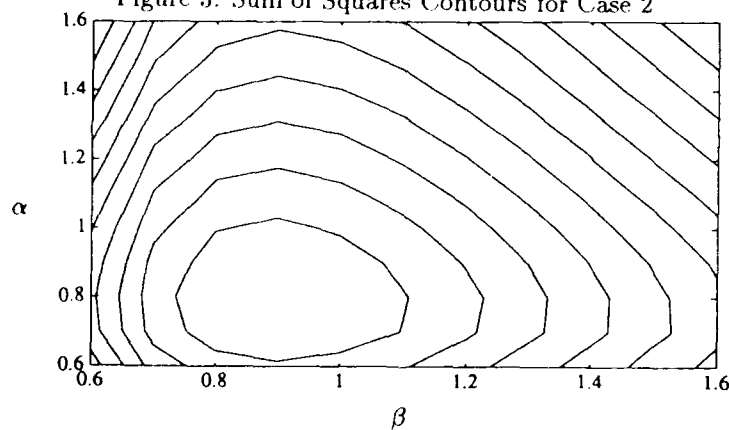
Figure 4: Sum of Squares Contours for Case 3

References

Allen, J.J., Martinez, D. R., "Techniques for Implementing Structural Model Identification Using Test Data," Sandia National Laboratories Report Number SAND90-1185

Bates D. M., Watts, D. W., 1988, *Nonlinear Regression Analysis & Its Applications*, John Wiley and Sons, New York

Bates D. M., Watts, D. W., "Relative Curvature Measures of Nonlinearity," J. R. Statist. Soc., Vol. 42, No. 1, pp. 1-25, 1980

Donaldson J.R., Schnabel, R. B., "Computational Experience With Confidence Regions and Confidence Intervals for Nonlinear Least Squares," Technometrics, Vol. 29, No. 1, pp.67-82, 1987

Gill, P. E., Murray, W., Wright, M. H., *Practical Optimization*, Academic Press, London, 1981

Himmelblau, D. M., 1970, *Process Analysis by Statistical Methods*, John Wiley and Sons, New York

Ratkowsky, D. A., *Nonlinear Regression Modeling*, Marcel Dekker, New York, 1983

Strang, G., *Linear Algebra and Its Applications*, Harcourt Brace Jovanovich, San Diego, 1988

Witkowski, W. R., "Model Identification and Parameter Estimation of Crystallization Processes," Ph. D. Dissertation, University of Texas at Austin, 1990

Table 1: Truss Weighted Least Squares Parameter Estimation Results: Theoretical verses Experimental Frequencies (* Indicate Regressor Variables for Each Case)

Mode	Modal Test Frequencies Freq. (Hz)	Case 1 (modes 2-8) Freq. (Hz)	Error (%)	Case 2 (modes 1-7) Freq. (Hz)	Error (%)	Case 3 (modes 1 and 2) Freq. (Hz)	Error (%)
1	3.53	3.60	1.98	3.57*	1.13	3.55*	0.57
2	10.28	10.30*	0.19	10.32*	0.39	10.28*	0.00
3	10.84	10.84*	0.00	10.85*	0.09	10.80	0.37
4	19.86	19.46*	2.01	19.50*	1.81	19.42	2.21
5	21.28	21.35*	0.33	21.40*	0.56	21.31	0.14
6	45.70	46.18*	2.16	46.28*	2.16	46.10	0.88
7	60.45	59.91*	0.89	60.04*	0.68	59.81	1.06
8	62.46	63.09*	1.01	63.23	1.23	62.97	0.82

Table 2: Truss Weighted Least Squares Parameter Estimation Results: Parameter Estimates and Marginal Confidence Intervals Using Three Different Approximation Schemes for **A**.

		α	$\pm\delta\alpha$	β	$\pm\delta\beta$
Case 1 ($s^2 = 1.46E\text{-}4$)	$\mathbf{A}_a$	0.781	0.0188	0.923	0.265
	$\mathbf{A}_b$	0.781	0.0190	0.923	0.267
	$\mathbf{A}_c$	0.781	0.0190	0.923	0.269
Case 2 ($s^2 = 1.47E\text{-}4$)	$\mathbf{A}_a$	0.785	0.0184	0.909	0.0403
	$\mathbf{A}_b$	0.785	0.0188	0.909	0.0420
	$\mathbf{A}_c$	0.785	0.0182	0.909	0.0438
Case 3 ($s^2 = 7.22E\text{-}6$)	$\mathbf{A}_a$	0.778	0.00966	0.899	0.00898
	$\mathbf{A}_b$	0.778	0.00966	0.899	0.00917
	$\mathbf{A}_c$	0.778	0.00966	0.899	0.00937

The predictive accuracy of structural dynamic models

Timothy K. Hasselman and Jon D. Chrostowski

Engineering Mechanics Associates, Inc.
Torrance, California

Timothy J. Ross

University of New Mexico
Albuquerque, NM

ABSTRACT: This paper previews results from a two–year study to develop
methods for evaluating the predictive accuracy of structural dynamic models.
A model uncertainty database has been compiled from correlated sets of modal
analysis and test data. It is used to assess the predictive accuracy of other
structural models belonging to the same generic categories. Results in the form
of interval predictions on frequency response amplitude and phase for a
deployable truss beam are compared with actual test data. The test data are
shown to fall within the intervals of predictive accuracy.

1. INTRODUCTION

Structural dynamic models are used in a wide variety of applications including
design verification, test support, flight load prediction, and in–flight control. These
models offer what may be called "point prediction" in the sense that the models,
which are themselves deterministic, yield deterministic response when acted upon
by deterministic inputs. Occasionally, stochastic inputs are applied to yield
stochastic response. In this case, response may be expressed in terms of response
intervals, e.g. the mean plus or minus one standard deviation. Rarely is the model
itself considered to be stochastic [e.g. Pannossian, (1988)]. In practical applications,
model uncertainty is accounted for either by perturbing selected model parameters,
or by adjusting input levels in an attempt to offset model uncertainty. Heretofore,
there have been no general tools for objectively evaluating the effects of model
uncertainty on response predictions.

The problem lies in acquiring and processing the data necessary to quantify
model uncertainty. Attempts have been made to express model uncertainty in
terms of design parameters at the finite element level, such as material properties
and local geometry. However, it is not practically feasible to gather sufficient data
at this level because of the diversity of materials, shapes, sizes and methods of
fabrication. Other attempts have been made to gather data at the modal level.
These data, however, have been limited to modal frequencies and damping. Mode
shape data have not been used, possibly because a means for homogenizing the data
has not been apparent.

2. MODEL UNCERTAINTY

Model uncertainty is herein defined as the difference between analysis and test results. It is expressed in terms of modal parameters with two distinct advantages: (1) data are readily available with which to quantify the uncertainty of modal parameters, and (2) model uncertainty expressed in terms of modal parameters is easily propagated through a model to assess predictive accuracy. This paper describes a recently completed effort to develop generic uncertainty models from prior analysis and test experience, and apply them to evaluate the predictive accuracy of other models [Hasselman and Chrostowski (1991)].

Modal mass and stiffness uncertainty are derived form the differences between analysis and test eigenvalues, $^{\circ}\lambda$ and λ, respectively,

$$\Delta\lambda = \lambda - {}^{\circ}\lambda$$

and the cross–orthogonality between the corresponding analysis and test eigenvectors, $^{\circ}\phi$ and ϕ,

$$^{\circ}\phi^{\mathrm{T}}\, {}^{\circ}\mathrm{M}\phi = \psi$$

where $\Delta\lambda$, $^{\circ}\lambda$ and λ are diagonal matrices, $^{\circ}\phi$ and ϕ are rectangular matrices, and $^{\circ}\mathrm{M}$ is the analytical mass matrix. Differences in the modal mass and stiffness matrices based on perturbation analysis [Hasselman and Chrostowski (1991)] are found to be

$$\Delta\mathrm{m} = (\mathrm{I} - \psi) + \mathrm{I} - \psi)^{\mathrm{T}}$$

$$\Delta\mathrm{k} = \Delta\lambda + {}^{\circ}\lambda\,(\mathrm{I} - \psi) + (\mathrm{I} - \psi)^{\mathrm{T}}\,{}^{\circ}\lambda$$

The difference in modal stiffness is placed in dimensionless form by dividing by frequency squared, where $^{\circ}\omega^2 = {}^{\circ}\lambda$.

$$\Delta\bar{\mathrm{k}} = {}^{\circ}\omega^{-1}\,\Delta\lambda\,{}^{\circ}\omega^{-1}$$

The difference in modal damping, $\Delta\xi$, is placed in dimensionless form by dividing by frequency.

$$\Delta\zeta = (2\,{}^{\circ}\omega)^{-1/2}\,\Delta\xi\,(2\,{}^{\circ}\omega)^{-1}$$

The diagonal elements of ξ and ζ are related as

$$\xi_{jj} = 2\,{}^{\circ}\omega_j\zeta_{ii}$$

The modal differential mass, stiffness and damping matrices are then vectorized by the operation

$$\Delta \tilde{r} = \left\{ \begin{array}{l} \text{Vec} (\Delta m) \\ \text{Vec} (\Delta \tilde{k}) \\ \text{Vec} (\Delta \zeta) \end{array} \right\}$$

where Vec (Δm) is a vector containing all of the upper triangular elements of the differential modal mass matrix, Δm, and similarly for $\Delta \tilde{k}$ and $\Delta \zeta$. A covariance matrix of this composite vector is then computed as

$$S_{\tilde{r}\tilde{r}} = E[\Delta r \Delta \tilde{r}^T] = \frac{1}{N} \sum_{k=1}^{N} [\Delta \tilde{r} \Delta \tilde{r}^T]_k$$

for N generically similar structures.

Covariance matrices for four generic categories of model–structure combinations have been derived: (1) Research Models of Large Space Structures (LSS), (2) Pretest Models of Conventional Space Structures (CSS), (3) Posttest Models of Conventional Space Structures, and (4) Combined Categories (1) – (3). Singular value decomposition was performed on all four covariance matrices yielding the eigenvalues shown in Table 1. The number of non zero eigenvalues corresponds to the number of model–structure combinations in the respective database. The sum of eigenvalues, equal to the trace of the matrix, is a measure of the total uncertainty reflected in that database. Posttest CSS models are thereby shown to have approximately half the uncertainty as pretest CSS models.

3. RESPONSE UNCERTAINTY

The covariance matrix of model uncertainty for large space structures was applied to a finite element model of the NASA Mini–Mast structure shown in Figure 1 [Pappa, et. al., (1989)]. In this example, modal damping is assumed to be lognormally distributed with a standard deviation of 0.176 on log ζ, where $10^{0.176} = 1.5$. An interval of $\pm 1\sigma$ on log ζ then corresponds to the interval [$^0\zeta/1.5$, $^0\zeta \times 1.5$] on ζ where $^0\zeta$ is the nominal value of modal damping. The frequency response at Node 14 in the Y direction due to force applied at Node 23 in the Y direction is shown in Figure 2. The left side of Figure 2 shows plots of amplitude and phase as functions of frequency. The nominal (analytically predicted) FRF is indicated by the small "o" symbols. Uncertainty intervals of $\pm 1\sigma$ are indicated by the vertical dashed lines. The range of frequencies is from 0.5 Hz to 5.5 Hz. This range includes two visible poles (resonances) and zeros (anti–resonances). Actually, an additional pole and zero occur near the first resonance because of two closely spaced modes in the X and Y coordinate directions. However, these characteristics are not discernible in the plots.

Two different methods are used for computing the uncertainty intervals. Linear covariance propagation is used when the excitation frequency is not near a pole or zero. With "u" denoting response in terms of log–amplitude and phase, the covariance matrix of response is given by

$$S_{uu} = T_{u\tilde{r}} S_{\tilde{r}\tilde{r}} T_{u\tilde{r}}^T$$

Table 1. Non-zero Eigenvalues of Modal Mass
and Stiffness Covariance Matrices

No.	LSS Research Models	CSS Pretest Models	CSS Posttest Models	LSS & CSS Combined Models
1.	0.570	0.933	0.582	0.599
2.	0.337	0.293	0.059	0.125
3.	0.226	0.171	0.047	0.120
4.	0.125	0.075	0.028	0.110
5.	0.089	0.043	0.014	0.069
6.	0.030	0.022	0.003	0.058
7.		0.010	0.001	˙0.032
8.				0.024
9.				0.024
10.				0.016
11.				0.010
12.				0.006
13.				0.005
14.				0.004
15.				0.004
16.				0.002
17.				0.001
18.	*These singular values were			0.000*
19.	smaller than 0.001 but			0.000*
20.	non zero.			0.000*
Trace	1.347	1.547	0.734	1.210
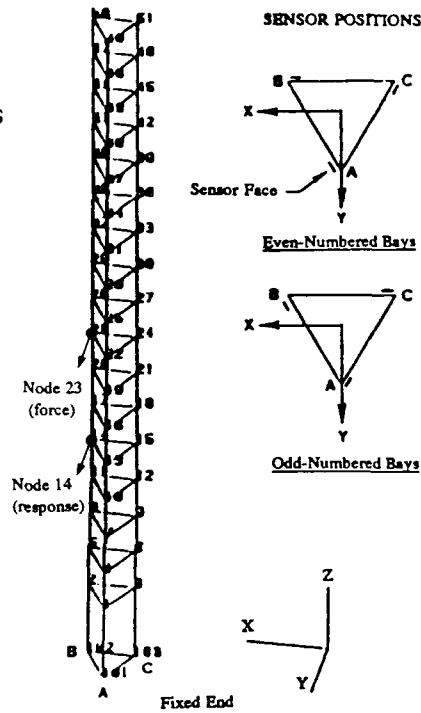
Figure 1. NASA Mini-Mast Structure.

where $T_{u\bar{r}}$ is the derivative matrix, $\partial u / \partial \bar{r}$.

Linear covariance propagation breaks down near the poles and zeros because the derivatives of amplitude and phase with respect to modal mass and stiffness become very large. A different method is needed to evaluate uncertainty intervals near these frequencies. Fuzzy sets offer an alternative to random variables for repre—senting uncertainty [Klir and Folger, (1988)]. Whereas the uncertainty of a random variable is measured in terms of probability, the uncertainty of a fuzzy variable is measured in terms of possibility. Fuzzy set methods can be used to bound response uncertainty near the poles and zeros of an FRF. Thus, whereas the uncertainty intervals obtained from linear covariance propagation tend to diverge near poles and zeros, the possibility intervals obtained from fuzzy set analysis are meaningful.

The uncertainty intervals shown in Figure 2 which are near the frequencies associated with poles or zeros are possibility intervals derived form the Vertex Method of fuzzy sets [Dong and Shah, (1987)]. When a function, such as FRF amplitude or phase, is continuous in parameter space and no extreme point exists in this region (including the boundaries), then the possibility interval (upper and lower bounds) of response is obtained by evaluating all possible combinations of the upper and lower bounds of the parameter intervals. Each combination of parameter values
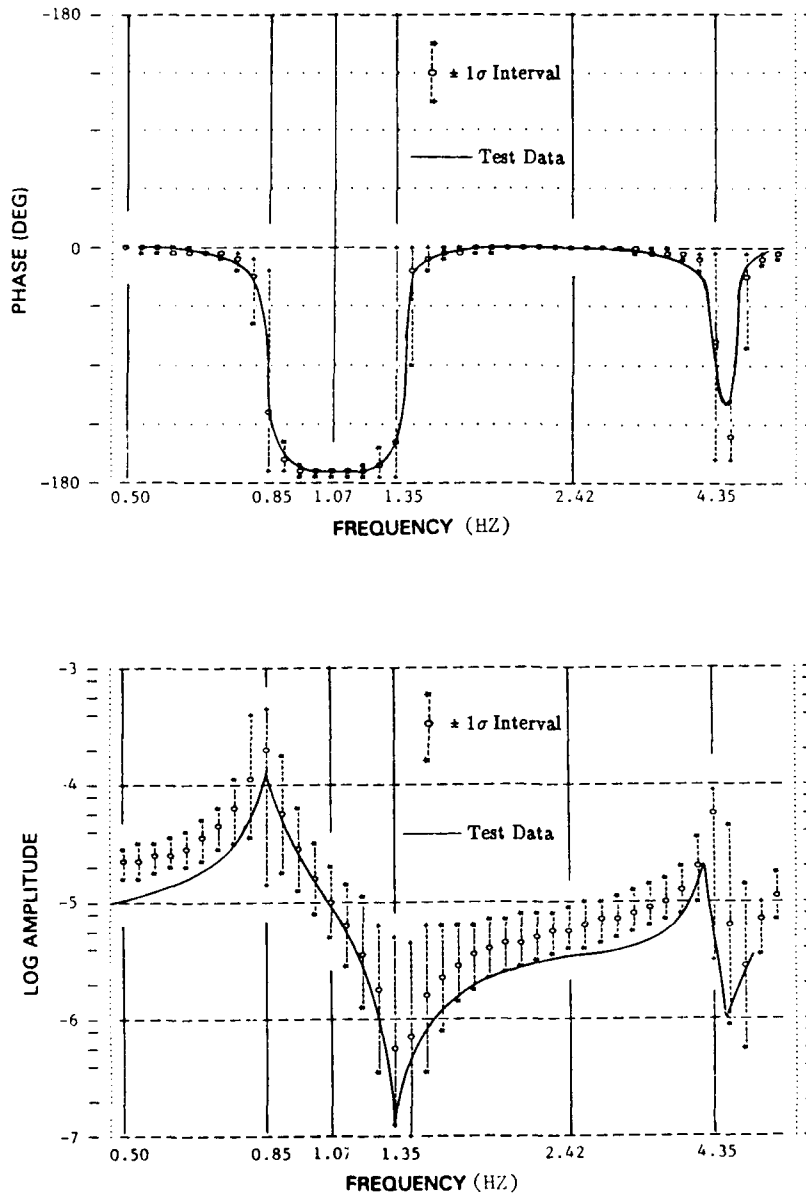
Figure 2. Interval Prediction for
LaRC Mini-Mast Structure.

corresponds to a vertex of a rectangular parallelepiped in the n–dimensional hyperspace defined by n parameters, hence the name "Vertex Method." In this application of the Vertex Method, however, extreme points do occur within the parameter space defined by parameter intervals. They must be located, evaluated and then combined with response at the vertices when determining the possibility intervals of response. Various search techniques have been employed for this purpose.

The $\pm$ 1σ response intervals near poles and zeros have a different meaning than the $\pm$ 1σ response intervals away from poles and zeros. In the case of linear covariance propagation, the uncertainty intervals reflect the nominal response $\pm$ one standard deviation (assuming a log–normal distribution on amplitude). In the case of the Vertex Method, the uncertainty intervals reflect upper and lower bounds based on $\pm$ 1σ parameter intervals.

Distributions of log–amplitude and phase are shown in Figure 3. These correspond to the selected frequencies indicated on the FRF plots. They were obtained by Monte Carlo simulation, assuming a multivariate normal distribution of the modal parameters. The LSS covariance matrix, $S_{\tilde{r}\tilde{r}}$, was first diagonalized; then the resulting generalized parameters with variances given by the eigenvalues of $S_{\tilde{r}\tilde{r}}$ were treated as independent normally distributed random variables for purposes of the Monte Carlo simulation. The resulting distributions are scaled to a maximum value of unity.

The distributions are seen to be consistent with the response intervals shown on the FRF plots. The distribution of log–amplitude near the poles and zero tend to be skewed in the positive direction. The phase distributions tend to be bimodal with modes occurring near 0 or 180 degrees, where most of the response tends to cluster. Phase distributions away from poles and zeros tend to be nearly delta functions at either 0 or 180 degrees. The distributions of log–amplitude away from the poles and zeros were expected to be more nearly Gaussian, based on earlier results for a single–degree–of–freedom model, which indicated that the distributions of log–amplitude off resonance tended to be Gaussian [Hasselman and Chrostowski (1989)]. In this case the distributions tend to be negatively skewed to the left of resonance, and positively skewed to the right of resonance.

4. CONCLUSIONS

The predictive accuracy of a structural dynamic model of a truss–type space structure has been evaluated on the basis of actual analysis and test experience derived from other structures. This is believed to be the first time such an evaluation has been made. Similar efforts in the past have limited model uncer-tainty to uncorrelated modal frequency and damping parameters. This effort considers the correlated variabilities of all modal mass and stiffness matrix elements, as well as modal damping.

The analysis utilizes a database compiled from twenty–two analysis/test data sets. These data sets are partitioned into three generic categories representing both pretest and posttest models of conventional space structures, and research models of large truss–type space structures. The statistics of these three data sets were compared with each other and with those of the combined data set. The data set for large space structures is used in the present example.
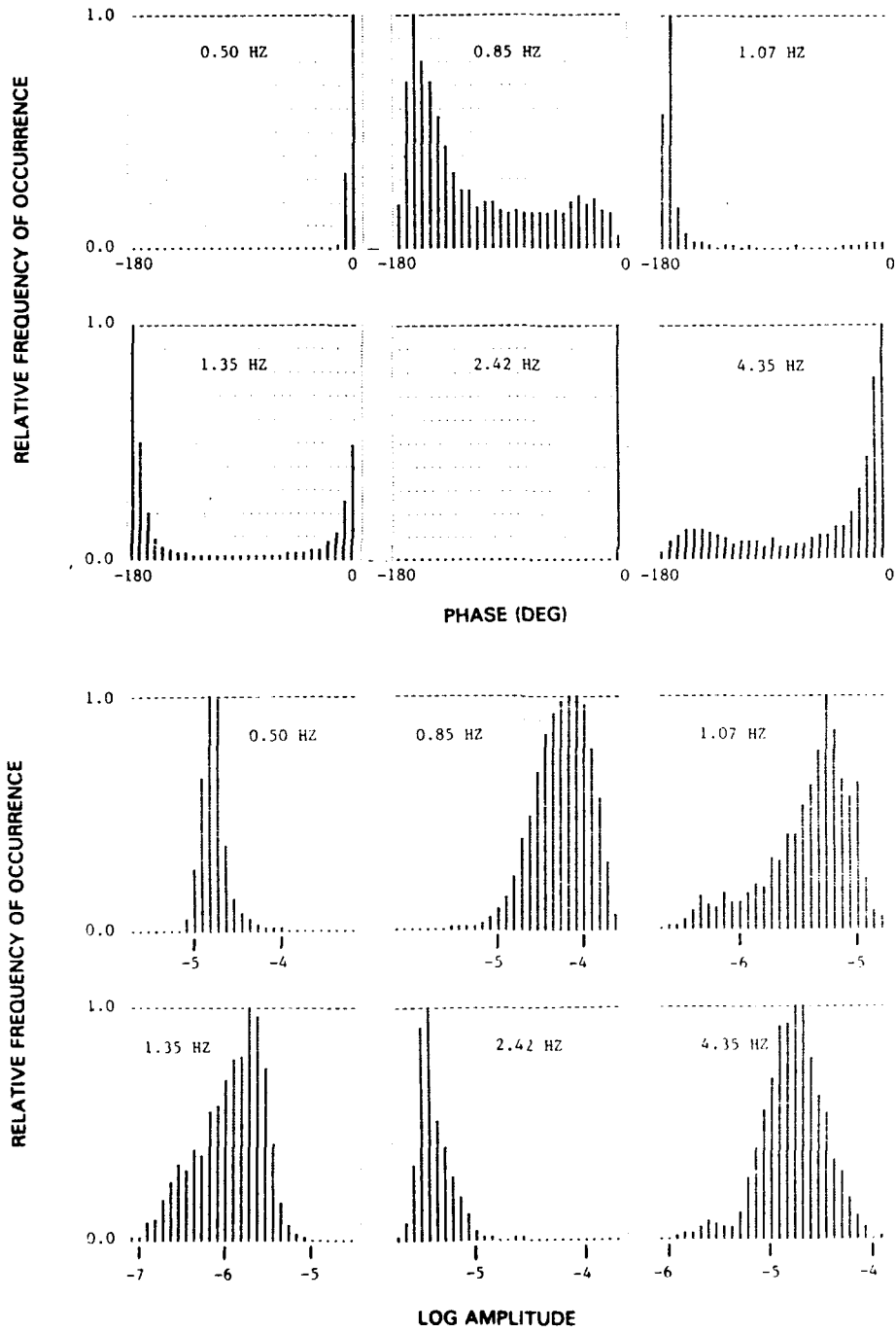
Figure 3. Distributions of Log-amplitude and Phase at
the Selected Frequencies Shown in Figure 2.

Three methods for evaluating predictive accuracy were employed, including a linearization method, a fuzzy set method and a numerical simulation method. The linearization method is appropriate to use at frequencies which are not close to poles or zeros. The fuzzy set method is appropriate to use near poles and zeros, but impractical to use elsewhere. Numerical simulation can be used anywhere but is computationally expensive. Nevertheless, it serves as a good check on the other two methods, and provides distributions of response.

The data and methods introduced here should be useful in the design of control systems for large flexible space structures where a trade-off is made between performance and robustness. The ability to realistically quantify the predictive accuracy of structural dynamic models should enable control system designers to avoid unnecessary conservatism, thereby enhancing performance.

ACKNOWLEDGEMENTS

REFERENCES

Dong, W., and Shah, H., "Vertex Method for Computing Functions of Fuzzy Variables", Journal of Fuzzy Sets and Systems," Vol. 24, pp. 65–78, 1987.

Hasselman, T.K. and Chrostowski, J.D., "Methods for Evaluating the Predictive Accuracy of Structural Dynamic Models" Engineering Mechanics Associates Technical Report No. TR–91–1152, prepared for the National Aeronautics and Space Administration, 1991.

Hasselman, T.K. and Chrowstowski, J.D., "Evaluation of Predictive Accuracy in Structural Dynamics Models", Seventh International Modal Analysis Conference, Las Vegas, NV, February 1989, Vol. 1, pp. 360–366.

Klir, G and Folger, T., "Fuzzy Sets, Uncertainty and Information," Prentice Hall, Englewood Cliffs, NJ, 1988.

Pannossian, Hagop V., "Optimal Stochastic Modeling and Control of Flexible Structures," HR Textron Report No. AFWAL–TR–88–3066, prepared for the Flight Dynamics Laboratory, Wright–Patterson Air Force Base, September, 1988.

Pappa, R., et. al., "Mini–Mast CSI Testbed User's Guide," NASA Langley Research Center, March, 1989.

Control structure optimization of active/passive damping in large flexible structures

G L Slater*, J Xu*, M D McLaren+

* University of Cincinnati, Cincinnati, OH 45221

+ LORAL/Space Systems, Palo Alto, CA 94303

Abstract. Optimal passive and active damping control can be considered in the context of a general control/structure optimization problem. Using a mean square output response approach, it is shown how an optimal mix of active and passive elements can be determined for a flexible structure along with the optimal structural elements.

1. INTRODUCTION

Because of the low inherent damping of the typical large flexible structure, some form of vibration control methodology is necessary to reduce the vibration response to an acceptable level. The control community has traditionally addressed this problem from an active control viewpoint, and has proposed a multitude of mathematical techniques for solving this difficult feedback control problem. While elegant in their mathematics, these analyses often show little consideration for the mass, cost, and reliability of the hardware required for these control strategies. An alternate approach to active vibration control is to implement vibration suppression through some type of passive means. Passive schemes have a long history of use due to their reliability and effectiveness. See e.g., McLaughlin.

The question which we address in this paper is the determination of the optimal combination of active and passive techniques for a structure to use. In previous work, the authors have proposed a stochastic approach to optimal control/structure design whereby the optimization problem is to find a minimum weight structure subject to fixed output constraints and to fixed control energy constraints (see Slater(88), McLaren(90)). The structure configuration as well as the controller structure is assumed to be specified. For example, in a perfect information environment, a full state controller yields the best controller performance, and hence the minimum weight structure (assuming a fixed controller mass.

If feedback is restricted to outputs, either with or without additional measurement noise, then the control structure can be modified to a direct output feedback, or filter feedback form. Using this approach one can, for example, determine the mass reduction possible through additional sensors.

Our approach to include passive control is to consider the passive damper as a special type of output controller. For example, a linear dashpot is an element

which generates a force opposing relative motion between two connected locations. This can be considered as an output controller, where the controller gain is the damping coefficient associated with that element. The task required to complete the optimization is a difficult one. If we are attempting to minimize the total mass of the structure, we must first ascertain the mass penalty associated with the controller (either active or passive). In fact, we are in no position to answer that question completely in this paper. Rather our approach will be to consider the problem parametrically, so that sensitivities of the optimal solution to component masses can be ascertained. The actual optimum can be obtained when appropriate information is available to the designer.

2. MATHEMATICAL FRAMEWORK FOR CONTROL/STRUCTURE OPTIMIZATION

The approach taken in this analysis is to consider the structure from a dynamic response point of view. We assume that the fundamental structural constraint is to support a load, or to hold various sub-system components (experiments, etc.) together to a required degree of accuracy in the presence of some form of excitation. The effect of the control system on this design problem is to effect a trade-off to reduce the effect of flexibility. As the structure is made lighter and more flexible, the control system can be used to reduce deflections and stresses to acceptable levels.

The mathematical approach taken to quantify the control-structure relationship is to initially regard the controller structure as fixed and satisfying certain control magnitude constraints, which for this analysis will be assumed to be a mean square control energy bound. Similarly the external force environment on the structure is known and is assumed to be stochastic with known mean square energy and spectrum. Within this framework the optimal structure-control design problem is to find the structural parameters and the control law to minimize a performance index while satisfying control energy and displacement constraints. This may be posed as a mathematical programming problem.

Assume the system is given as

$$
\begin{aligned}
\dot{x} &= Ax + Bu + Gd \\
y &= Cx \\
z &= Hx + v
\end{aligned}
\tag{1}
$$

where we have the conventional definitions of the state(x), control(u), performance output(y), measured output(z), and input and output disturbances (d, v, respectively). Here we will assume that d is Gaussian white noise, $d \sim N(0, D)$ For this system we pose the following optimization problem:

Minimize the function $J(p_1, p_2, \ldots)$, where the p_i are structural parameters such as mass, stiffness, area, etc., and find the feedback law

$$
u = f(z)
\tag{2}
$$

where $f(\cdot)$ is a specified functional form based on the controller type desired.

For example, if $z \equiv x$, then the problem is full state feedback and $f(\cdot)$ becomes naturally a gain matrix. The resulting optimization becomes a special form of the linear quadratic regulator. The functional $f(\cdot)$ can specify an (unknown) dynamical system in the general output feedback problem. For the problem considered in this paper we consider the controller to consist of two parts: The first is the passive controller which consists of unknown damping coefficients at specific locations. The second part is a "conventional" full state active controller. The active controls must satisfy the control energy constraints

$$\mathrm{E}[u^T R u] = \beta^2 \tag{3}$$

while the outputs satisfy

$$\mathrm{E}[y^T W_i y] \leq w_i \qquad \text{(Output disturbance Inequalities, } i = 1, \ldots, n) \tag{4}$$

The rationale for a fixed control energy constraint is that for an active control implementation, the desired control should utilize the full control capability to reduce the structural loading. The output inequalities may be several, in which case one or more constraints may be equality constraints, but others will be strict inequalities.

Using the Gaussian disturbance case, the expectations can be converted to simple operations on the covariance matrix, which is determined by a Lyapunov equation (assuming here linear controls). For details on this see the references. Using this approach the optimization framework is quite flexible and can be adjusted to a variety of special types of constraints and controllers. Numerically the resulting optimization problem can be solved by a variety of general non-linear optimization software. For the full state feedback case, linear regulator software can be incorporated also.

The physical details of the active and passive components are not explicitly considered in this paper. In general however we may consider the mass added by active control elements to be proportional to the mean square energy (β^2), while the mass of the passive damping elements is proportional to the damping element "c". Results using this parametric form are discussed in the next section.

3. APPLICATION TO DRAPER I TRUSS

In solving an optimal structure/controller problem (McLaren(90) determined the optimal mass of the tetrahedral truss model model known as "Draper I" (see Figure 1) for various types of controller implementations. For this structure there are six control actuators, situated in each of the base legs of the truss, and six collocated velocity sensors, giving the longitudinal velocity of each truss leg. The advantage of full state information is shown dramatically by comparing the minimum mass structure using full state active control with the minimum mass using only the six

velocity sensors. For this case the problem was to design the optimal structural elements to minimize the mass and to simultaneously design the controller. The controller energy is β^2 while the output constraint is $E(y^2) = \alpha^2$. Note in both of these cases, no damping or controller mass penalty was assumed. For these two cases the final masses are shown in Figure 2. The results indicate that generally full state designs may achieve almost 50% less mass than the optimum velocity feedback designs. Based on the large mass reduction from full state feedback, its seems reasonable that for this, and probably for most structures, the advantage of an active feedback scheme is real and can be quantified explicitly.
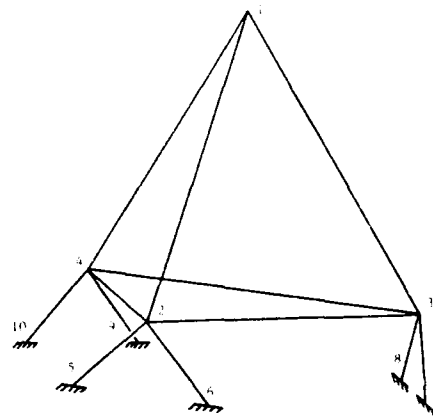
Figure 1: The DRAPER I truss

We also consider the case of a fixed structure and examine the optimal combination of active control and purely local passive damping. Numerically this case is computed by insertion of a damping matrix and a full state feedback design. The output constraint and control constraint remains as in the prior case. Due to the symmetry of the DRAPER structure the damping elements were broken into three components. The first component is equal damping added to the three main legs connecting the base to the vertex. The second is damping added to the base triangle of the structure, and the third is damping added to the six legs connecting the structure to ground. As expected, damping #2 in the base plane has little effect on response, however the role of damping #1 and damping #3 indicates a useful and interesting tradeoff between the passive damping added, and the amount of active control energy required. The most important point to be made is that the addition of passive damping is not necessarily beneficial. Indeed the location and size of the disturbance, the displacement constraint amplitude, and the relative mass penalty associated with the passive and active control components all play a large part in establishing the optimum combinations. If the disturbance is applied at the top vertex, the base damping is relatively unimportant, while a moderate amount of damping in the legs can substantially reduce the active control costs. A typical cost curve for a particular weighting of active and passive control costs is shown in Figure 3. Although not displayed on this graph it can easily be shown that decreasing the allowable tip deflection, generally decreases the amount of passive damping which required.

If the disturbance enters through the base of the structure, then the relative importance of the two damping components becomes more complicated. For very tightly controlled displacements, zero leg damping results in the lowest active control cost. As the displacement constraint on the tip is allowed to grow, then the

leg damping can aid the overall active control costs. These trends are shown in Figure 4. The optimal blend will of course depend on the relative cost penalty of the damping components.
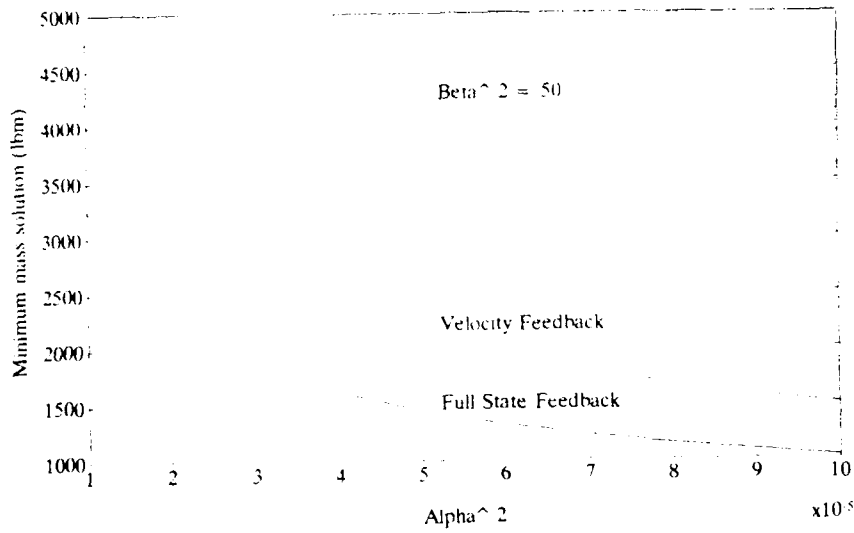
Figure 2: Optimal DRAPER I mass for full state vs. velocity feedback
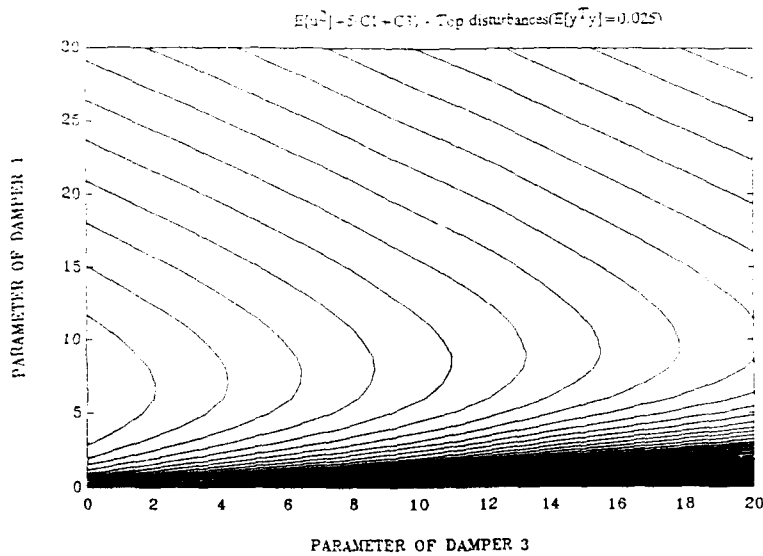
Figure 3: Cost contours showing optimal allocation of passive damping
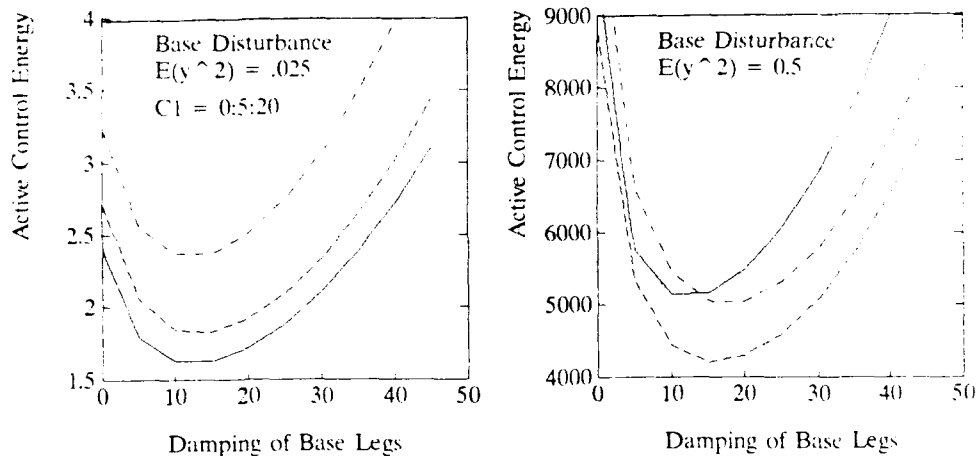
Figure 4: Effect of passive damping on active control energy required

4. CONCLUSIONS

The results shown indicate that there is an easy way to explicitly characterize the relative merits of an active versus a passive control scheme. No attempt here is made to quantify the exact trade-off due to the uncertainty in mass figures associated with the controller types. This, and further exploration of controller trade-offs, are subjects of continuing research.

ACKNOWLEDGEMENTS

REFERENCES

Slater G L, "A Disturbance Model for the Optimization of Control/Structure Interactions for Flexible Dynamic Systems", Paper 88-4058, AIAA Guidance & Control Meeting. Minneapolis, MN, August, 1988.

McLaren M D, Slater G L, "A Disturbance Based Control/Structure Design Algorithm", Proceedings of the 3rd Annual Conference on Aerospace Computational Control, August, 1989, Pasadena, CA.

McLaren M D, Slater G L, "A Covariance approach to Integrated Control/Structure Optimization", Paper 90-1211, AIAA Dynamics Specialist's Conference, April, 1990.

McLaughlin F A, "Integrated Structural Damping and Control design System design for High Order Flexible Systems", Ph.D. Dissertation, Stanford University, SUDAAR 601, December 1990.

Synergism of passive viscoelastic damping and active control in a high modal density structure

Dr Lynn Rogers
Consultant
3945 N Lake Shore Dr
Jamestown OH 45335-1119
(513) 675-2258

ABSTRACT

Generalizations of control-structure-interaction are drawn for the case of passive viscoelastic damping and active control for challenging vibration suppression in high modal density structure. The results of several analytic studies are summarized together with selected experimental results. Passive damping has been shown to remove large amounts of vibratory energy, lower the response of the structure to excitation, stabilize any active control system, and make an active system more robust. For extremely challenging vibration suppression requirements, an optimum blend of active and passive is the only practical approach.

INTRODUCTION

The necessity and/or desirability of suppressing the noise or vibration of a large variety of structures which are characterized by their complexity and consequent high modal density has become commonplace. This is true especially in certain high performance military satellites, but also in many other types of applications. The performance criteria may be resonant high cycle fatigue life, survival of the launch environment, providing micro-gravity orbital operations, precision pointing, settling time, jitter suppression, alignment of optical elements, noise suppression, etc.

Passive damping technology has reached a degree of maturity to the point that many applications are practical, and opportunities for further advancement are apparent. Similarly, active control is a well known technology.

The hierarchy of vibration suppression approaches is well established. Ordinarily, the dynamic disturbances are minimized. Then, if possible, the disturbance is isolated. The receiver is isolated if practical. Re-design of natural frequencies, stiffness, etc., is then appropriate. Beef-up in the instance of high cycle fatigue rarely extends life significantly because the disturbance is typically wide band, and resonant conditions are still encountered. Passive damping technology may be appropriate at any point in the design cycle, but especially if it is early in the design. Active control technology is typically the last in the hierarchy, especially if separate sensors and actuators are required.

Disturbances may be categorized in degree of difficulty. If the disturbance is sinusoidal of fixed frequency, it is typically easy to accommodate during design. If

disturbance frequencies are swept over a significant range, it will probably be difficult to avoid resonances. If the disturbance is broad band random, it is generally impossible to avoid resonances.

Passive damping may provide adequate performance if the criteria is vibration level, either peak to peak or rms. It may also be satisfactory in the case of jitter, settling time, noise or harshness. There are also types of applications where passive damping generally does not work, namely, flexible rotor modes, noise thru transmission of flexible structure, and others.

The measure of damping which is almost universally understood is "Q", the quality factor borrowed from electrical engineering and resonant circuits. The viscous critical damping fraction is also used widely. The modal loss factor, the reciprocal of Q, is typically used by viscoelastic material damping engineers.

DEFINITION OF THE PROBLEM

The most challenging problem is considered to be broadband vibration suppression of questionably modelled, modally dense structure. This situation has occurred and will continue to occur repeatedly in the future.

Practical structures are modally dense. It is didactic to consider beams (one dimensional structure) and plates (two dimensional), but realistic structure is three dimensional, large and flimsy. The significance of this is that structure will possess many natural vibration modes with ratios of adjacent frequencies nearly equal to unity.

The questionably modelled aspect arises because analytical predictions are not sufficiently accurate and also because the in-service identification of the plant is severely challenging. The relative difficulty of identification depends greatly on the modal damping in the structure; very low damping requires long observation times. It is here asserted that the optimum structure incorporates levels of modal damping on the order of five per cent of critical viscous. These levels present challenges of their own with regard to identification. When it is considered that plant geometry and mass properties may vary dramatically, the situation becomes clear regarding plant identification.

The problem is also broadband, both because the disturbances will be a wide range of frequencies and will include random, and because the natural global and local frequencies of the structure will cover an extremely wide range. The confrontation is with both a wide range of disturbances and a wide range of resonances.

The need for high precision in this situation provides the ultimate definition of the problem.

SELECTED STUDIES

A study by von Flotow and Vos provided a summary which indicated that flexible modes beyond the control bandwidth must be gain stabilized; furthermore, flexible modes within the control bandwidth must be robustly phase stabilized. Passive damping allows modelling infidelity. This is necessary for stability without regard for performance, which is the essential consideration.

A paper summarizing a design study by Garibotti considered a retargeting maneuver of a space based laser. The requirement was on settling time for line of sight. Twenty-four flexible modes and 21 collocated sensor/actuator pairs were used. Three values of Young's

modulus were used. To simplify the results dramatically, the control force and the control energy drops considerably at 9 % passive damping.

Another paper study by Bicos analyzed the settling time of a space station model and of a neutral particle beam after a retargeting maneuver. Again to simplify, high specific stiffness materials improve performance. High strain energy members were considered to be damped. It was concluded that both active and passive are required.

The PACOSS program, which was a $5.3M design, fabricate and test effort, provided several conclusions. Major experimental articles were designed, fabricated and tested. The Dynamic Test Article had 27 global modes under 10 Hz. There were 5 general types of viscoelastic damping designs used. Modal damping as high as 13% was achieved. It was established that viscoelastic damping is designable, mode by mode. Experimental identification of the DTA proved to be challenging. Fully half of the program resources were expended on active control investigations. Five control algorithms were experimentally implemented. It was established that there is a strong synergism between active control and passive damping. Viscous dampers were investigated as well as viscoelastic.

These studies establish that the required active control energy is dramatically reduced for viable amounts of passive damping and that both active and passive are required.

PASSIVE DAMPING IS A DESIGN PARAMETER

Numerous hardware investigations and viscoelastic passive damping applications have established that analysis and experiment correlate very well. On multiple occasions, viscoelastic damping has been developed on an accelerated time scale and used to enable launch of a satellite and its orbital performance. Satisfactory results have been achieved on these occasions using conventional finite element analysis programs.

Damped laminated steel is in production for automotive valve covers, oil pans, etc., in the USA. In Japan, it is used widely in household appliances. It can be deep drawn, welded, shaped, painted, etc. Damped computer disc drives are in wide production in the US.

RECOMMENDATIONS

It is clear that, in many cases, active/passive vibration/noise/jitter suppression engineers are severely challenged in meeting system performance requirements. The necessity for heroic efforts and breakthrus are commonplace.

It is equally clear that confidence levels in technical/cost/schedule are not adequately established for active/passive techniques to the point that program managers believe payoffs are commensurate with risks.

A quantum leap in jitter performance thru extensive viscoelastic structure is guaranteed and is affordable. Several programs to design, fabricate and test hardware as close as possible to future system hardware is essential.

REFERENCES

anon, DAMPING '89, West Palm Beach FL, Feb 8-10 1989, WRDC-TR-89-3116 (3 vols).

anon, DAMPING '91, San Diego CA, Feb 13-15 1991, WL-TR-91-3078 (3 vols).

Anderson E and Jacques R, The Role of Passive Damping in a Controlled Structures Testbed, Active Materials and Adaptive Structures Conference, Nov 4-8, 1991.

Bicos A S, Damping of a Large Space Platform, DAMPING '89, Paper HBB.

Edberg D L and Bicos A S, Design and Development of Passive and Active Damping Concepts for Adaptive Space Structures, Active Materials and Adaptive Structures Conference, Nov 4-8, 1991.

Garibotti J, Payoff of Passive Damping in Active Control of Large Space Structures, DAMPING '89, Paper HBC.

Hanks B and Gilbert M G, Research on the Structural Dynamics and Control of Flexible Spacecraft, Active Materials and Adaptive Structures Conference, Nov 4-8, 1991.

Henderson J P and Stover P E, Technology Integration Requirements for Adaptive Structures in Space, Active Materials and Adaptive Structures Conference, Nov 4-8, 1991.

Lurie B, O'Brien J, Sirlin S, and Fanson J, The Dial-a-Strut Controller for Structural Damping, Active Materials and Adaptive Structures Conference, Nov 4-8, 1991.

von Flotow A, Hagood N, Johnson C D, Keinholz D, and Davis L P, Case Studies in Passive Piezoceramic, Viscous and Viscoelastic Damping, Active Materials and Adaptive Structures Conference, Nov 4-8, 1991.

von Flotow A and Vos D W, The Need for Passive Damping in Feedback Controlled Flexible Structures,. DAMPING '91, Paper GBB.

Yiu Y P, Austin E M, and Ginter S D, Passive Damping Design for Control System Stability on the SPICE Testbed, Active Materials and Adaptive Structures Conference, Nov 4-8, 1991.

The optimal mix of passive and active control with actuator selection

Jae H. Kim and Robert E. Skelton

School of Aeronautics and Astronautics, Purdue University, West Lafayette, IN47907

ABSTRACT : This paper shows how to redesign a structure to make it easier to control. Given an initial structure, a set of noisy actuators and a controller are selected to minimize the control effort subject to the output RMS inequalities. The initial structure and the Output Variance Constrained (OVC) controller constitute a closed-loop system which yields the required performance. Then the structure and the controller are simultaneously redesigned to minimize the active control effort, while preserving all the closed-loop properties of the original closed-loop system.

1. INTRODUCTION

The selection of actuators (their number, type, size and locations) is one of the most important problems in the synthesis of a control system. The cost, reliability and weight of the input devices limits their characteristics. Superfluous actuators can increase plant disturbances or model uncertainties without contributing much to the system performance [1]. Furthermore, an unfavorable selection resulting in a plant poorly conditioned (in the sense of input-to-output characteristics) may lead to controller design difficulties. Hence, simplistic design methods have to be replaced by more sophisticated ones for which unnecessarily excessive effort must be made. The size (i.e., dynamic range) of the devices must also be taken into account during the selection process because any physical device has its own limitation. In general, a good choice of actuators can be made when a closed-loop (rather than open-loop) system performance is considered as a selection criterion. So the selection algorithm must be integrated with the controller design process. In the first part of this paper, a set of actuators is selected which consumes minimum control energy while output variance constraints are satisfied. The actuator selection procedure is an iterative algorithm composed of two parts; an output variance constrained control and an input variance constrained control algorithms.

Structure design and control design have been independently optimized to improve the dynamic response of various mechanical structures [2], but these theories have not been integrated in any tractable way. However, a *combined* structure redesign and active control design can achieve better performance than simply designing the controller *after* the structure is designed. In order to get the required performance, the control effort required of a strictly active control system might be excessively large. In this case, one can benefit greatly by both structure and control redesign in a coordinated way. One approach is to *simultaneously* optimize the structural and control parameters, [3-4]. This leads to nonlinear mathematical programming problems with no guarantee of stability, nor a globally optimal solution, nor the convergence of algorithms. Our approach guarantees stability and a globally optimal solution in a finite number of iterations.

Recently [5], the idea was advanced that the controller should be designed *first* for the given plant, then both the structure and the controller should be redesigned to yield the same response as the original plant with the original controller. Hence, for specified closed-loop system performances achieved by some (given) controller acting on the original structure, the best combination of passive control (structure redesign) and active control (control redesign) for mechanical structures was derived by minimizing the active control effort required to yield the same closed-loop system matrix as the original controlled system. However, in [5] only a static output feedback controller was used before and after structure redesign. We shall extend these results to the dynamic feedback case. Furthermore, the initial controller is designed with optimally selected actuators.

2. ACTUATOR SELECTION

In this section we propose an iterative algorithm which simultaneously solves both the actuator selection problem and control problem while closed-loop performance is taken into account during the selection process. Consider a plant described by

$$\dot{x}_p = A_p x_p + B_p \beta(u + w_a) + D_p w_p \ , \quad y = C_p x_p \tag{2.1}$$

where $x_p \in \mathbb{R}^{n_x}$, $u \in \mathbb{R}^{n_u}$ and $y \in \mathbb{R}^{n_y}$ are the vectors of plant state, input and output. The diagonal matrix β is to be selected with the i-th diagonal element $\beta_i = 0$ or 1. $\beta_i = 1$ means that the i-th actuator is selected for a controller design. The columns of B_p matrix are dictated by the locations and types of available actuators. The actuator noise w_a and the plant disturbance w_p are assumed to be zero mean Gaussian white noise processes with intensity W_a and W_p, respectively. The problem under consideration may be stated as follows:

Optimal Actuator Selection (OAS) Problem

Given a positive definite input weighting matrix R_0 and upper bounds of output variances σ^2, find the N actuator locations (or location index matrix β) out of $n_u (> N)$ available locations, and the corresponding control law u such that

$$\underset{\beta, u}{\text{Min}} \ \mathcal{E}_\infty (\beta u)^T R_0 (\beta u) \quad \text{subject to} \quad \mathcal{E}_\infty y_i^2 \le \sigma_i^2 \ , \quad i = 1, 2, \cdots, n_y \tag{2.2}$$

where $\mathcal{E}_\infty \triangleq \lim_{t \to \infty} \mathcal{E}$ is the expectation operator.

Notice that in the OAS Problem, β is a matrix of "complicating variables" in the sense that when β is temporarily held fixed, the remaining problem is considerably more tractable. In our case, when β is fixed we have the OVC control problem for which there are well-developed algorithms [6-8]. This favorable observation is our motivation to use the following iterative algorithm to select a set of actuators.

First we consider the following two problems which are closely related to the OAS problem; here Ω denotes a set of stabilizing control laws:

Output Variance Constrained (OVC) Control Problem

For given *diagonal* matrix $R_0 > 0$ and σ_i^2's,

$$\underset{u \in \Omega}{\min} \ \mathcal{E}_\infty u^T R_0 u \quad \text{subject to} \quad \mathcal{E}_\infty y_i^2 \le \sigma_i^2, \quad i = 1, \cdots, n_y \ . \tag{2.3}$$

Input Variance Constrained (IVC) Control Problem

For given *diagonal* matrix $Q_0 \ge 0$ and μ_j^2's,

$$\underset{u \in \Omega}{\min} \ \mathcal{E}_\infty y^T Q_0 y \quad \text{subject to} \quad \mathcal{E}_\infty u_j^2 \le \mu_j^2, \quad j = 1, \cdots, n_u \ . \tag{2.4}$$

The following theorem provides the relationship between the OVC and IVC control problems. See also [11] for solutions of problems similar to OVC/IVC.

Theorem 1 [8]

Let $\bar{u}$ and q be, respectively, the solution and the optimal multiplier vector of the OVC Control Problem. Suppose that for the IVC Control Problem we choose

$$Q_0 = \text{diag}(\bar{q}) \quad \text{and} \quad \mu_j^2 = \mathcal{E}_\infty \bar{u}_j^2 \ , \ j = 1, 2, \cdots, n_u \ , \tag{2.5}$$

then $\bar{u}$ is also a solution to the IVC Control Problem and the corresponding multipliers are the diagonal elements of R_0 given in the OVC control problem.

Before we provide an actuator selection algorithm, we consider another closely related problem whose solution is dependent on a perturbation parameter:

Perturbed IVC Control Problem

For a given matrix $Q_0 \geq 0$ and a vector μ^2,

$$\min_{u \in \Omega} \mathcal{E}_\infty y^T Q_0 y \quad \text{subject to } \mathcal{E}_\infty u_j^2 \leq \mu_j^2 + \varepsilon_j, \quad j = 1, \cdots, n_u \tag{2.6}$$

where the perturbation parameters ε_j's are considered to be fixed.

The perturbed problem (2.6) has been studied by many mathematicians (see [9] and references therein). Under mild conditions [9], we have the following theorem;

Theorem 2 [9, Theorem 5.4.1]

For ε in a neighborhood of 0, the gradient of the optimal value function is

$$\frac{\partial}{\partial \varepsilon_j} \left[\mathcal{E}_\infty \bar{y}^T Q_0 \bar{y} \right] = -r_j(\varepsilon) \tag{2.7}$$

where $\bar{y}$ is the output vector when $\bar{u}$ is used in (2.1).

Theorems 1 and 2 are basis of the following algorithm for solving the OAS in (2.2);

An OAS Algorithm

Step 1 *Set $k = 0$ and $\beta_j^{(k)} = 1$ for all j.*

Step 2 *Solve the OVC control problem with $R_0 > 0$ and calculate the optimal input variances $\mathcal{E}_\infty \bar{u}_j^2$ for all j such that $\beta_j^{(k)} = 1$. The multiplier vector $\bar{q}$ is a part of solution.*

Step 3 *Solve the IVC control problem with $Q_0 = \text{diag}[\bar{q}_1, \bar{q}_2, \cdots, \bar{q}_{n_y}]$ and an upper bound of input variance, μ^2 (from (2.9a). The multiplier vector $\bar{r}$ is a part of solution.*

Step 4 *Calculate the actuator effectiveness values*

$$\alpha_j = \bar{r}_j \text{ (from Step 3)} \times \frac{\mathcal{E}_\infty \bar{u}_j^2 \text{ (from Step 2)}}{\mu_j^2} \quad \text{for j such that } \beta_j^{(k)} = 1 . \tag{2.8}$$

Step 5 *Set $k = k + 1$ and delete one actuator which has the smallest value of α_j (i.e., set $\beta_j^{(k)} = 0$ for the corresponding actuator).*

Step 6 *Repeat Steps 2 thru 5 until $N = \sum\limits_{j=1}^{n_u} \beta_j^{(k)}$.*

The final controller would be the one from Step 2. Hence the output variance constraints are guaranteed to be satisfied. In case there are variance constraints on each actuator, they should be used for the upper bound μ_j^2 in Step 3 to solve the IVC control problem. Otherwise, the following value is recommended;

$$\mu_j^2 = \gamma_j \mathcal{E}_\infty \bar{u}_j^2 \quad \text{for all j such that } \beta_j^{(k)} = 1 \tag{2.9a}$$

where $\mathcal{E}_\infty \bar{u}_j^2$ is available from the solution of the OVC control problem in Step 2 and

$$\gamma_j = 1 - \mathcal{E}_\infty \bar{u}_j^2 / \sum \mathcal{E}_\infty \bar{u}_j^2 . \tag{2.9b}$$

Notice from Theorem 1 that if we choose $\gamma_j = 1$ for all j, we have $\bar{r}_j =$ the j-th diagonal element of R_0. By Theorem 2, $\bar{r}_j$ is a marginal change (or sensitivity) of the optimal value $\mathcal{E}_\infty \bar{y}^T Q_0 \bar{y}$ when the j-th input variance bound μ_j^2 varies from $\mu_j = \mathcal{E}_\infty \bar{u}_j^2$. For example, if $\bar{r}_j = 0$, then the sensitivity of the IVC objective function with respect to the j-th input perturbation is zero. Hence the corresponding actuator is a candidate for deletion. The second term on the right hand side of (2.8) is to consider the role of each input in the OVC control problem relative to the constraint in the IVC control problem.

Notice that the above algorithm does not use any integer programming (which requires intensive computation). This algorithm does not guarantee that the solution will be globally optimal. If the actuator noise is much greater than the external plant disturbances our algorithm fails to find the optimal solution in one example. The final OVC controller will be used for redesigning the system in the next section.

3. THE OPTIMAL MIX OF PASSIVE AND ACTIVE CONTROL

We consider vector second order systems described by

$$\dot{x}_p = A_p x_p + B_p u \ , \ z = M_p x_p \ , \ x_p^T \triangleq [q^T \ \dot{q}^T] \ , \ q \in \mathbb{R}^{n_q} \ , \ z \in \mathbb{R}^{n_z} \ , \qquad (3.1a)$$

where

$$A_p \triangleq \begin{bmatrix} 0 & I_{n_q} \\ -M^{-1}\mathcal{K} & -M^{-1}\mathcal{D} \end{bmatrix} , \ B_p \triangleq \begin{bmatrix} 0 \\ M^{-1}\mathcal{B} \end{bmatrix} , \ M_p \triangleq [M_q \ M_{\dot{q}}] \ , \qquad (3.1b)$$

where I_{n_q} is an identity matrix of size n_q, z is a noise free measured signal which is fed back to a controller, and u is an actuator signal generated by any linear dynamic controller of order n_c given by

$$\dot{x}_c = A_c x_c + B_c z \ , \ u = C_c x_c + D_c z \ , \ x_c \in \mathbb{R}^{n_c} \ , \ u \in \mathbb{R}^{n_u} \ . \qquad (3.2)$$

Our plant is a mechanical system, hence we refer to the plant as a "structure". In fact our motivation is to design flexible structures for better "controllability", in some sense to be made precise. Suppose an OVC controller has already been designed so that the required performance of the system (3.1) is achieved. *After* structure redesign, the mass, damping and stiffness matrices are changed by ΔM, $\Delta \mathcal{D}$ and $\Delta \mathcal{K}$, respectively. So we have

$$\dot{x}_p = \tilde{A}_p x_p + \tilde{B}_p \tilde{u} \ , \ z = M_p x_p \qquad (3.3)$$

where

$$\tilde{A}_p \triangleq \begin{bmatrix} 0 & I_{n_q} \\ -(M+\Delta M)^{-1}(\mathcal{K}+\Delta\mathcal{K}) & -(M+\Delta M)^{-1}(\mathcal{D}+\Delta\mathcal{D}) \end{bmatrix} , \ \tilde{B}_p \triangleq \begin{bmatrix} 0 \\ (M+\Delta M)^{-1}\mathcal{B} \end{bmatrix} .$$

The controller (3.2) will also be changed to

$$\dot{x}_c = \tilde{A}_c x_c + \tilde{B}_c z \ , \tilde{u} = \tilde{C}_c x_c + \tilde{D}_c z \ . \qquad (3.4)$$

The controller (3.4) is to be designed so that specified closed-loop properties of systems (3.1) with (3.2), and (3.3) with (3.4), are identical. Define the active control effort after the redesign as follows:

$$\tilde{J} \triangleq \sum_i \int_0^\infty \tilde{u}^T(i, t) R \tilde{u}(i, t) dt \qquad (3.5)$$

where R is a given positive-definite weighting matrix and $\tilde{u}(i, t)$ denotes $\tilde{u}(t)$ when only the i-th initial condition ($i = 1, \cdots, n_x + n_c$) of the closed-loop system is applied.

The optimal mix problem under consideration is stated as follows :

The Transfer Equivalence Optimal Mix (TEOM) Problem

Find the structure redesign matrices ΔM, $\Delta \mathcal{D}$ and $\Delta \mathcal{K}$ which minimize the active control effort (3.5) while preserving the closed-loop system matrix after structure redesign. That is,

$$\underset{(\Delta M, \Delta \mathcal{D}, \Delta \mathcal{K})}{\text{Min}} \ \tilde{J} \ \text{subject to} \ \begin{cases} A_{cl} = \tilde{A}_{cl} \ , \\ M + \Delta M \geq \underline{M} \ , \ \mathcal{D} + \Delta \mathcal{D} \geq \underline{\mathcal{D}} \ , \ \mathcal{K} + \Delta \mathcal{K} \geq \underline{\mathcal{K}} \end{cases} \qquad (3.6)$$

where A_{cl} ($\tilde{A}_{cl}$) is the closed-loop system matrix before (after) structure and controller redesign, and $\underline{M}$, $\underline{\mathcal{D}}$ and $\underline{\mathcal{K}}$ represent the lower bounds of mass, damping and stiffness matrices allowed in the redesign.

The controller redesign part is embedded in $\tilde{A}_{cl}$. Hence, the TEOM problem *simultaneously* redesigns the plant and the controller.

After some algebraic manipulation, the equation in (3.6) may be reduced to

$$\mathcal{B}\,\tilde{G}_u M = \mathcal{B}\,G_u M + |\Delta\mathcal{K} \quad \Delta\mathcal{D} \quad \Delta\mathcal{M}|\,L \quad \text{and} \quad \tilde{A}_c = A_c \,, \, \tilde{B}_c = B_c \tag{3.7a}$$

where

$$G_u \triangleq |D_c \quad C_c| \,, \quad \tilde{G}_u \triangleq |\tilde{D}_c \quad \tilde{C}_c| \,, \tag{3.7b}$$

$$L \triangleq \begin{bmatrix} I_{n_u} & 0 \\ 0 & I_{n_u} \\ \mathcal{M}^{-1}(\mathcal{B}\,G_u M - |\mathcal{K} \quad \mathcal{D} \quad 0|) \end{bmatrix} \,, \quad M \triangleq \begin{bmatrix} M_p & 0 \\ 0 & I_{n_c} \end{bmatrix} \,. \tag{3.7c}$$

The last two equations (3.7a) imply that the *dynamic* characteristics of the controller are not influenced by structure redesign if the closed-loop system matrix is to be preserved. The following theorem will be essential to the development of a solution:

Theorem 3 (|10|, Theorem 2.3.2)

If $\mathcal{B}$ has full column rank and M_p has full row rank, $\tilde{G}_u$ satisfying (3.7a) exists if and only if the following equation is satisfied:

$$\mathcal{B}\mathcal{B}^+|\Delta\mathcal{K} \quad \Delta\mathcal{D} \quad \Delta\mathcal{M}|\,L\,M^+ M = |\Delta\mathcal{K} \quad \Delta\mathcal{D} \quad \Delta\mathcal{M}|\,L \tag{3.8}$$

where superscript + denotes the Moore-Penrose pseudoinverse |10|. Furthermore, if a $\tilde{G}_u$ exists, it is uniquely given by

$$\tilde{G}_u = G_u + \mathcal{B}^+|\Delta\mathcal{K} \quad \Delta\mathcal{D} \quad \Delta\mathcal{M}|\,L\,M^+ \,. \tag{3.9}$$

Hence replacing the equation in (3.6) by (3.8) and (3.9) results in an equivalent statement of the TEOM Problem. It can be shown [7] that J can be calculated by

$$J = tr(\tilde{G}_u M X M^T \tilde{G}_u^T R) \tag{3.10}$$

where X satisfies $A_{cl}X + XA_{cl}^T + X_0 = 0$ and $X_0 = diag[\cdots x_i^2(0) \cdots]$ for one-at-a-time application of initial conditions $x_i(0)$.

Notice that the minimization of (3.10) subject to (3.8) and (3.9) is a quadratic programming problem. In fact, it can be shown that the problem is convex |8|. Hence, every local solution is globally optimal. A globally optimal solution can be obtained in a finite number of iterations. See |8| to transform the problem into a standard form of the quadratic program so that any existing software can be used to solve the TEOM problem.

Even though mass is not penalized in our optimization, one might guess that our minimization of control power would cause mass to be reduced in the redesign, since it takes less power to push around smaller masses. The following corollary describes an extreme case of the TEOM problem which more or less confirms this trend. Indeed, the problem (3.6) degenerates to the following obvious solution when $\mathcal{M} = \mathcal{K} = \mathcal{D} = 0$ in (3.6).

Corollary 1 |8|

Suppose that $\mathcal{M} = 0$, $\mathcal{D} = 0$ and $\mathcal{K} = 0$ in (3.6), and that $\mathcal{B}$ and M_p have full column and row rank, respectively. Then the solution of the optimal mix problem (3.6) is given by

$$\Delta\mathcal{M} = -\mathcal{M}, \, \Delta\mathcal{D} = -\mathcal{D}, \, \Delta\mathcal{K} = -\mathcal{K} \text{ and } \tilde{G}_u = 0 \,. \tag{3.11}$$

This result simply states that if there are no lower bounds on the mass then the minimal energy control is accomplished by reducing the system mass to zero. Physical constraints usually do not allow the lower bounds on mass and stiffness to be zero, but the reasonable trend expressed by the extreme of Corollary 1 is that it takes less control energy to push around smaller masses.

4. SUMMARY

This paper shows how to redesign a structure to make it easier for OVC control. The initial controller satisfying multiple output RMS performance requirements is simultaneously obtained when an optimal set of actuators is selected thru the suggested algorithm. The actuator selection process is an iterative algorithm composed of two parts; an output variance constrained control and an input variance constrained control algorithms. Once the initial controller is obtained, both the structure and the controller are redesigned to minimize the active control effort, while preserving all the closed-loop properties of the original closed-loop system.

REFERENCES

[1]   Skelton, R.E. and DeLorenzo, Michael, "Selection of Noisy Actuators and Sensors in Linear Stochastic Systems", *Large Scale Systems,* Vol 4, pp. 109-136, 1983.

[2]   Meirovitch, L., "Dynamics and Control of Structures", *A Wiley-Interscience Publication,* New York, 1990.

[3]   Kosut, R.L., Kabuli, G.M., Morrison, S. and Harn, Y-P, "Simultaneous Control and Structure Design for Large Space Structure", *1990 American Control Conference,* San Diego, California, May 1990.

[4]   Onada, V. and Hattka, R.T., "An Approach to Structural/Control Simultaneous Optimization for Large Flexible Spacecraft", *AIAA Journal,* Vol. 25, No. 8, 1987.

[5]   Smith, M.J., Grigoriadis, K.M. and Skelton, R.E., "The Optimal Mix of Passive and Active Control", *1991 American Control Conference,* Boston, Massachusetts, June 1991.

[6]   Hsieh, Chen, Skelton, R.E. and Damra, F.M, "Minimum Energy Controllers Satisfying Inequality Output Variance Constraints", *Optimal Control Applications & Methods,* Vol 10, No 4, pp. 347-366, 1989.

[7]   Skelton, R.E., "Dynamic Systems Control ; Linear Systems Analysis and Synthesis", *Wiley,* New York, 1988.

[8]   Kim, J.H., "Model Redection, Sensor/Actuator Selection and Control System Redesign of Flexible Structures", *PhD Dissertation, in preparation*

[9]   Fiacco, A.V., "Introduction to Sensitivity and Stability Analysis in Nonlinear Programming", *Academic Press,* New York, 1983.

[10] Rao, C.R. and Mitra, S.K., "Generalized Inverse of Matrices and Its Applications", *John Wiley & Sons, Inc.* New York, 1971.

[11] Khargonekkar, P.P. and Rotea, M.A., "Multiple Objective Optimal Control of Linear Systems; The Quadratic Norm Case", *IEEE Trans. Automatic Control,* Vol 36, No 1, pp. 14-24, 1991.

Optimal passive damper placement and tuning using the Ritz model reduction method

Cheng-Chih Chu, Mark H. Milman, and Andy Kissil

Jet Propulsion Laboratory, California Institute of Technology, Pasadena, CA 91109

Abstract. A problem of considerable importance in Control Structure Interaction (CSI) technology development is the placement and tuning of passive viscous dampers to improve system stability and enhance control system performance. This paper addresses several aspects of this problem, including the development of a mathematical problem formulation, optimization and model reduction strategies for solving the problem, numerical simulation of the procedure, and finally the implementation of passive dampers on a complex testbed facility.

1. Introduction

The motivation for studying the optimal placement and tuning problem has been discussed previously by Chu *et al* (1990) where the general placement problem for both active and passive elements was considered. However, little attention has been paid to the tuning aspect of passive dampers.

This paper addresses both the placement and tuning problem for passive viscous dampers. where the tuning parameters are the damper stiffness and damping coefficient. Our approach to this problem is to treat these two tuning parameters as the gain factors in an equivalent colocated position and *velocity feedback* system respectively. The relative velocity feedback gain is simply the damping coefficient. However, the relative displacement feedback gain is the difference between the structural element stiffness at the location replaced by the passive damper and the actual damper stiffness. The objective of the tuning process is to "optimally" adjust these two feedback gains such that certain performance measures are optimized. However, it is impractical to use the "full-order" model in the tuning process because of the computation overhead. Hence, a reduced-order model must be used in the process.

In this study that the Ritz model reduction method is applied to derive a reduced low-order model for predicting damper effectiveness and the "damped" system performance with high fidelity. It is noted that this method has been used to derive the reduced order model for computing the dynamic response of the open-loop (undamped) system (Kline 1986) It has also been extensively used in the structural analysis community for model reduction via various component mode synthesis techniques (Craig and Bampton 1968). The approach presented in this paper has been successfully applied to the placement and tuning problem of one passive damper on the JPL's CSI Phase B Testbed (O'Neal *et al* 1991). Results generated provide not only the specifications for the Honeywell D-struts (Wilson and Davis 1987) but also candidate locations for placement.

2. Modeling and Ritz Model Reduction Method

Assume that the dynamics of the undamped structure can be described by

$$M\ddot{z} + Kz = B_d d, \quad y_o = C_{op}z + C_{ov}\dot{z} .$$

Here z denotes the n dimensional vector of generalized coordinates, d is the n_d dimensional external forcing input vector, y_o is the p dimensional controlled output vector, M is the $n \times n$ symmetric, positive definite, mass matrix, and K is the $n \times n$ symmetric, positive semi-definite, stiffness matrix.

If the passive viscous damper is modeled as a spring in parallel with a dashpot. The dynamic structural model with the inclusion of n_p passive dampers can be represented as:

$$M\ddot{z} + \left(\sum_{j=1}^{n_p} k_{v_j} b_j b_j{}^T\right)\dot{z} + \left(K + \sum_{j=1}^{n_p} k_{p_j} b_j b_j{}^T\right)z = B_d d . \tag{1}$$

The fundamental issue of passive damper placement and tuning is to find "best" locations, k_{p_j}, and k_{v_j} such that a certain "performance measure" is optimized. Since n is typically very large, it is impractical to carry out any optimization problem using the full order model. a reduced-order model with the order much less than n must be developed.

The model reduction method used in this study is called the "Ritz model reduction method" where the Ritz transformation matrix comprises the first m ($m << n$) eigenvectors corresponding to the lowest m eigenvalues, $\{\omega_1, \omega_2 \ldots, \omega_m\}$, and additional Ritz vectors to account for the static correction for each of forcing inputs. Define the transformation matrix $\mathcal{P}$ as $\mathcal{P} = [\Phi_m \quad \Phi_{ritz}]$ where the matrix Φ_m contains the first m eigenvectors and Φ_{ritz} comprises all required Ritz vectors. The reduced-order model is then obtained by applying $\mathcal{P}$ to Eq. (1)

$$(\mathcal{P}^T M \mathcal{P})\ddot{x} + \mathcal{P}^T \left[\sum_{j=1}^{n_p} k_{v_j} b_j b_j{}^T\right] \mathcal{P}\dot{x} + \mathcal{P}^T \left[K + \sum_{j=1}^{n_p} k_{p_j} b_j b_j{}^T\right] \mathcal{P}x = (\mathcal{P}^T B_d)d .$$

3. Optimal Passive Damper Placement and Tuning

In the optimal passive damper placement/tuning problem, two types of performance criteria are considered. The first one is the structural modal damping for selected modes. The computation involved is to solve for the eigenvalues of the "A"-matrix for a given damper configuration with corresponding damper stiffness and damping coefficients. The second type of criterion requires both the external disturbance input vector and the controlled output vector to be specified. A meaningful and numerically tractable criterion for the associated optimization problem is to minimize the $\mathcal{H}_2$-norm of the transfer function from d to y_o. In addition, a weighting

function W_d can be used to model spectral property of d and a weighting function W_p can be used to improve the performance of y_o over certain frequency ranges.

The general $\mathcal{H}_2$-optimal placement/tuning problem for multiple passive dampers can be posed as

$$\min_{K_p \in \mathcal{K}_p} \min_{K_v \in \mathcal{K}_v} \min_{B_p \in \mathcal{B}_p} \|W_p G_p(s; B_p, K_p, K_v) W_d\|_2 \tag{2}$$

where $G_p(s; B_p, K_p, K_v)$ is defined as the transfer matrix from the d to y_o with a given damper configuration of locations corresponding to B_p and the corresponding stiffness and damping coefficients K_p and K_v.

The above optimization problem is a combined "continuous+discrete" optimization problem where the selection of locations (B_p) is a combinatorial problem and the the selection of K_p and K_v (tuning) is a continuous optimization problem.

4. Application – Placement/Tuning of One Passive Damper

A detailed description of the JPL's CSI Phase B Testbed can be found in O'Neal *et al* (2991). There are 186 candidate locations on the truss structure considered for placing the passive dampers and the model has 252 mass degrees of freedom, i.e., $n = 252$.

To study the placement and tuning problem, the $\mathcal{H}_2$-optimization formulation was described in Chu *et al* (1990). Our approach is to first fix the damper stiffness k_s to be constant since passive viscous damper usually improves system performance much better if the damper stiffness is lower. For example, the lowest possible stiffness for the Honeywell D-struts is 8000 *lb/in* (approximately) which will the the damper stiffness used in this study. The optimal k_v can be found between 0 and 1000 *lb-sec/in* by solving the nonlinear optimization problem in one variable for each of locations. A uniform modal damping of 0.1% for all modes is assumed in the undamped model.

The $\mathcal{H}_2$-norm cost for the undamped system is equal to $1.1661E - 03$ and location 133 (located at first bay of the tower) is found to be the best location for placing a single passive damper with a cost of $2.0827E - 04$ with corresponding optimal $k_v = 370.07$ *lb - sec/in*. It is observed that there are significant number of candidate locations where the corresponding closed-loop systems show either no or little improvement in performance. Since our ultimate objective is to place and tune multiple passive dampers, the combinatorial optimization problem arisen is known to be a notorious problem due to the fact that the number of candidate locations is typically much larger than the number of passive dampers. This study could also provide us useful information for the pruning process (Chu *et al* 1990) to simplify the associated combinatorial optimization problem.

The specifications for the stiffness and damping coefficient of Honeywell D-struts are recommended based on the study presented here. Figure 1 presents experimental result with a D-strut placed at the location 133. Clearly, remarkable performance improvement was achieved with only one appropriate "placed and tuned" D-strut.
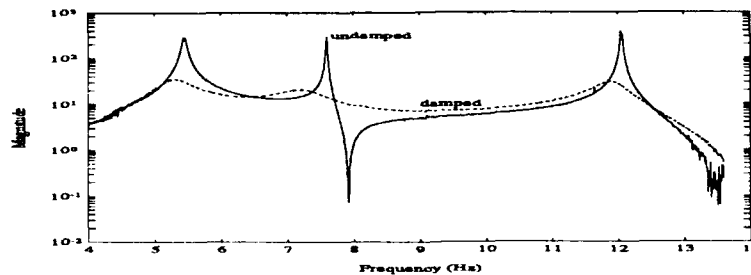
Figure 1: Comparison of undamped and damped responses

5. Conclusions

In this paper, the general optimal passive damper placement and tuning problem is formulated. The effectiveness of the Ritz model reduction method as a means to obtain a reduced order model enables us to effectively predict the damped system performance. A detailed study was carried out for placement and tuning of one passive damper on the JPL's CSI Phase B Testbed. Results generated from this study provide not only the specifications for the Honeywell D-struts but also candidate locations for experimental verification which shows excellent results.

The multiple damper placement and tuning problem is a combined "continuous+discrete" optimization problem. The computation involved is extremely intensive. To develop an efficient and effective approach to solve such a problem is an area of our ongoing research.

Acknowledgments

References

Craig, R. R. Jr. and Bampton, M. C. C., "Coupling of Substructures for Dynamic Analysis", AIAA Journal, Vol. 6, No. 7, July 1968, pp. 1313-1319

Chu, C.C., Fanson J.L., Milman M.H., and Eldred D.B., "Optimal Active Member and Passive Damper Placement and Tuning", 4th NASA/DoD Control/Structures Interaction Technology Conference, Orlando, FL, November 5-7, 1990

Kline, K.A., "Dynamic Analysis Using a Reduced Basis of Exact Modes and Ritz Vectors," AIAA Journal, Vol. 24, No. 12, December, 1986, pp. 2022-2029

O'Neal, M., Eldred, D., Liu, D, and Redding, D., "Experimental Verification of Nanometer Level Optical Pathlength Control on a Flexible Structure", 14th Annual AAS Guidance and Control Conference, Keystone, CO, February, 1991

Wilson, J.F. and Davis, L.P., "Viscous damped space structure for reduced jitter", Vibration Symposium, Huntsville, AL, August, 1987

633

Finite element method for numerical simulation of the actuator performance of a composite transducer array

Liang-Chih Chin, Vasundara V. Varadan and Vijay K. Varadan

Research Center for the Engineering of Electronic and Acoustic Materials
The Pennsylvania State University,University Park, PA 16802

ABSTRACT: A general finite element approach is developed for the analysis and the design of a composite transducer array with selective electrical excitation of one of the the piezoceramic elements. This finite element simulation can incorporate a transducer structure with general material damping, dielectric loss and can take into account the effect of fluid loading, backing and matching layers. Natural frequencies and mode shapes are calculated using model analysis. The excited voltage on the adjacent electrode, the equipotential distribution in the transducer, and the input electrical admittance are studied in the dynamic response analysis.

1. INTRODUCTION

Piezoelectric composite transducers combine a piezoelectric ceramic and a passive host material. This kind of transducer offers several advantages in a variety of applications which have been well documented. The finite element approach is a powerful means to simulate the performance of composite transducers since it can be applied to any arbitrary geometry for any arbitrary set of material properties and multi-field boundary conditions. The basic finite element formulation can be found in the work of Allik (1970) and Kagawa (1976). In this paper, we introduce a new actuator equation for the dynamic analysis of a composite transducer array. For the actuator function of a transducer, we are interested in the displacement and stresses on the face of the transducer induced by a known applied voltage to one or more elements of the transducer array. The effect of fluid loading is combined with a material damping matrix which facilitates the calculation process. A very interesting study is the physical connection between the excited voltage on the adjacent electrode and the input electrical admittance when only some elements of the array are excited.

2. FINITE ELEMENT FORMULATION

Allik and Hughes (1970) have applied the finite element formulation to the analysis of vibration modes of piezoelectric materials. This paper will follow their basic formulation and notation. Additional capabilities are developed in the actuator equation.

The geometric configuration of the two-dimensional composite transducer array to be analyzed is shown in Fig. 1. In this example, the dimensions in x- and y- direction are larger than the thickness of the transducer array. If the distribution of piezoelectric elements or unit cell is periodic, we can consider just one period as our object of analysis in the x-direction and use Floquet modes to simplify our problem. In this example, a selective PZT element is excited by a known voltage. Selective excitation of the array destroys periodicity, however, we expect only a few nearest neighbors to be influenced by the excited element. Periodicity can be reinvoked by assuming 1) alternate elements are excited, 2) every third element is excited and so on. This way, we can compare the results and study the convergence of the calculations and assess the effect of selective excitation on neighboring elements. We will examine the input electrical admittance, the excited voltage on the neighboring PZT element and the equipotential distribution in the transducer. We first model one and half of one unit cell. The length of the unit will be extended if numerical convergence is not satisfied.
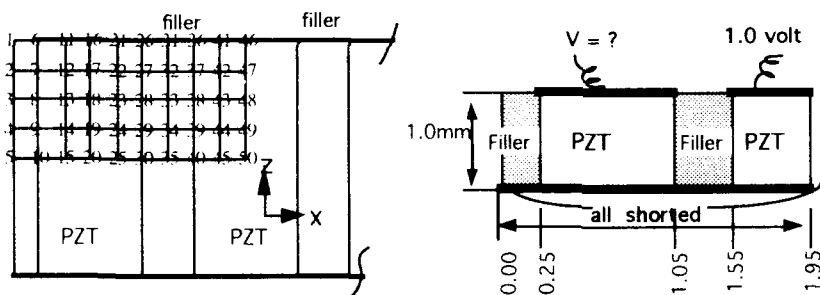
Fig. 1(a). Model for a two-dimensional composite transducer array. 1(b) model with a quarter of three periodic unit cells.

The equations which define the motion of a piezoelectric structure can be obtained from the principle of minimum virtual work by means of a variational functional approach. With the virtual nodal displacement system and potential system being arbitrary in the variational form, we construct the finite element matrix form (1) in terms of the arbitrary displacement $\{\delta u\}$ and electrical potential $\{\delta \varphi\}$ at the element node points.

$$\begin{bmatrix} [K_{uu}] & i\omega[D] - \omega^2[M] & [K_{u\phi}] \\ [K_{u\phi}]^t & [K_{\phi\phi}] \end{bmatrix} \begin{Bmatrix} \{u\} \\ \{\phi\} \end{Bmatrix} = \begin{Bmatrix} \sum_{i=1}^{n} \iint_{S_i} [N]^t \{\bar{T}\} dS_i = \{F\} \\ \sum_{j=1}^{m} \iint_{S_j} [N]^t \{\bar{\sigma}_s\} dS_j = \{Q\} \end{Bmatrix} \quad (1)$$

3. Electroelastic Free Vibration Analysis

The free vibration of the transducer differs from elastic free vibrations in that it involves electric boundary conditions on the electric terminals. With different electric boundary

conditions, the free vibration of the transducer can be divided into two extreme cases in which the electric terminals are shorted and open-circuited. In (1) the nodal potential vector $\{\phi\}$ can be divided into two groups, $\{\phi_p\}$ and $\{\phi_q\}$, where subscript 'p' denotes the element nodes at the electrodes and 'q' the nodes at other electrodes in (1).

For the short-circuited case, $\{\phi_p\} = \{0\}$, the corresponding row and column are removed and the (1) becomes

$$\left| ([K_{uu}] - [K_{uo}]_q [K_{oo}]_{qq}^{-1} [K_{ou}]_q) - \omega^2 [M] \right| = 0 \tag{2}$$

For the open-circuited case, there is no $\{Q\}$ in (1) and the eigen-equation is expressed as

$$\left| ([K_{uu}] - [K_{uo}][K_{oo}]^{-1}[K_{ou}]) - \omega^2 [M] \right| = 0 \tag{3}$$

The natural frequencies from the free electromechanical vibrations are shown in Table 1.

Table 1. natural frequencies for short and open-circuited case

Freq.(MHz)	f1	f2	f3	f4	f5	f6
ShortCase	0.3180	0.5548	0.7834	0.7840	1.2279	1.3170
OpenCase	0.3210	0.5550	0.8803	0.8951	1.2286	1.3240

In Table 1., we only find that the third and fourth modes have significant difference between their resonance (shorted) and antiresonance (open) which are the thickness vibration modes. They display strong electromechanical coupling. In transducer applications, we operate the transducer at its thickness mode in order to obtain a higher transmission efficiency.

4. Actuator Dynamic Response Analysis

Since the transducer array is periodic, we can expects the acoustic field in the fluid as a summation of Floquet modes. The forcing vector in (1) is due to a fluid loading matrix which can be transferred to the left hand side and becomes part of the damping matrix $[D]$ in the generalized stiffness matrix $[\tilde{K}_{uu}]$ in (4). If we consider the transducer as an actuator device interacting with the surrounding medium Eq. (1) can be expressed into the new form,

$$\begin{bmatrix} [\tilde{K}_{uu}] & [K_{uo}] \\ [K_{uo}]^T & [K_{oo}] \end{bmatrix} \begin{Bmatrix} \{u\} \\ \{\phi\} \end{Bmatrix} = \begin{Bmatrix} \{0\} \\ \{Q\} \end{Bmatrix} \tag{4}$$

where

$$[\tilde{K}_{uu}] = [K_{uu}] - i\omega([D] - [D_f]) - \omega^2 [M]$$

For a given driving voltage we can use (4) to get the admittance values. The admittance is defined as

$$Y \text{ (Admittance)} = \frac{j\omega}{V} \sum_i Q_i$$

(5)

where V is a applied voltage, Q_i is the electrical charge of element nodes on the electrodes. The admittance plot is shown in Fig. 2.

Electrical Admittance (Material Loss)
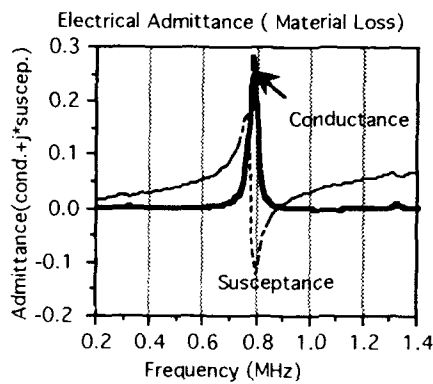
Fig. 2 Input Electric Admittance

Voltage Excited on the Neighboring Electrode
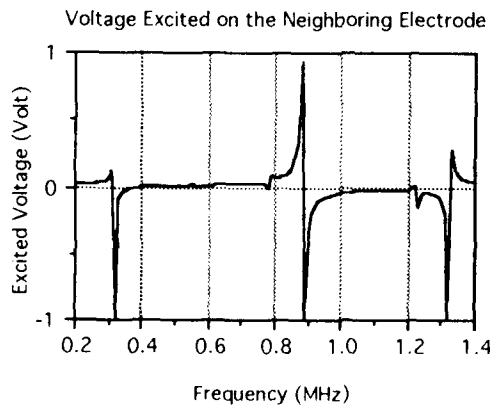
Fig. 3 Excited Voltage on Adjacent Electrode

The excited voltage on the adjacent electrode plotted in Fig. 3 illustrates that the maximum voltage excited occurs at the open-circuited operation which is in reasonable agreement with realistic sensor application.

As the operating frequency approaches the thickness resonance the equipotential contour gradually forms a circle and therefore diverges out after resonance. Here, we only show the equipotential distribution at its thickness vibration mode in Fig.4.

Equipotential Distribution in a Transducer (CB@0.78MHz)
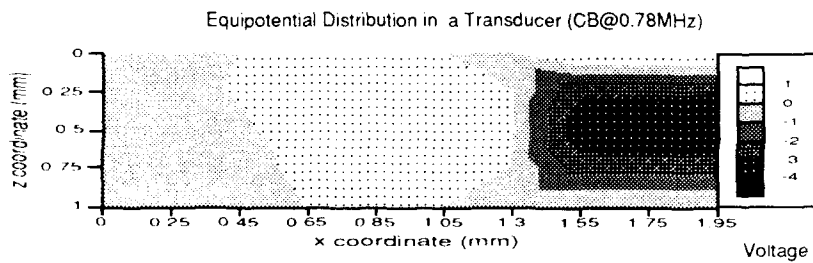
Fig. 4. The euqipotential distribution in the composite transducer array

5. CONCLUSIONS

The finite element approach for the analysis and design of composite piezoceramic actuator transducers has been developed in a more general form. This finite element approach allow for electroelastic vibration analyses, dynamic analysis including general material damping and dielectric loss terms. An example based on a two-dimensional composite transducer array illustrates the electroelastic vibration analyses for both shorted and open-circuited cases. An input electrical admittance spectrum is presented for a transducer with material losses. The material damping is not restricted to a proportional damping in our computation. Also, by use of Floquet's theorem, the fluid loading effect can be easily combined with the material damping matrix. For an applied voltage on a selective PZT element, the voltage excited on neighboring electrodes can be calculated to determine the cross-talk effect between adjacent PZT elements. Stress analysis and deformation are also available upon design requirement.

6. ACKNOWLEDGMENT

7. REFERENCES

Allik H and Hughes T J R 1970,International Journal for Numerical Methods in Engineering, Vol. 2,pp.151-157

Kagawa Y and Yamabuchi T 1976, IEEE Transactions on Sonics and Ultrasonics, Vol. Su23, No. 4,pp. 263-272

Piezoelectric finite element formulation applied to design of smart continua

H. S. Tzou [1,2], C. I. Tseng [3], and H. Bahrami [4]

[1] Department of Mechanical Engineering
University of Kentucky, Lexington, Kentucky 40506–0046 USA

[2] Institute of Space and Astronautical Science, Kanagawa 229, Japan [††]

[3] SDRC, Detroit, Michigan (Currently, Feng–Chia University, Taiwan, R.O.C.)

[4] IBM, Lexington, Kentucky 40511 USA

ABSTRACT: Studies on smart continua with integrated sensor/actuator for structural identification and control have drawn much attention in recent years. This paper is devoted to a new piezoelectric finite element development with applications to smart continua. Hamilton's principle and variational equation are used to derive the thin piezoelectric solid element. Proportional feedback — constant gain — feedback control is also implemented in the finite element program. A square plate with four–pair colocated segmented distributed sensors and actuators is studied. Finite element results are closely compared with analytical solutions.

1. INTRODUCTION

Smart continua integrated with distributed sensors and actuators suggest a great potential for design of new–generation high–performance structures and systems. In this paper, thin piezoelectric layers are coupled with conventional elastic continua and are used as distributed sensors or distributed actuators in smart continua. Piezoelectric materials, rigid and flexible, were used in a number of smart structural design and applications. Flexible piezoelectric PVDF was used in vibration control and active damping of beam structures (Tzou, 1987; Plumb, et al., 1987). Rigid crystalline piezoceramics were also applied to a distributed sensor/actuator for beam structures (Hanagud & Obal, 1988; Crawley & de Luis, 1987) and a longitudinal actuation in space truss structures (Fanson & Garba, 1988). A theory on multi–layered shells coupled with the piezoelectric shell actuators was derived and evaluated (Tzou & Gadre, 1989). New distributed sensing/control theory for a generic shell continuum was also proposed and evaluated (Tzou, 1991). In this study, a new thin piezoelectric finite element is formulated and a general purpose computer code capable of analyzing elastic/piezoelectric coupled continua is developed.

Piezoelectric isoparametric hexahedron and tetrahedral finite elements were formulated and applied to piezoceramic transducer designs (Nailon, et al., 1983; Allik & Hughes, 1979). However, the derived isoparametric elements are too thick for thin continuum applications. In this paper, development of a new "thin" piezoelectric

---

solid element with internal degrees of freedom (DOF) is presented and application to distributed structural identification and control of continua is demonstrated.

2. A THIN PIEZOELECTRIC ELEMENT

In this section, a thin piezoelectric finite solid element with internal DOF's is derived using a variational principle. The system matrix equation is also formulated via assembling all element matrices. The variational equation for a piezoelectric solid can be derived as (Tzou & Tseng, 1990)

$$
\int_V \left[\rho\{\delta\dot{q}\}^t\{\dot{q}\} - \{\delta S\}^t[c]\{S\} + \{\delta S\}^t[e]\{E\} - \{\delta E\}^t[e]\{S\} - \{\delta E\}^t[\epsilon]\{E\} \right.
$$
$$
\left. + \{\delta q\}^t[P_b] \right] dV + \int_{S_1} \{\delta q\}^t\{P_s\} \, dS_1 - \int_{S_2} \delta\phi \; \sigma \, dS_2 + \{\delta q\}^t\{P_c\} = 0 , \qquad (1)
$$

where ρ is the mass density, $\dot{q}$ the velocity (time derivative of the displacement q), $\{S\}$ the strain vector, $[c]$ elasticity matrix, $\{E\}$ electric field vector, $[e]$ the dielectric permittivity matrix, $[\epsilon]$ the dielectric matrix, $\{P_b\}$ is the body force, S_1 the effective surface area, $\{P_s\}$ the surface force, $\{P_c\}$ the concentrated load, ϕ the electric potential, and σ the surface charge. Note that $\{\cdot\}^t$ or $[\cdot]^t$ denotes vector or matrix transpose. To derive the electroelastic matrix relationship for a piezoelectric finite element, one needs to define shape function matrices $[N_q]$ and $[N_\phi]$ and express displacement $\{q\}$ and strain $\{S\}$ in terms of nodal coordinates. As discussed previously, the distributed piezoelectric sensor/actuator is about two to three orders thinner than the master elastic continua. Thus, three internal DOF's are added into the thin eight−node solid element formulation (Tzou & Tseng, 1990). Thus, the system equations can be derived as

$$
\begin{bmatrix} [M_{qq}] & 0 \\ 0 & 0 \end{bmatrix}\begin{Bmatrix} \{\ddot{q}\} \\ \{\phi\} \end{Bmatrix} + \begin{bmatrix} [C_{qq}] & 0 \\ 0 & 0 \end{bmatrix}\begin{Bmatrix} \{\dot{q}\} \\ \{\phi\} \end{Bmatrix} + \begin{bmatrix} [K_{qq}] & [K_{q\phi}] \\ [K_{\phi q}] & [K_{\phi\phi}] \end{bmatrix}\begin{Bmatrix} \{q\} \\ \{\phi\} \end{Bmatrix} = \begin{Bmatrix} \{F\} \\ \{G\} \end{Bmatrix} , \qquad (2)
$$

where $[M_{qq}]$, $[C_{qq}]$, and $[K_{q\phi}]$ denote the system mass, damping (proportional damping), and stiffness matrices, respectively; $\{F\}$ is the external mechanical excitation; and $\{G\}$ is the electrical excitation. In active vibration control applications. $\{G\}$ can be used as feedback voltages determined by control algorithms. Note that the mechanical equation is closely coupled with the electrical equation. In order to improve computation efficiency, Guyan's reduction scheme is implemented in the finite element code. A congruent transformation matrix $[T_c]$ can be calculated using the static system equation.

$$
[T_c] = \left[[I] , - [K_{q\phi}][K_{\phi\phi}]^{-1} \right] . \qquad (3)
$$

Thus, the condensed system equation becomes

$$
[M_{qq}]\{\ddot{q}\} + [C_{qq}]\{\dot{q}\} + [K^*]\{q\} = \{F\} - [K_{q\phi}][K_{\phi\phi}]^{-1}\{G\} , \qquad (4)
$$

where $[K^*] = [K_{qq}] - [K_{q\phi}][K_{\phi\phi}]^{-1}[K_{\phi q}]$. Note that there are two excitation forces associated with the piezoelectric structures, i.e., the mechanical forces and the electric forces. Time history responses of the piezoelectric smart system are calculated using a time–domain direct integration algorithm — the modified Wilson–θ method and a pseudo–force method (Tzou & Schiff, 1987) to accommodate the control forces. Note that the derived piezoelectric finite element was verified using both analytical techniques and laboratory experiments for simple cases.

3. SMART CONTINUA

The basic configuration of a smart continuum is composed of a master elastic structure coupled and/or embedded with piezoelectric thin layers acting as distributed sensors and the actuators, respectively. In general, distributed piezoelectric sensor layer can respond to structural vibration and generate electric signal representing the current dynamic state. The electric potential vector $\{\phi\}$ can be calculated by

$$\{\phi\} = [K_{\phi\phi}]^{-1}\left[\{G\} - [K_{\phi q}]\{q\} \right] . \tag{5}$$

Note that $\{G\}$ is usually zero in the distributed sensor layer. Thus, the distributed sensor output is estimated by

$$\{\phi\} = [K_{\phi\phi}]^{-1}\left[-[K_{\phi q}]\{q\} \right] . \tag{6}$$

That is the nodal output amplitude vector is contributed by nodal displacement vector at a given time or state. The distributed sensor generates voltage outputs when the structure is oscillating; and the signal can be amplified and fed back into the distributed actuator. Thus, the control strategy is established such that the control (counteracting) moment generated will oppose the motion in the transverse direction.

In feedback controls, the electric force component can be regarded as a feedback control force $\{F_f\}$:

$$\{F_f\} = [K_{q\phi}][K_{\phi\phi}]^{-1}\{G\} . \tag{7}$$

Note that $\{G\}$ is a function of feedback voltage in terms of the output signal from the distributed sensing layer. Thus, the system equation with velocity feedback can be rewritten as

$$[M_{qq}]\{\ddot{q}\} + \left[[C_{qq}] - [K_{q\phi}][K_{\phi\phi}]^{-1}[C][K_{\phi\phi}]^{-1}[K_{\phi q}]\right]\{\dot{q}\} + [K^*]\{q\} = \{F\} , \tag{8}$$

where $[C]$ is a gain matrix which can be determined by various control algorithms to achieve different control effectiveness. The control force induced by the feedback surface voltage/charge can effectively enhance the system damping and therefore suppress the vibration of a smart continuum. Constant gain proportional feedback control is implemented in the program. In this case, the feedback gain is constant while the feedback amplitude varies with respect to the negative oscillating velocity (*negative velocity, constant gain proportional feedback control*), i.e.,

$$\{G\} = [K_{q\phi}] [K_{\phi\phi}]^{-1} [C] [K_{\phi\phi}]^{-1} [K_{\phi q}] \{\dot{q}\} .\tag{9}$$

Time history responses are calculated by a time–domain integrated technique (Tzou & Schiff, 1987).

4. CASE STUDY

A square plate (40cm×40cm×1.6cm) made of plexiglas is coupled with four pair of segmented distributed piezoelectric polyvinylidene fluoride (PVDF) polymer layers (40 μm) on the top and bottom surfaces. Figure 1. The bottom four distributed pieces are used as segmented sensors and the top four pieces as segmented actuators. Note that the sensor and actuator are colocated on the square plate. The plate has simply supported boundary conditions. It is intended to use the segmented sensors to monitor the plate oscillation and the actuators to control the plate oscillation. It is also assumed that the plate has a 1% initial damping.
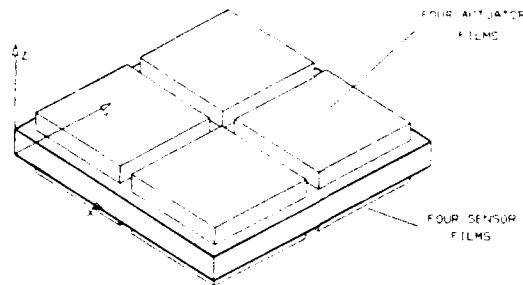
Fig.1 A plate with four–pair colocated segmented distributed piezoelectric sensor/actuator.

The three–layered square elastic plate is divided into 289 elements and the signal piece of piezoelectric sensor or actuator is divided into 49 elements. There are 3924 degrees of freedom initially and it is reduced to 324 degrees of freedom after reduction. The first three natural frequencies are calculated analytically and numerically: (1,1)–mode: 15.4 (theory) and 15.9 (FEA); (1,2)–mode: 38.4 (theory) and 41.7 (FEA); (2,2)–mode: 61.4 (theory) and 70.6 (FEA). The natural frequencies are compared well for the lower modes and deviated for the higher modes. The error for the first mode is 3.2%. Active control of the first mode oscillation using the segmented sensors and actuators is studied next.

As discussed previously, there are four pairs of these colocated sensors and actuators. The sensor information are processed and fed back to the top colocated actuators using the control algorithm. Control effectivenesses of various feedback gains are compared. Note that only the first bending mode is studied. An initial displacement of the first mode is imposed for the square plate and the snap back responses, uncontrolled and controlled, are studied. The snap–back free response of the square plate is shown in Figure 2.
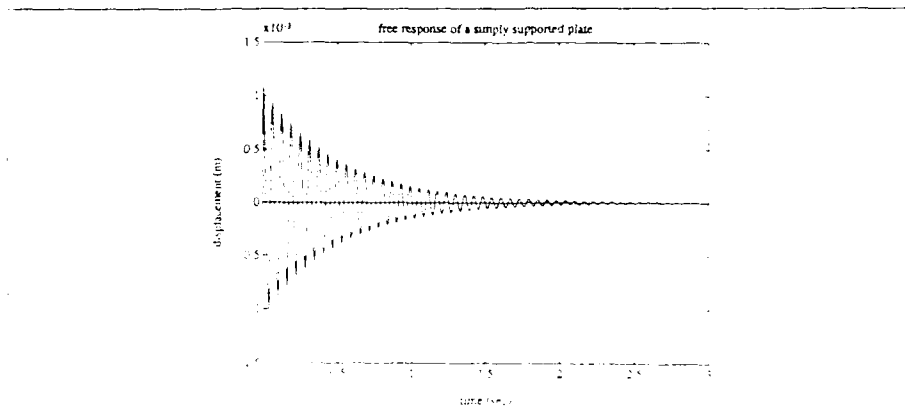
Fig.2. Snap back response of the plate.

Ten-percent settling time for the free oscillation is estimated to be 2.38 sec and a theoretical calculation is 2.41 sec. Closed-loop feedback controls of the plate using the four-pair colocated segmented sensors and actuators are also studied. Control response via the constant gain feedback control has similar time history which converges faster than Figure 2. (Due to page limitation, it is not shown here.) Ten-percent settling time for the above case is estimated to be 0.98 sec while a theoretical estimation is 0.85 sec. Note that the mechanical properties of the segmented sensors/actuators were not considered in theoretical calculation. Figure 3 shows the 10% settling time of the plate with various control gains.
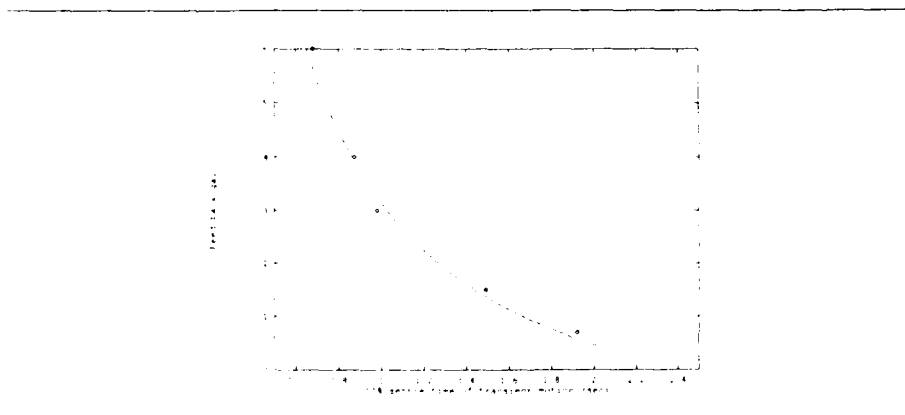
Fig.3. 10% setting time v.s. feedback gains.

It shows that as the feedback gain increases, the snap back response converges faster, i.e., the plate is better controlled.

5. CONCLUDING REMARKS

Smart continua with integrated sensors and actuators provide great potentials in many engineering designs and applications. In this paper, a new thin piezoelectric finite element was developed and application to structural monitoring and control

illustrated. A variational principle and a finite element discretization technique were used to derive the dynamic system equations. Constant gain feedback control was also implemented in the computer program.

A simply supported thin square plate with four-pair colocated segmented distributed piezoelectric sensors and actuators was studied and effectiveness evaluated. It showed that the plate settles faster as the feedback gain increases. Finite element results were compared with the theoretical solutions favorably. However, it should be noted that the feedback voltage is limited by a "breakdown" voltage. That is the piezoelectric material becomes useless in both distributed sensing and control applications.

ACKNOWLEDGEMENT

REFERENCES

Allik H. and Hughes, T.J., 1979, "Finite Element Method for Piezoelectric Vibration," *Int. J. of Numerical Methods Eng.*, Vol. 2, pp.151–168.

Crawley E.F. and de Luis, J., 1987, "Use of Piezoelectric Actuators as Elements of Intelligent Structures," *AIAA Journal*, Vol.25, No.10, pp.1373–1385.

Fanson J.L. and Garba, J.A., 1988, "Experimental Studies of Active Members in Control of Large Space Structures," AIAA Paper 88–2207, *Proc. of AIAA/ASME/AHS 29th SDM Conference*, pp.9–17.

Hanagud S. and Obal, M.W., 1988, "Identification of Dynamic Coupling Coefficients in a Structure with Piezoelectric Sensors and Actuators," *Proc. of AIAA/ASME/AHS 29th Structures, Structural Dynamics, and Materials Conference*, (Paper No.88–2418), Part–3, pp.1611–1620.

Nailon, M., Coursant, R.H., and Besnier, F., 1983, "Analysis of Piezoelectric Structures by a Finite Element Method," *ACTA Electronica*, Vol.25, No.4, pp.341–362.

Plump, J.M., Hubbard, J.E., and Baily, T., 1987, "Nonlinear Control of a Distributed System: Simulation and Experimental Results," ASME *J. Dynamic Systems, Measurement, and Control*, pp.133–139.

Tzou, H.S., 1987, "Active Vibration Control of Flexible Structures via Converse Piezoelectricity," *Developments in Mechanics*, Vol.14–c, pp.1201–1206.

Tzou, H.S., 1991, "Distributed Modal Identification and Vibration Control of Continua: Theory and Applications," ASME *J. Dynamic Systems, Measurement, and Control*, Vol.(113), No.(3).

Tzou, H.S. and Gadre, M., 1989, "Theoretical Analysis of a Muli–Layered Thin Shell Coupled with Piezoelectric Shell Actuators for Distributed Vibration Controls," *Journal of Sound and Vibration*, Vol.132, No.3, pp.433–450.

Tzou, H.S. and Schiff, A.J., 1987, "Development and Evaluation of a Pseudo–Force Approximation Applied to Nonlinear Contacts and Viscoelastic Damping," *Intl. J. Comptr. & Structures*, Vol. 26, No.3, pp.481–493.

Tzou, H.S. and Tseng, C.I., 1990, "Distributed Piezoelectric Sensor/Actuator Design for Dynamic Measurement and Control of Distributed Parameter Systems," *Journal of Sound and Vibration*, Vol.138, No.1, pp.17–34.   (C/PzFEA–ADPA.PzShl3)

Stress reduction in an isotropic plate with a hole by applied induced strains

M. J. Palenterä , P. K. Sensharma , R. T. Haftka
Virginia Polytechnic Institute and State University, Blacksburg, VA 24061

ABSTRACT: Recently there has been much interest in adaptive structures that can respond to a varying environment by changing their properties. Shape memory alloys and piezoelectric materials can be used as induced strain actuators to reduce stresses in the regions of stress concentration. The objective of our work was to find the maximum possible reduction in the stress concentration factor in an isotropic plate with a hole by applying induced strains in a small area near the hole. Induced strains were simulated by thermal expansion.

1. INTRODUCTION

Recently there has been much interest in adaptive structures that can respond to a varying environment by changing their properties. Piezoelectric materials and shape memory alloys (SMA) are often used to create such adaptivity by applied energy, usually electric current. Due to these adaptive properties, SMA and piezoelectric materials can be used as actuators as shown by Rogers and Lin (1991) and Crawley and Luis (1987). These actuators can be used to induce strains in structures and reduce stresses in regions of stress concentration.

The objective of our work was to find the maximum possible reduction in the stress concentration factor in an isotropic plate with a hole by applying induced strains in a small area near the hole. Induced strains were simulated by thermal expansion. Both analytical optimization methods and numerical optimization based on finite element simulations were used to obtain optimal axisymmetric and non-axisymmetric induced strain distributions.

2. PROBLEM DEFINITION

A thin 30 in. square plate with a 1 in. circular hole under uniaxial tensile loading S (10ksi), as shown in Figure 1 was used throughout this study. The plate is made of aluminium with Young's modulus E = 1.0E07 psi , Poisson's ratio v = 0.3, and coefficient of thermal expansion α = 2.3E-05 $1/^0$ C. The plate was treated analytically as an infinite plate. The radial stress (σ_r), tangential stress (σ_θ), and shear stress ($\tau_{r\theta}$) distributions for this case are given by Timoshenko (1970).

Our goal was to reduce the stress concentration as measured by Von-Mises or the maximum shear stress criteria by adding axisymmetric and non-axisymmetric induced strain fields over a minimal region of the plate. Without the induced strain field, σ_θ varies from 3S to -S around the edge of the hole. Since it is the only nonzero stress component there, the stress concentration factor is 3. An

axisymmetric induced strain can lower that stress concentration no lower than 2 (when the variation will be between 2 and -2).

In the non-axisymmetric case, however, the stress concentration factor can be reduced below 2 because the stresses can be reduced at one point (i.e., $\theta = \frac{\pi}{2}$) without affecting stresses at other points (i.e., $\theta = 0$).
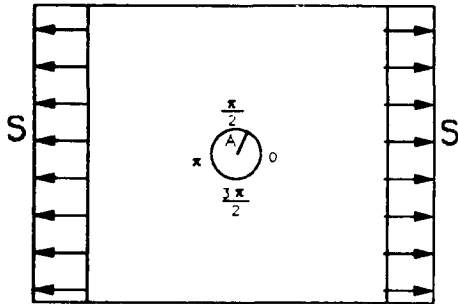
Figure 1: Plate with a hole subject to uniaxial loading
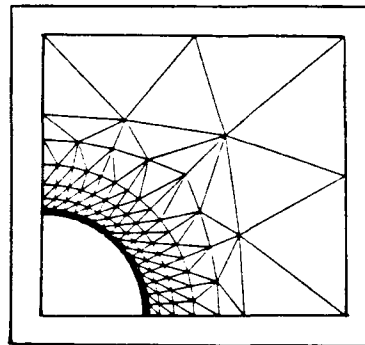
Figure 2: Finite element mesh at the hole region

For the finite element analysis, a quarter plate model shown in Figure 2 was analyzed using the EAL. The basic element mesh of the plate was formed by four-node quadrilateral elements. The hole region, as well as the transition from dense to coarser element mesh was modeled with 3-node triangular elements. The model consists of 234 three-node and 176 four-node membrane elements. The plate was loaded in unidirectional tension by applying a constant displacement at one end of the quarter plate model. Axisymmetric induced strain variation is applied separately to five constant-width rings of elements around the hole. The inner and outer radii of these rings are 0.500-0.515 in., 0.515-0.530 in., 0.530-0.580 in., 0.580-0.650 in., and 0.650-0.750 in.. In the non-axisymmetric case, the induced strain distribution in the tangential direction was formed by dividing the five rings into constant strain sectors.

3. PROBLEM FORMULATION

For the numerical optimization we seek the induced strain distribution that minimizes the maximum stress in the plate. However, the maximum stress is not a smooth function of the design variables. This problem is solved by adding the value of the maximum stress, σ_{max}, as an additional design variable.

The optimization problem is then formulated as

$$minimize \quad \sigma_{max}$$

$$such \ that \quad \sigma^j_{eq}(\varepsilon^i_k) \leq \sigma_{max} \quad j = 1, \dots, n_e \tag{1}$$

where ε^i_k, $k = 1, 2, \dots, n$ are the design variables, which are the values of the induced strains in n regions of the plate. The other design variable is σ_{max} which is also the objective function. The constraints require that the equivalent stress, σ_{eq} is lower than σ_{max} at n_e element centers.

Numerical optimization was carried out with the finite element model described in the previous section. The optimization employs sequential linear programming using the MINOS package, Murtagh and Saunders (1983).

4. ANALYTICAL OPTIMIZATION

4.1. Axisymmetric case

As mentioned earlier, the plate was treated analytically as an infinite plate. We consider a circular ring around the hole with induced strains $\varepsilon_r^i = \varepsilon_\theta^i = \varepsilon^i$. The stresses and deformations in a circular ring with radial induced strain variation will be a function of radius only. The stress distributions are given in Burgreen (1971). It was found that applying axisymmetric induced strains in an isotropic circular ring does not have any effect on the interior stresses. This property was used to find the optimized induced strain distributions. For a general case, where K is the desired stress concentration factor, the optimized induced strain distribution to reduce the tangential stress to K (K = 2 in this case) was obtained as

$$\varepsilon^i(r) = \frac{S}{E} \left[K \frac{A}{r} + \left(\frac{A}{r} \right)^4 + 2(1 - K) \right] \tag{2}$$

Induced strain distributions for Von-Mises and maximum shear stress criteria were also obtained by integrating ODE. All three induced strain distributions are shown in Figure 3. We can see that for these three stress criteria, the induced strains are applied over $r \leq 1.25A, r \leq 1.21A$, and $r \leq 1.17A$ respectively. The maximum shear stress criteria gives the smallest region over which the induced strains are applied. Optimized induced strain distribution for this case can be approximated very closely by the following expression

$$\varepsilon^i_M(r) = \frac{S}{E} \left[K \left(\frac{A}{r} \right)^2 + \left(\frac{A}{r} \right)^4 + 2(1 - K) \right] \tag{3}$$

To better simulate fiber type actuators, the problem was solved with only tangential strain (i.e., $\varepsilon_r^i = 0$). Optimized induced strains were found slightly higher than that required for the isotropic induced strain case.

4.2. Non-axisymmetric case

Analytical solutions of stresses for non-axisymmetric induced strain distributions were obtained using a stress function $\phi(r, \theta)$ developed by Forray (1958) for the

case of applied temperature $T(r, \theta)$. The plane-stress equations of equilibrium and compatibility are satisfied if the stress function $\phi(r, \theta)$ is obtained such that

$$\nabla^4 \phi = - E\alpha\nabla^2 T \tag{4}$$

For the case of isotropic induced strains, $\varepsilon_r{}^i = \varepsilon_\theta{}^i = \varepsilon^i$, we can replace αT by ε^i. For a prescribed induced strain distribution $\varepsilon^i(r, \theta)$ in the form

$$\varepsilon^i(r, \theta) = P_o(r) + \sum_{i=1}^{\infty} \left[P_n(r) \cos n\theta + Q_n(r) \sin n\theta \right] \tag{5}$$

the complete solution of equation (4) can be found in Forray.

Similar to axisymmetric case, we apply induced strain distributions over a region $A \leq r \leq R$, where $R = 1.5A$. The non-axisymmetric induced strain distribution was chosen as

$$\varepsilon^i(r, \theta) = - \quad (r) \cos 2\theta \tag{6}$$

The above induced strain distribution was chosen because it produces compressive stresses over $45^0 \leq \theta \leq 90^0$ and tensile stresses over $0^0 \leq \theta \leq 45^0$ of the plate and hence will reduce the stress concentration over the critical region.
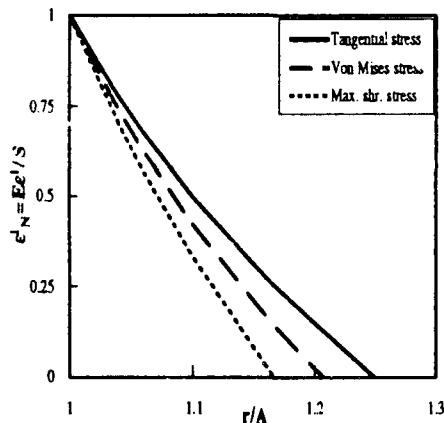
Figure 3: Optimized induced strain distributions for axisymmetric case (analytical solution)
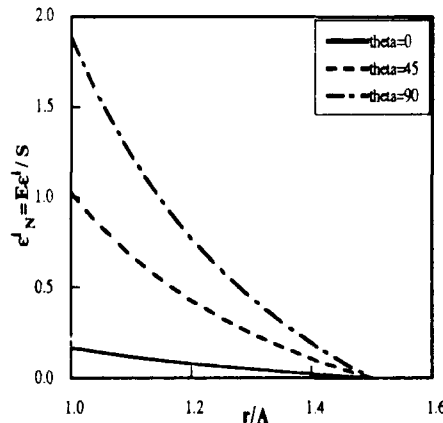
Figure 4: Induced strain distributions for maximum shear stress (analytical solution)

To optimize the induced strain distribution, the induced strain was assumed to be of the form

$$\varepsilon^i(r, \theta) = \lambda_A \varepsilon^i_A(r) - \lambda_N \varepsilon^i_N(r) \cos 2\theta \tag{7}$$

Equations (2) and (3) were used as $\varepsilon^i_A(r)$ and $\varepsilon^i_N(r)$ respectively. The values of K were adjusted such that the induced strains become zero at $r = 1.5A$. The two variables λ_A and λ_N were found by sequential linear programming problem using MINOS. The stress concentration factor for maximum shear stress

criterion was reduced to 1.46 and corresponding values of λ_A and λ_N were obtained as 0.7612 and 0.5414 respectively. The induced strain distributions at $\theta = 0^0, 45^0, 90^0$ are shown in Figure 4.

5. NUMERICAL OPTIMIZATION

5.1. Axisymmetric case

The analytical solution for the tangential stress minimization of eqn. (2) was used as a starting point for the numerical optimization. The optimal applied strain distributions for the three stress criteria are shown in Figure 5. The stress concentration factor for tangential, Von-Mises and maximum shear stress criteria were reduced to 1.96, 1.97 and 1.98 respectively. The same problem was solved for the case $\varepsilon_r^i = 0$ and optimized induced strain distributions were slightly higher than the strains required for the isotropic expansion case.

5.2. Non-axisymmetric case

Strains were first applied on the five rings for a sector $45^0 \le \theta \le 90^0$ in the *quarter plate model*. The optimal strain distributions are shown in Figure 6. The stress concentrations, as measured by the Von-Mises and maximum shear stresses, were reduced to 1.62 and 1.56, respectively. Next, strains were also applied on the sector $0^0 \le \theta \le 45^0$, thus leading to a ten-variable representation of the strain distributions. Very little improvement was observed. Finally, the strain distribution was obtained by dividing the quarter plate into four sectors, 22.5^0 each, leading to a twenty-variable representation of the strain distribution.
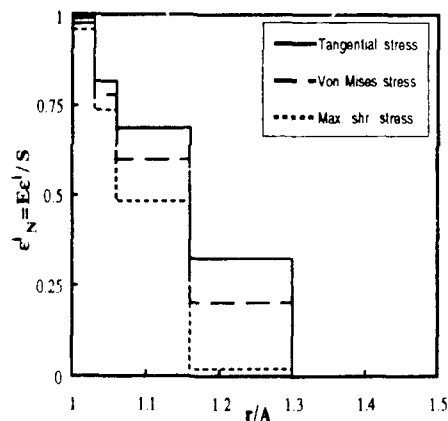
Figure 5: Optimized induced strains for axisymmetric case (numerical solution)
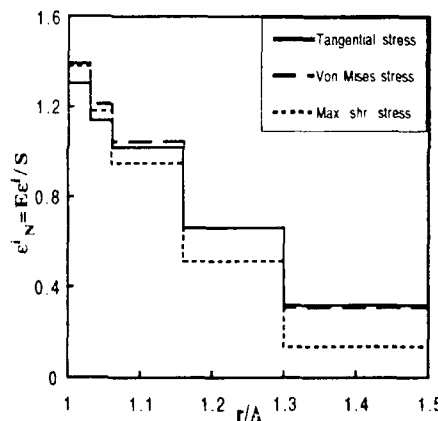
Figure 6: Optimized induced strain distributions (strains applied over $45^0 < \theta < 90^0$)

Again, almost no improvement over the five-variable case was observed. However, the induced strain distributions obtained for these two cases are quite different. Optimal induced strain distributions to minimize Von-Mises and maximum shear stresses were also found for four different cases, in which the

induced strain values were constrained. The four cases were: (1) $\varepsilon^i \geq 0$, (2) -1.38E-3 $\leq \varepsilon^i \leq$ 1.38E-3, (3) -1.15E-3 $\leq \varepsilon^i \leq$ 1.15E-3, (4) 0 $\leq \varepsilon^i \leq$ 1.38E-3. Practically the same reductions are achieved in the constrained cases as in the non-constrained case.

6. CONCLUSIONS

Analytical and numerical optimization were used to demonstrate that stress concentration factors for a plate with a hole can be reduced substantially by applying induced strains over a small area of the plate. With axisymmetric induced strain distributions the stress concentration factor was reduced from 3 to 2. Induced strains were required in a ring around the hole with an outer diameter of 1.17 times the hole diameter. When induced strains were applied only in the tangential direction, the same stress reduction was achieved with a slightly different induced strain distribution. Non-axisymmetric induced strain distributions were able to reduce the stress concentration factor to 1.46 with induced strains applied to an area with outer diameter 1.5 times the diameter of the hole. By increasing this area larger stress reductions could be achieved. Constraints imposed on the the magnitude of the applied induced strain led to only slightly higher maximum stresses. The results obtained by analytical optimization and numerical optimization were quite close.

REFERENCES

Burgreen, D., *Element of Thermal Stress Analysis*, C. P. Press, 1971.

Crawley, E.F. and de Luis, J., *Use of Piezoelectric Actuators as Elements of Intelligent Structures*, AIAA Journal, 1987, Vol 25, No 10, pp 1373-1385.

Forray, M., *Thermal Stress in Rings*, The Journal of the Aero Space Sciences, 1958, page 310-311.

Lin, M.W. and Rogers, C.A., *Analysis of Stress Distribution in a Shape Memory Alloy Composite Beam*,AIAA-91- 1164-CP, Proceeding, AIAA/ASME/ASCE/AHS/ASC 32nd Structures, Structural Dynamics and Materials Conference, Baltimore, MD, April 8-10, 1991.

Murtagh, B. A. and Saunders, M. A., *MINOS 5.0 User's guide*, Technical Report Sol 83-20, Stanford University, 1983.

Rogers, C.A., Liang, C. and Li, S., *Active Damage Control of Hybrid Material Systems Using Induced Strain Actuator*, Center for Intelligent Material Systems and Structures, Virginia Polytechnic Institute and State University, Blacksburg, VA, Unpublished.

Timoshenko, S.P. and Goodier, J.N., *Theory of Elasticity*, McGraw-Hill, 1970.

Interferometric signal processing for strain and vibration sensing using two-mode and Bragg grating fiber sensors

A. D. Kersey and T. A. Berkoff [‡]

Optical Techniques Branch, Code 6574, Naval Research Laboratory,
Washington, D.C. 20375

ABSTRACT: Phase shift detection techniques for two beam fiber optic interferometric sensors are well developed and have been used in a number of important system demonstrations of the technology. In this paper we discuss fiber sensor types which utilize variant interferometric signal processing techniques to provide high resolution strain and vibration sensing for smart structures applications.

I. INTRODUCTION

A range of interferometric fiber optic sensors have been demonstrated over the years to monitor a variety of different parameters [1] including magnetic [2] and acoustic [3] fields. With these sensors, the measurand field induces fiber strain which in turn results in a phase shift in the interferometer output. Several different methods have been demonstrated to recover phase shift information from a remote two-beam interferometer in a passive mode [4,5] using laser frequency modulation concepts. These techniques have also been adapted to measure not just relative phase changes, but absolute changes in interferometer phase [6,7] and thus optical path imbalance. Here we show how such interferometric-type signal processing concepts can also be used with other sensor types, specifically dual-mode e-core and fiber grating based fiber sensors.

II. PRINCIPLE

A fiber interferometer with a path imbalance ΔL between the arms is a wavelength-dependent device. If the source light coupled to the device is frequency modulated, the interferometer output is phase modulated and can described by

$$I = A\{1 + k\cos(\phi_0 + \Delta\phi\sin\omega t)\} \qquad (1)$$

where A is a constant determined by the source power, losses in the system due to couplers, etc., k is the interference visibility, which depends on polarization differences between the recombining beams, splitting ratio of the couplers, and the source coherence properties, ϕ_0 is the bias phase term of the interferometer and $\Delta\phi$ is the laser-modulation-induced phase carrier amplitude given by

$$\Delta\phi = 2\pi\Delta v\Delta Ln/c \qquad (2)$$

with, Δv the frequency deviation of the laser emission frequency, ω the modulation frequency, ΔL the optical path difference, and n the effective index. Expansion of Eqn (1) shows that this phase modulated output contains a series of even and odd harmonics of ω that vary as cosine and sine respectively of the phase term ϕ_0. By synchronous detection at the first and second harmonics of ω, the following quadrature phase signals can be obtained:

$$I_1 = 2AkJ_1(\Delta\phi)\sin\phi_0 \tag{3.a}$$

and;

$$I_2 = 2AkJ_2(\Delta\phi)\cos\phi_0 \tag{3.b}$$

where J_1 and J_2 are the Bessel functions of the first kind. These two signals can be balanced by adjusting the depth of FM modulation to $\Delta\phi = 2.6$ radians where J_1 is equal in magnitude to the J_2 Bessel function. With these quadrature phase signals available, a linear output corresponding to fiber strain can be readily obtained either by differentiate and cross multiply [4], or other phase tracking [8] schemes. This laser-FM based signal processing concept is widely used in interferometric sensor systems for the passive remote interrogation of sensors designed for the detection of weak time-varying strain. The scheme can also be used to track larger phase excursions caused by higher strain levels using, for example, directional fringe counting [9]. This technique, however, suffers from the problem of ambiguity; the phase shift measured indicates only a relative change in fiber strain and not the absolute change. The information required to assess the absolute shift is, however, contained in the interferometer output (Eqns. 1 and 2). From Eqn. 2, the amplitude of the laser-FM induced phase shift $\Delta\phi$ is directly proportional to the interferometer path imbalance ΔL. Consequently, changes in ΔL can be monitored by precisely determining the induced phase carrier $\Delta\phi$ at a given laser frequency modulation deviation Δv. A number of approaches based on this adaptation of the basic phase generated carrier (PGC) technique have been described for achieving quasi-static (DC) strain sensing capability using an interferometer. We have investigated two schemes, one based on a J_1/J_2 Bessel ratiometric approach, and the second on a J_0 Bessel function tracking scheme (see refs. 6 and 7 for details). In the following sections we discuss how this same type of signal processing concept can be used with other sensors types, namely two-mode e-core and Bragg grating sensors, to allow the remote passive detection of strain.

III. E-CORE FIBER STRAIN SENSOR

Two-mode elliptical core fiber sensors have been widely proposed for use in smart materials and structures applications [10,11]. A two-mode fiber sensor can be viewed as a form of common fiber two-beam interferometric device, where the two beams are formed by the two spatial modes in the fiber. Due to their different propagation constants, there is an effective optical path difference between the modes within the fiber. For a range of e-core fiber parameters, a suitable delay can be achieved between the two modes so that there is a phase dependence on laser frequency of the form described by Eqn 2. This dependency can be expressed as

$$\Delta\phi = 2\pi \; \kappa(\beta_{01} - \beta_{11}) \, \Delta v \tag{5}$$

where the coefficient $\kappa(\beta_{01} - \beta_{11})$ is dependent on the difference in the propagation constants β_{01} and β_{11} of the LP_{01} and LP_{11} even modes respectively, which are determined by the e-core fiber parameters and source wavelength. This dependence on laser frequency allows interferometric demodulation techniques to be used with two-mode e-core sensors to provide passive remote phase interrogation.

The use of phase-generated carrier demodulation with a two-mode fiber sensor was demonstrated using the configuration shown in Figure 1. Light from a 0.83 μm laser diode source was coupled to single mode fiber which guided the light to the e-core sensing fiber. This fiber, which was ~ 10 m in length, was wound on a piezoelectric transducer so that test strains could be applied. The output of the e-core fiber was spatially filtered using single mode fiber in an offset splice to produce a cosinusoidal phase signal at the single-mode fiber output. Modulation was applied to the laser supply current to produce a FM induced phase carrier at the photodetector output. Figure 2 shows an example of the photodetected signal when sinusoidal modulation is applied to the laser diode supply
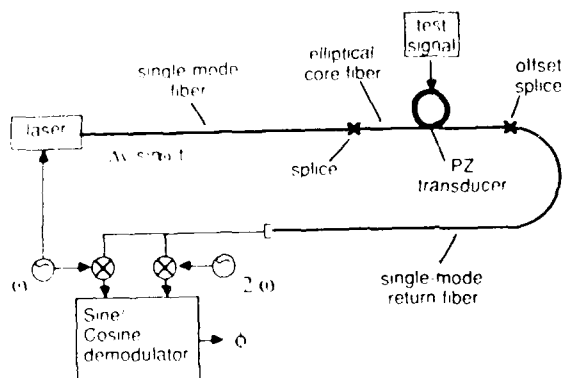
Figure 1. Passively phase interrogated e-core fiber sensor arrangement.
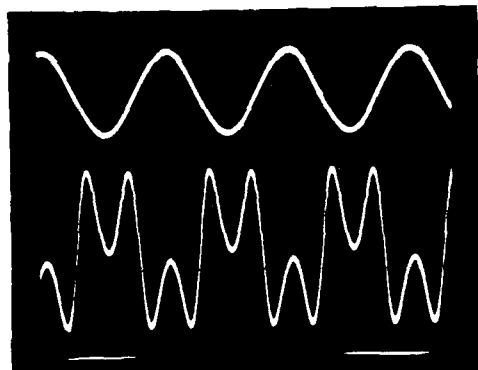
Figure 2. E-core sensor output response to a sinusoidal laser frequency modulation.
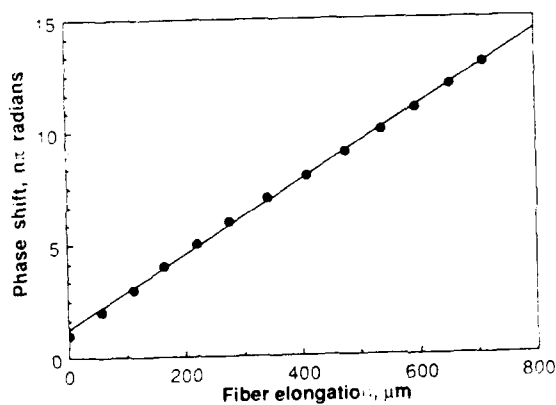
Figure 3. Phase shift responsivity of the e-core sensor to strain induced by a
piezoelectric cylinder.

current. To obtain sine/cosine quadrature phase signals a high frequency carrier of 40 kHz was used which was then synchronously detected at the photodetector output. Phase shift responsivity to fiber strain was determined by monitoring a phase carrier signal while applying voltage to the piezoelectric transducer and is shown in Figure 3. From this measurement the strain responsivity of the fiber (fiber elongation for a 2π phase shift) was calculated to be 119 μm. To fully demodulate the sine/cosine signals and provide an output proportional to dynamic fiber strain, a differentiate and cross multiply circuit was used. The noise floor of this arrangement was recorded at several different frequencies over the signal band: a phase sensitivity of 50 μrad/√Hz or better was achieved from 20 to 1000 Hz which corresponds to a fiber length change smaller than 1 nanometer, or a strain resolution of 10^{-10} for the 10 m length used.

IV. FIBER GRATING SENSOR

In-fiber Bragg grating sensors [1,2] have attracted considerable interest over the past few years because of their intrinsic nature and wavelength-encoded operation. These sensors are particularly attractive for quasi-distributed sensing, as many gratings can be written into a length of fiber and addressed using either wavelength-division multiplexing or time-division addressing. Consequently, these devices are potentially useful for a variety of applications, particularly in the area of advanced composite materials or 'smart structures', where fibers can be embedded into the materials to allow real time evaluation of load, strain, temperature, vibration etc.

The primary drawback of this sensing approach lies in the detection of the wavelength shift, $\Delta\lambda$, of the sensor returns. This function can be provided by a spectrometer or monochromator, or by a more simple arrangement involving a dispersive element coupled with a image array, such as a CCD detector array. These systems are unattractive due to the bulk-optical nature, size and lack of ruggedness, and limited resolution capability.

The means used to detect the wavelength shift of a grating sensor described here is based on the use of an unbalanced fiber interferometer wavelength discriminator. The proposed system for a single grating sensor is shown in Figure 4. Light from a broadband source is coupled into the fiber which transmits the light to the grating element. The wavelength component reflected back along the fiber towards the source is tapped off using a coupler and fed to a unbalanced Mach-Zehnder interferometer. This light effectively becomes the source light into the interferometer; wavelength shifts induced by perturbation of the grating resemble a wavelength (optical frequency) modulated source. The interferometer output is thus of the form described by Eqn 1, i.e. $I(\lambda) = A\{1 + k\cos[\psi(\lambda) + \phi]$, where $\psi(\lambda) = 2\pi n\Delta L/\lambda$, λ is the wave-length of the return light from the grating sensor (sensor signal) and ϕ is a bias phase offset of the Mach-Zehnder interferometer. The wavelength shift of the grating signal is proportional to the fiber strain, $\Delta\varepsilon$, i.e. $\Delta\lambda = \gamma \Delta\varepsilon$, γ is the strain-to-wavelength shift responsivity of the grating. For a dynamic strain induced modulation in the reflected wavelength, $\Delta\lambda\sin\omega t$, from the grating sensor element, the change in phase shift $\Delta\psi(t)$ is thus: $\Delta\psi(t) = -\{2\pi n\Delta L/\lambda^2\}\Delta\lambda\sin\omega t$.

In the experimental demonstration of the scheme, the broadband source used was a diode-pumped Er-doped fiber superfluorescent source, producing ~ 300 μW of output power with a ~35 nm bandwidth (1530 - 1565 nm). The sensing grating, with nominal Bragg wavelength of 1545 nm, was attached to a piezoelectric transducer, which introduced known dynamic strain signals. Figure 5 shows the fiber grating transmission spectrum over the wavelength range 1544 to 1546 nm. The returned light was coupled to a fiber Mach-Zehnder interferometer of 10 mm (± 2 mm) fiber imbalance which was held in quadrature by a feedback applied to a p/z cylinder fiber stretcher in one arm. Balanced photodetection of the interferometer output was used to provide intensity noise rejection. Figure 6 shows a power spectrum of the interferometer output observed with a dynamic strain perturbation of 0.12 με rms applied to the fiber grating at a frequency of 500 Hz. The signal to noise of the component at 500 Hz of 46 dB relative to a 1 Hz bandwidth and relatively flat noise floor
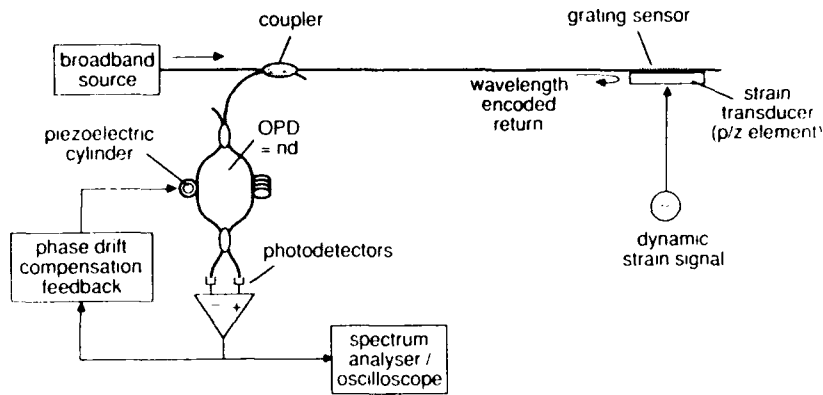
Figure 4. *Fiber grating system with interferometric wavelength shift determination.*
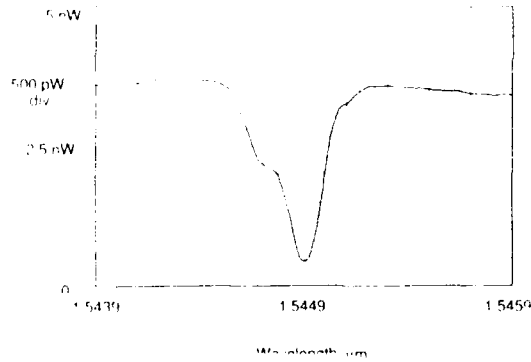
Figure 5. *Grating transmission spectrum.*
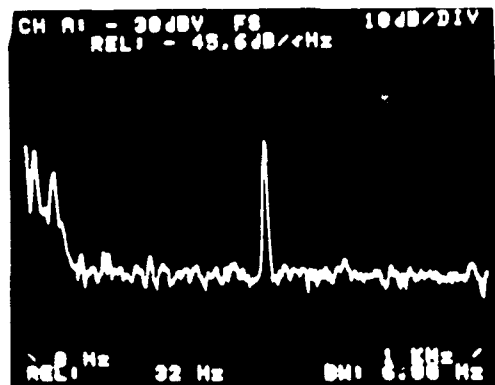
Figure 6. *Interferometer output power spectrum showing ~ 4 millirad signal rms at 500 Hz induced by dynamic 0.12 με rms strain applied to the fiber grating.*

above 100 Hz, sets a minimum detectable strain perturbation of ~ 0.6 nε/√Hz (nano-strain/√Hz) for frequencies greater than 100 Hz. The actual phase noise floor corresponds to a level of ~ 20 μrad/√Hz at frequencies above 100 Hz, limited by photodetector noise. The increased noise below 100 Hz is attributed to direct environmental perturbations of the MZ, which could be greatly reduced by shortening and shielding of the fiber arms.

V. CONCLUSIONS

In summary, we have demonstrated the use of a common interferometric signal processing concept for strain sensing using two-mode e-core and Bragg grating based sensors. High resolution detection of weak dynamic strain induced shifts in the reflection wavelength from an in-fiber Bragg grating sensor element has been demonstrated (dynamic strain resolution of ~ 0.6 nε/√Hz at frequencies > 100 Hz).

VI. ACKNOWLEDGEMENTS

VII. REFERENCES

1. E. Udd, ed., Fiber Optic Sensors: An Introduction for Engineers and Scientists., John Wiley & Sons, Inc., New York, 1991.
2. F. Bucholtz, et. al., "Fiber Optic Magnetic Sensor Development", proc. SPIE 718, Fiber Optic and Laser Sensors IV, Cambridge, Mass., p. 56, 1987.
3. A. M. Yurek, A. B. Tveten, and A. Dandridge, "High Performance Fiber Optic Hydrophones in the Artic Environment", Proc. Optical Fiber Sensors '90, p. 321, 1990.
4. A. Dandridge, A. B. Tveten and T. G. Giallorenzi, " Homodyne demodulation scheme for fiber optic sensors using phase generated carrier", IEEE J. Quantum Electron., QE-18, p. 1647, 1982.
5. D. A. Jackson, A. D. Kersey and M. Corke, " Pseudo-heterodyne detection scheme for optical interferometers", Electron. Lett., 18, p. 1081, 1982.
6. M.J. Marrone, T.A. Berkoff, and A.D. Kersey, "Fiber-Optic Temperature and Pressure Sensors in the All Optical Towed Array Using Bessel Ratio Interrogation Technique", Naval Research Laboratory Memorandum Report # 6639, May 25, 1990.
7. T.A. Berkoff and A.D. Kersey, "Interferometric Fibre Displacement/Strain Sensor Based on Source Coherence Synthesis", Electronics Letters, Vol. 26, No. 7, p. 452, 1990.
8. T.A. Berkoff, A.D. Kersey, and R.P. Moeller, "Novel Analog Phase Tracker for Interferometric Fiber Optic Sensor Applications," Proc. Fiber Optic and Laser Sensors VIII, SPIE Vol. 1367, p. 53, San Jose Sept., 1990.
9. E.R. Peck and S.W. Obetz, "Wavelength or Length Measurement by Reversible Fringe Counting", Journal of the Optical Society of America, Vol. 43, No. 6, p. 505, 1953.
10. B.Y. Kim, et. al., "Use of Highly Elliptical Core Fibers for Two-Mode Fiber Devices", Optics Letters, Vol. 12., No. 9, p. 729, 1987.
11. K.A. Murphy, et. al., "Elliptical-Core Two-Mode Optical-Fiber Sensor Implementation Methods, Vol. 8, No. 11, p. 1688, 1990.
12. G. Meltz, W.W. Morey, and W. H. Glenn, "Formation of Bragg gratings in optical fiber by a transverse holographic method," Optics Lett., 14, p. 823, 1989.
13. W.W. Morey, " Distributed Fiber Grating Sensors," Proc. OFS,90, p. 285, Sydney, Australia, Dec. 1990.
14. W.W. Morey, J. R. Dunphy and G. Meltz, "Multiplexed fiber Bragg grating sensors", Proc. 'Distributed and Multiplexed Fiber Optic Sensors', SPIE vol. 1586, paper #22, Boston, Sept. 1991.

† - SFA Inc., Lanover, Md. 20785.

Optical fiber Fabry–Perot sensors for smart structures

C. E. Lee, J. J. Alcoz, Y. Yeh, W. N. Gibler, R. A. Atkins, and H. F. Taylor

Department of Electrical Engineering
Texas A&M University, College Station, Texas 77843

ABSTRACT : A fiber Fabry-Perot interferometric (FFPI) sensor with internal mirrors is developed to sense temperature, strain, acoustic waves and other physical perturbations. These sensors have been successfully embedded in composites and metal structures. The performance of the FFPI sensor is demonstrated and application of these sensors to smart structures is discussed.

1. INTRODUCTION

Fiber optic sensors are being developed widely for smart structures because they provide immunity to electromagnetic interference (EMI), high sensitivity and are amenable to multiplexing. Numerous studies on embedding of fiber sensors in composites and plastic have been conducted. However, most sensor designs have not provided both high sensitivity and localized parameter measurement.

Interferometric sensing schemes generally provide much higher sensitivity than other fiber sensors. Most of the interferometric sensors investigated to date utilize Mach-Zehnder, Michelson or Sagnac interferometers. These interferometers require a fiber coupler which presents major impediments to both miniaturazation and to embedding. They also may require compensation for polarization induced signal fading. The Fabry-Perot configuration, in which the interferometer is formed by two reflectors in a single mode fiber, has been shown to provide high sensitivity "point" sensing and multiplexing capability.

2. THE FIBER FABRY-PEROT INTERFEROMETER

2.1 Fabrication of Internal Mirrors

Over the past several years, a novel fusion splicing technique for fabricating internal mirrors in continuous lengths of optical fibers has been developed at Texas A&M University. This technique produces a permanent joint between a coated with a thin dielectric layer and an uncoated fiber[1]. The mirror reflectance can be adjusted during the fusion process. Typical coating thickness is 1000Å for low finess FFPIs. Reflectances of the individual mirrors ranging from less than 1% to larger than 85% have been demonstrated[2], with excess losses of only a few percent. Two of these mirrors separated by a length of single mode fiber, typically one centimeter, form the cavity of a fiber Fabry-Perot interferometer (FFPI).

The internal mirrors have good mechanical properties (tensile strength is approximately 40 kpsi), which enable them to withstand the thermal and mechanical stresses experienced during the process of embedding them in a variety of materials. FFPIs produced at Texas A&M have been embedded in graphite-epoxy composites in materials laboratories at McDonnell Douglas and Stanford University. Recently, we have also succeeded in producing cast aluminium parts containing embedded FFPIs.

2.2 Principle of Fabry-Perot Inteferometer
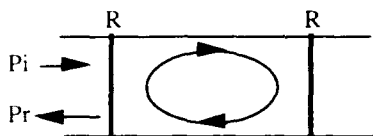
Fig. 1. Fabry-Perot Interferometer

A reflectively monitored FPI is illustrated in Fig. 1. For the FPI with low reflectance mirrors, R <<1, the ratio of the reflected optical power Pr to the incident power Pi can be approximated by[3]

$$Pr/Pi = 2R (1- \cos \phi)$$

where ϕ is the round-trip phase shift inside the cavity, given by $\phi = 4\pi nL/\lambda$ with L the length of the cavity, n its index of refraction, and λ the free space wavelength of the light source. This result indicates that parameters such as temperature, strain or ultrasound pressure, which perturb the optical length nL of the cavity can induce the reflected power to sweep through maxima and minima of interference fringes. By observing the reflected power from the FFPI, the perturbation can be measured.

3. PERFORMANCE OF FFPI SENSORS

3.1 Temperature Sensing

Experiments with these FFPI sensors have been carried out using pulse modulated 1.3 µm laser diode light sources, with the output signal monitored in reflection. A FFPI temperature sensor with a 1.5mm-long cavity has been operated from -200°C to +1050°C[4]. We believe that this is still the greatest range of operating temperature reported for any fiber-optic sensor. Also, the performance of this sensor in a strong electromagnetic field environment has demonstrated[5].
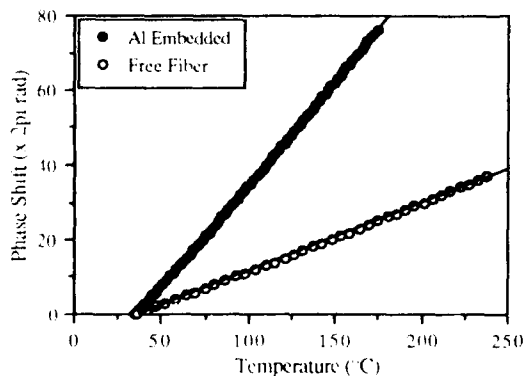
Fig. 2. Temperature dependence of phase shift for two FFPI sensors and their linear fits.

A FFPI sensor embedded in 8 layers of graphite-epoxy panel was produced to measure the temperature change of the composite sample[6]. Sensitivity of this embedded sensor was calculated and the thermal expansion coefficient of the composite along the fiber axis was estimated. Recently produced cast aluminium parts containing embedded FFPIs were tested and the temperature sensitivity was measured[7] to be almost three times greater than for the same sensor in air as shown in Fig. 2. The difference is attributed primarily to the length change in the fiber due to the large thermal expansion coefficient of the aluminium.

3.2 Strain Sensing

For strain testing of the composite, the FFPI sensor was embedded between the
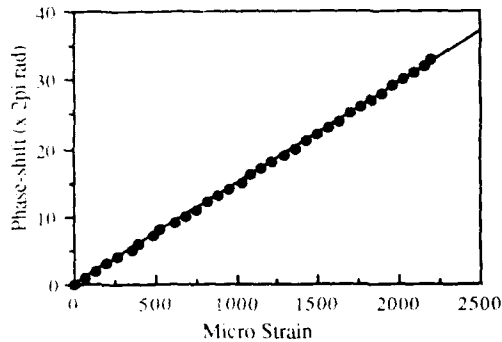
Fig. 3. Dependence of FFPI phase shift on strain.

second and third layer of a 16-layer graphite/PEEK coupon. Two electric strain gauge (ESGs) were bonded to opposite side of the sample, above and below the embedded FFPI. A strain is generated by applying a load to the center of the coupon. Fig. 3 shows strain response of the sensor calibrated by ESGs at the position of the fiber (2/16) in the coupon. The strain sensitivity is determined from Fig. 3 to be 9.1 x 10^{6} rad/m. This value is consistent with the previous reports measured with a He-Ne laser source[8]. Measurements were also made at elevated temperatures. Both the FFPI and ESG showed good linearity
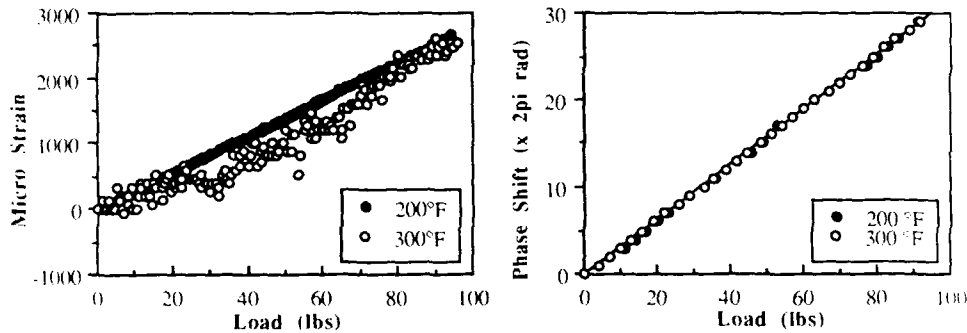
Fig. 4. Response of (a) ESG and   (b) FFPI sensor at 200 and 300 °F.

at 200 °F. However, as indicated by the data of Fig. 4 (a), at 300 °F the ESG response was unstable. By contrast, the FFPI sensor gave the same linear load profiles at 200 and 300°F in Fig. 4(b).

3.3 Ultrasound Sensing

Ultrasound sensors are widely used for non-destructive evaluation (NDE) of structures. Typical applications are acoustic emission detection and pulse-echo testing using piezo electric elements. These sensors are rugged and sensitive, but their response is strongly dependent on the acoustic frequency. Also, they are subject to EM interference.

Ultrasound sensing experiment were conducted on composite and cast aluminium parts with embedded FFPIs over the frequency range of 0.1 to 8 MHz. Phase modulation indices were 0.5[3] and 1.5 rad[7] for composite and aluminium respectively. The "pencil breaking" technique which is sometimes used for transducer calibration was carried on these samples. The acoustic shock waves generated on the composite were detected by a FFPI sensor as in Fig. 5. A signal for triggering the oscilloscope was provided by a PZT transducer attached on the surface of the sample. The PZT was also used to generate an acoustic pulse, and the reflected acoustic pulse wave was monitored with the fiber sensor, as in Fig. 6. The acoustic delay of the reflected pulse corresponds to the transit time across the sample thickness of 5.4 mm.
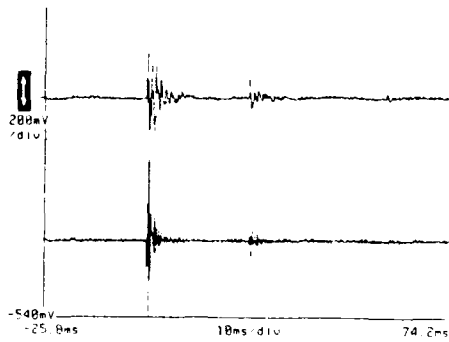
Fig. 5 Detected pencil-breaking (upper) and the PZT trigger signal (lower trace).
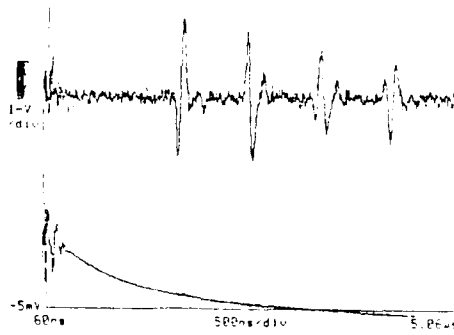
Fig.6 Acoustic pulse-echo signal (upper) and the pulser trigger signal (lower trace).

4. DIGITAL SIGNAL PROCESSING

Signals from the reflectively monitored FFPI sensors are well suited for processing by digital means under microprocessor control. A processing system which samples reflected waveforms from a sensor FFPI and a reference FFPI to produce a digital readout the sensor temperature has been demonstrated in our laboratory. This design can be easily extended to the processing of signals from a time-division-multiplexed sensors using a single light source and photodetector.

5. CONCLUSION

In conclusion, FFPI sensors have been embedded in structural materials of interest for "smart skins" applications - graphite composites and cast aluminium. High sensitivity and point sensing capability for measurement of temperature, strain, and ultrasound waves have been demonstrated. Also a sensing system utilizing a digital processor with time-domain multiplexing capability has been developed.

6. REFERENCES

(1) C. E. Lee and H. F. Taylor, Electron. Lett. 13, 1038, 1988.
(2) C. E. Lee and H. F. Taylor, submitted to J. of Lightwave Tech.
(3) J. J. Alcoz, C. E. Lee, and H. F. Taylor, IEEE Trans. UFFC-37, 302, 1990.
(4) C. E. Lee, R. A. Atkins, and H. F. Taylor, Opt. Lett. 13, 1038,1988.
(5) Y. Yeh, C. E. Lee, R. A. Atkins, W. N. Gibler, and H. F. Taylor, J. Vac. Sci. Tech. A(8), 3247, Jul/Aug, 1990.
(6) C. E. Lee, H. F. Taylor, E. Udd, and A. M. Markus, Opt. Lett. 14, 1225, 1989.
(7) C. E. Lee, W. N. Gibler, R. A. Atkins, J. J. Alcoz and H. F. Taylor, will be published on Opt. Lett., 1992.
(8) T. Valis, D. Hogg, and R. M. Measure, Proc SPIE 1370,154, 1990.

Hybrid fiber optic strain sensor resolves directional ambiguity of time multiplexed Fabry-Perot

J. P. Andrews

Martin Marietta Aero & Naval Systems

Baltimore, Maryland 21220

Abstract

The sensor described in this paper is a hybrid design combining an extrinsic Fabry-Perot interferometer with a longitudinal misalignment strain sensor. Using two techniques simultaneously resolves the directional ambiguity of the interferometer and the lead fiber sensitivity of the intensity sensor. Further, this design is easily time-multiplexed. The basic principle of operation is proven in a laboratory experiment and strain in a unclamped cantilever beam is measured.

Sensor Design

The sensor consists of two sections of optical fiber and one section of hollow tubing whose inner diameter is very slightly larger than the outer diameter of the optical fibers. For the prototype the hollow tubing is silica capillary tube drawn from a preform using the same technique as in optical fiber manufacturing. As shown in Figure 1 the two sections of fiber are inserted into the tube such that the air gap, s, is ~100μm . The fibers are then either tacked into place with a fusion "weld" for embedded applications or left unbonded for external "attached" applications.
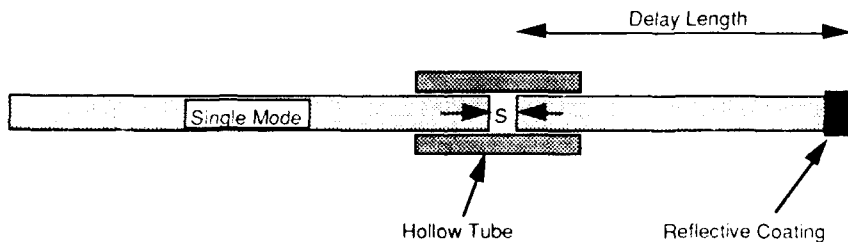
Figure 1.

As shown in Figure 2 the optical source for this system is an Optical Time Domain Reflectometer, OTDR. This system contains a laser that launches short pulses into the single mode lead fiber. Upon reaching the "air gap splice" two Fresnel reflections are created. One from the glass-air interface of the lead-in fiber and one from the air-glass interface of the lead-out fiber. These two reflections are out of phase by an amount proportional to the length of the air gap, s. Because of the relatively long coherence length of some OTDR systems (~1.3mm in air) these two reflections interfere and go through constructive and destructive interference fringes as the air gap, s, changes by multiples of $1/2$ wavelength. A limitation of

this sensor alone, however, is that the sensor response for increasing strain is the same as that for decreasing strain. This "directional ambiguity" is a problem with most interferometers. To overcome this problem a hybridization of two sensor concepts is used.
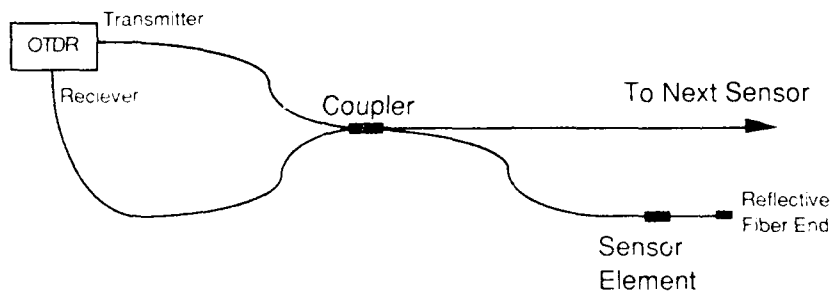
Figure 2.

Referring back to Figure 1 a third reflection is created at the far end of the lead-out fiber. The magnitude of this reflection is increased with the application of a reflective coating to the fiber end. This reflection is resolvable in time from the splice double-reflection providing the lead-out fiber is of sufficient length. For commercially available OTDR systems this length needs to be >4cm. The amplitude of this reflection is proportional to the air gap length, s. The original pulse from the OTDR system is attenuated by Fresnel reflections and the longitudinal misalignment, s, on its first pass through the air gap splice. Upon reflection from the far end of the lead-out fiber the pulse is again attenuated at the splice by an amount proportional to the gap length, s. Therefore when the host material is put into tensile strain the gap, s, increases causing more splice loss thus decreasing the amplitude of the far end reflection. Hence a direct correlation between reflected intensity and strain can be determined. For the purposes of this sensor, however, it is only the direction of amplitude change that is of interest. An increasing pulse amplitude indicates decreasing strain and vice versa. This information resolves the directional ambiguity of the Fabry-Perot interferometer.

Just as the interferometer working alone suffers from directional ambiguity, intensity sensors also have their limitations. Typical intensity based sensors are subject to erroneous data from intensity changes due to loss mechanisms affecting the lead fibers. In this configuration, however, if an intensity change is not accompanied by a corresponding number of fringes from the interferometer the intensity change can be ignored. Thus the interferometer resolves the fundamental problem of the intensity based sensor just as the intensity based sensor resolved the fundamental problem, directional ambiguity, of the interferometer.

This sensor design offers two other significant attributes. Interferometers are highly susceptible to thermal drift. Thermal drift is erroneous data from thermally induced phase shifts caused by the thermo-optic effect. In addition, polarization changes in the two interfering waves can cause the fringes to disappear. This occurs when the two interfering waves have their polarizations rotated such that the two waves are orthogonal. This is caused by changes in birefringence in the fibers. The degree of birefringence can be altered by physical perturbations and temperature changes and therefore is a significant problem for most applications.

This sensor overcomes these problems in the following way. The region in which the two interfering waves are separated is the air gap itself. Any perturbations to the signal will therefore have to occur in the air gap. The thermo-optic coefficients of a gases, air, are

orders of magnitude below that of silica therefore the thermo-optic effect is reduced by orders of magnitude nearly eliminating thermal drift. Second, air is a gas and therefore is not birefringent. Zero birefringence eliminates the problem of polarization fading which occurs in all-fiber interferometers. This occurs in fiber interferometers when the sensing *or* reference fiber is physically perturbed.

Experimental Results

Two experiments were performed to prove the validity of the sensor concept. The system was set-up as shown in Figure 2. The first test was to verify the air gap intensity sensor portion of the device. Longitudinal displacement was accomplished by mounting the lead-in and lead-out fibers on two alignment stages. Then, with piezo-electric controls, the lead-out fiber was moved back and intensity data recorded. Recall it is the reflected intensity from the far end of the lead-out fiber that is recorded and not the intensity from the splice double-reflection. The data for z-displacement vs. reflected intensity is shown in Figure 3.

Longitudinal Displacement vs. Normalized Power
(Far end reflection of lead-out fiber)

Longitudinal Displacement, μm
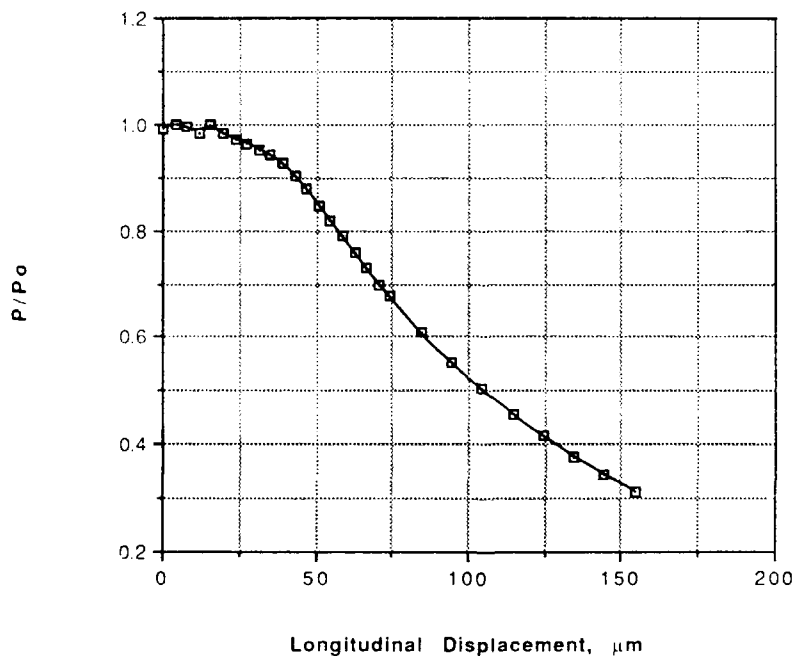
Figure 3.

The second experiment verified the interferometer part of the sensor. The sensor was mounted to a cantilever beam whose tip was incrementally displaced by a micropositioner. This time, however, the intensity information recorded was that of light reflecting off of the air gap splice itself. It is expected that the intensity will oscillate through fringes as the beam deflection causes the air gap, s, to expand through multiples of π, or 625nm. As shown in

Figure 4, the fringes are very clear. The data is displayed as strain vs. fringe number in Figure 5.

Strain vs. Sensor Response

Figure 4.

Cantilever Beam Strain vs. Number of Fringes

Microstrain
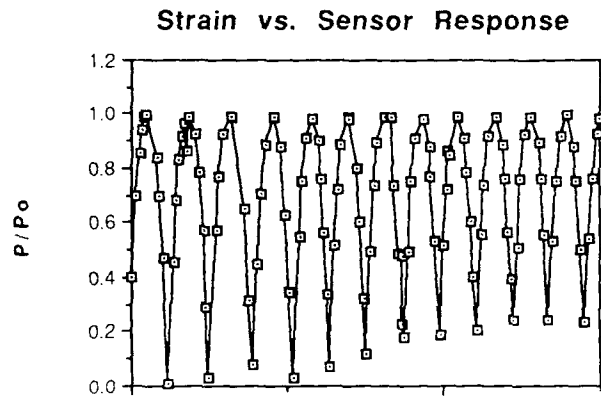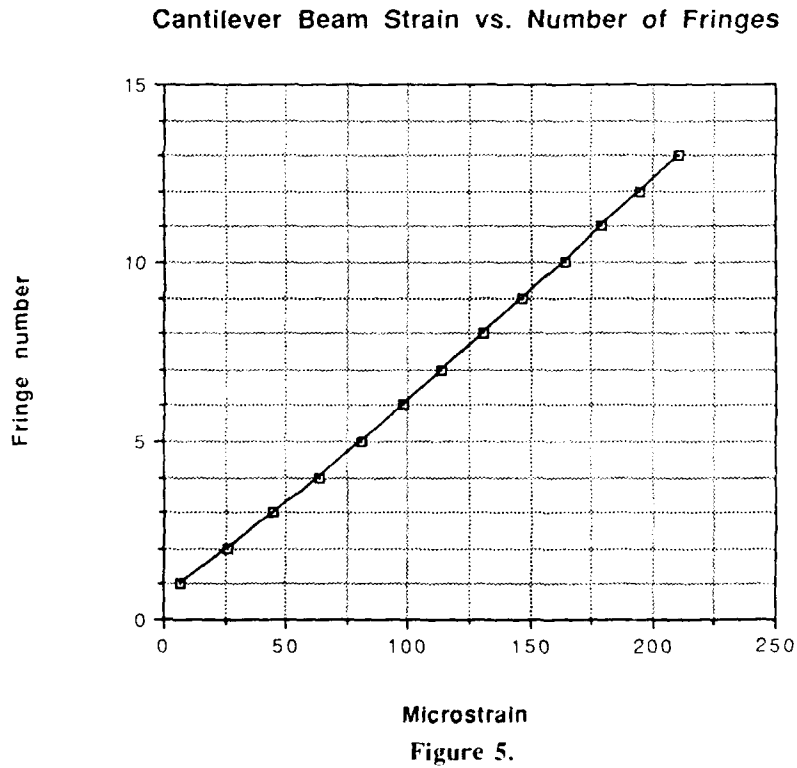
Figure 5.

Some error does exist in the data however the fact that manual data acquisition was possible is a tribute to the stability of the sensor. Typically interferometers will drift through many fringes in one minute whereas this design appears to have drifted only one fringe in the 21 minutes it took to record this data. The stability of the interferometer is attributed to the fact that the region in which the two interfering waves are separated is the air gap. As expected thermal drift and polarization fading are not a problem with this design.

One supporting experiment was also performed. The issue of lateral displacement is of some concern therefore the data was taken measuring the optical loss through the sensor vs. displacement in the radial direction. This data is shown in Figure 6. Because the capillary tubing allows a total of only 3 microns of movement, the power fluctuation will be ≤1%.

Lateral Misalignment vs. Normalized Power

Lateral Displacement, µm
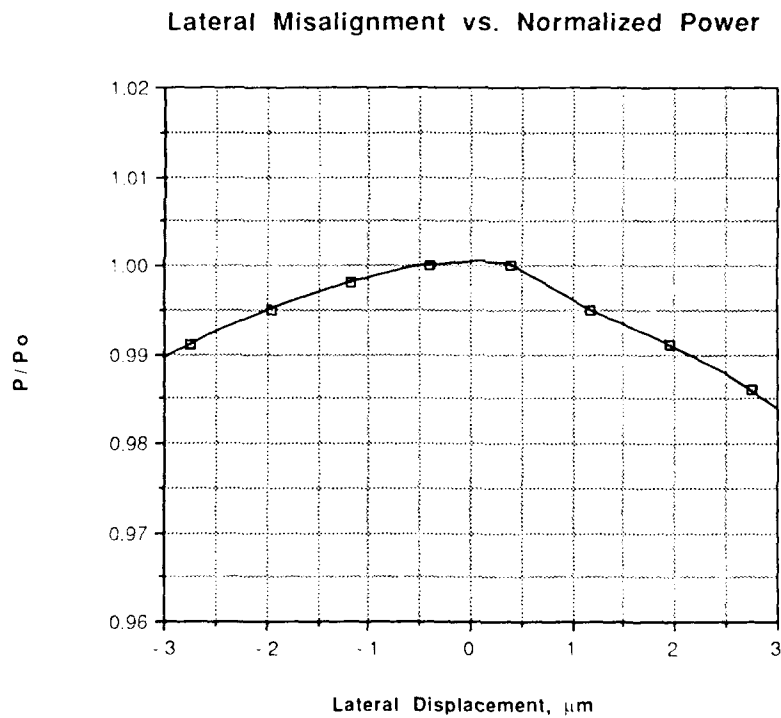
Figure 6.

Conclusion

It has been demonstrated that an optical time domain reflectometer can be used for interferometry. A new hybrid strain sensor using OTDR has been designed and tested with promising results. This design is easily multiplexable in addition to being very stable. Most importantly this sensor resolves the directional ambiguity of the interferometer.

Development of a fiber Fabry–Perot (FFP) strain gauge system

Dayle Hogg, Beck Mason, Tomas Valis,
and Raymond M. Measures

FiberMetrics Corporation, 4925 Dufferin Street,
Downsview, Ontario, CANADA, M3H 5T6

University of Toronto, Institute for Aerospace Studies,
4925 Dufferin Street, Downsview, Ontario, CANADA, M3H 5T6

ABSTRACT

The current status of fiber Fabry-Perot (FFP) strain sensors suitable for smart structure applications is reviewed. A high reflectivity, single-end, FFP strain gauge in conjunction with a pseudo-heterodyne demodulation technique capable of tracking high strain rates is presented. The linear nature and dynamic response of the system is demonstrated.

1. FFP STRAIN GAUGE

The fiber Fabry-Perot (FFP) sensor has been identified by our group and others as one of the leading candidates for strain monitoring in active material applications. The FFP sensor has a number of advantages over other fiber-optic sensors such as the Bragg and modal-domain type sensors. The primary advantages of the FFP sensor over other designs are its high sensitivity, ease of demodulation, and its single fiber / single ended nature. A portion of this work has been previously reported by the authors[6].

The FFP sensor has been developed by a number of groups using a variety of fabrication techniques. Claus et al.[1] at Virginia Polytechnic Institute fabricated an FFP sensor by supporting two cleaved single-mode fibers inside a hollow core fibre. The air-gap between the two fibers then forms the sensing cavity. Leilabady[2] at Amphenol also developed an FFP sensor from two semireflective air-gaps. A semireflective air-gap was fabricated by limiting the current during fusion splicing of two cleaved fibers, thus forming an air-gap in the core region of the fiber. A second air-gap reflector was then added to complete the FFP sensing cavity. A metal sheath placed over the two air-gap fusion splices provided mechanical strength. Both of these techniques rely on an air / glass interface to achieve a 4% reflectivity. Lee & Taylor[3] at Texas A&M developed a technique where titanium oxide was sputtered over the entire endface of an optical fibre, a second optical fiber was then fusion spliced on to form a semireflective splice. A second semireflective splice was then added to form the FFP cavity. Figure 1 illustrates the above mentioned FFP fabrication techniques.
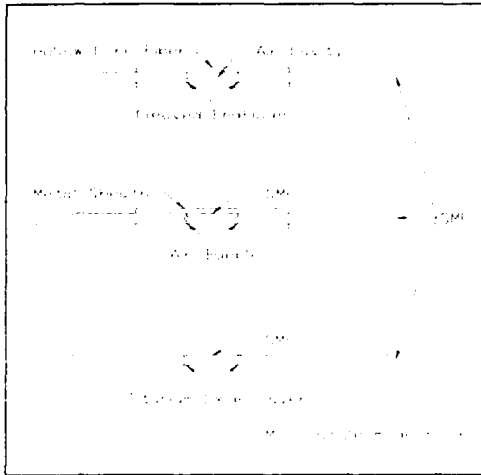
Figure 1: Methods of fabricating Fabry-Perot strain sensors in single-mode optical fibers.
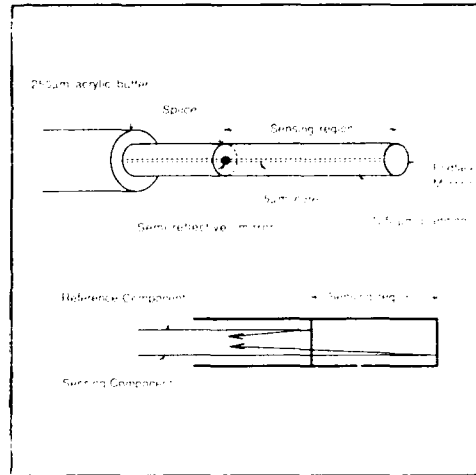
Figure 2: An intrinsic FFP sensor configuration using a localised semireflective fusion splice with a fully reflective second mirror.

In order to obtain a good depth of modulation with any of the above FFP fabrication techniques, a second matched, semireflective splice is required to complete the sensing cavity. Light from the two semireflective mirrors (approximately 4%) then propagates back to the demodulation optoelectronics. Since only a small percentage of the incident light at the sensor is reflected back to the detector, care must be taken to prevent light originating in the lead-out fiber from propagating back to the detection optoelectronics. This is usually accomplished by index-matching the end of the lead-out fibre with a suitable index-matched gel.

Present thinking on active material applications has strain sensors embedded within the composite materials which make up the structure. It is therefore desirable to have a sensor with a cross sectional area no larger than the lead-in/out fiber. Sensors which are fabricated from the fiber itself and require no external support members are termed intrinsic, while those requiring external mechanical support members are termed extrinsic.

A method of fabricating intrinsic FFP sensors which overcomes the above difficulties and makes better use of the incident light from the sensing region has been previously reported by the authors[4,5,6]. Figure 2 illustrates the sensor geometry used. A high reflectivity (>10%), and high loss (<80%) semireflective front splice is used. This allows for the use of a totally reflective second mirror, thus eliminating the need for an index-matched lead-out fiber. This approach also represents a substantial increase (from 8% to 20%) in the optical power being reflected back to the sensor's detection optoelectronics, thus increasing the signal to noise ratio of the sensing system.

2. STRAIN DEMODULATION

Signal demodulation refers to the extraction of the measurand of interest (i.e., strain, pressure, or temperature) from the optical signal present at the detector. All low finesse interferometers have essentially a sinusoidal response to a linear change in strain, pressure, or temperature, see Figure 3. Thus a signal demodulation scheme is required to determine the magnitude and direction of any change in the measurand coupled to the sensing region.

Figure 4 illustrates a strain demodulation system. Light from a laser diode is coupled to a 2×2 coupler through an optical isolator to prevent backreflected light from entering the lasing cavity and damaging the laser diode. A polarisation maintaining FC (PM-FC) connector is then used to connect the FFP strain gauge to the phase demodulation optics. Light returning from the FFP sensor is then coupled to a photodiode through the 2×2 coupler. A pseudo-heterodyne phase demodulation system is then used to interpret the change in optical length of the sensing region as a function of the measurand of interest, in this case strain.
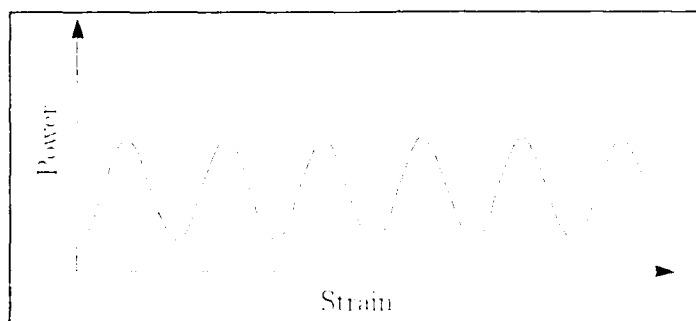
Figure 3: Experimentally obtained sinusoidal response of a low finesse FFP strain gauge.

The present demodulation system interfaces with 5 - 20 mm gauge length FFP sensors and achieves a strain resolution of 10 με, with a strain range of ±50 000 με. The system can track a strain rate of dc - 10^6 με/s. This represents the current state of the art for fiber-optic strain gauges.

The linear nature and dynamic strain response of the system was tested by bonding the FFP strain gauge to a cantilevered beam. A resistive foil strain gauge with the same gauge length was bonded to the opposite side of the beam as a reference. Figure 5 illustrates the linearity of the system, while Figures 6 and 7 demonstrate the dynamic response of the system.

3. CONCLUSIONS

The Fiber Fabry-Perot (FFP) sensor is one of the most promising sensor candidates for strain sensing in active materials. A review of three methods of fabricating FFP sensors was given, and a preferred method introduced. A sensor demodulation system with a resolution of 10 με, a range of ±50 000 με, and a strain rate range of dc - 10^6 με/s was demonstrated.
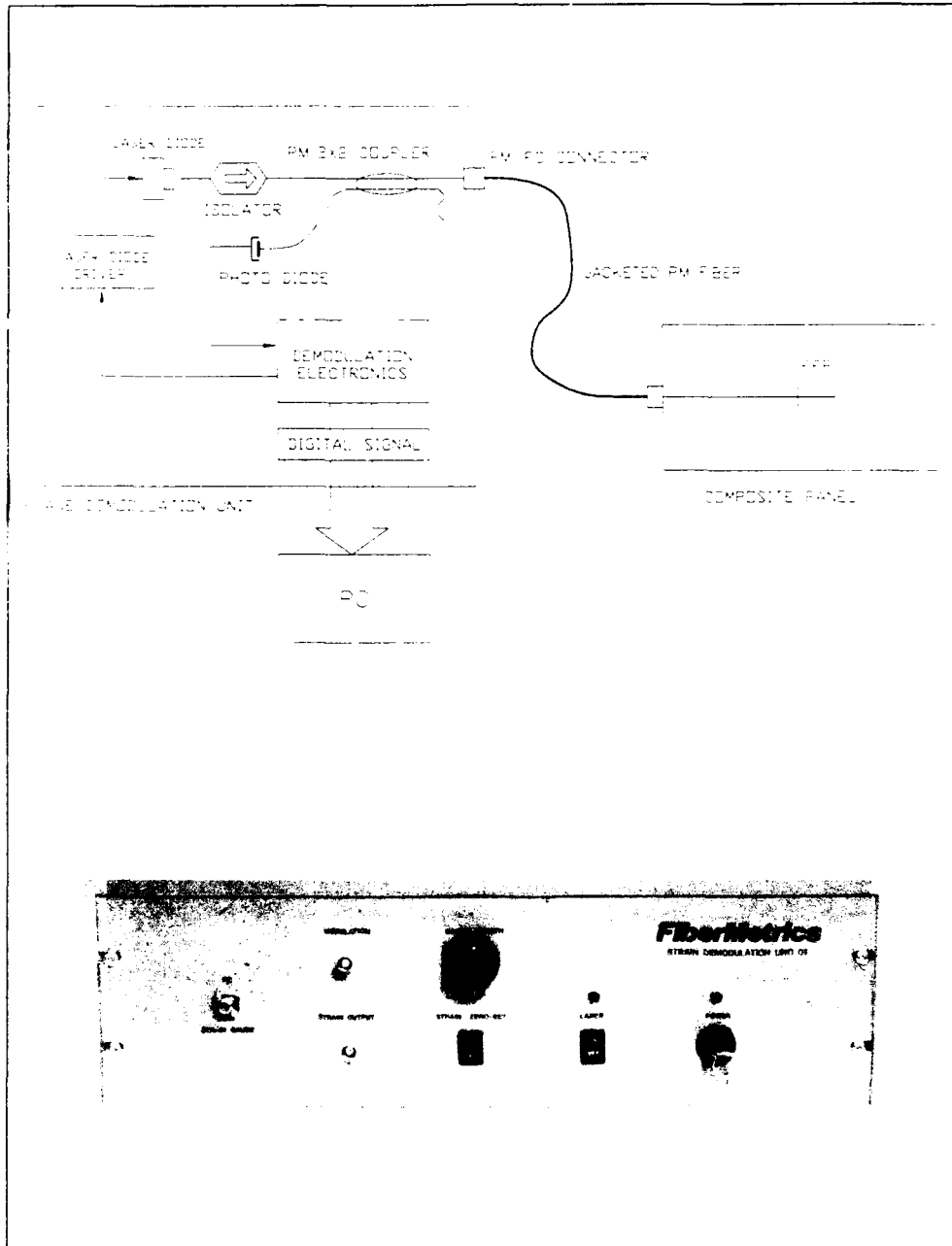
Figure 4: FFP strain demodulation system.
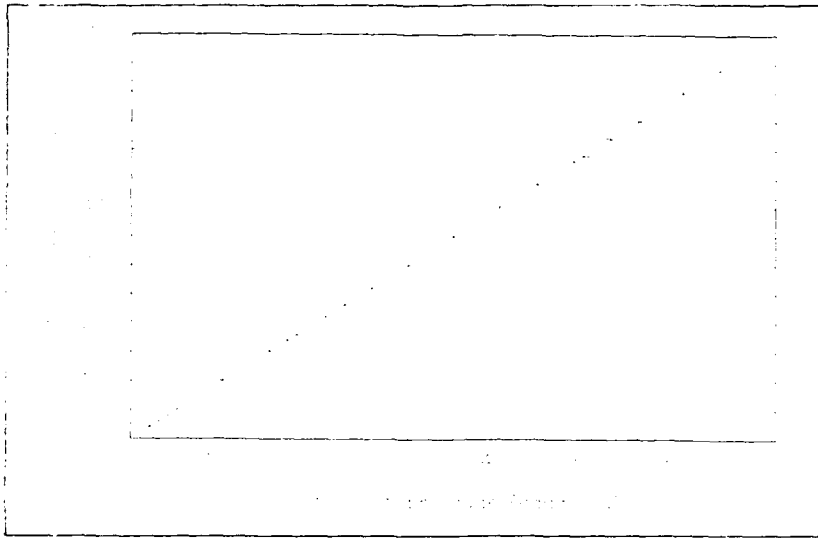
Figure 5: Linear response of the FFP strain gauge versus a resistive foil strain gauge.
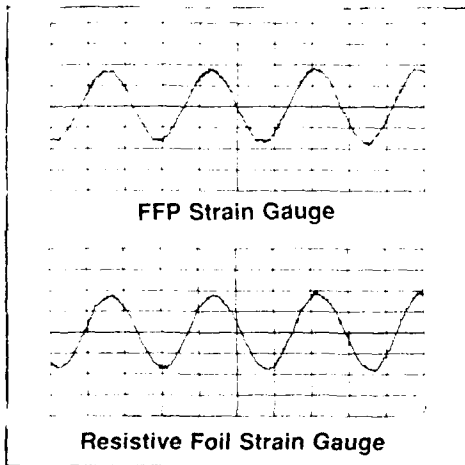
Figure 6: Natural vibration frequency of a cantilevered beam, 50µε / 20 ms per division.
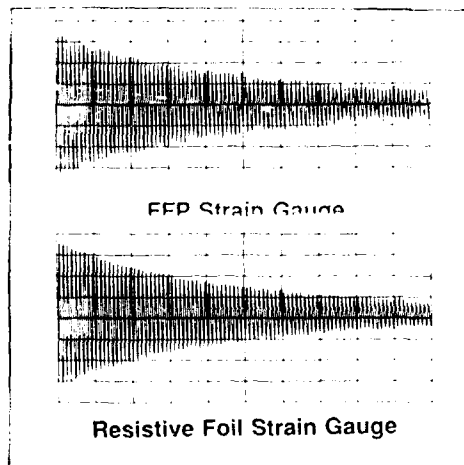
Figure 7: Dampening of a cantilevered beam, 20 µε / 0.5 s per division.

4. REFERENCES

1.   Tran, T.A., W.V. Miller, K.A. Murphy, A.M. Vengsarkar, R.O. Claus, "Extrinsic Fabry-Perot fiber optic sensor for surface acoustic wave detection", in *Proc. Fiber Optic and Laser Sensors IX*, SPIE vol. **1584**, paper 1584-25, Sept. 4, 1991.

2.   Leilabady, P.A., "Optical fiber point temperature sensor", in proceedings *Fiber Optic and Laser Sensors V*, SPIE Vol. 838, pp. 231-237, 1987.

3.   Lee, C.E. and H.F. Taylor, "Fiber Optic Sensor Research at Texas A&M University", *SPIE Conference on Smart Structures and Skins II*, SPIE vol. **1170**, 1989.

4.   Valis, T., W.D. Hogg, and R.M. Measures, "Fiber Optic Fabry-Perot Strain Gauge", *IEEE Photonics Technology Letters*, Vol. **2**, No. 3, pp. 227-228, March 1990.

5.   Valis, T., W.D. Hogg, and R.M. Measures, "Composite material embedded fiber-optic Fabry-Perot strain rosette", in *Proc. Fiber Optic Smart Structures and Skins III*, SPIE vol. **1370**, San Jose CA, pp. 146-161, 1990.

6.   Hogg, W.D., D. Janzen, T. Valis, and R.M. Measures, "Development of a fiber Fabry-Perot strain gauge", in *Proc. Fiber Optic Smart Structures and Skins IV*, SPIE vol. 1588, Boston MA, 1991.

Active structural control for damping augmentation and compensation of thermal distortion

S. W. Sirlin

Jet Propulsion Laboratory, California Institute of Technology, Pasadena, CA 91101

ABSTRACT: An end-to-end simulation of the optical performance of a large space-based interferometer (FMI) has been developed and used to demonstrate impedance-based adaptive structural control and control of thermal disturbances.

1. INTRODUCTION

The Control/Structure Interaction (CSI) program goal is to develop and demonstrate the technology necessary for precise control of future large space structures. One such candidate future mission is a space-based interferometer, termed the Focus Mission Interferometer (FMI) (Laskin 1989). An FMI-class instrument (some $26m$) must maintain optical pathlengths through the system at the 5 nanometer level. This paper focuses on replacement of 25 structural members with active piezoelectric members (Sirlin 1990).

2. STRUCTURAL AND OPTICAL MODEL

Each active strut is composed of a passive truss element and an active piezoelectric element in series. The specific stiffness of the active element was designed to be the same as that of the truss elements for complete interchangeability with other elements. The active members have embedded force and displacement sensors A NASTRAN finite element model of the FMI structure was built incorporating 527 modes. Rather than combining the models for the plant and controllers in state space, which would produce state space models of order around 1300, (plant plus controllers) models were combined in the frequency domain. Since each block of the model is brought into the frequency domain separately, special knowledge of each block can be used (Sirlin 1989). The modal analysis of the structure was done in NASTRAN. The damping was taken as 0.1%. For the vibration analysis, the disturbance source used was the imbalance force from 4 Hubble Space Telescope reaction wheels spinning from 0 to 1200 RPM (Sirlin 1990).

Each interferometer takes light from two siderostats, compressing the beam, adi-

justing the pathlength and tilt to compensate for structural vibration, and combines the beams at a focal plane. One of the three interferometers of the FMI has been modeled using the Controlled Optics Modeling Package (COMP, based on Redding 1991). The optical train consisted of 19 elements, 9 on the +Y half, 9 on the -Y half, and the focal plane. COMP was used to determine the partial derivatives of the optical pathlength to the motion of the individual optical elements, the transformation from structural vibration to optical pathlength.

3. STRUCTURAL DAMPING WITH THE DIAL-A-STRUT CONTROLLER

A more robust way of implementing a softening controller than (Sirlin 1990) is with bridge feedback (Lurie 1986,1991, Chen 1990) using both force and displacement measurements. At JPL a Dial-a-Strut controller has been developed that has a simple form, can easily be adjusted to work with a wide variety of structures, and is insensitive to plant and control parameter variations.

An approximate model of the Dial-a-Strut is given by $v_d = h_f(s)v_f + h_r(s)v_r$.

$$h_r(s) = -h_f(s)rK_rsZ_d, \quad h_f(s) = qK_2h_c(s), \quad Z_d(s) = \left(C_1s + \frac{C_2s}{1+RC_2s} \right)^{-1}.$$

The voltages v_f, v_r, and v_d correspond to the force and displacement sensors, and the piezoelectric strain command respectively. K_2 and K_r are constant gains, and $h_c(s)$ is a smooth rolloff filter. The adjustable part of the Dial-a-Strut lies in the constant gains q and r (less than 1), and the capacitors C_1 and C_2 and resistor R. The resulting impedance of the active element as seen by the structure is defined by $Z(s) = \frac{v_r(s)}{f(s)}$. As the control gains diminish, $h_f(s), h_r(s) \to 0$, the impedance approaches the original impedance (a simple spring) $Z(s) \to \frac{s}{k_a}$. As the control gains grow, $h_f, h_r \to \infty$, the impedance approaches a weighted ratio of the two paths. $Z(s) \to \frac{1}{rZ_d(s)}$.

The tuning of the Dial-a-Strut controllers is done by first smoothing (in the frequency domain) the structure driving point impedance. This desired impedance is then approximated by the Dial-a Strut controller. Figure 1 shows the open loop impedance of a particular active element (Z_0), the impedance of the structure as seen by the strut (Z_s), and the closed loop active element impedance (Z_c). The impedance is positive real, hence the system is stable with any other additional positive real elements added, and will only help the implementation of any other global control. Each of the 25 Dial-a Strut controllers is identical.

4. VIBRATION CONTROL PERFORMANCE

Vibration isolation was implemented by suspending the reaction wheels in the same manner as is done on the Hubble Space Telescope. To control the optical pathlength directly, a controller similar to that used in (Laskin 1989) is implemented. The primary difference is that in the previous work the bandwidth was limited to 10 Hz due to light levels. Current studies (Short 1991) indicate that this is overly conservative, and a bandwidth of 1kHz range is feasible. Combining the various control strategies yields the pathlength control results shown in Table I. The table shows that
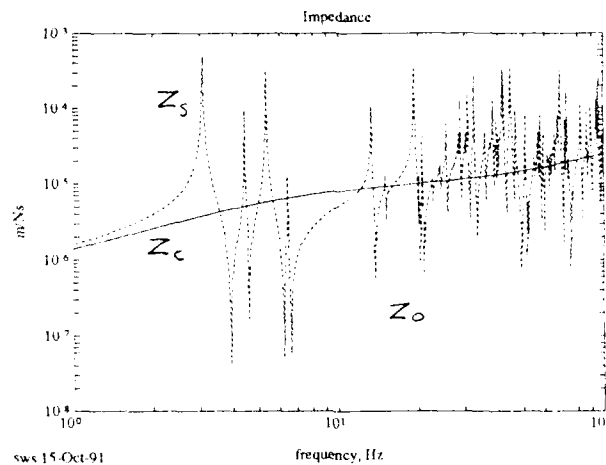
Figure 1. Impedance magnitudes at strut 13.

Table I. Optical Performance

Control	RMS pathlength error (nm)
1. None	992
2. Dial-a-Strut	271
3. Dial-a-Strut + Isolator	66.0
4. Dial-a-Strut + Pathlength	5.40
5. Dial-a-Strut + Isolator + Pathlength	1.16

all the various layers are necessary to get below the 5nm level, even though the largest reduction comes from the pathlength controller.

5. THERMAL DISTURBANCES

Using a coefficient thermal expansion of $5.0 \times 10^{-7} 1/^\circ C$ (40 times better than aluminum) thermal displacements are expected to be on the order of 1 - 60 μm throughout the structure at worst. Displacements along the arms can be compensated for at high bandwidth. Displacements transverse to the optical pathlength cannot be compensated for by the optical system however. The suitability of the active members for eliminating these deformations was investigated by considering the required active element forces and strokes necessary to control a single siderostat in three degrees of freedom to the 60μm level. The results are shown in Table II. The stroke and force requirements are much larger than for simple vibration control (Sirlin 1990), in fact just above current active member capabilities (25.4μm, 445N). The worst case direction is along the arm (Y direction) however, which need not be controlled.

6. CONCLUSIONS

The Dial-a-Strut controller is simple to tune, robust, and provides excellent per

Table II. Active Member Requirements for Thermal Control			
	Control Direction		
	x	y	z
Stroke, μm	6.0	27.6	6.3
Total Element Force N	207	728	138

formance in vibration suppression. The active members are just barely capable of controlling thermal distortion. Reliable thermal control will require somewhat larger members with larger force and stroke capabilities.

7. ACKNOWLEDGEMENT

8. REFERENCES

Chen G S et al 1990 "Active Member Control for Vibration Suppression in Truss Structures" International Workshop on Intelligent Structures Taipei Taiwan

Fanson J L Lurie B J O'Brien J F Chu C-C Smith R S 1991 "System Identification and Control of the JPL Active Structure," AIAA/ASME/ASCI/AHS/ASC Structures, Structural Dynamics and Materials Conference

Laskin R A San Martin A M 1989 "Control/Structure System Design of a Spaceborne Optical Interferometer" AAS/AIAA Astrodynamics Specialist Conference

Lurie B J 1986 Feedback Maximization (Deadham MA: Artech House)

Lurie B J Sirlin S W O'Brien J F Fanson J L 1991 "The Dial-a-Strut Controller for Structural Damping" ADPA Active Materials & Adaptive Structures Conference

Redding D C Breckenridge W G 1991 "Optical Modeling for Dynamics and Control Analysis," AIAA Journal of Guidance, Control, and Dynamics Volume 14 Number 5

Short K 1991 "Orbiting Stellar Interferometer, Preliminary Mission and System Study Results" (internal document)

Sirlin S W Laskin R A 1990 "Sizing of Active Piezoelectric Struts for Vibration Suppression on a Space-Based Interferometer" 1st Joint U.S./Japan Conference on Adaptive Structures

Sirlin S W 1989 "Pro-Matlab Functions for Frequency Response" JPL EM 343-1163 (internal document).

Inertial d oupling in the application of actuators to flexible structures

Ephrahim Garcia

Smart Structures Laboratory, Department of Mechanical Engineering
Vanderbilt University, Nashville, Tennessee 37235

ABSTRACT: The application of reactive mass actuators are seen as one avenue for the control of unwanted dynamics in future space structures. The effects of parasitic mass in proof mass actuators tends to decouple the dynamics of the actuator from the dynamics of the structure. Actuator-structure interaction is essential for the dissipation of structural vibratory energy, and hence, this decoupling is detrimental to the control performance.

1. INTRODUCTION

Inertial force actuators have received much attention over the last decade because of their potential as actuators in space. These actuators are generally referred to as space-realizable because these devices generate force by the acceleration of a proof mass. That is to say, force is generated without having attached the device to ground, or some other reference point, hence, the term space-realizable. These actuators are usually referred to as proof mass actuators, or reaction mass actuators. Theoretical and experimental investigations of these systems have been investigated by Juang (1984), Zimmerman and Inman (1990), and Garcia, et al. (1991). These references site other important works which are omitted here for brevity.

Reaction mass devices can be classified as passive, semi-active and active. The passive reactive mass device is that of the well known vibration absorber (see for instance, Den Hartog, 1934), which has been well understood for some time. A generalization of the vibration absorber was carried out by Juang (1984) for continuous structures which was modified to include the modal participation factor of the structure at the point of absorber placement. Since this work, other researchers have implemented PMAs in what will be define as semi-active and active modes of vibration. Semi-active is defined as a PMA whose dynamic characteristics can be adjusted or tuned by adjusting electrical constants of the devices. Nominally, the proof mass is centered within the stroke-length of the actuator via a position derivative (PD) controller. This generates a position feedback constant which can be approximated as an equivalent servo stiffness, and a velocity feedback constant which can be approximated as an equivalent viscous damping term. The term active will refer to the integration of PMA into an active control law. Here the control law generates an error signal that causes the actuator's proof mass to accelerate away from its center position. The reaction force has been used successfully for control purposes.

The application of actuators to flexible systems can actually alter the dynamic characteristics of the flexible structure. Under certain conditions, this can reduce the effectiveness of the active control system. Considered will be the effect of PMA parasitic mass on the control authority of the actuator system.

2. MODELING ACTUATOR STRUCTURE INTERACTION

PMAs can be simply represented as a parasitic mass, the actuator dynamics, and a proof mass. The internal dynamics of the actuator derive from the fact that the proof mass needs to be centered with the actuator stroke length. For the case of a simple PD controller, the position centering controller can be approximated by an equivalent spring stiffness and viscous damper. These coefficients are generated electro-mechanically.

Consider the system of Figure 1. This schematic represents a simple beam with a single reaction mass actuator located at the tip.

k_r, c_r · actuator dynamics   L   beam length
m_d · parasitic mass ρ · lengthwise density
m_r · reaction (proof) mass   EI · flexural rigidity
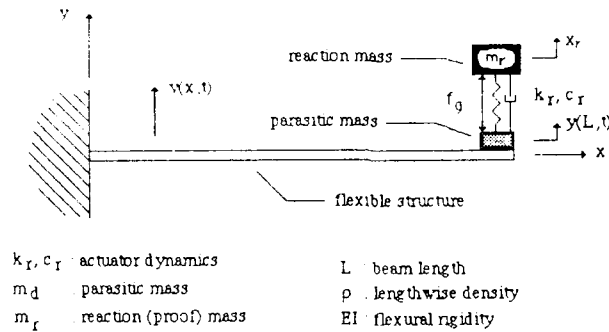
Figure 1. Schematic of a simple beam with connected to a proof mass actuator.

The equations of motion for an actuator attached to a simple beam structure can be derived by applying Hamilton's principle to the conservative system elements. Applying a Rayleigh-Ritz model for the system, the motion of the structure, $y(x,t)$, can be written as a sum of a finite set of time invariant shape functions, $\phi_i(x)$, thus yielding the equations of motion for the system.

$$
\begin{bmatrix} m_r & \mathbf{0}_{1 \times n} \\ \mathbf{0}_{n \times 1} & m_d \phi_i(L)\phi_j(L) + \int_0^L \rho \phi_i(x)\phi_j(x)dx \end{bmatrix} \begin{bmatrix} \ddot{x}_r(t) \\ \ddot{q}_i(t) \end{bmatrix}
$$

$$
+ \begin{bmatrix} k_r & -k_r\phi_j(L) \\ -k_r\phi_i(L) & k_r\phi_i(L)\phi_j(L) + \int_0^L EI\phi_i''(x)\phi_j''(x)dx \end{bmatrix} \begin{bmatrix} x_r(t) \\ q_i(t) \end{bmatrix} = \begin{bmatrix} 1.0 \\ -\phi_i(L) \end{bmatrix} f_g \qquad (1)
$$

This expression is for one mode of the system; rows and columns can easily be added to increase the number of modes, n, used in the simulation. The term $\phi_i(L)$ defines the modal participation factor for the flexible motion of the system at the actuator location. Since the viscous damper is collocated with the actuator spring stiffness, the terms of the damping matrix must have the same effect on the system dynamics as does the spring. Hence, the damping matrix of Eq. (1) is

$$
D = \begin{bmatrix} c_r & -c_r\phi_j(L) \\ -c_r\phi_i(L) & c_r\phi_i(L)\phi_j(L) \end{bmatrix} \qquad (2)
$$

These equations of motion were also solved by Juang (1984) who applied a relative (as opposed to an absolute) reference frame for the motion of the actuator.

3. EFFECTS OF PARASITIC MASS

While much work has been accomplished in the theoretical and experimental implementation of proof mass actuators, little attention has been paid to the overall effects of the actuator design on the control. An investigation of the dynamic interaction of the actuator and structure is performed. Two parameters are proposed for the application of proof mass actuators to flexible structures. These are 1) the ratio of structural mass to parasitic mass, η, and 2) the ratio of reaction mass to total actuator mass, designated as η_{eff}. The mass ratio, η, defines a constraint on the structure. That is, this parasitic mass restricts the free vibration of the structure at the point where the actuator is attached. This reduces the dynamic interaction between the beam and the actuator. It is this interaction that allows structural vibratory energy to be dissipated in the actuator. Naturally, if it is shown that the parasitic mass of a structure is detrimental to the overall system performance, then the efficiency ratio should be as close to unity as possible.

First let us consider a case where the actuator dynamics and proof mass are set equal to zero. The remaining system is a clamped-free beam with parasitic mass acting at tip. The modal participation factors of the system for an input force are defined as, $\phi(x_i)$, where x_i signifies the actuator location along the structure. Figure 2 represents the mode 2 of the structure and the absolute value of the mode shape which is the modal participation factor along the length of the beam, $|\phi_i(x)|$.
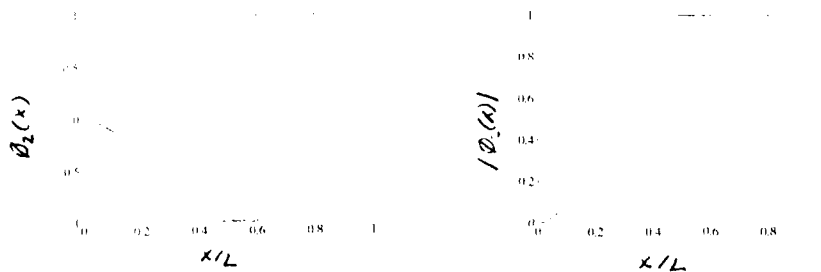
Figure 2. Mode 2 of a cantilevered beam with various degrees of parasitic mass.

The ratio of the beam mass to the tip mass, η, is plotted in Fig. 2 for values {1, 5, 10}, represented by the dotted, dashed and solid lines, respectively. The parasitic mass has negligible effect on the first mode shape of vibration. Note that for the higher modes of vibration the parasitic mass acts as a nodal attractor, i.e., the nodes of the mode shapes moved closer to the actuator for increasing amounts parasitic mass. Additionally, the modal participation factor at the actuator location, $\phi_i(L)$, decreases with increasing parasitic mass. Similar trends are present for other higher modes of vibration.

4. FEEDBACK CONTROL

A local velocity feedback (LVF) control law is applied to the system of Figure 1 to illustrate the effects of the parasitic mass on the control of flexible systems. The LVF controller feedbacks the absolute velocity of the structure. For this system, the control force produced is

$$f_g = -K_v \, \dot{y}(L,t) = -K_v \sum_{i=1}^{n} \phi_i(L) \dot{q}_i(t) \tag{3}$$

This generates an asymmetric damping matrix, which is composed of damping terms from the damping of the actuator, c_r, plus the damping generated by the active controller. A gain K_v was chosen so that all modes of the system remained stable and increased damping was exhibited in the flexible modes, see Figure 3.

a.

b.
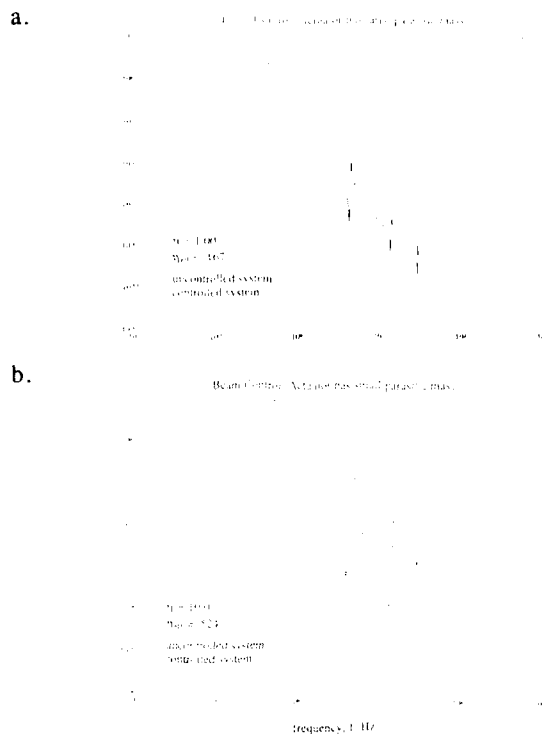
Figure 3. Controlled and Uncontrolled response for systems for various η.

It can be seen in Figure 3a that when the ratio of parasitic mass is large with respect to structural mass, the ability of the actuator to dissipate higher modes of vibration is reduced. However, when the degree of actuator-structure interaction is increased, as shown in Figure 3b, for a system with small parasitic mass, then even this simple velocity feedback controller can control the higher frequency flexible modes.

5. REFERENCES

Juang J N 1984 Optimal Design of a Passive Vibration Absorber for a Truss Beam, *AIAA Journal of Guidance, Control and Dynamics* 7 6 pp 733-739

Den Hartog J P 1934 *Mechanical Vibrations*
    (Mineola, New York: Dover) pp 87-104

Zimmerman D C and Inman D J 1990 On the Nature of Interaction Between Structures and Proof Mass Actuators, *AIAA Journal of Guidance Control and Dynamics*, 13 1 pp 82-88.

Garcia E, Webb S, Pokines B J, and Carlin R A 1991 *Feedback Control Formulations for a Complex Flexible Structure Utilizing Reaction Mass Actuators, Proceedings of the American Control Conference*

Modification of damping in a structure with coincident modes

Steven G. Webb, Daniel J. Stech, Jeffrey S. Turcotte, M. Scott Trimboli

United States Air Force Academy, Colorado 80840–5701
Frank J. Seiler Research Laboratory, USAF Academy CO 80840–6528

ABSTRACT: This paper presents the results of analytical and experimental studies of the interactions between a low–order structure with either closely spaced or coincident modes and a reaction mass actuator acting as a passive vibration absorber. The actuator significantly reduced the peak amplitude ratios of the first two structural modes for the structure with closely spaced modes. This effect was observed at all points on the structure even if the actuator and disturbance were not collocated. When the actuator and disturbance were collocated on the structure with coincident modes, the structural vibrations were likewise damped at all points on the structure. However, with the disturbance occurring at a point away from the actuator, the magnitude of one of the structure's first two resonant modes was enhanced at certain points on the structure.

1. INTRODUCTION

It is anticipated that future space structures will be large and very flexible. Such structures will possess a tremendous number of resonant modes, many of which may be closely spaced or even coincident. Closely spaced and coincident modes, it turns out, present an interesting control challenge, and will be the focus of this paper. To minimize unwanted vibrations, both passive and active control schemes will have to reduce or eliminate the vibrations associated with all of the structure's significant resonant modes, some of which may be closely spaced or coincident. In some cases it may be difficult to determine if closely spaced or coincident modes are even present. Hence, effective control schemes must be robust enough to account for the effects of closely spaced or coincident modes.

This paper examines the interactions between a passively tuned reaction mass actuator and a flexible structure. The structure was designed to have tunable resonant bending and torsion modes at low frequencies; the first two modes could be adjusted from being closely spaced to being coincident. A finite element model of this structure was generated and verified experimentally. A study was then conducted to examine the interactions between the structure and the actuator. Specifically, the extent to which the actuator reduced the structure's vibrations was analyzed when the resonant modes were either closely spaced or coincident.

2. EXPERIMENTAL SET–UP

The experimental structure used in this study exhibited two dominant low–frequency structural bending and torsion modes on the order of five Hertz. The higher modes were at frequencies at least three times that of the first two. A 144–degree of freedom finite element model of the structure was generated using MSC/NASTRAN.
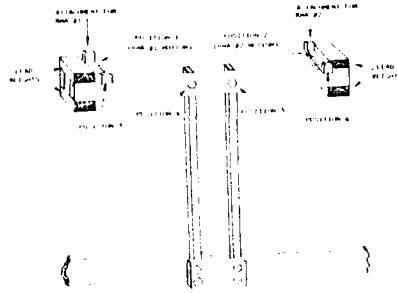
Figure 1. Sketch of the Low Order Structure

The structure was designed such that the first two frequencies could be altered by moving the four lead weights that were attached to the horizontal beams. A sketch of the structure in Fig. 1 shows that there are two brackets on the horizontal beams; these serve as supports for two reaction mass actuators (RMAs). Only one actuator was used in this study. For the configuration illustrated in Fig. 1, the first three resonant frequencies of the analytical model were found to be 4.6417, 5.1904, and 109.4542 Hertz. The first resonant frequency corresponded to a torsional, or twisting motion about the vertical axis, with a node at the center of the horizontal beams. The second frequency corresponded to a bending motion about the horizontal axis parallel to the horizontal beams.

By positioning the actuator brackets at the outboard positions on the horizontal beams and moving the lead weights towards the center of the structure, the torsional frequency could be raised while maintaining roughly the same bending frequency. Through a trial and error process of positioning the lead weights at various locations on the structural model, a structure with coincident modes was obtained. The first two resonances occurred at 5.2190 and 5.2195 Hertz, respectively, with the third mode at 133.57 Hertz. Even this model possessed closely spaced modes rather than true coincident modes since a separation of 0.0005 Hertz actually existed between the two modes. However, it is difficult, if not practically impossible, to construct a structure with identical modes.

Because high order analytical models present computational difficulties with the available equipment, the NASTRAN model was reduced to fourth–order using an accurate modal reduction technique outlined by Hallauer (1980). The reduced model could then be used to determine the actuator's optimum natural frequency and damping with an existing MATLAB routine.

The analytical model was validated with an experimental structure (Webb, 1990a,b). The first two experimental resonances of the structure with closely spaced modes were 4.618 and 5.113 Hertz, which agreed well with the analytical model (0.5 and 1.5 percent errors, respectively). For the coincident mode configuration, the first resonance occurred at 5.075 Hertz, a 2.759 percent error from the analytical model. It should be noted that both analytical and experimental frequency response functions of the structure with coincident modes showed only one peak at the first resonance, indicating that the first two resonant frequencies were the same.

3. DAMPING OF THE STRUCTURE WITH CLOSELY SPACED MODES

The method used to determine the optimum actuator tuning parameters (natural frequency and damping ratio) was one adapted from Duke (1990), which described

how to calculate the optimal tuning of an actuator attached to a multi–degree of freedom system. For this study, the RMA was attached at Position 3 and the structure was disturbed at Position 3 (refer to Fig. 1).

For the structure with closely spaced modes, the optimum natural frequency for the RMA was computed to be 4.441 Hertz, with an optimum damping ratio of 0.082218. The actuator, when passively tuned to the structure's first resonant frequency, introduced a new resonant mode to the system due to the additional degree of freedom. In addition, the actuator significantly altered the structure's first modal response by shifting the frequency higher and reducing the peak amplitude ratio by almost 95 percent. The actuator also altered the structure's second resonant mode by raising the frequency and reducing the peak amplitude ratio by 99 percent. Higher modes were not affected by the addition of the passive RMA.

To determine the effectiveness of the passive damper at other locations on the structure, frequency response functions of both baseline and optimally passively damped structures were generated for Positions 4, 5, and 6. In each case, the disturbance was introduced at Position 3, with the RMA also located at Position 3. The actuator acted as a passive vibration absorber for the entire structure, even though it was attached to just a single point on the structure. Once again, higher modes were not altered. It is clear that the actuator's ability to reduce the structure's vibrations diminishes significantly for frequencies well beyond the resonant frequency of the RMA.

With the RMA still attached to Position 3, the structure was then disturbed at Positions 4, 5, and 6, in turn, and the corresponding frequency response functions were generated. Once again, in each case the passive damper reduced the structure's vibrations at all points on the structure, regardless of where the structure was disturbed.

The above results were repeated experimentally by attaching a reaction mass actuator to the experimental structure. The RMA was passively tuned to a natural frequency of 4.418 Hertz and a damping ratio of 0.082218. With the RMA assembly attached to the structure at Position 3, the structure was disturbed at Position 3. The frequency response function of the passively tuned structure was then obtained and compared to the response of the baseline structure. The experiment yielded results virtually identical to the analytical predictions in each of the cases tested and reported above.

It is clear that adding a single passively tuned absorber to the structure with closely coupled modes reduces the magnitudes of the resonances in the vicinity of the RMA's frequency. Higher modes are not affected. Furthermore, the RMA dampens the vibrations at all points on the structure, no matter where the RMA is attached or, for that matter, where the structure is disturbed.

4. DAMPING OF THE STRUCTURE WITH COINCIDENT MODES

The analytical and experimental procedures described above were repeated for the case of coincident modes. Analytically, the RMA's natural frequency was 4.9621 Hertz, and the damping ratio was 0.13619. The RMA was experimentally tuned to a natural frequency of 4.8252 Hertz and a damping ratio of 0.13619. As before, the RMA was attached at Position 3 and the structure was disturbed at Position 3.

The responses are similar to those obtained when a passive vibration absorber is attached to a single degree of freedom system (Den Hartog, 1956, Miller, 1988). The baseline structure's response was similar to that of a single degree of freedom system

since the coincident modes generated a single peak in the frequency response function. It appears that the RMA damped equally the vibrations of the first two structural resonances, and the resulting response simply mirrored that of a single degree of freedom system with a passive vibration absorber attached. Experimentally, the analytical results were verified.

To observe the effects of the passive RMA at other points on the structure, analytical frequency response functions of the structure's responses at Positions 4, 5, and 6 were obtained. As before, the RMA was attached at Position 3 and the structure was disturbed at Position 3. Although the RMA damped the structure's first two resonances at all points along the structure, the damping of one of the structural resonances was diminished further from the RMA. For instance, at Position 6, while the damping of one structural resonance was similar to that obtained at Position 3, the frequency of the other mode was unaltered, and the mode exhibited less damping than at either Positions 3, 4, or 5. Once again, these results were verified experimentally.

Further investigations revealed that the passive RMA would only damp the entire structure if the disturbance was collocated with the RMA. For example, with the RMA at Position 3 and the structure disturbed at Position 5, frequency responses corresponding to Positions 3, 4, 5, and 6 were obtained. At Position 3, both structural resonances were damped; however, an anti-resonance appeared between the two resonant peaks. At Position 4, even though one structural resonance was heavily damped, the frequency of the other mode was essentially unchanged and the mode was only slightly damped as a result of adding the passive RMA. The response at Position 5 was almost identical to the baseline structure's response. The RMA's resonant mode was barely noticeable, as was one of the structure's resonant modes. hence, the passive RMA was still effective in damping one resonant mode, although the response of the other structural resonance was only very slightly damped. Finally, at Position 6, it appears that the structural response with the RMA attached was actually worse than the baseline structural response. In reality, although the passive RMA damped one structural resonance, this occurred at the expense of the other structural resonance. Experimental results were once again identical to the analytical results.

Disturbing the structure at Position 6 with the RMA attached at Position 3 likewise yielded some intriguing results. The frequency response for Position 3 showed one resonance to be damped as before, but the resonant frequency of the other mode was unaltered and the magnitude of vibration was, in fact, larger than the first resonance. The responses at Positions 4 and 5 again showed that the passive RMA damped the vibrations of only one of the structural resonances, while the other structural resonance was less damped than before. Finally, at Position 6 one resonance was effectively eliminated; adding the passive RMA resulted in a slight dampening effect on the structure's other resonant mode. These results were all verified experimentally.

The above results clearly differ from the results obtained with the passive RMA attached to the structure with closely spaced modes. Root locus plots of the structure's first two modes (with the passive RMA attached) were computed as a function of the position of the lead weights. These plots show that when the modes are coincident, the real parts of one of these modes is zero. In fact, it was observed that this mode is uncontrollable. Therefore, when the actuator is attached to the structure, one mode is damped out while the other mode is unaffected. If a steady state disturbance is introduced to this system, it is possible that the energy in the controllable mode is "funneled" to other parts of the structure, resulting in an increase in vibrations at some other point in the structure.

Obviously, a structure with coincident modes behaves differently than a structure which has modes that are close but separate. If one of those modes remains uncontrollable, then control of the entire structure is compromised. Hence, a control scheme which uses passive damping must be able to discriminate between the various structural resonance, or the control system itself may not be able to eliminate a structure's vibrations.

5. CONCLUSIONS

Based on the analytical and experimental results presented, a passive reaction mass actuator reduces the resonant vibrations of a structure with closely spaced modes, provided the resonances are close to the actuator's resonant frequency. The effects of this damping diminish with resonant modes further from the actuator's tuned frequency. In addition, the vibrations are reduced everywhere on the structure, no matter where the structure is disturbed.

On the other hand, if the structure has coincident modes, the passive reaction mass actuator can actually enhance the resonance of one of the structure's coincident modes. If the absorber and disturbance are collocated, the vibrations are reduced all along the structure. However, if the disturbance is at some other point on the structure, there are places along the structure where the vibrations are actually less damped *with the absorber attached than without the absorber.* Thus, control schemes for structures with coincident modes may not eliminate structural vibrations if controllability of the structure is not taken into account.

REFERENCES

Den Hartog J P 1956 **Mechanical Vibrations** (New York: McGraw–Hill) pp 87–103
Duke J P, Webb S G and Vu H 1990 **Proc AIAA Guidance, Navigation, and Control Conference** AIAA Paper 90–3499
Hallauer W L Jr and Barthelemy J–F M 1980 **Proc. 21st AIAA Structures, Structural Dynamics, and Materials Conference** Paper No. 80–0806
Miller D W and Crawley E F 1988 **Journal of Guidance, Control and Dynamics** Vol 11 No 5 pp 449–458
Webb S G and Fisher C A 1990a **Proc. First Joint US/Japan Conference on Adaptive Structures**
Webb S G and Turcotte J S 1990 **Proc. 1990 AIAA Guidance, Navigation and Control Conference** AIAA Paper 90–3500

Shear mode piezoceramic sensors and actuators for active torsional vibration control

Chia Chi Sung*, Xiao-Qi Bao, Vasundara V. Varadan and Vijay K. Varadan

Department of Engineering Science and Mechanics, Center for the Engineering of Electronic and Acoustic Materials, The Pennsylvania State University, University Park, PA 16802

ABSTRACT: This paper presents an investigation of pure torsional vibration control of circular tubes using piezoelectric sensor/actuators. A theoretical analysis for shear mode sensors/actuators is presented. Two types of sensors/actuators are fabricated and tested with a velocity feedback control system. An increase in the damping factor and a decrease in the resonance peaks of the transfer function curves are observed for various tubes. The investigation shows the feasibility of using the piezoceramic shear mode sensors/actuators to actively control the torsional vibration of tubes.

1. INTRODUCTION

There is a growing interest in the application of piezoceramic sensors and actuators in active vibration control. Most published works in this area are focused on beam, truss and plate vibration control. This paper investigates pure torsional vibration control of tubes using piezoelectric sensors/actuators. Two types of PZT sensor/actuators are designed. Both of them can be attached to the surfaces of circular tubes and are sensitive or effective only to the torsional vibration of the tubes. The coupling of the sensors/actuators to the resonant modes of the tubes are formulated.

The performance of PZT shear mode sensors/actuators applied to active vibration control are experimentally tested with a velocity feedback control system. Closely located one-sensor/one-actuator arrangement is used. Two different methods are used to judge the control performance: one is to measure the damping factor from the waveform in time domain, the other is to compare the frequency responses of the transfer function from an exciter to the sensor in the cases with and without active control.

Several different cases are tested: 1) structure -circular tubes with and without end mass; 2) material of the tube - phenolic and pyrex; 3) sensor/actuator - ring type and shell type; 4) control - single mode and multiple modes. An increase in the damping factor by a factor of 2.6 to 3.4 times or a decrease in the resonance peaks of the transfer function curves from 4 to 9 dB are achieved by the active control technique.

---

* Current address: Istitute of Naval Archtecure, National Taiwan University, Taiwan, R.O.C.

2. SHEAR MODE TRANSDUCERS FOR CIRCULAR TUBES

Circular shear mode transducers are designed as sensors/actuators of shear stress/strain exhibited on pure torsional vibration of a circular tube. The transducers are made of piezoelectric ceramics (PZT), which has higher electromechanical coupling coefficients than other piezoelectric materials. The constitutive equations of PZT can be written as:

$$S_p = s^E_{pq}T_q + d_{ip}E_i$$

$$D_i = d_{iq}T_q + \varepsilon_{ik}E_k$$

where i,k=1, 2, 3 and p,q=1, 2....., 6, and the piezoelectric constants are in the form of following matrix:

$$d_{ip} = \begin{bmatrix} 0 & 0 & 0 & 0 & d_{15} & 0 \\ 0 & 0 & 0 & d_{15} & 0 & 0 \\ d_{31} & d_{31} & d_{33} & 0 & 0 & 0 \end{bmatrix}$$

From the equations, it is obvious that, when the electrodes of the transducer are perpendicular to the axis 1 or 2, the transducer will sense or affect to the shear stress or strain only. Two different type transducers used in the experiments are shown in Fig. 1. The original electrodes in the figures are the electrodes used in the polarization process.

(a) Ring type   (b) Shell type
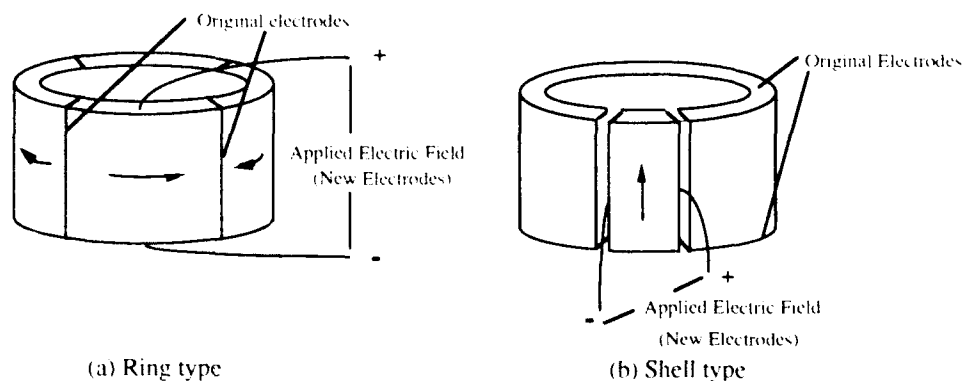
Fig. 1 Electrode arrangements of shear mode transducers. (arrow indicates poling direction)

Theoretical analysis of the ring type shear mode transducer shows that, when it is used as a sensor, the output current with short circuit $I_s(t)$ is

$$I_s(t) = K\sum|\phi_i(x_1)-\phi_i(x_2)| \, dq_i(t)/dt, \qquad (i=1,2,.......)$$

where the $\phi_i(x_1)$ and $\phi_i(x_2)$ are the displacement distribution (angle) of the i-th mode at two ends of the ring respectively, $dq_i(t)/dt$ is the modal velocity of the i-th mode, and

$$K = (2\pi r_t/l) \, d_{15}/s^E_{44}.$$

where r is the average radius of the ring, t_r is the wall thickness of the ring, l is the length of the ring, and s^E_{44} is the elastic compliance constant.

When used as an actuator, the equivalent force (torque) for the j-th mode $F_j(t)$ is as follows:

$$F_j(t) = K[\phi_j(x_1)-\phi_j(x_2)] \, V_a(t), \qquad\qquad (j=1,2,\ldots\ldots)$$

where $V_a(t)$ is the voltage applied to the actuator. The modal displacement distribution can be found by finite element approach.

3. EXPERIMENTAL SETUP AND RESULTS

To demonstrate the ability of the shear mode sensors/actuators, experiments are performed on circular tubes with one clamped end. A velocity feedback control algorithm is applied. One sensor and one actuator, which are closely located near the clamped end, are utilized in the control system.

Five tubes are tested in the experiments. The tubes are hollow shafts with clamped-free or clamped-endmass boundary conditions. Two materials, phenolic and pyrex , are chosen for the tubes. Table 1 exhibits detailed descriptions of the tubes.

Table 1   Descriptions of tubes

Tube No.	Material	Length (mm)	OD (mm)	Wall (mm)	Transducer Type	Boundry Condition	End Mass Moment of Inertia ($\times 10^{-4}$ kg·m²)
1	Phenolic	152.4	12.7	1.6	Ring	Clamped-End Mass	6.24
2	Phenolic	203.2	14.22	1.6	Shell	Clamped-End Mass	6.24
3	Phenolic	228.6	11.18	1.6	Ring	Clamped-End Mass	6.24
4	Phenolic	228.6	11.18	0.81	Ring	Clamped-Free	—
5	Pyrex	228.6	11.18	0.81	Shell	Clamped-Free	—

The dimensions of the ring type transducers are 12.7 mm in outside diameter, 0.787 mm in wall thickness and 6.35 mm in length. Both the ring and shell type transducers are bonded onto the surface of the tubes by a regular epoxy.

Two different setups as shown in Fig. 2 are tested in our experiments.   In setup 1, a heavy end mass is attached to the free end of the tube. The centers of transducer 1 (actuator) and

transducer 2 (sensor) are located 4 mm and 10.4 mm respectively from the clamped end. A velocity feedback control algorithm is applied. The feedback loop includes an current amplifier, a filter, a phase shifter, a preamplifier, and a power amplifier. A digital oscilloscope recorded the free decaying vibration of the tubes with and without active control. Damping ratios are calculated according to the recorded data. The dominated vibrations excited in our experiments with setup 1 are the first mode of the tubes. This setup is applied to tubes 1, 2 and 3. A typical waveform is presented in Fig. 3. Controlled results are summarized in Table 1. Damping factors are increased by 2.6 to 3.36 times.

Configuration 1   Configuration 2
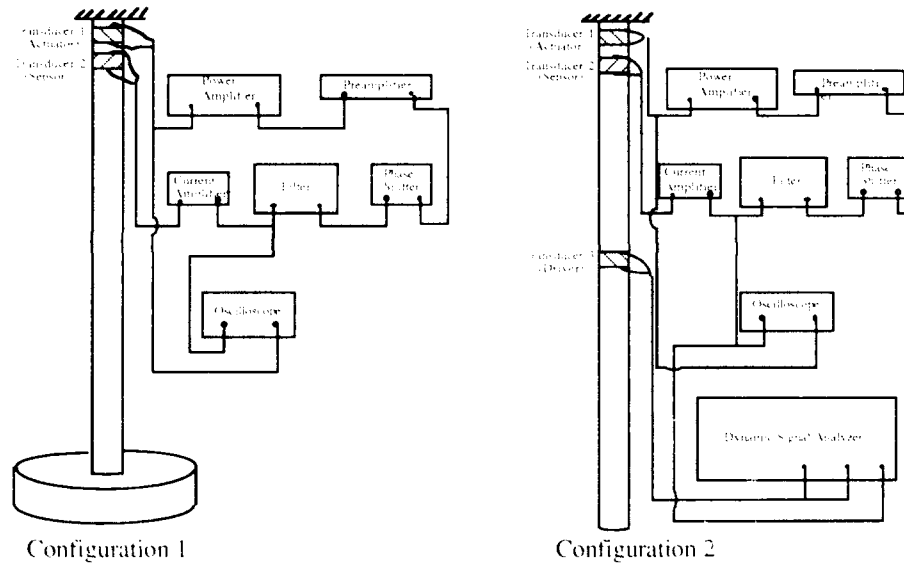
Fig. 2 Structure and transducer arrangement. of tubes.
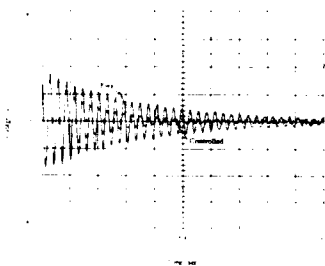
Fig. 3 First mode control of tube 3.

Table 2. Control results for tubes 1, 2 and 3.

Tube No	1st Mode Freq (Hz)		Damping Ratio		Control Gain (dB)	Damping Ratio Increased Factor
	Exp	Anal	Free	Controlled		
1	42.4	41.9	0.0014	0.0047	280	3.36
2	42.8	42.4	0.0025	0.0065	281	2.7
3	34.3	34.8	0.0013	0.0034	285	2.6

In setup 2, there is no end mass. A third transducer (driver) is applied on a selected location of the tube to provide the external driving force. The location selected is 10.7 cm from the center of transducer 3 to the clamped end. A dynamic signal analyzer is connected to the driver and

sensor to measure the transfer function from the driver to the sensor. This setup make direct measurements in the frequency domain possible and is applied to tubes 4 and 5. Both capabilities of controlling the first three modes separately (single mode control) and simultaneously (multimode control) are tested. Typical curves of transfer functions are presented in Figs. 4 and 5. Reductions about 5 to 9 dB in the resonance peaks are obtained in single mode control. In multimode control of tube 4, 6.3 dB, 4 dB and 9.4 dB reductions are achieved for the first, second and third modes respectively.
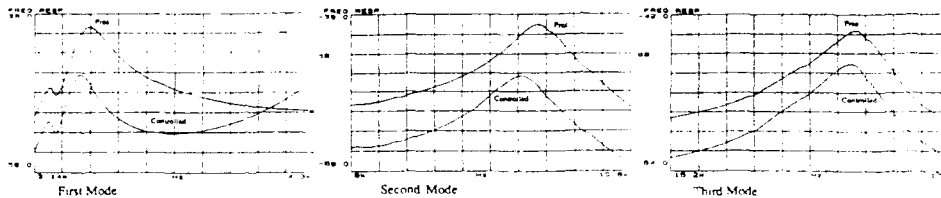
Fig. 4 Single mode control of tube 5.
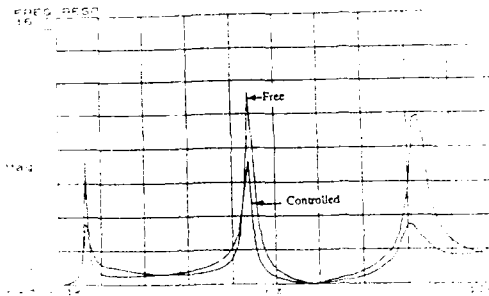
Fig. 5 Multimode control of tube 4.

4. SUMMARY

Two types of shear mode PZT sensors/actuators are designed and fabricated for active tube torsional vibration control. The sensors/actuators are tested with an analog velocity feedback control system. The control performances are studied in both time and frequency domains. The increases in the damping factors are obviously observed for all the tested tubes with both types of sensors/actuators. This investigation shows the feasibility of using the piezoceramic shear sensors/actuators to actively control the torsional vibration of tubes.

Fabrication of multilayer ceramic actuators

A P Ritter, A E Bailey, F Poppe, and J Galvagni *

Martin Marietta Laboratories, 1450 South Rolling Rd., Baltimore, MD 21227; *AVX Corp., Myrtle Beach, SC 29577

ABSTRACT: Fabrication of layered ceramic actuators using techniques developed for production of multilayer ceramic capacitors allows flexibility in actuator design and permits significant volume-cost benefits that are needed for practical implementation of active elements in smart structures. Key design issues include required stroke, hysteresis, operating temperature and stress, bandwidth and related system-specific parameters.

1. INTRODUCTION

Ceramic materials employed to provide active control of moving structures have relatively small field-induced strains (typically 0.01 - 0.1 % strain at 1 MV/m applied field) although they generate large forces because of their high stiffness. In order to obtain usable displacements, ceramic thickness is increased; however, operating voltages needed to achieve needed field strengths ($\sim$ 1MV/m) can get extremely large. For example, a 1-cm-tall block of monolithic ceramic may be capable of producing 8- to 10-μm displacement, but would require about 10 kV to attain requisite field strength. By dividing that block into very thin layers (e.g., 0.1 - 0.2 mm), connected in series mechanically and in parallel electrically, comparable displacement can be obtained, but drive voltages are reduced by about 2 orders of magnitude. The essence of multilayer actuator fabrication is to first select optimum active materials and then utilize methods that allow extremely thin layers to be produced and interconnected with uniform, reproducible displacement, at reasonable cost and quantity. Techniques employed to produce multilayer ceramic capacitors have demonstrated applicability to the low-cost, high-volume production of high-performance actuator components.

This paper is an overview of the multilayer actuator fabrication process which will clarify relationships among different parts of the process and thus highlight the practical tradeoffs that must be made when designing and applying an actuator for active structure control.

2. ACTUATOR FABRICATION

Central to the fabrication process is the need to obtain very thin ceramic layers in order to reduce operating voltages to practical levels, i.e., hundreds of volts. In that these devices are multilayer

capacitors, they must be designed to withstand the electrical stresses to provide robust, long-lived performance. Unlike multilayer capacitors, actuators are also mechanically active, and can have significant internal stress gradiants that ultimately limit performance and reliability. However, given proper internal electrode designs and well-controlled fabrication methods (Takahashi et al. 1985, Winzer et al. 1989) devices can sustain electrical and mechanical stresses for at least 100's of millions of cycles with no degradation of performance. The basic actuator fabrication process (Fig. 1) includes powder selection and processing, tapecasting to produce thin unfired ("green") layers, printing with noble metal electrode inks to create internal electrode patterns for subsequent termination, near-net-shape forming of unfired laminated devices, burnout of organic components, and sintering to produce a densified, co-fired composite made up of alternate layers of ceramic (hundreds of μm thick) and electrode (5-10 μm thick). The steps are reviewed in greater detail in the following section.
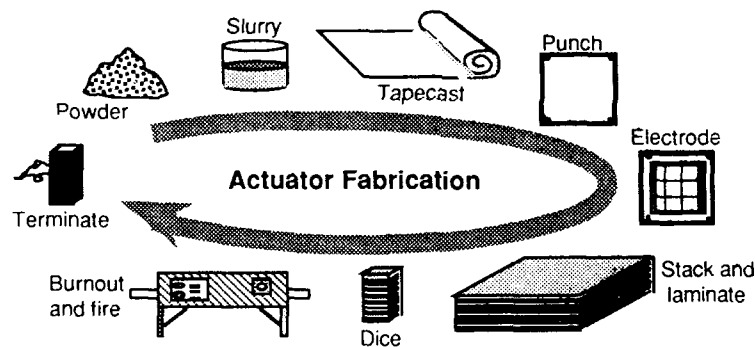
Figure 1. Multilayer actuator fabrication process

Selection of the proper material for construction of the actuator is predicated on an understanding of the fundamental properties of different classes of ferroelectric compounds, including hard and soft piezoelectrics and high strain, low hysteresis electrostrictive ceramic materials. Inherent properties of these materials can be accented for different applications, where needs for absolute stroke, hysteresis, linearity, operating temperature range, force output and electrical efficiency are traded against one another. In general, hard piezoelectric materials provide the most linear behavior, lowest electrical and mechanical losses (among piezoelectrics), and greatest stability over wide temperature and pressure ranges of operation. This stable performance comes at the expense of field-induced strains -- hard piezoelectrics produce the smallest displacements per unit length (~0.03% strain @ 1 MV/m). Piezoelectric materials that produce large strains (~0.06% strain @ 1 MV/m) have a "soft" domain structure that is affected to a greater degree by changes in temperature and prestress and has inherently higher losses. Relaxor electrostrictive materials produce the greatest field-induced strains (up to 0.1% strain @ 1 MV/m) with extremely low hysteresis; however, their response is quadratic and most susceptible to variation with

temperature. Each material has special attributes for specific applications, and all can be processed with equal facility in multilayer ceramic actuators.

Ceramic powders for actuator fabrication can be produced using industry standard mixed-oxide techniques at costs of 10s of dollars/kg in quantities up to 2000 kg in a single run. Meticulous process control is crucial in that all subsequent steps rely on controlled, reproducible powder properties for consistent results. Important considerations are chemical purity, compositional stability and powder morphology.

Tapecasting is a process that spreads a slurry of ceramic particles and organic binders into a thin film that is dried, printed with electrode patterns and then laminated, without adhesives, into a monolithic stack of unfired ceramic / electrode layers. Like control of powder morphology, control of slurry rheology is crucial to obtaining reproducible tape casts. Slurries typically contain about 40% solvents and 60% solids, including ~90 vol% ceramic and 10 vol% binders, plasticizers and dispersants. Dried ceramic tapes typically are 25- to 250-μm thick, thin tape layers produce lower operating voltage (and low impedance) devices. Ceramic tapes undergo approximately 20% linear shrinkage upon firing.

After the tapecast films are dried, they are punched or mounted in a metal frame to provide registration during the electroding, stacking and laminating steps. Good registration techniques allow horizontal alignment to be maintained within approximately 20-30 μm during stacking. Prior to stacking, individual tape layers are screen printed with metal ink electrode patterns. The ink layers serve as internal electrodes to the stacked ceramic layers after the device is fired. Noble metals (e.g., Au or Pt) are better choices for internal electrodes, despite their cost, since they are significantly less mobile than lower cost electrode materials (e.g., Ag). Migration of electrode material in the presence of electric field and humidity is one of the limiting factors in the long-term performance of multilayer ceramic components. Nonetheless, electrodes are ultimately the primary cost driver in high volume fabrication, and development opportunities exist in this area.

Electroded ceramic tapes are stacked and laminated to form the near-net-shape component. It is at this stage that one of the principal advantages of the multilayer fabrication process becomes apparent. Because the ceramic is as yet unfired, there is flexibility in the shape, size and stacking sequence of the device being made. This allows layer thickness within the stack to be varied, controlling the field (stress) gradients to improve reliability. Device cross-sections can be circular, square or rectangular. The devices can have very low aspect ratios with relatively few active layers ("bimorphs") and high aspect-ratio parts with hundreds of active layers (stacks), all of which may be produced without significant changes to the fabrication process. This flexibility means that parts can be specifically tailored for an application at low risk and cost.

Binders and plasticizers must be removed (burned out) from the laminated actuator prior to firing. Removal is accomplished by heating in air to allow organics to oxidize and escape through the intergranular porosity. Heating is done at very low rates, over a period of days, to allow gases to escape without building up pressure that delaminates or deforms the stack. After the organics are removed, the ceramic / metal powders are cofired at high temperature (> 1000°C) to produce the dense, stiff ceramic actuator. Electrical interconnection is provided by a second firing step where conducting strip electrodes are bonded to the alternate layers. For the piezoelectric devices, the fabrication process is completed by applying a poling field at elevated temperatures; electrostrictive materials do not require this step.

3. ACTUATOR PERFORMANCE

Properly designed multilayer actuators have the same behavior as the bulk material used in their fabrication. Using the multilayer fabrication methods, actuators up to 3-4 cm in length, containing 100s of active layers, have been produced (Fig. 2a). These devices produce displacements of up to 35 μm. Depending on the type of active material used, voltage / displacement behavior may be radically different (Fig. 2b), and thus useful for a wide variety of structure control applications, as either discrete components or embedded arrays.

a)   b)
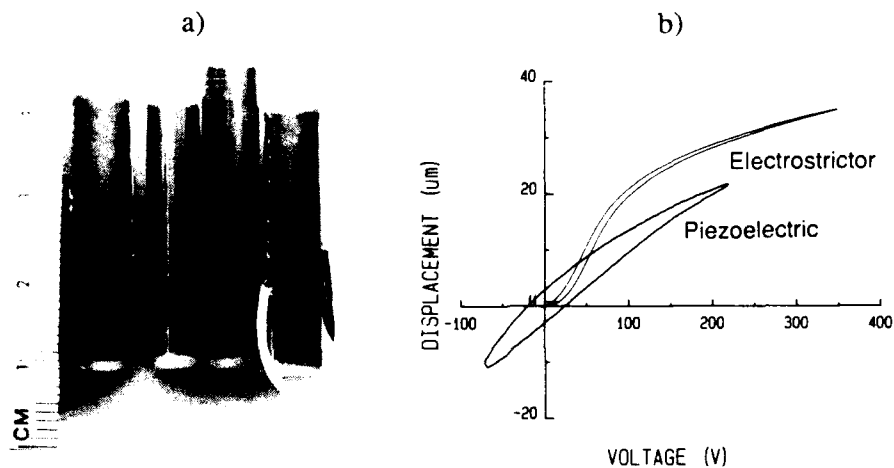
Figure 2. Multilayer actuators a) may have hundreds of active layers and b) produce 10's of μm displacment with several hundred volt drive. The response is distinctly different for piezoelectric and electrostrictive materials.

4. REFERENCES

Takahasi S, Yonezawa M, Ochi A, Yano T, Hamatsuki T and Fukui I 1985 June 11, US Patent No. 4,523,1213.
Winzer S R, Shankar N and Ritter A 1989 *J. Am. Ceram. Soc.*, 72 [12] 2246-57.

Smart structural composites with inherent sensing properties

Nisar Shaikh
Department of Engineering Mechanics and
Center for Materials Research and Analysis
212 Bancroft Building
University of Nebraska-Lincoln
Lincoln, NE 68588-0347

ABSTRACT: A true smart material is being researched that does not require embedded sensors. The carbon-epoxy composites are developed with self-sensing capability, by sputtering the carbon fibers with piezoelectric Zinc Oxide. An electric field is developed when the composite structure is strained, thus allowing the vibration measurement. The research in progress is aiming for complete health monitoring of the composite structure.

Carbon epoxy composites are some of the most important structural materials for the present and future needs of the Department of Defense. The fundamental research in progress is leading to structural composites that have inherent intelligent properties, achieved without embedded sensors. This research is being pursued by synthesizing "sensitive" carbon filaments deposited with thin films of piezoelectric Zinc Oxide (ZnO). The carbon fibers may be intercalated to enhance their electrical and thermal conductivity. Through these synthesized fibers, features of sensing, actuation, and controllability can be imparted to composites. Smart materials can be developed to carry out desired functions, which depend on the application. For example, in certain structural applications, smart materials can continuously monitor the structure's state (vibration), make decisions on the proper response, and act (actuate) accordingly. Thus, smart structural composites can themselves carry out functions that are now the aim of smart skin patches and fiber optic sensors.

The feasibility of inducing strain sensing properties in a material has been demonstrated (Shaikh and Dillon 1990) with beam samples made from stainless steel strips deposited with a thin film of piezoelectric ZnO. The technique of sputtering fibers with ZnO was initially

developed by coating Ni-Cr wires of 143 micron diameter. The synthesis of intelligent carbon strands progressed systematically, starting with simple stainless steel strips and eventually moving to carbon fibers through models of increasing sophistication. Initially the electrical conductivity of carbon fibers was increased by intercalation with bromine to enhance the sensor's capability, but in later development it was found unnecessary.

Structural beam specimens were fabricated from various strips and fibers deposited with ZnO and tested for self sensing of vibration. Figure 1 shows a cantilever beam made of unidirectional carbon-epoxy composites. The carbon strands synthesized with ZnO are laid at an angle to the longitudinal axis of the beam. The carbon in the coated strand acts as one of the electrodes while the uncoated carbon epoxy acts as a ground electrode. Both electrodes were directly connected to a digital scope without any preamplifiers.
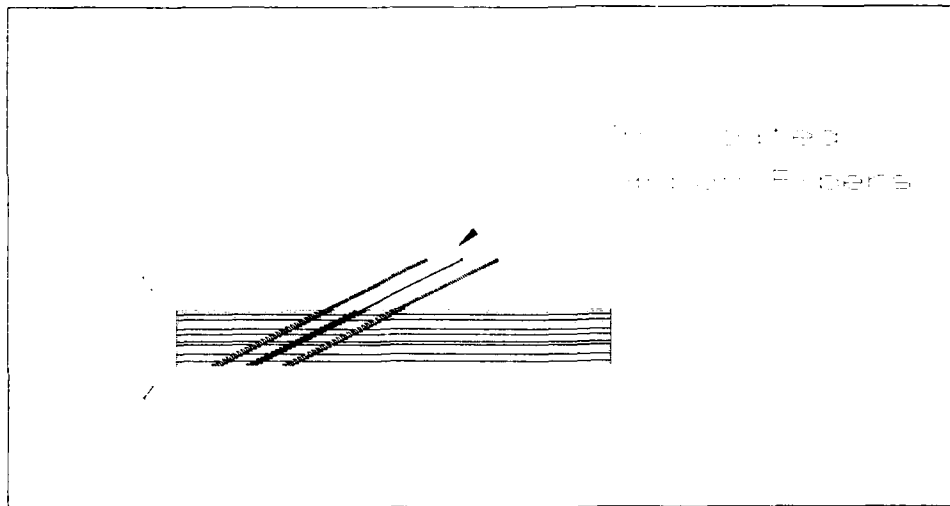
Figure 1: Carbon epoxy sample

The beam was tested for its inherent ability to sense vibration. The test consisted of forced vibration through a shaker as well as natural vibration by impulse. Figure 2a shows the voltage developed in the coated strand when a small ball is dropped at the end of the beam. A damped natural vibration containing both low and high frequency modes is seen. Figure 2b shows the results of a forced vibration test. The fixed end of the cantilever beam is vibrated on a shaker table. The bottom signal is from an accelerometer mounted on the

fixed end of the beam. while the top signal is the voltage developed in the carbon strand. These signals were not amplified or smoothed through averaging.
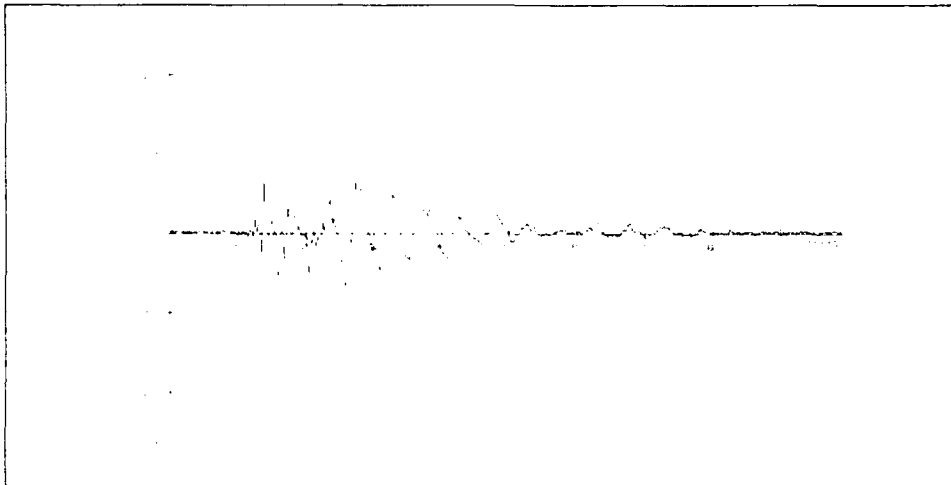
Figure 2a: Carbon Epoxy Beam: Natural Vibration

Piezoelectric Signal

Accelerometer Signal
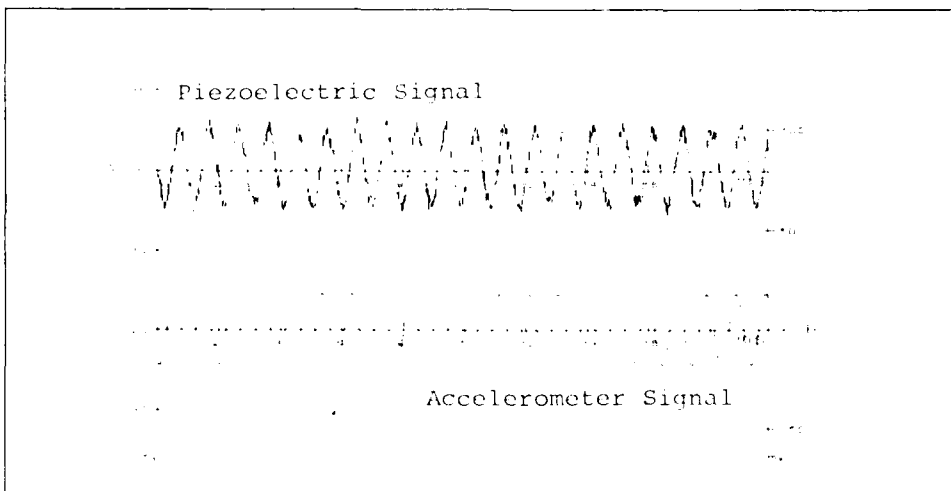
Figure 2b: Carbon Epoxy Beam: Forced Vibration

CONCLUSION

The feasibility of a true smart material has been demonstrated by a microstructure synthesized with piezoelectric material, which imparts a self-sensing property to the material. The same concept is being extended to the actuation capability through a biomorph construction.

ACKNOWLEDGEMENTS

REFERENCES

Shaikh, Nisar and Dillon, Rod, "Smart Structural Composites," U.S. Japan Work Shop on Smart Intelligent Materials and Systems, 1990, pp 287-293.

Fabrication and curing of laminates with multiple embedded piezoceramic sensors and actuators

Shiv P. Joshi and W.S. Chan

Center for Composite Materials, Aerospace and Mechanical Engineering Departments, University of Texas at Arlington, Arlington, Tx 76019

ABSTRACT: Existing fabrication and curing procedures for advanced laminated composites have been standardized by trial-and-improvement over a period of time. The presence of multiple embedded piezoceramic sensors and actuators necessitate some modification of fabrication and curing procedures. A detailed discussion of fabrication procedure is presented in this article. The effect of curing cycle on the piezoelectric properties is also briefly discussed.

1• INTRODUCTION

Fabrication and curing processes for advanced laminated composites have been optimized for the last two decades. Curing processes involve control of pressure and temperature over the curing time. Recent research in this area has increased our understanding of the curing processes and resulted in real time control of curing parameters (Kranbuehl et.al.,1988). Real time control of curing processes has reduced the costs and time associated with a trial and improvement procedure for thick laminated composites (Tam and Gutowski, 1988).

The fabrication and curing processes for smart composite laminates involve additional parameters arising from the placement of sensors and actuators. This paper describes various aspects of fabrication and curing processes for laminates with multiple embedded piezoceramic sensors and actuators. Graphite epoxy laminates with embedded piezoceramic wafers are discussed in detail.

Chapin and Joshi (1991)considered residual thermal stresses due to curing process in deciding the optimum placement of piezoceramics in a laminate. Shaw et.al. (1990) discussed edge stress distribution due to presence of piezoceramic layers in a laminate. Crawley and Luis (1989) briefly discussed manufacturing aspects of intelligent structures with embedded piezoceramics. The following is a detailed discussion of fabrication and curing methodology.

2• PIEZOCERAMICS

The discussion of fabrication and curing process in the following sections is limited to placement of a piezoelectric material known as Lead Titanate Zirconate (PZT). The piezoceramic, commercially known as G-1195, is selected on the basis of some desirable properties

such as curie temperature, relatively high elastic moduli etc. The fabrication and curing processes are modified to reduce the risk of mechanical or electrical failure to the network of embedded piezoceramics. In addition, it is necessary to minimize the deterioration, if any, of piezoelectric and mechanical properties of sensors and actuators.

3. FABRICATION

The lay-up and geometry of the structural elements are known at the time of the fabrication. In addition, the planer positions and through-the-thickness placement of actuators and sensors in the laminate is provided to the fabricator. Figure 1 shows a schematic of a laminated plate lay-up with multiple piezoceramic wafers. Piezoceramic wafers are placed in cut-outs in
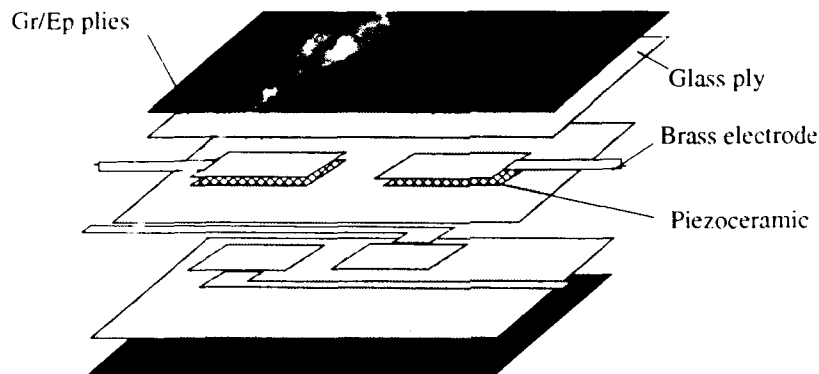
FIGURE 1. Schematic of a laminated plate lay-up with multiple piezoceramic wafers

a glass-epoxy prepreg ply. The brass electrodes run on the opposite sides of the glass-epoxy ply. This ply with piezoceramics placed in cut-outs is placed between two glass plies to insulate piezoceramics and electrodes from the conductive graphite-epoxy plies.

The brass ribbon electrodes (thickness 0.001 inch) cut in a required pattern are bonded to piezoceramic wafers. The electrodes are bonded prior to the placement in the glass-epoxy ply with cut-outs. Echo bond 57C conductive epoxy is used for bonding electrodes because it does not require application of heat which can adversely affect the piezoelectric properties. The bonding epoxy should be applied uniformly. The brass electrodes should cover the piezoceramic area completely but should not extend over the edges. Electrodes extending over the edges may short-circuit the piezoceramic wafer. One should also be careful in applying the conductive epoxy to avoid short-circuiting. An uneven application of the conductive epoxy will result in cracked piezoceramic wafers after curing. An x-ray radiograph of cured laminates showing cracked piezoceramic wafers as a result of the uneven application of the conductive epoxy is shown in figure 2.

FIGURE 2. X-ray radiograph showing undamaged and damaged embedded piezoceramic wafers in the insulating glass/epoxy plies.

The brass electrode pattern is chosen to avoid overlap of reverse polarity electrodes. Although an insulating glass/epoxy ply is between the electrodes, even in the case of cracked glass/epoxy ply, such a pattern will reduce a possibility of sparking. Cut-outs of same size as the wafers are cut in the glass/epoxy ply and wafers are placed in the cut-outs with electrodes running on the opposite sides of the ply. A glass/epoxy ply is placed on each side to encapsulate piezoceramic wafers and electrodes to avoid a connection between conductive graphite epoxy plies and sensors and actuators. These multiple sensors and actuators encapsulated in glass/epoxy plies are placed at required locations in a stacking sequence of a graphite/epoxy laminate. Figure 3 shows nine piezoceramic wafers with brass strip terminals in insulating glass/epoxy plies. Note that brass electrodes do not cover the whole surface of the wafers which resulted in cracked wafers after curing. There is no specific requirement on the width of the brass strips extending out from the wafers to the edges of the laminate. The brass electrodes are chosen on an ad-hoc basis. They can be replaced by any other type of electrodes.

The vacuum bagging procedure is the same as the commonly used bagging procedure. The procedure may vary depending on the complexity of the structural part. However, extra precautions should be taken to avoid breaking electrode terminals extending out of the laminate for external electric connections.
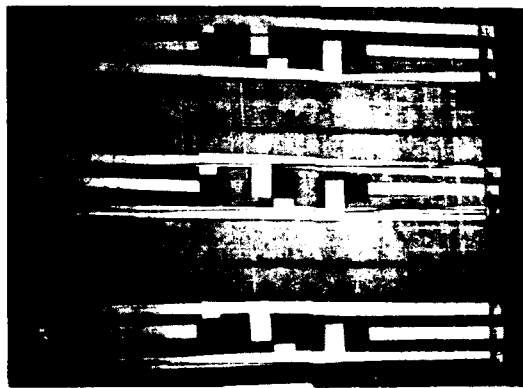
FIGURE 3. Piezoceramic wafers with brass terminal strips encapsulated in glass/epoxy insulating plies.

4• CURING PROCEDURE

Two curing procedures are tried. The first one is a recommended curing procedure for graphite/epoxy (AS4/3501-6) laminates of moderate thickness. In our case the laminate also contains glass/epoxy and piezoceramic wafers (G-1195). The maximum temperature and pressure applied in this cycle are 350 °F and 80 psi, respectively. The 350 °F temperature is slightly higher than the one half of the curie temperature. Curie temperature is the temperature at which ceramic loses piezoelectric properties. Piezoelectric properties deteriorate if the piezoceramic is subjected to temperatures higher than one half of the curie temperature.

The second curing procedure uses the recommended curing cycle for glass/epoxy laminates to separately cure glass plies containing piezoceramics. These cured plies are then placed in graphite/epoxy pre-preg lay-up and cured according to the first cycle. Second curing procedure almost doubles the curing time. However, it has certain advantages over the first curing procedure. The second curing procedure minimizes the piezoceramic wafer cracking and shorting between brass terminals and graphite fibers. The shorting between graphite fibers and brass terminals occurs frequently in the single cure cycle procedure because graphite fiber penetrated the epoxy rich areas of the glass/epoxy pre-preg during co-curing. Cured glass/epoxy plies with embedded piezoceramics can be screened for cracks in piezoceramics and electric connections before curing them with graphite/epoxy lay-up. This results in a higher percentage of undefective specimens.

The two cycle curing procedure is now routinely used in preparing test specimens at the University of Texas at Arlington laboratory facilities.

5• EFFECT OF CURING ON A PIEZOCERAMIC

Piezoceramic wafers are subjected to the curing cycle's pressure and temperature without embedding them in a laminate. These wafers are tested to evaluate the effect of the curing cycle on piezoelectric properties. The piezoelectric strain coefficient (d_{31}) is compared with virgin wafers. Figure 4 shows the variation of the in-plane normal strain induced by the electric field applied in the thickness direction of the wafer.

The strain data is recorded after they stabilize over time. Strain readings are stable for virgin wafers. However, the wafers subjected to the cure cycle become stable after a minute or so. It is clear that the curing cycle deteriorates piezoelectric properties. The microscopic inspection of virgin piezoceramic and the piezoceramics subjected to the curing cycle shows no difference between the microstructure at five to ten micron scale. It rules out the effect of microcraking induced deterioration in piezoelectric properties. The effect of curing cycle on piezoceramic properties are being studied at present and are beyond the scope of this article.

6• ACKNOWLEDGMENTS

The authors acknowledge the help from students D. Shaw, S. Subramanian. A.

Howard, V. Jacklin, C. Bauer, J. Stephens and R. Lawrence. The research is sponsored by the Army Research Office. Dr. G. Anderson is the project monitor.
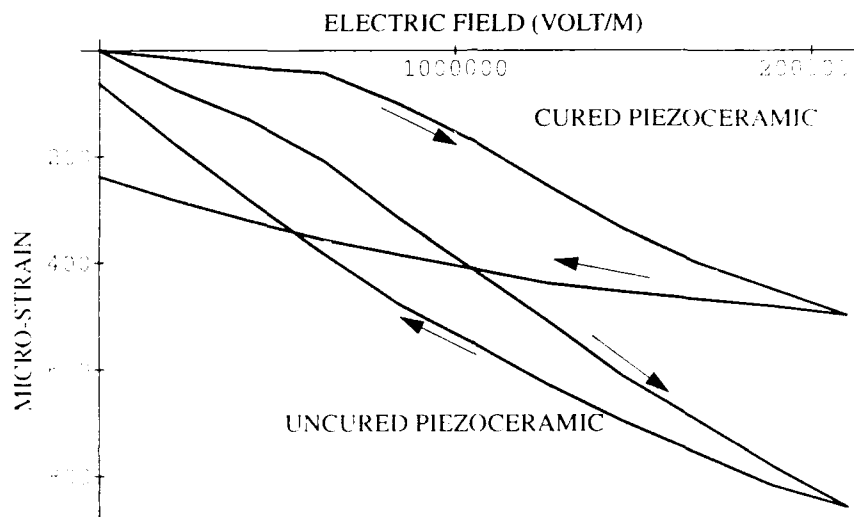
FIGURE 4. Variation of the in-plane normal strain due to application of electric field in the thickness direction

7• REFERENCES

1. Chapin, C.M. and Joshi, S.P., 1991, *Composites Design, Manufacture, and Application. ICCM VIII, Hawaii*, ed. S.W. Tsai and George S. Springer (Covina: SAMPE) pp. 30-D-1.10.

2. Crawley, E.F. and Anderson, E.H., 1989, *American Institute of Aeronautics and Astronautics, Inc.*, pp. 2000-2010.

3. Kranbuehl, D.E., Hoff, M., Eichinger, D.A., Loos, A.C., Freedman, W.T., Jr., 1988, *Proceedings of the American Society for Composites, Third Technical Conference*, (Lancaster: Technomic) pp. 313-323.

4. Shah, D.K., Chan, W.S., Joshi, S.P., and Subramanian, S.,1990, *Recent Developments in Composite Materials Structures*, Ed. D. Hui and C.T. Sun, AD-Vol. 19, AMD-Vol. 113. The American Society of Mechanical Engineers, pp. 19-24.

5. Tam, A.S. and Gutowski, T.G., 1988, *Proceedings of the American Society for Composites, Third Technical Conference*, (Lancaster: Technomic) pp. 255-262.

Experiments on active vibration control of a thin plate using disc type piezoceramic actuators and sensors

Suk-Yoon Hong, Vasundara V. Varadan and Vijay K. Varadan

Research Center for the Engineering of Electronics and Acoustic Materials
The Pennsylvania State University, University Park, PA 16802

ABSTRACT: For the vibration control of a two dimensional structure such as a thin plate clamped along all sides, the piezoelectric ceramic, PZT was chosen as sensor, actuator and vibrator because of its large electro-mechanical coupling constant that in turn allows the actuators to output sufficiently large power and it also serves as an accurate sensor. A series of active vibration control experiments have been performed for several lower modes with different types of control algorithms. In direct feedback multi-mode control, by superposing each signal from particularly positioned sensors, coupled mode signals could be simplified without using filters. Alternatively, modified coupled mode control using optimal control algorithm has also been used. In these experiments, the idea for a uni-disc type colocated sensor (inner disc) and actuator (outer ring) has been proposed to implement actual colocation of sensors/actuators and to minimize the numbers of transducers used. The performance has been verified experimentally.

1. INTRODUCTION

For the vibration control of a two dimensional structure such as a thin plate clamped along all sides, the piezoelectric ceramic, PZT (Lead-Titanate-Zirconate) was chosen as sensor, actuator and vibrator because of its large electro-mechanical coupling constant. A series of active vibration control experiments have been performed for several lower modes with different type of control algorithms for analog control as well as digital control. Although the system structure is stiff because of the material characteristics of the plate and due to the clamped edges, we could implement effective vibration control with optimally selected positions and sizes of sensors and actuators.

Coupled multi-mode steady-state quadratic optimal control procedures for the plate have been developed. General closed-form expressions for the mode shapes do not exist for the rectangular plate. Therefore, we have used the Rayleigh-Ritz procedure to obtain the approximated mode shape constants. For the modal equation, proportional type damping has been considered to obtain a closed-form solution of the differential eigenvalue problem for the damped system. Sensing signal conversion has been performed to change the curvature signal to a displacement signal. The actuating signal can also be converted. PZT actuators can be approximately converted to point force actuators with appropriate conversion constants which function as the final control gain.

In developing multi-mode velocity feedback analog control systems, we selected a

specific sensing mode cancellation idea which serves as a filter by adding or subtracting each signal. We believe that this idea could improve the control performance. In this research, the idea for uni-disc type colocated sensors and actuators is proposed and the performance is verified experimentally.

To take the advantages of digitalized system such as the flexibility of control program and increased logic capability and to simplify the experimental system especially for multi-mode control, a digital control system composed of a microcomputer and a data acquisition board has been recommended

2. MODE SHAPE AND MATERIAL PROPERTIES OF CONTROL STRUCTURE

The first six mode shapes of the all-clamped sides square plate are shown in Fig.1 and for the plates used in system 1 (analog control system) and system 2 (optimal digital control system), some modal frequencies are shown in Table 1. The control structure is made of aluminum and two different piezoelectric transducers have been used as sensors and actuators. Details are summarized in Table 2 and 3, respectively.

Table 1   Mode Frequencies   (Hz)

Mode	System 1	System 2
(1,1)	74.5	44.4
(2,1)	149	71.5
(2,2)	248	92.0

Table 2   Properties of Control plate

	System 1	System 2
Material	Aluminum	Aluminum
Size (m x m)	0.305 x 0.305	0.305 x 0.305
Thick. (mm)	0.8	0.4
Density(kg/m^3)	2.16	1.08

Table 3   Properties of Transducers

	Large Disc	Small Disc
Material	PZT-4	PZT-5
Diameter (mm)	39.5	25.4
Thickness (mm)	0.51	0.89
Weight (g)	4.5	3.4
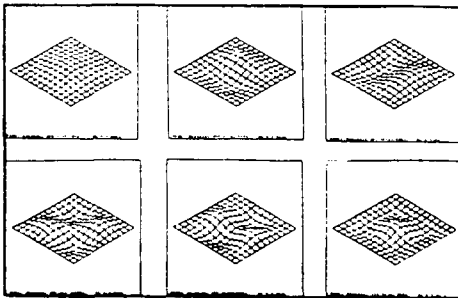
Fig.1 All Sides Clamped Square Plate Mode Shapes

3. MULTI-MODE ANALOG CONTROL (SYSTEM 1)

The configuration of the adaptive structure and system are shown in Fig.2. The adaptive structure is composed of two groups of sensors/actuators and each group has two sensors and one actuator. Vibrator V1 and V2 have been used to generate mode (1,1), (2,1) vibration signal, respectively. By adding the signals from the two sensors S1 and S2, mode (2,1) signals are canceled out by the 180° phase difference of mode (2,1) at the sensor positions

used. Therefore, only mode (1,1) signals go through the system A. Similarly, by changing the poling direction of S4 to negative (-), we can filter only mode (2,1) signals that go through the system B. Fig.3 shows the sensing signals from each sensor or sensor group. The advantages of these *smart filters* are summarized as follows and experimental results obtained are shown in Fig.4.

- Almost 100% bandpass filtering effect (actual reproduction of each single mode signal)
- Some change of system resonance frequency or vibrator (source) frequency does not decrease filtering efficiency.
- Additional filtering effect (some other even/odd modes can be canceled.)
- Simple and low cost
- For other modes of interest, we can design smart filters by considering the mode shapes.

4. MULTI-MODE OPTIMAL CONTROL (SYSTEM 2)

The all clamped square plate does not have a closed form solution for the mode equations. Therefore, mode shape approximations are necessary to formulate steady-state quadratic optimal control. By using the Rayleigh-Ritz method, we can approximate the control mode shape as in Eq.(1).

$$w_{ij}(x,y) = \sum_m \sum_n a_{mnij} \ w_m(x) \ w_n(y) \tag{1}$$

$w_{ij}(x,y)$: ij mode shape of plate
$w_m(x), w_n(y)$: beam mode shape which satisfies the B.C. on the edges (x=0,L y=0,L)
a_{mnij} : Rayleigh-Ritz method constant

(a) Sensing signal from sensor 1, S1

(b) Sensing signal from S1+S2, mode(1,1)

(c) Sensing signal from S3+S4, mode(2,1)
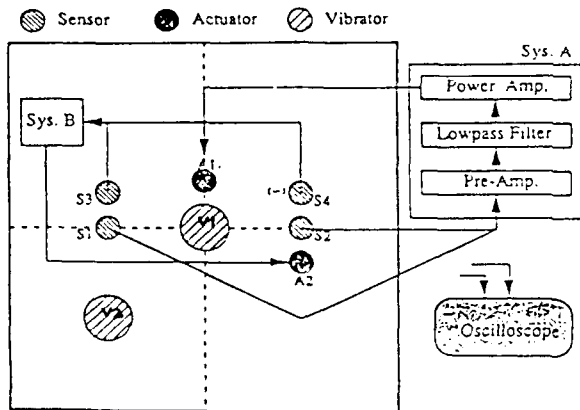
Fig.2 Experimental Scheme (System 1)
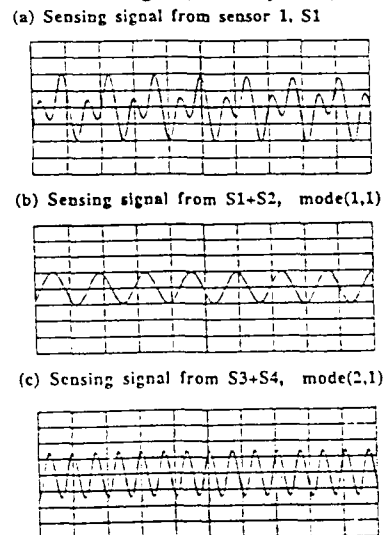
Fig.3 Signals from System 1 Sensors
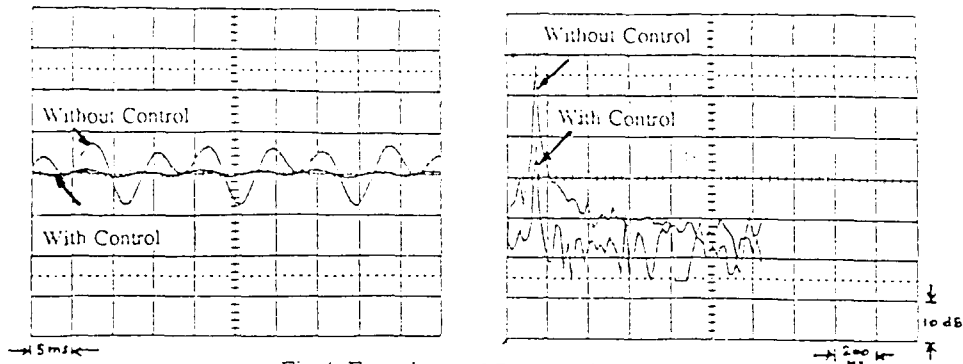
Fig.4 Experimental Results (System1)

From modal equation, Eq.(2) and with Table 4, we obtain the modal state equation as Eq.(3). After selecting the performance index of quadratic form and the sampling frequency by pretest, we could follow a regular optimal digital control procedure using a Kalman filter.

$$\ddot{\eta}_r(t) + 2\,\zeta_r\,\omega_r\,\dot{\eta}_r(t) + \omega_r^2\,\eta_r(t) = f_r(t) \tag{2}$$

η_r : modal coordinate

ω_r : modal frequency

ζ_r : modal damping factor (0.004)

f_r : modal force

Table 4 Numerical Value of System Variables

	Freq.(Hz)	ω_r	ω_r^2	ζ_r	$2\,\zeta_r\,\omega_r$
(1,1)	44.5	279	77826	0.004	2.232
(2,1)/(1,2)	71.5	449	201824	0.004	3.594
(2,2)	92.0	578	334145	0.004	4.624

$$
\begin{bmatrix} \dot{x}_1 \\ \dot{x}_2 \\ \dot{x}_3 \\ \dot{x}_4 \\ \dot{x}_5 \\ \dot{x}_6 \\ \dot{x}_7 \\ \dot{x}_8 \end{bmatrix} =
\begin{bmatrix}
0 & 1 & 0 & 0 & 0 & 0 & 0 & 0 \\
-77826 & -2.23 & 0 & 0 & 0 & 0 & 0 & 0 \\
0 & 0 & 0 & 1 & 0 & 0 & 0 & 0 \\
0 & 0 & -201824 & -3.59 & 0 & 0 & 0 & 0 \\
0 & 0 & 0 & 0 & 0 & 1 & 0 & 0 \\
0 & 0 & 0 & 0 & -201824 & -3.59 & 0 & 0 \\
0 & 0 & 0 & 0 & 0 & 0 & 0 & 1 \\
0 & 0 & 0 & 0 & 0 & 0 & -334145 & -4.62
\end{bmatrix}
\begin{bmatrix} x_1 \\ x_2 \\ x_3 \\ x_4 \\ x_5 \\ x_6 \\ x_7 \\ x_8 \end{bmatrix} +
\begin{bmatrix} 0 \\ 4.94 \\ 0 \\ 5.66 \\ 0 \\ 5.66 \\ 0 \\ 6.09 \end{bmatrix} \cdot F
\tag{3}
$$

Sensing signal conversions have been performed to change curvature signals to displacement signals using Eq.(4). Every sensed signal from PZT give us the information for curvatures but, to implement optimal control with displacement sensors, we need the displacement values. In case of single mode, the conversion is straight forward but in multimode case, only limited points on the plate satisfy the conversion requirements. Those points could be found using numerical calculation and could be decided as optimum sensor points. The actuating signal also should be converted. PZT actuators can be approximately converted to point force actuator with appropriate conversion constants which serves as the final control gain. To do this conversion, a finite element method package program, ANSYS has been used considering equivalent loading for the applied PZT moments.

$$V_s = [-\alpha \ (h) \ (t) \ (d_{31}/\epsilon_{33}{}^T) \ / \ (s_{11}+s_{12})] \ [\ 1/A \ \iint_A (\partial^2 W/\partial x^2 + \partial^2 W/\partial y^2) \ dx \ dy \ ]$$

$$= \ -0.8(0.455 \times 10\text{-}3)(0.2 \times 10\text{-}3)(-10.6 \times 10\text{-}3) \quad [\ \text{Ave.Curvature} \ ]$$
$$\quad (12.3 \times 10\text{-}12\text{-}0.31 \times 12.3 \times 10\text{-}12)$$

$$= \ [\ -91.0 \ ] \ [\ \text{Ave.Curvature} \ ] \tag{4}$$

α : bonding effect   h : neutral axis distance   t : sensor thickness   A : sensor area

d_{31} : piezoelectric const. ϵ_{33} : dielectric const. s_{11}, s_{12} : elastic compliance

The experimental scheme and the results obtained are shown in Fig.5 and 6, respectively. By partially removing the electrode on the PZT surface, we could make an uni-disc type sensor/actuator which results in a colocated sensor/actuator as in Fig.5.

5. CONCLUSION

Piezoelectric ceramics are promising materials as actuators/sensors in structural vibration control. And also, circular disc shaped PZT elements are recommended in two-dimensional structural vibration control. For the filtering of object signal, mode signal superposition concepts have been proposed and gives us confidence in the use of *smart filters*. A reliable colocated sensor/actuator system can be implemented using uni-disc sensor/actuator type transducers.

We can expect multi-mode optimum control with a suitably positioned minimum number of transducers using advanced control algorithms (e.g., steady-state quadratic optimal control) by changing the number of control modes, sensors/actuators and the positions of sensors/actuators.
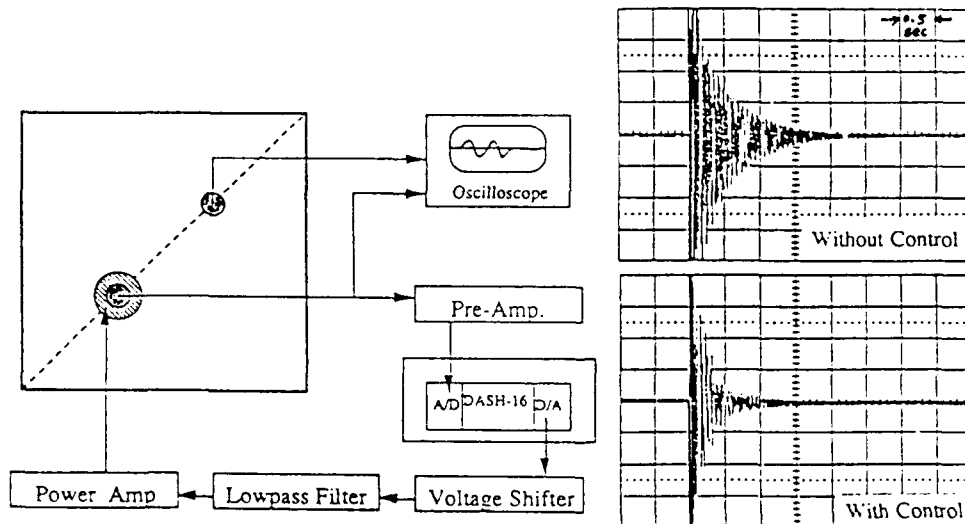
Fig.5 Experimental Scheme (System 2)   Fig.6 Experimental Results (System2)

713

Vibration characteristics of a composite beam with semi-active piezo-actuators

Sung J. Kim and James D. Jones

Ray W. Herrick Laboratories, School of Mechanical Engineering, Purdue University

ABSTRACT: A new and novel semi-active control strategy using surface-mounted piezoelectric actuators to alter the vibration response of a composite beam model is analytically investigated. Non-linear equations of motion of the composite beam are developed, which incorporate the influence of initial in-plane loads generated by the piezoelectric layers. It is shown that the natural frequencies of a simply-supported composite beam can be varied substantially by applying a constant voltage to the piezoelectric layers or by varying the electric conditions of the electrodes.

1. INTRODUCTION

Piezoelectric actuators have attracted significant attention in recent years because of their distributed character of actuation which allows them to be tailored to selectively reduce structural modes with little control spillover. Piezo-actuators also have several other inherent advantages over conventional actuators. They are inexpensive, space efficient, lightweight and they can be easily shaped and bonded-to (or embedded-in) a variety of surfaces. Furthermore, in contrast to point actuators, piezo-actuators do not require a back reaction.

In past research, there have been two main areas of relevant research for the use of piezoelectric actuators for control of structural sound and vibration. One important area has been a development of mathematical models which describe the substructure/piezo-actuator coupling. Lee (1987) developed the equation of motion for the composite plate with piezo-actuator layers based on Love's theory. However, when piezo-actuators of high piezoelectric coupling constant are considered, Lee's model does not represent the true characteristics of the piezo-actuators since the variation of electric condition was neglected in the analysis.

The second important research area covers the development of control strategies. Active control strategy whereby a time-varying electric field is applied to surface mounted piezo-actuators to directly control the structure vibration have been widely studied by many investigators (Bailey 1985 and Hagood 1990). Further, Hagood (1991) introduced a novel passive control strategy which uses passive electric circuits to shunt the electrodes of the surface-mounted piezoelectric element in order to dissipate structural vibration energy.

Recently, a passive adaptive approach to controlling structural sound and vibration using adaptive materials such as shape memory alloys (SMAs) has been demonstrated. Bliss and Gottward (1990) experimentally demonstrated the concept of alternating resonance tuning (ART) which involves arranging arrays of panels with adjacent panels tuned to have the resonance frequencies just above and below a given operating frequency.

One of the interesting characteristics of piezoelectric materials is that their elastic properties, such as Young's moduli and Poisson's ratio, depend on the electric conditions of the electrodes. Although, the Young's moduli variations of SMAs are far greater than those of piezoelectric

materials, there are some clear advantages of piezoelectric materials including fast response times and simple electric control circuits. Further, piezo-actuators can be used to change the system dynamic characteristics by generating in-plane forces rather than bending moment of active control strategy.

In the current study, a semi-active control strategy is investigated to study the influence of the in-plane loads generated by the piezo-actuators and the variations of the electric conditions of the electrodes on the dynamic characteristics of the composite beam model. Since conventional composite plate theory (Lee 1987) cannot accommodate the variation of the changes on the electrode conditions, a new mathematical model is introduced. Also, since linear beam theory cannot accommodate the in-plane loads in the transverse dynamic characteristics of the beam, a non-linear beam theory is introduced. Variations in the composite beam natural frequencies with changes in the applied electric field are presented. The influence of composite beam length and composite geometric configuration on the changes of natural frequencies are also investigated.

2. ELASTIC PROPERTIES OF PIEZOELECTRIC MATERIALS

Piezoelectric materials in this study are assumed to be of a hexagonal structure of 6mm=C_{6v} which has 5 independent elastic constants, 3 independent piezoelectric constants and 2 electric constants (IEEE 1978). However, the application of piezoelectric materials in this study is limited to the case of thin composite plates. Thus, the piezoelectric layer is also assumed to be thin and consequently, a plane stress state is assumed. Also, the applied electric field is assumed to be in the thickness direction. It is not difficult to show that the elastic properties of the piezoelectric materials under these assumptions have following relationships;

$$Y^D = \frac{Y^E}{1-k_{31}^2} , \quad v^D = \frac{k_{31}^2 + v^E}{1-k_{31}^2} \quad \text{where, } k_{31}^2 = \frac{d_{31}^2 Y^E}{1-(v^E)^2} \tag{1}$$

where Y and v represent Young's modulus and Poisson's ratio, respectively. Superscripts D and E are the open- and short-circuited conditions, respectively, while the variables d_{31} and k_{31} represent the piezoelectric strain and coupling constants. Figure 1 shows the ratios of Young's modulus and Poisson's ratio ((Y^D/Y^E and v^D/v^E)) as a function of coupling constant k_{31}. Note that the open-circuited Young's modulus and Poisson's ratio are greater than those of the short-circuited. It is also demonstrated that the Poisson's ratio shows greater variation than the Young's modulus. Note here that the typical values of coupling constant k_{31} for piezo-ceramic materials (PZT) and piezo-polymer materials (PVDF) are about 0.3 and 0.1, respectively.

3. EQUATIONS OF MOTION

As discussed above, Lee (1987) developed the Love equations of motion for the composite plate with embedded piezoelectric layers. In the analysis, Lee assumed that the electric field was constant over the piezo-actuator thickness. Since mechanical strains for the structure in flexural motion are functions of thickness, Lee's assumption lead that the electric displacement is constant with respect to the thickness variation. However, Gauss law, which is analogous to the mechanical continuity equation, states
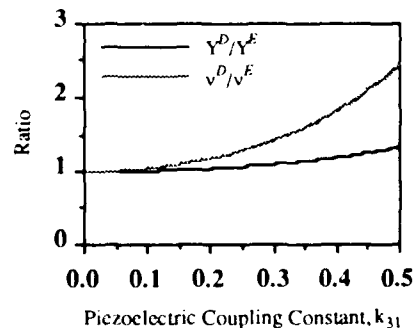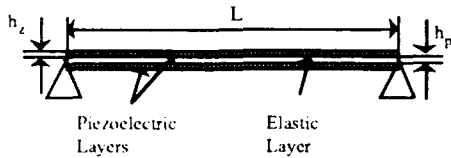
Figure 1. The Variation of Elastic Properties of the Piezoelectric Materials

$$\frac{\partial D_3}{\partial z} = 0 \tag{2}$$

Therefore, it is the the electric displacement rather the electric field that is constant over the thickness variation.

It is not difficult to derive the Love equations of motion with the utilization of above constraint. In this study, the effect of large deflection and initial in-plane loads are also included into the equations of motion of the composite plate by introducing new strain-displacement relationships (von Karman assumption) which includes a non-linear relationship of strain-displacement, and a new set of equilibrium equations (Leissa 1967). Since a detailed derivation is lengthy, only the final equation of motion for specific example is presented. The equation of motion for a composite beam as shown in Figure 2 can be expressed as

$$D_c \nabla^4 u_3 + T_c \nabla^2 u_3 - \nabla^2 m_{pz} + m_c \ddot{u}_3 = q_3 \tag{3}$$

Piezoelectric Layers   Elastic Layer

Figure 2. Simply-Supported Composite Beam

where u_3 is the transverse displacement and q_3 is the external transverse force. Here the variables T_c, D_c and m_c are the initial in-plane load, flexural stiffness, and mass of the composite plate, respectively. The third term in Equation (3) represents the piezo-actuator control force. The composite variables can be found from a summation of the individual material properties of each layer as shown below.

$$D_c = D_p + 2D_z^D(1-\xi), \quad m_{pz} = 2e_{31}\left[\left(\frac{h_p}{2}+h_z\right)^2 - \left(\frac{h_p}{2}\right)^2\right]\frac{V_o}{h_z}, \quad m_c = \rho_p h_p + 2\rho_z h_z \tag{4}$$

$$D_p = \frac{Y_p}{12(1-v_p^2)}h_p^3, \quad D_z^D = \frac{Y_z^D}{3(1-v_{zd}^2)}\left[\left(\frac{h_p}{2}+h_z\right)^3 - \left(\frac{h_p}{2}\right)^3\right] \tag{5}$$

$$\xi = \frac{3}{2}\bar{\delta}_z \frac{k_{31}^2}{1-k_{31}^2} \frac{1+v_{ze}}{1-v_{ze}} \frac{\left[\left(\frac{h_p}{2}+h_z\right)^2 - \left(\frac{h_p}{2}\right)^2\right]}{\left[\left(\frac{h_p}{2}+h_z\right)^3 - \left(\frac{h_p}{2}\right)^3\right]}, \quad \text{where } \bar{\delta}_z = \frac{h_p+h_z}{2} \tag{6}$$

$$T_c = 2\frac{Y_z^E}{1-v_{ze}}d_{31}h_z E_f, \quad \text{where, } E_f = \frac{V_o}{h_z}. \tag{7}$$

Here, the variable v_{ze} and v_{zd} represent the short- and open-circuited Poisson's ratios, respectively. Note here that when the polarization of the applied voltages (V_o) are arranged to generate the bending moment, the in-plane force (T_c) in Equation (7) becomes zero whereas when they are arranged to generate in-plane force, the effective moment (m_{pz}) in Equation (4) becomes zero which is the case of this study. Note also that when the electrodes are electrically open (i.e., $\xi=0$), the flexural rigidity (D_c) becomes D_c'' in Equation (8). Note further that the flexural rigidity by Lee is D_c' in Equation (8):
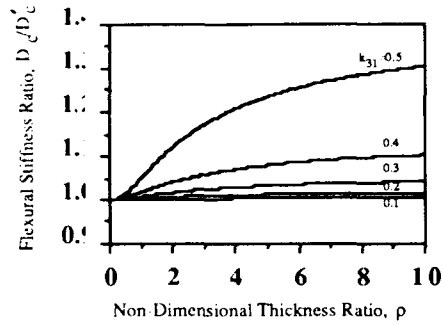
Figure 3. The Flexural Rigidity Ratio
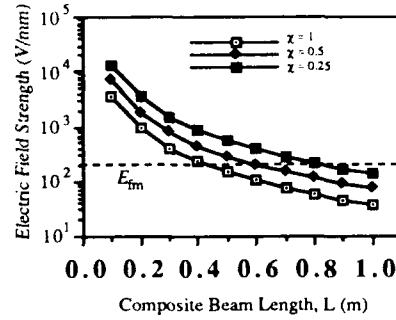
Figure 4. Critical Buckling Electric
Field Strength

$$D_c' = D_p + 2D_z^E \ , \quad D_c'' = D_p + 2D_z^D \ . \tag{8}$$

Figure 3 shows the flexural rigidity ratio (D_c/D_c'). Note that when the coupling constant k_{31} is high, noticeable discrepancies exist between D_c and D_c'. Further, when the thickness ratio, $\rho = h_z/(h_p/2)$, is high, the discrepancies become even greater. Therefore, Lee's assumption (i.e., constant electric field across the thickness) is not valid in these cases.

4. DISCUSSION

Since the beam under consideration in this study is simply-supported, the m-th natural frequency (ω_m) can be estimated as

$$\omega_m^2 = \frac{D_c\left(\dfrac{m\pi}{L}\right)^4 + T_c\left(\dfrac{m\pi}{L}\right)^2}{m_c} \tag{9}$$

4.1 Critical Buckling Electric Field

It is interesting to note that the natural frequency in Equation (9) can be zero when T_c is negative (i.e., the in-plane forces are in compression). Leissa (1969) defined the critical buckling load for symmetric beam as the load which makes the first natural frequency equal to zero (which means that the beam loses its flexural rigidity completely). Figure 4 shows the variation of the buckling electric field strength as a function of the beam length (L) and the piezo-actuator thickness ratio (χ) which is defined as the ratio $(\chi=(h_z/2)/h_t)$. The piezo-actuator and substructure are assumed to be PZT and aluminum, respectively.

It is clear that as the length of the beam increases the critical buckling electric field strength decreases, which is plausible since, in general, longer beams have lower critical buckling loads. However, as the piezo-actuator thickness ratio (χ) decreases (i.e., the fraction of piezo-actuator thickness to the total composite beam thickness decreases), the critical buckling electric field strength increases. This can be explained by the fact that the in-plane load due to the piezo-actuator layer becomes smaller as the piezo-actuator thickness ratio (χ) decreases. It is not difficult to see that the critical buckling electric field strength approaches infinity when the piezo-actuator thickness ratio (χ) approaches zero.
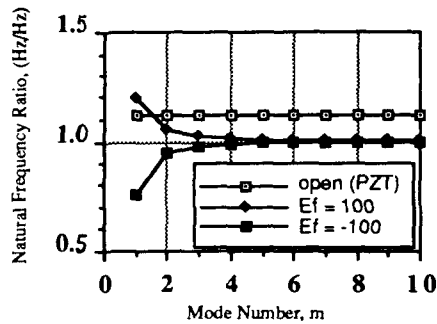
Figure 5. The Natural Frequency Ratios of the Composite Beam for PZT Actuators with $\chi = 0.5$ and L = 0.5 (m).
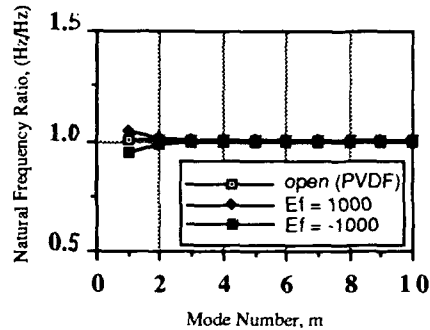
Figure 6. The Natural Frequency Ratios of the Composite Beam for PVDF Actuators with $\chi = 0.5$ and L = 0.5 (m).

For most PZT piezo-actuator materials, the maximum allowable electric field strength (E_{fm}) is about 200 V/mm for continuous usage. If the applied field strength is exceeded, the piezo-actuator experiences de-polarization which causes the actuator to rapidly lose its piezoelectric properties. In Figure 4, the dotted line represents the maximum allowable field strength (E_{fm}). Therefore, the composite beam under that line will experience buckling if the maximum allowable field strength is applied. Due to the existence of asymmetries in every real composite beam which tend to reduce the critical buckling electric field strength, this cannot be easily verified by experiments. However, an important observation in this result is that the dynamic characteristics of the composite beam can be substantially varied by an applied electric field within practical limits.

4.2 Variations of Natural Frequency

Figure 5 shows the natural frequency variations of a composite beam as a function of mode number (m) for select electrical conditions of the piezo-actuator. The piezo-actuator thickness ratio (χ) and the beam length (L) are arbitrary chosen to be 0.5 and 0.5 (m), respectively. The applied electric field strength (E_f) is chosen to be 100 V/mm, well below the maximum allowable field strength (200 V/mm for PZT).

It is clearly shown that applied in-plane loads due to the piezo-actuator greatly influences the lower order modes of the composite beam. The first natural frequency can be varied by more than 20 % by applying a constant electric field to the piezo-actuator. It is interesting to note that the influence of the in-plane load decreases with the increasing mode number (m).

In Figure 5, the effects of opening the electrodes (open-circuited) are also demonstrated. The natural frequencies of the open-circuited composite beam differ by approximately 12 % from those of the short-circuited composite beam irrespective of the mode. Note here that the opening the electrode might be more useful than applying a constant electric field to control the higher order modes because the in-plane load does not create sufficient natural frequency variations in the higher order mode range.

Figure 6 shows the natural frequency variations when the piezo-actuator is PVDF. The applied electric field strength is chosen to be 1000 V/mm which is 10 times greater than that of PZT since PVDF has a greater maximum allowable field strength, typically 2000 V/mm. The variation of the first natural frequency with PVDF actuator is about 2.5 % whereas that of the composite beam with PZT actuator is more than 20 %. Since the PVDF has a lower stiffness

than PZT, the in-plane load generated by PVDF is smaller than by PZT and consequently, the PVDF composite beam has lower natural frequency variations than the PZT composite beam.

PVDF has an electro-mechanical coupling coefficient (k_{31}) of 0.12, which is significantly smaller than that for PZT which has a nominal value of 0.33. Therefore, the Young's modulus of the open-circuited PVDF is about 1 % greater than that of the short-circuited actuator. Accordingly, the variations of the natural frequencies by opening the electrodes (open-circuited beam) are less than 1 %. Therefore, no significant changes are shown in Figure 6 when the electrodes are open because the high stiffness of the substructure as compared with the PVDF actuator prevents significant natural frequency variations. Thus, due to their high stiffness and the high coupling coefficient, PZT actuators will generally provide a more significant natural frequency variations than PVDF. Nevertheless, for plates and beams of significant dimensions, large sheets of PVDF actuators can easily be manufactured. However, because of the highly brittle nature of PZT materials, actuators of large dimensions are not currently possible, although an array of PZT actuators may prove equally effective.

5. CONCLUSIONS

The non-linear governing equation of the motion of a beam which incorporates the effects of large deflection and in-plane loads due to the piezo-actuator layers is developed. It is demonstrated that the open-circuited Young's modulus of the piezo-actuator in plane stress state is different from that of short-circuited piezo-actuator. Furthermore, it is shown that buckling can be caused by applying an electric field to the piezo-actuator embedded in a beam if a critical buckling electric field strength is exceeded. The natural frequencies can be substantially decreased or increased by the in-plane load, i.e., by applying a positive or negative electric field to the piezo-actuator. The natural frequency variations are more significant for the lower order modes and longer beams. It is also demonstrated that the natural frequencies can be controlled substantially by changing the electrode condition. These changes in the natural frequencies are independent of the boundary conditions, composite thickness and the beam length. Finally, it is shown that, due to their stiffness and the higher coupling coefficient, PZT actuators provide a more significant natural frequency variations than PVDF actuators.

ACKNOWLEDGEMENTS

REFERENCES

Anders W, Rogers C and Fuller C 1991 *AIAA*-**91-1163**
Bailey T and Hubbard J 1985 *AIAA J. of Guid. and Control* **6** 605
Bliss D and Gottwald J 1990 Submitted to the *AIAA Journal of Aircraft.*
Hagood N, Chung W and Flotow A 1990 *J. of Intell. Mater. Syst. and Struct.* **1** 327
Hagood N and Flotow A 1991 *J. Sound and Vib.* **140** 243
Leissa A 1969 Vibration of Plates *NASA* **SP-160** U. S. Government Printing Office Washington D. C. pp. 276-277
Lee C 1990 *J. Acoust. Soc. Am.* **87** 1144

Adaptive piezoelectric structures: theory and experiment

H. S. Tzou [1,2] and J. P. Zhong [3]

[1] Department of Mechanical Engineering
University of Kentucky, Lexington, KY 40506-0046

[2] Institute of Space and Astronautical Science, Kanagawa 229, Japan [§]

[3] Conmec Inc., Allentown, PA 18103

ABSTRACT: Active "smart" structures with controllable and/or adaptive dynamic characteristics have extensive potential applications in a variety of high-performance systems, e.g., aircraft/space structures, robots, "smart" machines, etc. In this study, an active adaptive structure made of piezoelectric materials is proposed and evaluated. Electromechanical equations of motion of a generic piezoelectric shell subjected to mechanical and electrical excitations are derived using Hamilton's principle and the linear piezoelectric theory. Structural adaptivity is achieved by a voltage feedback (open or closed loops) via the converse piezoelectric effect. Applications of the theory are demonstrated.

1. INTRODUCTION

Active structures with controllable and/or adaptive static/dynamic characteristics have great advantages over traditional elastic or passive structures. A control system integrated with the active structures can add an "intelligence" and an adaptive control capability in which the system tracks any disruptive excitation, frequency and amplitude, and automatically self-adjusts to adapt the "new" environment. This new technique can be applied to a variety of new engineering systems, such as advanced aerospace structures [1,2], noise and vibration controls [3–6], flexible robot manipulators [7], high-precision isolation and control [8,9], etc. In this study, the adaptive structures are made of a piezoelectric material in which the adaptivity is contributed by the converse piezoelectric effect and controlled by external feedback voltages. Damping enhancement of piezoelectric coupled beam structures was studied recently [1,3,10,11]. Tzou and Gadre derived a theory on a multi-layer shell with distributed shell actuators [4]. An integrated distributed sensing/control theory of shells was proposed and applied to distributed sensing/control of plates/shells [6]. Tzou and Tseng also derived a new piezoelectric finite element applied to distributed sensing and control of distributed parameter systems — shells and plates [12]. In the above studies, active vibration control — damping enhancement — was the primary goal. Frequency variation of the piezoelectric structures was not investigated. Besides, structural adaptivity of piezoelectric shells was not studied. In this paper, a piezoelectric shell theory which accommodates the direct/converse effects and mechanical/electrical excitations is derived. Equations of motion and boundary conditions of a generic piezoelectric shell are formulated. Applications of the generic shell theory to an adaptive piezoelectric bimorph beam.

---

2. THEORY OF A PIEZOELECTRIC SHELL

Dynamic characteristics of a piezoelectric structure can be controlled by injecting a high voltage into the structure. In this section, the dynamic equation of a generic piezoelectric shell is presented.

It is assumed that the piezoelectric shell is defined in a curvilinear coordinate system, i.e., α_1 and α_2 axes define a curvilinear surface and α_3 the transverse axis. Note that these three axes are orthogonal to each other. Assumptions associated with the thin elastic shell structures follow the linear Love–Kirchhoff theory [6]. It is also assumed that the electrodes are fully covered the top and bottom surfaces. Localization and discretization of the electrodes can be achieved by defining Dirac delta functions and/or step functions which are not shown here. It is also assumed that a transverse electric field E_3 and non–symmetrical in–plane dielectric permittivity coefficients e_{31} and e_{32}. (Note that for a symmetrical hexagonal piezoelectric material, e_{32} is equal to e_{31}.) Besides, the injected control voltage is usually much larger than the self–generated voltage due to the direct effect. Using Hamilton's principle and calculating the variations, one can obtain the equations of motion of a piezoelectric thin shell [13].

$$-\frac{\partial}{\partial\alpha_1}[(N_{11}-e_{31}\int_{\alpha_3}E_3d\alpha_3)A_2] - \frac{\partial(N_{21}A_1)}{\partial\alpha_2} - N_{12}\frac{\partial A_1}{\partial\alpha_2} + (N_{22}-e_{32}\int_{\alpha_3}E_3d\alpha_3)\frac{\partial A_2}{\partial\alpha_1}$$

$$- A_1A_2\frac{Q_{13}}{R_1} + A_1A_2\rho h\ddot{u}_1 = A_1A_2q_1 , \tag{1}$$

$$-\frac{\partial(N_{12}A_2)}{\partial\alpha_1} - \frac{\partial}{\partial\alpha_2}[(N_{22}-e_{32}\int_{\alpha_3}E_3d\alpha_3)A_1] - N_{21}\frac{\partial A_2}{\partial\alpha_1} + (N_{11}-e_{31}\int_{\alpha_3}E_3d\alpha_3)\frac{\partial A_1}{\partial\alpha_2}$$

$$- A_1A_2\frac{Q_{23}}{R_1} + A_1A_2\rho h\ddot{u}_2 = A_1A_2q_2 , \tag{2}$$

$$-\frac{\partial(Q_{13}A_2)}{\partial\alpha_1} - \frac{\partial(Q_{23}A_1)}{\partial\alpha_2} + A_1A_2[-\frac{1}{R_1}(N_{11}-e_{31}\int_{\alpha_3}E_3d\alpha_3)$$

$$+ \frac{1}{R_2}(N_{22}-e_{32}\int_{\alpha_3}E_3d\alpha_3)] + A_1A_2\rho h\ddot{u}_3 = A_1A_2q_3 ; \tag{3}$$

where Q_{13} and Q_{23} are defined in the following two equations:

$$Q_{13}A_1A_2 = \frac{\partial}{\partial\alpha_1}[(M_{11}-e_{31}\int_{\alpha_3}\alpha_3E_3d\alpha_3)A_2] + \frac{\partial(M_{21}A_1)}{\partial\alpha_2} + M_{12}\frac{\partial A_1}{\partial\alpha_2}$$

$$- (M_{22}-e_{32}\int_{\alpha_3}\alpha_3E_3d\alpha_3)\frac{\partial A_2}{\partial\alpha_1} , \tag{4}$$

$$Q_{23}A_1A_2 = \frac{\partial(M_{12}A_2)}{\partial\alpha_1} + \frac{\partial}{\partial\alpha_2}[(M_{22}-e_{32}\int_{\alpha_3}\alpha_3E_3d\alpha_3)A_1] + M_{21}\frac{\partial A_2}{\partial\alpha_1}$$

$$- (M_{11}-e_{31}\int_{\alpha_3}\alpha_3E_3d\alpha_3)\frac{\partial A_1}{\partial\alpha_2} , \tag{5}$$

where N_{ij} and M_{ij} are the force and moment resultants [4]; A_i is Lame's parameter; R_i is the radius of curvature; ρ is the mass density; h is the thickness, and q_i is the external mechanical force. Note that transverse shear deformations and rotary

inertias are neglected. Boundary conditions can be derived accordingly, which include both mechanical and electric effects. Note that these equations of motions could include the effect of non–uniform voltage distribution. This could be introduced by the resistance of surface electrodes or spatially segmented electroded surfaces. It should be noted that the boundary conditions are different from the conventional expressions by the introduced voltages. System "adaptivity" of a piezoelectric shell structure is achieved by controlling voltage injections.

The derived shell equations are very general and can be simplified to account for many other commonly occurred geometries, such as plates, cylindrical shells, spheres, cones, arches, beams, etc. In the following case studies, the derived piezoelectric shell theory is applied to a piezoelectric bimorph beam made of two piezoelectric layers with opposite polarity. Analytical solutions are compared with laboratory results.

3. AN ADAPTIVE PIEZOELECTRIC BEAM

For a bimorph beam with opposite polarization, the resultant stress of each layer is in opposite sign when an external electrical field is applied across its thickness. The resultant normal stresses introduce a moment with respect to the neutral axis. It is intended to use this action to control the beam. For a transversely vibrating beam, the Lame's parameters $A_1 = 1$ and $A_2 = 1$, $R_1 = R_2 = \infty$. Simplifying the shell equations of motions to a transversely vibrating beam with a uniform electrical field (electrode resistance is neglected), one can find the equation of motion:

$$YI \frac{\partial^4 u_3}{\partial x^4} + \rho h \frac{\partial^2 u_3}{\partial t^2} = 0 . \tag{6}$$

where Y is Young's modulus and I is the area moment of inertia. In order to control the structural adaptivity, a control system is required as illustrated in Figure 1. In this case, the electrical field is controlled using a displacement transducer – a proximeter – output located at the free end.
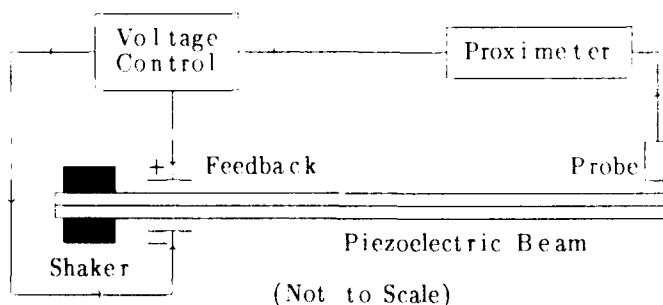
Fig.1 A control system for the piezoelectric adaptive beam.

The voltage supplied to the beam is proportional to the displacement at the free end, i.e., $V = G S u_3(x = L, t)$ where G is the control gain and S is the transducer sensitivity. The control moment can be defined as

$$M = \frac{bh e_{31} GS}{4} u_3(L,t) , \tag{7}$$

where b is the beam width. Thus, boundary conditions at the free–end of the

adaptive bimorph beam are defined as: 1) shear force $Q_{13} = 0$ and 2) moment $M = K$ $u_3(x=L, t)$, i.e.,

$$\frac{\partial^3 u_3}{\partial x^3} = 0 \ ; \tag{8}$$

$$\frac{\partial^2 u_3}{\partial x^2} = -\frac{K}{YI} u_3 \ ; \tag{9}$$

where $K = bhe_{31}GS/4$. Note that the boundary conditions at the clamped end are the same as any conventional cantilever beam. Substituting the boundary conditions into the equation and considering harmonic motion, one can derive a characteristic equation:

$$\cosh(\lambda L)\cos(\lambda L) + 1 = \frac{2K}{YI\lambda^2}\sinh(\lambda L)\sin(\lambda L) \ , \tag{10}$$

where $\lambda^2 = (\omega^2 \rho h/YI)^{1/2}$ and ω is the circular natural frequency. Solving this characteristic equation gives the natural frequencies of the adaptive bimorph beam. Note that eigen–solutions depend on K when material and geometry are specified, i.e., the solution is a function of feedback gains and the transducer sensitivity. Thus, the natural frequencies and mode shapes can be manipulated based on the feedback control systems, i.e., controlling the gain can vary the natural frequency of the beam, so that the system is adaptive and active control can be achieved.

For a beam with b = 10 mm, h = 1 mm, L = 100 mm, $Y = 4.704 \times 10^9$ N/m^2, $d_{31} = \frac{e_{31}}{Y} = 23 \times 10^{12}$ C/N, the first three natural frequencies are 23.9 Hz, 112.4 Hz, and 222.2 Hz. Change of natural frequency with different feedback gains was investigated. These calculations are summarized in Figures 2–3 for the first and the second natural frequencies, respectively. Note that each natural frequency is evaluated from negative to positive feedback.
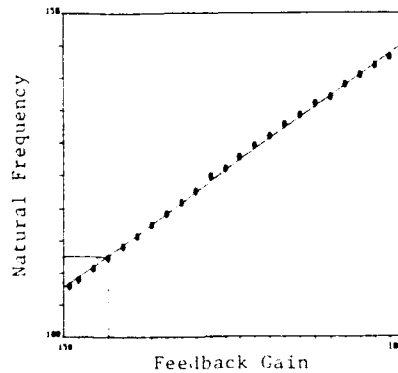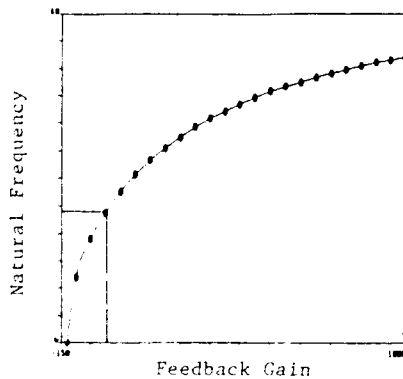
Fig.2 1st natural frequency control.   Fig.3 2nd natural frequency control.

It is observed that the two natural frequencies increase when the control gain increases. However, the influence to each mode is different. (Note that the results presented in Figure 2–3 are for a cantilever beam without tip mass.)

To validate the theory derived previously, a piezoelectric bimorph cantilever beam was design and tested in Dynamics and Systems Laboratory. White noise signal was input into a shaker which directly excites the beam. The displacement of free–end was picked up by a proximeter. This signal was amplified and then fed back into the piezoelectric beam. This model was only tested its first mode with gains from − 100 to + 100. Note that an eddy–current sensor was used for measuring displacement signal in the experiment, a metal mass (tip mass) was attached on the beam tip to introduce an eddy–current. Thus, this model is different from the above model which does not have a tip concentrated mass. The frequency spectrum of the structure was analyzed by a signal processing system. The finite difference (5–point) solution was also calculated to compare with the experiment results, Table 1.

Table 1 Comparison between theory and experiment.

Gain	−100	−50	0	50	100
Feedback Valtage (v)	−200	−100	0	100	200
Calculating Value (Hz)	8.53	10.48	12.39	14.25	16.04
Experiment Value (Hz)	9	11	13	15	17
Error	5.2%	4.7%	4.7%	5%	5.6%

The difference between the numerical solutions and experimental data is primarily introduced by the tip–mass location. In the finite difference model, the tip–mass was considered at the free–end. However, the mass is about 5% inside in the experimental model, which introduces higher natural frequency. Besides, the electrode stiffness was not considered in the theoretical model and the finite difference calculation. This could explain why the numerical solution is lower than the laboratory data.

4. SUMMARY AND CONCLUSIONS

Active structures with adaptive static/dynamic properties are of importance in modern high–performance structures. In this study, an adaptive piezoelectric structure is proposed, in which the structural adaptivity is contributed by the converse piezoelectric effect and is controlled by voltage injections. A generic theory of the active piezoelectric shell structure was proposed and the system dynamic equations were formulated using Hamilton's principle and the piezoelectricity theory. Assumptions, limitations, and applications of the theory were discussed. The generic theory can be simplified to account for many other common components, e.g., spheres, plates, cylinders, etc, using four system parameters: two Lame's parameters and two radii of curvatures. Natural frequencies of a an adaptive piezoelectric bimorph beam were manipulated by controlling the voltage injections to the piezoelectric bimorph beam. Analytical solutions were compared favorably with experimental results. In practice, some potential problems, such as breakdown voltage, electrode properties, etc., associated with the adaptive piezoelectric structures should be noted.

ACKNOWLEDGEMENT

REFERENCES

1.   E. F. Crawley and J. de Luis, 1987, *AIAA Journal,* Vol.25, No.10, pp.1373–1385. Use of piezoelectric actuators as elements of intelligent structures.

2.   J. L. Fanson and J.A. Gabra, 1988, AIAA Paper 88–2207, Experimental studies of active members in control of large space structures.

3.   H. S. Tzou, 1987, *Developments in Mechanics,* Vol.14–C, pp.1201– 1206. Active vibration control of flexible structures via converse piezoelectricity.

4.   H. S. Tzou and M. Gadre, 1989, *Journal of Sound and Vibration,* Vol.132, No.3, pp.433–450. Theoretical analysis of a multi–layered thin shell coupled with piezoelectric shell actuators for distributed vibration controls.

5.   H. S. Tzou, 1989, *Journal of Wave–Material Interaction,* Vol.(4), No.1–3, pp.11–29, 1990. Distributed sensing and controls of flexible plates and shells using distributed piezoelectric elements.

6.   H. S. Tzou, 1990, *Mechanical Systems and Signal Processing,* Vol.(5), No.(3), pp.215–231. May 1991. Distributed Vibration Control and Identification of Coupled Elastic/Piezoelectric Shells: Theory and Experiments.

7.   H. S. Tzou, 1989, *Journal of Robotic Systems,* Vol.(6), No.(6), pp.745–767, December 1989.   Integrated distributed sensing and active vibration suppression of flexible manipulators using distributed piezoelectrics.

8.   H. S. Tzou and M. Gadre, 1988, *AIAA Journal,* Vol.(26), No.8, 1014–1017. Active vibration isolation by piezoelectric polymer with variable feedback gain.

9.   H. S. Tzou and M. Gadre, 1990, *Journal of Sound and Vibration,* Vol.136, No.3, pp.477–490. Active vibration isolation and excitation by a piezoelectric slab with constant feedback gains.

10.   S. Hanagud and M.W. Obal, 1988 AIAA paper No.88–2418, Identification of dynamic coupling coefficients in a structure with piezoelectric sensors and actuators.

11.   J. M. Plump, J. E. Hubbard, and T. Baily, 1987, *J. Dynamic Systems, Measurement, and Control,* pp.133–139. Nonlinear control of a distributed system: simulation and experimental results.

12.   H. S. Tzou and C. I. Tseng, 1990, *Journal of Sound and Vibration,* Vol.(138), No.(1), pp.17–34. Distributed piezoelectric sensor/actuator design for dynamic measurement/control of distributed parameter systems: a finite element approach.

13.   Tzou, H.S. & Zhong, J.P., 1991, *Structural Vibration and Acoustics,* Edrs. Huang, Tzou, et al., ASME–DE–Vol.34., pp.7–15, 1991 ASME Design Technical Conference, Miami, FL, September 22–25, 1991. Theory on Hexagonal Symmetrical Piezoelectric Thick Shell Applied to Smart Structures.

(C/AdptShl–ADPA.PzShl3)

Nanometer level optical control on the JPL phase B testbed

John T. Spanos and Michael C. O'Neal
Jet Propulsion Laboratory, California Institute of Technology, Pasadena, CA 91101

Abstract. This paper describes experimental research currently in progress at the Jet Propulsion Laboratory aimed at developing and validating control concepts arising out of NASA's Control Structure Interaction program. The design methodology for optical pathlength control on a flexible structure is described and experimental results are presented.

1. Introduction

To meet the technical challenges of the next generation of space missions, the Jet Propulsion Laboratory (JPL) has developed a ground testbed facility, known as the Phase B Testbed, to validate new design methodologies developed by NASA's Control Structure Interaction (CSI) program. The Phase B Testbed is an eight-foot tall flexible truss structure equipped with an optical motion compensation system (Eldred and O'Neal 1991). The research described in this paper investigates the direct control of optical elements on the Phase B Testbed.

The optical elements on the Testbed represent a delay line for a stellar intereferometer. For the interferometer to perform its mission successfully, the variations in the length of the path traveled by light through the vibrating structure must be no larger than a few nanometers (Laskin and San Martin 1989). The pathlength control problem is emulated by the Testbed's optical motion compensation system which is encased in a flexure-mounted frame called "trolley." The trolley is firmly attached to one of the truss bays on the structure. A fine motion piezoelectric actuator (PZT) and a gross motion voice coil actuator (VC) provide high bandwidth optical pathlength control.

Previous experiments (O'Neal and Spanos 1991) were performed using an optical configuration that isolated the trolley from most structural motion, and the pathlength was effectively controlled to 10 nanometers RMS. The current configuration shown in Figure 1 couples structural motion directly into the pathlength. This paper describes the control system design and reports on the experimental results obtained with the new optical configuration.

2. Control System Design

The transfer functions for the two-input, one-output system were measured via band-limited white noise excitation, windowing and spectral averaging, a task facilitated with a Tektronix 2630 Fourier analyzer. The transfer function from PZT actuator to pathlength measurement sensor is not affected by the flexible dynamics of the Testbed partly due to the fact that the mass of the PZT mirror is sufficiently small and partly
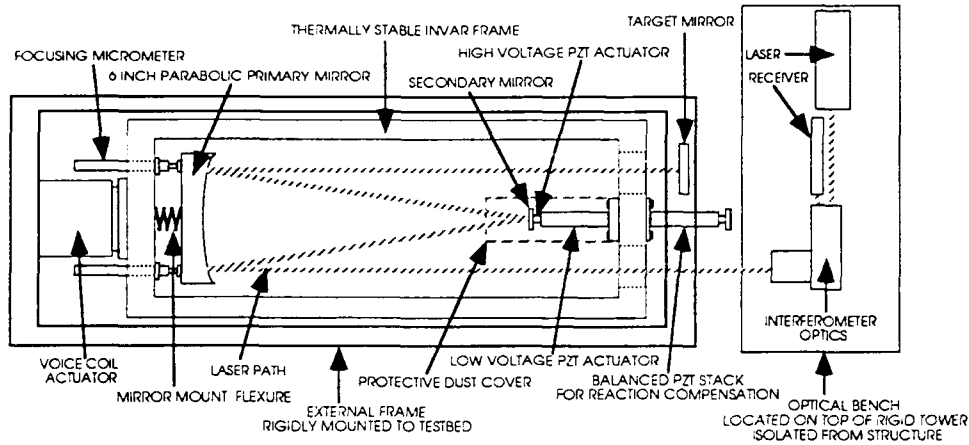
Figure 1. Optical elements on the Phase B Testbed

due to the presence of the balanced PZT stack used for reaction compensation. As a result, the pathlength/PZT transfer function was found to be unity over the frequency range 1-4000 Hz. On the other hand, the VC loop transfer function shown in Fig. 2 is impacted significantly by the effects of structural flexibility.

The dominant peak at 0.7 Hz represents the frequency of the trolley flexure mode. Other peaks in the magnitude of the VC loop transfer function correspond to higher frequency structural modes which are controllable by the VC actuator and observable by the laser pathlength measurement sensor. The important point to note here is that the low frequency pole-zero pairs are alternating which indicates that the corresponding modes will interact stably with the control system.

The design architecture of the two-input, one-output control system is illustrated in Figure 3. Classical methods (Bode 1945) were used to design the optical controller by shaping the gain of the open loop system in the frequency domain. It is important to point out that, unlike most modern control design methods (i.e., LQG, H$_\infty$, etc.), classical loop shaping methods do not require a parametric model of the plant (plant: system to be controlled). Generally, a non-parametric model as, for example, the measurement shown in Fig. 2 is sufficient for synthesizing a robust, high bandwidth controller.
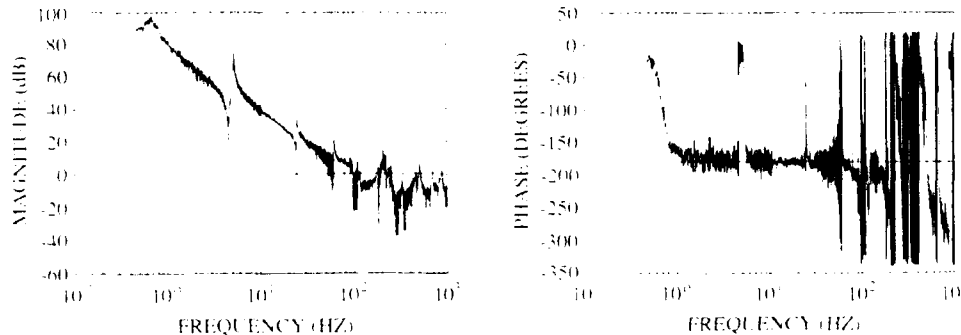
Figure 2. Voice coil transfer function
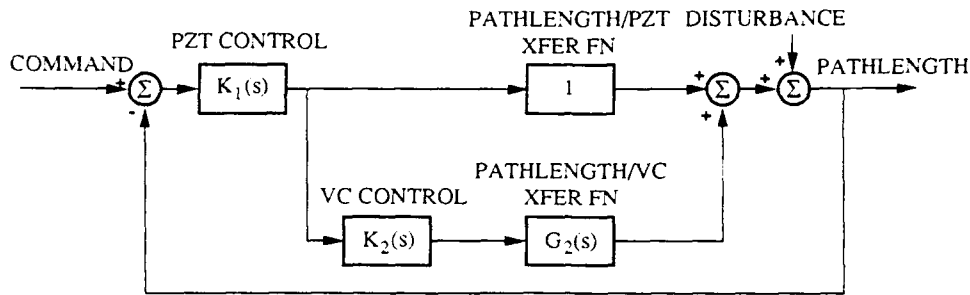
Figure 3. Control system architecture

The control architecture adopted herein follows that of Colavita *et al* (1991) in the sense that the output of the PZT compensator is used to drive both the PZT actuator and the VC compensator. In this arrangement the objective of the VC loop is to desaturate the limited stroke PZT actuator by keeping the control command to the PZT actuator near zero.

From the block diagram of Fig. 3 the transfer function of the open loop system is

$$L = K_1 (1 + K_2 G_2)$$ (1)

where. G_2 is the pathlength/VC transfer function. K_1 and K_2 are transfer functions representing the PZT and VC control laws respectively. We shall refer to $K_2 G_2$ as the VC loop gain. $K_1 G_1$ as the PZT loop gain, and L as the total loop gain of the system. Note that the PZT loop gain $K_1 G_1$ is identical to the PZT controller gain K_1 since $G_1 = 1$ over the frequency range of interest.

The control objective is to design each of the two compensators such that the closed loop system is stable, and the total loop gain. L, is as large as possible over the largest achievable bandwidth. Thus, the design requirements are placed in the frequency domain and specifically on the total loop gain. This is due to the fact that when $L \gg 1$, then $|L|$ is proportional to disturbance rejection. a key measure of the overall closed loop system performance. Three observations can be made directly from (1):

1. When $|K_2 G_2| \gg 1$. $|L| \approx |K_1 K_2 G_2|$
2. When $|K_2 G_2| \ll 1$. $|L| \approx |K_1|$
3. When $|K_2 G_2| = 1$. $|L| \approx \phi |K_1|$

where $\phi = angle(K_2 G_2) + \pi$ and $angle(K_2 G_2)$ is the phase angle (in radians) of $K_2 G_2$ at the frequency where $|K_2 G_2| = 1$. In Bode design terminology, the positive angle ϕ is the phase margin and the frequency at which it occurs is the loop gain crossover frequency. The third of these observations represents an approximation not as straightforward as the other two and valid only if the angle ϕ is sufficiently small (i.e., $\phi \leq 1$ *rad*). These observations imply that when the VC loop gain is large, the total loop gain is the product of the VC and PZT loop gains. As the VC loop gain tends to zero, the total loop gain approaches the gain of the PZT controller. At the VC loop

gain cross-over frequency the total loop gain is the product of the PZT gain and the phase margin associated with the VC loop.

With these observations in mind, the design of the control system was carried out one loop at a time. First, the VC controller was designed to stabilize the system assuming that (a) it is driven directly by the laser pathlength measurement (i.e., $K_1 = 1$), and (b) the PZT actuator is disconnected (i.e., $G_1 = 0$). Using frequency-domain loop shaping techniques (Bode 1945), a VC controller with transfer function

$$K_2(s) = (0.117) \underbrace{\left(\frac{s - 52}{s - 303} \right)}_{\text{LEAD}} \underbrace{\left(\frac{773.777}{s^2 - 352s + 773.777} \right)}_{\text{LOW PASS}}$$

was designed. The controller consists of (a) a first order lead filter providing phase at the gain cross-over frequency, (b) a second order low pass filter that attenuates the magnitude of the lightly damped, high frequency structural modes present in the VC transfer function. The low pass filter is essential in ensuring a stable control-structure interaction. The cross-over frequency of the VC loop gain was chosen to be 20 Hz. The phase margin at this frequency is in excess of 40 degrees which, in accordance with observation 3 above, implies that the total loop gain is expected to drop by about 4 dB in the neighborhood of the cross-over frequency (20 Hz). Similarly, a third order PZT controller was designed and its transfer function is given below:

$$K_1(s) = (3.137) \underbrace{\left(\frac{s - 378}{s} \right)}_{\text{LAG}} \underbrace{\left(\frac{s + 4.000}{s^2 + 440s + 394.784} \right)}_{\text{LOW PASS}}$$

The purpose of the first order lag is to increase the total loop gain at low frequencies. On the other hand, the purpose of the second order low pass filter is to allow steep roll-off of the PZT loop gain while still maintaining adequate phase margin for stability robustness. The bandwidth of the PZT was limited by high frequency noise, digital implementation time delays, and phase lag from the power amplifier. The Bode diagram of Fig. 4 summarizes the design by showing the total loop transfer function L as well as its high frequency approximation K_1. The effect of time delays due to computer implementation were taken into account. The frequency responses shown in Fig. 4 are clearly in agreement with the three aforementioned observations.
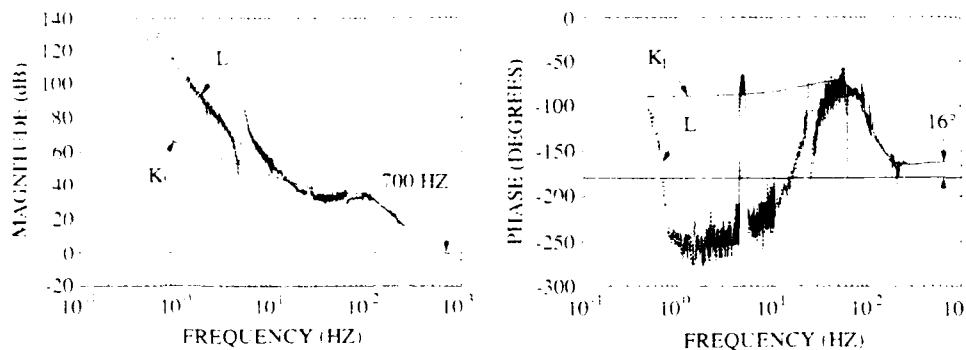
Figure 4. Bode plot of loop gain and phase

Both control laws were discretized using the bilinear transformation and prewarping was used to match them to their analog counterparts at their respective gain cross-over frequencies. The low bandwidth VC controller was implemented at 2.000 Hz and the high bandwidth PZT controller at 12.000 Hz. The phase lags associated with the sample-and-hold and control computation were modelled as pure time delays since the sampling frequencies of both controllers are much higher than their respective bandwidths. It is important to emphasize that the control design presented herein was developed by shaping the frequency response measurement directly and did not involve the use of analytical transfer function models.

3. Experimental Results

Figure 5 shows the performance achieved by the two-loop controller in view of the ambient laboratory disturbances. The closed loop variation in optical pathlength is approximately 15 nanometers RMS. Since the number of light reflections in our delay line exceeds that of a stellar interferometer by four, the equivalent optical pathlength error is 3.75 nanometers RMS. Spectral analysis of the closed loop time record has indicated that most of this error is due to noise occuring at frequencies beyond the control bandwidth (> 1.000 Hz).

Figure 6 shows a closed loop experiment where the disturbance is induced by a shaker attached to the structure. The disturbance profile is a sinusoid tuned to the frequency of the first truss mode at 5.5 Hz. During the first 5 seconds when the controller is off, the pathlength error is dominated by the 5.5 Hz sinusoidal disturbance. When the controller is turned on, the disturbance is attenuated by a factor of 5.000 which is in agreement with the loop gain of Fig. 4.
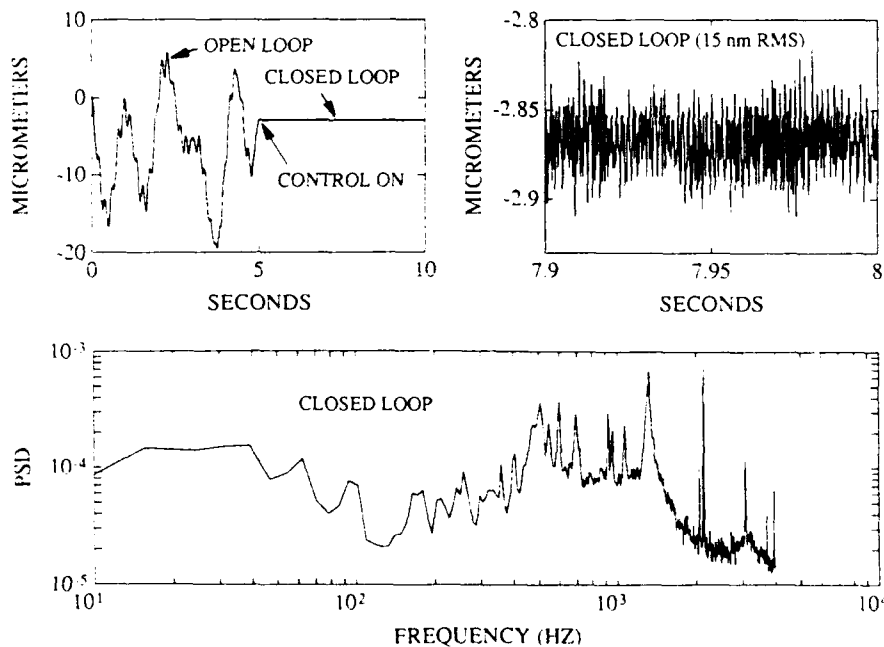
Figure 5. Experimental results with ambient laboratory disturbance
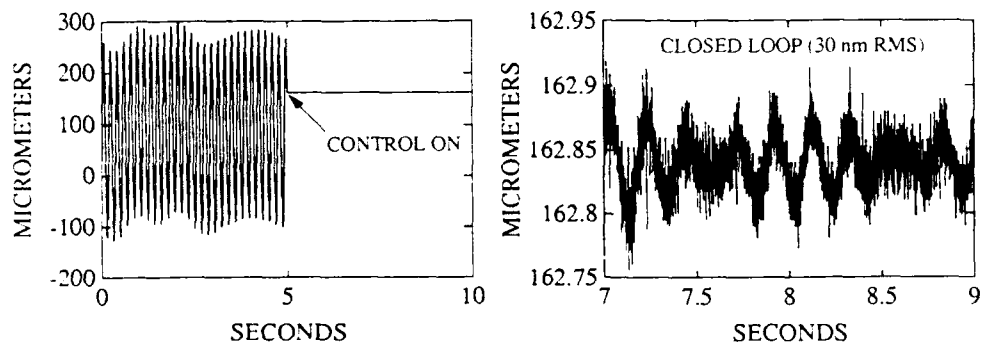
Figure 6. Experimental results with fundamental structural mode (5.5 Hz) excited

4. Conclusions and Future Work

The experimental results obtained thus far on the JPL Phase B Testbed indicate that nanometer level optical pathlength control is feasible in space. The control system design described herein involved shaping the measured plant transfer function in the frequency domain and did not require the identification and use of parametric models.

Future work on the Testbed will focus on reconfiguring the optical path in order to introduce a larger degree of coupling between the delay line controller and structural flexibility. Furthermore, other layers of control (passive/active damping, disturbance isolation, etc.) will be introduced as necessary to counter the stability and performance problems that are expected to degrade optical performance.

Acknowledgements

References

Bode H W 1945 Network Analysis and Feedback Amplifier Design (NY: Van Nostrand)

Colavita M M et al 1991 "Prototype High Speed Optical Delay Line for Stellar Interferometry" SPIE Intl Symposium on Optical Applied Science and Engineering

Laskin R A and San Martin A 1989 "Control/Structure System Design of a Spaceborne Optical Interferometer" AAS/AIAA Astrodynamics Specialist Conference

Eldred D B and O'Neal M C 1991 "The JPL Phase B Testbed Facility" ADPA Active Materials & Adaptive Structures Symposium & Exhibition

O'Neal M C and Spanos J T 1991 "Optical Pathlength Control in the Nanometer Regime on the JPL Phase B Interferometer Testbed" SPIE Intl Symposium on Optical Applied Science and Engineering

Microgravity isolation for spacecraft payload

M. Mercadal, [2] C.A. Blaurock, [3] A.H. von Flotow, [4] and N.M. Wereley [5]
Department of Aeronautics and Astronautics; Massachusetts Institute of Technology,
Rm 37-335; Cambridge, MA 02139

ABSTRACT: A laboratory prototype of a six axis microgravity isolation mount is presented, to provide a microgravity or micro-GEE ($9.81 \times 10^{-6} m/s^2$) vibration payload environment on board a milli-GEE ($9.81 \times 10^{-3} m/s^2$) spacecraft. The design can be adapted for NASA space shuttle or Space Station Freedom missions. The mount accomodates data, power, and cooling umbilicals of limited stiffness. Actuators are currently implemented using piezoelectric film.

1. MICROGRAVITY ISOLATION REQUIREMENTS

Mission specialist Bonnie Dunbar, on mission STS-32, measured acceleration levels above 10 mGEE ($9.81 \times 10^{-2} m/s^2$), especially when the crew members perform treadmill exercise. Figure 1 from [1] shows a typical vibration time history measured in the orbiter cabin. Preventive actions, such as shutting off unnecessary motors or restricting crew physical exercise, can reduce vibration during vibration sensitive experiments, but is impractical for extended periods.

Current NASA/ESA specifications consider harmonic disturbances only. More stringent requirements on the combined effects of broad-band GEE-jitter (crew motion, control thruster firings, sound etc.) and narrowband disturbances (antennae motion, rotating machinery, breathing etc.) need to be developed [2]. The single harmonic concept puts upperbounds on known narrowband disturbances and produces a curve of environmental disturbances as shown in Figure 2a [3]. The desired curve is Figure 2b, a combination of [4] and NASA specifications [2] from [3]. The two curves clearly emphasize the need for isolation.

2. MIT SIX AXIS ISOLATION MOUNT

The vibration isolation concept involves softly mounting an inner box to the shuttle, so that vibrations of an outer container are not transmitted to the inner box. A 2 cm gap is provided between the inner box and the outer box, following recommendations by [3]. A mount travel of 1 cm is accomodated before the mount "bottoms out" on rubber bumpers. This is four times greater than the travel implied by the transmissibility specification of Figure 2. A 1 cm sinusoid at 0.01 Hz produces 4 micro-GEE of acceleration.

The soft mounts are implemented using piezo-electric (PVDF) film. The film, in appropriate shape configurations, behaves like a soft spring to mechanically isolate the inner box from the outer box. Second, the film deforms when voltage is applied, and can be used as an actuator. Active feedback control is used to increase damping, and to further soften the mount. Combined

Figure 1: Shuttle middeck vibration time history during STS 32 flight
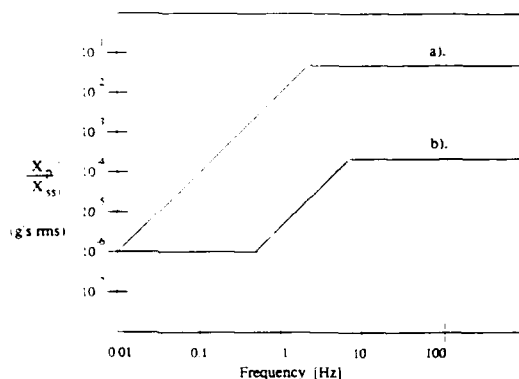
Figure 2: Single harmonic vibration requirements by Jones *et al*

active and passive action limits the need for active control; open loop performance of the mount is quite good, even though it falls short of the specifications in Figure 2.

Actuators were mounted so that three translations and three rotations of the inner box can be equally well controlled. Coupling between the six degrees of freedom is minimized to simplify control application. Each actuator is paired with an accelerometer. Decoupling the dynamics enables the entire system to be identified on the ground with partial tests only. This reduces the requirement for on-orbit identification. The control system can also be validated on the ground before launch.

From a survey of proposed microgravity experiments, flow of information, power, coolant, and vacuum must occur between the payload and spacecraft. Utility umbilicals will add stiffness to the system which is undesirable, so that umbilical stiffness should be minimized in order to achieve as soft a passive mount as possible, reducing the need for feedback control.

3. EXPERIMENTAL APPARATUS

The isolation system has been sized so that the isolated payload fits inside two standard NASA Space Shuttle middeck lockers. Wyle Laboratories [5], has developed the Universal Small Experiment Container (USEC) system shown in Figure 3, which fits inside two space shuttle mid-deck lockers and satisfies NASA safety standards for experiments flown on the shuttle. The USEC is proposed since microgravity payloads such as crystal growth or biological experiments require this degree of containment. The isolation system is part of the payload as far as the integration process is viewed by NASA.

The piezo-film actuators were modelled as a displacement source in series with a spring. The primary role of the actuators is to overpower the utility umbilicals and soften the mount. The payload box is nominally still, so that little control effort is used to overpower payload inertia. The utility umbilicals were lumped together and given a stiffness equivalent for all axes. Thus, the force on the actuator is the umbilical stiffness times the box relative motion. The derivation of actuator stiffness and free deflection is detailed in [6]. The actuators, as configured in Figure 4, actuate all six axes, and each kinematically actuates only one degree of translation and rotation. Rear actuators were doubled up to maintain equal control authority in the X axis. The actuators were nominally flat to maximize payload volume. The total mount stiffness measured was 5 N/m per axis. The mount was designed to handle an umbilical with 20 N/m stiffness. The design and fabrication of the actuators is detailed in [6].

The experiment focused on actuator validation, so that a mock-up of the locker and payload
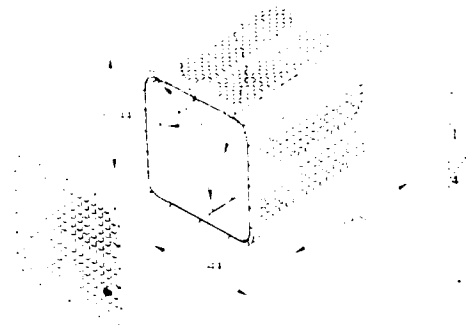
Figure 3: The Wyle Laboratories USEC containment box satisfies NASA's containment specifications for the shuttle middeck.
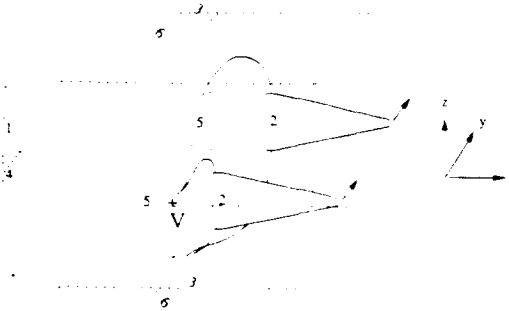
Figure 4: Actuators are configured such that two push at each location.
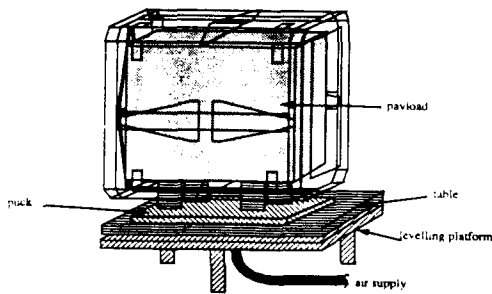
Figure 5: Experiment hardware.
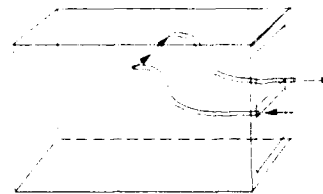
Figure 6: Placement of coolant umbilical.

was fabricated with representative dimensions and properties. During proof of concept, easy access to system components was required. As shown in Figure 5, the front panel was open to permit payload removal. Bumpers prevented damage to the actuators due to excessive payload motion. Actuator attachment locations were provided on all four longerons, and at the rear vertical bar. The actuator attachment hardware allowed nominal centering of payload. The payload rested on an air table with minimial damping, to permit free movement in the horizontal plane.

Actuator power was supplied by three Kepco BOP 1000M high voltage amplifiers, for which their maximum current output of 40 milliamps proved to be barely sufficient. Three shakers were used to excite the system, one for axial motion, and two at the side of the locker, to allow 2 translations, and rotation around the vertical axis. The shaker heads were connected to the core of an LVDT linear position sensor, so that transmissibility from locker motion to payload acceleration could be measured directly.

Sundstrand QA-1400 accelerometers were mounted on an adjustable platform that could be tilted to remove the accelerometer's DC bias by cancelling it with a component of gravity. Looped computer ribbon cable was used for the sensor umbilical. The modes of the experiment

with the ribbon cable in place were compared to the dynamics of the payload with accelerometer connections of very thin magnet wire. Utility umbilicals consisting of accelerometer cabling and a simulated coolant hose, sufficient for 1 KW of cooling with less than 50 degrees Celsius temperature increase, were implemented. The system ID places constraints on the umbilical locations, since some coupling terms in the stiffness matrix cannot be identified [6]. The umbilicals were attached symmetrically about the payload center of mass, as shown in Figure 6 to minimize unidentified coupling. Each coolant hose was looped, so that the hose was never stretched. The stiffness was found to be 8.2 N/m in the X direction, and negligible in the Y axis.

4. SYSTEM IDENTIFICATION

Ref. [6] details an analytical model of the system based on system geometry, its mass and inertia characteristics, the umbilical and actuator stiffnesses. This model is valid at low frequency (below about 10 Hz) where the control system exercises most of its authority.

Mechanical properties, such as mass, inertia, or stiffness, can be measured, or computed from detailed engineering drawings. However, system identification of the physical system should prove convenient information suitable control design. The six axis mount could be identified on-orbit. However, system ID would be time consuming due to low natural frequencies of the mount, with computational requirements far exceeding those for closed loop control. Thus, we propose six axis ground-based system ID, using three sets of three axis system identification tests. A single three axis test consists of resting one side of the inner box on an air table while suspending the outer box appropriately. This setup allows two translations and one rotation, and permits the identification of a projection of the unrestricted six degree of freedom motion. The accuracy and the validity of this strategy depends strongly on the decoupling of the dynamics. After the three 3-axis tests are performed, the identified stiffness matrix, K, is known except for those entries designed to be small, that is, identification cannot determine: helicoidal spring constants where a translation produces a torque in the same axis or torsional spring constants not aligned with one of the geometrical axes. Such springs have however been eliminated by design. Details of the 3-axis system identification is deferred to Appendix 1 of [6].

Single-input multi-output system ID of the three axis testbed was performed using a Tektronix 2630 Fourier analyzer, which computed transfer functions, and coherence functions. An ensemble average of 15 runs takes 39 min 45 sec. A weighted least mean square algorithm was used to determine a state space model [6]. The test was performed on the system equipped with two rubber hoses attached on the Y sides of the inner box to simulate the cooling apparatus. Excellent agreement is obtained for both magnitude and the phase. The resonant frequencies are at 0.124 Hz and 0.181 Hz for the Y and X translational modes (the umbilical separates the frequencies) and at 0.273 Hz for the rotational Z mode. Comparing with a second test performed without umbilical, the umbilical stiffness is estimated at 8.2 N/m, which is within design specifications.

Modal damping was identified to be between 1% and 6%. Also, the damping matrix, C, was not aligned with the stiffness matrix, so that modal decoupling was not completely effective. In Figure 7, the transfer function (magnitude only) of the decoupled plant is plotted. The off-diagonal elements of the transfer function matrix are substantially smaller than those on the main diagonal, but are not negligible.
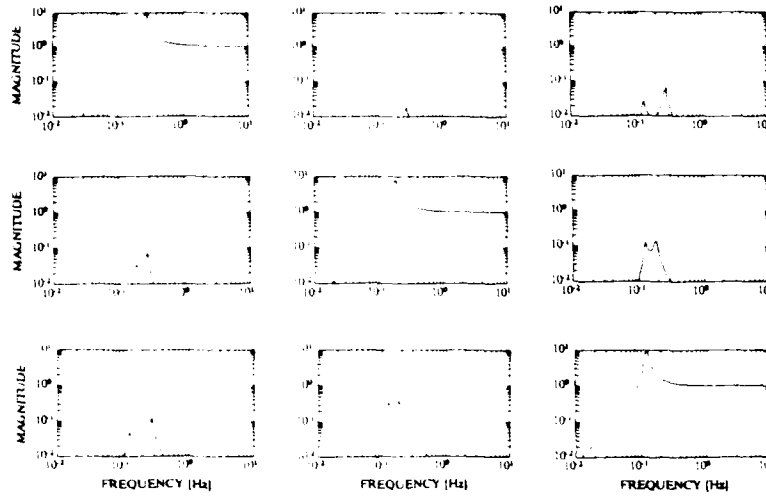
Figure 7: Decoupled identified transfer functions of the 3 axis test with umbilical: magnitude

5. CONTROL OBJECTIVES

The control objectives set by the NASA/ESA guidelines. [3], require the closed loop poles of the isolated payload to be at 0.05 Hz (curve a) or 0.01 Hz (curve b), with a damping ratio above 0.707. The control strategy is to combine sensor and actuator signals to modally decouple the system, and close a single input single output (SISO) control loop around each of the 6 decoupled modes. The advantage of the decoupling strategy over purely localized control between collocated sensors and actuators is that *spread in modal frequencies can be equalized* due to the spread in the stiffness matrix. With such a well-conditioned plant, however, six localized feedback loops are still possible, one for each (local) sensor/actuator pair. In order to drive the fastest mode to the required frequency, the localized scheme will require higher gains.

To reduce the natural frequency of the system, modal mass must be increased, or modal stiffness must be decreased. To improve modal damping and phase margins, velocity feedback was implemented. Acceleration feedback was selected for this application, over position feedback, because accelerometers were much less expensive than gap sensors of comparable sensitivity. Gap sensors can be easily accomodated in the current controller framework, and may be implemented in future work.

The design target will be to set the closed loop modal frequencies $\omega_{cl} = 0.01$ Hz (requirement a) or $\omega_{cl} = 0.05$ Hz (requirement b), with damping $\zeta_{cl} = 1$ to eliminate overshoot. However, phase losses from digital controller implementation and anti-aliasing filters will decrease closed loop damping.

The high-pass filter is a two-pole filter with corner frequency at 0.02 Hz. The corner frequency of the high pass filter was selected to prevent saturation of the actuators due to biases and bias drifts present in accelerometers and associated conditioning amplifiers. The filters ensure that modal mass is added only in the frequency range of interest. The high-pass filter adds phase lead and may reduce the amount of damping provided by the feedback loop, especially if the filter frequency is too high. The low-pass filter is a one-pole filter at 0.3 Hz followed by a two-pole filter at 10 Hz. The double pole filter at 10 Hz reduces high frequency accelerometer
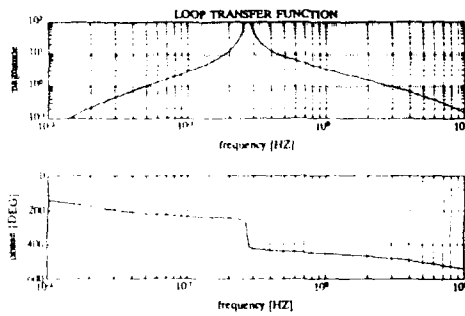
Figure 8: Loop transfer function of Z rotation mode, 0.2726 Hz. with filters
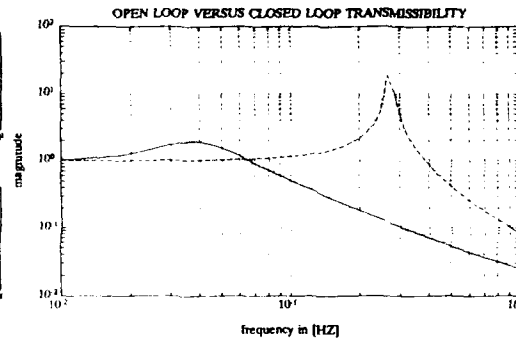
Figure 9: Open versus closed loop transmissibility of Z rotation mode

noise, and serves as anti-aliasing filters. In order to maintain stability, a one pole roll off is needed at cross over with enough phase lead to prevent instabilities. The corner frequency of 0.3 Hz was selected for that purpose.

The filters have a significant effect on the closed loop dynamics since their corner frequencies are close to the natural frequencies of the system, be it closed or open loop. The high-pass filter reduces the phase lag introduced by the integrator and will therefore reduce the amount of passive damping in the system. However, the 0.3 Hz low-pass filter adds some phase lag and compensates somewhat for the lead. The choice of the m_i and c_i must therefore be iterated until a satisfactory compromise is reached. The closed loop frequencies and damping will be very different from the prediction based only on the second oscillator model for the modes. The target for the closed loop is to set the modes at 0.04 Hz with as much damping as the wash-out filter can allow. The acceleration feedback gain, $m_{(\cdot)}$, and the velocity feedback gain $c_{(\cdot)}$, chosen in the experiment are: X Translation Mode, 0.1807 Hz. $m_x = 4$, $c_x = 4$; Y Translation Mode, 0.1236 Hz, $m_y = 2$, $c_y = 2$; Z Rotation Mode, 0.2726 Hz, $m_z = 10$, $c_z = 10$. The nominal closed loop poles are: Y translation, 0.0141 Hz, 35% damping; X translation, 0.042 Hz, 41% damping; Z rotation, 0.040 Hz, 40% damping.

The loop transfer function, the predicted closed loop versus open loop transmissibility and the sensor noise to acceleration spectrum is plotted for the stiffer Z rotation mode in Figures 8-9. These results are representative of all three modes.

6. CLOSED LOOP 3 AXIS GROUND EXPERIMENT

Control system was implemented part analog and part digital. Analog low-pass filters served the double purpose of attenuating the sensor noise and anti-aliasing. The control computer was an IBM Model PS/30 286. The accelerometer signals were sampled with an Analog Devices RTI-800 A/D converter. The control algorithm was implemented in Microsoft Quick C and ran at 18.2 Hz. The high pass filter was realized digitally due to its very low time constant. The digital control signal was passed to the Analog Devices RTI-802 D/A output. The D/A output to the current amplifier drove the piezo electric actuators.

First, we compare the open and closed loop transient responses. Figure 10 shows the three open loop accelerometer time traces recorded simultaneously for 40 seconds developed after a impulsive disturbance was applied (the experimenter blew on the inner box). The three
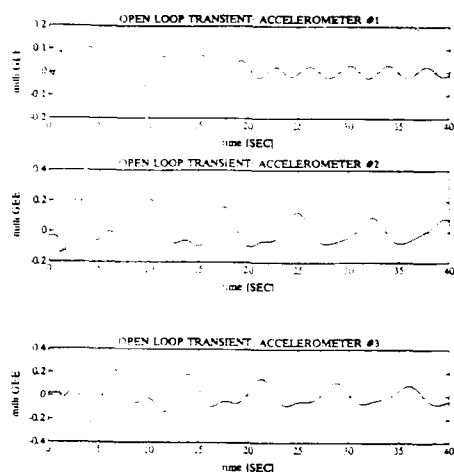
Figure 10: Open loop acceleration transient
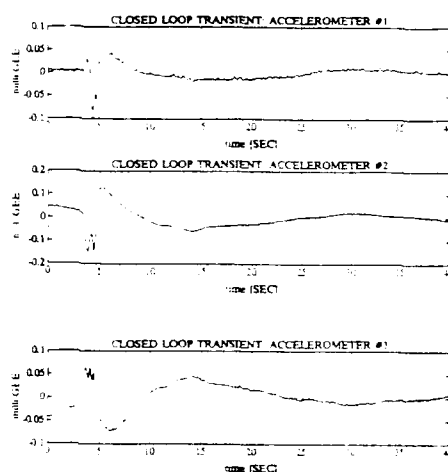
Figure 11: Closed loop acceleration transient

modes of the system are excited and damping levels are small. Figure 11 shows the three accelerometer time traces reocordered simultaneously for 40 seconds with active control. The impulsive disturbance was applied to a corner of the inner box designed to to excite all three modes. The time period of the oscillation is close to 25 seconds, or 0.04 Hz. The motion is also more strongly damped.

Experimental transmissibility curves were also obtained. A single shaker was used to excite all three modes, Z rotation, X and Y translations. Shaker motion was measured by a LVDT displacement sensor. The transmissibility, or the transfer function between accelerometer output and LVDT output, was obtained using the Textronix Fourier analyzer. Transfer function units are Accelerometer Volt / LVDT Volt. The DC gain is not equal to 1 as predicted by the analytical model. Figure 12 compares the open and closed loop transmissibility for accelerometer #3. Note that the open loop natural frequencies have shifted due to the umbilical stretching over time, thereby increasing stiffness. Damping has greatly increased, and the closed loop natural frequency has decreased. The maximum attenuation seen in the transmissibility is observed at 0.3 Hz on Figure 12 where the attenuation is greater than 36 dB, or reduced by a factor of 70.

7. SUMMARY

The six axis microgravity isolation mount prototype developed at MIT is a practical solution to isolating vibration sensitive payloads on board milliGEE spacecraft such as the NASA space shuttle or space station. The isolation system can be visualized as two boxes. The inner box, containing the payload, is mounted to an outer box the volume of two NASA Space Shuttle middeck lockers. The inner box is attached to the outer box via several soft springs made of piezo-electric film, and soft utility umbilicals. The passive mechanical isolation is then enhanced actively using the piezo-film actuators. The payload has provision for cooling, datalink and power through umbilicals of limited stiffness.
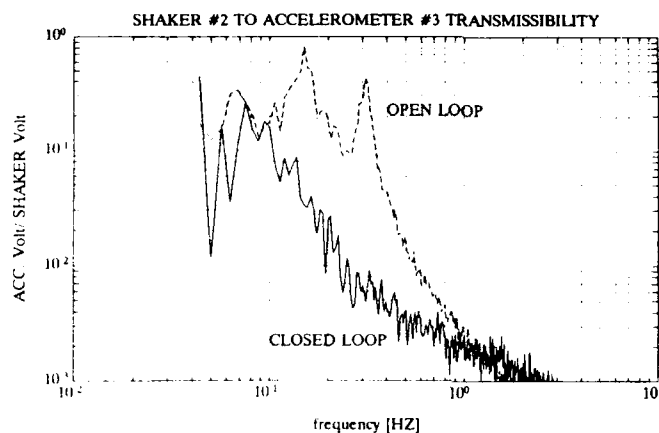
Figure 12: Comparison of experimental closed loop and open loop transmissibility between shaker no. 2 and accelerometer no. 3

The mount is designed to minimize interaxis coupling. Thus, ground-based system identification via three axis tests is sufficient to identify the six axis system, and provides enough information for control system design. The inertia and stiffness matrix are nominally diagonal and the location of the sensors and actuators makes modal control the natural approach. Active damping and mass are added to each mode via velocity and acceleration feedback, respectively, such that the compensator is essentially a lag compensator. The control philosophy has been validated by the test performed on the 3 axis identification testbed.

REFERENCES

[1] B. J. Dunbar, D. A. Thomas, and J. N. Schoess, "The microgravity environment of the space shuttle Columbia middeck during STS-32," Tech. Rep., NASA, 1991.

[2] E. S. Nelson, "An examination of anticipated g-jitter on space station and its effects on material processes," Tech. Rep., NASA, April 1991. NASA Technical Memorandum 103775.

[3] D. I. Jones, A. R. Owens, and R. G. Owen, "A microgravity isolation mount," *Acta Astronautica*, vol. 15, pp. 441–448, 1987.

[4] C. Tiby and D. Langbein, "Allowable g levels for microgravity payloads," Tech. Rep., Batelle Institute, Frankfort, 1985. ESTEC contract 5504/83.

[5] R. Giuntini, "Developing payload systems: there is a lot to it," Tech. Rep., WYLE Laboratories, 7800 Governors Drive, PO Box 07777, Huntsville, AL, 1991.

[6] M. Mercadal, C. Blaurock, A. H. von Flotow, and N. M. Wereley, "Laboratory prototype of a six axis microgravity ioslation mount," Tech. Rep., Dept. of Aeronautics and Astronautics, M.I.T., 1991. Final Technical Report submitted to McDonnell Douglas Space Systems Company.

The dial-a-strut controller for structural damping

B. J. Lurie, S. W. Sirlin, J. F. O'Brien, J. L. Fanson

Jet Propulsion Laboratory, California Institute of Technology, Pasadena, CA 91101

ABSTRACT: This paper presents experimental and computer simulation results on the application of a bridge feedback Dial-a-Strut controller applied to a piezo-electric active member of a truss structure. It explains why the control law is insensitive to the setting of control parameters and to plant parameter variations, and why SISO and MIMO systems built with these controllers are stable and robust.

1. INTRODUCTION

Piezoelectric active members with bridge feedback Dial-a-Strut controllers have been successfully employed for structural damping enhancement of a variety of flexible structures (Chen and Lurie 1989,1990, Lawrence 1990, Fanson 1990). The controllers were tuned in three simple steps:

1. The structure driving point impedance facing the active strut was determined. It can be done by calculation or experimentally using the sensors in the active member.

2. The desired active member impedance was calculated, by smoothing the structure driving point impedance. This desired impedance is then approximated by a function of the form $Ks(s + z_1)/(s + p_2)$.

3. The desired active member impedance was implemented by feeding back to the piezoelement the signals from the collocated force and velocity sensors in the proper ratio. This ratio is adjusted via dials on the controller's front panel that determine the values of two capacitors and a resistor.

Our experience is that with the above procedure, the control law parameter settings are not critical, and controller adjustment and test take no longer than a couple of hours (most frequently less than a half an hour). In fact, the design and test procedures turned out to be so simple that in most cases we left out a part of the control law design which is commonly considered indispensable: computer simulation. In the

following report, we make up for the previous omissions by comparing the experimental results with the performance of Pro-Matlab models, and discuss the robustness issues.

2. ROBUSTNESS OF IMPEDANCE MATCHING METHOD FOR VIBRATION ENERGY DISSIPATION

The impedance matching method of introducing structural damping is aimed at maximizing the vibration energy dissipated in the active member. The effect of matching can be seen in an analog electrical circuit Figure 1. Given the source impedance $Z_s = RS + jXS$ (the impedance of the structure facing the active member), the power dissipated in the load (in the active member) is maximized when the load impedance $Z_L = RL + jXL$ is the complex conjugate of the source impedance. This power $P_l = E^2/4RS$ where E stands for the for the electromotive force (which is the equivalent of the free velocity difference of the structure at the port if the mechanical impedance is defined as velocity/force).
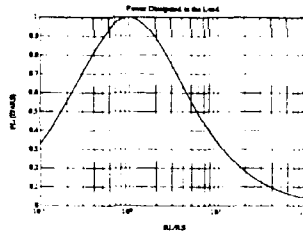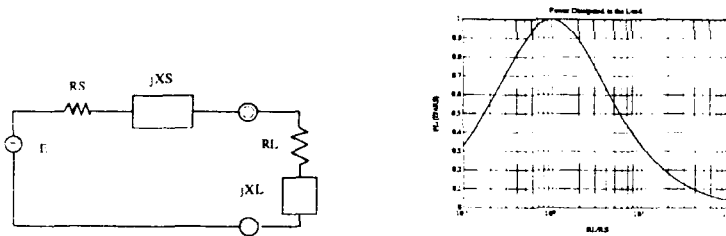
Figure 1. General electrical circuit.   Figure 2. Power dissipated in the load.

When the load impedance deviates from the optimum, the performance deteriorates gracefully. In particular, when $XS + XL \ll RS + RL$, the power dissipated in the load depends on RL as shown in Figure 2. For example, it requires +92% or -48% (a factor of 1.92) in load resistance deviation from the optimal to reduce the dissipated power by 10%. On the other hand, when $RS = RL$, presence of the reactive component of the contour impedance up to RL reduces the energy dissipation by less than 20%, which is often quite acceptable for vibration reduction. Thus the accuracy to calculate and implement ZL need not be better than 30%. This allows for control design without precise knowledge of the structure and results in insensitivity of the performance to plant parameter variations and control law parameter settings.

When the active member imitates a passive system (i.e. ZL is positive real), the requirement for the imaginary component of the contour impedance not to exceed the real component of the active member impedance cannot be satisfied over an arbitrarily wide frequency band. The bigger $|XS|$, the smaller is the bandwidth over which it can be adequately compensated by $|XL|$. This bandwidth can be calculated with Bode integrals (Bode 1945, Lurie 1986).

Although the described analogy may not seem applicable to lightly damped struc-

tures whose driving point impedances are nearly imaginary, the analogy is still valid when we use the notion of the structure's wave impedance, which can be viewed as the source impedance (Lurie 1990). When this impedance is matched by the load impedance, the structure is completely damped. Nonuniform structures can be approximated by uniform structures over finite frequency bands (Lurie 1990).

3. IMPLEMENTATION OF THE DESIRED ACTIVE MEMBER'S IMPEDANCE

Blackman's formula expresses the input impedance of a feedback system as

$$Z = Z_0 \frac{T(0) + 1}{T(\infty) + 1}, \tag{1}$$

given as a function of the system impedance without the feedback Z_0, the return ratio (loop transfer function) $T(0)$ in the case of the active member clamped (force feedback), and the return ratio $T(\infty)$ measured when the active member is free to expand (velocity feedback). When the both the force and velocity feedback are large (the case of large bridge feedback), the 1's in (1) can be neglected so that

$$Z \cong Z_0 \frac{T(0)}{T(\infty)}. \tag{2}$$

At lower frequencies where the feedback is large, the active member's impedance imitates that of a passive mechanical system and, therefore, a structure incorporating any number of the controllers remains passive and poses no instability danger. At higher frequencies, however, where the feedback reduces, the the angle of (1) might exceed ± 90 deg which will indicate that this function is not positive real and, therefore, there exists a passive load (and, particularly, a conservative load) which will cause oscillation (Lurie 1962).

4. STABILITY ISSUES

Figure 3 shows a feedback system with collocated force and velocity loops. In experiments, the velocity signal was obtained from an eddy current sensor whose displacement reading was processed in an analog link of the form $Ks/(s + p)$ to approximate the velocity over a bandwidth of up to $500Hz$.
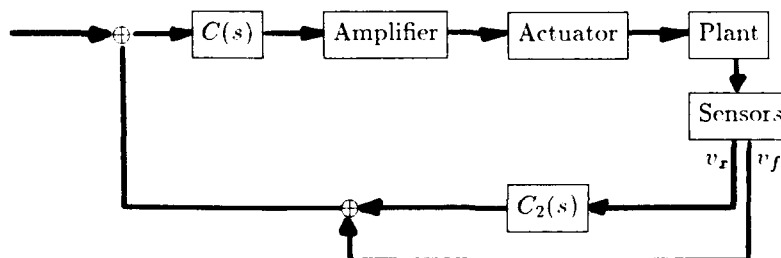
Figure 3. Dial-a-Strut system block diagram.

Without the feedback, the active member impedance (as the ratio of velocity over force) is $Z = s/k_a$ where k_a is the stiffness coefficient of the piezoelement, so that the impedance phase angle is 90 deg.

With the chosen compensator transfer function (Chen et al 1990)

$$C = K_c \left(\frac{1}{R_{c0}} + \sum_{j=1}^{7} \frac{C_{cj}s}{1 + C_{cj}R_{cj}s} \right)^{-1} .$$

(where K_c is an appropriate constant gain), setting the gain coefficients in the force and velocity loops (based upon the experiments described below), the transfer functions for the force and velocity loops are

$$T(0) = k_a \alpha_d h_A(s)C(s),$$

$$T(\infty) = -\alpha_d h_A(s)C(s)C_2(s),$$

which are plotted in Figure 4. The phase difference $\arg(T(0) + 1) - \arg(T(\infty) + 1)$, and the impedance phase angles $\arg(Z)$ and $\arg(Z_0)$ are plotted in Figure 5. Note that $|\arg(Z)| < 90$ deg over the entire frequency range. Since the impedance is positive real, the system is stable with any other additional positive real elements added. Therefore including such active members into the structure will not create a danger of oscillation, and will only help implementation of any global structural control (for example optical pathlength control for an interferometer). If however, the gain in the Dial-a-Strut loops is set too high, these conditions will not be preserved, and stability not guaranteed. Based on the simulation, the gain increase necessary is a factor of 779.
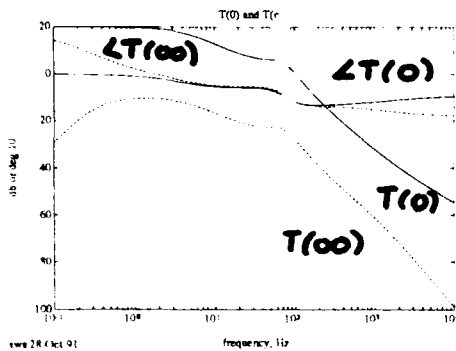
Figure 4. The return ratio T.   Figure 5. The impedance phase angle.
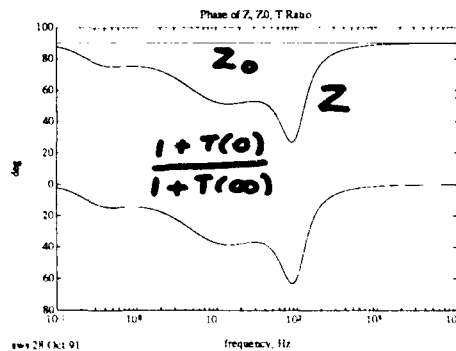
5. THE EXPERIMENTAL SET-UP

Two piezoelectric active members replaced two adjacent longeron elements in the base of the JPL Phase B structure (O'Neal et al 1991). The sensor measuring performance was an accelerometer in the direction of motion of the delay line (motion

in this direction will cause changes in optical pathlength). The first three resonances of the structure were the targeted modes for this experiment. The performance metric for the experiment is the transfer function from a force input due to a shaker (about halfway up the structure) to the accelerometer.

6. COMPUTER SIMULATION

The above system was modeled in Pro-Matlab, with analytical models of the Dial-a-Strut controller, amplififer, and piezoelectric transducer. In addition, experimentally determined open loop transfer functions were used to predict the closed loop performance. Shown in Figure 6 is the transfer function from shaker to accelerometer for the open loop case, and the case with two Dial-a-Strut. Both the predicted and the measured closed loop response are shown. All experimental data in the later plot have been smoothed.

7. EXPERIMENTAL RESULTS

Examining Figure 6, it is seen that the experimental results show a reduction in the amplitude of the first and third modes of 0.5 and 0.61 respectively, and elimination of the second mode completely. The computer simulation matches the third mode results, but misses the elimination of the second mode and the broadening of the first. The discrepancy between the experiment and the computer simulations are less than 5db except at low frequency (less than 5 Hz). In this region the experimental data itself is only good to 10 db. The exact source of the discrepancy has not been determined yet, but may be due to changes in the behavior of the amplifier under load.
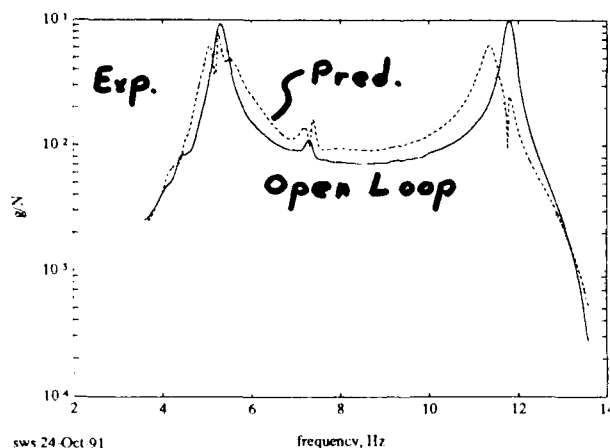
Figure 6. Experimental and predicted closed loop performance, two Dial-a-Strut.

8. CONCLUSIONS

The results of the experiments are in good agreement with computer simulation.

Therefore, in the future work, it is sufficient to obtain the data either way, depending on which is more convenient for particular plants.

The bridge feedback controller proved to be simple, robust, and efficient. A MIMO control system including several properly designed Dial-a-Strut controllers remains stable due to the positive real nature of the Dial-a-Strut impedance. The resulting Dial-a-Strut system can be used to complement a global controller (Neat et al).

9. ACKNOWLEDGEMENT

REFERENCES

Bode H W 1945 *Network Analysis and Feedback Amplifier Design*, (NY: Van Nostrand)

Chen G-S and Lurie B J 1989 "Bridge Feedback for Active Damping Augmentation" AIAA paper 90-1243

Chen G-S et al 1990 "Active Member Control for Vibration Suppression in Truss Structures" International Workshop on Intelligent Structures Taipei Taiwan

Fanson J L et al 1990 "Damping and Structural Control of the JPL Phase 0 Testbed Structure" ibid.

Lawrence C R et al 1990 "Active Member Vibration Control Experiment in KC-135 Reduced Gravity Experiment. First US/Japan Conference on Adaptive Structures" Maui Hawaii

Lurie B J 1962 "Synthesis of Active Two-Pole" Ph. D. Thesis Institute of Communications St. Petersburg

Lurie B J 1986 *Feedback Maximization*, (Deadham MA: Artech House)

Lurie B J 1990 "Active Damping of Flexible Structures" JPL Engineering Memorandum 342-1207

Neat G W et al "JPL - Langley Structure Control Experiment" to be reported

O'Neal M, Eldred D 1991 "The JPL Phase B Testbed Facility" ADPA Active Materials & Adaptive Structures Symposium & Exhibition

Concept verification of an electro-rheological torsional steering system damper

James R. Salois

General Motors Corporation Saginaw Division

ABSTRACT: This report investigates the use of an electro-rheological torsional damper in the steering system of an automobile. This damper would be attached to the lower steering shaft of the steering column and optimize the turning efforts perceived by the driver at all speeds.

1. INTRODUCTION

The steering system in an automobile provides directional control for the vehicle. It accomplishes this task by:

1) Providing a kinematic relationship between the steering wheel (hand wheel) and vehicular direction.

2) Controlled compliance between the components in the system.

3) Energy absorption from road inputs.

4) In the case of a power steering system, a boost mechanism.

In addition to the items above the steering system also provides a force feedback mechanism to the driver.

The major components in this system are shown in Figure 1 and interact in the following manner. The steering wheel provides an initial input to the system to alter the vehicular direction. This input is transmitted through the steering columns steering shaft through a linkage referred to as an intermediate shaft into the steering gear. The main function of the steering gear is to convert the rotary motion of the steering shaft into the lateral motion required to turn the vehicles' wheels. This lateral motion is transmitted through the tie rods which are attached to the steering arms. The steering arms provide a lever arm pivot perpendicular to the wheel. Thus they receive the

lateral motion from the steering gear and convert it back to a rotational motion that ultimately turns the wheels.

In a typical turning maneuver, the rotational input from the driver is converted to the lateral motion required to turn the wheels. Upon completion of the turn, the aligning forces between the tires and the road tend to realign the vehicle to a straight ahead position.

However, as the realigning forces work their way back through the steering system they get an additional boost from the rotational inertia generated from the steering wheel returning toward center. This tends to produce a very small oscillation from the straight-ahead position. This small oscillation, although not performance related, may affect driver pleasability.

FIGURE 1
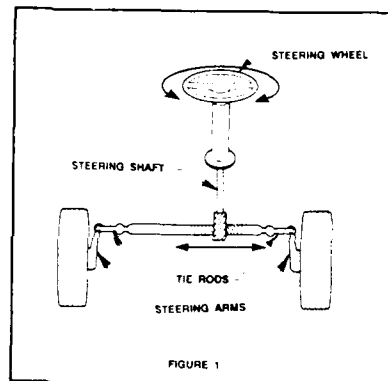
To minimize the effect of the rotational inertia of the steering wheel, the efficiency of the steering gear is slightly reduced. This corrects the small oscillations felt by the driver during higher speed maneuvers but, by reducing the overall efficiency of the steering system, adversely affects turning efforts at slower speeds.

During a slow speed maneuver, the driver must exert more effort to compensate for the reduced steering system efficiency. Herein lies the difficulty of tuning the steering system for low effort turning at low speeds yet minimizing oscillations from higher speed maneuvers.

Current technological devices such as viscous dampers and coulomb dampers do not produce the desired effect on the steering system. Viscous dampers, which depend largely on velocity, are ineffective at controlling the small, low velocity oscillations produced at the completion of a higher speed turn. They also negatively affect parking maneuvers when the steering wheel is typically turned at a higher rate of speed.

Coulomb dampers, which produce the desired effects on the higher speed turns, adversely affect parking maneuvers as they provide a near constant torque on the steering shaft requiring the driver to overcome this additional effort.

The device concepted here provides the variable damping required to optimize turning efforts at all speeds.

2. EXPERIMENTAL APPARATUS

The experimental hardware used to obtain the experimental results is shown in the accompanying schematic diagram. Figure 2. The components were designed to duplicate typical steering system values except for the added damping due to the friction in the bearings, damper seals, and the electrical slip ring contact.

The damper consists of a two piece aluminum outer housing (stator) rigidly attached to the electrically isolated support structure and an aluminum rotating disk (rotor) attached to the drive shaft. Each half of the housing contains a seal that insulates the drive shaft from the housing and also prevents the fluid from leaking out of the damper. The rotating disk is rigidly attached to the drive shaft and centered between the two halves of the housing with the clearance fixed at 1.5 millimeters.

The damping results from the shearing of the electro-rheological fluid between the rotating disk and the stationary housing. The fluid used in all of the tests was a mixture consisting of 35% corn starch and 65% silicone oil.
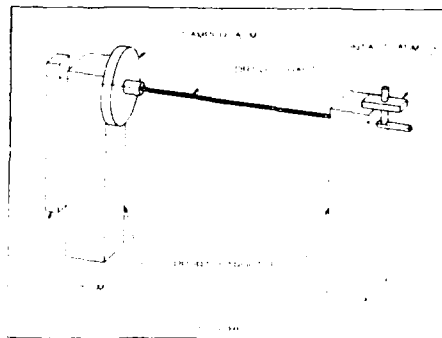
A nylon pendulum was constructed to simulate the rotational inertia generated by tne steering wheel and connected to the drive shaft near the damper.

The drive shaft was constructed as a three piece aluminum assembly. The

largest section was a 25.4 mm diameter rod which allowed for the mounting of the rotor and pendulum. A smaller 6.35 mm diameter section acted as a torsional spring. The final section of the shaft was a 12.5 mm diameter shaft that served as a contact ring. The shaft was supported at both of the larger ends by bearings in the electrically isolated support structure.

The electrical path required to activate the fluid consisted of a slip ring contact connected to the shaft which provided the voltage through the drive shaft to the rotor. The stator of the damper provided the return path to complete the circuit.

2.1 Testing

Two different types of tests were conducted on the damper assembly. The first was a dynamic test. This test consisted of applying an oscillatory input to the drive shaft and recording the resulting oscillations of the pendulum with various voltage increments applied to the damper.

The oscillatory input was produced through a frequency generator which was programmed to produce a sine wave of 9.5 Hz. This was then used as an input to a Bruel and Kjaer oscillator which was connected to the drive shaft through a linkage. The resulting pendulum oscillations were recorded with a Bruel and Kjaer laser motion detector and recorded on a Bruel & Kjaer frequency analyzer.

The procedure used to conduct this portion of the experiment consisted of applying the oscillatory input to the damper assembly, applying the appropriate voltage and recording the results. The voltages were applied at 400 volt increments with the voltage turned off, and the system allowed to return to its natural oscillatory response in between applications. The results of this portion of the experiment are shown in Figure 3.

The second test performed on the damper assembly was to measure the free response of the system. This portion of the experiment consisted of raising the pendulum 90 degrees, releasing the pendulum and recording

the subsequent oscillations. The angular response of the pendulum was measured by a rotational resistive element sensor attached to the drive shaft. This sensor uses a voltage input across a resistive element and outputs a voltage measured through the resistive element. The voltage change recorded by the sensor was used as the input to a Bruel & Kjaer frequency analyzer which recorded the oscillations.

The appropriate voltages were applied in 400 volt increments when the pendulum was raised to 90 degrees with the resulting system response shown in Figure 4.
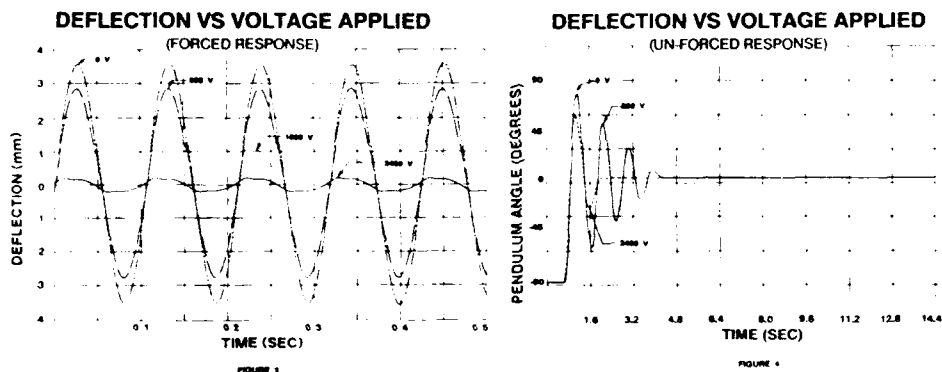
3. DISCUSSION

In the first portion of the experiment, the dynamic response, the system illustrated a high degree of damping was obtainable with this configuration. With as little as 400 volts applied the response began to show the damping imparted to the system. The higher voltages applied continued to illustrate the increared damping until 2800 volts where the damper absorbed the total input to the system. At this point the testing was suspended because there were no more oscillations to record. In the second portion of the experiment the free response of the system displayed a very underdamped response. This was expected since the only means of damping consisted of the friction of the bearings, seals, and electrical slip ring contact. The electro-rheological fluid in the damper also supplied a small amount of damping in the non-excited state but this was very small due to the low viscosity silicone oil that compromised the bulk of the fluid. The free response of the pendulum

with the application of 400 volts began to illustrate the damping effect. The peak oscillation and number of oscillations steadily decreased with the higher voltages until 2400 volts were applied and the test suspended. At this point the system showed the response curve of a slightly underdamped system. Using the method of logrithmic decrement this correlated to a fourfold increase in the damping factor of the system.

4. CONCLUDING REMARKS

The preliminary results illustrated above serves as a positive indicator that an electro-rheological damper could be successfully implemented into a steering system. The values recorded through the testing are appropriate for typical steering system damping requirements.

The damper used in this development was constructed of the simplest design and could be modified to provide greater damping at much lower voltages. Some suggested modifications that could be made include the basic modifications that also work on conventional viscous dampers. Increased shearing surface area and added roughness to both the stator and rotor will increase the damping produced. Further improvements may also be realized through the use of more sophisticated fluids.

A damper utilizing an electro-rheological fluid could be effectively implemented using only the vehicles speed as the controlling input to the voltage applied to the fluid. Thus, the voltage into the fluid could be increased linearly with the vehicles speed producing the desired turning efforts.

This does not imply that the speed would be the only input to the system. The almost instantaneous response of the electro-rheological fluid in the damper also serves itself well for use with a feedback algorithim that could dampen the steering during any turning maneuver. For example, when a turn has been executed a very predictable return of the steering wheel to center could be achieved by monitoring the vehicles speed, degree of turn just performed and adjusting the voltage to the damper correspondingly.

An innovative class of smart materials and structures incorporating hybrid actuator and sensing systems

M.V. Gandhi, B.S. Thompson, S.R. Kasiviswanathan,
S.B. Choi[1], B. Hansknecht[2], M. Soomar, X. Huang
Intelligent Materials and Structures Laboratory
C. Chmielewski
Department of Chemical Engineering
C. Foiles
Department of Physics
Michigan State University
East Lansing, MI 48824-1326

ABSTRACT

An innovative class of smart materials and structures incorporating *embedded hybrid multiple actuation systems* which capitalize on the diverse strengths of both electro-rheological (ER) fluids and piezoelectric materials, and operate in conjunction with fiber optic, and/or conventional sensing systems is proposed herein for the active continuum vibration control of structural and mechanical systems. By judicious selection, the smart-materials designer can synthesize numerous classes of hybrid actuation systems from a variety of actuator systems to satisfy a broad range of performance specifications that cannot be satisfied by deploying a single class of actuator systems alone. This work is focused on tailoring the elastodynamic characteristics of beam and plate-like structures, and a variety of mechanical systems in real time, therefore, the hybridization of ER fluids and piezoelectric actuator systems is proposed. This hybridization philosophy enables vibration-tailoring capabilities to be accomplished in real-time with minimal energy consumption and high reliability due to the inherent characteristics of ER fluids and piezoelectric materials.

1. INTRODUCTION

The insatiable demand in the international marketplace for high-performance structural and mechanical systems for the aerospace, defense, and advanced manufacturing industries has triggered the evolution of advanced composite materials [1]. These diverse high-performance applications have mandated that designers tailor both the materials and the material microstructural characteristics in order to ensure optimal performance of mechanical and structural systems. Designers have responded to these challenges by developing optimal design methodologies for a broad class of composite materials. Typically, these methodologies have been employed to optimally select the individual constituents, their micromechanical characteristics, and the spatial distribution of these constituents in order to synthesize a viable structure or subsystem with the desired mass, stiffness, and damping properties, for example [2-4]. However, these optimization strategies for traditional advanced composite materials yield an optimal design which is passive in nature.

The almost instantaneous response-time of the ER fluids, and piezoelectric materials, and the inherent ability of these materials to interface with solid-state electronics and modern control systems provides designers, for the first-time, with a unique capability to synthesize ultra-advanced smart composite structures whose continuum elastodynamic response characteristics can be actively controlled in real-time.

---

[1]currently at Korea Institute of Machinery and Metals

[2]currently at Ford Motor Company, Plastic and Trim Products   Division

Small and moderate changes in the geometrical characteristics can be accomplished in real-time by employing piezoelectric materials in order to substantially improve the performance of structures, for example.

Some of the recent developments in these aspects of smart materials are presented in [5-15]. The principal research activities presented in this paper on an innovative class of smart materials and structures are mainly focused on electro-rheological fluids, piezoelectric materials and fiber optic sensors. Various methodologies for synthesizing smart structures are based on integrating these smart actuator materials in a structural context to create a smart structure which is capable of changing its characteristics in a controlled manner. All of these methodologies have distinct strengths and weaknesses and distinct domains of applicability. It is expected that ultimately these various technologies will need to be integrated in a coherent manner in order to develop smart structural systems that would meet the diverse stringent high-performance requirements of future systems.

This paper is focused on the development of a new generation of self-adapting mechanical and structural systems featuring multifunctional smart actuation and sensing capabilities. It is anticipated that the hybridization philosophy proposed herein for vibration-tailoring capabilities will result in a viable comprehensive knowledge-base, which will catalyze the evolution of a new generation of truly autonomous smart materials and structures. This knowledge-base will be crucial in exploiting the unique capability of smart materials to interface with modern solid-state electronics by the successful incorporation of intelligent sensor technologies and modern control strategies.

2. SMART MATERIAL AND STRUCTURAL SYSTEMS

Smart materials and structures are innovative class of materials and structures which have self-inspection and inherent adaptive capabilities. Typically, the ingredients of a smart structure are a host structural material, a network of sensors, a network of actuators, microprocessor-based computational capabilities, and real-time control capabilities. Furthermore, these smart structures must demonstrate the following characteristics:

(i) The ability to respond almost instantaneously to changes in external stimuli

(ii) They must feature an inherent ability to interface with modern microprocessors and solid-state electronics

(iii) They should possess the inherent ability to integrate modern control systems.

In this novel class of materials and structures, the network of actuators provides the muscles to make things happen; the network of sensors provides the nervous system to monitor and communicate the external stimuli; the structural material provides the skeleton; and the microprocessor-based computational capabilities provide the brains which process the data provided by the nervous system prior to ensuring the optimal performance of the overall system. Smart materials and structures exploit the muscular characteristics offered by electro-rheological fluids, and piezoelectric materials, for example.

Some of the most promising dynamically-tunable actuator technologies are electro-rheological fluids, and piezoelectric materials. These actuator systems have diverse characteristics, with distinct advantages and disadvantages. Electro-rheological fluids enable the stiffness and damping characteristics and hence the natural frequencies of a smart structure to be dramatically changed in milliseconds by actively changing the electrical field imposed on the ER fluid domains. Piezoelectric actuators permit controlled voltages to generate axial forces or bending moments on a structure depending upon their electrical configuration which permit the structure to develop moderate changes in geometry.

Hybrid smart material and structural systems feature embedded hybrid multi-functional actuation systems which capitalize on the diverse strengths of electro-rheological fluids, piezoelectric materials, and which operate in conjunction with fiber optic sensing systems. This paper presents experimental investigations which clearly demonstrate, the ability to dramatically change the vibrational characteristics of mechanical systems fabricated in smart composites featuring ER fluids, piezoelectric materials, by controlling the external stimuli imposed upon them. This work has provided tools for the design of a variety of prototype laboratory platforms including robotic systems, linkage mechanisms.

3.   SMART STRUCTURES FEATURING ER FLUIDS AND PIEZOELECTRIC MATERIALS: EXPERIMENTAL INVESTIGATION

In this section a summary of experimental investigations on smart structures incorporating ER fluids

and piezoelectric actuator systems is proposed in conjuction with fiber optic and/or conventional sensing systems. Experimental results on characterizing the constitutive characteristics of hydrous and anhydrous electrorheological fluids were obtained by employing a Rheometrics RMS 800 mechanical spectrometer which had been upgraded with a high-voltage attachment which could impose a potential difference of 5000 volts across the double-walled couette test fixture containing the ER fluid sample under examination retrofitted in order to impose a variety of electrical fields on ER fluid specimens.

Typical result from this investigation is presented in Figure 1. Figure 1 shows the log-log graphical presentation of experimentally determined stress versus shear rate characteristics measured at different voltages for a hydrous ER fluid comprising of 45 percent corn starch and 55 percent silicon oil by weight. The Bingham-body model, featuring a linear relationship between the shear rate and the shear stress is clearly demonstrated in this figure. Furthermore, the increase in the static stress as a function of increasing voltage is also evident from this figure.

The investigations on characterizing ER fluids and piezoelectric materials were instrumental in the development of smart structural systems featuring composite and monolithic materials with embedded ER fluids and surface bonded piezoelectric actuator elements. Subsequently experimental investigations on the free and forced vibration characteristics of beams and plates featuring ER fluids and piezoelectric materials were undertaken. Figures 2 through 6 present some of the results obtained from these experimental investigations.

In Figure 2 a set of experimental results is presented for a smart beam with an embedded ER fluid actuator subjected to a number of discrete voltages with field intensities varying from 0 kV/mm of fluid thickness to 2.09 kV/mm. This data emphasizes and illustrates the ability to tailor the dynamic behavior of this class of smart structural materials by controlling the natural frequencies and energy-dissipation characteristics. Figures 3 and 4 show the transient responses of a smart beam featuring piezoelectric actuator with zero voltage and finite voltage, respectively. Figures 6 and 7 show the results obtained from a composite plate with embedded ER fluids.

Figure 5 shows the response of the plate under forced excitation at its first natural frequency (15.5Hz) with the ER fluid activated at different voltages. It is evident from the figure that the amplitude of the vibration is a function of the applied voltage. At 2kV/mm the amplitude of the vibration becomes almost equal to the amplitude of the excitation imparted by the shaker with the resonating response becoming almost negligible.

Figure 6 shows the frequency response of the same ER plate with and without ER fluid activation in the frequency range 0-100Hz. It is again clear from the figure that with the application of electric field (2kV/mm), the stiffness characteristics of the plate can be drastically changed. It can be observed that the natural frequencies of the plate in these two cases are totally different from one another clearly demonstrating their dependence on the applied electric field.

Control strategies and methodologies have also been developed to actively control the elastodynamic response of these structures in an autonomous manner. Fiber-optic and/or conventional sensors have been employed in implementing these control strategies. Investigations have also been undertaken to control the elastodynamic response characteristics of structural systems which exhibit a chaotic behavior. Typical waterfall plots from these investigations are shown in Figure 7, which presents a time-frequency amplitude plot of the beam demonstrating how a chaotic regime ensues when the initial voltage state of 1 kV imposed upon the beam is subsequently reduced to 0 kV. It is evident from the experimental data that upon removing the electrical potential from the ER fluid domain, the somewhat deterministic response is overwhelmed by a chaotic regime with no distinct repetition characteristics. This somewhat preliminary study clearly suggests that the chaotic behavior of certain classes of structures deployed in engineering practice could conceivably be alleviated by fabricating these structures in smart materials.

The above work on developing smart materials featuring ER fluids and piezoelectric materials has been extended to the development of smart mechanisms and also robotic systems. The objective of these investigations was to actively control the elastodynamic response of these complex mechanical members. Figure 8 shows typical results of investigations focused on the control of a single-link robotic system featuring an embedded ER fluid. This figure presents the measured step responses to a commanded step angular position of 7.2 degrees with the compensator zero $Z_c = -2$. Feedback gains of $K_p = 0.5$ and $K_v = 0.25$

were employed. The external input voltage of 2.0 kV/mm and 0 kV/mm were continuously imposed on the ER fluid domain throughout the two manoeuvers. It is clear from the figure that the response characteristics of the robot arm with and without the voltage imposed on the ER fluid domain are dependent upon the magnitude of this voltage. The amplitude of the tip deflection of the robot arm in the absence of the electric field was reduced by approximately 35 perce..t when the input voltage of 2.0 kV/mm was imposed on the ER fluid actuator. It is also observed from this response that the settling-time is approximately 1.3 seconds when a voltage is imposed on the ER fluid domain, while it is approximately 1.6 seconds when an external voltage is not imposed on the ER fluid embedded within the robot arm. Thus the elastodynamic performance of the robotic system can be greatly enhanced by carefully orchestrating the input signal to the electrical motor and also electrical signal to the ER actuator embedded within the robot arm.

Investigations of linkage mechanisms have also been undertaken and Figure 9 presents the elastodynamic response characteristics of the midspan of a flexible connecting rod of a slider crank mechanism when operating at 95 rpm. It is evident from the experimental results that the amplitude and frequency of the elastodynamic response of the articulating member, which is being subjected to both parametric and forced excitations, can be controlled by adjusting the external voltage imposed upon the ER fluid domain within the smart structural member. The behavior of the link is clearly a function of the applied voltage.

Figure 10 shows the preliminary results of the investigations focused on the hybridization of ER fluids and piezoelectric actuators which operate in conjunction with fiber optic and/or conventional sensing systems.

4. CONCLUSIONS

An innovative class of smart materials and structures incorporating *embedded hybrid multiple actuation systems* which capitalize on the diverse strengths of both electro-rheological fluids and piezoelectric materials has been proposed. The experimental results obtained for beams and plates incorporating ER fluids, piezoelectric materials and fiber optic sensing systems show the viability of this class of materials for the active continuum vibration control of structural and mechanical systems. By exploiting their capability to be interfaced with modern solid-state electronics, this class of smart materials could provide the basis for the evolution of a new generation of truly autonomous smart materials and structures.

REFERENCES

[1]   Gandhi, M.V., and Thompson, B.S., (1991), *Smart Materials and Structures*, (Chapman and Hall: London) U.K.(in press).

[2]   Gandhi, M.V., Thompson, B.S., and Fischer, F., (1990), *Composites Manufacturing*, 1, pp. 32-40.

[3]   Gandhi, M.V., Thompson, B.S., and Choi, S.B., (1989), *Journal of Sound and Vibration*, 135, pp. 511-515.

[4]   Huang, X., Thompson, B.S., Gandhi, M.V., and Choi, S.B, (1991), to be presented at the *2nd National Mechanisms Conference*, Cincinnati, Ohio.

[5]   Winslow, W.M., (1949), *Journal of Applied Physics*, 20, pp. 1137-1140.

[6]   Stangroom, J.E., (1983), *Journal of Physics Technology*, 14, pp. 290-296.

[7]   Batchellor, C.R., Dakin, J.P. and Peace, D.A.J., (1987), *International Journal of Optic Sensors*, 2, pp. 407-411.

[8]   Choi, S.B., (1990), Ph.D. Thesis, Department of Mechanical Engineering, Michigan State University, East Lansing, MI, USA.

[9]   Block, H., and Kelly, J.P., (1988), *Journal of Physics D; Applied Physics*, **21**, pp. 1661-1677.

[10]   Claus, R.O., McKeeman, J.C., May, R.J., and Bennet, K.D., (1988), *U.S. Army Research Office Workshop on Smart Materials, Structures, and Mathematical Issues*, Blacksburg, Virginia.

[11]   Bailey, T. and Hubbard Jr. J.E., (1985), *AIAA Journal of Guidance and Control*, **8**, pp. 605-611.

[12]   Crawley, E.F., and de Luis, J., (1987), *AIAA Journal*, **25**, pp. 1373-1385.

[13]   Plump, J.M., Hubbard Jr., J.E., and Baily, (1987), *AIAA Journal of Dynamic Systems, Measurement and Control*, **109**, pp. 133-139.

[14]   Tzou, H.S., and Gadre, M., (1989), *Journal of Sound and Vibration*, **132**, pp. 433-450.

[15]   Gandhi, M.V.,Thompson, B.S. and Choi, S.B., (1989), *Journal of Composite Materials*, **3**, pp. 1232-1255.
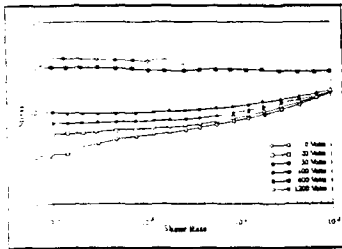
Figure 1   Stress versus Shear-rate Characteristics Measured at Different Voltages for a Hydrous ER Fluid

Figure 2   Frequency Response of a Smart Cantilevered Beam Subjected to Discrete Voltage States
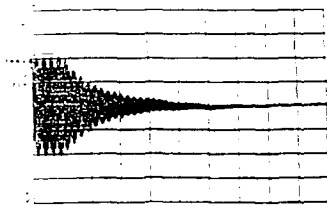
Figure 3   Transient Response of a Smart Beam Featuring Piezoelectric Actuator: Zero Volts.

Figure 4   Transient Response of a Smart Beam Featuring Piezoelectric Actuator with Finite Voltage.

Figure 5   Plate Response at Different Voltages With Excitation at 25.5 Hz
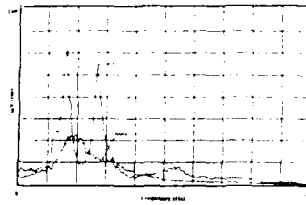
Figure 6   Frequency Response of the Plate With and Without ER Fluid Activation
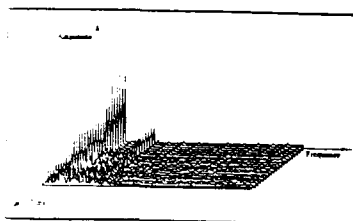
Figure 7   Waterfall Plot of the Elastodynamic Response of a Double Enclette Beam Subjected to Dynamical Excitation
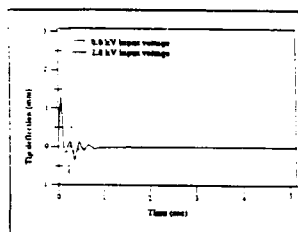
Figure 8   Measured Step Response with Feedback Gains of $K_y = 0.5$ and $K_c = 0.25$
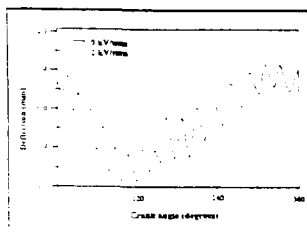
Figure 9   Transverse Deflections of the Tunable Connecting Rod Operating Speed 45 rpm
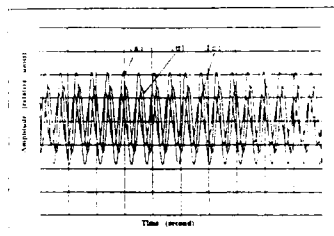
Figure 10   Vibration Reduction in Hybrid Beams (a) Without ER fluid and piezo film actuated (b) With ER fluid actuation (c) With ER fluid and piezo film actuators

Design of anhydrous electrorheological (ER) suspensions and mechanism study

Wei-Ching Yu, Rex C. Kanu and Montgomery T. Shaw

Institute of Materials Science, The University of Connecticut, Storrs, CT 06269-3136

ABSTRACT: Particle polarization in ER fluids was approached in terms of models for Maxwell-type composites. Anhydrous ER systems based on semiconducting polymers were designed to demonstrate the role of conductivity to the ER performance, an outcome of the composite analysis. A dielectro-rheological technique was developed to characterize the dielectric response and ER performance under high fields simultaneously. The results demonstrate the appropriateness of the chain theory.

INTRODUCTION

Electrorheological (ER) fluids are suspensions of highly polarizable fine particles dispersed in an insulating oil. The attractive features of the fluids for practical application are the speed and reversibility of the liquid-to-solid and solid-to-liquid transition when an electric field is turned on and off. With these characteristics, ER fluids will change the fundamental design of hydraulic systems and devices; they make possible the instantaneous control of such devices by computer. However, the many conceivable applications of ER technology have yet to be realized because the performance of available fluids is deficient. The disadvantages of available water-activated ER fluids include corrosion to the devices and a narrow temperature range over which they operate properly. Anhydrous systems have been reported but are not highly developed. Until recently, alumino-silicate (Filisko and Radzilowski 1990) and poly(acene quinone) (Block et al 1990, 1988) were the principal candidates. However, the mechanism of the alumino-silicate system is not clear, while the poly(acene quinone) suffers from a high current density. Clearly designing an efficient fluid requires a full understanding of the ER mechanism.

In this study, our efforts were directed toward (1) understanding the electronic polarization in particles, (2) designing anhydrous ER suspensions, and (3) developing a dielectro-rheological technique for characterizing the dielectric response of the fluid under high electric fields and in the presence of shear.

POLARIZATION IN PARTICLES

Particle polarization in ER suspensions can be understood qualitatively in terms of the relationships developed for Maxwell-type composites. The particles in the ER suspensions are randomly distributed and chained before and after application of an external field, respectively, while those in the Maxwell-type composites are randomly distributed. Using

an analysis for Maxwell-type composites (Banhegyi 1990), we found that the role of particle conductivity is crucial to the particle polarization. The maximum local polarization is also influenced by such particle parameters as geometry, anisotropy and orientation. For an ellipsoidal particle, the long axis aligned with the external field gives greater particle polarization than the short axis. The polarization of a spherical particle lies between the two cases. More complicated is the analysis when particle anisotropy is combined with orientation at an arbitrary angle to the external field. We developed a two-component model to simplify the case (Figure 1). The maximum polarization increases with decreasing angle of the long axis to the external field. The anisotropy in conductivity and dielectric property is important in the environment field. Particle conductivity is again the key parameter for determining the speed and magnitude of the polarization.

Figure 1 A two-component model for the dielectric properties of a Maxwell-type suspension.

poly(p-phenylene-2,6-benzobisthiazole)

poly(pyridinium salt)
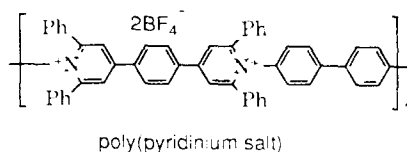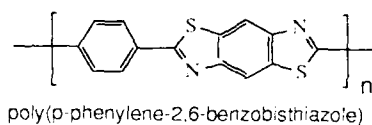
Figure 2 Chemical structures of poly(pyridinium salt) and poly(p-phenylene-2,6-benzobisthiazole) (PBZT).

DESIGN OF ANHYDROUS ER FLUIDS

From these findings, we designed anhydrous ER suspensions based on semiconducting materials, I_2-doped poly(pyridinium salt) and poly(p-phenylene-2,6-benzobis-thiazole) (PBZT) (Figure 2). The I_2-doped particles were further processed to form an insulating skin, which reduces interparticle conduction (Figure 3). The designed anhydrous suspension showed a strong ER effect (Figure 4) and low current density (Figure 5), demonstrating the importance of conductivity and the insulating skin. PBZT, a robust liquid crystalline polymer featuring a highly aromatic, ladder-like structure is also being studied as the dispersed phase. Rheological measurements have revealed that PBZT is a good candidate for the dispersed phase of an ER fluid. In steady shear measurements for 10 v% of PBZT particles in mineral oil, the shear stress increased by 40% for an electric field of 4 kV/mm. The dynamic elastic modulus G' for the fluid comprising 20 v% of PBZT particles in silicone oil showed a positive dependency on electric

undoped I_2-doped I_2-doped and insulating skin

Figure 3 Structures of poly(pyridinium salt) particles.
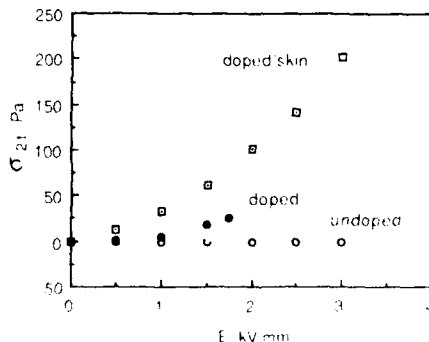
Figure 4 Apparent shear stress of fluids with 20 v% of poly(pyridinium salt) particles in mineral oil. The shear rate is 0.5 s^{-1}.

field in the range of 0.7 to 3.5 kV/mm (Figure 6). Further evidence of ER behavior of the PBZT suspension by optical microscopy showed that the stiffening of the ER fluid, portrayed by the increase in G' with electric field, is due to particle chaining.

A DIELECTRO-RHEOLOGICAL (DR) TECHNIQUE

An effective technique was developed to evaluate the dielectric response and ER performance of the fluid under high fields simultaneously. Conventional methods for measuring dielectric constants are to monitor the charge accumulation on the capacitor that contains the test sample. Because ER suspensions are used at high fields, the conventional methods become unrealistic and difficult. To overcome this problem, we monitor the attractive force between the capacitor plates instead. The dielectric constant under high field can be extracted from the measured attractive force as follows.

$$F_z = -\frac{d\,\text{Energy}}{dh} = -\frac{d}{dh}\left[\frac{1}{2} C V^2\right]$$

$$= -\frac{d}{dh}\left[\frac{1}{2} \frac{C h}{\varepsilon_o A} \frac{\varepsilon_o A}{h} V^2\right]$$

$$= -\frac{1}{2} \varepsilon_{eff} \varepsilon_o A \frac{d}{dh}\left[\frac{1}{h} V^2\right]$$

$$= \frac{1}{2} \varepsilon_{eff} \varepsilon_o A E^2 \qquad (1)$$

$$\frac{F_z}{A} = N_s = \frac{1}{2} \varepsilon_{eff} \varepsilon_o E^2 \qquad (2)$$

where C and V are the capacitance and the voltage, respectively; A and h are the area and the gap of the electrodes, respectively. F_z is the attractive force of the electrodes with a field (E). Thus, the normal stress (N_s) can be employed to evaluate the dielectric constant (ε_{eff}) of the suspension under high fields. To verify this new method, the effective dielectric constant of mineral oil was measured by this method and found to be consistent with that from the conventional measurement.

The excess normal stress (ΔN) is defined as the difference of the normal stresses be-
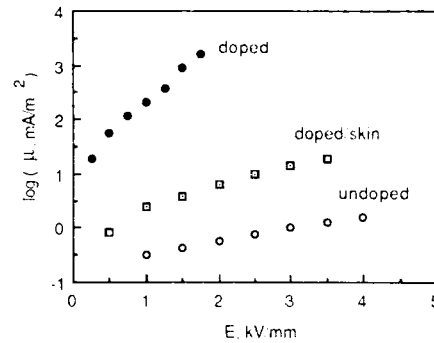
Figure 5 Current density of fluids with 20 v% of poly(pyridinium salt) particles in mineral oil.
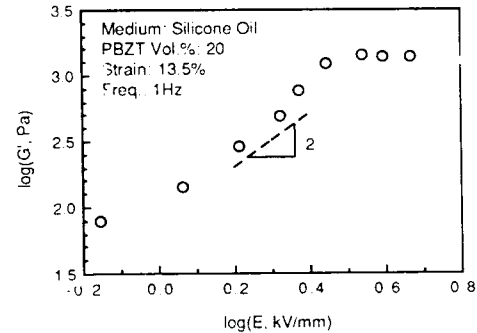
Figure 6 Stiffness dependence of PBZT-based ER fluid on electric fluid.
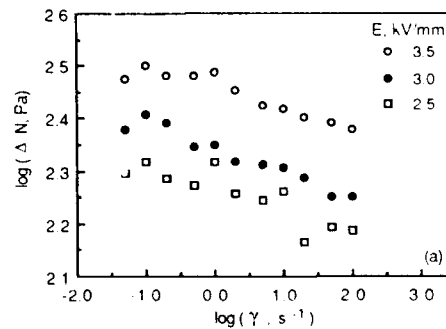
Figure 7(a) Dielectric interaction force (ΔN) vs strain rate [I_2-doped poly(pyridinium salt) (15 v%) in mineral oil].

tween the suspension and the suspending medium. Therefore, ΔN represents the sum of dielectric interaction force of the particles in the suspension. Previously, the dielectric interaction force has been estimated from the difference in dielectric constants of the dispersed particle and the suspending medium. Not included in this estimate are the effects of the spatial structure of the particles, and the geometry and actual dielectric response of the particle. In contrast the present technique measures the dielectric interaction force directly and thus takes all these factors into account.

In the designed anhydrous ER system comprising I_2-doped poly(pyridinium salt) in mineral oil, we found that a higher shear rate gives a smaller value of the dielectric interaction force (i.e. dielectric constant) of the suspension (Figure 7a). The apparent shear stresses (σ_{21}) were measured simultaneously with the dielectric interaction force by using the DR technique. The apparent shear stress also show a similar trend (Figure 7b). This implies that the chain structure of the dispersed phase was progressively destroyed with increasing shear rates. The disrupted structure, in which the particles are more randomly distributed, has a smaller value of interaction force among particles and thus a lower permittivity. This trend was consistent with measurements by

Figure 7(b) Apparent shear stress (σ_{21}) vs strain rate (the system in Figure 7(a)).
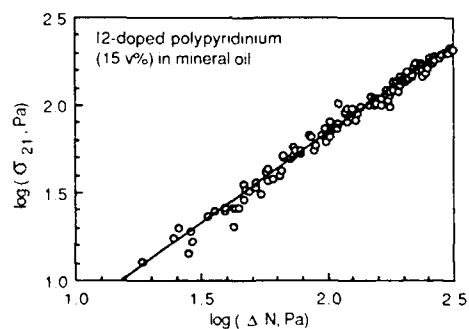
Figure 8 Relationship of apparent shear stress (σ_{21}) and dielectric interaction force (ΔN) (the same system as in Figure 7).

conventional dielectrometry before and after the dispersed phase in the suspension was aligned with a high field.

The apparent shear stress arising from ER effect was linearly proportional to the dielectric interaction force (ΔN) (Figure 8). The universal response is a demonstration, in essence, of the appropriateness of the chaining theory for the ER effect.

REFERENCES

Banhegyi G 1988 *Colloid & Polymer Sci.* **266** 11
Block H, kelly J P, Qin A and Watson T 1990 *Langmuir* **6** 6
Block H and Kelly J P 1988 *J. Phys. D:Appl. Phys.* **21** 1661
Filisko F E and Radzilowski L H 1990 *J. of Rheology* **34(4)** 539

An analytical and experimental investigation of electrorheological fluids

S.R. Kasiviswanathan, B.S. Thompson, M.V. Gandhi

Intelligent Materials and Structures Laboratory

Department of Mechanical Engineering

and

C. Chmielewski

Department of Chemical Engineering

Michigan State University, East Lansing, MI 48824, U.S.A.

ABSTRACT: This paper presents a summary of analytical and experimental investigations on characterizing the constitutive characteristics of electrorheological (ER) fluids. The steady-state rheological properties of an ER fluid are investigated, and a constitutive rheological equation is proposed for the ER fluid. A variety of ER fluids are considered here with different particulate suspensions in a dielectric medium. In this paper, the nature of an ER fluid, the influence of important variables such as shear stress, shear rate, electric field strength, field frequency, temperature, and fluid composition are presented. The results obtained from the experimental investigations are employed in the mathematical modeling of the constitutive rheological equation of the ER fluid.

I. INTRODUCTION

Electro-rheology is the phenomenon in which the rheology of fluids is modified by the imposition of electric fields. Since the invention of electro-rheological fluids by Winslow (1949), the rheological properties of ER fluid have attracted the attention of many researchers. Analytical aspects of the fluid dynamics research involve development of both linear and non-linear dynamic fluid models. Electro-rheological fluids in these models are described by non-Newtonian constitutive equations based on the rheological measurements. The dependence of viscoelastic properties of ER suspensions on the applied electric field has been determined experimentally by Vinogradov *et al.*(1986).

The ER phenomenon will not show itself in pure oil for example, but when an amount of corn starch is added the effect will occur. Most of the information reported is experimental with very few concerning the nature of the phenomenon. The analysis of literature and patents shows that the ER effect is suggested for application in the fields of control the flow of liquids through narrow channels, friction devices, clamping and positioning devices in machining of materials, switching components in fluidic control devices, clutches, brakes, shock absorbers, in controlling the vibration on the space structure and machinery parts, to control the vibrational response of aircraft wings, helicopter rotor-blades, and robot arms Gandhi *et al.* (1989a,b). Most of the information reported is experimental with very few concerning the nature of the phenomenon. The ER phenomenon is not only of academic interest, but also has tremendous applicability in engineering technology, Gandhi and Thompson (1991).

It took sometime for researchers to get momentum to exploit the mechanical properties of an ER fluid though several scientists and engineers are working in this field. Arguelles *et al.*(1974) have discussed a theoretical model for steady electroviscous flow between parallel plates. Adriani and Gast (1988) have modeled an ER fluid as a concentrated suspension of hard spheres with aligned field-induced electric dipole moments and they have presented a clear insight into the relationship between the macroscopic properties of the ER fluid and the microscopic structural changes.

Klass and Martinek (1967) and Block (1986) have been convinced that this phenomenon is due to the electric double layer interaction and overlap, as in the primary and secondary electroviscous effects. Stangroom (1983)has stated that the induced changes in rheology are due to the formation of aggregates of particles by dipole-dipole interactions and to the resulting fibrillated network. The dependence of viscoelastic properties of the ER suspensions has been suggested by Vinogradov *et al.* (1986). In spite of a number of theoretical and experimental investigations of the ER effect there is a considerable controversy concerning the primary underlying mechanism. Choi *et al.* (1990) have studied the vibration characteristics of a composite beam containing ER fluid. A review article on the nature of the fluids active in this role has been published by Block and Kelly (1988) which also presented and assessed various models for ER fluid. Whittle (1990) has reported a Brownian dynamics computer simulation of an ER fluid. Gamota and Filisko (1991) have presented the dynamic mechanical studies of ER materials, which was a combination of alumino-silicate particles and paraffin oil, at moderate frequencies. They have also introduced a rheological model to account for the ER materials qualitatively. McLeish *et al.* (1991) have calculated the linear frequency dependent modulus of a model ER fluid at low and intermediate concentrations, assuming that particle strings are the dominant structures. This paper is focused on the analytical and experimental investigations on the rheological properties of the ER fluid which were studied while subjected to electric fields ranging from 0 to 2.2 kV. The experimental work was undertaken on a Rheometrics RMS 800 mechanical spectrometer, upgraded with high voltage capability (5 kV). Using a double walled couette fixture, steady shear measurements were made at rates ranging from 0.1 to 100 s^{-1}. In addition, all measurements were made at temperatures ranging from 24° to 29° C. These studies not only illustrate the rheological effects of an electric field on ER fluids, but also provide an insight for the development of future experimental programs and procedures. The rheological investigations on these ER fluids indicate that higher imposed voltages apparently lead to more rigid fluid structures resulting in observed increases in the shear viscosity of the fluid.

2. ANALYTICAL AND EXPERIMENTAL INVESTIGATIONS

For Newtonian fluids the shear stress is in phase with the shear rate and there are no normal stresses. For polymeric fluids the response is different from linear fluids. So, often the data are presented in terms of real and imaginary parts of complex viscosity, η^*. The complex viscosity η^* is defined by $\tau^*_{21} = \eta^* \gamma_{21}$. Now it is necessary to allow η^* to be complex in order to account for the phase difference between shear stress and the shear rate. Hence $\eta^* = \eta' + i\eta''$, η' being the dynamic viscosity which could be thought of as elastic contribution associated with energy storage. The function which polymer rheologists use is $G^* = i\omega\eta^* = G' + iG''$, where ω is the frequency of oscillation in the experiment. In the above expression G' is known as the storage modulus, G'' is known as loss modulus and loss tangent is defined as $\tan\tau = G'/G''$.

The rheological properties of ER fluids consisting of Argo corn starch and Silicon oil suspension at different percentages were studied with varying electric field ranging from 0 to 2.2 kV. These experiments were conducted at temperatures varying from 24° to 29° C. Steady shear measurements were made at rates ranging from 0.1 to 100 s^{-1} and the dynamic strain data were taken at strains ranging from 0.1 to 100 percent at a frequency of 1.0 rad/s.

Figure 1 shows the variation of the non-Newtonian viscosity η with the rate of strain $\dot\gamma$ at 24° C. For the fluid without electric field, η decreases as $\dot\gamma$ increases. There is a monotonic decrease of the viscosity with shear rate, which is commonly referred to as viscous shear thinning. For the fluid in the presence of an electric field, at rates less than 0.4 s^{-1} the suspension exhibits a Newtonian like zero shear viscosity of 300 Pa.s. At rates higher than 0.4 s^{-1} there is a monotonic decrease of the viscosity with shear rate. We observe that there is a big change in the non-Newtonian viscosity in the presence of an electric field. The non-Newtonian viscosity appears to be higher for the fluid in the presence of an electric field than that for the fluid without electric field for a given shear rate.

Figure 2 shows the shear rate dependence of the shear stress at 24° C with and without electric field. It is observed that in the absence of electric field the shear stress varies non-linearly with the rate of strain. We also observe that there is a sudden jump in τ - $\dot\gamma$ graph in the presence of an electric field of 1 kV which may be regarded as that the ER fluid flows only at higher shear stresses. If we can measure the shear rates to the order 10^{-5} then we can observe more on the characteristics of ER fluid. When the electric field is 1 kV, notice the rate dependence of shear below 4s^{-1} and then it appears that

the shear stress is independent of the shear rate.

Figure 3 shows the shear stress dependence on shear rate of the ER fluid subjected to different voltages at 29° C. The main feature of this figure is that at voltages greater than 20 V there is an independence of shear stress with shear rate over a certain limited range of shear rates. Then, for investigations made for voltages between 20 and 600 V, shear stress is a monotonically increasing function of shear rate after a critical rate. For voltages greater than 600 V the stress seems to be independent of shear rate except for a small range of shear rates of 2 s^{-1} to 10 s^{-1} and for some observations $\dot{\gamma}$ is not measured beyond 2 s^{-1}. This may be likely due to the temperature variations while conducting the experiments or due to the difference in levels of the ER fluid filled in the gap between the cylinders of the rheometer. Figure 4 shows the dependence of the shear stress τ with the applied voltage. For the values of the shear rate up to 10 s^{-1}, shear stress varies gradually and after a critical applied voltage the variation in the shear stress is very low. When the shear rate is 100 s^{-1}, shear stress is independent of voltage up to 100 V and beyond this voltage shear stress increases monotonically upto 1 kV and remains constant after that. Figure 5 shows the behavior of an ER fluid with lesser concentration of corn starch. Under an electric field of varying intensities a solid structure is built up in the fluid which is seen from this figure as a larger stress response to the shearing rate as the voltage is increased. It is observed that the ER effect is less as the concentration is lesser for this ER fluid.

Figure 6 shows the monotonically increasing yield stress of an ER fluid of lower concentration (35%) with the changing electric field. This confirms our earlier result that a more global solid structure is built up under the varying intensities of electric field. In addition, with the higher voltages there is an excessive resistance for the fluid to flow, however, it begins to flow once the respective yield stress was reached. Figure 7 shows the storage modulus strain response of the fluid at 25.3° C with an applied voltage of 1 kV at an oscillatory frequency of 1.0 rad/s. There is no storage modulus for the fluid over a strain range of 0 to 2.75 percent and there is a sudden increase in storage modulus over a strain range of 3.75 to 5.75 percent with a plateau region beyond 5.75 percent. The storage modulus being zero up to the strain of 3.75 percent means that corn starch under the applied voltage of 1 kV does not have the elastic property till this percent strain is reached and its elastic response is enormous from a strain range of 3.75 to 5.75 percent and it remains constant after this percent. Figures 8 and 9 show the graph of the storage modulus of an ER fluid of lower concentration (35%) with percent strain. In the absence of an electric field, the continuous decrease in the storage modulus over the range of strains between 5 and 100 percent indicates a continuous break up of the fluid structure. Same interpretation can be applied for strain sweeps performed at voltages beyond 200 V the storage modulus is no longer found to be strictly monotonically decreasing function of strain. But, at sufficiently low strains the storage modulus is zero, indicating pure viscous type of behavior. At a critical strain the material quickly takes on elastic properties.

3. DISCUSSIONS AND CONCLUSIONS

Electro-rheological fluids are suspensions of particles on which the application of electric field increases the strength of the fluid structure. Even in the absence of an electric field a suspension tends to form some local structure on the result of aggregation of solid particles. These aggregates are easily broken up under the imposition of steady shear and result in shear thinning of the fluid as seen in Figures 1 and 2. For larger shear rates, the viscosity of the suspension decreases further and the fluid takes on the rheological properties of the solvent with non-interacting particles and a plateau region tends to form which is not fully recognized in the figures.

The fluid becomes more difficult to break as the voltage is increased due to more powerful solid structure formed by the application of electric field. This is seen from Figure 3 as the stress response is larger for the shear rate as the voltage increases. From Figure 4 we see that there is certain kind of relationship among τ, $\dot{\gamma}$ and the electric field E as the slope of the curves for the electric field varying from 90 V to 1 kV are more or less two. At low shear rates and under an imposed electric field, it is typical for the stress of the fluid to be independent of the shear rate. This flow behavior does not represent a solid like response or does not behave like a viscous or viscoelastic fluid since in viscous liquids a result of molecular momentum transport is that the stress depends on the strain rate. But, still we observe that this fluid may have a rheological equation whose $\dot{\gamma}$ and the yield stress τ_0 depend on the electric field. Considering all these aspects of the fluid an empirical rheological equation may be written as

$$\tau = \alpha E^X 0 \qquad \qquad \text{for } \dot{\gamma} \leq \dot{\gamma}_c$$
$$\tau = \alpha E^X 0 + \eta \, \dot{\gamma} \, (E) \qquad \text{for } \dot{\gamma} \geq \dot{\gamma}_c$$

where τ and X_0 are constants and $\dot{\gamma}_c$ is a critical strain rate. But, it seems, we can not generalize this kind of behavior for all ER fluids under an applied electric field.   Barnes and Walters (1985) have concluded that the yield stress concept is an idealization using the data obtained from constant stress rheometers. They have also concluded that by using Deer Rheometer Mk II, which can give results at shear rates as low as 10^{-5} s^{-1}, fluids which flow at high stresses will flow at all lower stresses and there is no yield stress. This departure from the concept of yield stress makes us to feel skeptical about the usage of the constitutive equation of Bingham model for ER fluid.

From Figures 7 - 9, the implication of a zero storage modulus at lower percent strains means that the fluid behaves like a Newtonian fluid and it is significant when this is compared with that of Shulman *et al.* (1989). An empirical rheological equation has been suggested by (1989), which also incorporates yield stress. If the ER fluid in question has yield stress than it would mean that for low strains the material would behave as an elastic solid. The corn starch ER fluid is not an elastic solid but rather a viscous fluid. Higher applied voltages on the fluid would lead to more rigid fluid structures. Below some critical percent strain the storage modulus was found to be zero indicating pure viscous fluid type behavior. But this contradicts with current constitutive equation which uses a yield stress to describe ER fluid behavior. The yield stress idea exists in isotropic materials, but still work has to be done whether this exists for anisotropic materials.

ACKNOWLEDGEMENTS

REFERENCES

Adriani, P.M. and Gast, A.P., (1988), *Phys. Fluids*, **31**, pp 2757-2768.

Arguelles, J., Martin, H.R. and Pick, R., (1974), *J. Mech. Engng. Sci.*, **16**, pp 232-239.

Barnes, H.A. and Walters, K., (1985), *Rheol. Acta.*, **24**, pp 323-326.

Block, H. (1986), *Polymers in Solutions*, ed. Forsman (New York: Plenum Press), pp 111-147.

Block, H. and Kelly, J.P., (1988), *J. Phys. D: Appl. Phys.*, **21**, pp 1661-1677.

Choi, Y., Sprecher, A.F. and Conrad, H.,(1990), *J. Intell. Mater. Syst. and Struct.*, **1**, pp 91-104.

Gamota, D.R. and Filisko, F.E., (1991), *J. Rheol.*, **35**, pp 399-425.

Gandhi, M.V. and Thompson, B.S., (1991). *Smart Materials and Structures*, (London: Chapman and Hall).

Gandhi, M.V., Thompson, B.S., Choi, S.B. and Shakir, S., (1989) *ASME J. Mech. Trans. and Auto. in Design*, **111**, pp 328-

Gandhi, M.V.,Thompson, B.S. and Choi, S.B., (1989) *J. Comp. Matls.*, **23**, pp 1232-

Klass, D.L. and Martinek, T.W., (1967), *J. Appl. Phys.*, **38**, pp 67-

McLeish, T.C.B., Jordan, T. and Shaw, M.T., (1991), *J. Rheol.*, **35**, pp 427-448.

Shulman, Z.P., Korobko, E.V and Yanovskii, Yu. G., (1989). *J. Non-Newtonian Fluid Mech.*, **33**, pp 181-196.

Stangroom, J.E., (1983), *Phys. Tech.*, **14**, pp 290-296.

Vinogradov, G.V., Shulman, Z.P., Yanovskii, Yu.G, Barancheeva, Korobko, E.V, and Bukovich, I.V., (1986), *Inzh. Fiz. Zh.*, **50**, pp 605-609.

Whittle, M., (1990), *J. Non-Newtonian Fluid Mech.*, **37**, pp 233-263.

Winslow, W.M., (1949). *J. Appl. Phys.*, **20**, pp 1131-1148.
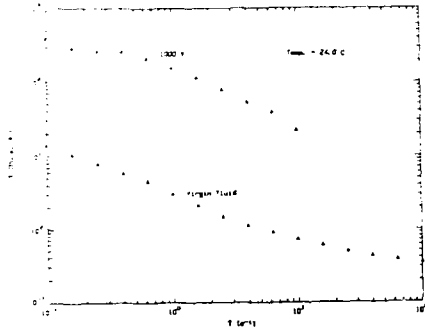
Figure 1 Non-Newtonian Viscosity
Versus Rate of Strain.
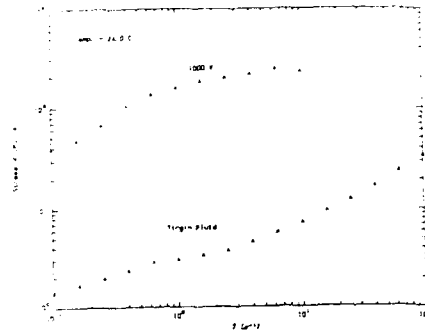
Figure 2 Shear Stress Versus
Shear Rate
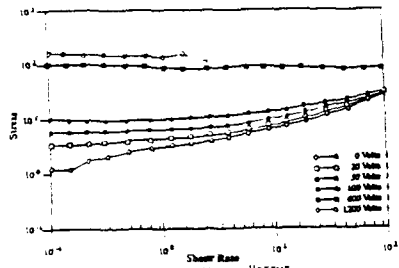
Figure 3 Shear Stress Versus
Shear Rate at Different
Voltages.
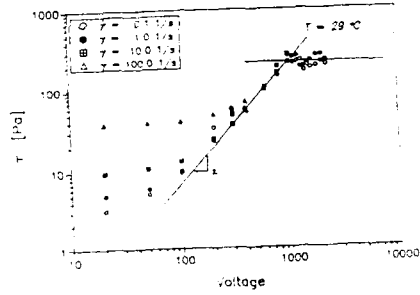
Figure 4 Shear Stress Versus
Applied Voltage
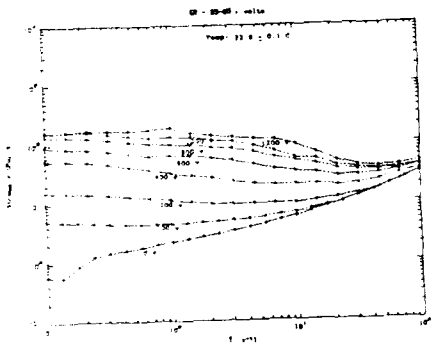
Figure 5 Shear Stress Versus
Shear Rate for Lesser
Concentration
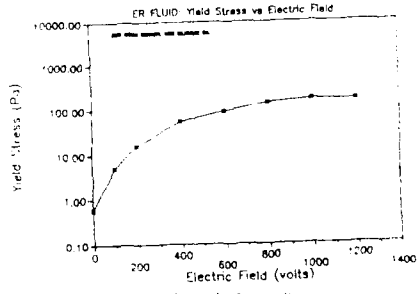
Figure 6 Yield Stress Versus
Electric Field.
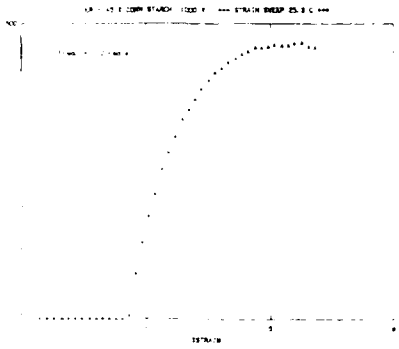
Figure 7   Storage Modulus Versus
            Percent Strain
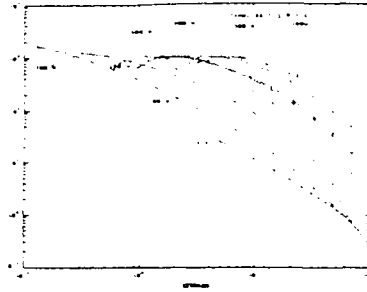
Figure 8   Storage Modulus Versus
            Percent Strain for Lesser
            Concentration
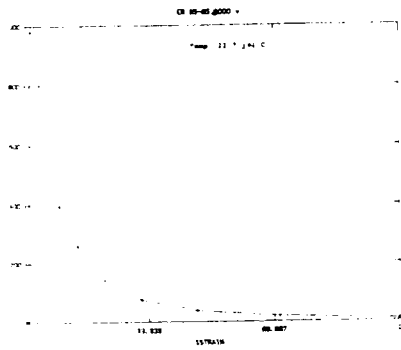
Figure 9   Storage Modulus Versus
            Percent Strain for Lesser
            Concentration

Single fiber simultaneous optical communications and sensing

P. L. Fuhr
P. J. Kajenski
University of Vermont
Electrical Engineering Department
Burlington, VT   05405

W. B. Spillman, Jr.
Catamount Scientific
Vergennes, VT   05491

Abstract

The idea of using a single optical fiber for simultaneous sensing and communications has been mentioned for many years. Initial studies using a single analog tone frequency and vibration sensing were first described within the last few years. We have extended that earlier work to the domain of high bandwidth communication signals and speckle pattern-based vibration sensing along a single multimode optical fiber. By adding a frequency subcarrier to the laser diode light source, it is possible to shift the vibration signal away from low frequency noise sources (e.g., line noise, 1/f noise) and obtain a significantly higher SNR and thus improved vibration signal detection. Experimental results and system configurations will be described as will the overall cross-talk effects of the communication channel and the vibration sensing signal.

Introduction

Over the past few decades there has been a great deal of interest in using optical frequencies for communication systems. This interest has been motivated by improved optical sources, notably the laser, and the development of the optical fiber. The advantages of using optical frequencies lie in the large potential bandwidth available, immunity from the effects of electromagnetic interference and other noise sources, and the ability to use low loss optical fibers for data transmission. Today optical fibers with losses of less than 1.0 dB/Km are readily available from a number of commercial sources, and long distance fiber optic networks have been installed worldwide.

Although optical fibers were developed for telecommunications use, they have also been successfully deployed in sensor applications. Fiber optic sensors offer a number of

advantages over conventional sensors, such as increased sensitivity, geometric versatility in that the sensor can be configured into nearly any shape, and immunity from the effects of electromagnetic interference (EMI). Fiber optic sensors have been developed to measure a number of different parameters, such as strain, magnetic fields, radiation, and rotation[2-4].

Fiber sensors can be embedded in composite materials, fiberglass, concrete, and other such materials. At present there is considerable interest in embedding these sensors in composite materials used in aircraft and other structures, creating what is known as "smart skins." In the interest of reducing the weight of the completed craft further, it has been suggested that multipurpose purpose sensor and communication systems be developed.

Vibration Sensing with Multimode Fiber Sensors

A multimode optical fiber can be used as a vibration sensor. Figure 1 shows a diagram of a multimode fiber vibration sensor, based on the phenomena of modal noise. When light from a laser is launched into a multimode optical fiber, a speckle pattern is formed at the fiber output. This pattern is the result of interference and coupling of the different modes propagating down the fiber. When the fiber is vibrated the phase and intensity of each mode is modulated, each to a varying degree. Due to the differential modulation of the modes the *distribution* of the light intensity in the pattern will change, though the intensity of the overall pattern will not vary. If the output pattern is spatially filtered (as would occur at splices, connectors, etc.) then the amplitude of the signal at the photodetector will be modulated. Vibration sensing based on this principle has been demonstrated in numerous application areas.

Simultaneous Communications and Sensing

Experiments were designed to show that a multimode fiber can be used simultaneously as a vibration sensor and a communications link. The experimental configuration is shown if Figure 1. The transmitter signal was a 34 Mb/s pseudo random bit sequence, in a Non Return to Zero (NRZ) format. First, the vibration rate was set to zero, and the bit error rate as a function of the received optical power was determined.

Next the power of the transmitted signal was reduced so that the $\log_{10}$ of the BER was approximately -7.2. The frequency vibration of the bar was set to 67 Hz, and the $\log_{10}$ of the BER as a function of the vibration amplitude was measured. The results of this experiment are shown in figure 4. It was noted that when the transmitter power was set so that the BER was less than -8.0, the BER was not affected at all by vibrating the fiber.

100/140 fiber aluminum bar
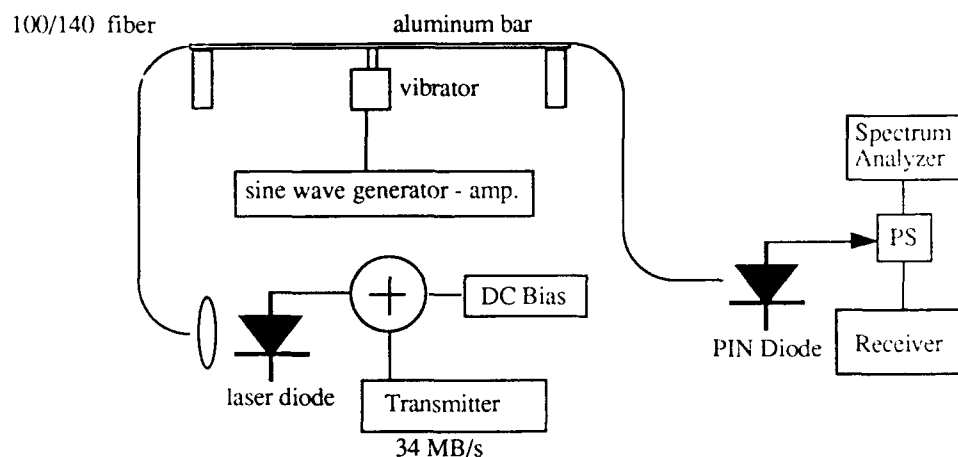
Figure 1. Simultaneous communications and vibration sensing experiment.

The final experiment was intended to demonstrate how the communications signal could degrade the vibration sensor signal. The vibration frequency of the bar was set at 67 Hz, with a displacement of approximately 0.5mm. It was determined that the vibration signal can be recovered with the transmitter on, the noise floor is increased by about 20 dB, limiting the minimum detectable signal to -45 dB. However, if the power of the communication signal is increased, it is possible that the vibration signal can be completely obscured.

Summary

These preliminary studies have demonstrated that a single multimode fiber can be used simultaneously as a vibration sensor and communications link. When light from a source with a sufficiently narrow spectral output (i.e. sufficiently long coherence time) is launched into a multimode optical fiber, a speckle pattern is formed at the fiber output. Any undesired modulation of the pattern is referred to as modal noise, and can occur when the fiber is subjected to any mechanical perturbation. Whereas modal noise can be detrimental in a communications system, it can be used to an advantage in a sensor system. It has been demonstrated that the modal can be used to determine the frequency and amplitude of the fiber perturbation.

The modal noise from the vibration signal will degrade the communications channel. One way of reducing the impact of the modal noise is to increase the number of speckles

received by the photodetector. This can be accomplished by either using a light source with many (greater than 10) longitudinal modes, or varying the extent of spatial filtering of the speckle pattern. Of course, it should be noted that using either of these two methods will reduce the amplitude of the vibration signal. Alternatively, the power of the transmitted signal can be increased. If sufficient optical power is delivered to the receiver, the desired bit error rate can be achieved, despite the modal noise.

The advantage of multiplexing sensor and communication signals is the reduced cost of the overall sensor system. A frequency multiplexing scheme is preferred over time division multiplexing, since for equivalent peak powers, the average power is higher for the former. Higher signal to noise ratios are therefore possible, and it is possible to multiplex a greater number of sensors.

BER vs Amplitude of Vibration
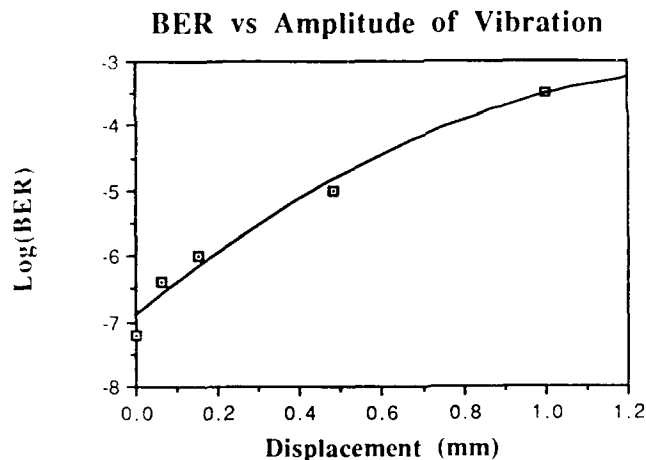
Figure 2. The bit error rate when the fiber is vibrated.

References

1. B. Culshaw. *Optical fibre sensing and signal processing* , (Peregrinus Press, London, 1984).

2. H. J. Arditty and H. C. Lefevre, "Sagnac effect in fiber gyroscopes," *Opt. Lett.*, Vol. 6, No. 8, pp. 401-3, Aug 1981.

3. F. Bucholtz, D. M. Dagenais and K. P. Koo, "Mixing and detection of RF signals in fiber optic magnetorestrictive sensors," *Electron. Lett.*, Vol. 25, No. 19, pp. 1285-6, 14 Sept 1989.

4. P. J. Kajenski, P. L. Fuhr and W. B. Spillman, "Spectral sampling technique for wavelength encoded fiber optic sensors,"," *ISA*, Vol. pp. 1989.

Non-destructive evaluation of PMN actuator elements for active structures

John A. Wellman

Litton/Itek Optical Systems
10 Maguire Road, Lexington, Massachusetts 02173-3199

ABSTRACT: Non-destructive techniques are needed to improve the performance and reliability of actuator elements incorporated into active and adaptive structures. Ultrasonic velocimetry is presented as a non-destructive technique for testing Lead Magnesium Niobate (PMN) multilayer stacked actuator segments. Acoustic velocity of PMN actuator segments was measured and found to correlate with the actuator's strain field sensitivity. The acoustic velocity of PMN was found to vary under an applied electric field, corresponding to morphic changes in the crystal structure.

1.0 INTRODUCTION

Actuators are incorporated into active structures as critical structural elements to apply forces and precisely distort the structure in a predetermined manner. The actuators ability to provide the required mechanical strain or displacement with the necessary precision determines the performance and reliability of the active structure. The reliability of a complex active structure with a large number of actuators and electronics must be addressed before for this technology can transition from laboratory experiments to critical applications. Development of non-destructive testing techniques for actuator elements is the first step towards improving performance and reliability of active structures. Acoustic energy is commonly used in the non-destructive detection of flaws and evaluation of materials. Pulses of high frequency ultrasonic waves are propagated through a sample while the reflected and transmitted energy is measured. Information about the sample is deduced from the propagation time, amplitude and waveform of the transmitted wave. This experimental investigation has been undertaken to establish the relationship between longitudinal acoustic velocity and the electromechanical behavior of PMN multilayer actuators. The relationships established can be used for non-destructive characterization of PMN multilayer actuators by ultrasonic velocimetry.

2.0 PMN ACTUATOR PHENOMENOLOGY

Over the past decade, Litton/Itek Optical Systems has pioneered the development of PMN multilayer actuators for active structural components. PMN is an electrostrictive material that offers several inherent advantages over PZT materials for adaptive structures applications. The strain sensitivity of the material and high Young's modulus provide excellent displacement resolution. The material requires no poling and exhibits exceptional set point accuracy due to its low hysteresis. The material is very thermally stable due to a very low thermal expansion coefficient and low energy dissipation. Table 1 provides an overview of the typical properties for the proprietary Itek PMN composition.

The actuators are fabricated from a ceramic powder process. The PMN powders are prepared and then tape cast to form individual layers. Two different electrode patterns are printed on the tapes. Tapes with alternating electrode layers are then stacked together to form a greenware block. The PMN block is then sintered and discretized to form individual actuators. The electrodes in the finished actuator are connected electrically in parallel. While the ceramic layers act in series combining the strain from each layer to produce the actuator stroke. Electrical and structural properties can vary between actuators resulting from the microstructure of the ceramic, contamination, manufacturing tolerances, and uncontrolled process variables. Typical defects that effect the performance of the actuator include porosity, delaminations, voids, interstitials and

cracks. The consequences of these defects include actuator breakage, dielectric break down, variable strain field sensitivity and altered mechanical or electrical properties. Evolution of the actuator fabrication process through design and process controls has led to major improvements in the yield, stroke, response uniformity and reliability of the actuators. Figure 1 illustrates some of the standard SELECT actuator configurations manufactured by Itek. Large stroke actuators are produced by bonding smaller standard actuator segments together to provide the required number of actuator layers.

PMN is a relaxor ferroelectric ceramic material. Under an applied electric field the ceramic undergoes an electrostrictive phase transformation inducing mechanical strain. The strain is unidirectional and proportional to the squared power of the electric field. The electrostrictive behavior of PMN is governed by thermodynamic equations derived from the elastic Gibb's function. The Gibb's function is a generalized equation that relates the strain response of a material to applied forces, fields and temperature. The familiar form of the eletrostriction strain equation is obtained by eliminating all unrelated, higher order and non-linear terms.

$$x = sX + mE^2 \tag{1}$$

where E is the applied electric field, m is the electrostrictive constant, s is the elastic compliance of the ceramic, and X is stress within the actuator.

3.0 TESTING METHODOLOGY

Non-destructive testing techniques are required for process control during fabrication and final inspection to assure desired performance and reliability of actuators being incorporated into active structures. A useful test procedures, particularly for process control, should be cost and time effective, minimizing setup and sample preparation. Information about the elastic properties can be obtained by measuring the acoustic velocity of the bulk material. Acoustic testing methods have been investigated by previous authors in the testing and evaluation of multilayer capacitor structures. Acoustic resonances and acoustic emission techniques have been employed for testing of multilayer capacitor structures. The longitudinal acoustic velocity of a material is related to the elastic stiffness and density by

$$c_\ell = \sqrt{\frac{E(1-v)}{\rho(1+v)(1-2v)}} \tag{2}$$

where E is Young's modulus, ρ is density and v is poisson's ratio. The measurement of the longitudinal velocity by it's self is not sufficient to calculate the elastic modulus of the test sample. Usually the acoustic shear velocity is also measured which allows for both Young's modulus and poisson's ratio to be derived. Measurement of the shear velocity is rather difficult particularly with the small size and shape of the actuators. The longitudinal velocity by it's self provides more of a qualitative measure of the elastic properties of the material. The potential for ultrasonic velocimetry to be utilized as a non-destructive evaluation method is based on the dependance of both the electromechanical strain and acoustic velocity on the elastic properties of the PMN ceramic material.

A Panametrics model 5252 ultrasonic velocimeter was used for the investigation to measure the longitudinal acoustic velocity of PMN actuator segments. Two piezoelectric transducers are mounted on the jaws of a digital caliper. One transducer produces a 20 mhz acoustic pulse, and the second senses the transmitted pulse on the other side of the sample. The acoustic velocity is derived by measuring the transit time for the puls to propagate through the thickness of the

specimen. Test samples are clamped between the transducers by means of the caliper, and are coupled to the transducers by a liquid couplant. The thickness of the sample is measured by the calipers and automatically recorded by the velocimeter. The velocimeter precisely measures the transit time delay and calculates the acoustic velocity.

$$c_l = \frac{x}{(t - t_o)} \tag{3}$$

where c_l is the longitudinal acoustic velocity of the sample, x is the thickness of the sample, and $t-t_o$ is the measured transit time. The accuracy of the velocimeter is within +/- 0.2 percent full scale. Outputs from the velocimeter also allow the waveform of the transmitted waves to be recorded with a digital oscilloscope. The echo pattern and attenuation of the wave pulse can be used to deduce additional information about the properties of the sample.

Actuator segments were tested along the longitudinal axis through the multilayer structure. Because this test is non electrical, actuators can under go testing and screening prior to expending the cost of applying electrical contacts and wires. Thus, The expense of handling and processing defective actuators can be saved. The testing time for each actuator is very short allowing for large numbers of actuators to be tested cost effectively.

4. EXPERIMENTAL RESULTS

Experimental testing was performed on a group of 69 actuators segments that included rejected and left over actuator segments from a production run. Each segment was tested for capacitance, loss tangent, stroke at 120 volts and acoustic velocity. Two independent velocity measurements were made for each actuator to provide an indication of the accuracy and repeatability of the measurements. The acoustic velocity was then correlated to the actuator stroke data that was measured with a Dektak profilometer. Figure 2 presents the experimental results that indicate a direct correlation between the measured velocity and electromechanical sensitivity of the actuators. Stroke between actuators at 120 volts ranged from 1.8 to 4.0 microns, and is linearly proportional to a 8.6 percent variation in acoustic velocity. PMN actuator segments with lower acoustic velocity exhibited greater strain sensitivity. The repeatability of the velocity measurements is depicted by the error bars.

A second experiment was performed to investigate the nonlinear effect of an applied electric field on the elastic properties of the ceramic. Variations of the elastic properties under an applied electric field are the result of morphic changes in the crystal structure of the ceramic. The actuator was connected to a variable power supply. The acoustic velocity of the actuator was measured while the voltage was incrementally increased. Figure 3 shows that the acoustic velocity of a PMN actuator decreases by roughly 4 percent under an applied electric field corresponding to 120 volts. The decrease in the acoustic velocity under the applied electric field indicates a decrease in the stiffness of the ceramic that effects the actuator's displacement response under load.

5. CONCLUSIONS

The purpose of this study has been to establish the feasibility of ultrasonic velocimetry as a technique for non-destructive evaluation of PMN multilayer actuators. Experimental results have demonstrated a direct correlation between the acoustic velocity and the electromechanical sensitivity of the actuators. Acoustic velocity measurements have also been used to measure the sensitivity of PMN elastic properties to an applied electric field. The velocimetry test procedure meets the desired objectives of cost effective, accurate and rapid testing of actuators for process

control and final acceptance. The full potential of the Panametrics ultrasonic velocimeter as a tool for non-destructively characterizing multilayer PMN actuators has not yet been established. Future work will investigate correlations of attenuation and echo patterns to the structural integrity and other key performance characteristics of PMN multilayer actuators.

6. REFERENCES

Blackwood G.H., Davis P.A. and Ealey M.A. 1991 *Proc. SPIE* **1543**
Boser O., Kellawon P., and Geyer R. 1989 *IEEE Trans. Comp. Hybrids Manu. Technol.* **12** 1
Ealey M.A., Davis P.A. 1990 *Optical Engineering* **29** 11
Ealey M.A., Wellman J.A. 1989 *Proc. SPIE* **1167** 66-84
Ealey M.A. 1991 *Proc. SPIE* **1543**
Internal Itek Report, UDRI Characterization of PMN
Kahn S.R. and Checkaneck R.W. 1983 *IEEE Proc. 33rd Electronic Comp Conf.* pp. 77-87
Krautkrmer J., Krautkrmer H. 1977 *Ultrasonic Testing of Materials* (Springer-Verlag) 2nd Ed.
Mason WP 1958 *Physical Acoustics And The Properties Of Solids* (Princton: D.Van Nostrand)
Megherhi MH.1988 *The Effect of Additives, Microstructure, and Macrostructure on the Fracture Behavior of Lead Magnesium Niobate-Based Ceramic Actuator* (PSUMasters Thesis)
Panametrics Inc. 1987 *Instruction Manual, Velocimeter Model 5252*, REV A
Taylor D.J., Newnham R.E., and Carlson W.B. 1988 *Ferroelectrics* **87** 81 34

Young's Modulus	17.5 x 10⁶	psi
Thermal Expansion	1.0 x 10⁵	°F
Thermal Conductivity	2.54	BTU/ft-hr-°F
Density	0.275	lb/in³
Tensile Strength	>3500	psi
Fatigue Life	>2 x 10⁹	cycles
Curie Temperature	32	°F
Dielectric Constant	23,000	
Sensitivity	7.1	A/V/layer
Temperature Coefficient	2.0%	/°F
Hysteresis	< 1%	

Tab. 1 PMN material properties   Fig. 1 Itek PMN actuators
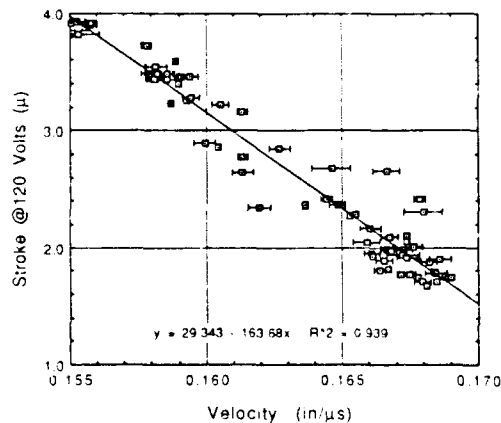
Fig. 2 Actuator Stroke vs acoustic velocity.   Fig. 3 Velocity vs applied electric field.
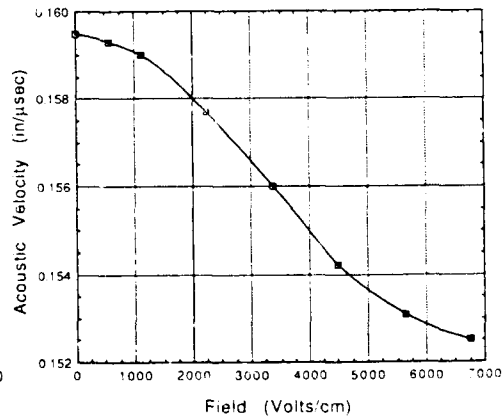
Composite-embedded fiber optic data links and related material/connector issues

R E Morgan, S L Ehlers, and K J Jones

Naval Avionics Center, 6000 East 21st Street, Indianapolis, IN 46219-2189

ABSTRACT: The objective of this effort is to utilize composite-embedded
optical fibers in airborne electronic packaging. Embedded evanescent
couplers are being developed. Also, an embedded spiral is being tested
for signal distribution by means of evanescent coupling from a
motherboard to individual circuit cards. A design for an embedded
connector array is being assembled and tested. High temperature optical
fibers are being investigated for embedment in metal-matrix composites.

1. INTRODUCTION

Future electronic packaging designs will require new design concepts and
material systems that meet severe military environmental constraints while
reducing weight, increasing performance and reliability, and reducing life
cycle costs. New material systems must be developed and transitioned into
all aspects of avionic packaging, including circuit modules, enclosures,
equipment racking, and cabling. Future aircraft and installed electronic
systems will be composed of composite materials of various types. They
will also incorporate fiber optic sensors and data links. As part of the
Naval Avionics Center's (NAC) total packaging concept, the NAC composite/
optical fiber team is combining these technologies and investigating the
embedment of optical fibers in composite materials and experimental avionic
components to develop intra-aircraft data links. Experimental circuit
module and enclosure hardware using composite-embedded optical fiber data
links are being designed and fabricated to conform to the physical and
environmental constraints of avionics packaging. This technique will
reduce aircraft weight penalties through reduced copper wiring volume and
will enhance both platform and air crew performances through enhanced
signal transmissions due to the signal carrying capabilities of the optical
fibers.

The goal of this project is to fabricate an electronics chassis/circuit
module demonstration entirely "wired" with embedded and interconnected
optical fibers (see Figure 1). Previous publications by the authors
(Morgan, et al., 1991; Ehlers, et al., 1991; Ehlers, et al., 1990; Morgan,
et al., 1989) have reported progress toward this goal. This paper will
report on three areas considered essential to avionics composite-embedded
data links: (1) embedded couplers and signal distribution, (2) embedded
connectors, and (3) material and environmental characterization of embedded
optical fibers in polymer-matrix (PMC) and metal-matrix composites (MMC).
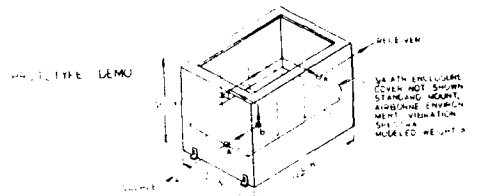
Fig. 1. Chassis with circuit cards.

2. EMBEDDED COUPLERS AND SIGNAL DISTRIBUTION

In order to achieve the avionics data links depicted in Figure 1, methods
are being developed for coupling a signal from the motherboard to a circuit
card and for signal distribution within the motherboard. Previous papers
(Ehlers, et al., 1991; Ehlers, et al., 1990; Morgan, et al., 1989) have
reported on using evanescent coupling for tapping composite-embedded
optical data links. Signal distribution is achieved within the motherboard
by means of a single fiber embedded as a flattened spiral (Morgan, et al.,
1991).

Spiral-oriented optical fibers have been reported by Newton, et al., (1983)
for use as a variable delay line or transversal filter. A similar
application, a spectrometer, was reported by Zürn and Ulrich (1990). A
planar fiber optic acoustic sensor configured in a planar spiral and
embedded in polyurethane was reported by Bucaro et al. (1991) and Lagokos
et al. (1988). An embedded spiral avoids loss due to coupling, fusion
splices and bending, and may be thought of as a folded delay line.

Coupling has been achieved by evanescent coupling of embedded optical
fibers in two parallel links (see Figure 2.). Signal distribution has been
demonstrated in evanescent coupling of an optical fiber embedded in a
spiral configuration (see Figure 3.). Three loops were tapped. The
spiral-embedded optical fiber allows for sequential tapping of a single
data link without losses from fusion splicing, fused biconical couplers or
tight bends. Ongoing work is involved with two essential steps: (a)
measurement of coupling loss (i.e., power input versus power output from
evanescent tap plus outgoing embedded optical fiber), and (b) measurement
of power output versus transverse displacement of a top (non-embedded)
directional coupler with respect to the tap of the embedded optical fiber.

3 EMBEDDED CONNECTORS

Embedded optical fibers in composites will require interconnection
technology to provide "panel joints" between composite sections. A
composite-embedded connector must achieve optical connection of composite-
embedded optical fibers between different boards while preventing breakage
of the embedded optical fibers. Also, the embedded connector must not
compromise or weaken the structural integrity of the composite panel.
Silicon V-grooves (Watson 1991) have been used for years for single mode
connectors. These are, however greater than 140 microns in diameter, and
would weaken the composite structure if embedded. Lu and Blaha (1991) have
reported embedding a ceramic ferrule and a single mode connector in a
composite panel. Again, these structures will likely weaken the composite
panel because they exceed 140 microns in diameter. The intent in avionics
packaging is to use relatively thin material cross-sections.

A design for an embedded connector array is being developed (see Figure 4.). Ongoing work is involved with assembling this device and demonstrating that it not only fulfills the requirement of a panel joint, but also the requirements of avionics environments.

4. MATERIAL AND ENVIRONMENTAL ISSUES

Previous publications by the authors (Morgan, et al., 1991; Ehlers, et al., 1991; Ehlers, et al., 1990) have described results of work performed on the embedment of optical fibers in graphite/epoxy panels and the subsequent vibration testing of the panels during simultaneous optical transmission.

Since future avionic circuit boards are expected to utilize optical fibers and metallic conductors with devices requiring thermal management heat sinking, embedment of optical fibers in metals and metal-matrix composites (MMC) is also being investigated. Successful embedment of a sapphire hollow waveguide in aluminum (without material damage or changing the optical transmission properties) was reported earlier (Morgan, et al., 1991) (see Figure 5.). Baldini, et al., (1991) reported embedment of Ge-doped optical fiber in titanium matrix composites. Lee, et al., (1991) reported embedment of silica fibers in aluminum parts and structures.

Work is currently in progress to evaluate the sapphire-aluminum interface for material interactions, formation of phases, presence of voids, etc. Figure 6 shows a cross-section of the sapphire hollow waveguide embedded in aluminum. Ongoing work in this effort involves the embedment and characterization of other types of optical fibers (and coatings) in aluminum. Solid sapphire optical fibers as well as aluminum-coated silica optical fibers have been acquired. Potential methods of embedding optical fibers in MMC are being investigated.

5. FUTURE WORK

Future work will involve designing a composite-embedded data bus for signal distribution within the chassis/circuit card system. This design will be based on coupling and connector losses as well as a power budget for the entire system.

6. ACKNOWLEDGEMENTS
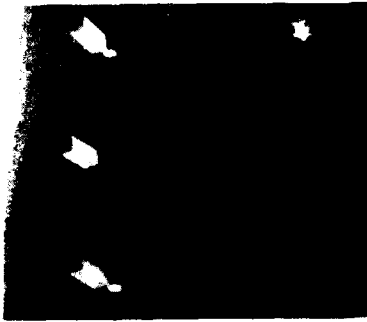
Fig. 2. Output of two surfacing
fibers next to arrows
on left. Light at RH
is from outgoing fiber.
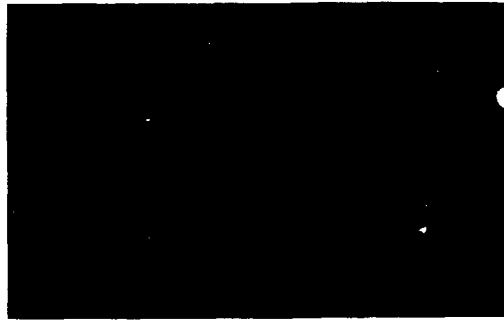
Fig. 3. Output of three surfacing
(LHS) loops of the embedded
spiral. Light at RH is
output of existing optical
fiber.
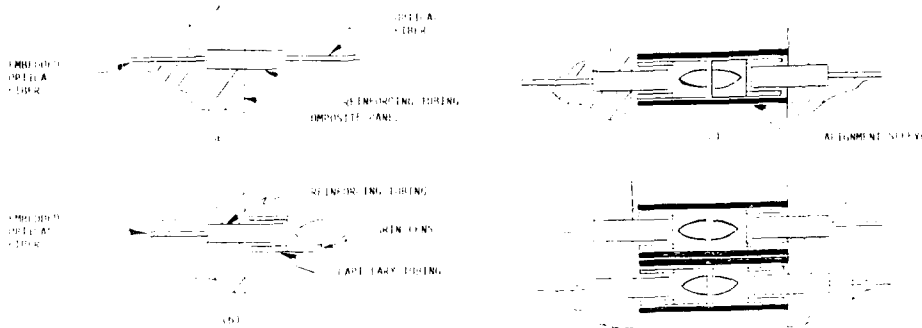
Fig. 4. Diagram of embedded connectors between two panels.

Fig. 5. Sapphire hollow wave-
guide embedded in alu-
minum.
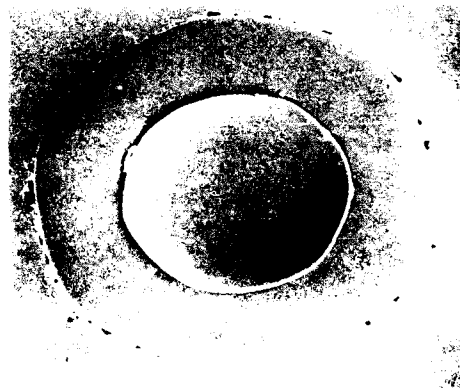
Fig. 6. SEM of cross-section of
sapphire hollow waveguide
embedded in aluminum.

7. REFERENCES

Bucaro J A, Lagokos N, Houston B H, and Dandridge A 1991 J. Lightwave Tech 9 1195

Ehlers S L, Jones K J, Morgan R E, and Hixson Jay CDR USN 1991 Fiber Optic Sensor-Based Smart Materials and Structures Workshop, April 3 & 4, 1991.

Ehlers S L, Jones, K J, Morgan R E, and Hixson Jay CDR USN 1990 Fiber Optic Smart Structures and Skins III (SPIE) Conference 1370 pp 346-355

Lee C E, Gibler W N, Friebele E J, Claus R O, Rogowski R S, and Nowakowski 1991 Fiber Optic Smart Structures and Skins IV (SPIE) Conference 1588 (to be published)

Lagokos N, Ehrenfeuchter P, Hickman T R, Tveten A, and Bucaro J A, 1988 Optics Letters 13 788

Lu Z J, and Blaha F A 1991 Fiber Optic Smart Structures and Skins IV (SPIE) Conference 1588 (to be published)

Morgan R E, Ehlers S L, and Jones, K J 1991 Fiber Optic Smart Structures and Skins IV Conference 1588 (SPIE) (to be published)

Morgan R E, Mitkus V V, Jones K J, and Hixson Jay CDR USN 1989 International SAMPE Electronics Conference Series 3 191

Newton S A, Jackson K P, and Shaw H J 1983 Appl Phys Lett 43 149

Watson H A 1991 Integrated Photonics Research Monterey CA April 9-11, 1991 pp 149

Zurn M, and Ulrich R 1990 Optics Letters 15 463

Active and adaptive optical components: a general overview

Mark A. Ealey

Litton/Itek Optical Systems
10 Maguire Road, Lexington, Massachusetts 02173-3199

ABSTRACT:

Since the revolutionary development of the laser in the late 1950's, the optics industry has strived to achieve optical components and systems with near diffraction limited performance. Optical components were designed and manufactured with precision tolerances to minimize fixed distortions. As the laser device improved in terms of power and beam quality, time-varying distortions induced by laser gain medium nonlinearities, atmospheric turbulence, and thermal blooming impeded system performance. A new generation of active optical components and adaptive techniques were realized to correct the time-varying distortions in real time.

1. INTRODUCTION:

Litton/Itek Optical Systems (**Tables 1** and **2**) has built adaptive optical components for use in high quality optical systems for two decades - see Ealey (1989). The shearing interferometer developed in 1973 remains the standard for wavefront measurement. The monolithic piezoelectric mirror (MPM), which was introduced in 1974, has been the quality product against which all other visible wavelength compensators have been compared. The Real Time Atmospheric Corrector (RTAC) system, which was built in 1974 using a monolithic piezoelectric mirror (MPM) and a grating based shearing interferometer wavefront sensor, was a landmark demonstration of concept feasibility of this technology (Hardy 1978). The stacked actuator deformable mirror (SADM), first delivered in 1980, set new performance standards for infrared systems. In 1981 Itek began the development of a new concept in deformable mirrors, the low voltage electrodistortive mirror (LVEM). Itek in 1984 began the development of cooled silicon electrodisplacive mirror (CSEM) technology to serve the high energy laser community (Ealey and Washeba 1990). Itek has also begun developing a cost efficient cooled mirror technology compatible with moderate flux levels and quantity production. The PMN SELECT electrostrictive actuator developed in 1988 features unsurpassed resolution and accuracy while operating at low voltage. The SELECT deformable mirrors delivered in 1990 offer enhanced reliability and performance even when compared with those first landmark components.

2. ELECTROSTRICTIVE ACTUATOR TECHNOLOGY:

The PMN SELECT actuators made by Litton Itek Optical Systems (see **Figure 1**) provide several inherent advantages over PZT (Ealey and Davis 1990). The sensitivity or strain is superior to that of the best piezoelectric ceramics. The transfer function exhibits low hysteresis, typically less than 1% at room temperature, and a usable linear electrostrain of about 1000 ppm. The strain is a linear function of the square of the electric polarization implying that the displacement is proportional to the square of the number of active layers. With recent material

and process advances, full stroke response can be achieved with as little as 100 volts over a range of stroke increments. PMN being a relaxor ferroelectric material requires no poling and exhibits exceptional positional set-point accuracy due to its low hysteresis. A very high elastic modulus (17 x 10^6 PSI) produces a high stiffness device capable of generating large deflection forces. The actuators also exhibit negligible thermal growth due to a small coefficient of thermal expansion (1 x 10^6 ppm/°F) coupled with very low power dissipation (micro-watts).

3. DEFORMABLE MIRROR TECHNOLOGY:

Fig. 1. Electrostrictive SELECT PMN Actuators

The PMN actuators were used to develop a new generation of low-voltage electrodistortive deformable mirror (LVEM). The LVEM consists of a glass facesheet, PMN actuators, a glass base reaction structure, printed circuit cards, and an electronic driver system. The facesheet contains actuator attachment pads machined directly into the thin glass wafer. The PMN actuators consist of 80 active ceramic layers connected mechanically in series and electrically in parallel. In the new generation mirrors, drive voltages have been reduced to +/- 75 volts taking advantage of the latest PMN material composition. The base structure has slots machined into the glass to facilitate integration of the electronic circuit cards. The actuators are adhesive bonded onto the base and the actuator addressing electrodes are connected to the card to make the all important electrical connection. The facesheet is bonded onto the actuator array and is then polished to an optical figure of λ/20 p-p at a wavelength of 0.6328 microns and an optical finish of better than 7 Å RMS. The electronic driver system consists of an

Fig. 2. Low Voltage Deformable Mirror (LVEM)

operational amplifier and power transistor stage to source voltage to the capacitive load. The 241 channel mirror shown in **Figure 2** represents a build-to-print design which features 4 microns of displacement with resolution of better than one hundredth of a micron.

In 1984 Itek began developing high performance cooled deformable mirrors (**Figure 3**) to address the needs of new generation high energy laser systems. The effectiveness of a laser mirror is measured by its ability to redirect incident radiation in a distortion free manner. The mirrors are required to reflect in excess of 99% of the laser radiation while surviving the remaining absorbed load as heat energy. To minimize such thermal distortion effects, the mirror must be necessarily be liquid cooled and made from thermally conductive materials such as silicon. All cooled deformable mirror structures include a polished mirror faceplate, an actuator population, a faceplate support structure in situ within the heat exchanger, and a stiff base

structure. The cooling is done by circulating a
liquid such as water in a compact heat exchanger
directly beneath the surface faceplate. Simply put,
a liquid such as water is flowed between two very
thin plates which are supported by a ribbed channel
or pin-post type structure. The liquid coolant is
used to "scrub" the heat away from the mirror
surface and effect mirror cooling. Typically, cooled
mirrors contain a 20 cm cooled aperture with
approximately 250 actuators arranged in a square
zonal array. Displacement and dynamic
performance of the cooled mirrors is similar to
those measured for uncooled components.

4. WAVEFRONT SENSOR TECHNOLOGY:

Fig. 3. Cooled Silicon Deformable Mirror (CSEM)

Developed originally at Itek in 1973, the grating lateral shear interferometer used a double frequency grating to produce the two sets of orthogonal gradients. The shearing interferometer as the name indicates is an interference based device. A diffractive element is used to produce multiple images or replicas of the reference at the image plane (Horwitz 1990). The image pupil is then imaged onto the detector array. Tilt can be determined by measuring the relative intensity variations in each of the detector subapertures. A modification in 1974 adapted the two frequency grating interferometer to be used with a white light reference source. In 1975 the AC lateral shear interferometer shown in **Figure 4** was developed which basically combined the Ronchi knife edge test with the shearing interferometer. A rotating radial grating was used to temporally modulate the optical beam and take advantage of heterodyne detection

Fig. 4. Shearing Interferometer Wavefront Sensor

schemes. Optical calibration requirements were virtually eliminated since the same grating was used to shear all the subapertures. Sensitivity to detector calibration is also eliminated since the wavefront gradient is proportional to the relative electrical phase.

5. REFERENCES

Ealey M A 1989 Proc. SPIE **1167** 48
Ealey M A and Washeba J F 1990 Opt. Engr. **29** 1191
Ealey M A and Davis P 1990 Opt. Engr. **29** 11
Hardy J W 1978 Proc IEEE **66** 651
Thorburn W G and Kaplan L 1991 Proc. SPIE **1543**
Horwitz B A 1990 Opt. Engr. **29** 1223

TABLE 1
ITEK DEVELOPMENTS IN DEFORMABLE MIRROR TECHNOLOGY

YEAR	DESCRIPTION	APPLICATION	TYPE	CHANNELS	CUSTOMER
1973-1974	Real Time Atmospheric Compensation	Turbulence Compensation (Imaging)	MPM	21	DARPA/RADC
1974	Deformable Mirror System	Turbulence Compensation (Imaging)	MPM	21	AFWL/MIT-LL
1974-1975	Real Time Atmospheric Compensation II	Image Compensation	MPM	21	DARPA/RADC
1976	Multidither Optical System	Multidither Techniques	MPM	241	MIT-LL
1975-1982	Compensated Imaging System	Turbulence Compensation (Imaging)	MPM	>200	DARPA/RADC
1979-1981	High Bandwidth Deformable Mirrors	Infrared Image Compensation	SADM	37	AFWL
1981-1983	Low Voltage Kduatuator DM	Turbulence Compensation	LVEM	1000+	DARPA/RADC
1982	Atmospheric Compensation Experiment	Turbulence Compensation (Outgoing)	MPM	69	MIT-LL
1983	Mid Scale DM Development	Turbulence Corrector Mid scale	LVEM	>500	DARPA/RADC
1984	Aberration Control System	HEL (ALPHA) Beam Cleanup	LVEM	100	TRW
1985	Short Wavelength Adaptive Technology	Turbulence Compensation	LVEM	241/341	MIT-LL
1985-1986	Field Scale DM Development	Turbulence Corrector Scaleup	LVEM	>2000	SDIO/RADC
1986	Ground Based FEL	HEL Brassboard	LVEM	69/97	Lockheed
1986-1989	Ground Based FEL Cooled DM	Turbulence Compensation (Outgoing)	CSEM	241/349	ARMY/MIT-LL
1987-1988	Phasar	Laser Phasing Brassboard	LVEM	69/97	Kaman/USAF
1987-1989	Thermal Blooming #1, #2	Thermal Blooming Experiments	LVEM	241/341	MIT-LL
1986-1989	Wavefront Control Experiment	STARLAB Flight Experiment	LVEM	69	AFWL
1986-1990	Integrated Wavefront Corrector	Ultra High Density Large Apertures	LVEM	10000+	SDIO/RADC
1984-1991	Silicon Deformable Mirror Technology	Cooled Mirror Development	CSEM	216/264	AFWL
1990	Sandia Optical Range Experiments	Turbulence Compensation (Imaging)	SELECT	241/341	AFWL
1990	Advanced Beam Control System	Beam Control Brassboard	SELECT	69/97	Hughes Danbury

TABLE 2
ITEK DEVELOPMENTS IN WAVEFRONT SENSOR TECHNOLOGY

YEAR	DESCRIPTION	APPLICATION	TYPE	CHANNELS	CUSTOMER
1973-1974	Real-Time Atmospheric Compensation	Turbulence Compensation (Imaging)	PMT Array	21	DARPA/RADC
1975-1982	Compensated Imaging System	Turbulence Compensation (Imaging)	PMT Array	>200	DARPA/RADC
1977-1980	Atmospheric Compensation Experiment	Turbulence Compensation (Outgoing)	PMT Array	69	MIT-LL
1984-1986	Aberration Control Experiment	HEL (ALPHA) Beam Cleanup	PbSe Array	100:800	TRW
1984-1985	Laser Wavefront Compensation System	Dye Laser Beam Cleanup	32x32 Reticon	64	LLNL
1985	EMRLD Adaptive Optics System	Excimer Laser Beam Cleanup	100x100 Reticon	132	AVCO
1985-1986	Field Scale Wavefront Sensor	Turbulence Compensation	64x64 Reticon	81+	DARPA/RADC
1986	Closed Loop Figure Sensor	Mirror Control and Diagnostics	128X128 Reticon	241:800	MIT-LL
1986	Wavefront Measuring Interferometer	Raman Look-through Experiment	256x256 Reticon	1024	MIT-LL
1987-1989	Wavefront Control Experiment	STARLAB Flight Experiment	PMT Array	69	Kaman/USAF
1987-1989	Wideband Wavefront Sensor	Thermal Blooming Experiments	Si Diodes	241	MIT-LL

Neural network applications in structural dynamics

M. E. Regelbrugge and R. Calalo

Structures Laboratory
Lockheed Palo Alto Research Laboratories
Palo Alto, CA 94304

Abstract. Neural network architectures and algorithms are discussed in application to the identification and classification of structural dynamics. The instant-learning, Probabilistic Neural Network paradigm is studied in examples illustrating dynamics identification in both time-domain and frequency domain. The network is shown to provide good identifications of complicated signals characteristic of structural dynamic motions.

1. Introduction

Effective utilization of active materials in adaptive structures depends on the proper synthesis of structural configurations, sensors, actuators and the means to direct these elements in harmony to achieve desired performance. Active materials promise a structure-integrated capability for large-scale, distributed sensing and actuation. Kinematically designed structures offer the necessary freedom to reconfigure and adapt load paths to changing conditions. Distributed and parallel-processing networks offer the needed capability to direct appropriate actuation and adaptation in response to external stimuli and changing conditions. One promising architecture for large-scale, distributed processing that appears ideal for adaptation is the neural network.

As in biological systems, artificial neural networks offer the means to quickly recognize a diversity of complicated patterns evident in external stimuli. Present neural network models attribute this capability to distributed storage of pattern information among a large number of highly interconnected yet simple elements. The network elements and interconnections typically have a limited number of parameters and weights that are adjusted through a learning process to yield repeatably correct classifications of input patterns. The highly parallel topology of the network admits fast response to a stimulus, while the distributed representation of learned pattern data has been shown in many cases to enable correct classification of input datasets whose contents are noisy or imprecise. These two properties have raised significant interest in applications of artificial neural networks to real-time recognition, classification and identification of real-world operational patterns of complicated systems.

This paper explores issues that arise in applying artificial neural networks to the identification of dynamic characteristics of structures. Important aspects of network integration with a dynamic structure are explored. Of particular interest are the synthesis of network input patterns appropriate to identify structural motions, and the selection of network schemes which preserve a robust autonomy in operation. Autonomy is critical for the practical use of neural networks to monitor dynamic characteristics of structures beyond immediate human accessibility, e.g. structures deployed in space.

Furthermore, fast-learning, autonomous networks may be employed to identify or estimate the dynamic characteristics of evolving structures (i.e. those with time-varying configurations or parameters).

The issue of autonomy in neural-network learning and operation hinges on the reliability of the learning algorithm to produce accurate identifications of observed patterns, where identification can be viewed as the expression of stimuli in terms of a limited set of useful (output) parameters. Inaccurate identifications can result in two ways:

1)   the learning algorithm can fail to adjust network parameters appropriately to identify a familiar stimulus, or

2)   the network may be faced with a stimulus sufficiently foreign as to preclude identification with any confidence.

In the first instance, the learning algorithm is not capable of configuring the network to respond to the observed system. In the second instance, the learning algorithm is not able to determine whether or not a stimulus is represented within the domain of the observed system. Naturally, some practical bounds exist on the degree to which any network, however sophisticated, can confidently identify unfamiliar stimuli. Autonomous learning requires the network to be able to differentiate between stimuli falling on either side of these bounds. One should note the complexity of such differentiation depends to a large degree on the constitution of the stimulus. For simple networks, stimuli should be simply constituted to avoid ambiguous or pathological identifications.

2. Neural Network Architectures

Several network architectures have been proposed for application to dynamics and signal identification tasks. Among these are perceptrons and other back-propagation (BP) networks used by Narendra and Parthasarathy (1990) and Cabell and Fuller (1991), Hopfield networks explored by Tank and Hopfield (1986) and Chu *et al.* (1990). Bayesian probability networks developed by Malkoff (1990) and Specht (1990) and Widrow's (1985) Adeline networks. Many of these networks have been applied to identification strategies resulting in adaptive active control.

Of these types of networks, perceptron, BP and Adeline networks learn by iteration. The topologies of the iteration networks are fixed initially and network-element interconnection weights are adjusted by a suitable learning algorithm to yield desired input-output behavior of the network. The learning algorithms are usually based on gradient descent methods such as steepest descent, conjugate gradient or, in certain special cases, Newton methods.

Unfortunate aspects of iterative learning schemes are that they may converge slowly and, during the process of convergence, they may produce incorrect identifications of previously learned input patterns. Furthermore, when converged, these networks will always yield identifications in terms of the learned pattern set, i.e. they have no capacity to recognize when stimuli fall outside the domain of their experience. This places a premium on adjusting network parameters over the entire expected domain of system performance. It also reduces the degree of autonomy in network learning and precludes adaptability to unforeseen evolutions of the system without explicit redirection

to undergo additional learning cycles. Finally, the establishment of robust network convergence criteria is absolutely critical to determine when the network becomes useful as an accurate identifier. This task is considerably complicated by uncertainties in system characteristics.

Hopfield networks are analog networks whose response to an initial stimulus converges to a stable, steady-state value which minimizes the energy state of the network. For the network to provide physically meaningful outputs, an energy functional must be synthesized in terms of the output quantities, and the network topology configured to mimic the synthesis of the functional.

Probabilistic Neural Networks

Bayesian, or probabilistic neural networks (PNN), as described by Specht (1990), alleviate the difficulties associated with fixed network topologies and iterative learning algorithms by instantly learning classifications based entirely on observations. Contrary to networks with fixed topologies that learn over time, PNNs learn instantly by increasing the number of neurons in the network. This is done by allocating a discrete neural element for each observed input pattern.

As illustrated in Figure 1, the PNN comprises three layers:

1) The *input layer* preprocesses sensory inputs distributes them to each element of the pattern layer

2) The *pattern layer* compares the input pattern to known patterns. Each element in the pattern layer (called a *pattern neuron*) contains a particular pattern vector from the network's experience (called an *exemplar*). Each neuron compares the input with its own exemplar, and outputs its own value of a local Gaussian probability density function centered about its exemplar. The output of ther i^{th} neuron is given by

$$p_i = \exp\left[-\frac{\|\mathbf{x} - \mathbf{x}_i\|^2}{2\sigma^2}\right]$$

where $\mathbf{x}_i$ is the pattern neuron's exemplar, and σ is a distribution scaling parameter. The value p_i is a measure of how much alike the input pattern and the ith neuron's exemplar are.

3) The output layer sums the contributions of the pattern neurons to determine the category to which the input belongs. Note that the categorization can be over many categories, not just the two implied by the hard limiter shown in Figure 1. The output layer also automatically computes the probability that the input pattern belongs to the same category as the summed pattern-neuron exemplars. This is given by $P(\mathbf{x} \in A)$ for all exemplars belonging to category A.

$$P(\mathbf{x} \in A) = \frac{1}{n_k} \sum_{i=1}^{n_k} p_i(\mathbf{x}) \qquad (\forall \mathbf{x}_i \in A)$$

If the input is not well characterized by the known exemplars (i.e. $P(\mathbf{x} \in A) << 1$) the network learns the new input by allocating a new pattern neuron with the present, unrecognized input as its exemplar. Thus, the next time an input pattern like the present one is presented to the network, the network will have learned to recognize and categorize it.
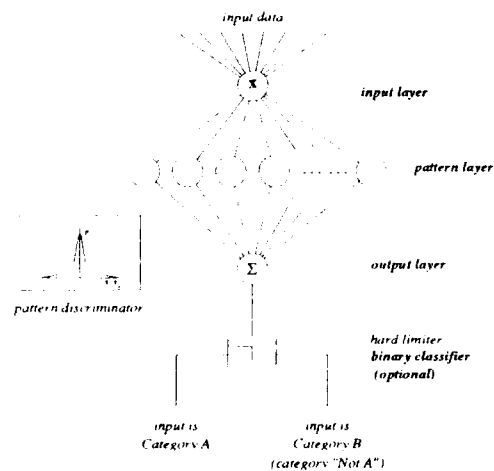
Figure 1. The Probabilistic Neural Network Architecture

A related network to the PNN is the Gaussian Potential Function Network (GPFN) described by Lee and Kil (1991). The GPFN contains additional parameters which are adjusted by back propagation. The GPFN is modeled by

$$p_i = \exp\left[-\frac{1}{2}(\mathbf{x} - \mathbf{x}_i)^T \mathbf{S}(\mathbf{x} - \mathbf{x}_i)\right]$$

$$S_{ij} = \frac{h_{ij}}{\sigma_i \sigma_j}$$

$$\mathbf{y}(\mathbf{x}) = \mathbf{C}\mathbf{p}(\mathbf{x})$$

where $\mathbf{y}$ is the output of the GPFN.

The GPFN does not learn instantly, but it offers a mechanism for adjustment without the necessity to expand the number of pattern neurons. The PNN is a specialization of the GPFN found by setting $\sigma_i = \sigma_j = \sigma$, $h_{ij} = \delta_{ij}$ ($\delta_{ij} = 1$ if $i = j$, $\delta_{ij} = 0$ otherwise), and $\mathbf{C}$ is established from the input pattern categorization.

The GPFN offers a practical a tradeoff between network order and learning time for a required accuracy.

3. Application to Structural Identification

The PNN or GPFN architectures may be employed to identify structural dynamic motions in several ways. Among these are schemes to identify the natural frequencies and modeshapes of the structural system (so-called *eigenstructure* identification, and schemes those that identify mappings between local histories of observed motions and the motions which follow them (the "future" motions). This latter scheme identifies a parametric analog of the state transition matrix, and is called *phenomenological* identification because identification is made exclusively by recording the observed input-output pairs.

The PNN was used to identify the eigenstructure of a simple structural model by presenting the network with input patterns consisting of a spatial distribution of the frequency response at frequencies corresponding to peaks in the response spectrum. The spatial distributions were presented as vectors normalized such that their length was made equal to the circular frequency at which they were measured. Thus, the PNN was able to construct a spatial-frequency map of motions in the structure.

Figure 2 shows the spectrum identified by the PNN eigenstructure identification algorithm for three of the members in the structure. The numbers adjacent to the peaks in the spectrum indicate the aggregate probabilities that the exact modeshape corresponding to the peak is embodied in the network's exemplars.
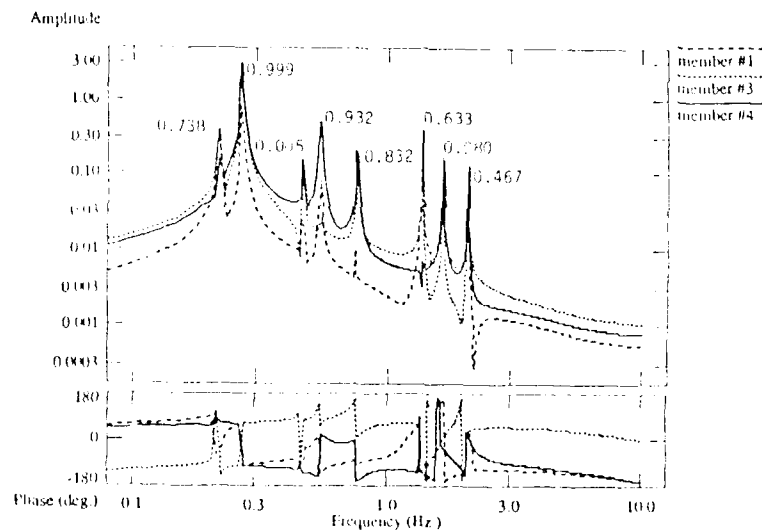
Figure 2. PNN Modal Identification from Frequency Response

Both the PNN and GPFN were also applied to the phenomenological identification of signals from an oscillatory system. In this application, the networks were presented with input patterns consisting of motion amplitudes at three previous sampling instants, and taught to classify these patterns in terms of the observed response at the next sampling interval. Thus when the network is presented with a learned motion history, it predicts the motion most likely to occur subsequently.

Results of the PNN and GPFN phenomenological identifications are shown in Figure 3, which illustrates observed and predicted motion histories for the two networks. Each network was allocated a maximum of 200 pattern neurons and the GPFN network was further allowed some 10,000 sample-iterations to converge to a predictive accuracy of 0.10%. As the figures show, a better predictive accuracy is obtained by the GPFN network albeit at a high cost in iteration.
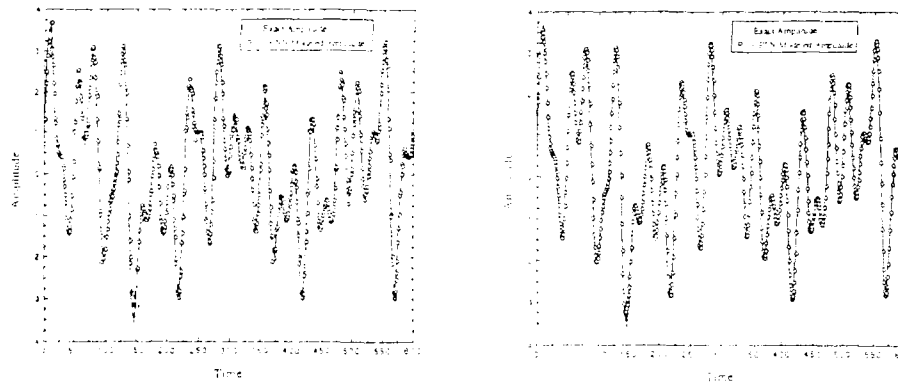
Figure 3. Phenomenological Identifications from PNN (left) and GPFN (right) schemes.

4. Conclusion

Probabilistic neural network schemes have been demonstrated for identification of motions typical of structural dynamic systems. These schemes require proper synthesis of input data if they are to make effective use of the neural network's pattern recognition properties. For example, a central issue in the application of such networks is the inherent tradeoff between how accurately they must identify observations and how fast they must respond to changing characteristics. This issue was illustrated by the differences in accuracy and speed observed between PNN (instant learning) and GPFN (iterative learning) identifiers. These characteristics and requirements need to be developed for applications on a system-specific basis.

Finally, one should note that networks of the type discussed can be applied to identify information locally within a large structure irrespective of global variations of response. Such a scenario may be especially useful to monitor integrity and pinpoint damage locations in very large structures.

References

Narendra, K. S. and Parthasarathy, K., "Identification and Control of Dynamical Systems using Neural Networks," *IEEE Trans. Neural Networks*, **1**, March 1990, pp. 4–27.

Cabell, R. H. and Fuller, C. R., "Pattern Recognition System for Automatic Identification of Acoustic Sources," *AIAA J.*, **29**, February 1991, pp. 180–186.

Tank, D. W. and Hopfield, J. J., "Simple 'Neural' Optimization Networks: An A/D Converter, Signal Decision Circuit, and a Linear Programming Circuit," *IEEE Trans. Circuits and Systems*, **33**, May 1986, pp. 533–541.

Chu, S. R., Shoureshi, R., Tenorio, M., "Neural Networks for System Identification," *IEEE Control Systems Magazine*, April 1990, pp. 31–35.

Malkoff, D. B., "A Neural Network for Real-Time Signal Processing," in *Advances in Neural Information Processing Systems* **2**, D. S. Touretzky, ed., Morgan Kaufmann Publishers, Palo Alto, CA, 1990, pp. 248–255.

Specht, D. F., "Probabilistic Neural Networks," *Neural Networks*, **3**, 1990, pp. 109–118.

Widrow, B. and Stearns, S. D., *Adaptive Signal Processing*, Prentice-Hall, Englewood Cliffs, NJ, 1985.

Lee, S. and Kil, R. M., "A Gaussian Potential Function Network with Hierarchically Self-Organizing Learning," *Neural Networks*, **4**, 1991, pp. 207–224.

Low level damping and hysteresis of damped structure

W Tse and D Werner

Lockheed Missiles and Space Co.

ABSTRACT: Active control of precision structure requires some damping for stability and low hysteresis for accurate positioning. Damping linearity of a built-up structure with and without constrained layer damping has been investigated down to sub-micron level. Hysteresis due to loading and unloading was measured. The measured damping shows little variation with vibration levels. The micro hysteresis time history indicates relaxation time is required for the structure to recover after unloading, and residual hysteresis does remain. The difficulty in measurement of damping and hysteresis at low levels is also addressed.

1. INTRODUCTION

The use of built-up precision structure in spacecraft results in low damping. To improve the performance and control of these systems, damping must be designed into the structure. There are concerns that the damping may decrease with the vibration level, thus the prediction or large amplitude test results may not be applicable to sub-micron vibration. Another concern for built-up structure with adhesive and epoxy is the micro-hysteresis that may exist after loading is removed. Precision pointing and positioning is more difficult to achieve if the structure does not return to the previous location after actuation. An aluminum honeycomb bonded cantilever structure 4 feet long was used to investigate low level damping and hysteresis concerns. Frequency and damping of the structure is measured before and after application of a constrained layer visco-elastic damping material. The displacement time history was monitored with displacement sensors during loading and after unloading to measure the residual hysteresis.

2. LOW LEVEL MEASUREMENT

Damping and hysteresis measurement for sub-micron displacement is a very challenging task. Response from ground and acoustic excitation can contaminate the measured data. The lower bound of the level is determined by sensors and force gauge resolution. The cantilever structure utilized has a fundamental frequency around 40 hz. For nano-meter displacement at this frequency, accelerometers must have a sensitivity below 1 micro-g. For vibration damping measurements, accelerometers from Wilcoxon Research with 0.2 micro-g sensitivity were used. Acceleration measurements of the floor indicated a 10 micro-g base input was possible. Ground vibration can cause amplified response of the test structure and limit the magnitude of low level measurement. The response to floor motion was attenuated by mounting the test structure on an optical bench supported by 1.5 hz air bag isolators.

Acoustic noise can induce sub-micron level vibration, especially on the bare structure with low damping. The noise producers can come from various sources such as fans, air conditioning, machinery, lights, wall motion, and air currents. Preforming the test in a vacuum chamber can solve this problem, but it is costly in terms of time and facilities use. Attenuation shielding around the test structure is not effective at the lower frequency range. Enclosures with wall densities over 5 lb. per square feet would be required to provide a 10 db reduction. A method called random decrement technique as suggested by Cole (1973) and further explained by Yang et al (1990) is used for the low level damping measurement. Random vibration inputs to the structure introduced by the acoustic noise creates random response at the accelerometers. The

acceleration time history is recorded and filtered to the desired resonance frequency. Whenever the data point crosses a certain threshold, a fixed length data segment after that point is shifted and summed. By summing and averaging many data segments, the random noise is smoothed. Figure 1 shows the initial random measurement and figure 2 shows the processed response for the structure without added damping. A clean decaying sinosoidal curve at the resonance frequency remains after the processing. The log decrement method can then be used to compute the percent critical damping.
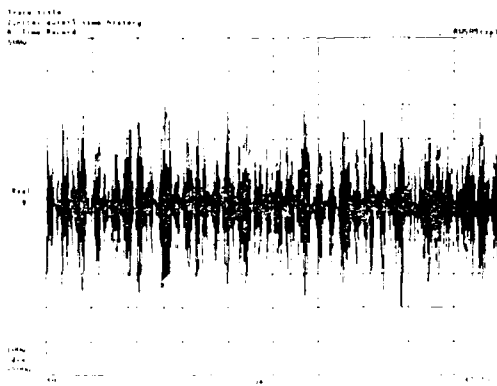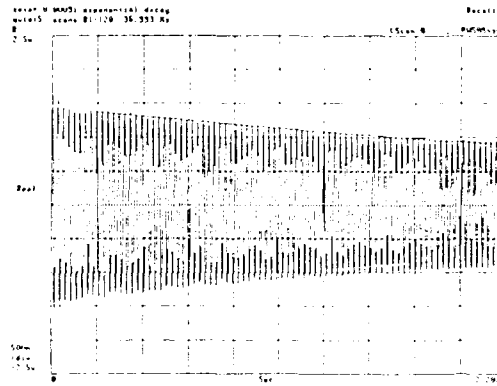
Fig. 1. Actual signal   Fig. 2. After processed

Hysteresis tests require direct displacement measurement. The Kaman 5100 differential sensor uses impedance variation caused by eddy currents induced in a conductive target located within range of the sensor. Two sensors are placed on opposite sides of the target plate, and motion of the plate caused impedance imbalance. This results in low noise and nano-meter accuracy for the static condition, and is used for the hysteresis measurement. The thermal drift of the sensor and the aluminum structure is a concern. Air currents can change the temperature of the structure, causing thermal gradients and bending. Temperature differences of 0.0015°F between the top and bottom plate can cause 100 nano-meter tip displacement. For the test, a foam enclosure was built to surround the test structure, sensors, and power amplifier. The power was turned on and the temperature was stabilized for 24 hours until the displacement time history from the sensor showed little drift. Since each hysteresis measurement requires less than 20 seconds, the error introduced from structural thermal distortion was deduced to be small.

3. DAMPING TEST RESULTS

The cantilever built-up structure has bending mode around 40 hz. and torsion mode about 70 hz. Figure 3 and figure 4 illustrate the mode shapes of the test structure for the 2 modes. The shorter edge of the pie shape structure is the anchoring edge of the cantilever. For large amplitude damping measurements, a shaker was used to excite the structure at the free edge. Narrow band sine sweeps were used to induce vibration. For lower amplitude excitation, shaker was attached to the anchoring block to move the whole table and introduced base motion to the cantilever. This allows larger force inputs to stay within the sensitivity range of the force gauge. The transfer function between the accelerometer and force gauge was used for circle fit to obtain the damping and frequency. Figure 5 shows the damping vs. vibration amplitude for the structure without added damping. The amplitude range varies from over 0.1 milli-meter to lower than 1 nano-meter. The damping varied from 0.115% to 0.134% for the bending mode, and varies from 0.068% to 0.077% for the torsion mode. Though the damping seems to

decrease slightly with decreasing amplitude for the bending mode and increase slightly for the torsion mode, the variation is not large enough to define a trend. The damping around 1 nano-meter acquired using the random decrement method has good agreement with that acquired with the shaker method.
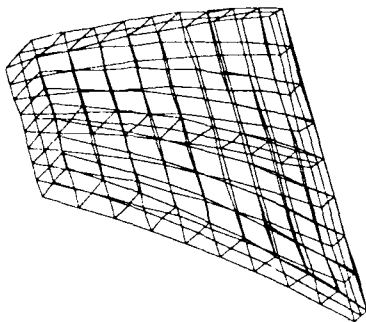
Bending mode

Torsion mode

Fig. 3. Bending mode

Fig.4. Torsion mode

Displacement (nano-meter)

Displacement (nano-meter)
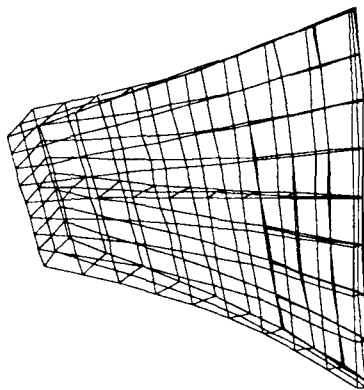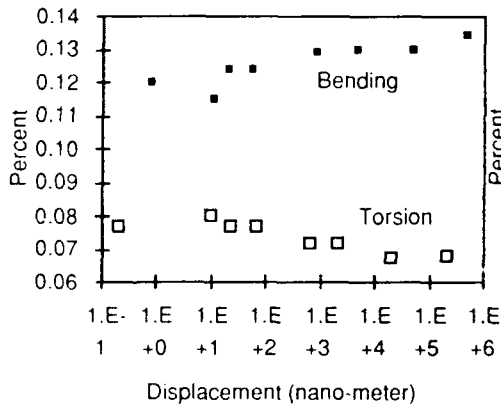
Fig. 5. Damping vs. Amplitude
Undamped structure
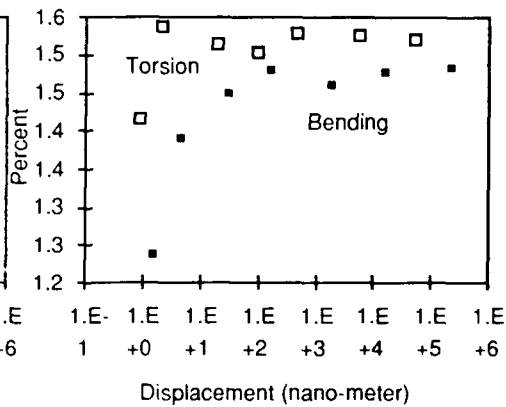
Fig. 6. Damping vs. Amplitude
Damped structure

For the damped structure, modal strain energy methods that have been used by Johnson *et al* (1981) were used to predict the damping. Prediction of the frequencies and damping correlated very well with the test results. Figure 6 shows the damping vs. vibration amplitude for the damped structure. The damping obtained with the random decrement method at amplitudes around 1 nano-meter is much lower than the damping obtained from the shaker method. The damping obtained using the shaker around 2 to 3 nano-meter does not indicate

the lower magnitude. Excluding the data point obtained with the random decrement method, the damping does not seem to have large variation with amplitude for the damped structure.

4. HYSTERESIS TEST RESULTS

Loading was applied at the tip of the structure to produce 33 microns of displacement. Different methods of loading were performed, including repeating sequences of loading with up down load reversal, load and hold for 2-3 seconds, and load and hold for 20 seconds. Figure 7 shows the hysteresis time history of a 20 seconds loading. The 33 microns of displacement decays down to 40 nanometers in about 5 seconds, and continue to move more than 25 seconds later. This decay phenomenon is present in all the hysteresis measurement performed on both the damped and undamped structure.
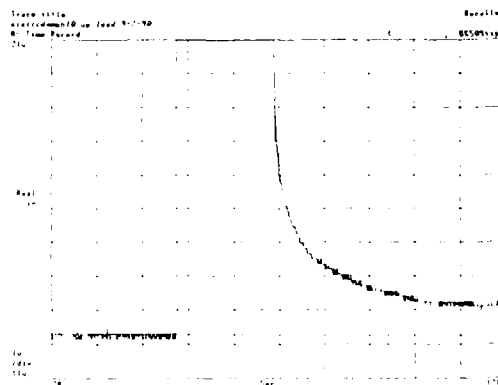
Fig. 7. Hysteresis time history

Table 1 shows the hysteresis as percentage of initial displacement at 5 seconds and 25 seconds after the load is removed. These results are the average of more than 10 measurements. For the 3 seconds loading of the undamped structure, some cases show no residual hysteresis after 25 seconds. For all the other loading method, and for the damped structure, residual hysteresis does remain. The longer loading time, and the damped structure produced larger residual hysteresis. These micro hysteresis effects must be considered in the design of active structure that requires precise positioning.

Table 1. Hysteresis test results

	Undamped		Damped	
	% of initial displacement			
	5 sec.	25 sec.	5 sec.	25 sec.
Repeating sequences	.03	.02	.08	.04
3 seconds load	.03	.01	.10	.02
20 seconds load	.15	.11	.27	.09

5. REFERENCE

Cole H A, *On-line Failure Detection and Damping Measurement of Aerospace Structures by Random Decrement Signatures*, NASA CR 2205, Mar. 1973

Johnson C D, Kienholz D A, Rogers L C, *Finite Element Prediction of Damping in Beams with Constrained Viscoelastic Layers*, Shock and Vibration Bulletin, No. 51, Part 1, May 1981, pp.78-81

Yang J C S, Qi G Z and Kan C D, *Mathematical base of Random Decrement Technique*, 8-th IMAC conference proceding, vol. 1, 1990

Structural control sensors for the CASES GTF

H.W. Davis [1] and A.P. Bukley [2]

[1] Ball Electro-Optics/Cryogenics Division (BECD)
[2] NASA/Marshall Space Flight Center (MSFC)

ABSTRACT: CASES (Controls, Astrophysics and Structures Experiment in Space) is a proposed Shuttle experiment to collect x-ray images of the galactic center and solar disk with unprecedented resolution. This requires precision pointing and suppression of vibrations in the long flexible structure that comprises the 32-m x-ray telescope optical bench. Two separate electro-optical sensor systems are provided for the ground test facility (GTF). The Boom Motion Tracker (BMT) measures eigenvector data for post-mission use in system identification. The Tip Displacement Sensor (TDS) measures boom tip position and is used as feedback for the closed-loop control system that stabilizes the boom.

1. CASES GTF DEVELOPMENT

The Controls-Structures Interaction (CSI) Advanced Development Facility (ADF) is under development a' 'larshall Space Flight Center (MSFC) for the purposes of supporting ground testing of future flight experiments, the investigation of advanced control and system identification methodologies, and structural dynamics studies. The baseline configuration of the facility is that of the Controls, Astrophysics, and Structures Experiment in Space (CASES), a proposed Shuttle-based flight experiment that will initiate on-orbit demonstrations of CSI technology. The experiment will provide active control of a 32-m extendible boom structure, using gas thrusters at the tip for pointing and angular momentum exchange devices (AMED) for active damping to suppress vibrations. The boom mechanically links an occulter plate at the boom tip with proportional counters located at the base to comprise an x-ray telescope. The controller goal is to provide accurate alignment of these devices for the purpose of x-ray observation of the galactic center and the Sun. Variations on this proposed experiment include a CASES without the x-ray devices (Controls And Structures Experiment in Space) or a free-flying version launched either by the Shuttle or an expendable booster.

The CASES ground test facility (GTF) will provide an environment in which advanced control laws, system identification techniques, failure detection and compensation schemes, real-time flight software, and experiment data handling techniques can be verified. Prototypes of

sensors, actuators, and flight computers can be functionally verified in the laboratory, as can actual flight hardware. Boom deployment and retraction dynamics, which will require active control, can also be investigated. Rapid reconfiguration capability in the laboratory will allow various flight configurations to be tested and verified, thus reducing development cost, time, and risk.

2.   FACILITY DESCRIPTION

The CASES GTF is located in the Load Test Annex high bay in Building 4619 at MSFC. The test article, the boom from the Solar Array Flight Experiment (SAFE) flown in 1984, is vertically suspended from a platform at the 62-m level. The disturbance system, comprised of two electromagnetic shakers, a tripod floated on air bearings, and an annular ring support surface, provides two translational degrees of freedom. A simulated Mission Peculiar Experiment Support Structure (MPESS), suspended from the center of the tripod through the annular ring support, interfaces the disturbance system with the test article to simulate a flight experiment interface with the Shuttle, MPESS, and the payload experiment. The boom supports a simulated occulting plate at the boom tip. The control objective of the flight experiment is to maintain alignment of the tip plate with the detector at the base of the boom on the Shuttle as the occulting plate is pointed towards a star to perform an x-ray experiment. Similarly, the ground experiment will strive to align the tip plate with the simulated detector at

the MPESS. Control authority will be provided by the AMEDs for vibration suppression and the bi-directional linear thrusters at the tip. Gravitational effects on the experiment will be processed out. Reference 1 provides a detailed description of the CASES GTF.

The key sensor systems to be used in the GTF are the Boom Motion Tracker (BMT) and the Tip Displacement Sensor (TDS) under development by BECD (Figure 1). The TDS will be used in closed-loop controller experiments as the feedback element, providing information on the precise alignment of the tip plate. The BMT will be used for the identification of boom mode shapes. Initially, the BMT data will be processed post-facto.
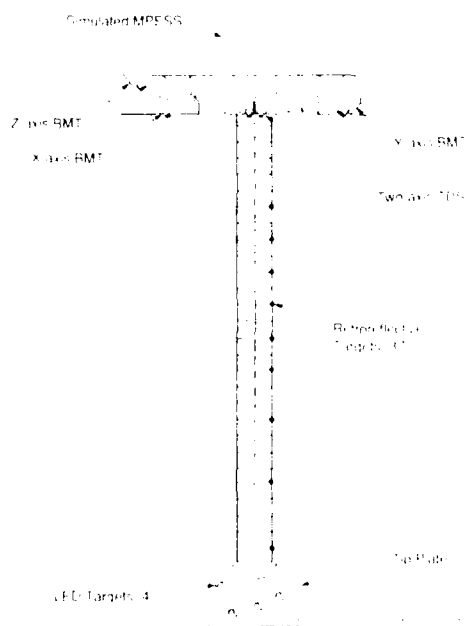
Fig. 1.

Future upgrades to the facility will provide the capability to use BMT data real-time in closed-loop control.

3.   ROLE OF THE RAMS SENSOR

The Remote Attitude Measurement Sensor (RAMS) was designed by BECD under IR&D to measure dynamic behavior of large, flexible space structures. RAMS provides an unobtrusive sensor with update rates, accuracies, and target capacities which exceed present technology. This capability is needed for both system identification and control feedback applications in space.

In the CASES GTF, the BMT observes and records dynamic behavior of the flexible boom structure. Three single-axis sensors are mounted at the base of the cantilevered boom and each monitors the translational displacements (within its sensitive plane) for 37 reflective targets distributed along the length of the boom. The X and Y sensors are offset equidistant from the base of the boom and oriented such that their sensitive planes are orthogonal to each other. The third (Z) sensor is offset further from the boom but along the same radial line as the X sensor. The increased offset distance improves sensitivity to z-axis motion, which is calculated by subtracting the effect observed by the X sensor. The BMT illuminates and monitors targets at ranges up to 32 m while measuring displacements to accuracies of 0.25 mm for the x and y axes. The Z sensor is less sensitive and measures displacements to an accuracy of 6 mm. Expected target motion for all three sensors is ±25 cm. The BMT updates the position of each target at 100 Hz. Displacement data is output to the CASES control processor in the form of BMT pixel number, with data for all targets multiplexed in digital format.

The TDS provides position feedback for the closed-loop control system that maintains tip position. Two single-axis sensors are mounted near the base of the cantilevered boom and measure 2-axis translational displacements for the four (4) light-emitting diode (LED) active targets. The targets are arranged in a fashion that ensures no overlap of targets in either sensed direction. The TDS observes the four targets at a range of 32.7 m and measures displacements to an accuracy of 0.2 mm. Update rate is selectable between 20 and 500 Hz. Displacement data is output to the CASES control processor in the form of TDS pixel number, with data for each target assigned to a dedicated line and in analog format. A ±10 V change in signal corresponds to a ±25 cm displacement of a TDS target.

4.   RAMS IN THE GTF

The RAMS design is derived from proven space sensor technology. The electronic design concepts and interpolation algorithms for RAMS have been demonstrated in space hardware, including the Retroreflector Field Tracker (RFT) that was flown on the Shuttle in 1984 and a variety of Ball-built star trackers. RAMS consists of a simple electro-optical design. It uses a cooperative light source (typically an LED) to illuminate reflective targets within its field of view (FOV). The reflected images are focused onto a linear charge-coupled device (CCD) detector by a cylinder lens to produce a line image. Displacement of a target causes the focused image to shift position on the CCD, giving an accurate indication of the angular displacement. Knowing the range of the target, translational displacement can be calculated.

RAMS (Figure 2) uses a CCD detector with 1 x 2,098 pixels and proprietary BECD interpolation algorithms that permit centroiding of target images to approximately 2% of a pixel. High update rates are achieved by pipeline processing of the CCD data in analog form. RAMS can provide resolution to better than 1:100,000 and update rates of 500 Hz for each of 50+ targets.   It uses off-the-shelf, low-cost parts such as Nikon OEM lens, Newport alignment flexures, Kodak CCD detectors, and AND brand light-emitting diodes. A detailed description of RAMS and CASES is provided in Reference 2.
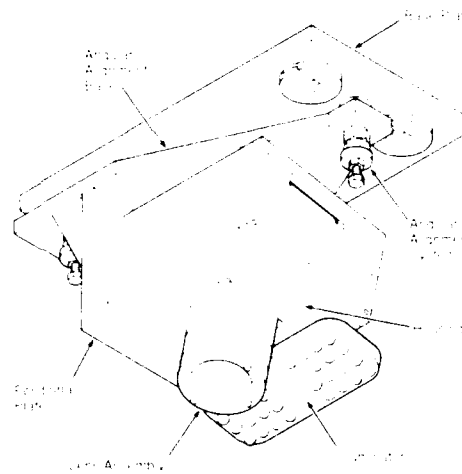
Fig. 2.

4.1 BMT Design

The BMT X and Y sensors are oriented such that their detectors are in the same plane as the boom and tilted at a slope that provides proper focus for every target. (This is guaranteed by the "Scheimpflug" condition.) The required FOV of each sensor (approximately 20 deg) is determined by the viewing geometry (e.g., offset distance from boom, distance to nearest and farthest targets, expected range of motion). The actual FOV exceeds this amount and is based on the detector pixel size, number of pixels, and the focal length of the lens (85 mm). The achievable resolution is determined by the angular subtense of each pixel and the degree to which subpixel interpolation can be achieved. Target distance varies from 3.6 m to 31.3 m. The major design challenge for the BMT is achieving the desired image shape and sufficient

optical return signal from the farthest target. This is influenced by the radiometric characteristics of the illuminator and by the size, shape, and retroreflective properties of the target material.

The BMT targets are made from 3M-brand Model 2000X retroreflective tape. This high-gain material contains microscopic corner cubes laminated beneath a protective film. The targets are square-shaped, as viewed by each sensor, and sized to subtend a specified angle within the FOV. Thus, target size will vary with range, but image width will remain constant. This condition is necessary in order to maintain precision in the interpolation algorithms. Incident light on this tape material is retroreflected with a luminance factor of 3000 and primarily within a 1.1 deg conical beam (full angle). The targets are illuminated by an array of 32 LEDs mounted on each sensor head. The illuminators must be positioned near the optical axis of the sensor because of the retroreflective nature of the targets. Most of the LEDs are aimed at the farthest target. The quasi-Gaussian beam shape provides an appropriate amount of radiance on the mid-range targets. Some LEDs are tilted towards the upper targets to illuminate them. Each LED is rated at 13 candelas and has a beam divergence of approximately 4 deg.

The sensor head is comprised of a thick-walled aluminum box on which a lens assembly is mounted. The lens assembly includes the off-the-shelf Nikon camera lens which is fitted with a cylinder lens to provide line images and a wide-band filter to reduce background illumination. The CCD detector, preamplifier circuitry, and detector mounting hardware are installed within the sensor head. Proper orientation and positioning of the detector with respect to the lens is crucial to accurate measurement of target position. The Kodak KLI-2103 CCD detector has 2,098 pixels, each 14 x 14 µm in size. This detector was selected for its low noise characteristics, high responsivity, and uniformity of photo-response between adjacent pixels. Data is transferred at rates exceeding 1 MHz and handed off to a separate electronics box containing the analog and digital processing circuitry. The analog pipeline processor detects the presence of targets, interpolates the position of each to within 2% of a pixel, and tags the data with a target number. This analog data is converted to digital form and multiplexed prior to output. The BMT data interface is a 32-bit parallel data word which is read by the CASES control computer upon generation of a strobe by the BMT.

4.2   TDS Design

The TDS sensors are mounted orthogonal to each other and observe the four (4) LED targets mounted on the upper surface of the tip plate. Using the known locations and unique pattern of the targets with respect to the tip plate, the motion of the tip plate reference point (i.e., center of mass) can be monitored. The required FOV of each TDS sensor (2.3 deg) is

determined by the target range, target spacing, and the maximum expected motions of ±25 cm. The actual FOV (15 deg) is larger than necessary because of the intentional use of common detectors for both the TDS and the BMT. Use of a slightly longer (105 mm) focal length lens for the TDS improves resolution compared to the BMT. The major design challenges for the TDS are high update rate, target range, and high resolution. The use of active (LED) targets rather than passive (retroreflector) targets improves the radiometric performance significantly and allows the shorter integration times needed for higher update rates. The four TDS targets consist of individual LEDs fitted with an adjustable spherical lens that expands the illumination beam to 15 deg. Beam divergence is based on the angular offset with respect to the sensor head plus an expected tilt of the tip plate of ±5 deg.

The TDS sensor head is identical to the BMT sensor, with two minor exceptions. There are no illuminators on the TDS sensor because active targets are used. The detector mounting block holds the detector normal to the optical axis (rather than tilted) because the targets are equidistant in range and require the same focal length. The TDS uses eight dedicated analog circuits to transmit analog position data for each of the four targets measured by each of the two sensor heads. Each target has a unique offset voltage at its stationary position, such that maximum resolution can be gained from the ±10 V range of the analog output.

5.   CURRENT STATUS

Fabrication and checkout of the BMT and TDS hardware are still in progress, so test results for these systems are not yet available. However, testing of the RAMS Prototype developed by BECD under IR&D has produced early, optimistic results. The Prototype has detected and tracked a retroreflective tape target at 31 m range under bright interior lighting conditions. Tracking of an LED target like that planned for the TDS has also been demonstrated. The Prototype has also demonstrated linearity across a single pixel as high as 1% of a pixel. (The TDS and BMT specifications can be met with errors equivalent to 5% of a pixel.) The new sensors are expected to show significant improvements in performance, due to larger pixel size, higher responsivity, improved uniformity of photoresponse, and lower noise from detector and processor circuitry. Tests results from these sensors are expected by Feb. 1992.

References:
1.   Jones, V.L., Bukley, A.P., and Patterson, A.F., "NASA/MSFC Large Space Structures Ground Test Facility," Proc. AIAA Guidance & Control Conf., New Orleans, LA, August 1991.
2.   Davis, H.W., Sharkey, J.P., and Carrington, C.K., "Structural Control Sensors for Control, Astrophysics, and Structures Experiment in Space (CASES)," Advances in Optical Structure Systems, Volume 1303, Proc. SPIE. Orlando, FL, April 1990.

Evaluation of acrylate and polyimide coated optical fibers as strain sensors in polymer composites

L. D. Melvin*, R. S. Rogowski*, M. S. Holben**, J. S. Namkung‡, K. Kahl†, J. Sirkis†

*NASA Langley Research Center M/S 231 Hampton, VA 23665
**Lockheed Engineering & Sciences, NASA Langley Research Center Hampton, VA 23665
‡College of William and Mary, NASA Langley Research Center Hampton, VA 23665
†Department of Mechanical Engineering, University of Maryland, College Park, MD 20742

ABSTRACT: Polyimide and acrylate coated optical fibers were embedded in 8 ply unidirectional graphite/epoxy composites. Strain was measured under tensile and cyclic loads with both surface mounted resistive strain gauges and the embedded optical fibers using an Optical Phase Locked Loop. The peak to peak amplitude of the acrylate sensor was 40% smaller in magnitude than that of the polyimide sensor. The acrylate sensor failed to respond between 100,000 and 120,000 cycles. Optical microscopy showed dramatic differences in the interfacial condition of the two sensor systems tested.

1.0 INTRODUCTION

The successful long term implementation of "smart", "adaptive" or "intelligent" structures will strongly depend on development of sensor systems that can accurately and consistently measure both static and dynamic changes to structural materials over their predicted lifetimes. The sensor system is composed of a chemically doped SiO_2 based core and cladding housed in a protective jacket. The optical fiber jacket or coating interaction with the host material plays a major role in determining the proper transfer of load from the structure to the optical fiber. Originally, Butter and Hocker (1978) demonstrated the ability to measure strains of $<0.4 \times 10^{-6}$ on a cantilever beam structure using an optical fiber. Since then many applications of this technology have been extended to making strain measurements using multimeasurand fiber configurations. This work focuses on determining what damage mechanisms cause hysteresis or complete optical signal loss when embedded sensors are subjected to large repeated load levels. The goals are to find optimum optical fiber coating/host material interface properties that will ensure sensor/host integrity over the structure's lifetime. Preliminary work has been performed on two "off the shelf" optical fibers, acrylate and polyimide coated.

2.0 EXPERIMENT

2.1 Sample Preparation

Strain measurements were made on two graphite epoxy composite samples using either a
Corning CPC3 50/125/250 μm (core/cladding/coating o.d.) acrylate or a Fiberguide
Thermocoat 50/125/145 μm polyimide coated optical fiber. Both composite samples
contained an acrylate and polyimide coated fiber for making interfacial comparisons using
microscopy after testing. The optical fibers were laid parallel to the 0° graphite fiber direction
between the fourth and fifth plies of an 8ply unidirectional composite. The composite
specimens were made of Hercules Magnamite graphite-epoxy pre-peg material following
ASTM standards (D 3039 - 76.). The optical fibers were approximately 0.63 cm apart placed
in the center of the 2.54 cm wide composite. Each specimen was approximately 30.5 cm long
and 0.11 cm thick. Teflon tubes were threaded over the optical fiber pigtails and embedded
0.63 cm into the laminate to provide protection during the cure process and subsequent
handling. The pigtails exiting the composite were fusion spliced to FC/PC connectors and
connected to the Optical Phase Locked Loop (OPLL). The samples were fatigue loaded in
tension at 5 Hz to 85% of their average 7650 lb ultimate tensile strength (UTS). Failure was
predicted to occur at 100,000 cycles for an AS4/3501-6 composite with $[0]_8$ layup.

2.2 Optical Setup

A schematic diagram of the OPLL is presented in Fig. 1. The electronics in this diagram are
similar to those from Heyman (1982) and Rogowski *et al* (1986), except that this system is
operated at a nominal frequency of 300 MHz, and a sinusoidal waveform is generated by the
oscillator. A voltage controlled oscillator (VCO) is used to directly modulate a diode laser and
to provide a reference signal to a double balanced mixer. The laser radiation passes through a
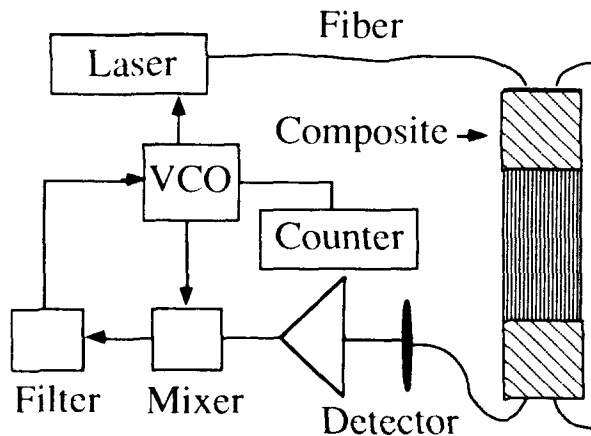
multimode embbeded optical
fiber, is detected, amplified,
and mixed with the reference
signal. The phases of the two
signals are maintained at
quadrature by feedback of the
DC error voltage from the
mixer to the VCO. The filter
removes the radio frequency
component coming from the
mixer. Any change in the
phase of the modulation is

Fig. 1. Schematic of optical phase locked loop and
composite with embedded optical fibers

expressed as an error voltage at the mixer and is compensated by a change in the modulation frequency. A change in path length, ΔL, of the optical fiber will produce a change in frequency, ΔF, according to Eq. 1. where L is the effective path length (optical plus

$$\frac{\Delta F}{F} = -\frac{\Delta L}{L} \qquad (1)$$

electronic) and F is the nominal frequency value. The VCO sensitivity is 1 μV per Hz In this experiment the error voltage and load cell were recorded with both a unix based data acquisition system and strip chart recorder to indicate strain.

3.0 RESULTS

A 2.5 second sample was recorded every 15 minutes over the entire fatigue test for both acrylate and polyimide coated sensors. The optical response to the applied cyclic 5 Hz load for the acrylate coated sensor is shown in Fig. 2. The frequency curve shows good agreement with the applied load for the sample set taken around 108,000 cycles. The peak to peak sensor response for the acrylate sensor was 40% lower than that of the polyimide sensor for the same 85% UTS load level. The acrylate sample however failed to respond between
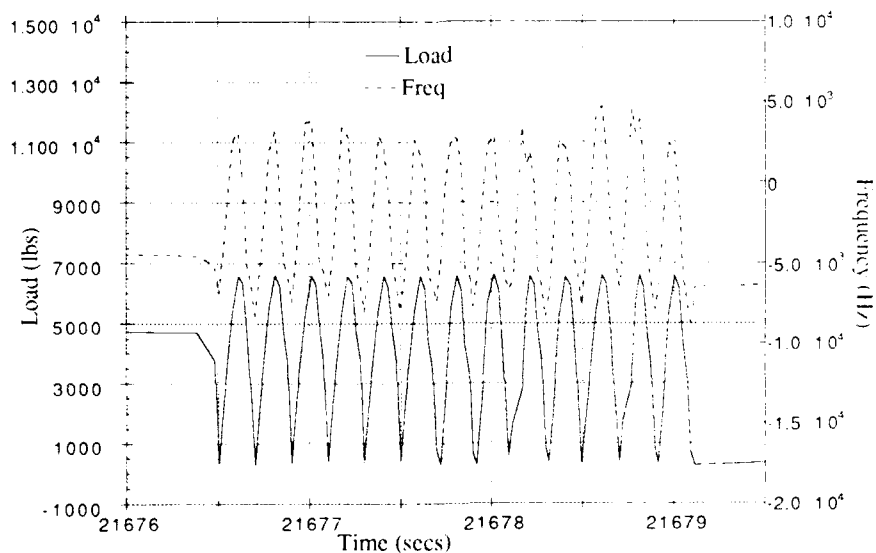
Fig 2. Applied cyclic load and optical fiber response
versus time for the acrylate composite system

100,000 and 120,000 cycles. Microscopy was performed after losing the acrylate optical signal. The polyimide sensor responded very similarly to the acrylate frequency curve shown in Fig. 2. The polyimide sensor continued to respond without any noticeable loss in peak to peak amplitude well beyond 139,000 cycles. A dc drift was observed in both tests and was attributed to a noisy detector power supply. Fig. 3 and 4. show cross sections of the acrylate and polyimide coated fibers respectively. The arrow in Fig. 3. points out cracks along the primary and secondary acrylate coating interface. Slippage of the glass along this interface could account for the reduction in peak to peak amplitude for the acrylate system. The polyimide coating system in Fig. 4. appeared to be well bonded to both the composite and the glass fiber.

Fig. 3. Acrylate coated fiber cross section after 122,000 cycles

4.0   CONCLUSIONS

Preliminary optical strain measurements were made on two composite samples with an embedded acrylate and polyimide coated optical fiber. The polyimide system withstood 139,000 cycles without exhibiting any fatigue related damage. The acrylate system however failed between 100,000 and 120,000 cycles. Microscopy showed interfacial damage which possibly contributed to the acrylate fiber response failure.
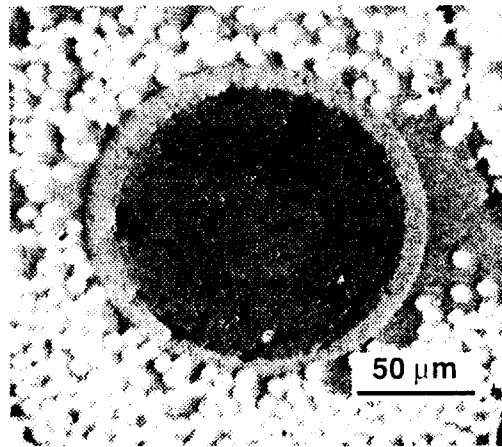
Fig. 4. Polyimide coated optical fiber cross section after 139,000 cycles

References

Butter C D and Hocker G B 1978 *Appl. Opt.* **17** (18) pp 2867-2869
Heyman J S 1982 U.S. Patent **4343242**
Rogowski R S, Heyman J S, and Holben M S, 1986 *Proc. SPIE* **663** pp 86-89

Embedded optical fiber sensors for monitoring cure cycles of composites

Mark A. Druy, Paul J. Glatkowski, and W. A. Stevenson

Foster-Miller, Incorporated, 350 Second Avenue, Waltham, MA 02154

ABSTRACT: The real-time in situ monitoring of the cure cycle of an epoxy resin/graphite fiber composite was monitored in an autoclave. In this work a short length of sapphire fiber was used as an embedded fiber optic sensor. The sapphire sensor was connected to infrared transmitting zirconium fluoride optical fiber cables which penetrated the wall of the autoclave and interfaced to a Fourier transform infrared spectrometer (FTIR). The results indicate that this technique is suitable for monitoring the degree of cure of the laminates throughout the entire cure cycle.

1. INTRODUCTION

The repeatable processing and manufacture of advanced composite materials is perhaps the major obstacle inhibiting the widest possible acceptance of resin matrix composites as aircraft structural elements. Considerable research and development has been expended in government, university and aerospace laboratories in efforts to improve the quality and reliability of this class of materials. We address this critical issue from a uniquely fundamental standpoint. The experimental technique involves the use of infrared spectroscopy and the development of infrared transmitting optical fibers as sensors for monitoring the cure of graphite fiber/resin matrix materials. In this paper we report the use of this experimental technique for monitoring the extent of cure in an autoclave environment and the correlation of the spectal data to mechanical test data.

The Foster-Miller fiber optic method is unique because it tracks a fundamental aspect of cure - the vibration of atoms and molecules associated with the dissociation and formation of chemical bonds which occur during the cure process. The information from the sensor is directly related to the chemical state of the resin.

2. EXPERIMENTAL PROCEDURES

The procedures used to lay-up the sensor fiber in the composite laminate, cure the laminates, and acquire the infrared spectra have been described in previous publications (Druy 1991). The composite system used was Fiberite 934 which consists of graphite fibers and a TGDDM/DDS epoxy. This resin system is known as a 350°F resin and is used in a number of aerospace structures. The principal components of the resin are Tetraglycidyl 4, 4' diaminodiphenyl methane epoxy (TGDDM) and 4, 4' diaminodiphenyl suf'₀.. e (DDS). Additionally there is present a catalyst, $BF_3 : NH_2C_2H_5$.

In an effort to determine if the spectral data obtained during a cure cycle could be used to determine extent of cure in an epoxy laminate, the cure cycle was altered by decreasing the duration of the 350°F hold. Spectral data was obtained during these runs and the panels were subjected to an Iosipescu shear test. This test utilizes a double-V-notch test specimen and is used to measure both the in-plane modulus and strength of a laminate. Figure 1 shows the configuration of the test specimen. This test is supposed to be sensitive to the degree of cure of the epoxy. Five test specimens were cut from each laminate that was cured.
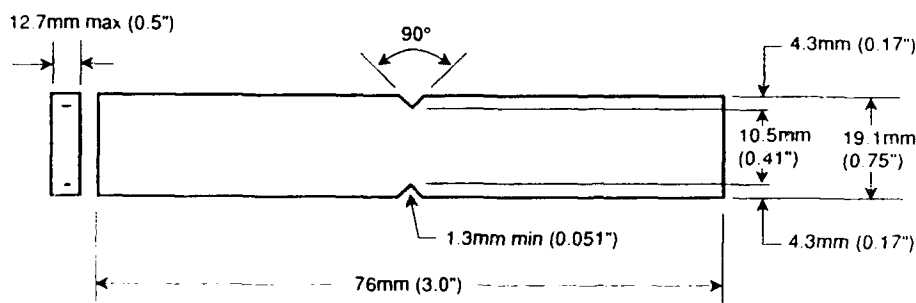
Figure 1. Configuration of Test Specimen for Iosipescu Shear Test

The standard cure schedule was a ramp from room temperature to 250°F, followed by a 45 min hold at 250°F, followed by a ramp to 350°F, followed by a hold at 350°F for 120 min. The altered cured schedules (which differed only in the extent of the 350°F hold) are shown in Table 1.

3. RESULTS AND DISCUSSION

The cure of this epoxy system involves two mechanisms (Morgan 1987). The first mechanism involves reaction of the epoxide ring with the amine functionality. This reaction occurs at relatively low temperature. The second mechanism involves the formation and

breakage of aliphatic C-H bonds which are indicative of subsequent cross linking reactions which build up the epoxy network.

Table 1. Cure Schedule For Composites

Sample	Interrupt point in Cure Cycle
1	Standard Cure, 120 min hold at 350°F
2	1 min hold at 350°F
3	105 min hold at 350°F
4	90 min hold at 350°F
5	75 min hold at 350°F
6	60 min hold at 350°F
7	15 min hold at 350°F
8	30 min hold at 350°F
9	45 min hold at 350°F

These spectral changes have been observed with the fiber optic infrared cure monitoring system (Druy 1991). In particular two peaks in the infrared are useful for determining the extent of cure during the late stages of the cure cycle. During the 350°F hold, the absorption at 2995 cm^{-1} decreases while the absorption at 2830 cm^{-1} increases.

For a Fiberite 934 laminate, a shear strength of 17 - 18 ksi is expected (Zimmerman 1991) for a fully cured specimen. Sample 4 (90 minute hold at 350°F) achieved this value. The expected values of ultimate shear strength were not reached for samples 1 and 3 because some of the panels appeared to be damaged during cutting. Comparison of the spectral data for samples 1 and 3 indicated that no further increase in the intensities of the C-H absorbance peak at 2830 cm^{-1} could be detected after 60 - 75 minutes into the 350°F hold. Similarly observation of the data for a 30 minute hold at 350°F, indicated that the C-H intensity at 2830 cm^{-1} was still increasing. This trend was confirmed by examing the data for a 60 min. hold (Sample 6). In a similar manner, the trend of the C-H absorbance peak at 2995 cm^{-1} can be analyzed. Its peak intensity tends to decrease up to ~ 90 min into the 350°F hold. The relationship between these absorbance peaks and the ultimate shear strength data is shown in Figure 2.

4. CONCLUSIONS

In conclusion, the monitoring of the spectral changes during cure of a TGDDM/DDS epoxy resin/graphite fiber composite can be correlated to the mechanical properties of the cured

laminate. This cure cycle suggests that for the given laminate dimensions (20 plies, 5 in. x 6 in.) full cure is obtained by the time a 90 min hold at 350°F occurs. Therefore, based on the data obtained with the sapphire sensor, the use of the FTIR cure monitoring system for standard epoxies might be best applied to determining whether a substantial amount of an undercured region exists in a part of complex geometry (i.e substantially differing thicknesses across the part).
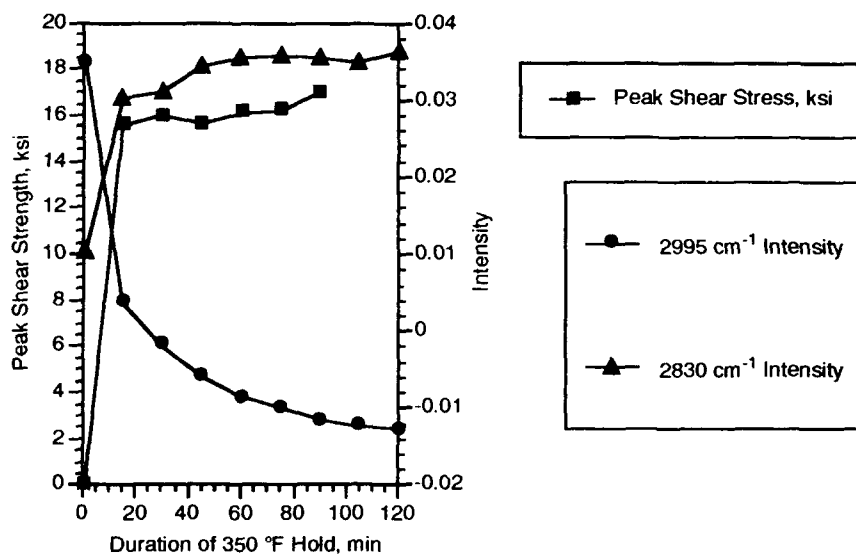
Figure 2.   Relationship Between C-H Absorbance Intensities And Shear Strength

5. ACKNOWLEDGMENTS

6. REFERENCES

Druy M A, Glatkowski P J, and Stevenson W A 1991 *SPIE Proceedings Vol. 1437 Applied Spectroscopy in Materials Science* pp 66-74 and references therein.

Morgan R S and Mones E T, 1987 *J. Appl. Poly. Sci.* **33** 999

Zimmerman D, Fiberite Inc., 1991 *private communication*

Fibre optic technique for simultaneous measurement of strain and temperature variations in composite materials

W.Craig Michie *, Brian Culshaw*, Scott S.J. Roberts**, Roger Davidson **

* University of Strathclyde, Glasgow, G1 1XW, UK.

** AEA Technology Harwell Laboratory, Oxon, OX11 0RA, UK.

ABSTRACT

A technique based upon the differential sensitivities of dual mode and polarimetric sensing schemes is shown to be capable of resolving simultaneously temperature and strain variations to within 20 $\mu\epsilon$ and 1 K over a strain and temperature excursion of 2 mϵ and 45 K.

Introduction.

Polarimetric and Dual moded sensing schemes have been reported as being suitable candidates for achieving high resolution measurements of strain and temperature variations (Butter, Kim). In the present experiment both techniques are used to simultaneously interrogate one single sensor in order to discriminate between the effects of temperature and strain.

The fibre sensor can be characterised in terms of the necessary temperature or strain variations required to produce a 2π radians rotation in the polarisation state. Thus the sensitivity of the fibre to temperature and strain variations (α_{Tpol} or α_{Tdual} (rads.K^{-1}) and $\alpha_{\epsilon pol}$ or $\alpha_{\epsilon dual}$ rads.$\mu\epsilon^{-1}$) can be determined.

Simultaneous interrogation of a sensor with both techniques permits two independent variables to be measured at the same time, provided that the relative sensitivities of the two sensing schemes are different. The application of a temperature and/or strain change to the sensed region will produce a phase change in the dual mode and polarimetric signals. Measurement of the phase changes allows the temperature and strain to be recovered corresponding to the relation,

$$\begin{bmatrix} \delta\epsilon \\ \\ \delta L \end{bmatrix} = \begin{bmatrix} \alpha_{\epsilon pol} & \alpha_{Tpol} \\ \\ \alpha_{\epsilon dual} & \alpha_{Tdual} \end{bmatrix}^{-1} \begin{bmatrix} \delta\varphi_{pol} \\ \\ \delta\varphi_{dual} \end{bmatrix} \qquad (1)$$

Experimentation.

Linearly polarised light from a laser diode ($\lambda = 820$nm) was combined with the output of a HeNe laser ($\lambda = 633$nm) and launched into a polarisation preserving fibre. This fibre was then subjected to controlled strain and temperature cycling and attempts were made to recover the sensed changes from the optical measurements. A typical example of temperature/strain recovery is displayed in Figure 1. Over the measurement range it can be seen that good agreement is observed between the applied and recovered variations. In general the estimation of the extension applied to the fibre is better than 20 μm. Temperature measurements are seen to be accurate to within 1-2 degrees in most instances and better than 5 degrees overall. In all of the measurements the general trend is correctly predicted. Over the increasing portion of the strain cycle the measured fibre extension was found to be 1694 μm with a corresponding temperature change of -44.9 C. This is in excellent agreement with the applied changes of 1700 μm and -45 K. The corresponding values for the relaxation cycle are -1700 μm applied extension versus -1689 μm measured and - 3 C applied versus - 4.2 measured which again indicates good experimental agreement.

Temperature/Strain Recovery with Embedded Sensor.

A uni-directional composite bar 650mmx25mmx5mm was press moulded from 40 layers of Ciba-Geigy 914C-TS-5-42 pre-preg. A single length of elliptical core polarisation maintaining fibre was located centrally between the 2nd and 3rd layer of the sample running axially and parallel to the reinforcment. This sample was subjected to simultaneous three point bending and thermal cycling. An example of the data recovery from such a measurement is indicated in Figure 2.

It is clear from this measurement that while the general trend of the tempeature and strain changes is correctly indicated, the data recovery from this experiment is less precise than in the unembedded case. The

reasons for this are the following. Firstly the sensing length of the fibre is much shorter than that used in the unembedded experiment. The sensitivity to the temperature changes is therefore reduced introducing errors in the calibration for thermal changes. Secondly the fibre used in the embedded experiment was taken from a different batch to the previous fibres and it had sensitivities which lead to a less well conditioned set of simultaneous equations describing the temperature/strain variations (Michie). Thirdly it is difficult to obtain an exact reference measurement of the thermal and strain changes within the composite sample. The fibre measurements were calibrated against estimations of temperature/strain changes taken from surface readings.

Conclusions.

Temperature/strain recovery with a single sensing length of optical fibre has been demonstrated to be successful to within 20 $\mu\epsilon$ and 1 K over a strain and temperature excursion of 2 mϵ and 45 K. The technique has been applied to embedded sensing where although a reduced sensitivity was observed this was not a direct result of the embedding process and the indications are that this technique is a suitable for temperature/strain recovery in composites.

Acknowledgements.

References.

Butter C.D., Hocker G.B. 'Fibre Optics Strain Gauge.' Applied Optics 17(18)
1978 pp2867-2869.

B.Y. Kim. J.N. Blake. S.Y. Huang. H.J. Shaw 'Use of Elliptical Core Fibres for Two-mode Fibre Devices' Opt. Lett. vol.12. p729.1987.

Michie W.C., Culshaw B.C., Roberts S.S.J., Davidson R. 'Fibre Optic Technique for Simultaneous Measurement of Temperature and Strain.'SPIE Boston 1991.
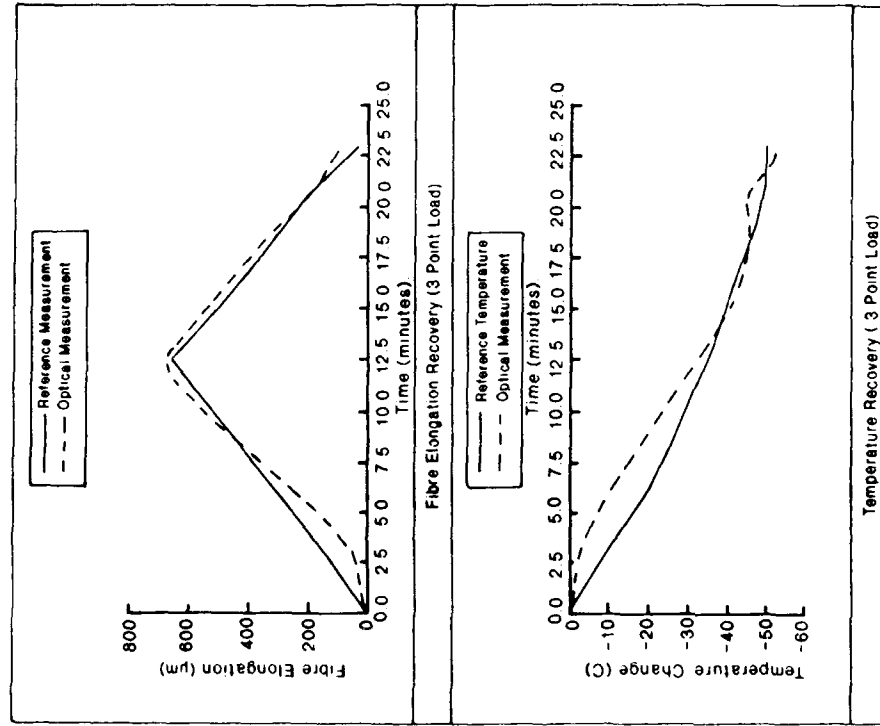
Figure 1
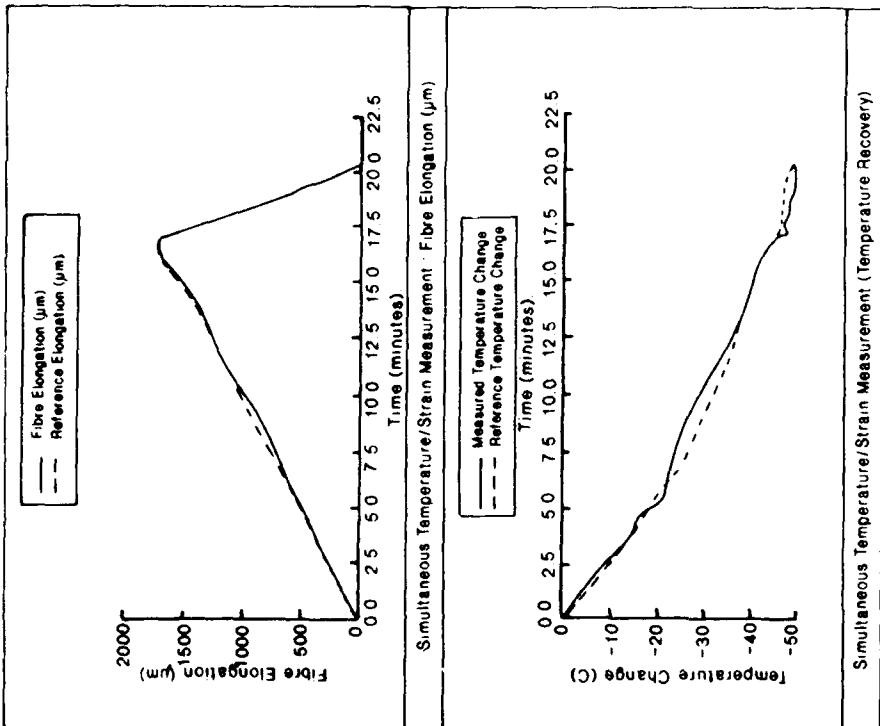
Figure 2

Bend-insensitive single mode fiber for embedding in composite materials

G. Orcel, R. May*, J. Greene*, R. Claus*

SpecTran Corporation, 50 Hall Road, Sturbridge, MA 01566
*Fiber & Electro-Optics Research Center, Virginia Tech, Blacksburg, VA 24061-0111

ABSTRACT: A single mode bend-insensitive (SMBI) fiber was designed using a depressed clad ($\Delta n = 0.003$) and a higher NA (0.15). The optical attenuation of such fiber embedded in 15 cm long graphite/epoxy composite panels and at $0°$ angle with respect to the reinforcing fibers in the adjacent plies is not affected by strain or temperature cycling.

1. INTRODUCTION

Optical fibers are being applied or contemplated for data transmission and sensing and diagnostic applications in advanced aircraft (Vendsarkar and Murphy). When the aircraft structure is constructed of composite materials, the optical fiber can be directly embedded in the material. Possible uses for embedded optical fibers include monolithic backplanes for avionics computers, and temperature and strain sensors for smart structures.

One difficulty in the use of embedded optical fibers is that structural reinforcing fibers often generate microbends in the optical fibers, inducing large optical attenuation (Bennett and Claus). The magnitude of these losses depends on the fiber's refractive index profile and coating modulus, and the type and orientation of the structural fibers (Jackson).

The purpose of this work is to design a single mode bend-insensitive fiber (SMBI) and to evaluate the optical performance of graphite/epoxy coupons with the embedded SMBI optical fiber when exposed to strain or temperature cycling.

2. EXPERIMENTAL PROCEDURE

The fiber preform was prepared using the Modified Chemical Vapor Deposition (MCVD) technique. The preform is then lowered into a graphite furnace under dry nitrogen atmosphere. Glass fiber is drawn to an outside diameter (OD) of 125 μm

and then coated on-line with either a polyimide resin to 150 μm OD or with an acrylate buffer to 250 μm OD.

The composite system is a Hercules 3501-6 epoxy resin matrix and AS4 graphite reinforcing fiber. The prepreg ply is 0.3 mm thick and the graphite fibers are linearly oriented.

The 15 cm long composite laminates were formed by applying 585 kPa pressure in a hot press at 175°C for 2 hours.

The optical fiber is embedded in the center of a 12-ply coupon (temperature test) or 6-ply coupon (strain test). The optical fiber is either oriented at 0° orientation, or at 90°, referred to as 90° orientation. A 12-ply composite coupon is described in Figure 1.
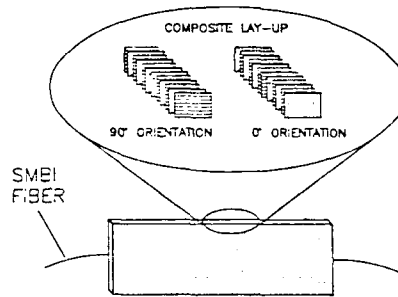
Fig. 1. 12-ply composite coupon with embedded fiber

3. RESULTS

The refractive index profile of the single mode bend-insensitive fiber is given in Figure 2. The clad is depressed by about 0.003, the numerical aperture is 0.15, and the core diameter is 6μm. The attenuation at 1300 nm is about 0.95 dB/km and the cut off wavelength is 1190 nm.
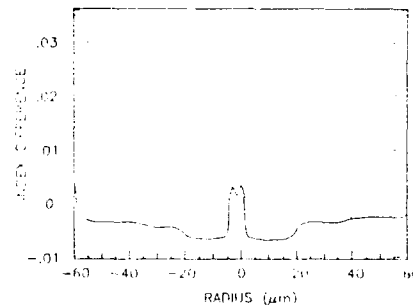
Fig. 2. Refractive index profile of a SMBI fiber

The results of a peel point attenuation test at 1300 nm (loss induced by a single quarter turn around a mandrel) are presented in Figure 3. The single mode bend insensitive fiber has a fraction of a dB loss for a 3mm diameter mandrel, while a matched clad single mode fiber (standard design) has about 5 dB loss.
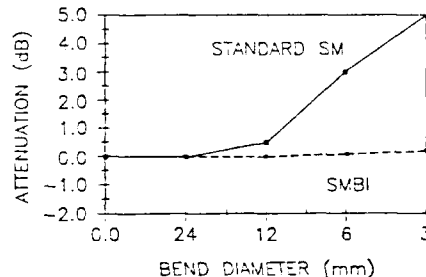
Fig. 3. Peel point attenuation test

The optical attenuation of the composite coupons was measured during a temperature cycle from -40°C to +85°C. A typical result for a SMBI fiber as well as the temperature schedule are given in Figure 4. Coupons with SMBI fiber as well as the temperature schedule are given in Figure 4. Coupons with SMBI fiber exhibited negligible loss. On the other hand, coupons with standard matched clad SM fiber displayed losses as high as 0.4 dB.
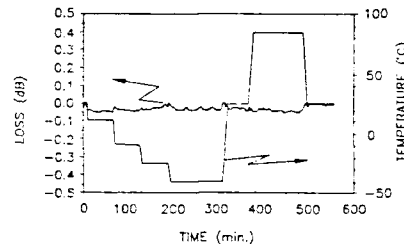
Fig. 4. Optical loss of P coated, embedded SMBI fiber during temperature cycling

The coupons with polyimide coated fibers embedded with a 90° orientation exhibited the highest losses during temperature cycle.

The optical loss of the embedded fibers was recorded as a function of strain. A typical plot for a coupon with polyimide coated, single mode bend-insensitive fiber is given in Figure 5. Coupons with standard, matched clad single mode fibers exhibited losses as high as 4 dB, while coupons with SMBI fibers exhibited a maximum loss of 0.5 dB.
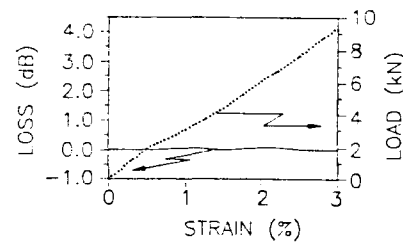
Fig. 5. Optical loss of P coated, embedded SMBI fiber during strain test

Loss is observed in the optical fiber after about 1 to 1.5% of strain is applied to the composite. Coupons with polyimide coated fibers embedded at 90° orientation exhibited the highest losses during the strain test, presumably due to the high elastic modulus of the polyimide.

Pull out tests were performed on dog-bone shaped samples prepared by embedding single fibers in neat resin. Cracks developed at the polymer/glass interface for loads of 44 and 107 N/mm for the acrylate and polyimide coated fibers, respectively. Crack propagation occurred for loads of 49 and 210 N/mm for the same samples. Only the polyimide coated fibers exhibited substantial stress transfer from the fiber to the matrix as evidenced by the development of stress patterns under polarized light.

Scanning electron micrographs of the fiber after failure clearly indicate that no coating is left on the glass fiber.

4.   DISCUSSION

The different tests indicate that the bend-insensitive single mode fiber is less affected by temperature cycles and strain than a standard matched clad single mode fiber. Bend insensitivity is essentially due to a reduced core diameter and a higher NA, and in part due to the depressed clad. Also, higher induced losses are observed for polyimide coated fibers than for acrylate coated fibers. There are two reasons for this behavior: 1) the polyimide coating is stiffer than the acrylate coating; and 2) the polyimide buffer is 12 μm thick while the acrylate buffer is about 60 μm thick. Consequently, the polyimide buffer transmits more outside perturbations to the optical fiber than the acrylate buffer. Finally, the single fiber pull out test indicates that adhesion of the polymer to the glass fiber is relatively weak. Weak adhesion of polymeric buffers to optical glass fibers is desirable because it provides a cushion and the buffer is less efficient in transmitting outside perturbation to the optical fiber.

5.   CONCLUSIONS

Graphite/epoxy composite panels with embedded optical fibers were manufactured. The influence of optical design, composite geometry, temperature cycling and strain on the optical attenuation of the coupons was determined. It was found that composite panels with embedded bend-insensitive single mode fibers were not affected by outside perturbations. It is best when the optical fiber is embedded at 0° orientation with respect to the reinforcing graphite fibers in the adjacent plies. Polyimide coated fibers transmit more outside perturbation to the optical fiber than acrylate coated fibers, because of the thinner and tougher polymeric layer.

6.   ACKNOWLEDGMENT

7.   REFERENCES

Bennett, K.D. and Claus, R.O., 1985 *J. Opt. Soc. Am. A* **13** 37
Jackson, B.S. 1984 *Optical Time Domain Reflectometry as a Nondestructive Evaluation Technique for Composite Materials*-Master of Science Thesis Virginia Polytechnic Institute
Vendsarkar, A.M. and Murphy, K.A. 1990 *Photonics Spectra* **4** 119

Piezoceramic/DSP-based integrated workstation for modal identification and vibration control

Joe Su, Michael Rossi, Gareth Knowles, Chien Huang

Grumman Corporate Research Center, Mail Stop A08-35, Bethpage, NY 11714

ABSTRACT: A PC/DSP-based integrated workstation was developed for modal parameter identification and vibration control of flexible structures. Utilizing a novel technique, the workstation was configured to perform very accurate estimation of the modal parameters of a cantilevered beam. Active vibration control of a cantilevered beam with a bonded piezoceramic bending motor and a bending generator was accomplished by configuring the workstation as a feedback control loop with a simple lag. Although all preliminary usage involved a cantilevered beam, the workstation proved to be an effective data acquisition, processing, and waveform generation system that can be employed for the modal identification and vibration control of any structure.

1. INTRODUCTION: We describe an ongoing effort to develop an integrated design that exploits recent advances in sensors and actuators to produce an automatic identification and control workstation for *in situ* modeling and vibration control of intelligent structures. The backbone of the system is the Texas Instrument TMS320C30 Digital Signal Processor (**Ref 1**) embedded in a Spectrum Signal Processing board (**Ref 2**). The workstation is an integrated system consisting of an AST 80486 personal computer (PC) with the Spectrum add-in board including 17 megabytes of private memory, 34 analog-to-digital (A/D) converters and 18 digital-to-analog (D/A) converters. There also is an Onsite Instruments Techfilter (**Ref 3**) add-in board with 16 analog channels of programmable anti-aliasing/smoothing filters. The filters have AC or DC coupling with adjustable gain and corner frequencies and exhibit 75 dB/Octave roll-off. The PC is the host to the DSP, and provides the interface between the user and the DSP. DSP software development, loading, and execution, as well as data visualization and postprocessing, all are performed in the PC environment. The DSP is the main processor which facilitates the analysis of sensor data and generates control signals to the actuators. The workstation can process data from up to 34 sensors and generate control signals for up to 18 actuators. Currently we are concentrating upon using piezoceramic actuators and fiber optic sensors (both collocated and non-collocated). The PC also contains an Excelan Ethernet board which supports TCP/IP/XWindows communication with the corporate Cray YMP supercomputer and various other workstations. The Grumman proprietary PROTOBLOCK computer-aided control system design package is implemented on several departmental workstations in this network. The preliminary test article consists of a cantilevered aluminum beam with non-collocated piezoceramic sensors and actuators. A set of eight 200-watt KEPCO BOP (**Ref 4**) power amplifiers provide the power to drive the piezoceramic bending motors. Instrumentation amplifiers provide gain, selectable from 1, 10, 100, or 1000, which gives full A/D resolution for piezoceramic sensor signals over a wide dynamic range.

2. SYSTEM IDENTIFICATION: Modal parameter estimation of the transverse vibrations of a cantilevered beam is accomplished with the workstation by measuring the steady-state response of the beam under sinusoidal excitation. The configuration of the experimental

Fig 1: FREQUENCY RESPONSE DETERMINATION USING THE PIEZOCERAMIC/DSP BASED WORKSTATION
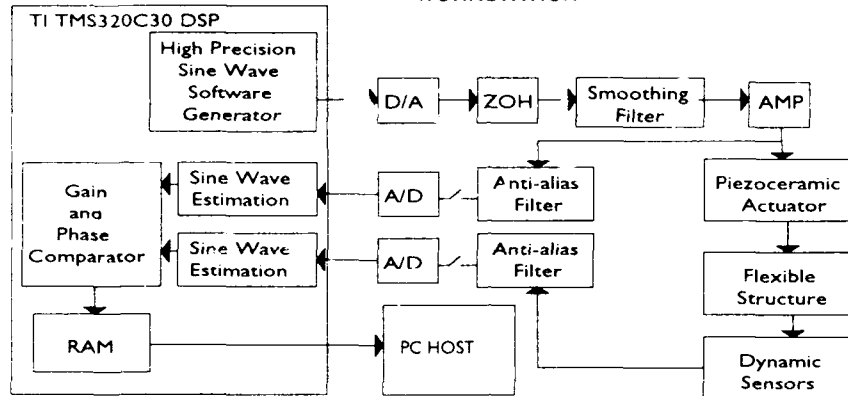
setup is illustrated in **Fig 1**. The waveform is generated with exceptionally high precision by interpolating a 1024 element floating point lookup table. The excitation is converted to analog form by the series connection of a digital-to-analog (D/A) converter, a zero-order-hold buffer (ZOH), and an analog smoothing filter. The resulting signal is fed to the KEPCO power amplifier which in turn drives the bending motor on the beam causing vibrations. The bending generator signal at steady state is passed to the Onsite anti-aliasing filter and sampled. With the corner frequency of that filter set to 40% of the sampling frequency, the recorded time sequence reflects true digitized vibration response. The excitation signal at the input of the PZT actuator is also filtered and sampled. The gain and phase of the beam's steady state response is determined by comparing this signal to that of the beam's response. From the viewpoint of implementation, it was important to maintain a real world environment throughout these procedures. Consequently, no attempt was made to isolate the experiments from the surrounding, rather noisy, environment. Another cause of loss of precision turned out to be entirely due to electronics when it was determined that the least significant five bits were unreliable due to nonlinear device effects of the A/D chip. Signal processing techniques were developed and utilized to improve the estimates for the steady state response. This includes a least-square-error estimation filter described as follows:

Given a noisy measurement vector,

$$M = \begin{bmatrix} m(0) & m(T) & \cdots & m(kT) & \cdots & m(nT) \end{bmatrix}, \text{ where}$$

$m(kT) = G\sin(\omega_c(kT) + \phi) + \eta(kT)$, steady state response + noise

T is sampling period, $\eta(kT)$ is uncorrelated with the response

Since any noise-free steady state response can be expressed as:

$$G\sin(\omega_c(kT) + \phi) = A\cos\omega_c(kT) + B\sin\omega_c(kT)$$

and since *sin* is orthogonal to *cos*, these functions serve as natural bases functions for this space. The optimal estimator, in the least squares sense, is the orthogonal projection of the measurement vector. Thus the "best" estimate will be given by:

$\hat{M} = Ac + Bs$, $c = \begin{bmatrix} 1 & \cos(\omega_c T) & \cdots & \cos(\omega_c(nT)) \end{bmatrix}$, $s = \begin{bmatrix} 0 & \sin(\omega_c T) & \cdots & \sin(\omega_c(nT)) \end{bmatrix}$,

$A = \dfrac{Mc'}{cc'}$, $B = \dfrac{Ms'}{ss'}$, M is the measurement, $\hat{M}$ is the optimal estimate

Hence, $m = \sqrt{A^2 + B^2}$ and $\phi = \arctan(A/B)$ are the optimal estimates for magnitude and phase. In order to estimate the actual frequency response from the measured data, we had to determine the individual effects due to the anti-aliasing filters, smoothing filter, power amplifier, etc. To do this we sampled the input signal to determine gain and phase brought about by the smoothing filter and power amplifier and then modified the response estimation accordingly. Thus, we are able to achieve very close estimates of the actual frequency response using this combination of high-precision sine wave generation, least squares estimation, and phase/gain compensation. **Fig 2** illustrates this procedure by a geometric analogy

FIG 2: GEOMETRIC ANALOGY FOR LEAST SQUARES ESTIMATION
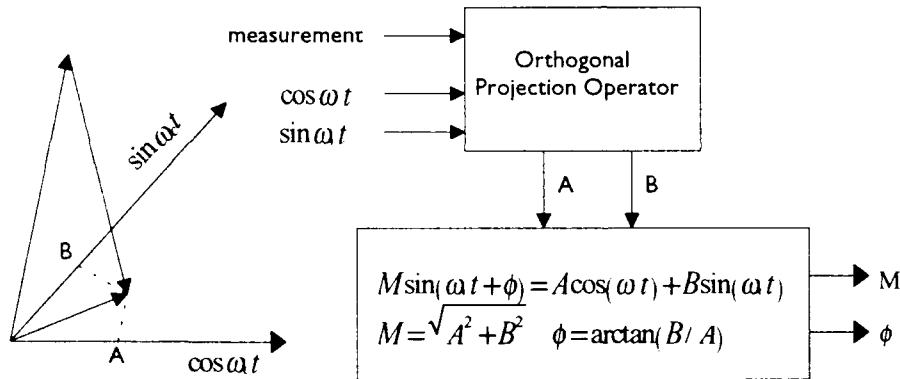
and a functional block diagram. To illustrate the effectiveness of this technique, the frequency response of the anti-aliasing and smoothing filters on the Spectrum board were measured in this way. The filters are fourth-order Butterworth in a Sallen-Key configuration which employ a set of 4 identical plug-in resistors to select each filter's corner frequency. The theoretical transfer function of the filter, assuming nominal component values, is:

$$\frac{E_o}{E_i} = \frac{1}{\left(R^2 C_1 C_2 S^2 + 2RC_1 S + 1\right)} \times \frac{1}{\left(R^2 C_3 C_4 S^2 + 2RC_3 S + 1\right)},$$ where R is the chosen restor value,

$C_1 = 2380\ pf, C_2 = 2780\ pf,\ C_3 = 1000\ pf, C_4 = 6800\ pf$.

Fig 3 illustrates the efficacy of our approach to system identification by showing a close fit of the estimated to the theoretical frequency response functions for the Butterworth filter for the case in which $R = 1.36\ M\Omega$. Virtually noiseless frequency response functions for the vibrating beam can be determined in this way over the frequency spectrum of interest. The natural frequencies and damping factors may be calculated by locating the frequency corresponding to a 90 degrees phase shift and then determining the 3 dB bandwidth at each resonant frequency. Accurate estimates were obtained even for low frequency modes. In addition, a positive real rational function estimation technique based on classical complex curve fitting (**Ref 5**) is used to realize the measured frequency response function of the vibrations of the beam (**Fig 4**).

Fig 3: BUTTERWORTH THEORETICAL vs EXPERIMENTAL vs FITTED RESPONSE
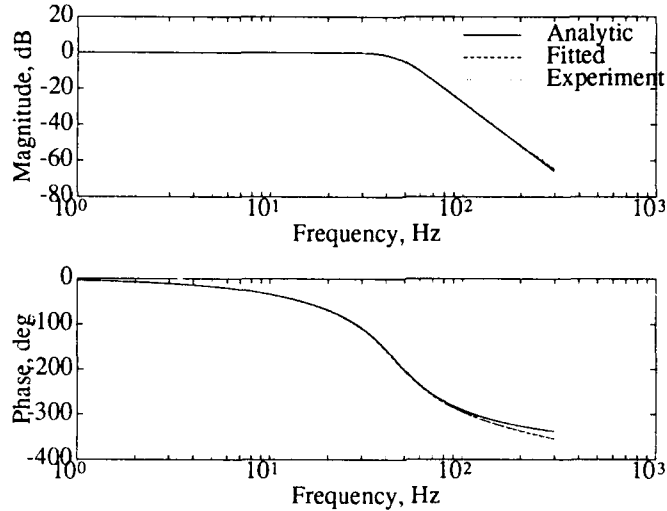
Fig 4: TRANSVERSE VIBRATIONS OF THE CANTILEVERED BEAM–THEORETICAL vs EXPERIMENTAL vs FITTED FREQUENCY RESPONSE
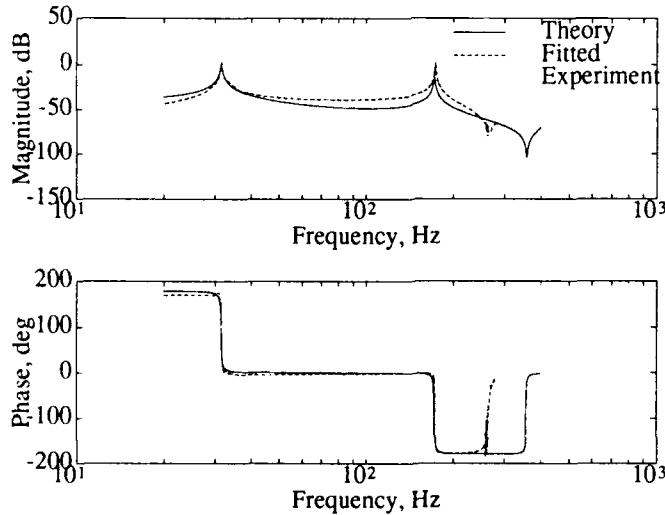
3. MODELS OF PIEZOELECTRIC SENSOR AND ACTUATOR DYNAMICS: The piezoelectric bending generator feeding the antialiasing filter in front of the A/D converter can be viewed as a current source in parallel with a capacitor and a resistor as shown in **Fig 5**. The current is proportional to the strain rate at that point in the beam. The voltage drop across the input impedance of the circuit would then have the illustrated transfer function. Note that at high enough frequencies, the voltage is proportional to strain. For the component values of the bending generator used and the input circuit on the workstation, $R_i = 10 \ \mathrm{K\Omega}$, $C_i = 34 \ \mathrm{nf}$, and $C_f = 216 \ \mathrm{nf}$, the frequency response function is depicted in **Fig 6**.

FIG 5: BENDING GENERATOR TRANSFER FUNCTION AND CIRCUIT MODEL

$$\frac{V}{\dot{\varepsilon}} = \frac{R_i}{R_i\left(C_f + C_i\right)S + 1}$$

where C_f = capacitance of Piezo

C_i = input capacitance of circuit

R_i = input resistance of circuit
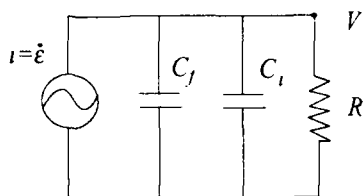
Fig 6: FREQUENCY RESPONSE FUNCTION OF THE BENDING GENERATOR
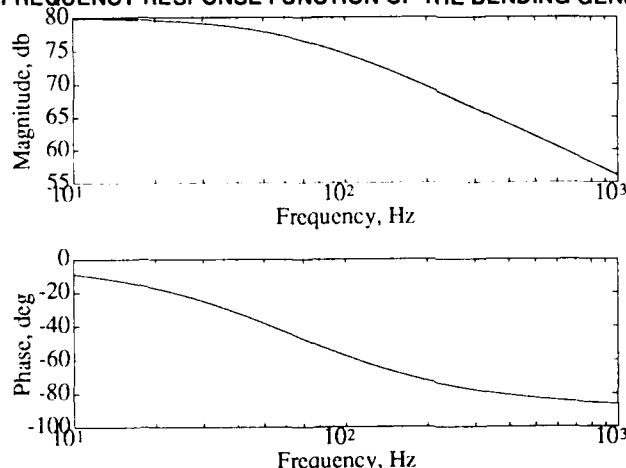
4. NONLINEAR ELECTRIC FIELD/STRAIN BEHAVIOR OF PIEZOCERAMICS:

We were surprised to observe in the laboratory the size of the nonlinear relation of electric field to induced strain in a piezoceramic bending motor. **Fig 7** illustrates the steady state output waveform for a sinusoidal excitation at a frequency just below resonance and for a range of amplitudes. The response is clearly far from sinusoidal. At low enough signal levels, the response is quasi-linear but noise becomes a dominating factor. To illustrate another view of the nonlinearities associated with piezoceramic actuators, consider **Fig 8** which shows changes in peak response, resonant frequency, and damping associated with the first bending mode at three different levels of excitation. Clearly, the response is dependent on the driving amplitude.

5. CONTROL SYSTEM DESIGN: Fig 9 illustrates the overall block diagram which

includes all of the components of the dynamic model of the system. Using the experimental procedures described above, we obtained the transfer functions of the cantilevered beam, the butterworth filter, the anti-aliasing filter, the sensor dynamics, and the power amplifier. For the single or two-mode models we were able to obtain substantial damping through feedback by exploiting a lag filter design. For simplicity we describe the single-mode results, the two mode results are exactly analogous. Initially all the models were ported into the PROTOBLOCK environment. Within this graphical environment we performed linear analysis which included a root locus technique to derive the closed loop system (**Fig 10**). It is interesting to observe that this plot clearly indicates that the structural modes do indeed become unstable for large enough gain. This was later verified experimentally where

Fig 7: NONLINEAR RESPONSE OF BENDING MOTOR--WAVEFORM
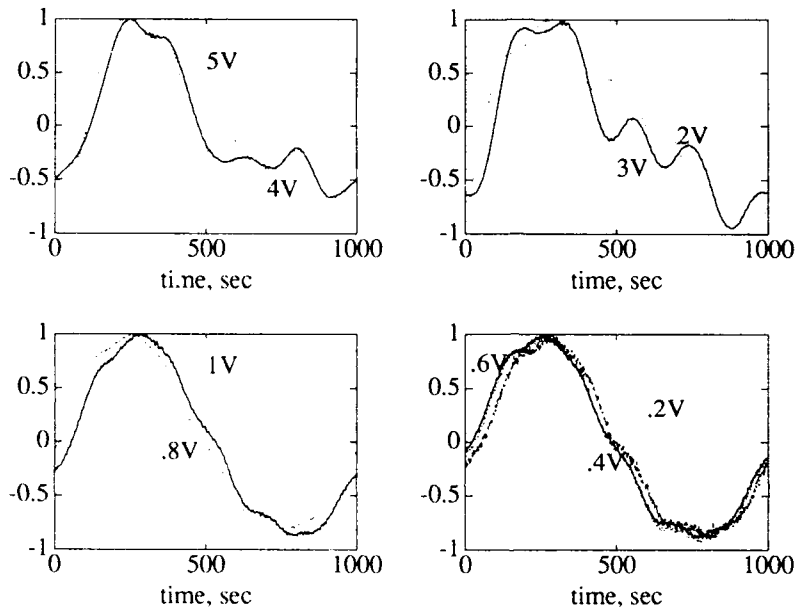
Fig 8: NONLINEAR RESPONSE OF BENDING MOTOR--FREQUENCY RESPONSE
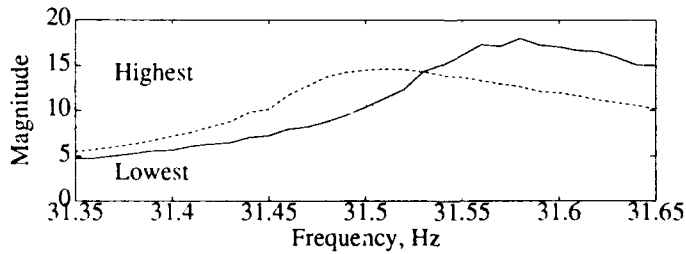
Fig 9: CANTILEVERED BEAM CONTROL BLOCK DIAGRAM
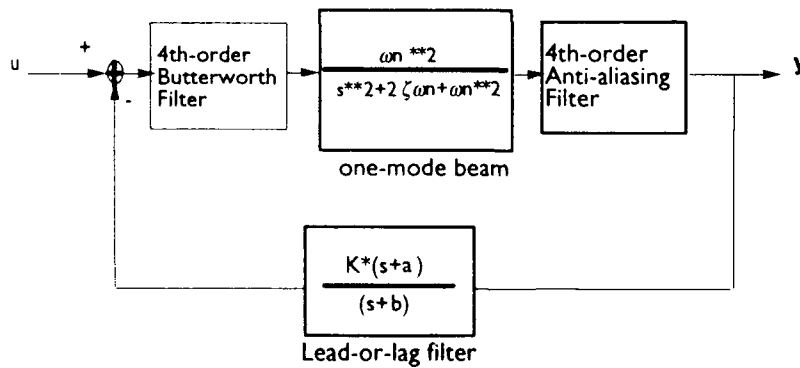
Fig 10: ROOT LOCUS PLOT OF THE COMPLETE SYSTEM
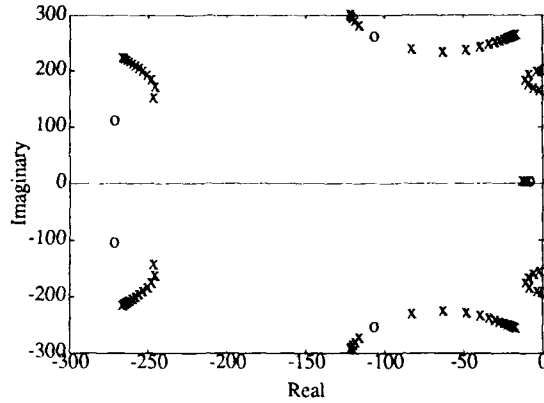
excellent correlation with the predicted instability was observed. The PROTOBLOCK environment allowed us to efficiently compare the root loci for a number of choices of lead or lag filters. For the single mode model it was quickly determined that choices of a = 10 and b = 20 gave an acceptable root locus plot. The required values of the gain are automatically generated through "clicking" on the desired location of the root locus graph. The closed loop response was simulated within the graphical environment and the predicted open and closed-loop time histories are displayed in **Fig 11**. The control system design is downloaded to the

Fig 11: ANALYTICAL–UNCONTROLLED vs CONTROLLED FIRST MODE RESPONSE
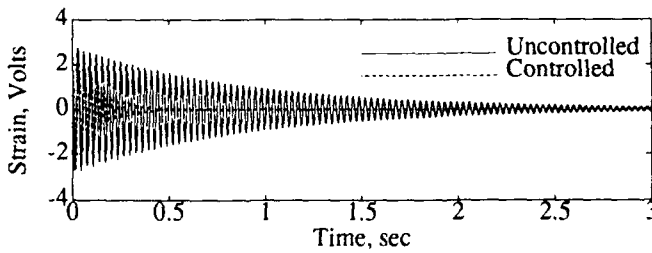
PC where the C30 implements the required algorithm to effect the lag filter controller design. We then proceeded to run the experiment using the piezoceramic bending motor driven with sinusoidal input at the first fundamental frequency of 31.4 Hz. Upon reaching steady-state, the input was removed and the time histories were sampled, stored, and displayed. The result of the one-mode experiment under open and closed-loop control is displayed in **Fig 12**.

Fig 12: EXPERIMENTAL–UNCONTROLLED vs CONTROLLED FIRST MODE RESPONSE
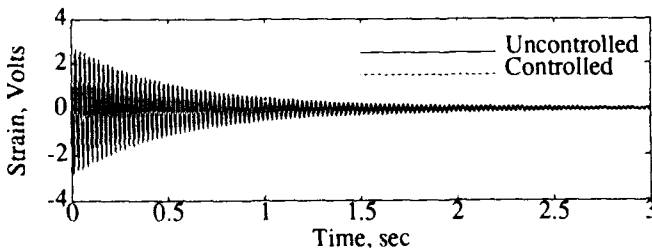
As can be clearly seen, we found excellent correlation between the simulated and experimental results.

6. CONCLUSION: The Piezoceramic/DSP-based integrated workstation has proved to be a great aid to research in smart materials and structures. It is now possible to quickly iterate between theoretical control system designs and actual hardware implementations employing embeddable real time digital controllers. This work illustrates the optimal combination of modern digital signal processing techniques, control system synthesis, system identification, and high speed computer networking. This symbiosis characterizes the essence of the kind of systematic approach which will lead to actual application of smart structures technologies.

7. REFERENCES:
1. TMS320C3x User's Guide, Texas Instruments, Dallas, TX, April 1990.
2. TF-16 TECHFILTER Technotes #2 & #4, Onsite Instruments, Mountain View, CA, Spring 1991.
3. TMS320C30 Real-Time System User's Manual, Spectrum Signal Processing, Westborough, MA, 1990.
4. BOP-200-1M Owner's Manual, KEPCO Power Supplies, Flushing, NY, 1990.
5. Levy, E. C., "Complex-Curve Fitting," IRE Transactions on Automatic Control, May 1959.

The intelligence between sensing and actuation in smart structures

Ümit Özgüner   Layne Lenning

Department of Electrical Engineering
The Ohio State University
2015 Neil Avenue
Columbus, Ohio, 43210

Abstract. It is claimed that smart structures require the implementation of distributed intelligence to work effectively. The local intelligence for flexible structures is based on local models of substructure dynamics. One possibility of realizing the local models is with analog circuits representing the substructures. The local models can then be the basis of different feedback control schemes.

1. Introduction

We claim that *adaptive* or *intelligent* structures require a nontrivial amount of *intelligence* to provide the *adaptation*, and that one of the key issues in this area is establishing a framework that is independent of the sensor and actuator technologies that are being considered. Thus, we have to understand the key characteristics of such structures:

- Sensors imbedded into substructures.

- Actuators imbedded into substructures.

- Substructures coupled to form a large structure.

- A distribution of control authority over the large structure.

- A distribution of sensor responsibility over the large structure.

Thus, the *intelligence* that connects the sensors and actuators must likewise fit into the above framework. That is, it must be imbedded into the substructures and must be "connectable" similar to the substructures. It must "understand" that it is part of a whole. It must show a distribution of intelligent processing power.

We now make a big jump to reach the claim that a major portion of *intelligence* or *intelligent action* is having an **internal knowledge of self**. In systems/control terminology, this is model based control.

The above general introduction leads us to the following two, somewhat more technical, observations:

1. A large class of interconnected structures, especially those comprised of physical systems, have models represented by electrical networks. These networks, which can actually be built and interconnected, will exhibit the same behavior as the nominal model of the original structure.

2. A large class of control approaches incorporate a nominal *model* of the system being controlled within the feedback control loop. [1]

In what follows, we shall summarize very briefly circuit based modeling of structures. This will also include the technology-dependent active materials portion of the structure. We will then show that physically having such an analogous circuit will directly aid in generating the feedback control for large structural systems.

2. Background: Circuit analogies

2.1. Modeling of Flexible Structures Using Circuit Analogies

Large structures may be viewed as an interconnection of several substructures where the vibration control problem can be approached as a question of power transfer—similar to problems in transmission line theory or electrical circuits. The propagation of disturbances may be analyzed in terms of *scattering parameters* or in terms of *circuit impedances*, just as in transmission lines or high frequency waveguides. We have been analyzing these analogies in detail, with the intent of exploiting the similarities (Lenning and Özgüner, 1991).

The first and simple motivation for this work is to reconsider existing results in circuit theory and microwave waveguides in order to transfer some of the results to the control of vibration damping in large, coupled, flexible structures.

The second and more unique motivation, which forms part of this paper, is to use these models to build the actual circuits. These circuits will then provide nominal models to be utilized jointly with the system as part of the control implementation.

Circuit analogies of mechanical systems have existed for many years. When the history of mechanical and electrical systems is considered, the complementary progress of the two areas is evident. Results of electrical network theory have many applications to acoustical, mechanical, and electromechanical systems. Included in these applications is vibration control of large flexible structures.

Typical examples of circuit analogies for mechanical systems are shown in Table 2.1. Using these variable and element analogies, the equations for electrical and mechanical systems are:

$$I_{ext} = C\dot{V} + \frac{1}{R}V + \frac{1}{L}\int V \, dt \tag{1}$$

$$F_{ext} = M\ddot{x} + \beta\dot{x} + Kx \tag{2}$$

$$\tau_{ext} = J\ddot{\theta} + \beta\dot{\theta} + K\theta \tag{3}$$

---

[1] This has at times been referred to as the *internal model principle*, although that term has also been used when the controller has a model of the disturbances.

ELECTRICAL	MECHANICAL (LINEAR)	MECHANICAL (ROTATIONAL)
voltage, V	velocity, v, $\dot{x}$	angular velocity, ω, $\dot{\theta}$
current, I, $\dot{q}$	force, F	torque, τ
charge, q	momentum, P	angular momentum, h
flux linkage, λ	displacement, x	angular displacement, θ
capacitance, C	mass, M	moment of inertia, J
inverse inductance, $\frac{1}{L}$	stiffness, K	rotational stiffness, K
inverse resistance, $\frac{1}{R}$	damping, β	damping, β

Table 1: Electrical / Mechanical System Analogies

Once n–port impedence matrices and scattering matrices are defined, circuit synthesis techniques can be applied to structure synthesis. Connecting substructures is analogous to connecting circuit subnetworks. The impedance or scattering parameters of the entire structure can be determined from the impedances of the interconnected substructures as one would determine the impedance of a circuit. In fact, Component Mode Synthesis methods in FEM have been studied in this context.

Using overlapping decomposition, the circuit/structure can be separated for decentralized controller design (Young 1990, Cagle and Özgüner 1989). Controllers may be designed to achieve certain scattering properties or to achieve certain voltage/velocity properties. H_2 or H_∞ design techniques could be used in these designs.

In conclusion, circuit analogies have been used to establish a framework for analyzing interconnected flexible structures. Our purpose here though, is in pursuing the possibilities that exist when these circuits are actually built.

2.2. Parallel Circuit Models of Flexible Structures

One advantage in actually developing the substructure building–blocks is that the assembly of the subnetworks will provide the same system response as the assembly of mechanical substructures. Thus, one can develop integrated circuit chips to represent portions of a truss, plates, appendages, etc., and assemble an analog representation of a total airplane wing or a space station. In fact, this would be quite similar to assembly of a total FEM of the same structures.

2.3. Inclusion of sensors and actuators

Sensors and actuators which have dynamics that cannot be ignored, can also be included in the circuit-based models described above. These may be proof mass actuators, piezo sensors and actuators, etc. Circuit equivalents for such systems
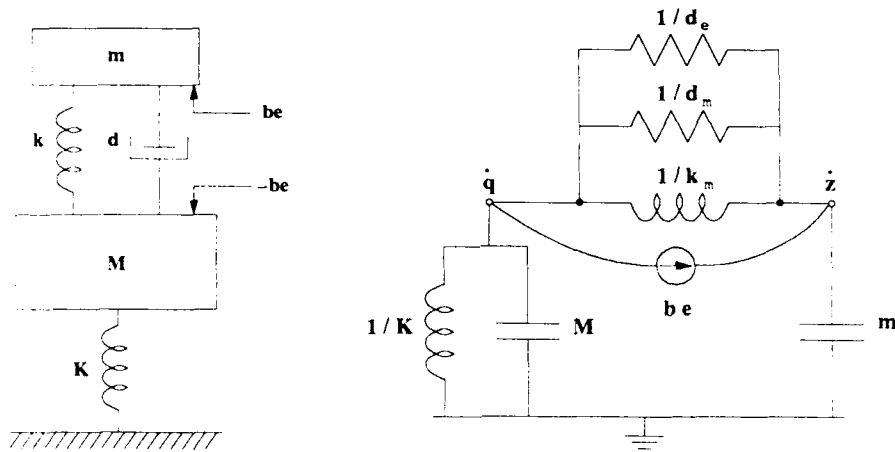
Figure 1: Single mode structure with proof–mass actuator and associated circuit model

are available and may be appended. See Figure 1 for an example of a proof-mass actuator with a mass-spring system that it is attached to.

3. Utilization of the structure model

3.1. Observer design

Observer design is an interesting application of circuit representations of flexible structures. Again, cost and size are key advantages of this application. The observer may be easily mounted to the structure or substructure to be controlled. Also, this observer can be implemented in analog. Thus, no microprocessor is necessary for this observer implementation.

The observer for the structure is equivalent to the observer for the equivalent RLC circuit. The state equations for a nondegenerate RLC circuit (no capacitance-voltage source loops and no inductance-current source cut sets) without controlled (dependent) sources can be written as

$$\mathbf{L}\frac{d\mathbf{i}_L}{dt} = \mathbf{R}\mathbf{i}_L + \mathbf{A}_c\mathbf{v}_c + \mathbf{B}_E\mathbf{E}(t) \tag{1}$$

$$\mathbf{C}\frac{d\mathbf{v}_c}{dt} = \mathbf{A}_L\mathbf{i}_L + \mathbf{G}\mathbf{v}_c + \mathbf{B}_I\mathbf{I}(t) \tag{5}$$

where the following are defined:

$\mathbf{i}_L$ vector of inductor currents
$\mathbf{v}_c$ vector of capacitor voltages
$\mathbf{E}(t)$ vector of independent voltage sources
$\mathbf{I}(t)$ vector of independent current sources

L	inductance matrix
C	capacitance matrix
R	matrix of resistances in writing loop (voltage) equations
	(row j shows resistances in the same loop as $\mathbf{L}_{jj}$)
A$_c$	matrix showing capacitor voltages in loop (entries ± 1 or 0)
B$_E$	matrix showing voltage sources in loop (entries ± 1 or 0)
G	matrix of inverse resistances in writing cut set (current) equations
A$_L$	matrix showing inductor currents in cut set (entries ± 1 or 0)
B$_I$	matrix showing current sources in cut set (entries ± 1 or 0)

Consider the case with *some* voltage (velocity) measurements. Thus,

$$y = \begin{bmatrix} \mathbf{0} & \mathbf{H} \end{bmatrix} \begin{bmatrix} \mathbf{i}_L \\ \mathbf{v}_c \end{bmatrix}. \tag{6}$$

One can design an observer, with error equation dynamics specified by the selection of matrices $\mathbf{F}_1$ and $\mathbf{F}_2$ and end up with the equations,

$$\mathbf{L}\frac{d\hat{\mathbf{i}}_L}{dt} = \mathbf{R}\hat{\mathbf{i}}_L + \mathbf{A}_c\hat{\mathbf{v}}_c - \mathbf{LF}_1\mathbf{H}\hat{\mathbf{v}}_c + \mathbf{LF}_1\mathbf{y} + \mathbf{B}_E\mathbf{E}(t) \tag{7}$$

$$\mathbf{C}\frac{d\hat{\mathbf{v}}_c}{dt} = \mathbf{A}_L\hat{\mathbf{i}}_L + \mathbf{G}\hat{\mathbf{v}}_c - \mathbf{CF}_2\mathbf{H}\hat{\mathbf{v}}_c + \mathbf{CF}_2\mathbf{y} + \mathbf{B}_I\mathbf{I}(t) \tag{8}$$

These equations imply that controlled (dependent) voltage sources must be added to the inductor element voltages and controlled (dependent) current sources must be added to the capacitive element nodes.

4.2. Sensitivity Functions

A second specific application, with the network analog being available, is using it in generating "sensitivity functions" of the structure. Indeed, it is known that the sensitivity functions (for example the state–sensitivity, defined as the variation of the state with respect to a parameter α of interest) can be generated from the nominal system *model* driven by the system outputs.

$$\mathbf{L}\frac{d\mathbf{s}_i}{dt} = \mathbf{R}\mathbf{s}_i + \mathbf{A}_c\mathbf{s}_v + \mathbf{S}_R\mathbf{i}_L - \mathbf{S}_L\frac{d\mathbf{i}_L}{dt} \tag{9}$$

$$\mathbf{C}\frac{d\mathbf{s}_v}{dt} = \mathbf{A}_L\mathbf{s}_i + \mathbf{G}\mathbf{s}_v + \mathbf{S}_G\mathbf{v}_c - \mathbf{S}_c\frac{d\mathbf{v}_c}{dt} \tag{10}$$

where the following are defined:

$$\mathbf{s}_i = \frac{\partial \mathbf{i}_L}{\partial \alpha} \tag{11}$$

$$\mathbf{s}_v = \frac{\partial \mathbf{v}_C}{\partial \alpha} \tag{12}$$

$$\mathbf{S}_c = \frac{\partial \mathbf{C}}{\partial \alpha} \tag{13}$$

$$\mathbf{S}_R = \frac{\partial \mathbf{R}}{\partial \alpha} \tag{14}$$

$$S_L = \frac{\partial L}{\partial \alpha} \tag{15}$$

$$S_G = \frac{\partial G}{\partial \alpha} \tag{16}$$

This is particularly appropriate for the configuration we propose.

One particular utilization of sensitivity functions is in real–time adaptive control algorithms, where they are used as part of gradient descent type of iterations.

1. Conclusions

It has been pointed out that distributed intelligence is required to have the intelligent/adaptive structures of the future perform as desired. In this paper, we claim that this distributed intelligence has to have local knowledge of the dynamic model of the substructures. Furthermore, we show that one way of implementing the local models is with analog circuits, which provides possibilities for developing many model-based control algorithms.

Acknowledgments

References

Lenning, L. and Ü. Özgüner, "Modeling and Control of Large Space Structures Using Circuit Analogies," Proc. 1991 AIAA Conf. Guidance, Navigation and Control, New Orleans LA, Aug. 1991

Young, K.D., "Distributed finite-element modeling and control approach for large flexible structures," *Journal of Guidance, Control, and Dynamics*, vol.13, No.4, 703–713, 1990

Cagle A. and Ü. Özgüner, "Optimal decentralized feedback control for a truss structure," Proc. 1989 AIAA Conf. Guidance, Navigation and Control, Boston MA, Aug. 1989

A workstation environment for design of vibration control for flexible structures using digital signal processors

William H. Bennett
Techno–Sciences, Inc.
7833 Walker Drive, Suite 620
Greenbelt, Maryland 20770

ABSTRACT Activities related to the design and evaluation of computational methods for design of vibration control systems based on frequency response measurements are described. A workstation is under development to support computation, design tradeoff analysis, realtime program development, simulation, and experimental evaluation. The realtime vibration control algorithms under develop use digital signal processing methods and are implemented using high speed, special purpose DSP processors. A benchmark multichannel vibration control experiment is planned.

Introduction

A principal concern in implementation of precision active vibration control systems for suppression and isolation in structures is the computational complexity for realtime, multichannel control processing. Recursive algorithms for realization of multichannel control laws can be readily designed from finite dimensional, state space models for structural flexure. For wide band vibration control in structures, model-based control law optimization is typically obtained for reduced order models of the structural flexure. Reduced models obtained from finite element analysis, are typically characterized by poor frequency resolution relative to the modal characteristics of a control configured structure. As a result, standard optimal control design methods are difficult to use for vibration control.

An alternate computational approach is to use direct measurement of system frequency responses for vibration control optimization. Tradeoffs in algorithm design can be assessed based on Wiener-Hopf optimal control methods for the high, modal density structural response to wide band disturbance excitation [1, 2, 3, 4]. The computational methods employed in this work offer an approach to optimization of vibration control for irrational transfer functions arising in distributed parameter models for structural flexure [4]. An optimal controller can be specified via a sampled data transfer function. The project described herein has the objective to validate active vibration control laws using realtime processing based on the frequency response optimization. Vibration control designs using realtime processing, based on Finite Impulse Response (FIR) algorithms, are currently being evaluated using a dedicated workstation which uses special purpose Digital Signal Processors (DSP) for the realtime control implementation.

In this paper we highlight the basis for design of vibration control in structures using frequency sampled data. Next we describe the functionality of a workstation for design and development of vibration control laws. We then provide overview of a benchmark vibration control experiment.

A Control Architecture for Vibration Suppression

An architecture for active vibration suppression which includes both feedback from downstream sensors and feedforward from upstream sensors is shown in Figure 1. Table 1 summarizes nomenclature for the signals and system model.

Table 1: Nomenclature
System transfer functions
$P(s)$ =commanded control force to downstream sensor
$P_o(s)$ =disturbance force to downstream sensor
$L_u(s)$ =disturbance force to upstream sensor
$C(s)$ =control process
$L_c(s)$ =feedforward compensator
Control loop signals
d =disturbance force
r =control command
y_{ds} =downstream sensor measurement
y_{us} =upstream sensor measurements
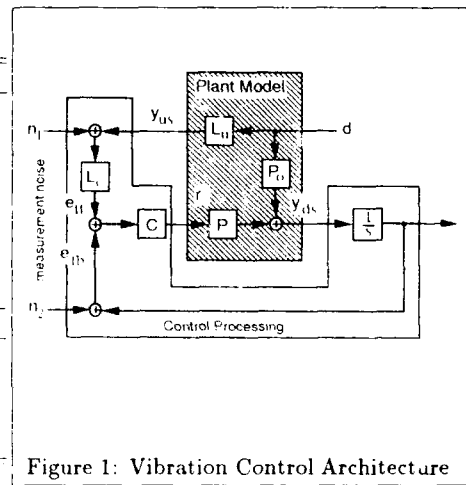
Figure 1: Vibration Control Architecture

Control Law Tradeoff via Wiener-Hopf Optimization

Important, quantitative tradeoffs in the design of the control processing can be addressed using Wiener-Hopf optimal control methods. For vibration suppression, the Wiener control objective is to minimize an averaged downstream displacement e given downstream y_{ds} (and possible upstream; i.e., feedforward) velocity measurements (y_{us})

$$Q_t = E \left\{ \frac{1}{2\pi} \int_{-\infty}^{\infty} e^*(\omega)e(\omega)d\omega \right\}$$

subject to a power-like constraint on the control, r,

$$Q_s = E \left\{ \frac{1}{2\pi} \int_{-\infty}^{\infty} r^*(\omega)r(\omega)d\omega \right\} .$$

The tradeoff of vibration suppression vs. control saturation is resolved by solving a Wiener-Hopf control problem [1, 2] that identifies a controller C which minimizes Q_t subject to constraint on Q_s. This is equivalent to minimizing the cost: $Q = Q_t + \mu Q_s$ over all controllers which maintain closed loop stability, where $\mu > 0$ is a Lagrange multiplier to be chosen during design.

A workstation for design and testing of DSP vibration control

A workstation for design, development, and testing of DSP-based vibration control is under development at TSI. The workstation supports all phases of the engineering design cycle for development of realtime processing for vibration control: 1) system frequency response estimation from finite element models and empirical measurments, 2) control law optimization, 3) realtime control algorithm design for DSP implementation, 4) control system simulation,

and 5) experimental (hardw..e in-the-loop) evaluation and testing. Workstation functionality is provided by software for control system simulation that supports an interactive, graphical interface for control configuration, data analysis and display. The software system runs on a host Everex 386 microcomputer equipped with two AT&T DSP32C boards each capable of 25MFLOPS of computational throughput. The control simulator functions in both simulator and test modes. In simulator mode, the dual DSP architecture is used to emulate vibration control system data interactions by simulating plant and controller dynamics asynchronously on separate processors. Data is transferred through the host's data bus and any desired control channel can be monitored on the host display. In test mode, a software activated data switch connects the dedicated DSP controller through a multiple channel, data acquisition system to actuator/sensor interface for closed loop control. Careful attention to the buffering and co-ordinated handshaking between multiple processors and data acquistion hardware allows the system to run synchronously at data rates of up to 1000 KHz for 16 control channels with transfers of up to 500 bytes of data and permits host microcomputer buffering and monitoring of all data channels.

A Vibration Suppression Benchmark Experiment

The vibration control workstation is currently being configured for interface with a 12 meter truss experiment at WRDC, Wright-Patterson AFB. The experiment plan will use inertial actuators (proof mass actuators) to suppress vibration induced motions at the tip of the 12 meter verticle truss which are induced by proof mass actuators acting at mid span. A vibration control algorithm for the 12 meter truss experiment has been designed. The experiment configuration is shown in Figure 2. The P-MA's at mid-station on the truss are to be used to excite the structure with a narrowband disturbance near its first bending mode. Actuators at the tip station will be used for active vibration suppression. The sensors include upstream measurements from the accelerometers at mid-station and feedback from the tip accelerometers. The objective is to suppress the deflection of the tip. The plant transfer function (PMA control commmand to displacement rate at tip station for X-Z plane bending) is shown in Figure 3. The downstream truss response is dominated by modes given in Table 2.
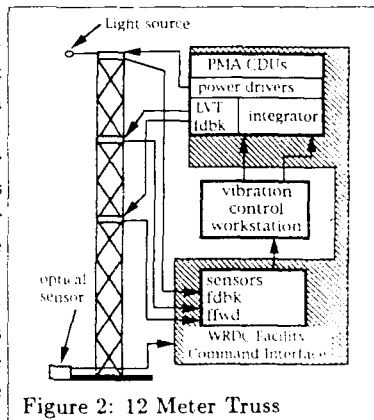
Figure 2: 12 Meter Truss

Table 2: Truss Flexure Modes

Frequency	Mode description
0.983 Hz	Actuator
1.770	First X-Z Bending
8.450	Second X-Z Bending
19.390	Third X-Z Bending
29.310	Fourth X-Z Bending
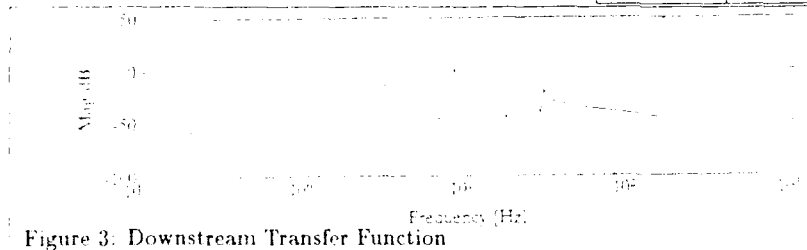
Figure 3: Downstream Transfer Function

Vibration Control Tradeoff Analysis

A suppression vs actuator saturation tradeoff analysis was performed using the Wiener-Hopf computation. The results, summarized in Figure 5, show that 0.07 v rms (corresponding to 0.05 in) displacement can be maintained with maximum actuator power (1 lb rms) for a narrowband disturbance centered near the first bending mode of the truss.

Frequency Sampled Controller

The Wiener-Hopf computation identifies an optimal controller for the vibration suppression problem as a sampled data transfer function as shown in Figure 5. The Figure compares the sample data computation for 200 Hz bandwidth with 1024 sample points with a state space approach computed based on a reduced order model for the truss X-Z bending response including the first 5 modes as in Table 2.
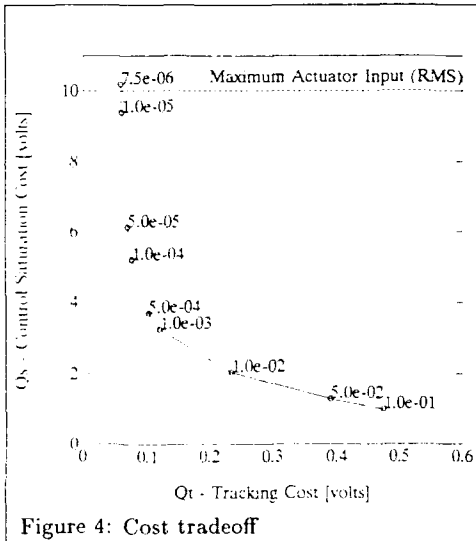
Figure 4: Cost tradeoff
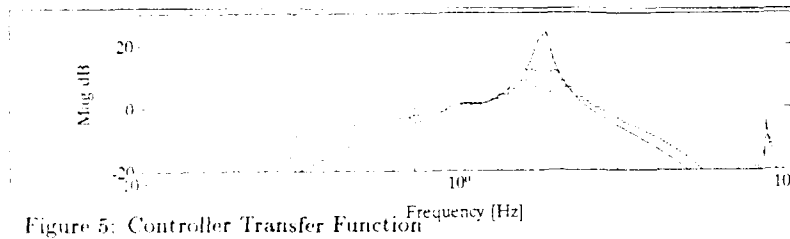
Figure 5: Controller Transfer Function

Workstation Simulation Mode

The workstation simulation mode for the truss vibration problem uses separate models for truss bending response, narrowband disturbance generation, and control processing. The truss bending response is simulated using a 21 mode truss model. Figure 6 shows the workstation simulator program interface for control channel configuration used for this experiment. The interface interface functions as a virtual patch panel.
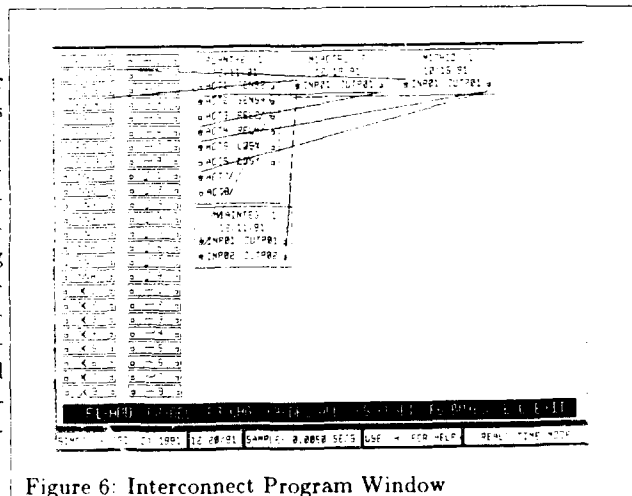
Figure 6: Interconnect Program Window

Boxes are displayed representing system components: $PLANT42$, truss bending response,

$M1ACTRL2$, the control process, $M1PHID$, narrowband disturbance, and $M1AINTEG$ integral processing for sensor/control law interface. A function generator, $FG1$, is assigned to generate a random, white noise excitation with variance of 14.14 volts.

The software patch panel provides virtual connections under user control via keyboard input. Each "patch cord" is programmed with a fixed gain and includes an assigned threshold value for detecting unstable responses or excessive transients. When data exceeds the programmed thresholds at these points the system automatically removes the connection and displays a warning.

The narrowband disturbance model drives midspan actuators. For downstream feedback vibration control, tip velocity sensors are connected to an integrator to provide displacement signals to the control process. Displacements are summed at the controller input. Another function generator, $FG2$, is assigned to produce white noise with variance 0.0424 volt and is used to simulate sensor measurment error due to A/D conversion. The control command is connected, using a patch cord providing a gain of -1 (i.e., negative feedback).

Data signals are assigned to data display windows via a graphical display and user interface. Time traces, X-Y plots, and frequency response windows are available. The realtime data display for closed loop simulated system responses for the control command and downstream velocity is shown in Figure 7. Time history is displayed in the upper window with an optional RMS counter display. Frequency responses for these channels are shown in the lower windows. The frequency responses are obtained from FFT computation from successive records. Open loop simulations are shown for comparison in Figure 8.
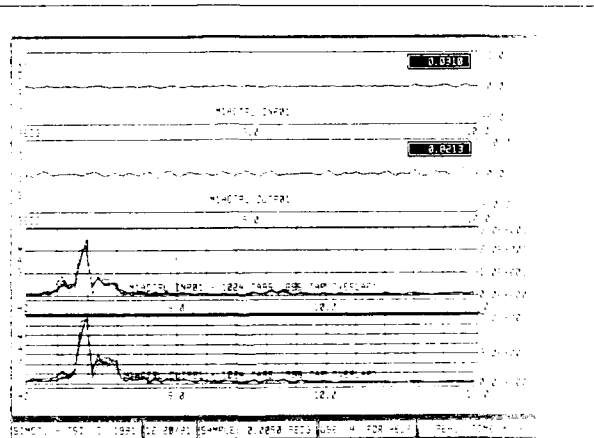
Figure 7: Closed Loop Simulation
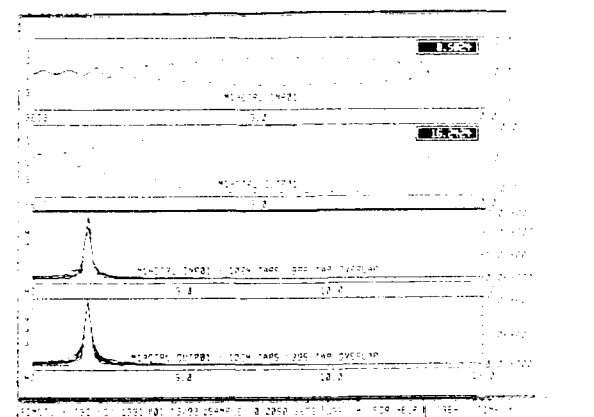
Figure 8: Open Loop Simulation

Conclusions

Direct methods for Wiener-Hopf optimization offer significant advantages for vibration control systems. Sampled data methods for frequency response modeling and control design can be integrated to support development of active vibration control for structures which integrates both feedback and feedforward processing of from available sensors. This project focuses on validation of such algorithms using a workstation to support the frequency response tradeoff analysis, design and simulation. The methods employed provide frequency response measures of known value in analysis and design of closed loop control systems. The workstation environment provides maximum flexibility for design, simulation, and experimental testing with a graphical user interface for ease of programming.

Acknowledgement

References

[1] W. H. Bennett, "Digital signal processing methods for control of vibrations in structures," in *Proc. Recent Adv. in Active Control of Sound & Vibration*, pp. 783–795, April 1991.

[2] W. H. Bennett, "Frequency response modeling and control of flexible structures: Computational methods," in *Proc. 3rd Annual Conf. Aerospace Comp. Control*, pp. 277–291, August 1989.

[3] W. Bennett and I. Yan, "A computer algorithm for causal spectral factorization," in *Proc. 1988 NAECON*, May 1988.

[4] W. Bennett and H. Kwatny, "Continuum modeling of flexible structures with application to vibration control," *AIAA J.*, vol. 27, pp. 1264–1273, September 1989.

Modal survey and test-analysis correlation of a multiply-configured three-stage booster

E. L. Marek, R. L. Mayes, and T. G. Carne

Sandia National Laboratories
Albuquerque, New Mexico
87185-5800

Abstract. This paper describes a procedure used to produce a test-validated finite element model of a three-stage solid propellant booster system. A series of system-level modal tests were performed for several inert and live propellant configurations. Test-analysis models (TAMs) were used to provide pretest support of the live propellant system tests. Confidence in the model was established by a test-analysis correlation procedure. Optimization techniques were used to determine appropriate model updates.

1. Introduction

A three-stage solid propellant booster system has been developed to launch a variety of payloads. Successful design of the booster control system depends upon a high level of confidence in the accuracy of elastic vibrational modes predicted by the booster analytical model for a number of critical flight times. Due to propellant burn and staging events, the booster configuration changes drastically from the initial to the final design time of interest.

A three-dimensional continuum finite element model (FEM) of the booster was assembled at Sandia National Laboratories using superelements and component mode synthesis (CMS) reduction techniques. The model is to be used to aid in the booster control system design, as well as in the performance of mission-specific payload loads analyses. The FEM was developed using MSC/NASTRAN Version 65 on a CRAY/XMP and Version 66 on a CRAY/YMP (MSC 1988). The goal of the modeling effort and the modal test series was to obtain a FEM which is equally validated at several critical flight times from launch until third stage burn-out. The FEM model is shown in Figure 1, where the major structural components are highlighted. There are approximately 70,000 degrees of freedom (DOF) in the (unreduced) model. The major superelements are the first stage motor, the 1st/2nd interstage, the second stage motor, the shroud, and a third stage collector. The third stage collector superelement (with shroud) is shown in Figure 2. It

---
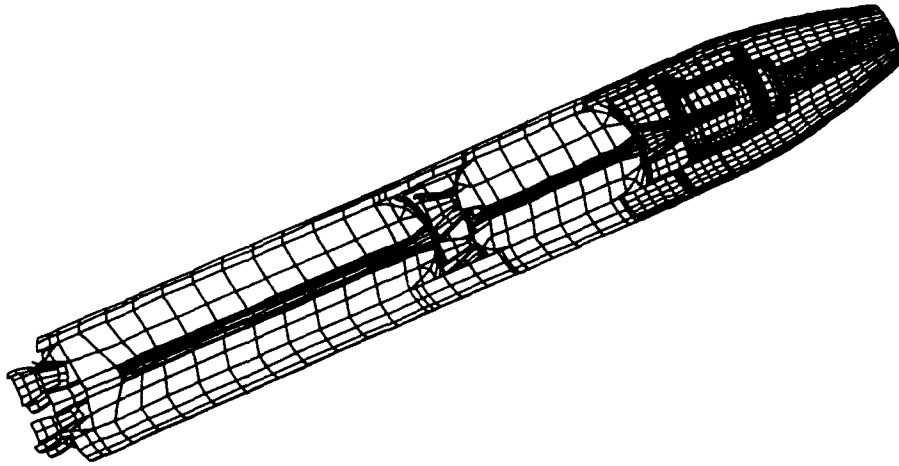
Figure 1: Finite Element Model of Booster
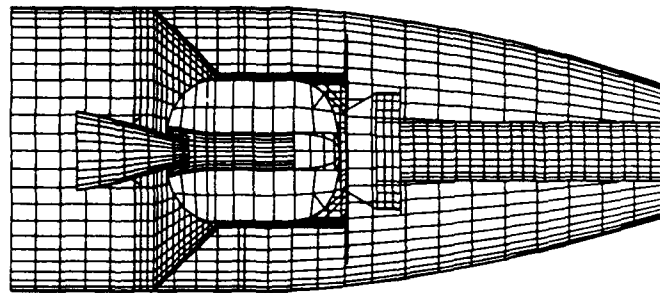
Figure 2: Finite Element Model of Third Stage

includes a section of magnesium alloy skin, a frustum from the skin to a twelve-sided motor enclosure called the dodecagon, a payload plate, a single payload simulator (mockup), and the third stage motor. This motor is attached at the junction of the dodecagon and the frustum. Booster guidance and control instrumentation (such as the rate gyro and IMU) are mounted to dodecagon surfaces. A vertical hoist assembly at the top of the shroud replaces the booster nose cap for the tests, and is represented as a rigidly connected lumped mass in the model.

Several parameters that are important to the booster behavior were very difficult to model or quantify. This necessitated the test-analysis correlation and verification process. The first and second stage booster motor cases are roughly 30 years old. They are made from filament-wound composite S-glass and manufactured by two separate suppliers. The material specifications and composite assembly procedures for these motors are not well defined. Their propellant grains are also

quite complex. The propellant is a visco-elastic material whose properties vary with temperature, frequency, and level of excitation. This is in addition to the uncertainty in propellant dynamic characteristics which has resulted from the aging process. The propellant and case dynamical properties must be accurately determined. The recently developed third stage motor also includes a composite case (graphite fiber). The new third stage structure and solid propellant motor have yet to be flight-tested. Hence, the ground tests provide critically important data for verifying these models.

Recent advances in modal test procedures, and in methods for test-analysis correlation, made a multiple-configuration approach feasible for this program. Correlation software provided by Structural Dynamics Research Corporation (SDRC) has been used successfully on a number of programs involving both inert and live propellants (Flanigan 1987, Brillhart *et al.* 1988 & 1990). In addition, the software is structured in such a way that multiple booster configurations may be handled simultaneously.

A total of five system-level tests were performed. Three tests were performed with available hardware and inert propellants, to obtain a maximum amount of structural response information early in the development program. Closer to first launch, two tests were performed using live propellants. A separate test of the mockup payload alone was also performed. Details of the tests, the FEM and TAM model development, and the correlation process are included in the following sections.

2. Inert Propellant Test Series

2.1. Setup

Schematic diagrams of the three all-inert propellant configurations appear in Figure 3. The configurations represent a booster at first stage burnout with stage 1 motor nozzles omitted (Test 1C), second stage ignition (Test 1B), and second stage burnout with stage 2 motor nozzles omitted (Test 1A). An annular TVC (thrust vector control) tank, mounted to the aft end of the second stage motor in a true flight unit, was not present for any of the all-inert tests. For each test, free-free conditions were closely approximated by suspending the booster vertically from an overhead bridge crane with a long flexible strap connected to the vertical hoist assembly. A photograph of the first stage burnout configuration test (1C) is shown in Figure 4.

2.2. Performance

For the 1C configuration, ten global modes and seven shell modes of the empty first stage motor case (all below 100 Hz) were determined. For the global modes, burst random excitation with 30 to 40 lb force peaks was achieved using two 50 lb
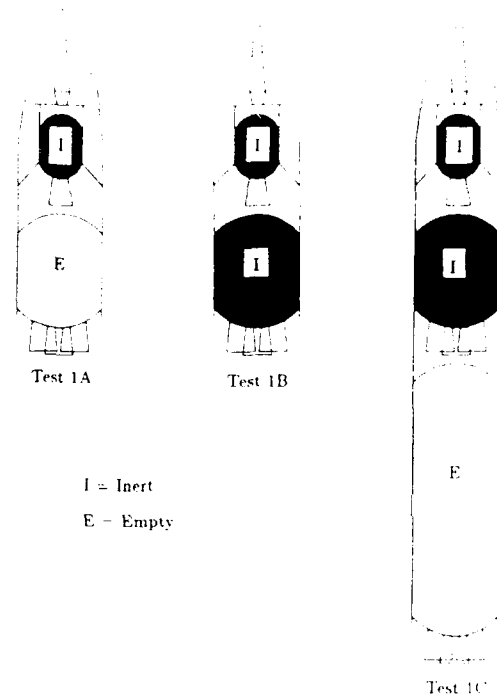
Figure 3: Schematic of Inert Modal Tests

electrodynamic shakers at the aft junction of the first stage motor case and skirt. The shakers were arranged to excite bending, axial, and torsional system modes. A limited nonlinearity check was performed using two input force levels, with a sine wave excitation tuned to produce a 90° phase difference between the force and response. Besides extensive fixed internal instrumentation, roving triaxial accelerometers were used every 90° around the booster at numerous stations. Shell modes of the empty motor case were desired to allow accurate correlation of equivalent orthotropic properties for the first stage case. Radial excitation was provided with an impact hammer, again at the bottom of the first stage motor case. The roving accelerometers were used every 30° around the circumference for this test.

Thirteen modes were found for the 1B configuration, using an impact hammer applied at two locations: the junction of the second stage motor forward skirt and the third stage skin; and, at the bottom of the second stage motor. Bending and torsional modes were excited. The roving triaxial accelerometers were placed every 45° around the circumference.

Ten modes were found for the 1A test. Burst random excitation was provided by two 50 lb shakers, placed at the bottom of the second stage motor so as to excite

Figure 4: Inert Modal Test 1C Setup

bending and torsional modes (no axial). The roving accelerometers were placed every 90° for this test.

3. Live Propellant Test Series

3.1. Setup

The two test configurations involving live propellant are shown schematically in Figure 5. These represented a booster at launch (right, Test 2B) and at second stage ignition (left, Test 2A). For these tests, only the third stage motor propellant was inert. No other major differences existed between these two test configurations and an actual flight unit.

Test 2A

L = Live

I = Inert

Test 2B
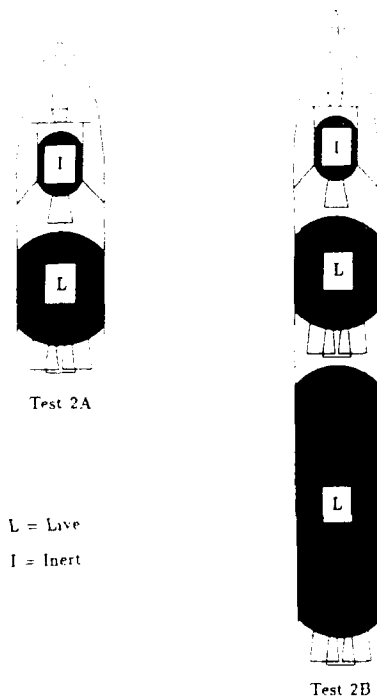
Figure 5: Schematic of Live Modal Tests

4.2. Suspension System Design

The booster was suspended from the vertical hoist assembly using an assembly of straps, rigid links, pulleys, cables, and a hydraset. This suspension system was attached to the boom of a truck-mounted hydraulic crane. During pretest calibrations with a rigid booster mockup, the suspension system was found to have significant coupling with the booster. In particular, the suspension system exhibited several modes which were close in frequency to the expected lowest missile bending mode at launch. This indicated that the suspension would not provide ideal free-free isolation of the test article. A finite element model of the suspension system was developed, correlated to the pretest modal data, and then altered to find a configuration which would minimize the effects of booster/suspension coupling. The transverse stiffness of the suspension system due to the axial load was modeled using elastic elements. The properties of these elements were derived using the analogous case of a string under tensile load. Inclusion of accelerometers at various positions on the suspension system during the actual tests allowed reliable correlation of the final booster/suspension model.

3.3. Performance

Three electrodynamic shakers were used in the launch configuration test. Two 100 lb shakers were placed at the bottom of the first stage motor to excite the bending, axial, and torsional modes. A 50 lb shaker at the bottom of the second stage motor was designed to aid the axial and bending excitation. This shaker was found to be fairly ineffectual because of local flexibility effects. Burst random input in the range from 8 to 64 Hz was used. A total of 13 modes were found between 8 and 40 Hz, with no strong modes above that frequency (perhaps because of high damping levels in the test article). The observed modes included four which were primarily bending in nature (occurring in pairs), one torsional, and several from the suspension system. Rigid body and suspension system modes below the first flexible booster modes were measured separately by manually exciting the booster. The first two suspension modes were extracted from impact data on the suspension system.

Two 100 lb electrodynamic shakers were mounted 90° apart on the vertical hoist assembly and used to excite the second stage ignition configuration. A combination of horizontal and vertical burst random input was used, in the range from 10 to 64 Hz. This input was successful in exciting the rigid body and lower suspension modes, as well as the flexible booster modes. Recorded modes above 40 Hz seemed to be affected by nonlinear behavior, perhaps caused by poor seating and rattling of the third stage motor nozzle. High confidence in the experimental mode shapes was therefore restricted to the first two bending modes in this test. These first two modal frequencies were considerably below the corresponding measurements in the all-inert second stage ignition test (20 % for the first and 50 % for the second). Possible sources of this difference were configuration and assembly variations and propellant properties. Post-test component weight comparisons suggested an apparent 12.7 % density discrepancy between live and inert second stage propellant.

Sixteen channels of data were simultaneously recorded for each configuration. The data was validated by using reciprocity checks and resynthesis of frequency response functions from the modal parameters for comparisons to the original data.

4. TAM and Pre-Test Analyses

4.1. TAM Background

A Test Analysis Model (TAM) is a reduced order representation of a finite element model (FEM). TAMs can be useful in the design and execution of modal tests on complex structures. An accurate TAM will represent a very close approximation to the stiffness and mass properties of the FEM. The TAM provides a mathematical link between the FEM and modal test results.

Two different TAM methods were used at the MSC/NASTRAN residual structure level for modal analyses of the live propellant test configurations. Static reduction (Guyan 1965) was used at the component level in each case, prior to the residual

analysis. Two TAM methods were compared for the residual analysis: static reduction and the Improved Reduced System (IRS) method (O'Callahan 1989). The residual structure static reduction TAM was found to be inadequate for the selected number of measurement DOF. Therefore, final pretest results were obtained using the IRS method for the residual analysis.

The IRS procedure is an extension of the Guyan reduction technique. It adjusts the reduced system modal matrices to include knowledge of system inertial effects. Let subscripts 'a' and 'd' represent active (instrumented) and deleted (noninstrumented) DOF, and let '~' and '—' underscores denote matrix and vector quantities, respectively. The active DOF 'a' correspond to MSC/NASTRAN A-set DOF in the residual structure TAM model. These correspond one-to-one with accelerometer channels used in the live propellant tests. The deleted DOF 'd' correspond to the MSC/NASTRAN B-set, C-set, and Q-set DOF present for the *residual* system run, minus the A-set DOF, and $n = a + d$.

The residual system static equation, $K_n X_n = F_n$, may be partitioned as:

$$\begin{bmatrix} K_{aa} & K_{ad} \\ K_{da} & K_{dd} \end{bmatrix} \begin{Bmatrix} X_a \\ X_d \end{Bmatrix} = \begin{Bmatrix} F_a \\ F_d \end{Bmatrix} \tag{1}$$

The lower partition of Equation (1) may be solved for X_d, the displacements of the deleted DOF:

$$X_d = -K_{dd}^{-1} K_{da} X_a + K_{dd}^{-1} F_d \tag{2}$$

Combining Equation (2) with the identity $X_a = X_a$ in a single partitioned equation, the result may be expressed as:

$$X_n = T_s X_a + X_n^{fd} \tag{3}$$

where T_s is the static Guyan condensation matrix, and X_n^{fd} is a displacement adjustment vector due to forces acting on the deleted DOF. The $n \times a$ matrix T_s may be expressed as:

$$T_s = \begin{bmatrix} I_{aa} \\ -K_{dd}^{-1} K_{da} \end{bmatrix} = \begin{bmatrix} I_{aa} \\ t_s \end{bmatrix} \tag{4}$$

where I_{aa} is the $a \times a$ identity matrix, and t_s is of size $d \times a$. The inertia forces at the deleted DOF are redistributed to the active DOF by the IRS formulation. This allows Equation (3) to be expressed as:

$$X_n = T_i X_a \tag{5}$$

where

$$T_i = \begin{bmatrix} I_{aa} \\ t_s + t_d \end{bmatrix} \tag{6}$$

is the IRS condensation matrix. and the expression for t_d contains the Guyan reduced system stiffness and mass matrices K_a and M_a:

$$t_d = K_{dd}^{-1} \left[M_{da} + M_{dd} t_s \right] M_a^{-1} K_a \tag{7}$$

The IRS reduced system stiffness and mass matrices are given by $K_a^i = T_i^T K_n T_i$ and $M_a^i = T_i^T M_n T_i$, respectively.

4.2. Live Propellant (2A/2B) Pre-Test Analysis

The TAM model for test 2B (not including the suspension system) included $a = 224$ DOF The TAM model for test 2A (not including the suspension system) included $a = 152$ DOF, a subset of those for the 2B TAM. A common global cylindrical coordinate system was used for both the TAM and test DOF. Orthogonality and cross-orthogonality checks between the FEM and TAM modes were used prior to the tests to verify the accuracy of the TAM. The fidelity of the TAM indicated that all modes of interest would be accurately measured using the chosen accelerometer distribution.

Using the FEM, frequency response functions (FRFs) were computed for every TAM accelerometer channel, using several potential exciter locations. The analytical FRFs were used to compute mode indicator functions (MIFs) and multivariate mode indicator functions (MMIFs). Review of this data, along with a careful examination of preliminary FEM mode shapes, allowed each exciter location to be evaluated prior to the tests. All booster modes of interest were successfully excited.

5. Model Correlation

Numerous researchers have used identification procedures to correlate structural models with the results of modal tests (Collins *et al.* 1974, Hart and Martinez 1982, Carne and Martinez 1987, Allen and Martinez 1990, Imregun and Visser 1991). This section summarizes the use of design sensitivity data from the FEM in conjunction with optimization techniques for performing test-analysis correlation via model parameter updating.

5.1. Correlation Using Design Sensitivity (CORDS)

MSC/NASTRAN provides a Design Sensitivity Analysis (DSA) capability which calculates the sensitivity of modal frequencies to (small) changes in model parameters. such as material and cross-sectional properties. This information is useful

in determining the appropriate set of model updates to achieve test-analysis correlation. The correlation software CORDS (Flanigan 1987) organizes this data and utilizes optimization techniques to determine parameter changes. The problem formulation is briefly reviewed here.

To a first order approximation, the change in each frequency (f_i) due to changes in parameter values (δp_j) is:

$$f_i^{mod} = f_i^{orig} + \sum_{j=1}^{n}(D_{ij}\delta p_j)$$

Where D_{ij} is the design sensitivity of f_i to a change in parameter p_j. D_{ij} is numerically equal to the derivative $\frac{\partial f_i}{\partial p_j}$.

Since this expression is only valid in a neighborhood of the nominal values (i.e. for small parameter changes) overall convergence is often improved by rolling off the effect of parameter changes:

$$f_i^{mod} = f_i^{orig} + \sum_{j=1}^{n}(\frac{D_{ij}\delta p_j}{1 + ||\delta p_j||})$$

The performance index is defined as:

$$P = \{W^f \cdot \sum_{i=1}^{m}(w_i^f \cdot ||\frac{f_i^{mod} - f_i^{targ}}{f_i^{targ}}||)\} + \{W^p \cdot \sum_{j=1}^{n}(w_j^p \cdot ||\delta p_j||)\}$$

This is the objective function to be minimized during the optimization. The f_i^{targ}, $i = 1,...,m$ are the target frequencies from the test data. Individual weights (w_i^f, w_j^p) and overall weights (W^f, W^p) are defined for both frequency errors (f) and parameter perturbations (p). Increasing the weights on frequency errors indicates greater confidence in the test data. Increasing the weights on parameter changes indicates greater confidence in the initial property values. Adjusting the weights to achieve a satisfactory trade-off between matching the test data and making justifiable model changes is a trial and error process requiring much engineering judgement.

The above equation for P applies for a single configuration (e.g. 2A). For simultaneous correlation using multiple configurations (e.g. 2A + 2B), the above relations are still applicable. If, configurations are to be simultaneously correlated the following interpretation is appropriate: concatenate the frequency error terms such that $m = m_I + m_{II} + \cdots + m_{N_c}$ and form the union of the parameter variation terms such that $n \leq n_I + n_{II} + \cdots + n_{N_c}$. That is, some parameters may be common to more than one configuration.

The CORDS software is designed to handle the multiple configuration case. Since frequency data alone is used, the parameters available for adjustment generally outnumber the data to be matched. Individual component tests which isolate specific structural elements along with simultaneous multiple configuration correlation yields a consistent and unique set of parameter updates. The current system

is somewhat modelable a priori and the modes are easy to comprehend. For more challenging systems, including some of the future payload systems which will fly on this booster, additional measures are required. Advanced system identification techniques are currently under development. These methods utilize shape data, frequency response data, local strain data, and statistical data. The challenge lies in interfacing these methods with FEM models and applying them to practical systems.

5.2. Payload Mockup Tests

The payload mockup is centered on the payload plate and is attached at four locations using "feet". In the FEM, these feet are modeled as equivalent bars connected to rigid elements which cover the footprint. A fixed-base payload test including the actual payload plate was performed to obtain data on payload attachment flexibility. Although the assembly is symmetric, noticable separation in the frequencies of orthogonal first bending modes occured. Subsequent investigation indicated that the flexibility of the payload/feet connection is heavily dependent on the preload and assembly procedures, including orientation. After mitigating these effects a reproducible configuration was obtained. This configuration was used in the live propellant tests. Figure 6 depicts the FEM modes for the fixed-base payload test
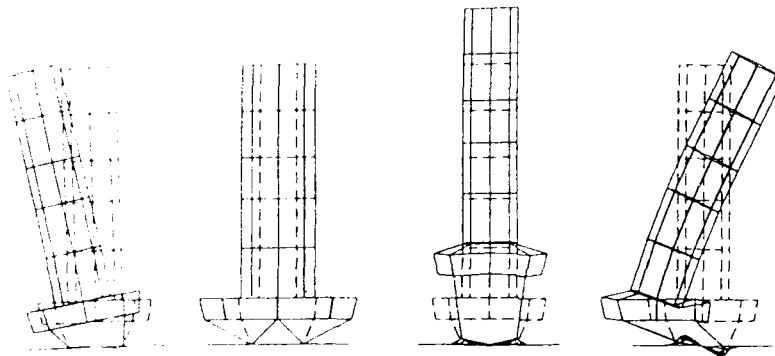
Figure 6: FEM Modes of Payload Test

(using a display model similar to the trace-links used to connect accelerometer locations for displaying modal test shapes). The frequencies of the correlated FEM are compared with the test data in Table 1. The frequencies of the first bending mode pair agree to within much less than 1%. For comparison, an initial model (symmetric and based solely on assembly drawings) exhibited errors in first bending frequencies of 6-11%.

5.3. First Stage Shell Modes

The inert tests were useful in designing the live tests and as a source of early, preliminary data. Uncertainties in the payload attachment flexibility and the inert

Table 1: Mockup Payload Frequencies

FEM	Test	Δ %	Description
26.32	26.30	+.08	1st Bending, Soft
27.79	27.80	-.04	1st Bending, Stiff
98.43	98.00	+.44	Torsion
135.9	139.6	-2.7	Axial
164.7	162.0	+1.7	2nd Bending, Soft
172.2	163.5	+5.3	2nd Bending, Stiff

Table 2: First Stage Shell Mode Frequencies

FEM	Test	Δ %	Mode
39.9	39.7	+.50	3,0
48.1	49.3	-2.4	4,0
54.4	54.8	-.73	2,0
73.3	74.0	-.95	5,0
79.5	78.1	+1.8	4,1
88.0	86.6	+1.6	5,1
96.3	97.1	-.82	3,1

propellant properties precluded using this data for quantitative correlation. However, seven orthogonal pairs of shell modes for the empty first stage were obtained. These modes are not heavily influenced by the uncertainties cited above. Two of these modes (FEM and test) are depicted in Figure 7. The indices (m, n) indicate the number of sine waves in the circumferential direction and the number of nodal lines in the longitudinal direction, respectively. The frequencies of the correlated FEM are compared with the test data in Table 2. The average frequency error of the seven shell modes is 1.3 %. For comparison, the average frequency error of the initial model was 11 %. The case properties changed up to 20 % from the initial estimates.

5.4. Live Propellant Tests

The live propellant tests were the main focus of the model verification effort. These tests were conducted at the launch facility using actual flight hardware for all systems except the third stage motor. As previously noted, the suspension system was designed within the constraints of the facility to alleviate coupling with the missile modes. The suspension system is modeled explicitly in the FEM using a combination of masses, rigid links, and elastic elements representing rotational connections and the transverse stiffness due to axial loading. Separate data for the lower modes of the suspension system were used to obtain initial estimates of the suspension system properties. These parameters were retained as variables in the overall correlation.

Configurations representing second stage ignition (2A) and launch (2B) were used in a simultaneous test-analysis correlation. The structural parameters of the

$m, n = 3,0$ $m, n = 3,1$
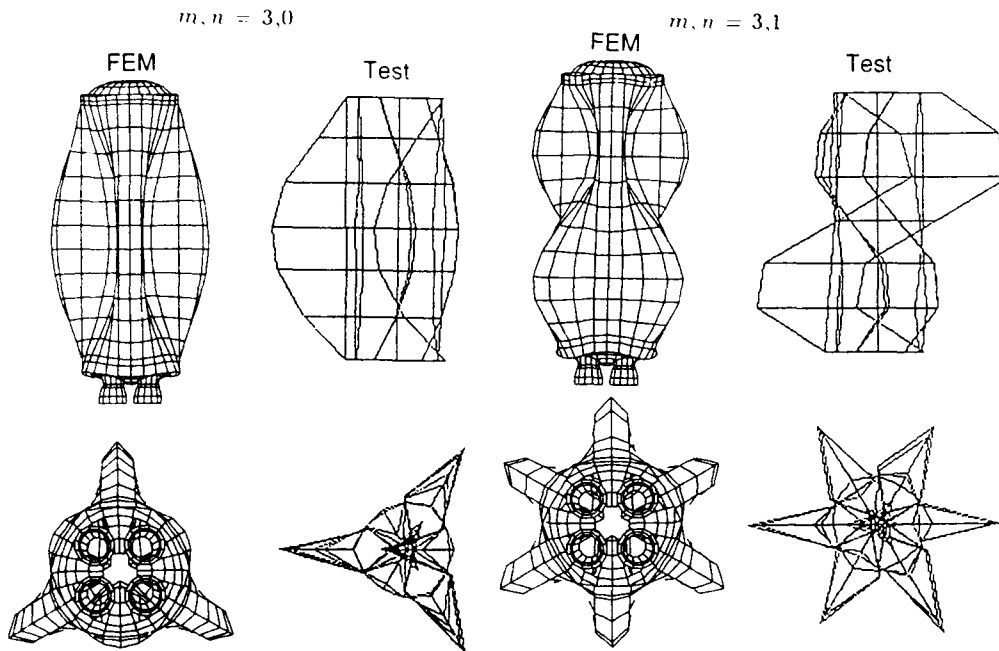
Figure 7: Test/FEM 1st Stage Shell Modes

second stage and above are common to both cases. The 2A/2B suspension system parameters are distinct due to different preloads. High confidence was placed in the payload attachment properties and the first stage case properties from prior component test-analysis correlation results. The six lowest frequency bending modes are depicted in Figure 8. The mode shapes are depicted in pairs. For each pair, the test shape appears on the left and the FEM shape appears on the right. The FEM plots utilize a display model, which is comprised of straight-line connections between selected nodes (corresponding roughly to accelerometer locations). The display models have a circumferential node spacing of 45° while the test accelerometer spacing is 90°. The suspension system is also shown. Some of the apparent difference in its motion (test vs FEM) is due to two factors: (1) the test data includes transverse degrees of freedom only and (2) some accelerometers are located within "rigid" elements rather than at the boundaries.

The frequencies of the correlated FEM are compared with the test data in Table 3 (the asterisks denote modes depicted in Figure 8). The first bending modes are the most significant for control design, particularly for first stage burn. The results indicate a frequency correlation error for these modes of less than 1% for first stage

Test   FEM

Test   FEM

Test   FEM

Test   FEM

18.60 Hz   18.32 Hz   12.19 Hz   12.22 Hz   18.83 Hz   18.93 Hz
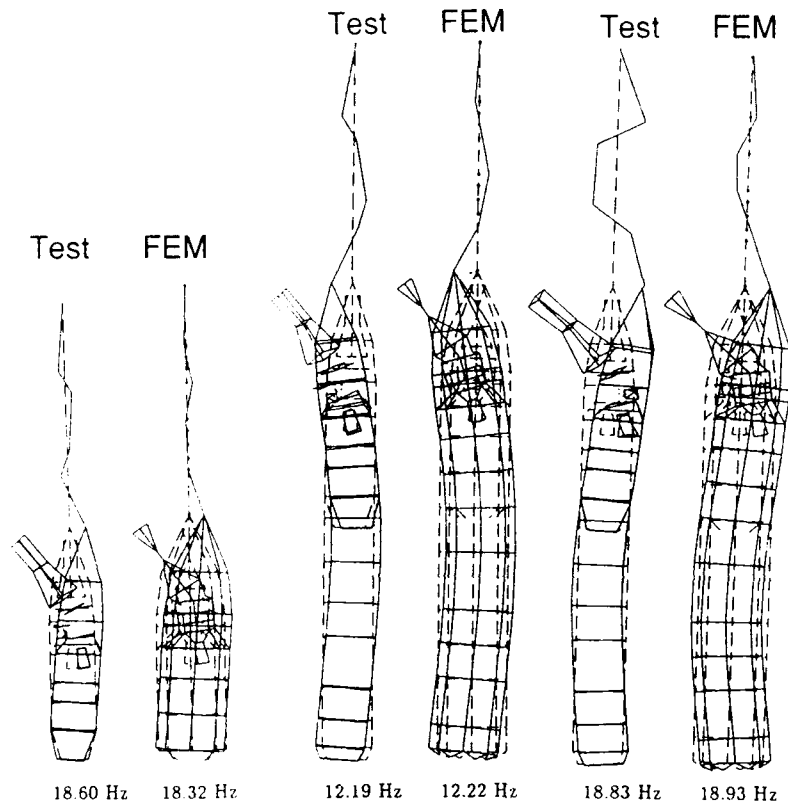
Figure 8: Test/FEM Configuration 2A/2B Bending Modes

burn and less than 2% for second stage burn. This compares with initial errors on the order of 10 % prior to the overall test-analysis correlation process. The larger part of this overall improvement is due to the component correlation (payload and shell modes). The final 2-3 % refinement is due to the 2A/2B data correlation. This implies that errors in the initial estimates of the first stage case properties and the payload flexibilities were the largest source of uncertainty.

6. Summary and Conclusions

This paper presented the results of a model verification and correlation effort for a multiple configuration booster system. A series of inert propellant tests were performed early in the program to provide timely preliminary data. Experience from these tests along with detailed pre-test analyses led to a successful set of live propellant tests. Modal data from several configurations were used to update a three-dimensional MSC/NASTRAN finite element model. These tests included payload mockup, empty first stage shell, live propellant second stage ignition and live propellant launch configurations. For each mission, test-verified payload models are

Table 3: Configurations 2A and 2B Frequencies

FEM	Test	Δ %	Description
14.72	14.80	-.54	2A Suspension System
15.60	15.60	0.0	2A Suspension System
18.32	18.60	-1.5	2A Payload Hinge*
18.64	18.90	-1.4	2A Payload Hinge
26.24	26.20	+.15	2A Suspension System
29.51	29.50	+.03	2A Suspension System
7.50	8.10	-7.4	2B Suspension System
7.72	8.40	-8.1	2B Suspension System
12.22	12.19	+.25	2B First Bend (PL In)*
12.32	12.41	-.73	2B First Bend (PL In)
18.93	18.83	+.53	2B First Bend (PL Out)*
19.10	19.23	-.68	2B First Bend (PL Out)
20.81	20.93	-.57	2B Suspension System
21.65	21.98	-1.5	2B Suspension System
29.34	28.53	+2.8	2B Second Bending
29.35	29.24	+.38	2B Second Bending
32.82	32.00	+2.6	2B First Torsion
35.67	34.40	+3.7	2B Suspension System

produced and coupled to the validated booster system model. This provides timely, efficient, and accurate prediction of the system modal characteristics throughout the flight trajectory.

7. Acknowledgements

References

MSC/NASTRAN User s Manual, Version 66, Los Angeles, California, MacNeal Schwendler Corporation, 1988.

Flanigan, C. C., "Test/Analysis Correlation of the STS Centaur Using Design Sensitivity and Optimization Methods", *Proceedings of the 5th International Modal Analysis Conference*, London, England, April 1987.

Brillhart, R. D., Hunt, D. L., and Kammer, D. C., "Modal Survey and Test-Analysis Correlation of the Space Shuttle SRM", *Proceedings of the 6th International Modal Analysis Conference*, Orlando, Florida, February 1988.

Brillhart, R. D., Freed, A. M., Hunt, D. L., and Chism, T. L., "Modal Test and Correlation of the Commercial Titan Dual Payload Carrier", *Proceedings of the 8th International Modal Analysis Conference*, Kissimmee, Florida, January 1990.

Guyan, R. J., "Reduction of Stiffness and Mass Matrices", *AIAA Journal*, Vol. 3, February 1965.

O'Callahan, J., "A Procedure for an Improved Reduced System (IRS) Model", *Proceedings of the 7th International Modal Analysis Conference*, Las Vegas, Nevada, January 1989.

Collins, J. D., Hart, G. C., Hasselman, T. K., and Kennedy, B., "Statistical Identification of Structures", *AIAA Journal*, Vol. 12, February 1974.

Hart, G. C., and Martinez, D. R., "Improving Analytical Dynamic Models Using Frequency Response Data - Application", *Proceedings of the 1982 Structures, Structural Dynamics, and Materials Conference*, Paper 82-0637.

Carne, T. G., and Martinez, D. R., "Identification of Material Constants for a Composite Shell", *Proceedings of the 5th International Modal Analysis Conference*, London, England, April 1987.

Allen, J. J., and Martinez, D. R., "Techniques for Implementing Structural Model Identification Using Test Data", *SAND90-1185*, Sandia National Laboratories, Albuquerque, New Mexico, June 1990.

Imregun, M., and Visser, W. J., "A Review of Model Updating Techniques", *Shock and Vibration Digest*, January 1991.

Comparison of four methods for calculating vibration mode shape sensitivities

Farhang Aslani, Nickolas Vlahopoulos

Staff Engineers, Automated Analysis Corporation, Ann Arbor , Michigan 48105

Ichiro Hagiwara

Research Scientist, NISSAN MOTOR Co., Yokosuka, Japan

ABSTRACT : Three available methods for calculation of vibration mode shape sensitivities and a new method developed by the authors are compared. These four methods include the Nelson's Simplified Method (NSM), Implicit Modal Superposition Method (IMSM), Direct Reduced Basis Method (DRBM), and Indirect Reduced Basis Method (IRBM). The methods were implemented in the general purpose MSC/NASTRAN finite-element program. The efficiency and accuracy of the four methods were compared using a 1000-node sample truck model having 46 design parameters. Efficiency were compared based on central processor unit (CPU) time needed by each method. The accuracy was compared with reference to the NSM results. It was found that the IMSM proposed by Wang is the most efficient and accurate method.

1. Introduction

Frequency and mode shape sensitivities are often needed in a process involving calibration or design optimization of a dynamic structural model. Either process uses an optimization scheme in which the sensitivity coefficients can be used to reduce the number of iterations needed to obtain a solution for optimum changes in design variables. Unlike mode shape sensitivities, frequency sensitivities involve minor computational effort. The earlier work by Fox and Kapoor (1968) provided the formulation for calculation of frequency sensitivities while the formulation given for mode shape sensitivities suffered from inaccuracy. Nelson (1976) suggested an exact method for mode shape sensitivities which was computationally intensive since it required one decomposition per mode of interest. The Nelson's Simplified Method (NSM) has been installed on MSC/NASTRAN (1986) and it proved to be very expensive for structures having several thousands of degrees of freedom.

In the search for a method more computationally efficient than the NSM, other methods have been suggested by Ojalvo (1986a, 1986b), Wang (1985, 1991). These methods are based on finite-difference or modal superposition. Hagiwara and Nagabouchi (1989) suggested an iterative scheme based on Gauss-Seidel method. Sutter (1988) compared the efficiency of these methods on two small structures. However, the results of comparisons are not valid for working-environment structures having thousands of degrees of freedom. The purpose of the stu   esented in this paper is :

1. To develop a new method for calculation of mode shape sensitivities based on finite difference method. It indirectly calculates the modes shapes of perturbed structure in a reduced space. The method will be called Indirect Reduced Basis Method (IRBM).

2. To implement the three methods in MSC/NASTRAN using Direct Matrix Abstraction Program (DMAP). These methods are a) the Implicit Modal Superposition Method (IMSM) by Wang(1991), b) Direct Reduced Basis Method (DRBM) by Wang (1990), c) the Indirect Reduced Basis Method (IRBM) developed by the authors.

3. To compare the accuracy and efficiency of the above three methods with the NSM using a 1000-node sample truck model having 46 design parameters. The comparison is based on central processor unit (CPU) time needed by each method. The accuracy was compared with reference to the NSM results.

2.   Summary of the Methods

2.1   Nelson's Simplified Method (NSM)

The eigenvalue problem for the baseline structure can be stated as:

$$([K] - \lambda_k [M]) \{\phi_k\} = 0 \tag{1}$$

where K, M, λ_k, and ϕ_k are the stiffness matrix, mass matrix, k^{th} eigenvalue, and the kth mode shape of the baseline structure, respectively. The differentiation of Equation (1) with respect to design variable x_i results in :

$$[Z_k] \frac{\partial \{\phi_k\}}{\partial x_i} = \{F_{ki}\} \tag{2}$$

where

$$[Z_k] = [K] - \lambda_k [M] \tag{3a}$$

$$\frac{\partial [Z_k]}{\partial x_i} = \frac{\partial [K]}{\partial x_i} - \lambda_k \frac{\partial [M]}{\partial x_i} - \frac{\partial \lambda_k}{\partial x_i} [M] \tag{3b}$$

$$\{F_{ki}\} = - \frac{\partial [Z_k]}{\partial x_i} \{\phi_k\} \tag{3c}$$

A direct solution of Equation (2) is not possible since $[Z_k]$ is a singular matrix. The NSM seeks to overcome the complication associated with this singularity.

2.2   Implicit Modal Superposition Method (IMSM)

In modal superposition method the mode shape sensitivities are expressed as a linear combination of the mode shapes of the baseline structure. Then the problem reduces to finding the modal contribution factor (MCF) for each mode of the baseline structure. Fox and

Kapoor (1968) have already developed the equations for the calculations of the MCF. In the analysis of a large structure, however, limited number of modes are extracted in the normal modes analysis of the baseline structure. These modes are typically in the range of 0-80 Hz for structural analysis and 0-300 Hz for acoustic-structural analysis. Therefore, the mode shape sensitivities suffer from the inaccuracy caused by modal truncation in the baseline structures, Aurora (1976) and Noor (1974). Recently, Wang (1991) suggested a method to include the effects of the higher modes which are not extracted in the normal modes analysis of the baseline structure. The method uses a mode-acceleration type approach, Craig (1981), by using a static solution to approximately include the effects of the higher modes. Wang's method has been programmed and tested in this study.

2.3 Direct Reduced Basis Method (DRBM)

In finite difference methods, the concept of reanalysis techniques is used in which the baseline structure is perturbed with slight change in a specific design parameter. Then, the information from moda. analysis of the baseline structure is used to extract the mode shapes of the perturbed structure. To reduce the computational efforts, the eigenvalue problem of the perturbed structure can be projected to a smaller space which is defined by 'h' mode shapes available from the normal modes analysis of the baseline structure. Then, the reduced eigenvalue problem is solved using any available method. The mode shapes of the perturbed structure can then be calculated by a simple back-transformation from the smaller space to the original space. Finally, having the normalized mode shapes of the baseline and perturbed structures. the finite difference method can be used to approximately calculate the mode shape sensitivities of the baseline structure with respect to a slight change in a specific design parameter. The method proposed by Wang (1990) was programmed in MSC/NASTRAN as an attempt to include the effect of higher truncated modes. However, analysis of a 1000-node sample problems resulted in numerical difficulties during eigenvalue extraction of some modes. Therefore, it was decided not to include the effects of higher modes since more work was needed to resolve the numerical problems faced during the eigenvalue extraction of the reduced problem.

2.4 Indirect Reduce Basis Method (IRBM)

Similar to the DRBM, the mode shapes of the perturbed structure are calculated in the IRBM. However, the method is called indirect since direct solution of the the reduced eigenvalue problem is not sought. The detailed development of the method will be published in another paper and will not be presented here due to space limitation.

3. DMAP Implementation in MSC/NASTRAN

The IMSM, DRBM, and IRBM were implemented in Version 66 of MSC/NASTRAN. New DMAP capabilities of Version 66 were employed to simplify the logic of the programs. Each method was programmed as a separate solution sequence. Any of the three solution sequences can be submitted as a RESTART from a normal modes analysis using Unstructured Solution Sequence (USS) SOL 63. The only restriction is that the normal modes analysis of the baseline structure should use the mass normalization option. The data deck for either of the three developed solution sequences is identical to the one used for SOL 53. However, some new parameters are added which control different options in the software.

4. Comparisons for Performance and Accuracy

A 1000-node finite element model of a sample truck was used in the accuracy and performance test of the three methods programmed in MSC/NASTRAN. For accuracy test, the results were compared with those from the NSM. This comparison assumes that the NSM is an exact method. This assumption becomes more valid as the amount of change in the design variables becomes smaller. Therefore, the analyses were performed for a 5% change in each design variable. Figure 1 shows the ratio of the mode shape sensitivities from each three methods to that calculated by the NSM. These data are presented for some selective degrees of freedom. The results of the analyses indicated that the IMSM is the most accurate method since it includes the effects of the higher modes not extracted in the normal modes analysis of the baseline structure.

As for CPU time performance, the effect of the number of design variables in the sensitivity analysis was studied. Twenty modes were included in all sensitivity analyses, whereas the number of design variables was increased in subsequent analyses. The CPU time needed in each analysis were compared with that needed by the NSM. The results are shown in Figure 2 which shows the ratio of the CPU time needed by each method to that needed by the NSM. The figure indicates that the IMSM takes the least CPU time which makes it the most efficient method. The superiority of the IMSM increases as the number of design variable increases.

Another attempt was made to examine how the CPU time performance is affected by the number of modes included in the sensitivity analysis. These analyses were performed for 20 design variables. The results are shown in Figure 3 and they again indicate that the IMSM is the most efficient method. The superiority of the IMSM increases as the number of modes of interest increases.

5. CONCLUSION

The IMSM proposed by Wang (1991) is the most efficient and accurate method. It requires 1/12 of the CPU time needed by the NSM in a bench mark test using a 1000-node sample truck model having 46 design variables and including the first 20 modes of vibration.
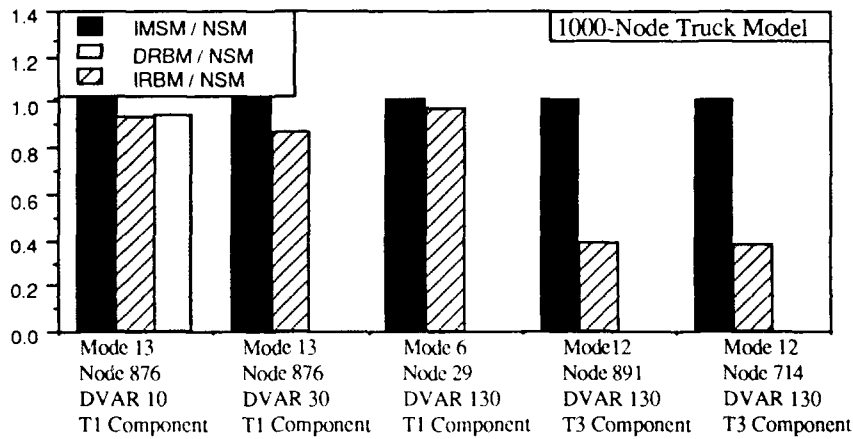
Figure 1 - Accuracy of the IMSM, DRBM, and IRBM Results
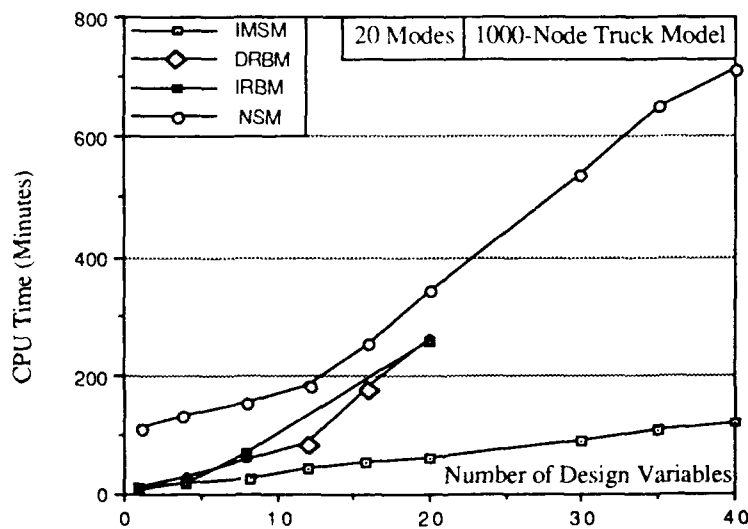
Figure 2 - CPU Performance of the IMSM, DRBM, IRBM, and NSM

for Different Number of Design Variables
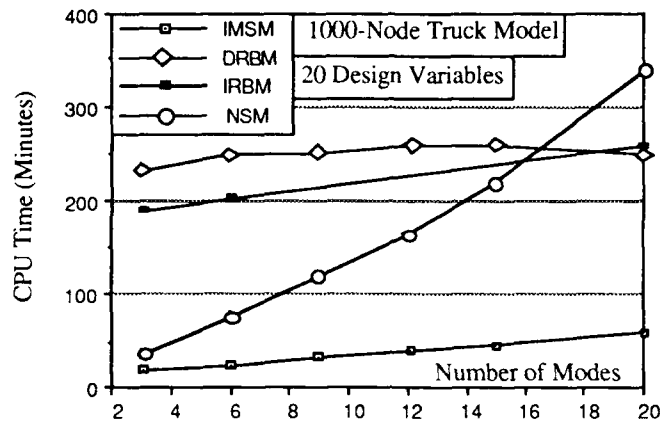
Figure 3 - CPU Performance of the IMSM, DRBM, IRBM, and NSM

for Different Number Modes of Interest

REFERENCES

Arora J S (1976) , " Survey of Structural Reanalysis Techniques", Journal of Structural Division, ASCE, Vol. 102, No. ST4.

Craig R R (1981), "Structural Dynamics, An Introduction to Computer Methods", John Wiley & Sons, New York.

Fox R L Kapoor M P (1968) , "Rate of change of eigenvalue and eigenvectors," AIAA Journal, Vol. 6, pp. 2426-2429.

Hagiwara I, Nagabuchi K, and Arai A (1989), "Study of Structure Identification Method Using Sensitivity Analysis," Transaction of Japanese Society of Mechanical Engineers (JSME), Vol. 32, No. 2, 1989 (in Japanese).

MSC/NASTRAN Application Manual (1986), " Application Notes - January 1986," Mac-Neal Schwendler Corporation, Los Angeles, California.

Nelson R B (1976), "Simplified Calculation of Eigenvector Derivative," AIAA Journal, Vol. 14, pp 1201-1205.

Noor A K and Lowder H E (1974), "Approximate Techniques of Structural Reanalysis," Computers and Structures. Vol. 4, pp. 801-812.

Noor A K and Whitworth S L (1988) , "Reanalysis Procedure for Large Structural Systems," International Journal for Numerical Methods in Engineering, Vol. 26, 1729-1748, 1988, pp. 1729-1745.

Ojalvo I U (1986a). "Gradients for Large Structural Models with Repeated Frequencies," Society of Automotive Engineers, SAE TP Series 861789.

Ojalvo I U (1986b), "Efficient Computation of Mode-Shape Derivatives for Large Dynamic Systems," AIAA Paper 86-0871, May 1986.

Wang B P (1985), "An Improved Approximate Method for Computing Eigenvector Derivative,"Presented at a Work-in-progress Session, 26th AIAA/ASME/ASCE/AHE Structures, Structural Dynamics and Material Conference, Orlando, Florida.

Wang B P, Caldwell S P, and Smith C M (1990), " Improved Eigensolution Reanalysis Procedures in Structural Dynamics," Proceedings of MSC/NASTRAN World Users Conference, Los Angeles, CA, March 26-30.

Wang B P (1991), "Improved Approximate Methods for Computing Eigenvector Derivatives in Structural Dynamics," AIAA Journal.

Structural identification using mathematical optimization within a production finite element analysis code

M S Ewing

Wright Laboratory, WL/FIBRA, Wright Patterson AFB, Ohio 45433-6553

ABSTRACT: Mathematical optimization techniques have been used to identify physical parameters which define a structural finite element model. Such an identification, alternatively termed finite element model updating, is based on minimizing one of a number of objective functions. The minimization is carried out with constraints on the differences between selected analytical and experimental free vibration frequencies and (normal) mode shapes. The special considerations necessary when integrating the techniques within production finite element analysis codes are discussed.

1. INTRODUCTION

During the development of complicated structures, the structural analyst is often called upon to compare a (usually small) set of measured static displacement or vibration responses with predicted responses. This almost always requires the mathematical model, most typically a finite element model, to be modified or "updated". In many circles, this process is termed "structural identification" since "proper" values of physical (*not* modal) constants which define a model are being identified.

A wide variety of techniques for identifying a model's physical properties have been developed over the last two decades. Numerous surveys of such methods have been written, including an excellent, recent survey by Imregun and Visser (1991). Unfortunately, few researchers address real structures and those who do generally report modest success. This is true because of the difficultly of arriving at a unique solution when there are a large number of physical variables involved (Berman 1971). Many researchers have chosen to concentrate on a small number of physical variables, especially those associated with support flexibilities.

In this paper, attention is given to techniques which can be used to update finite element models in terms of a small number of *physical* properties of the model's finite elements. In this way, a physical understanding of necessary model changes is possible. In contrast to most other efforts of this type, mathematical programming techniques are advocated for the identification task.

2. THE IDENTIFICATION PROBLEM

The basis of undamped, free vibration analysis using the finite element method is the equation of motion:

$$(K - \lambda_j M)\varphi_j = 0 \tag{1}$$

where K and M are the stiffness and mass matrices. λ_j is the jth eigenvalue (the square of the jth natural frequency, ω_j) and φ_j is the jth eigenvector (modeshape). The degree to which the analytical results match experimental (or operational) behavior are strongly dependent on the complexity (and accuracy) of the model.

2.1. Quantifying Modelling Error

If a given measured mode, φ_j, and eigenvalue, λ_j, are introduced into equation (1) in place of their analytical counterparts, the equation will not be exactly satisfied. The deviation from zero, or what has been called the "equation error" is the basis for many update methods. An alternative method of measuring error is to quantify the difference between measured modal properties and those predicted by an analytical method. This type of error is often termed "response error"; alternatively, the term "output error" is used since the measurements are the *output* of a (real or analytical) system.

The differences in the equation error and response error approaches result in striking differences in the *type* of mathematical difficulties encountered during an update. For an equation error update, it is clear that the number of degrees of freedom of an experimental model will (practically speaking) always be less than the number in an analytical model. Therefore, to calculate the equation error, either the analytical model must be reduced or the experimental model must be expanded. In any method requiring sensitivities of mass or stiffness matrices, the requirement for expansion or reduction sometimes imposes large computational penalties. On the other hand, response error methods will at most require expansion of eigenvectors. This would be required in the case in which eigenvector response is included in the error norm or a performance constraint (see section 3) and when the decision is made to compare mode shapes at other than measurement degrees of freedom.

2.2. Identification Strategies

Once an error measure has been defined, a decision must be made as to how the model will be updated to reduce the error. Early techniques focused on directly changing stiffness and mass matrices, term by term, without regard for whether or not the resulting matrices has any physical basis (Baruch and Itzhak 1978). Such an update is useful *if* the model is only to be used to make response predictions *and* will *not* be used to assess the effects of subsequent modifications to the structure.

In the case in which the updated model will be used to assess the effect of structural modifications or different boundary conditions, the model updating must be performed with attention to physically realizeable configurations (Kabe 1985). Acceptable methods include those in which physical variables such as thickness and cross-section variables are updated. More refined techniques allow these physical variables to be linked, thus reducing the number of variables and at the same time recognizing the uniformity of often large portions of stucture.

Historically, the most popular *mathematical* method of reducing an error norm is based on updating mass and stiffness matrices by amounts determined with a least-squares (Berman 1983) or weighted least-squares technique, such as Bayesian estimation (Collins *et al* 1974). The singular value decomposition (SVD) method is another possibility.

Yet another alternative is to pose the minimization problem as a mathematical programming problem which includes the enforcement of constraints on physical parameters or various performance measures. Many forms of mathematical programming techniques are possible including sequential quadratic programming, the method of feasible directions and at least a half a dozen others.

3. IDENTIFICATION WITH MATHEMATICAL PROGRAMMING

Consider a structural finite element model with physical parameters, r_i, as well as analytically determined mode shapes, or eigenvectors, $\underline{\phi}_j$ (with individual elements, ϕ_j^k), and natural frequencies, ω_j. (For notational convenience, $\lambda = \omega^2$.) The actual structure has physical parameters, $\bar{r}_i$, mode shapes, $\underline{\bar{\phi}}_j$, (with individual elements, $\bar{\phi}_j^k$), and natural frequencies, $\bar{\omega}_j$.

To identify the structure in terms of the model's physical parameters, the following optimization problem may be solved. Minimize:

$$\sum_{j=1}^{J_\omega} a_j \left(\frac{\lambda_j}{\bar{\lambda}_j} - 1 \right)^2 + \sum_{j=1}^{J_\phi} b_j |\underline{\phi}_j - \underline{\bar{\phi}}_j|^2 + \sum_{j=1}^{J_r} c_j (r_j - r_j^a)^2 + d (M - \sum_{j=1}^{J_d} m_j)^2 \quad (2)$$

subject to the constraints:

$$\frac{\lambda_j}{\bar{\lambda}_j} - 1 < e_j \quad for \; j = 1, 2, \ldots, J_e \quad (3)$$

$$|\phi_j - \bar{\phi}_j|^2 < f_j \quad for \; j = 1, 2, \ldots, J_f \quad (4)$$

$$M - \sum_{i=1}^{J_d} m_i < g_j \quad for \; j = 1, 2, \ldots, J_g \quad (5)$$

where, for example: J_ω is the number of natural frequency errors used in the objective function and J_e is the number of frequency constraints used; a_j is a weighting factor which reflects the confidence the analyst has in the jth natural frequency; e_j is a small number chosen to quantify how close to target is "close enough" for a frequency

constraint. In practice, only one of the summations in equation 2 need be included in the objective function. Likewise, only one type of constraint need be enforced. Computer experiments with simulated data has not revealed consistent rules for selecting the best combination of objective functions and constraints in the objective function (Ewing and Kolonay 1991).

As with any mathematical optimization, the sensitivities, or gradients, of the objective function and the constraints need to be calculated. In previous studies by the author, exact gradients were formulated in all cases. In particular, Nelson's method (Nelson 1976) was used to calculate eigenvector gradients. It is well-known that exact gradients are quite expensive computationally, but have been used widely due to a high level of confidence in the technique. Other more efficient techniques are available and should be explored further.

1. IDENTIFICATION WITHIN A PRODUCTION FINITE ELEMENT CODE

General purpose identification codes based on the finite element method and statistical estimation are available (Dascotte 1991) or under development (Hasselman and Christowski 1991, Ojalvo 1989). The author has developed a test-bed planar frame, finite element based identification code to evaluate the performance of mathematical programming techniques. Thus far, a sequential quadratic programming method has been used as the optimizer (Shittkowski 1976). Numerous "computer experiments" have been conducted to prove the worth of the method, including linear springs in series (Ewing and Venkayya 1991) and an intermediately supported beam (Ewing and Kolonay 1991). Results with operational data on the response of a tactical missile is forthcoming. A flow chart with the major steps required to impliment mathematical programming identification techniques within a production finite element code is shown on the next page.

Based on experiences with the aforementioned research, the author has concluded that the most general purpose identification code will have the ability to handle:

- both static and dynamic responses

- multiple boundary conditions and configurations

- alternative solution schemes (e.g., mathematical programming, Bayesian estimation, simple least squares)

- multiple eigenvalue extraction techniques, including repeated root capability

- alternative methods of comparing analytical and experimental mode shapes

- shifts in mode order during the update process (mode tracking)

- various types of damping

- update parameter linking

- a wide range of finite elements, including rigid elements

NONLINEAR MATHEMATICAL OPTIMIZATION PROCESS TO UPDATE FINITE ELEMENT MODELS
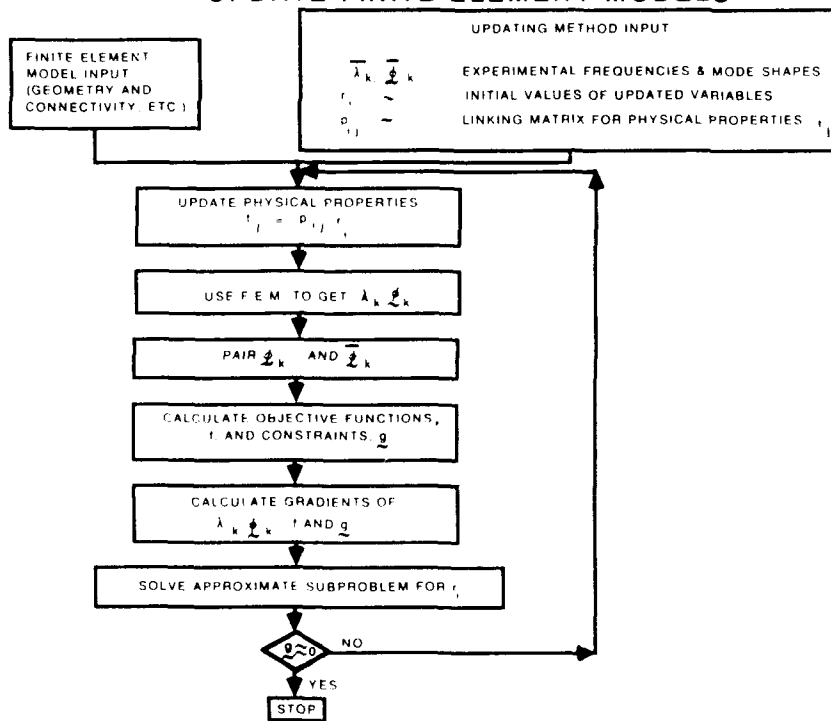
The Automated STRuctural Optimization System (ASTROS) (Johnson and Venkayya 1988) appears to be the ideal platform for development of a versatile identification code. ASTROS has a rich element library, but more importantly, is based on a state-of-the-art database system and an easily-used matrix manipulation language. Of special interest to the development of an identification code, ASTROS provides easy access to sensitivity information. For example, mass and stiffness sensitivities, which are needed for eigenvalue and eigenvector sensitivities, are used routinely within ASTROS.

A development program has begun to modify ASTROS to accomplish the identification task. The near-term goal is to allow the use of the objective functions and constraints given as equations 2-5 in conjunction with the method of feasible directions. Further enhancements will first add the capability of using other mathematical programming techniques as well as Bayesian estimation for the optimization task. Later, mode shape tracking, static deflection and damping capabilities will be added.

864 *Active Materials and Adaptive Structures*

References

Barach M and Bar Itzhack I Y 1978 "Optimal Weighted Orthogonalization of Measured Modes" *AIAA Journal* **16** (Apr) pp 346-351

Berman A and Flannelly W G 1971 "Theory of Incomplete Models of Dynamic Structures" *AIAA Journal* **9** (Aug) pp 1481-1487

Berman A and Nagy E J 1983 "Improvement of a Large Analytical Model Using Test Data" *AIAA Journal* **21** (Aug) pp 1168-1173

Collins J D, Hart G C, Hasselman T K, and Kennedy B 1974 "Statistical Identification of Structures" *AIAA Journal* **12** 2 (Feb) pp 185-190

Dascotte E 1991 "Applications of Finite Element Model Tuning Using Experimental Modal Data" *Sound and Vibration* **25** 6 (June) pp 22-26

Ewing M S and Venkayya V B 1991 "Structural Identification Using Mathematical Optimization Techniques" *Proceedings* AIAA 32nd Structures Structural Dynamics and Materials Conference, Baltimore MD, 8-10 April 1991 pp 840-845 (AIAA paper 91-1135)

Ewing M S and Kolonay R M 1991 "Dynamic Structural Model Modification Using Mathematical Optimization Techniques" *Proceedings* OPTI '91 — Computer Aided Optimum Design of Structures, Boston, MA, 25-27 June 1991 pp 285-295

Hasselman T K and Chrostowski J D 1991 "A Recent Case Study in System Identification" *Proceedings* AIAA 32nd Structures Structural Dynamics and Materials Conference, Baltimore MD, 8-10 April 1991 pp 2154-2168 (AIAA paper 91-1190)

Imregun M and Visser W J 1991 "A Review of Model Updating Techinques" *The Shock and Vibration Digest* **13** Jan. pp 9-20

Johnson E H and Venkayya V B 1988 "Automated STRuctural Optimization System (ASTROS)" *AFWAL-TR-88-3028*

Kabe A M 1985 "Stiffness Matrix Adjustment Using Modal Data" *AIAA Journal* **23** (Sep) pp 1431-1436

Nelson R B 1976 "Simplified Calculation of Eigenvector Derivatives" *AIAA Journal* **14** 9 (Sept) pp 1201-1205

Ojalvo I U, Ting T, and Pilon D 1989 "Practical Suggestions for Modifying Math Models to Correlate with Actual Modal Test Results" *Proceedings* 7th International Modal Analysis Conference, Las Vegas NV, Jan 1989 pp 347-354

Schittkowski K 1986 "NLPQL: A FORTRAN Subroutine Solving Constrained Nonlinear Programming Problems" *Annals of Operations Research* **5** pp 485-500

Sensitivity analysis of responses to dynamic loads

Warren C. Gibson, CSA Engineering Inc., 560 San Antonio Road, Palo Alto, CA

Abstract: Sensitivity analysis is a key element of structural optimization and optimization-based methods of parameter identification. Sensitivities of responses to dynamic loads pose special challenges because of the volume and complexity of data in a complete frequency spectrum or time record. An efficient method for computing the sensitivity of one or more peaks in a frequency spectrum or time domain is presented. The method accounts for shifts in peak location as well as changes in peak magnitude as design variables are varied. Brief examples are included.

1. Introduction: Sensitivity Analysis as an Adjunct to Structural Analysis

In the context of structural analysis, sensitivity analysis refers to the computation of partial derivatives of structural responses with respect to model parameters such as thicknesses, areas, spring rates, or added masses. Analysts or designers may sometimes make direct use of this information, but more often, it serves as a basis for automated optimization. Optimization can be used either for structural design purposes, seeking, for example, a configuration of minimum weight that satisfies performance or safety criteria. Alternatively, optimization methods may be used to adjust uncertain aspects of a model so that it predicts responses that more closely match measured responses (Ewing and Kolonay, 1989).

Sensitivity analysis may be programmed as an adjunct to finite element analysis. Some commercial FEA software packages provide sensitivity analysis and optimization; others such as NASTRAN (MacNeal-Schwendler, 1989) and ASTROS (Johnson *et al*, 1988) offer matrix programming languages that can be used to incorporate new sensitivity analysis functions without access to the source code. Sensitivity data can be coupled to a general-purpose optmizer such as ADS (Vanderplaats, 1983).

Although the developments presented here are applicable to a wide variety of structural problems, they have particular relevance to lightweight aerospace structures which are particularly susceptible to dynamic disturbances.

2. Sensitivity Analysis of Response Peaks in the Frequency Domain

The equations of motion for linear dynamic analysis, after discretization by finite

elements, may be written as

$$\mathbf{K}\mathbf{U}(t) + \mathbf{B}\dot{\mathbf{U}}(t) + \mathbf{M}\ddot{\mathbf{U}}(t) = \mathbf{P}(t) \tag{1}$$

in terms of stiffness, damping and mass matrices $\mathbf{K}$, $\mathbf{B}$, and $\mathbf{M}$; displacement vector $\mathbf{U}$, and load vector $\mathbf{P}$. For steady-state response, these equations are converted to the frequency domain and written as

$$[\mathbf{K}(1 + ig) + i\omega\mathbf{B} - \omega^2\mathbf{M}] \mathbf{U}(\omega) = \mathbf{P}(\omega) \tag{2}$$

where ω is the radian frequency and g represents structural damping. A classical response peak in the frequency domain is shown in Figure 1. If one were to calculate sensitivities at the peak frequency $\omega = \hat{\omega}$ by simply differentiating Eq. (2) and proceeding with optimization, the results would almost certainly be unsatisfactory. While the optimizer might succeed in reducing the response at that particular frequency, it would likely do so by simply shifting the peak to a neighboring frequency. Thus it is necessary to compute the total derivative of the peak so as to track its shift in frequency as well as its change in amplitude. Denoting a particular design variable as $\mathbf{X}_j$, we have

$$\frac{d\hat{\mathbf{U}}_i}{d\mathbf{X}_j} = \frac{\partial\mathbf{U}_i}{\partial\mathbf{X}_j}\bigg|_{\omega=\hat{\omega}} + \frac{\partial\mathbf{U}_i}{\partial\hat{\omega}}\frac{\partial\hat{\omega}}{\partial\mathbf{X}_j} \tag{3}$$

The first term on the right-hand side represents the sensitivity of the response at the peak frequency $\hat{\omega}$ and the second term accounts for the shift in the peak frequency.

Employing modal superposition and assuming that most of the response at a peak is due normal mode number n, we may express the peak displacement as

$$\hat{\mathbf{U}}_i = \frac{\Phi_i(\Phi^T\mathbf{P})}{k(1 + ig) - \hat{\omega}^2 m} \tag{4}$$

Figure 1. Classical frequency response function.

where Φ is the appropriate eigenvector and $k = \Phi^T\mathbf{K}\Phi$ is the modal stiffness and $m = \Phi^T\mathbf{M}\Phi$ is the modal mass.

For light damping, the peak occurs very near the undamped natural frequency ω_n, and since $k - \omega_n^2 m = 0$, the magnitude of the peak complex response is approximately

$$\hat{\mathbf{U}}_i \approx \frac{\Phi_i(\Phi^T\mathbf{P})}{kg} \tag{5}$$

From Eq. (5), it is clear that there are four ways to reduce $\hat{\mathbf{U}}_i$:

1. Reduce Φ_i. This means minimizing the participation of the mode in question at the particular response location. In a beam structure, for example, this might mean moving the nodes of the mode shapes toward the response point.

2. Reduce $\boldsymbol{\Phi}^T P$. This means reducing the modal participation of the load vector. In the case of a beam with a point load, again the node might be moved toward the load.

3. Increase k. Loosely speaking, this means increasing the structure's stiffness-to-mass ratio.

4. Increase the structural damping g.

Differentiating Eq. (5),

$$\frac{\partial \hat{U}_i}{\partial \mathbf{X}_j} = \frac{1}{kg}\left[\left(\frac{\partial \boldsymbol{\Phi}_i}{\partial \mathbf{X}_j} - \frac{2}{k}\frac{\partial \boldsymbol{\Phi}^T}{\partial \mathbf{X}_j}\mathbf{K}\boldsymbol{\Phi} - \frac{1}{k}\boldsymbol{\Phi}^T\frac{\partial \mathbf{K}}{\partial \mathbf{X}_j}\boldsymbol{\Phi} - \frac{1}{g}\frac{\partial g}{\partial \mathbf{X}_j}\right) + \boldsymbol{\Phi}_j\left(\frac{\partial \boldsymbol{\Phi}}{\partial \mathbf{X}^j}\mathbf{P}\right)\right] \quad (6)$$

All four of the aforementioned avenues are reflected in this equation. A general-purpose optimizer will take advantage of any of them, depending on how stiffness, mass, and damping are interrelated for a particular problem, and on other constraints that may be included in the optimization problem. In addition to stiffness and damping sensitivities, this expression requires eigenvector sensitivities, which may be calculated from stiffness and mass sensitivities (Nelson, 1976). The computation involved in this method is equivalent to one static analysis per mode, with one right-hand side per design variable.

LOAD
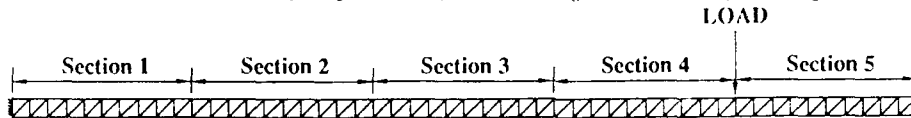
Figure 2. Long slender truss.

Table 1.

Truss optimization history for frequency response.

	Peak response, μ-radians	
Mode	Initial	Optimized
1	4735	1000
2	8.96	10
3	58.4	20

The sensitivity analysis described above was programmed in NASTRAN's DMAP language and coupled to the ADS general-purpose optimizer (Vanderplaats, 1983), using an approximate model (Schmit and Miura, 1976). The long slender cantilever truss shown in Figure 2 was optimized for a frequency-dependent load applied near one end. The optimizer redistributed the structural material so as to reduce the peak responses as shown in Table 1, at the same time achieving a slight weight reduction.

3. Sensitivity Analysis of Response Peaks in the Time Domain

As with steady-state loads, one can begin with the equations of motion, differentiate with respect to design variables, and solve for the required response sensitivity. Again, difficulties arise due to the tendency of peaks to shift as a result of design changes. For a peak $\hat{U}_i$ occurring at time t_p, the peak response sensitivity may be written as

$$\frac{\partial \hat{U}_i}{\partial \mathbf{X}_j}\bigg|_{t=t_p} = \frac{\partial \hat{U}_i}{\partial \mathbf{X}_j} + \frac{\partial \hat{U}_i}{\partial \mathbf{U}}\frac{\partial \mathbf{U}}{\partial \mathbf{X}_j} + \frac{\partial \hat{U}_i}{\partial t_p}\frac{\partial t_p}{\partial \mathbf{X}_j} \quad (7)$$

In computing the transient peak sensitivity we again assume that modal superposition is used. Depending on whether or not proportional damping is assumed, superposition

may or may not result in uncoupled equations of motion. Uncoupled equations may be solved independently by means of a convolution integral, whereas coupled equations may be solved by any of various forward integration procedures such as the Newmark Beta method (Gockel, 1983). A general second-order forward integration procedure may be expressed as

$$\mathbf{U}^{n+2} = f(\mathbf{K}, \mathbf{B}, \mathbf{M}, \mathbf{P}, \mathbf{U}^{n+1}, \mathbf{U}^{n}) \tag{8}$$

which may be differentiated

$$\frac{\partial \mathbf{U}^{n+2}}{\partial \mathbf{X}_i} = \frac{\partial f}{\partial \mathbf{K}}\frac{\partial \mathbf{K}}{\partial \mathbf{X}_i} + \frac{\partial f}{\partial \mathbf{B}}\frac{\partial \mathbf{B}}{\partial \mathbf{X}_i} + \frac{\partial f}{\partial \mathbf{M}}\frac{\partial \mathbf{M}}{\partial \mathbf{X}_i} + \frac{\partial f}{\partial \mathbf{P}}\frac{\partial \mathbf{P}}{\partial \mathbf{X}_i} + \frac{\partial f}{\partial \mathbf{U}^{n+1}}\frac{\partial \mathbf{U}^{n+1}}{\partial \mathbf{X}_i} + \frac{\partial f}{\partial \mathbf{U}^{n}}\frac{\partial \mathbf{U}^{n}}{\partial \mathbf{X}_i} \tag{9}$$

Just as modal superposition may be applied to the transient response equation, it may also be applied to the calculation of the peak sensitivity expression. These equations may be integrated separately or in parallel with the integration of Eq. (1). This procedure is generally economical when modal superposition is used because of the reduced number of degrees of freedom and possible uncoupling of the matrices. A precaution must be observed, however: more modes may be required for accurate computation of sensitivities than are required for accuracy in the response itself.

As an example, the same truss was subjected to the transient load shown in Figure 3. The optimizer was able to reduce the peak response by a factor of three with only an 80% increase in structural weight (Figure 4).
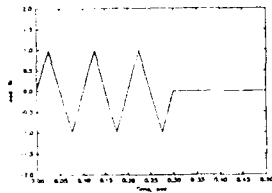
Figure 3. Transient load.
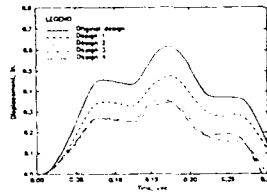
Figure 4. Optimized transient response.

References

Ewing M S and Kolonay R M 1991 "Dynamic Structural Model Modification using Mathematical Optimization Techniques," OPTI 91, Boston.

Gockel M A (ed.) 1983 *MSC/NASTRAN Handbook for Dynamic Analysis* MacNeal-Schwendler Corp., Los Angeles.

Johnson E H, Venkayya, V B, Neill D J, Herendeen D L and Hoesly R L 1988 "Automated Structural Optimization System (ASTROS)," AFWAL TR-88-3028. Volume I – Theoretical Manual, Volume II – User's Manual, Volume II – Application manual, Volume IV – Programmer's Manual.

MacNeal-Schwendler Corporation 1988 *MSC/NASTRAN User's Manual, Version 66*

Nelson R 1976 "Simplified Calculation of Eigenvector Derivatives," *AIAA J.*, Vol. 14, No. 9, pp. 1201-1205.

Schmit L A Jr and Miura H 1976 "Approximation concepts for Efficient Structural Synthesis," NASA CR2552.

Vanderplaats G N 1985 "ADS – a Fortran Program for Automated Design Synthesis," Engineering Design Optimization, Inc., Santa Barbara, CA.

869

Macromolecular smart materials and structures

D.H. Reneker, W.L. Mattice, R.P. Quirk, and S.J. Kim

Institute of Polymer Science, The University of Akron, Akron, Ohio 44325-3909

ABSTRACT: Macromolecules offer many possibilities for creating smart molecules. Smart molecules are designed to receive a stimulus, transmit or process it, and then to respond by producing a useful effect. New capabilities exist for the predictive design of polymer molecules from the rapid advances in computer modeling of the structure and properties of large molecules. Powerful chemical methods are available for the creation of polymeric modules which can be assembled into smart molecules. New tip scanning methods of microscopy make it possible to observe segments of polymer molecules attached to solid surfaces. This work brings these capabilities together to design, create, and characterize macromolecular smart materials.

1. INTRODUCTION

Our approach to smart materials based on polymer molecules is modular. The elementary functions of reception of a stimulus, transmission, processing, actuation, and the like are incorporated into oligomers which have reactive groups at the ends or at other strategic positions. Stimuli may include strain, stress, incident photons, small molecules, an electric field, hydrostatic pressure, or the like. Processing or transmission of the signal may include absorption of a photon, reaction with a small molecule, integration of a series of events, translation or rotation of segments of a polymer molecule, creation and motion of crystallographic defects or other localized conformations that produce reptation or twisting of segments[1], and the alteration of localized stress fields, for example. The useful effects produced may be a color change, a change in the index of refraction tensor, a change in the stress distribution, a different connectivity of the parts of a molecule or a network, or a change in volume.

The synthesis of such oligomers, and their attachment together, are active areas in state of the art polymer synthetic chemistry[2,3,4,5]. The reactive groups are used to assemble the desired set of functions required for a particular smart material by bonding together the oligomers that have the needed functions. The oligomers described above usually contain only one backbone chain and may involve only a few hundreds of atoms.

Alternatively, the elementary functions of a smart material based on polymers may be incorporated into a larger polymer molecule, or group of molecules. A few thousands of atoms may be involved. In this case, the properties of the module may be usefully described in terms of thermodynamic or bulk properties.

Contemporary computer modeling encompasses both of these size ranges[6]. The behavior of oligomers, and systems of connected oligomers, can be calculated from knowledge of the

electronic states of the molecules or from knowledge of the interatomic potential functions. Computer modeling can also predict the thermodynamic and bulk properties of the larger aggregates that may also be used to design polymeric smart material systems To distinguish these size ranges, we use the phrase "molecular scale" for the smaller and the word "nanophase" for the larger.

Information about the molecular scale behavior of smart materials is also available from the direct observation of oligomers, using the techniques[7] of atomic force microscopy and scanning tunneling microscopy. The attachment of oligomers to a solid surface is observed directly and used to help understand the behavior of a smart molecule system.

MODULES FOR A MOLECULAR SCALE SMART MATERIAL SYSTEM

An interesting example of a smart material system can be designed at the molecular scale to deal with the possibility that separation may occur at the polymer-matrix interface in a fiber reinforced composite when the composite is excessively deformed. See Figures 1 and 2.
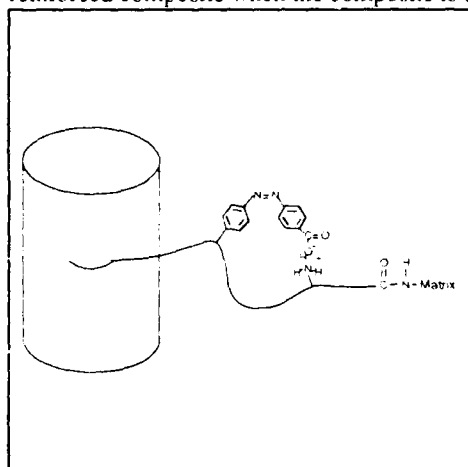
Figure 1. Diagram of a smart macromolecule at the interface between a fiber and its matrix.
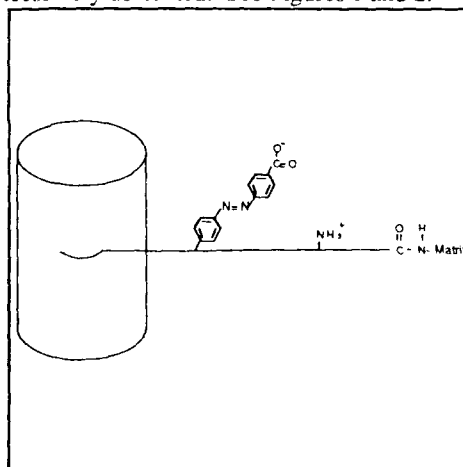
Figure 2. Diagram of the smart macromolecule after the fiber has begun to separate from the matrix.

Such a smart molecule would have an oligomer that attaches the smart molecule to the fiber. This attachment oligomer is connected to two branches. The first branch contains a stress sensitive chromophore and a weak link in series. The second branch contains a longer, strong chain which can carry the load when the weak link is pulled apart. The two branches are rejoined and connected to an oligomer that attaches to the polymer matrix. Figure 2 shows this smart molecule after the fiber has begun to separate from the matrix.

This smart material system receives and detects a signal from the strain field that separation at the interface is occurring as the point of attachment to the matrix moves away from the point of attachment to the fiber. The color change provides a signal that the separation has produced significant damage. The loose loop acts as a molecular "keeper chain" that tends to prevent the interfacial separation from growing to a catastrophic failure of the composite part. Such a smart material system is interesting in composite systems in which impact damage that produces little visible change can leave the composite unable to bear the expected compressive loads. Other oligomers that perform similar modular functions are being investigated.
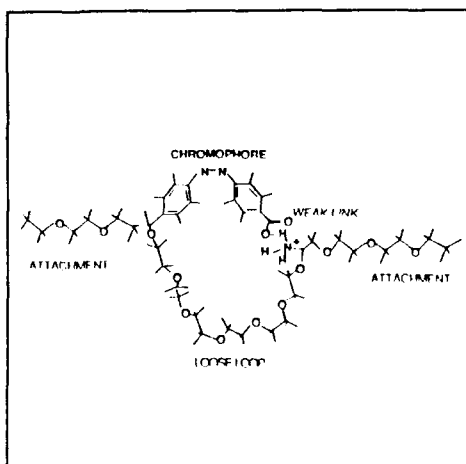
Figure 3. An atomic scale design for a smart macromolecule.

The modular functions that are needed are:

1. Attachment to the fiber.
2. A weak link that breaks as soon as a pre-determined amount of separation occurs.
3. A piezochromic group that changes its color when the separation occurs.
4. A loose loop of polymer which maintains a useful level of attachment even after the fiber and the matrix have separated by an anticipated amount.
5. Attachment to the matrix.

OLIGOMERIC MODULE FOR ATTACHMENT TO THE FIBER

The attachment of an oligomeric module to graphite was studied. The oligomer chosen for study is octadecyl amine, which might attach to reactive sites on the graphite through the amine group, or alternatively, through the Vanderwaals attraction of the hydrogen atoms to the graphite surface. Graphite was chosen because it is similar to the carbon or graphite fibers used in composites, and to the carbon black used in the manufacture of rubber. Graphite surfaces with monatomic steps were prepared by cleavage of highly oriented pyrolytic graphite. In some samples the cleavage surface was chemically oxidized to create steps that were one, or several, atomic layers high.

The objective of this work is primarily to demonstrate the modular approach to show how smart macromolecules can be designed and perhaps used. We recognize that a color change at the interface of a graphite fiber will be of limited usefulness. However, a very similar approach can be used for the design and characterization of smart molecules for the interface of glass or other transparent fibers if atomic force microscopy is substituted for the scanning tunneling microscopy which works so well on graphite crystals.

The attachment to graphite, of individual oligomers such as octadecyl amine, was directly observed with the scanning tunneling microscope and the atomic force microscope. The octadecyl amine molecules tend to lie flat on the graphite, with the molecule in a planar zig-zag conformation. See Figures 4 and 5.

Elastomers and plastics with stress-sensitive chromophores in the polymer backbone were synthesized. Using the methodology of living anionic polymerization, polymers can be prepared which have controlled molecular weight, molecular weight distribution, copolymer composition and microstructure, stereochemistry, tacticity, and branching. Because these are living polymerizations, the product is a polymeric carbanion which can be reacted with a variety of electrophiles to form end-functionalized polymers.

Figure 4. Scanning tunneling micrograph of octadecyl amine physically absorbed on the cleavage plane of graphite. Partly resolved carbon atoms surround the row of absorbed molecules.
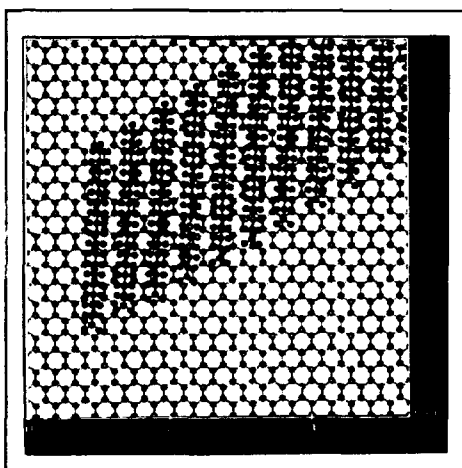
Figure 5. Computer generated drawing of octadecyl amine on graphite, showing how the scanning tunneling micrograph is interpreted.

Omega-carboxyl-terminated polystyrene and omega-carboxyl-terminated poly(styrene-block-butadiene) polymers were polymerized as shown in Scheme 1. The chain-end functionalized polymers were converted to the corresponding acid chlorides and then reacted with azodianiline to introduce the azo linkage into the polymer and couple the two chains together as shown in Scheme 2 below.
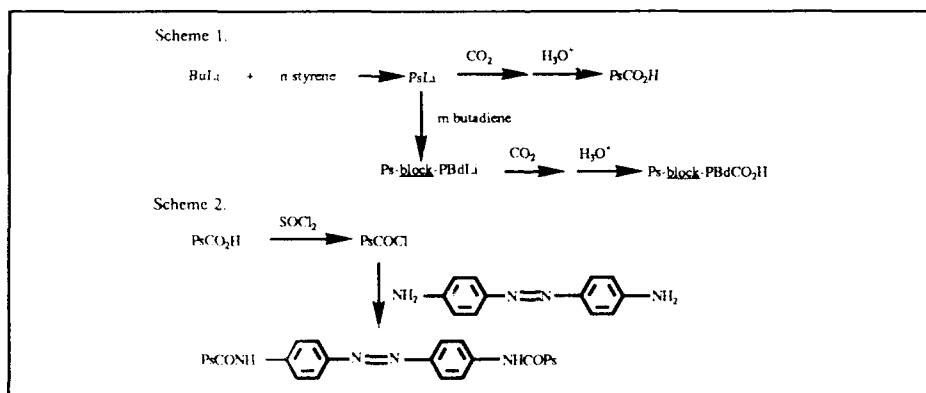
These polymers are being characterized with respect to their structure. The effect of irradiation and stress on their ultraviolet-visible absorption spectra is being measured. In order to increase the concentration of chromophores in the samples, alpha,omega-difunctional

elastomers are being prepared which will form segmented block copolymers upon reaction with difunctional chromophores such as azodianiline.

The relation between the conformational energy in an oligomer and the strain was calculated in the following way. The ends of the oligomer were constrained at a succession of points of increasing distance of separation in the stress direction. A minimum energy conformation of the segment was calculated for each distance, on the basis of the interatomic potentials. The value of the minimum energy was plotted as a function of the distance. The initial distance between the ends was used to calculate the strain for each separation distance. The energy was calculated with SYBYL molecular modeling software[8]. Molecular dynamics calculations are quite practical on molecules of this size, and would probably result in a more reliable estimate of the energy as a function of the separation of the chain ends.

Also, refined estimates of the stress associated with the light induced change in the conformation of azobenzene from trans to cis are being obtained. The molecules being considered are azobenzenes with different kinds of polymer chains appended in the para positions of each benzene ring. The approach utilizes a variation of the method described by Flory[9] for the computation of the average of the end-to-end vector of the attached polymer chains. The magnitude of the stresses induced by photo-isomerization are expected to be proportional to the differences in the end to end distances of the polymers caused by the trans to cis isomerization.

For a chromophore to change its conformation, or for a weak bond to separate, the energy from the strain field concentrated in that particular oligomer must be at least large enough to overcome the potential barriers of the sort described in the preceding paragraph. Thermally excited vibrations can provide some of the energy, but for the molecule to perform as intended, the thermal energy should not cause transitions in the absence of strain.

A useful starting point for predicting the response of such a molecule to a tensile force is the calculated curve of energy versus separation of chain ends. An effective spring constant that will store an energy equivalent to the maximum energy of the barrier when the spring is stretched to the strain at which the maximum occurs can be assigned to each segment. With each functional oligomer approximated as a linear spring, it is easy to calculate the strain and the elastically stored energy in each oligomer.

SUMMARY

The combination of molecular modeling, tunneling and atomic force microscopy, and state of the art polymer synthesis brings us to a new vista. Molecules of unusual complication can now be modeled easily and quickly. The parts of these molecules can be synthesized as modules and assembled together using the techniques of contemporary polymer synthesis. Direct observation of molecular scale features with new molecule resolving microscopes provides other useful information about the design, assembly and performance of these smart molecules.. This project brings all these things together. The early results on all three fronts of this project are most promising.

REFERENCES

1. Reneker, D.H. and Mazur, J.; Chapter 23, "Computer Simulation of Polymers", edited
    by R.J. Roe, Prentice Hall, 1990, page 331.

2. Quirk, R.P., Yin, J., Guo, S.H., Wu, X.-W., Summers, G., Kim, J., Zhu, L.-F., Ma,
    J.J., Takizawa. T., and Lynch, T., Rubber Chemical Technology, **64**, 648 (1991).

3. Rempp, P., Franta, E., and Herz, J.-E., Advances in Polymer Science, **86**, 145 (1988).

4. Teyssie, Ph., Makromolekulare Chemie, Macromolecular Symposium **22**, 83 (1988).

5. "Block Copolymers", Quirk, R.P., Kinning, D.J., and Fetters, L.J., in "Comprehensive
    Polymer Science", Allen, G., and Bevington, J.C., Editors, Pergamon Press, **7**, (1989)
    page 1.

6. R.J. Roe, editor, "Computer Simulation of Polymers", Prentice Hall, Englewood Cliffs,
    New Jersey 07632, (1990)

7. Reneker, D.H., Chapter 12 in " ew Characterization Techniques for Thin Polymer
    Films" John Wiley & Sons, (1990), page 327.

8. Sybyl is a comprehensive molecular modeling program supplied by Tripos, Incorporated
    of St. Louis, Missouri

9. Flory, P.J., Macromolecules, **7**, 381 (1974)

Nanosecond optical energy transfer in quinizarin doped sol-gel glasses

Drew L'Espérance and Eric L. Chronister

Department of Chemistry, University of California, Riverside CA 92521

ABSTRACT: Optical energy transfer and chromophore spatial distributions in quinizarin doped sol-gel glasses are investigated by time-resolved fluorescence anisotropy measurements. These results are discussed in terms of the potential of organically doped sol-gel glasses as novel fast response optical materials.

1. INTRODUCTION

Recent and continuing progress in the development of high intensity ultrashort laser sources illustrates the need for fast response optical materials. The chemical and structural versatility of organically doped sol-gel materials holds potential for the development of "smart" optical materials that can passively respond to optical input in a desired fashion, e.g. as an optical power limiter for the protection of sensitive solid state sensors. In this work we examine the transfer of optical energy between chromophores in organically doped sol-gel glasses on a nanosecond timescale.

Sol-gel glasses hold promise as versatile nonlinear optical materials since they can solvate a wide variety of chromophores at high concentrations. These materials can be prepared chemically at room temperature by the hydrolysis of a variety of metal alkoxides, and thin films are easily produced by dip coating or spin casting (Dislich H 1983). Dried gels result in rigid xerogel glasses which can have over 50% void volume with an average pore size from 20Å to 80Å depending on the sol-gel chemistry (Hensch L L *et al* 1990). The spectral changes upon complexation with aluminum and the possibility of photochemical hydrogen bond rearrangement make quinizarin a unique probe of optical response in metal-oxide glasses. In this study, the dynamics of optical energy transfer is used to probe the environments and distributions of quinizarin within xerogel glasses.

Although this paper focuses on organically doped sol-gel glasses as promising "smart" materials, the need for optical materials with power limiting capabilities has spawned a wide variety of efforts to develop other materials with the desired optical properties. Some of these include: optical nonlinearities in semiconductors and organometallic polymers; coherent energy exchange in photorefractive materials; intensity dependent internal reflection; optical breakdown and scattering by suspensions of absorbing particles; nonlinear Fabry-Perot etalons; and photochromism due to photochemical and photophysical changes (Tutt L and McCahon S 1990 *and references within*).

2.   EXPERIMENTAL

2.1   Preparation of quinizarin doped sol-gel films

Quinizarin doped aluminosilicate sol-gel glasses were produced by adding quinizarin to a 3:10:1 solution of diisobutoxyaluminoxytriethoxysilane (ASE), isopropanol, and water. Quinizarin-aluminum doped silicate sol-gel glasses were prepared by adding quinizarin and aluminum nitrate hemihydrate to a 6:17:2:1 solution of tetraethoxysilane, ethanol, 0.01M HNO₃, and Triton-X-100 (Hinsch A and Zastrow A 1990). Bulk samples were prepared by pouring these solutions into polystyrene molds and allowing the water and alcohol to evaporate, causing the solution to gel, shrink, and harden into glass (McKiernan J et al 1989). Thin films were prepared by dipcoating glass microscope slides in the solutions with a withdrawal rate of 2mm/s. Films and bulk samples were baked at 110° C. The resulting glasses had a density of about 1.6g/cm³ and film thicknesses of 0.5μm.

2.2   Time resolved fluorescence anisotropy apparatus

The polarized output of a nitrogen pumped dye laser (100μJ/pulse, 0.5ns pulsewidth, 30Hz) was used as an excitation source. Scattered excitation light was eliminated with a cutoff filter and the parallel and perpendicular polarization components of the sample fluorescence were selected and detected with a fast photomultiplier tube (0.8ns response time). The PMT signal was collected and averaged with an HP 400MHz digitizing oscilloscope (875ps risetime). Fluorescence depolarization decays were averaged for 2048 pulses and used to calculate the time-resolved fluorescence anisotropy.

3.   RESULTS AND DISCUSSION

3.1   Quinizarin chemistry and spectral changes
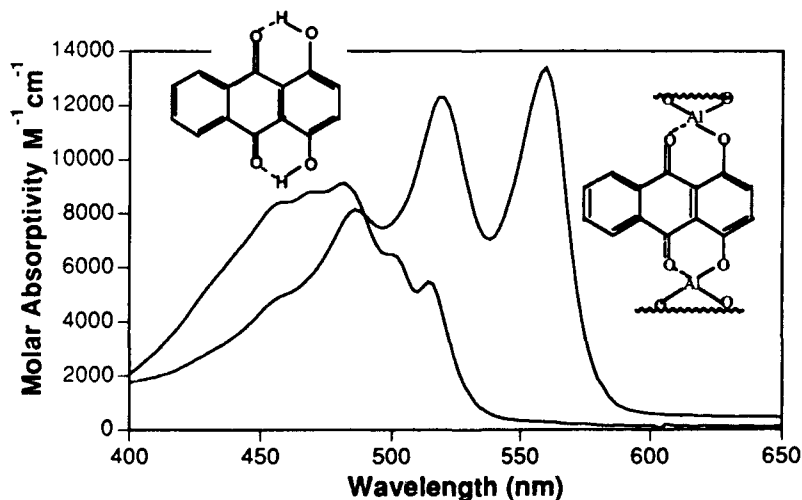
Fig 1. Absorption spectra of quinizarin versus that for the quinizarin-aluminum complex which forms when quinizarin is doped into an aluminosilicate glass. Also shown are the corresponding structures of the intramolecularly hydrogen bonded species and the quinizarin-aluminum complex.

Uncomplexed quinizarin has intramolecular hydrogen bonds between the hydroxyl proton and the quinoid oxygen. When complexed with aluminum, the 480nm absorption maximum of quinizarin red-shifts to 560nm and the absorption strength doubles. In addition, the room temperature fluorescence lifetime of the quinizarin-aluminum complex is 9.4ns versus 3ns for the uncomplexed molecule. Considerable vibrational structure is also apparent in the absorption spectrum of the quinizarin-aluminum complex. In addition, we succeeded in burning persistent photochemical spectral holes (λ=566nm) in quinizarin doped aluminosilicate glasses at 77K. Since hydrogen bond rearrangement is the most likely mechanism for photochemical hole-burning, the quinizarin molecules may only be complexed with one aluminum and retain some intramolecular hydrogen bonding. Similar holeburning results were recently reported for quinizarin adsorbed onto aluminum oxide powders (Basché Th and Bräuchle C 1991), indicating that some of the dopant molecules may be chemically adsorbed onto the inner surface of xerogel micropores.

3.2 Time-resolved depolarization in quinizarin doped sol-gel films

The rate of dipolar energy transfer between resonant energy levels on chromophores separated by a distance r is $\omega(r) = (1/\tau)(R_0/r)^6$, where τ is the fluorescence lifetime, and R_0 is the critical distance for energy transfer (typically in the range 10-60 Å) (Förster Th 1949). The time-resolved fluorescence anisotropy is defined as, $anis(t) = [I_{\parallel}(t) - I_{\perp}(t)]/[I_{\parallel}(t) + 2I_{\perp}(t)]$, where $I_{\parallel}$ and $I_{\perp}$ correspond to the emission intensity polarized parallel and perpendicular to the excitation polarization, respectively. In the absence of orientational diffusion, $anis(t)$ is directly proportional to the probability that the excitation resides on the originally excited molecule a time t after excitation, P(t).
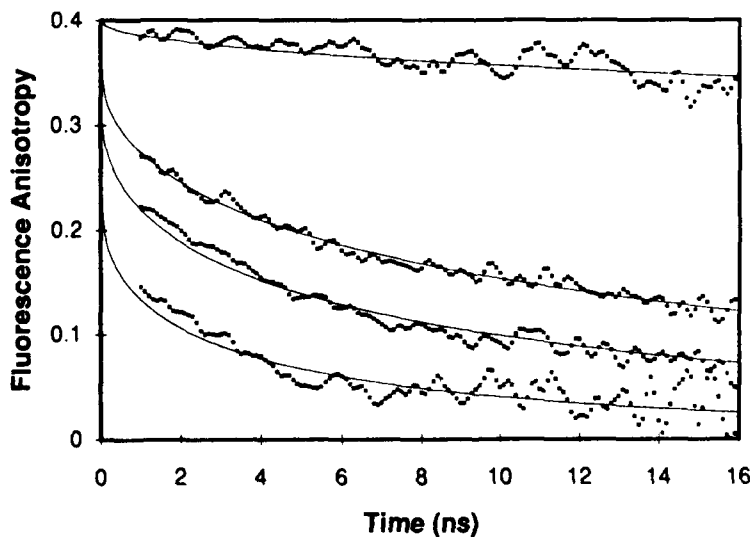
Fig. 2. Time-resolved fluorescence anisotropy decays for the quinizarin:aluminum complex doped into silica sol-gel films. From top to bottom, the quinizarin concentrations in the solid films are, $\leq$0.0001M, 0.009M, 0.015M and 0.038M respectively. The solid lines are best fits to Eq (1).

We neglect any donor trapping and analyze our results in terms of donor-donor transfer processes since our results were dispersionless (Stein A D *et al* 1990). For an arbitrary spatial distribution of chromophores this yields (Baumann J and Fayer M D 1986),

$$ln\ P(t)\ =\ -\rho \int_{o}^{\infty} (1\text{-}e^{\text{-}\omega t})\ u(r)dr \tag{1}$$

where u(r)dr is the probability that there is a chromophore a distance r from the initially excited chromophore and ρ is the number density of chromophores. In general, an experimentally determined P(t) can be used to evaluate a spatial distribution function u(r). For example, a random distribution function u(r) for an isotropic three dimensional solid yields the Eq (2), where α is proportional to both the chromophore concentration and R_0^3 (Baumann J and Fayer M D 1986).

$$P(t) = exp(-\alpha t^{1/2}) \tag{2}$$

Concentration dependent fluorescence anisotropy results for quinizarin doped sol-gel thin films are shown in figure 2. At low concentration the anisotropy changes little over two fluorescence lifetimes. This indicates that the dopant distribution function at low concentration does not have a large number of close neighbors. The higher concentration data in figure 2 consists of a fast unresolved component and a slowly decaying component to the fluorescence anisotropy. The solid lines in figure 2 are best fits to the data using Eq (1), assuming a bimodal distribution of chromophores, $u(r) = u_a(r) + u_b(r)$, consisting of both a random ($u_a(r)$ = constant) and a sharply peaked chromophore distribution ($u_b(r)$ = const for r < r_c). The fast component is unresolved and is simply the vertical change from $anis(0) = 0.4$ to the beginning of the slower decay. We conclude that dopant molecules are most likely incorporated into a collection of randomly distributed micropores within the sol-gel glass, but that as the concentration is increased, a significant fraction of the molecules reside in multiply occupied micropores. The micropore diameters, r_c, for the samples in this study are on the order of 30Å (Hench L *et al* 1990), and the fast component of the anisotropy decay is due to the fast energy transfer between closely spaced molecules within multiply occupied micropores. This picture is also consistent with our observation that the relative contribution of the fast component increases with chromophore concentration.

ACKNOWLEDGEMENT

REFERENCES

Basché Th and Bräuchle C 1991 *J.Phys.Chem* **95** 7130-7131
Baumann J and Fayer M D 1986 *J. Chem. Phys.* **85** 4087-4107
Dislich H 1983 *J. Non-Cryst. Solids* **57** 371.
Förster Th 1949 *Z. Naturforschung* **A4** 321
Hench L, West J, Zhu B, and Ochoa R 1990 *Sol-Gel Optics* (ed MacKenzie J D & Ulrich D) *Proc. SPIE* **1328** 230
Hinsch A and Zastrow A 1990 *SPIE Vol.* **1272** *Optical Materials Technology for Energy Efficiency and Solar Energy Conversion IX* 208-217
McKiernan J, Pouxviel J-C, Dunn B, and Zink J 1989 *J. Phys. Chem.* **93** 2129-2133
Stein A D, Peterson K A, and Fayer M D 1990 *J. Chem. Phys.* **92** 5622
Tutt L and McCahon S 1990 *Optics Letters* **15** 700

Parametric study of chiral composite materials

R. Ro, V. V. Varadan, and V. K. Varadan

Research Center for the Engineering of Electronic and Acoustic Materials
The Pennsylvania State University, University Park, PA 16802

ABSTRACT: Reflection and transmission characteristics of chiral composites are obtained for a normally incident, linearly polarized plane wave by employing a free-space measurement system in the frequency range of 8-40 GHz. The artificial chiral composites are fashioned by embedding chiral inclusions (metallic helices) into an epoxy medium (Eccogel). One reflection measurement is made for each sample since the reflected field is linearly polarized as the incident wave. Two transmission measurements at different polarization directions are needed in order to fully characterize the transmitted polarization ellipse. From one reflection and two transmission measurement data, the chirality parameters of chiral composites are for the first time computed numerically using a suitable inverse algorithm.

I. INTRODUCTION

For a normally incident, linearly polarized wave, the transmitted wave passing through the chiral medium not only is rotated but becomes elliptically polarized due to the existence of the chirality parameter. This results from the different phase velocities and different absorption for the left- and right-circularly polarized waves. Since electromagnetic waves can discriminate between objects of different handedness due to their transverse nature, the origin of chirality need not necessarily be molecular as in the case of optically active media. Effectively chiral composites can be constructed by embedding chiral microstructures in a host medium. The microstructure size should be large enough that the electromagnetic wave in the matrix can appreciate the handedness of the microstructure; at the same time, the microstructure size should be small enough so that the composite medium, consisting of a chiral phase, is effectively chiral.

The planar chiral samples made for this research are fashioned by embedding large numbers of micro-miniature helices in a host material. The matrix material, Eccogel 1365-90, produced by Emerson and Cuming, is a homogeneous, isotropic and low loss dielectric material. As Eccogel is a durable thermosetting plastic, samples then can be repeatedly used without changing their physical dimensions. The chiral inclusions have the dimensions pitch $P = 0.05292$ cm, radius $a = 0.05842$ cm, and 3 turns. Detailed information about the procedure to make isotropic, homogeneous chiral composites can be found in Guire (1988).

2. MEASUREMENTS OF ELLIPTICITY AND ROTATION ANGLE

The general procedure for measuring the angle of rotation in a free-space measurement system is illustrated in Fig. 1. The block diagrams shown in Fig. 1 are the cross-sections of the rectangular waveguide which connect the antennas and control the polarization directions of the antennas. The arrows in the figure indicate the directions in which each antenna is polarized as a result of the feed positions. At position A, both transmitting antenna (left) and receiving antenna (right) have the same polarization direction and they are said to be co-polarized. The free-space *TRL* calibration method (Ghogaonkar; 1989, 1990) is implemented next. Then the rectangular waveguide, which is connected to the receiving antenna, is rotated 90 degrees. This makes the antennas cross-polarized as shown in Fig. 1 position B, which implies that the directions of the antennas are 90 degrees with respect to each other and at this position the system is set to extinction. When the system is set to extinction, the chiral sample is inserted. Transmission increases because the chiral rotation causes a component of the transmitted wave ($S_{21cross}$) to be parallel to the polarization direction of the receiving antenna. The antennas are now rotated along their common axis until a minimum level of the transmission wave (S_{21min}) is achieved as shown in Fig. 1 position C. At this position, the angle rotated between the antennas is the measured rotation angle of the chiral sample.

Figure 2 shows the plot of the chirality parameter versus the frequency. For the racemic sample, both the real and imaginary parts of the chirality are approximately zero as they should be. The real parts of the chirality parameter have positive and negative values for the right- and left-handed samples, respectively, in the frequency range of 8-40 GHz. Their values are almost the same but with opposite signs. The imaginary parts of the right- and left-handed samples shown in Fig. 2 have almost the same values but with different frequencies.

3. CONCLUSION

It has been shown that the free-space measurement system can be used as a microwave polarimeter with very good accuracy. The chirality parameter β of the racemic samples has a value of approximately zero over the whole frequency range. For the handed samples, both the real and imaginary parts of the chirality parameter β increase as the volume concentration of the chiral sample increases. In addition, with the same volume concentrations, inversely handed samples have almost the same values but with opposite signs for the real and imaginary parts of the chirality parameter β.
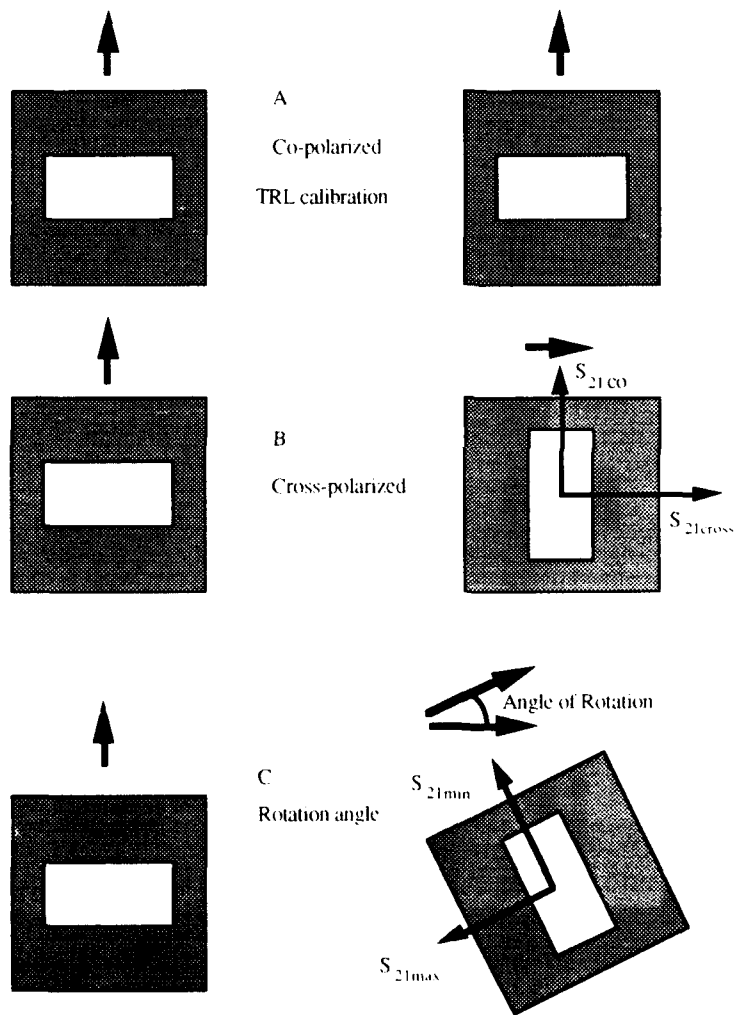
Fig. 1. Procedure of measurement of the rotation angle.
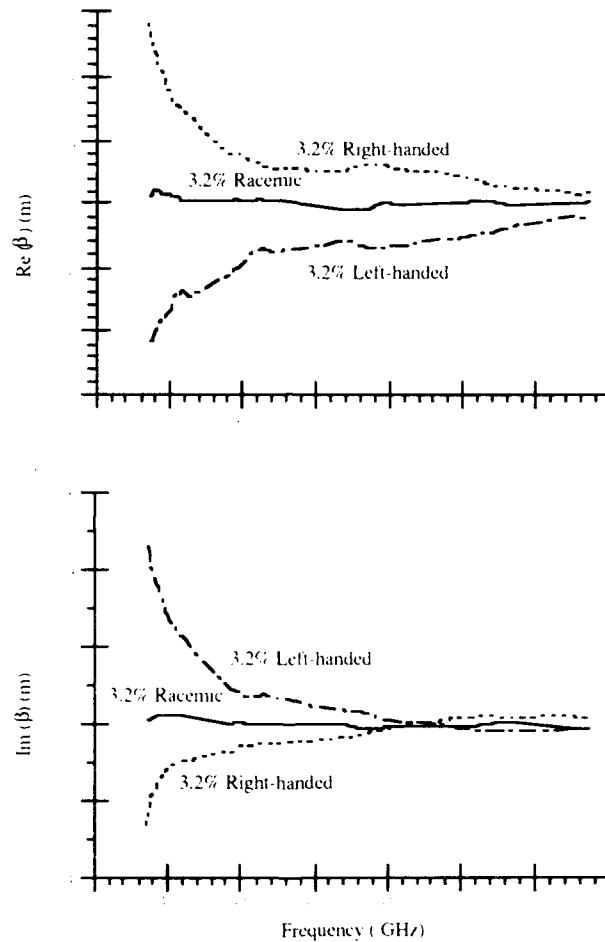
Fig. 2. The chirality parameters β of the 3.2% chiral composite samples.

REFERENCES

Guire, T., "Propagation Measurements on Chiral Composites at Microwave Frequencies,"
M.S. Thesis, 1988, Solid State Science, The Pennsylvania State University, University
Park, PA.

Ghodgaonkar, D.K., Varadan, V.V., and Varadan, V.K., *IEEE Transactions on
Instrumentation and Measurements* **IM-38**(3), 789 (1989).

Ghodgaonkar, D.K., Varadan, V.V., and Varadan, V.K., *IEEE Transactions on
Instrumentation and Measurements* **IM-38**(3), 387 (1990).

Prospects for electronic component distribution in intelligent structures

David J. Warkentin and Edward F. Crawley

Space Engineering Research Center, Department of Aeronautics and Astronautics, Massachusetts Institute of Technology, Cambridge, MA 02139

ABSTRACT: Some hardware implications of control system functionality distribution in intelligent structures are addressed; it is suggested that distributed and embedded systems can have substantially fewer external communications lines and faster control loop speeds than conventional approaches, at the cost of embedding electronic circuit chips. The application of a single-chip microcomputer to the control of a structural vibration problem demonstrates the potential for the development of monolithic integrated circuit devices capable of performing distributed processing tasks required for fully integrated intelligent structures.

1. INTRODUCTION

The application of fully integrated intelligent structures depends on the development of suitable actuators, sensors, processors, and algorithms. In the area of strain control, substantial work has been performed to demonstrate the operation of actuators such as piezoelectrics and shape memory alloys (Crawley and de Luis, 1987, Rogers et al, 1989), and sensors such as fiberoptics and other strain sensors (Turner et al, 1990), which would be suitable for embedding in an intelligent structure. Algorithms for the control of structures with large numbers of highly distributed sensors and actuators have also been suggested (Young, 1983, Hall et al, 1989). Recently, work has also been done to demonstrate the feasibility of physically embedding the electronic components used to implement the control algorithms (Warkentin and Crawley, 1991).

The actual application of intelligent structures technology will depend on the realization of tangible benefits and the existence of sufficiently powerful embeddable components. The purpose of this paper is to suggest some of those potential benefits and to demonstrate the implementation of structural control with single chip microcomputer.

2. BENEFITS OF DISTRIBUTION AND EMBEDDING

A substantial amount of circuitry is required to support the function of the actuators and sensors. Sensors and actuators must be powered, and signals to and from the transducers must be conditioned and perhaps digitized. The control processing, either in analog, digital, or hybrid form, must also be performed by integrated circuits. The components which perform these functions may be centrally located as in traditional control systems, or distributed to a greater or lesser degree. To quantify some of the implications of the level of distribution, we may consider the application of a control system to an idealized structure consisting of *n* nodes, each associated with an actuator and position and rate sensors, so that a full-state feedback control system could be implemented. The components which perform the control functions may be centrally located as in traditional control systems, or distributed to a greater or lesser degree, as illustrated in Options I and II in Figure 1. Option I shows a case in which only the sensor and actuator transducers themselves are integrated, so that at least one signal line from each transducer must leave the structure.
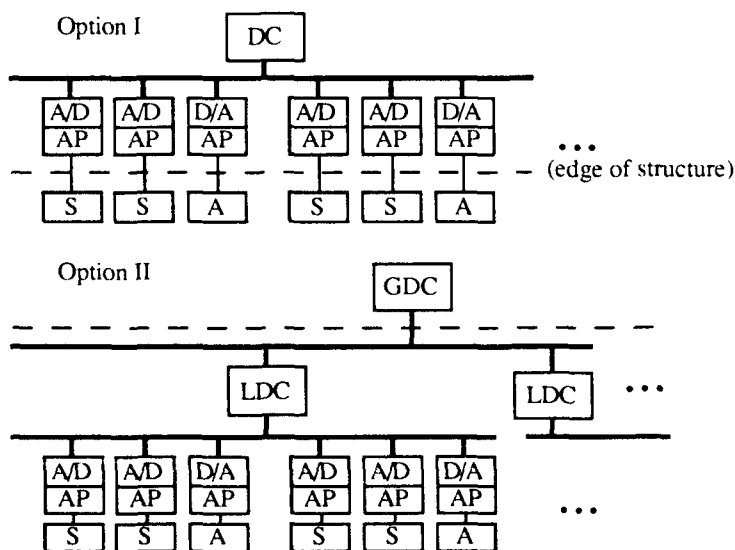
Fig. 1. Two options for distributing functionality. DC=digital computer, AP=analog processing, S=sensor transducer, A=actuator transducer, GDC=global digital computer, LDC=local digital computer.

Distributing analog processing as well as the transducers could improve signal to noise ratios at the cost of a small increase in the number of conductor lines and a number of chips proportional to the number of structural nodes. If the presence of those chips is supportable, however, a substantial savings in terms of lines can be obtained by distributing digital conversion and bus interface functions as well. At the cost of another slight increase in the

number of chips, the distributed processing in a hierarchic system could also be embedded, as shown in Option II of Figure 1. In this case, each local digital computer processes information from a group of transducers, and in turn is connected on a bus with the global computer. For concreteness, the number of local processors is taken to be the square root of the number of structural nodes n. Assuming an 8-bit parallel data bus structure with typical handshaking line requirements, as well as high and low voltage power lines, grounds, and a clock signal, we can produce a system in which the number of lines is a constant plus a term of order $O(\log_2 n)$, accounting for the number of lines required to address all the local processors. This line count reflects only those lines entering the structure.

An integrated digital bus could of course be implemented with out distributing the processing in a hierarchic fashion; the real benefits of this option are to be found in the comparison of control loop speeds achievable with undistributed and distributed computational power. Based on the algorithm presented in (Hall et al, 1989), the number of equivalent operations required for a fixed gain hierarchic controller may be computed and compared with the number required to implement a traditional centralized fixed gain controller such as a linear quadratic regulator. After making plausible assumptions as to relative computation and data transmission rates, the results of this comparison are presented in Table 1 along with the chip and line counts for the two options.

Table 1. Numbers of communications lines, distributed chips, and control loop durations for two levels of distributed functionality.

	Centralized	Hierarchic
Chips embedded	0	$3n + \sqrt{n}$
Communication lines	$3n + 2$	$16 + \max\left(8, \left[\frac{1}{2}\log_2 n\right]\right)$
Control loop duration (equiv. operations)	$O(n^2)$	$O(n)$

The table shows that by integrating electronic functionality in the structure along with the transducers a substantial reduction may be achieved in the number of power and signal lines entering the structure, at the cost of embedding some number of integrated circuits. The reduction in control loop speed can also be substantial, as suggested by the quadratic dependence on the number of structural nodes in the centralized option and the linear dependence in the hierarchic option.

The application of the hierarchic algorithm developed in (Hall et al, 1989) achieves its faster execution times by means of the inherent parallelism of the distributed local control, but also through model reduction at the global level. The separation into global and local levels allows a natural correspondence between fast local loops and high frequency motion, and between the relatively slow global loop and lower frequency motion. This structure does however incur

some penalty in the form of computational overhead and additional communications, so that for small systems the hierarchic approach can be slower than the centralized approach. As the problem size increases, though, the n dependence of the hierarchic loops quickly wins out over the n^2 dependence of the centralized loop, as shown in Figure 2.
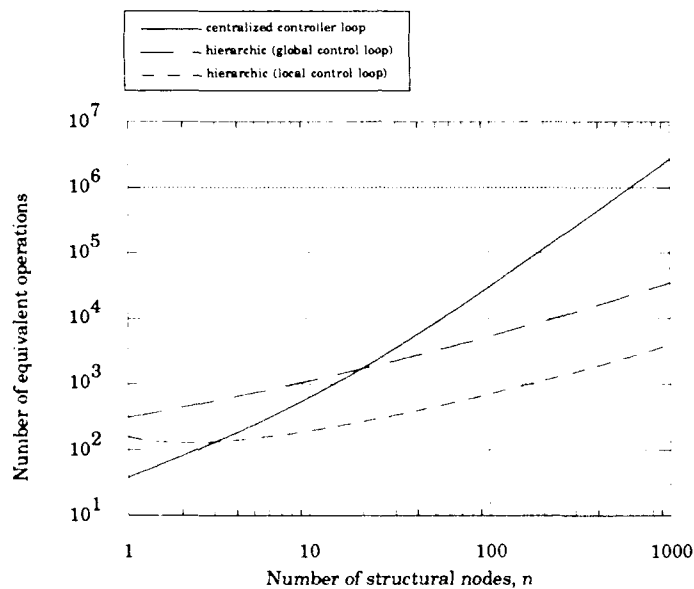
Fig. 2. Comparison of equivalent operations required by three control loops: the centralized system and global and local loops of the hierarchic system.

3. DEMONSTRATION OF SINGLE CHIP MICROCOMPUTER CONTROL

In contrast with conventional computer control systems which employ many specialized chips to perform the various functions of signal conversion, computation, storage, and communication, the embedded control system of an intelligent structure would greatly benefit from the use of processors which could combine as many functions as possible on a single chip. This would greatly simplify the interconnections as well as reduce the adverse effect on structural integrity.

The Intel 87C196KB is a commercially available microcomputer which incorporates on a single chip many functions (e.g., A/D and D/A conversion, high speed communication, memory) which are traditionally distributed among many separate chips. It is apparent that a wide variety of functions can now be combined to greatly reduce the number of chips required for a complete control system; combined with the ability to embed electronic components in general, this puts the development of true intelligent structures within reach. The presence of communication ports on these single chip microcomputers makes possible their incorporation into a network of such devices. This system could yield an efficient distribution of

computational load, perhaps in the implementation of a hierarchic controller of the type described above.

Burst random
disturbance input
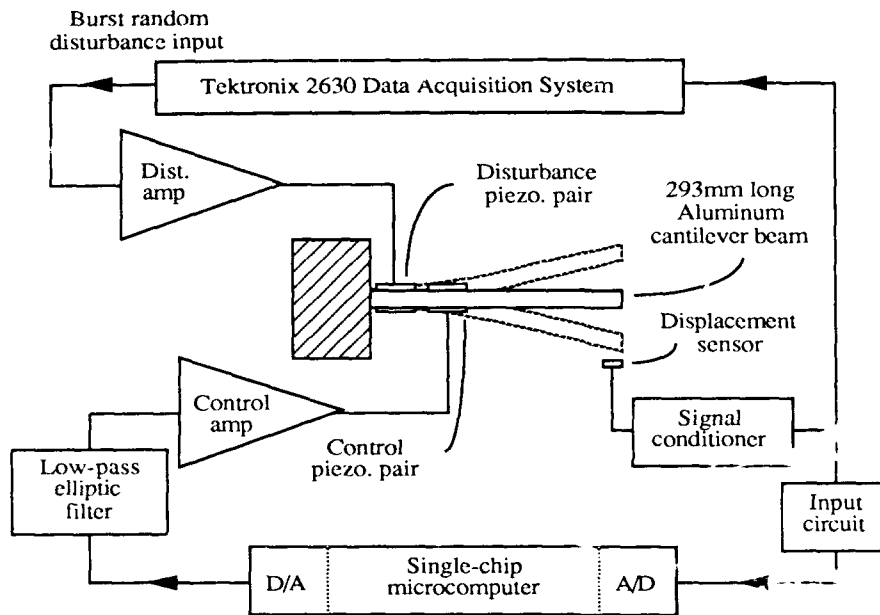
Fig. 3. Schematic of setup for single-chip microcomputer control experiment. Shows beam plant, actuators, sensor, and feedback loop components.

Figure 3 illustrates a simple structural control experiment in which the single chip microcomputer was used. As a commercial product with a wide range of intended applications, the microcomputer could not be expected to perform all dedicated signal conditioning and amplification functions required by the specific sensor and actuator hardware used in this experiment; a custom device might well absorb some of these functions as well. The classically designed compensator consisted of a zero at the origin and two real poles at 383 Hz, and a sampling rate of 14.7 kHz was attained. The tip displacement disturbance response of the cantilever beam with piezoelectric actuators was reduced by 20 dB from the open-loop level, and damping ratios of 31%, 4%, and 11% were achieved in the first three ι des, demonstrating a substantial degree of control effectiveness. Figure 4. shows the frequency response for the open loop case and for three closed loop gains; the large damping achieved in several modes is apparent, as is the authority exerted in shifting the frequency of the second mode. This achievement, together with the other, unused functions present on the chip, supports the conclusion that with a still greater level of functional integration, leading to a further reduction in the number of components and increased suitability for physical embedding, such a device or a near derivative might well be able to perform as a local controller in the hierarchic control architecture of an intelligent structure.

Disturbance piezo. transfer function - experiment
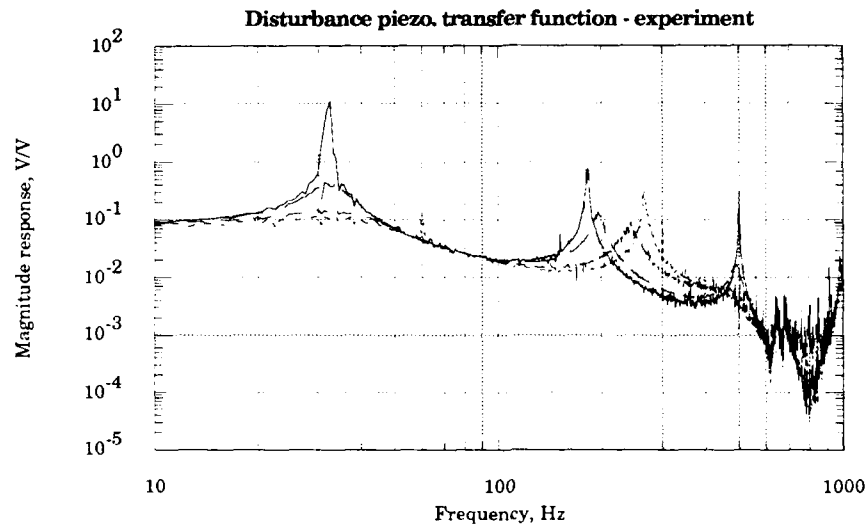
Fig. 4. Structural control with a single chip microcomputer. Response to disturbance at open loop and four closed loop gains.

References

Crawley, E. F. and de Luis, J., 1987, "Use of Piezoelectric Actuators as Elements of Intelligent Structures," *AIAA Journal*, Vol. 25, No. 10.

Hall, S. R., Crawley, E.F., and How, J., 1989, "A Hierarchic Control Architecture for Intelligent Structures," submitted to *AIAA Journal of Guidance, Control, and Dynamics*.

Rogers, C. A., Liang, C., and Barker, D. K., 1989, "Dynamic Control Concepts Using Shape Memory Alloy Reinforced Plates," Smart Materials, Structures, and Mathematical Issues, Technomic Publishing Co.

Turner, R. D., Valis, T., Hogg, W. D., and Measures, R. M., 1990, "Fiber-Optic Strain Sensors for Smart Structures," *Journal of Intelligent Material Systems and Structures*, Vol. 1, No. 1.

Warkentin, D. J., and Crawley, E. F., 1991, "Embedded Electronics for Intelligent Structures," *Proceedings. 32nd AIAA/ASME/ASCE/AHS/ASC Structures, Structural Dynamics, and Materials Conference*, Baltimore, MD.

Young, K. D., 1983, "An Application of Decomposition Techniques to Control of Large Structures," *Proceedings, 4th VPI & SU/AIAA Symposium on Dynamics and Control of Large Space Structures*.

889

Combining fiber optics, radio frequency and time reflectometry techniques for smart structure health monitoring

J S Schoenwald[*] and R H Messinger[**]

[*]Science Center, Rockwell International Corp., P.O. Box 1085, Thousand Oaks, CA 91358

[**]Space Systems Division, Rockwell International Corp., P.O. Box 7009, Downey, CA 90241-7009

ABSTRACT: Three optical fibers terminated with reflecting end coatings have been embedded in a graphite epoxy *double jointed bond* transverse to the load axis. Joint specimens were prepared with and without simulated disbonds. A technique has been developed of measuring the combined phase and amplitude swept radio frequency (rf) amplitude modulation reflections of the optical signal injected into the embedded fibers, obtaining the time domain response (TDR) from the rf frequency response and making a differential comparison between TDR signatures of a joint in its strained and unstrained state. Correct placement of the fibers is contingent on correct interpretation of finite element modeling of predicted strain.

1. INTRODUCTION

The phase-amplitude response of swept ultra-high frequency (UHF) laser amplitude-modulated light transmitted through composite embedded optical fibers is being used to measure strain in test structures subject to tensile loading. The objective is to identify differences in resulting strain fields due to the presence or absence of defects.

Culshaw and Dakin (1989) describe a broad variety of intensity and optical phase interferometric fiber optic sensors. This technique borrows from Rogowski, et al, [1988] in that the change in phase delay of the transmitted ultra-high frequency (UHF) modulation signal is a measure of integrated strain in the fiber embedded in the structure. Now, however, we seek to measure small spatial differences in strain imposed by transverse loading. This is accomplished by embedding several optical fibers of different penetration lengths, which are simultaneously illuminated by a single modulated laser source through a 3x3 fiber optic coupler. Each fiber is terminated with a cleaved, metalized end, causing the optical signal to reflect back efficiently through the optical splitter to a detector. The phase-magnitude characteristics of the reflected signals from the three fibers are determined

by a UHF network analyzer in the transmission measurement mode.   A fast Fourier transform (FFT) performed automatically by the network analyzer yields a transmission mode time domain image of the reflection from the fiber ends, which appear as distinct reflections. Time and frequency domain information are simultaneously available. Using a signal subtraction process, small strains are detected using differencing techniques, and information about the nature of the strain field should make identification of defect generation possible.

2. MODELING AND DESIGN OF BONDED JOINT SPECIMEN

A bonded joint was designed to test the feasibility of observing strain fields and strain anomalies due to joint disbonds by means of fiber optic sensors incorporated in the composite. The joint material is graphite/epoxy composite throughout. Figure 1 is a schematic of the specimens, showing where the optical fibers and simulated disbond Teflon inserts were placed relative to the bond region.   The fibers were placed in the mid-plane of the central tongue of the joint and penetrate to different lengths across the joint. The Teflon inserts were 0.5 and 1.0 inches in radius and were placed in two samples to form semicircular disbonds, as shown in the figure.
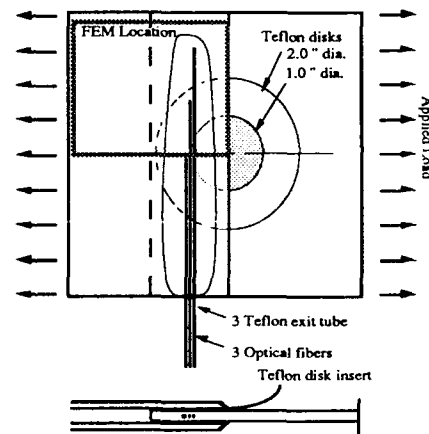
Specimens placed under tensile load experience lateral (transverse) contraction, parallel to the optical fibers, which undergo the same strain as the surrounding medium. The different degree of penetration of each fiber into the joint region would result in a different degree of net strain in each fiber. A 2.0 x 1.9 in.^{2} portion of the bonded region was modeled by finite element methods (FEM) to predict the two-dimensional stress field in the center tongue as a function of load and disbond area in one adjacent adhesive bond.

Transverse strain results of the analysis are shown in two-dimensional plots in Figure 2 for the specimen with a 0.5 in radius disbond. The strain experienced by the optical fibers, located at axial location 16, is thus indicated by values between curves at axial locations 15 and 17. Adherend compressive strain increases monotonically from the outer edge (axial location 21) as the adherend gradually accepts the distributed shear load. Transverse strain

levels vary from about 125 μ-inches/inch to 300 μ-inches/inch for an applied load of 1000 pounds per inch. Predicted strain in all three optic fibers will be about -160 micro strain. Results indicate that the transverse strain field remains unchanged only at the greatest distance from the disbond (lateral location 1). Compared to the no-disbond case, strain generally decreases near the disbond due to the lower total applied load. Within the disbond itself, however, compressive strain rapidly increases, caused by the elongation of the unloaded area in the axial direction. Along the optic fibers, strain levels remain unchanged between lateral locations 1 and 10, then decrease from about -170 microstrains at lateral location 10 to -100 microstrains at lateral location 18.
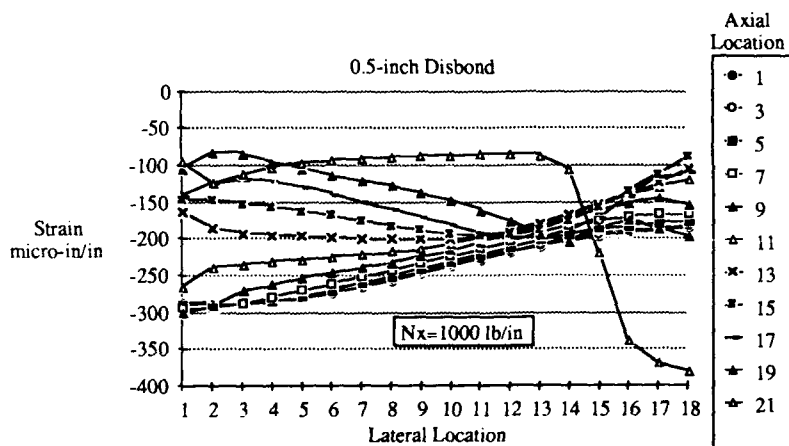
Figure 2. FEM predicted strain in bonded region with 0.5 in radius disbond.

3. FIBER OPTIC STRAIN SENSOR SYSTEM

The fiber optic system designed to measure strain in the double lap joint is shown in Figure 3. A network analyzer provided a swept rf signal from 300 kHz to 3 GHz [3]. This signal modulated the amplitude of a high speed diode laser transmitter [Ortel, TSL-300] and was coupled to a 50 micron core multimode fiber at the optical output port. This fiber was spliced to one fiber of a 3 x 3 beam splitting coupler (Canstar). The three output fibers were spliced to three fibers embedded in the center tongue of the double lap joint, as described earlier, and shown in Figure 3. Each embedded fiber is a 50 micron core/125 micron cladding step index mode fiber coated with polyimide to a total outer diameter of 145 microns. The lengths of the three fibers from the 3 x 3 coupler to the specimen are arbitrary, and can be chosen to

simplify signal processing, described later.
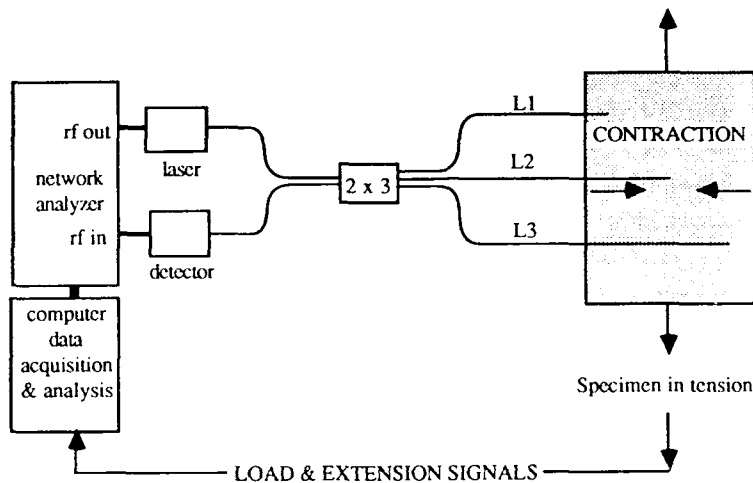
Figure 3. Configuration of optical fibers in specimen and data acquisition system.

The embedded fibers were end coated with gold to produce a substantial reflection. The reflected light returned through the coupler and is split three ways. Only the fibers carrying the light from the laser to the specimen and back to the detector are of interest - the third return fiber is ignored, and is not shown in the figure.

The high speed detector detector/receiver (Ortel, RSL-50) was ac coupled to the input port of the network analyzer (HP-8752A vector network analyzer). An rf transmission measurement previously described by Schoenwald, et al (1990) provides a magnitude and phase record of the sum of the three optical signals, which are of different path length, and which therefore produces a complex interference pattern in the frequency domain measured from 300 kHz to 3 GHz. Interpretation of strain effects from the frequency spectrum is difficult. Instead, we are able to perform a network analyzer-based Fast Fourier Transform (FFT) and convert the frequency domain information to a transmission time domain representation. In effect, reflections from the fiber ends are observable as optical sources at a given distance along the optical path. The FFT performed on the frequency domain data produces a time domain signal equivalent to an optical time domain reflectometer. To observe strain effects in the specimen using the fiber sensor, a subtraction procedure was used. As load was applied to the specimen, time-averaged waveforms of new time domain data (TDD) were subtracted from a reference waveform of TDD of the specimen in the zero load state. These differences

represent the degree to which the strained fiber endpoints have shifted relative to the unloaded state, and the dependence is predicted to be linear for small strains.

4. EXPERIMENT AND DISCUSSION

Tensile loads up to 16,000 lbs were applied to the specimen containing a 1.0 in. radius Teflon insert. Figure 4 is a representative set of curves for this specimen. The first difference curve indicates a nearly negligible response, whereas curves 2 and 3 indicate a trend of increasing signal with load, but with variations in the trends. These variations were somewhat repeatable with repetition of the measurements; since considerable time averaging was performed, noise is discounted as a probable reason for such variations. We suspect the variations are due to interfacial disbonding between the fibers and the composite matrix. Hysteresis lag during load reduction tends to support this interpretation. Further tensile testing and ultimately destructive sectioning and photomicrograph analysis may explain the observed behavior of the sensor. Interfacial adhesion between optical fiber coatings and both the fiber and composite matrix are of critical concern.
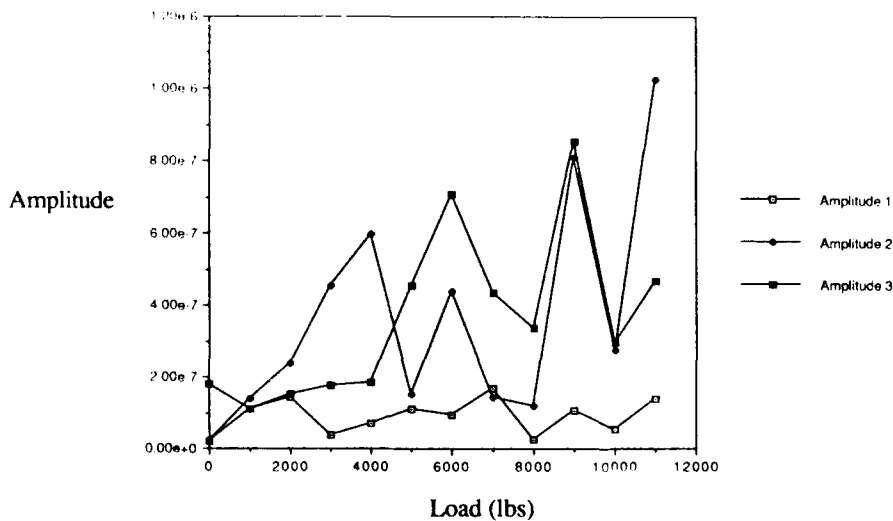
Figure 4. Differential signal response of FFT waveforms versus applied load

5. SUMMARY

We have described a fiber optic sensor designed to detect disbonds in double bonded joints of graphite/epoxy composite. The ability to observe such disbonds has implications for health monitoring systems applications in a variety of structures, including space launch

vehicles. The sensor is based on the signal processing of the complex amplitude and phase response of the summed reflections of radio frequency amplitude modulated light in three optical fibers embedded in a composite structure to different penetration distances. An FFT reduces the complex frequency information to a time domain representation of reflection pulses, which can be digitized and differenced from reference time domain waveforms. Observable trends indicate that fibers of greater penetration depth show greater strain response, but questions remain as to the bond integrity between the fibers and the composite matrix, and possible sources of noise which affect the predicted monotonic behavior of the processed signals.

6. ACKNOWLEDGEMENTS

REFERENCES

Culshaw B, and Dakin J 1989 *Optical Fiber Sensors: Systems and Applications* 2, (Norwood, MA: Artech House)
Rogowski R, Holben M, and Heyman, J 1988 *Rev. Prog. Nondestructive Evaluation* 7A ed D O Thompson and D E Chimenti (Plenum Press: NY) pp 559-63
Schoenwald J S, Messinger R H 1991 *Rev. Prog. Nondestructive Evaluation* 10B ed D O Thompson and D E Chimenti (Plenum Press: NY) pp 1239-46

Fiber-optic sensor integration and multiplexing techniques for smart skin applications

J. D. Muhs, S. W. Allison, C. J. Janke, S. Kercel, and D. B. Smith
Oak Ridge National Laboratory*

Abstract

Integration and multiplexing techniques for smart skin applications using optical fibers has become an increasingly important topic of research in recent years. This paper reviews the initial stages of research in this area at the Oak Ridge National Laboratory (ORNL). Specifically, results from first generation fiber-optic temperature and strain sensor development efforts are given, along with a discussion of various integration and multiplexing techniques proposed for future development.

1. Introduction

With the evolution of advanced composites for use in military, aerospace, and industrial applications, comes a growing need for sensors capable of monitoring the condition of these materials. Ideally, a single-sensor system will be able to evaluate several physical parameters simultaneously over the composite's lifetime to insure safety and reliability. "Smart" composite structures having a multitude of sensor arrays will also self-diagnose possible failure mechanisms prior to their occurrence and potentially be applicable during the curing phase of the composite fabrication process. To achieve these goals, further sensor experimentation by researchers is necessary to overcome some of the barriers associated with current state-of-the-art sensor systems.

Techniques in common use for detecting composite strength degradation after curing include the eddy current and ultrasonic methods. Using these techniques, determining the structural integrity of complex composite structures becomes cost intensive because of the (a) periodic and prolonged down-time required for nondestructive evaluation, (b) extensive time required to fully test the structures, and (c) difficulty in interpreting and drawing useful conclusions from the measurements. A new sensor technology using optical fibers has recently emerged as a potentially superior alternative to the conventional techniques for nondestructive evaluation because of the inherent advantages it possesses. A unique property of an optical fiber is its compatibility with composite structures. The small size of an optical fiber allows it to be embedded in a composite matrix without noticeably degrading the overall strength of the composite. Fiber-optic sensors are intrinsically safe, passive systems that require no shielding from electromagnetic interference. Optical fibers can also be made to detect a wide range of physical parameters and can act both as a transducer and a transmission medium. Such sensors also offer the potential for continuous, remote self-monitoring of composite structures during their service lifetime. This feature eliminates many of the problems associated with conventional nondestructive evaluation techniques.

Strain Measurement

In recent years, research has begun on strain measurements in fully cured composites using optical fibers. The need for such devices for structural fatigue, vibration, and delamination monitoring in composites is unquestionable. The embedded fiber-optic strain measurement techniques used by researchers to date consist of (a) multimode optical-fiber microbending, (b) singlemode fiber-optic interferometry, (c) modal domain crosstalk (using two-core optical fibers), and (d) optical time domain reflectometry (OTDR).[1-3,5-7]

Heat Damage Monitoring

The detrimental effects of overheating on composite strength has been well documented. For example, the strength of a 21-ply, epoxy-based IM6/3501-6 composite (manufactured by Hercules) decreases by approximately one order of magnitude when heated from 300°C to 600°C, although not visually detectable. Several techniques are currently being pursued for measuring surface heat damage after the high-temperature exposure has occurred.[4,6,8] However, most researchers feel that real-time temperature monitors using embedd_ _ensors will give the best indication of heat damage in composites. In the past, thermocouples have been used almost exclusively for this task. However, the attractive features of embedded fiber-optic sensors mentioned earlier make them a viable alternative, especially when multiplexed with other types of fiber-optic sensors.

Moisture Content Determination

In epoxy-based composite structures, moisture adversely effects the resin and decreases the overall strength of the structure. Furthermore, the added weight created by moisture can be detrimental to the structures survivability. Optical techniques capable of monitoring moisture in air (humidity) have been well documented in the past.[9-14] However, miniature fiber-optic moisture sensors must be developed for embedded composite sensor applications.

2. Preliminary Experimental Results and Discussion

Temperature Sensing

When excited by ultraviolet and/or visible laser light, certain phosphors will fluoresce in the visible portion of the electromagnetic spectrum. Hence, the technique chosen for further development at ORNL is based on UV-excited two-color (wavelength) fluorescence amplitude ratioing. The fluorescence amplitude of two separate wavelengths vary with temperature changes. As the temperature of the phosphor fluctuates, the ratio of the two fluorescence signals is altered. To insure the ultraviolet light interacts with the phosphor during the measurement, the optical fiber (in our case a 100/120μm glass-on-glass fiber) was etched using hydrofluoric acid until its core was exposed. Next, a temperature-sensitive phosphor was applied to the etched region using a epoxy binder. Figure 1 illustrates the experimental setup used. Preliminary results from one particular phosphor have shown the technique to be a viable method of discerning temperature changes.

The composite's epoxy resin itself will fluoresce when excited by broadband ultraviolet and/or laser light. Preliminary experiments at ORNL have shown that in some cases this intrinsic fluorescence phenomena is directly dependent on the maximum temperature experienced by the compounds, see Fig. 2.

Strain Sensing

The approach used at ORNL for strain sensing entails the use of singlemode optical fiber and incorporates the technique of OTDR. In general, the OTDR technique is based on the fact that if a very small duration light pulse is sent down an optical fiber, reflections at fiber discontinuities will send return signals back in the opposite direction, as depicted in Fig. 3. By measuring the time of flight, t_i, between consecutive reflections, one can determine the relative magnitude of the length of optical fiber located between the two discontinuities (reflections).

Recently, a preliminary proof-of-principle evaluation of the OTDR technique has been initiated at ORNL. In these experiments, a OTDR system (similar to the one depicted in Fig. 1) was assembled using off-the-shelf Tektronics and Opto-Electronics, Inc. components and experimental data taken. A fiber-optic strain sensor having a longitudinal gauge length of approximately one meter was hard-mounted at one end and affixed to a single-axis translation stage at the other. The

singlemode optical fiber was then elongated by moving the translation stage in increments of 400 μm. The relative changes in time-of-flight measurements were recorded. Figure 4 shows the results of five identical elongation sample experiments. The strain sensitivity of the system was ~400 microstrain, but with further refinement of the sensor architecture and improved components, the sensitivity is expected to improve by a factor of ~100.
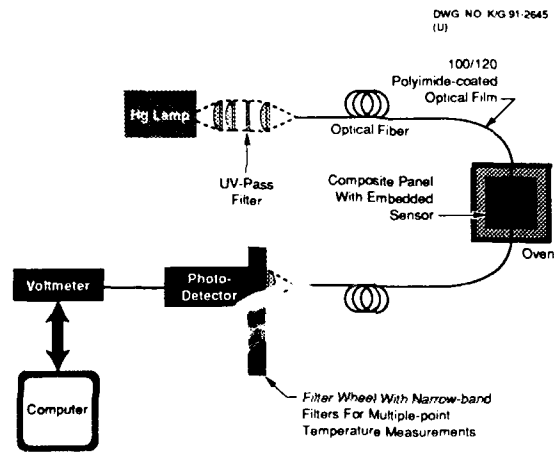
Fig. 1. Experimental arrangement for temperature sensing on optical fibers using thermographic phosphors.
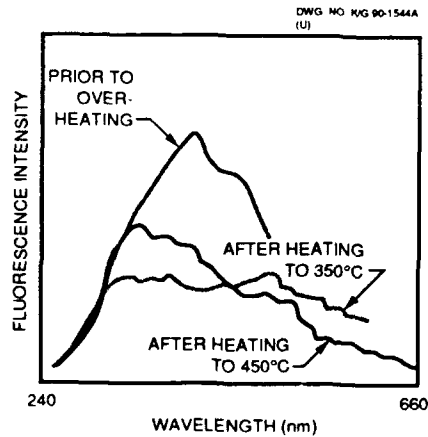
Fig. 2. Fluorescence spectra for composite epoxy sample before, during, and after curing.

Sensor Multiplexing and Integration

Several techniques for multiplexing the above sensors have been investigated for further development. For instance, wavelength division multiplexing will likely be implemented in the fluorescence temperature sensing system by depositing different phosphors at distinct locations along the length of an embedded optical fiber. In addition, the development of a proprietary optical fiber capable of multiplexing singlemode and multimode sensors is also being pursued at ORNL.

Samples of composite materials were fabricated using preliminary embedding techniques. The samples were fabricated from Hercules IM6G/3501-6, unidirectional, prepreg 12 inches wide in a 16-ply quasi-isotropic symmetrical layup - [+45/-45/90/0/+45/-45/90/0]. Optical fibers were embedded at three locations by placing groups of one, two, and three polyamide coated 100/120/130 μm multimode fibers side-by-side (a total of six fibers) in the composite (spaced approximately three inches apart). Testing that was performed on these panels included thickness measurements, interlaminar shear strength determinations, scanning electron micrographs, and optical photomicrographs. The results of these tests were (a) no abnormal thickness differences were evident between areas containing the embedded optical fibers compared to areas in which there were no embedded fibers, (b) tests showed that there was a large standard deviation in shear strength data (due to large void content and that the implementation of optical fibers had no discernable effect on the strength of the specimens, and (c) the scanning electron micrographs and optical photomicrographs identified several small voids adjacent to the optical fibers which likely resulted from poor flow of the epoxy resin system during cure.

3. Summary

This paper has reviewed integration and multiplexing techniques for smart skin applications using optical fibers being developed at ORNL, along with providing preliminary data on fiber-optic temperature and strain sensors.

4. Acknowledgements

5. References

1.   R. Czarnek, Y. F. Guo, D. D. Bennett, and R. O. Claus, "Interferometric Measurements of Strain Concentrations Induced by any Optical Fiber Embedded in a Fiber Reinforced Composite," *Proc. SPIE* **986**, 43-54 (1989).
2.   K. D. Bennett, J. C. McKeeman, and R. G. May, "Full Field Analysis of Modal Domain Sensor Signals for Structural Control," *Proc. SPIE* **986**, 85-89 (1989).
3.   W. B. Spillman, Jr., P. L. Fuhr, and B. L. Anderson, "Performance of Integrated Source/Detector Combinations for Smart Skins Incoherent Optical Frequency Domain Reflectometry (IOFDR) Distributed Fiber Optic Sensors," *Proc. SPIE* **986**, 106-118 (1989).
4.   M. A. Druy, L. Elandjiam, and W. A. Stevenson, "Composite Cure Monitoring With Infrared Transmitting Optical Fibers," *Proc. SPIE* **986**, 130-134 (1989).
5.   R. S. Rogowski, J. S. Heyman, M. S. Holben, Jr., C. Egalon, D. W. Dehart, T. Doederlein, and J. Koury, "Fiber Optic Strain Measurements in Filament-Wound Graphite-Epoxy Tubes Containing Embedded Fibers," *Proc. SPIE* **986**, 194-199 (1989).
6.   G. Meltz, et al., "Fiber Optic Temperature and Strain Sensors," *Proc. SPIE* **798**, 104-115

(1987).

7.   A. D. Kersey, T. G. Giallorenzi, and A. Dandridge, "Interferometric and Intensity Sensors Become More Sophisticated," *Laser Focus World*, 137-143 (July 1989).

8.   C. Janke, et al., "Composite Heat Damage: First Interim Draft Report," MMES Internal Report (In Press).

9.   P. B. Macedo, A. Barkatt, X. Fend, S. M. Finger, H. Hojaji, N. Laberge, R. Mohr, M. Penafiel, and E. Saad, "Development of Porous Glass Fiber Optic Sensors," *Proc. SPIE* **986**, 200-205 (1989).

10.   D. S. Ballantine and H. Wohljen, "Optical Waveguide Humidity Detector," *Anal. Chem.* **58**, 2883-2885 (1986).

11.   Q. Zhou, M. R. Shahriari, D. Kritz, and G. H. Sigel, Jr., "Porous Fiber-Optic Sensor for High-Sensitivity Humidity Measurements," *Anal. Chem.* **60**, 2317-2320 (1988).

12.   M. M. Budnov, A. A. Abramov, V. A. Bogatyrjov, and E. M. Dianov, "Silicon-Clad Fiber Sensor for Detecting of Water Penetration Into Optical Cables," *Proc. SPIE* **838**, 344-346 (1987).

13.   K. Tiefenthaler and W. Lukosz, "Integrated Optical Humidity and Gas Sensors," pp. 169-226 in *Proceedings OFS '84 2nd International Conference on Optical Fiber Sensors, Liederhalle Stuttgart, Federal Republic of Germany, September 5-7, 1984*, eds. R. Th. Kersten and R. Kist, FhG-PM, F.R.G.

14.   Q. Zhou, M. R. Sharriari, and G. H. Sigel, Jr., "The Effects of Temperature on the Response of a Porous Fiber Optic Humidity Sensor," *Proc. SPIE* **990**, 153-157 (1988).
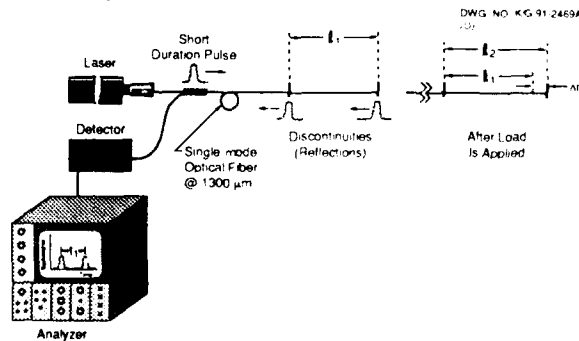
Fig. 3. Optical Time Domain Reflectometry (OTDR)-based fiber — optic strain sensor experimental arrangement.
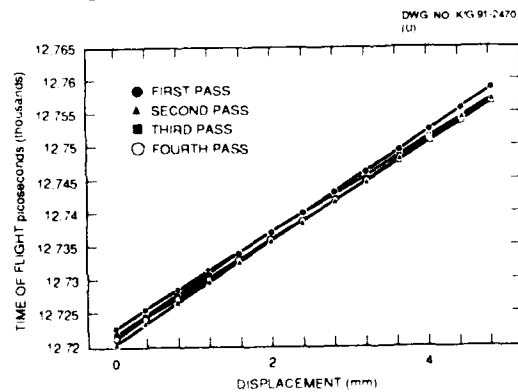
Fig. 4. Time-of-Flight vs displacement for 1 m gauge length OTDR strain sensor.

Control of smart traversing beam

A. Baz, J. Ro, S. Poh and J. Gilheany

Mechanical Engineering Department,   The Catholic University of America ,
Washington, DC 20064

ABSTRACT

Shape memory NIckel-TItanium alloy (NITINOL) is utilized in developing
SMART traversing beams for use in critical applications where weight and
deflection are of utmost importance such as the launching and crossing
operations of long support bridges.   The NITINOL fibers are placed at
critical locations inside the traversing beams to sense and control the
beam deflection.   With such capabilities, it would be possible to
manufacture light weight and long span support bridges which can be easily
handled in short emplacement time.
     A finite element model is developed to describe the static
characteristics of a thin-walled square cross section cantilever beam
subjected to concentrated moving loads.   The model accounts for the control
action provided by the phase recovery forces generated by the NITINOL
fibers due to their activation by the control system.   A closed-loop
computer-controlled prototype of the SMART beam is built to demonstrate the
feasibility of the concept.   The sides of the prototype beam are made of
photoelastic plates in order to monitor the stress distribution in the beam
with and without the activation of the NITINOL fibers.   The experimental
stress distribution and beam deflection are found to be in good agreement
with the predictions of the finite element model.   The results obtained
successfully demonstrate the effectiveness of the NITINOL fibers in sensing
and controlling the deflection of this class of SMART beams.

1. INTRODUCTION

     Emphasis has been placed recently on the development of a wide
spectrum of SMART structures that have built-in sensing, actuation and
control capabilities.   These structures can sense external disturbances,
actively compensate for them in appropriate time and revert back to their
undeflected shape as soon as these disturbances are removed.   Distinct
among these structures are those reinforced with **shape memory**
NIckel-TItanium alloy (NITINOL) fibers.   Such structures have been
considered for various critical applications because their static and
dynamic characteristics can be easily tailored to adapt to changes in the
operating conditions (Baz et al 1991, Rogers 1991 and Ikegami et.al 1990).
     In the present study, a SMART traversing beam is developed as shown in
Figure (1) to replace conventional traversing beams which are traditionally

manufactured from heavy metallic cross sections.   Such conventional beams
are launched from a truck provided with a massive counterbalance weight to
resist the tipping moment generated by the dead weight of the extended
beam.   The excessive weight of the metallic traversing beam imposes severe
stress and deflection constraints on the maximum length of its span which,
in turn, limits its use to narrow gap support bridges.   To avoid these
problems the **SMART** traversing beam concept offers a viable alternative as
the metallic beam is replaced by an actively controlled light weight
composite beam.   The **SMART** beam will operate with smaller counterbalance
weights over wider gaps.
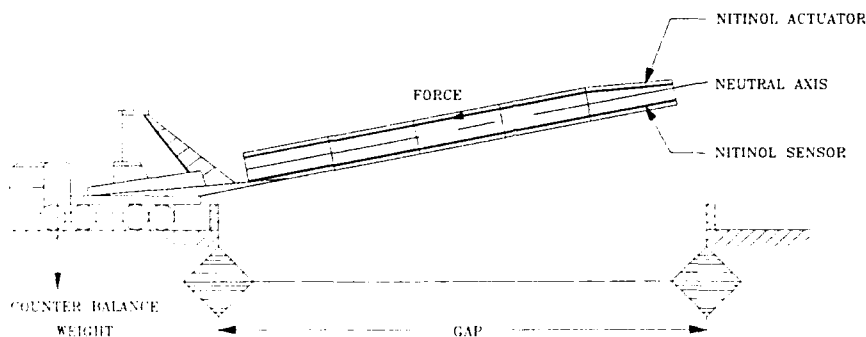
Figure (1) - The **SMART** traversing beam

The **SMART** beam relies in its operation on two sets of **NITINOL** wires
embedded in the composite fabric of its thin-walled hollow cross section.
The first set consists of large diameter wires to serve as actuators
whereas the second set of wires is made of much smaller diameter wires to
act as sensors.   When the set of sensors detects deflections, during
launching or cross over operations, a signal is generated which is
proportional to the external moment acting on the beam (Baz et al 1991).
This signal activates a appropriate number of actuator fibers by heating
them above their transition temperature (Duerig 1990, Perkins 1975).   The
resulting phase recovery forces times the distance to the neutral axis of
the beam generates a moment which counterbalances the gravitational moment
acting on the beam.   This action considerably reduces the beam deflection.

2. PROTOTYPE OF THE SMART TRAVERSING BEAM

A schematic drawing of a prototype of the **SMART** beam is shown in
Figure (2). The beam is a thin-walled square cross section beam which is
17.5cm x 5cm x 5cm. The wall thickness of the beam is 0.625 cm.   The sides
of the beam are made of a photo-elastic plate (PS-4 from Measurements
Group, Inc., Raleigh, NC) in order to monitor the stress distribution in
the beam. The top and bottom faces are made of fiberglass-polyester
composite plates. In the top face, a set of 0.55 rm diameter **NITINOL**
actuator fibers are embedded inside vulcanized rubber sleeves while in the
bottom face a single loop of a 0.15 mm diameter **NITINOL** sensor fiber is
bonded o the composite matrix. The actuator fibers are fixed to the free
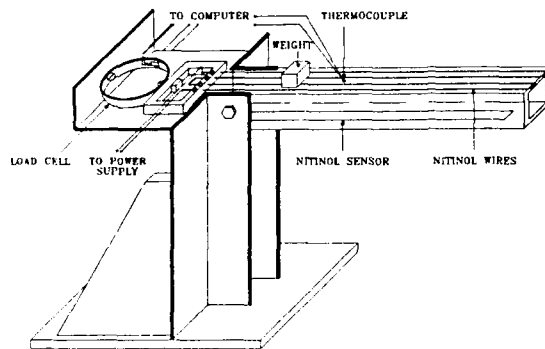
Figure (2) - Prototype of the **SMART** traversing beam

end of the beam and are connected to a load cell at the other end to
monitor the force generated by the actuators as they undergo their phase
transformation. The sensor fiber is connected to a Wheatstone bridge and
acts as a distributed strain gage. When a load is applied to the beam, the
sensor will detect the developed strains. The resulting signal is
amplified and sent to the computer to compute the required control action
based on an ON-OFF control strategy with a dead band as shown in Figure
(3). The control action is sent to a power amplifier to heat (activate)
the **NITINOL** actuator set in order to bring the beam back to its undeflected
position. The temperature of the **NITINOL** actuators is monitored with a
thermo-couple. The stress distribution inside the beam is also
continuously monitored by placing the beam inside a polariscope and
illuminating it with diffused light. The generated fringes are recorded by
the computer via a video camera during the different phases of operation.
The iso-chromatic fringes developed in the photo-elastic sides of the beam,
which represent the contours of constant shear stress, are compared with
the results of the finite element model.

The effectiveness of the **NITINOL**-based sensing and actuation is
evaluated by moving a weight at different speeds over the beam span and
monitoring the beam deflection with and without the activation of the
control system. This simulates the launching operation of the **SMART**
traversing beam where the bridge weight increases as it is extended over
the gap. Also, the performance of the control system is determined at
different values of the dead band and pre-load of the **NITINOL** actuator.
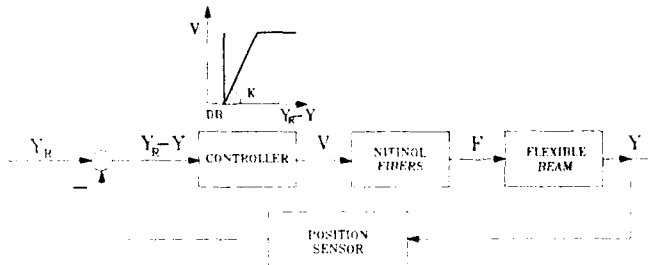
Figure (3) - Block diagram of the control system

3. PERFORMANCE OF SMART BEAM

3.1. Effect of actuator pre-load

Figures (4), (5) and (6) show the performance of the **SMART** beam when the pre-load of the **NITINOL** actuators is 0, 2.2 and 4.4 N, respectively. In all these figures, the controller dead band is set at 0.976 μm and the moving weight is pulled at a constant speed of 0.011 m/s over the beam span.   In Figure (4-A), the position of the moving weight is shown as a function of time and the corresponding deflection of the free end of the uncontrolled beam is shown in Figure (4-B). This deflection increases to a maximum value of 1.8 mm as the moving weight moves from the fixed end of the beam to its free end.   When the controller is activated the **NITINOL** actuators remain ineffective, as indicated in Figure (4-C), until their temperature starts exceeding their phase transformation temperature of about 40°C. This occurs at a time of about 10 seconds as shown in Figure (4-D).   Until such time is reached the beam deflection remains essentially equal to that of the uncontrolled beam.   However, as the time progresses the **NITINOL** actuators start generating their phase recovery forces as shown in Figure (4-C).   These forces bring the beam back to its undeflected position by compensating for the moment produced by the moving weight. Once the undeflected position is attained, at time = 13 s, the controller deactivates the **NITINOL** actuators.   This manifests itself by a drop in the actuator force and temperature.   Consequently, the beam deflection starts to increase beyond the desired dead band and the controller again activates the **NITINOL** actuators to compensate for this error. This process of activation and deactivation of the **NITINOL** actuators is repeated and it results in the oscillatory behavior displayed in Figures (4-B), (4-C) and (4-D).

Increasing the pre-load of the **NITINOL** actuators to 2.2 N and 4.4 N is observed to considerably improve the performance of the **SMART** beam as shown in Figures (5) and (6) respectively. This improvement is attributed to the increase in the phase recovery forces developed by the actuators as a result of increased pre-loads.   A summary of the effect of the pre-load on the **maximum** end deflection of the controlled and uncontrolled beam is displayed in Figure (7).

3.2. Effect of controller dead band

The effect of increasing the dead band on the controller performance is shown in Figure (8).   The figure indicates that increasing the dead band tenfold resulted in increasing the maximum deflection of the beam from 0.3 mm to 0.5 mm.   Such an increase is attributed to the delayed response of the controller which, in turn, resulted in delayed heating of the **NITINOL** actuators as clearly shown in Figure (8-D).

3.3. Effect of moving weight speed

The effect of varying the speed of the moving weight on the performance of the **SMART** beam is shown in Figure (9).   At low travel speeds, the controller response is adequate enough to compensate for the deflection error. However, as the speed of the weight increases the slow response of the **NITINOL** actuators becomes a limiting factor in correcting the displace-
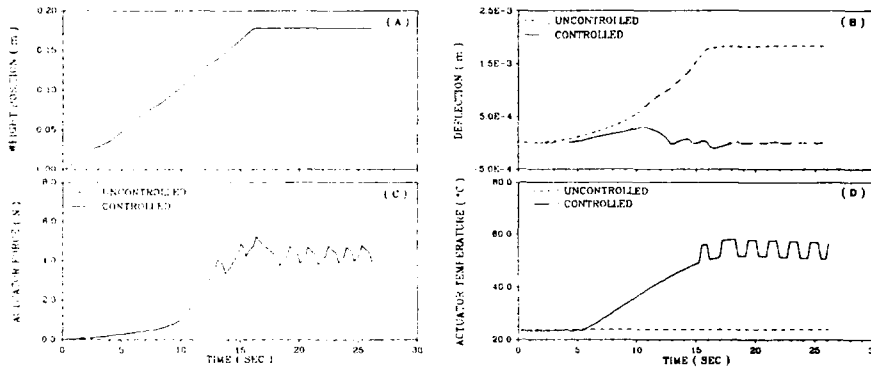
Figure (4) - Performance with actuator preload = 0 N and dead band =.976μm
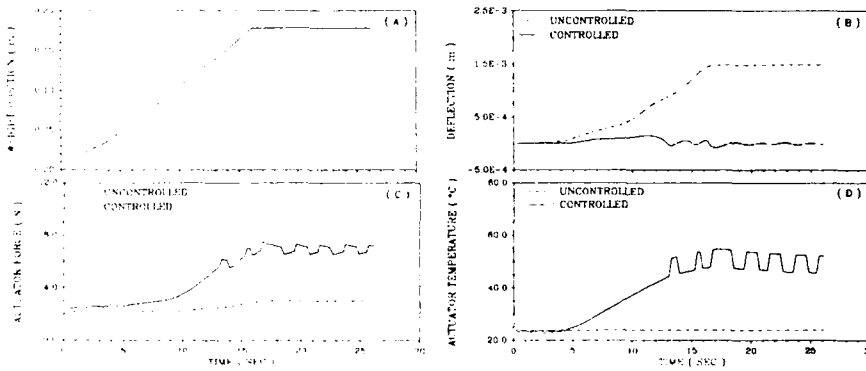
Figure (5) - Performance with actuator preload =2.2N and dead band =.976μm
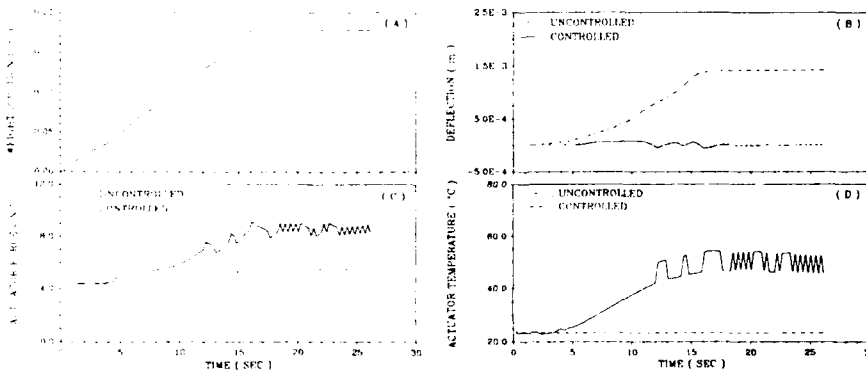
Figure (6) - Performance with actuator preload =4.4N and dead band = .976μm
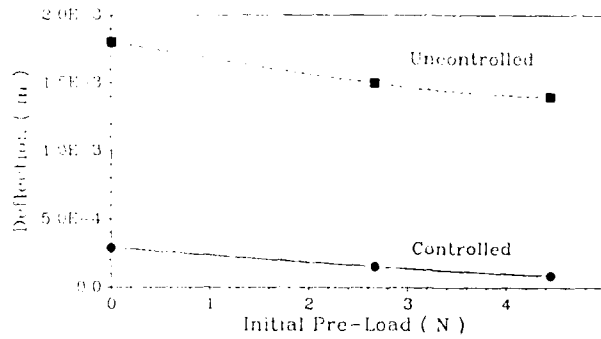
Figure (7) - Effect of preload on controlled and uncontrolled performance
(with dead band = .976μm).
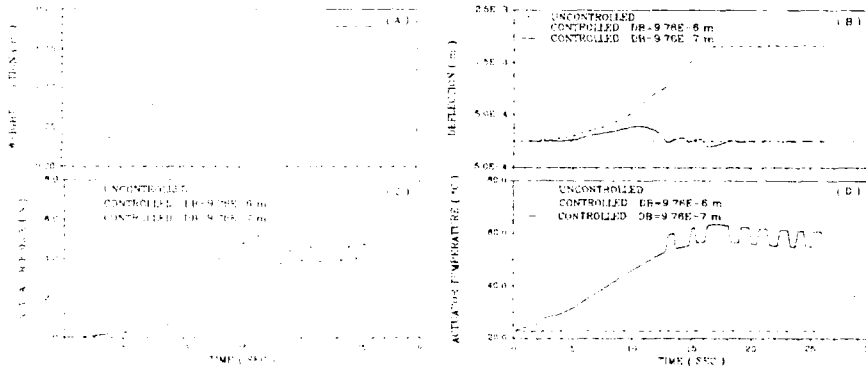
Figure (8) - Effect of dead band on performance with actuator preload = 0 N
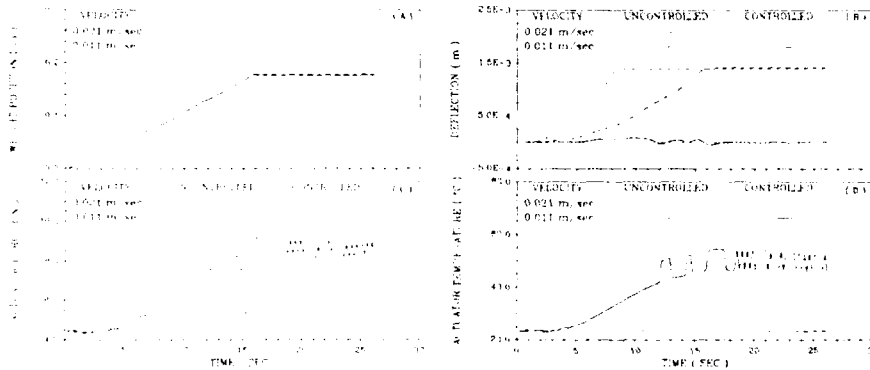
Figure (9) - Effect of moving weight speed on performance (actuator preload
= 4.4 N , dead band =.976μm)

ment error. This is clearly manifested in Figure (9-C) where the monitored maximum displacement error is 0.1 mm when the weight speed is 0.011 m/s and it increases to 0.9 mm as the weight speed is increased to 0.021 m/s.

4. STRESS DISTRIBUTION

4.1. Theoretical modeling

A finite element model is developed to model the stress distribution in the **SMART** beam. The model is obtained by dividing the beam into a set of **E** quadrilateral plate elements such that the displacement model within each element is assumed to be

$$U = [N] \; \delta^e, \tag{1}$$

where [N] is the matrix of shape functions and δ^e is the vector of nodal displacements of the element (Fenner 1975, Rao 1989). The strain vector ε is also expressed in terms of the nodal displacement vector δ^e by differentiating equation (1) to yield

$$\varepsilon = [B] \; \delta^e, \tag{2}$$

where [B] is the spatial derivative of the matrix of shape functions [N].

The vector of stresses σ are obtained from the constitutive model of the beam as follows

$$\sigma = [D] \; (\varepsilon - \varepsilon_0), \tag{3}$$

where [D] is the elasticity matrix and ε_0 is the vector of initial strains due to the pre-load of the **NITINOL** and the thermal loading.

Using the classical finite element approach, one can write the total potential energy of the beam and the necessary conditions for minimizing that energy to attain a static equilibrium configuration of the beam. This yields the following equation

$$\left(\sum_{e=1}^{E} [K^e] \right) \Delta = \sum_{e=1}^{E} \left(P_i^e + P_b^e \right) + P_c \tag{4}$$

where

$$[K^e] = \iiint [B]^T [D] [B] \; dV = \text{element stiffness}, \tag{5}$$

$$P_i^e = \iiint [B]^T [D] \; \varepsilon_0 \; dV = \text{element load vector} \atop \text{due to intial strain}, \tag{6}$$

$$P_b^e = \iiint [N]^T \; \Phi \; dV = \text{element load vector} \atop \text{due to body forces}, \tag{7}$$

$$\Delta = \text{the global vector of nodal displacements},$$

Φ = the vector of body forces per unit volume,

V = beam volume,

and P_c = concentrated loads and moments vector such that:

$P_c(\ell)$ = weight of moving mass **W** at node ℓ

$P_c(a)$ = moment of **NITINOL** actuators
(total actuators tension **T** x
distance to neutral axis **d**) at node a

otherwise $P_c(i)$ = 0 for all nodes i except i= ℓ or a   (8)

Equation (4) is used to calculate the nodal displacements due to the motion of the moving weight **W** over the beam span with, and without,   the activation of the **NITINOL** actuators (i.e. with and without the application of the control moment $P_c(a)= T \times d$).   Equations (2) and (3) are then used to compute the resulting strains ι and stresses σ.

The computed shear stresses τ_c are compared with the shear stresses τ_m measured using the photo-elastic technique (Kuske and Robertson 1974) which are given by

$$\tau_m = n \; f \; / \; (4 \; t),\qquad\qquad\qquad (9)$$

where **n** is the order of the iso-chromatic fringe on which τ_m acts, **f** is the material photoelastic constant and **t** is optical thickness of each side of the traversing beam.

4.2. Results

Figure (10) shows a comparison between the finite element model predictions and the photoelastic measurements of the shear stress distribution in the sides of the traversing beam.   The figure shows the theoretical and experimental stresses developed when the load is at the fixed end of the traversing beam as indicated in case (A).   Comparisons are also given when the load is placed at the free end of the beam with the controller unactivated (case B) and activated (case C).   It can be seen that there is close agreement between theory and experiments.
It is also important to note that the activation of the **NITINOL** actuators results in reducing the shear stresses in the beam particularly at its fixed end.   This is clearly manifested by the shifting of the iso-shear stress contours to the left and accordingly reducing the maximum order of the iso-chromatic fringes measured.

5. CONCLUSIONS

This study has presented a **SMART** beam with built-in sensing and actuation capabilities which are based on the utilization of shape memory fibers (**NITINOL**) to control the deflection under the action of a moving load.   Experimental and theoretical investigations performed successfully demonstrate the feasibility of the **SMART** traversing beam.   Increasing the
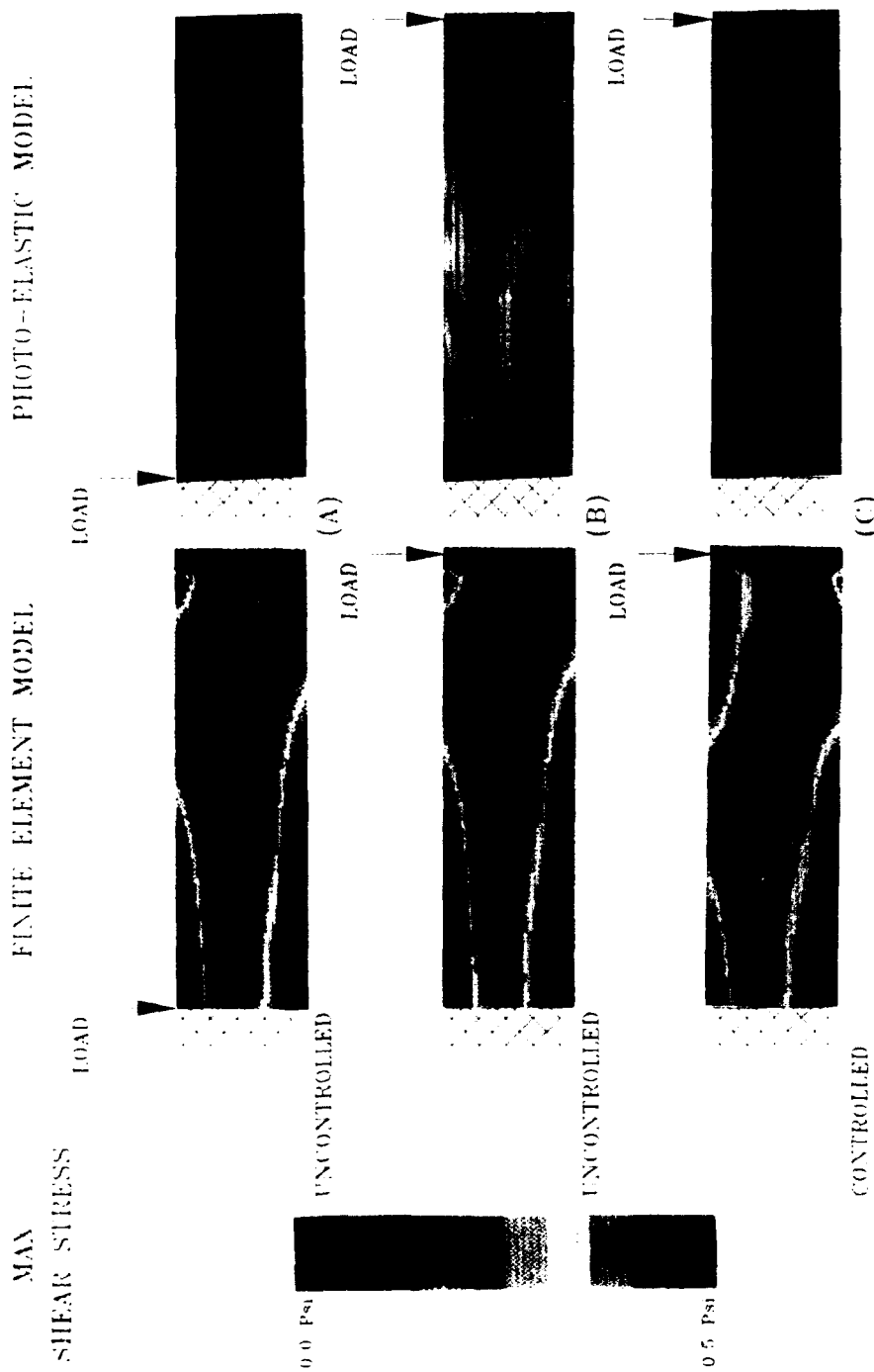
Figure (10) - Comparisons between theoretical and experimental stress distribution in the SMART beam sides (pre load = 4.4 %, moving weight = 0.8 N)

pre-load of the **NITINOL** actuators and reducing the controller dead band are found essential to improving the performance of the **SMART** beam. It is also observed that the travel speed of the moving weight should be compatible with the time response capability of the **NITINOL** actuators in order to achieve effective controller performance.

The results obtained suggest the potential of the **SMART** beam concept in providing light weight, high strength and low deflection beams that can be effective in designing critical structures such as long span support bridges.

REFERENCES

Baz, A., Ro, J., Mutua, M. and Gilheany, J., "Active Buckling Control of NITINOL-Reinforced Composite Beams", Proc. of Active Materials & Adaptive Structures Conference, Alexandria, VA, 4-8 November 1991.

Baz, A., Poh, S. and Gilheany, J., "A Multi-mode Distributed Sensor for Vibrating Beams", ASME Winter Annual Meeting, Atlanta, GA., Dec. 1991.

Duerig, T.W., Melton, K.N., Stockel, D. and Wayman, C., *Engineering Aspects of Shape Memory Alloys*, Butterworth and Heinemann Ltd., London, 1990.

Fenner, R.T., *Finite Element Methods for Engineers*., Macmillan Press Ltd., London, 1975.

Ikegami, R., Wilson, D. and Laakso, J., "Advanced Composites with Embedded Sensors and Actuators (ACESA)", Edwards AFB Technical Report # AL-TR-90-022 (F04611-88-C-0053), 1990.

Kuske, A. and Robertson, G. *Photo-elastic Stress Analysis*. J.Wiley & Sons, New York, 1974.

Perkins, J. *Shape Memory Effect in Alloys*, Plenum Press, New York, 1975.

Rao, S. *The Finite Element Method in Engineering*, Second edition, Pergamon Press, Oxford, U.K., 1989.

Rogers, C., Liang, C. and Jia, J., "Structural Modification of Simply-Supported Laminated Plates using Embedded Shape Memory Alloy Fibers", *Computers & Structures*, Vol.38, No.5/6, pp.569-580, 1991.

ACKNOWLEDGEMENTS

Active flexible rods with embedded SMA fibers

Dimitris C. Lagoudas and Iradj G. Tadjbakhsh

Department of Civil and Environmental Engineering, Troy, NY 12180

Abstract

Embedding of shape memory alloy (SMA) fibers in slender flexible bodies results in shape changes of the host medium, whenever shape recovery of the SMA fibers takes place. The shape change of a cylindrical rod with a single off—axis embedded SMA fiber is modeled in this paper. The distributed axial compressive force and bending moment due to phase transformation in the SMA fiber is evaluated using an approximate analytical model and the deformed shape of the flexible rod is found by solving the equations of equilibrium of the rod.

1. INTRODUCTION

The shape memory effect (Buehler and Wiley 1965, Perkins 1975) is connected with plastic strain recovery upon heating. SMA enhanced composites and SMA actuators have already proved very reliable (Liang and Rogers 1990a). Active flexible structures often consist of thin components such as rods, plates and shells that have been enhanced with shape memory fibers. Development of one or two dimensional theories that accurately describe the dynamic behavior of such composite elements poses special challenges. For, in addition to geometric nonlinearities that accompany large scale motions, one must now include complex material nonlinearity of the actuators (McNichols and Cory 1987, Liang and Rogers 1990b).

2. SHAPE CONTROL OF FLEXIBLE STRUCTURES

The general problem of controlling the shape of a flexible body according to a pre—determined configuration that is not its natural stress—free state requires development of new continuum models as well as new control strategies. The problem can be posed for either one— or two—dimensional media that execute three

dimensional motions. Control can be achieved by embedding SMA fibers in the body in orientations that create the necessary forces for maintaining the prescribed shape. The compliance of such a body changes with space and time.

Considering a thin rod enhanced with SMA fibers, a theory can be developed that will predict the shape of the rod when the SMA fibers undergo the martensitic–austenitic phase transformation. The same theory can also be used to consider the inverse, and conceivably more difficult, problem of determining SMA fiber placement when the shape of the rod is given. A prerequisite for success will be the correct modeling of the mechanisms of transfer of strain from SMA to the host medium and its conversion to distributed forces and couples.

A number of thin SMA fibers can be assumed to be embedded in the rod in various orientations including helical configurations. Assuming some initial prestraining of the SMA fibers before they are perfectly bonded to the rod, raising the temperature beyond A_f will induce strains in the surrounding matrix caused by the martensitic–austenitic phase transformation in the fibers and the constraint of the shape recovery imposed by the elastica. The variation in the forces on any cross section will give rise to resultant bending and twisting moments that will cause the curvature and torsion of the rod.

3. OFF–AXIS SMA FIBER EMBEDDED IN A CYLINDRICAL FLEXIBLE ROD

To demonstrate the idea of modeling configurational changes in flexible rods, a single SMA fiber is considered to be embedded in a long flexible rod of circular cross section as shown in Fig. 1. The SMA fiber is assumed to be in the martensitic phase and with initial permanent axial strain denoted by $-\epsilon^{sma}$. The strain ϵ^{sma} will denote the strain associated with the stress–free shape recovery upon heating, that is, when the temperature is raised above A_f. The strain ϵ^{sma} would be recovered provided that the SMA fiber were free to undergo the martensitic– austenitic phase transformation. Because of the constraints imposed by the host medium, a self–equilibrated internal stress state will develop instead, and the prestrain ϵ^{sma} will only be partially recovered.

An approximate model for the load transfer from the SMA fiber to the host medium is the cylindrical shear–lag model (Budiansky et al., 1986). According to this model, the axial strain of the host medium and the partial shape recovery of SMA takes place through deformation of a shear layer surrounding the SMA fiber. Assuming that the outer radius of the shear layer is $\rho=(\rho_T-d)$ and that the ends at $s=-L/2$ and

s=L/2 are traction–free (Figure 1), the following result is obtained for the shear stress on the interface between the SMA fiber and the host medium:

$$\tau_i = \frac{E_2 \, \epsilon^{sma} \, (\rho_2{}^2 - \rho_1{}^2)}{\rho_1{}^2 + (\rho_2{}^2 - \rho_1{}^2)E_2/E_1} \, \frac{\alpha \, \rho_1}{2} \, \frac{e^{-\alpha(L/2+s)} - e^{-\alpha(L/2-s)}}{1 + e^{-\alpha L}} \quad . \tag{1}$$

The constant α is given by

$$\alpha = \frac{1}{\rho_1} \sqrt{\frac{2G_2}{E_2 \ln(\rho/\rho_1)} \left(\frac{\rho_1{}^2}{\rho^2 - \rho_1{}^2} + \frac{E_2}{E_1}\right)} \quad . \tag{2}$$

As a result of the nonzero interface stress, a distributed axial force and a distributed bending moment is applied to the host medium by the SMA fiber. The distributed axial force is found by integrating the interface shear over the perimeter of the fiber and its non–zero component, along the axis of the rod, is given by

$$f_3 = -\int_0^{2\pi} \tau_i \, \rho_1 \, d\theta = F^{sma} \, \alpha \, \frac{e^{-\alpha(L/2+s)} - e^{-\alpha(L/2-s)}}{1 + e^{-\alpha L}} \quad , \tag{3}$$

with F^{sma} defined by

$$F^{sma} = -\pi \, \rho_1{}^2 \, \frac{E_2 \, \epsilon^{sma} \, (\rho_2{}^2 - \rho_1{}^2)}{\rho_1{}^2 + (\rho_2{}^2 - \rho_1{}^2)E_2/E_1} \quad . \tag{4}$$

Similarly, the distributed bending moment acts about an axis perpendicular to the plane formed by the SMA fiber and the axis of the rod. For the coordinate system selected in Figure 1 this is the x_2 axis and the magnitude of the distributed bending moment has the evaluation

$$m_2 = \int_0^{2\pi} \tau_i \, \rho_1 \, (d + \rho_1 \cos\theta) \, d\theta = -d \, f_3 \quad . \tag{5}$$

4. SHAPE CHANGE OF A FLEXIBLE ROD WITH AN EMBEDDED SMA FIBER

The equations of equilibrium of an inextensible rod, with applied distributed forces and distributed bending moments and a quadratic strain energy function, have the following form (Love 1944, Tadjbakhsh 1966):

$$F'_1 + \kappa_2 F_3 - \kappa_3 F_2 + f_1 = 0 \quad , \tag{6}$$

$$F'_2 + \kappa_3 F_1 - \kappa_1 F_3 + f_2 = 0 \quad , \tag{7}$$

$$F'_3 + \kappa_1 F_2 - \kappa_2 F_1 + f_3 = 0 \quad , \tag{8}$$

$$EI_{11}\kappa'_1 + GI_{33}\kappa_2\kappa_3 - EI_{22}\kappa_2\kappa_3 - F_2 + m_1 = 0 \quad , \tag{9}$$

$$EI_{22}\kappa'_2 + EI_{11}\kappa_1\kappa_3 - GI_{33}\kappa_1\kappa_3 + F_1 + m_2 = 0 \quad , \tag{10}$$

$$GI_{33}\kappa'_3 + EI_{22}\kappa_1\kappa_2 - EI_{11}\kappa_1\kappa_2 + m_3 = 0 \quad . \tag{11}$$

For the case of the off–axis SMA fiber embedded in a cylindrical rod, described in the previous section, we have $f_1 = f_2 = 0$, $m_1 = m_3 = 0$, while f_3 and m_2 are given by equations (3) and (5), respectively. The equations of equilibrium reduce in this case to the following ones:

$$F'_1 + \kappa_2 F_3 = 0 \quad , \tag{12}$$

$$F'_3 - \kappa_2 F_1 + f_3 = 0 \quad , \tag{13}$$

$$EI_{22}\kappa'_2 + F_1 + m_2 = 0 \quad . \tag{14}$$

The above system of nonlinear o.d.e.'s is supplemented by the kinematical relationships

$$\kappa_2 = \varphi'_2 \quad , \tag{15}$$

$$x_1 = \int_{-L/2}^{s} \sin\varphi_2 \, ds \quad , \quad x_3 = \int_{-L/2}^{s} \cos\varphi_2 \, ds \quad . \tag{16}$$

For a finite length rod, the above system of six o.d.e.'s (12)–(16) has been integrated numerically using a 4th order Runge–Kutta scheme. All mathematical manipulations have been carried out with MATHEMATICA (Wolfram, 1991). For a simply supported rod, schematically shown in Fig. 1, the boundary conditions are

$$x_1(-L/2) = x_3(-L/2) = F_3(-L/2) = \kappa_2(-L/2) = 0 \quad . \tag{17}$$

$$x_1(L/2) = F_3(L/2) = \kappa_2(L/2) = 0 \quad . \tag{18}$$

The shooting method has been employed to iteratively solve the above boundary value problem by a succession of initial value problems. After an initial guess for $\varphi_2(-L/2)$ and $F_1(-L/2)$ was made, the system of o.d.e. (12)–(16) was integrated from $s=-L/2$ to $s=L/2$ and the error in $\kappa_2(L/2)$ and $x_1(L/2)$ was used to update $\varphi_2(-L/2)$ and $F_1(-L/2)$ by adding to them increments found from the solution to the following system of linear equations:

$$
\begin{bmatrix}
\dfrac{\partial x_1(L/2)}{\partial \varphi_2(-L/2)} & \dfrac{\partial x_1(L/2)}{\partial F_1(-L/2)} \\[2mm]
\dfrac{\partial \kappa_2(L/2)}{\partial \varphi_2(-L/2)} & \dfrac{\partial \kappa_2(L/2)}{\partial F_1(-L/2)}
\end{bmatrix}
\begin{bmatrix}
\delta\varphi_2(-L/2) \\[2mm]
\delta F_1(-L/2)
\end{bmatrix}
=
\begin{bmatrix}
-x_1(L/2) \\[2mm]
-\kappa_2(L/2)
\end{bmatrix}
\tag{19}
$$

The partial derivatives in the coefficient matrix above were found numerically.

5. SELECTED RESULTS

As an example, the deformed shape of a rod of length 25d with an embedded SMA fiber is shown in Fig. 1. The rod is simply supported and is assumed to be straight in its original configuration, before the martensitic–austenitic transformation occurs in the SMA fiber. It is noted that for rod lengths below a critical value the deformed shapes are similar to the one shown in Fig.1. When the rod length exceeds that critical value, bifurcation of the solution occurs and multiple shapes are possible. This point is currently under investigation.

REFERENCES

Budiansky, B., Hutchinson, J.W., and Evans, A.G., 1986, "Matrix Fracture in Fiber–Reinforced Ceramics," *J. Mech. Phys. Solids*, Vol. 34, pp. 167–189.

Buehler, W.J., and Wiley, R.C., 1965, "Nickel–Base Alloys," U.S. Patent 3,174, p. 851.

Love, A.E.H., 1944, "A Treatise on the Mathematical Theory of Elasticity," Dover, New York.

Liang, C., and Rogers, C.A., 1990a, "Design of Shape Memory Alloy Actuators," Report, Smart Materials and Structures Laboratory VPI & Su, Blacksburg, VA.

Liang, C., and Rogers, C.A., 1990b, "One–Dimensional Thermomechanical Constitutive Relations for Shape Memory Materials," *J. of Intell. Mater. and Struct.*, Vol.1, pp.207–234.

McNichols, J.L. Jr., and Cory, J.S., 1987, "Thermodynamics of Nitinol", *J. Appl. Phys.*, Vol. 61, pp. 972–984.

Perkins, J., 1975, "Shape memory effects in alloys," Plenum Press, New York.

Tadjbakhsh, I.G., 1966, "The Variational Theory of the Plane Motion of the Extensible Elastica," *Int. J. Engng. Sci.*, Vol. 4, pp. 433–450.

Wolfram Research, Inc., 1991, *Mathematica*, Version 2.0, Wolfram Research, Inc., Champaign, Illinois.
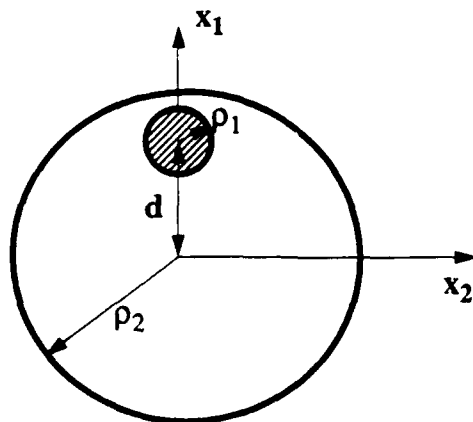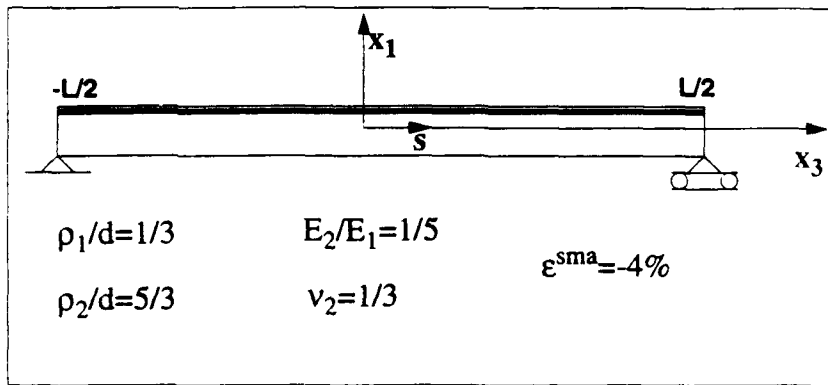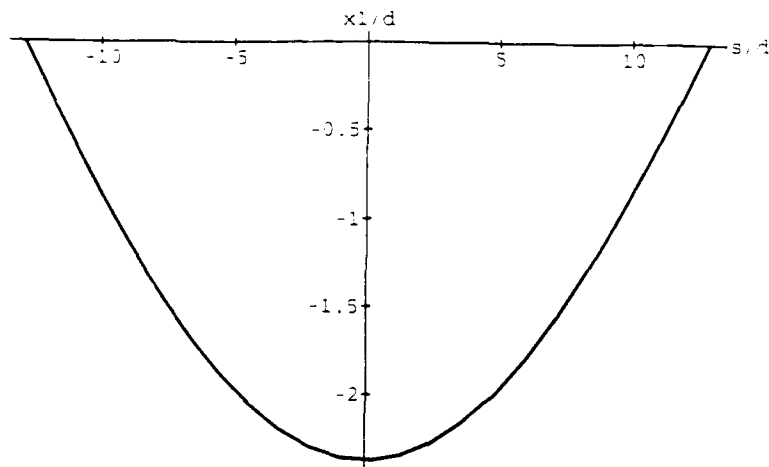
Fig. 1 Deformed Shape of a Flexible Rod with an Embedded SMA Fiber

AUTHOR INDEX

917

KEYWORD INDEX